2004
Solid-State Sensors, Actuators, and Microsystems Workshop

www.hh2004.org

Sponsored by the
Transducer Research Foundation, Inc.
Additional support provided:
Defense Advanced Research Projects Agency

Hilton Head Workshop
June 6 - 10, 2004 • Hilton Head, South Carolina
Editors: Thomas W. Kenny & Robert Sulouff

TRF Catalog Number: 04TRF-0001
Library of Congress Control Number: 2004105683
ISBN Number: 0-9640024-5-0
ISSN 1539-2058 (Print) • ISSN: 1539-204X (Electronic)
DOI 10.31438/trf.hh2004.0

2004

Solid-State Sensors, Actuators, and Microsystems Workshop

Hilton Head Island, South Carolina • June 6 - 10, 2004

TRF Catalog Number: 04TRF-0001
Library of Congress Control Number: 2004105683
ISBN Number: 0-9640024-5-0
ISSN 1539-2058 (Print) • ISSN: 1539-204X (Electronic)
DOI 10.31438/trf.hh2004.0

If you have questions regarding the installation, please contact:

The Printing House
Phone: +1-608-873-4500
Hours: Monday through Friday, 8 am - 5 pm CST
E-mail: graphics@printinghouseinc.com

Greetings from the General Chairman

The 2004 Solid State Sensor, Actuator and Microsystems Workshop is the twelfth in the biannual series of regional meetings that alternate with the world wide Transducer Conference. Every since the first meeting on Hilton Head Island in 1984 this workshop has enjoyed an atmosphere of high quality technical presentations in a venue of open collaboration and interaction. We are hear to learn together, share the fun of imagining new and different products and processes and perhaps the spark of a new company or solution to a common issue of mankind. Using the tools that offer us the ability to build a transistor cheaper than printing a single letter on this page we can fashion interesting products that sense, actuate or interact in a unique microsystem.

To insure the "cross-pollination" of applications, processes and device design, a wide range of topics is organized and held in a single session format. The technical program committee under the excellent leadership of Tom Kenny has selected oral presentations and a complementary collection of contributed poster papers to create the basis of this workshop. New this year is an oral introduction in the general session (poster shotgun) for each poster. Ample time is provided for discussion and questions after each presentation in a Gordon style format. Since there is much learning that occurs during out of session interactions, sufficient time has been allotted in the afternoons to trade process recipes and survivor stories from the last business cycle. The evening activities are organized to bring the participants back together for additional interaction.

Through the sponsorship of the Transducer Research Foundation Inc., this workshop has enjoyed an investment strategy in the future industry leaders. By encouraging outstanding technical contributions from graduate students and young professionals through the avenue of travel stipends, a strong base of expertise has fueled countless research groups that return with yet another generation of new and exciting ideas in subsequent Hilton Head Workshops. Several of this year's technical committee, as in previous years are a product of this cycle of learning and student sponsorship, attesting to the excellent return on invested efforts from the past workshops.

A special thanks to the contributions of individuals and organizations that have worked together to make this workshop a success. The Technical Program Chair, Tom Kenny collected an outstanding committee of 20 individuals and selected an impressive array of papers. The program committee gave countless hours for review and selection and meet for a long day of discussion and program finalization. Joe Brown developed corporate sponsorship and student travel support with great enthusiasm. The two major contributors were the Transducer Research Foundation (TRF) and DARPA. In addition Mark Allen (Local Arrangements) and Joe Giachino (Finances) combined there many years of experience in Hilton Head Workshops to produce yet another success. We are all aware and grateful for the professional management services provided by Katharine Cline and the team at Preferred Meeting Management Inc. (PMMI), perhaps some dead-line challenged authors more than others.

Most importantly, thanks for coming! Watch out for the alligators, don't get sunburned and think of the humidity as a beauty treatment, and oh yes dream, explore and network with your old and new friends, maybe optical or medical will need us soon.

Bob Sulouff
General Chairman

Organizing Committee

General Chairman	**Robert Sulouff** Analog Devices
Technical Program Chairman	**Thomas W. Kenny** Stanford University
Treasurer	**Joseph M. Giachino** University of Michigan
Local Arrangements	**Mark G. Allen** Georgia Institute of Technology
Student Travel Grants	**Joe Brown** Suss MicroTec

Technical Program Committee

David Arch
Honeywell Laboratories

Susanne C. Arney
AT&T Bell Laboratories

Bernhard E. Boser
University of California at Berkeley

James Bustillo
Georgia Institute of Technology

Gary Fedder
Carnegie Mellon University

Storrs Hoen
Agilent Technologies

Jay Jakubczak
Sandia National Laboratories

Hal Jerman
iolon Inc.

Jack Judy
University of California at Los Angeles

Thomas W. Kenny
Stanford University

Abraham P. Lee
University of California at Irvine

David J. Monk
Motorola, Inc.

Khalil Najafi
University of Michigan

Richard S. Payne
Polychromix, Inc.

Antonio J. Ricco
NASA Ames Research Center &
Stanford University

Leland “Chip” Spangler
Aspen Technologies

Robert Sulouff
Analog Devices, Inc.

Kimberely L. Turner
University of California at Santa Barbara

James Walker
Jay Walker Technical Consulting, LLC

Robert Sulouff
Analog Devices, Inc.

Jacob White
Massachusetts Institute of Technology

Acknowledgements

Special acknowledgement to the Transducers Research Foundation, Inc. and the Defense Advanced Research Projects Agency (DARPA) MTO/MEMS Program for their educational grant support of this meeting.

Solid-State Sensor, Actuator and Microsystems Workshop
June 6 – 10, 2004
Crowne Plaza Resort
Hilton Head Island, South Carolina

Sunday, June 6

6:00 p.m. –
9:00 p.m. Registration and Welcome Reception

Monday, June 7

7:30 a.m. **Breakfast**

7:45 a.m. **Welcome and Introduction** – Bob Sulouff, Chairman

Session 1 - Optical Sensors and Actuators
Session Chair – James Walker, JayWalker Technical Consulting

8:15 a.m. **Invited Speaker**
OPTICAL MEMS: LEGACY OF THE TELECOM BOOM 1
J.E. Ford
University of California, San Diego

9:00 a.m. *ELECTROSTATIC ACTUATORS WITH MECHANICAL BRAKES* 4
J.D. Grade, K.Y. Yasumura, and H. Jerman
iolon, Inc.

9:25 a.m. *CRYOGENIC CHARACTERIZATION AND TESTING OF MAGNETICALLY-ACTUATED MICROSHUTTER ARRAYS FOR THE JAMES WEBB SPACE TELESCOPE* 8
T.T. King[1], G. Kletetschka[1,2], M.A. Jah[1], M.J. Li[1], M.D. Jhabvala[1], L.L. Wang[1,3], M.A. Beamesderfer[1], A.S. Kutyrev[1,4], R.F. Silverberg[1], D. Rapchun[1,5], D.S. Schwinger[1], G.M. Voellmer[1], S.H. Moseley[1], and L.M. Sparr[1]
[1]NASA Goddard Space Flight Center, [2]The Catholic University of America, [3]Swales Aerospace Co., [4]Science Systems and Applications, Inc., and [5]Global Science and Technology

9:50 a.m. *A WAFER-BONDED, FLOATING ELEMENT SHEAR-STRESS SENSOR USING A GEOMETRIC MOIRÉ OPTICAL TRANSDUCTION TECHNIQUE* 13
S. Horowitz[1], T.-A. Chen[1], V. Chandrasekaran[2], K. Tedjojuwono[3], L. Cattafesta[1], T. Nishida[1], and M. Sheplak[1]
[1]University of Florida, [2]Massachusetts Institute of Technology, and [3]NASA-Langley Research Center

10:15 a.m. **Break**

Wednesday, June 9

Session 8 - Magnetic and MicroPower Systems
Session Chair – Jack Judy, University of California, Los Angeles

Contributed Posters

Late News Posters

TECHNICAL PAPERS

Solid-State Sensor, Actuator and Microsystems
Workshop

2004
Hilton Head Island, South Carolina
June 6-10

OPTICAL MEMS: LEGACY OF THE TELECOM BOOM

Joseph E. Ford
Electrical & Computer Engineering, University of California San Diego
La Jolla, CA 92093-0407

ABSTRACT

From 1997 to 2002 tens of billions of dollars were invested in optical MEMS technology for telecommunications, creating products just in time for a nearly complete market collapse. With the subsequent closure of R&D efforts and many entire companies, has this new technology been lost? In fact, many MEMS-based components survived the collapse and are selling into a slowly recovering market. More importantly, the technology developed is available for new applications in communications and other areas. In this presentation I will review optical MEMS technology developed, provide a status report on surviving components, and describe one example of how a device created for a specific application (a broad wavelength variable attenuator) has been modified to a completely different application in free-space optical communications (a retro-reflecting data modulator).

OPTICAL MEMS AND TELECOM

Any optical effect demonstrated with bulk components can be implemented, typically on a reduced physical scale, using optical MEMS fabrication. These basic functions are illustrated in Figure 1, which shows the four major categories of effects: movable first surface mirrors (analog or digital tilt mirrors on one or two axis), movable absorbing or refractive surfaces, tunable dielectric multilayer etalons (spectral phase and amplitude filters), translation stages (moving waveguides and shutters), as well as diffractive structures (variable phase delay or grating pitch).

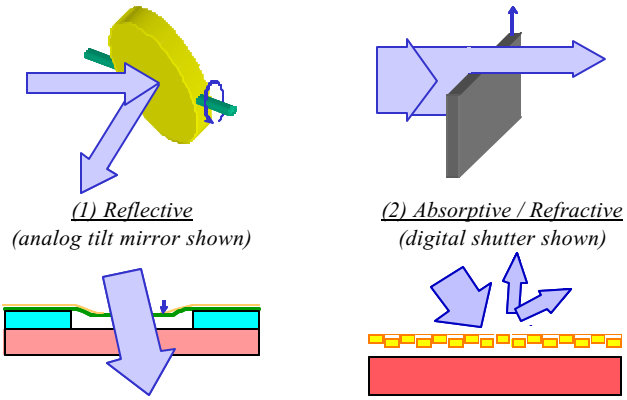

Figure 1. *Fundamentally different types of optical MEMS devices.*

The initial driving application for Optical MEMS devices was Texas Instruments' well-known DMD (digital mirror device) projection display, a 2D array of digital tilting micromirrors fabricated on a silicon VLSI drive circuit [1]. DMD displays are becoming the dominant technology for commercial and even consumer projectors, and optical MEMS devices have now been developed for applications including remote pressure and acceleration sensors, biotechnology, and adaptive optics. Still, the greatest driver for optical MEMS technology in terms of total investment has been telecommunications.

Early optical MEMS components intended for telecom applications were viewed with considerable skepticism; the technology was considered unproven and far off the consensus path of waveguide integrated optics. A reflective data modulator demonstrated in 1994 for fiber-to-the-home networks [2] may have been the first practical MEMS device for single mode fiber. This device was not developed into a successful product, but it was followed by a series of optical MEMS switches and filters for wavelength-multiplexed signals which demonstrated the broad applicability of optical MEMS components for optical communications. References [3] – [9] provide some examples.

By 1999, with increasing pressure to meet market demand for high-capacity networks, well-funded optical MEMS component efforts were under way at established and start-up companies. Many applications could be addressed with a range of technologies, but the large port-count provisioning switch (e.g., the Lucent "LambdaRouter" [10]) was a 'must-have' telecommunications component that simply could not be constructed with any other available technology. Optical MEMS was perceived as critical-path technology for high-capacity optical networks.

Demand for communications bandwidth had been greatly overestimated. The market peaked in mid 2000, and by 2002 technology investment was substantially over. Relatively few of the companies founded during the investment boom (by some estimates more than 3000 in total) survive to date. But though this process, a wide range of optical MEMS components were taken from laboratory demonstrations to fully packaged components, proven to meet critical Telcordia reliability tests, and built into fielded systems carrying live communications traffic. Despite the considerable disruption, a wide range of MEMS-based components are still commercially available, and have make the transition to a "bread and butter" technology.

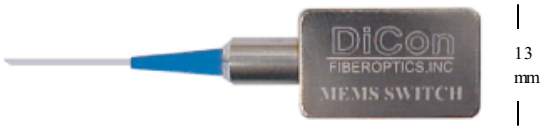

Figure 2. *A simple 1x2 protection switch is one example of the optical MEMS products now commonplace in telecom systems.*

TELECOM 'SURVIVORS'

The single best indication of this acceptance is the use of MEMS devices for protection switches, which are 1x2 and 2x2 switches used to direct traffic around faulty transmission systems, as for example due to a line cut. MEMS switches were shown to be more reliable than the electromagnetically-actuated (bulk optic component) opto-mechanical switches previously used, in addition to being smaller and more power efficient. Two current products

0-9640024-5-0/hh2004/$20©2004TRF
DOI 10.31438/trf.hh2004.1

Solid-State Sensors, Actuators, and Microsystems Workshop
Hilton Head Island, South Carolina, June 6-10, 2004

are JDSU's latching 2x2 switch, which is based on a SOI comb-drive actuator [11] and DiCon 1x2 switch with variable attenuation, which is based on an analog electrostatic tilt mirror. The DiCon switch pictured in Figure 1 has an insertion loss of 0.8 dB, switches in under 5 ms, requires only 15 V drive, and is guaranteed to operate over 100 million cycles [12].

Optical MEMS companies started during the boom have also survived to offer high-performance products to the slowly recovering component market. Beam-steering optical cross-connects based on two-dimensional arrays of analog tilt mirrors are available from Glimmerglass, which provides an 64x64 switch, and Calient Networks, which makes up to 256x256 switches [13]. Chromux offers 1x2 protection switch arrays, as well as scanning Fabry-Perot wavelength monitors.

Another important class of optical MEMS components integrates diffraction gratings to perform spectral demultiplexing onto the MEMS device to enable wavelength-selective filtering and switching. Dynamic spectral equalizers and wavelength-blocking switches are offered by LightConnect and Polychromix, while more general wavelength switching [4, 14] is offered by Capella Photonics. Figure 3 shows a representative sample.

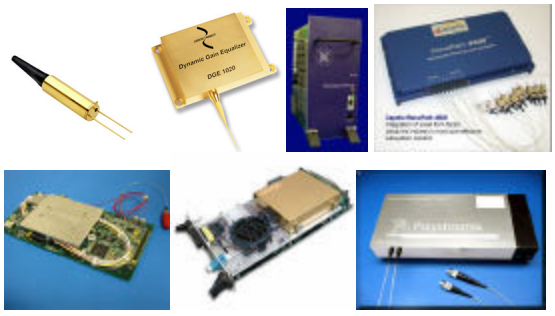

Figure 3. *Examples of currently available telecom products, clockwise from upper left: LightConnect variable attenuator and dynamic gain equalizer, Glimmerglass 64x64 switch, Capella Photonics wavelength selective switch, Polychromix wavelength blocker, Chromux protection switch array and wavelength monitor*

OPTICAL MEMS DEVICE PROGRESS

These basic functions have been demonstrated with various device structures, some of which were never publicized and which remain 'trade secrets' of technology holding companies. Device packaging and processing techniques are particularly difficult to obtain. However, some of the device technology has since been published in the open literature.

One good example is the feedback position control of electrostatic tilt mirrors used by Tellium in their modular crossconnect system [15]. Normally such mirrors are operated in a safe region, roughly half the full angular range, to avoid catastrophic snapdown as the voltage required to maintain a given angle quickly decreases. Tellium used a nonlinear controller with a novel technique for torque-to-voltage conversion [16] in combination with classic linear controller techniques with optical full-state feedback, state estimator, and reference input with feed-forward. They achieved stable angular positioning accuracy of <120 microradians over the full +/- 8° mechanical range of the mirrors, right up to the point of edge touchdown (Figure 4).

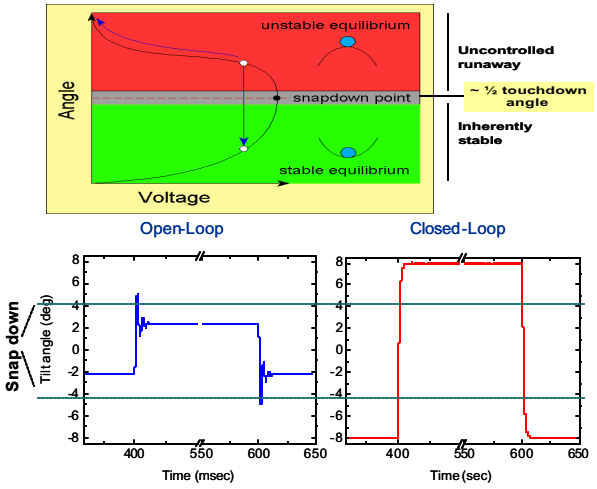

Figure 4. *Control of electrostatic mirrors through snapdown using optical feedback on the angular position [15, 16].*

Another area of technology development critical for low insertion loss optical MEMS devices is the accurate control of mirror (and etalon) curvature. Some of these efforts are widely available as improved tolerances and process yields from MEMS foundries (e.g., mirrors with >1 m radius of curvature, 10 - 100x improved over initial efforts). Also, basic work on thermal dependence of mirror curvatures has also been conducted at public universities including the University of Minnesota [17].

TECHNOLOGY RE-DEPLOYMENT: AN EXAMPLE

The basic technology development will have far-ranging impact on applications that have nothing to do with optical fiber networks. One example of this re-use is an on-going research project at UCSD involving the modification of a telecom-derived MEMS device for free-space (mobile) communications.

Fast, electrically-controlled optical fiber attenuators were needed for transient suppression in long-haul fiber communications. In 1996, a Bell Labs research project involved a novel MEMS wavefront modulator for this application [19]. A membrane reflector was formed over a hexagonal array of cavities so that electrostatic force could deform the normally flat reflector into a shape like the surface of a golf ball. A collimated beam illuminating the modulator is efficiently coupled into the output fiber, but when voltage is applied, a controlled fraction of light is aberrated away from the optical fiber core and discarded. The primary advantage of this device was that the mechanical response time was determined not by the overall optical aperture, but by the diameter of the individual membrane aperture.

This attenuator was successfully demonstrated using a variation on MARS etalon optical modulator process [2], where a silicon nitride membrane is held over the silicon substrate by a phosphor-silicate glass sacrificial layer. The only process change needed was to coat a uniform layer of gold over the top of the device. This device concept was independently conceived and demonstrated at the University of Delft in 1999 [20].

The new application of this device involved corner-cube retroreflectors (CCR), which are basically three mirrors are right angles to each other to form a hollow cube that faithfully reflects an incident optical beam towards it's point of origin. CCRs are used

to self-align free-space optical signals, as for example in a surveyor's rangefinder. A *retro modulator*, a retroreflector with an electrically-controlled reflectivity, can communicate data signals back to a laser source without needing to align a separate laser transmitter at the remote node.

Retro modulators can block the beam (amplitude modulation), but it is equally effective to phase-modulate the back-propagating wavefront so that the return signal is dispersed and does not arrive at the remote detector. A MEMS retro modulator demonstrated by UC Berkeley [18] for their 'Smart Dust" project used two fixed micro-mirrors assembled over a tilting MEMS mirror, so that the CCR angle could be switched away from 90°. The resulting device had a 1 mm aperture and a 2 kHz response. However, our goal was fabricate a retro modulator with a substantially larger aperture (10 to 25 mm) suitable for long-range (multi-km) optical communications, and operate the device at much higher speeds (>100 KHz) than possible moving a single large mirror. The Bell Labs attenuator device was ideal for this application.

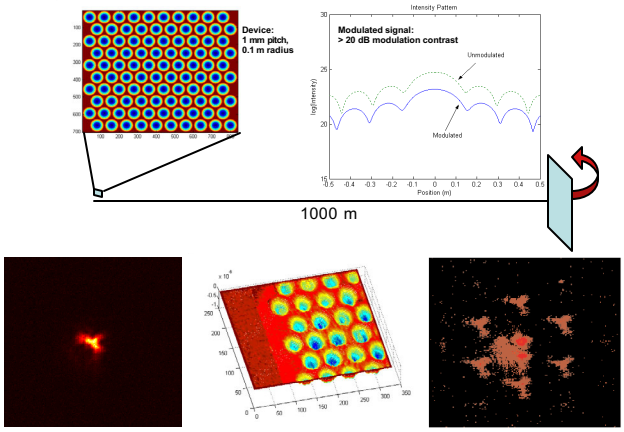

Figure 5. *Simulation (top) and experimental results from the membrane modulator used for free-space optical communications.*

A theoretical calculation of the wavefront propagating from a membrane modulator with 1 mm pixels with a 100 cm radius of curvature is shown at the top of Figure 5. More than 20 dB contrast is achieved over a wide range of angles, distances, and operating wavelengths. The lower three images are preliminary experimental results from a fabricated device. They show the optical far-field signal reflected from an undeflected modulator, the surface profile from the actuated device, and the dispersed signal reflected from the actuated modulator.

CONCLUSION

The telecom boom yielded a wealth of optical MEMS technology which, in addition to serving it's original purpose of telecom components, is available for new applications in sensing and communications. The next wave of research and development – hopefully less turbulent than the last – has already begun.

ACKNOWLEDGEMENTS

Research conducted at UCSD's Photonics Systems Integration Laboratory is supported by a grant from Cubic Corporation. The experimental results shown are the work of graduate student researcher Trevor Chan.

REFERENCES

1. P. Van Kessel et al, "A MEMS-based projection display," *IEEE Proceedings* 86(8), pp. 1687-1704 (1998).

2. K.W. Goossen, J. A. Walker, S. C. Arney, "Silicon modulator based on mechanically-active anti-reflection layer with 1 mbit/sec capability for fiber-in-the-loop applications," *IEEE Photonics Technology Letters* 6(9), pp. 1119 – 1121 (1994).

3. M. Wu, E. Vail, G. Li, and C. Chang-Hasnain, Widely and continuously tunable micromachined resonant cavity detector with wavelength tracking," *IEEE Phot. Tech. Lett.*, 8 pp.98–100 (1996).

4. L. Lin, E. Goldstein, R. Tkach, "Free-space micromachined optical switches with sub-ms switching time for large-scale optical crossconnects," *IEEE Phot. Tech. Letters* 10 pp. 525-527 (1998).

4. J. Ford, J. Walker, "Dynamic spectral power equalization using micro-opto-mechanics," *IEEE Phot. Tech. Lett.* 10(10), (1998).

5. J. Ford et al, "Micromechanical fiber-optic attenuator with 3 microsecond response," *IEEE J. Lightwave Tech.* 16(9), (1998).

6. P. Tayebati, P. Wang, D. Vakhshoori, and R. Sacks, "Widely tunable Fabry-Perot filter using Ga(Al)As/AlOx deformable mirrors" *Optical Society of America Conference on Optical Fiber Communications 1998*, pp. 22-27 (1998).

7. J. Ford, J. Walker, V. Aksyuk and D. Bishop, "Wavelength add/drop switching using tilting micromirrors," *IEEE J. Lightwave Tech.* 17(5), pp. 904-911, (1999).

8. C. Marxer and N. de Rooij, "Micro-opto-mech. 2 x 2 switch for single-mode fibers based on plasma-etched silicon mirror and electrostatic actuation" *J. Lightwave Tech.*17(1), pp. 2-6, (1999).

9. P. Hagelin et al, "Scalable optical cross-connect switch using micromachined mirrors," *IEEE Phot. Tech. Lett.* 12(7), pp. 882–884 (2000).

10. D. T. Neilson et al, "Fully provisioned 112×112 micro-mechanical optical crossconnect with 35.8 Tb/s demonstrated capacity," *OSA Conference on Optical Fiber Communications 2000*, postdeadline paper pp. 202 – 204, (2000).

11. B. Hichwa et al, "A Unique Latching 2x2 MEMS Fiber Optics Switch*", IEEE International Conf. on Optical MEMS*, (2000).

12. DiCon Fiber Optics product datasheet, http://www.diconfiberoptics.com/products/scd0061/index.htm

13. J. Xuezhe et al, "Three-dimensional MEMS photonic cross-connect switch design and performance," *IEEE Journal of Selected Topics in Quantum Electronics*, 9(2), pp. 571-578 (2003).

14. D. Marom et al, "Wavelength-selective 1x4 switch for 128 WDM channels at 50 GHz spacing," *Optical Society of America Conference on Optical Fiber Communications*, Paper FB7, 2002

15. J. Dadap et al, "Modular MEMS-based optical cross-connect with large port-count," IEEE Photonics Technology Letters, 15(12), pp. 1773 – 1775 (2003)..

16. I. Brener et al, "Nonlinear servo control of MEMs mirrors and their performance in a large port-count optical switch," *OSA Conference on Optical Fiber Communications* pp. 383-387 (2003).

17. K. Cao, W. Liu and J. Talghader, "Curvature compensation in micromirrors with high-reflectivity optical coatings," Journal of MEMS 10(3), pp. 409 – 417 (2001).

18. L. Zhou et al, "Corner-cube retroreflectors based on structure-assisted assembly for free-space optical communication, " IEEE J. MEMS 12(3), pp. 233-242, 2003.

19. J. Ford and J. Walker, "Technique for modulating optical signals in optical communications," United States Patent number 5,796,880, filed November 1996.

20. S. Sakarya, G. Vdovin and P. Sarro, "Micromachined SLM based on pixelated reflective membranes", SPIE Proc. 3760, November 1999.

ELECTROSTATIC ACTUATORS WITH MECHANICAL BRAKES

John D. Grade, Kevin Y. Yasumura, and Hal Jerman
Iolon, Inc.
San Jose, CA 95131

ABSTRACT

New DRIE actuator systems have been developed which use a high-force, linear actuator to wrap a flexible brake band around the rigid brake shoe of a large-deflection, rotary actuator. The brake can hold the rotary actuator at any arbitrary location within its full range of travel. A third actuator may be used to engage a pair of locking pins in order to keep the brake motor extended in the event of a power failure. The 100× increase in rotational stiffness after the brake is applied raises the fundamental resonant frequency by more than an order of magnitude, enabling precision optical adjustments over a large tuning range in the presence of external shock and vibration.

INTRODUCTION

With the improved stability from advances in suspension design, comb drive actuators are being deployed in applications requiring ever larger deflections. With total ranges in the hundreds of microns, the sub-micron positioning required for many applications is increasingly difficult to achieve, especially with the shocks and vibrations experienced in a product environment. This problem is commonly addressed in macroscopic applications by mounting small-deflection end effectors to large-deflection coarse positioners. However, this is less attractive with micromachined electrostatic actuators due to the additional fabrication complexity involved. An actuator with a mechanical brake provides similar functionality by increasing the suspension stiffness of the system to accomplish fine positioning once the coarse position has been set. Moreover, the brake may be used to implement a latching function, maintaining the actuated position of the motor in the event of a power failure or in applications requiring zero steady-state power.

As shown schematically in Fig. 1, DRIE actuators have been developed with mechanical braking mechanisms somewhat analogous to a drum brake in an automobile. Initial contact occurs between the vertical sidewalls in the center of the brake band, and the contact area increases as the brake actuator causes the band to wrap around the brake shoe.

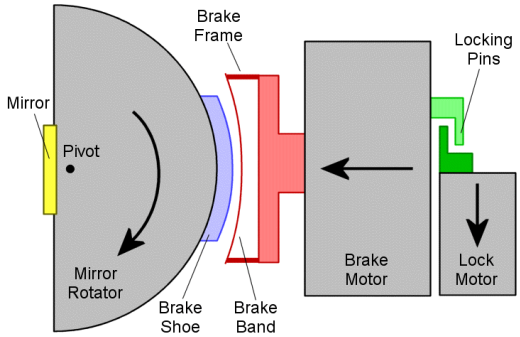

Figure 1. *Schematic diagram of a rotary actuator with a brake mechanism. A pair of locking pins can hold the brake motor in place in the event of a power failure. Compliance in the brake frame can allow a small amount of mirror rotation after the brake is applied.*

DRIE actuators have been developed with the mechanical braking mechanisms shown schematically in Fig. 1. In one example, the brake forms part of a latching optical switch, maintaining the actuated position of the motor in case of a power failure. Another example uses a brake to accomplish precision optical adjustments over a large tuning range in the presence of external shock and vibration. Unlike other power-safe schemes for electrostatic actuators [1-3], the mirror rotator in Fig. 2 may be held at any arbitrary location within its full range of travel.

DESIGN

The fabrication of the devices is identical to that used for optical devices described at HH2002 [4]. A cavity formed in an oxidized carrier wafer determines which portions of the final structure are fixed to the substrate and which are free to move. A second wafer is fusion bonded to the etched side of the carrier wafer and then ground and polished to a thickness of 85 µm. After contact holes and aluminum bonding pads are defined, the 85 µm thick silicon layer is DRIE etched to form the suspended electrostatic actuator, substrate anchored areas, bond pads, and electrical interconnects. The devices typically feature 4 µm wide suspension beams and 10 µm wide comb gaps, which are reliably obtained using available etching tools.

Fig. 2 shows a set of actuators for a latching optical switch [5, 6] which includes a mirror rotator, a brake motor, and a locking motor. After the mirror rotator has set the desired mirror rotation, the lock motor is retracted and the brake motor is extended. The flexible brake band wraps around the rigid brake shoe and inhibits further mirror rotation. Once the brake has been applied, the lock motor may be released. A single bi-stable actuator could replace the brake and lock motors [7], but this would provide little control over the force transition as the brake is applied.

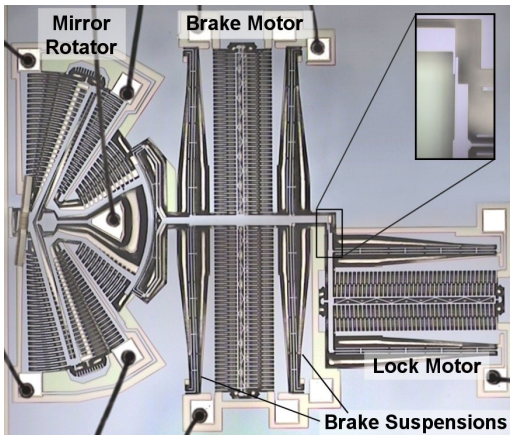

Figure 2. *Microscope photograph of an actuator for a latching optical switch, similar to the diagram in Fig. 1. The locking motor is holding the brake motor in the deflected position, and the brake band and shoe are in contact with the mirror held at a rotation of 5 degrees.*

0-9640024-5-0/hh2004/$20©2004TRF
DOI 10.31438/trf.hh2004.2

The motor device layer is 85 µm thick and the mirror (mounted out-of-plane) is 600×600×85 µm^3. The mirror rotator has a range of ±6° with 130 V and a resonant frequency of 900 Hz. The brake actuator requires 110 V to press the brake band into contact with the brake shoe.

The radius of the brake shoe was set to 80% of the brake band to ensure that the band wrapped around the shoe during operation. The contact area begins as a vertical line at the center of the brake band and grows with increasing brake motor force to include the entire band length.

Ideally, the activation speed of the brake motor would be much faster than that of the mirror rotator, the brake band would not move laterally when extending, and the motor would be essentially rigid once the brake has been applied. These requirements make a high-force, small-displacement actuator attractive; however, the fabrication process requires at least a 10 µm gap between the brake band and the brake shoe. The brake motor shown in Fig. 2 uses a symmetric, crab-leg suspension for lateral rigidity and linear actuation. Finite element analyses were used to determine suspension widths that brought the brake into first contact at 110 V and finished wrapping the band around the shoe after 150 V had been applied. To aid in overcoming potential stiction forces between the brake band and shoe, the initial brake motor designs featured opposed comb banks for bi-directional actuation, as shown in Fig. 2. As no stiction was observed, subsequent designs used single-sided actuation.

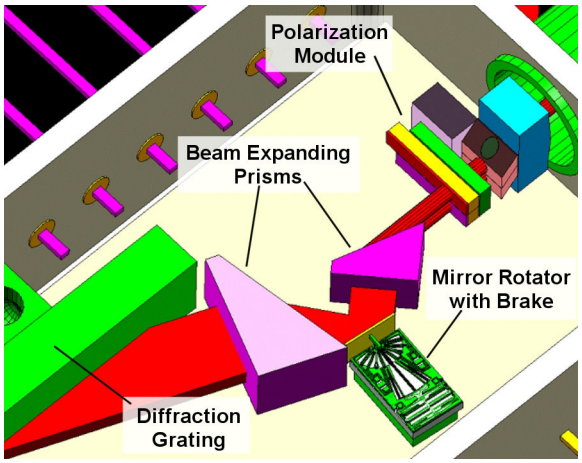

Figure 3. *Schematic drawing of a tunable optical filter containing a rotary actuator with a mechanical brake. A laser beam enters and exits a fiber pigtail. Rotating the mirror changes the retro-reflected angle of the beam on a grating, changing the center frequency of the filter.*

Fig. 3 and Fig. 4 show a tunable optical filter containing a rotary actuator with a mechanical brake that is used for coarse and fine position control rather than for power-safe operation [8]. The coarse servo system sets the initial rotation of the mirror, and then the brake is applied. The compliance of the frame supporting the brake band was designed to allow the mirror to be adjusted by 1% of the full range after braking, enabling precision optical adjustments in the presence of external shock and vibration while maintaining the large tuning range.

The optical design for the tunable filter requires an out-of-plane mirror that is quite large (2500×1270×85 µm^3). Since the motor device layer is only 85 µm thick, two different tactics are employed to reduce the out-of-plane vibration response. First, as shown in Fig. 5, the mirror is mounted off the left side of the chip, and it extends above and below the motor along the z-axis. This reduces the mirror's out-of-plane inertia by a factor of 4 and causes the mirror and motor masses of the resulting system to balance each other about all three axes. The downside is a relatively complex two-piece attachment between the mirror and the motor. Second, the mirror rotator includes flexural suspension beams at the pivot point (±70 degrees from the long axis of the chip) and at the center of the device (±15 degrees from the long axis). Partially compliant portions of the outer frame accommodate differences in suspension foreshortening during motor rotation. This arrangement provides excellent stiffness in both pitch and roll. It also allows the brake to be applied far from the pivot point, reducing the tendency of the brake to slip due to any torques induced by external shock or vibration.

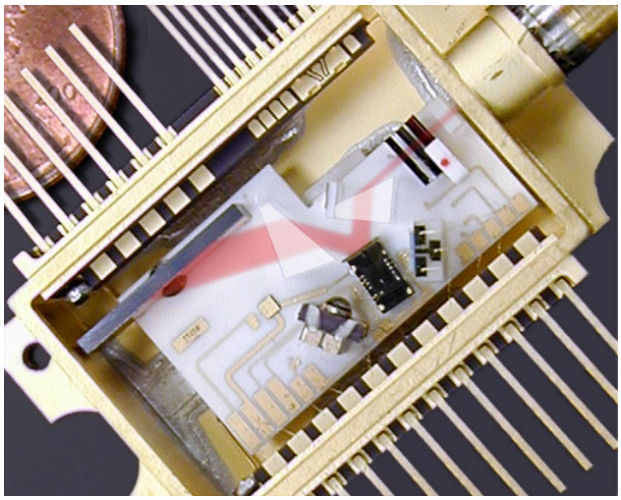

Figure 4. *Assembled tunable optical filter containing a rotary actuator with a mechanical brake (center).*

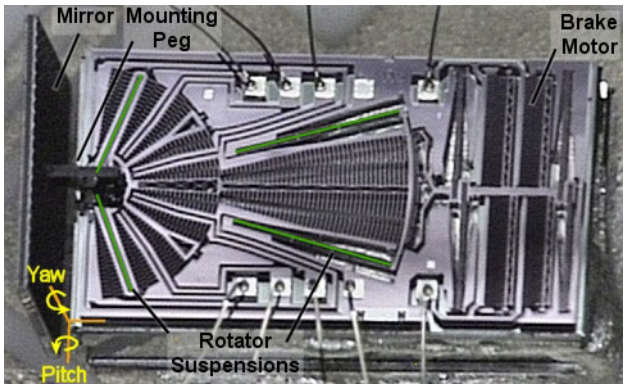

Figure 5. *An example actuator for a tunable filter in which the brake mechanism is used for fine positioning and vibration rejection.*

EXPERIMENTAL RESULTS

The performance of the rotary actuator in Fig. 2 was verified using a 670 nm laser reflected off the out-of-plane mirror onto a position sensitive detector (PSD). Voltage was first applied to the mirror rotator to set the desired mirror angle as shown in Fig. 6. A cosine-shaped voltage transition was used in order to reduce ringing in the mirror position. Voltage was then applied to the brake motor to press the brake band firmly against the brake shoe. Finally, the voltage was removed from the mirror rotator, with the mirror angle maintained only by the brake.

A small amount of compliance in the brake frame allowed a shift in mirror angle of 0.2% of the full-scale deflection when the mirror rotator was deactivated. As shown in the photograph in Fig. 2, the locking motor could also be used to keep the brake engaged when all voltages were removed.

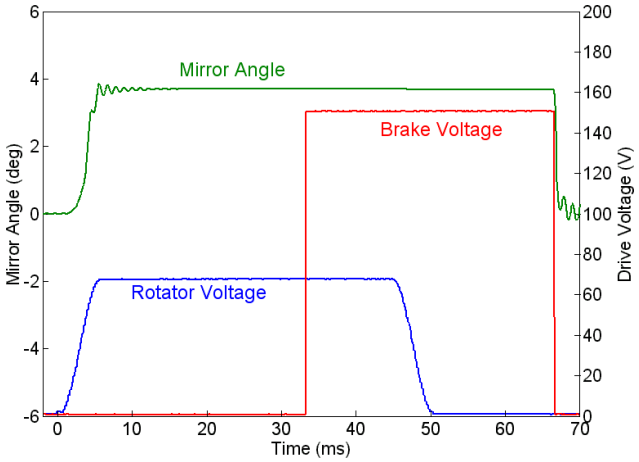

Figure 6. *Example operation of the brake mechanism in Fig 2. After the mirror angle was set, the brake was applied, and the voltage was removed from the mirror rotator.*

The same PSD measurement setup was used to characterize the actuator for the tunable optical filter. For this application, the brake was intended to improve resistance to shock and vibration by reducing the low frequency response by at least 100×, and by raising the fundamental resonance by an order of magnitude.

Fig. 7 shows the change in mirror rotator frequency response with braking. The brake reduced the DC rotational stiffness by 160× and raises the fundamental resonance above from 850 Hz to 12.5 kHz. The out-of-plane resonant frequency rose by almost a factor of two, from 3.3 kHz to 5.8 kHz.

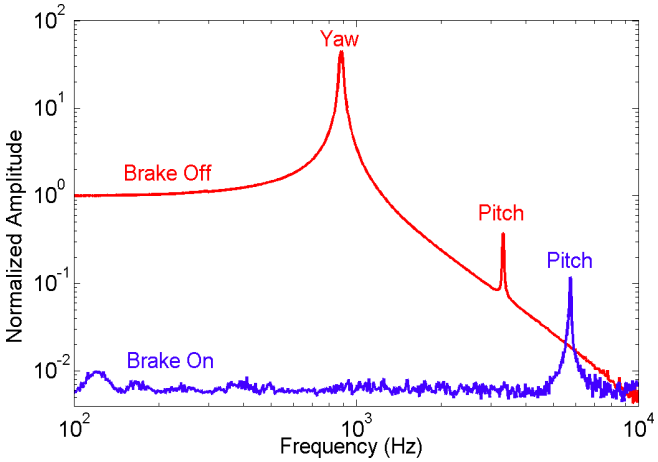

Figure 7. *Measured, open-loop, frequency response of a tunable filter actuator. Applying the brake raised the fundamental resonant frequency (mirror yaw) from 850 Hz to 12.5 kHz and raises the second mode (mirror pitch) from 3.3 kHz to 5.8 kHz.*

Several factors may combine to introduce errors in the final mirror position after the brake has been applied. Large radial loads applied by the brake may induce motion in the mirror rotator due to buckling of the individual suspension beams or compliance of the mirror motor frame. These errors should be a continuous function of the angle of the mirror motor, and they should be symmetric about the rest position. Discretization of the curves defining the brake may create facets that snap together and change the mirror angle slightly. Similarly, sidewall roughness arising from the DRIE step may cause the brake to engage preferentially at locations where the brake shoe and band have matching asperities. These sidewall effects would create angular shifts that are not correlated to the mirror position. The fine servo controller could compensate for angular shifts below 1% of the full-scale deflection, or 38 mdeg.

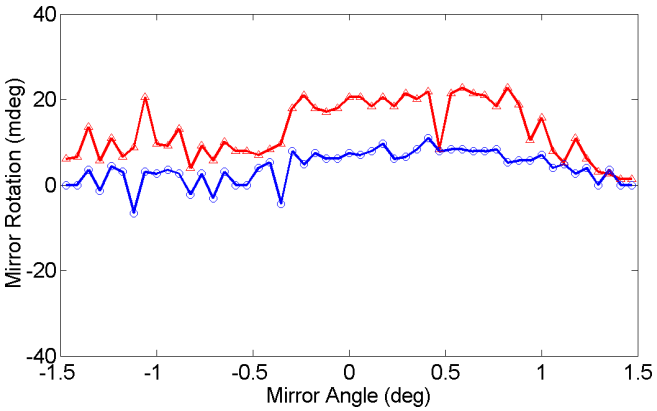

Figure 8. *Change in mirror angle after application of the brake as a function of initial mirror position. The brake was driven sinusoidally with amplitudes of 150 V (triangles, top curve) and 90V (circles, bottom curve). Brake slip occurred at 75 V.*

Fig. 8 shows a measurement of the post-brake angular shift as a function of mirror angle. The brake actuator was driven with a sinusoidal waveform to reduce the chances of the brake micro-bouncing when engaged at high speed. Measurements using a square wave showed no angular dependence and more than 5× the average angular shift. For both waveforms, lowering the brake force reduced post-brake angular shift, with the 90 V sinusoid yielding a maximum angular shift of 10 mdeg.

To more closely examine the effect of the brake force on the angular shift, the brake was applied repeatedly using a voltage that increased from 80V to 150V. As shown in Fig. 9, the post-brake shift increases with increasing brake voltage.

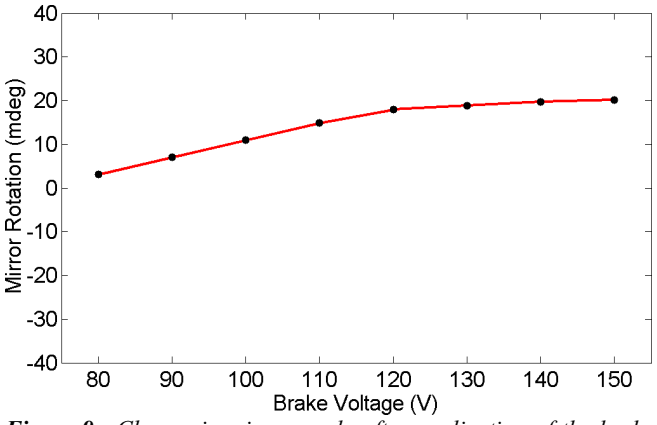

Figure 9. *Change in mirror angle after application of the brake as a function of the brake voltage. The initial mirror angle was set to the center position, or zero degrees.*

Two potential failure mechanisms, brake slip and brake stiction, have also been investigated. Brake slip is directly related to the coefficient of static friction between the brake shoe and

brake band, which likely depends on the DRIE sidewall roughness. Fig. 10 shows the calculated electrostatic forces for the mirror rotator and brake actuator at the brake slipping point. Mirror rotator forces of approximately 60 μN (torques of 0.17 mm-mN) caused slipping with the brake activated and caused full-scale deflection (±6º) with the brake deactivated. Only shocks exceeding 5000 g's would generate forces sufficient to cause brake slip in mechanically balanced rotators [4]. A linear fit to the data yields a friction coefficient of 0.67, which is within the range of reported values [9].

In the course of generating the friction measurements, it became clear that the friction coefficient could be raised by repeatedly overdriving the main actuator with the brake applied. This had the effect of removing small asperities, essentially burnishing the brake sidewall surfaces. The coefficient of friction rose quickly for the first few kilo-cycles and stopped rising after a few hundred kilo-cycles. Measurements of the slip voltage before and after burnishing indicated that the coefficient of friction had risen to 1.5 and that less than 0.5 microns of material had been removed.

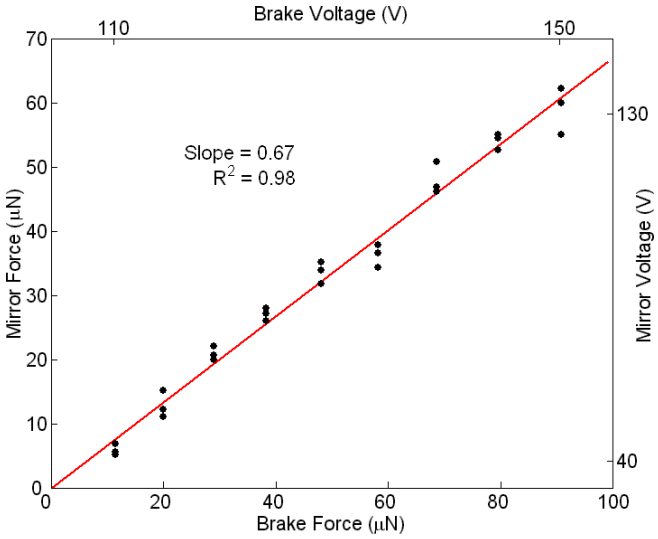

Figure 10. *Relationship between the mirror rotator force and the brake motor force at which a burnished brake begins slipping. The slope of the least squares fit through the data indicates a coefficient of static friction of 0.67.*

Stiction is another concern when using a mechanical brake. To reduce stiction forces, the maximum contact area between the brake band and shoe was kept small (less than 0.04 mm^2), and the brake band was designed to wrap on and peel off of the brake shoe. No hysteresis was observed in the quasi-static transfer function for the brake actuator, suggesting stiction-free operation. To simulate a high-humidity environment and guarantee that a liquid meniscus formed between the brake band and shoe, a very small amount of water was manually applied to the brake. The suspensions of the brake actuator readily overcame the capillary forces during this worst-case test.

CONCLUSIONS

A new strategy has been demonstrated for achieving precision optical adjustments in the presence of external shock and vibration without sacrificing total deflection range. The use of mechanical brakes allows an actuator to be held at any arbitrary location and can raise the fundamental resonant frequency by more than an order of magnitude. Burnishing and using a low brake force can reduce brake-induced motor rotation to levels that can be compensated by servo control.

ACKNOWLEDGEMENTS

The authors would like to thank C. Tan and K. Jackson on the iolon development team for their help in preparing and testing the actuator devices.

REFERENCES

1. A. Neukermans and R. Ramaswami, "MEMS Technology for Optical Networking Applications," *IEEE Communications Magazine*, *39*, January 2001, pp. 62-69.

2. R. Yeh, S. Hollar, and K. Pister, "Single mask, large force, and large displacement electrostatic linear inchworm motors," *Proceedings of the 14th Annual International Conference on Microelectromechanical Systems*, Interlaken, Switzerland, January 2001, pp. 260-264.

3. M. S. Rodgers and J. J. Sniegowski, "5-level polysilicon surface micromachine technology: application to complex mechanical systems," *Technical Digest 1998 Solid State Sensor and Actuator Workshop*, Hilton Head Isl., SC, June 1998, Transducer Research Foundation, Cleveland (1998), pp. 144-149.

4. H. Jerman and J. D. Grade, "A mechanically-balanced, DRIE rotary actuator for a high-power tunable laser," *Technical Digest 2002 Solid State Sensor and Actuator Workshop*, Hilton Head Isl., SC, June 2002, Transducer Research Foundation, Cleveland (2002), pp. 7-10.

5. J. D. Grade, H. Jerman, and T. W. Kenny, "A large-deflection electrostatic actuator for optical switching applications," *Technical Digest 2000 Solid State Sensor and Actuator Workshop*, Hilton Head Isl., SC, June 2000, Transducer Research Foundation, Cleveland (1994), pp.97-100.

6. H. Jerman, US patent publication number 20030034709, "Micromechanical device having braking mechanism," February 2003.

7. B. Hichwa *et al*., "A Unique Latching 2x2 Fiber Optics Switch," *Proc. 2000 IEEE/LEOS Int'l. Conf. Opt. MEMS*, Kauai, HI, August 2000, post-deadline paper.

8. J.D. Berger, F. Ilkov, D. King, A. Tselikov, and D. Anthon, "Widely tunable, narrow optical bandpass Gaussian filter using a silicon microactuator," in *Optical Fiber Communication Conference*, OSA Technical Digest, (OSA, Washington, DC, 2003), TuN2.

9. K. Deng and W. H. Ko, "A study of static friction between silicon and silicon compounds," *J. Micromech. Microeng. 2*, March 1992, pp. 14-20.

CRYOGENIC CHARACTERIZATION AND TESTING OF MAGNETICALLY-ACTUATED MICROSHUTTER ARRAYS FOR THE JAMES WEBB SPACE TELESCOPE

T.T. King[*], G. Kletetschka[*,†], M.A. Jah[*], M.J. Li[*], M.D. Jhabvala[*], L.L. Wang[*,‡], M.A. Beamesderfer[*], A.S. Kutyrev[*,§], R.F. Silverberg[*], D. Rapchun[*,+], D.S. Schwinger[*], G.M. Voellmer[*], S.H. Moseley[*], L.M. Sparr[*]

[*]NASA Goddard Space Flight Center, Greenbelt, MD 20771, USA

[†]The Catholic University of America, Washington D.C. 20064, USA

[‡]Swales Aerospace Co., Greenbelt, MD 20705, USA

[§]Science Systems and Applications, Inc., Lanham, MD 20706, USA

[+]Global Science and Technology, Greenbelt, MD 20770, USA

ABSTRACT

Two-dimensional MEMS microshutter arrays (MSA) have been fabricated at the NASA Goddard Space Flight Center (GSFC) for the James Webb Space Telescope (JWST) to enable cryogenic (~35 K) spectrographic astronomy measurements in the near-infrared region. Functioning as a focal plane object selection device, the MSA is a 2-D programmable aperture mask with fine resolution, high efficiency and high contrast. The MSA are close-packed silicon nitride shutters (cell size of 100 x 200 μm) patterned with a torsion flexure to allow opening to 90 degrees. A layer of magnetic material is deposited onto each shutter to permit magnetic actuation. Two electrodes are deposited, one onto each shutter and another onto the support structure side-wall, permitting electrostatic latching and 2-D addressing. New techniques were developed to test MSA under mission-similar conditions (8 K ≤ T < 300K). The "magnetic rotisserie" has proven to be an excellent tool for rapid characterization of MSA. Tests conducted with the magnetic rotisserie method include accelerated cryogenic lifetesting of unpackaged 128 x 64 MSA and parallel measurement of the magneto-mechanical stiffness of shutters in "pathfinder" test samples containing multiple MSA designs. Lifetest results indicate a logarithmic failure rate out to ~10^6 shutter actuations. These results have increased our understanding of failure mechanisms and provide a means to predict the overall reliability of MSA devices.

INTRODUCTION

In the quest to reveal the origins of galaxies, clusters, and large-scale structures in the universe, scientists and engineers at the NASA GSFC have begun work on JWST scheduled to launch in 2011. To fulfill its primary mission of observing galaxies at the peak of the star-forming and merging era, JWST will carry the Near Infrared Spectrograph[a] (NIRSpec) which will provide the required spectrographic coverage in the near-infrared wavelength region from 0.6 to 5 μm. To increase observation efficiency, simultaneous analysis of multiple astronomical bodies in the JWST/NIRSpec field of view will be enabled by a programmable aperture mask (PAM) that will select objects to optimally fill the focal plane without spectral overlap [**1**].

The science requirements on the PAM are that it must cover a large optical field of view in the focal plane (7.7 x 7.0 cm format area) with high resolution (100 x 200 μm pixel dimensions), exhibit high on/off contrast ratio (> 2000), and a high fill factor (> 70%). Furthermore, to minimize thermal emissions into NIRSpec and since the JWST second Lagrange point orbit will be inaccessible to space shuttle re-servicing missions, the PAM must operate in a cryogenic (~35 K) vacuum environment reliably over a 10 year mission lifetime without repair after launch. Additionally, any device built to fly in space must, in general, have very tight constraints on mass, volume and power dissipation. In light of these mission requirements, microelectronic mechanical systems (MEMS) technologies are ideally suited for the design and development of the PAM.

MICROSHUTTER ARRAY DESIGN

A team at the NASA GSFC is developing a MEMS-based microshutter array (MSA) for application as the PAM on the JWST/NIRSpec [**2**, **3**]. The MSA will represent the first mission-critical MEMS device to be flown in space. The MSA design has been driven by the aforementioned science and mission requirements and will be verified through extensive characterization and testing under flight-similar conditions. The MSA flight concept consists of a 2 x 2 format mosaic of four 384 x 175 arrays of close-packed shutters with a unit cell size of 100 x 200 μm placed in the JWST optical path at the focal plane. Individual shutters are designed with a torsion flexure hinge and are magnetically actuated by scanning a permanent tripole magnet across the MSA and electrostatically held open to allow the high-contrast transmission of light from specific celestial objects into NIRSpec. The selective nature of the MSA is achieved electrostatically via a three-voltage level, cross-point addressing scheme operating on orthogonally oriented column and row electrodes driven by external electronics [**4, 5**].

The challenges facing the MSA program are 1) the successful fabrication and packaging of the MSA, and 2) the development of a comprehensive test plan with MSA-specific test techniques to fully evaluate MSA parts under flight-similar conditions. This paper will highlight the progress achieved in these two areas and discuss recent results.

MICROSHUTTER ARRAY FABRICATION

The current MSA development focuses on refining fabrication and testing techniques on smaller 128 x 64 MSA prototypes before scaling up the design to flight-sized 384 x 175 MSA dice. The 128 x 64 MSA die are fabricated from silicon-on-insulator (SOI) wafers with a 0.5 μm thick silicon nitride layer pre-deposited onto the oxide[b]. The processing on the front-side (the side for shutters) includes multi-layer metal deposition and patterning to create aluminum front-side electrodes, cobalt-iron

[a] To be built by the European Space Agency.

[b] Obtained from MEMS Exchange, Reston, VA 20191.

0-9640024-5-0/hh2004/$20©2004TRF
DOI 10.31438/trf.hh2004.3

magnetic stripes[c]. A front side reactive ion etch (RIE) carves the shutters and torsion flexures out of the nitride membrane such that the front-side electrodes and magnetic stripes are made on each shutter blade. Each column of shutters is electrically contiguous through a single front-side strip electrode but electrically isolated from adjacent columns. An additional front-side metal deposition and patterning step is performed to build aluminum light shields around each shutter for blocking light leaks through the gap between the shutter and the silicon frame. The processing continues on the back-side (the side without shutters) with an anisotropic wafer-thinning back-etch, followed by a deep RIE back-etch to form a silicon frame support structure and to free the shutters from the silicon/oxide substrate. Additional back-side metal deposition, and patterning form back-side electrodes onto the silicon frame support structure and one of the side-walls. Each row of shutters is electrically contiguous through a single back-side strip electrode but electrically isolated from adjacent rows [4, 5, 6]. A schematic representation of an individual shutter cell in cross-section and secondary electron micrographs of a fabricated 128 x 64 MSA die are displayed in Figures 1 and 2, respectively.

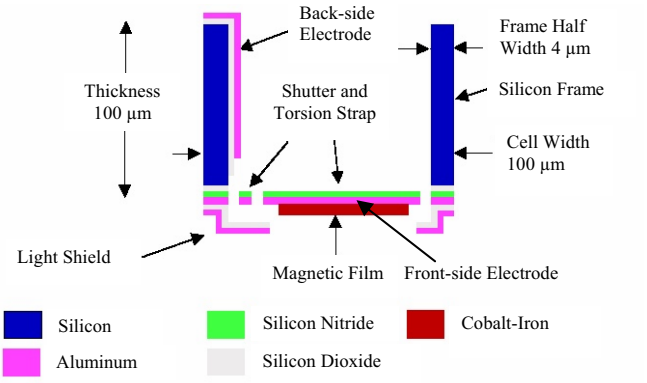

Figure 1. *Schematic cross-section of a shutter cell.*

Current packaging of 128 x 64 MSA dice involves bump-bonding the front-side electrode pads, and wire-bonding the back-side electrode pads to gold traces on a 500 µm thick silicon substrate. The silicon substrate is then wire-bonded to a printed circuit board (PCB)[d] equipped with electrical pin connector interfaces to the drive electronics.

MICROSHUTTER ARRAY TESTING

A MSA test plan has been developed to evaluate 128 x 64 MSA parts that are produced to quickly refine the design and fabrication process to meet the PAM science and mission requirements. A host of MSA-specific test techniques and capabilities have been developed and are applied at various stages in the 128 x 64 MSA development. Some tests conducted on partially processed 128 x 64 MSA dice include (a) microscopic

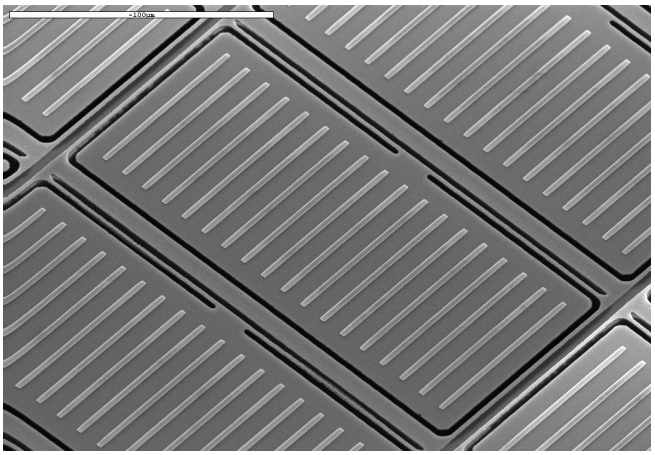

(a)

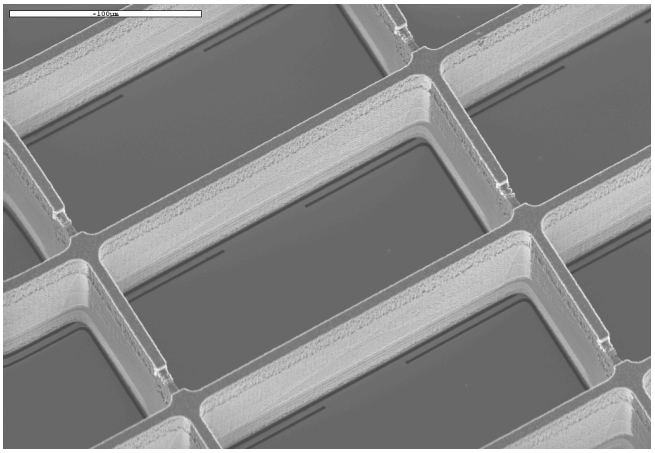

(b)

Figure 2. *Secondary electron micrographs of a 128 x 64 MSA die (scale indicates 100 µm). (a) Front-side view shown without light shields for clarity. (b) Back-side view.*

alignment inspections, (b) electrical continuity and isolation tests, (c) shutter release verification, (d) cryogenic magnetic property characterization, (e) cryogenic shutter bowing characterization, and (f) shutter in-plane twisting resistance tests. Tests performed on fully processed, but unpackaged 128 x 64 MSA dice include (g) cryogenic magneto-mechanical stiffness characterization, and (h) accelerated cryogenic lifetests. Tests performed on fully packaged (i.e. silicon substrate and PCB) 128 x 64 MSA include (i) electrical latching and two dimensional addressing tests, (j) optical functionality tests, (k) accelerated cryogenic lifetests, (l) thermal cycling tests, (m) vibration and acoustical tests, and (n) radiation exposure tests.

MAGNETIC ROTISSERIE LIFETEST METHOD

One important component of the MSA test plan is accelerated cryogenic lifetesting of unpackaged 128 x 64 MSA dice. The goal of this test is to actuate shutters to 10^6 actuations, one order of magnitude beyond the 100% mission lifetime requirement of 10^5 actuations, in a cryogenic environment and evaluate the resultant failures. In the MSA flight concept, shutter actuation is generated magnetically through the interaction between an external magnetic field provided by a permanent tripole magnet and the cobalt-iron film deposited onto each shutter blade. The specific nature of this

[c] Cobalt-iron film deposited by the U.S. Naval Research Laboratory, Washington, DC 20375.

[d] Bonding done by the Johns Hopkins University Applied Physics Laboratory, Laurel, MD 20723.

interaction is dependent upon the tripole magnet geometry. A tripole magnet has been modeled and constructed such that the magnetic field lines, emanating and terminating from the three poles, assume a carefully prescribed shape as illustrated in Figure 3. As the tripole magnet is scanned past a shutter cell at a specific distance above the pole tips, the shutter blade is torqued to align with the direction of the applied magnetic field vector. The cobalt-iron film on the shutter blade initially magnetizes in the applied field direction and then rotates to follow the rotating magnetic field vector until it is fully open against the back-side electrode on the silicon frame side-wall at which time it can be electrostatically latched open.

Though the scanning tripole magnet actuation method with electrostatic latching has been successfully demonstrated on packaged and unpackaged 128 x 64 MSA at room temperature and 30 K and is ideal for the flight MSA design [**3**], the scanning mechanism required to translate the tripole magnet back and forth operates very slowly: one complete sweep takes ~10 s. At this rate, a single lifetest to 10^6 actuations would require ~116 days to complete; too long given the aggressive MSA development schedule. In order to acquire lifetest data to refine the fabrication process in a timely manner, accelerated lifetesting is necessary.

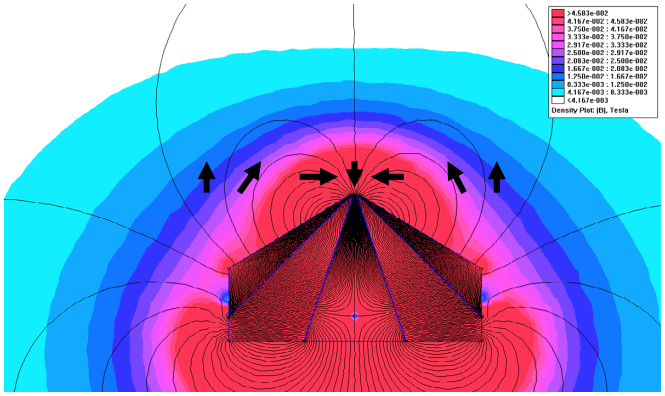

Figure 3. *Flux model of tripole magnetic field. Black arrows indicate the rotation of the magnetic field vector at different locations above the tripole magnet tip.*

To accomplish accelerated lifetesting, a rapid magnetic actuation method, called the magnetic rotisserie method, was developed. Instead of slowly translating a tripole magnet, the magnetic rotisserie rapidly spins a MSA within a stationary, unidirectional, homogenous magnetic field to simulate the rotating magnetic field vector required to open the shutters. The shutter actuation sequence (top view) is illustrated in the schematic diagram of Figure 4 (not drawn to scale). The green arrows indicate the direction of the homogeneous magnetic field generated between two electromagnet poles (green rectangles). The two black lines and black dot represent, in cross-section, the silicon frame support structure and torsion flexure, respectively, of a single shutter cell. The blue and red arrows represent a shutter blade: the color and arrow direction indicate the magnetization direction of the cobalt-iron magnetic material. The actuation sequence begins at 0˚ with the shutter cell oriented such that the shutter blade is parallel to the homogeneous field direction. The homogenous field, H, is turned on and the cobalt-iron magnetic material is initially magnetized away from the torsion flexure as indicated by the blue arrow. As the shutter cell is spun in a clockwise direction (indicated by the orange arrow), a torque is produced in the magnetized cobalt-iron material which attempts to maintain alignment with the applied homogeneous magnetic field by rotating about the torsion flexure axis against the restoring spring force of the torsion flexure as indicated at 45˚. At 90˚, the shutter blade makes first contact with the silicon frame support structure: the shutter cell is fully open. As the shutter cell continues to spin, the shutter is pushed along by the silicon frame support structure: the shutter cell is still fully open. At ~180˚, the combined effects of the torsion flexure restoring force and a sudden magnetic reversal of the cobalt-iron magnetization direction, now pointing towards the torsion flexure, causes the shutter blade to swing closed as indicated by the red arrow. As the shutter cell continues to spin, the remagnetized cobalt-iron again experiences a torque which forces the shutter blade to rotate open (225˚) and the entire actuation process repeats itself: 270˚ fully open, 315 ˚ fully open against silicon frame support. At 360˚, the combined effects of the torsion flexure restoring force and another magnetic reversal in the cobalt-iron again causes the shutter blade to swing close as indicated by the blue arrow. Thus, one revolution of the shutter cell in the magnetic rotisserie results in two complete shutter actuations.

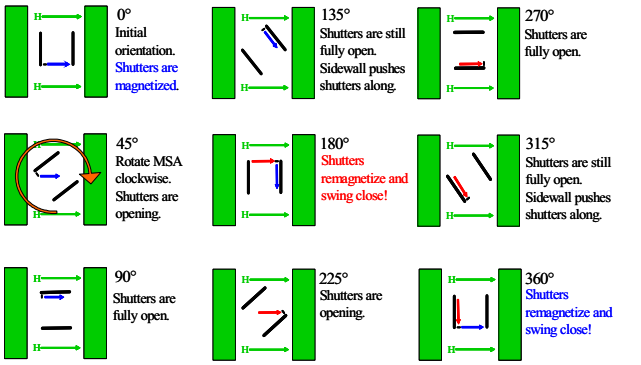

Figure 4. *Schematic diagram (top view) illustrating the magnetic rotisserie actuation sequence.*

Two accelerated cryogenic lifetest facilities have been constructed based upon the magnetic rotisserie method: a liquid nitrogen-cooled system (LN_2 rotisserie) and a liquid helium-cooled system (LHe rotisserie). The LHe rotisserie is depicted in Figure 5. Unpackaged MSA dice samples are inserted into a non-magnetic, liquid helium dewar and suspended above the surface of the liquid helium coolant. The dewar is situated within a uniform, homogeneous magnetic field generated by a pair of water-cooled electromagnets. The magnetic field strength is adjustable ($-3\ T \leq H \leq 3\ T$) and monitored by a Gaussmeter. The MSA samples are attached to a drive shaft and motor assembly which provides the spinning motion which can attain shutter actuation rates up to 30 Hz. A mechanical counter monitors drive shaft revolutions which are converted to total shutter actuations. The sample temperature is monitored by two silicon diode sensors mounted on the MSA sample holder. The LN_2 rotisserie and the LHe rotisserie are capable of cryogenic testing between $90\ K \leq T \leq 105\ K$ and $8\ K \leq T \leq 30\ K$, respectively.

MSA samples are optically inspected through a set of dewar windows via transmitted light microscopy. Figure 6 displays typical images of an entire 128 x 64 MSA without light shields in the closed (0˚) and open (345˚) positions that demonstrate the validity of the magnetic rotisserie method for actuating shutters to

the open position[e]. Use of fast camera shutter speeds during image acquisition also verifies shutter actuation while the MSA sample is spun at 900 rpm (or 30 Hz shutter actuation rate).

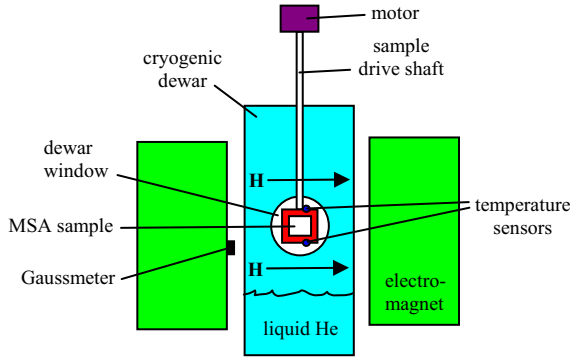

Figure 5. *Schematic diagram (side view) of cryogenic magnetic rotisserie.*

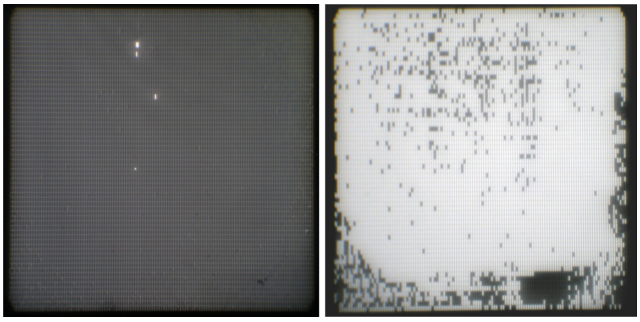

Figure 6. *Transmitted light micrographs of a 128 x 64 MSA without light shields in the LHe rotisserie in the (a) fully closed position at 0˚ and, (b) fully open position at 180˚ with H = 0.4 T. The active area of the MSA is 1.3 cm across.*

Accelerated lifetests were conducted on five MSA samples with the magnetic rotisserie method to evaluate two failure conditions for individual shutter cells: "failed open" (light leaking through a supposedly closed shutter cell) and "failed closed" (light blocked by a supposedly open shutter cell). The as-received, beginning-of-life (BOL), condition of all five MSA samples were imperfect, containing ≤ 3% "failed open" and ≤ 11% "failed closed" failures. Shutter cells exhibiting these BOL failures were excluded from subsequent lifetest analyses. On average, over 7,500 shutter cells per sample participated in cryogenic lifetesting.

None of the rotisserie-tested MSA samples contained light shields (LS). The cobalt-iron on each shutter of all of the MSA samples was of an earlier design, configured as a single square or rectangular pad instead of multiple stripes. One sample, a 128 x 128 MSA from an earlier design with a 100 x 100 µm shutter cell size (SOI 27-1), was lifetested at room temperature in ambient air. Cryogenic lifetesting between 90 - 105 K in nitrogen vapor was performed on four 128 x 64 MSA samples of a more recent design with a 100 x 200 µm shutter cell size (SOI 47-C, SOI 48-C, SOI 61-B, SOI 61-D). Two samples (SOI 47-C, SOI 61-B) underwent additional cryogenic lifetesting between 8 - 30 K in helium vapor.

[e] This particular MSA sample had known processing imperfections (i.e.: missing and stuck shutters) but was still suitable for verifying shutter actuation.

The torsion flexure geometry (width and length) of all of the MSAs varied between the samples.

Images of the entire MSA in an open and closed position were recorded at BOL and repeated at a minimum at every order of magnitude of shutter actuation throughout the lifetest. The total change in the number of "failed open" and "failed closed" shutters from one inspection to the next was counted and the associated number of shutter actuations was noted. A summary of the lifetest results is presented in Figure 7.

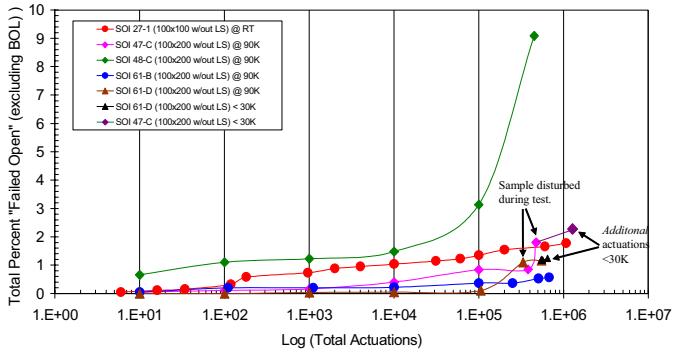

(a)

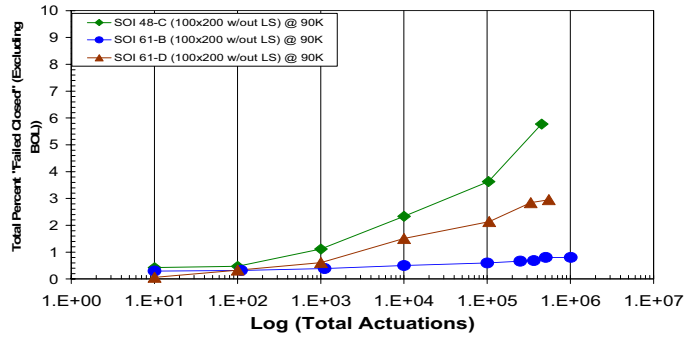

(b)

Figure 7. *Summary of lifetest results for (a) "failed open" failures, and (b) "failed closed" failures.*

For four of the MSA samples lifetested the "failed open" failure rate increased logarithmically adding < 2.3% failures at 10^6 actuations. Scanning electron microscopy (SEM) analysis indicates that the predominant failure mode in these cases was shutters missing due to fracture on the torsion flexure or near the shutter blade neck. The anomalous behavior of the "failed open" failures of sample SOI 48-C is currently under investigation. The "failed closed" failure rates also increased with actuations. The primary failure mode was contact between the shutter blades against the silicon frame side-walls preventing shutter actuation. This type of failure would occasionally "heal" itself: a shutter cell qualifying as a "failed closed" failure in one optical inspection would not always qualify as a failure in the next inspection. Slight misalignments between the shutter blade and the surrounding silicon frame and out-of-plane shutter blade twisting due to low cobalt-iron coercivity may be the cause of the "failed closed" failures. Improving the front-to-back alignment with newly acquired fabrication tools and modifying the cobalt-iron magnetic pad into a multiple stripe design with higher coercivity may reduce the number of "failed closed" shutters in future accelerated lifetests.

MAGNETO-MECHANICAL STIFFNESS

Since the functional performance of shutter actuation is dependent upon a combination of effects, namely the restoring spring force of the torsion flexure and the magnetic reversal in the cobalt-iron material, the magneto-mechanical stiffness is an important parameter for MSA design purposes. The magnetic rotisserie lifetest method conveniently enables this measurement for all shutters in a MSA in parallel and at cryogenic temperatures.

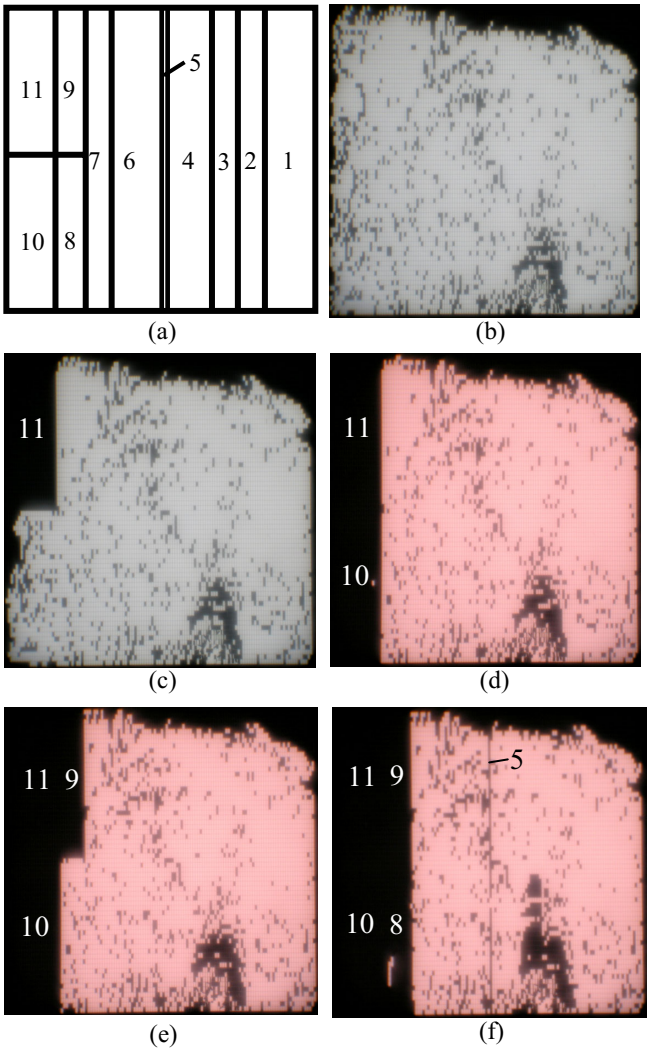

Figure 8. *Magneto-mechanical stiffness characterization of "pathfinder" 128 x 64 MSA. (a) Schematic of 11 different test regions. (b) All regions open at 0.200 T. (c) Region 11 closed at 0.160 T. (d) Region 10 closed at 0.145 T. (e) Region 9 closed at 0.130 T. (f) Region 8 closed (95%), Region 5 closed (95%) at 0.120 T.*

A "pathfinder" 128 x 64 MSA sample was fabricated containing 11 test regions each with a different torsion flexure geometry (variables were width and length) and/or magnetic stripe design (variables were number of stripes per shutter and stripe width) and is schematically represented in Figure 8 (a). To characterize the magneto-mechanical stiffness, the "pathfinder" MSA sample was placed in the magnetic rotisserie lifetest apparatus and slowly spun in the magnetic field (H = 0.200 T) until all shutters in the array were open. The sample was held at this angle (relative to the applied magnetic field direction) and the magnetic field strength was slowly decreased. As the torsion flexure restoring force and magnetic reversal in the cobalt-iron of a particular test region combined to overcome the applied magnetic field, the shutters within that test region swung close. Shutters within test regions that were magneto-mechanically stiff closed at higher applied magnetic fields than shutters within test regions that were magneto-mechanically more compliant as illustrated in Figure 8 (b-f). These results have been used to finalize a specific torsion flexure geometry and magnetic stripe design for the next generation of MSA.

CONCLUSIONS

The MSA development team at the NASA GSFC has successfully fabricated 128 x 64 MSA devices. A comprehensive test plan has been implemented and MSA-specific cryogenic testing and characterization techniques have been developed. The magnetic rotisserie lifetest method which has been demonstrated at cryogenic temperatures indicate a logarithmic "failed open" failure rate that adds < 2.3% failures at 10^6 actuations. This method has increased our understanding of different failure modes and provides a means to predict device reliability. Near-term efforts include additional cryogenic lifetesting on the next generation 128 x 64 MSA samples with light shields and fabrication of flight-like 384 x 175 MSA devices.

REFERENCES

1. H.S. Stockman, The Next Generation Space Telescope: visiting a time when galaxies were young, The Association of Universities for Research in Astronomy, Inc., 1997.

2. S.H. Moseley, et al., "Status of the Development of 128x128 Microshutter Array", in MOEMS and Miniaturized Systems, Proceedings of SPIE 4178, 2000.

3. A.S. Kutyrev, et al., "Programmable microshutter arrays for the JWST NIRSpec", accepted for publication in the Journal on Selected Topics in Quantum Electronics on Optical Microsystems, March 2004.

4. M.J. Li, et al., "Fabrication of Microshutter Arrays for Space Application", in Microelectronic and MEMS Technologies, Proceedings of SPIE 4407, 2001.

5. D.B. Mott, et al., "Magnetically Actuated Microshutter Arrays", in Micro-machining and Microfabrication, Proceeding of SPIE 4561, 2001.

6. M.J. Li, et al., "Microshutter Arrays for Near-Infrared Applications on the James Webb Space Telescope", Proceedings of SPIE 4981, 2003.

A Wafer-Bonded, Floating Element Shear-Stress Sensor Using a Geometric Moiré Optical Transduction Technique

Stephen Horowitz, Tai-An Chen, Venkataraman Chandrasekaran*, Ken Tedjojuwono§, Louis Cattafesta, Toshikazu Nishida, and Mark Sheplak†

Interdisciplinary Microsystems Group, PO Box 116250, University of Florida, Gainesville, Florida 32611-6250
† (352) 392-3983, FAX: (352) 392-7303, ms@mae.ufl.edu

*Department of Aeronautics and Astronautics, MIT, Cambridge, MA 02139

§Advanced Measurement and Diagnostics Branch, NASA-LaRC, Hampton, VA 23681-2199

ABSTRACT

This paper presents a geometric Moiré optical-based floating-element shear stress sensor for wind tunnel turbulence measurements. The sensor was fabricated using an aligned wafer-bond/thin-back process producing optical gratings on the backside of a floating element and on the top surface of the support wafer. Measured results indicate a static sensitivity of 0.26 $\mu m/Pa$, a resonant frequency of 1.7 *kHz*, and a noise floor of 6.2 $mPa/\sqrt{Hz}$.

INTRODUCTION

The MEMS community has developed both thermal [**1**] and floating element [**2-7**] shear-stress sensors. Thermal sensors are robust and simpler to fabricate; however, they are based on a heat transfer analogy and absolute calibration for quantitative measurements is difficult [**8**]. Conversely, floating-element structures respond directly to wall shear stress and provide the best opportunity to obtain quantitative, time-resolved measurements in a controlled wind tunnel environment. Several transduction methods exist for measurement of the shear-stress induced deflection of the floating element, including capacitive, [**2, 3, 7**] piezoresistive, [**4, 5**] and differential optical shutter techniques [**6**]. An ideal sensor is truly flush-mounted with no wire bonds that generate flow disturbances and is immune to non-shear stress inputs (i.e., electromagnetic interference (EMI), pressure fluctuations, vibrations, etc.). Only one existing device does not possess front-side wire-bonds, but it was not designed for turbulence applications and possesses too low a sensitivity [**5**]. The optical shutter technique [**6**] provided immunity to EMI and pressure fluctuations, but it possessed wire bonds and was sensitive to tunnel vibration due to the separation of the light source from the sensor. Additional information comparing these devices is given by Naughton and Sheplak [**8**] in their review of MEMS-based shear stress sensors.

An alternative transduction technique for measurement of small displacements involves the use of Moiré patterns [**9-11**]. This technique was specifically applied for motion detection of MEMS structures by Tran et al. [**11**], who reported a 50 *nm* displacement resolution using a simple image processing technique with a phase detection resolution of 5°. Our device employs an optical geometric Moiré transduction technique for measurement of shear-stress induced floating-element displacement. The geometric Moiré floating element sensor (Figure 1) possesses immunity from EMI and transverse element movement due to pressure fluctuations and/or vibrations. The flow disturbance is minimal because the incident and reflected light comes through the backside of the Pyrex wafer.

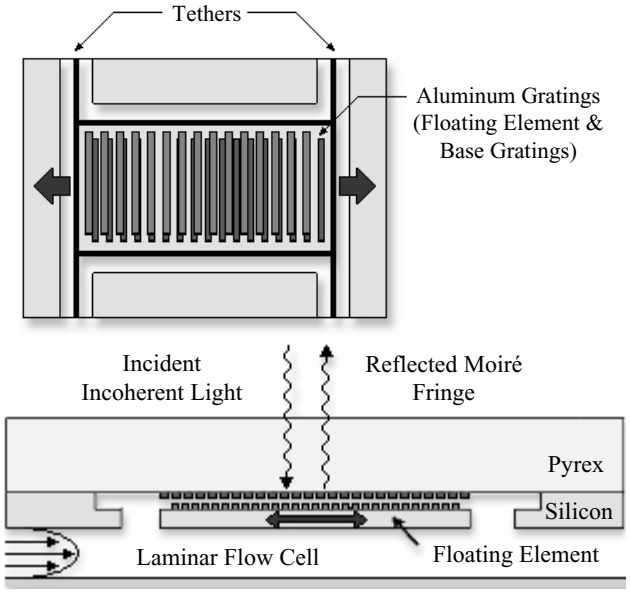

Figure 1: *Top view and cross sectional schematic of the first-generation optical shear-stress sensor.* ***Note:*** *drawings not to scale.*

SENSOR DESIGN

A schematic of a generic MEMS floating element structure is given in Figure 2. The floating element possesses a length, L_e, width, W_e, and thickness, t. The floating element is suspended over a recessed gap g by silicon tethers that also serve as restoring springs. The displacement δ of the floating element as a function of wall shear stress, τ_w, is determined via Euler-Bernoulli beam theory to be

$$\delta = \tau_w \frac{L_e W_e}{4Et}\left(\frac{L_t}{W_t}\right)^3\left\{1+2\frac{L_t W_t}{L_e W_e}\right\}, \qquad (1)$$

where L_t is the tether length, W_t is the tether width, and E is the elastic modulus of the tether [**2**]. Euler-Bernoulli beam theory assumes small deflections such that the strain at the neutral axis of

Travel support has been generously provided by the Transducers Research Foundation and by the DARPA MEMS and DARPA BioFlips programs.

the beam can be neglected. The limits of this approximation can be approximated via a large-deflection energy-based solution,

$$\delta\left[1+\left(\frac{3}{4}\right)\left(\frac{\delta}{W_t}\right)^2\right]=\frac{\tau_w W_e L_e}{4Et}\left[\frac{L_t}{W_t}\right]^3\left[1+2\frac{W_t L_t}{W_e L_e}\right]. \qquad (2)$$

It is clear that if the maximum deflection of the floating element is a significantly less than the tether width, then Eq. (2) reduces to the small deflection solution given in Eq. (1).

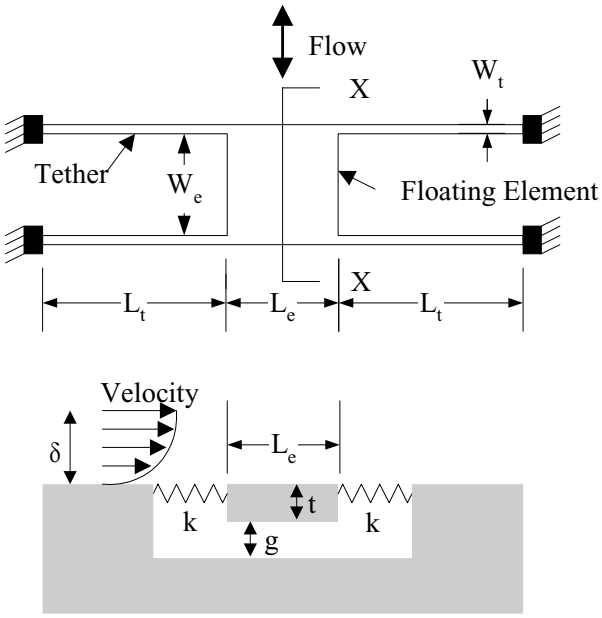

Figure 2: *Schematic plan view and cross-section of a typical floating-element sensor.*

The element possesses an effective mass, M, and the tethers possess an effective spring constant, k. The mechanical sensitivity of the sensor with respect to the integrated shear stress force, $F_\tau = \tau_w W_e L_e$, is directly proportional to the compliance of the tethers, $1/k$, given by

$$\frac{1}{k}=\frac{\delta}{F_\tau}=\frac{1}{4Et}\left(\frac{L_t}{W_t}\right)^3\left\{1+2\frac{L_t W_t}{L_e W_e}\right\}. \qquad (3)$$

The compliance of the device will be limited either by failure at the maximum applied shear stress or from the onset of geometric non-linearities in the force-displacement relationship shown in Eq. (2). The requirement of high spatial resolution requires the measurement of very small forces. For example, a sensor possessing a *100* μm^2 floating element structure would need to measure a *10 pN* force to resolve a shear stress level of *1 mPa*, thus requiring a highly compliant structure. If $L_e W_e >> L_t W_t$, then the effective mass is approximated by $M \approx \rho L_e W_e t$, where ρ is the mass-averaged density of the element material. Assuming a perfectly-damped or under-damped system, the bandwidth is proportional to the first resonance of the device, $\sqrt{k/M}$. Therefore, the shear-stress sensitivity-bandwidth product for the device is proportional to

$$\frac{1}{\sqrt{kM}} \propto \sqrt{\frac{1}{4E\rho L_e W_e t^2}\left(\frac{L_t}{W_t}\right)^3}. \qquad (4)$$

The sensitivity-bandwidth product is a useful figure of merit to investigate the scaling of mechanical sensors analogous to the gain-bandwidth product of an operational amplifier. The increase in the sensitivity-bandwidth figure of merit with decrease in M while maintaining the tether compliance illustrates that MEMS-enabled scaling is favorable for the development of low mass, compliant mechanical sensors possessing superior sensitivity-bandwidth products relative to conventional sensors. As is the case in all transducers, the minimum detectable signal will be determined by the electronic and/or thermal-mechanical noise floor of the measurement system [**12**]. The favorable miniaturization scaling of the mechanics of the structure is somewhat mitigated by the requirement to measure very small displacements that can be $O(\text{Å})$ [**6**].

Our device structure consists of a 1280 μm *x* 400 μm silicon floating element of 10 μm thickness, suspended 2.0 μm above the surface of a 500 μm thick Pyrex wafer by four 545 μm *x* 6 μm tethers of 10 μm thickness. The Moiré pattern is realized by patterning aluminum lines of pitch g_2 on the bottom of the floating element and g_1 on the Pyrex wafer. The superimposed top and bottom gratings create a translation-dependent Moiré fringe pattern with spatial period G (Figure 3). The period of the Moiré fringe can be derived by considering that for every Moiré period, the smaller grating has one extra line than the larger grating, thus

$$G = n \cdot g_2 = (n+1) g_1, \qquad (5)$$

where n is the number of lines of the larger grating [**9**]. By eliminating n from Eq. (5), the spatial period of the Moiré fringe can be given by

$$G = g_1 g_2 / (g_2 - g_1). \qquad (6)$$

Furthermore, the displacement of the Moiré fringe, Δ, is amplified as compared to the grating displacement δ, as given by

$$\Delta = \delta\left(\frac{G}{g_1}\right). \qquad (7)$$

Therefore, the Moiré amplification of the sensor can be adjusted by appropriate choice of the grating dimensions. For the design presented here, $G/g_1 = 100$.

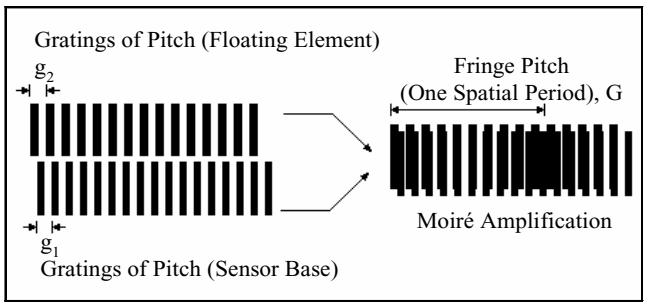

Figure 3: *Geometric Moiré pattern generated from two gratings where* $g_1 = 9.9\,\mu m$, $g_2 = 10\,\mu m$, *and* $G = 990\,\mu m$.

SENSOR FABRICATION

The sensor was fabricated using an aligned wafer-bond/thin-back process that produces optical gratings on the backside of a floating element and on the top surface of the support wafer. The wafer-bond/thin-back process is outlined in Figure 4. The process begins with one silicon-on-insulator (SOI) wafer and one Pyrex wafer. First, a 2 μm recess is etched into the top silicon layer of

the SOI wafer using reactive ion etching. This recess will later function as a cavity above which the floating element will move. Aluminum gratings of 0.25 μm thickness are then sputter deposited and patterned within the cavity as well as on the top surface of the Pyrex wafer. The inverted SOI wafer is then aligned and anodically bonded to the Pyrex wafer using an EV-501 Wafer Bonder. Following this, the backside of the SOI wafer is thinned-back via potassium hydroxide etching, stopping on the buried oxide (BOX) layer. The BOX layer is then removed prior to deep reactive ion etching that forms the tethers and releases the floating element (Figure 5).

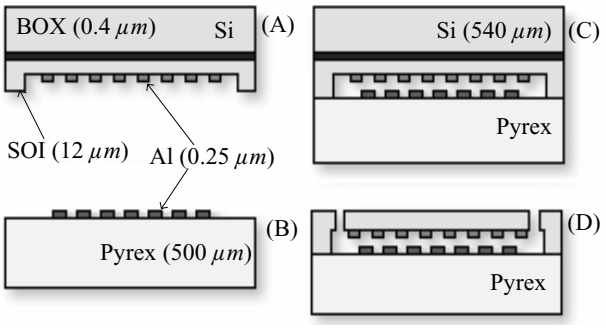

Figure 4: *A schematic of the fabrication sequence: (A) Etch 2 μm recess in Si-overlayer of SOI wafers, then deposit and pattern device gratings. (B) Deposit and pattern handle gratings on the Pyrex wafer. (C) Align, then anodic bond the Pyrex and SOI wafers. (D) Thin-back the bulk of the SOI wafer, then use DRIE to release the floating element and tethers. Note: schematics not to scale.*

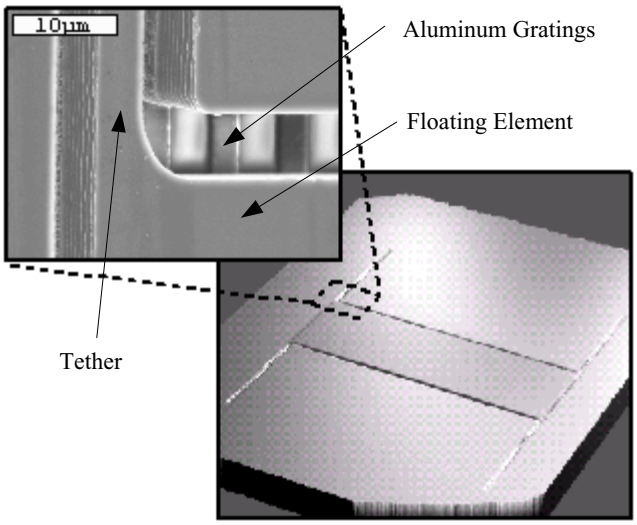

Figure 5: *Top-view of the shear stress sensor using an optical profilometer. Inset: Close-up of tether and aluminum gratings taken using scanning-electron microscope (SEM).*

The finished device was then packaged by flush-mounting the sensor die in a Lucite plug with back-side imaging optics, providing a 5x optical magnification, and a Thomson-CSF TH78CE13 linescan CCD camera (Figure 6). The CCD camera contains an array of 1 x 1024 pixels, each 10 μm in width.

RESULTS AND DISCUSSION

For static calibration, the packaged device was then mounted into a 100 *mm x* 1 *mm* flow cell that provides a variable mean shear stress via a laminar, incompressible, fully developed, 2-D pressure driven flow in a slot [**13**] (Figure 6). A block diagram of the static calibration procedure is given in Figure 7. The differential pressure between two locations in the fully-developed region of the laminar flow cell is measured via a Heise pressure sensor, which is then used to compute the applied shear stress to the sensor. This differential pressure measurement is averaged 100 times and used to compute the applied shear stress τ_w via

$$\tau_w = -\frac{h}{2}\frac{\Delta p}{L}, \qquad (8)$$

where Δp is the differential pressure, h is the height of the channel, and L is the distance separating the pressure ports.

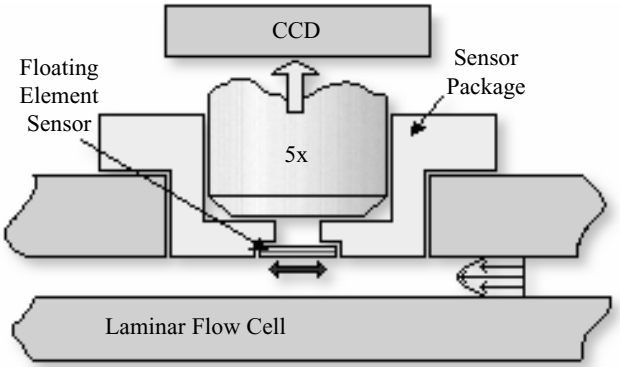

Figure 6: *Schematic diagram of static calibration experimental setup illustrating backside imaging optics for 2-D laminar flow cell.*

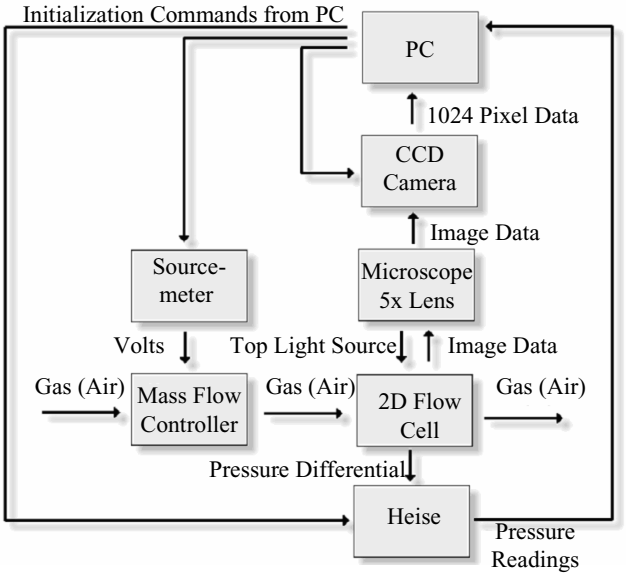

Figure 7: *Schematic diagram of experimental setup for static calibration.*

The Moiré fringe pattern is captured using the CCD camera, through the backside imaging optics. For the static calibration, 600 successive frames are obtained for averaging purposes. The imaged fringe pattern for zero applied shear stress is shown in Figure 8, where the first 100 successive frames from the camera are stacked vertically. The peak in relative intensity corresponds to the brightest region in the grayscale image.

From the captured image, relative pixel intensities are obtained for each frame and averaged over the 600 frames. The

averaged relative pixel intensities obtained for two different shear stresses are shown in Figure 9. The Moiré pattern was found to have a spatial period of 1002 μm, before the 5x optical amplification, compared to the physical grating period of 9.9 μm. The Moiré amplification for the sensor was then found to be 101.2 compared to our designed value of $G/g_1 = 100$.

The resulting averaged intensity pattern is normalized by a calibration image to eliminate pixel gain variations and non-uniform illumination effects. Following this, a spatial Fast-Fourier Transform (FFT) is performed on the normalized fringe pattern, from which the phase of the Moiré pattern is then extracted. This phase is then compared against the phase calculated for zero applied shear stress to obtain the phase shift and the corresponding pixel shift. Using knowledge of the Moiré pattern and optical magnification, the corresponding mechanical displacement of the floating element is computed to give a direct measurement of the wall shear stress.

Following the procedure outlined above, the pixel shift of the Moiré fringe pattern was determined for a range of applied shear-stress. The results are shown in Figure 10, along with the corresponding mechanical displacement. The mechanical sensitivity, as found from the slope of this curve, is 0.26 $\mu m/Pa$, while the Moiré fringe, after the 5x optical amplification, moves by 130.02 $\mu m/Pa$. Figure 10 illustrates a linear response up to 1.3 *Pa.*

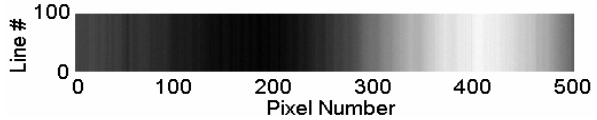

Figure 8: *Moiré fringe pattern for a static shear stress of 0 Pa as seen by 1024 pixel linescan camera. Successive frames from the camera are stacked vertically.*

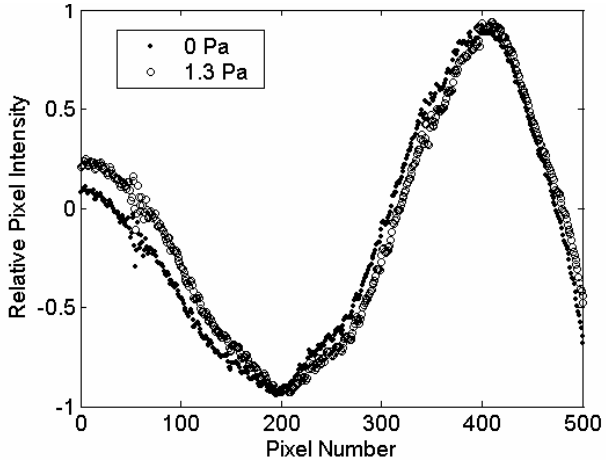

Figure 9: *Measured relative pixel intensity for mean shear stresses of 0 Pa and 1.3 Pa.*

The recessed gap under the floating element gives rise to pressure-gradient induced errors. The magnitude of the effective shear-stress, τ_{eff}, acting in the presence of a pressure gradient has been shown to be

$$\tau_{eff} = \left(1 + \frac{g}{h} + \frac{2t}{h}\right)\tau_w, \qquad (9)$$

where h is the channel height of the wind tunnel used for calibration, g is the recessed gap, and τ_w is the actual wall shear stress [**2**]. The second and third terms in the bracket are the error terms associated with flow under the floating element and the pressure gradient acting on the lip of the element, respectively. For the current device and experimental apparatus, this component of the calibration error is 2%.

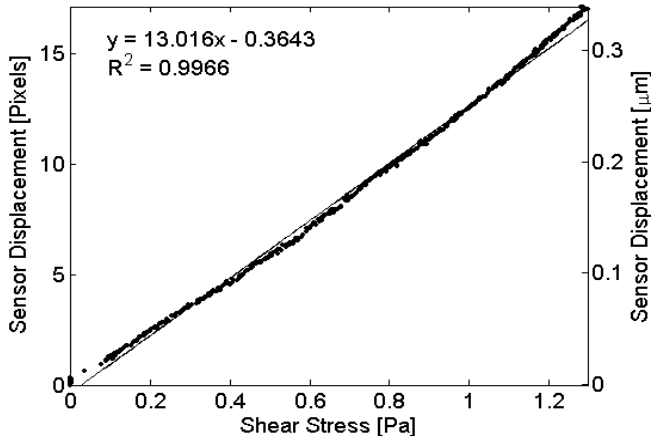

Figure 10: *Static response of the sensor in terms of Moiré fringe pixel displacement and corresponding mechanical displacement as a function of mean shear stress. The static sensitivities are 13.0 pixels/Pa and 0.26 μm /Pa.*

Dynamic calibration was performed in a plane-wave tube, with a 25.4 mm x 25.4 mm cross section, using a Stokes Layer excitation technique (Figure 11). This technique utilizes acoustic plane waves in a duct to generate known oscillating wall shear stresses [**14**]. The plane waves are generated by a JBL 2426H speaker mounted to the end of the plane wave tube. The packaged shear stress sensor is flush mounted to the side wall of the plane wave tube directly across from a Brüel & Kjær 4138 1/8" microphone. As with the static setup, the Moiré pattern is recorded by the CCD camera. In the dynamic calibration, however, the camera is programmed to record 16,384 lines at a line rate of 11.42 *kHz*. The microphone signal is recorded by a data acquisition (DAQ) card via an SRS-560 preamplifier for AC coupling. A synchronization pulse from the camera is used to trigger sampling by the DAQ card.

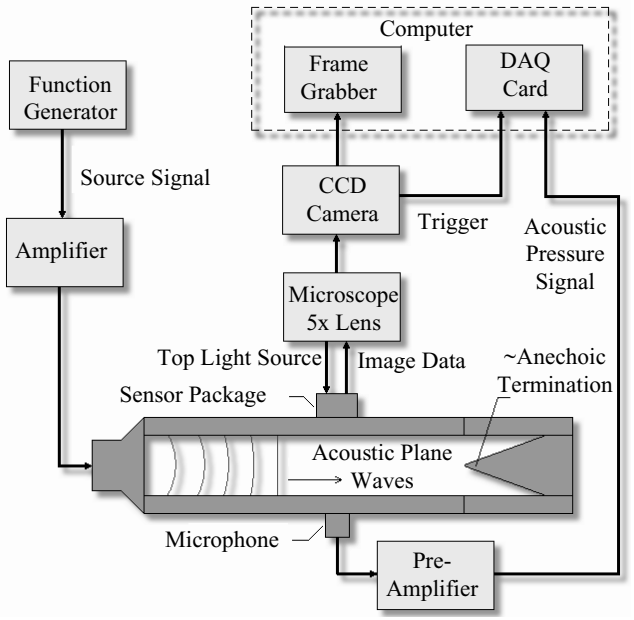

Figure 11: *Schematic diagram of experimental setup for dynamic calibration via Stokes' Layer Excitation [14].*

The recorded Moiré fringe pattern image for a sinusoidal shear stress of amplitude 0.061 *Pa* and frequency of 1 *kHz* is shown in Figure 12. This image shows 40 successive lines from the line scan camera stacked vertically, illustrating temporal oscillations of the phase of the fringe pattern. The sinusoidal time trace on the right represents the input oscillatory shear stress.

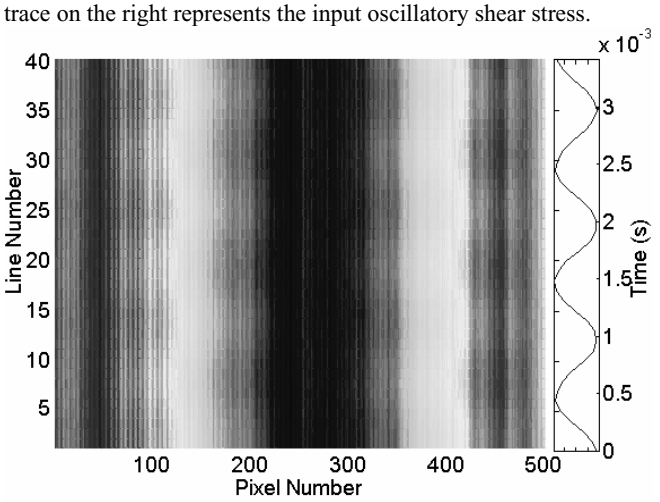

Figure 12: *Moiré fringe pattern for a 1 kHz sinusoidal shear-stress input of 0.061 Pa. Successive frames from the camera are stacked vertically illustrating the oscillatory fringe pattern. The sinusoidal time trace on the right represents input oscillatory shear stress.*

Time series data illustrating the dynamic response of the sensor in terms of Moiré fringe pixel displacement and corresponding mechanical displacement for a 1 *kHz* sinusoidal input of 0.061 *Pa* is shown in Figure 13. The amplitude of the sensor displacement is approximately 3 *pixels* or 0.06 μm .

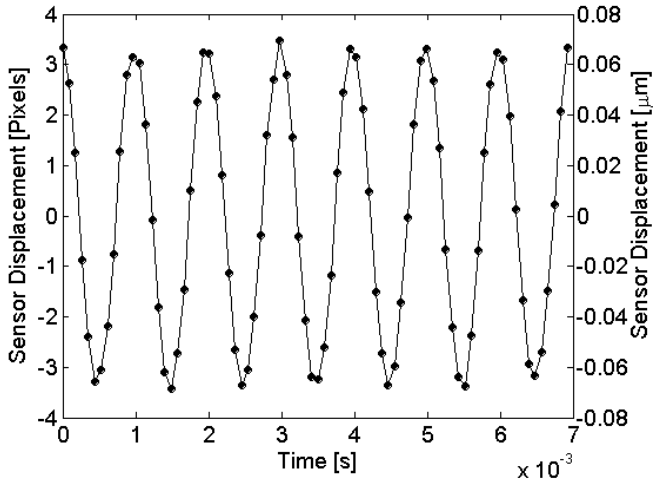

Figure 13: *Time series data illustrating the dynamic response of the sensor in terms of Moiré fringe pixel displacement and corresponding mechanical displacement for a 1 kHz sinusoidal input of 0.061 Pa. The dots are the actual samples taken and the line is a curve fit to the data.*

From the time series data, the frequency response function can be easily found. A preliminary estimate of the frequency response function gain factor is shown in Figure 14. Results indicate a first lateral mode resonant frequency at 1.7 *kHz*. The corresponding phase has not been accurately estimated due to synchronization issues between the linescan CCD and the microphone channel analog-to-digital converter. This issue arose despite the trigger signal from the CCD camera that is used to trigger the start of microphone sampling. It is believed that round-off error in the sampling rate of the DAQ card leads to a gradual loss of synchronization over time. Further work is necessary to elucidate the precise nature of this issue.

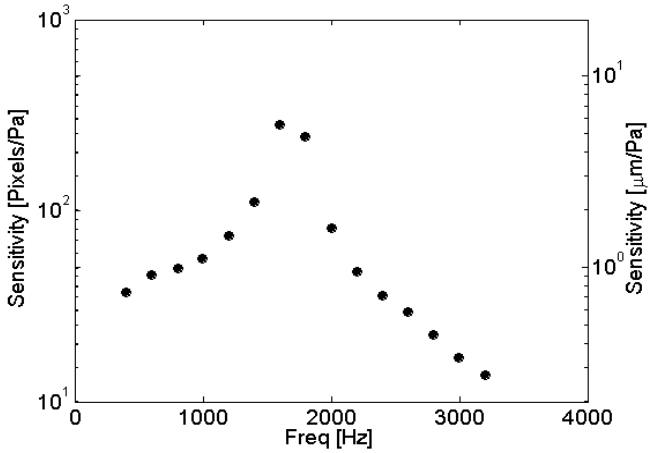

Figure 14: *Magnitude of frequency response function illustrating a resonance at approximately 1.7 kHz.*

The noise floor spectrum was obtained by recording microphone and CCD data with no acoustic input signal. An estimate of the noise floor magnitude is shown in Figure 15. For a 1 *Hz* bin centered at 1 *kHz*, the noise floor is 1.6 *nm/√Hz* or 0.08 *pixels/√Hz*, which corresponds to a minimum detectable shear stress of 6.2 *mPa/√Hz*. The dynamic range spans three orders of magnitude (6.2 *mPa*-1.3 *Pa*).

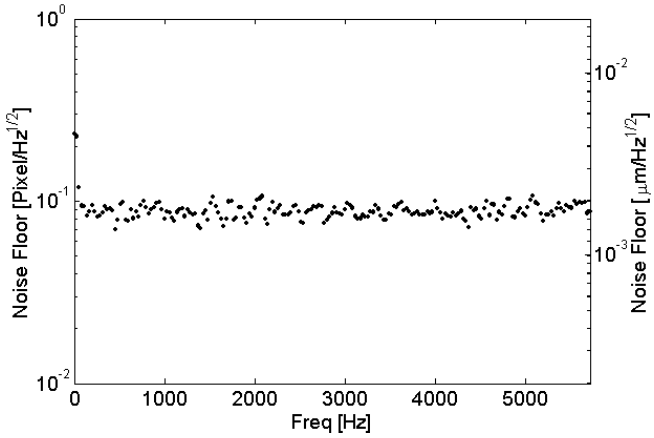

Figure 15*: Noise floor spectrum of the sensor with a 1 Hz binwidth.*

CONCLUSIONS AND FUTURE WORK

A proof-of-concept micromachined, floating element shear-stress sensor was developed that utilizes a geometric Moiré interferometric technique. A static characterization of the device indicated a linear response up to 1.3 *Pa*. Noise floor measurements indicate a minimum detectable shear stress of 6.2 *mPa* for a 1 *Hz* binwidth. Therefore, the experimentally determined dynamic range is 6.2 *mPa* – 1.3 *Pa*. The upper end of the dynamic range as predicted by Eq. (9) for a 3% static non-linearity is 21.7 *Pa*. This, however, could not be verified due to constraints in our static calibration apparatus. A comparison of the specifications of various shear stress sensors including the sensor presented here is given in Table 1.

In the dynamic experiments, the device exhibited a lower resonant frequency than was expected. Fabrication-induced

geometric errors have not yet been quantified, but this may be the underlying cause for the discrepancy. The measured displacement resolution was found to be 1.6 *nm/√Hz* for the current sensor and optical setup. There are several mechanisms by which this performance can be improved. The sensor and testbed and can be subdivided into three gain stages, consisting of mechanical sensitivity, Moiré amplification, and optical magnification. The mechanical sensitivity of the sensor can be increased but at the expense of decreased resonant frequency, in a typical gain bandwidth tradeoff. Additionally, the Moiré amplification can be increased, through two mechanisms. As the amplification is dependent upon the ratio of G/g_1, increasing G or decreasing g_1 has the same overall effect, an increase in Moiré amplification. Nevertheless, it is necessary to have at least one full Moiré period within the field of view of the CCD camera to allow accurate determination of the phase of the Moiré pattern. This places an upper limit upon G, and makes the reduction of g_1 the most desirable method of increasing the Moiré amplification. Ultimately, g_1 and g_2 are also limited, in this case by the photolithographic resolution of the gratings. Furthermore, as the grating pitch decreases, diffraction effects become more significant, leading to a blurring of the image and a reduction in fringe contrast.

***Table 1**: Comparison of specifications for various MEMS shear-stress sensors. The bandwidth, BW, of each of the sensors is listed in the far right column.*

Author	Type	Dyn. Range	Sensitivity	BW
Schmidt et al.[**2**]	Direct	0.01-1*Pa*	52 *mV/Pa*	10*kHz*
Pan et al. [**3, 15**]	Direct	0.5-3.8 *Pa*	1 *V/Pa*	n/a
Padmanabhan et al. [**6**]	Direct	1.4*mPa*-10 *Pa*	0.4 *mV/Pa*	10*kHz*
Liu et al. [**1**]	Thermal	n/a	1 *v/Pa*	25*kHz*
Liu et al. [**1**]	Thermal	n/a	30 *mv/Pa*	18*kHz*
Sheplak et al. [**14**]	Thermal	9 μ *Pa* - 1.7*Pa*	11 *mV/Pa*	8*kHz*
Horowitz et al.	Direct	6.2*mPa* - 1.3*Pa*	13 *pixels/Pa*	1.7*kHz*

The final mechanism by which the sensitivity can be increased is via a higher optical magnification. The advantage of this technique is that the sensitivity can be increased even after device processing is completed. The main disadvantage is a corresponding amplification of relative package and optical testbed vibrations, although this can be compensated by improvements in the packaging, and a reduction in optical depth of field. It should be noted that the package vibrations are not amplified by the Moiré amplification as only relative vibrations between the two gratings are amplified. Additionally, the field of view of the camera limits the maximum magnification, as once again it is necessary to have a minimum of one full Moiré period in view.

There are several issues regarding the reliability of the sensor. First, the floating element is designed with a hard stop after 7 μm to prevent damage to the sensor due to excessive shear stress. Additionally, temperature issues can play a role in both sensitivity and reliability, however, silicon and Pyrex have similar thermal expansion coefficients, so negligible thermal-induced stresses are expected.

Future work will include more rigorous dynamic and static characterization, noise floor studies, and sensitivity to non-shear stress inputs, as well as resolving the dynamic calibration synchronization issue. In addition, a borescope based imaging system will be implemented to reduce package size and improve portability. A second-generation device is planned in which the sensor geometry and Moiré fringe design will be optimized.

ACKNOWLEDGEMENTS

The authors would like to thank Professor Peter Ifju, Hamed Kourouma, Jhoanna Peña and Julio Castro for their assistance in this project. This work was supported through NASA-LaRC grant NAG-1-2133 and NASA-KSC grant NAG-10-316.

REFERENCES

1. C. Liu, J.-B. Huang, Z. Zhu, F. Jiang, S. Tung, Y.-C. Tai, and C.-M. Ho, "A Micromachined Flow Shear-Stress Sensor Based on Thermal Transfer Principles", *J.MEMS*, 8, (1999), pp. 90-9.
2. M. A. Schmidt, R. T. Howe, S. D. Senturia, and J. H. Haritonidis, "Design and Calibration of a Microfabricated Floating-Element Shear-Stress Sensor", *IEEE Tr. on Elect. Dev.*, 35, 6 (1988), pp. 750-57.
3. T. Pan, D. Hyman, M. Mehregany, E. Reshotko, and S. Garverick, "Microfabricated Shear Stress Sensors, Part 1: Design and Fabrication", *AIAA J.*, 37, (1999), pp. 66-72.
4. J. Shajii, K.-Y. Ng, and M. A. Schmidt, "A Microfabricated Floating-Element Shear Stress Sensor Using Wafer-Bonding Technology", *J. MEMS*, 1, 2 (1992), pp. 89-94.
5. H. D. Goldberg, K. S. Breuer, and M. A. Schmidt. "A Silicon Wafer-Bonding Technology for Microfabricated Shear-Stress Sensors with Backside Contacts", in *Solid-State Sensor and Actuator Workshop*, Hilton Head, (1994), pp. 111-5.
6. A. Padmanabhan, H. D. Goldberg, M. A. Schmidt, and K. S. Breuer, "A Wafer-Bonded Floating-Element Shear-Stress Microsensor with Optical Position Sensing by Photodiodes", *J. MEMS*, 5, (1996), pp. 307-15.
7. J. Zhe, K. R. Farmer, and V. Modi. "A MEMS Device for Measurement of Skin Friction Using Capacitance Sensing", in *Proc. of IEEE MEMS 01*, Berkeley, CA,, (2001), pp. 4-7.
8. J. Naughton and M. Sheplak, "Modern Developments in Shear-Stress Measurement", *Prog. Aero. Sci.*, 38, (2002), pp. 515-70.
9. D. Post, B. Han, and P. Ifju, *High Sensitivity Moiré*, NY, Springer (1994).
10. O. Kafri and I. Glatt, *The Physics of Moiré Metrology*, NY, Wiley (1990).
11. A. Tran, J. Lee, K. Zhang, and Y. Lo, "Ultrafine Motion Detection of Micromechanical Structures Using Optical Moiré Patterns", *IEEE Phot. Tech. Letters*, 8, 8 (1996), pp. 1058-60.
12. T. Gabrielson, "Mechanical-Thermal Noise in Micromachined Acoustic and Vibration Sensors", *IEEE Elect. Dev.*, 40, (1993), pp. 903-9.
13. M. Sheplak, V. Chandrasekaran, A. Cain, T. Nishida, and L. Cattafesta, "Characterization of a Micromachined Thermal Shear Stress Sensor", *AIAA J.*, 40, 6 (2002), pp. 1099-1104.
14. M. Sheplak, A. Padmanabhan, M. A. Schmidt, and K. S. Breuer, "Dynamic Calibration of a Shear Stress Sensor Using Stokes Layer Excitation", *AIAA J.*, 39, 5 (2001), pp. 819-23.
15. D. Hyman, T. Pan, E. Reshotko, and M. Mehregany, "Microfabricated Shear Stress Sensors, Part 2: Testing and Calibration", *AIAA J.*, 37, 1 (1999), pp. 73–8.

3D Silicon Transformation using Hydrogen Annealing

Ming-Chang M. Lee and Ming C. Wu
Department of Electrical Engineering, University of California at Los Angeles
Los Angeles, CA 90095-1594

ABSTRACT

Fabricating smooth, round structures in silicon is challenging by conventional processing methods. In this paper, we report on a novel 3D shaping technique for producing microspheres, microdisk toroids, submicron wires, and circular beams in Si using hydrogen annealing. Microspheres with 1 μm radius, submicron wires with 0.5 μm radius, and a microdisk toroid with 0.2 μm toroidal radius have been successfully demonstrated.

INTRODUCTION

Thermal annealing in hydrogen ambient has been extensively used in the IC industry as an *in situ* cleaning step to remove native oxide for silicon epitaxy[1]. In addition, it can reduce surface roughness of as-etched silicon to levels comparable to commercial polished wafers [2][3]. It is believed that heated hydrogen facilitates Si migration at temperatures much lower than the melting point of Si (1414°C). Due to this mass transport effect, a sharp corner on an etched step can be rounded by annealing. Recently, Sato *et al.* demonstrated several types of buried voids by annealing etched Si trenches in pure hydrogen at 1100°C [4]. However, most of the previous studies focused on the transformation of deep trenches [5]. The deformation of mesa structures on different substrates has not been examined yet.

In this paper, we investigate the effect of hydrogen annealing on the sidewall profiles of microstructures on silicon-on-insulator (SOI). Circular beams and microspheres are fabricated by heating rectangular beams and cylinders, while submicron wires and toroidal microdisks are manufactured by annealing partially released lines and disks on thin SOI.

PRINCIPLE

The dissociative adsorption of hydrogen on silicon surface increases by many orders of magnitude when the substrate is heated at high temperature [6]. At such temperature, the reaction of hydrogen with silicon enables silicon atoms to migrate on the surface. For features with sharp edges, this mechanism, which is similar to reflow, leads to rounded corners and reduced surface roughness to minimize the surface energy. This is illustrated in Figures 1, which shows the cross-sectional profiles of a comb structure (1-μm fingers with 1-μm spacing and 2.5-μm height) etched on bulk Si before and after hydrogen annealing. Rounding of sharp corners was clearly observed. The structures remain monocrystalline after annealing.

(a)

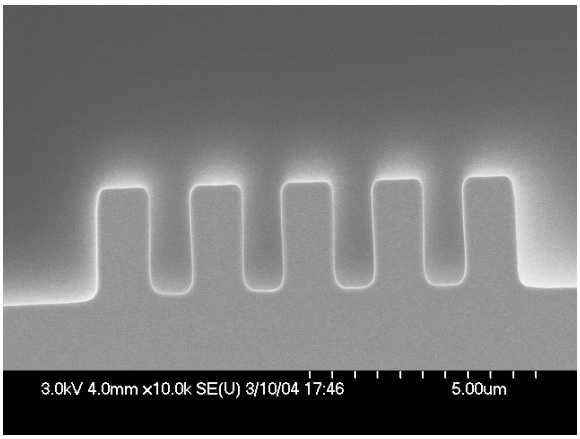

(b)

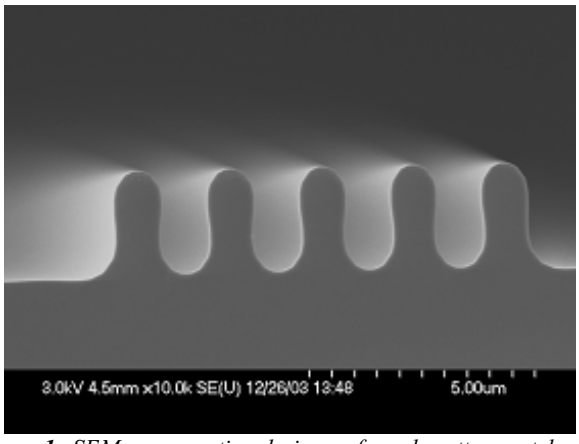

Figure 1 *SEM cross-sectional views of comb patterns etched on bulk silicon* ***(a)*** *before and* ***(b)*** *after hydrogen annealing (1100°C and 10 Torr).*

The surface migration depends on the annealing temperature, the gas pressure, and the reaction time. To investigate the temperature dependence, a 2.5-μm-tall mesa was etched on a bulk silicon substrate. Then, the wafer was annealed (ASM Episilon II single wafer epitaxial reactor) in pure hydrogen at 10 Torr for 5 minutes. Sharp corners at both the top and the bottom of the mesa became rounded. Figure 2 displays the radius of curvature at the corners versus annealing temperature. It increases from 0.59 μm for annealing temperature of 1000°C to 0.86 μm at 1100°C. Higher temperatures produce more rounded corners.

0-9640024-5-0/hh2004/$20©2004TRF
DOI 10.31438/trf.hh2004.5

Solid-State Sensors, Actuators, and Microsystems Workshop
Hilton Head Island, South Carolina, June 6-10, 2004

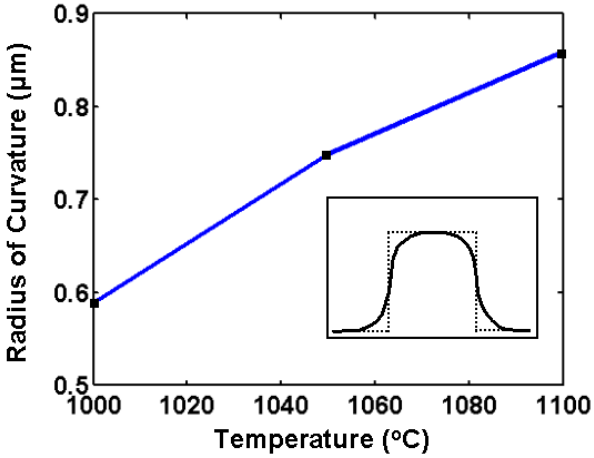

Figure 2. *The radius of curvature on the corner of a mesa structure after annealing for 5 minutes at 10 Torr versus annealing temperature.*

The sidewall profile produced by hydrogen annealing also depends on bottom interface of the structure. Figure 3 compares the cross sections of the annealed steps on bulk silicon and SOI. The SOI wafer was etched to expose the buried oxide, while the bulk Si wafer was time-etched to the same depth. Then, both wafers were annealed in pure hydrogen at 1100 °C, 10 Torr for 5 minutes. In the bulk silicon sample (Fig. 3(a)), the annealed step exhibits both convex (top) and concave (bottom) corners. In the SOI wafer (Fig. 3(b)), both corners are convex. Furthermore, a slit developed between the etched Si and the SiO_2 due to undercut at the interface. Similar undercut has been observed previously [7]. The undercut can be understood by examining the chemical reactions at the silicon–silicon dioxide interface:

$$Si - H + SiO_2 \longrightarrow Si^* + H_2O_{(g)} \quad (1)$$

$$Si^* + SiO_2 \longrightarrow SiO_{(g)} \quad (2)$$

$$Si + 2H_2O_{(g)} \longrightarrow SiO_2 + 2H_2 \quad (3)$$

In Eq. (1), the hydrogen atoms attached on silicon react with silicon dioxide to yield water vapor and adsorbed silicon. These silicon atoms are prone to react with silicon dioxide to form volatile SiO. Some of the water vapor re-oxides the exposed silicon to form silicon dioxide. As shown in Eq. (2) and (3), both Si and SiO_2 are consumed at the interface. This phenomenon explains the existence of the slit at the interface. The width of the slit is typically between 0.1 to 0.2 μm. The length of the undercut region increases with decreasing pressure or increasing temperature.

The undercut at the interface partially release the etched Si mesa, and after subsequent annealing, a convex corner similar to that at the top of the mesa was observed at the interface, as shown in Fig. 3(b). We can exploit this phenomenon to make circular cross-sectional profiles with very smooth surfaces from rectangular silicon features on SOI substrates.

(a)

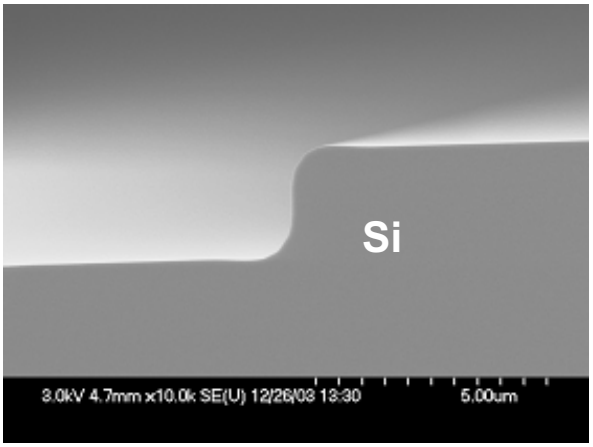

(b)

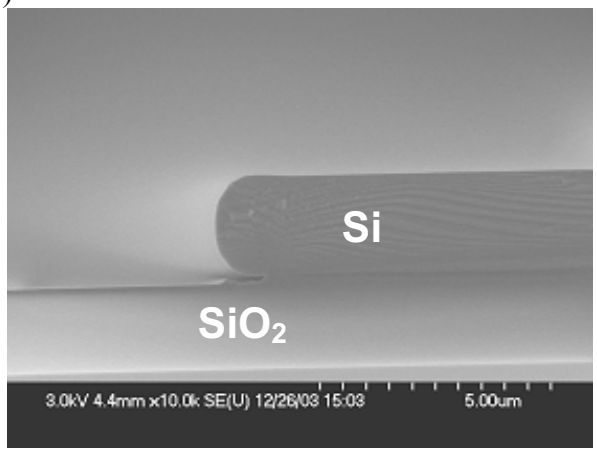

Figure 3 *SEM pictures of step profiles on* ***(a)*** *a silicon substrate and* ***(b)*** *an SOI wafer. Both wafers have the same step height and were annealed at 1100°C and 10 Torr for five minutes. In SOI wafer, the edge of the Si mesa is partially released from the SiO_2, resulting in a convex bottom corner.*

EXPERIMENTAL DETAIL

A. Circular Beams and Microspheres

Circular beams were fabricated on SOI wafers with 1.5-μm-thick Si films. First, a microbeam array was patterned by lithography. The widths of these lines are comparable to the thickness of the Si film. In this experiment, 1-μm lines with 1-μm spacing were employed. After lithography, the structures were dry-etched down to the buried oxide with vertical sidewalls. Before thermal annealing, the as-etched sample was dipped in diluted hydrofluoric (HF) acid to remove residual oxide, which could create surface pits during hydrogen annealing [8]. Finally, the sample was annealed in pure hydrogen at 1100°C and 10 Torr for five minutes.

Figure 4(a) shows the scanning electron microscopy (SEM) picture of the microbeams after hydrogen annealing. The rectangular beams became circular beams with rounded tips. The beams were released due to the undercut effect described earlier. The microbeam array was anchored to a large-area pad shown on the left of the picture.

Microspheres were created using a similar process. First, an array of circular cylinders with 1-µm radii were created by photolithography and dry etching. The sample is then annealed in pure hydrogen. Figure 4(b) shows the SEM micrograph of the microspheres after hydrogen annealing. The annealing time is controlled to prevent complete release of the microspheres.

(a)

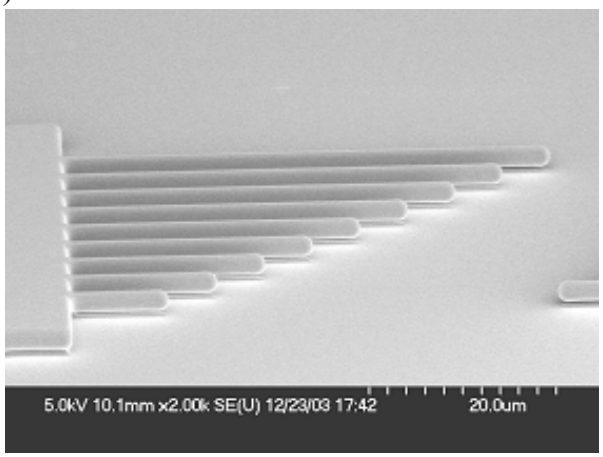

(b)

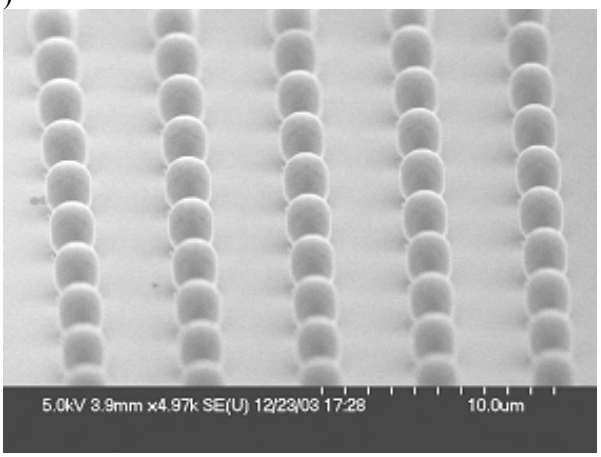

Figure 4(a). *Circular microbeams and* ***(b).*** *microspheres. The radius of the microsphere and the diameter of the microbeam is 1 um. Both SEM pictures were taken from an oblique view. The features are made on SOI.*

B. Submicron wire and Toroidal Microdisk

For suspended thin silicon structures, the morphology changes more dramatically, especially at the edges, after hydrogen annealing. Silicon atoms tend to accumulate around the edge to reduce the total surface energy but still maintain a monocrystalline lattice structure.

To demonstrate this effect, an SOI with 0.2-µm-thick Si film and 3-µm-thick buried oxide was patterned to form an array of 1-µm-wide lines with 1 µm spacing. The top and the cross-sectional views of the lines are shown in Fig. 5(a). After releasing in buffered oxide etch (BOE), this array was annealed in hydrogen ambient at 1100°C for five minutes. The SEM images are shown in Figure 5(b). The cross-sections of the Si beams were transformed from 0.2 x 1 μm^2 rectangles to 0.5-µm-diameter circles. Note that the cross-sectional areas are conserved during the annealing process. Using this technique, sub-micron features can be made without advanced lithography.

(a)

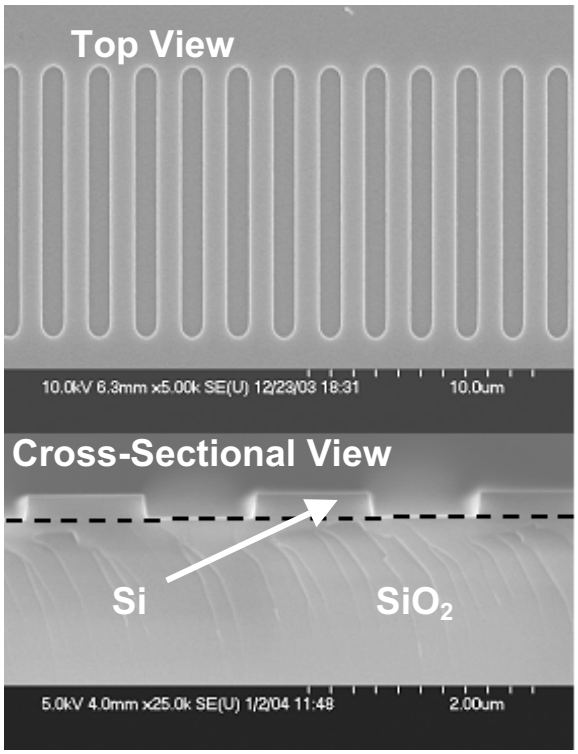

(b)

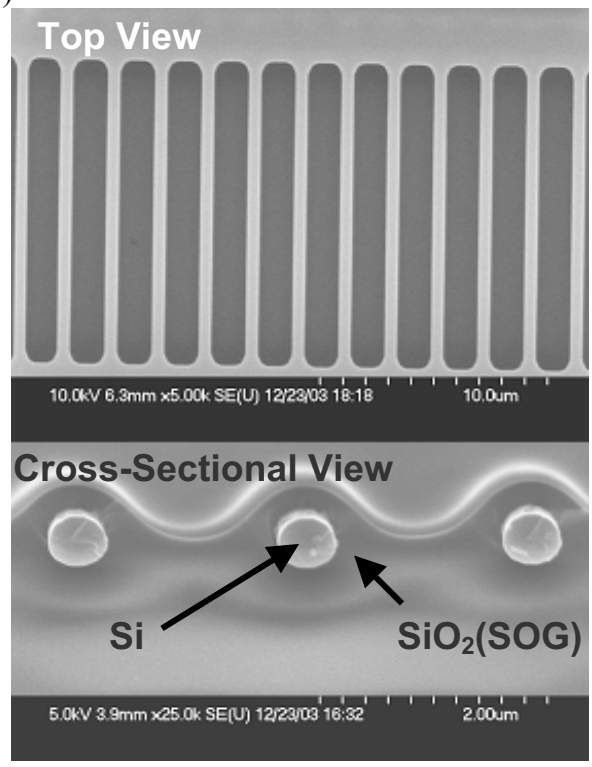

***Figure 5.**. Top- and cross-sectional views of the microbeam array **(a)** before and **(b)** after annealing. The SOG (spin-on-glass) in (b) was coated after annealing to hold the suspended structure.*

For thin SOI structures with large areas (diameter >> 1 μm), the migration of Si atoms happens primarily at the edges. As a result, a thick rim is formed on the edges of the structure. This can be exploited to make Si microtoroid structures. Circular disks with 10-μm radii were first patterned on 0.2-μm-thick SOI wafers. The disks were partially released in HF to create overhangs at the edges. After annealing in hydrogen, the microdisk was transformed into a toroidal structure with a very smooth surface. Figure 6(a) shows the SEM of a 10-μm-radius microtoroid disk. Figure 6(b) shows the cross-sectional view of the toroid. The edges of the disk was not only rounded but also expanded in the vertical direction. The toroidal radius is 200 nm. The microtoroid disks offer several advantages for optical microresonator applications[9].

(a)

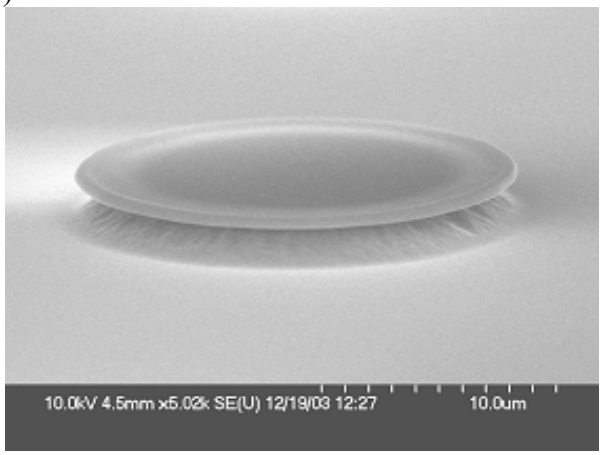

(b)

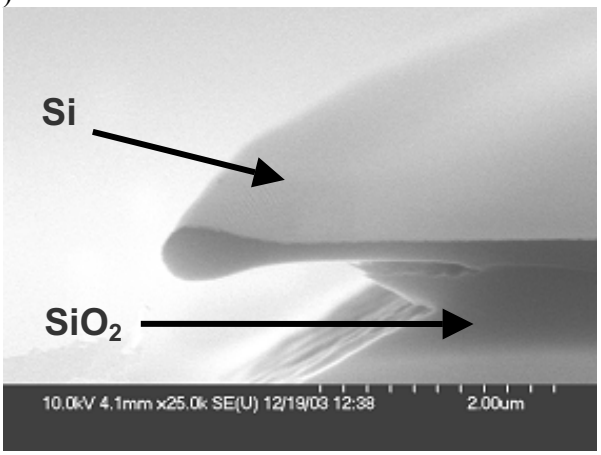

***Figure 6. (a)** A toroidal structure after hydrogen annealing. **(b)** A close-up view of the disk cross section. Thickness around the edge is expanded.*

CONCLUSIONS

In summary, we have demonstrated a 3D silicon transformation method using hydrogen annealing. By controlling process temperature, hydrogen pressure, and annealing time, the radius of curvature on the sidewall profile can be engineered. Circular microbeams, microspheres, submicron Si wires, and microtoroid structures have been successfully demonstrated.

ACKNOWLEDGEMENT

This project is supported by DARPA Optoelectronics Center (#MDA972-00-1-0019) and the CS-WDM programs (#MDA972-02-1-0019).

REFERENCES

[1] K. Morishima, et al., *Jpn. Pat., No. JP03123027, 1991*

[2] Nobuhiko Sato and Takao Yonehara, "Hydrogen Annealed Silicon-on-insulator", *Applied Physics Letter,* Vol. 65, No. 15, Oct. 1994, pp.1924~1926.

[3] Yang-Kyu Choi, Leland Chang, Pushkar Ranade, Jeong-Soo Lee, Daewon Ha, Sriram Balasubramanian, Aditya Agarwal, Mike Ameen, Tsu-Jae King, and Jeffery Boker, "FinFET Process Refinements of Improved Mobility and Gate Work Function Engineering", *International Electron Devices Meeting. Technical Digest, 2002, pp259~262*

[4] Tsutomu Sato, Nobutoshi Aoki, Ichiro Mizushima, and Yoshitaka Tsunashima, "A New Substrate Engineering for the Formation of Empty Space in Silicon (ESS) Induced by Silicon Surface Migration", *IEDM 1999,* pp. 517~520

[5] Hitoshi Kuribayashi, Reiko Hiruta, Ryosuke Shimizu, Koichi Sudoh, and Hiroshi Iwasaki, "Shape Transformation of Silicon Trenches during Hydrogen Annealing", J. Vac. Sci. Technol. A 21(4), Jul/Aug, 2003, pp 1279-1283.

[6] Peter Bratu and Ulrich Hofer, "Photon-Assisted Sticking of Molecular Hydrogen on Si(111)-(7X7)", Physical Review Letters, Vol. 74, No. 9, Feb. 1995, pp 1625-1628

[7] S. T. Liu, L. Chan, and J. O. Borland, "Reaction Kinetics of SiO2/Si(100) Interface in H2 Ambient in A Reduced Pressure Epitaxial Reactor", *Proc. Electrochem. Soc.,* 87-88, 1987, pp428~434

[8] Hitoshi Habuka, Hitoshi Tsunoda, Masanori Mayusumi, Nato Tate, and Masatake Katayama, "Roughness of Silicon Surface Heated in Hydrogen Ambient", *J. Electrochem. Soc.*, Vol. 142, No. 9, Sep. 1995, pp. 3092-3098

[9] D. K. Armanl, T. J. Klappenberg, S. M. Splllane and K. J. Vahala, "Ultra-high-Q Toroid Microcavity on A Chip", *Nature,* Vol. 421, 27 Feb., 2003, pp.926~928

A BATCH FABRICATED RUBIDIUM-VAPOR RESONANCE CELL FOR CHIP-SCALE ATOMIC CLOCKS

Chung-Hoon Lee, Hang Guo, Shankar Radhakrishnan, and Amit Lal
School of Electrical and Computer Engineering, Cornell University
Ithaca, NY 14853

Csaba Szekely, and Thomas A. McClelland
Frequency Electronics, Inc.
Mitchel Field, NY 11553

Albert P. Pisano
Department of Mechanical Engineering
University of California, Berkeley
Berkeley, CA 94720

ABSTRACT

We present a batch-fabrication process for Rubidium^{87} (Rb^{87}) vapor cells appropriate for chip-scale atomic clocks. The Rb^{87} cells are fabricated by anodic bonding of glass to bulk micromachined cavities in silicon, enabling batch production of hundreds of cells per (four-inch) wafer. We describe a method to enable parallel filling of the sealed cavities with Rb^{87}. We present a novel method by which the cells containing Rb^{87} are wax-sealed to produce individual Rb^{87} cells after dicing. For the fabricated Rb^{87} cells, we measured a hyperfine interaction linewidth of 956.8 Hz at the center frequency of 6.84 GHz, realizing a quality factor of 7.14 X 10^6.

INTRODUCTION

Atomic clocks are used for satellite communications, global positioning systems (GPS), cellular phone communications, radar and other applications requiring precision timing. Currently their use is limited due to their large volume (150-250 cm^3) and high power consumption (>10 Watts). Hence, the feasibility of realizing a microscale low-power chip-scale atomic clock (CSAC) is intriguing and could have high payoffs for precision timing applications. Atomic clocks are based on the hyperfine energy shifts of the electronic states due to the electron-nucleus spin interactions. In most cases alkali atoms are used due to a single electron in the outermost shell, resulting in a well-defined singular hyperfine transition. The energy shifts in many cases are in the gigahertz range. By populating the atoms in the higher energy state by optical pumping, and then measuring the absorption under a microwave signal corresponding to the hyperfine energy, one can obtain a very pure microwave frequency source. The purity or the quality factor of these sources is limited by the coherence time of the atoms, which is determined by collisions the atoms undergo with other atoms and the chamber. In many atomic clocks, the coherence length is maintained by creating polarized atomic beams that are used up when they hit the detector. In the most common rubidium or cesium clocks, the alkali atoms are immersed in a package filled with inert gas such as argon, neon, or nitrogen. The atomic collision of the alkali atoms with the gas atoms is elastic leading to the preservation of the alkali atom hyperfine atomic energy state. However if the atoms collide with the chamber surfaces, the coherence is lost. Therefore, miniaturization of the alkali-vapor-inert gas chamber could lead to broadening of the atomic transition due to higher surface to volume ratio. Hence, a key question is if the linewidth of a micromachined device can be as narrow as that of macroscale resonance cells. In this paper we demonstrate that a batch fabricated micromachined cell can have linewidths less than one kilohertz (1 kHz). A second consideration in clock design is the method of atomic interrogation.

One popular candidate for miniaturized atomic clocks is the use of VCSELs (vertically cavity surface emitting laser) with the output wavelength tuned at the optical transition of the alkali atoms [1,2] using the coherence population trapping technique. The laser light is modulated at half the hyperfine frequency to create coherent population trapping of atoms in the laser beam pathway. The laser modulation frequency is stabilized by feedback of the absorption of the light. One drawback of this approach is the drift in the laser frequency due to temperature variations, necessitating very accurate temperature control. The temperature control will require considerable power, making the advantage of the small size optical source less useful. In contrast the traditional Rb-based clocks utilize plasma lamp-based pumping. In this approach the resonance cell is pumped with photons from a Rb^{87}/buffer gas plasma lamp. The emitted photons are then filtered by Rb^{85} atoms which absorb photons corresponding to only one of the emitted photon energy levels. The Rb^{85} can be mixed in the lamp itself, or can be a separate filter cell. The resulting photon flux is then incident on a resonance cell where the absorption of these highly specific photons is measured as the frequency of a microwave magnetic field is phase modulated. The advantage of plasma lamp technique is that the lamp-generated photons are already specifically tuned to that needed to sample the resonance cell rubidium atoms, requiring less temperature tuning compared to that for VCSELs. The temperature stability requirement for the lamp is to control the temperature to within one Kelvin, which is easier than that for VCSELs. The disadvantages of the plasma lamp approach include possible high power consumption for realizing spectrally pure plasma at the microscale.

We present a clock architecture using the plasma lamp and RF interrogation of the resonance cell using Rb^{87}. Commercially available atomic clock systems typically use resonance cells fabricated out of glass tubing. The fabricated glass cells are individually filled with Rb^{87} and sealed by fusing the glass inlet. Some of the recent chip-scale resonance cell fabrication has been done using anodic bonding but each cell is filled serially, which would still keep the cost of the end products prohibitively high. In this work, we present a novel way of batch fabricating Rb^{87} cells to address some of these issues. We also present results of linewidth measurements using batch fabricated cells. We experimentally confirm the hyperfine-resonance by RF-interrogation of the fabricated cells inside a commercially available clock resonant cavity.

MICROMACHINED CAVITIES FOR Rb^{87} CELLS

A method for batch fabrication of Rb^{87} cells is described in the following sections. Rb^{87} cell fabrication uses anodic bonding of a bulk-micromachined silicon wafer to a glass wafer, which

Travel support has been generously provided by the Transducers Research Foundation and by the DARPA MEMS and DARPA BioFlips programs.

0-9640024-5-0/hh2004/$20©2004TRF
DOI 10.31438/trf.hh2004.6

poses thermal constraints. Anodic bonding requires high temperature (~ 400˚C) processing, while the melting point of Rubidium (39.3˚C at 1 atm) is low. Therefore Rb^{87}/buffer-gas cannot be placed before the bonding process. To solve this, we have developed a method to fill an entire wafer of cavities (after wafer-bonding) with Rb^{87}-vapor and buffer gas, and then seal each cell with a low-melting-point high-molecular-weight wax.

Figure 1 describes the three-mask process flow to batch fabricate the Rb^{87} cells. We use four-inch double-side-polished high-resistivity silicon wafers to realize the cells.

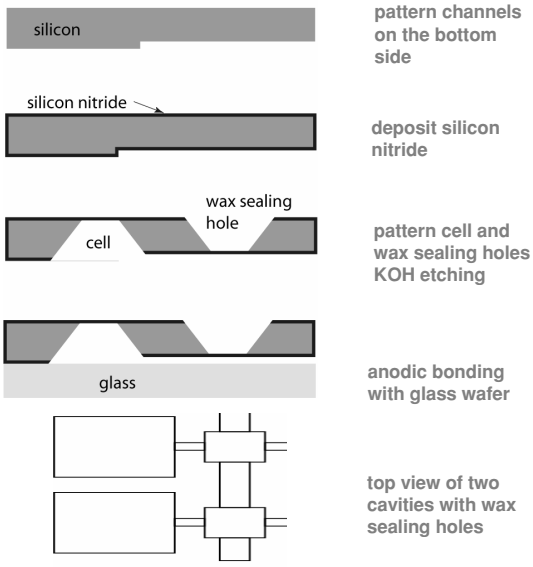

Figure 1. *Batch fabrication of Rb^{87} cells using anodic bonding and wax-sealing.*

The first mask step defines channels on the back side of the wafer. We then deposit 1 µm of low-stress LPCVD Silicon nitride (SiN) to act as an etch mask, and form membranes for subsequent process steps. Mask 2 and 3 define the back side cell cavity and the front side wax sealing hole. An anisotropic etch (20 % KOH, 80˚C) of the results in the final structure. Several cavities on the backside are connected by the channel, and in turn to an input cavity. Finally, the cavities on the backside are sealed by anodically bonding to glass wafer (Corning 7740) forming a wafer sandwich.

THERMAL CHASING OF Rb^{87}

Figure 2 shows an input cavity connected to a cell cavity. A glass capillary is attached to the inlet using a commercially available vacuum-compatible epoxy-based seal (Torr seal). Anodic bonding of a square glass capillary is also a way to attach the glass tubing to the wafer sandwich.

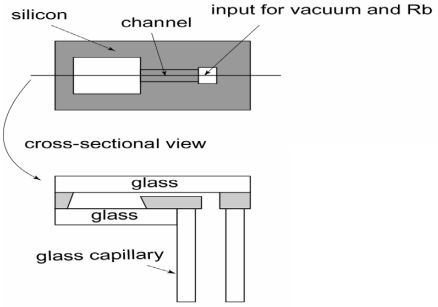

Figure 2. *An input cavity connected to several cells. The attached glass capillary connects to a Rb^{87} reservoir.*

The wafer sandwich is pumped down to ~10^{-8} torr by connecting the inlet pipe to an ultra-high vacuum (UHV) system via glass blowing. A molecular flow resistance and capacity models for the flow path was developed to calculate the time to reach 10^{-6} torr pressure in the deepest cavity. This calculation yields a pumpdown time of about two hours. The entire wafer is kept at 70˚C and pumped down overnight to bake out any impurities. After the pumpdown, the wafer is filled with nitrogen to 20 torr pressure. The glass cavity is filled with Rb^{87} from a small glass transfer chamber. Then the inlet with solid Rb^{87} is sealed, creating a Rb^{87} reservoir at the entry point of the wafer (Figure 3). The wafer sandwich is then heated uniformly at 70˚C. The Rb^{87} reservoir is heated to 90˚C. The cavities are flooded with a pool of isotopically pure Rb^{87} by creating a pressure driven flow or thermal "chasing".

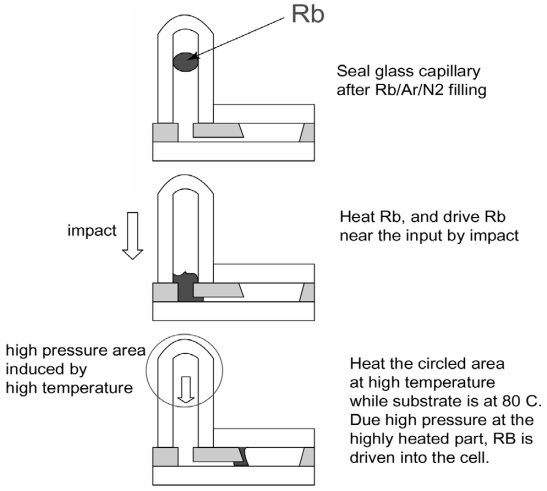

Figure 3. *Pressure driven flow from reservoir in to Rb^{87} cells.*

THE WAX-SEALING PROCESS

After filling the cavities with Rb^{87}, the individual cells are sealed and isolated as illustrated in Figure 4 (left). First, the wax is molded into a micromachined mold to form wax strips that intimately fit into the anisotropically etched wax seal holes.

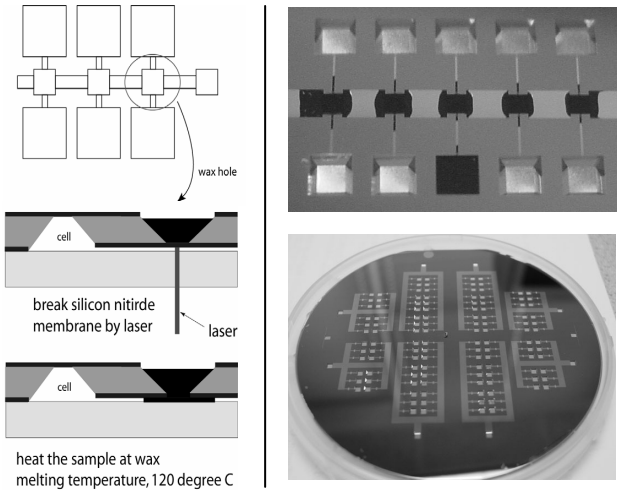

Figure 4. *(Left)Laser drilling is used to create holes that allow wax to penetrate and seal channels after Rb^{87} and buffer gases are filled. (Right).Photographs of one section of formed cells and an entire wafer of Rb^{87} cells.*

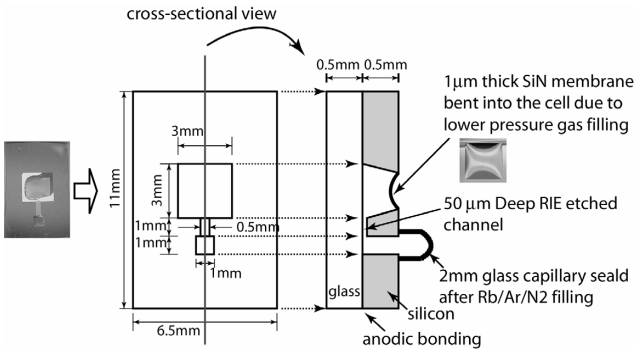

Figure 5. *The cross-section of a diced resonance cell and a pool of Rb^{87} in a bent-in SiN membrane indicate filled-in resonance cell.*

Next the wafer is heated to the wax softening temperature (90˚C). This causes the wax flow into the microchannels inside silicon nitride bulk micromachined windows through laser cut holes in the nitride membrane to form airtight seals. The wax (W-40) chosen has a low vapor pressure of 10^{-9} torr at 100˚C, which is higher than the sealing temperature (90˚C) and the clock operation temperature (75˚C).The wafer is then diced using a high speed saw to obtain 100 to 120 cells (Figure 4 right). Figure 5 shows the dimensions of a typical Rb^{87} cell fabricated by this method and the photograph of a Rb^{87}-filled cell.

LINEWIDTH MEASUREMENT

A RF absorption spectroscopy system as shown in Figure 6 is used to measure the linewidth of the fabricated Rb^{87} cells. The fabricated devices were placed in a RF cavity to measure the hyperfine resonance. The output of a RF-excited Rb^{87} lamp is projected into a temperature-controlled microwave cavity consisting of a filter cell consisting of Rb^{85}.

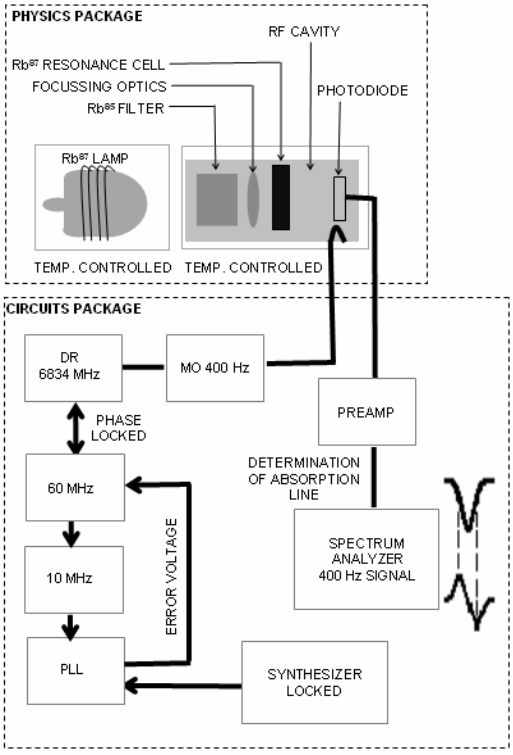

Figure 6. *Current atomic clock architecture*

The temperature control at 75˚C is necessary to maintain Rb in gas phase. A RF field of 120 MHz is projected into the microwave cavity, which is designed to have a TE 101 mode [4]. The microwave cavity resonates at its 57th harmonic, which is generated using a step-recovery diode mode with a modal frequency equal to the hyperfine frequency of Rb^{87}. A low phase noise quartz oscillator is used in a voltage controlled oscillator (VCO) loop to achieve a stable, low phase noise frequency to drive the cavity. Figure 7 shows a photograph of the physics package of the clock architecture shown schematically in Figure 6.

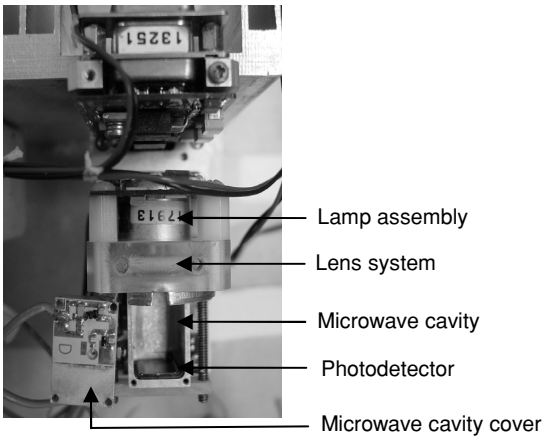

Figure 7. *RF-cavity of commercially available Rb atomic clock from Frequency Electronics, Inc. to measure atomic resonance of the Rb in the resonance cell.*

RESULTS AND DISCUSSIONS

For linewidths measurements, a 120 MHz input for RF field projection in to the microwave cavity was generated by using a 12 X multiplication of a 10 MHz input from a function generator. This frequency is swept over a small range (50 Hz) to observe the hyperfine resonance of Rb^{87}.

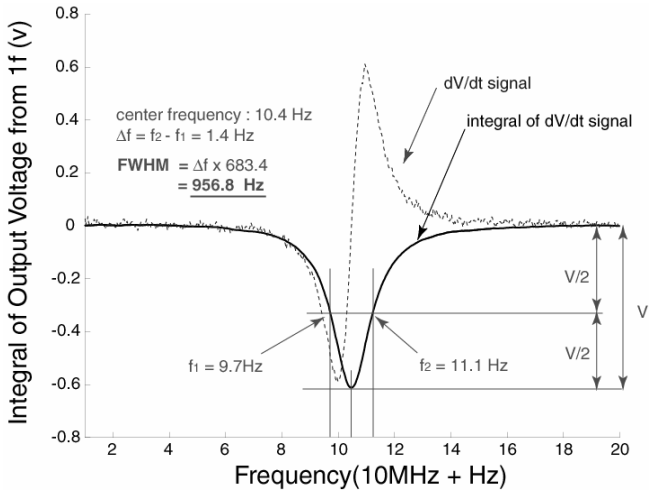

Figure 8. *A sub-1kHz linewidth measured with silicon resonance cell using setup in Figure 7, over the center frequency of 6.84 GHz.*

Figure 8 shows the first derivative of the microwave double resonance spectral line, obtained by modulating the microwave frequency at 120 Hz. A computer code finds the integrated output

of the measured data to obtain the hyperfine resonance linewidth of the cell of 956.8 Hz at the center frequency of 6.84 GHz, realizing a quality factor of 7.14 X 10^6.

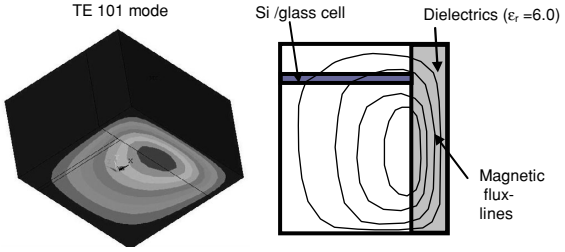

Figure 9. *Left: 3-D finite element analysis (using ANSYS) showing TE 101 mode for the RF cavity partially loaded with dielectrics (to reduce the physical dimensions of the cavity). Right shows a schematic sketch of the cavity containing a Si/glass cell. Change in resonant frequency between glass and Si cell, Δf = 37 MHz.*

The use of silicon poses a RF-design issue. The higher silicon substrate resistance increases loss for the RF cavity, and the higher dielectric constant reduces the effective speed of light. The electric field is more focused near the silicon cell, as compared to when a glass cell is placed. Figure 9 shows a finite element simulation of the resonant frequency of TE101 mode and field crowding at the resonant mode. Simulations for a glass resonance cell show a resonant frequency that is ~37 MHz higher than that for a Si resonance cell. The cavity resonance frequency shift implies that the microwave gain from the signal to atomic absorption was not as high as possible.

CLOCK ARCHITECTURE

Given our fabrication and demonstration of the resonance cells, and a process to fill bulk-micromachined cavities with Rb^{87}, we are pursuing to implement a complete physics package (Figure 10) that would enable power and volume reduction to the required for a CSAC. The resonance cell will be attached to a plasma lamp which utilizes radioactive thin films to excite the Rb^{87} and buffer gas mixture, in addition to high frequency and dc magnets to induce a low power plasma [5]. Two bulk micromachined cavities made out of Silicon are bonded in an inert ambience (glove box) to result in a sealed cavity with a small amount of Rb^{87}. This forms the Rb^{87} plasma lamp for optical pumping into another Rb^{87} resonance cell (top cavity in figure 10). A radioactive thin film of Nickel^{63} (Ni^{63}) can be used to project electrons in to the lamp cavity that induce optical transitions resulting in photons [5]. A RF coil integrated underneath the lamp cavity could be used to generate regulated plasma. The Allan deviation, $\sigma_y(\tau)$ of the atomic clock is expected to be

$$\sigma_y(\tau) \propto \frac{1}{Q \times S/N \times \sqrt{\tau}},$$

where Q is the physics package quality factor, S/N ratio is the signal to noise ratio dominated by the photo detector for light absorption, and τ is the integration time. Given the measured Q with 1 kHz linewidth is 7.14 X 10^6, and the required Allan deviation is 10^{-11} integrated over one hour, the signal to noise ratio required is 233. Our estimate is that in the case of shot noise limited optical detection, the required number of photons detected is 10^{10} photons/seconds or approximately 2.5 nW of optical power. This flux should be obtainable from the kinetic energy emitted from a 1-5 mCi radioactive source. The micro magnets are integrated into the cavities to create a magnetic field in the cavity that increases the residence time of the projected electrons in the lamp cavity, thereby increasing the plasma efficiency. The preliminary results we have obtained so far from the analysis and simulations of the proposed structure are merely a feasibility study and the results would be reported elsewhere. Further, the results underscore the importance of developing an inexpensive way of fabricating Rb cells for CSAC.

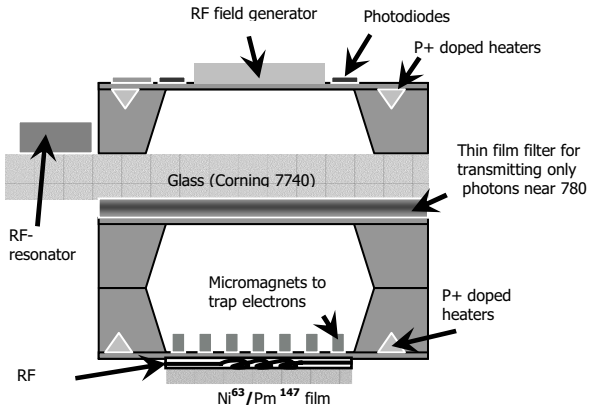

Figure 10. *Proposed Chip-scale atomic clock architecture. Two cavities filled with Rb^{87} and nitrogen buffer gases are required. The RF interrogation requires a SiN membrane with RF coils or micromechanical choppers to project B field into resonance cell.*

CONCLUSIONS

The main accomplishment presented in this paper is the realization of sub-1 kHz linewidth for a batch fabricated Rb^{87}/nitrogen cells. A process flow utilizing wax sealing was developed to address the conflicting requirements of vacuum filling and low-temperature sealing of microfabricated resonance cell. The rubidium hyperfine linewidth was measured using a RF-interrogation technique implemented using a commercial RF cavity used in commercial atomic clocks. The high quality factor obtained for the chamber confirms the possibility of achieving CSACs.

ACKNOWLEDGEMENTS

This project was funded under DARPA–MTO CSAC program. This research was conducted in part at the Cornell Nanofabrication facility, and Frequency Electronics, Inc.

REFERENCES

1. L. Lewis and M. Feldman, "Optical pumping by lasers in atomic frequency standards" *Proceedings 35th Annual Freq. Control Symp.* USAERADCOM, May 1981, pp. 612-624.

2. J. Kitching, S. Knappe, M. Vukicevic, L. Hollberg, R. Wynands, W. A. Weidmann, "Microwave frequency reference based on VCSEL-driven dark line resonances in Cs vapor", *IEEE Transactions on Instrumentation and Measurement*, Vol. 49, (6), 2000 pp. 1313 - 1317

3. M. Hashimoto, M. Ohtsu , "Experiments on a semiconductor laser pumped rubidium atomic clock", *Quantum Electronics*, IEEE Journal of , Volume: 23 , Issue: 4 , Apr 1987 pp. 446 - 4511.

4. H. E. Williams, T. M. Kwon, and T. McClelland, "Compact rectangular cavity for rubidium vapor cell frequency standards", *Proc. 37th Annual Frequency Control Symposium*, 1983; New York, IEEE, 1983, xi+529 pp. 12-17.

5. Hang Guo, Amit Lal, "Self-powered photon source", *TRANSDUCERS*, 12th International Conference on Solid-State Sensors, Actuators and Microsystems, June 2003 , Vol. 2 pp. 1474 – 1477.

EVOLUTION OF INTEGRATED INERTIAL MEMS TECHNOLOGY

Michael W. Judy
Analog Devices, Inc.
Micromachined Products Division
Cambridge, MA 02139-3556

ABSTRACT

Integrated inertial surface-micromachined MEMS technology is presented as an example of how accelerometers and angular-rate sensors are evolving in response to competition, innovation and customer requirements. These market forces are commoditizing the products and impacting key technologies such as fabrication, assembly, packaging, test, and design. Current and future directions of integrated inertial MEMS technology will be disclosed, as well as how these advances will enable both future inertial and non-inertial MEMS products.

BACKGROUND

Micromachined inertial products have been manufactured in volume since the mid 1980's, although initially in small volumes and for characterization and instrumentation applications [1,2]. These non-integrated accelerometers and gyros were bulk-micromachined sensors using predominately piezoresistance to measure the displacement resulting from an applied acceleration or angular rate. The limited application of MEMS inertial sensors was due to their high cost relative to other simpler devices. Low-performance applications, such as measuring tilt or bump detection, were adequately met by mercury switches and pendulums. When the US government mandated that all cars must have airbag safety systems, it created what Peterson called a "starved market segment" [3]. This market required a high-volume (>10^7units/year), low-cost, high-reliability, high-quality, and high-performance accelerometer. Although the bulk micromachined sensors met the performance specifications, they were lacking on the other criteria, especially a path to low cost.

Polysilicon surface micromachining, which had been developed during the early 1980's, offered an attractive alternative that sacrificed some performance specifications for lower costs and higher quality. The reduced performance was due to the much smaller inertial masses that are created using surface micromachining. A typical bulk micromachined sensor mass is approximately 1 mg while a surface micromachined sensor mass is 1 µg, or 1000 times lower. The lower mass translates into more Brownian noise, higher resonant frequencies and lower spring constants or restoring forces. Surface micromachining; however, promised much lower costs through smaller sensors and resulting die sizes, more compatibility with standard IC fabrication and assembly techniques, and reduced integration complexity between circuits and MEMS.

Recent competition to access the rapidly growing market for inertial sensors in cars, in particular the burgeoning low-g market, has been quite acute. There are more than a dozen companies with over 100 products to address these markets. Two broad classes of MEMS integration strategies have been developed: one-chip and two-chip solutions – otherwise known as integrated and unintegrated. The technology followed by most companies (e.g., Bosch, Motorola, STMicro, Infineon, Kionix, etc.) is the two-chip solution where a MEMS-only chip and a companion electronics chip are combined in a single package. The primary advantage of this approach is that the MEMS and circuit processing do not interact, thus allowing each process and design to be optimized independently and quickly. This approach allows the company to focus its resources on the value added parts of the product: the circuit and MEMS design and the MEMS process. The other advantage of this approach is that the total processing cycle time is less. The disadvantage is that a considerably larger sensor is required to compensate for the additional parasitic capacitances. This makes it very difficult to migrate to smaller less expensive packages. The one-chip solution, or integrated solution, has the advantage of a smaller MEMS structure and thus resulting die size. This provides access to much smaller packages and thus a path to lower costs. The down side is that this process has more complexity, predominately due to circuit-MEMS interactions, and has longer fabrication time and thus longer product development time. Neither approach, integrated or unintegrated, has dominated the market, nor are they likely to do so in the near future.

The application of accelerometers and gyros in cars over the last decade has multiplied from one accelerometer in the center module to more than a dozen accelerometers and gyros participating in not only passive but also active safety systems. The passive safety systems include all of the airbag systems, seat-belt tensioners and rollover protection. In an active safety system, like vehicle dynamic control (VDC), certain systems within the automobile are temporarily under the control of the VDC system, not the driver. As a result of this relinquishment of control, the criteria for MEMS quality and reliability have become even more stringent. The low-g market has been much more dynamic with excitement about a given application followed by a moderation as the real demand for the application did not materialize into high-volume demand. An example of this type of market is using inertial inputs for computer game controllers (e.g., Nintendo Gameboy). The emerging low-g markets are in laptops, cell phones, and PDAs. In these new markets the sensors are used for all manner of bump/shock sensing and tilt sensing such as menu scrolling and selecting.

TECHNOLOGY EVOLUTION THEMES

High-volume inertial sensors, as with all markets, have been subject to the following pressures through competition and the generation of new market opportunities:

1. Lower cost
2. Smaller size and weight
3. Higher quality & reliability
4. Higher performance
5. Total ownership cost

The first, and many would argue the second and third priority, is reducing the price of the MEMS component. For all high volume markets, price is the governing criteria. If the component suppliers

0-9640024-5-0/hh2004/$20©2004TRF
DOI 10.31438/trf.hh2004.7

are unable to meet the price expectations, the system manufacturer will likely either stick with an existing solution that may have worse performance or delay the entire program. Depending on the market there are different levels of quality and reliability requirements. Automotive suppliers, for example, demand <1 ppm failures in the field, while consumer electronic equipment suppliers have less stringent requirements.

In response to the market pressures discussed above three different technology development themes have been followed by every competitor:

1. Higher levels of efficiency (e.g., die size)
2. Increasing use of standard IC equipment (e.g., foundries)
3. Product differentiation (e.g., performance & support)

Increasing efficiency affects every aspect of design and manufacturing. All competitors have worked hard to produce smaller structures and packages with more functionality and higher performance. This evolution puts ever more emphasis on collaboration between all aspects of design and manufacturing, to resolve both yield and quality issues, but also to design the next-generation sensor with improved performance. The interdisciplinary nature of MEMS demands this intimate collaboration. The special processing-equipment requirement for MEMS devices means that additional fixed expenses must be incurred beyond those typical for any microelectronics facility. Improving the technology to remove these requirements provides access to lower cost foundry and assembly facilities; however, it also creates dependence as well. The final step of product differentiation usually focuses on some aspect of the product, such as package size or a performance specification. It is also vital to provide an adequate customer-support organization to help customers with implementation of the components in both their production lines as well as their intended applications. This goes beyond conventional design-in assistance and extends into system (i.e., mechanical design) and manufacturing process development.

FRONT-END INTEGRATED MEMS PROCESS TECHNOLOGY

A current high-volume integrated inertial MEMS process technology is the Analog Devices process called *i*MEMS®. This process has been developed over the past 15 years and is a robust 3-µm BiCMOS process integrated with a surface-micromachined polysilicon MEMS device (Figure 1) [4]. Other important characteristics of the process include: laser trimmed thin-film resistors and both 5-V and 24-V devices. Over the last several years at ADI a next-generation integrated MEMS technology named SOIMEMS has also been developed and will also be discussed.

There is another integrated technology that is currently being commercialized at MEMSIC, where a thermal accelerometer is integrated with foundry CMOS. This process incorporates a low fixed cost manufacturing process with an X-Y accelerometer that is not susceptible to several failure mechanisms intrinsic to capacitive based sensors. The performance of these devices appears to be limited, but time will tell if the emerging applications will be able to use these devices. If so, this approach will be very effective within its niche.

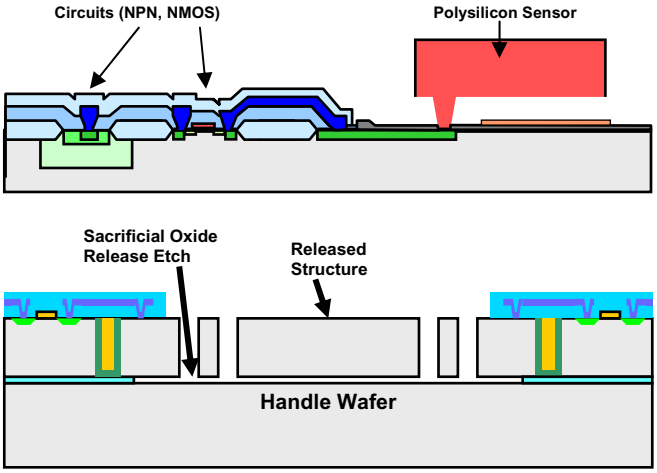

Figure 1: *a) i*MEMS*: 3-µm BiCMOS interleaved with 2-4 µm polysilicon. b) SOIMEMS: 0.6-µm CMOS integrated with 10-µm SOI MEMS devices.*

***i*MEMS:** The circuit-processing and MEMS-processing steps are interweaved in *i*MEMS. The process begins with the circuit process up to gate planarization, and then continue with all MEMS processing prior to release, then finishing the circuit process (i.e., metallization and passivation), and finally removing the sacrificial oxide. Several different versions of the core *i*MEMS technology have been used in production. Each version improved on the key metrics of performance, yield, reliability, and area utilization. The primary feature is the migration to thicker polysilicon for the device layer. Increasing thickness, or rather increasing the aspect ratio of the resulting capacitor gap, increases the sensitivity of the differential capacitors, provides a stiffer suspension and produces a more heavily damped sensor. The original polysilicon thickness was 2 µm and has migrated to 4 µm. In addition, the number of interconnect layers under the released structure were increased to two, which facilitated complex designs such as the ADXRS150 gyro. Finally, the sacrificial oxide thickness was increased to reduce the parasitic capacitance of the structural layer, which impacts noise performance.

Table 1: *Details of the different versions of the i*MEMS *process. *Version 3 has reduced parasitics for the MEMS interconnect layers.*

*i*MEMS Version	Ground Layer	Interconnect Layers	Sacrificial Oxide	Poly Si Thickness
0	Bare Si	1	1.6 µm	2 µm
1	Poly Si	2	1.6 µm	3 µm
2	Poly Si	2	2.0 µm	4 µm
3*	Poly Si	2	2.0 µm	4 µm

SOIMEMS: To meet the demands of higher efficiency, higher functionality and more robust structures, ADI has been developing a next-generation process over the last several years. The result is a 0.6-µm BiCMOS double-metal process with post-package trim capability. The process integrates MEMS and electronics using a 10-µm-thick SOI layer for both the electronics and MEMS structures (Figure 1). The MEMS structures are isolated from the surrounding SOI by trench isolation. The integration strategy is similar to *i*MEMS in that there is MEMS processing at the beginning (trench isolation) and the end of the entire process (structure etch and release), but has the advantage that all of the circuit processing is done in one process module.

This process module is run in a circuit foundry instead of a custom fabrication facility, thus reducing fabrication cost.

The primary challenge for this approach has been to engineer the pre-processed wafers, such that there is a minimal impact on the foundry process module. The complexity of this task should not be trivialized and the adoption of a finer geometry CMOS process would be met with similar development challenges and times.

Release & Surface treatment: Both *i*MEMS and SOIMEMS use a release process where temporary photoresist pedestals prevent the structures from collapsing during drying. Vapor HF is a viable alternative that is used by many of the MEMS-only competitors that removes the requirement for photoresist pedestals. An alternative protection layer, such as polyimide, is required since photoresist is permeable to vapor HF.

An effective surface treatment is also required to insure that the MEMS devices do not stick when brought into contact during subsequent handling. In the original anti-stiction coating process at ADI, the coating agent was dispensed into the ceramic package just prior to lid seal. Several years ago a wafer-level anti-stiction coating process was put into production. This improved the uniformity of the coating as well as removed the requirement for a special processing step in assembly.

BACK-END PROCESS TECHNOLOGY: ASSEMBLY, PACKAGING & TEST

The main items of interest in back-end processing are how to prevent the released MEMS device from being damaged or contaminated during the assembly process and to protect the device from the environment during its intended and unintended use.

Dicing: The initial assembly flow starts with dicing the completed wafers. To protect the released MEMS devices from the slurry during dicing, a temporary cap is created from two layers of tape suspended on a film frame [6]. One layer of tape is uniform and one has holes punched though it to create a cavity that will cover the MEMS device during dicing.

Wafer Capping: While the above dicing process works well, the released MEMS devices are still exposed to the environment of the assembly facility during the remainder of the assembly flow. This requires working with the assembly contractor to improve cleanliness and to institute process monitoring and inspections to insure that contamination is minimized to an acceptable level. Since the current failure rate in cars of the airbag accelerometers built with this process is <1 ppm the goal has been achieved. However, this assembly flow is custom and thus costs a premium when compared with open-market assembly of integrated circuits. This cost driver has motivated the development of a wafer-capping approach (Figure 2). The cap is fabricated with a combination of deep silicon etching and wafer sawing and is bonded to the MEMS die directly over the circuitry using a screen printed glass-frit seal [7]. These techniques provided a cap with tight design rules that protect the structure during the assembly flow as well as establish improved control over the environment surrounding the release structure. The capped wafer can then be sent to any assembly contractor, which will significantly reduce cost.

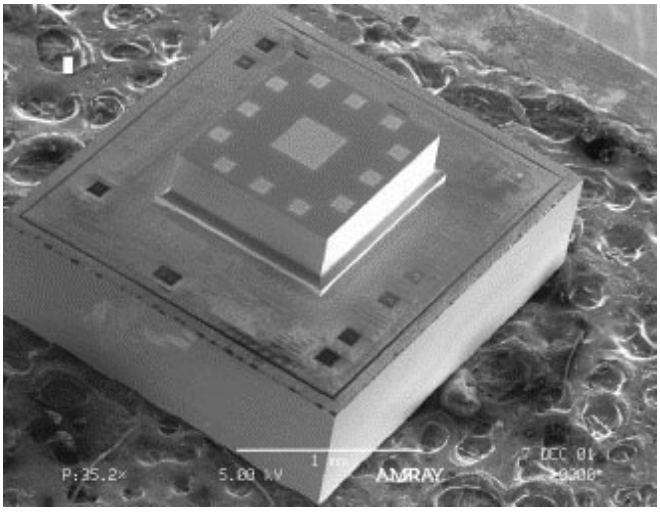

Figure 2: *SEM image of a capped iMEMS® accelerometer.*

Package evolution: MEMS packaging has traditionally been the most expensive part of the manufacturing process so there is great incentive in adopting lower cost packaging solutions. ADI is no exception to this industry wide trend. Figure 3 shows the evolution of the accelerometer packages at ADI with each package shown at the same scale. At each stage of development a standard IC package was adopted for integration with the MEMS devices. For the first 3 packages, hermetic cavities were created to house the released MEMS dies. With the development of the capping technology described above, low cost plastic packaging has become accessible. The most prevalent plastic package is the Lead Frame Chip Scale Package (LFCSP); commonly known by the trademarked assembly contractor names of MLF, QFN and MLP. This leadless package produces a smaller and lighter package than an equivalent leaded package such as an SOIC. The LFCSP package is also desirable from a manufacturing point of view as it uses a very similar process to leaded transfer molded packages, thus reducing capital investments.

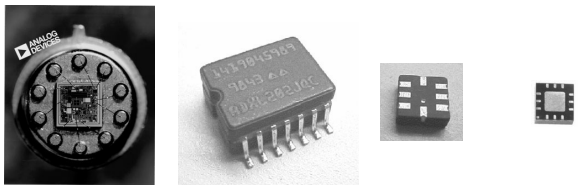

	Header	Cerdip/Pak	LCC	LFCSP
X_{mm}	10	10	5	4
Y_{mm}	10	10	5	4
Z_{mm}	7	5	3	1.5 → 0.9

Figure 3: *The package development of ADI's accelerometer product line: TO-100, CERPAK, LCC, LFCSP. The packages are shown at the same scale.*

Test: In high-volume markets, automated testers are used to keep costs at a minimum. Figure 4 shows a typical IC tester and handler combined with a shaker which applies the appropriate input acceleration or angular rate. Although the tester-handler is standard equipment, the incorporation of a shaker means that the resulting platform is custom equipment and thus more expensive than on the open market. In addition to the typical electrical tests, the following sensor specifications must be measured; sensitivity,

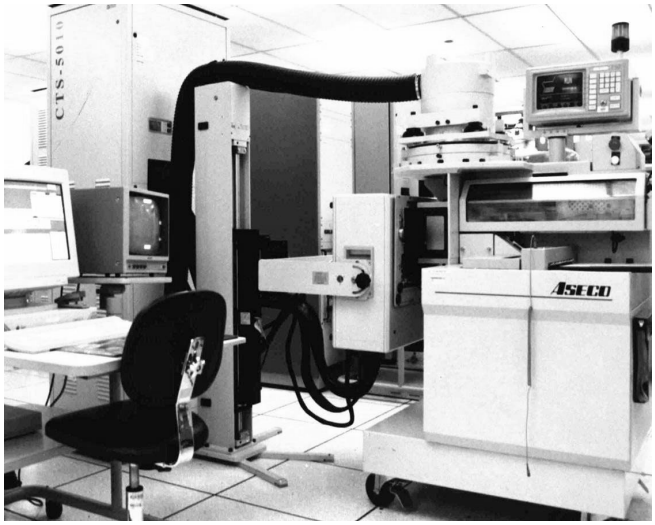

Figure 4: *Automatic tester with integrated handler.*

offset, self-test, and noise. Insuring sensitivity is measured to within ±1% is a difficult challenge that is accomplished by using calibration standards that are measured at the same time as the device under test. Noise is a critical performance parameter, and great care must be taken to insure that electrical as well as mechanical noise and vibration do not interfere with this measurement. This has become an even greater challenge as the throughput rates of the testers are pushed faster. The development of multi-axis accelerometers and gyroscopes have also pushed the test technology.

DESIGN

Figure 5 shows the product evolution of the airbag-accelerometer family at ADI. The most obvious characteristic is the factor of 4 reduction in die size through all 4 generations. The first 3 reductions were due to improved circuit architectures as well as MEMS designs using the subsequent generations of *i*MEMS. The ADXL50 was chosen to be a force-feedback design because the stability of the polysilicon was not well established.

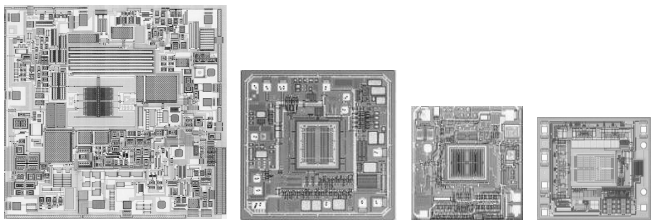

	ADXL50 (1994)	ADXL76 (1996)	ADXL78 (2001)	ADXL40 (2004)	
Die Area	10.8	5.4	2.7	2.5	mm^2
MEMS Area	0.43	0.38	0.27	0.22	mm^2
% MEMS	4.0%	7.0%	10%	8.8%	
Cs	100	100	40	160	fF
fo	25.0	24.5	24.5	12.5	kHz
Noise	6.0	1.0	1.0	1.0	mgee/ rt.hz
Offset	3.0	1.0	0.5	0.5	gee

Figure 5: *The airbag crash sensor family of ADI – from the original ADXL50 (1991) to the 4th-generation accelerometer using the new SOIMEMS process technology.*

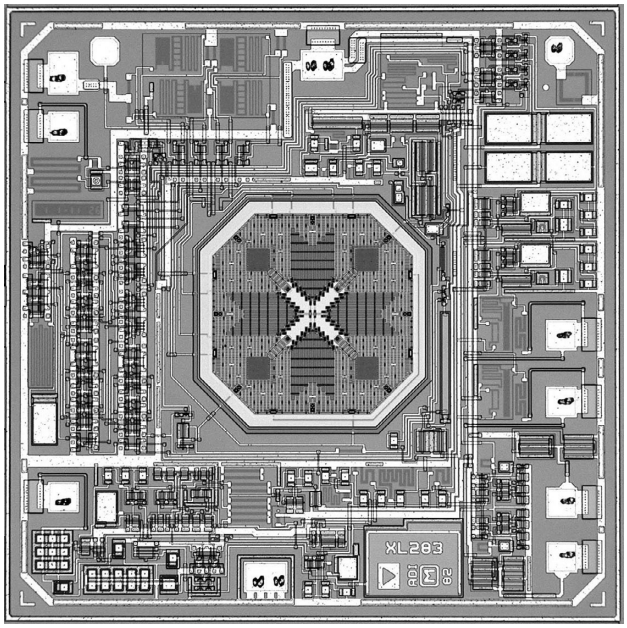

Figure 6: *ADXL203: a 2-axis accelerometer with ±50 mgee null bias stability and 110 µgee/rt.hz noise.*

After proving the stability of polysilicon as a structural material, an open-loop architecture was implemented in the ADXL76, which provided a factor of two decrease in die size.

The next factor of 2 decrease in die size with the ADXL78 also produced a more robust sensor to overload accelerations. This had become a requirement when the accelerometers were placed in the periphery of the automobile, which is exposed to much higher accelerations during impacts (i.e., side impacts). This device uses a differential circuit and MEMS architecture and feedback (i.e., not force feedback) to help reduce any undesirable overload response.

The most recent step in airbag crash sensors is the ADXL40, which uses the SOIMEMS technology with post-package trim. The scale factor and bandwidth of the part can be electrically selected by the user. Like the MEMS-only sensors that have similar electrostatic gap aspect ratios, the ADXL40 uses squeeze film damping to preserve velocity during an overload event.

In addition to the reduction in die size, improving key performance specifications has also been a goal. A good example of how the performance of a MEMS device has been improved is the ADXL203, a second-generation dual-axis accelerometer with ±1.7 gee full-scale dynamic range (Figure 6). The first dual-axis accelerometer, the ADXL202, had a null accuracy of 500 mgee which made DC measurement of tilt difficult. With the advent of VDC systems in cars, it was recognized that there was a clear market for a DC capable dual axis accelerometer. Since post-package trimming was not available at the time, the designers needed to produce a device that would be inherently insensitive to packaging and thermal stresses. It was recognized early that by changing the mounting of the spring-mass and differential capacitor finger system from perimeter to die center that the magnitude of the die distortion that causes the offset shifts would be significantly reduced. Through experimental test chips and extensive modeling, the optimal position of anchors was obtained. The resulting ADXL203 improved the null accuracy to a typical value of 25 mgee and a total of ±50 mgee over the operating

temperature (-40º C to 125º C). The noise of the accelerometer was also reduced to 110 µgee/rt.hz by improving the beam biasing architecture. These performance improvements allowed the product to measure absolute tilt to 3 degrees and resolve tilt differences of less than 0.01 degrees.

The most challenging device by far to develop has been the ADXRS150, a vibratory rate gyro (Figure 7) [8,9]. The two uncoupled structures are oscillated in anti-phase and the resulting coriolis motion is synchronously detected by the integrated accelerometer. The minimum detectable coriolis displacement is $1.6x10^{-4}$ Å or about 2 orders of magnitude lower than the ADXL203. This level of performance requires the structures to be manufactured with improved precision in order to prevent structure imperfections from producing feedthrough of resonator motions into the coriolis signal. The development of the gyro is a great example of the strong design and manufacturing interaction that is required by all MEMS products. During the development of this device the designers requested that the process engineers guarantee the CD matching within a gyro structure be 20 nm. Initially, this level of matching was viewed as a show stopper for a high-yield gyro. However, through careful data collection, experimentation, and design improvements the manufacturing requirements of the gyro were met successfully.

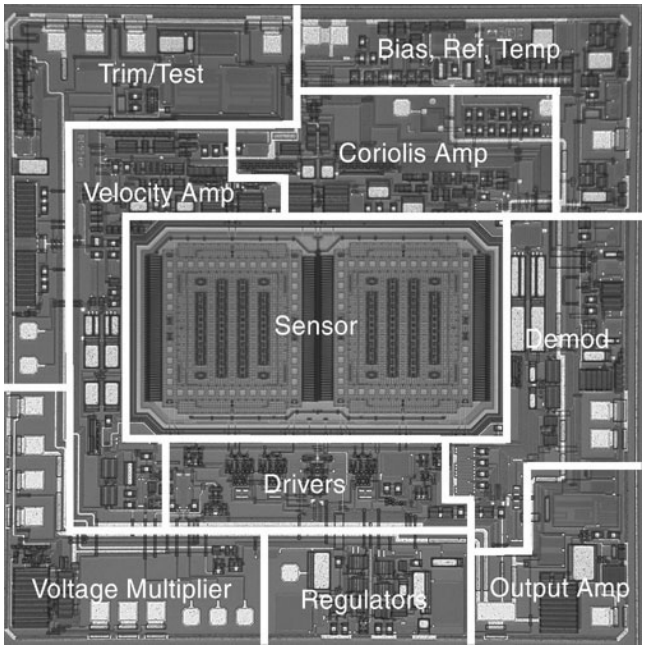

Figure 7: *ADXRS150: a z-axis gyroscope with 0.05 deg/rt.sec noise integrated on a 3x3 mm die.*

DESIGN-MANUFACTURING INTERACTION

As stated earlier, MEMS products require a very tight coupling between design/product development and manufacturing. Around each product at ADI is a cross-functional team of design and manufacturing people. This highly integrated product-development method is in stark contrast with what typically transpires with most integrated-circuit products, especially purely digital circuits. Here the designer works in isolation of the circuit technology, relying solely on the design and layout specification to guide their design. Even though integrated MEMS technology has become a mature process, it is these close working relationships that have enabled the successful release and enhancement of all of the integrated inertial MEMS products at ADI.

There are of course layout and design specifications that are provided to the MEMS designers. Manufacturing tolerances are also provided, such as the mean and standard deviation of all the critical MEMS geometry and material properties. Some of these parameters are a result of in-line monitoring of product wafers, while others are tracked or characterized on a more infrequent basis. The incorporation of these tolerances into the design is vital to producing high-yield products. Use of statistical-processing controls, such as C_{pk} monitoring, can be use to monitor and control the health of the manufacturing line. The close working relationship between design and manufacturing has produced MEMS products with yields the same as integrated circuits products without MEMS as well as a profitable business.

FUTURE TECHNOLGY & PRODUCTS

The next generation of products to address the inertial automotive and consumer electronics markets will continue down the paths of higher efficiency/utilization, increased use of standard IC equipment, and further product differentiation. As described throughout this paper, the die sizes will continue to drop. A 1-mm^2 die accelerometer is within reach with the integrated approach, which will drop the die cost by another factor of 2.5. It is unlikely that the two-chip approaches will reach even 3-mm^2 due to the large sensors required by the extra parasitic capacitances. A successful *in-situ* capping technology might be released to manufacturing, which would reduce the die sizes even further.

Most inertial-sensor manufacturers are working on or have released a LFCSP-style package. The next stages will reduce the size and thickness of these packages. The thickness, surprisingly, is the more stringent requirement which should approach the industry standard of 0.9 mm. Eventually, the wafer-scale packaging (WSP) trend in integrated circuits will be adopted by MEMS companies. In this package the plastic package is completely removed and the silicon die is flip-chip mounted directly to the board.

Testing of inertial devices will also be an area of very active development and should evolve to the point where the application of an acceleration or angular rate will not be required. Instead, an electrical stimulus will be adequate to insure the device has met the required performance tolerance. With the evolution to smaller and lighter packages, such as WSP, there will be many more challenges with simply handling the packages and making reliable contacts. Part of this progress will be the increased understanding of the customers to the real requirements for their applications. For example, does a product need to have DC response when relative responses are all that are required? As a result, sensor-specification requirements might relax if lower prices can be obtained.

The evolving capping and packaging technologies and integration techniques will lead to other product developments beyond inertial sensors. The core technology of surface micromachining using polysilicon and SOI has already demonstrated a great variety of devices, such as oscillators, variable capacitors, pressure sensors, and microphones. However, the cost of these devices has been prohibitive for the development of most of their corresponding high-volume markets. The cost structures and technology evolution of inertial MEMS will

eventually allow access to these other high-volume non-inertial markets.

SUMMARY

Inertial MEMS products are commodities. The selection of a part is made almost solely on the unit price because there are at least two vendors who provide similar performance, quality, and reliability for most high-volume products. To continue to be competitive both in the existing markets and emerging markets, a highly active technology development is ongoing throughout the entire industry. Even though ADI produces 10^6 MEMS devices/week it is nowhere near enough to independently drive to the lowest cost on a custom process. To meet customer expectations, MEMS manufacturers must adopt existing capacities and capabilities anywhere possible for fabrication, assembly, and test. Perhaps in the not-too-distant future, when accelerometers reach $1/axis or less, will the total market revenue be great enough to begin to drive the costs down. Until that time, we can look forward to many more evolutions of inertial MEMS products and likely a few new applications that leverage this technology base.

ACKNOWLEDGEMENTS

Thanks go to everyone who has contributed to the success of ADI's inertial MEMS technology. This paper presents the accumulated accomplishments and hard work by everyone within the Micromachined Products Division. The author would also like to thank the MPD management team for supporting the publication of the overview of ADI's technology evolution.

REFERENCES

1. S. C. Terry, "A Miniature Silicon Accelerometer with Built-In Damping," *Solid-State Sensor and Actuator Workshop*, Hilton Head Island, S.C., June 1988, pp. 114-116.
2. P. W. Barth, F. Pourahmadi, R. Mayer, J. Poydock, and K. Peterson, "A Monolithic Silicon Accelerometer with Integral Air Damping and Overrange Protection," *Solid-State Sensor and Actuator Workshop*, Hilton Head Island, S.C., June 1988, pp. 35-38.
3. K. E. Peterson, "Bringing MEMS to Market," *Solid-State Sensor and Actuator Workshop*, Hilton Head Island, S.C., June 2000, pp. 60-64.
4. T. A. Core, W. K. Tsang and S. J. Sherman, "Fabrication Technology for an Integrated Surface Micromachined Sensor," *Solid State Technology*, Oct 1993, pp. 47-53.
5. K. H.-L. Chau, R. E. Sulouff, Jr. "Technology for the high-volume manufacturing of integrated surface-micromachined accelerometer products," *Microelectronics Journal*, vol. 29, 1998, pp. 579-586.
6. C. M. Roberts, Jr., L. H. Long, P. A. Ruggerio, "Method for Separating Circuit Dies from a Wafer," U.S. Patent 5,362,681, 1994.
7. L. E. Felton, M. Duffy, N. Hablutzel, P. W. Farrell, and W. A. Webster, "Low-Cost Packaging of Inertial MEMS Devices," *Proceedings of 36th International Symposium on Microelectronics*, Boston, MA, Nov. 2003, pp. 402-406.
8. J. A. Geen, "A Path to Low Cost Gyroscopy," *Solid-State Sensor and Actuator Workshop*, Hilton Head Island, S.C., June 1998, pp. 51-54.
9. J. A. Geen, S. J. Sherman, J. F. Chang, S. R. Lewis, "Single-Chip Surface Micromachined Integrated Gyroscope With 50°/hr Allan Deviation," *Journal of Solid-State Circuits*, vol. 37, no. 12, pp. 1860-1866.

PHASE NOISE AMPLITUDE DEPENDENCE IN SELF-LIMITING WINE-GLASS DISK OSCILLATORS

Seungbae Lee and Clark T.-C. Nguyen

Center for Wireless Integrated Microsystems(WIMS)
Department of Electrical Engineering and Computer Science
University Of Michigan Ann Arbor, Michigan 48109-2122, U.S.A.
Tel.:(734)764-3352, Fax:(734)647-1781, email:seungbae@umich.edu

ABSTRACT

Self-limiting 46.4-MHz series resonant reference oscillators employing a wine-glass mode disk micromechanical resonator to avoid hard limiting without the need for ALC have achieved measured phase noises of -113 and -134 dBc/Hz at 1kHz and far-from-carrier offsets, respectively. When divided down to 10MHz frequency for fair comparison with other oscillators, these values correspond to -126 dBc/Hz and -147 dBc/Hz, which now satisfy specifications for low-end cellular handsets. For these oscillators, $1/f^3$ phase noise is found to be independent of vibration amplitude for amplitudes below critical Duffing, which pares down the list of possible mechanisms to those that are amplitude independent.

I. INTRODUCTION

Although their exceptional Q (>10,000) and superb thermal and aging stability make quartz crystals the resonators of choice for precision reference oscillators in portable applications [1], their size and incompatibility with integrated circuits preclude true system-on-a-chip wireless solutions. On the other hand, electrostatically transduced vibrating micromechanical ("μmechanical") resonators have become increasingly attractive as frequency-setting elements in reference oscillators for communication applications due to their potential for direct integration or bonded merging with transistors onto single chips [2]-[5]. In particular, phase noise performance nearing the requirements of the GSM cellular telephone standard have recently been demonstrated via an oscillator referenced to an extensional-mode single-crystal silicon vibrating bar with a Q of 200,000, constructed using a thick-device-layer SOI process [6]. Although the resonator used in [6] lacked adequate temperature stability, another resonator based on surface micromachined polysilicon structural material was recently demonstrated with a temperature coefficient as low as -0.24 ppm/°C [7], a Q of 4,000 at 10 MHz, and a proven integrability with transistor electronics [2][5]. However, an oscillator based on this polysilicon resonator exhibited a $1/f^3$ phase noise component farther from the carrier than expected that prevented the oscillator from achieving GSM-like phase noise specifications (e.g., for 10 MHz reference oscillator, better than -120 dBc/Hz at 1kHz offset frequency, -130 dBc/Hz preferred) [8].

Recently, automatic level control (ALC) circuitry designed to limit the vibration amplitude of a micromechanical resonator in an oscillator has been found to successfully remove this $1/f^3$ phase noise [9], suggesting resonator transducer or mechanical nonlinearity as the source of this noise. Unfortunately, ALC removes $1/f^3$ noise at the price of carrier power, so the phase noise performance of ALC'ed oscillators still falls well below the needs of today's cellular wireless standards [9]. In addition, although a mechanism linked to resonator amplitude has been identified, an analytical model that accurately predicts the measured $1/f^3$ component has so far been elusive.

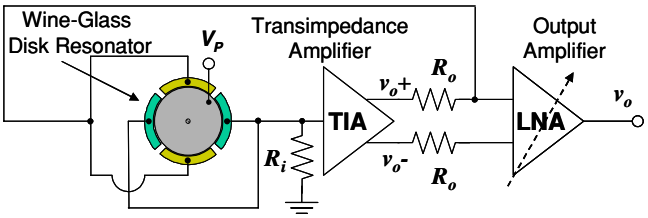

Fig. 1: Schematic of the series oscillator with transimpedance sustaining amplifier utilizing a wine-glass mode disk μresonator tank.

Pursuant to both better understanding the source of $1/f^3$ noise and achieving better overall phase noise performance, this work harnesses a recently demonstrated polysilicon wine-glass mode vibrating disk μresonator with high-Q even in air [10], and with higher power handling ability (i.e., linearity) than previous surface-micromachined resonators, to attain oscillators that self-limit before critical point Duffing nonlinearity without the need for ALC. By avoiding hard nonlinearity, these oscillators achieve 10-MHz-effective phase noises of -123 dBc/Hz at 1kHz offset and -147 dBc/Hz far-from-carrier under atmospheric pressure, which now satisfy specifications for some cellular handsets. Equally importantly, these oscillators also provide better insight into the amplitude dependence (or independence) of $1/f^3$ phase noise.

II. OSCILLATOR TOPOLOGY AND OPERATION

Like a previous oscillator design [9], the oscillator of this work uses a series resonant topology, shown in Fig. 1, in which the wine-glass disk is embedded in a positive feedback loop together with an off-chip NE5211 transresistance sustaining amplifier possessing sufficient gain to initiate and sustain oscillation. As shown, since the micromechanical resonator used for this work is a multiport device (as opposed to the one port devices used in previous work [8][9]), the dc-bias voltage V_P is directly connected to the resonator structure without the need for the bias tee used in [8][9]. Other than this and the use of a more advanced micromechanical resonator, the criteria governing start-up and sustenance of oscillation are identical to those described in [9]:

1. For Start-Up: $R_{amp} > R_x + R_i + R_o$
2. In Steady-State: $R_{amp} = R_x + R_i + R_o$
3. Loop Phase Condition: 0^o around the positive feedback loop

where R_{amp}, R_i, and R_o are the gain, input resistance, and output resistance, of the transresistance sustaining amplifier, respectively; and R_x is the series motional resistance of the wine-glass disk. As

Travel Support has been generously provided by the Transducers Research Foundation and by the DARPA MEMS and DARPA BioFlips programs.

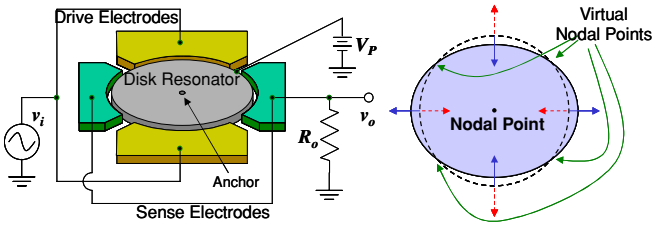

Fig. 2: (a) Perspective-view of a wine-glass disk resonator illustrating a typical two-port bias and excitation scheme, and (b) its mode shape.

will be described, this oscillator limits when its resonator R_x increases with amplitude to the point of satisfying criterion 2 above.

III. RESONATOR AMPLITUDE LIMITATIONS

Fig. 2(a) presents a more detailed schematic of the disk resonator with electrodes configured to excite the fundamental wine-glass mode shape shown in Fig. 2(b). The dc-bias voltage V_P applied to the disk effectively amplifies the force and motional output current induced when a resonance ac excitation voltage v_i forces the disk into resonance vibration. The motion is constrained entirely to the plane of the disk, with its perimeter expanding along one axis and contracting in the orthogonal axis about the center point, which remains stationary, acting as a node. Although four additional quasi-nodal points exist on the disk perimeter and thereby allow greater flexibility in the choice of support structure [10], this work simply anchors the disk at its center in order to maximize the available electrode area. The wine-glass resonance frequency f_o, goes as the inverse of its radius R, and can be obtained by solving the mode frequency equation given in [10]

At the amplitudes experienced during oscillator vibration, the force F needed to achieve a given vibration amplitude x for this electrostatically driven resonator becomes of a function of third-order Duffing nonlinearity [11] and is governed by the expression

$$\frac{F}{m_r} = \ddot{x} + \frac{\omega_o}{Q}\dot{x} + \frac{k_1}{m_r}x - \frac{k_3}{m_r}x^3 = \ddot{x} + \frac{\omega_o}{Q}\dot{x} + \omega_o^2(x - \mu x^3) \quad (1)$$

$$\text{where, } k_1 = k_{m1} - k_{e1}, \quad k_3 = k_{e3} - k_{m3}, \quad \omega_o = \sqrt{\frac{k_1}{m_r}}, \quad \mu = \frac{k_3}{k_1}, \quad (2)$$

and where m_r is effective mass of resonator; k_{m1} and k_{e1} are the linear mechanical and electrical spring constants, respectively; and k_{m3} and k_{e3} model their third-order spring nonlinearities. For the resonators of this work, the electrode-to-resonator gaps d_o are quite small, so $k_{e3} > k_{m3}$ (i.e., the third-order coefficient in (1) is negative), so *spring softening* occurs as the vibration amplitude increases. The resonance frequency then decreases as the resonator amplitude increases, resulting in a frequency response curve that bends leftward as amplitudes increase, as illustrated in Fig. 3, where the amplitude dependence of the peak (radian) frequency ω is governed by the expression [11]

$$\omega^2 = \omega_o^2 - \frac{3}{4}\frac{k_3}{m_r}x^2 \quad (3)$$

where ω_o is the radian resonance frequency at small amplitudes.

When the peak vibration amplitude exceeds the critical point:

$$X_{crit} \approx \frac{1.52}{\sqrt{\mu Q}} \quad (4)$$

the amplitude versus frequency curve bends to a point where there

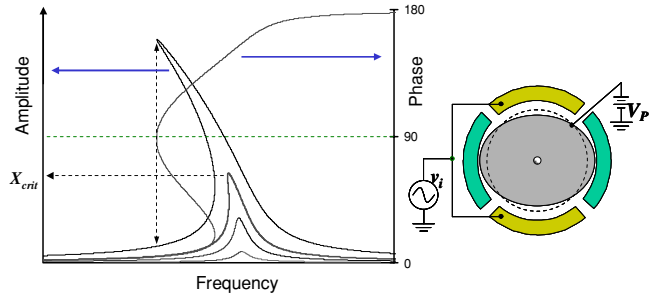

Fig. 3: Schematic depiction of the theoretical Duffing curve expected for large amplitudes.

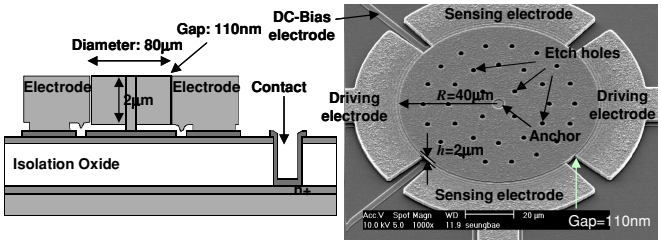

Fig. 4: Cross section and SEM of a 46.4-MHz wine-glass mode disk polysilicon μresonator, with dimensions indicated.

are three theoretically valid amplitudes for each frequency in the bent portion of the curve. This amplitude ambiguity leads to unstable steady-state operation [2], which then results in excessive phase noise. Needless to say, operation at amplitudes past the critical point are not recommended, so X_{crit} effectively defines an amplitude threshold that then sets the maximum rms power handling ability of the resonator to

$$P_o = \frac{1}{2}\frac{\omega_o k_1}{Q}x^2 \le \frac{1}{2}\frac{\omega_o k_1}{Q}X_{crit}^2 = 1.16\frac{\omega_o k_1}{\mu Q^2} \quad (5)$$

IV. EXPERIMENTAL RESULTS

46.4-MHz polysilicon wine-glass mode disk resonators were designed and fabricated using a process similar to a previously reported self-aligned stem process [12], except for the use of a chemical mechanical polishing (CMP) step to reduce topography at the end of the process. Fig. 4 presents the final cross section and scanning electron micrograph (SEM) of one such resonator, identifying key features and dimensions. With 80-μm diameters, the disks of this work are larger than previous ones, so etch holes are now used to keep release etch times under 15 minutes. This is needed to prevent HF attack of the nitride isolation layer underneath the devices, which occurs when the nitride is exposed to 49 wt.% HF for longer than 35 minutes. Structurally, the etch holes reduce the resonator stiffness, resulting in a slight reduction of its resonance frequency. Finite element simulation using ANSYS predicts frequencies of 46.7-MHz and 48.1-MHz for wine-glass mode disk resonators with and without etch holes, respectively.

Fig. 5 presents frequency spectra measured for the device of Fig. 4 under 50 mTorr pressure in a custom-built vacuum chamber, and in air as well, where the dependence of frequency on dc-bias-derived electrical stiffness [13] and on increased gas damping in air can be clearly seen. In vacuum, the Q is 30,267. In air, although a larger dc-bias V_P is needed to achieve the same motional resistance, the Q is still a respectable 5,091. The oscillator circuit of Fig. 1 was implemented on a printed circuit (pc) board shaped to allow placement within the custom-built vacuum chamber. Dies containing fabricated wine-glass mode disk μresonators were glued to this

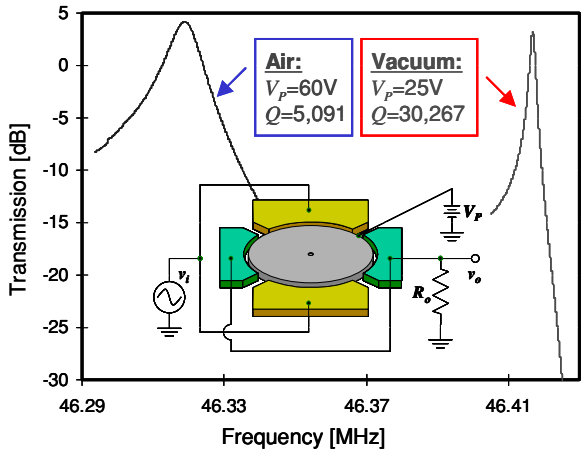

Fig. 5: Measured frequency characteristics for the wine-glass mode disk μresonator in air as well as in vacuum, with an inset specifying the measurement setup.

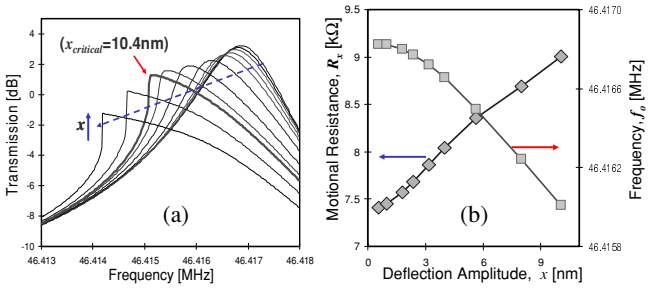

Fig. 6: Measured plots summarizing the displacement amplitude dependence of the wine-glass disk resonator: (a) frequency responses, showing Duffing nonlinearity; and (b) motional resistance R_x and resonance frequency; all measured under 50 mTorr vacuum.

board over specially grounded regions and bonded to board-mounted electronics.

Fig. 6(a) presents measured plots of transmission versus frequency for a 46.4-MHz wine-glass mode disk under increasing drive force amplitudes, where spring softening Duffing behavior is clearly seen. In particular, the peak frequency clearly decreases with increasing displacement amplitude. In addition, a decrease in peak transmission is also seen, consistent with [2], where either Q or transducer electromechanical coupling, or both, may be decreasing with displacement amplitude. This reduction in transmission corresponds to an increase in series motional resistance R_x with displacement amplitude, plotted in Fig. 6(b) (along with frequency), which then provides a convenient mechanism for self-limiting of an oscillator referenced to a wine-glass mode micro-disk. In particular, at oscillator start-up, when the R_x of the resonator is smaller than the transresistance gain of the sustaining amplifier R_{amp}, the overall loop gain is greater than unity, so oscillations build up. As the amplitude of the resonator grows, however, R_x grows until it equals R_{amp} minus other series loop resistances (e.g., amplifier input and output resistance), at which point, the oscillation amplitude stops growing, and steady-state operation is achieved. In this mode of operation, the steady-state oscillation amplitude can be set by setting the initial difference between R_x and R_{amp}, which can in turn be set by choice of dc-bias voltage V_P [9]. The wine-glass disk of this work has an advantage over other resonators in that its power handling and R_x versus amplitude characteristic are such that oscillation with sufficient output power can be achieved at vibration amplitudes well below critical Duffing, which is one of

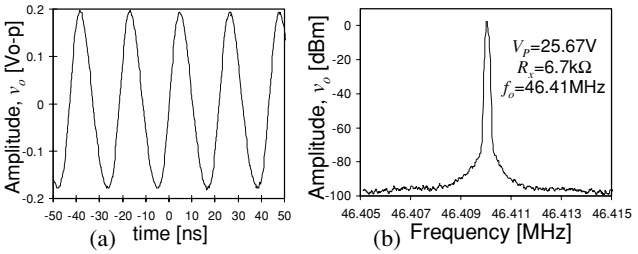

Fig. 7: Measured output (a) waveform and (b) Fourier spectrum for the self-limiting wine-glass disk micromechanical oscillator.

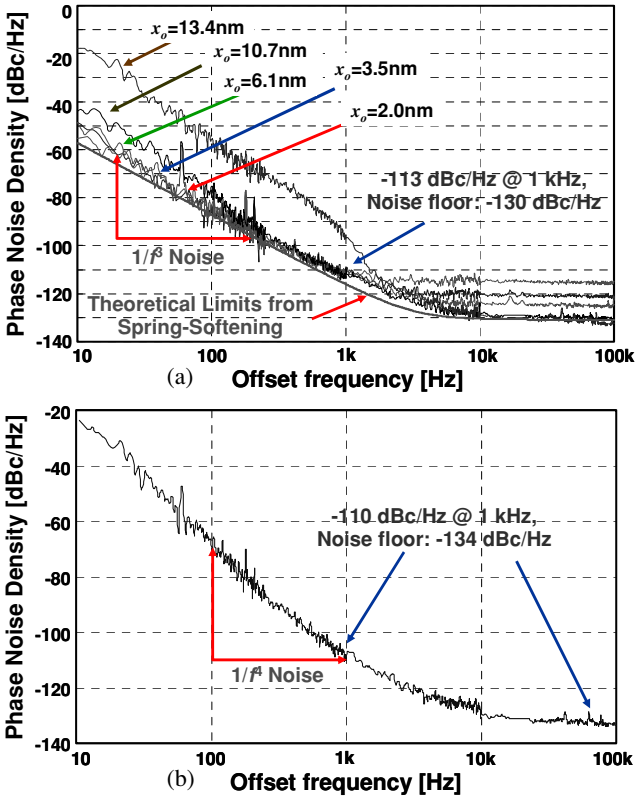

Fig. 8: Measured phase noise density-to-carrier power ratio versus carrier offset frequency for the μmechanical resonator oscillator in (a) vacuum and (b) in atmosphere.

the criteria for good oscillator stability in Section III.

Fig. 7 presents the measured output waveform and Fourier spectrum for a self-limiting wine-glass disk oscillator hooked up as in Fig. 1 and operated under conditions summarized in the inset. Fig. 8 presents plots of phase noise density versus frequency offset for the 46.4-MHz wine-glass disk oscillator, with displacement amplitude as a third variable, measured (a) under 50 mTorr vacuum and (b) in air, using an HP E5500 Phase Noise Measurement System. Operational specifics for each curve are summarized in Table I. In vacuum, a $1/f^3$ component is seen close to the carrier, and this noise clearly depends upon the oscillation amplitude, becoming considerably worse when the amplitude of oscillation becomes larger than the critical Duffing amplitude (10.4 nm), where multiple operating amplitudes are possible in the curves of Fig. 6(a), verifying that operation past the critical point should be avoided.

In vacuum, the phase noise at 1kHz offset from the carrier is of the $1/f^3$ variety, as expected, but curiously it remains fairly constant at -113 dBc/Hz for amplitudes below the critical amplitude. On the other hand, the far-from-carrier phase noise has a rather strong

Table I. Operational Data for Various Oscillation Amplitudes

Amplitude, x[nm]	**2.0**	**3.5**	**6.1**	**10.7**	**13.4**
V_P **[V]**	24.54	24.67	24.93	25.67	26.96
R_x **[kΩ]**	7.323	7.245	7.095	6.691	6.066
f_o **[MHz]**	46.4131	46.4124	46.4116	46.4093	46.3990
v_i **[mV]**	34.6	61.5	109.4	194.5	259.4
$L[f_m$**=1kHz]**	-111	-111	-112	-113	-97
Noise Floor	-115.2	-121.4	-125.3	-130.5	-132.3

dependence on amplitude, getting smaller with larger displacement amplitude, and attaining its lowest value of -130 dBc/Hz at an amplitude of 10.7 nm, right at the edge of critical Duffing. When divided down to 10MHz for fair comparison with other standard oscillators, the phase noise for the 10.7 nm displacement case at 1kHz and far-from-carrier offsets are -126 and -143 dBc/Hz, respectively, which are now in the range of acceptable values for cellular handsets, although some sticklers might still demand -130 and -150 dBc/Hz. If needed, these values should be attainable via a redesign to provide a more favorable Duffing response curve (e.g., by optimizing the electrode-to-resonator gap spacing).

In air (Fig. 8(b)), although a mysterious $1/f^4$ phase noise component introduces itself at carrier offset frequencies below 1kHz, the overall performance of the oscillator matches that of the vacuum-operated version past 1kHz, despite its lower Q. The performance even exceeds that in vacuum at far-from-carrier offsets, achieving 4dB better in this region. The reason: In air the amplitude required to make R_x=R_{amp} is smaller than that needed in vacuum, and the dc-bias voltage V_P needed is larger—a combined condition that allows both small displacement amplitude for good close-to-carrier phase noise, but large current output amplitude (provided by the larger V_P) for good far-from-carrier noise.

V. INSIGHTS INTO $1/f^3$ PHASE NOISE

The observation that $1/f^3$ phase noise is independent of vibration amplitude for amplitudes below critical Duffing pares down the list of possible mechanisms to those that are amplitude independent. Among these mechanisms is the previously proposed [8] shaping of aliased $1/f$ noise by the resonator passband, leading to a $1/f^3$ phase noise component governed by

$$L[f_m]=\left[\frac{1}{4Q_l^2V_P^2}+\frac{1}{4k_1^2}\frac{(\varepsilon_o A_o)^2}{d_o^6}V_P^2\right]\cdot 2qK_1I_BR_{amp}^2\frac{f_o^2}{f_m^3} \qquad (6)$$

where d_o and A_o are the electrode-to-resonator gap and overlap area, respectively; and K_1(50kHz) and I_B(50μA) are the $1/f$ noise constant and base current, respectively, of the bipolar transistor at the input of the sustaining transimpedance amplifier with gain R_{amp}, 14 kΩ.

Another possible mechanism arises when $1/f$ noise on the dc-bias voltage V_P leads to electrical-stiffness-induced frequency instability, which then generates a $1/f^3$ phase noise component governed by

$$L[f_m]\approx\frac{1}{2}\left(\frac{\varepsilon_o A_o V_P}{k_{m1}d_o^3}\right)^2 2qK_1I_BR_{amp}^2\frac{f_o^2}{f_m^3} \qquad (7)$$

Unfortunately, neither of the above equations exactly matches the measured phase noise of Fig. 8. In particular, using the data in the 4th column of Table I, (6) predicts -124 dBc/Hz at 1 kHz offset, while (7) yields -120 dBc/Hz—each more than -7 dBc/Hz from the measured value. A new formulation based on frequency shifts due to Duffing distortion (3) leads to the expression

$$L[f_m]\approx\frac{1}{(2\pi)^4 f_o^2}\cdot\left(\frac{3k_3}{4m_r}\right)^2\frac{4Q^2V_P^2}{k_1^2}\cdot\frac{(\varepsilon_o A_o)^2}{d_o^6}\cdot 2qK_1I_BR_S^2\cdot\frac{x^4}{f_m^3} \qquad (8)$$

This expression yields -115 dBc/Hz at 1kHz using the data in the 4th column of Table I, which is very close to the measured value. However, this expression also exhibits a dependence on amplitude not seen in measurement, so cannot be entirely correct.

Perhaps the previous observation that ALC or limiting via electronics rather than the resonator eliminates $1/f^3$ phase noise is more telling. In particular, the mechanism for $1/f^3$ phase noise is likely tied to the Duffing distortion-based limiting mechanism described in Section III. Efforts to properly model $1/f^3$ phase noise are ongoing.

VI. CONCLUSIONS

A 46.4-MHz μmechanical resonator reference oscillator has been demonstrated using a series resonant oscillator topology in which a transimpedance amplifier with zero phase shift sustains the oscillation of a high stiffness wine-glass mode μmechanical disk resonator. Due to the high-Q, high power handling, and large stiffness (relative to previous micromechanical devices), of the wine-glass disk resonator, this oscillator achieves a phase noise performance consistent with the needs of commercial wireless communications without the need for ALC. This performance is attained as long as the vibration amplitude of the resonator is kept below the critical Duffing amplitude; otherwise, excessive phase noise ensues. In addition, without ALC or some electronic means for limiting, this oscillator still exhibits the $1/f^3$ close-to-carrier phase noise seen in previous micromechanical oscillators, further verifying that limiting via resonator nonlinearity (e.g., Duffing-related nonlinearity) is likely responsible for this noise. The fact that $1/f^3$ noise is found to be independent of vibration amplitude for operation below critical Duffing sheds more light on the roots of this noise phenomenon.

Acknowledgment: This work was supported under DARPA Cooperative Agmt. No. F30602-01-1-0573.

References:

[1] R. J. Matthys, *Crystal Oscillator Circuits*. New York: Wiley, 1983.
[2] C. T.-C. Nguyen, *et al*., *IEEE J. Solid-State Circuits*, vol. 34, no. 4, pp. 440-455, April 1999.
[3] T. A. Core, *et al*., *Solid State Technology*, pp. 39-47, Oct. 1993.
[4] A. E. Franke, *et al*., *Tech. Digest*, 12th Int. IEEE MEMS Conf., Orlando, Florida, Jan. 17-21, 1999, pp. 630-637.
[5] A.-C. Wong, *et al*., *Dig. of Tech. Papers*, Transducers'01, Munich, Germany, June 10-14, 2001, pp. 992-995.
[6] T. Mattila, *et al*., *Sensors and Actuators*, A 101, pp. 1-9, 2002.
[7] W. -T. Hsu, *et al*., *Tech. Digest*, 2002 IEEE Int. Micro Electro Mechanical Systems Conf., Jan. 20-24, 2002, pp. 731-734.
[8] S. Lee, *et al*., *Digest of Technical Papers*, Transducers'01, Munich, Germany, June 10-14, 2001, pp. 1094-1097.
[9] S. Lee, *et al*., *Proceedings of 2003 IEEE Frequency Control Symposium*, Tampa, Florida, May 5-8, 2003, pp.341-349.
[10] M. A. Abdelmoneum, *et al*., *Technical Digest*, 16th Int. IEEE Micro Electro Mechanical Systems Conf., 2003, pp. 698-701.
[11] S. Timoshenko, D. H. Young, and W. Weaver Jr., *Vibration Problems in Engineering*. 5th ed. New York: Wiley, 1990.
[12] J. Wang, *et al*., *Dig. of Tech. Papers*, Transducers'03, 2003, pp. 947-950.
[13] F. D. Bannon III, *et al., IEEE J. Solid-State Circuits*, vol. 35, no. 4, pp. 512-526, April 2000.

DRY-RELEASED POST-CMOS COMPATIBLE CONTOUR-MODE ALUMINUM NITRIDE MICROMECHANICAL RESONATORS FOR VHF APPLICATIONS

Gianluca Piazza and Albert P. Pisano

Berkeley Sensor and Actuator Center (BSAC)
University of California Berkeley, Berkeley, CA 94720
Tel: (510) 642-8713, Fax: (510) 643-6637, Email: piazza@eecs.berkeley.edu

ABSTRACT

This paper reports experimental results on a new class of dry-released, post-CMOS compatible, contour-mode aluminum nitride resonators spanning a frequency range from 23 MHz to 225 MHz showing high quality factors both in vacuum (Q_{max}=5,830 at 43.26 MHz) and air (Q_{air}=3,700), and low motional resistance (~600Ω at 89 MHz). For the first time, thin-film aluminum nitride technology has been used to fabricate circular and rectangular plates, which were successfully excited in contour modes in both fundamental and higher order modes. Dilation-type modes were excited in AlN rectangular plates demonstrating frequencies as high as 224.6 MHz with Q of 2,580. A 50μm radius disk vibrating in a wineglass contour mode exhibited Q of 5,830 at 43.26 MHz. Uncompensated temperature coefficients of frequency were measured to be ~-14ppm/°C for the disk and ~-22ppm/°C for a 200x50μm^2 rectangular plate vibrating in its 3rd mode.

INTRODUCTION

Recent demand in wireless communication for miniaturized, low-power, low-cost, on-chip and high-Q resonators to be employed in front-end RF filters or as frequency references has focused research efforts towards the development of new vibrating micromechanical structures, capable of substituting existing off-chip, bulky resonator technologies. Very promising alternatives to currently adopted solutions (SAW or ceramic devices) have been demonstrated [1,2] using in-plane, electrostatically-transduced, micromechanical resonators made of polysilicon or polydiamond. Although extremely high quality factors have been reported at UHF, the exhibited impedance values are too high for these resonators to be directly coupled to antennas in RF systems. Also, the high temperature fabrication steps involved with the deposition of the structural layers ultimately complicate the integration of these devices with state-of-the-art microelectronic components.

FBAR technology [3,4] has proven itself as a valid solution to replace conventional RF filters, demonstrating relatively high quality factors (Q~2,500), and extremely small (several Ω) impedances. The fundamental frequency of these devices is set by the film thickness. This constitutes a major challenge to the manufacturing of FBARs. In order to obtain reasonable yields, a thickness tolerance of 0.1% must be met. Also, multiple frequency selective arrays of resonators cannot be fabricated on a single chip. The new class of devices described here is not subject to these limitations.

This work introduces a new class of aluminum nitride micromechanical resonators that exhibit high quality factors, small impedance values (~600Ω at 89 MHz) and are fabricated using a low-temperature, post-CMOS compatible surface micromachining process. For the first time, thin film aluminum nitride technology has been used to fabricate circular and rectangular plates, which were successfully excited in contour modes in both fundamental and higher order modes. The use of contour modes specifically enables the fabrication of arrays of piezoelectric microresonators with different frequencies on a single chip. Other piezo-on-silicon rectangular plates have been described in the literature [5], however these resonators did not employ the same contour modes. The research described in this paper has led to resonators with low insertion losses, demonstrating that a fully aluminum nitride resonator body can effectively reduce the equivalent motional resistance and simultaneously achieve high quality factors. Most importantly these devices can be operated in air without significant Q degradation (Q_{vacuum}=3,280 and Q_{air}=2,680 for a 200x50μm^2 plate). Low, uncompensated temperature coefficients of frequency (TCF) of ~-14ppm/°C for disks and ~-22ppm/°C for a 200x50μm^2 plate (~2X smaller than reported in [5]) have also been demonstrated. In addition, the center-frequency has been tuned both up and down by purely piezoelectric means. A tuning range of ~6kHz was obtained for a 22.97 MHz rectangular plate using a 30V DC power supply.

CONTOUR MODES IN AlN PLATES

Figures 1a and 1b show schematic views of the AlN rectangular plates vibrating in dilation-type contour modes. A vertical electric field applied across the film thickness induces extensional mechanical stress in the plane of the film (through the d_{31} piezoelectric coefficient) and excites the structures in a dilation-type contour mode.

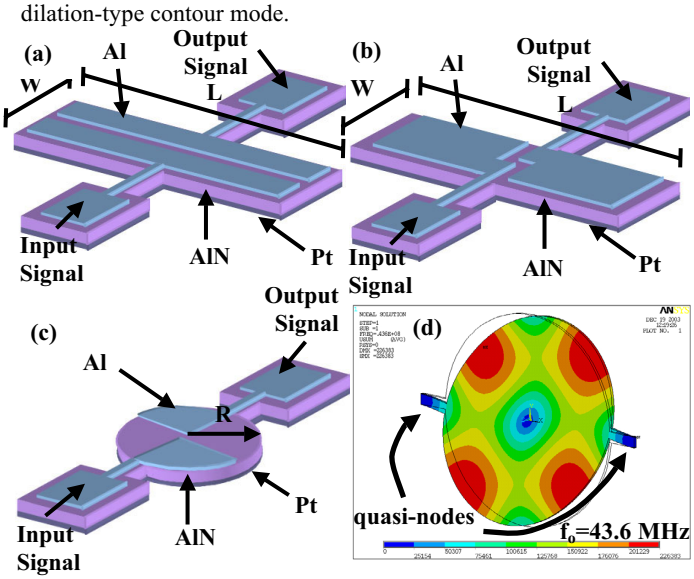

Figure 1. *Two-port AlN micromechanical resonators: (a) schematic view of an AlN rectangular plate with electrodes placed parallel to the plate length; (b) schematic view of an AlN rectangular plate resonators with electrodes placed parallel to the plate width; (c) schematic view of an AlN circular plate excited in a wineglass contour mode shape (d). Mode shapes for (a) and (b) are shown in Fig.2.*

0-9640024-5-0/hh2004/$20©2004TRF
DOI 10.31438/trf.hh2004.9

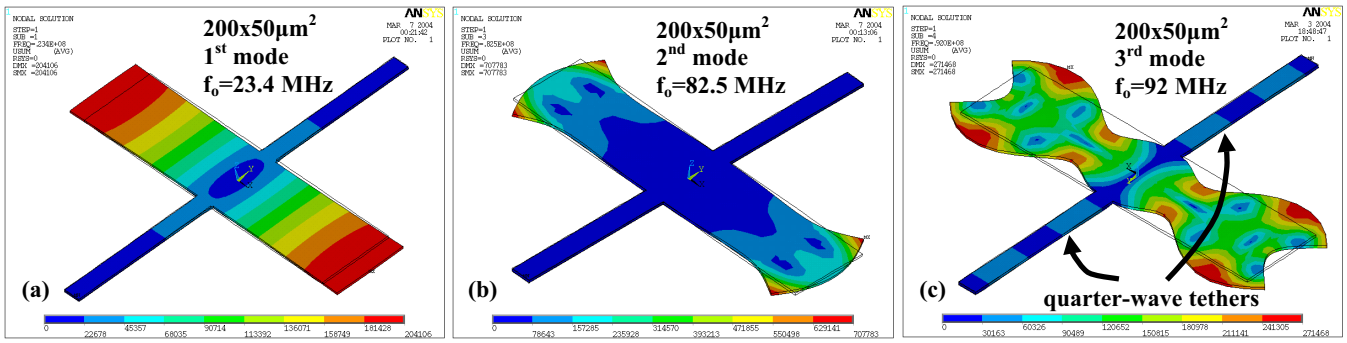

Figure 2. *Dilation-type contour modes (via FEA) excited in two-port AlN rectangular plate(200x50μm²) resonator: (a) fundamental length-extensional mode shape (denoted as 1st mode in this paper); (b) 1st width-extensional mode shape (denoted as 2nd mode in this paper); (c) 2nd width-extensional mode showing effective "quarter-wavelength" tethers design (denoted as 3rd mode in this paper).*

Two-port configurations were implemented by patterning the top electrodes symmetrically with respect to the length or the width of the plate. In order to minimize anchor losses, the resonators were suspended by two "quarter-wavelength" tethers.

Several in-plane contour mode shapes can be excited in these resonators [6], but either electrode configurations or energy loss mechanisms limit the detectable mode shapes to the one shown in Fig.2. The resonator can most effectively be excited in length-extensional (Fig. 2a) [7] and width-extensional (Fig. 2b-c) dilation-type contour modes. An important parameter that characterizes the relative strength of each of the resonances and sets the value of the equivalent motional resistance is the electromechanical coupling, η_{em}. It can either be defined as the ratio of the output force to the input voltage, or the ratio of the output charge to the mechanical displacement. For a symmetric electrode topology such as the one used in this work, η_{in} and η_{out} are the same; specifically:

$$\eta_{em} = \frac{\iint_A (d_{31}T_1 + d_{31}T_2)dA}{Z_{\max}} = \frac{\frac{2E}{1-\sigma} d_{31} \iint_A \left(\frac{\partial u}{\partial x} + \frac{\partial v}{\partial y}\right) dA}{Z_{\max}} \quad (1)$$

where T_1 and T_2 represent normal stresses in the x and y directions respectively, d_{31} is the piezoelectric coefficient, u and v are the displacements in x and y directions [8], E is the Young's modulus, and σ the Poisson ratio for AlN, A is the electrode area, and Z_{max} is the maximum displacement for the structure. Taking this into account the electrodes were placed so that η_{em} is maximized.

WINEGLASS MODE IN AlN DISKS

In Fig.1c is shown a schematic view of an AlN micromechanical disk to be excited in a wineglass contour mode. Thanks to in plane symmetry of AlN films, radial and compound mode shapes [9] can be effectively excited in thin circular disks through the d_{31} piezoelectric coefficient. In order to minimize anchor losses, the disk was pinned at two of its quasi-nodal points (Fig.1d).

A two-port configuration is implemented by having each of the two top electrodes cover a quadrant of the disk. By placing the electrode in such a fashion, maximum electromechanical coupling is achieved. In this specific case η_{em} is given by:

$$\eta_{em} = \frac{\frac{2E}{(1-\sigma^2)} d_{31} \iint_A \left[\frac{\partial u}{\partial r} + \sigma\left(\frac{u}{r} + \frac{1}{r}\frac{\partial v}{\partial r}\right)\right] dA}{Z_{\max}} \quad (2)$$

where E, σ, A and Z_{max} are the same as defined in equation (1), u and v represent the radial and tangential displacements [9], respectively, and r is the radial coordinate for the circular plate. Due to the isovoluminal nature of the mode shape and the electrode covering just half of the plate top surface, the electromechanical coupling for the disk is relatively smaller (~ 8X) than that for AlN plates of comparable frequency.

FABRICATION PROCESS

A simple three-mask, low-temperature (T_{max}<350˚C), post-CMOS compatible process has been used to fabricate rectangular and circular AlN plates (Fig.3). A thin (~50nm) AlN buffer layer is deposited on a Si wafer to provide electrical isolation. A 1.5μm AlN film is sandwiched between a bottom platinum electrode and a top aluminum electrode. AlN is reactively deposited using an Advanced Modular Sputtering Inc., AMS 2003 sputtering tool. Cl_2-based dry etching has been used to pattern AlN and yields fairly straight (within 16° of vertical) sidewalls (Fig.5) with an etch rate of ~80nm/min. Oxide deposited by electron cyclotron resonance is used as a hard mask during the AlN etching step and the ion milling of the Pt layer. Openings to contact the bottom electrode are quickly wet etched through AlN in a hot (160°C) phosphoric bath. The top Al electrode is evaporated and strategically patterned so that maximum electromechanical coupling is obtained. The structures are released by dry etching of silicon in XeF_2. This novel dry release step for fully AlN resonators eliminates stiction forces and significantly increases yield compared to other processes that use wet release techniques [5].

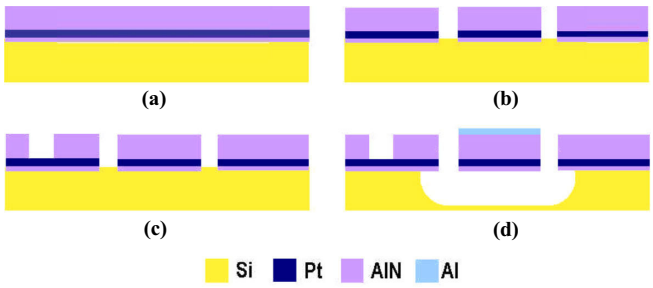

Figure 3. *Fabrication process flow for AlN micromechanical resonators: (a) AlN,Pt and AlN are sputter-deposit on a Si wafer; (b) trenches are open through AlN and Pt by Cl_2-based dry etching and ion milling, respectively; (c) Openings to the bottom electrode are wet etched through AlN in hot (160°C) H_3PO_4; (d) Al top electrodes are evaporated and patterned by lift-off.*

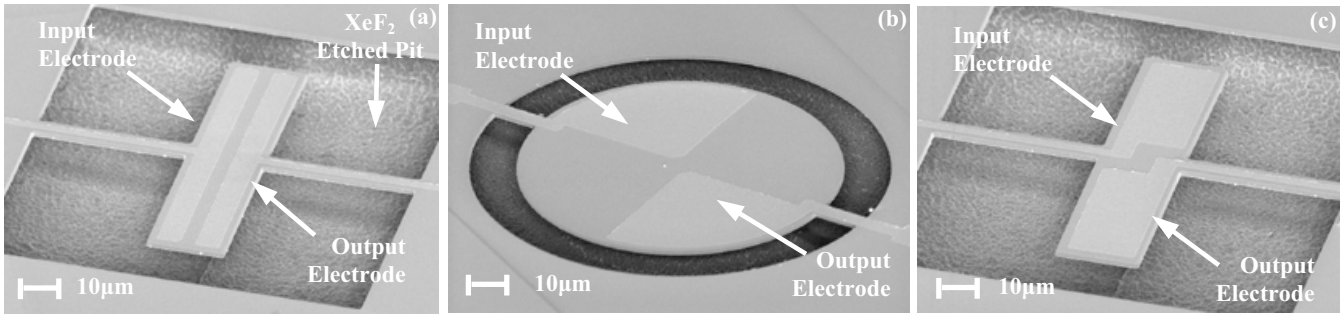

Figure 4. *Scanning electron microscope pictures showing: (a) 80x20μm² AlN rectangular plate with electrodes parallel to the resonator length; (b) 50μm radius AlN circular plate to be excited in a wineglass mode shape; (c) 80x20μm² AlN rectangular plate with electrodes parallel to the resonator width.*

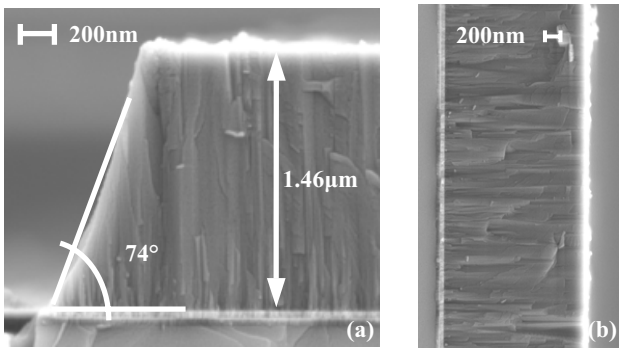

Figure 5. *Cross-section views of AlN films: (a) 74° sidewalls are obtained after Cl_2 dry etch and ion milling; (b) closely-packed, highly crystalline AlN film is obtained using AMS sputtering tool (rocking curve value: best FWHM ~ 1.9°).*

All the deposition steps occur at low temperature (T_{max} ~350˚C when sputtering AlN) and can potentially be integrated with state-of-the-art microelectronic components. Fig. 4 shows rectangular and circular plates that were fabricated using the aforementioned process.

EXPERIMENTAL RESULTS

The fabricated micromechanical resonators were tested in a Janis micro-manipulated RF vacuum probe system in 5mTorr vacuum and at atmospheric pressure. Ground-Signal-Ground (GSG) probes from Picoprobe were used. The bottom Pt electrode was grounded, whereas each of the two top electrodes was used for either sensing or driving the device under test. No interface circuitry between the resonator and the network analyzer was needed. Given the low impedance values, it was possible to directly measure the frequency response of the resonators using an Agilent 4195A network analyzer.

A. Frequency Response of AlN Rectangular Plates

Various rectangular plates with length to width ratios of 2 and 4 were fabricated and tested. The resonators varied in length from 80 to 200μm. All resonators, despite their size and electrode configuration, exhibited the fundamental length-extensional mode. Fig. 6a represents the typical response in vacuum of a 200x50μm² plate, showing Q of 3,280 and a motional resistance, R_x, of only ~150Ω when vibrating in its 1st HF mode (Fig.2a). It was also possible to excite higher order modes in plates with electrodes placed parallel to the plate length and having a length to width ratio of 4. Q as high as 4,470 were obtained from the 2nd mode

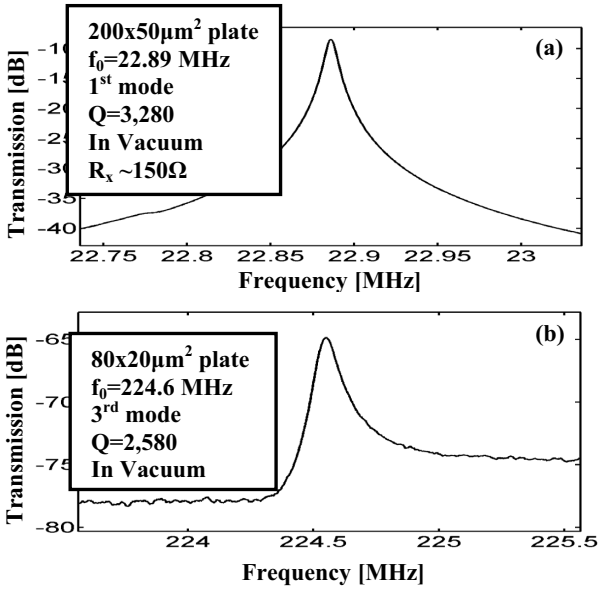

Figure 6. *(a) Typical frequency response of a 200x50μm² rectangular plate excited in its fundamental mode in vacuum; (b) frequency response for a 80x20 μm² rectangular plate excited in its 3rd mode in vacuum.*

(Fig.2b) of a 200x50μm² plate at 80.57 MHz in vacuum. A 80x20μm² plate achieved the highest measured frequency of 224.6 MHz with Q of 2,580 (Fig. 6b) in vacuum, when vibrating in its 3rd mode (Fig. 2c). The use of quarter-wavelength tethers minimized the energy lost through the anchors and enabled achieving quality factors higher than the one recorded for the 1st mode. The same plate could not be excited in its 2nd mode. The low electromechanical coupling exhibited by this mode shape is most likely why it cannot be detected at higher frequencies. It is interesting to note that these resonators could be actuated in air without significant Q degradation. Recorded Q reduction was about 20-30% for all resonators. For example, Q of 2,000 in air and Q of 2,580 in vacuum were recorded for a 80x20μm² plate vibrating in its 3rd mode. Experimental measurements for dilation-type contour modes in AlN rectangular plates are summarized in Table I. Recorded frequencies match within 3% to ANSYS finite element analysis (electrode loading was not taken into account for FEA).

A 200x50μm² resonant plate exhibited a linear TCF over a temperature range of 28-100°C. TCF values of ~-26ppm/°C, ~-25ppm/°C, and ~-22ppm/°C were recorded for the same plate vibrating in its 1st, 2nd and 3rd mode, respectively. Furthermore it was possible to tune the center-frequency of a plate both up and

down by purely piezoelectric means. A constant strain was induced in the resonator by superimposing a DC voltage to the ac signal on the two top electrodes. This tuning mechanism resulted in a ±3kHz linear tuning range for a 22.97 MHz rectangular plate using a 30V power supply (slope ~ 4.4ppm/V). Such a tuning scheme could potentially be employed to implement low-power active frequency compensation for temperature variations of ±10°C.

Table I. *Summary of most significant experimental measurements for dilation-type contour modes in AlN rectangular plate. A and B next to the plate size refer to the top electrode configuration: A indicates resonators with electrodes parallel to the length of the plate, B indicates resonators with the electrodes parallel to the width of the plate. I.L. stands for insertion loss. Modes are numbered as defined in Fig.2.*

Size LxW [MHz]	Mode	F_O [MHz]	Q (in vacuum)	I.L. [dB]
200x100 A	1	22.88	2,820	-16.7
200x50 A	1	22.89	3,280	-9
	2	80.57	4,470	-23.1
	3	88.99	4,200	-21.8
140x70 A	1	32.66	1,360	-32.2
140x35 A	1	32.65	1,860	-29.4
	2	115.3	2,870	-32.9
	3	127.3	1,520	-36.4
140x35 B	1	32.72	3,320	-32.2
80x20 A	1	57.67	1,940	-40.6
	3	224.6	2,580	-64.8
80x20 B	1	57.40	1,885	-39.1

B. Frequency Response of AlN Disks

50μm radius AlN disks vibrating in a wineglass contour mode shape exhibited Q as high as 5,830 at a frequency of 43.26 MHz in vacuum (Fig. 7). A high quality factor of 3,700 was recorded in air for the same type of resonators. Using fairly small tethers (5μm wide) and anchoring the disk at its quasi-nodal points (tangential displacement is non-zero at this locations) resulted in the highest Q for contour modes in AlN plates. Despite its high Q the resonator shows a motional resistance (~73kΩ) much higher than the one recorded for rectangular plates. Although, having the electrodes over the whole resonator surface could decrease the motional resistance by a factor of 4, the equivoluminal nature of the mode shape makes its excitation very difficult in AlN films. The same resonator exhibited a linear TCF of ~-14ppm/°C for a temperature range of 28-100°C. The smaller value of TCF compared to the one recorded for rectangular plates is probably a consequence of the isovoluminal mode shape.

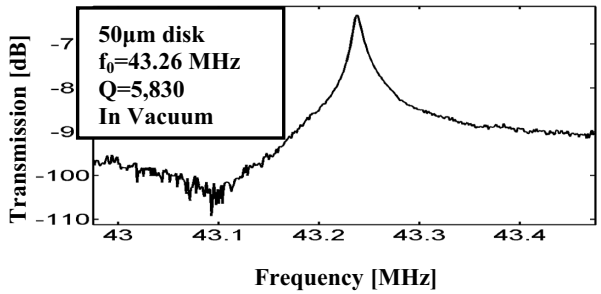

Figure 7. *Characteristic frequency response of 50μm radius AlN disk excited in a wineglass contour mode, showing Q of 5,830 at 43.26 MHz. Antiresonance peak appears before series resonance peak because the output voltage is 180° out of phase with respect to the input voltage[10].*

CONCLUSIONS

For the first time contour-modes were excited in thin-film AlN micromechanical resonators spanning a frequency range from 23 to 225 MHz. Rectangular and circular plates were fabricated using a dry-release surface micromachining process that is potentially post-CMOS compatible. Thanks to the use of a fully AlN resonator body and an intrinsically high electromechanical coupling, rectangular plates exhibited impedance values as low as ~150Ω. Three fundamental contour modes were observed in thin rectangular plates, showing Q as high as 4,470 at 80.57 MHz. Quarter-wavelength supports enabled achieving high frequencies and high Q at the same time. Compared to commercially available piezoceramics used for VHF applications, these rectangular plate resonators offer key advantages in terms of size reduction and possible integration with state-of-the-art microelectronic, while maintaining the same quality factors. Contour-mode shapes were also uniquely excited in circular plates. The highest Q of 5,830 was recorded for a 50μm radius disk excited in a wineglass mode. Ongoing research efforts focus on extending this promising technology to GHz frequencies.

ACKNOWLEDGMENT

The work was supported by DARPA grant No. NBCH1020005. The authors wish to thank AMS Inc. for depositing AlN films. Special thanks to UCB microfabrication laboratory staff, Phil Stephanou and Brian Bircumshaw for their help. Travel support has been generously provided by the Transducers Research Foundation and by the DARPA MEMS and DARPA BioFlips programs.

REFERENCES

1. S.-S. Li, *et al*., "Micromechanical "Hollow-Disk" Ring Resonators", *IEEE MEMS 2004,* January 2004, pp. 821-824.
2. J. Wang, *et al*, "1.51-GHz Nanocrystalline Diamond Micromechanical Disk Resonator with Material-Mismatched Isolating Support", *IEEE MEMS 2004,* January 2004, pp. 641-644.
3. R. Aigner, *et al.*, " RF-Filters in Mobile Phone Applications", *Transducers'03*, June 8-12, 2003, pp.891-894
4. R. Ruby, *et al.*, "Ultra-Miniature High-Q Filters and Duplexers Using FBAR Technology", *IEEE International Solid-State Circuits Conference*, Feb. 2001, pp.121-122.
5. S. Humad, *et al.*, "High Frequency Micromechanical Piezo-On-Silicon Block Resonators", *IEDM*, 2003, pp. 957-960.
6. R. Holland, "Contour Extensional Resonant Properties of Rectangular Piezoelectric Plates", *IEEE Transaction on Sonics and Ultrasonics*, Vol. Su-15, No.2, April 1968, pp. 97-105.
7. B. Antkowiak, *et al.*, "Design of High-Q, Low-Impedance, GHz-Range Piezoelectric MEMS Resonators", *Transducers' 03*, June 8-12, 2003, pp. 841-846.
8. R.A. Johnson, *Mechanical Filters in Electronics*, New York, NY Wiley, 1983.
9. M. Onoe, "Contour Vibrations of Isotropic Circular Plates", The Journal of the Acoustical Society of America, Vol. 28, No. 6, pp. 1158-1162.
10. G.Piazza, *et al.*, "Voltage-Tunable Piezoelectrically-Transduced Single-Crystal Silicon Micromechanical Resonators on SOI Wafer", *IEEE MEMS 2003*, January 2003, pp.149-152.

A NEW MEMS-BASED QUARTZ RESONATOR TECHNOLOGY

David T. Chang, Frederic P. Stratton, Deborah J. Kirby,
Richard J. Joyce, Tsung-Yuan Hsu, Randall L. Kubena
Sensors and Materials Laboratory, HRL Laboratories, LLC
Malibu, CA 90265-4799

ABSTRACT

We report on the development of a new quartz resonator technology that allows for the processing and integration of VHF to UHF high-Q oscillators and filters with high-speed silicon or III-V electronics. This paper describes the successful demonstration of new wafer bonding and dry plasma etching processes that make quartz-MEMS technology possible. In addition, we present impedance, Q, and temperature sensitivity data along with comparison to 3-D harmonic and thermal analysis of VHF-UHF resonators.

INTRODUCTION

Modern communication systems such as programmable radios and GPS receivers require ultra small, high frequency filters or oscillators with extremely good temporal and thermal stabilities, high resonant quality-factors, and excellent RF matching characteristics. Discrete bulk acoustic wave devices such as quartz resonators have been the prevailing choice for such applications because single crystal quartz has several attractive material properties. It is a low loss (high Q) piezoelectric material with zero temperature coefficient and stress compensated crystal cuts. In addition, its chemically inert surface makes quartz a candidate for stable frequency operations. However, current manufacturing technology for quartz resonators does not provide a straightforward method for reducing the size and thereby increasing the frequency of operation into the UHF range [**1**]. Furthermore, integrating large arrays of precisely tuned structures with high-frequency RF electronics and vacuum packaging the resulting chip at wafer level are not possible with present techniques. Polysilicon surface micromachining technology has enabled the creation of on-chip UHF resonators with high Q values [**2**]. However, these devices suffer from extremely large motional resistance (> 1 kΩ), making them less desirable for low impedance (~50Ω) RF applications.

Recent advancements in microfabrication, especially in the areas of precision wafer bonding and plasma etching, have enabled us to fabricate miniaturized quartz on-chip resonators working in the VHF-UHF frequency range. These resonators retain the excellent properties of discrete quartz devices while providing a low-cost path for on-chip integration with electronics and wafer-scale packaging.

DEVICE DESIGN AND SIMULATION

In quartz resonator design, it is important to optimize energy trapping and motional resistance and to exclude spurious oscillation modes by adjusting electrode and quartz plate dimensions. We worked with Coventor to establish the first commercial piezoelectric 3-D finite element modal and impedance analysis software to design thickness-shear mode (TSM) quartz resonators and predict their frequency characteristics.

Figure 1 shows the finite element simulation result for an AT-cut TSM quartz resonator of dimensions 265 µm (L) x 80 µm (W) x 10 µm (T) with top and bottom gold (Au) electrodes of dimensions, 200 µm (L) x 50 µm (W) x 0.12 µm (T). The 3-D modal analysis indicates that at 149 MHz this design has excellent energy confinement under the electrodes and pure thickness-shear oscillation without any anharmonic modes near this resonance.

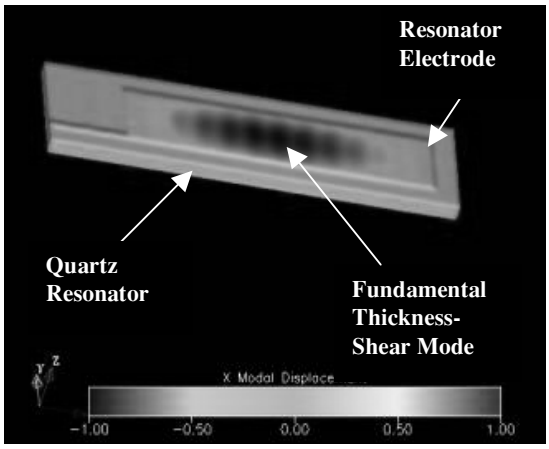

Figure 1. *3-D modal pattern of a 149 MHz thickness-shear quartz resonator.*

Impedance analysis of this resonator design provides the frequency-dependent I-V characteristics of the device. Using the admittance routines available from the Coventor software package, we calculated the admittance versus frequency plots for several of the designs on our current mask set. Figure 2 shows the admittance vs. frequency plot for the aforementioned 149 MHz resonator design.

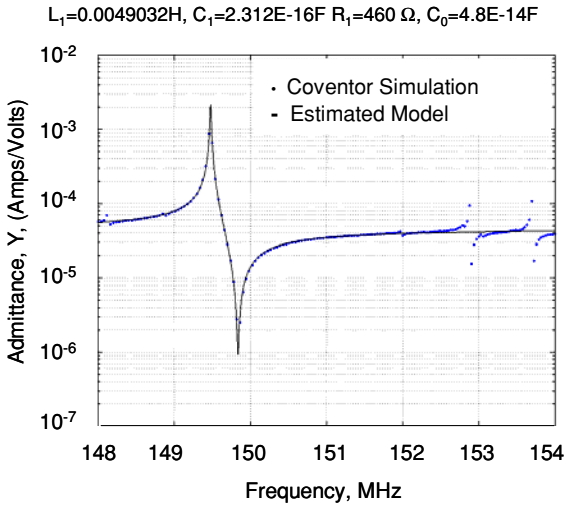

Figure 2. *Simulated admittance vs. frequency plot of a 149 MHz thickness-shear quartz resonator.*

0-9640024-5-0/hh2004/$20©2004TRF
DOI 10.31438/trf.hh2004.10

The simulation results were then used to extract the equivalent circuit parameters for a Van Dyke circuit, and the results compare favorably with analytical data. For an assumed Q of 10,000, a 265 x 80 micron design yielded a motional resistance R_1 of 460 Ω, motional inductance L_1= 4.9 mH, motional capacitance C_1= 0.23 fF and a static capacitance of C_0= 48 fF.

FABRICATION

The quartz resonator fabrication process is illustrated in figure 3. The starting materials for this process are: 1) a 300-µm-thick, double-side polished AT-cut single crystal quartz blank, 2) a 500-µm-thick, <100>-oriented, n-type, 1-10 ohm-cm, silicon handle wafer, and 3) a 300-µm-thick host substrate such as a GaAs or a silicon wafer. The process begins with a plasma cavity etch into the silicon handle wafer (~2 microns depth) to later accommodate the top metal electrodes of the quartz wafer. The quartz wafer is metallized with electrodes (200 Å Cr / 1000 Å Au) and then aligned and directly bonded to the silicon handle wafer using plasma-assisted room temperature bonding with EV Group's EV-620 aligner and EV-501 bonder. The bonded quartz is subsequently thinned to a thickness of approximately 10 µm using conventional lapping and polishing techniques. Its thickness is further reduced to less than 10 µm using an SF_6-based plasma etch in a Unaxis inductively-coupled, high-density plasma etcher. Veeco surface profilometer measurements of the final quartz surface after thinning give a surface roughness of 2 nm.

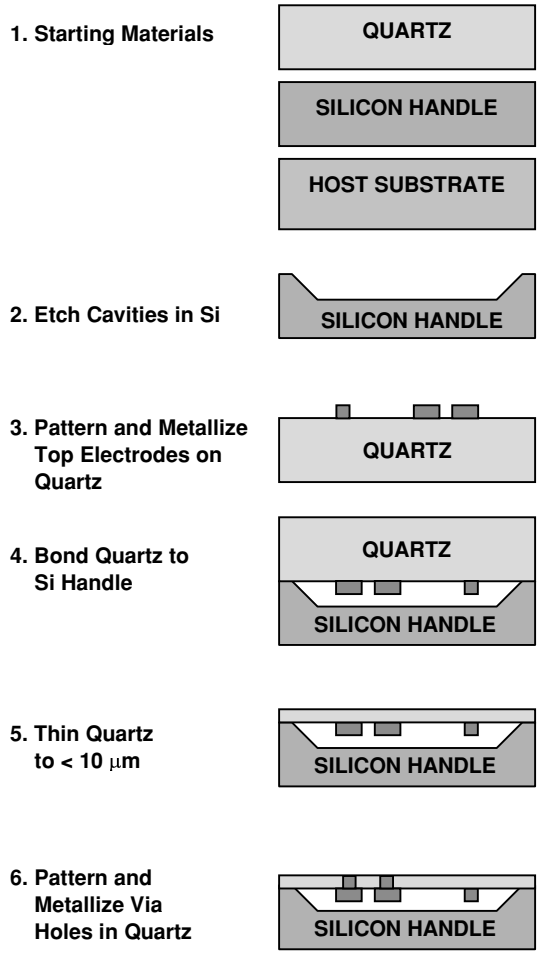

Figure 3. *Fabrication process flow for the quartz resonators.*

A deep reactive ion etching (DRIE) process with CF_4 chemistry and bottom-side metallization (200 Å Cr/ 1000 Å Au) create the through-wafer vias and metal interconnects to bridge the top-side metallization to bottom-side bonding pads. The continuous sheet of quartz is then patterned and etched using a thick Shipley SJR-5740 photoresist mask and a second DRIE step to delineate the resonator patterns. (Fig. 4) The detailed description of the DRIE process is presented in an earlier publication [**3**].

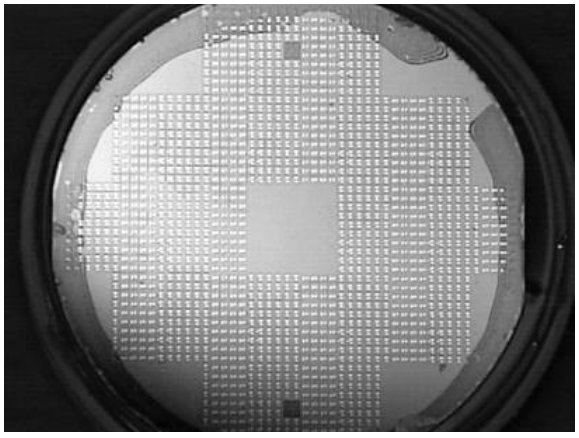

Figure 4. *Quartz resonator patterns on silicon handle wafer after process step 8.*

For the host substrate, it is first patterned and etched to create 5-μm-tall protrusions on its surface. Then, metals are deposited on the protrusions to form the bond pads (200 Å Cr / 5000 Å Au) for the subsequent thermal compression bond. In this bonding step, the Si/quartz pair is first aligned to the host substrate using EV Group's EV-620 aligner and then bonded at 300°C in the EV-501 wafer bonder using a compression pressure of 10 MPa. Finally, the silicon handle wafer is removed using either an SF_6 plasma etch or a wet TMAH process to leave the individual quartz resonators on the host substrate. Completed resonators are shown in both the microscope photograph (Fig. 5) and an SEM image. (Fig. 6)

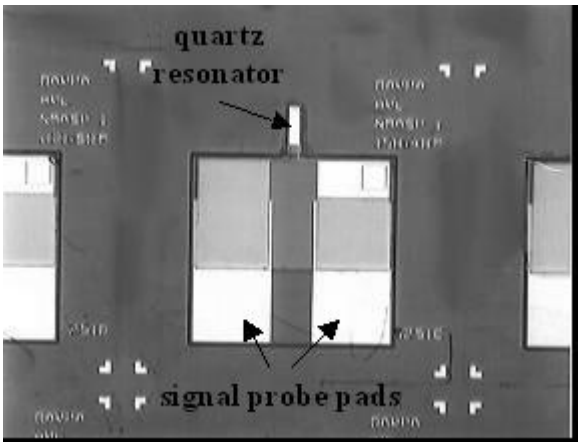

Figure 5. *Microscope photograph of a completed resonator.*

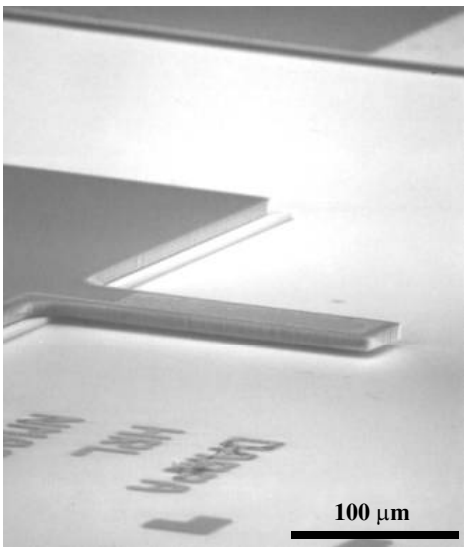

Figure 6. *SEM photograph of a completed resonator.*

This fabrication process provides a path for integrating large resonator arrays with high frequency RF electronics since the low-temperature process is compatible with standard silicon and III-V compound semiconductor processes. It also allows conventional packaging techniques such as anodic, glass frit, and solder bonding to hermetically seal the resonators at the wafer level because the permanent Au-Au thermal compression bond for the resonators can withstand a post-processing temperature of at least 400°C, which is ample for the aforementioned sealing processes.

EXPERIMENTAL DETAILS

Several different designs of AT-cut shear-mode resonators have been tested using Cascade microprobes and an Agilent 4991A impedance analyzer at room temperature. One of the keys to making measurements on ultra-small piezoelectric resonators is compensating for stray capacitance during wafer-level probing. Capacitance compensation below 10^{-13} F is generally required. For a 1.49-μm-thick quartz resonator with electrode dimensions of 160 μm x 50 μm x 0.1 μm, we obtained a fundamental frequency of 591 MHz and a Q value of 13,470 in air for this device (Fig. 7). This yields an f x Q product of 8 x 10^{12} Hz, which is within a factor of two of the highest frequency–Q product reported to date for any quartz resonator [**4**]. The motional resistance of this resonator was measured to be 40 Ω, thus providing good impedance matching to external transmission lines. These results indicate that we have obtained good energy confinement and very low damage of the quartz during processing. In addition, temperature test data showed that these devices have a linear temperature coefficient of frequency of about –5 ppm/°C near room temperature (RT), which is within a factor of two of the best reported temperature coefficient to date for an on-chip resonator without external compensation [**5**]. Thermal analysis of our designs and quartz cut-angles predict a linear frequency shift near room temperature of –4 ppm/°C. Previous data for AT-cut resonators indicate that a maximum frequency deviation of 50 ppm from –40°C to 85°C (near zero TC at RT) is possible with an optimized quartz cut [**6**].

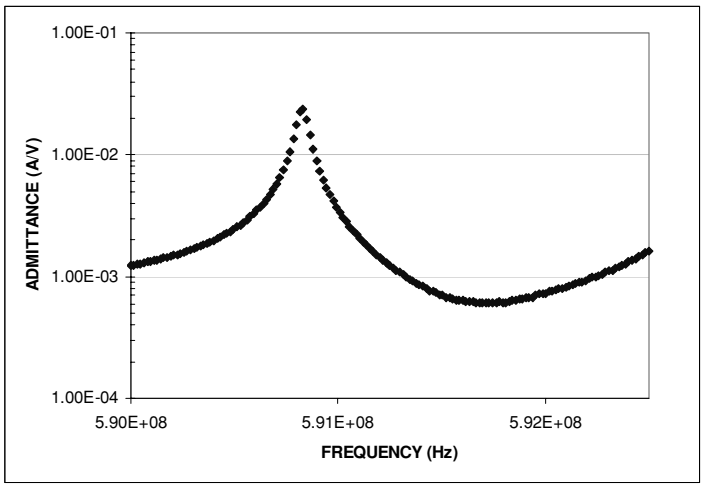

Figure 7. *Measured admittance vs. frequency for a 1.49-μm-thick, AT-cut shear-mode resonator with electrode dimensions of 160 μm x 50μm x 0.1 μm.*

FREQUENCY TUNING OF RESONATORS

For precision frequency adjustments after fabrication, we have demonstrated an ultra clean and high-resolution method of real-time mechanical tuning using focused-ion-beam (FIB) micromachining. A beam of gallium ions is focused and scanned over the surface of the top Au resonator electrode. The interaction of the ion beam with the electrode results in a controlled ejection of Au atoms from the resonator with sub-monolayer precision. The reduction in electrode mass leads to an increase in device

frequency. Figure 8 depicts the modified FEI focused-ion-beam system used for frequency tuning of our quartz resonators.

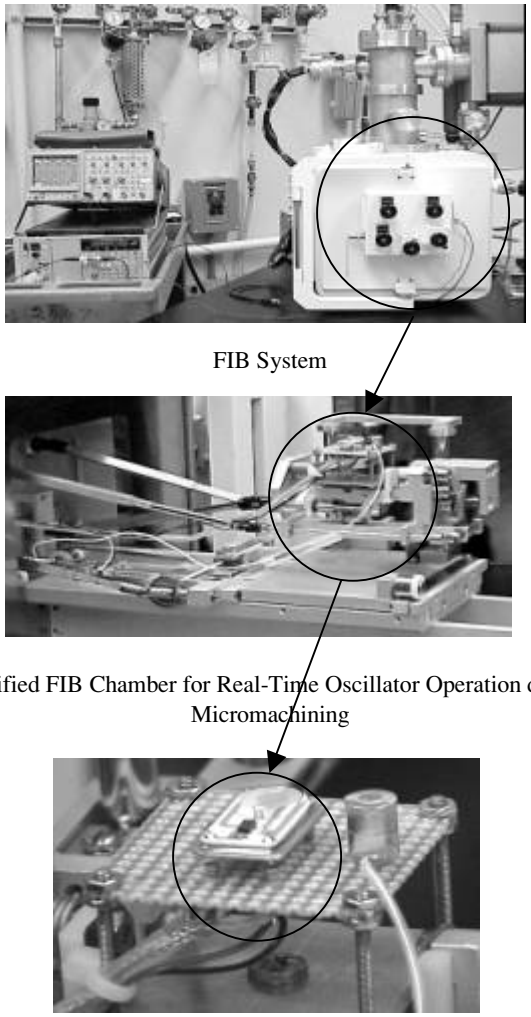

Figure 8. *Focused-ion-beam (FIB) system for frequency tuning of quartz resonators.*

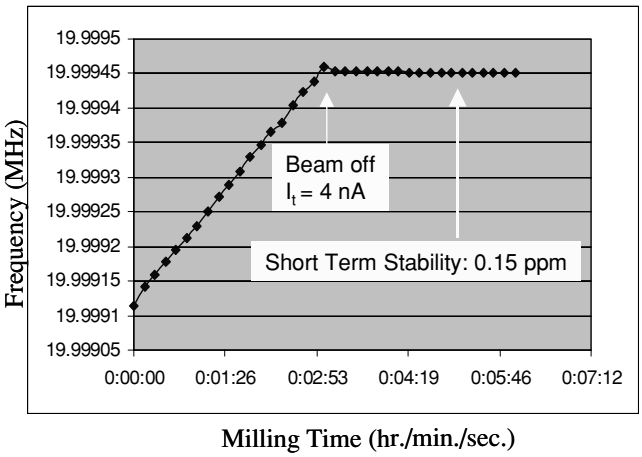

Figure 9. *FIB tuning of an AT-cut quartz resonator. The initial resonant frequency of the resonator was 19.999113 MHz. After the ion beam is turned off, the resonant frequency became 19.999454 MHz. The frequency eventually stabilized to 19.999451 MHz to represent a short- term stability of 150 ppb.*

We achieved a frequency modification of 338 Hz on a 20 MHz AT-cut quartz resonator after 3 minutes of milling under a beam current of 4 nA and a voltage of 25 kV. (Fig. 9) After removal from the FIB vacuum chamber and a re-pump down to vacuum (10^{-5} Torr), the frequency stability was observed to be roughly 1 Hz for this 20 MHz quartz resonator. For ultra-small UHF resonators, FIB tuning is ideal due to its high spatial resolution and monolayer milling control.

CONCLUSIONS

We have developed a new VHF-UHF quartz resonator technology which can be integrated with RF electronics and is compatible with MEMS-based wafer-scale vacuum packaging. For a quartz thickness-shear mode resonator thinned to 1.49 μm, we measured a resonant frequency of 591 MHz and a Q of 13,470 in air. This device has an excellent motional resistance of 40 Ω and a temperature coefficient of –5 ppm/ ^{o}C. We have also demonstrated that FIB micromachining can be used for precise frequency tuning of resonator with 150 ppb accuracy. Future work will emphasize higher frequency performance using thinner aluminum electrodes and optimizing the temperature stability.

ACKNOWLEDGMENTS

The authors would like to thank Dr. John Vig of US Army CECOM and Prof. Yook-Kong Yong of Rutgers University for their valuable technical discussions and support. We also acknowledge the modeling support of Matt Lim and Prof. Robert M'Closkey from UCLA. This project is being funded by DARPA's Microsystems Technology Office under contract DAAB07-02-C-P613.

REFERENCES

1. Statek Corporation, Technical Note 28, Rev. A, "An Ultra-Miniature Low-Profile AT Quartz Resonator."

2. C. T.-C. Nguyen, "Frequency-Selective MEMS for Miniaturized Low-Power Communication Devices," *IEEE Transactions on Microwave Theory and Techniques,* vol. 47, no 8, pp 1486-1503, 1999.

3. D. Chang, F. Stratton, R. Kubena, R. Joyce, "Optimized DRIE Etching of Ultra-Small Quartz Resonators," *Proceedings of the 2003 IEEE International Frequency Control Symposium*, pp 829-832, 2003.

4. R. Smythe and R. Angove, "Chemically-Milled UHF SC-Cut Resonators," *Proceedings of the 1988 IEEE International Frequency Control Symposium*, pp 73-77, 1988.

5. W.-T. Hsu, J. R. Clark, C. T.-C. Nguyen, "A Sub-Micron Capacitive Gap Process for Multiple-Metal-Electrode Lateral Micromechanical Resonator," *Proceedings of the 14th IEEE International Conference on Micro Electro Mechanical Systems,* pp. 349 – 352, 2001.

6. Microchip Technology, Inc. Technical Note AN 588.

REDUCTION IN THERMOELASTIC DISSIPATION IN MICROMECHANICAL RESONATORS BY DISRUPTION OF HEAT TRANSPORT

Rob N. Candler[1], Matthew Hopcroft[1], Woo-Tae Park[1], Saurabh A. Chandorkar[1], Gary Yama[2], Kenneth E. Goodson[1], Mathew Varghese[3], Amy E. Duwel[3], Aaron Partridge[2], Markus Lutz[2], and Thomas W. Kenny[1]

[1]Stanford University, Departments of Mechanical and Electrical Engineering
Stanford, CA 94305

[2]Robert Bosch Corporation, Research and Technology Center, North America
Palo Alto, CA 94304

[3]Charles Stark Draper Laboratory
Cambridge, MA 02139

ABSTRACT

Micromechanical resonators have been fabricated with a novel geometry, designed to disrupt thermoelastic dissipation (TED), which is heat flow that can limit the quality factor, Q. Finite element simulations were used to design resonators with heat flow-interrupting slits that have achieved Q's higher than a simple beam achieves and higher than a simplistic application of Zener theory predicts. The new structures have a Q as much as 4X the value of those without the new geometry, 40,000 as compared to 10,000 for a ~550kHz resonator. This result shows the necessity of modeling the complex interaction between the thermal and mechanical modes, and demonstrates a tool to engineer specific Q values for micromechanical resonators.

INTRODUCTION

With the growing interest in the use of micromechanical resonators for communications applications [1], understanding the operation of these resonators has become essential. The ability to predict and control the essential parameters (e.g resonant frequency and quality factor) of these resonators is a prerequisite to their inclusion in useful systems. Quality factor, Q, determines how well the given resonator can store energy, and it has an impact on the signal-to-noise ratio of the device. There are many mechanisms that can limit the Q, including air damping, material quality, energy dissipation on the surface, anchor loss, and thermoelastic dissipation. Thermoelastic dissipation (TED) is a phenomenon, discussed in the 1930s by Zener [2], whereby a strain gradient produces a thermal gradient in a structure. The finite thermal conductivity of the material allows this thermal gradient to relax via the flow of heat across the beam. The result of this process is a loss in energy, because an energy input was required to generate the thermal gradient. This energy loss can limit the quality factor of the resonator, especially if the thermal time constant associated with the loss is of the same order as the period of the mechanical resonance. The theory developed by Zener was for simple geometries and predicted a curve of theoretically limited Q, as shown in Fig. 1.

This theory is accurate for predicting Q limited from TED in simple beams [3]. However, the question remains open about the TED-limited Q for more complex structures. Theories have recently been developed about the effect of more complex situations, such as TED due to stress on polysilicon grains [4] and the addition of thermal paths due to process-induced geometries [5]. The present work couples novel simulation techniques [6] with a series of targeted experiments to extend TED theory and understand the interaction of multiple thermal modes with the mechanical resonance. Resonators were designed with purposefully placed slits to disrupt the flow of heat across the flexed beams.

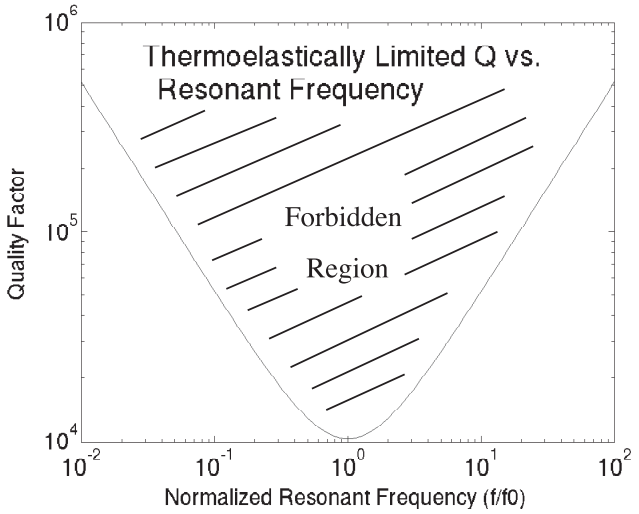

***Figure 1**. Theoretical limit of quality factor of a flexural beam with Zener theory.*

MODELING AND DESIGN

In a weakly coupled thermoelastic model (high Q), multiple thermal modes contribute to damping, with separate weighting functions defining the damping contribution [2, 7]. In Zener's formulation, a weighting factor and a time constant for every thermal mode that contributes to damping must be calculated. For the flexural mode of a simple beam, Zener showed that a single thermal mode dominates the damping, with a weighting factor of 0.97 and a characteristic time constant determined by the beam width,

$$\tau = \left(\frac{b}{\pi}\right)^2 \frac{C_v}{\kappa} \qquad (1)$$

where τ is the time constant, b is the width, C_v is the specific heat per unit volume at constant pressure, and κ is the thermal conductivity. Fig. 2 shows the Q for the single thermal mode (as

Travel support has been generously provided by the Transducers Research Foundation and by the DARPA MEMS and DARPA BioFlips programs.

the solid line), given by the following equation using Zener's method.

$$Q_{TED}^{-1} = \left(\frac{E\alpha^2 T_0}{C_v} \right) \frac{\omega\tau}{1+(\omega\tau)^2} \tag{2}$$

E is the Young's Modulus, T_0 is the equilibrium temperature of the beam, α is the coefficient of thermal expansion, and ω is the angular frequency.

The introduction of slits in the beam will modify the thermal modes of a simple beam, and multiple modes may contribute to damping. Even if one mode dominates, the weighting factor may be significantly modified. Consider the case of only one dominant mode (assumed weighting factor = 1) with a characteristic time constant determined by half the beam width. The corresponding Q is plotted in Fig. 2 (as the dashed line).

Others have interpreted their data by looking for rough characteristic length scales for the thermal modes and by considering the possibility that multiple modes may contribute to Q [4, 5]. In all examples above, the weighting factors were neglected to obtain an analytically tractable solution. In general, the effect of multiple thermal modes on Q with weighting factors is as follows,

$$Q_{TED}^{-1} = \left(\frac{E\alpha^2 T_0}{C_v} \right) \sum_n \frac{\omega\tau_n}{1+(\omega\tau_n)^2} f_n \tag{3}$$

where τ_n is the characteristic time constant for a given mode, and f_n is the weighting factor [7]. For arbitrary geometries, it may not be possible to identify characteristic thermal time constants by inspection. It is possible to evaluate both characteristic thermal time constants as well as weighting factors numerically, and this offers valuable intuition.

In this work, however, a very different approach is used to evaluate the Q. We find the complex eigenvalues of the fully coupled thermo-mechanical equations using a finite elements solver [6, 8]. The coupled thermo-mechanical equations are re-formulated in 2D by using plane stress approximations. This reduces the number of degrees of freedom, minimizing memory requirements and reducing computation time. Fig. 3 shows the simulated eigensolutions for a simple beam and a beam with slits. The materials parameters used in the simulations are summarized in Table 1.

Silicon Parameter	Value
Density, ρ	2330 kg/ m^3
Young's Modulus, E	157 GPa
Poisson ratio, ν	0.3
Specific Heat, C_v	700 J/ kg•K
Thermal Conductivity, κ	90 W/ K•m
Coefficient thermal expansion, α	2.6 ppm/K
Ambient Temperature, T_0	300 K

Table 1. *Silicon parameters used in TED simulations*

Simulated Q values as a function of frequency are also included in Fig. 2. For the beam without slits, the Zener formula with one mode matches the simulations well. When slits are included, a single Q minimum still appears. Interestingly, the frequency of the Q minimum is close to the frequency of Q minimum for a thermal time scale corresponding to half the beam width. The symmetry of the minimum and the value of Q deviate significantly from the amended Zener minimum. These simulations indicate that Q at a particular frequency can be improved by engineering the geometry of the resonator.

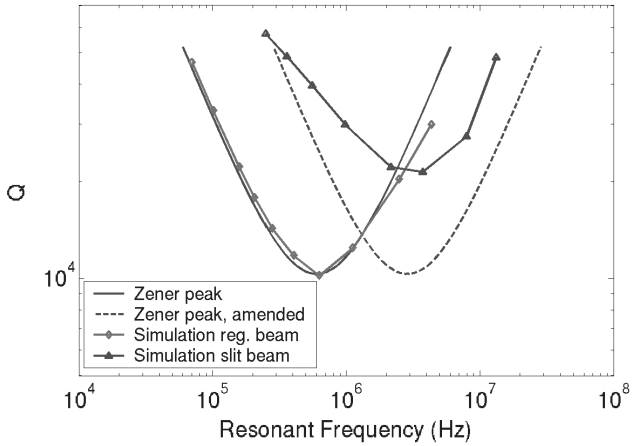

Figure 2*. Theoretical limit of Q by various methods: Zener theory, Zener theory amended to model a beam with slits, FEMLAB eigenvalue simulation for regular beam, and FEMLAB eigenvalue simulation for beam with slits.*

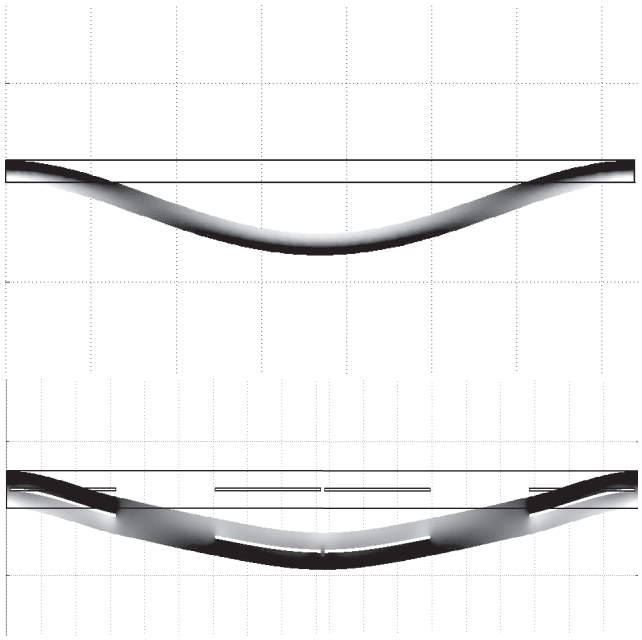

Figure 3. *FEMLAB plot of eigensolutions to thermoelastic equations for a regular beam (top) and a beam with slits (bottom). Deformation shows mechanical solution, and grey scale indicates the local temperature variation. Lighter tone correlates to higher temperatures. The slits isolate the hot and cold regions and also modify the overall damping.*

The resonators were designed to examine different mechanical resonant frequencies while maintaining similar thermal modes. In order to do this, a control set of resonators without slits was included in the design. The width in the direction of resonance was fixed at 12μm to keep a constant thermal time constant across the beam. The length of the beam was altered to produce resonators with different resonant frequencies. A second set of resonant beams with slits designed to disrupt the flow of heat

across the beam was included with the purpose being to understand the effect of additional thermal paths. The structures were all doubly-clamped tuning forks, as seen in Fig. 4, with the slit configuration shown in Fig. 5.

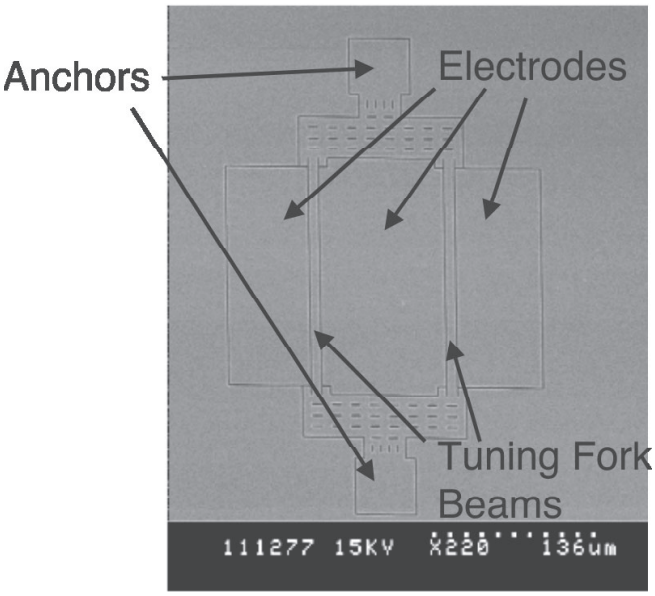

Figure 4. *Top view SEM of tuning fork, showing beams, anchors, and electrodes.*

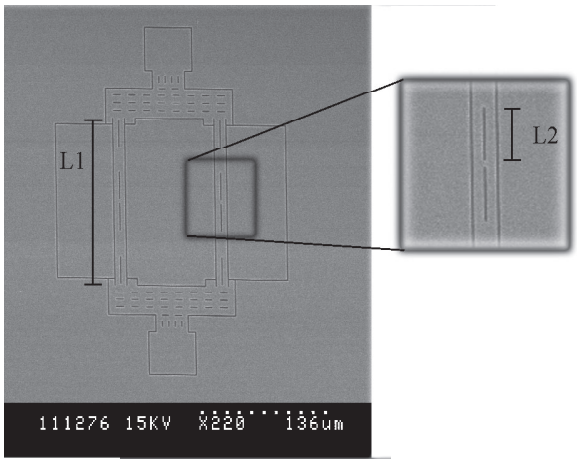

Figure 5. *Top view SEM of tuning fork with heat flow interrupting slits. Each beam has 4 slits. The slit-to-beam length ratio, L2:L1, is 1:6. A range of values for L1 was used to vary frequency, but the ratio of L2:L1 was kept constant.*

FABRICATION

The devices were fabricated using a wafer scale, single-wafer encapsulation technique. Features of this process include a HF vapor release process and deposition of an epitaxial polysilicon encapsulation layer [9]. Process details can be seen in Figs. 6 and 7.

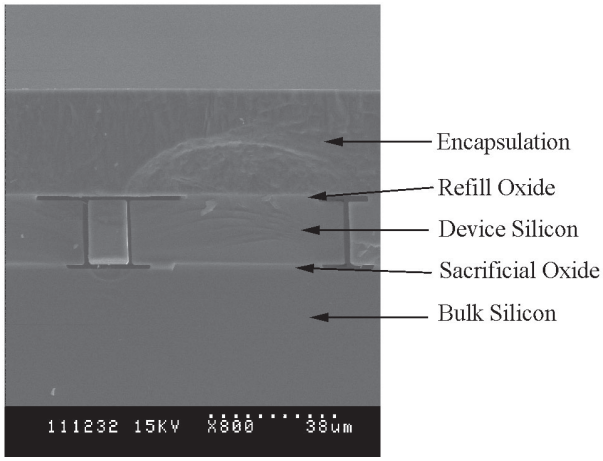

Figure 6. *Cross section of fabricated wafer, showing device under silicon encapsulation.*

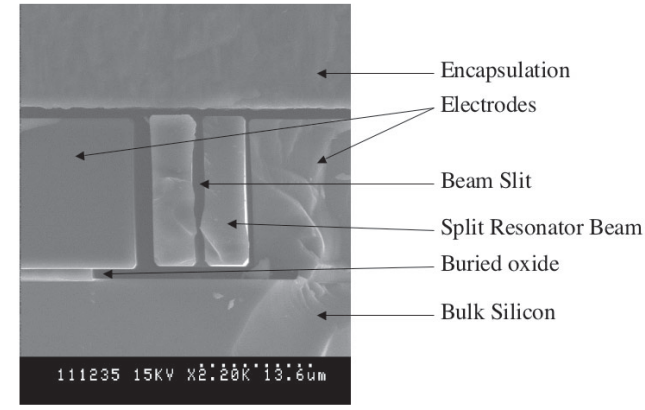

Figure 7. *Cross-section of slit beam, showing electrodes on either side of a beam with a slit*

RESULTS

Resonators with and without slits were fabricated and tested. A Bode Plot for a typical resonator is shown in Fig. 8.

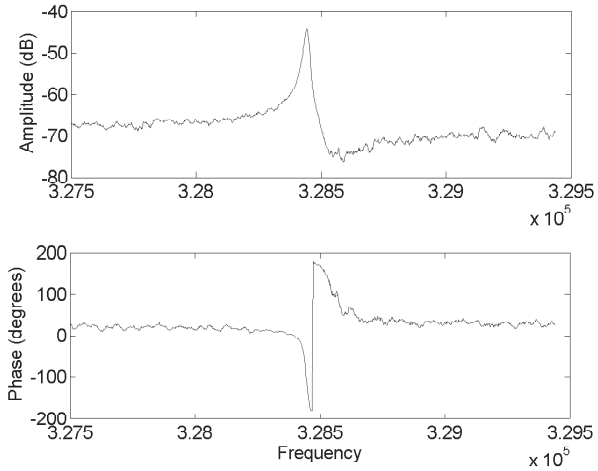

Figure 8. *Bode plot for a 328.5 kHz resonator.*

Both sets of resonators, with and without slits, were tested to determine resonant frequency and Q. Results were shown to be in good agreement with the simulations, as shown in Fig. 9.

The effect of other damping mechanisms is likely minimal with respect to the effect of TED for these measurements. The two sets of structures, with and without slits, have identical anchors, which should give them similar clamping loss. Also the addition of slits will minimally change the air damping. Since the slit beams have a similar structure but significantly higher Q than those without slits, it is reasonable to conclude that the beams without slits must be limited by a mechanism other than pressure or clamping, namely TED. The close following of the slit beams with simulation suggest that these results are also from TED. The parts were measured in their wafer-scale encapsulation, which was found to have a pressure of ~3 Pa. The package has shown no noticeable degradation in pressure over the past several months. In addition, the lowest frequency, highest Q parts were measured under vacuum conditions to guarantee that pressure limitation was not a factor.

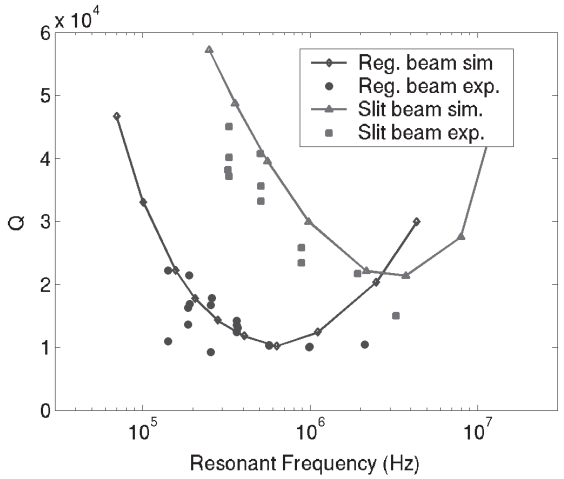

Figure 9. *Simulation and experimental results for TED limited single crystal silicon resonators. Regular beams and beams with slits show different TED limitation. Both types of devices agree well with simulation results.*

CONCLUSION

Novel modeling techniques have been used to study thermoelastic dissipation in complex structures and engineer resonators to improve Q. A wafer scale encapsulation process was used to fabricate devices to provide experimental evidence which, when coupled with the models, enable a more in-depth understanding of TED, and capture the complex interaction between mechanical and dissipative thermal modes. The micromechanical resonators were fabricated using the modeling as a design guide, and the experimental results were found to be in good agreement with the modeling.

ACKNOWLEDGEMENTS

This work was supported by DARPA HERMIT (ONR N66001-03-1-8942), Bosch Palo Alto Research and Technology Center, a CIS Seed Grant, The National Nanofabrication Users Network facilities funded by the National Science Foundation under award ECS-9731294, and The National Science Foundation Instrumentation for Materials Research Program (DMR 9504099).

REFERENCES

[1] C. T.-C. Nguyen, "RF MEMS for wireless applications," *Device Research Conference*, pp. 9-12, 2002.

[2] C. Zener, "Internal Friction In Solids: II. General Theory of Themoelastic Internal Friction," *Physical Review*, vol. 53, pp. 90-99, 1937.

[3] T. V. Roszhart, "Micromachined Silicon Resonators," presented at Electro International, 1991, 1991.

[4] V. T. Srikar and S. D. Senturia, "Thermoelastic damping in fine-grained polysilicon flexural beam resonators," *Journal ofMicroelectromechanical Systems*, vol. 11, pp. 499-504, 2002.

[5] R. Abdolvand, G. K. Ho, A. Erbil, and F. Ayazi, "Thermoelastic damping in trench-refilled polysilicon resonators," *TRANSDUCERS, 12th International Conference onSolid-State Sensors, Actuators and Microsystems*, vol. 1, pp. 324-327, 2003.

[6] B. Antkowiak, J. P. Gorman, M. Varghese, D. J. D. Carter, and A. Duwel, "Design of a High-Q Low-Impedance, GHz-Range Piezoelectric MEMS Resonator," *TRANSDUCERS, 12th International Conference on Solid-State Sensors, Actuators and Microsystems*, pp. 841-846, 2003.

[7] A. S. Nowick and B. S. Berry, *Anelastic Relaxation in Crystalline Solids*, 1972.

[8] J. P. Gorman, "Finite Element Model of Thermoelastic Damping in MEMS, Master's Thesis," in *Materials Science and Engineering*: Massachusetts Institute of Technology, 2002.

[9] R. N. Candler, W.-T. Park, H. Li, G. Yama, A. Partridge, M. Lutz, and T. W. Kenny, "Single wafer encapsulation of MEMS devices," *IEEE Transactions on Advanced Packaging*, vol. 26, pp. 227-232, 2003.

A MASS SENSOR BASED ON PARAMETRIC RESONANCE

Wenhua Zhang and Kimberly L. Turner
Department of Mechanical and Environmental Engineering, University of California
Santa Barbara, CA 93106

ABSTRACT

We present a parametric resonance-based mass sensor, comprised of a single-crystal silicon micro-oscillator with sensitivity at the pico-gram (10^{-12} *g*) level when operating in air. This mass sensor detects mass change by measuring frequency shift at the boundary of the first order parametric resonance 'tongue'. High sensitivity is achievable due to the sharp jump in amplitude caused by parametric resonance at predictable drive frequencies. Pt deposition using focused ion beam and water vapor are used to change the mass of the testing oscillator. The results show that the sensitivity can be > 1 order higher than the same oscillator working at simple harmonic resonance mode. The effect of noise on mass sensing ability in this nonlinear dynamic system is considered as well.

INTRODUCTION

The concept of tracking resonant frequency shifts of micro/nano-oscillators in simple harmonic resonance mode to measure mass change is a well–established technology in applications of chemical and biological sensing. In a micro-cantilever array, information on cantilever resonance frequency shifts can be used for recognition of a variety of chemical substances, such as water, primary alcohols, and alkanes **[1]**. A single cell with an estimated mass of about 0.7 pico-gram has been detected based on a micro-cantilever **[2]**. By creating even smaller oscillators, such as in nano scale, the ability of detecting femtograms or even attograms of mass change should be achievable **[3]**.

One of the factors which limit the sensitivity of the simple harmonic resonance (SHR) based mass sensors is the quality factor (*Q*). Micro/nano-oscillator with high *Q* can detect small mass changes in the system because of the ability to resolve small frequency shift. Very low pressure and temperature is desired in many of these high-sensitive mass sensors, which makes the applications very limited. The sensitivity of mass detection can be dramatically lowered when operating in air or water, where *Q* can be less than 10.

In previous work, we have reported the concept of mass sensing using parametric resonance phenomenon **[4, 5]**. This mass sensor detects mass change by measuring frequency shift of the stability boundary of the first order parametric resonance tongue **[4, 5]**. This transition at the boundary is very sharp, thereby making small frequency changes easily detectable and the resolution high **[5, 6]**. Since quality factor will not affect the sharpness of the transition, very small mass change can be detected in high pressure, even in air.

In this work, we present the first results on a mass sensor based on parametric resonance phenomenon. This preliminary device has sensitivity at the pico-gram (10^{-12} *g*) level when operating in air. This mass sensor is comprised of a single crystal silicon micro-oscillator (Fig.1), in which the backbone is supported by four folded beams to provide recovery force for the oscillation and driven by a set of non-interdigitated comb-fingers using fringing-field electrostatic force. Parametric resonance can be activated at certain frequencies because the non-interdigitated comb-fingers tune the stiffness of the oscillator **[5]**. To 'create' mass change to test the concept, Platinum is deposited on the backbone using Focused Ion Beam (FIB). A similar micro-oscillator is designed as a reference in the same package to improve the sensitivity of mass sensing through common-mode rejection.

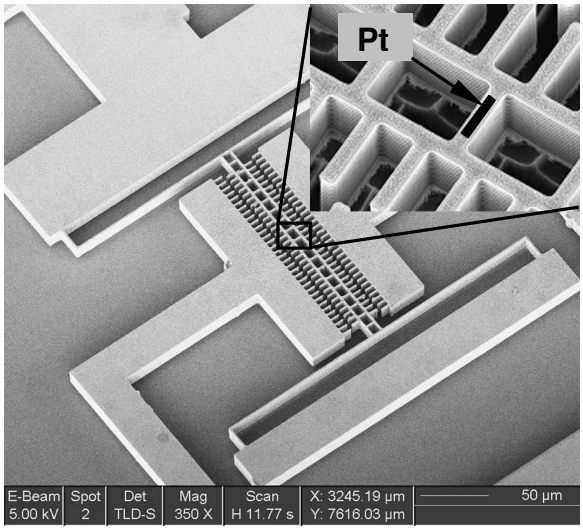

Figure 1. *A SEM picture of the mass sensor. It has a backbone, 4 springs with folded beams to provide recovery force and one set of non-interdigitated comb-fingers to drive the oscillator. Pt deposition to change mass is schematically shown in this picture.*

A noise analysis has been completed to determine the effect of noise on the device sensitivity. Because of the nonlinear dynamics nature of parametric resonance, the noise mechanism differs from normal simple harmonic resonance based mass sensors. Thermal noise, Brownian motion and actuation voltage fluctuation have been considered here. Both the experiment and analysis show that Brownian motion is the main noise source in mass sensing application of parametric resonance in air.

The ultimate sensitivity of the conceptual mass sensor is studied by testing water vapor content change in the environment. Less than 1 *pg* of mass change in the oscillator has been detected in air. Significant improvements of this technology are achievable by reducing the size of the structure. This is discussed later in the paper.

THEORY

In previous work, we have discussed the parametric resonance dynamics of a similar oscillator in detail **[5, 7]**. The

Acknowledgement: *Travel support has been generously provided by the Transducers Research Foundation and by the DARPA MEMS and DARPA BioFlips programs.*

micro-oscillator, shown in Fig.1, can be simplified as a mass-spring system with electrostatic force as the driving force. When electrical signal is applied on the non-interdigitated comb-fingers, the electrostatic force generated is dependent on the position of the oscillator. In the experiments presented here, we use a square rooted AC voltage signal $(V_A(1+\cos 2\omega t)^{1/2})$ to isolate the parametric resonance from direct harmonic response **[6]**. The movement of the device is governed by nonlinear Mathieu equation **[5]**.

$$\frac{d^2x}{d\tau^2}+\alpha\frac{dx}{d\tau}+(\beta+2\delta\cos 2\tau)x+(\delta_3+\delta_3^{'}\cos 2\tau)x^3=0 \qquad (1)$$

where $\alpha=\frac{2c}{m\omega}$ $\beta=\frac{4(k_1+r_1V_A^2)}{m\omega^2}$ $\delta=\frac{2r_1V_A^2}{m\omega^2}$

$\delta_3=\frac{4k_3+4r_3V_A^2}{m\omega^2}$ $\delta_3^{'}=\frac{4r_3V_A^2}{m\omega^2}$

m, k_1 and k_3 are the mass, linear and cubic mechanical stiffness of the oscillator, c is the damping coefficient, r_1 and r_3 are linear and cubic "electrostatic stiffness" and $\tau=\omega t$ is a normalized time **[5]**.

Figure 2 schematically shows the dynamics of this nonlinear Mathieu equation in β-δ plane defined above **[5]**. According to dynamic characteristics, β-δ plane can be divided into three areas. Area II inside the "tongue" is the resonance area of the first order parametric resonance with one non-trivial solution, while area I and III are non-resonance area with one trivial solution in area I and One trivial solution plus one non-trivial solution in area III. The characteristics of solutions in each area are schematically shown in Fig.2 as well, where "S" means stable and "U" means unstable. Here we only consider stable solution, since unstable solution cannot be observed experimentally. The dynamics can be more easily understand in an experimental frequency response as shown in Fig.3.

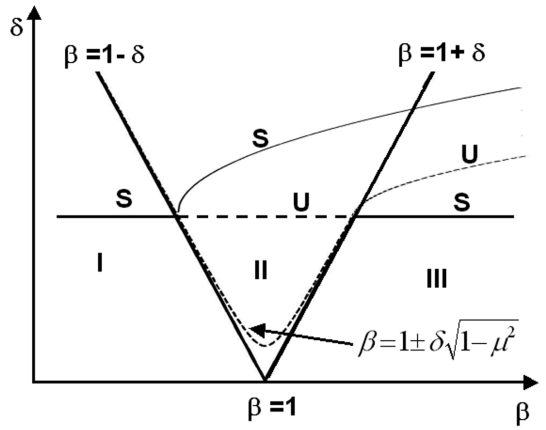

Figure 2. *Dynamic characteristics of Nonlinear Mathieu Equation in the β-δ plane. $\beta=1\pm\delta$ are the transition curves, which divide β-δ plane into Area I, II, III. Note the damping effects on transition curves and how the positions of the stable (dark trace) and unstable (broken trace) points vary as β and δ are varied quasi-statically.*

Figure 3 shows the typical frequency response of parametric resonance inside resonance area (area II) and outside of the resonance area (area I and III). As the driving frequency goes up, the amplitude of the oscillator increases from the left boundary of area II and keeps increasing past the boundary of area III. The frequency where the drop happens depends on initial condition of the frequency applied. When sweeping down the driving frequency from area III, movement of the oscillator jumps to a large value from zero at the right boundary of area II and reduces in amplitude thereafter until it reaches zero at the left boundary of area II. The frequency at the right boundary of area II, where the "jump" happens, is given by $f=\frac{1}{2\pi}\sqrt{4k+2rV_A^2/m}$, where k, m, V_A and r are stiffness, mass, driving voltage amplitude applied and the coefficient of electrostatic force respectively. A small mass change (Δm) in the oscillator causes this "jump" frequency to shift (Δf). Therefore, this mass change can be detected by measuring the frequency shift. Figure 4 shows the mechanism of parametric resonance based mass sensor, where the mass change is given by $|\Delta m|-2m\left|\Delta f\right|/f_0$.

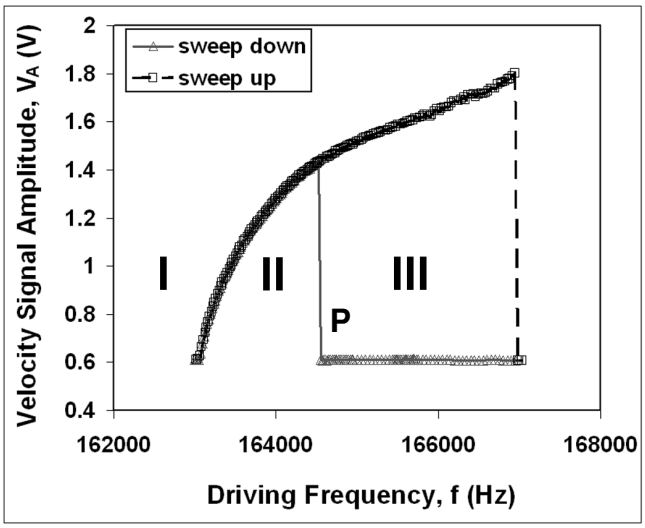

Figure 3. *A frequency response curves of the first order parametric resonance inside and outside of stability region. Area II is inside of "tongue", as shown in Fig.2, while I and III are outside. When sweep frequency down, resonance only happens in area II and there is completely no movement in area I and III. A jump happens at the right boundary of area II.*

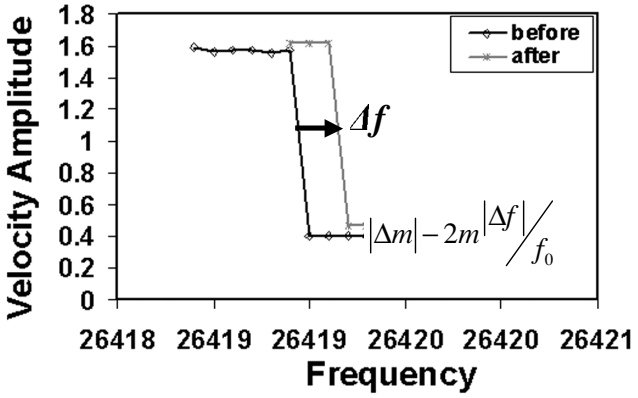

Figure 4. *Schematic of the mechanism of parametric resonance-based mass sensor. By measuring the frequency shift at right side of area II (Fig.3), mass change in the oscillator can be found.*

The sensitivity of parametric resonance based mass sensor depends on the smallest frequency shift we can measure. Since the "jump" is a characteristic of nonlinear dynamics, the detectable frequency shift can be very small. In our previous work, a 0.001*Hz*

frequency shift has been observed **[6]**. Damping affects the resonance boundary of the tongue, as shown in Fig.2. At high damping, for example in air, actuation of parametric resonance requires more energy than at low pressure. However, the characteristics of dynamics will not change. Therefore, damping has little effect on the sensitivity of parametric resonance based mass sensors.

EXPERIMENT

DEVICE FABRICATION

The micro-oscillators are fabricated from SOI wafer with highly doped device layer. After patterning, a deep silicon etch process, BOSCH, is performed to form the micro structure, following by removal of photo resist left and wet chemical release of the buried silicon oxide layer to form the suspended MEMS structure. The thickness of the device is about 18 μm, which is defined by the thickness of the top device layer. The fabricated oscillator is a single crystal silicon device and electrically conductive.

Eight devices with different dimensions and configurations have been made. Two of them are tested here, named as device#3 and device #4. The two devices have the same dimensions, except that the springs of device#3 are of 1.5 μm wide and that of device #4 are of 2.0 μm wide. The backbone mass of the two devices is about 30 *ng* and the natural frequencies are about 49 *kHz* and 83 *kHz*.

MASS SENSING WITH Pt DEPOSITION

As s proof of concept, we change the mass of the oscillator by attaching a set volume of Platinum (Pt) on device#3 using a FIB (Focused Ion Beam), as shown in Fig.1. Three such mass changes, about 1, 4 and 0.4 μm^3 Pt deposition (corresponding to about 20, 80 and 8 *pg*), have been made. We record the frequency change at the right boundary of the first order parametric resonance area as discussed earlier before and after the deposition in air using laser vibrometry **[8]**. Meanwhile, device#4 works as a reference sensor and the frequency information is also recorded as a reference to environmental fluctuation, such as humidity and temperature.

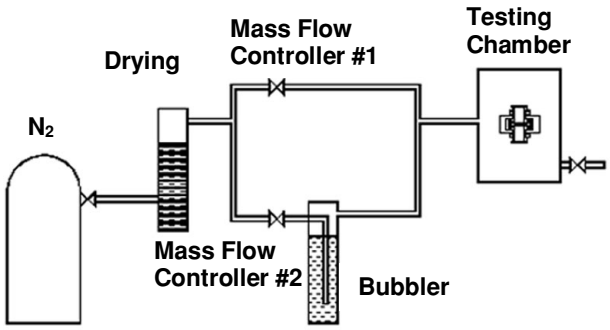

Figure 5. *Gas handling setup*

MASS SENSING WITH WATER VAPOR

To perform a more sensitive test, the mass sensor was also tested using adsorption of water vapor. A gas handling setup is built to control the water vapor content in testing chamber, as shown in Fig.5. A dry nitrogen gas flows through mass flow controller #1 directly to the testing chamber and another dry N_2 through mass flow controller #2 with water vapor from the water bubbler. By setting the flow rates of the two mass flow controllers, relative water content can be adjusted. The frequency information of device #4 at the right boundary of the first order parametric resonance area is recorded, as water content in the testing chamber is adjusted. Because of the native silicon oxide on the surface of the oscillator **[9]**, water molecules are absorbed on the surface and the mass of the oscillator is changed. By measuring this frequency shift, mass change can be determined.

RESULTS AND DISCUSSION

The results of frequency shift in Pt deposition test are shown in Fig.6. After each mass change, the "jump" frequency is recorded many times in a few days. The results are rectified according to frequency change in reference oscillator. As shown in Fig.6, the average frequency shift is about 36, 151 and 17 *Hz*, corresponding to 1, 4 and 0.4 μm Pt deposition. Good correlation is shown in these tests between the volume of Pt and "jump" frequency shift, as we discussed earlier, mass change is linearly dependent on frequency shift, $|\Delta m| - 2m\left|\Delta f\right| / f_0$, when mass change in the oscillator is small. The minimum mass change here is about 8 *pg*.

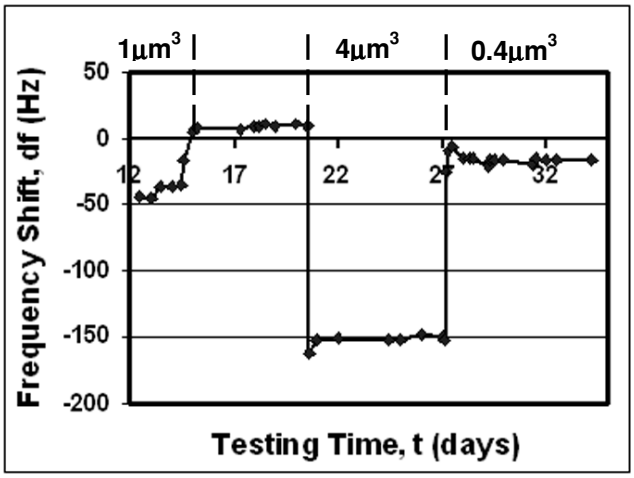

Figure 6*. Frequency shift in Pt deposition tests. Three mass changes have been made, 1, 4 and 0.4 μm^3 corresponding to about 20, 80 and 8 pg respectively.*

As with most micro-sensors **[10-12]**, noise is an important issue in mass sensing using parametric resonance technology. The ability to detect ultra-fine frequency shift because of the nature of parametric resonance is compromised by noise problems in the oscillator. As we mentioned earlier, a 0.001 *Hz* or even smaller frequency shift has been observed **[6]**. However, in our current experiment, the frequency fluctuation is much larger than this value and the standard deviation of this frequency fluctuation we measured in these two oscillators is about 0.8 *Hz* at room temperature. To analyze noise problems in mass sensing, we consider thermal noise, Brownian motion and Driving voltage fluctuation. Because of the complexity of parametric resonance, numerical simulation method is used to calculate the effects of these noise sources. Brownian motion of oscillators is attribute to be the main noise source in parametric resonance mass sensing. In room temperature, the standard deviation of Brownian motion is estimated about 0.5 *Å*, which brings about 0.7 *Hz* of frequency fluctuation. The result agrees well with measured result.

Certainly, there are other issues, which can be considered noise effects in mass sensing, such as frequency drift caused by humidity fluctuation and temperature fluctuation in the

environment. We notice that noise caused by this frequency drift can be larger than that caused by Brownian motion even with reference sensor when the test lasts days. These issues are currently being addressed.

To find the ultimate sensitivity of this mass sensor based on parametric resonance, we use the micro-oscillator to detect water content change in the testing chamber. By adjusting the water content, we observe the frequency shift simultaneously. Figure 7 shows the results of frequency shift of Device#4 as the relative water content is changed in air. When water content is switched between 5% and 10% as shown in Fig.7 from A-B, the rate of frequency shift changes. As water vapor is turn on and off from B-C, the results shows good consistency between frequency shift and water vapor content. The smallest controllable frequency shift as shown in Fig.7 is about 2 *Hz*, which is equivalent to mass change of 0.7 *pg*.

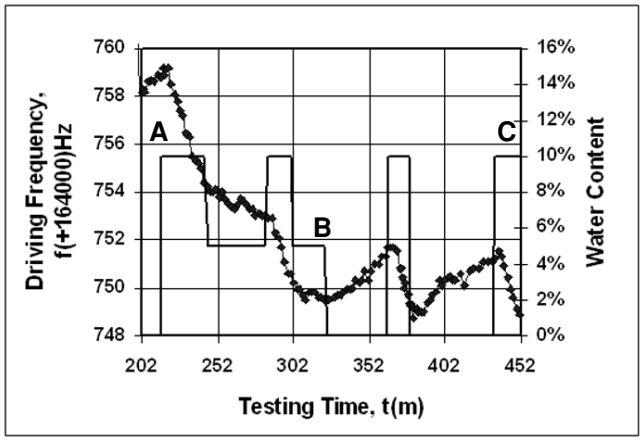

Figure 7. *Frequency shifts at the right side of the first parametric resonance area as adjusting water content.*

Because of damping effect, the sensitivity of simple harmonic resonance (SHR) based mass sensor decrease dramatically in air. It is difficult for the devices we tested here to resolve 100 *Hz* shift in SHR mode with Q about 50. Using parametric resonance, the sensitivity can improve more than 1 order of magnitude. Damping has little effect on the sensing ability when operated in a parametric resonance mode.

The devices are just prototype mass sensors to test the concept of parametric resonance mass sensing. By tailoring the oscillator dimensions (for example, the cantilever geometry), increasing resonance frequency, or designing oscillator arrays, the sensitivity can be further improved, thus extending their application to DNA, virus and other analytes with mass in the order of attograms. We calculated the noise level of device#3 with dimensions reduced by a factor of 5. The equivalent mass resolution will be at femto-gram level in air pressure. Now, many smaller micro/nano oscillators have been made with higher frequency, such as micro-cantilever and nanowire **[13, 14]**, and parametric resonance has been realized in these devices. Thus, the possibility of significant improvements in cantilever based sensors is achievable, and currently underway.

CONCLUSIONS

Parametric resonance based mass sensor has been developed in this work. The measurement, taken in air, demonstrates that parametric resonance-based mass sensors can improve sensitivity 1-2 orders compared to the same sensor working in harmonic mode. The prototype mass sensors can detect mass changes at pico gram level when operating in parametric resonance mode. By decreasing the mass of oscillator and increasing resonance frequency, the sensitivity can be further improved.

REFERENCES

1. F.M. Battiston, J.P. Ramseyer, H.P. Lang, M.K. Baller, C. Gerber, J.K. Gimzewski, E. Meyer, and H.J. Guntherodt, "A chemical sensor based on a microfabricated cantilever array with simultaneous resonance-frequency and bending readout", *Sensors & Actuators B-Chemical*, B77, 122 (2001).
2. B. Ilic, D. Czaplewski, M. Zalalutdinov, H.G. Craighead, P. Neuzil, C. Campagnolo, and C. Batt, "Single cell detection with micromechanical oscillators", *Journal of Vacuum Science & Technology B*, 19, 2825 (2001).
3. Z.J. Davis, G. Abadal, O. Kuhn, O. Hansen, F. Grey, and A. Boisen, "Fabrication and characterization of nanoresonating devices for mass detection", *J. Vac. Sci. Technol. B, Microelectron. Nanometer Struct.*, 18, 612 (2000).
4. K.L. Turner and W. Zhang, "Design and analysis of a dynamic MEM chemical sensor", *Proceedings of the 2001 American Control Conference*, Arlington, VA, USA, 25-27 June 2001, pp. 1214-1218.
5. W. Zhang, R. Baskaran, and K.L. Turner, "Effect of cubic nonlinearity on auto-parametrically amplified resonant MEMS mass sensor", *Sens. Actuators A, Phys.*, 102/1-2, (2002).
6. K.L. Turner, P.G. Hartwell, F.M. Bertsch, and N.C. MacDonald, "Parametric resonance in a microelectromechanical torsional oscillator", *ASME International Mechanical Engineering Congress and Exposition Proceedings of Microelectromechanical Systems (MEMS)*, Anaheim, CA, USA, 15-20 Nov. 1998, ASME, New York, NY, USA.(1998), pp. 335-340.
7. W. Zhang, R. Baskaran, and K.L. Turner, "Tuning the dynamic behavior of parametric resonance in a micromechanical oscillator", *Appl. Phys. Lett.*, 82, 130 (2003).
8. K.L. Turner, "Multi-dimensional MEMS motion characterization using laser vibrometry", *Transducers'99 The 10th International conference on solid-state Sensors and Actuators, Digest of Technical Papers*,, Sendai, Japan, 7-10 June 1999, pp. 1144-1147.
9. H.P. Lang, M.K. Baller, F.M. Battiston, J. Fritz, R. Berger, J.P. Ramseyer, P. Fornaro, E. Meyer, H.J. Guntherodt, J. Brugger, U. Drechsler, H. Rothuizen, M. Despont, P. Vettiger, C. Gerber, and J.K. Gimzewski, "The nanomechanical NOSE", *Proceedings of 12th International Workshop on Micro Electro Mechanical Systems - MEMS*, Orlando, FL, USA, 17-21 Jan. 1999, pp. 9-13.
10. A.N. Cleland and M.L. Roukes, "Fabrication of high frequency nanometer scale mechanical resonators from bulk Si crystals", *Appl. Phys. Lett.*, 69, 2653 (1996).
11. J.R. Vig and K. Yoonkee, "Noise in microelectromechanical system resonators", *IEEE Transactions on Ultrasonics Ferroelectrics & Frequency Control*, 46, 1558 (1999).
12. T.B. Gabrielson, "Mechanical-thermal noise in micromachined acoustic and vibration sensors", *IEEE Trans. Electron Devices*, 40, 903 (1993).
13. Y. Min-Feng, G.J. Wagner, R.S. Ruoff, and M.J. Dyer, "Realization of parametric resonances in a nanowire mechanical system with nanomanipulation inside a scanning electron microscope", *Physical Review B-Condensed Matter*, 66, 073406/1 (2002).
14. M. Napoli, R. Baskaran, K. Turner, and B. Bamieh, "Understanding mechanical domain parametric resonance in microcantilevers", *Proceedings IEEE Sixteenth Annual International Conference on Micro Electro Mechanical Systems*, Kyoto, Japan, 19-23 Jan. 2003, pp. 169-172.

MICROGEIGER: A MICROFABRICATED GAS-BASED BETA RADIATION DETECTOR

Chester G. Wilson* and Yogesh B. Gianchandani
Department of Electrical Engineering and Computer Science, University of Michigan, Ann Arbor

ABSTRACT

This paper reports a micromachined Geiger counter fabricated from a glass-Si-glass stack of wafers. As a beta particle passes through, a bias applied between two enclosed electrodes generates electron cascades in the gas between them. This results in a current pulse or "count". A single die of 2 cm^2 had 6 independent chambers ranging in size from 8X8 mm to 1X3 mm. He, Ne, and a He/air mixture, which have different voltage bias requirements, are separately evaluated as background gases. Counting rates are lower in a Ne background gas than in He, but Ne is more suitable for packaging. In tests the device was found to detect incident beta particles from a Uranium-238 source. Counting rates of up to 22 counts/min were measured. As with conventional Geiger counters, the rates varied inversely with distance from the source. The microGeiger was tested with pure He and Ne background gas with ^{90}Sr, ^{60}Co, and ^{204}Tl, all beta emitting isotopes. Rates up to 24 counts/min. were measured.

I. INTRODUCTION

Radioactive materials, particularly uranium, are stockpiled in large and small quantities all over the world with varying degrees of security. There is a perpetual risk of their potential use in "dirty bombs," which use conventional explosives to disperse dangerous radioactive materials. Uranium-238 naturally decays into ^{234}Th and then ^{234m}Pa, emitting 0.8 MeV beta particles, which are essentially high energy electrons. Other possible dirty bomb ingredients include a number of beta sources, including ^{90}Sr and ^{204}Tl. The former is a particularly hazardous material, as it is easily absorbed into the human body, where it displaces calcium in bone, remaining there with a radioactive half-life of 27 years. Thus, there is considerable motivation to develop miniaturized sensors for radioactive materials.

Since a few radioactive materials emit X-rays, one possibility is to exploit X-ray detectors, which have benefited from solid-state technology in recent years [1]. Unfortunately, most radioisotopes are not sources of X-rays, and the best way to detect most of the target species for dirty bombs is through their emission of beta particles. Solid-state detectors for beta particle exist, but they are relatively large, with sizes on the order of 1 cm^2. They typically require cryogenic cooling to distinguish radiation type and energy, and are particularly subject to radiation damage [2]. Another type of device uses pixelated silicon structures at room temperature to provide spatial imaging of beta particle flux [3].

Geiger counters, however, are the preferred sensors for detecting beta radiation [4]. Typical Geiger counters utilize a tube held under vacuum, with a rod-like anode and concentric cathode. (Fig. 1). The tube is biased at 500-1000 volts, and a thin window – typically mica – allows passage of beta radiation. This radiation ionizes the gas at some statistical rate, resulting in an avalanche breakdown, which is measured by circuitry as a "count" corresponding to one event. These gas-based detectors are very reliable, temperature insensitive, require only simple circuitry, and measure over a much wider range of radiation species and energies. Miniaturized gas-based detectors exist, but work only for detection of photon based radiation, such as X-rays [5]. Again, as very few isotopes emit X-rays, there is a compelling need for a micromachined beta radiation detector.

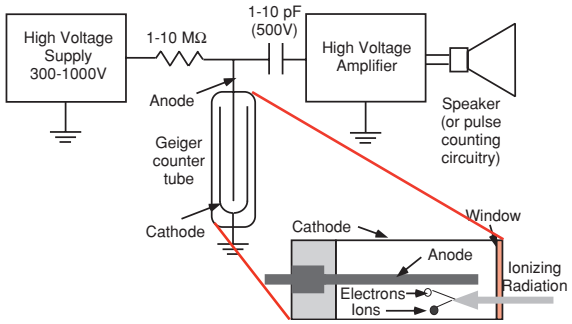

Fig. 1: Traditional Geiger counters utilize a tube under partial vacuum, and a high voltage supply applied through a resistor to a small capacitor.

II. DEVICE CONCEPTS AND OPERATION

The microGeiger device is fabricated by anodic bonding a glass-silicon-glass stack, where the silicon is EDP etched to form an anode-cathode configuration. When DC power is applied to this configuration two electrostatic regions are formed: a drift and amplification region (Fig. 2). As beta particles pass through the glass window into the drift region, they ionize the background gas. The electrons are slowly accelerated into the amplification region. In the amplification region the electrons are quickly accelerated

* *Corresponding author:* chwilsn@engin.umich.edu.

0-9640024-5-0/hh2004/$20©2004TRF
DOI 10.31438/trf.hh2004.13

Solid-State Sensors, Actuators, and Microsystems Workshop
Hilton Head Island, South Carolina, June 6-10, 2004

through a higher field region resulting in an electron cascade. Designing the drift region to be much larger than the amplification region allows consistent pulses that are not a function of the entry position of the beta particle.

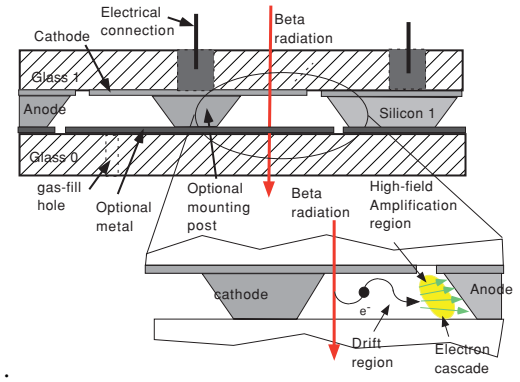

Fig. 2: The microGeiger device utilizes dissolved silicon bonded to glass as the anode-cathode configuration. Beta radiation passing through the drift region creates liberated electrons, which travel to the amplification region, creating an electron cascade.

Macroscale gas-based devices have been widely used in the field of radiation detection [6]. Virtually all gas-based detectors rely on the impinging radiation ionizing the fill gas, with the resulting electrons accelerated by an electric field, ionizing more neutral species, thereby creating an avalanche breakdown. The general form of the electron density in a cascade of length x is given by:

$$n(x) = n(0)\exp(\alpha x) \qquad (1)$$

Here, α is the first Townsend coefficient of the gas, a function of the gasses ionizability, and electron capture cross section.

Typical detectors fall into four regimes of operation, defined by the applied electric field, electrode geometry, and the pressure and species of fill gas (Fig. 3). The four regimes all have electric discharges with differing physical properties. (These regimes apply to both beta particles and photons like X-rays and gamma particles). The regime with the lowest voltage is the ion saturation region, where the only charge collected is by gas directly ionized by impinging radiation. As the voltage across the device is increased, avalanche breakdown begins to occur, and the amount of collected current increases. This is the proportional region: the amount of current is roughly proportional to the energy of impinging X-rays or gamma particles, as photon radiation is completely absorbed by the background gas. In contrast, impinging beta particles impart only a portion of their kinetic energy to the ionization of gas, so the resulting current created is not correlated to the beta energy; the proportional region is more limited for beta particles.

As the voltage is increased, the dependence of the current pulse upon the energy of the radiation is diminished even for photon radiation. This non-linearity is primarily due to the difference in mobilities between ions and electrons. In the limited proportionality regime, the much slower ions are sufficient in quantity to create a space-charge region which distorts the local electric fields. This limits the total charge, such as created by avalanching and is dependent on the electric fields. (Similar space-charge regions have been found to be the reason for lower charge densities in previously reported microplasmas [6].) As the voltage is increased further, the impinging radiation generates a self-sustaining discharge; this is the Geiger-Muller region. The total amount of current collected in this region for a cylindrical proportional counter is given by:

$$\ln M = \frac{V}{\ln(b/a)} \cdot \frac{\ln 2}{\Delta V}\left(\ln\frac{V}{pa\ln(b/a)} - \ln K\right) \qquad (2)$$

Here, M is the multiplication factor, the quantity of electrons from a single incident. V is the applied voltage, a and b are the anode and cathode radii, respectively; p is the ambient gas pressure, and ΔV and K are constants of the background gas, related to electron mean free path and ionizability.

For the characteristic dimensions, and gas species of the microGeiger device, a corresponding cylindrical configuration would provide an M, multiplication factor ranging from 10 to 10^5 as the operating voltages are varied. The actual multiplication of the microGeiger device is in the range of 1-2 $\times 10^{13}$. This is because the microGeiger device operates in the Geiger-Muller regime, where the initial charge multiplication is further amplified by secondary emission from the anode. This serves as compensation for the small size of the microGeiger, in which the amplification region is smaller than in traditional devices.

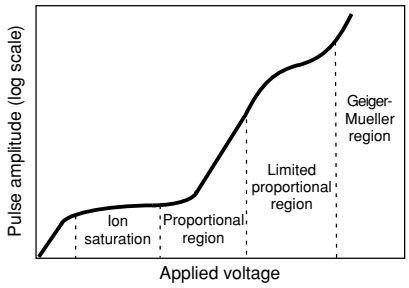

Fig. 3: Gas-based radiation detectors have four regimes of operation, that are defined by the applied voltage.

III. DEVICE FABRICATION

The microGeiger device is fabricated in either a two or three mask process (Fig. 4). The first mask defines a boron-diffused etch stop. Mask two patterns an oxide which defines a region where silicon is etched. This silicon wafer is anodically bonded to a pyrex wafer, which forms the beta window. The silicon is etched, forming structural offsets, and boron-doped anodes and cathodes. The stack is diced and bonded to a second glass wafer, providing the capability

of gas packaging. Photographs of the final die with six independent cavities is shown in Fig. 5.

IV. EXPERIMENTAL RESULTS

Unsealed devices were tested in a flow chamber to permit the comparison of various fill gasses (Fig. 7). The background gas flows into the microGeiger device through input ports machined into the glass window. The gasses which were evaluated included He, Ne, and a He/Air gas mixture. Helium was chosen for its lower ionization energy; this allows a larger current pulse at microscale dimensions. Neon also has a lower ionization energy, but does not leak through metal. In the test set-up DC power was provided to a capacitor which powers the anode; the cathode was grounded. Figure 8 shows a uranium ore sample that was used to test the devices. For all uranium tests a He/Air gas mixture was used as the background fill gas. Figure 9 illustrates the counting rate of one chamber in the microGeiger as a function of the distance from the detector. The normalized decline in counts is similar to that measured with a conventional detector, an Electro-Neutronics CDV-700.

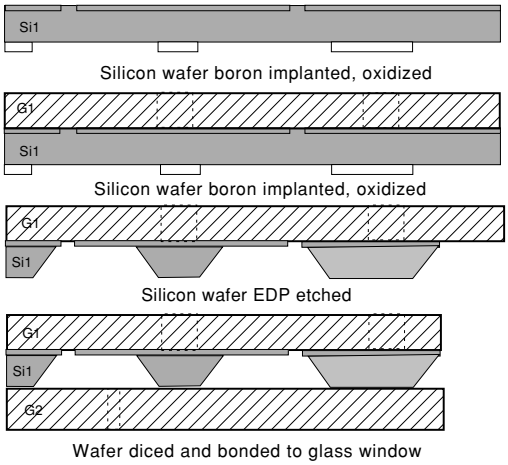

Fig. 4: Process flow of the microGeiger device. Mask 1 defines a boron etch stop, mask 2 a patterned oxide. EDP etching, anodic bonding, and additional glass processing define the microGeiger cavities.

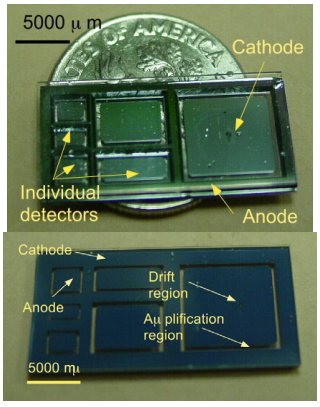

Fig. 5 (a-upper) The microGeiger die contains multiple detector cavities and is orders of magnitude smaller than traditional tubes. (b-lower) Backside of the microGeiger device.

Figure 10 shows the counts per minute as a function of the thickness of the glass windows. As the thickness of the window increases, more beta radiation is absorbed before it reaches the encapsulated gas as the glass thickness is increased. This illustrates that standard glass wafers from 500 μm – 750 μm can be utilized for fabrication.

As the discharge capacitor that powers the microGeiger device is charged to increasing voltages the charge delivered in each pulse increases, however, the final voltage on the discharge capacitor after ignition remains fairly constant (Fig. 11). This provides evidence that a self-sustaining discharge is created in the device that terminates when the capacitor reaches a certain voltage.

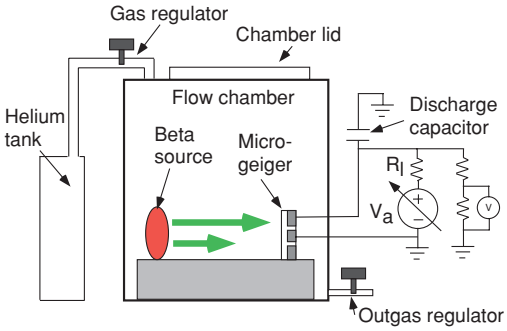

Fig. 7: Preliminary test setup for the microGeiger device; tank allows for helium filling, and pulse discharge measurement. Final microGeiger devices have the gas sealed within them, and do not require the chamber.

Fig. 8: Uranium ore sample used to test device.

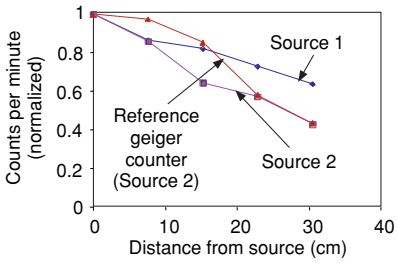

Fig. 9: Normalized counts per minute for the microGeiger and a reference Geiger counter as a function of source distance.

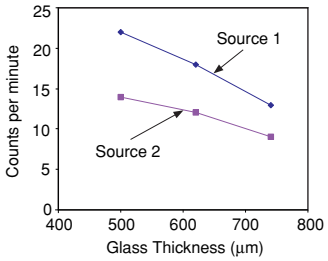

Fig. 10: Over 20 counts per minute are realized on the microGeiger. 200 μm thickness of glass reduces the counting rate by about a factor of 2.

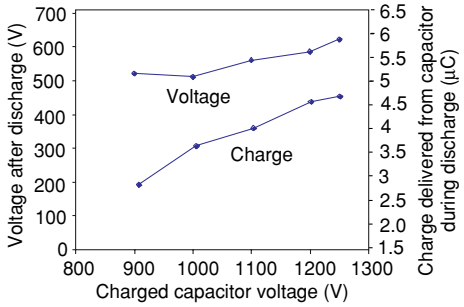

Fig. 11: Increasing the capacitor bias increases the amount of charge delivered to the discharge. The residual voltage on the capacitor remains fairly constant

The microGeiger device was tested with a variety of radioactive isotopes, and fill gases. The corresponding results are shown in Figs. 12-14. Figure 12 illustrates data for a 500 μm thick Pyrex window, and He fill gas. Count rates were measured for three different cavity dimensions (8X8 mm, 4X4.5 mm, and 2X2 mm), and two isotopes, ^{90}Sr and ^{60}Co. ^{90}Sr emits 0.546 MeV beta particles, and ^{60}Co provides a range of beta particles, with a maximum energy of 0.314 MeV. The count rate can be seen to increase as the cavity size increases, providing more collection area, for both isotopes. Figure 13 provides data for Ne fill gas, using ^{90}Sr and ^{204}Tl isotopes. ^{204}Tl produces a spectrum of beta particles with a maximum energy of 0.776 MeV. Again, the counting rate is seen to increase as the collection area increases.

Eventually, as the voltage is increased in the microGeiger device, a continuous arc breakdown occurs across the anode-cathode gap. Pulsed breakdown due to the impinging beta particle occurs at voltages that are lower, but still sufficiently high to develop the avalanche breakdown. This defines the allowed voltage operating range for the device, which is shown for three different background gasses in Fig. 14. Helium provides the lowest operating voltages but can be difficult to package long term, as it leaks through metal. Neon eliminates this problem with only a slight increase in operating voltage. He/Air mixtures provide a much wider range of allowed voltages, however the counting rate becomes a function of the operating voltage.

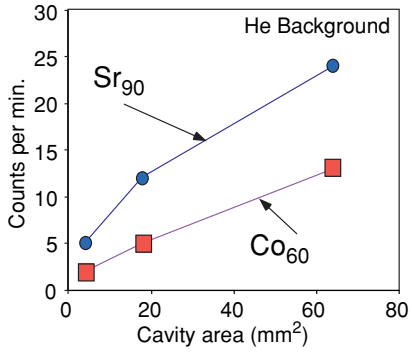

Fig. 12: Counting rates for a He packaged device, for varying cavity sizes.

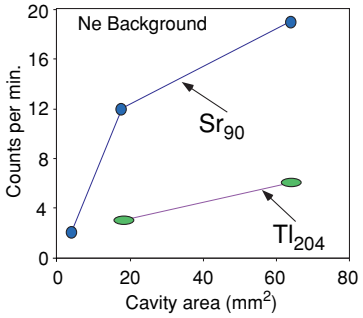

Fig. 13: Counting rates seen in a Ne packaged device, with varying cavity sizes.

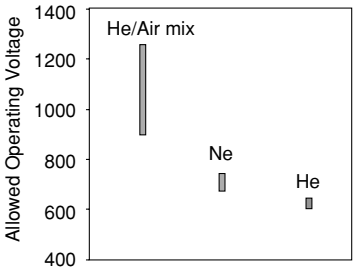

Fig. 14: Operational range of voltage on the microGeiger device for various fill gasses.

V. CONCLUSIONS

The microGeiger device was found to measure beta radiation produced from Uranium-238 ^{90}Sr, ^{60}Co, and ^{204}Tl, all beta emitting isotopes. Counting rates of up to 24 counts per minute were measured, and were found to fall as the source moved away in distance with similarly to a laboratory grade Geiger counter. He and Ne were evaluated as background gasses, as they provide a reduced operating voltage. The voltage required for a He/Air mixture is higher, but it provides a larger range of biasing.

ACKNOWLEDGEMENTS

This work was supported primarily by the Engineering Research Centers Program of the National Science Foundation under Award Number EEC-9986866. The facilities used for this research include the Solid State Electronics Laboratory (SSEL) at the University of Michigan. The authors are grateful to Mr. Ramon Torres-Isea, for use of the Advanced Physics Laboratory. Travel support has been generously provided by the Transducers Research Foundation and by the DARPA MEMS and DARPA BioFlips programs.

REFERENCES

[1] S. A. Audet, E. M. Wouters, and M. H. Kim, "High-Purity Silicon Soft X-Ray Imaging Sensor", Sensors and Actuators, (A22) nos. 1-3, Mar. 1990 pp. 482-486

[2] R. Wunstorf, "Radiation hardness of silicon detectors: current status", IEEE Transactions on Nuclear Science, (44) nos. 3, June 1997 pp. 806-14.

[3] E. Bertolucci, et. al., "BETAview: A Digital β-Imaging System for Dynamic Studies of Biological Phenomina," Nucl. Inst. and Methods, A381, 1996 pp. 527-530

[4] W. J. Price, Nuclear Radiation Detection, McGraw-Hill, 1964, pp. 123.

[5] G. Charpak, et. al., "Micromegas, a multipurpose gaseous detector," Nucl. Inst. and Methods, A478,2002 pp. 26-36

[6] G.F. Knoll, "Radiation Detection and Measurement," *John Wiley and Sons,* 2000, pp 161

[7] C.G. Wilson, Y.B. Gianchandani R.R. Arslanbekov, V. Kolobov, and A.E. Wendt, "Profiling and Modelling of DC Nitrogen Microplasmas," *Jour. of Applied Physics,* 94(5) Sept 2003, pp. 2845-51

RESONANT MICROCANTILEVER GAS SENSOR FABRICATED IN CMOS TECHNOLOGY FOR THE DETECTION OF CHEMICAL AGENTS

Ioana Voiculescu[1], Mona Zaghloul[1], R. Andrew McGill[2], Eric J. Houser[2], Stanley Stepnowski[2], Evgueni Sokolovski[2], Jennifer Stepnowski[2], Joe Vignola[2] and Gary K. Fedder[3]

1. George Washington University, Mechanical & Aerospace Engineering, 801- 22nd Street, NW, Washington, DC 20052, phone: (571) 338-2048, fax: (202)767-5301, e-mail: ioana@gwu.edu

2. Naval Research Laboratory, Washington, DC. 20375

3. Carnegie Mellon University, Dept. of Electrical & Computer Engineering, Pittsburgh, PA. 15213

ABSTRACT

The design, fabrication, and testing of a resonant cantilever in CMOS technology is presented in this paper. The new cantilever design described here includes interdigitated fingers for electrostatic actuation, and a piezoresistive Wheatstone bridge arrangement to read out the deflection signal. The reference resistors of the Wheatstone bridge are fabricated on auxiliary cantilevers that are immediately adjacent to the actuated device. The entire device is fabricated using a 0.6 μm three metal, double poly CMOS (complementary metal oxide semiconductor) process, combined with subsequent micromachining steps. A thin polymer coating is applied to the surface of the microcantilever to provide a sorbent layer for chemical nerve agents. Exposing the sensor with the nerve agent simulant dimethylmethylphosphonate (DMMP), allowed demonstrated detection at a concentration of 20 ppb or 0.1 mg/m³.

I. INTRODUCTION

A chemical sensor is a device, which converts analytic chemical information into a useful signal. Chemical sensors are important for a variety of industrial and environmental applications, including the detection of hazardous chemicals, quality control in the food, perfume, and beverage industries, and for medical applications.

A typical configuration for a chemical sensor includes a sorbent layer deposited on the active area of a transducer [**1**]. The interaction of a gas and the sorptive layer can be monitored as a function of physicochemical changes in the coating, and transduced into an electrical signal for ease of recording or display. The advent and maturation of microelectromechanical systems (MEMS) technology now offers many opportunities to dramatically reduce the size, cost, and power consumption of chemical sensors.

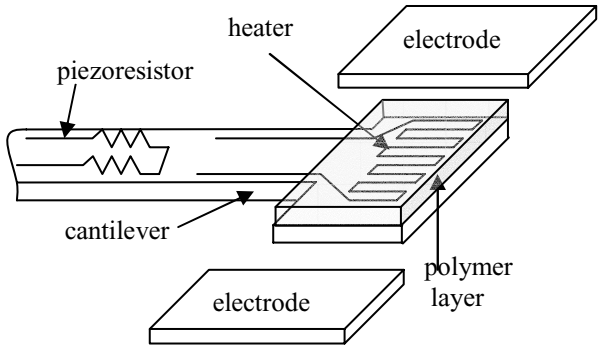

Figure 1. *Microcantilever gas sensor. Electrodes are used for electrostatic actuation of the cantilever.*

II. SENSOR TECHNOLOGY AND DESCRIPTION

A cantilever chemical sensor consists of two key components: a gas sorptive layer, such as a polymer, and the cantilever transducer as shown in Fig.1. In this design, only the cantilever tip is used for polymer coating. The uptake of different gases is monitored as a shift in the device frequency, which is reversible if the gas-polymer chemical interactions are reversible. The cantilever gas sensor is a resonating microbalance, with mass increases normally leading to a decrease in the cantilever resonance frequency. Electrostatic actuation is used to operate the cantilever in a resonant mode, and the resonance frequency is measured by a set of piezoresistors connected in a Wheatstone bridge configuration.

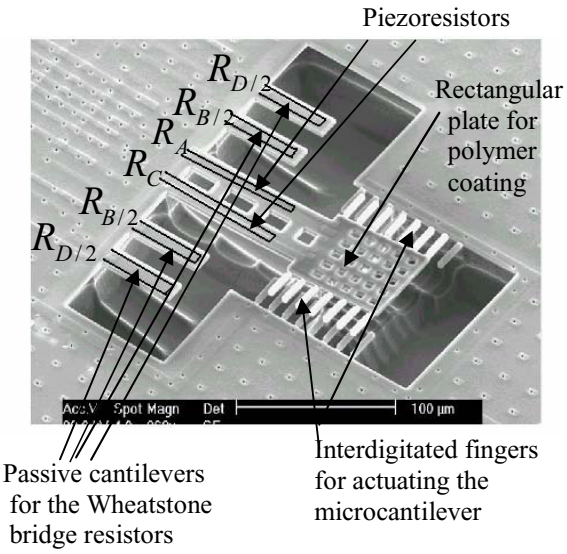

Figure 2. *SEM image of cantilever. R_A, R_B, R_C and R_D resistors are arranged in the on chip Wheatstone bridge.*

The full Wheatstone bridge has two piezoresistors, R_A and R_C, positioned on the active cantilever, and two reference resistors R_B and R_D situated on neighboring short, auxiliary cantilevers, as shown in Fig.2.

The chip was designed in CMOS-MEMS technology using MEMSCAP-Xplorer software installed under Cadence. The custom style used for the CMOS-MEMS process was developed at Carnegie Mellon University (CMU) [**2**]. Typical die size for this process is 2.5 mm by 2.5 mm. The foundry used in this work was Austrian Microsystems (AMS) (0.6 μm, 3-metal, 2-poly CMOS).

Travel support has been generously provided by the Transducers Research Foundation and by the DARPA MEMS and DARPA BioFlips programs.

The standard CMOS-MEMS process was followed by two maskless dry etch steps to release the microstructures that are protected by the top-most metal layer [**2**].

III. VIBRATION AMPLITUDE AND RESONANCE FREQUENCY

The surface motion of the microcantilever oscillator was characterized with a scanning laser doppler vibrometer (LDV) system developed at the Naval Research Laboratory (NRL). The NRL LDV system has been previously described in detail [**3**]. The system illuminates the sample surface with light from an argon-ion laser (spot size = 2.5 μm). Scattered light for the sample surface is mixed on the surface of a photo detector with the frequency shifted, reference light. The photodetector produces a frequency modulated signal that, once demodulated, is proportional to the surface displacement at a single location. Fig.3 shows the measured vibration amplitude at the tip of a bare microcantilever.

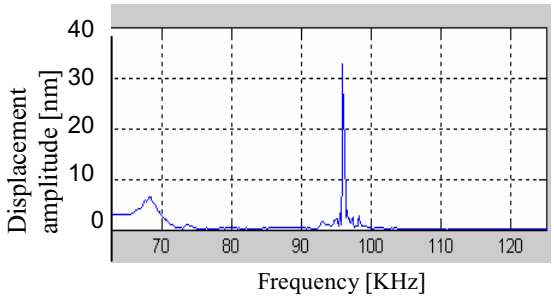

Figure 3. *Vibration amplitude of the microcantilever as a function of frequency.*

Using the identified fundamental resonance frequency, the cantilever chip was then characterized using a spectrum analyzer. The cantilever device was operated electrostatically by driving it with a small varying ac signal imposed on a constant dc bias. Breadboard electronics and a sensor manifold were later designed and fabricated to provide a portable platform being developed towards a palm-sized system.

IV. VAPOR TEST MEASUREMENTS AND CONCLUSION

The cantilever was coated with a custom NRL functionalized sorbent carbosilane polymer [**4**-**5**]. The tests were carried out by exposing the sensor to the nerve agent simulant, dimethylmethylphosphonate (DMMP) with isothermal conditions

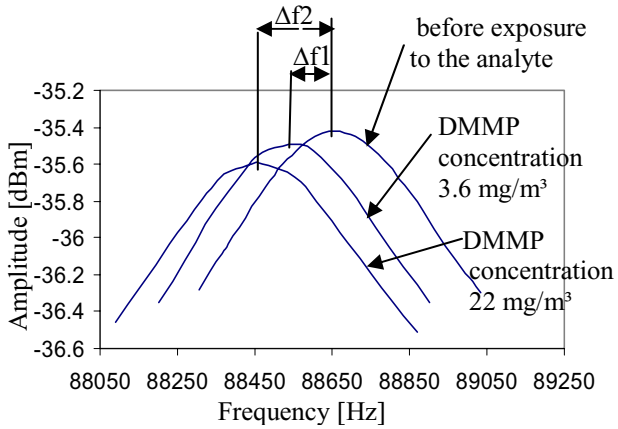

Figure 4. *Cantilever response upon exposure to various DMMP concentrations. Frequency shifts are marked Δf1 and Δf2.*

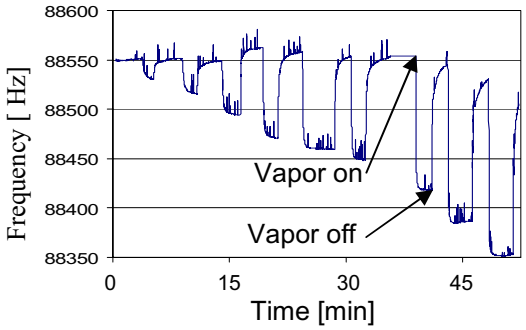

Figure 5. *Frequency response to increasing DMMP concentration.*

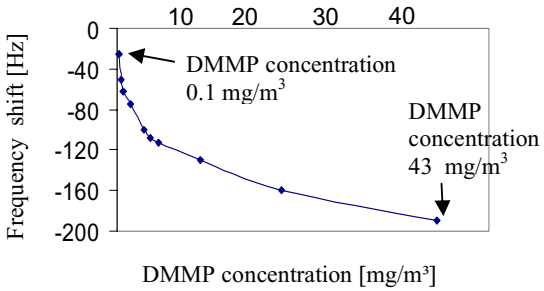

Figure 6. *Cantilever response upon exposure to DMMP concentrations varying from 0.1 to 43 mg/m³.*

at vapor concentrations which were ramped up and down from 0.1 mg/m³ to 43 mg/m³ in a repeated fashion.

The cantilever sensor response, as a function of DMMP concentration, is shown in Fig. 4 and Fig. 5. The lowest DMMP concentration tested was 0.1 mg/m³ or 20 ppb, see Fig. 5 & 6. At this concentration, the signal frequency shift recorded was 20 Hz, with an estimated signal noise level of about 1 Hz. The sensor time constant to 90% of signal was approximately 10 s.

These initial promising results were attained with a relatively simple design, fabricated in standard CMOS, which could offer an inexpensive option for production of a miniature chemical detector, with on chip electronics integrated to the cantilever.

REFERENCES

[1] R. A. McGill, M. H. Abraham, J. W. Grate, "Choosing polymer coatings for chemical sensors," *CHEMTECH 24*, pp. 27-37, 1994.

[2] H. Xie, L. Erdmann, X. Zhu, K. J. Gabriel, G. K. Fedder, "Post-CMOS processing for high-aspect-ratio integrated silicon microstructures", J. *Microelectromech. Sys*., vol. 11, pp.93-101, 2002.

[3] J. F. Vignola, X. Liu, S. F. Morse et al., Rev. Sci. Instrum Vol. 73, Nr.10, pp.3584 -3588, (2002).

[4] E. J. Houser, D. L. Simonson, J. L. Stepnowski, R. A. McGill "Linear and Hyperbranched Hydrogen Bond Acidic Poly(silylene methylene)s for Chemical Sensor Applications" PMSE Preprints 2003, 88, 548

[5] R. A. McGill, and E. J. Houser, "Linear chemoselective carbosilane polymers and methods for use in analytical and purification applications", U.S. Patent 6,660,230

ACKNOWLEDGEMENTS

The authors are indebted to Mr. John Petrella from the George Washington University for his contribution to the circuit design used to drive the resonant beam and his assistance. This work was supported in part by the Transportation Security Administration (TSA), and the Bureau of Alcohol, Tobacco, Firearms, and Explosives (ATF), and the Office of Naval Research (ONR).

INTERNAL ELECTROSTATIC TRANSDUCTION FOR BULK-MODE MEMS RESONATORS

Sunil A. Bhave and Roger T. Howe
Berkeley Sensor & Actuator Center, 497 Cory Hall, University of California, Berkeley, CA 94720

ABSTRACT

This paper demonstrates a new approach to electrostatic drive and detection of bulk acoustic resonators in which the electrode-gaps are filled with a high dielectric constant material. *Internal electrostatic transduction* has much higher efficiency than air-gap electrostatic transduction for bulk-mode resonators, which results in improved electrical performance. As a proof-of-concept, we demonstrate this phenomenon by electrostatic actuation of a 1.9GHz AlN ($\kappa \sim 9$) film bulk acoustic resonator (FBAR).

INTRODUCTION

Surface micromachining technology supports fabrication of multi-frequency, electrostatically transduced lateral bulk resonators. A single mask can include multi-frequency filters, oscillators and mixers. However, lateral bulk acoustic resonators have very large motional resistance due to reduced transducer area [**1**] and inefficient air-gap electrostatic transduction (compared to piezoelectric transduction [**2**]). Creative approaches to increasing transducer area include forming a coupled array of resonators [**3**] and large diameter bulk annular ring resonators [**4**]. However, to reach motional resistances on the order of 50Ω, we would need a coupled array of 100 resonators or a 400μm diameter ring resonator. The signal routing challenges for these structures will be daunting at GHz frequencies and the chip area occupied by these resonator designs will be larger than an FBAR (which has motional resistance of 2Ω).

The electrostatic force and motional current for a parallel-plate electrostatic transducer are:

$$f = V_{DC} \cdot \frac{\varepsilon_0 \cdot A}{g^2} \cdot v_{in} \quad ; \quad i = V_{DC} \cdot \frac{\varepsilon_0 \cdot A}{g^2} \cdot \omega \cdot x$$

Both terms are proportional to the permittivity of capacitor dielectric (ε_0 for air or vacuum). We propose to fill the electrode gaps of the bulk acoustic resonators with a dielectric material having much higher permittivity than air. The high-κ dielectric will enhance both the force density of the electrostatic actuator as well as the sense capacitance, thereby reducing the motional resistance of these resonators by κ^2.

Bouwstra *et al* demonstrated that audio-frequency cantilever beams can be driven and sensed using silicon nitride dielectric capacitors embedded in a silicon resonator [**5**]. The resonator made use of Poisson's ratio to convert applied strain perpendicular to the beam's thickness into strain along the beam, which coupled into the fundamental bending mode. The approach was deemed inefficient because air-gap capacitive transduction provided larger displacement, the preferred performance metric at that time.

BULK-MODE INTERNAL ELECTROSTATIC TRANSDUCTION

Bulk-mode resonators have significantly different design requirements compared to flexural resonators. These resonators typically have displacements on the order of a few nanometers. In principle, we can enhance the transduction efficiency of bulk resonators by filling the air-gaps with a low Young's modulus, high-κ dielectric material. A more practical approach would be to find a dielectric with similar acoustic velocity as the resonator material and 'build-in' an internal electrostatic transducer at the maximum strain 'anti-nodes' rather than the maximum displacement nodes. This approach would minimize bulk energy losses due to acoustic velocity mismatch and optimize transduction efficiency of the resonator. TiO_2 with relative permittivity $\kappa \sim 80$ and bulk acoustic velocity 7900m/s is an attractive material for this purpose.

In order to benchmark the performance of the internal electrostatic transducer, we evaluate its performance in a 3rd overtone lateral bulk acoustic resonator. This class of resonators has been demonstrated with air-gap electrostatic [**1,4**] and piezoelectric transduction [**2**]. The 3rd overtone can be excited and detected by introducing layers of TiO_2 at the two anti-nodal planes, as shown in Figure 1.

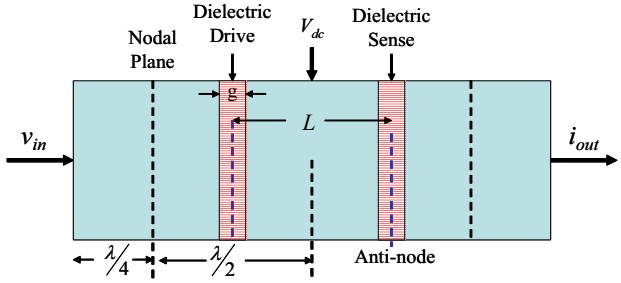

Figure 1. *Schematic of electrostatically transduced 3rd overtone bulk acoustic resonator*

The motional resistance of this resonator is

$$\frac{1}{R_{electrostatic}} \approx \frac{V_{DC}^2 \cdot \kappa_{TiO_2}^2 \cdot \varepsilon_0^2 \cdot A^2}{g^4} \cdot \frac{\omega \cdot Q}{E \cdot A/L}$$

By replacing the electrode-gap with TiO_2 at the antinodes, we can reduce the motional resistance by $\kappa^2 = 6{,}400$.

A 14MHz bulk acoustic resonator with 1μm air-gap electrostatic transducers has a motional resistance of 590kΩ [**1**]. The 3rd harmonic of an identical resonator with TiO_2 dielectric transduction would have a motional resistance of 275Ω. Similarly, the motional resistance of the 1.2GHz 3rd harmonic ring resonator [**4**] would scale down from 282kΩ to 44Ω.

ELECTROSTATIC EXCITATION OF AN FBAR

We used Agilent Technologies' AlN FBAR [**6**] to demonstrate internal electrostatic transduction. AlN has a relative permittivity of $\kappa \sim 9$ and the resonator has a mechanical quality factor $Q \sim 1350$

Travel support has been generously provided by the Transducers Research Foundation and by the DARPA MEMS and DARPA BioFlips programs.

at a resonant frequency of f_0 = 1.92GHz. Electrostatic force is quadratic; therefore we can actuate the FBAR with an input signal at half the resonant frequency (Figure 2). This ensures that there is no piezoelectric actuation of the resonator. A low-pass-filter was added to prevent any harmonics from the RF synthesizer from reaching the input electrode.

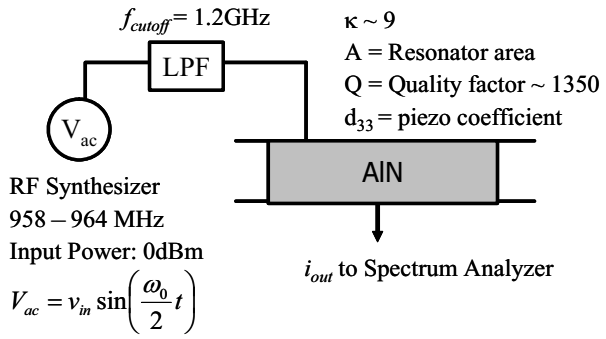

Figure 2. *Test equipment setup for half-frequency measurement. The Spectrum Analyzer is set to MAX_HOLD as the synthesizer frequency is swept near half-resonance frequency.*

Electrostatic actuation will generate stress in the resonator at the resonant frequency:

$$T_{electrostatic}(f_0) = \frac{1}{4} \cdot \kappa_{AlN} \cdot \varepsilon_0 \cdot \frac{v_{in}^2}{t^2}$$

This electrostatic stress generates dielectric displacement and results in piezoelectric displacement current:

$$i_{out,piezo}(f_0) = \omega_0 \cdot A \cdot Q \cdot d_{33} \cdot \frac{1}{4} \cdot \kappa_{AlN} \cdot \varepsilon_0 \cdot \frac{v_{in}^2}{t^2}$$

The output current also has an electrostatic component due to the quadratic electrostatic force. However, this component is extremely small compared to the piezo component due to the relatively large resonator thickness.

By sweeping the RF synthesizer frequency from 958MHz to 964MHz and using the MAX_HOLD function [7] on the 8562EC Spectrum Analyzer, we were able to construct the mechanical transfer function and extract *Q* of the FBAR (Figure 3).

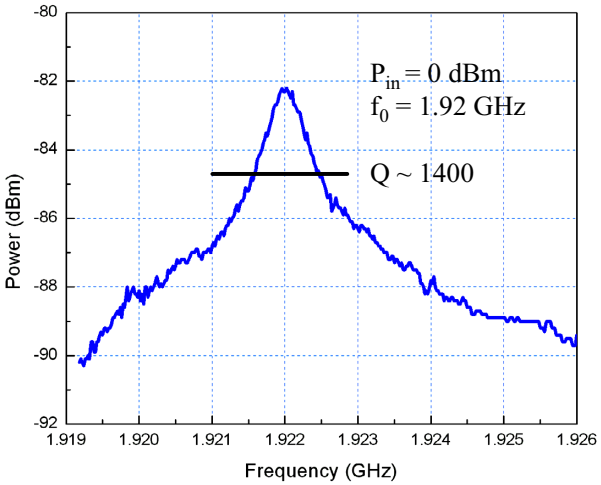

Figure 3. *FBAR transmission spectrum obtained using half-resonance electrostatic actuation. Q ~ 1400 was extracted from the shape of the transfer function.*

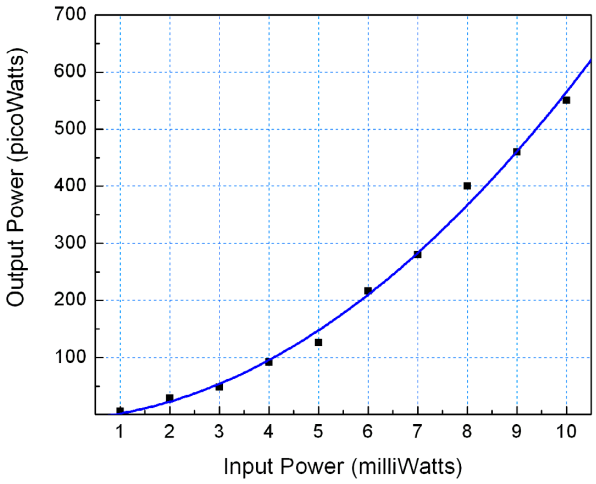

Figure 4. *Output power is proportional to the square of the input power, verifying internal electrostatic actuation of the FBAR.*

While the output current is due to piezoelectric effect, the mechanical motion of the FBAR is due to electrostatic stress. Hence, both the mechanical motion and output power are proportional to square of the input power (Figure 4).

The FBAR is a one-port device and hence is not suitable for electrostatic transduction. However, these two measurements provide preliminary experimental verification of internal electrostatic drive for bulk-mode resonators.

CONCLUSION

Internal electrostatic transducers using high-κ dielectrics can achieve κ^2 higher efficiency than conventional air-gap transducers. This new approach will enable us to fabricate arrays of small foot-print lateral bulk acoustic resonators with motional resistances <1kΩ. It will also open up the opportunity to design microwave frequency resonators with reasonable motional resistances. As a proof-of-concept, we excited an FBAR at 1.92GHz with internal electrostatic actuation.

ACKNOWLEDGMENT

The authors wish to thank Dr. Dan Radack and the DARPA NMASP program, whose generous grant (#N66001-00-1-8955) has made this research possible.

REFERENCES

1. T. Mattila, *et al*, "Micromechanical Bulk Acoustic Wave Resonator," *2002 Ultrasonics Symposium*, pp. 945-948.
2. S. Humad, *et al*, "High Frequency Micromechanical Piezo-on-Silicon Block Resonators," *IEDM 2003*, pp. 957-960.
3. M. Demirci, *et al*, "Mechanically Corner-Coupled Square Microresonator Array for Reduced Series Motional Resistance," *Transducers 2003*, pp. 955-958.
4. S.-S. Li, *et al*, "Micromechanical "Hollow-Disk" Ring Resonators," *MEMS 2004*, pp. 821-824.
5. S. Bouwstra, *et al*, "Excitation and Detection of Vibrations of Micromechanical Structures using a Dielectric Thin Film," *Sensors and Actuators*, 17 (1989), pp. 219-223.
6. R. Ruby, *et al*, "Ultra-Miniature High-Q Filters and Duplexers using FBAR Technology," *ISSCC 2001*, pp. 120-121.
7. J. Wang, *et al*, "1.14-GHz Self-Aligned Vibrating Micromechanical Disk Resonator," *RFIC 2003*, pp. 335-338.

A VERSATILE MEMS GAS CHROMATOGRAPH FOR DETERMINATIONS OF ENVIRONMENTAL VAPOR MIXTURES

E. T. Zellers,[1,2] W. H. Steinecker,[2] G. R. Lambertus,[2] M. Agah,[3] C.-J. Lu,[1] H. K. L. Chan,[3] J. A. Potkay,[3] M. C. Oborny,[1] J. M. Nichols,[2] A. Astle,[4] H. S. Kim,[3] M. P. Rowe,[2] J. Kim,[5] L. W. da Silva,[6] J. Zheng,[7] J. J. Whiting,[2] R. D. Sacks,[2] S. W. Pang,[3] M. Kaviany,[6] P. L. Bergstrom,[7] A. J. Matzger,[2] Ç. Kurdak,[5] L. P. Bernal,[4] K. Najafi,[3] K. D. Wise[3]

Engineering Research Center for Wireless Integrated Microsystems (WIMS),
Departments of [1]Environmental Health Sciences, [2]Chemistry, [3]Electrical Engineering and Computer Science,
[4]Aerospace Engineering, [5]Physics, [6]Mechanical Engineering, University of Michigan, Ann Arbor, MI 48109;
[7]Department of Electrical and Computer Engineering, Michigan Technological University, Houghton MI, 49931
e-mail: ezellers@umich.edu

ABSTRACT

A microfabricated gas chromatograph (μGC) with several innovative and enabling design features is described. The microsystem incorporates capabilities for particulate exclusion, on-board calibration, sample preconcentration and thermal desorption, pressure- and temperature-modulated separations, and "spectral" detection with array of microsensors. It is intended to permit rapid determinations of complex mixtures of environmental contaminants at trace concentrations. The ultimate goal is to embed microcontroller and rf communications modules for deployment in high-performance distributed environmental monitoring networks, among other possible applications. Ultra-low power dissipation is therefore a priority. This presentation reports on progress, to date, with an emphasis on the MEMS sensors and actuators employed. Device design, processing, and integration issues are reviewed. Pressure-tuned separations with a dual micro-column ensemble are demonstrated for the first time to effect the resolution of 13-vapor mixture at room temperature in under 4 minutes. A first-generation hybrid prototype μGC capable of performing mixture separations in as little as 30 seconds with detection limits in the low part-per-billion concentration range is also presented.

INTRODUCTION

Measurements of gases and vapors in complex mixtures are critical for accurate human exposure assessments, air quality forecasting, industrial emission monitoring/ mapping, emergency spill/release response, and biomedical surveillance and diagnosis. Several portable instruments capable of multi-vapor analyses are now commercially available [**1**], but reductions in size and complexity as well as improvements in analytical performance are necessary before routine *in-situ* determinations of multiple trace-level contaminants are possible at reasonable cost.

Microsensor arrays have been applied successfully to the determination of vapors in simple mixtures [**2,3**] and to comparative analyses of mixture composites in so-called 'electronic nose' configurations [**4**]. In addition, progress continues toward micro-spectrometers based on ion-mobility [**5**], infrared absorbance [**6,7**], atomic emission [**8**], and mass analysis [**9**]. It must be appreciated, however, that quantitative analysis of vapor mixtures of complex and variable composition invariably demands temporal/spatial separation prior to measurement, regardless of the detector employed. Furthermore, for most environmental health applications a preconcentration step is required to detect vapors in the range of regulatory limits, which can be as low as a few parts-per-billion (ppb) by volume.

Since the first report by Terry et al. [**10**], a number of researchers have described micromachined gas chromatographic separation channels coupled with one or another sampling, pretreatment and/or detection devices [**11-14**]. Most notable among these is the Sandia μChemLab®, which incorporates a membrane preconcentrator with a short, DRIE-Si separation column and an integrated acoustic-wave sensor array into a fieldable hybrid microsystem designed principally for national security applications [**12,14**].

The Michigan Engineering Research Center for Wireless Integrated Microsystems (WIMS) has recently engaged in a broad-based effort to develop generic micro-instrumentation platforms for biomedical and environmental monitoring applications [**15**]. The archetypical WIMS design couples interconnected sensing and actuation subsystems, which can be customized for specific applications, with an embedded controller, RF-MEMS wireless transceiver, and (battery) power supply. The primary focus of the environmental monitoring development effort is a versatile, high-performance micro gas chromatograph (μGC).

A block diagram of the analytical components of the μGC is shown in Fig. 1 (center). Analysis requires a sequence of operations. Air samples are drawn by the pump through the inlet particulate filter, past the calibration-vapor source and through the multi-stage, adsorbent preconcentrator/focuser (μPCF). After collection of a finite sample volume, trapped vapors are rapidly thermally desorbed from the μPCF and backflushed into the dual-column separation module, which can be pressure- and temperature-programmed for adjusting (i.e., tuning) retention. The vapors in the mixture are separated spatially as they reversibly partition into the thin polymeric stationary phases lining the walls of the two columns. Compounds elute from the columns and are passed over the array of microsensors for recognition and quantification – responses from the sensors vary with the strength of the transient interactions occurring between the analyte vapors and sensor interface layers. Pressure and temperature sensors, as well as heater structures, are integrated within several devices.

MEMS processing methods are being used to fabricate the entire system with the ultimate goal of creating an autonomous micro-instrument that occupies only 1-2 cm^3, requires an average power of <<100 mW per analysis, and provides determinations of complex environmental vapor mixtures at low- or sub-ppb

0-9640024-5-0/hh2004/$20©2004TRF
DOI 10.31438/trf.hh2004.16

Solid-State Sensors, Actuators, and Microsystems Workshop
Hilton Head Island, South Carolina, June 6-10, 2004

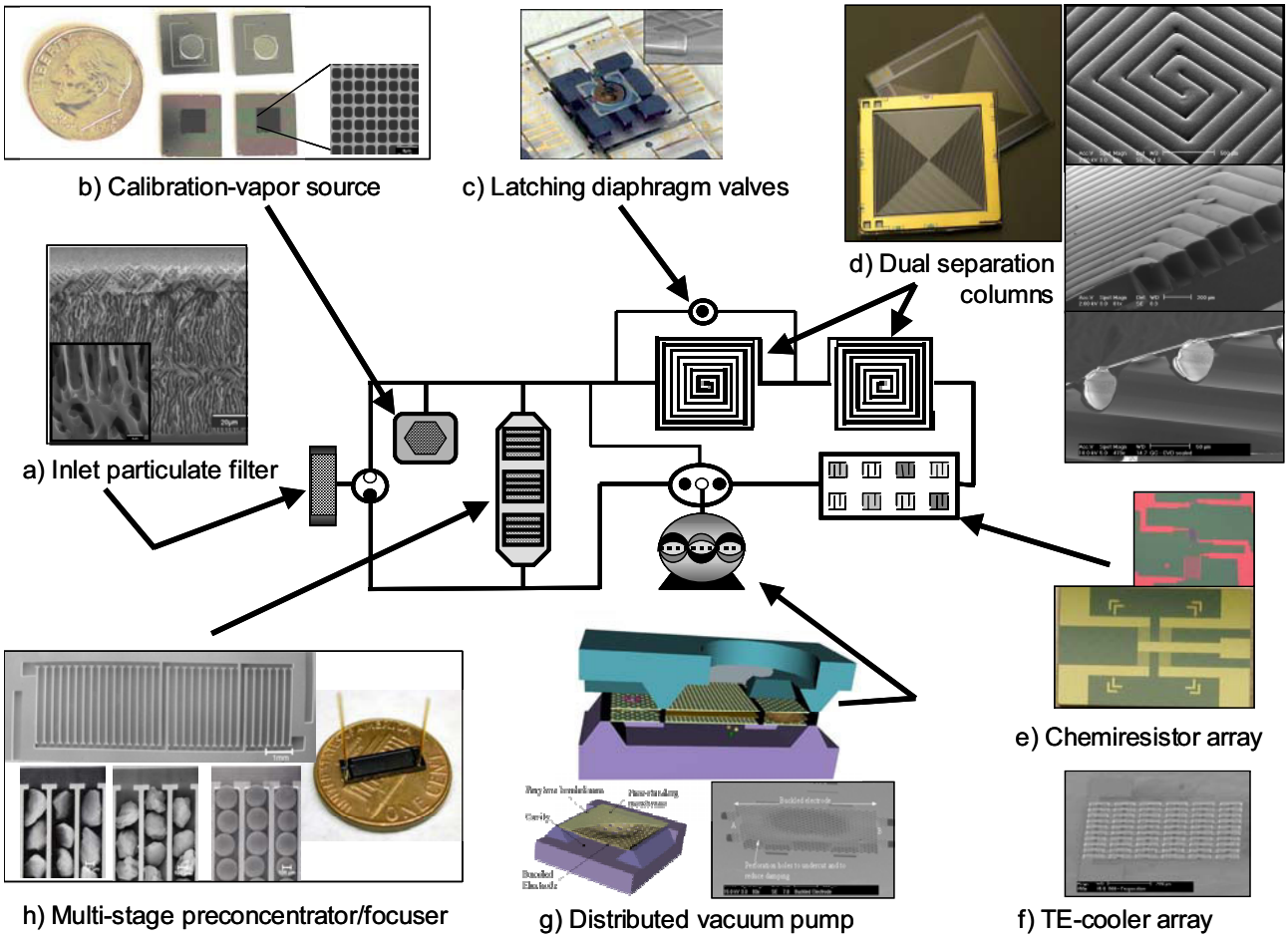

Figure 1. *Layout of the analytical components of the WIMS μGC (center); a) SEM image of a porous silicon superlattice with inset showing the tortuous-path cross section that will enhance particle collection efficiency; b) pair of calibration-vapor sources prior to sealing, with DRIE diffusion paths in top layer and PS reservoir in bottom layer (left), and SEM image of through-wafer straight-pore PS sample with uniform 3.5-μm pores (right); c) thermopneumatically actuated electrostatically latched microvalve with inset showing the elevated heater d) clockwise: photo of two 3-m Pyrex-Si DRIE columns on 3.3 x 3.3 cm die; backview of one column, cutaway showing channel cross-section, and cutaway of a 2nd-gen. ultra-low-mass CVD-sealed column; e) integrated 4-chemiresistor (CR) array with 15-μm electrode spacings (left) and CR sensors with electrode spacings of 1, 0.3, and 0.1 μm (right); f) SEM image of an array of 60 TE cooler elements for reducing sensor-array temperature; g) conceptual illustration of vacuum pump (two stages shown), and diagram and SEM image of buckled electrodes with Parylene membrane; h) 3-stage μPCF with granular adsorbents packed between transverse heat exchanger slats (left) and packaged μPCF on a U.S. penny (right).*

concentrations with a cycle time of a few minutes. Low-power interface, control, and RF-MEMS wireless communication devices to be integrated with the μGC are being developed in parallel efforts within the WIMS Center [**15,16**]. Fig. 2 presents a conceptual diagram of one monolithic μGC configuration.

Descriptions of several μGC components and subsystems can be found in recent published reports [**2,17-31**]. Here, we provide a review of current status that focuses on the important attributes of the MEMS sensors and actuators being employed, the challenges of achieving high performance at low power, and our latest results showing tuned separations and high-speed mixture analyses with a first-generation hybrid μGC prototype.

MICROSYSTEM FEATURES

Inlet Filter and Calibration-Vapor Source. An inlet filter is needed to prevent particle entrainment into the system. We are attempting to construct the filter from a large membrane of porous silicon (PS). The challenge is to create a tortuous path in order to efficiently capture particles with diameters down to the sub-micron range while maintaining sufficient porosity to minimize the pressure drop at the sampling flow rate, currently anticipated to be ≤25 cc/min. By varying the anodization conditions it is possible to adjust the size and orientation of the PS macropores with depth, alternating between regimes where pore growth is dependent on crystal orientation (anisotropic) and the direction of applied current (isotropic) [**30**]. We have succeeded in creating beds ~100 μm thick with the right morphology (Fig. 1a) and are working to extend the superlattice through the entire wafer.

The calibration-vapor source (Fig. 1b) is designed to generate calibrant vapor at a constant rate by passive diffusion from a liquid reservoir. Analysis of this "internal standard" along with vapors captured from the environment provides the means to assess and compensate for aging and drift. It is a 3-layer structure whose base contains a deep PS reservoir for retaining the volatile-liquid calibrant (n-decane for most tests to date), a Pyrex spacer layer with a wide, central aperture that defines the headspace region, and a Si cap that contains a DRIE diffusion channel and exit port. The device has a footprint of 8.5 x 9.0 mm and is 2.2 mm thick. To avoid pore-induced vapor pressure depression effects, PS reservoirs are being fabricated under conditions that yield straight vertical pores having diameters on the order of 2-8 microns (Fig. 1b) [**29**]. Constant vapor generation over many hours operation has been demonstrated with a temperature dependence that agrees closely with theory [**25**].

Preconcentrator-Focuser (μPCF). The three-stage μPCF is designed to capture organic vapors quantitatively and to thermally desorb them into a much smaller volume thereby increasing the effective concentration and providing a sharp injection plug, which facilitates high-speed chromatographic separations. Quantitative capture of vapors in complex environmental mixtures requires a large adsorbent surface area. However, subsequent desorption of trapped chemicals with a wide range of vapor pressures demands a gradient of adsorbent surface area that increases in the direction of air flow in order to avoid irreversible adsorption or thermal degradation. Rapid desorption at minimum power also requires efficient heating structures. Indeed, the demand for rapid heating represents a significant challenge to low power operation. The current μPCF (Fig. 1h) contains a set of transverse, high-aspect-ratio slat-type DRIE-Si heat exchangers, 380 (h) x 50 (w) x 3000 μm (l), spaced from adjacent elements by 220 μm. The base is a 50-μm-thick doped-Si resistively-heated membrane occupying 27 mm^2 [**26**]. The interior volume is packed with three different porous, carbon-based adsorbents (total mass ~ 5mg) in order of increasing specific surface area [**32**]. The loaded μPCF is sealed by RTA with a Si cover plate having etched grommets designed to accept the capillary interconnections. Capture/release of 30 vapors has been demonstrated but heating to 280 °C to effect desorption currently requires about 800 mW per stage. Further miniaturization and vacuum encapsulation promise significant reductions in power. Devices are also being designed to accommodate novel adsorbent materials being developed with tailored surface areas and porosities as well as high-surface-area, thermally stable materials that can be produced *in situ* within the heater structures by CVD.

Dual-Column Separation Module. The separation stage determines much of the resolution, speed, and power dissipation of the overall microsystem. Power is especially critical since the columns must be heated to ~100°C in operation, and when temperature programming is used the temperature changes can be rapid. This requires a very high thermal resistance between the columns and the ambient to achieve low power as well as ultra-low thermal mass to achieve a rapid response time. The length of the separation column, among other factors, determines the resolving power, the number of separable compounds, and the analysis time. Column length is also subject to constraint because of the pressure drop created since the pressure-driven flow provided by the micropump is limited.

To address the tradeoffs of resolution, length, and time, we are employing two series-coupled separation columns having a pressure-control valve at their junction point and independent temperature control. The two columns have complementary stationary phases so that retention differs between them for each analyte. A non-polar polydimethylsiloxane stationary phase is employed in one column and a moderately polar poly-trifluoropropylsiloxane phase in the second column. Placing a tap at the midpoint permits adjustment of the time spent in each column by the analytes. Flow can be stopped in the first column and simultaneously accelerated in the second column during an analysis, and strategically timed stop-flow intervals can enhance separations. Independent temperature control of each column provides another powerful mechanism of adjusting resolution. Collectively, these features allow maximum use of available column length and maximum flexibility for specific applications.

An initial goal for the system is to achieve sufficient resolution to separate/analyze 30 or more volatile organic compounds in a single separation of ≤10 minutes duration. Two discrete columns are employed currently, each consisting of a convolved square-spiral DRIE-Si channel 150 μm (w) x 240 μm (h), 3 m length, on square die 3.3 cm on a side [**20,21**]. To allow for peripheral inlet/outlet ports, two parallel channels were created in each column that meet at the center of the chip where the flow direction is reversed. The latest columns also have integrated pressure and temperature sensors. Degenerative boron doping of the channel floor facilitates removal of un-needed substrate as well as subsequent column heating. Wafer-level low-pressure anodic bonding is used to seal the channel with a Pyrex cover plate and fused-silica capillaries are epoxied into recessed side ports for fluidic connections. Fig. 1d shows front, back, and cutaway images of sealed columns having thinned Pyrex covers to reduce total mass. Power for sustained heating to 100 °C is projected at < 100 mW with proper packaging [**31**].

Stationary phases are deposited dynamically from a dilute solution under a positive pressure of inert gas and then cured to improve stability. Tests have shown that these columns can provide between 5500 and 8200 theoretical plates each. The separation of 15-20 compounds on each column in an air matrix in a matter of a few minutes has been demonstrated [**20-22**].

Fig. 3 shows the first example of a pressure-tuned separation with a dual DRIE-Si column ensemble The columns were mounted within a conventional GC oven and connected to a heated split-flow injector, compressed-air carrier gas, pneumatic mid-point valve, and a flame-ionization detector (FID). Syringe injection of a 13-compound mixture yielded the upper trace, with several co-elutions. By incorporating a series of pre-determined stop-flow intervals of a few sec each, resolution of all 13 compounds was possible in < 4 min at room temperature.

Next-generation monolithic dual-column ensembles are currently in fabrication. These low-mass columns are made from bulk-etched spiral channels with circular cross-sections formed in Si by undercutting a silicon/dielectric mask. The mask openings are subsequently sealed with CVD dielectrics. The column walls are boron-doped Si, permitting the wafer to be dissolved at end of process to yield a single-crystal Si tube supported at each end (Fig. 1d). The columns achieve minimum thermal mass and are engineered to set the tradeoffs between thermal isolation and thermal time constant. Vacuum sealing will eliminate convective losses and low-emissivity coatings minimize radiation loss. Thermal response times for heating of < 100msec and power <<100 mW are anticipated.

Chemiresistor Array. The integrated array of chemiresistors (CR) is designed to produce a "spectrum" of responses to vapors eluting from the separation module that can be combined with column retention times to identify the vapors. The magnitudes of the CR responses reflect the vapor concentrations. CR sensors consist of a set of interdigital electrodes with a thin,

chemically responsive overlayer. They are particularly well-suited for miniaturization due to the simplicity of their design and required supporting drive and measurement circuitry, ease of fabrication, and their favorable scaling laws. Work to date has focused on integrated arrays of 4 CR sensors with electrode spacings of 15 μm (Fig. 1e) and interfacial films of Au-thiolate monolayer-protected nanoclusters (MPC), 50-300 nm thick, whose dc resistances increase to different extents upon sorbing vapors [17,19,28,33]. MPCs tested include those having the following thiolate ligands: n-octanethiol (C8); 4-mercaptodiphenylacetylene (DPA); 1-mercapto-6-phenoxyhexane (OPH); and 7-mercaptoheptanitrile (CCN). The coated array is sealed with a Macor® lid to create a 3-μL detector cell. Preliminary results obtained with such arrays have been very encouraging [**17-19,28**].

With a goal of further reductions in sensor size (which will also permit a modest increase in the number of sensors in the array) we have tested CR devices with electrode spacings as small as 100 nm and found that this 150x reduction in gap size has no significant effect on sensitivity but allows a reduction in cell volume and required sample mass (which in turn will permit a reduction in the size and power requirements of the μPCF). Consistent with sorption-governed responses, sensitivity increases of 2-4x are observed upon cooling sensors by only 18 °C. Micro-thermo-electric (TE) cooling by use of arrays of Bi-Te and Sb-Te thin-film column-type TE cooling elements of micron dimensions is being investigated. Such structures have been produced by co-evaporation of the elements (Fig. 1f) and are currently being tested [**24**].

In exploring the fundamental aspects of electron tunneling through MPC films, we have observed non-linear I-V characteristics in C8-Au films on 100-nm electrode arrays even at room temperature. In addition, sensors exhibit 1/f noise that increases by ~100-fold upon toluene exposure while the resistance changes by only a factor of two [**34**].

Valves and Pump. Valves are required in three locations within the microsystem (Fig. 1). In order to minimize fluidic constrictions, valve throws > 10 μm are desirable. Actuation times <100 msec, low leakage at differential pressures of 0.5 atm, and operation at very low power are also among the design specifications. Building on prior work [**35**], we have fabricated a "smart" valve that utilizes a thermally isolated thermopneumatic actuator and an electrostatic latch, coupled with a capacitive position-sensing capability. Prototype stand-alone microvalves 1-mm in diameter (Fig. 1c) produce 500Torr of actuation pressure at 100mW of input power and provide a throw of 30 μm. The valve seat position is determined with a sensitivity of 4.3fF/Torr and the valve latches at 40V at a cavity pressure of 600Torr. Leakage is < 0.02 sccm at 0.5 atm differential pressure. Hold power (open or closed) is negligible.

Sample transport through the μGC will ultimately be provided by distributed 18-stage, peristaltic vacuum (compression) air pump currently in fabrication. Each stage comprises two checkerboard valves and an electrostatically actuated pump chamber. The overall pump dimensions are 1cm x 1cm x 1mm. Dynamic operation modeling predicts flow rates of 2-50 sccm at back pressures of 0.2-0.5 atm with a power dissipation < 40 mW [**23**]. Fabrication entails the use of Parylene membranes patterned, bonded, metallized and transferred over perforated electrodes. A novel two-sided stress-buckled (curved) electrostatic drive is also being used to create large-deflection (~8 μm) actuation at relatively low voltages (~150 V) (Fig. 1g).

1ST-GENERATION PROTOTYPE PERFORMANCE

Fig. 4 shows our first-generation prototype which combines the calibration-vapor source, μPCF, single (non-polar) column, and 4-CR array with commercial mini-valves on a Pyrex-on-Si substrate. The substrate has etched channels and micromilled access ports for fluidic interconnections, as well as metal traces for electrical interconnections to interface, control, and rf-communication boards upon which it will be mounted.

Flow velocity can have dramatic effects on desorption profiles from the μPCF, chromatographic resolution, and response profiles from the sensors. Reconciling flow velocity is one of the challenges to effective microsystem integration. Optimal flows through the μPCF during desorption are typically much higher than those providing optimal chromatographic resolution, particularly when using air as the carrier gas, however the heating rate of the μPCF, the initial separation-column temperature, and the analyte vapor pressures are all important cofactors. Models to address these issues are being developed.

Fig. 5 shows a single-sensor (OPH-Au) chromatogram obtained for a mixture of vapors captured on the μPCF and then desorbed and analyzed under one set of flow/heating conditions. These tests were performed with the same components as shown in Fig. 4 but in a slightly modified configuration. The column used a Kevlar-embedded resistive heater for temperature programming and a small commercial suction pump for air flow [**17,18**]. As shown, sharp, well resolved peaks can be produced under these conditions and the 10-compound mixture could be separated in about 2 min. This separation would require 5-10x longer on a conventional GC. Limits of detection for these vapors are all below 100 ppb assuming a 0.25-L preconcentrated air sample.

Fig. 6 shows a set of responses from the entire 4-CR array obtained under different operating conditions, adjusted to increase analysis speed for this set of more volatile vapors. A split-flow bypass (Fig. 1) was used to shunt a portion of the flow passing through the μPCF around the column so that a high desorption flow rate could be used while maintaining a lower column flow rate [**17**]. In addition a different heating profile was used for μPCF desorption. The 7-vapor mixture is separated remarkably rapidly (~30 sec), though at somewhat lower resolution. Response patterns shown for a subset of four vapors (Fig. 6) reflect the diversity of sensor responses and provide chemical information that can facilitate determinations of analyte identities [**36**].

CONCLUSIONS

This work has demonstrated that rapid, quantitative analysis of mixtures of organic vapors is possible with a MEMS gas chromatograph and that detection limits in the ppb-range can be achieved for modest sample volumes. Response patterns from the sensor array are combined with retention times to distribute the analytical burden between the separation and detector stages. Coupled with dual-column retention tuning, this microanalytical system affords unprecedented levels of performance and versatility. Achieving such high performance at the greatly reduced levels of power dissipation required for incorporation into distributed wireless environmental monitoring networks remains a formidable challenge. However, paths to lower power operation based on novel design and packaging schemes have been identified and are being implemented

ACKNOWLEDGMENTS

. The authors wish to thank Prof. Craig Friedrich for micro-milling the fluidic substrate, cover plate, and detector-cell lids, Robert Gordenker and Katherine Beach for fabrication, and Dr. Frank Dorman (Restek Corp.) for early assistance with stationary phase deposition. This work was supported by the Engineering Research Centers Program of the National Science Foundation under Award Number ERC-9986866.

REFERENCES

1. C.M. Harris, "GC to Go," *Anal. Chem*., 74, 585A (2002).

2. M.D. Hsieh, E.T. Zellers, "Limits of Recognition for Simple Vapor Mixtures Determined with a Microsensor Array", *Anal. Chem*., (web release date March 5th, 2004).

3. J. Park, W.A. Groves, E.T. Zellers, "Vapor Recognition with Small Arrays of Polymer-Coated Microsensors--A Comprehensive Analysis" *Anal. Chem.,* 71*,* 3877 (1999).

4.. K.J. Albert, D.R. Walt, D.S. Gill, T.C. Pearce, "Optical Multibead Arrays for Simple and Complex Odor Discrimination," *Anal. Chem.,* 73, 2501 (2001).

5. R.A. Miller, E.G. Nazarov, G.A. Eiceman, A.T. King, "A MEMS Radio-Frequency Ion-Mobility Spectrometer for Chemical Vapor Detection," *Sens. Actuat. A*, *91*, 301 (2001).

6. C. Charlton, F. de Melas, A. Inberg, N. Croitoru, B. Mizaikoff, "Hollow-Waveguide Gas Sensing with Room-Temperature Quantum Cascade Lasers", *IEE Proc.-Optoelect., 150* 306 (2003).

7. G.Hocker, D. Youngner, E. Deutsch, A. Volpicelli, S. Senturia, M. Butler, M. Sinclair, T. Plowman, A. Ricco, "The Polychromator: a Programmable MEMS Diffraction Grating for Synthetic Spectra," *Digest Solid-State Sens. Actuat. Workshop,* Hilton Head, SC, Transducer Res. Corp., June, 2000, pp. 89-91.

8. J.C.T. Eijkel, H. Stoeri, A. Manz, "A DC Microplasma on a Chip Employed as an Optical Emission Detector for Gas Chromatography", Anal. Chem., 72, 2547 (2000).

9. J. Moxom, P.T.A Reilly, W.B Whitten, J.M. Ramsey, "Analysis of Volatile Organic Compounds in Air with A Micro Ion Trap Mass Analyzer, *Anal. Chem., 75,* 3739 (2003).

10. S.C. Terry, J.H. Jerman, and J.B. Angell, "A Gas Chromatograph Air Analyzer Fabricated on a Silicon Wafer", *IEEE Trans. Electron Dev., 26,* 1880 (1979).

11 A. de Mello, "On-Chip Chromatography: The Last Twenty Years," *Lab on a Chip*, 2, 48N (2002).

12. G. Frye-Mason, R. Kottenstette, P. Lewis, E. Heller, R. Manginell, D. Adkins, G. Dulleck, D. Martinez, D. Sasaki, C. Mowry, C. Matzke, and L. Anderson, "Hand-Held Miniature Chemical Analysis System (μChemLab) for Detection of Trace Concentrations of Gas Phase Analytes", in *Proc. Micro Total Analysis Systems Workshop*, Enschede, NE (2000) pp. 229-232.

13. H. Noh, P.J. Hesketh, G.C. Frye-Mason, "Parylene gas chromatographic column for rapid thermal cycling," *JMEMS. 11*, 718 (2002).

14. R.P. Manginell, M. Okandan, R.J. Kottenstette, P.R. Lewis, D.R. Adkins, J.M. Bauer, R.G. Manley, S. Sokolowski, R.J. Shul, "Monolithically Integrated μChemLab for Gas-Phase Chemical Analysis", *Proc. 7th Int. Conf. Miniatur. Chem .& Biochem. Anal. Sys –μTAS'03*, Squaw Valley, CA (2003) pp. 1247-1250.

15. K.D. Wise, K. Najafi, D.M. Aslam, R.B. Brown, J.M. Giachino, L.C. McAfee, C.T.-C. Nguyen, R.O. Warrington, and E.T. Zellers, "Wireless Integrated MicroSystems (WIMS): The Coming Revolution in the Remote Gathering of Information," Technical Digest Sensors Expo, Chicago, IL (2001) pp. 175-182. (website: http\\:www. wimserc.org)

16. K.D. Wise, K.Najafi, R. D.Sacks, E.T. Zellers, "A Wireless Integrated Microsystem for Environmental Monitoring," *Digest IEEE Int. Sol.-St. Circuits Conf.*, San Fran.CA(2004) pp. 434-436.

17. C.-J. Lu, W.H. Steinecker, W.-C. Tian, M.C. Oborny, J.M. Nichols, M. Agah, J. Potkay, H.C.K Chan, J. Driscoll, R.D. Sacks, S.W. Pang, K.D. Wise, E.T. Zellers, "First-Generation Hybrid MEMS Gas Chromatograph", *Lab on a Chip,* (under review).

18. C.-J. Lu, W.-C. Tian, W.H. Steinecker, A. Guyon, M. Agah, M.C. Oborny, R.D. Sacks, K.D. Wise, S.W. Pang, E.T. Zellers, "Functionally Integrated MEMS Micro Gas Chromatograph Subsystem," *Proc. 7th Int. Conf. Miniatur. Chem .& Biochem. Anal. Sys –μTAS'03*, Squaw Valley, CA (2003) pp. 411-415.

19. W.H. Steinecker, M.P. Rowe, A.J. Matzger, and E.T. Zellers, "Chemiresistor Array with Nanocluster Interfaces as A Micro-GC Detector," *Proc. 12th Int. Conf. Solid-State Sens., Actuat. & Microsys. -- Transducers '03,* Boston, MA (2003) pp. 1343-1346.

20. M. Agah, J.A. Potkay, J. Driscoll, R. Sacks, M. Kaviany, K.D. Wise, "Thermal Behavior of High-Performance Temperature-Programmed Microfabricated Gas Chromatography Columns," *Proc. 12th Int. Conf. Solid-State Sens., Actuat. & Microsys - Transducers '03,* Boston, MA, June (2003), pp. 1339-1342.

21. G. Lambertus, A. Elstro, K. Sensenig, J.A. Potkay, M. Agah, S. Scheuering, K.D. Wise, F. Dorman, R.D. Sacks, "Design, Fabrication and Evaluation of Micro-Fabricated Columns for Gas Chromatography," *Anal. Chem.*, (in press).

22. W.-C. Tian, S.W. Pang, C.-J. Lu, and E.T. Zellers, "Microfabricated Preconcentrator/Focuser for A Micro-Scale Gas Chromatograph," *JMEMS., 12,* 264 (2003).

23. A. Astle, L. P. Bernal, P. Washabaugh, H. Kim, K. Najafi, "Dynamic Modeling and Design of a High Frequency Micro Vacuum Pump," *Proc. Int. Mech. Engin. Congress & Expos.*, Washington, DC, ASME, November, 2003, # IMECE 2003-41493

24. L.W. da Silva, M. Kaviany, A. DeHennis, J. Dyck, "Micro Thermoelectric Cooler Fabrication: Growth & Characterization of Patterned Sb_2Te_3 and Bi_2Te_3 Films, "Proc. Int.Conf. Thermoelectics, La Grande Motte, FR, August(2003),pp. 665-668.

25. M.C. Oborny, J.Zheng, J.M. Nichols, C-J. Lu, P.L. Bergstrom, R.P. Manginell, G.C. Frye-Mason, E.T. Zellers, "Passive Calibration-Vapor Source for A Micro Gas Chromatograph," *Proc. 7th Int. Conf. Miniatur. Chem. and Biochem. Anal. Sys. –μTAS '03*, Squaw Valley, CA, October (2003), pp. 1243-1246.

26. W.-C. Tian, H.K.L. Chan, C.J. Lu, S. Pang, E.T. Zellers, "High-Sensitivity Three-Stage Microfabricated Preconcentrator-Focuser for Micro Gas Chromatography," *Proc. 12th Int. Conf. Solid-State Sens., Actuat. and Microsys. -- Transducers '03,* Boston, MA, June (2003), pp. 131-134.

27. H.S. Kim, K. Najafi, P. Washabaugh, L. Bernal, "Large Deflection Out-of-Plane Electrostatic Buckled-Electrode Actuators" *Proc. 12th Int. Conf. Solid-State Sens., Actuat. & Microsys - Transducers'03,* Boston, MA, June(2003),pp. 794-797.

28. Q.Y. Cai, E.T. Zellers, "Dual-Chemiresistor GC Detector Employing Monolayer-Protected Metal Nanocluster Interfaces," *Anal. Ch*em., 74, 3533 (2002).

29. J. Zheng, M. Christophersen, P.L. Bergstrom, "Thick Macroporous Membranes Made of p-type Silicon", *Digest 4th Int. Conf. on Porous Semicon. Sci. Tech.*, Valencia, Spain (2004).

30. J. Zheng, M. Christophersen, P.L. Bergstrom, "Formation Technique for Macroporous Morphology Superlattice", *Digest 4th Int. Conf. on Porous Semicon. Sci. Tech..*, Valencia, Spain (2004).

31. M. Agah, J. A. Potkay, A. Elstro, G. Lambertus, R. D. Sacks, K. D. Wise, “High Performance Temperature Programmed Gas Chromatography Column,” (2004), this volume.

32. C.-J. Lu, E.T. Zellers, "Multi-Adsorbent Preconcentration/ Focusing Module for Portable-GC/Microsensor-Array Analysis of Complex Vapor Mixtures," *Analyst ,127,* 1061 (2002).

33. M.P. Rowe, K.E. Plass, K. Kim, E.T. Zellers, A.J. Matzger, “Single-Phase Synthesis of Functionalized Gold Nanoparticles,” *Chem. Materials* (under review).

34. J. Kim, A. Kuo, Ç. Kurdak, M. P. Rowe, A. J. Matzger, W. H. Steinecker, E. T. Zellers, "1/f Noise in Au Nanoparticle Chemosensors,” *J. Microelectronics* (under review).

35. C. A. Rich, K. D. Wise, "A High-Flow Thermopneumatic Microvalve with Improved Efficiency and Integrated State Sensing," *JMEMS* , 12, 201 (2003).

36. C.J. Lu, J. Whiting, R.D. Sacks, E.T. Zellers, "Portable GC with Tunable Retention and Microsensor Array Detection for the Determination of Complex Vapor Mixtures," *Anal. Chem. 75,* 1400 (2003).

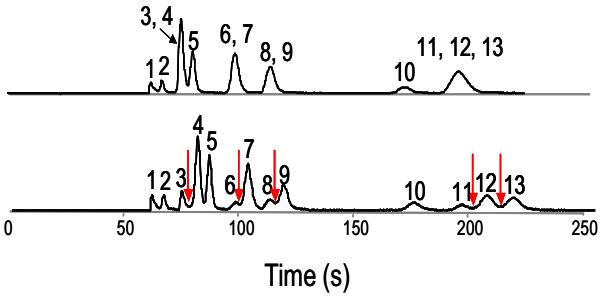

Figure 3*. 13-vapor chromatograms with dual-column ensemble (FID detection, air carrier gas). Top trace shows four co-elutions under initial conditions. Bottom trace shows resolution of compounds via brief stop-flow intervals at t = 40, 85, and 125 sec. Arrows show the resulting separations (1 acetaldehyde; 2 methanol; 3 ethanol; 4 pentane; 5 isoprene; 6 propionaldehyde; 7 cyclopentane; 8 acetone; 9 1-hexene; 10 butyraldehyde; 11 ethyl acetate; 12 benzene; 13 cyclohexene).*

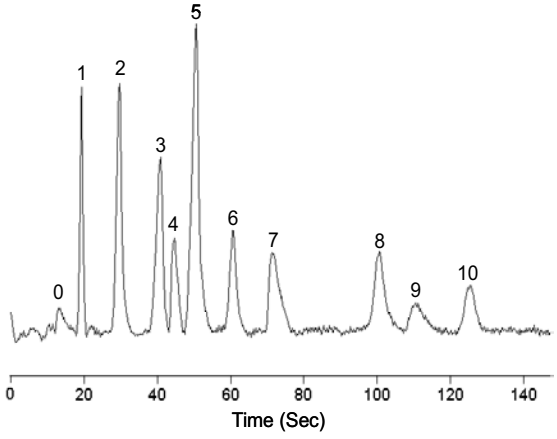

Figure 5. *10-vapor chromatogram from the μGC prototype system (only the OPH-Au coated chemiresistor response is shown), illustrating sharp, well-resolved peaks. The non-polar column was held at 25° C for 40 sec, then ramped at 0.85° C/sec to 65° C and held for the remainder of the separation. Compounds: 0 water; 1 TCE; 2 toluene; 3 perchloroethylene; 4 n-butyl acetate; 5 chlorobenzene; 6 m-xylene; 7 2-heptanone; 8 mesitylene; 9 3-octanone; 10 n-decane.*

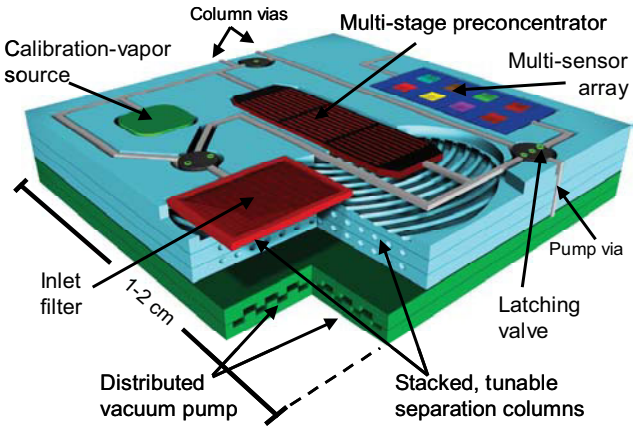

Figure 2.*. Conceptual Diagram of a Monolithic μGC.*

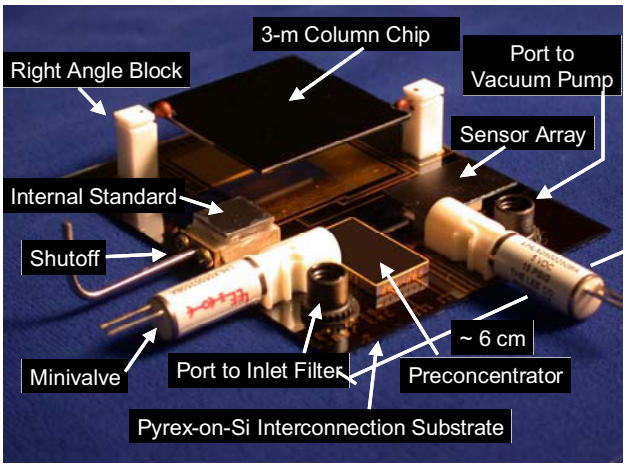

Figure 4. *1st-generation μGC prototype with MEMS and non-MEMS components on a fluidic/electrical interconnection substrate 6x8cm.*

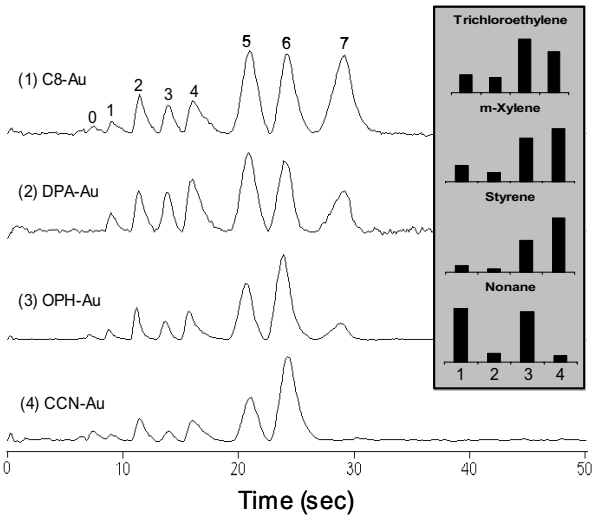

Figure 6. *High-speed 4-CR-array chromatograms of a 7-vapor mixture analyzed in 30 sec at 25 ℃ with the μGC prototype. Each trace is labeled with the corresponding nanoparticle sensor interface layer. Inset shows response patterns for a subset of vapors. Split-flow injection was employed. Cmpds: 0 water; 1 trichloroethylene; 2 toluene; 3 perchloroethylene; 4 n-butyl acetate; 5 m-xylene; 6 styrene; 7 n-nonane.*

A MEMS-Based Renal Replacement System

M.R. Kaazempur-Mofrad
Departments of Mechanical Engineering and Biological Engineering, Massachusetts Institute of Technology
Cambridge, MA 02139

J.P. Vacanti and N.J. Krebs
Department of Surgery, Massachusetts General Hospital
Boston, MA 02114

J.T. Borenstein
Biomedical Engineering Center, Draper Laboratory
Cambridge, MA 02139

ABSTRACT

Over the last decade, medicine and the biological sciences have benefited from advances in microfabrication technologies and microdevices originally developed for consumer and industrial electronics, automotives and aerospace, and national defense. Real-time miniaturized diagnostic tests, implantable drug delivery and minimally invasive imaging technologies are on the verge of revolutionizing the delivery of health care. Beyond these products lies the field of regenerative medicine, a merger of cell biology, computational biology, microfabrication and biomaterials, aimed at replacing the function of failing tissues and/or organs in patients with end stage organ failure. One of the most critical applications is in the field of renal dialysis, in which waste products in the blood are filtered in an intermittent, invasive and costly manner, with very poor patient outcomes. It is the aim of this work to develop a minimally invasive, continuous hemodialysis capability that utilizes a combination of advances in computational fluid dynamics, MEMS fabrication and biomaterials. Here, early ultrafiltration results are reported, using a microfabricated biopolymer blood processing unit, designed, built and tested in a model system containing a single vascular and dialysate layer.

BACKGROUND

End-Stage Renal Disease (ESRD) is a significant cause of morbidity and mortality in the United States, with 72,000 ESRD deaths reported annually. Standard clinical care for most of the 250,000 renal failure patients is three, four-hour hemodialysis sessions per week, costing nearly $12 billion each year. However, these treatments only provide intermittent filtration and reabsorptive function, and patients are at higher risk for further complications. Moreover, life expectancy drops to less than 20% for patients on renal dialysis treatments for periods of five years or more. Recent advances have been reported in bioartificial kidney technology [**1**], nanofabricated ultrafiltration membranes [**2**], and MEMS-based micro-degassing devices for dialyzers [**3**]. In this work we report early design, fabrication and ultrafiltration results for a novel MEMS-based system for renal replacement that incorporates fractal microvascular network designs and micromolded flow chambers. This microfabricated device could ultimately provide a smaller, less invasive and less expensive therapy for ESRD. Preliminary studies show that the high surface area and precision of this MEMS-based hemofiltration system offers a significant improvement in the clearance efficiency of uremic wastes over current hemodialysis technologies. Additionally, the miniature aspect of this system enables it to be portable and potentially wearable. Most importantly, however, it will provide for *continuous* renal replacement therapy.

DESIGN AND ANALYTICAL APPROACH

The kidney is essentially a microfluidic device that processes and removes wastes while maintaining the proper balance of electrolytes including sodium, potassium, calcium and magnesium, as well as the retention of sugars and blood proteins such as albumin. Consequently**,** hemodialysis requires high rates of blood filtration and well-controlled processing of the blood in order to precisely regulate critical levels of electrolytes, sugars and other blood constituents. Dialysis membranes serve as the engine for hemodialysis, filtering out large molecules, which must remain in the bloodstream while removing smaller molecules such as urea and creatinine and routing them to the excretory system. Because electrolytes and sugars are also filtered from the blood, they must be reabsorbed into the bloodstream rapidly and in a highly regulated fashion. Renal proximal tubular cells, endothelial cells and other cells work in concert to provide this exquisite regulation of the full spectrum of blood constituents processed by the kidneys. For this early demonstration MEMS ultrafiltration device, however, cells have not been incorporated into the construct, since the focus has been the development of an acellular construct capable of separating blood components by size at high densities and with suitably biocompatible and hemocompatible materials.

Development and testing of a finite element based algorithm for simulation of intra- and extra-vascular transport within the kidney is critical. The governing partial differential equation for mass transport is as in Eqn. (1):

$$\frac{\partial c}{\partial t} + \vec{V}\nabla c = D\nabla^2 c \cdot \qquad (1)$$

Here, $c(x,y,z,t)$ is concentration of the transported species e.g. ions (sodium, potassium, magnesium, phosphorous, calcium), blood proteins (albumin), D is the diffusion coefficient for these species, and $\vec{V}$ is the time and space dependent velocity field. The mass transfer in the intravascular and extravascular regions of the device is expected to be characterized as advective and diffusive, respectively. The advective transport will be treated using a characteristic Galerkin algorithm, while the diffusive region will be solved using standard Galerkin methods. This novel mass transfer algorithm will be used to evaluate the mass transport and filtration efficiency in the device.

Design of the vascular portion of this device is accomplished through the generation of a model network that mimics the requisite physiological features of the renal microcirculation. The computational fluid dynamic model utilized to generate this design has been described previously [**4**]; it is a fractal-based approach that produces ordered structures amenable to assembly by photomasking and microfabrication techniques. Among the physiological parameters most critical to successful operation of

0-9640024-5-0/hh2004/$20©2004TRF
DOI 10.31438/trf.hh2004.17

the device are the blood flow rates, pressure losses, and the distribution of hematocrit (red blood cells) within the network. In Figure 1, the distribution of hematocrit across one such model network is illustrated, showing regulation within a narrow range.

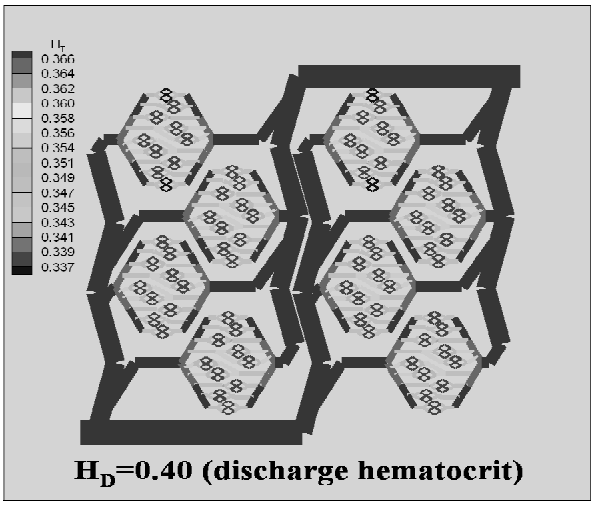

Figure 1. *Distribution of hematocrit across a model microvascular network, illustrating the ability of the model to provide for uniform spreading of mixed-phase flow within a network.*

The unit cell for this hemodialysis approach is a bilayer device with lateral flows of blood and waste in a countercurrent fashion, separated by a thin ultrafiltration membrane. Each bilayer device contains a planar network of blood-carrying vessels and a compartment for waste (dialysate), sandwiched together with an intervening ultrafiltration membrane (Figure 2.) Replacement of current dialysis therapy in a wearable device will require a microfabricated device with large filtration capacity. Calculations show that a device of approximately 100 layers is necessary to provide sufficient blood processing capacity on a wearable, continuous device. Thus, current designs that are produced on a 100 mm diameter wafer platform, will be vertically integrated to produce a 100-layer device by stacking individual bilayer devices together. Experiments reported here are based on single bilayer devices. However, current efforts are aimed at scaling the system to 35 – 100 layers for large-scale *in vitro* and *ex vivo* studies.

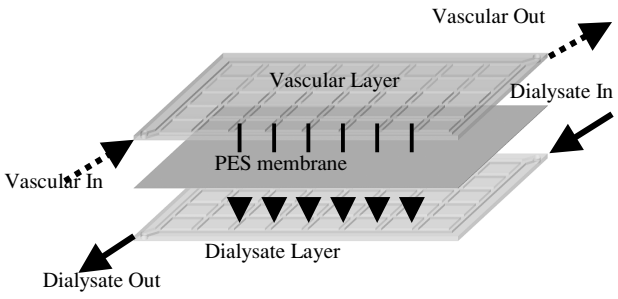

Figure 2. *Experimental design for bilayer ultrafiltration device.*

EXPERIMENTAL DETAILS

The computational algorithm described above was developed to generate a fractal microvascular network that mimics proper anatomical and physiological conditions for flow and mass transport in the device (Figure 3.) This algorithm has been used to design vascular compartments for vital organ tissue engineering, in which the density of small blood vessels must be maximized to provide sufficient oxygenation of growing tissue. In the current application, these algorithms remain useful because the ultrafiltration device must process large volumes of blood rapidly, requiring a very high density of blood vessels and maximal surface area between the vascular network and the dialysate network. No such algorithms were used to design the dialysate layer, which carries waste blood products back out of the device. Consequently, for the first generation system, the dialysate layer has been represented by a simple microfluidic compartment rather than a network.

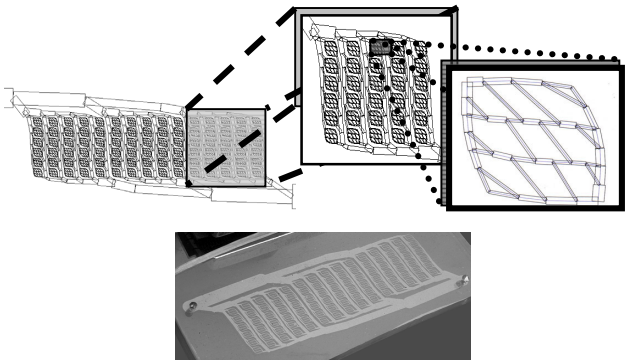

Figure 3. *Design process for generation of microvascular networks, with capillary beds (right inset) arranged in rectangular arrays in each device layer. Bottom photograph: Replica-molded PDMS layer cast in the inverse image of the designs shown.*

Based on these algorithms, bilayer devices have been fabricated using silicon micromachining and polymer replica molding processes [**5-6**]. Vascular and dialysate layer designs were generated using L-Edit (Tanner Research), and produced as transparencies on high-resolution 5080 dpi printers (PageWorks). Next, transparency masks were used to pattern silicon wafers, which were then etched to a depth of 35 microns using an isotropic silicon etching recipe in a standard plasma etcher (STS). Passivation layers were deposited in a deep reactive ion etcher (STS) to promote release of replica-molded polymer films. Thin PolyDiMethylSiloxane (PDMS) films were repeatedly produced using solvent casting against the silicon wafer masters. Thicknesses of PDMS films as low as 100 microns were routinely produced from these molds, consistent with high packing densities for multilayer devices. For the single bilayer device demonstrations, however, PDMS thicknesses of ca. 2 mm were targeted for ease of handling during flow studies.

For the early ultrafiltration experiments in acellular constructs, properties of the membrane drive the performance of the device. Membrane materials such as polysulfone and polyethersulfone (PES) are commonly used as dialyzer membranes, because they are proven to be capable of effective ultrafiltration while possessing outstanding hemocompatibility with patients' blood. Furthermore, these membranes are preferred over other membrane materials for their uniform pore size control,

durability, and ability to be chemically modified. The hemodialysis system design for this device consists of a PDMS structure with membranes interspersed between alternating layers of the vascular and dialysate bed. Since the incorporation of PES membranes into MEMS-based polymeric constructs has required substantial process development and is not yet completed, initial device fabrication and testing has incorporated polycarbonate (PC) membranes (Millipore), which are more amenable to current fabrication processes. Moreover, PC membranes have similar ultrafiltration properties to PES membranes; thus, they were used as an alternative initial model. However, PES membranes will be used in these devices once the process development is completed. Multilayer microfluidic constructs with PC and PDMS membranes have been reported elsewhere [**7-9**]. In this case, the PC membrane is readily incorporated through the use of a thin adhesive layers, which provides adequate connectivity between layers without adversely affecting the porosity of the interfacial layer.

To study the ultrafiltration capabilities of our devices, we examined clearances of urea and creatinine from the vascular stream into the dialysate stream at varying flow rates under single-pass countercurrent conditions. Fluid samples from each flow stream were taken at various time points up to five hours and analyzed for final concentration levels. These concentration values were used to calculate individual solute clearances. Finally, clearance values for urea and creatinine were normalized with respect to current hemodialysis parameters (surface area and flow rate) and compared for overall efficiency.

RESULTS

Clearances (K_i in ml/hr) of urea and creatinine from a vascular stream into a dialysate/parenchymal stream were determined at varying flow rates under *single-pass countercurrent* conditions. For each ultrafiltration experiment performed, the vascular fluid consisted of ultra-pure water and dissolved urea and creatinine each at a concentration of 200 mg/dl, while the dialysate fluid consisted of only ultra-pure water initially. Thus, the urea and creatinine solutions are pumped through the vascular layer containing the microvasculature and the ultra-pure water/"dialysate" is pumped through the open dialysate chamber. Three separate flow-rate ratios of vascular flow (Q_B) to dialysate flow (Q_D) were examined:

1. ≈ 2:1 (Q_B:Q_D) at 0.9 and 2.0 ml/hr respectively
2. 1:1 (Q_B:Q_D) with both fluids at 1.0 ml/hr
3. 1:1 (Q_B:Q_D) with both fluids at 2.0 ml/hr

Each experiment was performed in an incubator at 37°C and a syringe pump was used to administer each fluid into its respective layer. Samples from each flow stream were taken at various time points, for up to five hours, and analyzed for final concentration levels. Concentrations of urea and creatinine from each fluid stream were tracked versus time; each showed slightly different trends with respect to the dialysate-side clearance values. However, both sets of data indicate that an approximate 2:1 vascular:dialysate flow rate ratio – with Q_B = 0.9 ml/hr and Q_D = 2.0 ml/hr – is the optimal ratio for the clearance of both solutes. This corresponds directly to the ratio used in conventional hemodialysis. A higher concentration gradient of solute is established between the vascular and dialysate networks when the vascular fluid is allowed to remain in the device longer, relative to the dialysate. The equation used to calculate dialysate-side clearance is:

$$K_D = Q_{Do}*(C_{Do}/C_{Bi}) \quad (2)$$

where K_D is the dialysate-side clearance, Q_{Do} is the flow rate of the dialysate at the outlet, C_{Do} is the solute concentration in the dialysate outlet, and C_{Bi} is the solute concentration at the vascular inlet. Finally, the calculated clearance values for urea and creatinine obtained from our experiments were normalized with respect to current hemodialysis parameters from a Preset Multiflow M-60 dialyzer, including overall total surface area for filtration (6.0 m^2) and flow rates used (500-2500 ml/hr). Our normalized values for urea and creatinine clearance were then compared with published clearance values for overall efficiency [**10**] (Brunet *et. al*.) The results of this comparison are summarized in Figures 4a and 4b. This normalized data is extremely useful because it enables us to determine the maximal solute clearances our devices can achieve in accordance with the minimal total surface area and flow rates that are needed for a fully functional, continuous, and wearable renal replacement device based on the number of 'stacked' layers of such a device.

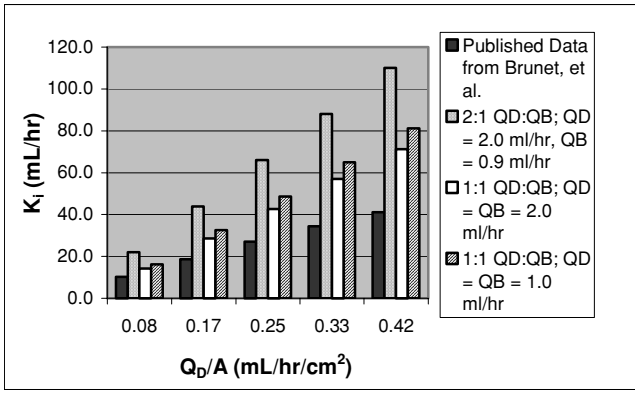

Figure 4a. *Experimental urea clearance at various flow rate conditions: Comparison with published data (Q_D and Q_B denote dialysate and blood flow rates, respectively, K_i is the solute clearance, and A is the total surface area for mass transport).*

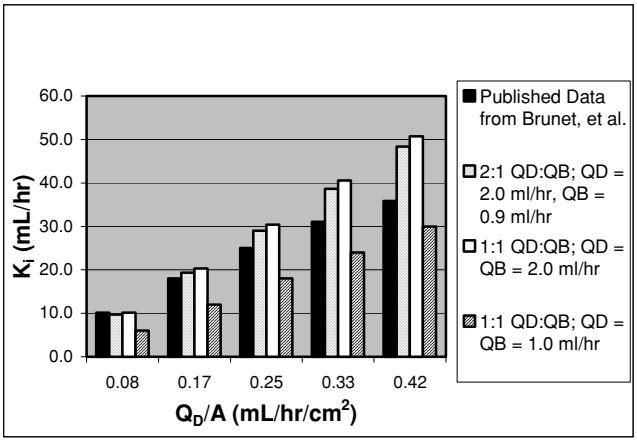

Figure 4b. *Experimental creatinine clearance at various flow rate conditions using the same nomenclature as in Figure 4a.*

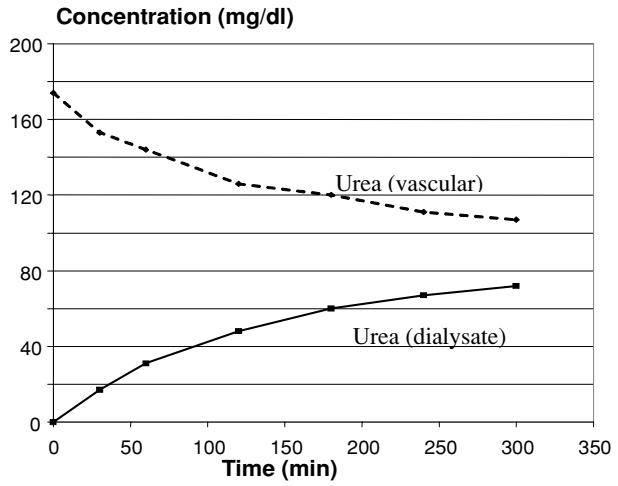

Figure 5. *Diffusion study conducted using PES membrane.*

These early results, obtained in a device constructed using a PC membrane, indicate that the filtration efficiency in the microfabricated device is quite high. However, the PC membrane does not offer optimal ultrafiltration performance with regard to hemocompatibility and molecular selectivity. Current efforts are focused on the construction and testing of microfabricated devices with a PES membrane for ultrafiltration. Initial diffusion studies with these membranes indicate that solute concentrations behave appropriately. Furthermore, PES membranes are invariant to surface treatments applied to the membrane for bonding purposes. Figure 5 illustrates the results of one such diffusion study, in which untreated and treated PES membranes (GE Osmonics) exhibited excellent urea filtration efficiency. Untreated PES membranes denote those obtained directly from the vendor, without any surface preparation aimed at promoting adhesion to PDMS. However, the surface chemistry of PES is such that weak bonding to PDMS is expected, and this has been observed in preliminary device assembly experiments. Therefore, PES membranes have been treated with various processing recipes designed to promote strong, permanent surface adhesion to PDMS. The PES membrane treatments in these cases included oxygen plasma exposure and various related processes.

CONCLUSIONS AND FUTURE OUTLOOK

Fractal microvascular networks designed using our computational models exhibit appropriate anatomical and physiological conditions, including uniform flow and hematocrit distribution, optimized flow resistance, and maximal surface area for exchange of gases, nutrients, and wastes. Microfabricated bilayer devices built based on these microvascular designs have been assembled using polycarbonate nanoporous membranes as a model system for a hemodialysis unit cell. Initial results of our ultrafiltration experiments show that when normalized and compared to conventional hemodialysis parameters, our bilayer devices are roughly twice as effective at removing uremic solutes from incoming vascular flow under optimized flow conditions.

Therefore, current *in vitro* data supports our first goal of creating an ultrafiltration unit capable of efficiently filtering uremic metabolites from incoming vascular flow. Next, we will incorporate renal proximal tubular cells into these MEMS-based devices to examine the re-adsorption of electrolytes, a critical hemostatic function not performed by standard hemodialysis treatment. Our microfabricated renal replacement system promises dramatic improvements over current hemodialysis technologies, including the potential for our system to be wearable and continuous.

ACKNOWLEDGEMENTS

The authors would like to thank members of the MEMS Group at Draper Laboratory, particularly Edward Barnard, Connie Cardoso, Brian Orrick, Mert Prince and Eli Weinberg. Thanks are also due to Kevin R. King of MIT for significant contributions to the microfabrication technology, and to Kimberly Morgan of Massachusetts General Hospital / Boston University for device construction. This project was sponsored by the Department of the Army, Cooperative Agreement DAMD-99-2-9001. The content of this paper does not necessarily reflect the position or the policy of the government, and no official endorsement should be inferred.

REFERENCES

1. E. Tziampazis and H.D. Humes, "Extracorporeal Kidney," in *Methods of Tissue Engineering*, eds. A. Atala and R.P. Lanza, (Academic Press, San Diego, 2002) p. 987.

2. W.H. Fissell, H.D. Humes, A.J. Fleischman and S. Roy, "Initial characterization of a nanoengineered ultrafiltration membrane," *J. Am. Soc. Nephrology* **13** 602A (2002).

3. Z. Yang, S. Matsumoto and R. Maeda, "A prototype of ultrasonic micro-degassing device for portable dialysis system," *Sensors and Actuators* **A95** 274 (2002).

4. M.R. Kaazempur-Mofrad, J.P. Vacanti and R.D. Kamm, R. D., "Computational Modeling of Blood Flow and Rheology in Fractal "Microvascular Networks," *Computational Fluid and Solid Mechanics 200*. ed. K.J. Bathe, (Oxford, Elsevier Science Ltd.), 864 – 867, (2001).

5. J.T. Borenstein, H. Terai, K.R. King, E.J. Weinberg, M.R. Kaazempur-Mofrad, J.P. Vacanti, "Microfabrication technology for vascularized tissue engineering," *Biomedical Microdevice,* **4** 167-175 (2002).

6. J.T. Borenstein, W. Cheung, L. Hartman, M.R. Kaazempur-Mofrad, K.R. King, A. Sevy, M. Shin, E.J. Weinberg and J.P. Vacanti, "Living Three-Dimensional Microfabricated Constructs for the Replacement Of Vital Organ Function," *Proc. 12th Int'l. Conf. Solid State Sensors, Actuators and Microsystems* (Transducers 2003), 1754-7 (2003).

7. J.R. Anderson, D.T. Chiu, R.J. Jackman, O. Cherniavskaya, J.C. McDonald, W. Hongkai, S.H. Whitesides and G.M. Whitesides, "Fabrication of topologically complex three-dimensional microfluidic systems in PDMS by rapid prototyping", *Anal. Chem.* **72** 3158-3164 (2000).

8. S. Hediger, A. Sayah and M.A.M. Gijs, "Biosystem for the Culture and Characterisation of Epithelial Cell Tissues," *Sensors and Actuators B* **63** 63-73 (2000).

9. S. Hediger, A. Sayah, J.D. Horisberger and M.A.M. Gijs, "Modular Microsystem for Epithelial Cell Culture and Electrical Characterisation," *Biosensors and Bioelectronics* 16 689-694 (2001).

10. S. Brunet, M. Leblanc, D. Geadah, D. Parent, S. Courteau and J. Cardinal, "Diffusive and convective solute clearances during continuous renal replacement therapy at various dialysate and ultrafiltration flow rates," *Am. J Kidney Dis*. **34** 486-492 (1999).

RAPID ON-CHIP SEPARATION OF PROTEINS AND IMMUNE COMPLEXES USING UV-INITIATED POLYACRYLAMIDE GELS

Amy E. Herr, Andrew A. Davenport†, Renée Shediac, Anup K. Singh
Biosystems Research, Sandia National Laboratories
Livermore, CA 94551-0969

ABSTRACT

Proteomics seeks to identify proteins present during biological processes with the intent of characterizing important proteins and protein interactions. Recent advances in the application of microtechnology to biology have enabled development of increasingly complex microsystems that hold promise for proteomics, and clinical diagnostics, due to enabled rapid analysis of low abundance species. To that end, microdevice-based analysis of complex samples necessitates system architectures with localized functionality.

We have developed a cross-linked polyacrylamide gel photopolymerization process for the *in situ* fabrication of gel structures as a functional component of microfluidic-based proteomic and diagnostic systems. The straightforward fabrication process yields spatially localized gel matrices with the potential to increase functionality and improve performance of on-chip separation systems. In particular, our work involving UV-initiated polyacrylamide gels as a separation medium for sodium dodecyl sulfate polyacrylamide gel electrophoresis (SDS-PAGE) of proteins and electrophoretic immunoassays involving cytokines is described. The fabrication technique has enabled direct adaptation of slab gel SDS-PAGE of proteins to a chip-based format. Comparison of SDS-PAGE on-chip to slab gel has shown promising advantages, including separation times up to two orders of magnitude more rapid than those performed in gels (30 s *vs*. 3600 s) and separation distances that are a fraction of those required for slab SDS-PAGE (7 mm *vs*. 50 mm).

INTRODUCTION

Conventional SDS-PAGE is a time-consuming and labor-intensive analytical technique conducted on a slab gel. Nevertheless, the technique is reliable, powerful, and yields valuable molecular weight information from complex samples. Coupled with isoelectric focusing, SDS-PAGE is considered the workhorse of proteomic analysis.[1] Much of the power of slab gel SDS-PAGE comes from the ability to tailor gel cross-linking to provide more or less sieving depending on the target sample (i.e., molecular weight, M_r, range of interest).

In the last decade, benchtop bioanalytical systems (slab gel and capillary-based) have been adapted for use in planar microfluidic format.[2,3,4,5] Use of microfluidic architectures has enabled rapid separations requiring short separation lengths. Exceptional performance improvements are attributed to the small-injected analyte plug widths realizable using the microsystem format and the high applied electric field strengths attainable owing to the heat dissipating qualities of the microsystem. Further, microdevice formats are amenable to complex, integrated system designs and have increased potential for automation. The aforementioned attributes of microfluidic systems make the approach promising for applications that require analysis of precious sample in a high throughput manner.

In an effort to leverage the strengths of sieving-type electrokinetic separations while addressing the limitations of macroscale analysis methods, researchers have employed polymeric structures for use in successful separations and analysis of DNA.[6,7] Even so, open channel zone electrophoresis (CZE) has been the method of choice for protein analysis. It is important to note that gel electrophoresis circumvents performance concerns and is superior to CZE in many respects, including: 1) high separation resolution due to low non-specific binding, 2) fast separations (seconds) using short length channels (mm) due to the high surface area of the gel, 3) ready tailoring of gel porosity for specific applications, and 4) spatial-localization of photopatterned polyacrylamide (useful in multiplexing and integration).

While system development of the *in situ* photopolymerization process continues, results presented here indicate successful completion of a suite of protein and immune complex analyses employing the PAGE technique. Polymer matrices can be customized and localized using the straightforward procedure. Results presented demonstrate high separation resolution, throughput, and the ability to extract quantitative information for a variety of biologically relevant species.

THEORY

Apparent electrophoretic mobility and size differences between proteins enable differentiation of various species (for a detailed treatment of electrophoresis see Probstein[8]). Fractionation of analytes based on differences in both charge and size is the goal of SDS-PAGE using sieving media with pore sizes of between 0.5 and 3 nm.[9] The ability to tailor the pore size of a cross-linked gel allows a system designer to optimize the separation media to resolve species within a size range of interest. Pore size is determined by the acrylamide monomer and bis-acrylamide cross-linker concentrations in the initial un-polymerized mixture. An empirical relation has been developed for the separation behavior of SDS-protein complexes, as is relevant to SDS-PAGE. That separation relation has been determined to be a direct proportionality between the logarithm of the molecular weight and the mobility of the protein.[10] This straightforward relationship makes SDS-PAGE a useful, near universal technique for sizing unknown proteins.

One area where an SDS-PAGE like sizing mechanism may be useful is in the detection and characterization of immune complexes. Figure 1 presents a schematic illustrating a direct or non-competitive immunoassay. Immunodiagnostics employing this approach employ either antibody or antigen probes (e.g. hepatitis). In this work, fluorescently-labeled antigen probes were mixed with antibody-containing sample. During an electrokinetic separation of the sample, the presence of antibody can be

†Now at Dept. Mechanical Engineering Stanford University, Stanford CA 94305.

0-9640024-5-0/hh2004/$20©2004TRF
DOI 10.31438/trf.hh2004.18

Solid-State Sensors, Actuators, and Microsystems Workshop
Hilton Head Island, South Carolina, June 6-10, 2004

determined through the formation of a second (lower apparent mobility) peak corresponding to the immune complex. The peak area/height of that second peak can be used as a measure of antigen concentration.

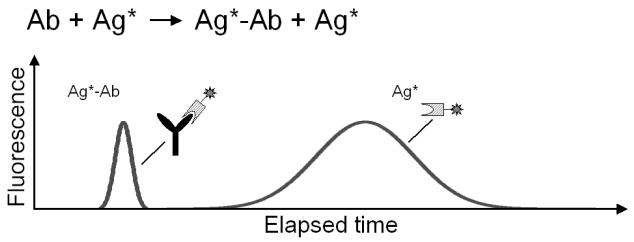

Figure 1. *Schematic depiction of a direct immunoassay. Incubation of fluorescently labeled antigen (Ag*) with unlabeled antibody (Ab) yields a fluorescent complex (Ag*-Ab) and excess Ag*. On-chip native PAGE is used to separate Ag* from the complex, thus allowing detection and quantification of the immune complex.*

To date, electrophoresis-based immunoassays have promised advantages over conventional immunoassay techniques. A capillary or microdevice-based electrophoretic immunoassay requires lower sample and reagent volumes, simultaneous determination of multiple analytes, rapid completion of immunoreaction, hence, rapid analysis, and direct detection of immune complex formation and dissociation, thus simplifying data interpretation.[11] As free solution electrophoresis separates species by differences in charge-to-mass ratio, the small degree of differentiation between the charge of antibody and immune complex make such separations difficult (i.e., in antigen-detecting systems). To address the difficulty, separations could be enhanced by either increasing electrophoretic mobility differences between antibody and immune complexes or by simply separating species based on relative size. The latter approach would benefit tremendously from tailoring of the pore size for high resolution in the antibody/immune complex molecular weight range.

EXPERIMENTAL DETAILS

Microchannel & Photopatterned Cross-linked Gel Fabrication. Bioanalytical devices were fabricated in glass substrates as previously described[12] using standard photolithography, wet etching, and bonding techniques. The substrate was Schott D263 glass wafers (4-in. diameter, 1.1-mm thickness; S. I. Howard Glass Co.). The channels were ~40 µm deep x ~100 µm wide with 6.7 cm long separation channels.

Prior to fabrication of the cross-linked gel, channels were functionalized with an acrylate-terminated self-assembled monolayer and subsequently coated with linear polyacrylamide using a two-step process similar to that described by Kirby *et al*.[13] The conditioning process enhances gel adhesion to the channel walls. Following the coating procedure, chips were flushed with deionized water for 5 minutes and stored filled with water at 5°C.

Polyacrylamide gel structures were fabricated, using the reaction shown in Figure 2, to form sieving matrices for electrophoretic separations employing microfluidic devices. Sieving media composed of various gel concentrations were fabricated *in situ* using the four-step process depicted in Figure 3. Total gel concentration, *T*% (monomer and cross-linker), was controlled by diluting a stock solution of 30% (37.5:1) acrylamide/bis-acrylamide (Sigma) with run buffer. The water-soluble photoinitiator 2,2'-azobis[2-methyl-N-(2-hydroxyethyl)propionamide] (VA-086, Wako Chemicals) was added in a 5 mg/mL concentration to the diluted monomer and cross-linker solution. This low viscosity monomer solution was then introduced, via pressure-driven flow, into all open channels of the microfluidic device (Figure 3). Select regions were masked using material opaque to UV-light (e.g., electrical tape, Rubylith) and the entire device was exposed to a UV source (λ = 365 nm, 4W) for 20 minutes. After the exposure step, all open channels were flushed with run buffer or water to remove unpolymerized acrylamide solution. As depicted in Figure 3, the UV exposure step resulted in localization of a cross-linked gel matrix in unmasked device regions. This process can be repeated to allow fabrication of gels having various porosities in different regions of a single device. During process development, voids or 'tears' have been observed forming in proximity to channel junctions upon application of an electric field. The tears may arise from stresses induced by electroosmotic flow in channels filled with a non-uniformly polymerized gel. Efforts to enhance gel robustness are currently underway in our lab.

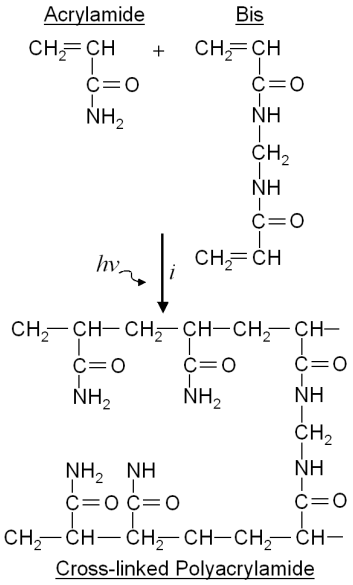

Figure 2. *Polymerization reaction of acrylamide. Structural representations of acrylamide, N,N'-methylenebisacrylamide (Bis), and a segment of cross-linked polyacrylamide are shown. The initiator, in this case VA-086, is indicated as "*i*", while exposure to light is indicated by "*hv*". The concentration of acrylamide and Bis determine the pore size and cross-linking characteristics of the final gel structure. Schematic adapted from Chrambach and Rodbard[9].*

Assays. Sample introduction and separation were performed using common electrokinetic injection methods.[14] The species transport was observed using standard epifluorescence microscopy techniques and digital image collection. Image analysis was conducted using available and in-house Java plug-ins developed using ImageJ (National Institutes of Health, Bethesda, MD, http://rsb.info.nih.gov/ij/). Images were corrected for background signal to adjust for spatial non-uniformities in the excitation and collection efficiencies.

For SDS-PAGE analysis, molecular weight markers (Sigma) consisted of five fluorescently labeled species in solution (62 mM Tris, 1mM EDTA, 3% sucrose, 0.5% dithiothreitol, 2% SDS and 0.005% bromphenol blue). The markers included: aprotinin (bovine lung), M_r 6.5 kDa; α-lactalbumin (bovine milk), M_r 14.2 kDa; trypsin inhibitor (soybean), M_r 20.1 kDa; carbonic anhydrase (bovine erythrocyte), M_r 29 kDa; and alcohol dehydrogenase (horse liver), M_r 39 kDa were prepared for on-chip SDS-PAGE per instructions from the supplier (heating to 65°C for 5 minutes). Prior to use, samples were diluted in tris/glycine/SDS run buffer by

a factor of 3. The proteins α-lactalbumin, trypsin inhibitor, carbonic anhydrase, and alcohol dehydrogenase were used as sizing standards for all gel concentrations in this work; aprotinin did not consistently provide sufficient signal-to-noise ratios to be used as a standard. Immunoassay results for the cytokine interleukin-2 (IL-2, M_r 17.1 kDa) relied upon fluorescent labeling (FITC) of that species for detection.

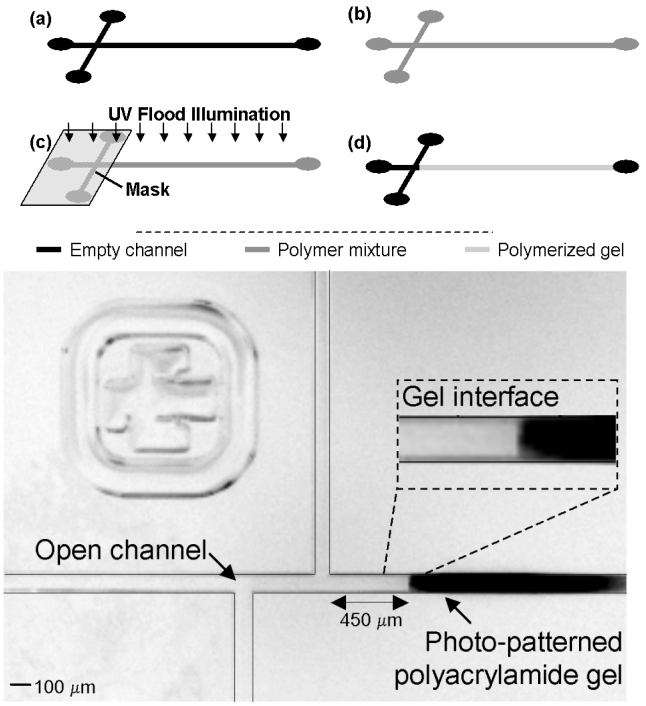

Figure 3. *(top) Schematic representing in situ photopolymerization process. Photopolymerization steps include: (a) microfluidic channels have been conditioned, (b) channels are filled with a solution of unpolymerized monomer and cross-linker, (c) select regions of the device are masked and the device is exposed to a UV light flood exposure, and (d) the final device contains channels filled with cross-linked polyacrylamide gel and open channels. (bottom) Inverted grayscale image of gel localized within the separation channel. For clarity, the gel has been dyed to appear dark in this image.*

RESULTS & DISCUSSION

On-chip SDS-PAGE. Directed experiments were conducted to assess the performance of on-chip SDS-PAGE in cross-linked gel sieving matrices. SDS-PAGE electropherograms are shown in Figure 4 for a mixture of five fluorescently labeled species for both 4% and 8% cross-linked gels. Under otherwise identical running conditions, the 4% gel is unable to resolve the species, while the 8% gel permits baseline resolution of all five species in elapsed separation times of 30 s or less. As an illustration of the exceptionally rapid SDS-PAGE possible with this technique, Figure 4 shows a near baseline-resolved separation that is complete in less than 5 s. Separation lengths were typically less than 7 mm. Conventional slab gel SDS-PAGE requires up to an hour for separation of species in gels having separation lanes 80 mm in length. Similarly, rapid near-baseline resolved on-chip protein separations were reliably achieved in cross-linked gels ranging from 6% to 12% total gel concentration.

Standard curves relating migration distance and molecular weight were generated to validate the separation mechanism governing the on-chip technique. Figure 5 shows an electropherogram corresponding to the SDS-PAGE separation from Figure 4 overlaid with a standard curve generated from that separation data. Standard curves were linear ($R^2 > 0.984$) for gel concentrations ranging from 4% to 10%. The linearity of the curves confirms the size-based separation mechanism of the technique, as is also the case in slab gel SDS-PAGE.

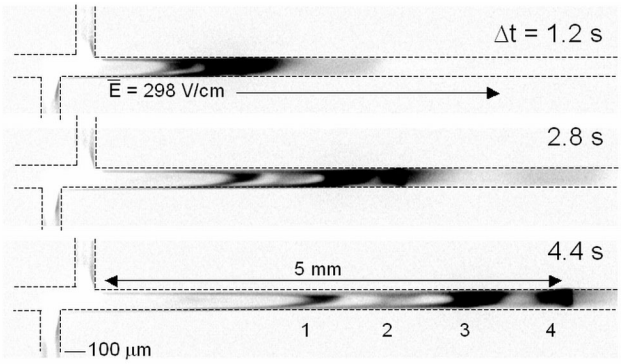

Figure 4. *Time-evolution of an on-chip SDS-PAGE separation of protein in an 8% gel. Transverse band asymmetry is attributed to a non-optimal offset injection and low diffusion of the species. Cross-linked gel was patterned in all channels of the device. Species are: (1) apotinin (2) α-lactalbumin, (3) trypsin inhibitor, (4) carbonic anhydrase II and (5) alcohol dehydrogenase. E = 298 V/cm.*

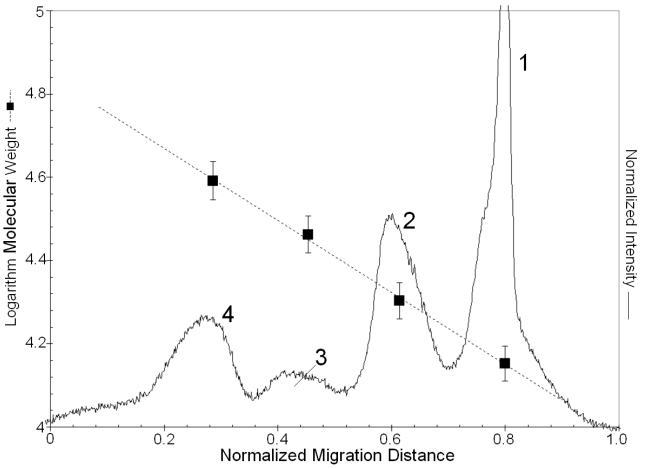

Figure 5. *Standard curve overlaid with axial concentration distribution for the separation of four proteins in a 8% acrylamide SDS-PAGE separation. E = 298 V/cm.*

The *in situ* photopatterning technique allows fabrication of various gel concentrations. Results for separations of M_r 6.5 to 39 kDa proteins using 4% and 8% gels are shown in Figure 6. The results highlight the importance of tailoring gel concentration for optimum resolving power for a given assay (i.e. M_r range of interest). Further, gel porosity customization enables development of quantitative system calibration curves employing Ferguson analysis. Protein standards were separated on gels having gel concentrations ranging from 4% to 10%. The apparent mobility of each species was measured in those gel systems. Plotting logarithm mobility *vs.* gel concentration for each standard results in an effective retardation coefficient for each species. For the gel system reported in this work, a calibration curve relating this retardation coefficient to molecular weight was found to be governed by the equation: $K_r = 2.2\text{x}10^{-3} \times M_r - 0.001$ (R^2 =

0.996). Generation of such calibration curves based upon protein standards allows determination of M_r for unknown proteins.

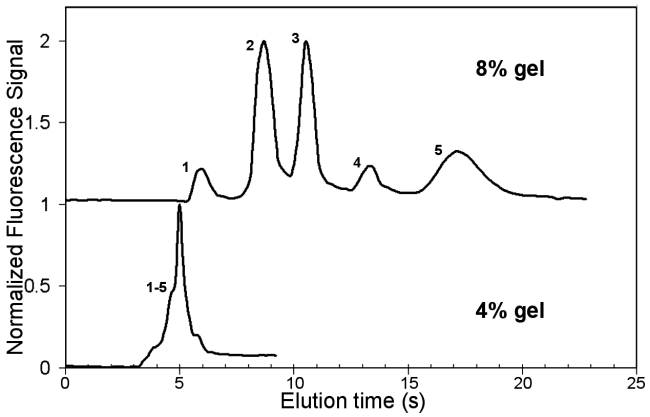

Figure 6. *On-chip SDS-PAGE separation resolution dependence on gel acrylamide concentration (4% and 8%). Separation of five SDS-protein complexes was not attained in the low concentration gel, while the higher concentration gel clearly resolves all species. Aside from variation of gel concentration, conditions were constant. E = 298 V/cm.*

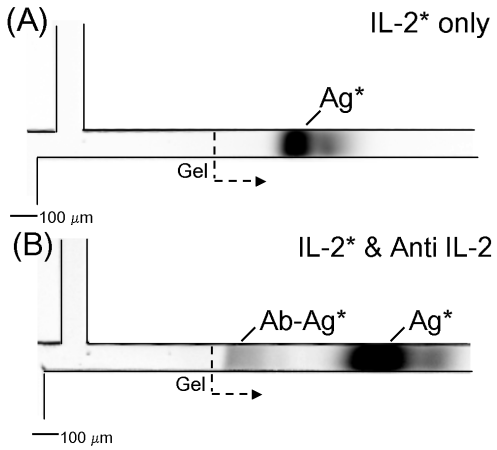

Figure 7. *Native PAGE separation of free and immune-complexed IL-2. Inverted grayscale images of: (A) native PAGE of IL-2*, and (B) native PAGE of the immune-complex with a 2x molar excess of IL-2*. Species were separated in less than 15 s and within 2 mm of the injector. E = 460 V/cm.*

Immunoassays. Sensitive detection of cytokines is of interest to clinical diagnostics as such disease markers are involved in the immune response to invading species. Traditional immunoassays can be multi-step procedures, while electrophoretic immunoassays are rapid, sensitive, and amenable to automation. While not universally applicable, non-denaturing native PAGE can sometimes resolve free antigen from immune-complexed species without destroying immune complexes. Denaturing SDS-PAGE tends to disrupt immune complexes. Figure 7 shows on-chip immunoassays resulting in ultrafast native PAGE characterization of the cytokine interleukin 2 (IL-2). In these experiments, the antigen (Ag) was labeled used as a fluorescently labeled probe for the target antibody (Ab). Figure 7A shows native PAGE results for an IL-2* sample with no antibody present. A companion native PAGE analysis of IL-2* in solution with anti-IL-2 (M_r 150 kDa) is shown in shown Figure 7B. Figure 7 shows an additional, lower mobility band resolving from the antigen. The slower band corresponds to the large antigen-antibody immune-complex. Differentiation between the free IL-2* and the IL-2 immune complex occurred within 15 s in a 2 mm separation length.

CONCLUSIONS

Cross-linked polyacrylamide gels, photolithographically patterned *in situ*, have been demonstrated for use as components of microfluidic bioanalysis systems. The fabrication process is compatible with the microfluidic format and has been introduced as a means to define cross-linked sieving matrices at specific locations in a microfluidic device for use in protein sizing and electrophoretic immunoassay applications.

The fabrication technique has enabled direct adaptation of slab gel SDS-PAGE of proteins to a chip-based format, resulting in substantial performance improvements. Comparison of SDS-PAGE on-chip to slab gel reveals separation times up to two orders of magnitude more rapid than those performed in gels (30 s *vs*. 3600 s) and separation distances a fraction of those required for slab SDS-PAGE (7 mm *vs*. 50 mm). Further work extends the approach to separations of biomarkers, in this case IL-2 and the associated immune complex. Our lab is currently exploring this material as a component of an integrated diagnostic instrument.

REFERENCES

1. S. Mouradian, "Lab-on-a-chip: applications in proteomics" *Current Opinions in Chemistry and Biology 6,*1 (2002).
2. D. J. Harrison*, et al.*, "Capillary Electrophoresis and Sample Injection Systems Integrated On a Planar Glass Chip" *Anal. Chem. 64,*17 (1992).
3. C. S. Effenhauser, A. Manz and H. M. Widmer, "Glass Chips For High-Speed Capillary Electrophoresis Separations With Submicrometer Plate Heights" *Anal. Chem. 65,*19 (1993).
4. S. C. Jacobson*, et al.*, "High-Speed Separations On a Microchip" *Anal. Chem. 66,*7 (1994).
5. A. T. Woolley and R. A. Mathies, "Ultra-High-Speed Dna-Sequencing Using Capillary Electrophoresis Chips" *Anal. Chem. 67,*20 (1995).
6. S. N. Brahmasandra*, et al.*, "Electrophoresis in microfabricated devices using photopolymerized polyacrylamide gels and electrode-defined sample injection" *Electrophoresis 22,* (2001).
7. K. G. Olsen, D. J. Ross and M. J. Tarlov, "Immobilization of DNA hydrogel plugs in microfluidic channels" *Anal. Chem. 15,*74 (2002).
8. R. F. Probstein (1994). Physicochemical Hydrodynamics: An Introduction. New York, John Wiley & Sons, INC.
9. A. Chrambach and D. Rodbard, "Polyacrylamide Gel Electrophoresis" *Science 172,* (1971).
10. A. L. Shapiro, E. Vinuela and J. V. Maizel, "Molecular Weight Estimation of Polypeptide Chains by Electrophoresis in SDS-Polyacrylamide Gels" *Biochem. Biophys. Res. Commun. 28,* (1967).
11. W. S. B. Yeung*, et al.*, "Capillary electrophoresis-based immunoassay" *J. Chromatogr. B 25,*797 (2003).
12. D. J. Throckmorton, T. J. Shepodd and A. K. Singh, "Electrochromatography in microchips: Reversed-phase separation of peptides and amino acids using photopatterned rigid polymer monoliths" *Anal. Chem. 74,*4 (2002).
13. B. J. Kirby*, et al.*, "Programmable modification of cell adhesion and zeta potential in silica microchips" *Lab Chip 3,* (2003).
14. S. C. Jacobson*, et al.*, "Effects of Injection Schemes and Column Geometry On the Performance of Microchip Electrophoresis Devices" *Anal. Chem. 66,*7 (1994).

ACKNOWLEDGEMENTS

This work was financially supported by a National Institute of Dental and Craniofacial Research grant (U01DE014961). Sandia is a multi-program laboratory operated by Sandia Corp., a Lockheed Martin Co., for the United States Department of Energy under Contract DE-AC04-94AL85000.

CORIOLIS MASS FLOW, DENSITY AND TEMPERATURE SENSING WITH A SINGLE VACCUM SEALED MEMS CHIP

D.Sparks, R.Smith, S.Massoud-Ansari, N.Najafi
Integrated Sensing Systems Inc., 391 Airport Industrial Dr,
Ypsilanti, MI 48198 www.mems-issys.com

ABSTRACT

A new microfluidic system for measuring the mass flow rate, dose, chemical concentration, fluid density, specific gravity and temperature has been developed. Vacuum packaged, resonating silicon microtubes are employed to form both a Coriolis mass flow and density sensor. The micro Coriolis mass flow sensor has 10 times the resolution of the best commercially available macro Coriolis mass flow sensors. An on-chip temperature sensor (RTD) has been added to the microchip, enabling accurate fluid temperature monitoring. At constant temperature the density resolution/or output stability approaches 1 over 1 million (6 digits) in the new system. Also a new method of chip-level gettering was developed to achieve the milliTorr pressures needed for adequate resonator signal quality for the vacuum packaged microsensors. Applications for both mass flow measurements and density sensing are discussed.

INTRODUCTION

Conventional Coriolis mass flow sensors have been commercially available for over 30 years. The basic function of an ideal resonating Coriolis mass flow sensor can be expressed by the following equations and is illustrated in Fig. 1. The mass flow rate q is given by:

$$q = K_s \vartheta/(4\omega L r)$$

Where, K_s angular spring constant of the flow tube, ϑ is the twisting angle of the tube, ω is the resonance frequency, L is the length of the tube and r is the radius of the U-bend of the tube. Therefore, the mass flow rate is directly proportional to the twisting angle and inversely proportional to the resonance frequency. The density of a liquid ρ is given by the expression:

$$\rho = 1/V\ [(K_s/4\pi^2 f^2) - m_t]$$

where V is the internal volume of the resonant tube, m_t is tube mass, K_s is the spring constant of the tube and f is the resonance frequency of the tube. As can be seen by the expression above, the density is inversely proportional to the square of the resonance frequency.

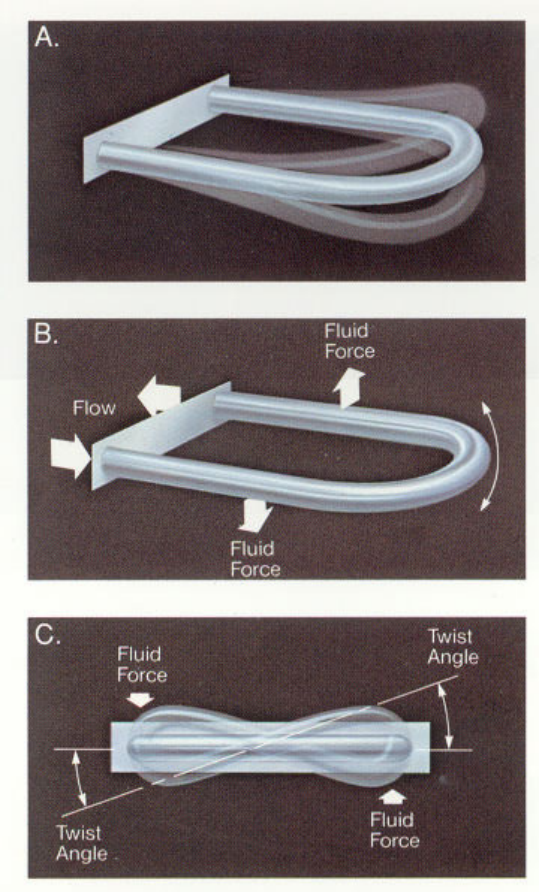

Fig. 1. Explanation of the Coriolis mass flow sensor tube motion: (a) vibration in the primary mode - used for density measurements, (b) forces acting on the sensing tube in upward motion, (c) end-on view of the sensor tube indicating force couple and tube twist.

The microfluidic sensor discussed in this paper is based on a MEMS chip concept first published in 2001 [1]. This early work as well as one other MEMS study [2] entailed the development of an R&D micromachined chip only, and employed a laboratory vacuum chamber and instrumentation to both enable and sense resonance. At the core of the new sensor is a U-shaped, vacuum-sealed resonating silicon microtube. The fabrication process uses a combination of plasma and wet etching, photolithography, along with various types of wafer-to-wafer bonding to form the microfluidic chips [3-5]. While filled with a fluid, the tube is driven into

0-9640024-5-0/hh2004/$20©2004TRF
DOI 10.31438/trf.hh2004.19

resonance electrostatically and its motion sensed capacitively using metal electrodes under the tube and accompanying electronic circuits connected to the MEMS chip via wire bonding.

MICROMACHINED SENSOR FABRICATION

The silicon MEMS fabrication process used to form the microtubes has been described in previous publications [3,4]. A photograph of the resonant microtube chip is shown in Fig. 2. The doped silicon tube is anodically bonded to a metallized Pyrex wafer. Holes for the passage of fluid are predrilled into the Pyrex wafer. The metal pattern on the Pyrex forms capacitor plates, feedthroughs, electrical runners, a temperature sensor and silicon contacts.

A quality factor or Q value above 1000 was desired to obtain sufficient frequency and hence density resolution with the sensor. Initial test data on R&D samples were made using a vacuum chamber and

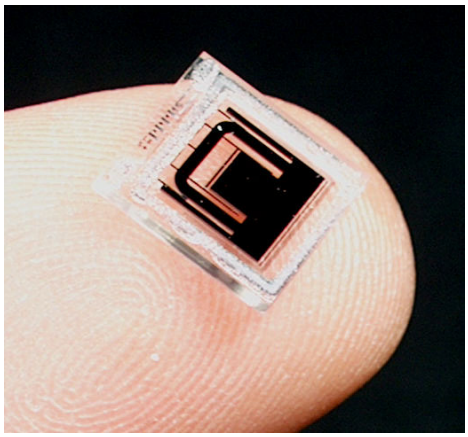

Fig. 2. The U-shaped microfluidic chip.

indicated that a cavity pressure of under 100mTorr would be needed to obtain an acceptable sensor signal. Conventional anodic bonding produces cavity pressures in the 100 - 400 Torr range [6,7], while glass frit and solder sealing produces cavity pressures of 1-2 Torr [8]. For this microfluidic device, a cavity pressure of 1.4 Torr was obtained with glass frit sealing and due to squeeze-film damping and molecular interaction, the Q value was limited to 40 for this wide vertical resonator.

After initially using NonEvaporable Getters (NEGs) with poor results, a new approach to MEMS gettering was developed [9-11]. This method was integrated into a wafer bonding process. A capping wafer, generally either silicon or glass was patterned and etched to form both a cavity that encloses the active micromachine and opens up access to the electrical bond pads. At this point the getter, called NanoGetters™, was applied and patterned on the top portion of the cavity, as shown in Fig. 3. The NanoGetter™ is comprised of a proprietary, patent

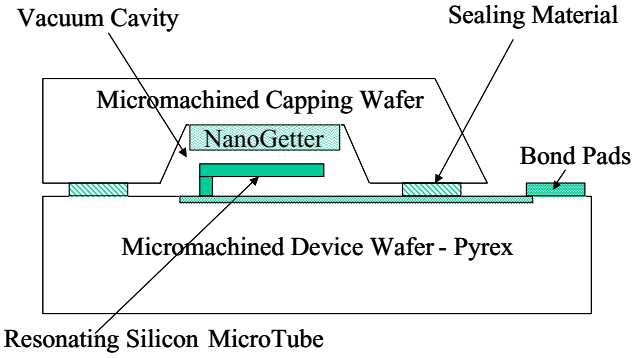

Fig. 3. Cross-sectional illustration of the vacuum packaging and gettering approach.

pending, multi-layer structure and as the name implies the thickness of the film layers are in the nanometer - 5nm to 500nm range. Since thin film deposition techniques are employed in a cleanroom environment, the new getter is virtually particle free compared to conventional NEGs formed using powder metallurgy. The thin film deposition method also enhances the ability to easily integrate the getter into most typical MEMS processes.

RESULTS

Through wafer-to-wafer bonding with getters, the vacuum level obtained was found to be under a milliTorr, resulting in Q values ranging from 2000 to 45,000 for the silicon tube resonator. Extensive life testing of the hermetic glass frit seal and getter has been performed to insure that the basic MEMS device is reliable. Fig. 4 shows that the average Q of the resonators did not vary in a statistically significant manner whether the parts were at room temperature or

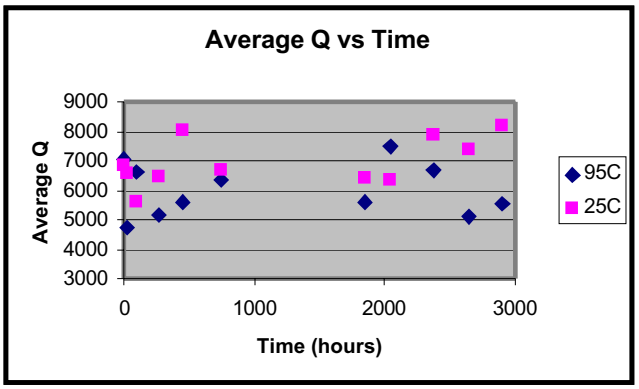

Fig. 4. Average Q versus time at 25°C and 95°C for 24 silicon resonators vacuum packaging using the NanoGetter™.

elevated temperature. In previous resonator reliability studies, Q values were found to decrease at high temperature when getters were not employed due to gas desorption from the microcavity walls [8].

The first product that was developed with this technology was a static density meter [3,12]. The commercially available density meter is shown in Fig 5. The development of a density meter was simpler and hence faster than that of a Coriolis mass flow sensor since the tube twisting did not have to be monitored. The resonant frequency of the microtube varies from 11KHz empty, down to 6KHz when filled with a dense liquid.

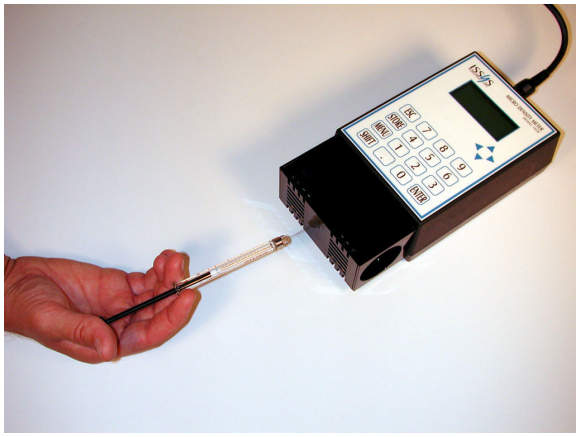

Fig. 5. Syringe loading of the temperature controlled microfluidic sensing system [3].

The system has been used to measure various petrochemicals, pharmaceuticals, beverages and aggressive chemical reagents. Micro density testing offers an advantage in saving time and money in distillation and fermentation applications as well as with the analysis of very expensive, small samples

Fig. 6. Industrial in-line flow and density meter.

such as perfumes and drug library samples.

Chemical concentration can be measured with this MEMS-based instrument using a mass-based solution approach. Sodium chloride (saltwater/saline) solutions are used for intravenous drug infusion. Sucrose and dextrose solutions are employed in IV drug infusion as well as in beverage and food processing. Measurement of alcohol solutions see application in fuel cells, fuel blending and alcoholic beverages. An in-line meter has followed the launching of the static density meter. The same chassis used for this in-line density meter has been adapted for the Coriolis mass flow sensor. Fig. 6 shows the in-line package housing with the outer module casing removed.

Mass flow tests were performed using both nitrogen and argon gas. An ATC IL-05CC, traceable gas calibration sensor was used to measure the flow data. Fig. 7 shows the results of this initial testing. Good sensor output linearity was observed. Further improvement at the system board level is underway to

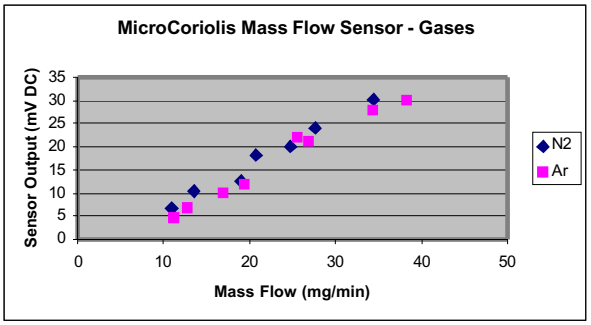

Fig. 7. Micro Coriolis mass flow output for gases.

reduce noise and improve overall sensor accuracy of these prototypes.

The same sensing elements have been used to measure the mass flow of water, methanol and various solutions. Fig. 8 shows how for liquid flow

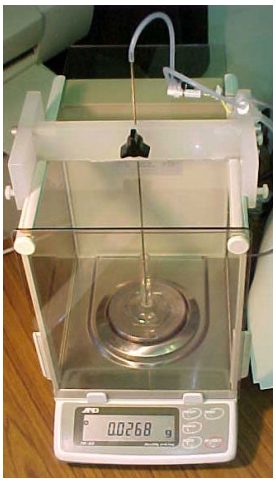

Fig. 8. Microscale system used to measure very low liquid mass flow rates.

monitoring a microscale was employed to measure the true mass of the liquid as it travels through the sensor and associated tubing. Precautions against air-flow related errors, temperature variation and evaporation were taken into account in this test system. The sensor was connected to a commercially available elastomeric drug infusion pump, rated at 0.5mL/hr. These low

pump supplied flow rates were measurable with this new sensor and confirmed with the microscale. This same microtube device has measured flow rates as in excess of 110 ml/hr using a gravity fed and syringe supplied fluid test system. In comparison the lowest flow rate, commercially available Coriolis mass flow sensor, the Quantim, which uses small metal tubes, has a minimum flow rate limit of 5ml/hr [14]. Another MEMS Coriolis flow sensor developed by Enoksson et al. [2], in which the tubes were fabricated using wet silicon etching, had minimum flow rate measurements of 300ml/hr, due to the relatively large silicon tube size. Being able to measure flow rates below 100ml/hr, along with the sensor's small size and low power consumption, make this technology ideal for drug infusion applications. By integrating the mass flow with respect to time, the delivered dose and dose rate can be monitored. This sensor offers improved drug infusion safety features as well as a lower dose delivery capability.

One of the benefits of using Coriolis mass flow sensors is that a fluid density or specific gravity output is available. This can enable the user to monitor what type of fluid is traveling through the sensor. In medical applications this can prevent the delivery of the wrong drug and gas bubbles. Other applications for this low flow rate and density sensing technology are also found in the areas of drug discovery and development, leak detection, and the mixing and metering of industrial chemicals like pesticides, perfumes, flavor agents, fuels, dopants and additives.

CONCLUSIONS

A new microfluidic system for measuring the mass flow rate, dose, chemical concentration, fluid density, specific gravity and temperature has been developed. Vacuum packaged, resonating silicon microtubes are employed to form both a density meter and a Coriolis mass flow sensor. An on-chip temperature sensor has been added to the microchip, enabling accurate fluid temperature monitoring. As part of this development effort, a new method of gettering was developed to achieve the sub-milliTorr pressures needed for adequate resonator signal quality. With this NanoGetter™, Q values above 45,000 were obtained. MEMS-based, Coriolis mass flow and density sensors have been developed that are suitable for medical, industrial and laboratory applications.

ACKNOWLEDGMENTS

The authors would like to acknowledge the financial support of the Michigan Life Science Corridor, National Institute of Standards and Testing, and assistance in gas testing provided by ATC personnel.

REFERENCES

1. Y. Zhang, S. Tadigadapa and N. Najafi, "A micromachined Coriolis-force-based mass flowmeter for direct mass flow and fluid density measurements," Transducers'01, p.1460, 2001.
2. P. Enoksson, G. Stemme and E. Stemme, "A silicon resonant sensor structure for Coriolis mass-flow measurements, J.MEMS, vol. 6, p.119, 1997.
3. D. Sparks, R. Smith, M.Straayer, J.Cripe, R.Schneider, A.Chimbayo, S.Ansari, N.Najafi, "Measurement of density and chemical concentration using a microfluidic chip," Lab Chip, vol. 3, p.19, 2003.
4. S.Tadigadapa, C.Tsai, Y.Zhang and N.Najafi, "Micromachined fluidic apparatus," US Patent 6,477,901, 2002.
5. D.Sparks, "Integrated microtube sensing device," US Patent 6,647,778, 2003.
6. H.Henmi, S.Shoji, Y.Shoji, K.Yoshimi and M. Esashi, "Vacuum packaging for microsensors by glass-silicon anodic bonding," Sensors and Actuators A, vol. 43, p. 243, 1994.
7. M.Esashi, et al. "Vacuum-sealed silicon micromachined pressure sensors," Proc. IEEE, vol. 86, no. 8, p.1627, 1998.
8. D.Sparks, et al., "Wafer-to-wafer bonding of nonplanarized MEMS surfaces using solder," J. Micromech.&Microengr., vol. 11, no. 6, p.630, 2001.
9. D. Sparks, S. Massoud-Ansari, N. Najafi, "Chip-level vacuum packaging of micromachines using nanoGetters," IEEE Trans. Adv. Packaging, vol. 26, no. 3, p.277, Aug. 2003.
10. www.nanogetters.com
11. N.Najafi, S. Massoud-Ansari, S.Tadigadapa, and Y.Zhang, "Methods for prevention, reduction, and elimination of outgassing and trapped gases in micromachined devices," US Patent 6,499,354, 2002.
12. D.Sparks,R.Smith,M.Straayer,J.Cripe,R.Schneide, S.Ansari,N.Najafi, "A microfluidic system for the measurement of chemical concentration and density," Transducers'03, Boston, MA, 2C2.5, p. 300, 2003.
13. M.Tanaka et al., "Recommended table for the density of water between 0°C and 40°C based on recent experiemental reports," Metrologia, Vol. 38, p.301, 2001.
14. Quantim Coriolis Mass Flow Sensor, http://www.brooksinstrument.nl/PDS/QM/QmIP40-Pe-0102.pdf, Jan. 2002.

ADDRESSABLE MICROLENS ARRAY TO IMPROVE DYNAMIC RANGE OF SHACK-HARTMANN SENSORS

Hyuck Choo and Richard S. Muller
Berkeley Sensor & Actuator Center
Department of Electrical Engineering and Computer Sciences
University of California at Berkeley
Berkeley, California 94720-1774 USA

ABSTRACT

We demonstrate an addressable array (5-by-5) of high-quality microlenses applied to a Shack-Hartmann (SH) sensor in a micro-optical system. Specific lenses in the array can be addressed using a new selection scheme (that we have designed, built, and tested) in which the mechanical resonant frequencies of individual lens-support carriages are varied. Thus, by changing the frequency of the drive voltage, we require only two electrical connections per row in the lens system to identify the selected lens by its resonating focal image. We show that using this lens-identification method allows us to improve the dynamic range of Shack-Hartmann sensors by 2600-4600% over values attained in conventional SH designs.

INTRODUCTION

Shack-Hartmann sensors are widely used in astronomical telescopes and ophthalmic-analysis systems as monitors for wavefront aberrations. They are fast, accurate and, in contrast to interferometers, generally insensitive to vibrations. When used in conjunction with adaptive mirrors, Shack-Hartmann sensors are able to improve the image quality of astronomical telescopes by performing real-time corrections on the wavefront aberrations that are inherently generated as starlight traverses the earth's atmosphere.

In Shack-Hartmann systems, a microlens array dissects an incoming wavefront into a number of segments (Figure 1). Each microlens in the array creates a focal spot within the assigned sub-aperture on the CCD (typically made of 40 CCD pixels). Because light travels in a straight path normal to the wavefront, the position of these focal spots is related to the average wavefront slope over each microlens aperture. Thus the pattern of spots at the focal plane contains information about the spatially-resolved waveform slope that can be integrated to reconstruct the wavefront [1]. The dynamic range (the range of measurable wavefront slope/curvature) of a conventional SH system has fundamental design limits that must be kept in mind; a SH system produces false results if the curvature or the slope of the wavefront being measured is too large. Figure 2 shows one of such cases in which a focal point of one microlens dislocates into an adjacent sub-aperture assigned to a focal point of another microlens.

Researchers have attempted to overcome this dynamic-range limitation of SH systems using at least three methods: (1) employing a modified unwrapped algorithm,(2) using a SH array of microlenses with well-defined astigmatism, or (3) positioning a spatial-light modulator in front of the SH microlens array as a shutter [2-4]. Research showed that the first two methods had very limited practical use because they worked only with certain types of wavefronts. Method (1) works with highly sloped planar wavefronts but not with highly curved wavefronts. Method (2) fails if the incoming light contains astigmatic characteristics, possibly canceling out the well-defined astigmatism of the lens array and thereby making it impossible to identify where the focal points come from. Method (3) which employs a spatial-light modulator is also impractical on three grounds: the modulator absorbs a great deal of light (at least 50% in the case of an LCD illuminated with unpolarized light); it increases the noise in the measurement; and it introduces additional aberrations to the wavefront being measured. In addition, spatial-light modulators may have polarization dependences, and they are typically very expensive.

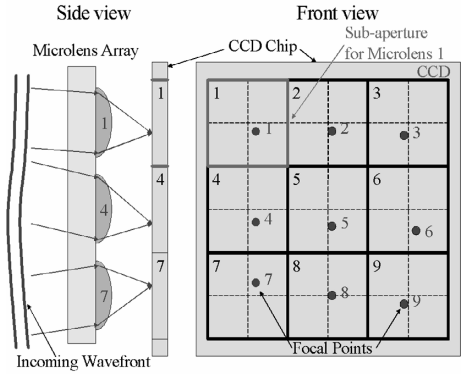

Figure 1. *Wavefront-slope measurement using microlens array: Each microlens has its own sub-aperture consisting of forty CCD pixels (divided into four quadrants), and the focal point of the microlens must be located within the assigned sub-apertures*

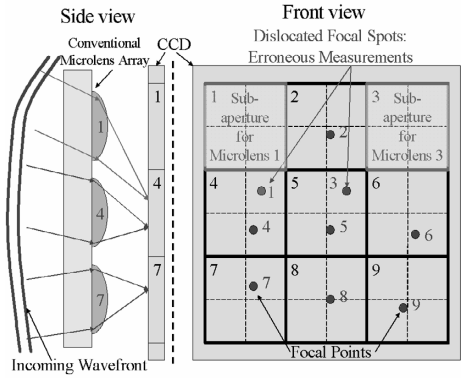

Figure 2. *Limited dynamic range of a conventional Shack-Hartmann sensor (left): A highly curved- or steeply sloped-wavefront causes the focal points of microlenses #1 and #3 to mis-locate onto the sub-apertures assigned to microlenses #4 and #5, respectively, causing erroneous measurements.*

Using MEMS technologies developed in the Berkeley Microlab, we have created densely packed active microlens arrays that are individually controlled to resonate at given frequencies. When a lens resonates, its focal point will move parallel to it; hence by energizing one microlens, we identify its focal point

0-9640024-5-0/hh2004/$20©2004TRF
DOI 10.31438/trf.hh2004.20

through its movement (Figure 3). We have varied the mechanical resonant frequencies of individual lens-support carriages so that, by changing the frequency of the drive voltage, we require only two electrical connections per row in the lens system to identify the selected lens. Figure 4 shows a schematic diagram of a microlens array and an enlarged view of an active MEMS microlens unit. Through our design, a lens focal point can be identified outside its associated sub-aperture (usually 40 pixels), anywhere in the sensing array. This identification allows the dynamic range of the SH sensor to be dramatically improved-- a factor of 26 to 46 better than that achieved in conventional Shack-Hartmann systems.

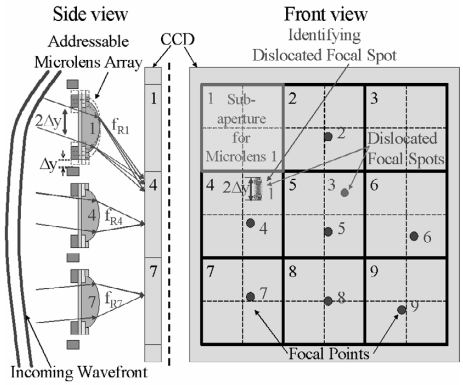

Figure 3. *By making each microlens resonate individually, we can identify its associated focal point, even if the focal point is located outside the assigned sub-aperture.*

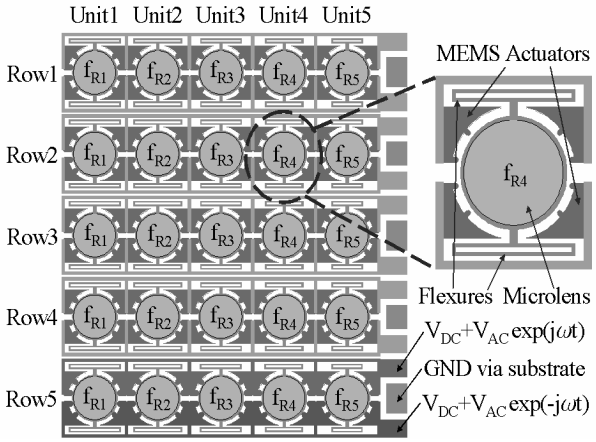

Figure 4. *Schematic diagram of addressable microlens array: Our resonant-frequency addressing method requires only a single pair of electrical lines per row to control each unit individually.*

DESIGN CONSIDERATIONS AND FABRICATION

Our addressable microlens array for Shack-Hartmann sensors has been based on the following design principles: 1. Maximizing the clear aperture of the system (or microlens area) by minimizing the areas for actuators and interconnects; 2. Reducing mechanical cross-talk between different units as much as possible in order to avoid errors in identifying a lens 3. Assuring that only the desired lens moves appreciably even when it must be actuated with the highest driving voltage for lenses in its row. The resonant frequency of each structure is varied by decreasing the support-flexure lengths from 900 to 500 μm in steps of 100 μm. Theoretical analysis of the system predicts that when one of the units is at full resonance of ±20 μm, the other four units move less than a few microns.

Our 5×5 addressable-lens arrays, fabricated using SOI wafers, are pictured in the SEM photographs shown in Figure 6-9. Each addressable unit (1.5mm square) contains one 800μm-diameter microlens with lens-support carriage and actuators. The microlenses are precisely formed using our polymer-jet printing technology (described earlier [5]) within the 20μm-deep circular wells (etched in the device layers of SOI wafers) having 2μm-thick silicon-nitride-membrane floors. The boundaries of the circular wells define the lens diameters, and the polymer surface tension creates a high-quality optical surface. Figure 5 illustrates the processing steps. The buried- oxide mask is used in order to pattern fine features such as comb fingers and flexures after creating 20μm-deep contact holes and circular wells. The handling layer is also used as electrical ground, and the moving structures are electrically connected to the handling layer through the contacts, preventing any unwanted electrostatic pulling forces.

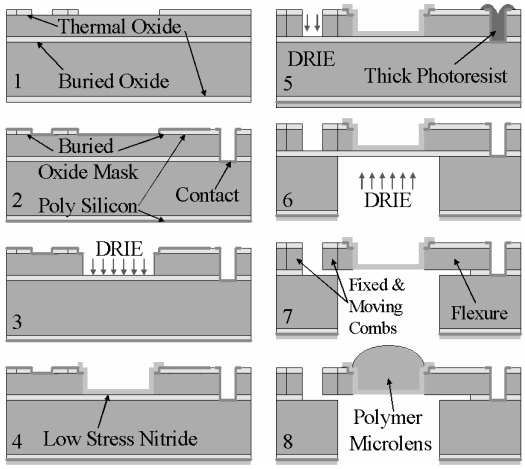

Figure 5. *Fabrication process: **1**. Grow 1μm-thick thermal oxide on a SOI wafer. Define combs, flexures, supports, and lens frames to make buried oxide-layer mask; **2**. DRIE halls and deposit 0.5μm-thick LPCVD poly-Si layer to create electrical contacts from the device layer to the handling layer (GND). Poly-Si layer also protects the oxide mask; **3**. DRIE circular trenches in the device layer; **4**. Deposit and pattern silicon nitride layer (tensile stress, ~250MPa); **5**. DRIE silicon parts (combs, flexures, supports, and lens frame) using the buried oxide mask; **6**. Open the backside of the lens using DRIE; **7**. HF Release; **8**. Make microlenses using polymer-jet printing technology. The boundary of the trench defines the diameter of the lens.*

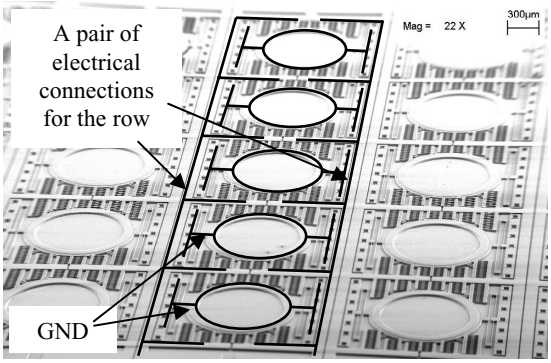

Figure 6. *SEM picture of the fabricated addressable microlens array before microlens fabrication*

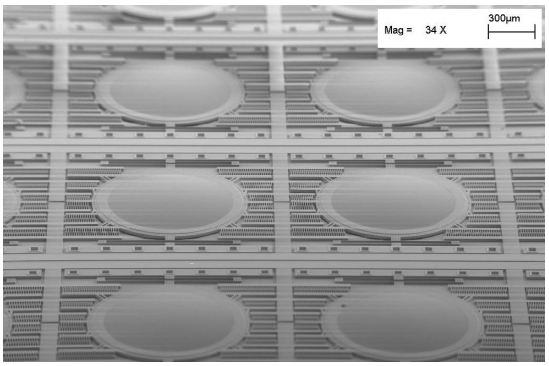

Figure 7. *SEM picture of the fabricated addressable microlens array before microlens fabrication*

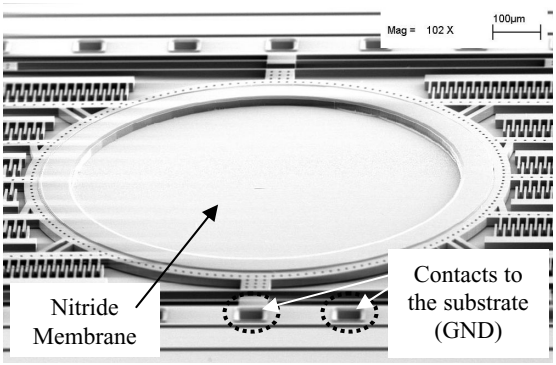

Figure 8. *SEM picture of the fabricated addressable microlens unit before microlens fabrication*

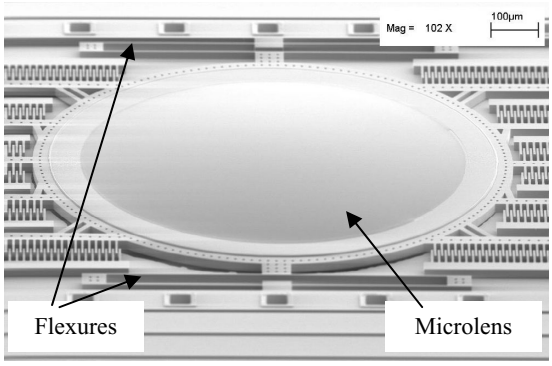

Figure 9. *SEM picture of the fabricated addressable microlens unit after microlens fabrication*

EXPERIMENTAL RESULTS

Polymer-jet printing technique in circular wells has produced microlenses with effective focal lengths (EFL) ranging from 1.94 to 7.48mm as adjusted by controlling the volume of the microlenses. Twenty-five microlenses (average EFL=2.09mm), fabricated using this method, showed ≤5% variation (peak-to-peak) in EFL. Using WYKO-NT3300, we measured the surface profiles of the low-stress (~250MPa) tensile-nitride-membranes and microlenses (EFL=5.5mm) (Figure 10). Within a 200μm-radius, the membranes are virtually flat (radius-of-curvature≥3m) and the microlenses closely follow an ideal circle (radius=2.2mm).

The measured mechanical resonant frequencies of the MEMS-microlens units 1 through 5 with {without} microlenses (EFL=2.09mm) are 0.654{2.03}, 0.789{2.46}, 0.989{3.06}, 1.241{4.08}, and 1.744{5.43} kHz (Figure11). The corresponding Q-factors with {without} microlenses (EFL=2.09mm) are 65.4{18.5}, 105.1{24.6}, 142.1{30.6}, 174.8{58.3}, and 205.2{90.5} (Figure12). The maximum variation of resonant frequencies between rows is approximately 5 % {2 %}. All units achieve 40μm resonant excursions (±20μm) when applying actuation voltages (|VAC+VDC|) lower than 50V (Figure13). Figure14 shows an optical demonstration of microlens identification and its associated focal point using our scheme. We have only observed mechanical crosstalk between units 1 and 4. When unit 4 is resonating with amplitude of 40μm, the unit-1 lens shows an approximately 3μm-oscillation, which is too small to cause identification error.

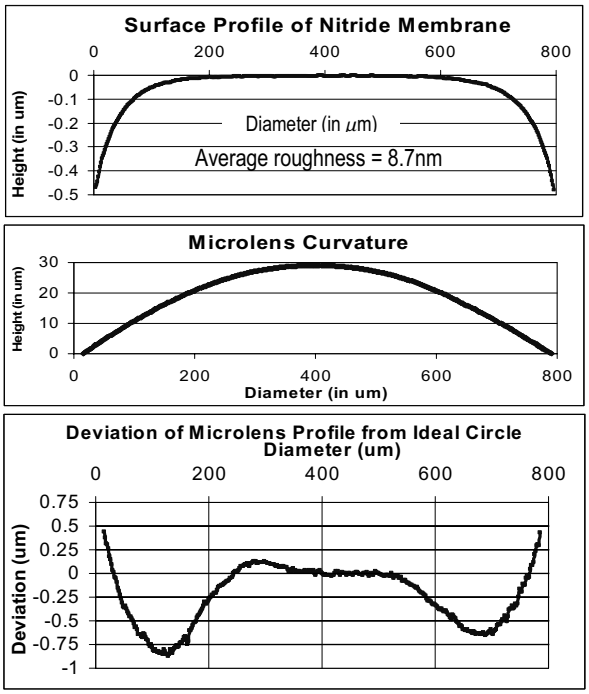

Figure 10. *Low tensile-stress (250MPa) nitride membrane is very flat (radius of curvature≥3m) within 200μm radius. Its profile deviates from an ideal flat surface near the edge. The microlens (f=5.5mm) profile follows closely with an ideal circle (radius=2.2mm) within 200μm radius. Its deviation near the edge may be influenced by the profile of the nitride membrane underneath it.*

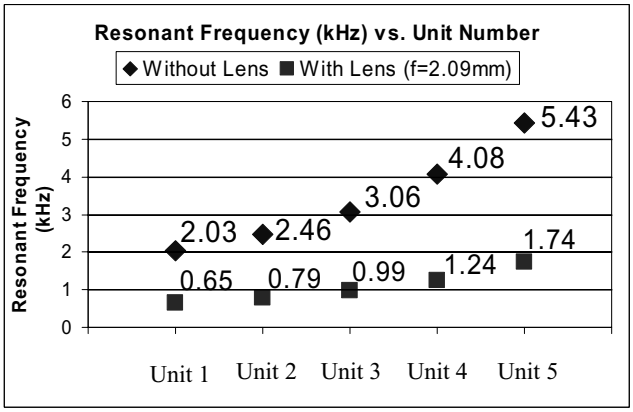

Figure 11. *Resonant frequencies of the fabricated addressable microlens array before and after microlens fabrication*

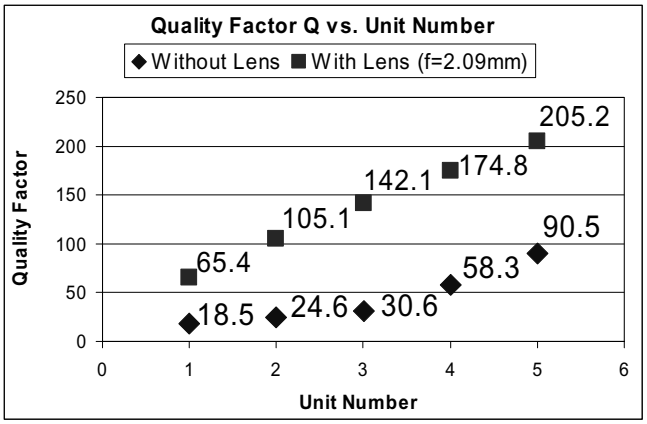

Figure 12. *Q-factors of the fabricated addressable microlens array after microlens fabrication*

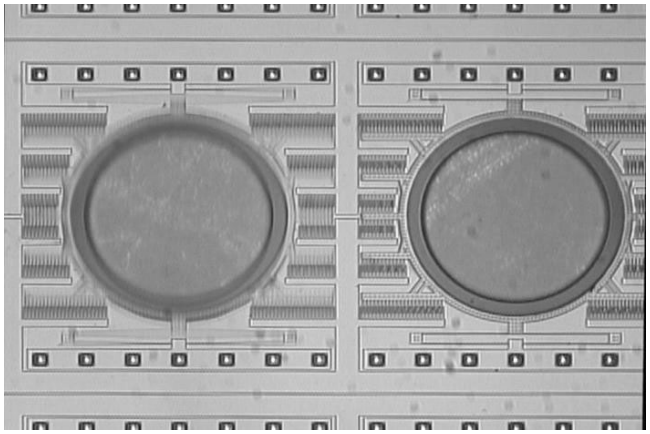

Figure 13. *Unit1 (left) is at resonance. All other units in the row show no movement. Non-uniform metallic texture seen on the nitride membrane is a reflection of the surface of the copper wafer-chuck of the optical microscope.*

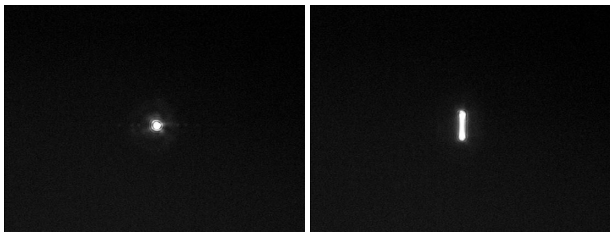

Figure 14. *Demonstration of focal point identification: As the microlens resonates, its focal point turns into a scanning line, and the focal point and its associated microlens can be identified. The focal length f of the microlens is 2.09mm, and the CCD imager is placed at 9.84f from the lens. The focal point travels 40μm×9.84f or 0.3936mm on the CCD imager.*

CONCLUSIONS

We have demonstrated an addressable array (5-by-5) of high-quality microlenses which can be applied to a Shack-Hartmann (SH) sensor in a micro-optical system to improve its dynamic range. Specific lenses in the array can be addressed using our new design in which the mechanical resonant frequencies of individual lens-support carriages are varied. The measured mechanical resonant frequencies of the MEMS-microlens units 1 through 5 with {without} microlenses (EFL=2.09mm) range from 0.654{2.03}, up to 1.744{5.43} kHz. The corresponding Q-factors with {without} microlenses (EFL=2.09mm) were between 65.4{18.5} and 205.2{90.5}. All units achieve 40μm resonant excursions (±20μm) when applying actuation voltages ($|V_{AC}+V_{DC}|$) lower than 50V. Optically observed mechanical cross-talk between different units was negligible. The frequency selection of MEMS structures that is demonstrated in this project has clear advantages for other applications.

ACKNOWLEGEMENT

The authors would like to thank Joseph Seeger for technical discussions on actuator design, Hanjun Kim of Hewlett Packard Lab (Palo Alto, CA) for helpful discussion on nitride-membrane fabrication, and Justin Black for wire-bonding. This project has been funded by the Berkeley Sensor & Actuator Center. Travel support has been generously provided by the Transducers Research Foundation and by the DARPA MEMS and DARPA BioFlips programs.

REFERENCES

1. D. R. Neal, E. Hedlund, M. Lederer, A. Collier, C. Spring, and W. Yanta, "Shack-Hartmann wavefront sensor testing of aero-optic phenomena," *20th AIAA Advanced Measurement and Ground Testing Technology Conference*, June 15-18, 1998, pp.2-13

2. J. Pfund, N. Lindlein, J. Schwider, "Dynamic range expansion of a Shack-Hartmann sensor by use of a modified unwrapping algorithm," *Optics Letters, vol.23, no.13,* July 1998, pp.995-7. Opt. Soc. America, USA.

3. N. Lindlein, J. Pfund, J. Schwider, "Expansion of the dynamic range of a Shack-Hartmann sensor by using astigmatic microlenses," *Optical Engineering, vol.39, no.8,* Aug. 2000, pp.2220-5. SPIE, USA.

4. N. Lindlein, J. Pfund, J. Schwider, "Algorithm for expanding the dynamic range of a Shack-Hartmann sensor by using a spatial light modulator array," *Optical Engineering, vol.40, no.5,* May 2001, pp.837-40. SPIE, USA

5. H. Choo and R. S. Muller, "Optical properties of microlenses fabricated using hydrophobic effects and polymer-jet-printing technology," *2003 IEEE/LEOS International Conference on Optical MEMS and Their Applications,* August 18-21, 2003, pp.169-170. Waikoloa Beach Marriot, Waikoloa, Hawaii

HIGH-RESOLUTION WAVEFRONT CONTROL USING MICROMIRROR ARRAYS

Julie A. Perreault and Thomas G. Bifano
Boston University, College of Engineering, Boston MA, 02215

ABSTRACT

Silicon deformable mirrors have the potential to modulate spatial and temporal features of an optical wavefront. This capability is critical for systems in which aberrations affect optical beam quality, including many applications in laser communication, medical imaging, astronomy, and target tracking. The main goal of the work presented here was to design, build, and test a 1024 actuator wavefront controller for real-time modulation of an optical wavefront.

INTRODUCTION

This work builds on the heritage of several generations of silicon micro-machined deformable mirrors and spatial light modulators that were fabricated over the past several years. Previous work focused on smaller SLM arrays. Results from these devices laid the foundation for a 32x32 array device with regard to design[1] manufacturing[2,3] and characterization[4]. New work includes layout, fabrication, and packaging of this kilo-pixel device, characterization of high-speed mirror dynamics in air and in vacuum, and integration of the device in an optical test bed for high-speed holographic compensation of aberrations.

DEFORMABLE MIRROR

The kilo-pixel SLM is made up of 1024 individually addressable surface-normal electrostatic actuators with center posts that support individual optical mirror segments. Each electrostatic actuator consists of a silicon membrane anchored to the substrate on two sides above a silicon electrode (Figure 1).

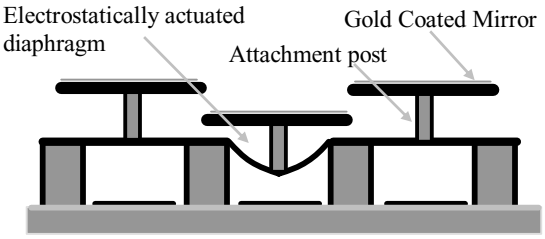

***Figure 1**. Schematic cross section of a gold coated spatial light modulator with a central deflected actuator.*

A post centered on each actuator supports a 338µm x 338µm x 3µm optically coated mirror segment. The SLM has an aperture of 10mm, actuator stroke of 2µm, and a position repeatability of 3nm. Devices were fabricated with a combination of silicon surface micromachining and several custom fabrication processes to ensure optical quality. Chemo-mechanical polishing was used to remove surface roughness and ion machining was used to remove curvature. A stress-free gold coating process was also developed to increase reflectivity. The devices were packaged by wire-bonding 1024 bond pads around the periphery of the device to a custom-made ceramic package (Figure 2).

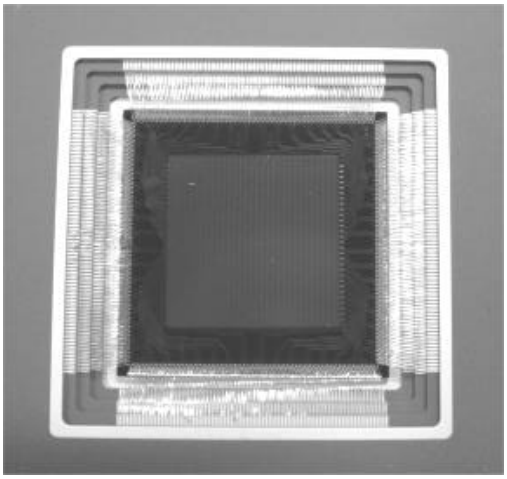

***Figure 2.** Photograph of kilo-pixel SLM*

BACKGROUND

There are currently a number of research groups working on the development of MEMS-based deformable mirrors for adaptive optic correction. Early work in this field included aluminum spatial light modulators demonstrated by Texas Instruments more than twenty years ago[5]. These one-bit, segmented, phase-adjusting devices predated the more well-known amplitude modulating micromirror arrays that were developed by Texas Instruments for projection display applications. More recently, segmented micromirror devices based on silicon micromachining were pioneered by the Air Force Research Laboratory, using the SUMMiT IV process. This group was among the first to report the use of micromirrors for adaptive optics compensation[6].

Only a few efforts to produce MEMS deformable mirrors have resulted in devices with sufficient stroke, resolution, and optical quality (smoothness, flatness, and reflectivity) for use in optical imaging applications. One of these, the first commercially available MEMS-based deformable mirror was developed at Delft University and later commercialized[7]. This device was comprised of a silicon nitride membrane suspended over an array of addressable electrodes[8]. Subsequently, similar MEMS-based deformable mirrors were designed and manufactured at Stanford University[9], and later commercialized[10]. A two-level silicon surface micromachining approach was employed by researchers at Boston University to produce MEMS deformable mirrors using an original architecture described in Figure 1[11]. These devices were manufactured at a commercial MEMS foundry[12] and were later commercialized[13].

Recently, many researchers have reported on the use of these and other MEMS-based deformable mirrors in adaptive optics applications. Mirrors of different architectures and designs have been compared in recent reviews to delineate their optical and electromechanical performance[14,15].

0-9640024-5-0/hh2004/$20©2004TRF
DOI 10.31438/trf.hh2004.21

DEVICE CHARACTERIZATION

Mirror characterization included measurements of electromechanical actuator performance and optical surface contour. Dynamic measurements included *frequency response* in air and vacuum, *motion repeatability*, and *strobed surface mapping* of a single spatial light modulator segment.

For closed loop operation, it is important to know the temporal response of the micro mirror system. The bandwidth of a spatial light modulator (SLM) was measured in air using a laser Doppler vibrometer (LDV). An individual mirror segment was driven with a sinusoidal 1Vpp signal offset by 100V while monitoring velocity with the LDV. Velocity measurements were made over a discrete range of input frequencies and integrated to yield displacement data.

Frequency response measurements made with a high speed Doppler laser vibrometer indicate an actuator bandwidth of approximately 60kHz at low pressure. There was considerable air damping when operated at atmospheric pressure (Figure 3).

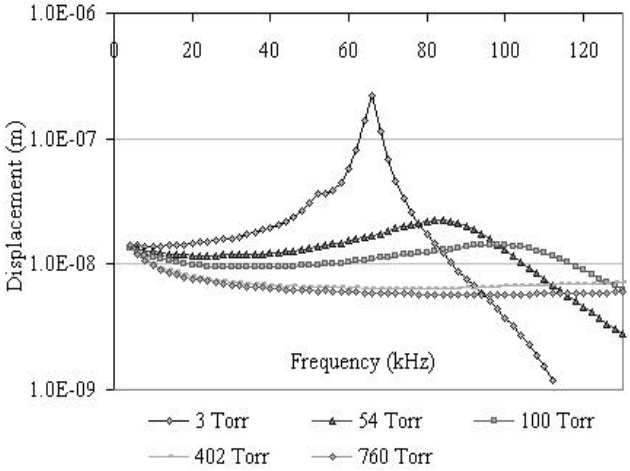

Figure 3. *Mirror response characterization in air and in partial vacuum, illustrating the 60kHz natural frequency and the effects of air damping.*

An important measure of device performance is position repeatability, defined as the standard deviation of a set of measurements of deflection made on a single actuator subjected to repeated, identical voltage excursions. Position repeatability was measured for a single actuator on a continuous membrane mirror through ensemble averaging of the data from a series of tests.

Position repeatability measurements were made with a dynamic single point interferometer that uses a focused laser beam to measure normal displacement with a position resolution of 2.5nm, a range of ±250µm, a frequency bandwidth of 0-133kHz, and a lateral averaging area of ~30µm. Measurements were made over several hours while the mirror was enclosed in a chamber at a partial pressure of 200Torr. Repeatability was demonstrated to be within 4nm. (Figure 4), roughly corresponding to the noise floor of the measurement system.

A similar repeatability measurement was made at the Jet Propulsion Laboratory (JPL) using an instrument with higher measurement resolution. The JPL laser metrology measurement system was used to measure the small signal actuator response with an offset of 10V. Response data was recorded for sinusoidal input excitation frequency of 35Hz and amplitudes ranging from 1Vpp to 2Vpp in 0.1Vpp steps. It was found that the actuator position repeatability was approximately 13pm (one standard deviation), over that measurement range (corresponding to excursions ranging from ~2.5nm at 1Vpp to ~5.0nm at 2Vpp). This repeatability measurement corresponded to the approximate noise floor of the instrument at this frequency.

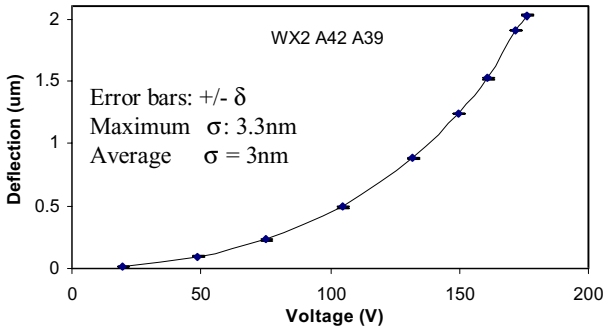

Figure 4. *Voltage versus deflection measurements of a single actuator on a spatial light modulator with a repeatability of ~4nm.*

To study high-speed system response, a strobed interferometric surface mapping instrument was used to characterize the complex motion of a mirror segment in real time (Umech Technologies MMA-G2). A custom vacuum chamber was designed and built to fit in the measurement system. A 100V square wave input was applied to a single pixel on the SLM and the response was measured while the mirror was maintained at 38Torr or 349Torr. Strobed interferometric contour mapping measurements showed considerable flexure of the mirror segment in response to step changes in actuator position at lower pressures (Figure 5).

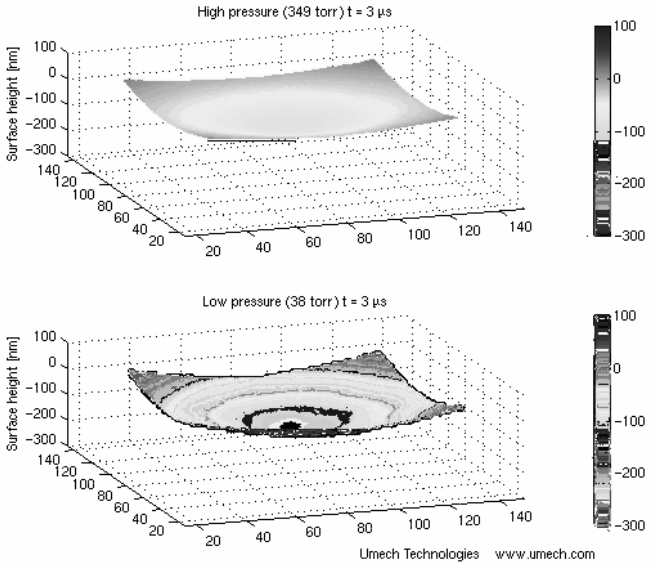

Figure 5. *Still frame capture from a dynamic measurement of mirror pixel step response at 349Torr (top) and at 38Torr (bottom) recorded 3?s after a step change on the actuator input.*

WAVEFRONT CONTROL

After characterization was completed, the SLM was integrated into a laboratory test bed and a field test bed for laser communication at Lawrence Livermore National Laboratories (LLNL).

The testbed was developed for use with this kilo-pixel MEMS SLM[16]. A holographic phase conjugation engine made use of the SLM to dramatically reduce the effects of horizontal path aberrations at a frame rate of ~890Hz. A diagram of the optical test bed is shown in (Figure 6). The system is comprised of a SLM, CCD, Laser, specialty phase-plates, quarter and half wave plates (QWP, HWP), hologram splitter, and bench top optics.

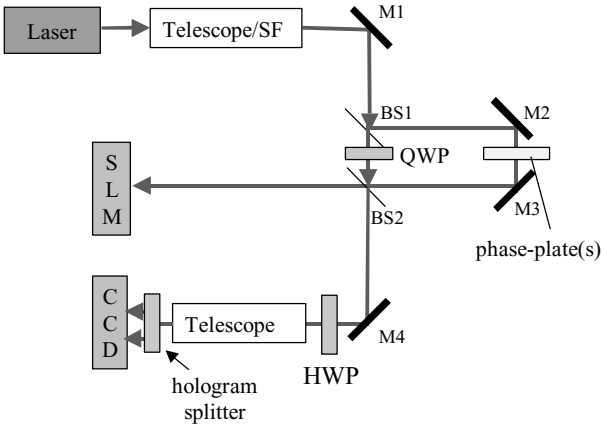

Figure 6. *Optical Test bed for open and closed loop aberration correction for laser communication.*

A 50/50 beam splitter (BS) is used to create a reference beam and probe beam from a vertically polarized laser. Specialty phase plates, designed to simulate atmospheric turbulence with a Kolmogorov phase structure function, were used to introduce aberration into the probe beam path. The reference beam is passed through a QWP to change it's vertical polarization to circular, which is used to form to interferograms with a $\pi/2$ phase shift. The aberrated probe beam is reflected from the SLM and recombined with the circularly polarized reference beam.

The recombined beams are then passed through a half wave plate to rotate the polarization by $\pi/4$. This rotation does not affect the phase shift between the horizontal and vertical components of the reference beam. It does produce equal amplitude horizontal and vertical components in the reference beam. A holographic splitter is used to spatially separate the pair of interferograms, which are then imaged onto the CCD camera with a telescope. This type of design was implemented to perform adaptive correction that exploits parallel control of all SLM pixels using direct optical feedback.

Strehl ratio, the peak intensity of an aberrated point image normalized by the peak intensity of an unaberrated point image, was measured in both the lab test bed and in the field, in work that is not yet published. The Strehl improvement in the lab was approximately a factor 25 which is an absolute Strehl of approximately 60%. Improvements in the field had an improvement by roughly a factor of 8, or an absolute Strehl of approximately 46%, which is still considered very good. The artificial distortions created on the lab bench setup by (rotating) phase screens were significantly more severe than the real atmospheric distortions in the field. This accounts for the higher improvement factor in the laboratory.

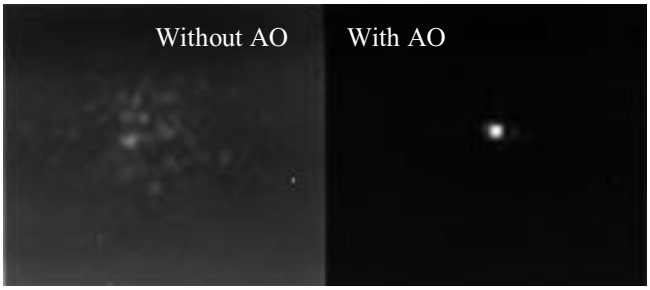

Figure 7. *Far-field image formed using a laser communication system with the kilo-pixel SLM, running open loop at a frame rate of 890Hz. Field tests were conducted at LLNL with support from DARPA via the Coherent Communication, Imaging, and Targeting Program (CCIT). Figures provided courtesy of Lawrence Livermore National Laboratories (LLNL).*

CONCLUSIONS

Static and dynamic behavior of individual actuators in the device have been measured, and their characteristic stroke of 2?m, repeatability of ~13pm, and frequency response >>1kHz have proven suitable for wavefront correction in an aberrated optical system. These high-resolution wavefront correctors may become an important element in future adaptive optical compensation systems.

ACKNOWLEDGMENTS

Travel support has been generously provided by the Transducers Research Foundation and by the DARPA MEMS and DARPA BioFlips programs. Support for the development and testing of SLMS was provided by a research contract from DARPA's Coherent Communications, Imaging and Targeting Program, and that work was conducted in collaboration with Boston Micromachines Corporation. Repeatability testing at JPL was supported by a grant from NASA through the Terrestrial Planet Finder Program. Control experiments were supported by an Army Research Office contract for Communicating Networked Control Systems, through a Multi-University Research Initiative. Graduate fellowship support was provided in part by the Army Research Laboratory, through the Boston University Photonics Center Co-op Program.

[1] Mali, R. K., Bifano, T. and Koester, D. A., "Design-based approach to planarization in multilayer surface micromachining," **J. Micromech. Microeng. [9],** pp. 294-299, 1999

[2] Horenstein, M.N., Bifano, T.G., Mali, R. K., Vandelli, N., "Electrostatic Effects in Micromachined Actuators for Adaptive Optics," **Journal of Electrostatics [42],** pp. 69-82, 1997

[3] Bifano, T. G., Johnson,, H. T, Bierden, P. and Mali, R. K., "Elimination of Stress-Induced Curvature in Thin-Film Structures" **J. Microelectromechanical Systems, [11],** pp 592-597, 2002

[4] Bifano, T. G., Perreault, J., Mali, R. K., and Horenstein, M. N., "Microelectromechanical Deformable Mirrors," **Journal of Selected Topics in Quantum Electronics, [5],** pp. 83-90, 1999

[5] Hornbeck, L. J., "128 x 128 deformable mirror device," **IEEE ED [30],** pp. 539-545, 1983

[6] Roggemann, M. C., Bright, V. M., Welsh, B. M., Hick, S. R., Roberts, P. C., Cowan, W. D., and Comtois, J. H., "Use of micro-electro-mechanical mirrors to control aberrations in optical systems: theoretical and experimental results", **Optical Engineering, [36]**, pp.1326-1338, 1997

[7] Flexible Optical B V, Delft, Netherlands Technologies

[8] Vdovin, G and Sarro P. M., "Flexible mirror micromachined in silicon," **Applied Optics [34],** pp. 2968-2972, 1995

[9] Mansell, J. D., and Byer, R. L., "Micromachined silicon deformable mirror," *Proc. SPIE Vol. 3353, Adaptive Optical System Technologies;* Domenico Bonaccini, Robert K. Tyson; Eds. pp. 896-901, 1998

[10] Intellite Corporation, Albuquerque, NM

[11] Krishnamoorthy, R., Bifano, T. G., Vandelli, N., and Horenstein, M., "Development of MEMS deformable mirrors for phase modulation of light," **Optical Engineering [36]**, pp. 542-548, 1997

[12] Currently MEMSCAP, Inc. Durham, NC

[13] Boston Micromachines Corporation, Watertown, MA

[14] Krulevitch. P., Bierden, P. A., Bifano, T., Carr, E., Dimas, C., Dyson, H., Helmbrecht, M., Kurczynski, P., Muller, R., Olivier, S., Peter, Y., Sadoulet, B., Solgaard, O., and Yang, E. H., "MOEMS spatial light modulator development at the Center for Adaptive Optics," *Proc. SPIE Vol. 4983, MOEMS and Miniaturized Systems III*, James H. Smith, Peter A. Krulevitch, Hubert K. Lakner, Eds., pp. 227-234, 2003.

[15] Weyrauch T., Vorontsov M. A., Bifano T. G., Hammer J. A., Cohen M., and Cauwenberghs G., "Microscale adaptive optics: wavefront control with a μ-mirror array and a VLSI stochastic gradient descent controller," **Applied Optics, [40]** 24 pp. 4243-4253, 2001

[16] Baker, K. L., Stappaerts, E. A., Wilks, S. C., Young, P. E., Gavel, D. T., Tucker, J. W., Silva, D. A. and Olivier, S. S., "Open- and closed-loop aberration correction by use of a quadrature interferometric wavefront sensor", **Optics Letters, [29],** pp. 47-49, 2004

SINGLE-CRYSTAL SILICON CONTINUOUS MEMBRANE DEFORMABLE MIRROR WITH PZT UNIMORPH MICROACTUATOR ARRAYS

Yoshikazu Hishinuma[†] , and Eui-Hyeok(EH) Yang
Jet Propulsion Laboratory, California Institute of Technology
4800 Oak Grove Dr., Pasadena, California 91109
[†] yoshikazu.hishinuma@jpl.nasa.gov

ABSTRACT

For the first time, this paper reports on fabrication, assembly and testing of piezoelectric unimorph-based deformable mirrors (DMs) with continuous single-crystal silicon deformable membranes. A PZT unimorph actuator of 2.5mm in diameter with optimized PZT/Si thickness and design showed a deflection of 5μm at 50V. DMs consisting of 10μm thick single-crystal silicon membranes supported by 4×4 actuator arrays were fabricated and optically characterized. An assembled DM showed a stroke of 2.5μm at 50V with a resonant frequency of 42 kHz and influence function of approximately 25%.

INTRODUCTION

The future deployment of ultra-large, light weight space telescopes is being envisioned by NASA. However, deploying conventional, large area, rigid primary mirrors in space is prohibitively expensive. Therefore, it is planned to construct telescopes with either segmented apertures or with relatively flexible monolithic primary mirrors whose large surface errors can be corrected using subsequent active or adaptive wavefront control **[1]**. These concepts could potentially involve wavefront errors greater than several wavelengths. Thus, the key optical component needed for effective wavefront compensation is an optical quality, large-stroke, continuous-membrane DM with high actuator density over large areas (Fig. 1). DMs with mirror surface quality of <10 nm can be fabricated using the membrane transfer technique demonstrated by our group **[2]**. Other desirable characteristics of DMs include mirror actuation of >2μm at <50V (<1μW per pixel), with a bandwidth of > 1kHz, and influence function of <30%. Micromachined DMs have been previously reported (Table 1), however they needed high-voltage operation due to electrostatic operation (100-700V) **[3-7]**, small stroke (<2μm) **[3-5, 7]**, marginal surface quality **[3,5]**, or high influence function (crosstalk) **[4, 5]**. In this paper, we present a single-crystal silicon continuous membrane DM, incorporated for the first time with underlying piezoelectric unimorph actuators.

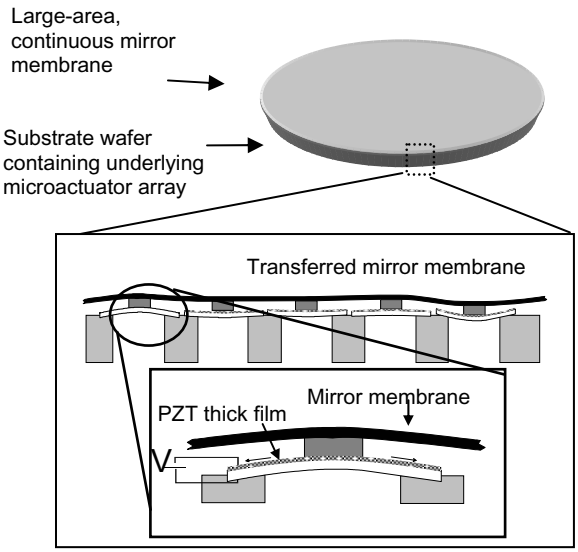

Figure 1. *Large-area continuous membrane deformable mirror (DM) concept. For minimizing the effect of print-through, the silicon mirror membrane is required to be thicker than 10 μm thick. The mirror membrane is backed by an array of piezoelectric unimorph microactuators. The advantage of this approach is that the small strains obtainable from a piezoelectric material at modest voltages are translated into relatively large displacements.*

	Requirements	Boston University[3]	Stanford University[4]	Grenoble, France[6]	Bell Lab[7]	JPL
Stroke (1 actuator)	> 2 μm	2 μm	1 μm	2 μm	2 μm	2.5μm
Bandwidth	> 1 kHz	7 kHz	2 kHz	1 kHz	4 kHz	40 kHz
Actuation voltage	Low	240 V	200 V	150 V	100 V	50 V
Actuation mechanism	--	Electrostatic	Electrostatic	Electrostatic	Electrostatic	Piezo-unimorph
Surface quality	< 25 nm	30 nm RMS	-	180 nm	-	30 nm RMS
Mirror membrane	--	2μm poly-Si	10 μm Si	1~5μm SC Si	1~3μm SC Si	10 μm SC Si

Table 1. *Comparison table of existing MEMS DM specifications*

0-9640024-5-0/hh2004/$20©2004TRF
DOI 10.31438/trf.hh2004.22

PZT UNIMORPH ACTUATOR

We have modeled, fabricated and characterized a series of PZT unimorph membrane actuators with various membrane designs in order to optimize the DM actuator geometry. Fig. 2 contains (a) a photograph of fabricated actuators of various types and (b) a schematic illustration of the actuator structure. Electrode designs which have been tested include: plain circles, concentric rings, spirals, and segmented electrodes.

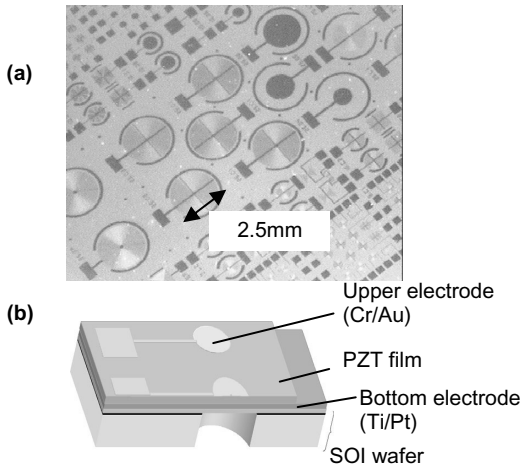

Figure 2. *(a)A photograph of PZT actuator array (b)Schematic diagram showing the structure of a PZT unimorph actuator*

The actuation principle is as follows: An electric field applied perpendicular to the piezoelectric layer plane induces contraction in the lateral direction, producing a large out-of-plane deflection because of its unimorph geometry. Compared to piezoelectric stacks that are widely used in commercial DMs, this actuation mechanism requires far less voltage and power to produce same amount of deflection. We have discovered that there are two regimes of unimorph membrane actuators depending on the PZT film / silicon membrane thickness ratio. For thin silicon membranes (less than or equal to the PZT layer thickness), concentric rings and spiral electrode designs produced more deflection than full circle electrodes, implying that the stress in the electrode film reduces the amount of deflection significantly. For actuators with thick silicon membranes (greater than twice the PZT thickness), full circle electrodes produced more deflection than the other electrode designs. Since actuators with thick Si membranes showed more promise for DM applications because of the higher deflection and ease of handling during fabrication, we focused our efforts in optimizing the full circle actuator design for thick Si membranes.

In order to optimize the geometry of the unimorph actuator structure, a mathematical model was developed using an energy minimization method **[8]**. In this model, the total energy of the unimorph membrane under deflection is calculated using a deflection profile predicted using thin plate deflection theory. Then the total energy, which is the sum of the elastic energy due to the bending of the membrane, the potential energy stored by the film stresses, and the work done by the piezoelectric moment, is minimized with respect to the deflection profile using a Lagrange multiplier method. Fig.3 shows a WYKO interferometer image of the deflection of the unimorph actuator. The measured thickness dependence of membrane deflection shows excellent agreement with our model (Fig. 4). Fig. 5 shows the deflection dependence versus the size of the electrodes relative to the membranes. The measured deflection for an optimized actuator is 5.4μm at 50V (for an actuator with 2.5mm diameter, PZT/Si = 2μm/15μm thick, 60% electrode diameter).

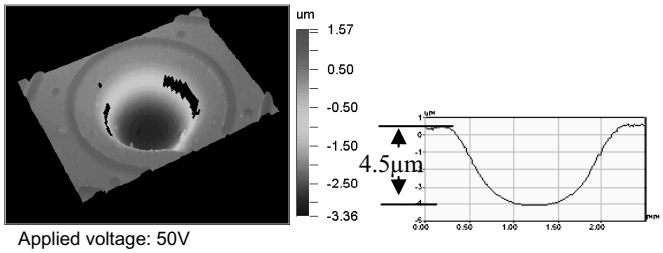

Figure 3*. WYKO interferometer image of a PZT unimorph actuator under deflection. The thicknesses of PZT/Si layers are 2μm/15μm.*

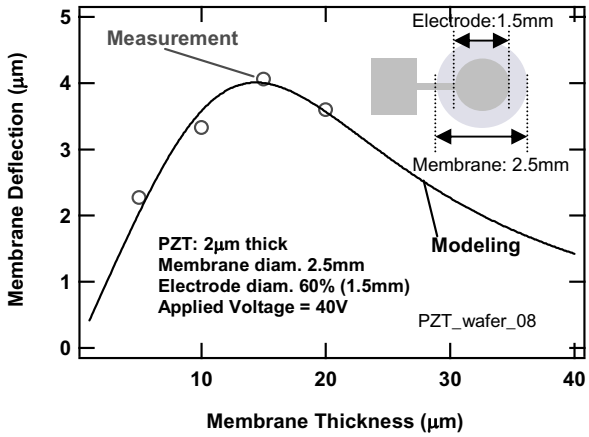

Figure 4*. Dependence of deflection on silicon membrane thickness. For membranes 2.5mm in diameter, the optimized Si/PZT thickness ratio is approximately 6. The data points represent an average of 10 separate measurements on 2 different pixels within a typical array.*

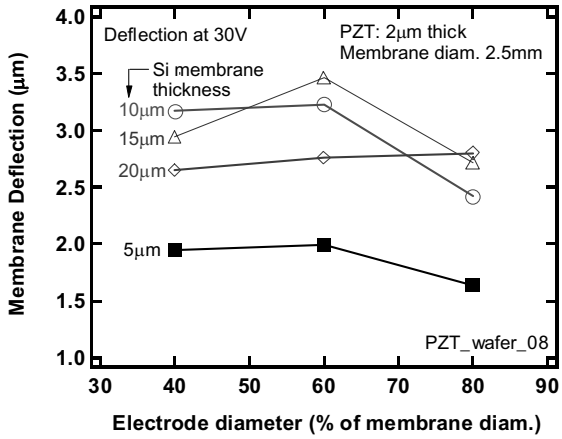

Figure 5*. Dependence of membrane deflection on electrode diameter. Optimum electrode diameter is approximately 60% of the membrane diameter.*

DEFORMABLE MIRROR

DMs consisting of 10μm thick single-crystal silicon membranes supported by 4×4 actuator arrays were fabricated and optically characterized. Fig. 6 contains (a) a schematic diagram of the DM structure and (b) a photograph of DMs and the microfabricated arrays of actuators (the upper mirror membrane is intentionally removed). The Si mirror membrane made from another SOI wafer was bonded onto the actuator wafer via indium posts at the centers of each actuator (Fig. 7).

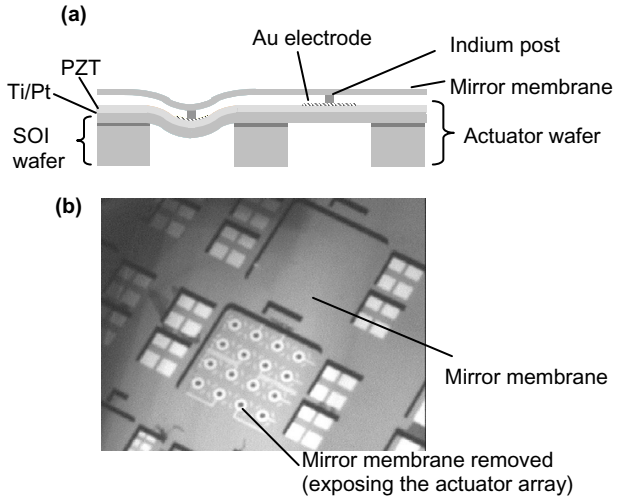

***Figure 6**. (a) Cross-sectional schematic of the deformable mirror (b) Photograph of microfabricated deformable mirrors with 4×4 actuator arrays*

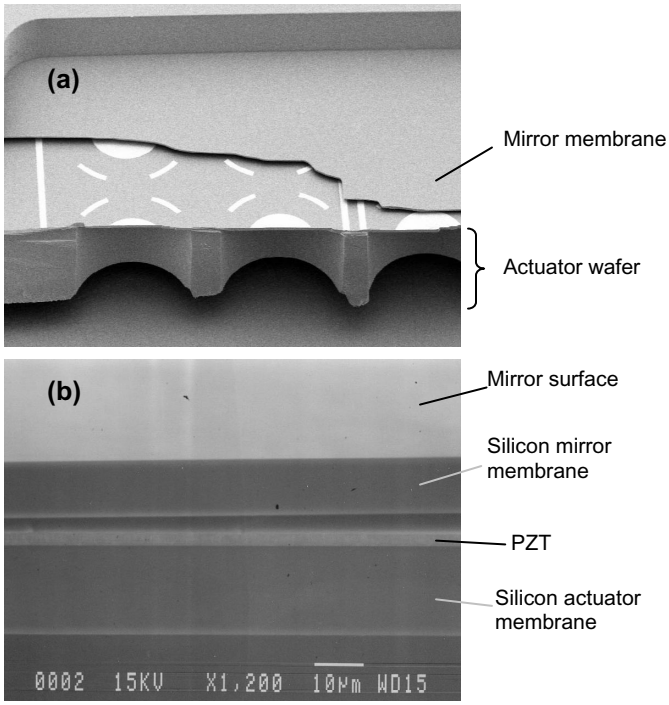

***Figure 7**. SEM micrographs of the assembled deformable mirror. (a) DM with mirror membrane partially removed. (b) Cross section of the DM: the mirror membrane is 10 μm thick to provide the necessary optical quality for the DM.*

The surface profile of an *actuated* deformable mirror using one underlying actuator is shown in Fig. 8. The measured influence function is 25%. Fig. 9 presents the measured deflection *vs.* the applied voltage for an actuator and a DM actuated using a single actuator. The DM shows stroke of 2.5 μm at 50 V. The stroke of the mirror membrane is approximately 40% less than that of the actuator alone. This stroke reduction can be adjusted by changing the mechanical compliance (e. g. optimizing the PZT/ actuator membrane/ mirror membrane thickness ratio). Frequency responses of the unimorph actuator and with the mounted mirror membrane were obtained using a laser-doppler vibrometer (Fig. 10). The measured resonance frequency of 42 kHz far exceeds the bandwidth requirement for most DMs.

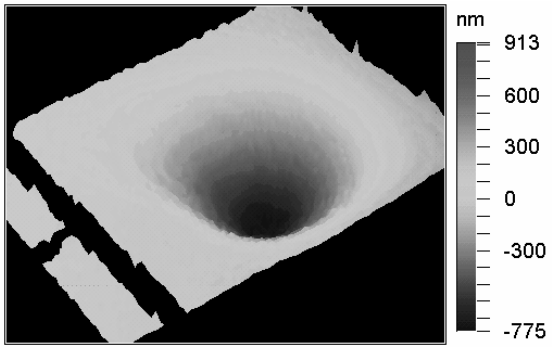

***Figure 8**. Deflection of a deformable mirror with one actuator activated. From this profile, the influence function (crosstalk between pixels) is approximately 25%.*

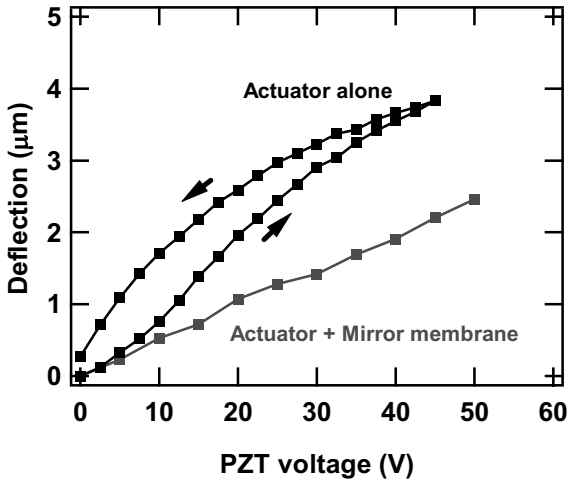

***Figure 9**. Relative deflection vs. applied voltage for a 2.5mm diameter actuator alone and with a mounted mirror membrane.*

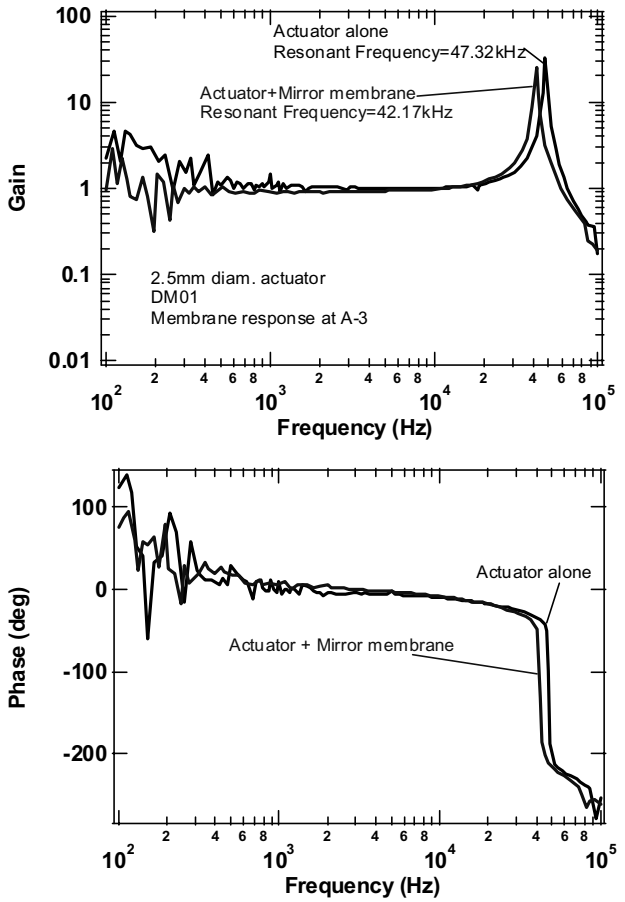

***Figure 10**. Measured frequency response of the piezoelectric unimorph actuator alone and with a mounted mirror membrane. These plots demonstrate that the DM is capable of high bandwidth operation. They also indicate the high-stiffness of the actuator membrane, which is important for high optical quality mirrors.*

CONCLUSIONS

In summary we have successfully demonstrated the proof-of-concept for a DM composed of a continuous single-crystal silicon membrane supported by piezoelectric unimorph actuator arrays. Piezoelectric unimorph actuators designed with optimized PZT/Si thicknesses can produce large strokes (as high as 5μm) at low voltage (50V). DMs consisting of 10μm thick single-crystal silicon membranes supported by 4×4 actuator arrays were fabricated and characterized optically. Improvements in the fabrication process for better optical quality mirror membranes and optimization of the DMs for larger strokes are underway. Additional optical characterization of fabricated DMs will also be performed.

ACKNOWLEDGEMENTS

The authors would like to thank Dr. Jian-Gong Cheng and Prof. Susan Trolier-McKinstry of Pennsylvania State University for providing PZT depositions on wafers. We would like to acknowledge Dr. Thomas George for his valuable comments throughout this research project. The research described in this paper was carried out at the Jet Propulsion Laboratory, California Institute of Technology, under a contract with the National Aeronautics and Space Administration. Travel support has been generously provided by the Transducers Research Foundation and by the DARPA MEMS and DARPA BioFlips programs.

REFERENCES

1. R. Dekany, *et al.*, "Advanced Segmented Silicon Space Telescopes (ASSiST)," *SPIE International Symp. On Astronomical Telescopes and Instrumentation, Adaptive Optical System Technologies II*, 8/22-28/02, Waikoloa, Hawaii (2002).

2. E. H. Yang and D. V. Wiberg "A wafer-scale membrane transfer process for the fabrication of optical quality, large continuous membranes," *IEEE/ASME Journal of Microelectromechanical Systems, 12(6)*, 804 (2003).

3. T. Bifano *et al.*, "Continuous-Membrane Surace-Micromachined Silicon Deformable Mirror", *Optical Engineering, 36(5)*, 1354, (1997); T. Bifano *et al.*, "Micromachined Deformable Mirrors for Adaptive Optics", *SPIE Conf. on High-Resolution Wavefront Control: Methods, Devices, and Applications IV*, Seattle, WA, 7/8-9/2002, SPIE Int. Soc. Opt. Eng.(2002), pp.10-13.

4. J. Mansell *et. al.*, "Silicon Deformable Mirrors and CMOS-based Wavefront Sensors," *SPIE Internatinal Conference, High-Resolution Wavefront Control*, San Diego, CA, 8/1-2/2000, SPIE Int. Soc. Opt. Eng. (2000), pp.15-25.

5. G. Vdovin, "Optimization-based Operation of Micromachined Deformable Mirrors," *SPIE Conf. on Adaptive Optical System Technology*, Kona, Hawaii, SPIE Int. Soc. Opt. Eng. (1998), pp.902-909.

6. C. Divoux, *et al.*, "A Novel Electrostatic Actuator for Micro Deformable Mirrors: Fabrication and Test", *International Conference on Solid State Sensors, Actuators, and Microsystems*, Boston, MA 6/8-12/03, IEEE(2003), pp.488-491.

7. P. Kurczynski, *et al.*, "Electrostatically actuated membrane mirrors for adaptive optics", *SPIE Conf. on MOEMS and Miniaturized Systems III*, San Jose, CA (2003), pp. 305-313.

8. P. Muralt, *et al.*, "Piezoelectric actuation of PZT thin-film diaphragms at static and resonant conditions", *Sensors and Actuators A, 53,* 398 (1996).

FEMTO-PHOTONICS: OPTICAL TRANSDUCERS UTILIZING NOVEL SUB-WAVELENGTH DUAL LAYER GRATING STRUCTURES

Dustin W. Carr, Gregory R. Bogart, Bianca E. N. Keeler
Sandia National Laboratories
Albuquerque, NM 87185

ABSTRACT

We have fabricated and measured a novel grating structure consisting of two levels that can be actuated relative to one another. Near-field optical effects result in strong sensitivity of the zero-order diffraction efficiency, making this useful as a transducer for sensing very small amounts of relative motion. We have observed a noise floor of 100 fm/Hz$^{1/2}$ at 100 mHz.

INTRODUCTION

Deformable diffractive optical structures have been studied for many years, mostly for applications relating to video displays or communications [**1**]. These structures have traditionally relied upon first-order gratings with feature dimensions significantly larger than the wavelength of light with which they are designed to interact. Recent studies have looked at a different type of diffractive structure that utilizes near-field optical effects that are very sensitive to the motion of the grating elements [**2**]. These designs result in optical resonant structures that can modulate the intensity of the reflected or transmitted zero orders, while moving only fractions of a wavelength. Such devices are very sensitive to wavelength, and could thus be used as tunable elements for spectrometry, as well as communications or inertial sensing.

Device designs utilizing multi-layer sub-wavelength gratings that can be translated in-plane have been studied computationally in the past [**3**]. In this work, we study the optical and mechanical properties of fabricated structures, shown schematically in Figure 1. While precise correlation with the optical theory is difficult, we have demonstrated the strong sensitivity to motion that has been predicted in the past. Of particular interest for our applications is the use of this device as a transducer for measuring very small amounts of relative motion between the two grating levels. Such a structure could be used in an inertial sensor system. Previous work has detailed the advantages of using an optical transducer for this application [**4**].

EXPERIMENTAL DETAILS

An SEM micrograph of a released dual grating structure is shown in Figure 2, with the bottom grating hidden beneath the top silicon layer. The grating elements of both layers are grounded to the substrate. Comb-drive fingers enable electrostatic lateral actuation of the top grating, while parallel plate electrodes on the first silicon layer apply forces vertically. Simultaneous actuation of these two sets of electrodes allows us to map out the optical response of the structures across a large operating range.

To experimentally observe the motion in the device, a 636 nm laser is focused on the device, and the reflected signal is detected using a balanced detector. A reference beam is also incident on the surface near the device, enabling the subtraction of noise related to the experimental apparatus. With this setup, we are able to study the static and dynamic properties of the devices. Studying the mechanical resonant response enables us to verify the mechanical and electrical properties, which we can then use to get a precise measure of the amplitude of motion at lower frequencies. The measured resonant frequencies of these devices are typically within 1% of those predicted using finite element analysis, an indication of the excellent control we have in the precision processing of these devices.

Figure 3 contains plots of the reflected intensity as a function of displacement from the rest position for the transverse electric (TE) and transverse magnetic (TM) modes, where the transverse direction is defined as perpendicular to the grating lattice vector. While the range of motion is very slight, we see a substantial change in the intensity of the reflected signal, approaching 15% modulation, normalized to the peak reflectance. This data is obtained by applying voltages to the two electrodes, and then translating these voltages into the known deflections of the device, which are calibrated through the use of computational models, along with dynamic resonant mode data. In this data, The two gratings have a period of 720 nm, with a silicon fill factor of approximately 2/3.

Figure 4 is an amplitude spectral density plot for a device that is being driven at 10 Hz. The total amplitude of motion is approximately 100 fm, while the noise level is 130 fm/Hz$^{1/2}$. This remarkable sensitivity at such low frequencies is largely enabled by the use of reference optical detection, which defeats many potential sources of 1/f noise that becomes dominant at these levels.

Sandia is a multiprogram laboratory operated by Sandia Corporation, a Lockheed Martin Company, for the United States Department of Energy's National Nuclear Security Administration under contract DE-AC04-94AL85000.

1. O. Solgaard, F. S. A. Sandejas, and D. M. Bloom, "Deformable grating optical modulator," *Optics Letters, 17*, 688 (1992).

2. B. E. N. Keeler, D. W. Carr, J. P. Sullivan, T. A. Friedmann, and J. R. Wendt, "Experimental demonstration of a laterally deformable optical NEMS grating transducer," *Optics Letters,* accepted for publication (unpublished).

3. W. Nakagawa and Y. Fainman, "Design of tunable optical cavity based on near-field optical coupling between subwavelength periodic nanostructures," 2003 IEEE/LEOS International Conference on Optical MEMS (2003) pp. 111-112.

4. R. L. Waters and M. E. Aklufi, "Micromachined Fabry-Perot interferometer for motion detection," *Applied Physics Letters, 81*, 3320 (2002).

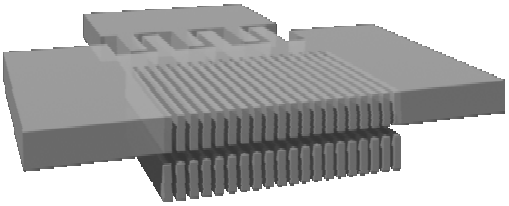

Figure 1. *The device under consideration is a two layer grating in silicon with features much shorter than the wavelength of light. The two gratings are separated by a small air gap, and the upper grating can be moved horizontally. We can observe the motion by detecting reflected light from a normal incident beam.*

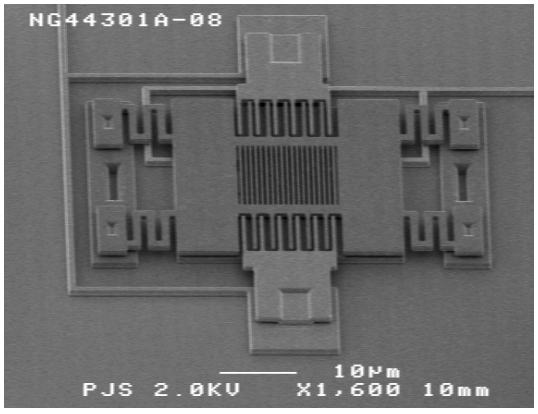

Figure 2. *SEM micrograph showing a test device. The comb-drive fingers enable electrostatic actuation in the plane, and electrodes on the first level enable vertical actuation. The grating shown has a period of 720 nm.*

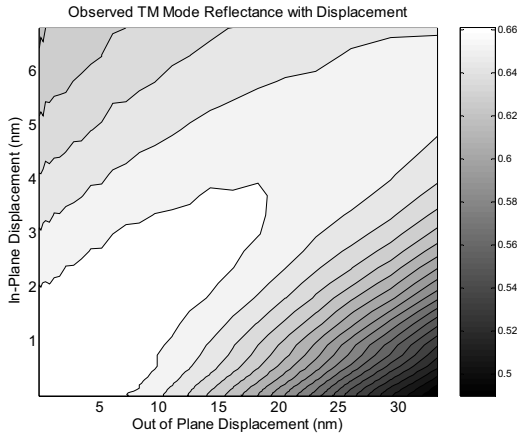

Figure 3. *Measured reflectance from the surface of a device identical to the one shown in Figure 2. This is raw data that is acquired at a rate of 10 Hz while the lateral and vertical actuation voltages are swept, producing the displacements shown.*

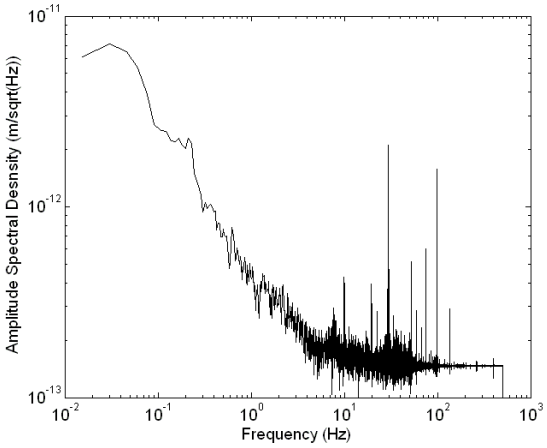

Figure 4. *Spectral density plot showing the signal at 10 Hz, and the noise floor of 140 fm/Hz$^{1/2}$ at 10 Hz.*

RF MEMS SWITCHES USING COPPER-BASED CMOS INTERCONNECT MANUFACTURING TECHNOLOGY

N. Hoivik, C. V. Jahnes, J. Cotte, J. L. Lund[1], D. Seeger and J. H. Magerlein

IBM T. J. Watson Research Center, PO Box 218, Yorktown Heights, NY 10598, USA
[1]Current address: 22822 Howard Chapel Road, Brookeville, MD 20833, USA

ABSTRACT

High-quality RF MEMS switches fabricated using a Cu-based integrated circuit interconnect technology have been demonstrated. The process technology allows the fabrication of switches within the interconnect layers of an RF integrated circuit for low packaged cost and superior performance, The switch design includes a beam fixed at both ends and actuation electrodes separate from the RF conductors. Switch isolation is better than 30 dB from 0-6 GHz, insertion loss is 0.3 dB, and actuation voltage is about 26 V for a switch with a gap of 0.2 μm. Optimizing switch performance requires careful attention to film stress.

INTRODUCTION

In a large number of RF applications, the many discrete, board-level components significantly increase assembly cost and overall size, as well as limiting performance. Thus integrated passive components would be desirable [1]. It is well recognized that RF-MEMS switches have been shown to exhibit superior performance compared to FET and diode switches; however most of these devices have been built using highly special processing techniques incompatible with integrated circuit fabrication. As a result, the implementation of RF MEMS devices into products has remained elusive [2].

This paper describes the first high-quality switches fabricated using a copper-based integrated circuit interconnect technology. The objective is to develop integrated switches for 2 GHz applications using standard "back-end" processing compatible with Bi-CMOS or SiGe technology [3], [4].

Typical RF design specifications for an integrated switch are presented in Table 1. The isolation required in the OFF state is more than 30 dB; while the insertion loss in the ON state should be less than 0.5 dB.

RF Performance @ 2GHz	
Isolation	> 30 dB
Insertion loss	< 0.5 dB
Actuation voltage	< 10-15 V
Switching speed	10 - 100 μsec
Power handling	10 - 100 mW

***Table 1**: Typical specifications for integrated MEMS switch*

SWITCH FABRICATION AND DESIGN

The integrated MEMS switch is fabricated using a conventional back-end copper based CMP (Chemical Mechanical Polishing) process. All of the dielectric and metal films are deposited at temperatures of 400° C or less using tools and processes typically used in CMOS processing. The MEMS structures are released using a dry release process [4].

Using a copper-based process to create free-standing MEMS devices adds to the complexity of the MEMS device. In order to prevent the copper from oxidizing, the metal structure must be encapsulated to prevent corrosion during processing. Therefore, the resulting micromechanical beam tends to have a complicated multilayer cross-section, and film stresses must be considered during fabrication to avoid overall compressive beam stress and severe stress gradients.

Figure 1 depicts a top-view photograph of a fabricated and released, MEMS switch. The two actuation electrodes are kept separate from the RF conductor (in center). The switch measures 24 x 105 μm, with a 2 μm space separating the actuation electrodes from the RF conductor.

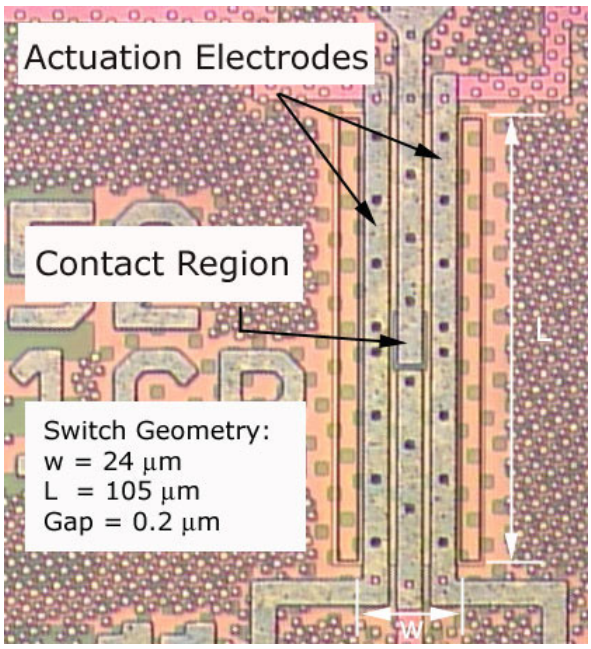

***Figure 1**: Top-view photograph of fabricated RF MEMS switch. The two actuation electrodes are separated from the RF conductor and contact region in the center of the bridge structure.*

0-9640024-5-0/hh2004/$20©2004TRF
DOI 10.31438/trf.hh2004.24

Figure 2 illustrates a side-view of the RF-MEMS switch. The switch is fixed at both ends to ensure an adequate restoring force compared to a cantilever design. However, the RF conductor only covers half of the suspended length to mimic a series cantilever switch. In order to balance stresses due to the mismatch between copper and dielectric materials, the bridge incorporates a "dummy" metal region. Furthermore, the upper contact region consists of several smaller contacts (18 contacts of 1x1 µm in C2), whereas the lower contact (C1) is a uniform contact region. Having the contact material formed in patches on the upper contact facilitates a larger contact force when the switch is actuated. Etch holes along the actuation electrodes and RF conductor both facilitates an improved release process as well as reducing squeeze film damping when operated in a N_2 environment.

The gap between the two actuation electrodes was designed to be 0.2 µm in order to obtain a low actuation voltage, while at the same time allow the switch to demonstrate an adequate isolation at the design frequency of 2 GHz.

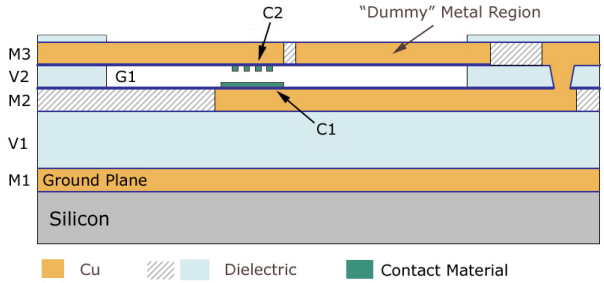

Figure 2: *Side-view schematic of the MEMS switch. The switch is anchored on both ends with a dummy metal region to balance stress. The upper contacts (C2) consist of 18 small (1x1µm) contacts whereas the lower contact (C1) is uniform.*

RESULTS AND DISCUSSION

All RF measurements were performed on wafer level in a controlled nitrogen environment. Microwave probes and an HP8753B network analyzer were used. The measured performance of the RF MEMS switch is presented in Figure 3. The measured isolation in OFF state was measured to be greater than 30 dB from DC to 6 GHz, corresponding to an up state capacitance about 6.5 pF, which also matches simulated values. The actuation voltage required to make initial contact was measured to be around 12-15 V, however 24 V was required to obtain an insertion loss of 0.3 dB. This actuation voltage was measured on repeated devices and no further reduction on insertion loss was observed up to 30 V, which indicates that a proper contact was made.

Further simulation of the MEMS switch indicated a deformation in the actuation electrodes around 0.15 µm (Figure 4). This deformation is not unexpected due to the nature of a multi-layer beam. However, the magnitude of stress was somewhat larger than expected, thus with a deformation on the order of the design gap separating the two electrodes, the actuation voltage would greatly be increased.

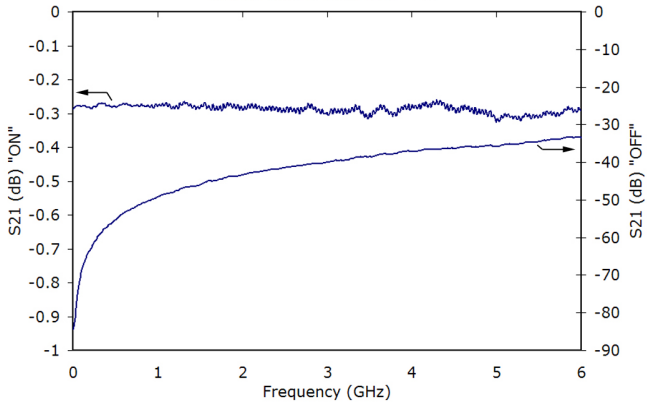

Figure 3: *Measured S21 transmission of MEMS switch with +10dBm power and using response calibration. The actuation voltage is 24V.*

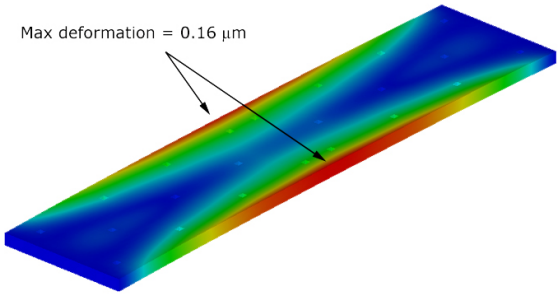

Figure 4: *Simulation of deformation in switch actuation electrodes due to a high stress gradient in the multilayer stack.*

SUMMARY

This paper describes an RF MEMS switch fabricated with a Cu CMP process suitable for direct integration with SiGe or Bi-CMOS IC's. A "direct integration" approach demonstrates the potential for a MEMS device to share existing mask levels, thus diluting the cost of the MEMS device into the base cost.

The measured RF performance is well within the initial specifications. Further reduction in stress is currently under investigation together with measurements of switching speed, reliability and power handling.

REFERENCES

1. D. Seeger et al. "Fabrication Challenges for next-generation devices: Microelectromechanical systems for radio-frequency wireless communications," *J. Microlith., Microfab., Microsyst*., Vol. 2 No. 3, pp 169 – 177 (2003).
2. Arthur S. Morris et al, "High-Performance Integrated RF-MEMS: Part 1- The Process", *11th GAAS Symposium - Munich 2003*, pp 325 – 328.
3. Jennifer L. Lund et al,"A Low Temperature Bi-CMOS Compatible Process for MEMS rf Resonators and Filters". *Solid-State Sensor, Actuator and Microsystems Workshop*, Hilton Head Island, June 2-6, 2002.
4. C. V. Jahnes et al. " Simultaneous Fabrication of RF MEMS Switches and Resonators using Copper-based CMOS Interconnect Manufacturing Methods", *MEMS 2004 Technical Digest, Jan 25-29,* pp 789 – 792.

CARDIAC SIGNAL RECORDING USING ULTRASONIC SILICON MICROPROBES

Xi Chen, Amit Lal
SonicMEMS Lab, Cornell University
Mark L. Riccio, Robert F. Gilmour
Biomedical Sciences, College of Veterinary School at Cornell University

ABSTRACT

For the first time we report on a silicon-based microprobe integrated with ultrasonic horn actuator that successfully penetrated isolated and perfused canine heart at low driving voltage ($6V_{pp}$) and recorded simultaneously the electrical signals on multiple sites within the heart. The penetration into tissues was not possible without ultrasound, and was made predictable and reliable using ultrasonic actuation. These recordings provide information for reconstruction of the physioelectrical wave propagation within heart tissue which is important in the study of the mechanism and development of cardiac arrhythmias.

INRODUCTION

Sudden cardiac death—mainly caused by ventricular fibrillation (VF)—is the leading cause of mortality in the industrialized world. Despite the chaotic nature of the disturbed cardiac rhythm during VF, researchers have hypothesized that just prior to VF, rotating spiral waves with distinct spatial and temporal order are generated and travel around the heart, breaking into multiple wavelets upon collision and eventually lead the heart to the chaotic state incapable of pumping and sustaining life. Such kind of spiral pattern has been observed on surface of isolated canine heart by staining the heart with voltage sensitive dyes [**1**]. However these studies could not provide information of the electrical activities underneath the surface. Since heart is a three dimensional entity with electrical pathways expanding in all three directions, it is important to obtain three dimensional mapping of physioelectrical wave propagation within cardiac tissue.

Silicon based microprobes have been reported for electrical activity recording in neural tissues [**2, 3**]. They provide high spatial resolution, reduced tissue damage, and the ease to integrate with microelectronics. These probes therefore become a good candidate for recoding cardiac signals inside the heart. However, these thin probes do not have enough flexural rigidity to go into the much denser and harder cardiac muscle tissues, when encountered with resistance from the cardiac tissue, they easily buckle and break. This is in contrast to neural tissue with much lower stiffness. Thicker probes provide greater rigidity but the increased probe dimension causes more damage to the tissue being investigated and may affect their physioelectrical activities.

We have reported before on microfabricated silicon ultrasonic surgical tools that reduce cutting force on biological tissues by actuating the surgical tool at its ultrasonic resonance [**4**]. In this paper we integrate ultrasonic horn actuator with microprobes that have multiple electrodes for 2-dimensional recordings on one device. Therefore by inserting a number of probes at different locations on the heart, we will be able to record the 3-dimentional distribution of electrical activities within the heart, and the wave propagation can be reconstructed and studied. Here we demonstrate the feasibility of measuring cardiac potentials, opening the way for the more involved 3D studies.

DESIGN AND FABRICATION

The design and fabrication of the silicon ultrasonic probe is similar to the ultrasonic surgical tools reported before [4], except that two tips (5mm long x 100μm wide x 70μm thick) are defined at the high-velocity section of the silicon ultrasonic horn. The Au/Cr electrodes on the tips are 20μm×20μm, there are 5 electrodes on each tip with 500μm spacing, forming a 2 by 5 electrode array. The catenary silicon horn is 6cm long, with end-to-tip area ration 15:1, and a longitudinal $\lambda/2$ resonance of 75kHz. The tips are of much smaller dimensions, so their longitudinal resonant frequency is much higher and will move in longitudinal direction at the same ultrasonic speed as the small end of the horn. To reduce unwanted bending and flexural motion of the tips, another silicon horn with same shape and dimension but without the two small tips are bonded to the one with tips to achieve symmetry in thickness direction. Figure 1 shows the entire process flow.

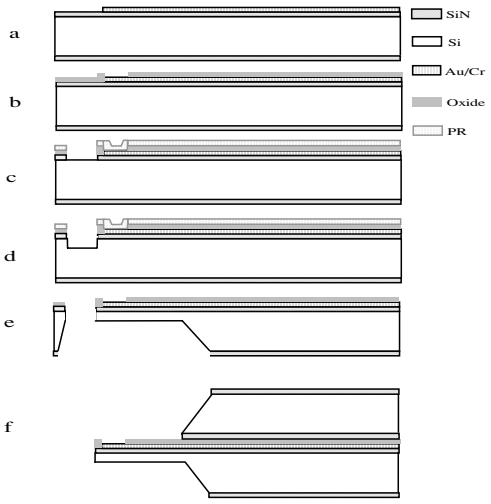

Figure 1. *Process flow for fabricating the silicon ultrasonic microprobe.* ***a****: Evaporate and pattern Au/Cr metallization on 4" wafer with LPCVD nitride layer;* ***b****: Deposit and pattern PECVD oxide passivation layer;* ***c****: Pattern photoresist defining the probe tips;* ***d****: DRIE with the PR mask for desired probe tip thickness;* ***e****: Backside-only KOH etching to release the device;* ***f****: Another silicon horn without tips is bonded to the device for symmetry and reducing bending mode of the tips.*

Next PZT-4 plates (6mm×20mm) are bonded to the probe at the displacement node. The probe is clamped to a customized PC board, also at the location of the displacement node. The Au/Cr pads on the probe are wire-bonded to the PC board and then connected to external circuit through ribbon cable. Figure 2 shows the assembled device.

**Travel support has been generously provided by the Transducers Research Foundation and by the DARPA MEMS and DARPA BioFlips programs*

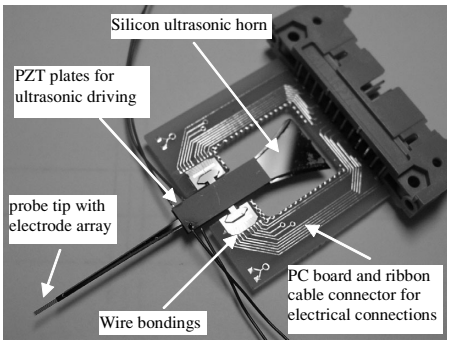

Figure 2. *Silicon ultrasonic microprobe packaged with PZT plates and printed circuit board*

EXPERIMENTAL RESULTS

The silicon ultrasonic microprobe was tested on chicken thigh sample first with ultrasonic driving voltage 0~10V_{pp}. The device was attached to and driven by a motorized micromanipulator at constant cutting speed 200μm/sec. The sample was fixed on a load cell to record the force applied by the probe. The penetration force is the maximum force the probe tip encounters during a penetration event. Figure 3 shows a typical penetration force vs. ultrasonic driving voltage curve. The penetration force decreases approximately linearly with the driving voltage after an initial flat region, which is probably due to a threshold energy necessary for the ultrasound to take effect, and is worth further investigation.

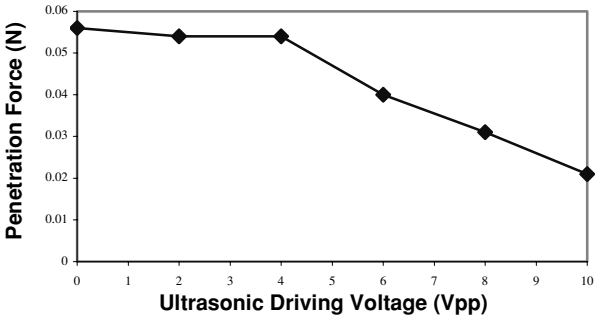

Figure 3. *Penetration force measurement of the ultrasonic microprobe on chicken thigh sample*

On canine heart experiment, the probes can be inserted into the cardiac tissue with >=6V_{pp} driving, at lower voltage the tips often buckle significantly and break. To test cardiac signal recording, perfused canine heart was used and all measurements were conducted within three hours after the heart was isolated from the subject. Diacetylmonoxime was added to the perfusion fluid to reduce the muscle contractions while still allow normal electrical activities. Figure 4 is a photo showing the probe tips penetrated and embedded into the heart tissue. The signals were amplified in unipolar configuration and sampled at 1kHz. Figure 5 is the recorded signal on four electrodes on one tip during ventricular fibrillation. The signals are at higher frequency (~500Hz) than that of normal rhythm and less regular. Figure 6 shows the five channel signals recorded when externally pacing the heart with a 300Hz square wave stimulator. Closer examination in time scale showed that the time delay between the furthest apart electrode pair (2mm away) is approximately 5ms. These results showed that our ultrasonic microprobe is suitable for penetrating the relatively tough cardiac tissue and can provide multi-site recordings with high resolution (currently 500μm which can be easily improved by reducing electrode spacing) and good signal quality.

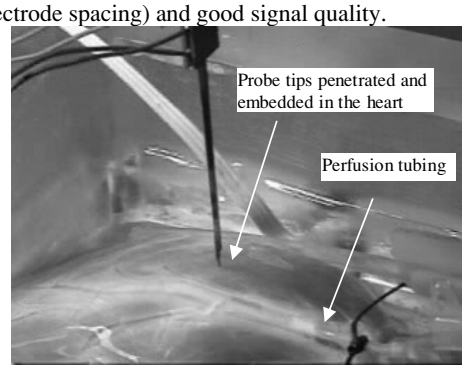

Figure 4. *The in-vitro canine cardiac recording experiment*

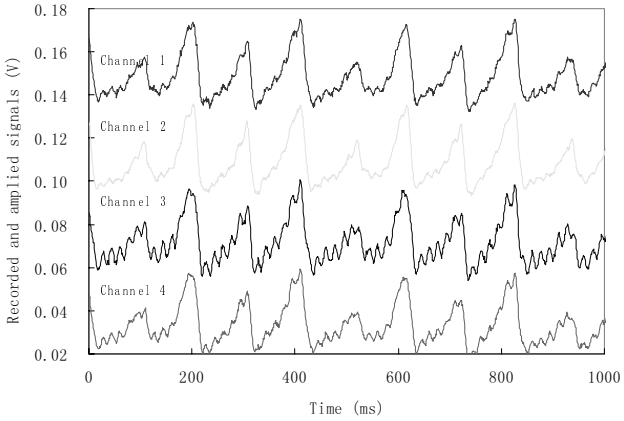

Figure 5. *Signals during VF from four electrodes on one tip. This is probing during ventricular fibrillation resulting in the measurement of the high frequency content.*

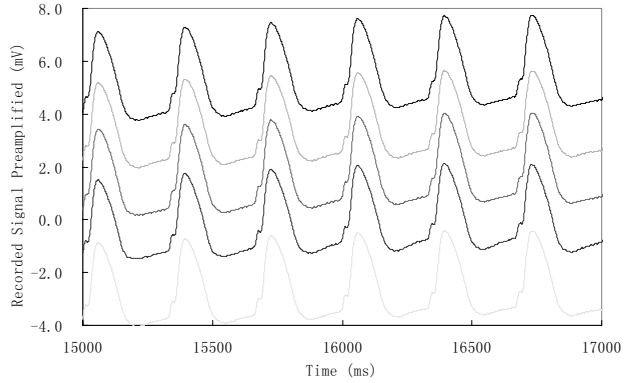

Figure 6.*Signals from five electrodes on one tip during external stimulation. The temporally shifted signals indicate that we are indeed measuring electric potential wave propagation along the probe.*

References:
[1]F. X. Witkowski et al., "Spatiotemporal evolution of ventricular fibrillation", *Nature*, Vol. 392, 5 March 1998, pp78-82
[2]T. H. Yoon, et at, "A micromachined silicon depth probe for multichannel neural recording", *IEEE Trans. Biomedical Engineering,* Vol. 47, no. 8, August 2000
[3]K. Najafi, et al, "A high-yield IC-compatible multichannel recording array", *IEEE Trans. Electron. Devices,* Vol. ED-32, no. 7, pp1206-1211, July 1985
[4]A. Lal, "Silicon-based surgical tools", *Proceedings of the IEEE EMBS conference*, Hong Kong, October 1998

MICROMACHINED AMPEROMETRIC NITRATE SENSOR WITH INTEGRATED MICROFLUIDICS

Dohyun Kim, Ira B. Goldberg, and Jack W. Judy
Department of Electrical Engineering, University of California, Los Angeles
Los Angeles, California, 90095

ABSTRACT

Nitrate-sensing system that consists of a micromachined sensor substrate, nitrate-permeable membrane, integrated microfluidic channels, and standard fluidic connectors has been designed, fabricated, assembled, and tested. Our microsensor was designed for *in-situ* monitoring of nitrate concentrations in ground water. A silver electrode was patterned for amperometric nitrate detection. An electrochemically oxidized silver electrode was used as a reference electrode. Microfluidic channels were fabricated as flow paths for the eluent and ground-water sample to the microelectrochemical (MEC) cell. The sensor also incorporates a nitrate-permeable membrane that is used for selective measurement of nitrate. The sensor has a linear response over concentration ranging from 1 μM to 1 mM.

I. INTRODUCTION AND MOTIVATION

NITRATE is considered to be a major contaminant in ground-water and surface-water systems, and can present significant risks to human health and the environment [1]. In addition, precise nitrate concentration management is needed for the growing field of precision farming [2]. Consequentially, federal health and environmental agencies, ecological scientists, environmental engineers, and farmers have a great need for small, low-power, reliable, and yet sensitive nitrate sensors that can be remotely operated and can measure concentrations in the range of 1 μM to 1 mM [3].

Commercially available nitrate-sensing systems based on ion chromatography, spectrometry, or electrophoresis, usually require expensive and massive instrumentation, complex measurement procedures, and are not currently amenable to remote operation or large-scale deployment. Electrochemical measurements, such as amperometry and potentiometry, are relatively simple, easily miniaturizable, low power, and yet sensitive enough for the targeted applications (i.e., 1 μM to 1 mM). Of these electrochemical techniques, amperometry usually offers simpler analyses to be performed and lower detection limits to be achieved than potentiometry [4]. Selectivity is a major concern in electrochemical measurements and many surface-modification approaches have been used, including immobilized enzymes, freshly-deposited electrode surfaces, and complexing metal ions. However, these approaches increase technical and procedural complexity, without significantly improving performance [4]. Instead, a nitrate-ion-permeable membrane provides the selectivity for our sensing system. Our ultimate research goal is to develop a remotely operable, field-deployable and miniaturized nitrate-sensing system that meets the requirements mentioned above. With the sensitive amperometric detection techniques, a nitrate-permeable membrane, and MEMS-fabrication technology, such a sensing system can be realized.

II. DESIGN AND FABRICATION

A schematic diagram of the sensing system and an illustration of its operation are shown in Figure 1. The sample reservoir is filled with a ground-water test sample and the microelectrochemical (MEC) cell is filled with an electrolytic eluent (10 mM NaOH) (Figure 1b). The sample-fluid reservoir and the MEC cell are adjacent to each other but separated by the ion-selective membrane. Hydroxide ions diffuse across the membrane due to an extreme concentration gradient, and exit the cell while nitrate ions diffuse through the membrane and enter the cell to maintain charge balance. After equilibrium is reached (~5 minutes in our design), the nitrate ions previously in the sample reservoir are transferred to the MEC cell and the amperometric measurements are performed (Figure 1c). When other anions are present in sample solution, they are also transferred across the membrane. However, nitrate diffuses much faster than the other interfering ions due to its larger diffusion coefficient in the membrane. Such a separation method is called Donnan dialysis and allows the selectivity for nitrate measurements [5, 6].

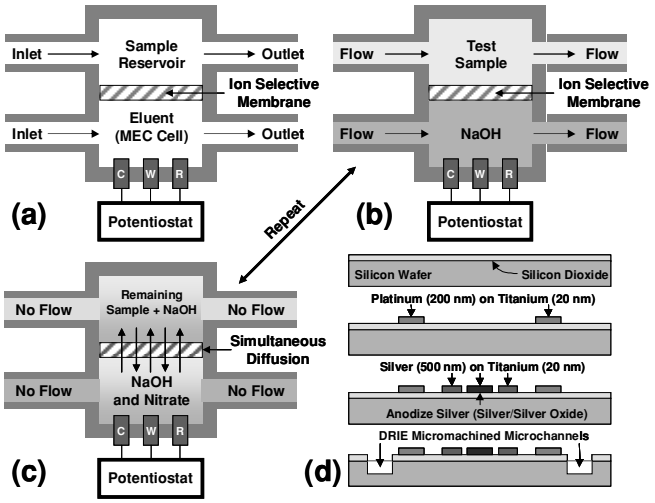

Figure 1. *Schematic diagrams of the electrochemical-sensor system, microfludics (a, b, c), and its fabrication process (d). The electrodes shown are: counter electrode (C), working electrode (W), and reference electrode (R).*

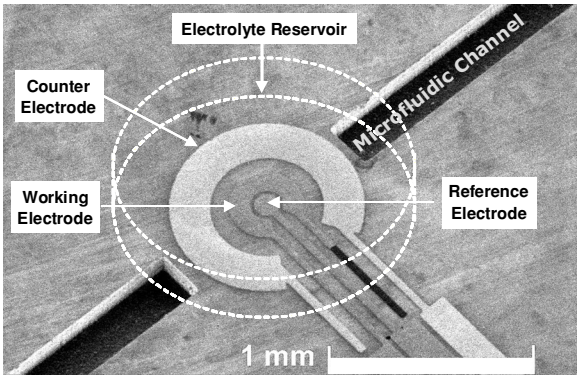

Figure 2. *SEM image of the micromachined electrodes and the 180-μm-deep microchannels in the substrate.*

The microfabrication process was used to produce the microelectrode substrates with integrated microfluidic channels (Figure 1d). Electrode materials widely used for amperometry, such as Pt, Au, and glassy carbon, are not electrochemically active for nitrate detection. We chose to use silver as the working-electrode material after through electrochemical studies in a 10-mM NaOH supporting electrolyte, since silver has an excellent activity for reducing nitrate to nitrite or ammonia [7, 8]. Therefore, the MEC cell has a silver working electrode patterned on a silicon-dioxide substrate. To simplify fabrication, the reference electrode

Travel support has been generously provided by the Transducers Research Foundation and by the DARPA MEMS and DARPA BioFlips programs.

0-9640024-5-0/hh2004/$20©2004TRF
DOI 10.31438/trf.hh2004.26

was made of silver that is electrochemically anodized in 10-mM NaOH to form silver oxide. The counter electrode was made of platinum. The metal electrodes are deposited using a CHA e-beam evaporator. Titanium was used as an adhesion later instead of chromium since it is not electrochemically etched during measurements. A pair of 180-μm-deep microchannels are dry etched with the BOSCH-DRIE process. A SEM image of the concentric electrodes and the microchannels are shown in Figure 2. The microsensor chip is then assembled into a sensor unit with the ion-permeable membrane and EDPM (ethylene-propylene-diene-methylene) rubber plates that define the reservoir and fluidic ports sized to accept standard connectors (Figure 3). The completed and assembled sensor unit is shown in Figure 4.

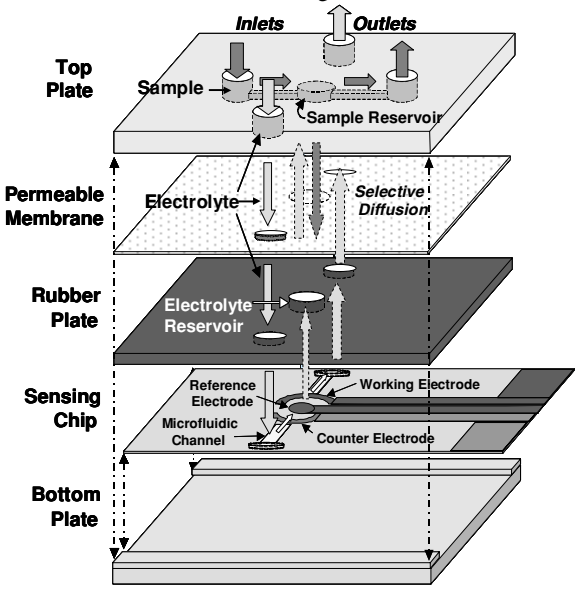

Figure 3. *Exploded schematic diagram of the complete sensor unit.*

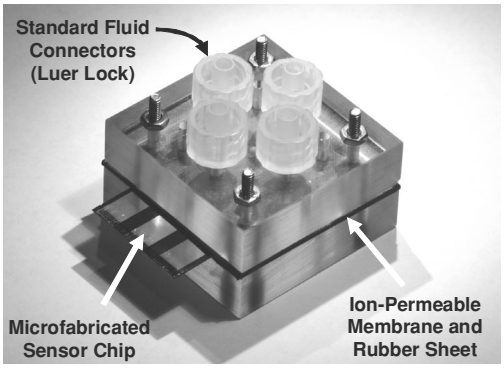

Figure 4. *Assembled sensor unit with standard connectors.*

III. EXPERIMENTAL RESULTS

Reagents were prepared by standard methods. Measurements of the electrochemical process were done using a laboratory potentiostat and data-acquisition system.

In order to obtain repeatable and sensitive measurements, the working electrode needs to be activated before analysis [8]. This is done by sweeping potential from -1.2 V to 0.8 V vs. Ag/AgCl a total of 20 times at a sweep rate of 1 V/s. Calibration curves for nitrate were obtained using chronocoulometry (Figure 5), in which the working electrode is biased at -0.85 V vs. Ag/AgCl and the nitrate reduction current is integrated for 0.5 s. With standard addition methods (1, 2, 5, 10, 20, 50, 100, 200, 500, 1000 μM nitrate), the integrated current (charge) is plotted with respect to concentration and slopes are calculated with linear regression. The calibrations represent the greatest and smallest slopes of the sensing chips tested. The data also illustrates the linearity of our amperometric method. The detection limit of the microsensors is ~1 μM of nitrate.

In order to examine the selectiveness of our microsensor, its response to 100-μM nitrate in a mixture of typical interfering ions in ground water (i.e., 100 μM each of PO_4^{-2}, SO_4^{-3}, F^-, Cl^-) was measured. The sensor output is only 13.9% higher than the average response for 100-μM nitrate without interfering ions.

IV. CONCLUSIONS

By incorporating amperometric detection techniques, a nitrate-permeable membrane, and MEMS-fabrication techniques, we successfully demonstrated the feasibility of using a microsensor system to monitor nitrate concentration in ground water. The performance of the nitrate microsensor is sufficient for this application (i.e., detection range from 1 μM to 1 mM with good selectivity). Long-term qualification tests are presently underway. Once integrated with a chip-scale potentiostat, miniature pumps, check valves, and a wireless sensor node, we anticipate that a revolutionary instrument for nitrate monitoring in water systems could be realized.

ACKNOWLEGEMENTS

We would like to gratefully acknowledge that our research was funded by the NSF and Center for Embedded Network Sensing at UCLA (NSF CCR-0120778).

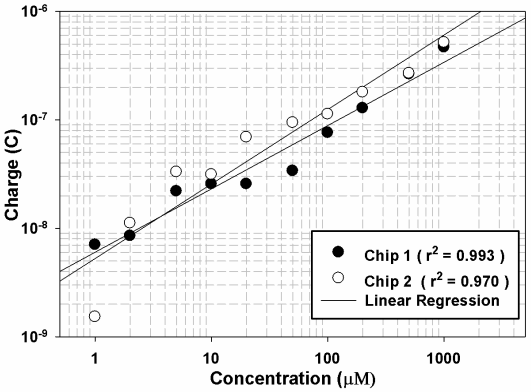

Figure 5. Calibration curves for the nitrate-sensor system with a minimum detection level of ~1 μM.

REFERENCES

[1] C.S. Bruning-Fann and J.B. Kaneene, "The effects of nitrate, nitrite, and N-nitroso compounds on human health: A review", *Veterinary and HumanTtoxicology*, vol. 35, pp. 521, 1993.

[2] P. Robin and D.A. Barrow, "Microsystems technology for remote monitoring and control in sustainable agricultural practices", *Journal of Environmental Monitoring*, vol. 2, pp. 385, 2000.

[3] Environmental Protection Agency, "List of contaminants & their maximum contaminant level (MCLs)", *http://www.epa.gov/safewater/contaminants/dw_contamfs/nitrates.html*

[4] M.J. Moorcroft, J. Davis, and R.G. Compton, "Detection and determination of nitrate and nitrite: a review", *Talanta*, vol. 54, pp. 785, 2001.

[5] T.A. David, J.D. Genders, and D. Pletcher, *A First Course in Ion Permeable Membranes*, England, pp. 245, 1997.

[6] H. Miyoshi, "Diffusion coefficients of ions through ion exchange membrane in Donnan dialysis using ions of different valence", *Journal of Membrane Science*, vol. 141, pp. 101, 1998.

[7] M. Fedurco, P. Kedzierzawski, and J. Augustynski, "Effect of multivalent cations upon reduction of nitrate ions at the Ag electrode " *Journal of the Electrochemical Society*, vol. 146, no. 7, pp. 2569, 1999.

[8] J. Krista, M. Kopanica, and L. Novotny, "Voltammetric determination of nitrates using silver electrodes", *Electroananlysis*, vol. 12, pp. 199, 2000.

AN INTEGRATED MICROFLUIDIC INKING CHIP FOR SPM NANOLITHOGRAPHY

Kee Suk Ryu, Xuefeng Wang, Kashan Shaikh, Edgar Goluch, David Bullen, Jun Zou and Chang Liu
Department of Electrical and Computer Engineering, University of Illinois at Urbana-Champaign
Urbana, IL 61801

ABSTRACT

We report a new architecture of a microfluidic chip for dressing (inking) a high-density array of nanolithography tips in a parallel and multiplexed fashion. The microfluidic chip consists of a matching array of precision patterned thin PDMS films serving as porous inking pads. Inks are supplied from loading reservoirs to the inking pads through embedded microfluidic channels. The thin PDMS membrane allows trapped gas and molecules to permeate through while preventing liquid itself from overflowing or evaporating. The new inking chip provides high density inking, easy loading of inks, and reduced evaporation loss. The fabrication process and results of inking commercial nitride probe and scanning probe contact printing (SP-CP) probes are presented.

INTRODUCTION

Scanning Probe Microscopy (SPM) has been widely used for patterning sub-micron features [1]. The SPM instrument can be used to direct-write chemical and biological molecules with sub-micron precision for applications such as producing proteomic and gene arrays, functionalizing sensors and circuits, or catalyzing surface chemical reactions. For example, Dip Pen Nanolithography (DPN) [2] utilizes the positioning capability of SPM instruments to deposit chemicals onto substrate with sub-100-nm linewidth. DPN tips are first coated ("inked") with a chemical of interest. When the probe is placed in contact with a writing surface, molecules transfer from the tip to the substrate via meniscus at tip-substrate interface. Recently, a new technique called scanning-probe contact printing (SP-CP) was invented [3]. It utilizes an SPM probe with an integrated tip made of polydimethylsiloxane (PDMS). In the SP-CP process, chemicals are first absorbed into the elastomeric tip. The probe is then moved to a desired location using a commercial SPM. Each contact printing action creates individual dots, analogous to dot-matrix printing. SP-CP process combines the chemical versatility and performance advantage of microcontact printing.

The throughput of SPM-based nanolithography methods can be increased by using arrays of probes [4], arrayed in one- or two dimensions. Certain future applications require inking different tips with different chemicals. However, existing methods for inking DPN or SP-CP probes require exposing tips to vapors or liquids. These inking methods are not suitable for arrayed tips either because of cross-contamination or difficulty of putting different inks to neighboring tips in a dense array (e.g., with tip to tip spacing on the order of 500 μm or smaller in one or two axes). Inking using open channels or capillary wells incur rapid ink loss and cross contamination since the ink solution is open to air [5]. In addition, it would require an active control to maintain the level of liquid to interact with multiple tips simultaneously.

A successful method for parallel, multiplicity inking must be practical, scalable (to hundreds of tips per inking session or more), and low cost, while providing high density and low ink loss.

DESIGN AND FABRICATION

We report a new method of "inking" tips taking advantage of thin (5 μm thick on average) PDMS membrane patches as permeable inking pads. The patches are arranged in array format, matching the density and number of nanolithography tips.

***Travel support has been generously provided by the Transducers Research Foundation and by the DARPA MEMS and DARPA BioFlips programs.**

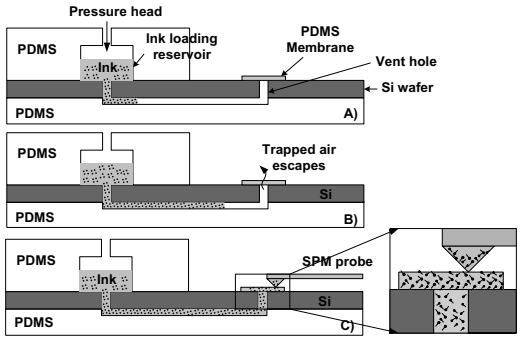

***Figure 1**. The inking chip with a single inking site shown. PDMS membrane allows gas to escape and the positive pressure head at the reservoir keeps the "ink" at the membrane.*

As shown in *Figure 1*, a thin PDMS membrane (5 μm-thick) is patterned in registration with vent holes made in a silicon wafer. Reservoirs and connecting fluidic channels, formed by PDMS molding, are bonded on the top and bottom of the Si wafer, respectively. Once the reservoir is filled with ink (*Figure 1*(A)), the positive pressure head at the reservoir will move the "ink" towards the inking site (membrane). Trapped air escapes through the thin PDMS membrane (B), allowing inking liquid to contact the bottom of the membrane. The ink, over time, diffused through the membrane to the other side and is picked up by a tip in contact mode. The diffusion of ink molecules through the membrane can be expressed with Fick's first law, i.e., $J = -D(dC/dx)$, where D is the diffusion coefficient of the ink molecule in PDMS, C is the concentration of the ink in the solution, and x is the thickness of the PDMS membrane. The diffusion coefficient D is an experimental parameter that varies with the ink molecules and the PDMS elastomer. Membranes must be thin to allow fast diffusion.

Advantages of this method are following: (1) No active pump or valve required, (2) Cross contamination of adjacent PDMS membranes is minimal, (3) Evaporation of liquid is minimal, (4) high-density inking sites are possible.

We first form throughholes in silicon with DRIE and pattern Al around the holes (*Figure 2*). A recently method for making precision PDMS thin film [6] is used to form PDMS patches. The Al is removed from back. Finally, the top and bottom pieces of PDMS are molded, aligned and assembled. *Figure 3* shows the assembled chip with 144 (four groups of 4 x 9 arrays) inking sites.

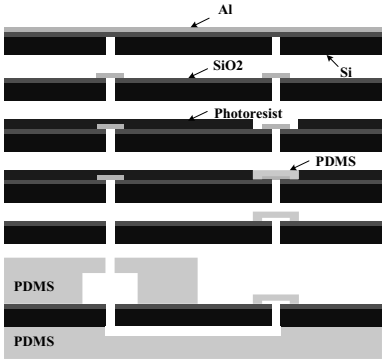

***Figure 2.** Microfabrication steps including PDMS patterning.*

0-9640024-5-0/hh2004/$20©2004TRF
DOI 10.31438/trf.hh2004.27

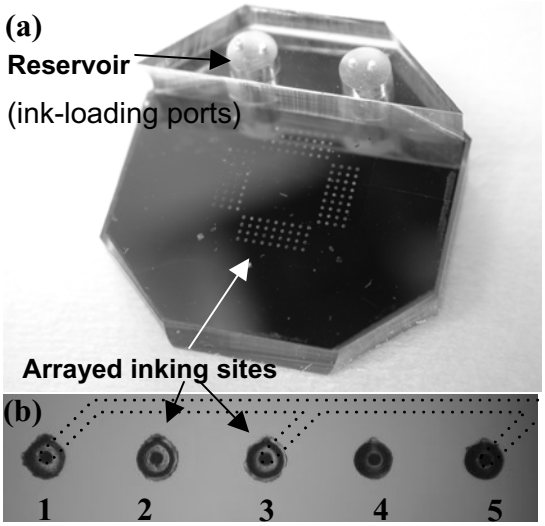

Figure 3. *An assembled inking chip with 144 inking sites. (a) Perspective view of chip with two loading ports; (b) Close view of PDMS membranes. The distance to nearby membrane is 500 μm. Dotted line indicates backside channels.*

TEST RESULTS

Inking of tips by organic molecules has been performed by filling one of the two reservoirs with a 4 mM ethanolic ODT solution. 5 μl of the solution was fed into the reservoir. Ink travels to the membrane sites in 2-3 sec. After 6 hr to let the PDMS membrane to be saturated with ODT, SPM tips are made to contact the inking pads to initiate ink transfer from the pad to the tips (*Figure 4*). Ink loss through vaporization is minimal and can be minimized even more in future. It was found the 5 μl of solution completely dries up in about 12 hr. With bigger reservoir (~100 μl) in the future, the concentration change in the ink can be minimal. Nanolithography tips (including a silicon nitride Microlever tip and a SP-CP tip) were then placed directly on top of the PDMS inking patching but not over the vent hole aperture. After 30 minutes of "inking", the nitride probe and SP-CP probe were used to write on Au surfaces. For comparison, "Inking" by making contact to bulk PDMS soaked for 12-24 h in a solution at least takes 10 minutes. The inking speed is still limited by diffusion but parallelism and ink multiplexity capabilities are gained.

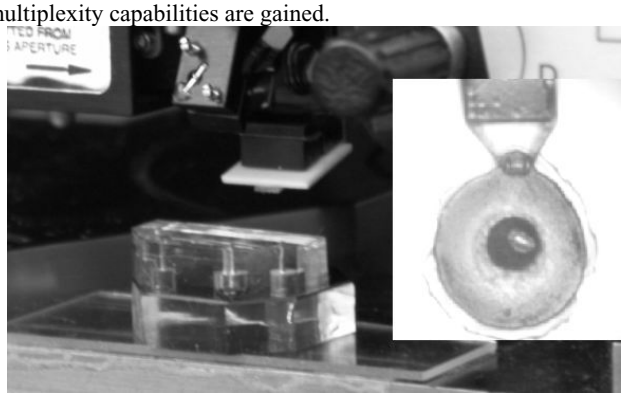

Figure 4. *Optical picture of setup in a scanning probe microscope nanolithography station. The inking chip is located below and a SP-CP probe is being brought into contact to "ink" the probe. Enclosed optical micrograph shows SP-CP probe being "inked" through PDMS membrane by contact.*

Figure 5 (a) shows lines drawn by a commercial nitride probe with the writing speed of 0.1 μm/s. Increasing the writing speed results in narrower line widths as shown in *Figure 6*. *Figure 5*(b) shows dots drawn by a SP-CP probe. 10 s, 30s, and 1 min of contact printing resulted in patterns in the sizes of 600 nm, 1.3 μm, and 1.8 μm.

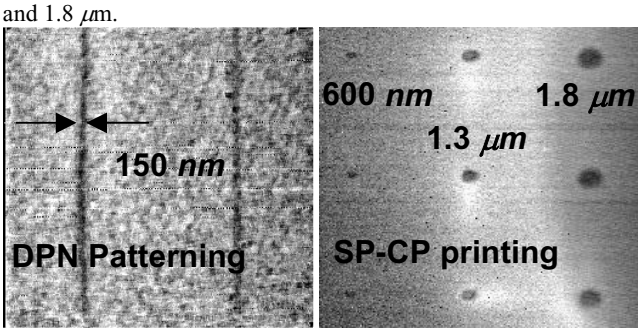

Figure 5*. (a) AFM scan image of lines drawn by a nitride DPN tips; (b) ODT dots created by a single SP-CP probe. Large size dots are useful to print coarse features for selected applications.*

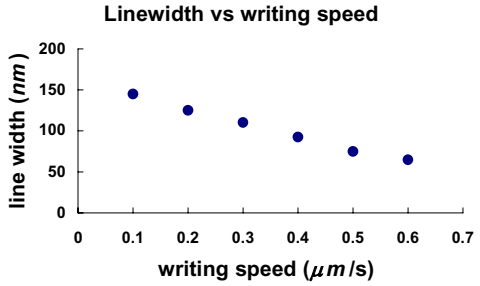

Figure 6. *Writing speed and resulting line width plot for commercial nitride probe in DPN writing mode.*

Cross contamination was experimentally found to be minimal. We supplied ODT to odd-numbered inkpads (i.e., #.1, 3, 5 inkpads shown in *Figure 3(b)*) and making a contact to even-numbered inkpads, which are not being fed by ink. We performed writing after 30 min of contact but no visible pattern was created by either probe. We concluded that no appreciable cross contamination occurs, 6 h after filling.

CONCLUSION

This paper reports a novel method for inking scanning probes for nano lithography with high efficiency. Thin PDMS membranes were used as inkpads and as a membrane which minimize the evaporation of the ink and thus cross-contamination between inking sites. Inking operation has been confirmed. Cross-contamination has been experimentally confirmed to be minimal, at least within 6 hours of filling. The overall inking speed is diffusion limited (even with 5-μm thick PDMS membrane) and will be a subject of future improvement.

REFERENCE

[1] H. T. Soh, K. W. Guarini, and C. F. Quate, *Scanning Probe Lithography*: Kluwer Academic Publishers, 2001.

[2] R. D. Piner, J. Zhu, F. Xu, S. Hong, and C. A. Mirkin, ""Dip-Pen" Nanolithography," *Science*, vol. 283, pp. 661-663, 1999.

[3] X. Wang, K. Ryu, D. Bullen, J. Zou, H. Zhang, C. A. Mirkin, and C. Liu, "Scanning Probe Contact Printing," *Langmuir*, vol. 19, pp. 8951-5, 2003.

[4] D. Bullen, S.-w. Chung, X. Wang, J. Zou, C. A. Mirkin, and C. Liu, "Parallel dip-pen nanolithography with arrays of individually addressable cantilevers," *Applied Physics Letters*, vol. 84, pp. 789-791, 2004.

[5] D. Banerjee, J. Fragala, T. Duenas, R. Shile, and B. Rosner, "Planar Capillary Pumped Ink Delivery Apparatus For Dip Pen Nanolithography (DPM)," presented at 7th International Conference on Miniaturized Chemical and Biochemical Analysis Systems, Squaw Valley, CA, 2003.

[6] K. Ryu, X. Wang, K. Shaikh, and C. Liu, "A Method for Precision Patterning of Silicone Elastomer and Its Applications," *IEEE/ASME Journal of Microelectromechanical Systems*, vol. In press, 2004.

A QUANTITATIVE UNDERSTANDING OF TRANSIENT BUBBLE GROWTH IN MICROCHANNELS USING μPIV

Evelyn N. Wang, Shankar Devasenathipathy, Carlos H. Hidrovo, David. W. Fogg, Jae-Mo Koo, Juan G. Santiago, Kenneth E. Goodson, Thomas W. Kenny
Stanford University, Departments of Mechanical Engineering
Stanford, CA 94305

ABSTRACT

Various fluidic MEMS structures require a better fundamental understanding of microscale bubble growth dynamics. Much of the work in this area has been qualitative observations of bubble formation and growth. This paper presents an approach to obtain quantitative estimates of forces acting on bubbles by obtaining liquid velocity fields using micron-resolution particle image velocimetry (μPIV). These velocity fields aid in determining parameters such as viscous stresses acting on the bubble, vapor and local liquid pressure, and bubble departure criteria. The ability to obtain these velocity fields in a transient bubble growth process is demonstrated in a microfabricated silicon channel with an integrated heater. These measurements offer a step towards understanding and developing accurate models for MEMS structures associated with the presence of bubbles.

INTRODUCTION

Bubbles are prevalent in several different MEMS devices. Examples include thermally-actuated pumps and valves [1-3] and two-phase microchannel heat sinks for IC cooling applications [4-6]. However, little is understood about the bubble formation and growth process in these microscale structures. A robust understanding of these phenomena is needed in order to optimize the performance of these MEMS devices.

This paper presents an experimental methodology which can potentially determine forces on growing vapor bubbles in a microchannel. By acquiring the liquid velocity field in a region near the bubble using micron-resolution particle image velocimetry (μPIV), important parameters such as viscous stresses, vapor and local liquid pressure, and bubble departure may be assessed. This important information will aid in a better fundamental understanding of bubble actuated devices, and boiling in microchannel heat sinks; and the methodology be extended to other MEMS structures and applications. In this paper, we demonstrate this approach for the first time in a heated microchannel system during heterogeneous nucleation and boiling for the future development of a robust two-phase heat sink model and design.

EXPERIMENTAL APPROACH

The μPIV setup consists of an epi-fluorescent microscope (Nikon TE300) with a mercury lamp illumination source as shown in Figure 1. Imaging is achieved using a 20X objective lens (NA = 0.75) and a 12-bit resolution interline cooled CCD camera (Roper Scientific CoolSnap HQ). A constant hydrodynamic head in a graduated cylinder generates flow through the microchannel test structure. Deionized water is seeded with 700 nm fluorescent polystyrene particles (Duke Scientific) at a particle density of 0.025 %. A concentration approximately half of the critical micelle concentration of Triton-X (Sigma) nonionic surfactant is used to reduce particle adsorption to the channel walls.

The liquid velocity fields surrounding a growing bubble are obtained using μPIV by cross-correlating image pairs in designated interrogation regions. The PIV algorithm used in these experiments was developed by Meinhart *et al.* [7] to determine time-averaged velocity fields. An average correlation method is used to improve the signal-to-noise ratio of the correlation function. The measurement depth, beyond which image intensity has only a negligible effect on velocity measurements, is 4.7 μm.

Figure 2 shows silicon microchannels which are fabricated with integrated aluminum heaters with standard MEMS processing technology. The channels all have hydraulic diameters less than 150 μm. Power is applied to the microchannel to initiate bubble generation in the channel from heterogeneous nucleation sites.

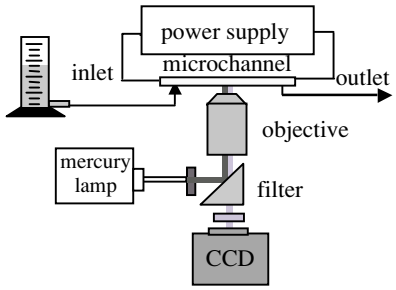

Figure 1. *Schematic of μPIV imaging system used to image bubble formation and growth in a microchannel .*

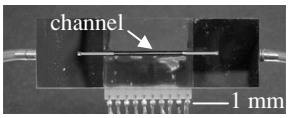

a. Chip front side with single microchannel.

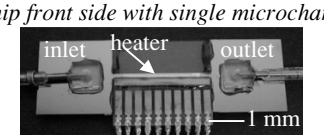

b. Chip back side with heater.

Figure 2. *Image of silicon microchannel with integrated sensors and uniform heater.*

EXPERIMENTAL RESULTS

Vapor bubble growth processes were studied under two-phase conditions in a microchannel as a function of increasing power. Figure 3 shows images of the growth of a bubble in a hydraulic diameter, D_H = 140 μm channel. Surface tension forces dominate in this Stokes flow regime, (Re_D = 0.02), where the bubbles do not depart from the walls. The intensity of the images near the liquid-vapor interface is higher due to diffraction and potential particle coalescence as the vapor bubble grows.

0-9640024-5-0/hh2004/$20©2004TRF
DOI 10.31438/trf.hh2004.28

Solid-State Sensors, Actuators, and Microsystems Workshop
Hilton Head Island, South Carolina, June 6-10, 2004

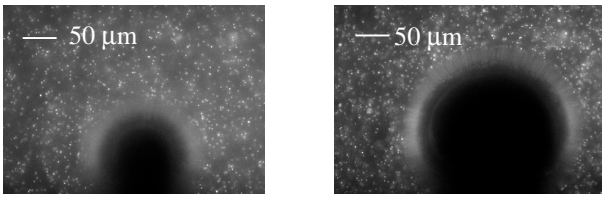

(a) P = 0.98 W *(b) P = 1.4 W, 13.8 s later*

Figure 3. *Images of bubble growth in a D_H = 140 µm microchannel with particles seeded in the flow.*

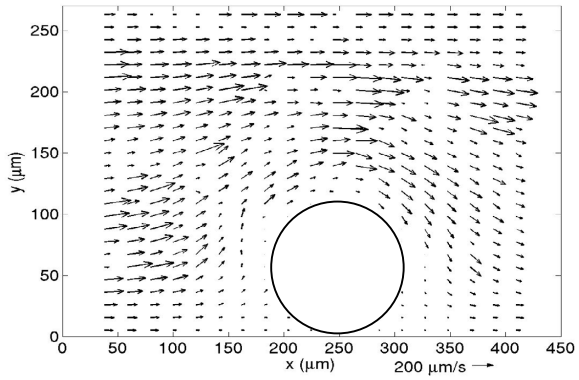

(a) P = 0.98 W

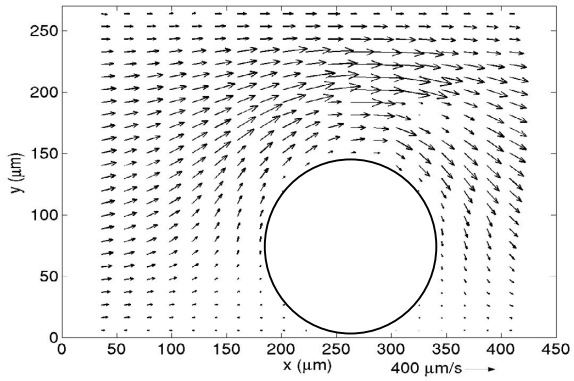

(b) P = 1.4 W, 13.8 s later

Figure 4. *Liquid velocity fields in the region around a growing vapor bubble which corresponds to images in Figure 3.*

Figure 4 shows velocity fields that correspond to the images of a vapor bubble growing in the microchannel in Figure 3. As the power level increases from 0.98 W to 1.4 W, the liquid velocity near the stationary bubble increases as the liquid flow area around the bubble is constrained. The maximum observed velocities in this experiment are 250 µm/s and 420 µm/s, respectively, corresponding to Figures 6(a) and 6(b).

Figure 4 is an example of the transient liquid velocity fields that can be obtained using µPIV when bubbles are created by applying heat to the microchannel. Quantitative estimates of viscous stresses on the bubble can be obtained directly from these velocity data, in place of approximate correlations based on integral quantities of idealized conditions such as drag coefficients [8, 9].

To proceed further, pressure fields within and outside of the bubble can be found using a momentum balance on control volumes in the bubble region and relations for the surface tension on the free surfaces. In such measurements, we would obtain two-dimensional velocity fields at different depths of the bubble, such that the entire three-dimensional flow field can be obtained.

The ultimate goal of this work is determining criterion for bubble departure from the channel wall, once pertinent forces are quantified. These velocity measurements are an important step in this direction and a contribution to understanding bubble dynamics in a microchannel structure.

CONCLUSIONS

Progress towards understanding important parameters in bubble growth in a microchannel is demonstrated using µPIV. Preliminary measurements of liquid velocity fields surrounding vapor bubbles suggest that quantitative values of forces acting on a bubble should be attainable. Further work is required to extract these forces and determine bubble departure criteria. The method should provide an essential tool for a fundamental understanding of bubble growth in many MEMS devices and ultimately aid in the design of optimized microscale structures.

ACKNOWLEDGEMENTS

The work is supported by MARCO. Travel support has been generously provided by the Transducers Research Foundation and by the DARPA MEMS and DARPA Bio-Flips programs. The project made use of the National Nanofabrication Users Network facilities funded by the National Science Foundation under award number ECS-9731294.

REFERENCES

1. R. A. Braff, A. L. Gerhardt, M. A. Schmidt, M. L. Gray, and M. Toner, "A Microbubble-Powered Bioparticle Actuator", *Hilton Head Solid-State Sensor, Actuator, and Microsystems Workshop*, Hilton Head, SC, 2002.
2. A. P. Papavasiliou, A. Pisano, and D. Liepmann, "High-Speed and Bi-Stable Electrolysis-Bubble Actuated Gate Valves", *Transducers*, June 10-14, 2001, Munich, Germany, 2001.
3. T. Jun, and C.-J. Kim, "Valveless Pumping Using Traversing Vapor Bubbles in Microchannels", *Journal of Applied Physics, 83,* 11, 5658-5664 (1998).
4. L. Zhang, J.-M. Koo, L. Jiang, M. Asheghi, K. E. Goodson, J. G. Santiago, and T. W. Kenny, "Measurements and Modeling of Two-Phase Flow in Microchannels with Nearly-Constant Heat Flux Boundary Conditions", *Journal of Microelectromechanical Systems, 11,* 1, 12 -19 (2002).
5. M. Steinke, and S. G. Kandlikar, "Flow Boiling and Pressure Drop in Parallel Flow Microchannels", *1st International Conference on Microchannels and Minichannels*, April 24-25, 2003, Rochester, New York, 2003.
6. L. Jiang, M. Wong, and Y. Zohar, "Phase Change in Microchannel Heat Sinks with Integrated Temperature Sensors", *Journal of Microelectromechanical Systems, 8,* 4, 358-365 (1999).
7. C. D. Meinhart, S. T. Wereley, and J. G. Santiago, "A Piv Algorithm for Estimating Time-Averaged Velocity Fields", *Journal of Fluids Engineering, 122,* 2, 285-289
8. J. F. Klausner, R. Mei, D. M. Bernhard, and L. Z. Zeng, "Vapor Bubble Departure in Forced Convection Boiling", *International Journal of Heat and Mass Transfer, 36*, 651-662 (1993).
9. R. Clift, J. R. Grace, and M. E. Weber, *Bubbles, Drops and Particles*. 1978, New York: Academic Press.

Paramagnetic Capture Mode Magnetophoretic Microseparator for Blood Cells

Ki-Ho Han, and A. Bruno Frazier
School of Electrical and Computer Engineering, Georgia Institute of Technology
Atlanta, GA 30332-0250

ABSTRACT

This paper presents the characterization of a continuous paramagnetic capture (PMC) mode magnetophoretic microseparator for separating white and red blood cells from whole blood by using a high gradient magnetic separation (HGMS) method and microfabrication technology. The PMC microseparator directly separates blood cells based on their native magnetic properties without the use of additives such as magnetic tagging or inducing materials. Experimental results show that the present PMC microseparator can continuously separate out 68.2% of the red blood cells (RBC's) from whole blood in 5 minutes by applying an external magnetic flux of 0.2T using a permanent magnet.

INTRODUCTION

Conventional magnetophoretic macroseparators [1] using HGMS have been used for separating particles from liquids because of characteristics such as a non-hydrolytic separation force, simple structure, and ease of use. In ref. [2], we reported the development of a diamagnetic capture (DMC) mode magnetophoretic microseparator, which separated WBC's, and RBC's. The DMC mode utilized a permanent magnet to apply an external magnetic field perpendicular to the plane of the bonded glass substrate. Through FEM modeling and experimental verification of the DMC microseparator, it was found that the DMC microseparator had characteristic limitations. For instance, using the geometries of the designed DMC microseparator, RBC's placed within ~25µm of a square wire along the bottom of the microchannel, were not affected by the separation force, thereby decreasing the separation efficiency. While the PMC mode (Fig.1) is more difficult to fabricate than the DMC mode, the simulation analysis (Fig.2) shows that the PMC mode has definite advantages in this application including a stronger magnetic separation force generated around the square wire, which exponentially increases at a distance of ~50µm from the wire edge toward the wire's edge along the bottom of microchannel. This paper describes the design and fabrication of the PMC microseparator (Fig.3), and reports on the quantitative performance of the PMC microseparator for separating WBC's from whole blood for genomic analysis and for removing a large percentage of the RBC's that act as inhibitors [3] for subsequent genomic analysis.

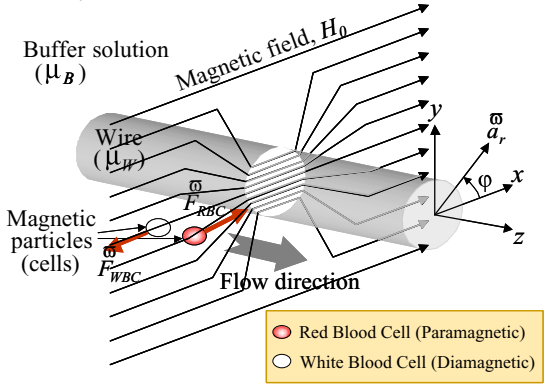

Figure 1. *The working principle of the PMC microseparator.*

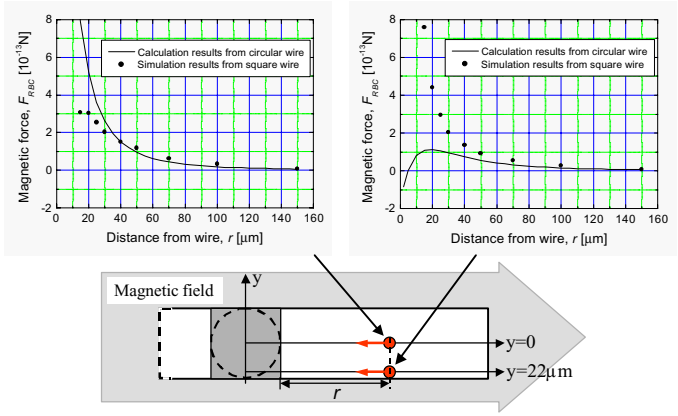

Figure 2. *Calculation and simulation magnetic forces on RBC.*

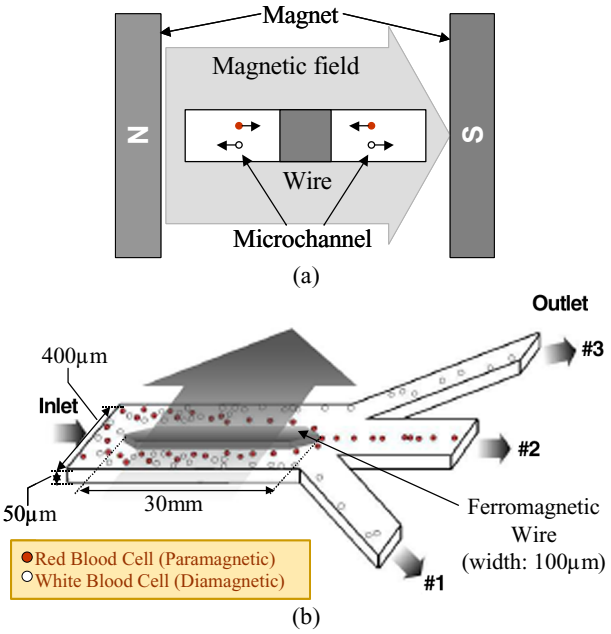

Figure 3. *Illustrations of the PMC microseparator having one inlet and three outlets: (a) cross section view; (b) perspective view.*

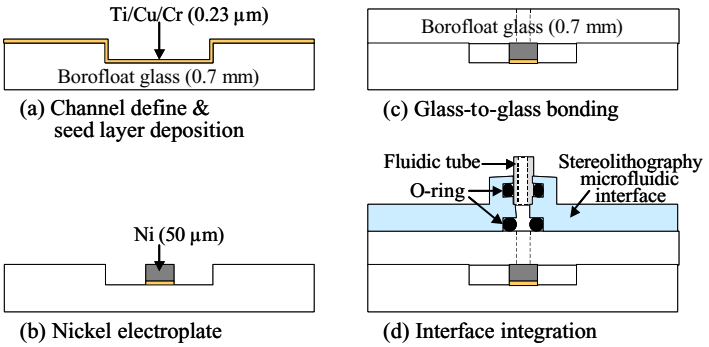

Figure 4. *Microfabrication process.*

0-9640024-5-0/hh2004/$20©2004TRF
DOI 10.31438/trf.hh2004.29

Solid-State Sensors, Actuators, and Microsystems Workshop
Hilton Head Island, South Carolina, June 6-10, 2004

RESULTS AND CONCLUSION

Figure 4 illustrates the microfabrication process of the PMC microseparator. Figure 5 shows the fabricated microseparator and instrumental setup implemented using a permanent magnet to create the external magnetic flux of 0.2T. Figures 6(a) and (b) show images of blood cells flowing at a velocity of 0.2mm/s through the microchannel with and without an external magnetic field applied. Figures 7(a) and (b) display images of blood cells flowing at velocities of 0.1mm/sec and 0.6mm/s. The images show that RBC' s are forced towards the wire with the application of an external magnetic field and accumulate at the wire edge. The relative percentage of RBCs at the outlets (Fig.8(a)), measured using a hemacytometer, shows that the PMC microseparator separates out 68.2% RBC' s from whole blood at 0.1mm/s flow velocity, agreeing well with the estimated results from FEM modeling (Fig.8(b)). By monitoring WBC' s dyed with a fluorescent probe (Fig.9), the relative percentage of WBC' s at the outlets was measured as shown in Fig.10, and shows that WBC' s are not influenced by a 0.2T external magnetic flux applied to the PMC microseparator and separate away from the integrated wire due to Fickian diffusion.

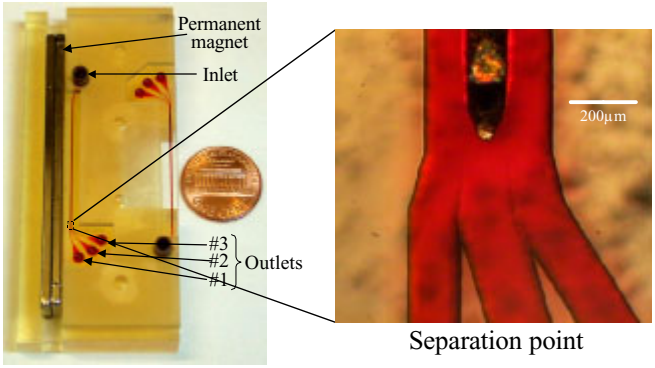

Figure 5. *Fabricated microseparator and instrument setup.*

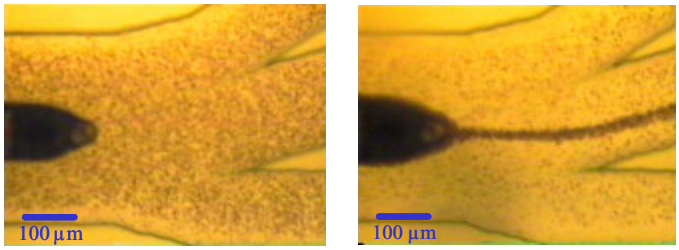

(a) Without magnetic field (b) With 0.2T magnetic field

Figure 6. *Blood cells passing through the microchannel of the PMC microseparator at a velocity of 0.2 mm/s.*

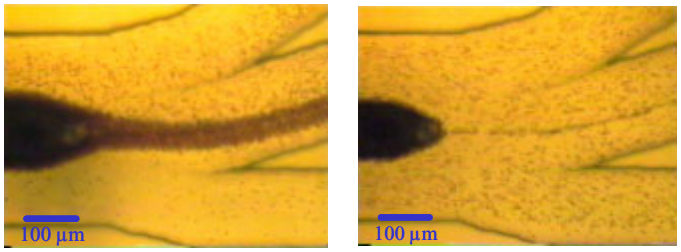

(a) 0.1 mm/s (b) 0.6 mm/s

Figure 7. *Blood cells passing through the microchannel of the PMC microseparator at varying flow velocities with 0.2T magnetic field applied.*

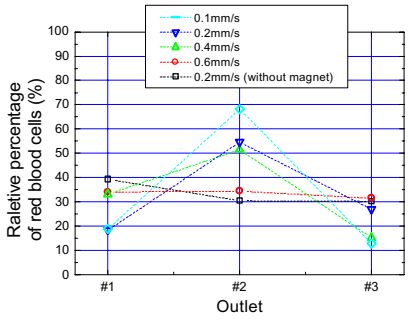

(a) Measured results

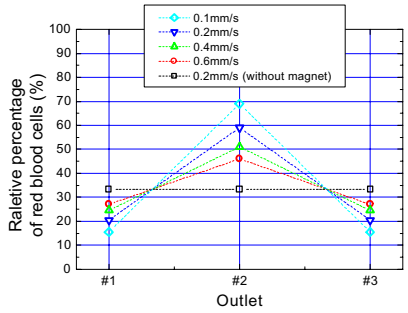

(b) Estimated results

Figure 8. *The relative percentage of RBC' s from the outlets of the PMC microseparator for varying flow velocity.*

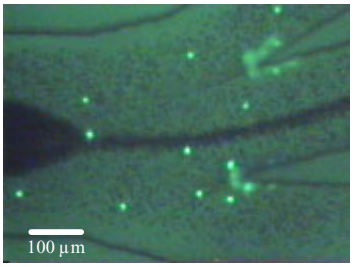

Figure 9. *Fluorescent probed WBC' s passing through the microchannel of the PMC microseparator at a velocity of 0.2 mm/s.*

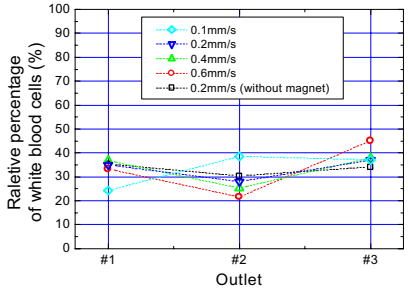

Figure 10. *The relative percentage of WBC' s from the outlets of the PMC microseparator for varying flow velocity.*

ACKNOWLEDGEMENTS

This work was supported by the National Institutes of Health (NIH) / National Institute for Environmental Health Sciences (NIEHS) under Grant ES10846.

REFERENCES

1. M. Franzreb, W. Holl, and C. Hoffmann, U.S. Patent No. 2002/0088741.
2. K.-H. Han, J. P. Landers, and A. B. Frazier, *Transducers' 03*, pp.1229-1232.
3. M. M. Hämäläinen, J. U. Eskola, J. Hellman, and K. Pulkki, *Clinical Chemistry, 45*, 465 (1999).

MEMS REQUIREMENTS FOR AN EPI-RETINAL PROSTHESIS

Robert Greenberg
Second Sight Medical Products Inc.
Sylmar, California 91342
bob@2-sight.com

ABSTRACT

Two approaches have been pursued to restore vision to blind patients – electrically stimulating the visual cortex and the retina. MEMS techniques have played a role in each of these research efforts and will continue to play a role going forward. Progress towards these goals will be discussed in the talk.

I. INTRODUCTION AND BACKGROUND

In 1755 LeRoy discovered that an electric charge delivered to the blind eye produced a sensation of light [1]. Ever since, humanity has pondered the possibility of making the blind see. However, it was not until the age of modern electronics that building such a device became possible.

II. STIMULATING THE VISUAL CORTEX

In the 1960's, Dr. Brindley in England elicited sensations of light in blind subjects by electrically stimulating their visual cortex (the back side of their brain) [2]. In the 1970's, Dr. Dobelle in the U.S. repeated these experiments with some success [3]. However, the resolution achieved by these early devices was very poor. At best, these patients could read Braille by the flashing lights (phosphenes).

By the time the visual image has reached the brain, a significant amount of processing has already occurred - making fine resolution difficult to achieve. Another problem with this approach was that the surgery was very invasive and dangerous for these volunteer patients.

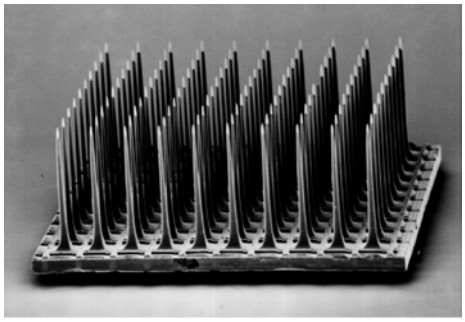

Fig. 1*. Visual cortex electrode array courtesy of Dick Normann at the University of Utah.*

III. STIMULATING THE RETINA

Over the past decade at Johns Hopkins and now at USC, we discovered that there is a subpopulation of blindness (outer retinal degenerations such as Retinitis Pigmentosa and Macular Degeneration) in which a majority of the retina and visual system is intact, allowing stimulation more peripherally - at the retina [4].

By electrically stimulating the retinas of over two dozen of these patients in the operating room, we were able to achieve formed vision. Stimulating the retina has the potential to provide a much higher resolution device than stimulating the visual cortex and there are now half a dozen groups around the world pursuing this line of research. In the Los Angeles area, we formed a company called Second Sight, which has embarked on creating the first artificial retina (a long-term implantable system which will allow the blind to see) [5].

At the time of this writing, three patients have been chronically implanted with a first generation retinal prosthesis. This device has 16 independently controllable electrodes. The completely blind patients are able to perceive individual spots of light corresponding to each of the electrodes and perform simple visual tasks despite the simplicity of the device.

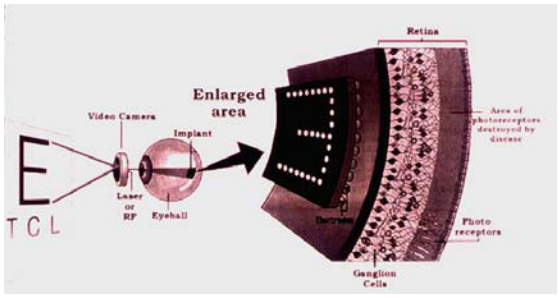

Fig. 2*. Visual prostheses concept based on simulating the retina.*

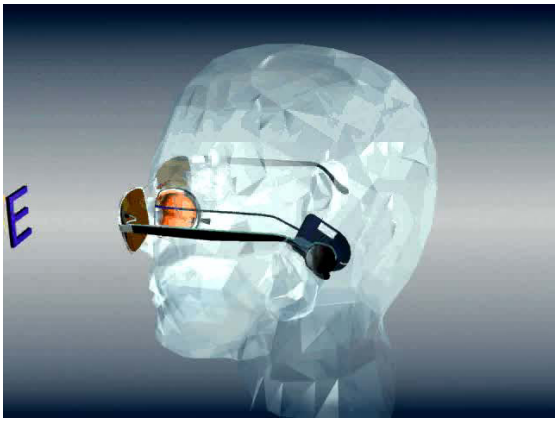

Fig. 3*. Second Sight / USC Model 1retinal prosthesis*

IV. MEMS APPLICATIONS IN RETINAL PROSTHESES

Second Sight Medical Products is working on future-generation devices with higher resolution. This is where the need for MEMS technology comes in. In order to produce higher electrode counts, MEMS-like approaches for the fabrication of the electrodes are necessary. As we continue down our path towards 1000 electrodes and beyond, new techniques will need to be

0-9640024-5-0/hh2004/$20©2004TRF
DOI 10.31438/trf.hh2004.30

developed. The following technology areas must be advanced for truly high-resolution retinal prosthetics to be developed:

- a method of producing small high-resolution electrodes that do not degrade when passing high current levels in saline
- high-density hermetic packaging
- fully integrated electronics including power supplies
- bidirectional high-rate data telemetry

Research towards these goals is underway at Second Sight in conjunction with its partners [6-8]. Details of the progress accomplished to date will be presented.

III. CONCLUSIONS

Although significant progress has already been made, the challenges are great and more progress is needed. Feel free to contact us if you have an interest in this area.

ACKNOWLEGEMENTS

I would like to thank Jack Judy for his help and advice in preparing this manuscript.

REFERENCES

[1] J. Clausen, "Visual Sensations (Phosphenes) Produced by AC Sine Wve Stimulation", *Acta Physiol. Neurol. Scand. Suppl.* Vol. 94, pp. 1-101 (1955)

[2] G.S. Brindley, he Site of Electrical Excitation of the Human Eye", *J. Physiol (Lond)*, vol 127, pp. 189-200 (1955)

[3] R.A. Normann, "Visual Neuroprosthetics – Functional Vision for the Blind", *IEEE Eng. Med. & Biol.*, Jan/Feb, pp. 77-83 (1995)

[4] M.S. Humayun, E. de Juan, Jr., G. Dagnelie, R.J. Greenberg, R. Propst and D.H. Phillips, "Visual Perception Elicited by Electrical Stimulation of the Retinal in Blind Humans", *Arch. Ophthalmol.*, vol. 114, pp. 40-46 (1996)

[5] Second Sight Medical Products, Inc., www.2-sight.com

[6] Andy Hung, David Zhou, Robert Greenberg, and Jack W. Judy, "Micromachined Electrodes for High Density Neural Stimulation Systems", IEEE Micro Electro Mechanical Systems Workshop (MEMS 2002), Las Vegas, Nevada, (January 20-24, 2002), pp. 56-59.

[7] Andy Hung, David Zhou, Robert Greenberg, and Jack W. Judy, "Dynamic Electrochemical Simulation of Micromachined Electrodes for Neural-Stimulation Systems", 1st International IEEE EMBS Neural Engineering Conference, Capri, Italy (March 20-22, 2003).

[8] W. Liu, R. Bashirulla, G. Lazzi, M. Humayun, and J. Weiland, "A Smart Bi-directional Telemetry for Retinal Prosthesis," ARVO 2002

A WIRELESS MICROSYSTEM FOR MULTICHANNEL NEURAL RECORDING MICROPROBES

Hao Yu, Roy H. Olsson, Kensall D. Wise, and Khalil Najafi
Center for Wireless Integrated Microsystems
Department of Electrical Engineering and Computer Science,
The University of Michigan
Ann Arbor, MI 48109-2122

ABSTRACT

The first fully wireless microsystem has been developed to record neural signals from multichannel microprobes. The bio-implantable microsystem can sample and digitize neural signals and accomplish wireless bi-directional data and power transmission. It can reliably receive power from an external transmitter through a 5.12MHz inductive RF link over a distance of 1mm to 15mm. A bit rate of 33kbps is achieved for sending command data to the implant, and a bit rate of 2.56Mbps is achieved for recorded data transmission over a range of 10mm. The microsystem has been used to record neural signals from a rat's motor cortex *in-vivo*. The minimum detectable signal of this microsystem is 28.8 μVrms. The entire microsystem, including the active microprobe and coils, weighs 1.2g and consumes 12.7mW. The telemetry chip is fabricated in 1.5μm AMI ABN CMOS process with a die size of 4.6 x 4.7 mm^2.

INTRODUCTION

Chronic recording of multichannel neural electrical activity by microprobes is desirable and extensively used for understanding the operation of the nervous system [1]. Electrophysiological recording of interest ranges from the potentials generated by large populations of cells to the action potentials generated by individual neurons. All of these signals are small amplitude AC signals that must be detected from a background of interfering signals from other bioelectrical activities and other noise sources. Three-dimensional multi-channel recording arrays and additional on-chip signal processing circuits have been developed to achieve high quality, high selectivity recording [2, 3].

Current usage of battery-powered or wired systems for neural recording shortens the implant life. A battery is a potential source of failure if it leaks, and electrical leads and connectors carrying DC voltages and neural signals are particularly difficult to insulate and are a source of infection. Therefore, it is desirable to design an implantable telemetry system to receive power and command data from the outside world using inductive coupling, provide power and control signals to multi-channel microelectrodes, digitize the neural signals and transmit the results outside. This kind of telemetry microsystem can be used in many other applications related to remote sensing, powering and biomedical prosthesis and it is a typical implementation of a wireless integrated microsystem (WIMS).

This paper explores the idea of using Radio Frequency (RF) inductive coupling to transmit power and bi-directional data in neural recording applications. The system diagram is shown in Figure 1. The implantable part of the microsystem is composed of a telemetry chip interfaced with an active microprobe, a power receiving coil and a transmitter antenna. An external transmitter/receiver fulfills the tasks of delivering power and transmitting/receiving data to/from the implant.

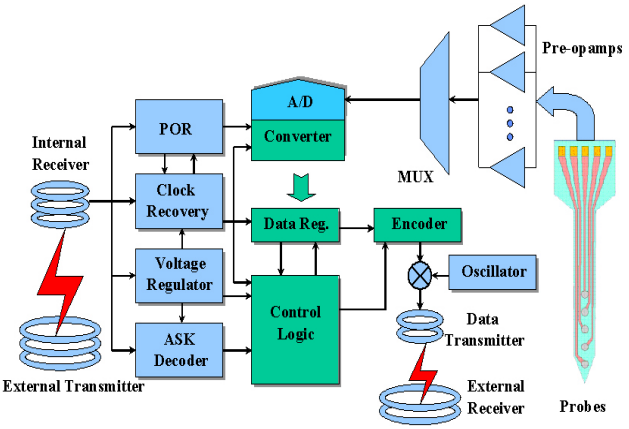

Figure 1. *Block diagram of the microsystem.*

REQUIREMENTS FOR A WIRELESS SYSTEM

Many limitation and challenges exist in the design of the implantable telemetry system, which are analyzed below:

1. Radiation Limit

The external transmitter drives the external coil to transmit power and command data to the implant. Because RF power needs to pass through biological tissues and intensive RF electromagnetic (EM) fields may cause damage to tissues, the energy absorbed by the object exposed to the EM fields is of concern. IEEE recommends a standard for safety with respect to RF exposure [4]. It is noted that different limits are adopted for electric and magnetic fields, because they have different biological effects. Usually the magnetic field limits are more relaxed than electrical field limits in high frequency. The maximum fields depend inversely on the frequency, which dictates the use of low frequency carriers (<20MHz) for power transmission. Since the coupling coefficient between an external transmitter and a small receiver coil is typically less than 5% for distances of about 10mm, care should be taken in the design of the telemetry link. To maximize efficiency, a class-E amplifier could be used for power transmission, and the physical configuration of the transmitter and receiver coils and their distance could be optimized. In addition, an appropriate RF frequency should be used to reduce transmission loss. Carrier frequency from 1MHz to 10MHz has been used in this application.

2. Temperature Increase Limit

The implanted microsystem's power dissipation should result in less than 1^{o}C temperature rise in the surrounding tissues to avoid tissue damage. A simple model is used to calculate the maximum allowable power dissipation for the microsystem [5]. If the implant size is 15 mm x 15 mm x 2 mm, a power dissipation of at least 22.6mW is needed to increase tissue temperature by 1^{o}C. If the total power dissipation of the microsystem is less than

Travel support has been generously provided by the Transducers Research Foundation and by the DARPA MEMS and DARPA BioFlips programs.

15mW, it can satisfy the maximum 1°C temperature rise requirement.

3. Channel Capacity of Data Link

Shannon's theorem gives a fundamental upper bound to the capacity of a link, C, in bits per second (bps), as a function of the available bandwidth, W, received power, P, and the channel noise modeled by an Additive White Gaussian Noise (AWGN) with power spectral density of N_0 watts/Hz, by the following:

$$C = W * Log_2(1 + \frac{P}{W * N_0})$$

It is obvious that wider channel bandwidth and higher signal power are preferred for higher channel capacity. But higher signal power increases the power consumption of the system, requiring a tradeoff between power and channel capacity.

4. Low Noise Design

Low noise electronics is another challenge in this neural recording application. Microelectrodes must be within 50-100μm of a neuron to record a usable action potential and they usually pick up signals from several adjacent neurons, which may need to be discriminated based on small differences in their waveforms. Even relatively low noise levels may degrade the reliability of such discrimination. Consequently, low noise amplifier (LNA) is necessary, especially for the active microprobe of the microsystem.

SYSTEM DESIGN AND RESULTS

The system block diagram is shown in Figure 1. It consists of the front-end circuitry that receives the RF signal from the outside transmitter, the logic and control circuitry, the on-chip Analog/Digital (A/D) converter, the active microprobe and the on-chip transmitter. The function of each of these subsystems is discussed below [3, 6].

Front-End Circuitry

The telemetry front-end receives power through the inductive link, generates regulated supply voltages, clock, reset and command data for other implantable circuits. The important front-end circuit blocks include voltage regulators, bandgap reference, ASK (amplitude shift keying) demodulator, clock regenerator and POR (power on reset). The detailed operation of these circuits is presented in [6].

For voltage regulators, line regulation is better than 1mV/V when the line voltage exceeds 6.5V, load regulation is better than 0.05V/mA when supplying a current of up to 25mA. The performance of the regulator ensures stable power supplies for implantable electronic circuits. The half-wave rectifier removes the noise by 36dB at 5.12MHz. The Power Supply Rejection Ratio (PSRR) of the regulator alone is 30dB at 5.12MHz.

The amplitude of RF carrier is modulated to transmit command bits to the implant. The ASK demodulator senses the amplitude shift of the carrier and generates raw command data. The ASK demodulator is fully-functional for data rates from 10 kbps to 400 kbps. The clock regenerator recovers the clock from the carrier and provides to the implanted electronics, which works well for carriers of up to 12MHz. The POR Circuitry generates a 303μs POR pulse whenever the microsystem is powered up to reset the entire system.

Logic Circuitry

After the ASK demodulator generates raw command data, it is further decoded by a Manchester decoder and command bits are latched into FIFO (First In First Out) registers. Manchester coding is used so that incoming data contains self-timing information after decoding, independent of the carrier frequency. If the command bits are correctly received, they will be stored in the command registers to control the functionality of the entire microsystem. Both the power supplies and time multiplexing control for the active probes are provided from the telemetry chip. The probe can be set up for single channel or multichannel recording. The control signals and operation for multichannel recording are illustrated in Figure 2.

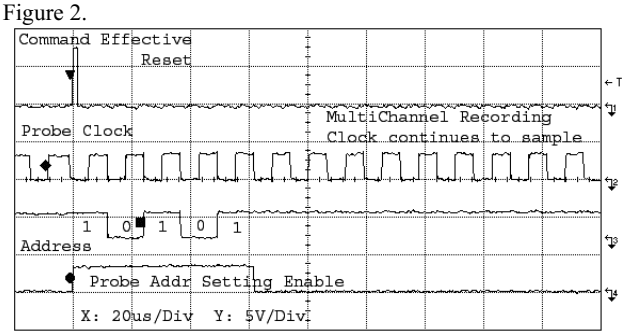

***Figure 2**. Setting up the microprobe for multichannel neural recording.*

Analog-Digital Converter

An on-chip 10-bit charge distribution ADC converts analog neural signals to digital format. The ADC sampling rate is 160kS/sec in order to sample from 8 channels with a per-channel bandwidth of 10 kHz. The maximum magnitudes of Differential Nonlinearity (DNL) and Integral Nonlinearity (INL) are less than 0.6 and 0.8 LSB, respectively. The 3dB bandwidth of the A/D Converter is 40 kHz, shown in Figure 3 and Effective Number of Bit (ENOB) is 9.3bit for input frequency below 10kHz.

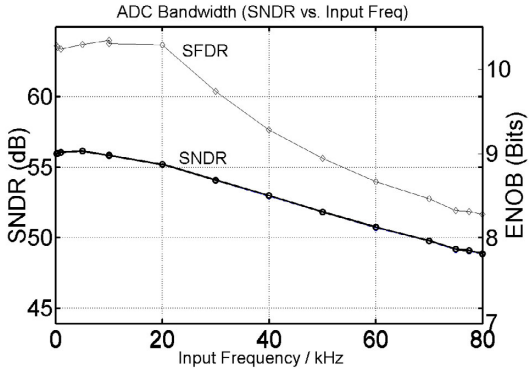

***Figure 3**. ADC bandwidth.*

Active Microprobe

A 64-site, 8-channel active neural recording array [3] has been developed as shown in Figure 4. The 100μm^2 iridium recording sites are arranged in an 8x8 array along the electrode shanks. The vertical center-to-center site spacing is 100μm while the horizontal spacing is 200μm. The shanks are 3mm in length, taper from a maximum width of 85μm at the base to a sharp tip, and are approximately 12μm thick. The probe features a 64:8 front-end selector, which allows 24 unique site combinations to be chosen for recording. Eight on-chip capacitively-coupled pre-

amplifiers [7] provide an in-band gain of 40dB while removing the dc baseline polarization of the electrode. These amplifiers have a tunable low-frequency cutoff for selective recording of action potentials alone or simultaneous recording of action and field potentials [8]. The time-division multiplexer samples the eight amplified channels onto one data lead and the active filter removes the clock artifact while providing an additional in-band gain of 20dB. The integrated circuitry occupies 5mm^2 of die area.

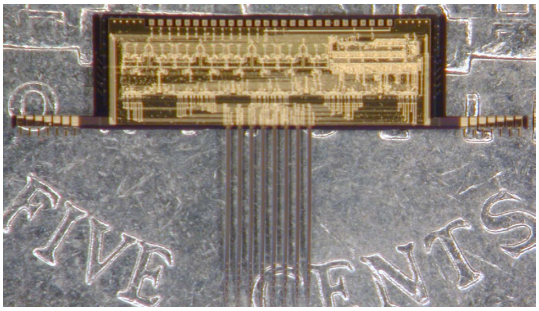

Figure 4. *Active neural recording probe on a nickel.*

On Chip Transmitter

Digitized results are sent to the external receiver by the on-chip transmitter, whose carrier frequency is adjustable in FCC unlicensed band from 88 to 108 MHz by trimming capacitors in the on-chip ring oscillator. Feature bits are used to synchronize external receiving scheme.

A measurement is carried out to test the data communication link. The transmitter's loop antenna is built by 7-turn of AWG #38 copper wire, with a diameter of 8mm. An external receiving antenna is built by 30 turns AWG 32 copper wire with a ferrite core, its diameter is 12mm and length is 20mm. These two antennas are placed 10mm apart from each other. After the signal is received by the external antenna, it is amplified, filtered and fed to an OOK (On-Off-Keying) demodulator. The real-time demodulated digital output is compared with on-chip transmitter input data in Figure 5, where the data rate is 2.56 Mbps. The recovered data is sampled and saved for analysis.

The BER (Bit Error Rate) is an important criterion to evaluate the quality of a digital communication channel. The BER is measured to be less than 10^{-7} when the transmission distance is less than 15mm in this measurement.

Detailed measurements of the BER have been carried out and generally indicate that for distances of up to 15mm, the system operates reliably for bi-directional data and command transmission. It has been shown that RF power transmission does not degrade the recorded data transmission quality. The carrier frequency of the on-chip transmitter is 103 MHz for the measurement. When the distance between two antennas is 5mm, the induced 103 MHz sinusoid across the external receiver loop antenna is 56 mV (p-p), while the induced 5.12MHz sinusoid across the external receiver loop antenna due to power transmission is 740mV (p-p). However, the 5.12MHz noise is effectively attenuated because of the usage of a VHF-UHF amplifier and bandpass filter in the external receiver. At the output of the bandpass filter, the ratio of 103MHz signal to the 5.12MHz noise is 52dB.

In-vitro Measurement

In-vitro testing is carried out to verity the functionality of the microsystem in a wireless single-channel recording configuration.

The microsystem is powered by an RF link and placed in a saline solution, while the active microprobe's power supply and control logic are provided from the telemetry chip. The distance between the power transmitter coil and the receiver coil is 5mm. An on-chip air-core loop antenna is separated by 5mm from an external ferrite-core loop antenna to transmit recorded data.

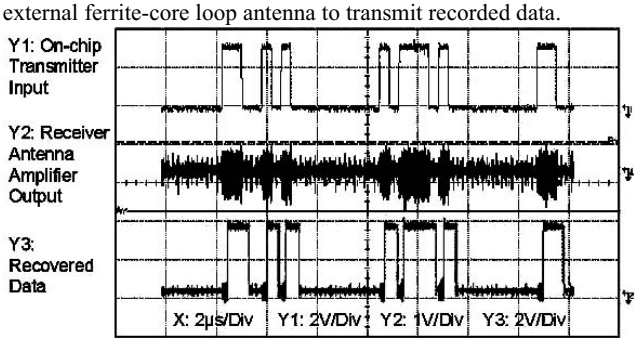

Figure 5. *Real time OOK communication (2.56Mbps).*

A 1 kHz sinusoid with an amplitude of 2mV (peak-to-peak) is fed to the saline solution, and the external antenna receives the transmitted digital results. The signals are reconstructed in MATLAB and its spectrum is plotted in Figure 6. SNDR (Signal to Noise & Distortion Ratio) in neural band (300Hz – 10 kHz) is 26dB, and the measured signal is 45-50dB above the noise floor. The noise of the microsystem was also characterized in *in-vitro* measurement to be 28.8 uVrms (root mean square), which dictates the MDS (minimum detectable signal) of the system.

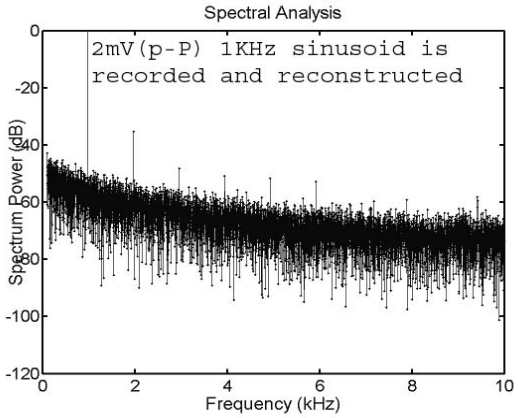

Figure 6. *Spectrum of the received signal for in-vitro testing.*

In-vivo Measurement

As shown in Figure 7, the implantable part of the microsystem is composed of a telemetry chip interfaced with an active microelectrode, a power receiving coil and a data transmission antenna. They were assembled on a flexible board, which could be easily bended and was chosen for the convenience of implanting.

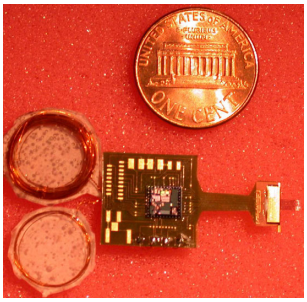

Figure 7. *The assembled microsystem.*

The microsystem shown above has been tested in animals to verify in-vivo operation in acute studies. The microsystem was

implanted in the motor cortex of the rat [9], and the animal was administered general anesthesia throughout the surgical procedure. The microprobe was inserted to the point where the recording sites were estimated to be 0.5–1.2 mm below the cortical surface.

The *in-vivo* results are shown in Figure 8, where each channel from 8 channels is recorded for 0.95 second. The preamplifiers provide a total gain of 1,600 in this measurement. If referred to the input of the active microprobe, the average noise of 8 neural channels is 52 Vrms in this measurement. The plotting is expanded to show a detailed spike in channel 6.

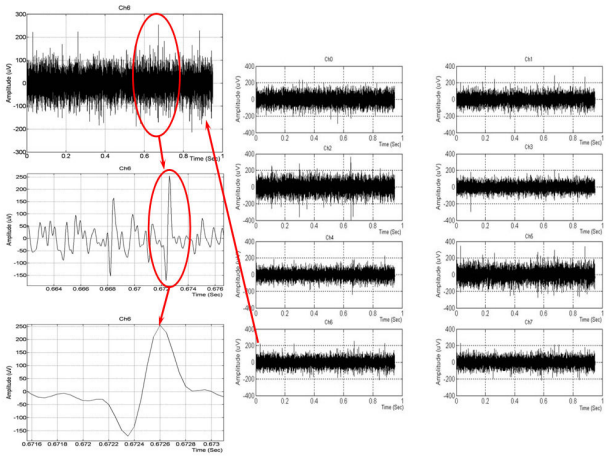

Figure 8. *The recorded multichannel neural signals in-vivo.*

Finally, Table 1 summarizes the performance specifications for the entire system and its individual circuit blocks.

Circuit Blocks	Specification	Power Consumption
Four Regulators	Line Regulation: <1mV/V (input 6.5-20V) Load Regulation <0.05mV/mA (I_{load} <25mA) VDD1 = 3.4V VDD2 = 1.7V	For Entire Front-End Circuitry 527µW
Clock Recovery	Recover up to 12MHz clock	
POR	POR Pulse width = 303µs	
ASK	Data rate: 10k-400kbps Carrier frequency: 5.12MHz Modulate depth: 30%	
Control Logic		3.1mW
On-chip Transmitter	Carrier Frequency: 88-108MHz Bit rate: 2.56 Mbps, Bit error rate < 10^{-7}	2.2mW
10-bit Charge Re-distribution ADC	Clock: 2.56MHz	1.1mW
	Speed: 160 kS/s	
	ENOB: 9.3 bit	
	|DNL|<0.6LSB, |INL|<0.8LSB	
	3dB Bandwidth: 40kHz	
Active Microprobe	8 Channel Time-multiplexing	2.73mW
Die Size	4.6 x 4.7 mm^2	Total Power 12.7mW
Process	Double poly, double metal AMI ABN 1.5µm CMOS	

Table 1. *Summary of the System Performance.*

CONCLUSIONS

The first fully wireless microsystem for multichannel neural recording has been reported. It includes a telemetry chip, an active neural recording microprobe, a power receiving coil, a data transmission antenna and an external transmitter/receiver. Powered by a wireless RF link, the bio-implantable microsystem can sample and digitize neural signals by using an on-chip 10-bit charge-redistribution A/D converter. Digitized results are sent to the external receiver by an on-chip OOK transmitter, whose nominal carrier frequency is in the FCC unlicensed band, from 88 to 108MHz. The command data is transmitted to the implant by modulating the amplitude of the 5.12MHz power delivery carrier. The microsystem has been tested *in-vitro* and *in-vivo*. Fully integration of the microsystem enhances the reliability and accuracy of the system. This microsystem consumes a total of 12.7mW and is fabricated in AMI ABN 1.5µm CMOS process.

ACKNOWLEDGEMENT

The authors thank Dr. D. Anderson, Dr. D. Kipke, B. Casey, K. Kong, A. Hoyord, R. Vetter for timely helps in testing. This project is supported by NIH-NINDS contract 5N01NS002329-001 and this work made use of Engineering Research Centers Shared Facilities supported by the National Science Foundation under Award Number EEC-0096866. Travel support has been generously provided by the Transducers Research Foundation and by the DARPA MEMS and DARPA BioFlips programs.

REFERENCES

1. T. Akin, K. Najafi, R. M. Bradley, "A Wireless Implantable Multichannel Digital Neural Recording System for a Micromachined Sieve Electrode," *IEEE J. Solid-State Circuits, Vol. 33, No. 1*, pp. 109-118, Jan. 1998

2. M. D. Gingerich, "A Programmable Multichannel Microstimulator with Bi-directional Telemetry", *Ph.D. Thesis, UM-EECS Technical Report No. SSEL-254*

3. R. H. Olsson III, M. N. Gulari, and K. D. Wise, "Silicon Neural Recording Arrays with On-Chip Signal Processing for In-Vivo Data Acquisition," *presented at IEEE-EMBS Special Topic Conference on Microtechnologies in Medicine and Biology, Madison, WI*, 2002

4. IEEE Standards Coordinating Committees, "IEEE Standard for Safety Levels with Respect to Human Exposure to Radio Frequency Electromagnetic Fields, 3kHz to 300GHz", *IEEE C95.1-1991,* pp13, pp20

5. K. Najafi, "Multielectrode Intracortical Recording Arrays with On-Chip Signal Processing", *Ph.D. Thesis, UM-EECS Technical Report No. SSEL-177*

6. H. Yu, K. Najafi, "Low-Power Interface Circuits for Bio-Implantable Microsystems", *ISSCC 2003*, San Francisco, Feb 2003

7. R. H. Olsson III, M. N. Gulari, and K. D. Wise, "A Fully Integrated Bandpass Amplifier for Extracellular Neural Recording," *1st International IEEE EMBS Conference on Neural Engineering*, Capri, 2003

8. R. H. Olsson III, D. Buhl, M. N. Gulari, G. Buzsaki, and K. D. Wise, "A Silicon Microelectrode Array for Simultaneous Recording and Stimulation in the Brain of Behaving Animals," *presented at 25th Annual Meeting of the Engineering in Medicine and Biology Society,* Cancun, 2003

9. D. R. Kipke, R. J. Vetter, J. C. Williams, J. F. Hetke, "Silicon-substrate Intracortical Microelectrode Arrays for Long-term Recording of Neuronal Spike Activity in Cerebral Cortex", *IEEE Transactions on Neural Systems and Rehabilitation Engineering, Volume: 11 Issue: 2 , June 2003,* pp. 151 -155

A MICROMACHINED PLANAR PATCH-CLAMP CHIP WITH INTEGRATED MICROFLUIDICS

Brian Matthews and Jack W. Judy
Department of Electrical Engineering, University of California, Los Angeles
Los Angeles, California, 90095

ABSTRACT

We have designed, fabricated, integrated, and tested microfabricated planar patch-clamp substrates and poly(dimethylsiloxane) (PDMS) microfluidic components suitable for use in an automated planar patch-clamp dose-response measurement system. Substrates with cell-patch-site aperture diameters ranging from 300 nm to 12 μm were produced using standard MEMS fabrication techniques. The resistance of the cell-patch sites and substrate capacitance were measured using impedance spectroscopy. The resistance of the cell-patch sites ranged from 200 kΩ to 47 MΩ for apertures ranging from 12 μm to 750 nm respectively. The substrate capacitance was 17.2 pF per mm^2 of fluid contact area for substrates with a 2-μm-thick layer of silicon dioxide. In addition, testing shows that the fluidic components are appropriate for driving human embryonic kidney cells (HEK 293) to patch apertures, for trapping cells on patch apertures, and for rapidly exchanging the extracellular fluid environment.

I. INTRODUCTION

ION-CHANNEL proteins, which are embedded in cell membranes, control the flow of ions through the membrane and are gated by chemical, electrical, or mechanical stimuli. The ionic currents generated from the gating of ion-channels control many cellular processes, such as cell-signaling pathways and have been studied extensively using the patch-clamp technique. The patch-clamp technique is a powerful tool for the investigation of many electrophysiological cell properties, such as the characterization of the kinetics and steady-state effects of toxins, chemical

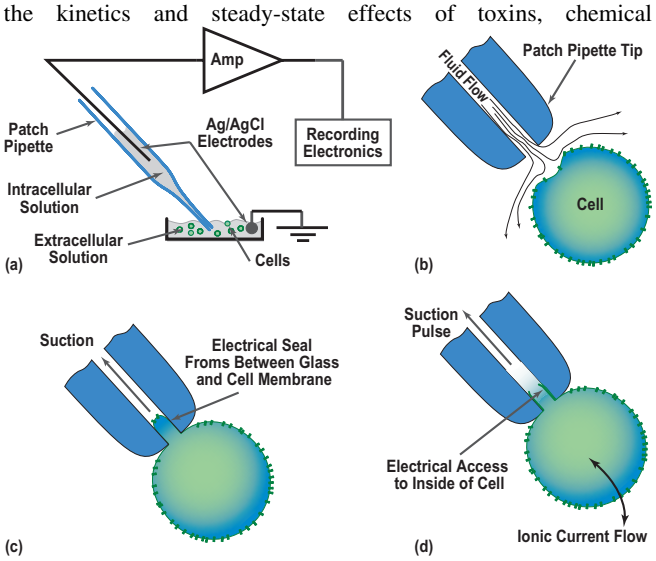

***Fig. 1**. (a) Schematic representation of a traditional patch-clamp system using a pulled-glass pipette. (b) The pipette is positioned close to a cell with positive pressure to prevent contaminating the tip with debris from the solution. (c) Suction is applied to the pipette and a highly resistive electrical seal (i.e., gigaohm seal) is formed at the interface between the glass and cell membrane. (d) A suction pulse is applied, and the cell membrane inside the pipette lumen is ruptured to provide direct electrical access to the inside of cell.*

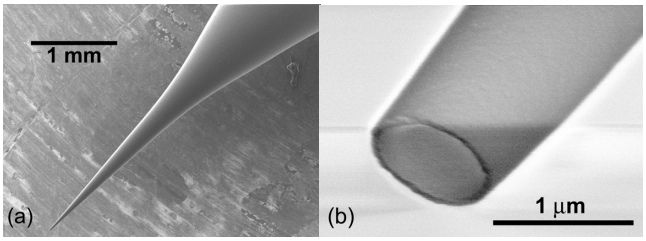

***Fig. 2**. (a) SEM of an uncoated traditional patch-clamp pipette and (b) close-up of the pipette tip.*

agonists, antagonists, and drugs in ion channels, transporters, and pumps [1]. Specifically, the patch-clamp technique enables the measurement of ionic current flowing through the cellular membrane by creating isolated electrical connections to the inside and outside of a cell membrane (Fig. 1). In the traditional patch-clamp technique, an approximately 1.5-mm-diameter glass capillary is heated and pulled apart to form a pipette with a tip diameter of 500 nm to 10 μm, depending on the intended application (Fig. 2) [2]. The pipette is filled with a suitable solution and electrically connected to electronics for amplification and recording, via a Ag/AgCl non-polarizable electrode. The pipette is then used to electrically isolate the intracellular and extracellular sides of a small patch of membrane. By forming a seal to the membrane and achieving electrical isolation on the order of gigaohms, the pipette is able to record currents passing through the membrane to a ground electrode (Fig. 1a). Using the configuration shown in Fig. 1, it is possible to investigate the electrical and chemical dependencies of ion channels. Although the traditional equipment used to perform the patch-clamp technique has been very successful, conventional pipettes are not easily adapted to all the applications for which the patch-clamp technique would be useful. Examples of electrophysiological applications that would benefit from uniquely tailored patch-clamp systems include measuring dose-response curves for single cells, high-throughput screening, applications needing optical access to the cell (e.g., confocal and florescence microscopy), and applications needing rapid intracellular perfusion.

II. MOTIVATION

With the advent of micromachining and micro-electromechanical systems (MEMS) technologies, specifically engineered patch-clamp systems can be realized. Microfabricated patch-clamp systems hold the promise of parallelism, microfluidic manipulation, uniformity, optical access, and automation that is currently impossible to obtain with traditional pulled-glass capillary systems. Although microfabricated structures have been used to patch to cells with gigaohm seals in academic and commercial laboratories, these devices do not patch with high reliability, have not been integrated into miniaturized systems, or have solely targeted high-throughput screening [4-13]. The ultimate goal of this work is to develop a set of microfabrication processes that are flexible enough to address a number of application-specific patch-clamp configurations and to create a microfluidic system capable of performing complex electrophysiological experiments on individual cells.

0-9640024-5-0/hh2004/$20©2004TRF
DOI 10.31438/trf.hh2004.32

Solid-State Sensors, Actuators, and Microsystems Workshop
Hilton Head Island, South Carolina, June 6-10, 2004

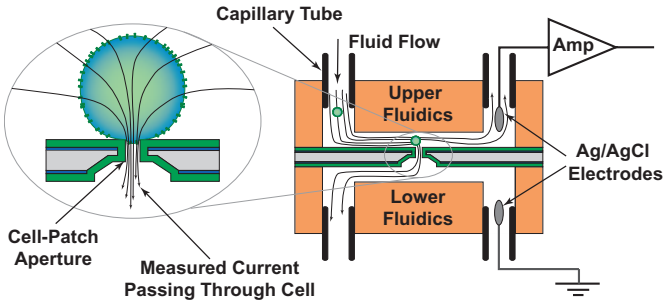

Fig. 3. Schematic diagram of a planar patch-clamp dose-response measurement system.

III. DESIGN

Our initial effort will be to microfabricate a system capable of automating the measurement of single-cell dose-response curves in stablely transfected human embryonic kidney (HEK), Chinese hamster ovary (CHO), and other cell lines. Dose-response measurements are used to evaluate the effect of chemical concentration on ion channels. Therefore, it is necessary for a dose-response system to be able to apply different concentrations of a chemical in a precise and repeatable way. Such an automated system will necessarily include the base components needed for most specialized patch-clamp experiments. Components such as: a suitable cell-patch site, Ag/AgCl electrodes, microfluidic components to precisely control intracellular and extracellular solutions, good optical access, and system-wide mechanisms to control the recording process.

The optimal diameter for cell-patch sites dependings on the particular application and the size of cell being investigated. Cell lines such as HEK, CHO, and others typically have cell sizes ranging from 7 µm to 10 µm. Acceptable cell-patch-site diameters, when working with cells of this size, are from 500 nm to 2.5 µm. Although, the target aperture size for this project was 1 µm, the design of the process allows for adjustments in this diameter to be made without changing the mask set. Silicon dioxide was chosen as the surface material for the cell-patch sites in an attempt to simulate traditional pulled-glass pipettes.

The initial design of the microfluidic components was made intentionally simple. The design of the topside microfluidic system includes eight ports that provide direct fluid access to a patched cell: a cell-injection port, six solution-exchange ports, and a waste port (Fig. 4). For this initial microfluidic system, the front-side channels are 30-µm wide and 30-µm deep.

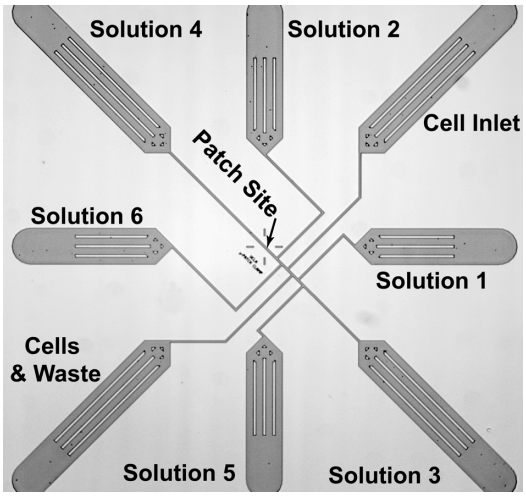

Fig. 4. Overview of the eight-port microfluidic system.

When used for conventional dose-response measurements, the six solution-exchange ports can be configured to provide a patched cell with six different premixed concentrations of a chemical. In this configuration the six predefined chemical concentrations are sequentially applied to a cell in a continuous fashion and for a period of time necessary for the cell response to reach equilibrium.

An alternative method of delivering chemical stimuli to a patched cell is with the use of sample plugs. A sample plug can be formed by a pair of offset solution-exchange channels crossing the cell-injection channel. This microfluidic configuration is similar to the sample-preparation methods used in capillary electrophoresis systems [14]. The sample plugs can be used to study the kinetics of ion-channel activation and deactivation. Currently backside fluidic connections consist of a simple two-port structure machined into the polycarbonate test fixture that connects to the backside of the cell-patch aperture

Similar to traditional patch-clamp pipettes, we anticipate that planar patch-clamp chips cannot be reused once a recording is made. Because of the single-use nature of the system, it is necessary for the planar system to have an easy method for exchanging chips. In order to facilitate quick macrofluidic connections, the microfluidics are fabricated with a thick layer of PDMS containing integrated access ports capable of accepting capillary tubing without the need for glue. The completed, assembled and plumbed system is shown in Fig. 5.

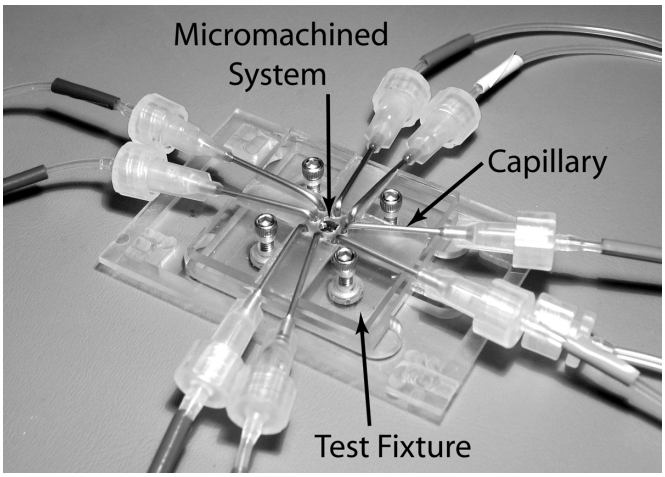

Fig. 5. Photograph of the macroscopic test fixture with eight capillaries connecting to the micromachined planar patch-clamp system.

IV. FABRICATION

A. Silicon-Based Patch-Clamp Substrates

The fabrication process of the substrates containing the cell-patch sites is a two-mask process and was carried out at the UCLA Nanoelectronic Research Facility. A schematic cross section of a substrate is given in Fig. 6a. The process begins with a 100-mm-diameter p-doped {100} silicon wafer. (Silicon Quest International).

The wafers are cleaned in 5:1 H_2SO_4 : H_2O_2 (piranha) and inserted into a low-temperature low-pressure chemical-vapor-deposition (LPCVD) furnace at 790 °C and 33 Pa (0.25 torr) with 40 sccm of SiH_2Cl_2 and 108 sccm of NH_3 in order to deposit 200 nm of silicon nitride (Si_3N_4) (Tystar Titan II). The first photolithography step is then performed on the backside of the wafers using AZ5214EIR photoresist (Clariant Ltd.) using a standard process provided by the resist manufacturer [13].

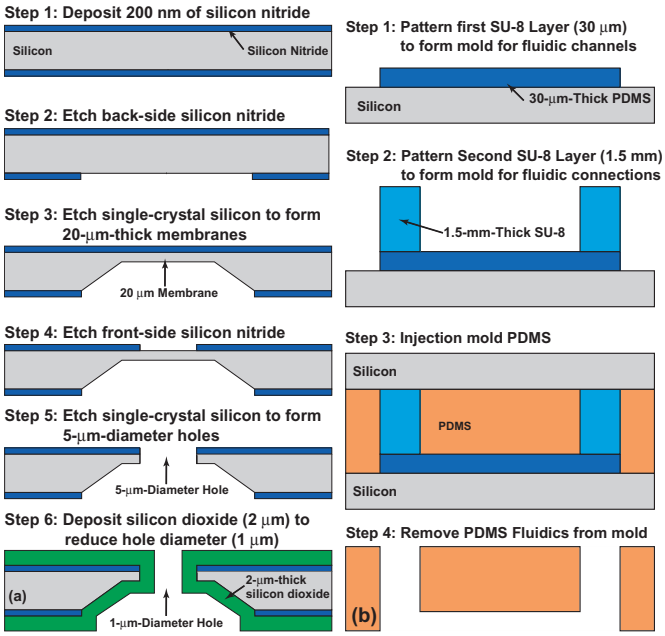

Fig. 6*. (a) Cell-patch-site fabrication process and (b) microfluidic fabrication process.*

Openings in the backside silicon nitride layer are then etched in a reactive ion etcher (RIE) at 13 Pa (0.1 torr), 200 W, and 5:1 CF_4:O_2 for 3 min (Techniques Fluorine RIE 800). The wafers are then striped of photoresist and submerged in a 30% solution of KOH to etch the single-crystal silicon to form membranes as defined by the backside silicon-nitride openings. As there is nothing to stop the KOH from completely etching through the wafer, it is necessary to carefully monitor the etch rate and remove the wafers at the appropriate time.

The wafers are then cleaned and the second photolithography step is performed, again using AZ5214EIR, to define the cell-patch sites. The front-side silicon nitride is then etched using the same RIE process as the backside silicon nitride. A deep reactive ion etcher (DRIE), using a standard Bosch59 process, is then used to create a hole through the membrane that forms the cell-patch site (PlasmaTherm SLR Series). Once the hole is formed, the wafers are cleaned in piranha for 20 min and then further cleaned in an oxygen plasma at 150 °C, 66 Pa (0.5 torr), and 200 W for 30 min (Tegal Plasmaline 515). This cleaning is necessary to remove the fluorine-based polymer deposited in the DIRE process.

The wafers are then cleaned again in piranha for 10 min and placed into either an LPCVD furnace or a thermal-oxidation furnace to deposit a layer of silicon dioxide (SiO_2) (Tystar Titan II). The 2-μm-thick layer of LPCVD SiO_2 is deposited at 450 °C and 33 Pa (0.25 torr) with 43 sccm of SiH_4 and 60 sccm of O_2. For wafers receiving thermal oxidation, the silicon nitride was removed from both sides of the wafer using the RIE process described above. The 2-μm-thick layer of thermal SiO_2 is grown at 1100 ºC for 8.5 hr in the presence of saturated water vapor. Because the oxide deposition techniques are conformal, the deposited film will coat the sidewalls of the hole, thereby reducing its diameter. Silicon dioxide, in addition to reducing the diameter of the hole, will form a surface onto which cells can form a tight seal. It is therefore possible to fabricate cell-patch sites with a wide range of diameters and with diameters smaller than the lithographic capabilities of our optical mask aligner. The wafers are then cleaved into 1-cm^2 dice in preparation for testing. After cleaving, the backsides of several substrates are bonded to 1–mm-thick poly(dimethylsiloxane) (PDMS) gaskets with 1-mm^2 openings in order to investigate the effect of fluid contact area on capacitance.

B. Microfluidics

The microfluidic components of the system were fabricated by molding PDMS onto a two-level SU-8 mold master [15]. Schematic cross sections of the process are given in Fig. 6b. The first layer of SU-8 is then deposited on a 100-mm-diameter silicon wafer using a standard process provided by the resist manufacturer [16]. This first layer is made from 30-μm-thick SU-8 2025 and forms the mold for the microfluidic channels. The second layer of SU-8 is fabricated from a 2-mm-thick layer of SU-8 2100 and forms the macroscale fluid-access ports. The fabrication process for the second SU-8 layer is adapted from a process developed by Lin *et. al.* and is described below [17].

Because a 2-mm-thick layer of SU-8 will flow off the edges of the wafer when brought above the glass transition temperature, a 2-mm tall casting barrier is first glued around the periphery of the silicon wafer containing the first SU-8 layer. The wafer is then dehydrated at 150 ºC for 10 min. A pre-measured amount of SU-8 2100 is then poured into the casting barrier to form a 2-mm-thick layer of SU-8. The pre-exposure bake is then performed at 120 ºC for 8 hr without initial ramping of the hotplate. At the end of the 8-hr softbake time, the hotplate was cooled to 60 ºC and held for 5 min. The temperature is then ramped down to 50 ºC at a rate of 20 ºC·hr^{-1}. The wafer is then exposed with a total exposure dose of 5.6 J·cm^{-2} (Karl Suss MA6). The post exposure bake is performed at 65 ºC for 10 min and then 100 ºC for 10 min starting from room temperature with a ramp rate of 150 ºC·hr^{-1}. The wafer is then submerged in SU-8 developer until the features are completely developed, a process that typically takes 1 to 2 hr (SU-8 Developer, Micro Chem). After being fully developed, rinsed, and dried, a flood exposure of 5.6 J·cm^{-2} and hard bake of 150 ºC for 10 min are then performed to further crosslink the SU-8 and drive off residual solvent.

Once complete, the SU-8 mold master is used to create the PDMS microfluidic components. In order to ensure that the macroscale fluidic access ports remain unoccluded during the casting process, a blank silicon wafer is then clamped on top of the SU-8 mold master and PDMS is then injected into the interstitial space between the two wafers. The PDMS is cured in an oven at 65 ºC for 1 hr (Blue M). Subsequent to curing the PDMS is removed from the mold master and cut to form 1-cm dice. The macroscale fluid-access ports provide an easily operated and robust fluidic connection technology that seals to capillary tubing without glue.

Patch-clamp substrates and PDMS microfluidics were aligned and bonded using a mask aligner/bonder (Karl Suss MA-6). Prior to bonding the patch-clamp substrates and PDMS microfluidics are exposed to an oxygen plasma (100 W for 1 min) to modify the PDMS surface to form a bond with adhesion strength greater than that of the bulk PDMS [18].

V. EXPERIMENTAL RESULTS

A. Physical Properties

The physical properties of the cell-patch sites were investigated using a scanning electron microscope (SEM) on uncoated samples (Hitachi S4700). The micrograph in Fig. 7 shows the smoothness and cleanliness of a cell-patch site prior to silicon dioxide deposition. It was found that if the cell-patch site had any residual polymer or other debris from the DIRE, the silicon dioxide layer would deposit in a non-uniform manner. The result is an out-of-round aperture unsuitable for seal formation. The micrograph in Fig. 8 is an example of typical cell-patch site.

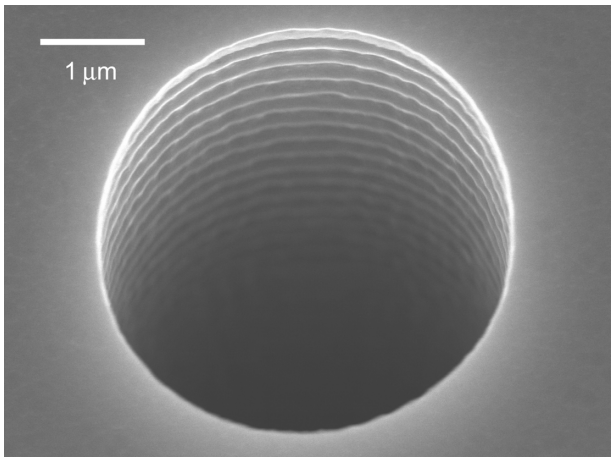

Fig. 7*. Cell-patch site before oxide deposition or growth.*

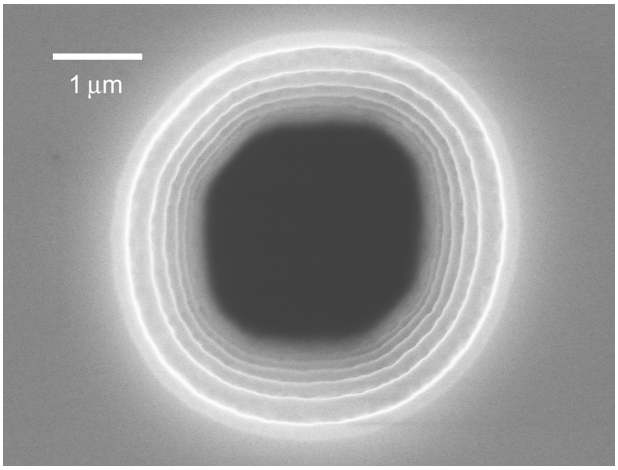

Fig. 8*. (b) An example of a 2.5-μm-diameter cell-patch site made of thermal SiO_2.*

B. Electrical Properties

The small signals generated by ion channels in patch-clamp experiments can be obscured by noise from the following general categories: biological sources, experimental apparatus, and the interface with the experimental apparatus to the biology. Contributions to the general noise categories are made by many sources in the experiment, such as the amplifier, cell membrane, glass-membrane seal, pipette holder, pipette, and interactions between all of these sources [19]. Because the proposed devices are replacing the pipette holder and pipette used in traditional patch-clamp experiments, the noise sources associated with these replaced components must be well understood. In conventional patch-clamp systems the pipette holder and pipette contribute to several noise terms through lossy dielectrics, capacitance added to the amplifier input by the pipette holder and pipette, distributed RC noise, and noise arising from the resistance of the pipette in series with the cell membrane. As a general rule, in attempting to perform low-noise single-channel recordings, it is advantageous to reduce both the series resistance and capacitance traditionally associated with the pipette. As an example, reducing the capacitance of the pipette will reduce dielectric noise that results from the thermal fluctuations in lossy dielectrics.

In order to extract the series resistance and capacitance of our substrates, a potentiostat was used to measure their impedance spectra (EG&G Instruments 283 and Solatron SI 1260). To perform measurements the samples were place in a testing apparatus and electrically isolated 100-mM-KCl electrolyte solutions were placed in contact with the frontside and backside of the substrate. An Ag/AgCl non-polarizable electrode was then placed into each KCl electrolyte solution. The Ag/AgCl electrodes were connected to the potentiostat and the impedance spectra were measured using a 10-mV excitation voltage with a 1 Hz to 10^5 Hz frequency range. The equivalent circuit, shown in Fig. 9a, was used to model the impedance spectra. The series resistance of the aperture and the substrate capacitance in the circuit model were fitted to the measured impedance spectra.

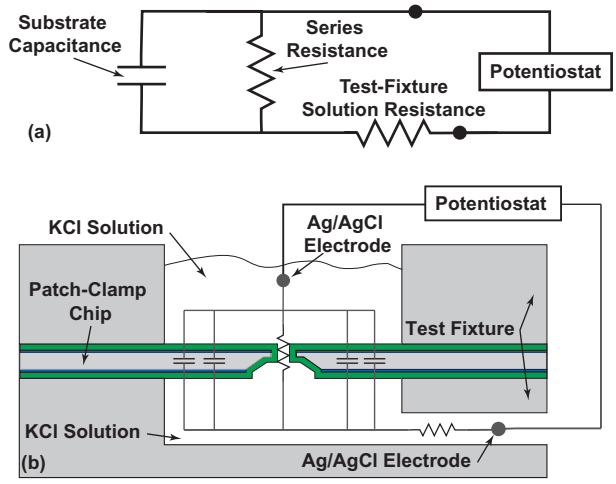

Fig. 9*. (a) Equivalent-circuit model of cell-patch-site substrates. (b) Schematic diagram showing physical locations of parameters in the equivalent circuit model.*

Simple resistance and capacitance models were developed for the substrates and are illustrated in Fig. 9b. The overall system resistance is dominated by the conductance of the cell-patch-site apertures because of their small dimensions relative to the rest of the conducting path. Therefore, system resistance can be acceptably modeled by only taking into account the cell-patch-site resistance. The cell-patch site can be modeled as a conductor with a resistivity matching that of the KCl solution. This model is given by

$$R = \frac{\rho l}{A} \tag{1}$$

with resistance R, resistivity of the KCl solution ρ, cross-sectional area of the conductor A (i.e. the area of the aperture), length of the conductor l (i.e. the thickness of the membrane).

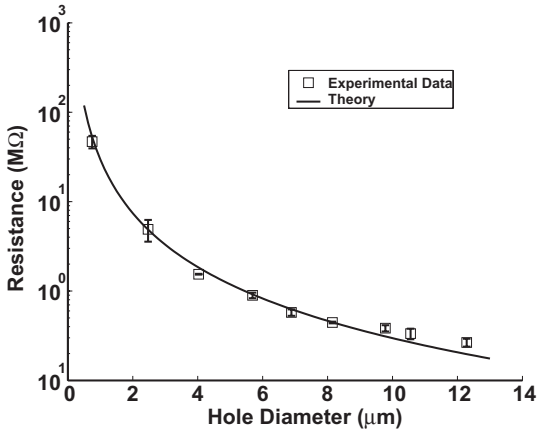

Fig. 10*. Modeled cell-patch-site resistance and measurements.*

The impedance spectra and cell-patch-site diameter for a total of 27 thermally oxidized substrates were measured. Fig. 10 shows good agreement between the average resistance of nine different cell-patch-site diameters (0.8, 2.5, 4.0, 5.7, 6.9, 8.2, 9.8, 10.6, and 12.3 μm) and the modeled cell-patch site resistance. The data points in the plot indicate the average of resistance measurements made from three different substrates while the error bars indicate the standard deviation.

The model for the capacitance of the substrate is given by

$$C = \left(\frac{1}{C_F} + \frac{1}{C_B} \right)^{-1} = \frac{\varepsilon_r \varepsilon_o A_F A_B d_F d_B}{A_F d_B + A_B d_F} \quad (2)$$

with total capacitance C, front-side and back-side capacitances C_F and C_B respectively, relative permeability of the dielectric material ε_r, permeability of free space ε_o, the area of fluid contact, A and thickness of the dielectric layer d on the frontside (F) and backside (B) respectively. Equation (2) models the two capacitors formed by the conducting parallel plates of KCl solution and the silicon substrate separated by the silicon dioxide dielectric. Fig. 11 shows good agreement of the experimental data with the theoretical model and indicates that a small fluid-contact area is critical to achieving low-noise recordings. The data points in the plot indicate the average of capacitance measurements made from three different substrates while the error bars indicate the standard deviation.

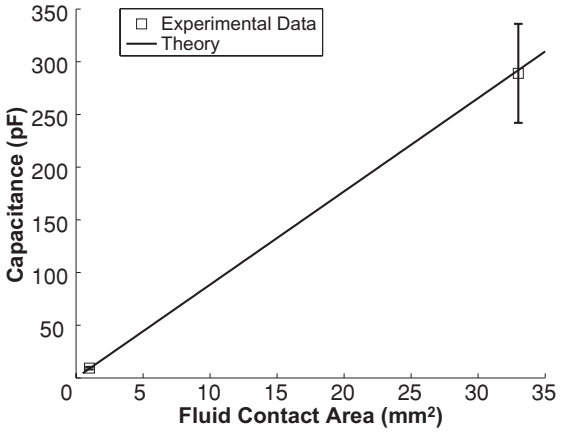

Fig. 11. Modeled substrate capacitance and measurements.

C. Microfluidic Properties

In operation, the fluidic system must be able to perform several tasks involving cell handling and fluid switching. For cell handling, the system must be able to drive a suspension of cells past the cell-patch aperture and trap a single cell from the suspension onto the aperture without damaging it. Once a cell is trapped on the patch site, the fluidic system must be able to switch fluids flowing past the patched cell in order to test the response of the cell to different test solutions. Qualitative tests have been made in order to test both cell trapping and fluid exchange properties of the microfluidic components of the system.

For the cell trapping tests, HEK cells are removed from cell-culture flasks and suspended in standard Hank's balanced salt solution (HBSS). The cells are driven from the cell-inlet port, past the cell-patch aperture via a pressure differential with the waste port. In order to trap a cell onto a patch aperture, a pressure deferential is applied between the cell-inlet port and the backside port so that there is a net flow of fluid through the cell-patch aperture. When a cell is trapped, the pressure differential across the

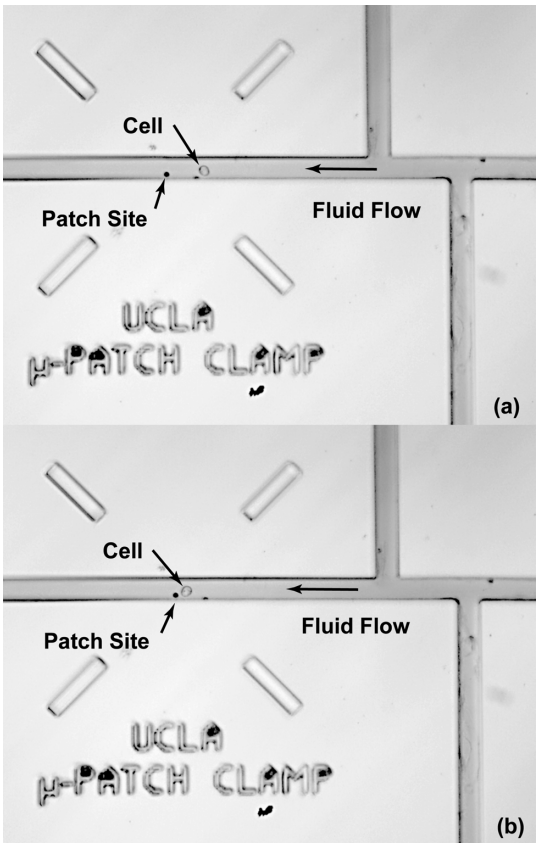

***Fig. 12**. Photograph of cell in microfluidic channel that is flowing toward a cell-patch site.*

cell-patch aperture should be no more than 4 kPa, because a higher pressure could result in cell rupture before seal formation [21]. Using this method HEK cells have been successfully driven through the fluidic system and trapped on a cell-patch aperture (Fig. 12,13). Once a cell has been successfully trapped on a cell-patch aperture and a gigahom seal is made and the effect of ion-channel gating compounds can be tested by flowing an alternating sequence of buffer and ion-gating compounds past the cell. In order to qualitatively test the switching characteristics of the fluidic system, dyes representing ion-channel-gating compounds were driven through the system simulating extracellular fluid exchange (Fig. 14).

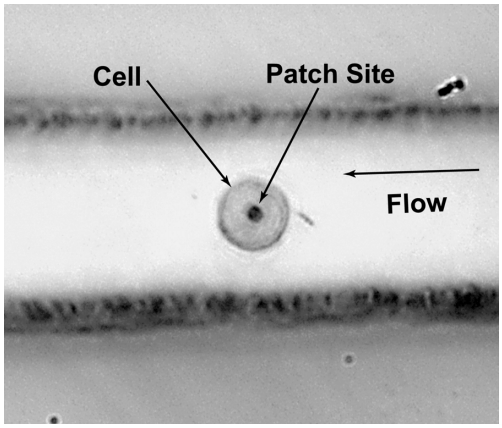

***Fig. 13**. Photograph of a cell in a microfluidic channel that has been trapped onto a cell-patch site.*

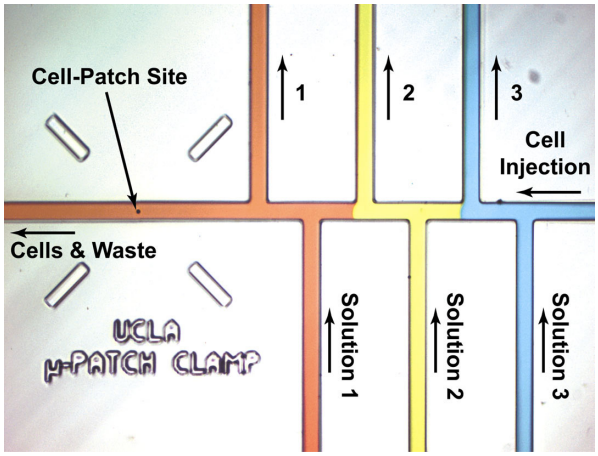

Fig. 14*. Higher magnification photograph of the microfluidic system shown in Fig. 4. Three solutions are being passed through the microfluidic system to illustrate the formation of sample plugs.*

D. Sealing

The formation of a gigaohm seal between the cell-patch aperture and the cell membrane is an essential component of patch-clamp measurements. Without this seal, ions can leak between the membrane and patch aperture resulting in measured current that does not pass through ion channels and therefore contributes to error in the desired measurement. Currently, we are unable to form gigaohm seals with the microfabricated cell-patch apertures. This issue is currently the critical-path item limiting progress in the overall system. The primary reasons for poor seal formation in the microfabricated patch-clamp chips are hypothesized to be (1) fouling of the surface during microfabrication, (2) inappropriate surface roughness, (3) incorrect geometry of the patch aperture, or (4) fouling of the surface during cell capture. Experiments are currently underway to understand the dependence of these problems on sealing performance.

VI. CONCLUSIONS

Specifically-engineered patch-clamp systems present an opportunity to simplify currently difficult-to-perform electrophysiology experiments. The first steps toward an automated single-cell dose-response-curve-measurement system have been made. To date, we have fabricated substrates containing cell-patch sites, fabricated PDMS microfluidic components, and integrated the two. The geometric and electrical properties of the silicon cell-patch substrates have been investigated and found to be suitable for patch clamping. Qualitative tests have been undertaken with the microfluidic components of the system to test cell handling and fluid switching. Although cells can be captured and different solutions can be controlled, gigaohm seal are elusive. Once gigaohm seals are reliably achieved, our patch-clamp system will hold the promise of parallelism, microfluidic manipulation, uniformity, optical access, and automation that is currently impossible to obtain with traditional patch-clamp systems.

ACKNOWLEGEMENTS

Supported by Center for Cell Mimetic Space Exploration (CMISE), a NASA University Research, Engineering and Technology Institute (URETI), under award number #NCC 2-1364. Travel support has been generously provided by the Transducers Research Foundation and by the DARPA MEMS and DARPA BioFlips programs. We would also like to acknowledge the support of Prof. Montemagno's laboratory for their assistance with cell culturing and the intellectual collaboration of our colleagues in the UCLA Neuroengineering Program.

REFERENCES

[1] D. Purves, G. Augustine, D. Fitzpatrick, L. Katz, A. LaMantia, and J. McNamara, Eds. Neuroscience, Sinauer Associates. Massachusetts, 1997.

[2] Neher, E., and Sakmann, B., 1976, Single-channel currents recorded from membranes of denervated from muscle fibers, *Nature* 260:799-802.

[3] R. Pantoja, D. Sigg, R. Blunck, F. Bezanilla, and J. R. Heath, "Bilayer reconstitution of voltage-dependent ion channels using a microfabricated silicon chip," *Biophys. J.,* vol. 81, pp. 2389–2394, 2001.

[4] C. Schmidt, M. Mayer, and J. Vogel, "A chip-based biosensor for the functional analysis of single ion channels," *Angew. Chem. Int.,* vol. 39, pp. 3137–3140, 2000.

[5] N. Fertig, C. Meyer, R. H. Blick, and J. Behrends, "A microstructured chip electrode for low noise single channel recording," *Biophys. J.,* vol. 80, pp. 337a, 2001.

[6] K. Cheung, T. Kubow, and L. P. Lee, "Individually addressable planar patch clamp array," *2nd Annual International IEEE-EMBS Special Topic Conference on Microtechnologies in Medicine and Biology*, pp. 71-5, 2002.

[7] K. G. Klemic, J. F. Klemic, M. A. Reed, and F. J. Sigworth, "Micromolded PDMS planar electrode allows patch clamp electrical recordings from cells," *Biosensors & Bioelectronics*, vol. 17, pp. 597-604, 2002.

[8] PatchXpress, Axon Instruments, www.axon.com.

[9] IonWorksHT, Molecular Devices, www.moleculardevices.com

[10] Nanion Technologies, www.nanion.de.

[11] Sophion Biosciences, www.sophion.dk..

[12] B. Matthews and J. Judy, "Characterization of a Micromachined Planar Patch Clamp for Cellular Electrophysiology," *IEEE-EMBS International Conference on Neural Engineering*, pp. 648-651, 2003.

[13] Clariant Ltd., Data sheet: AZ5200 series, Mutteuz, Switzerland, April, 2000.

[14] Harrison, D. J., Fan, Z., and Seiler, K., "Integrated Electrophoresis Systems for Biochemical Analysis," *Proceedings of the 1994 Solid-State Sensor and Actuator Workshop*, Hilton Head Island, SC, June 13-16, 1994, pp. 21-24.

[15] J. McDonald, D Duff, J. Anderson, D. Chiu, H. Wu, O. Schueller, G. Whitesides, "Fabrication of microfluidic systems in poly(dimethylsiloxane)," *Electrophoresis*, vol. 21 pp. 27-40, 2000.

[16] Micro Chem, Data sheet: NANO SU-8 2000 Negative Tone Photoresist Formlations 2002-2025, Newton, MA, Febuary, 2002.

[17] C. H. Lin, G. B. Lee, B. W. Chang, and G. L. Chang, "A new fabrication process for ultra-thick microfluidic microstructures utilizing SU-8 photoresist," *J. Micromech Microeng*, vol 12 pp. 590-597, 2002.

[18] K. Hosokawa, K. Hanada, and R. Maeda, "A polydimethylsiloxane (PDMS) deformable diffraction grating for monitoring of local pressure in microfluidic devices," *J. Micromech, Microeng*, vol. 12, pp.1-6, 2002.

[19] B. Sakmann, and E. Neher, Eds., *Single-Channel Recording*, Plenum Press, New York, 1983.

[20] R. E. Thompson, M. Lindau, and W. W. Webb, "Robust, high-resolution whole cell patch-clamp capacitance measurements using square wave stimulation," *Biophysical Journal*, vol. 81, no. 2, p. 937-948, 2001.

[21] Z. Ahang, M. A. Ferenczi, and C. R. Thoma, "A micromanipulation technique with a theoretical cell model for determining mechanical properties of single mammalian cells," *Chemical Engineering Science*, vol. 47, no. 6 p.1347-1354, 1992.

THE WIMS CUBE: A MICROSYSTEM PACKAGE WITH ACTUATED FLEXIBLE CONNECTIONS AND RE-WORKABLE ASSEMBLY

Asli B. Ucok, Joseph M. Giachino, and Khalil Najafi
NSF - Engineering Research Center for Wireless Integrated Microsystems (WIMS ERC)
University of Michigan
Ann Arbor, MI 48109-2101

ABSTRACT

This paper presents the first results of a packaging/assembly approach for Wireless Integrated Microsystems (WIMS) with flexible and actuatable cables. A typical microsystem consists of many substrates, including circuits, sensors, and actuators. These substrates are assembled on top of one another inside of a cube (the WIMS cube), and electrical/fluidic signal transfer between dice is achieved using rows of integrated flexible cables that are attached to cube walls and actuated during assembly, row-by-row, to make pressure contacts to each die. The cables can be actuated using various actuation mechanisms including electrostatic, electrothermal, and electromagnetic actuation techniques. Cubes with actuatable integrated Parylene cables have been fabricated. Electrothermal actuators have been tested both electrically and on a hotplate, and produced 100's microns of deflection with less than 28mA current through 530-630Ω resistive heaters. Electromagnetic and electrostatic actuators have also been fabricated and are undergoing testing.

INTRODUCTION

Previous research on packaging and assembly of microsystems include various techniques, none of which provides the flexibility and modularity needed for a microsystem containing substrates with sensors, actuators, and circuits fabricated using different technologies [**1**,**2**]. We introduced the concept of a packaging/assembly approach for Wireless Integrated Microsystems (WIMS cube) [**3**], Fig. 1. In this approach, multiple substrates containing circuits, sensors, and actuators are stacked on top of each other in a re-workable and modular fashion inside a cube, with interconnection between substrates provided through flexible cables [**4**].

Figure 1 shows the WIMS cube, which is typically a few millimeters on a side and holds different dice (top cover is not shown and side is flipped open to reveal stacked substrates/battery). Electrical/fluidic signals are transferred between dice using rows of integrated flexible cables attached to cube walls and actuated, row-by-row, to make pressure contacts to each die. At the start of assembly, all cables are retracted and pressed against the cube wall. After each die is "dropped" into the cube, a row of cables is actuated/released into position (Figure 2). A non-conductive elastomer sheet is then dropped over the die, acting like a cushion, followed by another die; the process is then repeated. Finally, the cube is covered by a lid, which presses against the dice and elastomers, forcing all cables into intimate contact with their substrate. Actuation is critical since all cables have to deflect >90°, and is needed only during assembly.

As the connections between cables and individual microsystem substrates are achieved using pressure contacts, they are not permanent. This allows the microsystem to be disassembled either if one of the dice fails after assembly, or if a different microsystem with a different set of sensors or actuators is needed for another application. As a result, this packaging/assembly approach results in maximum flexibility and modularity, two critical features for microsystems and MEMS applications.

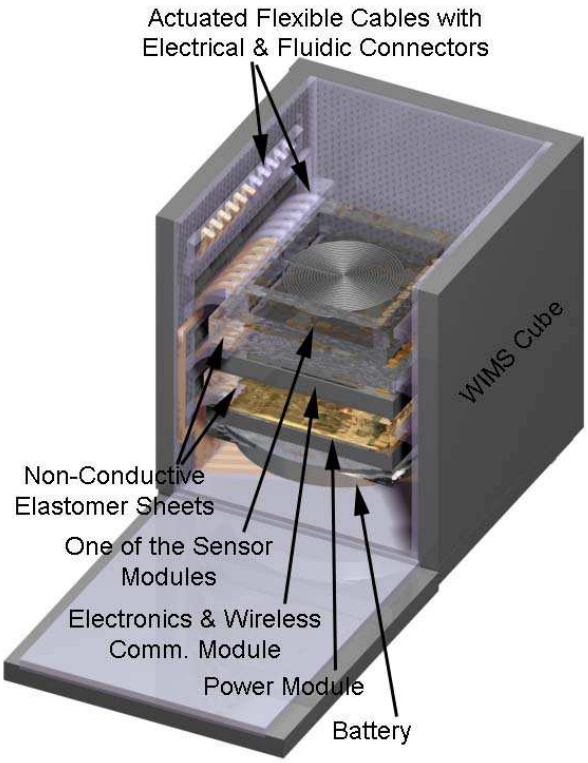

Figure 1. WIMS Cube: *Schematic of high-density mechanical connect/disconnect system for packaging of multi-substrate microsystems. The flexible connector cables make pressure contacts to pads and fluidic channel openings on the dice.*

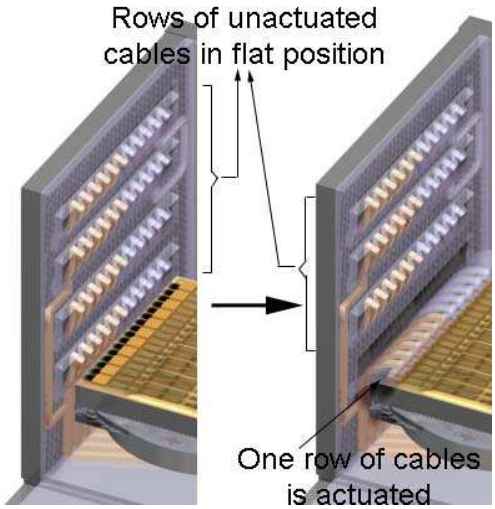

Figure 2. *Each row of cables is actuated (or released) in position after their corresponding die is "dropped" into the cube.*

0-9640024-5-0/hh2004/$20©2004TRF
DOI 10.31438/trf.hh2004.33

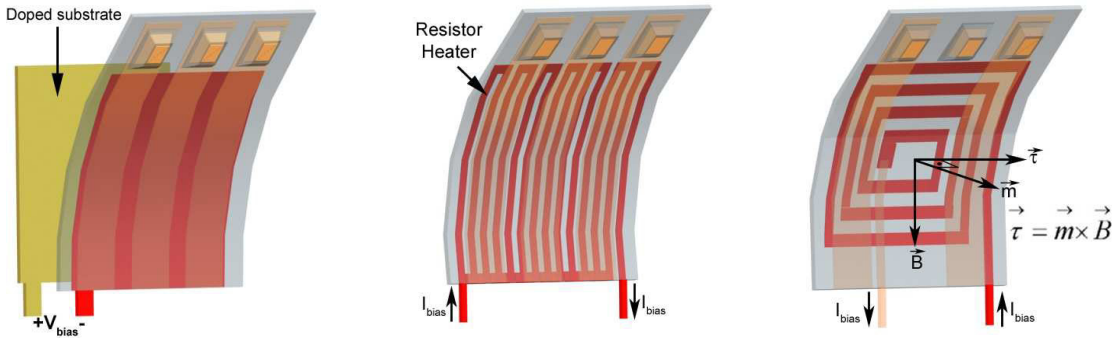

Figure 3. *(a) Electrostatic, (b) Electrothermal, and (c) Electromagnetic actuation mechanisms for flexible cables*

ASSEMBLY MECHANISMS

The WIMS cube is fabricated using planar silicon technology. The bottom and the four sidewalls of the cube are fabricated on a single substrate and are attached to each other by the flexible cable material, and a separate piece could be used as the lid of the cube. Each cube can then be handled easily and folded using a jig. The walls can next be glued/soldered to form the cube. During assembly, current/voltage is applied to the corresponding row of cables to actuate that row. Signals are applied using a long flexible cable that carries conductors to interconnect to each row. After the assembly is completed, right before closing the lid of the cube, the cable can be folded and placed inside the cube for any future assemblies of the same cube.

Cables can be actuated using various actuation mechanisms including electrostatic, electrothermal, and electromagnetic actuation techniques (Fig. 3). For electrostatic actuation, cables are in naturally-bent position due to intrinsic stress. A voltage applied between the cables and sidewall substrate pulls them into flat position. After a given die is placed inside the cube, the row of cables is released to naturally bend onto the die. Controlling the intrinsic stress of cables to get naturally bent position is a challenge. Therefore using only this mechanism to actuate the cables may not be a preferable actuation method.

In electrothermal actuation, the cables should initially be in a flat position and bend out of plane to connect to a substrate when heated. Heating is achieved using an embedded resistor, which is activated only during assembly. As long as we have cables that are not initially bent towards the substrate due to intrinsic stress, thermal actuation is a promising method as a means of cable actuation. An important point is to both design the cables so that they are flexible enough to have high deflection, and also make sure that high deflections are achieved without overheating the structure to prevent damage. Note that electrostatic and electrothermal actuation can be used together to obtain two-way actuation of cables as well.

In electromagnetic actuation, an external magnetic field is set up around the cube in an assembly jig. By passing current through a coil on the cable, one can achieve two-way actuation just by changing the direction of current on the coil. This is the most attractive of the three mechanisms, because the forces generated could be quite large with a very high magnetic field. However, one should be aware of keeping the current values low so that joule heating of the coil will not dominate cable actuation acting as a resistive heater [**5**]. Therefore, it is very important to have a high magnetic field in the assembly environment. The test setup can be prepared using high-strength permanent magnets placed in an assembly jig or an electromagnet so to create a magnetic field with a gradient around the cables.

FABRICATION

So far, we have fabricated WIMS cubes with electrical connectors. Figure 4 shows the fabrication process. Several candidate materials have been considered as the structural material for cables including silicon/polysilicon, inorganic dielectric materials such as silicon oxide/nitride, "soft" metal films such as gold, and finally polymers, such as polyimides, Parylene, and liquid-crystal polymers (LCP) [**4**]. Parylene is chosen due to its high-quality properties; conformal, pin-hole free and low stress coating with high quality barrier properties to moisture and gases, high chemical resistance, thermal mechanically flexibility up to 150°C, and no outgassing.

We start with a silicon wafer that is anisotropically etched in order to form small islands of silicon where each electrical connector will have extruding tips for better pressure-contact electrical connection. The wafers are then highly doped to form the bottom plate for electrostatically actuated cables. SiO_2 insulating layer is grown and etched at places where backside through-wafer deep reactive ion etching (DRIE) will be done later in the process. These include the areas that will be etched in order to get separate silicon walls of the cube. This step also enables to get contact to the doped substrate. Afterwards, photoresist sacrificial layer is patterned to enable the release of cubes and/or protect Parylene for any damage during backside through-wafer DRIE. The first Parylene layer is then deposited, and patterned to get contact to substrate for electrostatic actuation. Next, electrode metal layer, which forms the second plate for electrostatically actuated cables or the resistive heater and part of the coil for electrothermally and electromagnetically actuated cables, respectively, is deposited and patterned. A second Parylene layer is deposited and patterned for contact to electrode metal layer for coils on cables. The connector metal layer is the second metal layer deposited in fabrication. This layer forms the electrical connectors and the rest of the fabricated coils. A third and last Parylene layer can be deposited and etched to expose the ends of each connector on cables for pressure contact connection to system die pads during assembly. All Parylene layers are also etched to form the suspending cables. Lastly, backside through-wafer etch is performed to obtain separate cube walls, and cables are released by removing the sacrificial photoresist layer. Backside through-wafer etch can also be used to help release electrothermally and electromagnetically actuated cables without any need for special releasing and drying techniques to prevent stiction.

Figure 5 shows a silicon wafer with four $1cm^3$ unfolded cubes, and an unfolded cube with released Parylene flexible cables. At the center of the wafer you can see one cord for each cube to connect each pad substrate to its corresponding cube. The unfolded released cube, Fig. 5(b), has all the walls of the cube

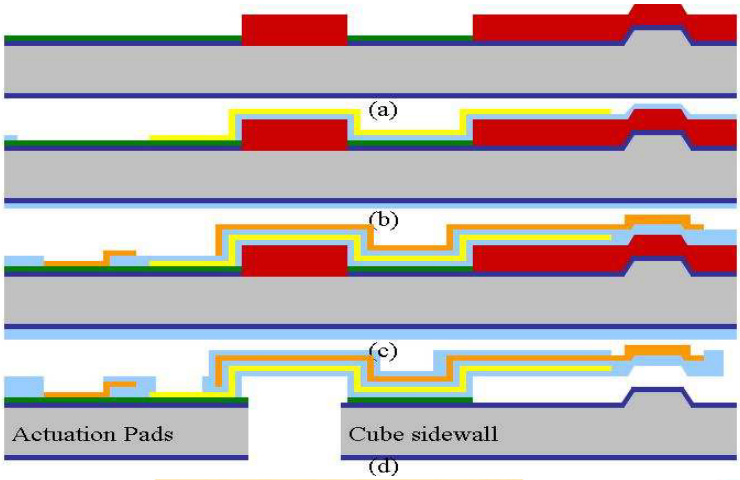

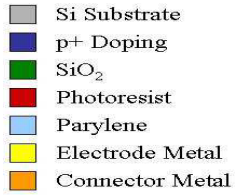

Figure 4. *Fabrication steps for the WIMS cube: (a) Anisotropic etch for tip formation, p+ doping, SiO_2 growth & lithography, sacrificial photoresist lithography, (b) Parylene1 deposition & lithography, electrode metal deposition & lithography, (c) Parylene2 deposition & lithography, connector metal deposition & lithography, and (d) Parylene3 deposition & lithography, backside through-wafer etch to separate cube walls and release cables*

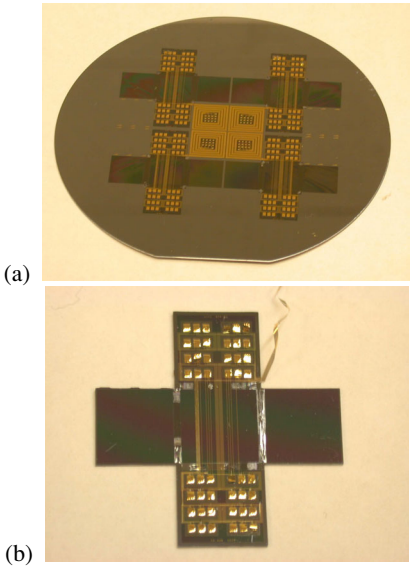

Figure 5. *(a) A silicon wafer with fabricated four unfolded $1cm^3$ cubes, and (b) An unfolded cube with released Parylene flexible cables.*

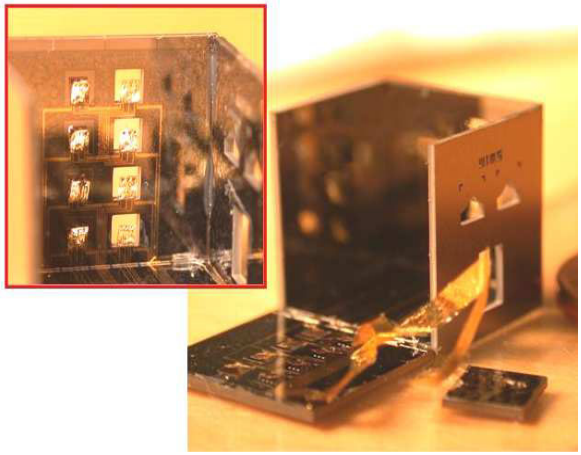

Figure 6. *A fabricated re-workable package (WIMS cube). The dimension of the cube is $1cm^3$, and the Parylene cable dimension is 1mm x 1.3mm. The small silicon piece in front of the cube, connected to the main structure by a wide and long cable, contains the pads where probe tips are used to actuate each row of flexible cables separately during assembly.*

attached to each other by the deposited Parylene layer during fabrication. Metal connector lines can also be seen running on the walls of the cube. The long cord leading to the pad substrate is also seen in this picture. Figure 6 shows a folded WIMS cube with released Parylene cables and a better view of the pad substrate.

DESIGN AND TESTING OF CABLES WITH ACTUATORS

We have designed and fabricated three different cable structures that are 1.3mm x 1mm and with thickness values of each layer given in Table 1. The basic electrostatic actuator calculations using a 3μm sacrificial layer between the cable and substrate resulted in 135V, 80.1V, and 81.4V of required pull-in voltage for the cables, respectively [**6**]. In this calculation, pull-in is assumed to be starting near the anchor of the curled cable, where the spacing between cable and substrate is smallest. The cables require characterization and adjustment of each deposition step in order to get an acceptable initially-bent position created by intrinsic stress. The high dependence of this design to fabrication variables makes it less reliable, and as a result, less attractive as mentioned earlier.

The electrothermally actuated cables are also designed to get large deflections. Figure 7 shows a released flexible cable with a resistive heater for thermal actuation. Design #1 was the first one to be designed and fabricated. The hotplate experiments showed 100's of microns of deflection (Fig. 8). Experimental data by applying current to the resistive heater has also proved that we can get large deflections with this design (Fig. 9).

Table 1. *Dimensions of fabricated flexible cables*

Design #1	**Design #2**	**Design #3**
Parylene1: 1.90μm	Parylene1: 1.82μm	Parylene1: 1.82μm
Cr/Al/Cr: 100Å/5000Å/100Å	Cr/Al/Cr: 200Å/5000Å/200Å	Cr/Au: 200Å/5000Å
Parylene2: 1.12μm	Parylene2: 0.56μm	Parylene2: 0.56μm
Cr/Au:4000Å/500Å	Cr/Au:500Å/5000Å	Cr/Au:500Å/5000Å
Parylene3:0.62μm	Parylene3:0μm	Parylene3:0μm

Due to releasing conditions, these thermally actuated cables, which have all the substrate underneath them etched, are in naturally bent position towards the etched opening in substrate. This is a preferred condition in terms of assembly of the cube. However, during testing, the cube sidewall with the cables touching the chuck surface hinders the movement at the beginning

of increasing current cycle. This results in the sudden increase of deflection near 25mA, instead of a smooth I^2 relation of deflection *vs.* current.

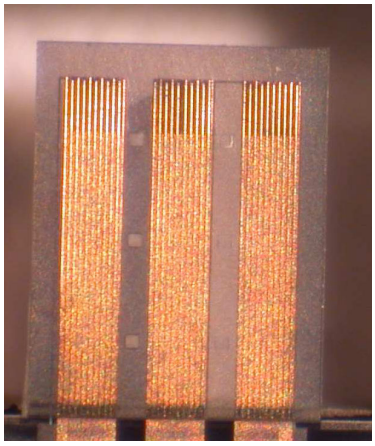

Figure 7. *A released flexible cable with resistive heater*

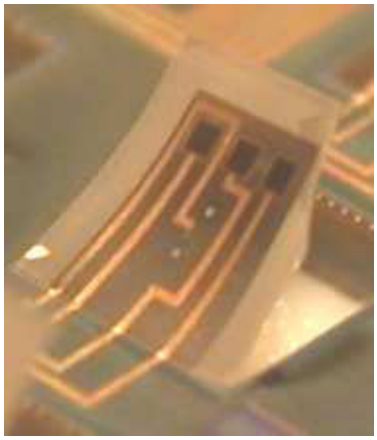

Figure 8. *A thermally actuated flexible cable (Design #1) on 120℃ hotplate. The cable dimension is 1mm x 1.3mm, and the deflection is 100's of microns as can be observed visually.*

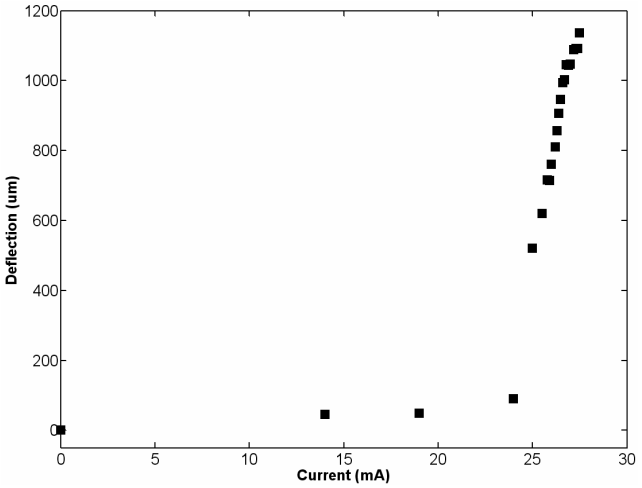

Figure 9. *Deflection vs. current characteristics of a Design #1 device with* 630Ω resistive heaters

In spite of the good deflection characteristics, this design is not preferable because of the expected high resistance of the connector metal. As a result, Designs #2 and #3, which will have comparably less deflection characteristics, but better electrical properties as a connector, are fabricated and are under test.

The design and testing of electromagnetically actuated cables continue.

CONCLUSIONS

We have proposed a modular and reusable stacked packaging approach for microsystems with flexible and actuatable cables making pressure contacts to the pads on the system dice. This modular approach serves as a re-workable platform for microsystems, which contain various substrates fabricated with different technologies. Parylene is used as the structural material for these connector cables because of its high flexibility, chemical inertness, and conformity of deposition. All cables have to be actuated to deflect >90°, which is needed only during assembly. They can be actuated using various actuation mechanisms including electrostatic, electrothermal, and electromagnetic actuation. Cubes with actuatable integrated Parylene cables have been fabricated. Electrothermal actuators have been tested both electrically and on a hotplate, and produced 100's of microns of deflection with less than 28mA current through 530-630Ω resistive heaters. Electromagnetic and electrostatic actuators are not tested yet.

ACKNOWLEDGMENTS

The authors would like to thank Robert Gordenker for his help in calibrating the test setup. This work was supported by National Science Foundation (NSF) Engineering Research Center for Wireless Integrated Microsystems (WIMS-ERC) under award number EEC-9986866. Travel support has been generously provided by the Transducers Research Foundation and by the DARPA MEMS and DARPA BioFlips programs.

REFERENCES

1. S. F. Al-Sarawi, D. Abbott, and P. D. Franzon, "A Review of 3-D Packaging Technology," *IEEE Transactions on Components, Packaging, and Manufacturing Technology*, 21, 1, pp. 2-14 (1998).

2. M. Schuenemann, K. A. Jam, V. Grosser, R. Leutenbauer, G. Bauer, W. Schaefer, and H. Reichl, "MEMS Modular Packaging and Interfaces," *Proc. of the 50th Electronic Components and Technology Conference*, pp. 681-688 (2000).

3. A.B. Ucok, J.M. Giachino, and K. Najafi, "Compact, Modular Assembly and Packaging of Multi-Substrate Microsystems," *Proc. of the 12th International Conference on Solid-State Sensors, Actuators, and Microsystems (Trans'03)*, Boston, MA, 6/9-12/03, pp.1877-1878 (2003).

4. A.B. Ucok, J.M. Giachino, and K. Najafi, "A High-density Flexible Connector Array for Multi-substrate Packages," *2003 ASME International Mechanical Engineering Congress and Exposition (IMECE'03)*, Washington, DC, 11/16-21/03, (2003).

5. C. Liu, T. Tsao, Y.-C. Tai, and C.-M Ho, "Surface Micromachined Magnetic Actuators," *Proc. of Micro Electro Mechanical Systems (MEMS '94),* pp. 57-62 (1994).

6. S. D. Senturia, 2001, "Microsystem Design," Kluwer Academic Publishers, Norwell, Massachusetts, USA

MAGNETICALLY-DRIVEN ACTUATION USING LIQUID-PHASE POLYMERIZATION (LPP) AND ITS APPLICATION: A PROGRAMMABLE MIXER

A.K. Agarwal[1], S.S. Sridharamurthy[1], T.M. Pearce[2], G.A. Mensing[2], D.J. Beebe[2], and H. Jiang[1]
[1] Department of Electrical and Computer Engineering, University of Wisconsin-Madison
[2] Department of Biomedical Engineering, University of Wisconsin-Madison
Madison, Wisconsin 53706

ABSTRACT

IC-derived microelectromechanical systems (MEMS) technologies have advantages in terms of precision and compatibility with standard fabrication processing. Polymer-based microsystems have recently facilitated promising advances in microfluidics. We present a first demonstration of the combination of these two platforms via the construction and testing of various magnetically-driven devices. Our fabrication process uses microfluidic tectonics (μFT) to produce the microscale systems. A programmable micromixer is fabricated that is controlled by an autonomous clutch-based mechanism using responsive hydrogels. Based on the environmental parameters, specifically pH, the micromixer is turned on and off despite the constant presence of an external rotating magnetic driving field. Micromixer mixing efficiencies are also investigated as a function of input flowrates.

INTRODUCTION

Integrated circuit (IC) based MEMS technology has been established with a solid foundation. Its ability to provide highly precise structures and compatibility with standard fabrication methods makes it very attractive to anyone working with microstructures. Recently, a surge in polymer-based microsystems has taken off and allowed for rapid advancement in microfluidic technology. In this work, we utilize a fabrication process, microfluidic tectonics (μFT), which uses liquid-phase photopolymerization (LPP) to allow for the rapid creation of microcomponents **[1]**.

We present here an approach to fabricating microsystems that leverages advantages of both aforementioned platforms (MEMS and μFT). This approach provides unique capabilities and can easily integrate existing sophisticated silicon-based microsystems with polymer-based microfluidics. Polymer-based microfluidics makes use of photosensitive polymers that can be patterned without the additional necessity of a cleanroom environment. Also, LPP is a low-temperature process (<100 °C). Unlike lithography requiring spinning/casting of photosensitive materials on entire substrates, LPP occurs at designated areas on the substrate.

In previous work, researchers demonstrated assembled externally-driven magnetic microstirrers **[2, 3]**. Many responsive hydrogels also exist that are sensitive to various stimuli, including light, temperature, electric fields, and pH **[4]**. Previously, pH-sensitive hydrogels that undergo volumetric changes (swelling in base solutions and shrinking in acidic solutions) have been used to form autonomous valves **[5]**.

We present a first demonstration via the construction and testing of various magnetically-driven devices, specifically a programmable micromixer. Fabrication of microcomponent devices *in situ* (inside the channel) and their programmable operation via local fluid parameters are shown here.

FABRICATION METHODS

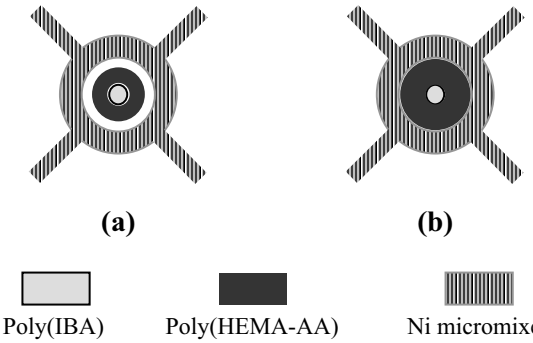

Figure 1. *Conceptual diagram of using poly(HEMA-AA)* ***[4]*** *to control the actuation of the Ni micromixer.* ***(a)*** *Low pH causes the hydrogel to shrink, allowing the micromixer to rotate freely.* ***(b)*** *High pH causes the hydrogel ring to expand in volume, constricting the micromixer's rotational movement.*

Magnetically-driven structures are fabricated using polymer-based microfluidics and nickel (Ni) electroplating.

Polymers

The polymer structures are formed using a liquid IBA-based pre-polymer and (responsive) hydrogels, both which are designed to be sensitive to ultraviolet (UV) light.

The pre-polymer solution consists of three constituents: isobornylacrylate (IBA), tetraethylene glycol dimethacrylate (TeGDMA), and 2,2-dimethoxy-2-phenylacetophenone (DMPA). IBA is the monomer; TeGDMA is the crosslinker; and DMPA is the photoinitiator. Exposure to a UV source causes the pre-polymer to harden (poly(IBA)) because of the photoinitiator.

Here, we use pH-sensitive hydrogels to control the actuation of micromixers (see Figure 1). This gel consists of four components: acrylic acid (AA), hydroxy ethyl methacrylate (HEMA), ethylene glycol dimethacrylate (EGDMA), and 2,2-dimethoxy-2-phenylacetophenone (DMPA). Exposure to UV light renders a gel matrix that changes its volume configuration depending on its surrounding (pH) environment.

Fabrication

Here, devices are fabricated on pre-cleaned microscope glass slides (76.2 mm × 25.4 mm × 1 mm) that have been coated with Ti/Cu/Ti (0.05/0.35/0.05 μm) using a DC sputterer. The bottom and top Ti-layers serve to promote adhesion to the glass and prevent oxidation of the underlying Cu-layer, respectively. The Cu-layer serves as the seed layer for future Ni electroplating. High resolution transparency masks (3600 dpi) are used to pattern the poly(IBA) structures. See Figure 2 for the process flow.

First, a poly(IBA) mold is formed that will serve as a masking layer during the Ni electroplating. A cavity is created between the glass slide and the transparency mask using 125-μm

0-9640024-5-0/hh2004/$20©2004TRF
DOI 10.31438/trf.hh2004.34

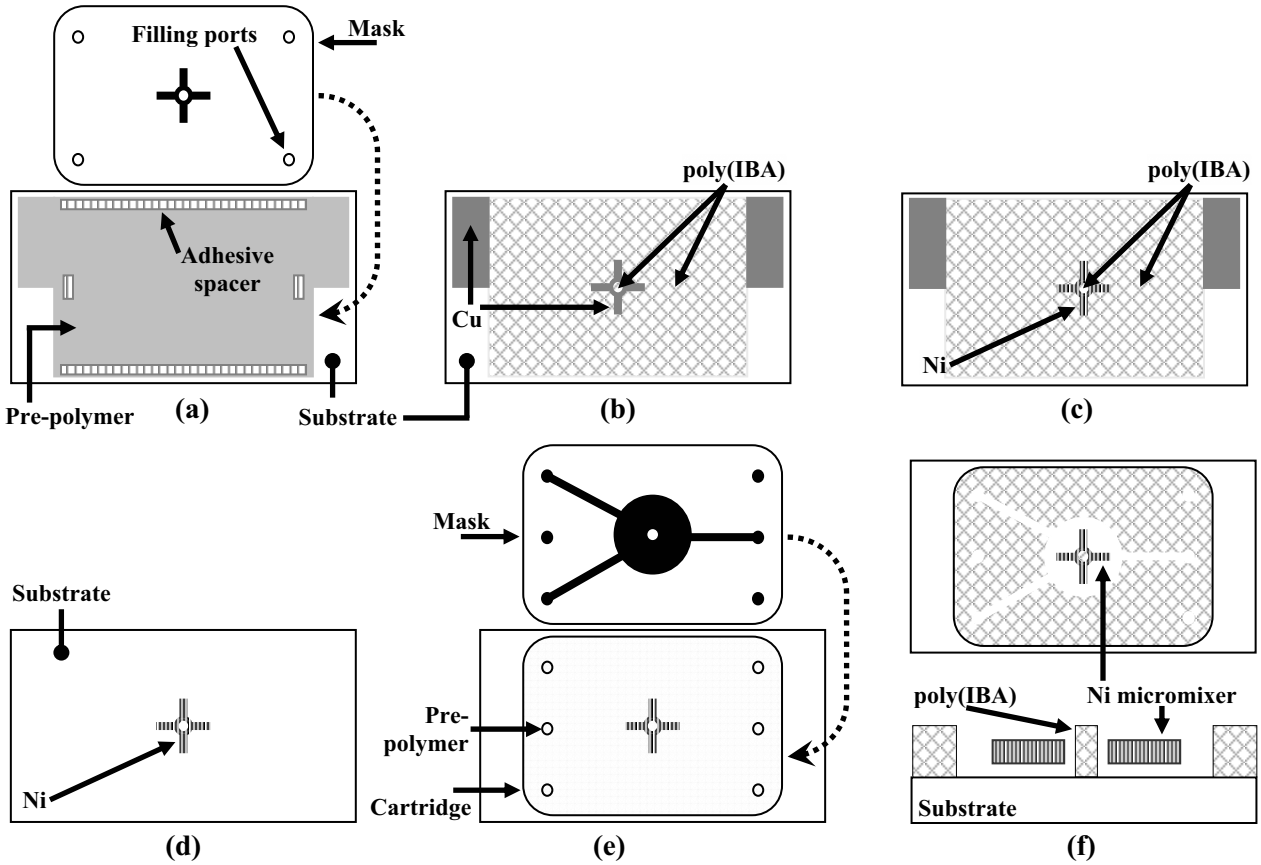

Figure 2. *General process flow for fabricating Ni-based devices (top view).* ***(a)*** *A cavity created between the substrate (coated with Ti/Cu/Ti) and high resolution transparency mask is filled with the pre-polymer mixture and exposed to UV light.* ***(b)*** *The top Ti-layer is removed, exposing the underlying Cu-layer.* ***(c)*** *Ni electroplating is performed with the poly(IBA) serving as the mold* ***[6]****.* ***(d)*** *The poly(IBA) is removed by soaking the device in methanol for several hours. The seed metal layers are also removed* ***[7]****.* ***(e)*** *The poly(IBA)-based channels, mixing chamber, and post are patterned and realized within a self-containing polycarbonate cartridge.* ***(f)*** *Top and side-view of a functional Ni micromixer post-release with a poly(IBA) post.*

thick double-sided adhesive tape. Depending on the desired thickness of the Ni structures, the depth of the cavity varies between 125–375 μm. The pre-polymer is flowed into the cavity (see Figure 2(a)). The pattern on the mask is transferred to the pre-polymer by exposure to UV light (dose ranges from 94 mJ/cm^2 to 131 mJ/cm^2 depending on desired poly(IBA) thickness). The remaining pre-polymer is washed away using ethanol.

Prior to Ni electroplating, the top Ti-layer is removed by placing the glass slide in a bath of HF:H_2O= 1:10, exposing the underlying Cu-layer (see Figure 2(b)). Once rinsed with H_2O, it is placed in a nickel sulfamate bath (Microfab® NI 100, Enthone-OMI, Inc., West Haven, CT) and Ni is electroplated (current density = 5×10^{-4} A/mm^2) **[6]**. Electroplated Ni thicknesses range from 125–250 μm (see Figure 2(c)) at a rate of approximately 125 μm/hour. The poly(IBA) mold is removed by soaking the device in methanol for several hours. The metal seed layers are also removed (see Figure 2(d)). HAC:H_2O_2:H_2O=1:1:10 is used to selectively etch Cu **[7]**.

The channels, fluidic chambers, and post are formed next. A polycarbonate cartridge (HybriWells™, Grace-Bio Labs, Inc., Bend, OR) with a spacer layer of 250 μm is affixed to the glass slide and filled with the pre-polymer using the filling ports (see Figure 2(e)). The pre-polymer is exposed through a transparency mask and subsequently rinsed using ethanol. If so desired, at this step, poly(HEMA-AA) hydrogel posts can be patterned (approximate dose is 680 mJ/cm^2) *in situ* to create a programmable micromixer (see Figure 1). Figure 2(f) shows the final device and cross-section. Access to the channels is accomplished by using plastic pipette tips cut at the end and glued directly onto the polycarbonate channel ports using a general 5-minute epoxy. The Ni structure is finally released by flowing in Ti and/or Cu-etching solutions.

EXPERIMENTS AND RESULTS

Experiments were videotaped directly to a computer using a Sony Hyper HAD CCD-Iris/RGB camera (Sony Corp., New York City, NY). An external rotating magnetic stirrer was used to drive the Ni microstructures (Cole Parmer, model 84000-00, Vernon Hills, IL). For controlled and stable fluid flows through the device channels, syringe pumps were used (Cole Parmer, model 74900 series, Vernon Hills, IL).

Experiments and Results

A programmable micromixer has been developed that is controlled by a clutch-based mechanism using a responsive hydrogel. The autonomous clutch here uses a parameter-sensitive hydrogel ring to control the clutch operation (on and off). It allows individual control of the micromixer despite the constant presence of a rotating external magnetic field (see Figure 1). The micromixer automatically turns on and off based on the local environmental parameter (pH for this device), thus providing

programmable mixing control where the 'program' is 'written' by the fluid in the channel (see Figure 3(a-c)). Figure 3(d) shows the feasibility of fabricating an array of micromixers on a single substrate, all possessing the ability to be individually turned on and off via local environmental parameters that can extend beyond pH, including light, temperature, and electric fields.

The fabrication approach also allows embedding Ni structures in free-moving poly(IBA) structures (Figure 4). A Ni rotor (~125 μm tall) is embedded in a 250-μm tall poly(IBA) gear. A second poly(IBA) gear is patterned next to the first gear such that the teeth engage with each other (width of each tooth is ~100 μm). Rotation of the first gear under the influence of an external rotating magnetic stirrer causes the second poly(IBA) gear to rotate in the opposite direction (a gear train). Because the process is liquid-based, the planarization of the poly(IBA) across large topography (i.e., the Ni rotor) is easily realized.

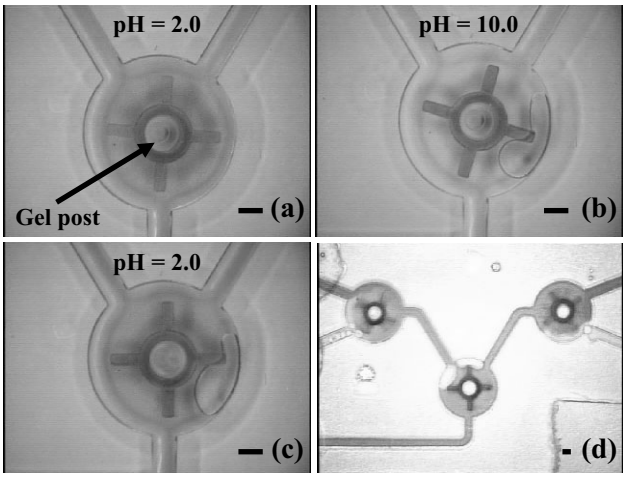

Figure 3. *A programmable micromixer that uses a pH-sensitive (poly(HEMA-AA)) hydrogel post (ϕ = 1.25 mm).* ***(a)*** *Blue buffer solution of pH=2.0 flows through the channel enabling the micromixer to rotate freely (t_0).* ***(b)*** *Yellow buffer solution of pH=10 flows through the channel causing the micromixer to stop spinning ($t_1 = t_0 + 40$ seconds).* ***(c)*** *Blue buffer solution of pH=2.0 flows through the channel causing the micromixer to rotate again ($t_2 = t_1 + 38$ seconds).* ***(d)*** *A system of micromixers mixing colored solutions. The scale bar represents 0.75 mm.*

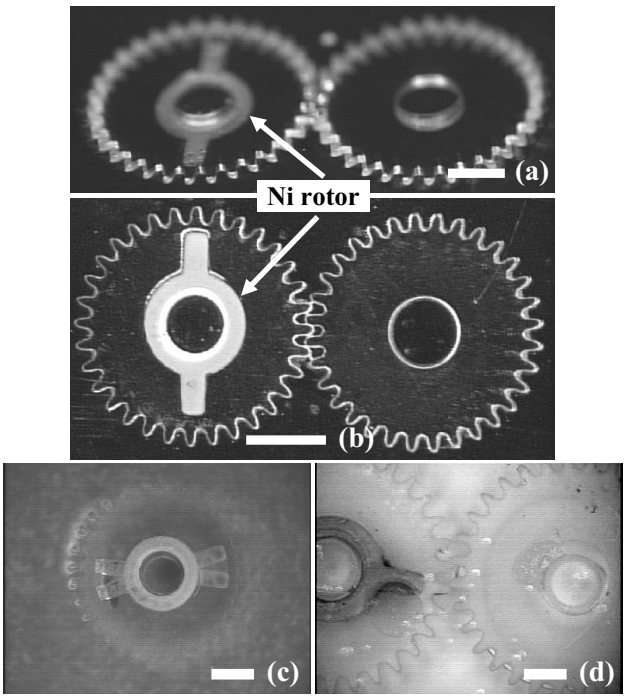

Figure 4. *Gear trains and embedded Ni structures.* ***(a)*** *Angled view of the gear train.* ***(b)*** *Top view of the engaged gear train.* ***(c)*** *A single Ni rotor embedded gear rotating freely around a post (open device with no cartridge).* ***(d)*** *The two gears rotating around their own poly(IBA) posts (open device with no cartridge). The scale bar represents 1.25 mm.*

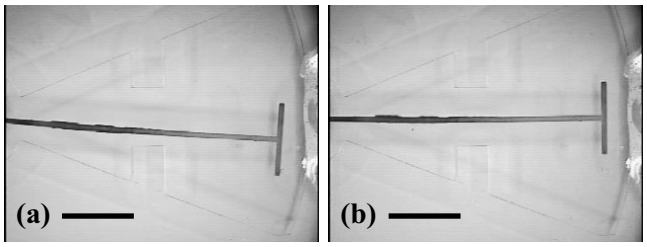

Figure 5. *A 20-mm long hammer structure with a 6-mm T-shape at one end, oscillating under the influence of an external magnetic stirrer.* ***(a)*** *The oscillating hammer moving down.* ***(b)*** *The oscillating hammer moving back up (within 1-2 seconds). The scale bar represents 6.0 mm.*

Figure 5 shows a Ni T-shaped hammer oscillating in a microfluidic channel responding to the rotating magnetic field. The poly(IBA) post (opposite end) cannot be seen in these pictures. The oscillating angle (here, ranging from approximately 2-12°) is dependent on the stirrer's RPM, i.e., the higher the RPM, the smaller the angle. With a constant RPM, the hammer's oscillation may also provide an assessment on fluid viscosity. It could also be applied in actuators such as vibromotors **[8]** or in an on-chip power source with the further integration of a wire coil.

An active micromixer was also fabricated and can be seen mixing two colored solutions in Figure 6 (total flowrate is 16.66 μL/min). FD&C Blue 1 and Yellow 5 food coloring dyes are used. The four blades measure 1.25 mm × 0.35 mm and channel widths are 0.75 mm. Using software NIH Image 1.61 **[2]**, intensity profiles of the cross-section ~3.0 mm past the mixing chamber were obtained. Mixing efficiencies, shown in Figure 7, are determined for several flowrates. And, since the micromixers are activated by an external rotating magnetic field, there is no need for on-chip power supplies.

This process allows for almost any design of poly(IBA) and Ni structures (see Figure 8). The high resolution transparency masks allow for rapid prototyping and fabrication (electroplating) of Ni structures and liquid-forming of poly(IBA). Thicknesses of these devices range from 100-300 μm. Dimensions of the device can range from tens of μm to mm.

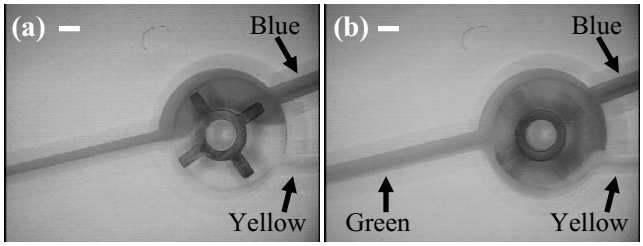

Figure 6. Micromixer mixing blue and yellow solutions. ***(a)*** *Micromixer at time, t = 0 second. The two fluids move through the channels in laminar flow without mixing.* ***(b)*** *Magnetic stirrer is activated causing the Ni micromixer to start rotating and mixing the blue and yellow solutions, resulting in a green-colored solution (t = 16 seconds). The scale bar represents 0.75 mm.*

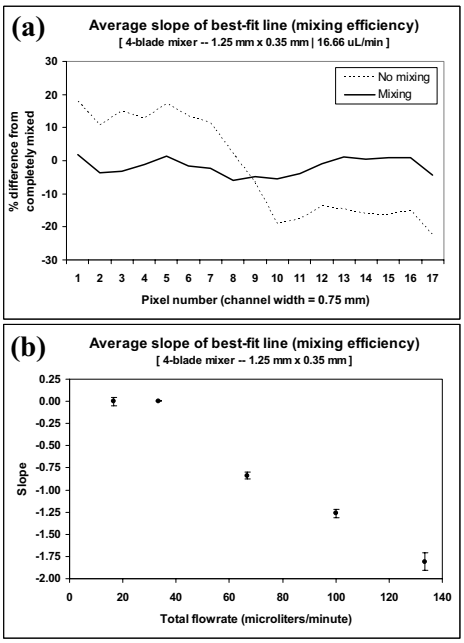

Figure 7. *Mixing efficiency plots.* ***(a)*** *Plot of percent difference in intensity between a control mixture, and trials before and after mixing.* ***(b)*** *Average slope as a function of total flowrate (slope = 0 corresponds to optimal mixing). Vertical bars represent standard deviation.*

DISCUSSION

At the macro scale, the response time of hydrogels to stimuli is very slow since the volumetric change is a diffusion-based process. However, by reducing the scale, the response time can be improved significantly. Because the response is governed by diffusion, the time response improves as the diffusion distance is squared (e.g., a 4-fold reduction in size results in a 16-fold reduction in response time). Thus, these materials are ideally suited to be used at the microscale. Here, instead of patterning a ring of poly(HEMA-AA), smaller and multiple posts may reduce the response time.

Mixing efficiencies depend on many variables, including micromixer dimensions (blade length, width, and thickness), mixing chamber diameter, channel widths, input flowrates, and height of the final poly(IBA) structures. Gear trains also have potential for being incorporated into various systems, including slide rulers, actuators, etc.

The fabrication method can act as a stand-alone process or append to an existing procedure. It allows for extrusion of 2-D structures to form 2.5-D ones, and true 3-dimensional structures can also be formed using stereo-lithography. Other substrates such as Si, SiN, and SiO_2 have been tested and pose no problems, further expanding the choice of substrates.

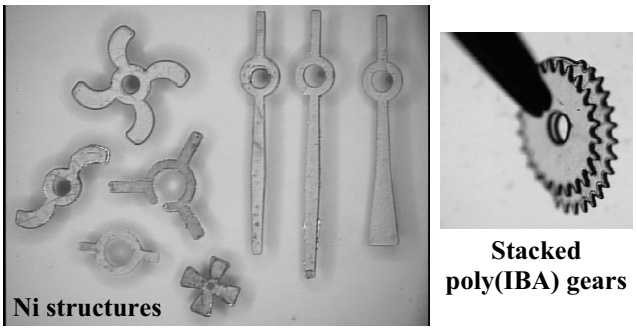

Figure 8. *Photograph of multiple Ni structures with different shapes and a two-layer poly(IBA) gear* ***[9]****.*

While seed-layer deposition in this work took place in the cleanroom, metal-coated substrates can be purchased, allowing all processes to be performed by researchers without access to a cleanroom facility.

CONCLUSION

Demonstration of a programmable mixer combining IC-derived MEMS and polymer technology has been shown here. Using responsive hydrogels, the on/off status of a single micromixer can be controlled using local environmental parameters. Preliminary experiments on mixing efficiency have also been conducted, showing that as total flowrate increases, mixing efficiency decreases.

The fabrication method can act as a stand-alone process or append to an existing procedure. Unlike conventional lithography requiring spinning/casting of photosensitive materials on entire substrates, LPP occurs at designated areas on the substrate. The process can be appended to MEMS structures that have been previously released. Since the process is liquid-based, topography is not a significant concern. Finally, the ability to control component operation via local fluid parameters expands control scheme possibilities while *in situ* processing simplifies fabrication and eliminates the need for assembly.

ACKNOWLEDGMENTS

This work is partly supported by the Wisconsin Alumni Research Foundation (WARF). Travel support has been generously provided by the Transducers Research Foundation and by the DARPA MEMS and DARPA BioFlips programs.

REFERENCES

[1] D.J. Beebe, J. S. Moore, Q. Yu, R.H. Liu, M.L. Kraft, B-H Jo, C. Devadoss (2000). "Microfluidic tectonics: A comprehensive construction platform for microfluidic systems," *PNAS*, Dec. 5, 97(25): 13488-13493.

[2] G.A. Mensing, T.M. Pearce, M.D. Graham, and D.J. Beebe (2003). "An externally driven magnetic microstirrer," accepted and to be printed in *Philosophical transactions: Mathematical, physical, and engineering sciences*.

[3] L-H Lu, K.S. Ryu, and C. Liu (2002). "A magnetic microstirrer and array for microfluidic mixing," *JMEMS*, October, 11(5): 462-469.

[4] D.T. Eddington and D.J. Beebe (2004). "Flow control with hydrogels," *Advanced Drug Delivery Reviews*, February 10, 56(2): 199-210.

[5] D.J. Beebe, J.S. Moore, J.M. Bauer, Q. Yu, R.H. Liu, C. Devadoss and B-H. Jo (2000). "Functional hydrogel structures for autonomous flow control inside microfluidic channels," *Nature,* 404: 588-590.

[6] Microfab® NI 100 data sheet, July 2000, Enthone-OMI Inc., West Haven, CT.

[7] J. Zou, C. Liu, J. Schutt-Aine, J. Chen, and S-M Kang (2000). "Development of a wide tuning range MEMS tunable capacitor for wireless communication systems," *Proc. IEDM*, December 10-13, 403-406.

[8] A.P. Lee, P.B. Ljung, and A.P. Pisano (1992). "Polysilicon micro vibromotors," *IEEE MEMS Proc*., Germany, Feb. 4-7.

[9] G.A. Mensing, T.M. Pearce, and D.J. Beebe (2004). "An ultra rapid method of creating 3D channels and microstructures," submitted to *JMEMS*.

A MICROSCALE VAPOR-FED FORMIC ACID FUEL CELL

J. Yeom[1], R. S. Jayashree[2], G. Z. Mozsgai[1], A. Asthana[2], E. R. Choban[2], M. Mitchell[2], P. J. A. Kenis[2], and M. A. Shannon[1]*

[1] Department of Mechanical and Industrial Engineering, University of Illinois, Urbana, IL 61801
[2] Department of Chemical and Biomolecular Engineering, University of Illinois, Urbana, IL 61801
* mshannon@uiuc.edu

ABSTRACT

A silicon-based microfabricated fuel cell running on formic acid vapor as a fuel has been developed to provide on-chip power for MEMS devices, without using any ancillary devices such as heaters, water management, air pumps, etc. As a demonstration instrument, an integrated silicon-based membrane electrode assembly and fuel evaporative structure was packaged in a plastic package to test the vapor-fed fuel cell concept. Initial results (0.4 V of the open circuit potential (OCP) and 2.3 mW/cm^2 of the peak power density) of the cell indicate that evaporation can potentially serve as a passive fuel delivery method for on-chip proton exchange membrane (PEM) fuel cells. The OCP is currently limited by anode reactions and the power density by both a slow anode catalyst (Pt) and low evaporation rates. Continued improvements will raise the cell potential and power by incorporating higher kinetic catalysts, faster evaporative structures, and lower oxygen crossover in the gas permeability membranes.

INTRODUCTION

A worldwide effort is underway to develop micro-fuel cells that utilize liquid fuels, such as methanol and formic acid [**1-4**]. However, the direct contact of liquid fuel with the membrane electrode assembly (MEA) leads to the several drawbacks. Direct liquid fuel delivery needs some pumping action and gas extraction from the exhaust, where the byproducts such as CO_2 form bubbles, potentially blocking fuel transport. Feedback systems are frequently used in large fuel cells to match the supply of fuel and water to the power load, and to avoid anode flooding. Reduced mass transport of the active fuel ingredients (MeOH, HCOOH, ethanol, etc.) can also be a problem associated with convection of fuel to the anode, and many research efforts try to alleviate it. These mitigation efforts become even more challenging at the *microscale*, as ancillary systems (pumps, gas extractors, water recycling, etc.) are harder to integrate into an efficient system.

Though little work has been done on passive vapor-fed fuel cells, the use of vapor phase fuel provides the following advantages over direct liquid fuel delivery. (1) Fuel is stored in concentrated form, so that higher effective energy density can be achieved. Liquids mixtures in direct feed are dilute (MeOH ~5% in 95% H_2O, HCOOH ~40%, etc). (2) No feedback system is required to deal with anode flooding. The condensation of vapor into liquid onto the anode is determined by the rate of consumption of fuel, driving the vapor off the equilibrium value of condensation occurring in the rest of the volume (determined by temperature). Thus, up to the maximum vaporization and condensation rate, the supply of fuel to the anode is automatic. (3) Exhaust gases can simply counter diffuse back from the anode as vapor condenses onto the MEA, thus preventing gas lock-up (bubble blocking), making exhaust/fuel separation an easier task if a membrane with different affinities to fuel and exhaust gases is available. (4) Flooding of the cathode with too much water is eliminated since water is not needed for evaporation. Methanol exhibits a higher vapor pressure (~95 mmHg at 20°C) than formic acid (~33 mmHg at 20°C). However, the kinetics of methanol electro-oxidation is prohibitively slow at room temperature, which leads us to an alternative fuel, formic acid, which has a much higher kinetics than methanol **[3]**. A comparison of fuel cell performance of the two different fuel mixtures in liquid form can be found elsewhere **[4]**.

In an effort to address these issues, we have developed and tested a microfabricated fuel cell running on formic acid vapor as a fuel. This microscale vapor-fed formic acid fuel cell has been prepared by various microfabrication technologies that will be described. An optical photograph of the Si-based fuel cell is shown in Fig. 1.

EXPERIMENTAL DETAILS

A complete silicon microfabricated vapor–fed fuel cell (Si-μVFFC) structure, as shown in Fig 1, comprises of two silicon electrodes, a proton conducting membrane, and a catalyst layer on electrodes. Two identical electrodes coated with Au and Pt-black were employed for both anode and cathode and sandwiched together to form a membrane electrode assembly (MEA).

Si-μVFFC electrodes were prepared using a series of MEMS fabrication processes adapted from our previous work. A 100 mm double-side polished silicon wafer (Silicon Quest; 500 μm thick, <100> oriented, 10 Ω·cm of resistivity) was chosen as a base structure. To enhance current collection of the Si-substrates, a 1000 Å Au layer was deposited using DC magnetron sputtering and patterned with a liftoff process. The front of the wafer was then coated with a polyimide spacer layer serving as both a dielectric layer for the electrodeposition of a catalyst and as the intermediate layer to promote a bonding between silicon substrate and Nafion^{TM} membrane, the polymer electrolyte. In the second photolithography step, the front mesh pattern was aligned to the etch pits on the back of the wafer. Feedholes in the Si-μVFFC electrode were created from the front of the wafer using a deep-trench reactive ion etcher (DRIE), and the back of the wafer was also etched by the same etching technique leaving a circular cavity. Figure 2(A) shows a scanning electron microscopy (SEM) image of the Si-μVFFC electrode of a 50 μm thick mesh with a 150 μm pitch and 100 μm square holes, facilitating rapid diffusion of fuel to the catalyst as well as transport of CO_2 generated at the anode from the interface.

Often for PEM type fuel cells, the catalysts are applied to the membrane by painting Nafion-based inks containing Pt or Pt-alloy catalysts with carbon supports. However, this type of method is not compatible with an integrated membrane electrode assembly (MEA). Therefore, a catalytic layer of Pt-black (Alfa AESAR) was electroplated directly onto the Au current collector of both

***Figure 1**. A photograph of a Si microfabricated vapor-fed fuel cell (Si-μVFFC). The MEA and the Si wicking structures are bonded temporarily with a PDMS membrane.*

Travel support has been generously provided by the Transducers Research Foundation and by the DARPA MEMS and DARPA BioFlips.

0-9640024-5-0/hh2004/$20©2004TRF
DOI 10.31438/trf.hh2004.35

Solid-State Sensors, Actuators, and Microsystems Workshop
Hilton Head Island, South Carolina, June 6-10, 2004

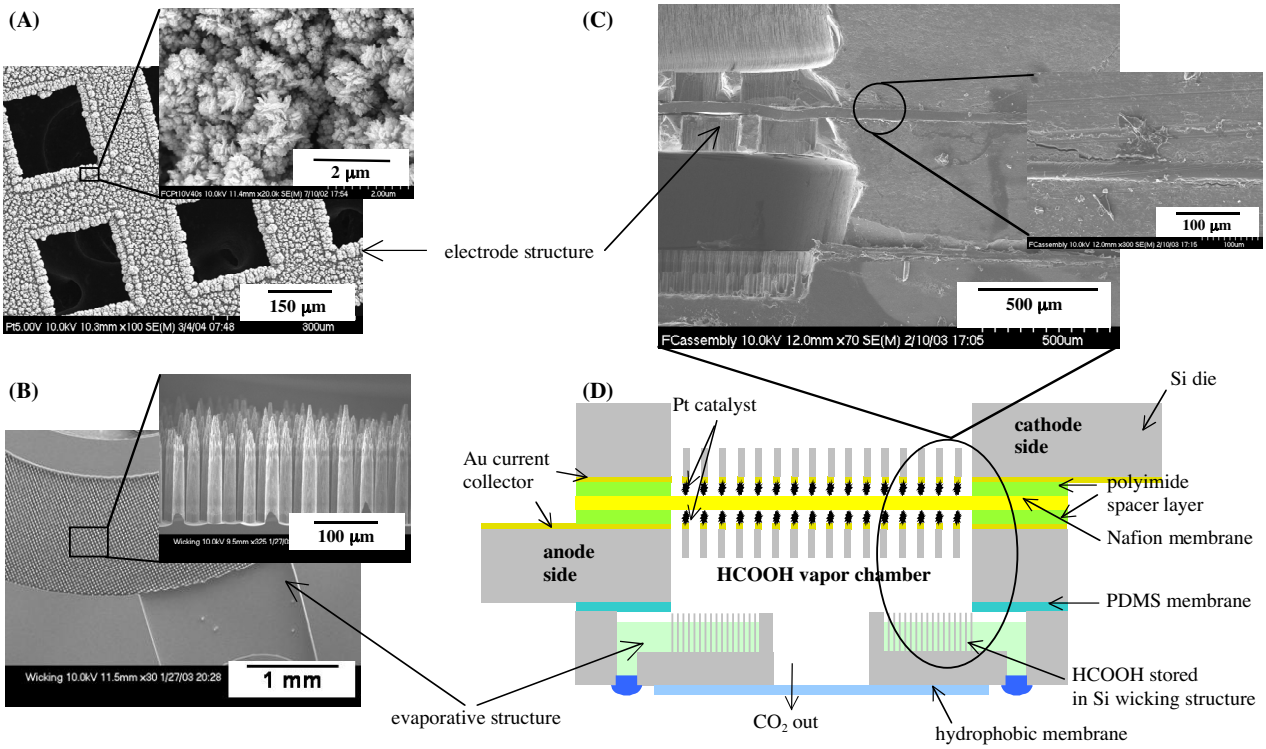

Figure 2. *(A) A SEM of the DRIE–etched Si electrode structure deposited with Pt–black catalyst. The exploded view shows the dendritic growth of the catalyst due to high current density electrodeposition. (B) A SEM of the Si wicking structure: an array of DRIE etched posts of a pitch of 50 µm, 15 µm width, and around 250 µm height (see the exploded view). (C) A SEM image of the cross-sectional view of the bonded fuel cell. The exploded view illustrates an excellent bonding between Si electrode and the Nafion™ membrane. (D) A schematic of the Si-µVFFC including fuel delivery structure.*

cathode and anode to reduce ohmic losses within the cell and to bring the catalyst into direct contact once assembled with both the current collector and the PEM. The plating bath consisted of 120 ml DI water, 5 g dihydrogen hexachloroplatinate ($H_2PtCl_6{\cdot}6H_20$, Alfa AESAR), and 30 mg of lead acetate ($Pb(CH_2COOH)_2{\cdot}3H_20$, Alfa AESAR). High (50 to 100 m^2/cm^3) surface areas were achieved by carrying out the deposition at relatively high current densities, ~1 A/cm^2. Cyclic voltammetry measured an increase in surface roughness of approximately 500. The dendritic growth of the Pt-black is shown in Fig. 2(A). This method, however, produces an undesirably high catalyst loading of over 5 mg/cm^2, dictating a need for the thorough characterization of the catalyst deposition.

Two catalyst-coated electrodes are bonded onto either side of a Nafion 112™ membrane to form a Si MEA. Prior to bonding, the Nafion 112™ membrane was protonated by soaking it at 80ºC in sequence in dilute H_2O_2, DI water, dilute H_2SO_4, and DI water for one hour each. The assembly was hot-pressed at 120ºC under ~ 200 N/cm^2 for 10 minutes.

High surface area evaporative (wicking) structures were fabricated to provide a high flux of formic acid into the anode. These Si wicking structures were etched in an ICP-DRIE Bosch process with a lithographically patterned mask of arrayed structures. Figure 2(B) shows an array of DRIE etched posts with a pitch of 50 µm, 15 µm width, and around 250 µm height. According to recent studies by our group, the evaporation rate of formic acid depends on the area and perimeter of the microstructures **[5]**. The evaporation rates of formic acid from the microstructures range from 10.5 to 11.5 mM/cm^2-hr, which corresponds to a theoretical ideal power density of 280 to 310 mW/cm^2 at a cell potential of 0.5 V.

The MEA and the Si-based wicking structure are bonded using polydimethysiloxane (PDMS) as an adhesive gasket. Figures 2(D) and 2(C) show a schematic diagram of the integrated structure of a complete Si-µVFFC and a SEM image of its cross-sectional view, respectively. In order to prevent loss of fuel by vaporization, membranes with selective permeability for carbon dioxide (but impermeable to formic acid and water) were used. In this study, a 500 µm thick PDMS membrane was used for the semi-permeable membrane, which was bonded on the exhaust port of the Si-µVFFC.

All tests were performed at room temperature (~20 C) after conditioning. Conditioning was performed by holding the cell at 0 V and the OCP, each for 15 minutes. This procedure was repeated twice. During the conditioning, the flow rates of H_2 and

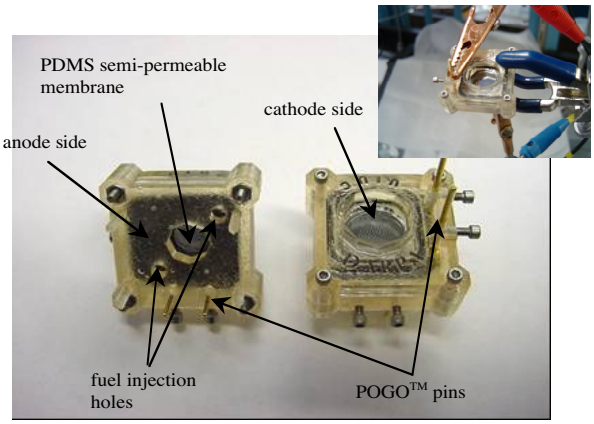

Figure 3*. A photograph of the integrated Si-µVFFC housed in a SLA package to make electrical connections. A simple test setup is shown in the top corner showing the stand-alone showing operation without ancillary devices.*

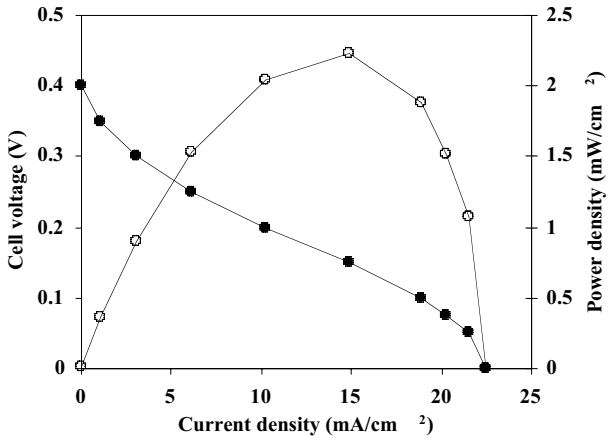

***Figure 4**. IV (dark circle) and power density (clear circle) profiles for the passive (vapor-fed) formic acid fuel cell, with 0.2 ml of 10 M formic acid evaporated at room temperature from the fuel Si wicking structure to the anode, while cathode is open to ambient.*

O_2 were 10 sccm. This preconditioning was required to properly hydrate the membrane, as significant drying occurs during the bonding process. The MEA was placed in a plastic housing made using a stereolithography apparatus (SLA, 3-D Systems) in order to make the external electrical connections for the experiments. Figure 3 shows the anode and cathodes side of the SLA package with a Si-μVFFC. An amount of 20 to 40 μL of 10 M formic acid solution (prepared from ACS grade, 96%, ACROS Organics) was injected in through a PDMS plug in the Si-μVFFC. Various concentrations of HCOOH-water mixtures were fed into the Si wicking structure, to study the effect of concentration on the performance of the cell. The cathode side is open to air. All voltage and current measurements were made using a potentiostat (Autolab PGSTAT 30) to regulate the load on the cell. The I-V curves were generated by holding the cell at various potentials.

RESULTS AND DISCUSSION

The Si MEAs were operated as hydrogen PEM fuel cells before bonding the MEAs with the evaporative structure to form a Si-μVFFC, in order to verify their performance. These H_2-O_2 MEAs delivered an open circuit potential of 0.95 to 0.98 V, and a short circuit current density of 80 to 100 mA/cm^2, matching the results in our previous study **[4]**. We have made at least 5 different Si-μVFFCs and compared the performance of the cells. The open circuit potentials and peak power densities varied within 10% from cell to cell.

Figure 4 shows the current density, cell potential, and power density for the Si-μVFFC with 10 M formic acid as the fuel, and quiescent air as the oxidizer. Measured currents were normalized to the nominal electrode area of 0.44 cm^2 to obtain the current density. The open circuit potential (OCP) was 0.4 V and the maximum power density obtained under these conditions was 2.3 mW/cm^2. These values are comparatively lower than those reported in our previous forced fed formic acid fuel cell studies (0.55 V of the OCP and 17 mW/cm^2 of the peak power density) **[4]**. Fukunaga *et al.* have reported lower OCP in the case of vapor feed direct methanol fuel cells **[6]**. They suggest that the chemical potential of methanol in the vapor phase is lower than that for liquid if the partial pressure of methanol is lower than the saturated vapor pressure. We speculate that the lower OCP in the current case could be due to similar reasons, as well as a mixed potential from the presence of oxygen at the anode. The current method of injecting fuel through the PDMS ports can admit significant

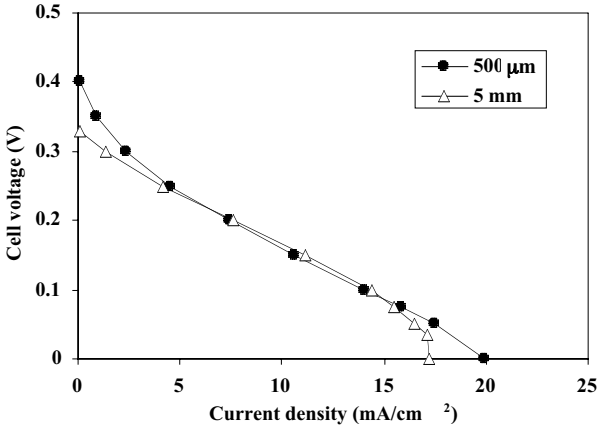

***Figure 5.** IV curves for Si-μVFFCs with a different thickness of PDMS membrane between the anode and the Si wicking structure, while running on 0.04 ml of 10 M formic acid vapor with the cathode open to ambient air.*

amounts of air to the anode side. In addition, the current and power densities for the Si-μVFFC are almost an order of magnitude lower than those of LF-FAFC. This lower current may be due to a mass transport limit of the evaporating formic acid-water mixture. It is also possible that the quiescent air-fed cathode is limiting the performance somewhat in comparison to the forced oxygen LF-FAFC. The crossover of fuel to the cathode from the anode can also be different than LF-FAFC. Finally, the overall kinetics of the catalysts for the condensing vapor fuel mixture at the anode may be quite different than that for a forced liquid flow.

One major issue with these Si-μVFFCs is whether the fuel mixture is delivered to the anode as a vapor and not as a liquid. If the liquid fuel injected into the Si wicking structure makes direct contact with the anode, the cell performance can be vastly different from the fuel being delivered as a vapor from the wicking structure. To confirm the utilization of vapor in these cases, cells with larger distances between MEA and the wicking structures were studied, and different amounts of fuel were injected. The increased distance was achieved by using a thicker PDMS block between the MEA and the evaporative structure to further separate the fuel reservoir from the anode when the same quantity (0.04 ml) and concentration (10 M) of the fuel mixture is injected. Figure 5 shows the polarization (I-V) curve for the Si-μVFFC with the PDMS blocks of 500 μm and 5 mm. The performance of the cells

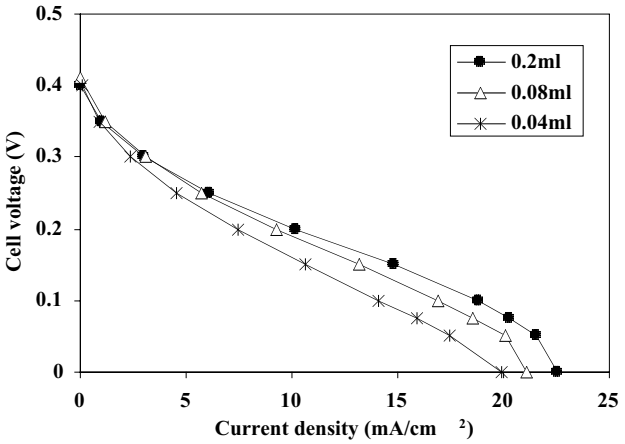

***Figure 6.** IV curves for Si-μVFFC's with various amount of 10 M HCOOH–H_2O mixture (from 0.04 ml to 0.2 ml) when the PDMS membrane thickness is fixed at 500 μm. No drastic change in cell performance ensures the fuel being delivered to anode as a vapor.*

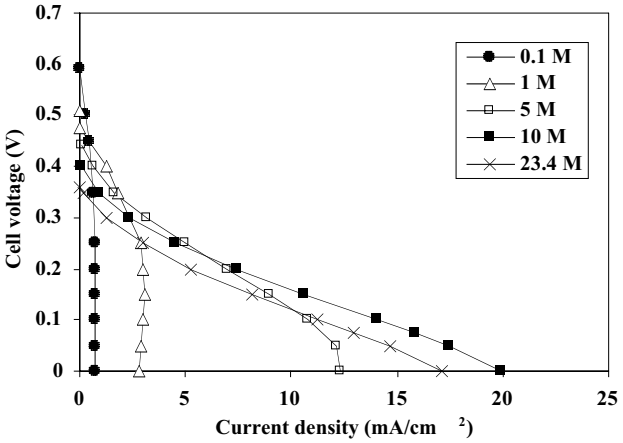

Figure 7. *The IV curves for Si-μVFFCs with a wide range of concentration of HCOOH–H_2O mixtures (from 0.1 M to 23.4 M). All testing was performed at room temperature (~ 20°C) with an ambient air-breathing cathode.*

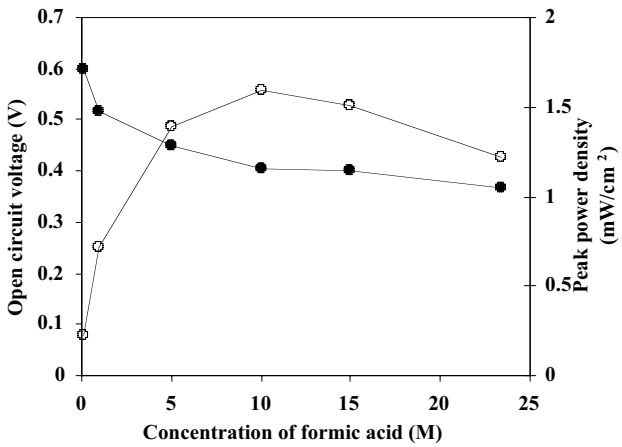

Figure 8. *Plots of formic acid feed concentration vs. OCP (dark circle) and formic acid feed concentration vs. peak power density (clear circle).*

did not vary with the distance between the MEA and the wicking structures, indicating that our fuel cells work in a vapor phase regime. In addition, for a fixed PDMS layer (500 μm), the amount of the 10 M HCOOH–H_2O mixture injected was varied from 0.04 ml to 0.2 ml. No significant change in the cell performance is observed in Fig. 6. Therefore, we believe that the fuel mixture is being delivered as a vapor in the Si-μVFFC.

Another major issue with the Si-μVFFC is the removal of the product CO_2 without the loss of formic acid and water mixture from the anode side of the fuel cell. In addition, as noted above, the exclusion of oxygen from the anode is important to avoid mixed potentials at the anode. Our approach in this Si-μVFFC is to employ a membrane that is permeable to CO_2, but is relatively impermeable to O_2, H_2O and HCOOH. We found that PDMS met these requirements and we tested a number of membranes with different thicknesses. The permeability of the 400 μm thick PDMS membrane utilized in this current work was measured to be 3.96 (10^{-4}) {cm^3(STP)·cm/cm^2·sec·(cmHg)} for O_2 and 2.55 (10^{-3}) {cm^3(STP)·cm/cm^2·sec·(cmHg)} for CO_2 at an inlet gas pressure of 100 torr. The permeability of CO_2 is found to be 5 times higher than the O_2 permeability, which makes PDMS an initial candidate for the semi-permeable membrane for the anode.

The Si-μVFFC's were also studied as a function of formic acid concentration ranging from 0.1 M to 23.4.M (88% by weight). The IV curves of Si-μVFFC with various concentrations of formic acid are shown in Fig. 7. As the concentration of formic acid increases, the current density increases to a maximum at about 10 M, which is consistent with forced LF-FAFC results [**3**]. The OCP, however, drops monotonically with increasing concentration, as seen in Fig. 8. The peak power density of these cells, though, increases with concentration until ~ 10 M concentration is reached, as shown in Fig. 8. The low power density of these cells at the lowest concentrations of formic acid could be due to mass transport limitations of the formic acid from the wicking structure to the anode. However, it is interesting to note that the cell potentials were higher with lower concentrations of formic acid.

At the highest formic acid concentrations tested, the cell performance decays slightly, which is significant since we would prefer to maximize the energy density of the fuel using high concentrations of formic acid. There are many potential mechanisms for this decay [**3**], but the dehydration of the membrane from the low water content at the anode at high formic acid concentrations will reduce proton conductivity through the Nafion, thereby reducing the current flow and power output. More experiments are being performed to understand the mechanisms associated with each of the unique aspects of operating vapor-fed fuel cells with formic acid as the fuel.

ACKNOWLEDGEMENT

The fuel cell work was supported by the Defense Advanced Research Projects Agency under US Air Force Grant F33615-01-C2172. All SEM work was conducted in the Center for Microanalysis of Materials, in the Frederick Seitz Material Research Laboratory, University of Illinois, which is partially supported by the U.C. Department of Energy under grant DEFC02-91-ER45439. Any opinions, findings, and conclusions or recommendations expresses in this publication are those of the authors and do not necessarily reflect the views of the Department of Energy, the U.S. Air Force, or the Defense Advanced Research Projects Agency.

REFERENCE

1. S. C. Kelley, G. A. Deluga, and W. H. Smyrl, "Miniature Fuel Cells Fabricated on Silicon Substrates," *AlChE J., 48*, 1071-1082 (2002).

2. W. Y. Sim, G. Y. Kim, and S. S. Yang, "Fabrication of Micro Power Source (MPS) Using a Micro Direct Methanol Fuel Cell (DMFC) for the Medical Application," *IEEE Intl. Conf. On MEMS, Tech. Digest*, *14*, 341-344 (2001).

3. C. A. Rice, S. Ha, R. I. Masel, P. Wazczuk, A. Wieckowski, and T. Barnard, "Direct Formic Acid Fuel Cells," *J. Power Sources*, *111*, 83-89 (2002).

4. J. Yeom, G. Z. Mozsgai, A. Asthana, B. R. Flachsbart, P. Waszczuk, E. R. Choban, P. J. A. Kenis, and M. A. Shannon, "A Silicon Microfabricated Direct Formic Acid Fuel Cell," *1st International Conference on Fuel Cell Science, Engineering and Technology,* Rochester, NY, 4/21-23/03, ASME (2003).

5. A. Asthana, E. R. Choban, M. Mitchell, R. S. Jayashree, and P. J. A. Kenis, "Formic Acid Evaporation from Microstructures Towards Passive Fuel Delivery Elements for Micro Fuel Cells", submitted.

6. H. Fukunaga, T. Ishida, N. Teranishi, C. Arai, and K. Yamada, "Impedance of Vapor Feed Direct Methanol Fuel Cells – Polarization Dependence of Elementary Processes at the Anode", *Electrochimica Acta*, *49*, 2123-2129 (2004)

MAGNETIC INDUCTION MACHINES EMBEDDED IN FUSION-BONDED SILICON

David P. Arnold*, Florent Cros, Iulica Zana, and Mark G. Allen
School of Electrical and Computer Engineering, Georgia Institute of Technology
Atlanta, GA 30332-0269

Sauparna Das and Jeffrey H. Lang
Dept of Electrical Engineering & Computer Science, Massachusetts Institute of Technology
Cambridge, MA 02139-4307

ABSTRACT

This paper presents the design, fabrication, and characterization of laminated, magnetic induction machines intended for high-speed, high-temperature, high-power-density microengine power generation systems. Innovative fabrication techniques were used to embed electroplated materials (Cu, $Ni_{80}Fe_{20}$, $Co_{65}Fe_{18}Ni_{17}$) within etched and fusion-bonded silicon to form the machine structure. The induction machines were characterized in motoring mode using tethered rotors, and exhibited a maximum measured torque of 2.5 μN·m and a projected torque density of 340 $N{\cdot}m/m^3$.

INTRODUCTION

The power demands of modern electronic devices are quickly outpacing the energy and power density of today's best batteries. This has driven the development of new compact, electric power sources in the 10-100 watt range for use in portable electronics, remotely located sensors, and robotic devices. One potential system, is a microengine [**1**,**2**]—a small (few cubic centimeters) gas-fueled turbine engine [**3**,**4**] coupled to an electrical power generator [**5**-**8**]. Such a system has the potential to reduce the mass, life-cycle costs, and cumbersome logistics of conventional batteries while providing uninterrupted high density power.

Both electric [**5**,**6**] and magnetic [**7**,**8**] induction machines have been investigated to convert the mechanical energy into electrical power, for use in a microengine. To achieve the desired power densities, the electrical generator must support high rotor spin (~1 Mrpm) and tip (500 m/s) speeds. Also, for integration with the multi-wafer-bonded turbine microengines, the machine must withstand high operating temperatures (~300°C) and use a compatible fabrication process.

As compared to their electric counterparts, magnetic machines may offer higher power densities, higher efficiencies (e.g. lower windage losses), less stringent fabrication tolerances (e.g. larger air gap), and simpler power electronics. They also operate at lower voltages and higher currents and are therefore easier to integrate with typical electronic devices. The previously reported magnetic induction machines were fabricated using SU-8 micromolding and multi-level electroplating of various metals [**7**,**8**]. These first-generation devices successfully demonstrated electromechanical power conversion, but were not integrable with the silicon-based microturbines and were limited in temperature due to the presence of the SU-8 polymer. This paper extends the previous research by demonstrating silicon-based, wafer-bonded, high-temperature, laminated, magnetic induction machines. This represents another step towards fully-integrated power generators for silicon-based microengines.

*Travel support has been generously provided by the Transducers Research Foundation and by the DARPA MEMS and DARPA BioFlips programs.

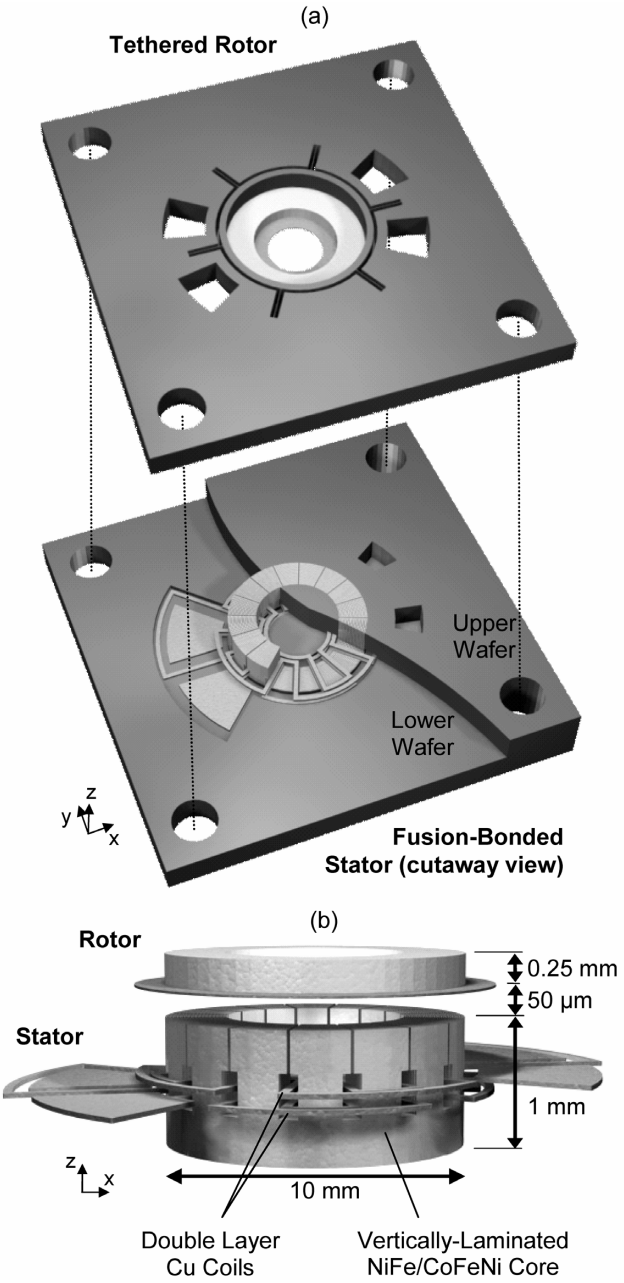

***Figure 1**. Renderings of the magnetic induction machine (z-axis expanded by 4x and air gap exaggerated). (a) Perspective view, showing a cutaway of the machine components embedded within the bonded silicon. (b) Side view, showing only the magnetic rotor and stator core and phase windings.*

0-9640024-5-0/hh2004/$20©2004TRF
DOI 10.31438/trf.hh2004.36

INDUCTION MACHINE DESIGN

The magnetic machine is designed for maximum power density and efficiency in the context of interoperability with a microturbine system. As a result, the design is constrained by system level compatibility issues and microfabrication limitations. First, the turbine-generator system is intended to operate with a 10 mm OD rotor spinning with a 500 m/s tip speed. Second, to support the high currents and magnetic fluxes needed for high power density, the machine must have relatively large geometric dimensions (~mm). Finally, as mentioned previously, the machine should withstand operating temperatures of ~300°C and be fabricated using silicon wafer-bond compatible processes.

Within these constraints, a planar induction machine was designed consisting of two primary components: a two-phase, 8-pole stator and a composite annular rotor, as shown in Fig. 1. Electromechanical energy conversion occurs through the interaction of a traveling magnetic wave in the rotor-stator air gap and the eddy currents induced in the rotor by the traveling wave [**9**]. In motoring mode, a traveling magnetic wave is established by applying two currents in quadrature to the two stator phases, resulting in a torque on the rotor.

The stator contains two phases made up of planar Cu coils wound in a three-dimensional, vertically-laminated ferromagnetic core, all supported by a silicon frame. The core laminations form onion-like concentric rings, where the lamination thickness is approximately one skin depth (~30 μm) to limit eddy current losses [**10**]. The rotor is a 250 μm thick ferromagnetic annular ring (10 mm OD, 6mm ID) with a 20 μm thick overlayer of Cu. The Cu extends beyond the magnetic region (12 mm OD, 4 mm ID) to enhance eddy current generation in the rotor for maximum torque. Machines were designed using either $Ni_{80}Fe_{20}$ or $Co_{65}Fe_{18}Ni_{17}$ as the ferromagnetic material. As compared to NiFe, the CoFeNi alloy has similar permeability and resistivity, but offers higher saturation flux density (higher power density) and higher Curie temperature (higher operating temperature) at the expense of a slight increase in coercivity (larger hysteresis loss) [**11**].

For testing purposes, the rotor was suspended above the stator using flexible silicon tethers that permitted angular rotation and a controllable air gap while avoiding the difficulties of supporting a spinning rotor. This simulates a blocked rotor test, commonly used to test macro-scale machines [**9**]. Six, 35 μm wide, 475 μm tall, 2.5 mm long silicon tethers were designed to provide an angular compliance of 25 rad/N·m with a stiffness in the axial direction of 4.2 μm/N to prevent rotor pull-in.

DEVICE FABRICATION

Innovative fabrication techniques were used to embed thick electroplated coils and cores within etched and wafer-bonded silicon to form the machine stators. The rotors and silicon tether structures were fabricated separately and assembled together for rapid prototyping with the stators.

Stators were fabricated by embedding coils inside of fusion-bonded silicon wafers and then building the magnetic core around the coils as depicted by Fig. 2. The process began with two highly-doped (~0.001 Ω·cm), n-type, 100 cm double-side-polished silicon wafers. In each wafer, 70 μm deep cavities were etched using deep reactive ion etching (DRIE) and a 200 nm thermal SiO_2 layer was grown. Then, a 400 nm Ta diffusion barrier and 200 nm Cu seed layer were DC sputtered across the surfaces of the wafers. Next, a thick negative photoresist was patterned in the cavities to define a mold for the coils, maintaining a minimum clearance of 50 μm from the cavity sidewalls. Patterning the mold within the cavities permitted uniform plating and prevented protrusions, which would inhibit wafer bonding. After plating, the photoresist, metallic seed layers, and SiO_2 were wet-etched back down to the pristine silicon surface, leaving the coil recessed in the cavity as shown in Fig. 3. The two wafers were then aligned and fusion bonded, sealing the coils inside. The bonding was performed at 500ºC for 4 hours under vacuum (<2 x 10^{-6} torr) with 200 kPa clamping pressure, resulting in a strong, uniform bond without degrading the embedded copper as reported in [**11**]. Next, a 3 μm PECVD oxide was deposited on the top and bottom surfaces of the bonded pair. Using this oxide layer and photoresist as masks, nested etches were performed from the bottom and top sides to form a silicon skeleton for the laminated core. Then, using a method detailed in [**12**], ~30 μm of NiFe or CoFeNi was selectively electroplated onto the conductive silicon sidewalls to form the magnetic laminations. The metals plated only on the etched silicon regions, with the SiO_2 layer on the top and bottom surfaces acting as a mask. Finally, contact openings were made from the top side by etching the silicon down to the buried coil contacts. Fig. 4 shows images of the completed stator.

The tethered rotor structures were built by assembling metallic rotors into tethered silicon rings. Rotors were built on a silicon substrate by first electroplating a 250 μm thick NiFe or CoFeNi annular ring on top of a 20 μm thick Cu ring using SU-8

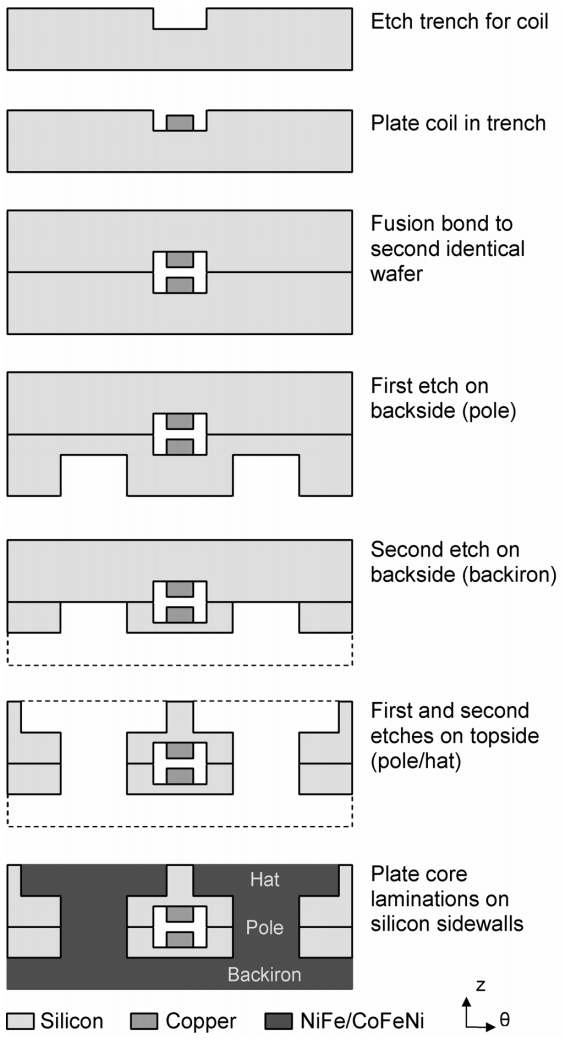

***Figure 2**. Simplified fabrication process flow for wafer-bonded machine stator, depicting cross sections in θ-z plane: two coil conductors pass radially through the laminated core structure (laminations not shown).*

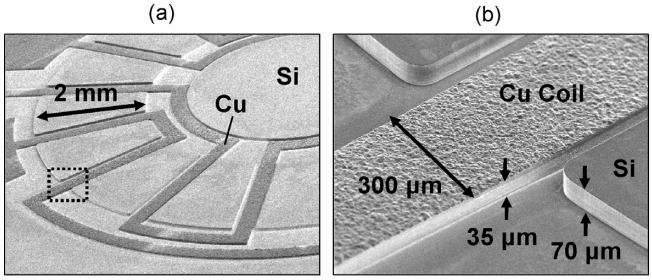

Figure 3. *(a) SEM of 35 µm thick, 300 µm wide, copper coil recessed in 70 µm deep silicon cavity before wafer bonding to a second identical wafer; (b) Detail.*

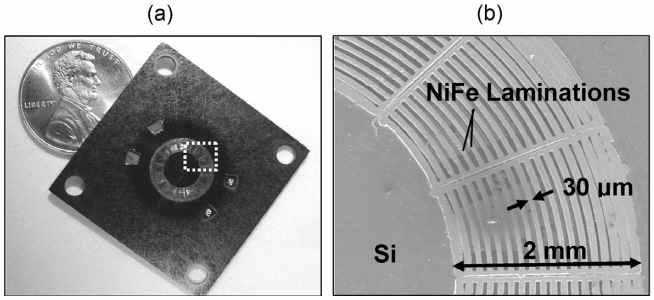

Figure 4. *(a) Fabricated wafer-bonded machine stator; (b) SEM of highlighted region showing 30 µm wide, 1000 µm tall, NiFe vertical magnetic laminations.*

molds. The SU-8 was then removed and the silicon substrate was etched away using KOH. The silicon tether structures were formed separately by through-etching a wafer using DRIE. The rotors were subsequently glued into the tethered retaining ring.

CHARACTERIZATION

For characterization, the rotor was suspended above the stator with flexible silicon tethers to avoid the difficulties of supporting and stabilizing a spinning rotor. The stator and tethered rotor components were clamped together and mounted on a water-cooled chuck as shown in Fig. 5. An air gap of 50 µm was maintained between the stator and rotor by using Kapton spacers.

Power electronics supplied a balanced current excitation in quadrature to the stator phases. The drive signals were routed through a circuit that could swap the phases at a given frequency (the *torque reversal* frequency) to control the direction of the traveling magnetic wave and resulting torque. Using this setup, the tethered rotor was excited at a torque reversal frequency much lower than the electrical frequency. A microvision image analysis system was used to dynamically measure the angular deflection of the tethered rotor under the influence of the oscillating torque input, as described in [**8**]. The torque was extracted by fitting a second-order response $T = J\ddot{\theta} + b\dot{\theta} + k\theta$ to the measured data.

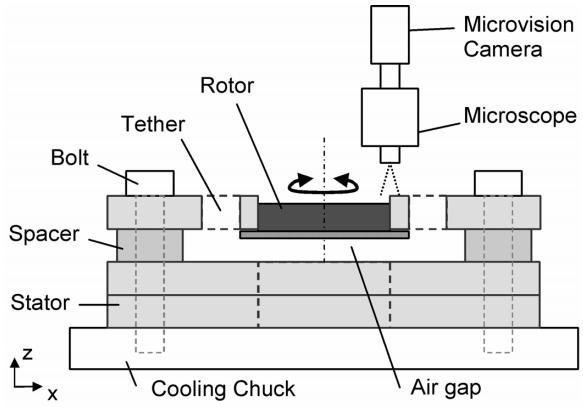

Figure 5. *Schematic of the measurement setup showing the tethered rotor structure clamped to the stator on the cooling chuck. The air gap was maintained at 50 µm.*

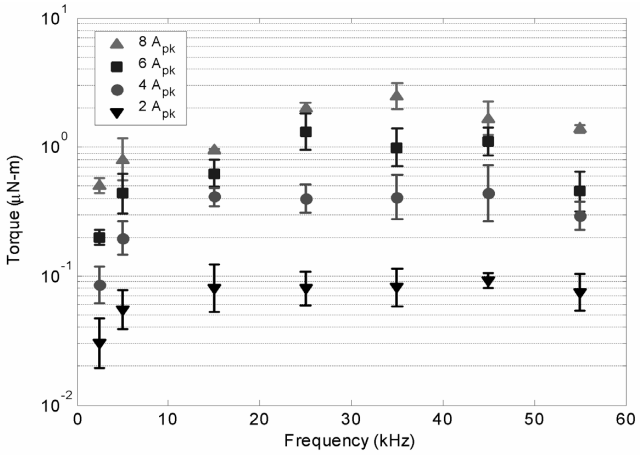

Figure 6. *NiFe machine measured torque vs. electrical frequency for currents of 2 – 8 A_{pk} with 50 µm air gap.*

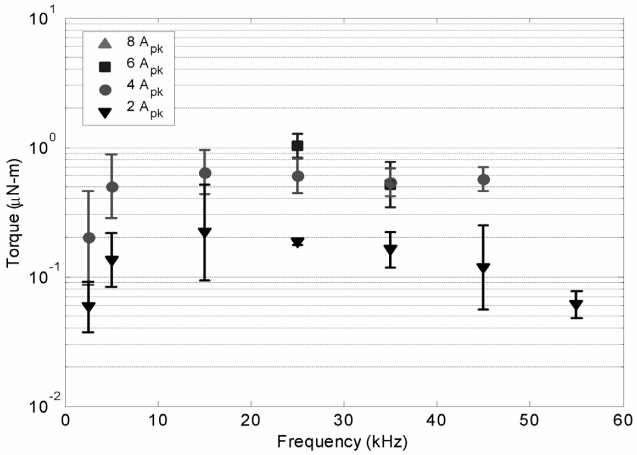

Figure 7. *CoFeNi machine measured torque vs. electrical frequency for currents of 2 – 6 A_{pk} with 50 µm air gap.*

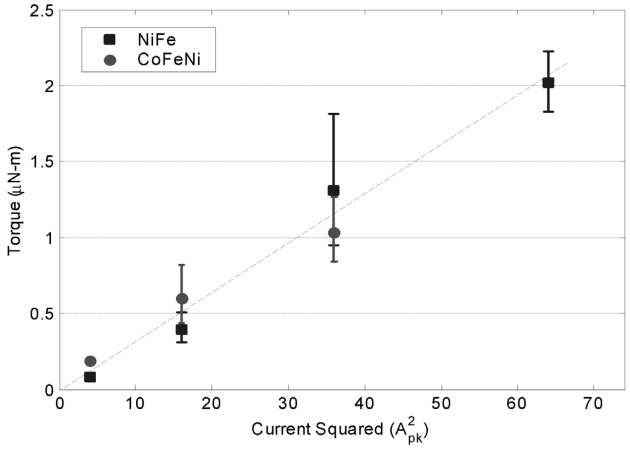

Figure 8. *Torque vs. square of stator current for NiFe and CoFeNi machines at 25 kHz with 50 µm air gap.*

Machines were analyzed in motoring mode by varying both the amplitude and frequency of the excitation currents. The machines show characteristic induction machine behavior as shown in Figs. 6 and 7. The error bars indicate 95% confidence intervals, based on the accuracy of the curve fit to the dynamic response data. The tethered motor testing was limited to a maximum of 8 A_{pk} (approximately 8 W per phase, for 0.25 Ω coil resistance) because the displacement of the rotor became non-linear and out-of-plane motion was detected, both causing large uncertainties in the torque extraction.

The NiFe machine shows a maximum torque of 2.5 μN·m at 8 A_{pk}, 35 kHz. Tests of the CoFeNi machine were corrupted at high currents by broken tethers, and only two data points were collected above 4 A_{pk}. Regardless, the CoFeNi machine demonstrated 1.0 μN·m at 6 A_{pk}, 25 kHz. At low currents, where no magnetic saturation occurs, the torque should show a quadratic dependence with current; upon saturation, the torque should increase linearly. Fig. 8 plots the torque vs. the *square* of current. The data follows this quadratic relation, indicating that neither machine had saturated, and that higher currents may be used to achieve even larger torques. While not measured, the machine should support currents of at least 32 A_{pk} (corresponding to a current density of 3 x 10^9 A/m^2). At this level, and assuming no saturation, the machine would exhibit ~40 μN·m of torque (340 $N·m/m^3$ torque density).

CONCLUSIONS & FUTURE WORK

These successful demonstrations of laminated, wafer-bonded, Si-based magnetic machines represent progress toward a fully-integrated microengine system. The materials, structure, and fabrication processes offer the potential for higher operating temperatures and direct integration with multi-wafer microturbine devices.

The performance of these silicon-based machines is comparable to the previously reported SU-8-based machine [**8**] as summarized in Table 1. Torque density normalizes the torque by the active volume of the machine. The average surface shear stress normalizes the torque generated on the surface of the rotor by surface area and moment arm. This is the average force per unit area generated in the rotor by the electromechanical interactions. Although higher torque densities and shear stresses have been reported for electric induction machines [**7**,**8**], those results were obtained using spinning, not tethered rotors.

Device	a (mm)	b (mm)	t (mm)	Max. Torque (μN·m)	Torque Density ($N·m/m^3$)	Shear Stress (N/m^2)
Magnetic SU-8-based [**8**]	1.0	2.0	2.0	0.3	12	20
Magnetic Si-based	3.0	5.0	1.5	2.5	21	12

Table 1. *Comparison of magnetic induction machine measured performances (a, b, and t are the inner radius, outer radius, and thickness, respectively, for the active machine volume—stator, rotor, and air gap, excluding the windings).*

It is believed that the performances of the machines reported here are limited by two fabrication issues. First, the teeth gaps between adjacent poles on the upper surface of the stator core are partially closed over due to overplating of the laminations. This shorts out the magnetic flux path between the stator and rotor and limits torque production. Second, in using highly doped silicon for the stator frame, the eddy currents, which would normally be confined to small loops around each lamination, are now allowed to circulate around an entire stator pole. These large eddy current loops reduce the flux linking the stator and rotor and limit the effectiveness of the laminations. The defective teeth gaps may be repairable and the machines retested. Alternatively, rebuilding machines with a nonconductive stator frame, larger coils, and more aggressive fabrication could also further improve the torque.

Future efforts will focus on enabling spinning rotors for testing in both motoring and generating mode. This will permit measurements of speed, power, and efficiency for additional characterization.

ACKNOWLEDGEMENTS

This work was supported by the Army Research Laboratory (DAAD19-01-2-0010) and Army Research Office (DAAG55-98-1-0292). The authors thank the staff of the Microelectronics Research Center at Georgia Tech for their assistance with fabrication and Dr. D. Freeman's group at MIT for use of the computer microvision system.

REFERENCES

1. A. H. Epstein, S. D. Senturia, et al., "Power MEMS and microengines," *Tech. Dig. Int. Conf. Solid-State Sensors and Actuators* (*Transducers '97*), June 1997, pp. 753-756.

2. A. H. Epstein and S. D. Senturia, "Macro power from micro machinery;" *Science*, vol. 276, no. 5316, p. 1211, May 1997.

3. A. Mehra, et al., "A six-wafer combustion system for a silicon micro gas turbine engine," *J. Microelectromech. Syst.*, vol. 9, pp. 517-27, 2000.

4. L. G. Frechette, et al., "Demonstration of a microfabricated high-speed turbine supported on gas bearings," *Tech. Dig. Solid-State Sensor and Actuator Workshop* (*Hilton Head 2000*), June 2000, pp. 43-7.

5. L. G. Frechette, et al., "An electrostatic induction micromotor supported on gas-lubricated bearings," *Tech. Dig. 14th IEEE Int. Conf. MEMS* (*MEMS 2001*), Jan. 2001, pp. 290-293.

6. C. Livermore, et al., "A high-power MEMS electric induction motor," *Tech. Dig. Solid-State Sensor and Actuator Workshop* (*Hilton Head 2002*), June 2002, pp. 251-254.

7. F. Cros, et al., "Micro-magnetic induction machines for portable power applications," *Proc. Army Research Lab Collaborative Technology Alliances, Power and Energy*, April 2003, pp. 17-21.

8. H. Koser, "Development of magnetic induction machines for micro turbo machinery," *Ph.D. Thesis*, Massachusetts Institute of Technology, Cambridge, MA, June 2002.

9. A.E. Fitzgerald, C. Kingsley, Jr., S. D. Umans, *Electric Machinery*, 6th Ed., New York: McGraw Hill, 2002.

10. J. Lammeraner and M. Stafl, *Eddy Current*, London: Iliffe, ch. 1-2, 1966.

11. R. M. Bozorth, *Ferromagnetism*, New York: IEEE Press, Reissue, pp.162-169, 1993.

12. D. P. Arnold, et al., "Electroplated metal microstructures embedded in fusion-bonded silicon: conductors and magnetic materials," *J. Microelectromech. Syst.*, (submitted).

13. D. P. Arnold, et al., "Vertically-laminated magnetic cores by electroplating Ni-Fe into micromachined Si," *IEEE Trans. Magn.* (in publication).

LIQUID-ROTOR ELECTRET MICROPOWER GENERATOR

Justin S. Boland, Yu-Chong Tai
Electrical Engineering, California Institute of Technology
Pasadena, California 91125

ABSTRACT

We present the world's first liquid-rotor electret power generator (LEPG), designed to harvest electricity from low-frequency mechanical vibrations. The device (figure 1) consists of a fixed-charged, Teflon-electret capacitor with an air-filled gap and a liquid droplet that moves by vibration. As the liquid moves into and out of the gap, a net voltage is generated across the capacitor as image charges (induced by the electret) on the two electrodes redistribute according to the position of the droplet. Experimentally, we have proven the feasibility of such a device and our first prototype can generate greater than 30Vpp open-circuit voltage and deliver a power as high as 0.43μW to a resistive load (at 28Hz and R_{load}=21MΩ). The LEPG may be an economical method to harvest power from vibrational environments to power remote sensing devices.

INTRODUCTION

Portable and remote electronics require power, generally provided by disposable or rechargeable batteries. These sources, however, must be replaced or replenished. Meanwhile, this time the device is not useful. This poses serious problems in placing sensors in remote location devices, such as sensor-net nodes and bio-implantable devices. Novel devices are needed to convert available energy to electrical power. Some solutions include photovoltaic and piezoelectric transducers [1]. The LEPG is the latest energy scavenging device.

Seiko has demonstrated the ability to harvest energy from rotational torque with an electromagnetic power generator in their Kinetic Series watches. We have previously demonstrated this same ability with an electrostatic solution, which takes advantage of MEMS process efficiencies and produces output voltage swings greater than 40 volts. Our previous generator converts rotational energy to electrical energy with a fixed-charge variable-area capacitor. Exploiting the relationship

$$V(t)=Q/C(t),\ C(t)=\varepsilon A(t)/d \qquad [1]$$

we are able to convert a variable area into a variable voltage for power harvesting.

To take advantage of linear oscillations, we could easily change the geometry of the previous device and fabricate a moving-mass suspended by springs. This is still a fixed-charge, variable-area capacitor. A fixed-charge, variable-distance capacitor is essentially a microphone, which has been previously reported [2-4].

The work presented here explores a variable-permittivity capacitor.

$$C(t)=\varepsilon(t)A/d \qquad [2]$$

The effects of a variable permittivity are explored in freshman E&M books [5], but those examples use a solid dielectric. This would quickly destroy the Teflon surface unless a mechanism is employed to maintain a gap while allowing relative motion. This causes more friction and thus consumes valuable energy. Instead of using solids and more processing steps to create micro springs or sliders, our solution exploits the near-zero friction of a high contact angle liquid on the dielectric.

Experiments with liquid water stalled when the liquid experienced electrowetting [6]. Using silicone oil to prevent electrowetting would enable the use of water, but it is not clear what effect this would have on the required fixed charge . Mercury is a liquid at room temperature, and does not appear to suffer from electrowetting. It has a contact angle of ~150° on Teflon. Mercury, a conductive metal, is equivalent to a dielectric of infinite permittivity.

With low friction and heavy mass, the mercury will remain fixed as we subject the capacitor to linear oscillatory motion.

THEORY

The LEPG can be described as a displacement current device, in which a constant charge embedded into the Teflon produces an image charge shared between the top and bottom electrodes.

$$Q = q_1(t) + q_2(t) = \sigma LW \qquad [3]$$

Where Q is total charge implanted, q_1 and q_2 represent the free charge available at the electrodes, σ is the measured charge density, and L and W are the length and width of the active channel as can be seen in figure 1. By fixing the position of the implanted charge and assuming the charge to be of uniform depth, it acts as a uniform intermediate electrode. The first approximation assumes the charge resides entirely on the surface of the Teflon layer. This intermediate electrode allows us to describe the system as four separate capacitors.

Starting with a single capacitor, C_0, we develop an expression for a variable-dielectric capacitor c_0' with a dielectric that enters the gap according to the area ratio $\alpha(t)$.

$$C_0 = \frac{\varepsilon_0 A_0}{G} \qquad [4]$$

$$c_0' = \frac{\varepsilon_0 A_0}{G}\left(1-\alpha(t)\right) + \frac{k_{liquid}\varepsilon_0 A_0}{G}\alpha(t) = C_0\left(1+\chi_{liquid}\alpha(t)\right) \qquad [5]$$

Where χ_{liquid} is k_{liquid}-1

Now, we add in a second capacitor in series to C_0 to account for the charge implantation at depth Δ.

$$C_1 = (C_0^{-1} + C_{Teflon}^{-1})^{-1} = \frac{\varepsilon_0 k_{Teflon} A_0}{\Delta + k_{Teflon} G} \qquad [6]$$

0-9640024-5-0/hh2004/$20©2004TRF
DOI 10.31438/trf.hh2004.37

Solid-State Sensors, Actuators, and Microsystems Workshop
Hilton Head Island, South Carolina, June 6-10, 2004

Incorporating a moving dielectric as shown in figure 1b and we get.

$$c_1 = \frac{k_{liquid}\varepsilon_0 A_0 \alpha(t)}{G},\ c_2 = \frac{\varepsilon_0 A_0 (1-\alpha(t))}{G},$$
$$c_3 = \frac{k_{Teflon}\varepsilon_0 A_0 \alpha(t)}{\Delta},\ c_4 = \frac{k_{Teflon}\varepsilon_0 A_0 (1-\alpha(t))}{\Delta} \quad [7]$$

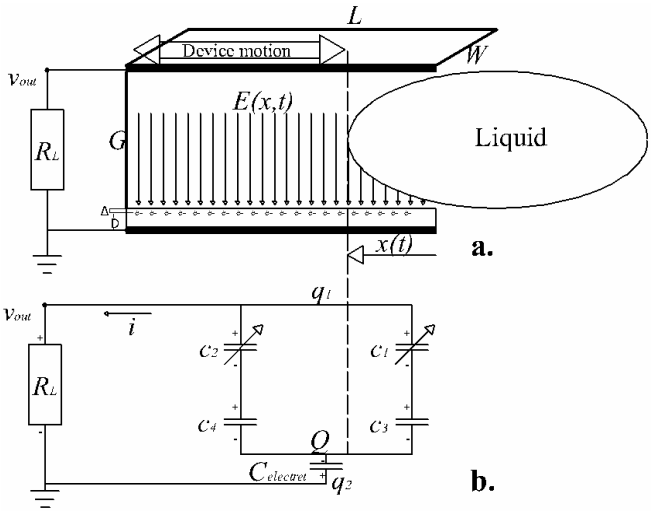

Figure 1. *a. Conceptual design b. Equivalent circuit.*

The four capacitors exist between the top electrode and the implanted charge layer and reduce to a single equivalent capacitor as follows

$$\left(\frac{1}{c_1}+\frac{1}{c_3}\right)^{-1} = \frac{k_{liquid}k_{Teflon}\varepsilon_0 A_0 \alpha(t)}{k_{liquid}\Delta + k_{Teflon}G},$$
$$\left(\frac{1}{c_2}+\frac{1}{c_4}\right)^{-1} = \frac{k_{Teflon}\varepsilon_0 A_0 (1-\alpha(t))}{\Delta + k_{Teflon}G} \quad [8]$$

Then the equivalent capacitor is expressed as

$$c_1' = \left(\frac{1}{c_1}+\frac{1}{c_3}\right)^{-1} + \left(\frac{1}{c_2}+\frac{1}{c_4}\right)^{-1} = C_1\left(1+\beta\chi_{liquid}\alpha(t)\right) \quad [9]$$

Which is similar to equation [5] - a single, variable-dielectric capacitor. The extra term is

$$\beta = \frac{k_{Teflon}/\Delta}{k_{liquid}/G + k_{Teflon}/\Delta} \quad [10]$$

For oscillatory motion with the droplet occupying the entire channel at t=0, the area of the channel that is affected by the liquid is described by

$$\alpha(t) = \left(\frac{1+\cos(\omega t)}{2}\right) \quad [11]$$

For simplicity we ignore the spherical nature of the droplet.

Using the familiar $V=Q/C$, we can write the loop voltage as

$$v_{out} = \frac{q_1}{c_1'} - \frac{q_2}{C_2} = q_1\left(\frac{1}{c_1'}+\frac{1}{C_2}\right) - \frac{Q}{C_2} \quad [12]$$

Where q_1 is the charge on the top electrode, q_2 is the charge on the bottom electrode, and C_2 is the capacitance between the implanted charge layer and the bottom electrode. q_2 was eliminated in favor of the constant charge Q and q_1 by substituting [3] into [12].

Noting the obvious,

$$v_{out} = iR_l = -R_l\frac{\partial q_1}{\partial t} \quad [13]$$

and substituting [12] into [13], v_{out} is eliminated:

$$-R_l\frac{\partial q_1}{\partial t} = q_1\left(\frac{1}{c_1'}+\frac{1}{C_2}\right) - \frac{Q}{C_2} \quad [14]$$

In standard form, this is a linear, first order ODE.

$$\frac{\partial q_1}{\partial t} + \frac{1}{R_{load}}\left(\frac{1}{c_1'}+\frac{1}{C_2}\right)q_1 = \frac{Q}{R_{load}C_2} \quad [14]$$

Using:

$$m = \frac{1}{R_{load}}\left(\frac{1}{C_1\left(1+\beta\chi_{liquid}\alpha(t)\right)}+\frac{1}{C_2}\right)$$
$$n = \frac{Q}{R_{load}C_2} \quad [16]$$

$$\mu(t) = e^{\int m dt} = e^{\frac{t}{R_{load}C_2}} e^{\frac{1}{R_{load}C_1}\int\left(\frac{1}{1+\beta\chi_{liquid}\alpha(t)}\right)dt} \quad [17]$$

the solution is given by:

$$q_1 = \frac{\int \mu(t) n dt}{\mu(t)} + \frac{Const}{\mu(t)} \quad [18]$$

Numerical methods must be employed to solve this equation. The current, output voltage, and power can then be described as:

$$i = -\frac{\partial q_1}{\partial t},\ v_{out} = iR_{load},\ P_{out} = iR_{load}^{\ 2} \quad [19]$$

FABRICATION

Fabrication of the LEPG is shown in figure 2. Glass plates with patterned metal are the starting capacitor electrodes. An 8μm thick Teflon AF is spun onto the bottom plate, and 0.5μm Teflon onto the top plate [4]. The Teflon AF layer on the bottom plate is then implanted with electrons from a back-lighted thyratron to form the electret [7]. The spacer (which also provides the liquid chamber) is made by casting Sylgard 184 PDMS onto a CNC-machined mold (figure 3) and bonded to the bottom plate with epoxy. For this demonstration, a liquid mercury droplet is used to partially fill the chamber on the bottom electrode. The top electrode plate is then bonded to the spacer to finish the device (figure 4). Cavity dimensions for Device 3 are W=2.3mm, L=4.812mm, and H=2.3mm for a droplet of 50μL. Cavity

dimensions for Device g are W=3.5mm, L=9.4mm, H=4.45mm for a droplet about 600μL.

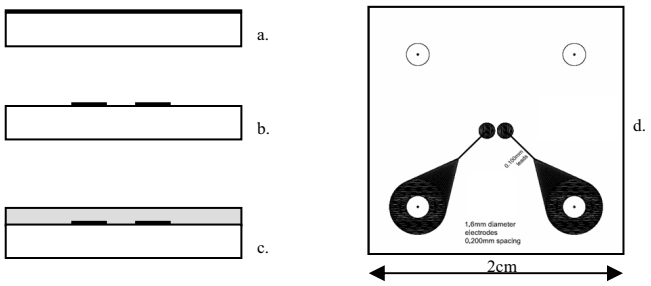

Figure 2. *Process Flow a. deposit metal on glass substrate b. pattern metal c. spin-on Teflon AF d. mask design used in step b.*

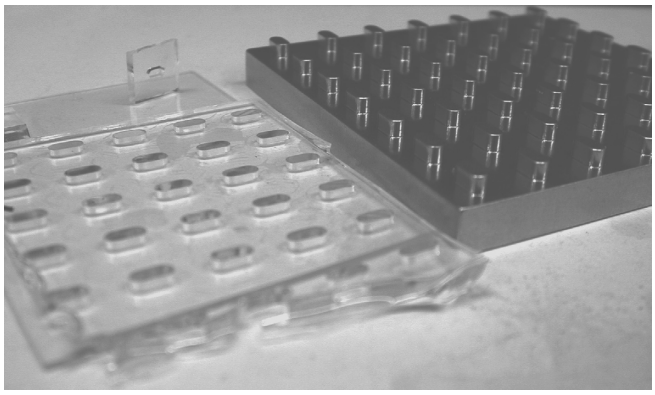

Figure 3. *Mold Master for Sylgard 184 and peeled PDMS.*

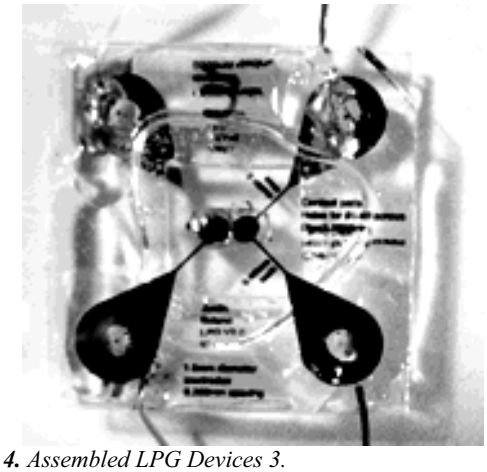

Figure 4. *Assembled LPG Devices 3.*

EXPERIMENTAL DETAILS

Power generation experiments are performed using a shielded box mounted to Labworks Inc. ET-132-2 electrodynamic shaker (figure 5.), which is driven sinusoidally by a HP33120A function generator through a power amplifier. The acceleration of the power generator is measured using an Endevco256HX-10 accelerometer. Both the acceleration and generator voltage waveforms are averaged over 256 data sets. The shaking frequency is varied from 10Hz to 60Hz, while the rms acceleration is kept constant through the experiments. The LEPG is connected to a resistive load and the voltage across the load is measured from a National Semiconductor LF356N op-amp used as a 10^{12}Ohm input impedance voltage buffer.

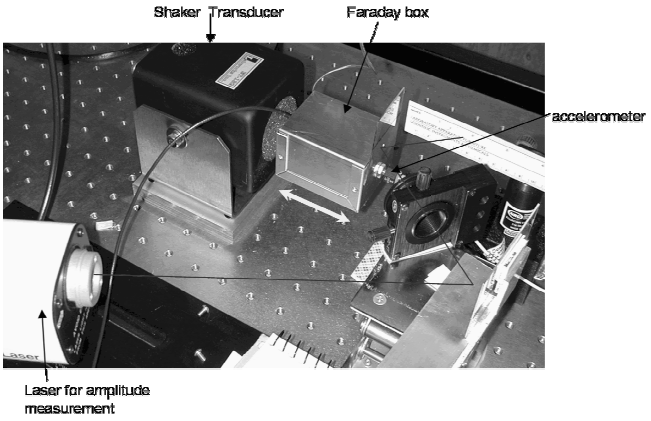

Figure 5. *Test Setup for LEPG*

DATA ANALYSIS

Power generated versus frequency from two LEPG devices of different size suggests that device geometry can be optimized for shaking parameters (figure 6). In this graph we see the maximum power of 0.25μW was produced with Device 3, the same shown in figure 4. The waveform of Device 3 appears to be frequency shifted by 19Hz with respect to Device g, with secondary peaks being larger in magnitude. The frequency shift is expected since channel length for Device g is ~50% longer than Device 3. The measured masses are: Device 3 is 2.7g and Device g is 5g, including mercury.

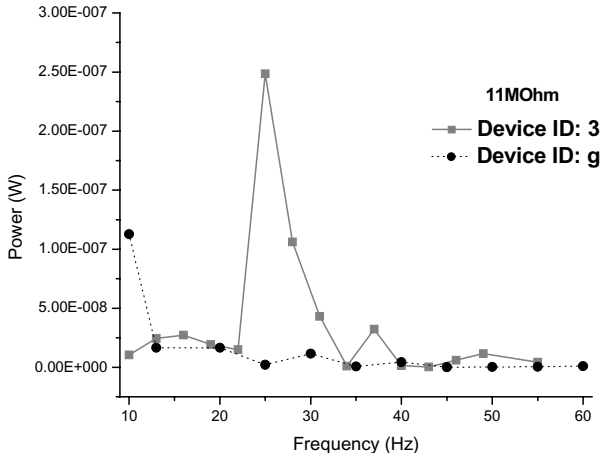

Figure 6. *Power versus frequency for 2 devices of different channel length and height.*

Figure 7 also shows that for a single device, power generation versus frequency is load dependent. The figure shows that power is scaled, but not translated in frequency for different loads. Thus far, insufficient testing precludes determining the optimum load.

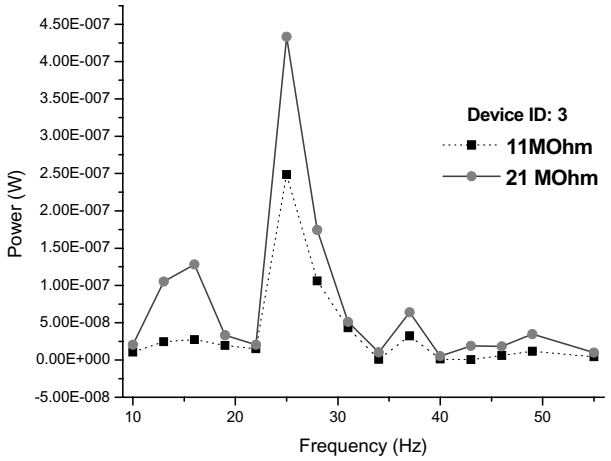

Figure 7. *Power versus frequency for a single device with 2 different loads.*

Figure 8 shows open circuit voltage increasing with acceleration up to 16Hz for a single device. From 16Hz to 24Hz the voltage output exceeds the buffer amplifier range of 30Vpp. For frequencies greater than 24Hz the mercury droplet begins to oscillate in multiple modes at frequencies other than the driving frequency. This lowers rms voltage output. The shaker setup does exhibit slight resonant modes in the y and z axes, however, this phenomenon is observed on all test samples, and appears to be related to cavity and/or liquid dimensions as shown in figure 6.

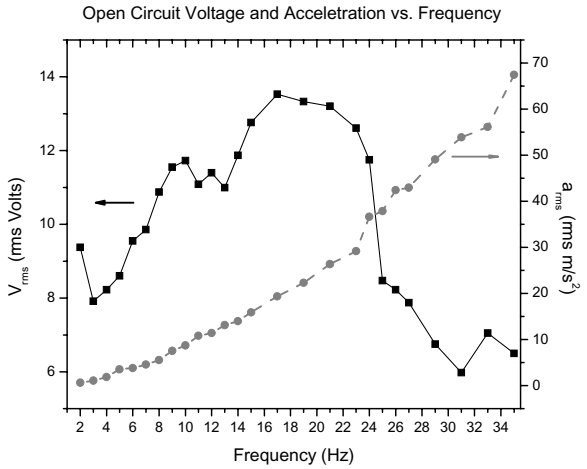

Figure 8. *Open circuit voltage and acceleration versus frequency for constant displacement.*

The voltage response of figure 9 is clipped, but it is apparent that system response is related to the driving function. The driving function being fed to the shaker is sinusoidal, but this frequency is below the specifications listed on the accelerometer. Watching the shaker, the motion is visibly not sinusoidal. As acceleration passes through its maximum, the voltage output passes through zero. Equivalently, current is proportional to velocity.

Lifetime tests were performed on Device g. The test consisted of a repeating, linear frequency sweep between 1 and 60Hz over 30second intervals for 2 weeks. There was no noticeable change in the output power or waveform over this time.

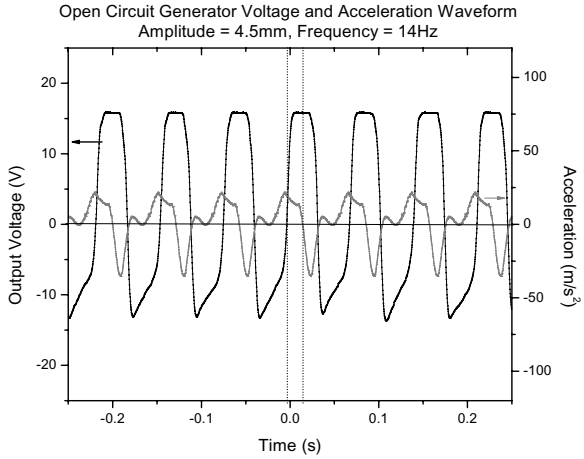

Figure 9. *Open circuit voltage and acceleration waveforms, at given amplitude and frequency.*

CONCLUSIONS

We have produced a variable-permittivity power generator with maximum power output of 0.25μW and over 30Vpp open circuit voltage. The trend shows an increase in power generated for smaller devices and higher frequencies. For load resistances tested, there is no evidence that maximum power output shifts in frequency with load resistance. Further work should probe the effects of scaling device dimensions and varying liquid volume fractions. Liquid dielectrics with dielectric constant less than infinity should also be explored.

*This work is supported by DARPA MPG program (*DAAH01-01-1-R002*) and NSF ERC Center for Neuromorphic Systems Engineering at Caltech (EEC-9402726). Travel support has been generously provided by the Transducers Research Foundation and by the DARPA MEMS and DARPA BioFlips programs.*

REFERENCES

1. S. Roundy, B. Otis, Y-H. Chee, J. Rabaey, P.K. Wright, “A 1.9 GHz Transmit Beacon using Environmentally Scavenged Energy.” *ISPLED 2003*, Seoul Korea, 2003 August 25-27, (2003).

2. W. Hsieh, T. Hsu and Y. Tai, "A Micromachined Thin-Film Teflon Electret Microphone", *TRANSDUCERS '97, Solid-State Sensors and Actuators*, Chicago; IL, 1997 Jun, IEEE (1997), pp. 2B2.02.

3. W. H. Hsieh, T.-J. Yao and Y.-C. Tai, "A High Performance Mems Thin-Film Teflon Electret Microphone", *TRANSDUCERS '99 The 10th International Conference on Solid-State Sensors and Actuators*, Sendai, Japan, 1999, Institute of Electrical Engineers of Japan (1999), pp. 1064-1067.

4. T.-Y. Hsu, W. H. Hsieh, K. Furutani and Y.-C. Tai, "A Thin Film Teflon Electret Technology for Microphone Applications", *Technical Digest of the 1996 Solid-State Sensor and Actuator Workshop*, Hilton Head Isl., SC, 1996 June, Transducers Research Foundation, Cleveland (1996), pp. 235-238.

5. D. J. Griffiths, "Introduction to Electrodynamics", Prentice Hall,0-13-481367-7, (1989).

6. H. Moon, S. Cho, R. Garrell and C. Kim, "Low Voltage Electrowetting-on-Dielectric",*Journal of Applied Physics*,92,[7],4080-4087(2002).

7. T. Y. Hsu, "A Novel Electron Beam Source Based on the Back-Lighted Thyratron", *Ph.D. dissertation, University of Southern California*,1992).

An Ultra High Efficiency Piezoelectric Direct Charging Radioisotope Micropower Generator

Rajesh Duggirala, Hui Li, and Amit Lal
*Sonic*MEMS Laboratory, School of Electrical and Computer Engineering, Cornell University
Ithaca, NY-14850

ABSTRACT

We demonstrate a novel piezoelectric radioisotope micropower generator that has an ultra high conversion efficiency of 7.2% from collected electron energy to electrical energy. The generator employs direct charging to convert radiated β-particle kinetic energy into stored electromechanical energy, and piezoelectricity to convert the stored electromechanical energy to extractable electrical energy. The radiated β-particles are used to *direct charge* an air-gap capacitor, formed by the collector plate at the tip of a piezoelectric unimorph cantilever beam and the thin-film radioisotope source. The emitted charges induce an electrostatic force which draws the two plates closer. The collector plate eventually makes contact with the source, discharging the air-gap capacitor and releasing the cantilever. The sudden release excites the unimorph mechanical impulse response, causing the cantilever to oscillate. The stored electromechanical energy is converted into electrical energy dissipated across the load. The vibrations die out and a new reciprocation cycle begins. Using a low-activity (0.5 millicurie) radioisotope source, we demonstrate a peak output voltage of 1.5 V across a load resistance of 1 MΩ, corresponding to a peak output power of 2.25 μW.

INTRODUCTION

A critical requirement for the success of autonomous remote systems is the realization of miniature micropower sources with long lifetimes. This demands a power source using a fuel with extremely high energy density, and a highly efficient conversion mechanism implementable at the small-scale.

Several technologies have been investigated for micropower applications. Traditional electrochemical batteries have very high conversion efficiencies (up to 50 %), but suffer from low energy densities (1-2 kJ/m^3 [1]). Hydrocarbon fuels have higher energy densities (20 kJ/m^3), but suffer from low conversion efficiencies at the small-scale. Demonstrated technologies for hydrocarbons conversion include micro-fuel cells [2] and micro-heat engines [3]. Micro solar cells [4] can potentially provide long lifetimes at an acceptable power density (10 mW/cm^2 under direct sunlight), but need light for operation.

In comparison, radioisotopes can have very high energy densities (~10^5 kJ/m^3) [5]. Additionally, since the half-life of radioisotope thin films can range from 100's of years to a few seconds, a power source with optimal lifetime can be designed with a suitable choice of radioisotope.

Early work on the conversion of radioactive energy focused on thermal heating [6], thermoelectric [7] and thermionic [8] conversion mechanisms. These mechanisms employ heat cycles and require high temperatures (300-900 K) for efficient operation. They are generally useful for the generation of power in the few watts-kilowatts range. But they do not scale down well for micro-power applications. They are also feasible only at the large-scale (volume > 0.1 m^3) as it is hard to achieve large thermal gradient at high temperatures in microsytems. An alternative to the aforementioned mechanisms is direct charging of capacitors with emitted charged particles [9]. These systems can generate very high voltages (100 kV – 10 MV), but the need for power conditioning circuitry at these voltages makes this approach untenable. An approach commonly used for micro-scale micropower operation is using the betavoltaic effect (emitted charge e-h$^+$ generation) [10]. Betavoltaic cells tend to be low power devices operating at low efficiencies (< 0.5 %). Moreover, they present a tradeoff between power output and lifetime as increased radiation doses can lead to limited lifetime due to impact damage.

We have previously reported a self-reciprocating direct charging cantilever beam [11] to show the feasibility of capturing the kinetic energy of emitted particles to actuate a cantilever beam, and convert the radiated kinetic energy to stored mechanical energy in the cantilever. In this paper, we report a milliscale micropower generator that utilizes the direct charging process to actuate piezoelectric unimorphs, which in turn generate electrical power. The piezoelectric unimorph supplies the load circuit with a directly usable voltage signal while shielding it form the high voltages generated due to direct charging. The generator uses a 0.5 millicurie thin-film Ni^{63} solid source emitting low-energy β radiation (average electron energy 17 keV, half-life = 100.2 years) with very low penetration depth (14 μm in copper). The low penetration depth of the emitted particles combined with the solid state nature of the source eliminates the need for elaborate measures for shielding, further enhancing the applicability of the microgenerator for microsystems such as remote sensor nodes.

THEORY

Figure 1 shows the schematic of the piezoelectric radioisotope micropower generator. The collector at the tip of the cantilever beam traps the charged particles emitted from the thin-film radioactive source. By charge conservation, the radioisotope film is left with equal and opposite charges. This leads to electrostatic force between the cantilever and the radioactive source, bending the cantilever and converting the radiated kinetic energy to stored mechanical energy. For suitable initial gap separations, the tip of the cantilever eventually makes contact with the radioactive thin-film and the accumulated charges get neutralized via charge transfer. As the electrostatic force is nulled, the cantilever is released. The sudden release excites oscillations, which lead to charges induced in the piezoelectric element at the base of the cantilever. With suitable termination to the electrical circuit, the cantilever system can be designed to behave as a resonant power source. A rectifier based circuit topology is commonly used to extract power [12]. The rectified output current of the micropower generator is used to charge up a storage capacitor or a rechargeable battery, which is used to power low-power circuits. In this work, a simple load resistor (Figure 2) is used to focus on the characteristics of the microgenerator.

The radiated kinetic energy E_r for one reciprocation cycle is

$$E_r = I_r E_{avg} (T_{rec} + T_{vib}) \cong I_r E_{avg} T_{rec}, \qquad (1)$$

Travel support has been generously provided by the Transducers Research Foundation and by the DARPA MEMS and DARPA BioFlips programs.

0-9640024-5-0/hh2004/$20©2004TRF
DOI 10.31438/trf.hh2004.38

Solid-State Sensors, Actuators, and Microsystems Workshop
Hilton Head Island, South Carolina, June 6-10, 2004

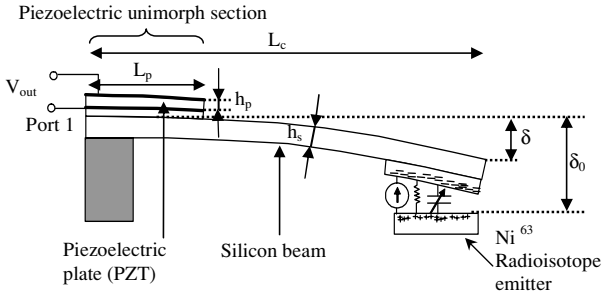

Figure 1: Cross-section showing the geometrical parameters of the structure and a model of the air-gap capacitor. The current source is due to emitted charges, R is due to ionization current/ secondary electron emission, and the source plate and the collector plate form a capacitor.

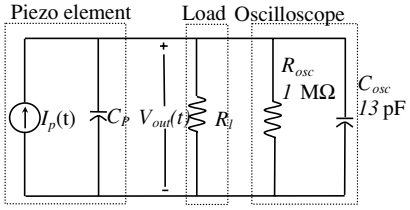

Figure 2. The circuit configuration for the characterization of the micropower generator

where I_r is the net current due to the collection of emitted charged particles, E_{avg} is the average kinetic energy of the emitted particles, T_{rec} is the reciprocation period, and T_{vib} is the duration for which the vibrations are sustained. The vibration period T_{vib}, is negligible compared to T_{rec} for the devices with high efficiency, as high charge voltages requiring long reciprocation times lead to high efficiency. The reciprocation period T_{rec}, can be calculated using

$$T_{rec} = \frac{Q_{final}}{I_r} = \frac{\sqrt{2\varepsilon A k \delta_0}}{I_r}, \qquad (2)$$

by modeling the air-gap capacitor as a current controlled electrostatic actuator. The electromechanical energy E_{em} stored in the cantilever just before discharge is

$$E_{em} = E_m + E_q = \frac{1}{2}k\delta_0^2 + \frac{Q_p^2}{2C_p} \cong \frac{1}{2}k\delta_0^2, \qquad (3)$$

where E_m is the stored mechanical energy, E_q is the stored dielectric energy in the piezoelectric element, k is the stiffness of the cantilever beam, δ_0 is the initial gap height, Q_p is the charge induced in the piezoelectric just before contact due to the bending deformation and C_p is the capacitance of the piezoelectric element. For the devices discussed here, $E_m \sim 1000 E_q$. The extracted electrical energy per cycle E_{ext}, across a load resistor R_l, is given by

$$E_{ext} = \int_0^{T_{vib}} \frac{V_{out}^2(t)}{R_l} dt, \qquad (4)$$

where $V_{out}(t)$ is the output voltage. The ratio of the extracted electrical energy to radiated kinetic energy η is

$$\eta = \eta_r \eta_{me} = \frac{E_{em}}{E_r}\frac{E_{ext}}{E_{em}} = \frac{E_{ext}}{E_r}, \qquad (5)$$

where η_r is the ratio of the stored electromechanical energy to radiated kinetic energy and η_{me} is the ratio of the extracted electrical energy to stored electromechanical energy. The ratio η_r can be maximized by designing the peak charging voltage of the air-gap capacitor, $V_{cap\max}$, to satisfy the following condition.

$$V_{cap\max} = \sqrt{\frac{8}{27}\frac{k\delta_0^3}{\varepsilon A}} = \frac{E_{avg}}{q}. \qquad (6)$$

The above equation is based on the simplifying assumption that the peak charging voltage is not limited by voltage breakdown in the gap and all the emitted particles have a kinetic energy of E_{avg}. Writing δ_0 in terms of $V_{cap\max}$ and substituting the expression for T_{rec} in the expression for η_r we get

$$\eta_{r\max} = \frac{1}{2}\sqrt{\frac{27}{16}} = 0.64. \qquad (7)$$

Modeling the resonant system as a single degree of freedom system [13], it can be shown that η_{me} can be maximized to

$$\eta_{me} = \frac{k_{me}}{k_{me} + 2C_p c 2\pi f}, \qquad (8)$$

by using an optimum value of R_l given by

$$R_{opt} = \frac{1}{C_p 2\pi f}. \qquad (9)$$

Here, k_{me} is the mechanical to electrical coupling coefficient dependant on the geometry of the cantilever beam system and the characteristics of the piezoelectric element, C_p is the dielectric capacitance of the piezoelectric element, c is the mechanical damping coefficient and f is the resonance frequency of the cantilever beam system given by [14]

$$f = \frac{\lambda_i^2}{2\pi}\sqrt{\frac{k}{(0.23m + m_s)}}, \qquad (10)$$

where λ_i= 1.875 for fundamental bending mode, m is the mass of the cantilever beam, m_s is the mass of the collector plate. The collector plate mass provides an additional degree of freedom in adjusting the resonant frequency without changing the stiffness of the beam (for keeping T_{rec} constant). From Equation 8, η_{me} approaches unity in the absence of mechanical damping, or,

$$\eta_{me\max} = \eta_{me}|_{c\to 0} = 1.$$

Therefore, the maximum possible conversion efficiency for the device is

$$\eta_{\max} \times 100 = \eta_{r\max}\eta_{me\max} \times 100 = 64\%. \qquad (11)$$

FABRICATION

Prototype devices are fabricated to test for the power generation characteristics and verify the conversion principle. A 100 μm thick silicon wafer is laser-cut [15] into the desired dimensions for the cantilever beam. A 125 μm thick PZT-5H (lead-zirconate-titanate oxide ceramic from Piezo Systems Inc.) plate is also laser-cut into the desired dimensions for the piezoelectric element and bonded at the base of the silicon beam. Two pieces of 125 μm thick copper sheet, cut into 1 cm × 5 mm plates, are adhesively bonded to the tip of the silicon beam to act as both a charge collector and a mass to lower the resonance frequency. A β-particle emitting ^{63}Ni radioisotope is used for all the experiments. The ^{63}Ni is electroplated as a 1 cm × 1 cm thin-film on a 1 mm thick Ni plate. A large device (5 cm × 5 mm) and a small device (15 mm × 2 mm) are fabricated and tested in a vacuum chamber (Figure 3 (a)). The smaller device is fabricated to demonstrate the feasibility of packaging the device in a ceramic DIP package (Figure 3 (b)).

TESTING AND RESULTS

Figure 3(a) shows the experimental test setup. The beam is clamped between two ceramic plates for electrical insulation. The source is clamped by two Teflon plates, which are mounted on a

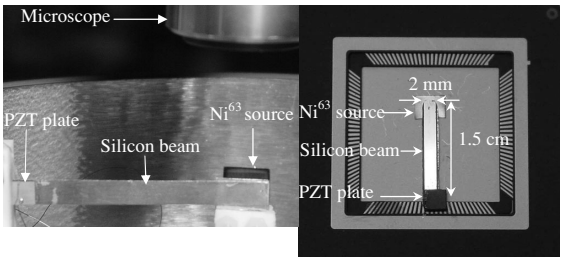

Figure 3. (a) The experimental setup used for testing the prototype device. (b) A prototype generator housed in a ceramic package

linear motion stage used to control the initial distance between the source and the cantilever collector. The setup is placed inside a vacuum chamber (p=10-20 mTorr) sealed with a glass top. A microscope connected to a CCD camera outside the chamber is used to monitor the motion of the cantilever tip. The two leads connected to an external circuit (Figure 2) are used to monitor the output signal.

Tests for characterizing the two components of the micropower generator, the direct charging air-gap capacitor and the piezoelectric unimorph beam are carried out before the characterization of the micropower generator.

The net current due to the transport of the emitted charges I_r, is measured by positioning a collector plate (1 cm × 5 mm) at a given separation from the thin-film source and measuring the short circuit (output terminals shorted) current using a semiconductor analyzer (Keithley 4200). The dependence of the charge collection on the gap separation is plotted in Figure 4. As the gap separation increases, the solid angle subtended by the collector at the source decreases, resulting in the lower number of captured particles and hence a lower current. The current is expected to be affected minimally by non-idealities in the system, such as secondary electron emission from the collector and ionization current of the residual gas molecules in the gap [12]. The measured value of the current, at a very small gap separation (δ_0=5 µm) where the effects of the non-idealities are considered to be the least, is used in the calculation of the available energy (Equation 1) from the radioisotope source.

The stiffness of the cantilever (k) is measured by deflecting the beam tip and measuring the generated blocking force using a Chatillon™ force meter mounted on a Sutter Instruments Co. MP-285 micropositioner. The measured values of the stiffness are 2.33 N/m and 19.3 N/m for the larger and the smaller beam respectively. The measured values which agree well with the theoretical estimates of 2.67 N/m and 23.5 N/m, calculated using bending beam theory.

Tests for characterizing the micropower generator are done by first positioning the radioisotope source at an initial separation δ_0 from the collector at the tip of the cantilever, and monitoring the system through the charge-discharge/release-oscillations cycle. The reciprocation cycle is timed by visually observing for the release event. Figure 5 plots the output voltage signal from the piezoelectric element of the larger beam, with an oscillation frequency of 17.6 Hz. The procedure is carried out for different values of δ_0 and R_l. The results for the larger device are presented first.

The reciprocation period T_{rec} measured as a function of the initial gap distance δ_0 is plotted in Figure 6. The reciprocation period is expected to increase with the square root of δ_0 (Equation 2), but the measured value of T_{rec} is always higher than the expected value due to the non-idealities present in the air-gap capacitor charging system. The net radiated current I_r decreases with increasing δ_0 (Figure 4), and the leakage current due to

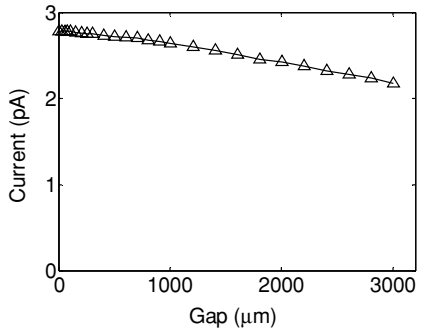

Figure 4. Measured net current due to the charge particles emitted from the radioisotope. Collector dimensions: 10 mm × 5 mm. The 2.8 pA corresponds to an effective activity of 0.5 millicurie.

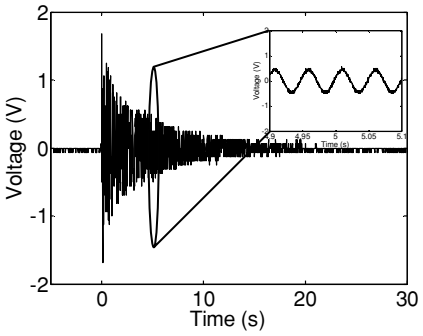

Figure 5. Measured output voltage across the piezoelectric element with a 1 Mohm load.

ionization of residual gas molecules increases [12] with increasing δ_0, resulting in higher than expected reciprocation times. Furthermore, reciprocation does not occur at all for initial gap separations of 3 mm and higher. The cantilever beam bends to about half of the gap separations, suddenly gets released and starts oscillating. This is because of the partial discharge occurring due to excessive buildup of voltage across the air-gap capacitor (estimated maximum electric field in the air gap for δ_0= 3 mm is 12.75 kV/mm), illustrated by the intersection of the air-gap capacitor voltage curve with the Paschen Curve in Figure 7.

The output voltage waveform is captured, and the modal damping ratio ζ, and quality factor Q, calculated using

$$\zeta = \frac{1}{(t_2 - t_1)2\pi f}\ln\left(\frac{V_{t1}}{V_{t2}}\right) = \frac{1}{2Q} \qquad (12)$$

where V_{t1} and V_{t2} are the voltage outputs at two instants t_1 and t_2 respectively, and f is the frequency of the oscillations. Figure 8 plots the Q-factor of the structure for different load resistors. As expected (Equation 8), the Q-factor peaks at a R_l of 1 MΩ.

From the output voltage waveform, the extracted electrical power E_{ext} is calculated using Equation 4. The radiated kinetic energy E_r is calculated by considering the effective number of particles captured by the collector. The effective number of particles is calculated from Equation 2. The energy conversion efficiency η, for different values δ_0 is plotted in Figure 9. The increase in η is primarily due to the increase in η_r. As δ_0 increases, the peak voltage across the air-gap capacitor $V_{cap\max}$, increases (Equation 6). This requires the emitted particles to expend more energy to get to the cantilever collector against the higher impeding voltage, resulting in larger stored electromechanical energy. So large gap separations are desirable for higher efficiency,

but the voltage breakdown of the gas in the air-gap limits the maximum efficiency achievable.

Table 1 summarizes the results obtained from the testing of both large and small devices. The larger device gives higher efficiency at a lower voltage while the small device gives lower efficiency at a higher voltage. Generally, beams with lower stiffness placed at higher gap separations are more efficient.

	δ_0 (μm)	T_{rec} (min)	T_{vib} (s)	V_{out} (V)	E_{ext} (μJ)	E_r (μJ)	η (%)
Large	2000	73	20	1.4	6	83.33	7.2
Small	750	126	2	4.4	1.42	66.67	2.1

Table 1. Summary of the test-results on the large (5 cm × 5 mm) and small (15 mm × 2 mm) devices.

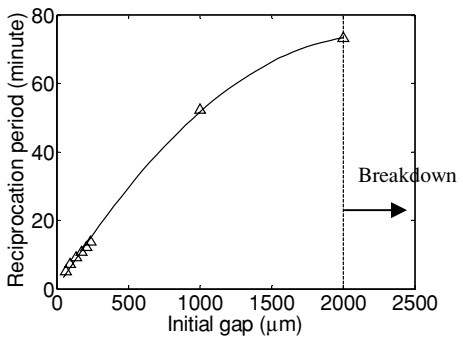

Figure 6. Measured reciprocation time vs. initial gap for a beam with a given stiffness of 2.34 N/m

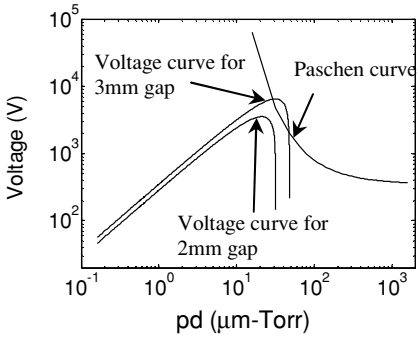

Figure 7. The breakdown at gap separations larger than 2 mm is illustrated by the intersection of the calculated Pachen curve and the voltage curve.

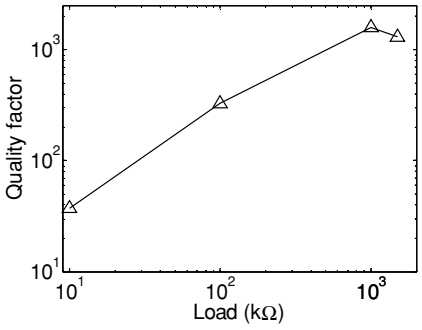

Figure 8. Q-factor vs. R_l. The graph shows the Q-factor rising steadily till the optimum load resistance of 1 Mohm.

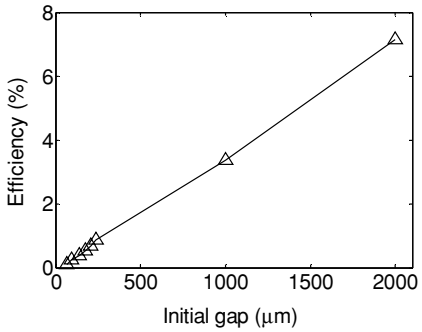

Figure 9. Absorbed kinetic energy to extractable electrical energy conversion efficiency vs. initial gap for beam stiffness =2.34 N/m

CONCLUSIONS

A high efficiency piezoelectric radioisotope powered micropower generator is designed, fabricated and experimentally characterized. The ultimate limits on efficiency are identified as being the breakdown of the gas due to high voltage across the capacitor. This limit can be further explored by investigating the dominant sources of breakdown. Furthermore, by arraying many phase-locked cantilevers it might be possible to achieve high power output.

ACKNOWLEDGEMENTS

This work was supported by DARPA-MTO under the MPG program, and contracted under the U. S. Army Aviation and Missile Research, Development, and Engineering Center.

REFERENCES

1. Bates J. B. et al., "Rechargeable Solid State Lithium Microbatteries**",** *Proceedings of MEMS '93*, pp. 82 – 86.
2. Holloday J. D. et al., "Microfuel Processor for use in a Miniature Power Supply", *Journal of Power Sources*, Vol. 108, pp. 21-27.
3. Schmidt V. H. et al., *Proceedings of the sixth IEEE International Symposioum on Applications of Ferroelectrics*, (1986), pp. 538-542.
4. Randall J. F., *On Ambient Energy Sources for Powering Indoor Electronic Devices*, Ph.D. Thesis, EPFL, Switzerland, May 2003.
5. Corliss W. R., Harvey D.G., *Radioisotopic Power Generation*, Prentice Hall, 1964.
6. Stephens C. W., *Dynamic Thermal Converters, Energy Conversion Systems Reference Handbook*, Vol. III (WADD,1960).
7. Brauer F. B. et al., US Air Force RADC-TR-56-130 "(1956).
8. Wilson V. C., *Astronautics and Aerospace Engg.* **1,** 62 (1963).
9. Coleman J. H., *Nucleonics* 11, 42 (1953)
10. Guo H. et al., "Nanopower Betavoltaic Microbatteries", *Digest of Technical Papers, Transducer'03*, Vol. 1, pp. 36-39.
11. Li H. et al., "Self-reciprocating Radioisotope-powered Cantilever", *Digest of Technical Papers, Transducers'01*, pp: 744-747.
12. Ottoman, G. K., "Adaptive Piezoelectric Energy Circuit for Wireless Remote Power Supply", *IEEE Transactions on Power Electronics*, Vol. 17, No. 5, pp. 669-76.
13. Lu F. et al., "Modeling and Analysis of Micro Piezoelectric Power Generators for Micro-electromechanical-systems Applications", *Smart Mater. Struct.* 13 (2004), pp. 57-63.
14. Young W. C., Roark's *Formulas for Stress and Strain*, McGraw Hill, 1989.
15. Duggirala, R et al., "A Pyroelectric - Piezoelectric Valve for Integrated Microfluidics"*, Digest of Technical Papers, Transducer'03*, Vol. 2, pp. 1554-1557.

A MEMBRANE BREATHER FOR MICRO FUEL CELL WITH HIGH CONCENTRATION METHANOL

De-Sheng Meng, Thomas Cubaud, Chih-Ming Ho, and Chang-Jin "CJ" Kim
Mechanical and Aerospace Engineering Department, University of California, Los Angeles
Los Angeles, CA 90095, U.S.A.

ABSTRACT

This paper introduces a breather for micro direct methanol fuel cell (μDMFC) that removes the gas byproduct (CO_2) from aqueous methanol fuel. The proposed breather aims to improve the efficiency of a fuel cell by preventing excessive accumulation of gas bubbles in the microchannel where the liquid fuel flows. The release of gas bubbles is visually demonstrated by developing a micro-breather, which integrates microchannels, nano-porous hydrophobic membrane, and an on-chip bubble intake mechanism. The breather achieves successful gas separation from methanol fuel with a concentration as high as 10M and with pressure tolerance as high as 35psi without leakage, fulfilling the requirement of the next-generation μDMFC. This breathing scheme can be useful for other microfluidic applications, where bubbles need to be eliminated from the system.

INTRODUCTION

Due to their potential for high energy capacity and environment-friendly nature, PEM (Proton Exchange Membrane) fuel cells have recently attracted considerable attention as a micro power source, with the μDMFCs [1] leading the way.

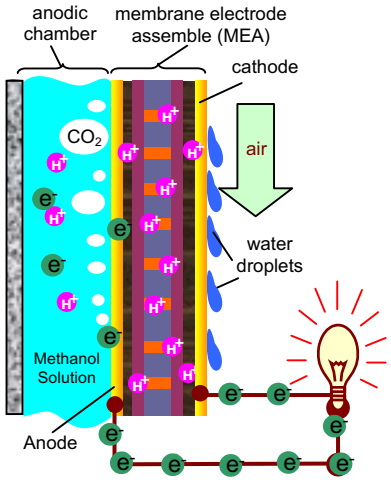

Figure 1. *Schematic of DMFCs' fuel stack*

In the fuel stack of direct methanol fuel cell as shown by figure 1, the electrochemical reaction is:

$$CH_3OH + H_2O \bullet 6e^- + 6H^+ + CO_2 \bullet \quad \text{(anodic side)}$$
$$1.5O_2 + 6e^- + 6H^+ \bullet 3H_2O \quad \text{(cathodic side)}$$
$$CH_3OH + 1.5O_2 \bullet 2H_2O + CO_2 \quad \text{(overall reaction)}$$

According to this reaction, DMFCs generate CO_2 gas bubble intrinsically. The small bubbles in large-scale DMFC may not cause much trouble. They are usually carried with the fuel flow to a downstream external gas/liquid separator, essentially an open tank, and get released there. But unique problems occur in their microscale counterparts, where channels may be as small as individual bubbles. As CO_2 bubbles fill the microchannel, flow resistance of fuel increases dramatically and the reaction area on PEM surface reduces substantially. Furthermore, pressure buildup by gas accumulation would worsen fuel cross-over of PEM.

It would be most ideal to breathe out these bubbles where they are generated. However, simple openings in the μDMFCs are not acceptable as the liquid fuel would leak out through the holes. Meng and Kim [2] have verified that hydrophobic microscale holes release CO_2 gas without leakage under moderate pressure. The ability to prevent leakage increases dramatically when the hydrophobic capillaries shrink down to sub-micrometer. In this paper, we report the use of nano-porous hydrophobic membrane for a breather suitable even for high-concentration methanol under high pressures, a challenging condition expected for the next-generation fuel cells. In addition to μDMFC, the breather's potential applications include microbial (glucose) fuel cell [3] , portable dialysis device [4] , water recycling system for space shuttle [5] , degasser for HPLC, and micro-mixer [6] .

BREATHING AND LIQUID HOLDING MECHANISM

Figure 2 represents a simple, idealized model to illustrate how liquid can be held from leaking by its own small meniscus. On the sharp corner of the breathing hole's entrance, this meniscus can assume a range of shapes, so as to balance under varying pressure according to the Laplace-Young equation:

$$P_f - P_0 = 2\sigma_f \cdot \cos(\pi - \alpha)/r \qquad (1)$$

where P_f is the pressure of the liquid fuel, P_0 is the ambient pressure, σ_f is the surface tension of fuel, α is the angle between meniscus and capillary wall, and r is radius of capillary. Since air bubbles in the fluid are not confined by this kind of interface, they can be breathed out freely.

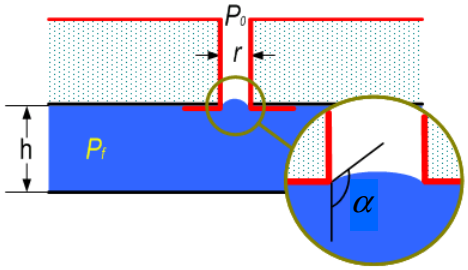

Figure 2. *Liquid meniscus in a hydrophobic capillary*

The pressure that a hydrophobic capillary can withstand is limited. Given a surface material and a liquid, the maximum contact angle is fixed (known as dynamic advancing contact angle

Travel support has been generously provided by the Transducers Research Foundation and by the DARPA MEMS and DARPA BioFlips programs.

or θ_a). The maximum pressure difference that can be resisted in this breathing hole is:

$$P_{\max} = Max(P_f) - P_0 = 2\sigma_f \cdot \cos(\pi - \theta_a)/r \qquad (2)$$

If the fuel pressure is higher than this critical pressure, leakage would happen. Here, we have assumed that the breathing hole is straight and the surface of its wall is smooth. The nanopores in the membrane, however, can be described better by a more realistic model with irregular capillary, as illustrated in figure 3, where the maximum pressure before leakage is defined as:

$$P_{\max}' = 2\sigma_f \cdot Max(\cos(\pi - \theta_{eff})/r_{eff}) \qquad (3)$$

with r_{eff} stands for the effective radius of breathing holes and θ_{eff} for the effective advancing contact angle inside the breathing holes. The "*Max*" implies that the leakage of each breathing hole is defined by its most constricted neck, as shown in figure 3.

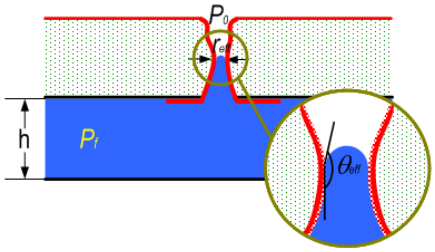

Figure 3. *Leakage pressure for irregular capillary*

According to equation 3, the irregular breathing holes can usually withstand larger pressure because a rough surface is known to increase the advancing contact angle [7] and the radius of the "neck" can be much smaller than the nominal radius specified by the manufacturer. These two factors tend to increase leakage pressure. Meanwhile, an opposite factor should also be taken into account: given a membrane with many distinct holes on it, the membrane-scale leakage happens on the most susceptible pores. So the leakage pressure of the membrane is:

$$P_{leak} = Min\left(P_{\max}'\right) = Min\left(2\sigma_l \cdot Max\left(\cos(\pi - \theta_{eff})/r_{eff}\right)\right) \qquad (4)$$

DEVICE FABRICATION AND TEST

We have recently demonstrated the removal of chemical-reaction-induced CO_2 bubbles from inorganic aqueous solution through Teflon®-coated silicon-micromachined breathing holes (50µm in diameter)[2] . However, the pressure it could withstand was limited because of the difficulties in the fabrication of microscale breathing holes with uniform hydrophobic coating and mechanically robust structure. Leakage cannot be prevented at all for high-concentration fuels, because the breathing holes are wet much easier by the concentrated fuel with lower surface tension and smaller contact angle. Table 1 summarizes our measurements of contact angles with methanol of various concentrations.

Table 1. Interfacial properties of methanol aqueous solution

		DI water	1M	2M	10M	Methanol
Contact angle on Teflon® flat surface	Advancing	122°	119°	120°	101°	67°
	Receding	105°	102°	99°	60°	60°
	Hysteresis	17°	17°	21°	41°	7°
Surface tension (dynes/cm)		72.8	66.5	57.4	39.7	22.7

Moreover, progresses of PEM (Proton Exchange Membrane) technology are expected to substantially reduce the cross-over problem and increase the feasible fuel concentration from current 0.5-2M to 8-10M to achieve higher energy efficiency. Challenged by the high concentration fuel, we identify intrinsically hydrophobic porous membranes to construct a breather for high-concentration methanol fuel. This category of membranes has originally been developed for the sample preparation of X-ray spectrochemistry, high performance liquid chromatography, and ultrafiltration. Their 0.1-5µm diameter pores are ideal for the gas breathing application. Advanced membrane technologies have provided diverse membrane materials, including some of the most hydrophobic polymers (e.g. PTFE) known.

Figure 4 shows the scheme to construct a gas permeable microchannel by sandwiched membrane. The breather chip and membrane holder are both fabricated from a same 400µm-thick (100) silicon wafer by DRIE etching. A cross-shaped gas-bubble generator [8] is also designed on the breather chip to produce adjustable liquid/gas two-phase flow, corresponding to µDMFC's fuel flow with CO_2 bubbles. Parts of the microchannel on the breather chip are protected by polyimide tape after the DRIE etching has reached the desired depth. After DRIE and subsequent Piranha cleaning, the breather/bubble generator chip is anodically bonded to a piece of Pyrex® glass. Then the membrane is sandwiched between breather chip and membrane holder chip with epoxy to construct a gas-permeable microchannel, analogous to µDMFCs' fuel chamber with integrated breather. During the epoxy adhesive bonding, through-holes on both chips are used as alignment marks. The alignment is assisted by strong illumination from below.

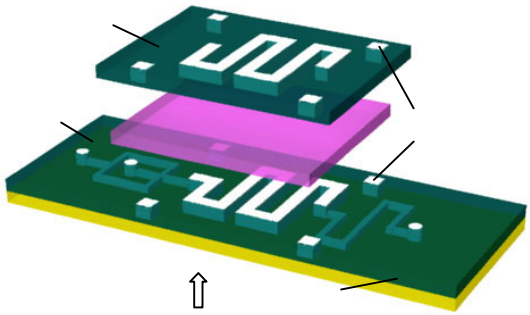

Figure 4. *Alignment and bonding setup*

The finished breather is shown in figure 5. Gas and liquid are injected via the tubing connected to the breather (not shown in the figure). Pressurized gas is used to inject CO_2 directly and water/methanol solution is provided indirectly via a liquid reservoir. Flow meters and pressure sensors are used to monitor the flow rate and pressure inside the microchannel. The experimental data are collected by a computer.

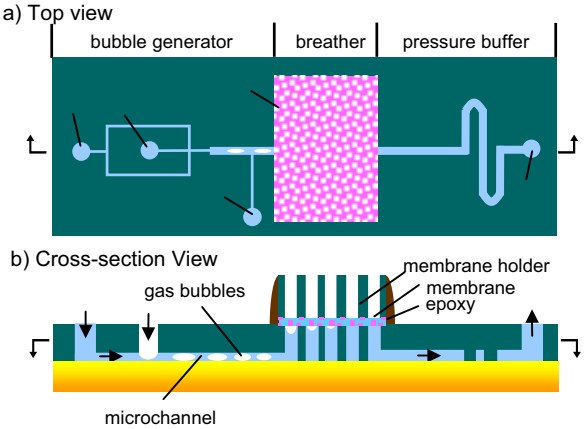

Figure 5. *Sandwiched membrane breather*

EXPERIMENTAL RESULTS

The experiments were carried out with both DI water and 10M methanol inside membrane breathers of porous PTFE membrane (with 3μm pore in diameter, from Millipore) and porous polypropylene membrane (with 0.2μm pore in diameter, from Chemplex® Industries Inc). During the experiments, the pressure inside the microchannel was controlled to 0.5-2psi. The breathing processes, recorded by a microscope equipped with a CCD camera, were proved to be highly repeatable. The time-series of 0.2μm polypropylene membrane breather are shown in figure 6. The 3μm PTFE membrane breather demonstrates similar breathing behavior but with a faster breathing rate.

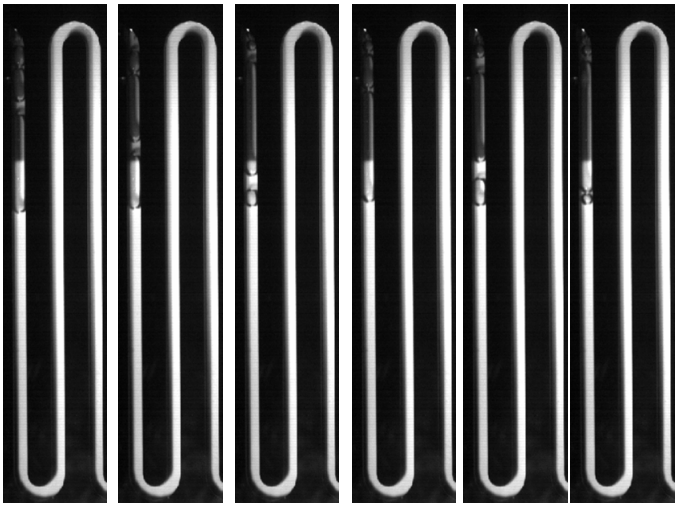

(a) breathing for DI water (no breathing activation)

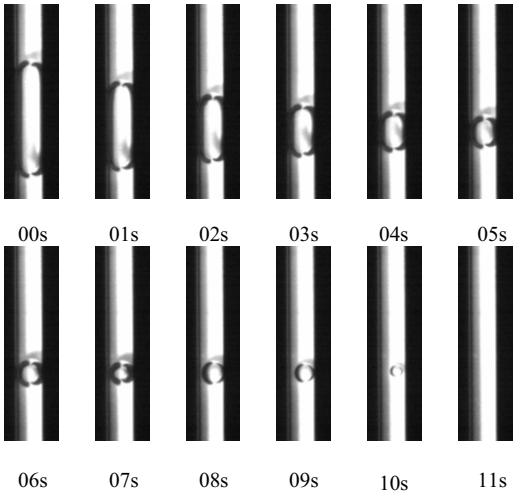

(b) reducing of a single bubble in 10M Methanol

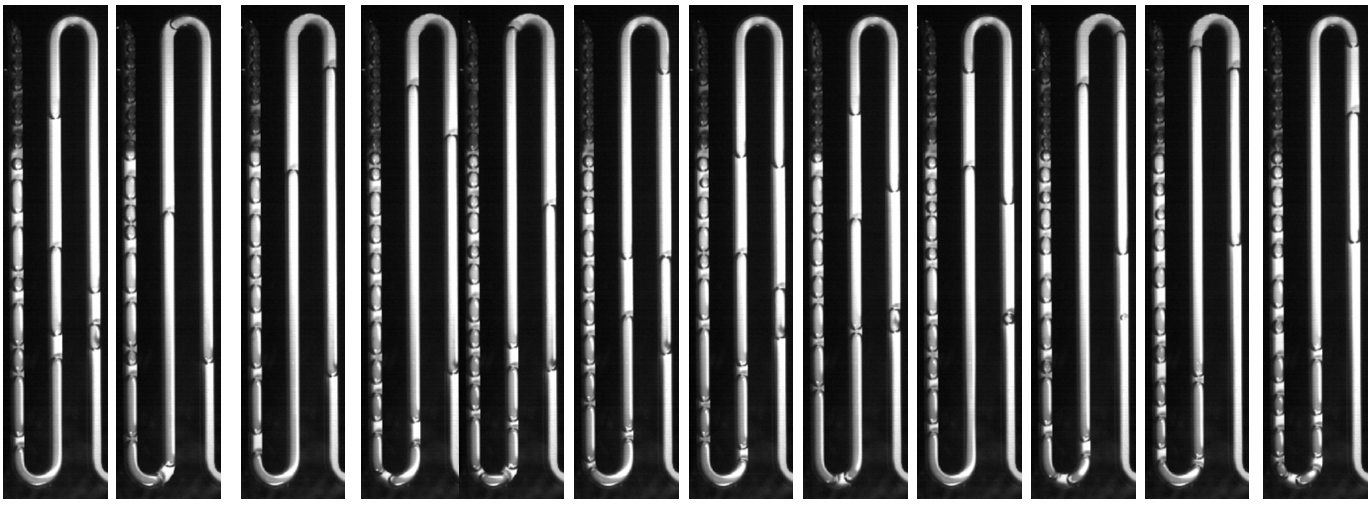

(c) Breathing for 10M methanol (with breathing activation)

***Figure 6**. Breathing process in gas permeable microchannel (transmembrane pressure = 0.8psi).*

As figure 6(a) shows, the bubbles in DI water are breathed out almost immediately after they touch the membrane. Usually, only the front meniscus is observed to be oscillating within a short distance from the non-permeable part of the microchannel, because breathing and injecting are competing there. Small bubbles can also break from the large one and get breathed out completely.

Figure 6(b) shows similar bubble reduction can also be obtained in high-concentration methanol. However, bubbles in high-concentration methanol tend to stay in the gas permeable microchannel for a longer period than DI water case before they are merged into the largest leading bubble in the very front and then breathed out completely (shown in figure 6(c)). Consequently, a bubble train behind the leading bubble is formed. Since bubbles stay intact for a short period before being breathed out, we state that a "breathing activation" is needed. An explanation is that a tiny liquid droplet can be trapped inside the small capillaries and block the breathing of gas (figure 7). Due to contact angle hysteresis, the contact angle on the head or tail of this droplet (θ_{head} and θ_{tail}) can be different. This introduces a corresponding pressure difference that can hold this droplet in the breathing hole temporarily. However, the eventual success of breathing suggests that the tiny droplet in this hydrophobic nano-pore is unstable. It can finally be removed to clear the breathing hole, or in another word, the breathing can be activated.

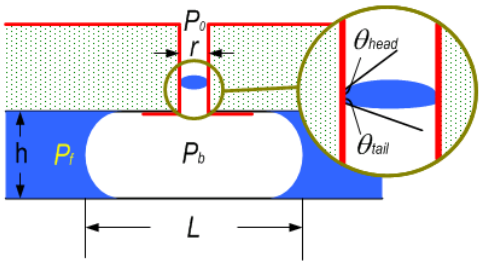

Figure 7. *Droplet trapped in a breathing hole*

This hypothesis is supported by two facts. First, experiments with DI water, whose contact angle hysteresis is much smaller than that of 10M methanol (refer to table 1), demonstrate less or no need for breathing activation. Second, the bubble train is observed to be much shorter when the flow rate is reduced. Trapped droplets can be a reasonable explanation, because bubble-covered membrane area gets more opportunities to eliminate the trapped droplets if the flow is slower. Nevertheless, more research is necessary to confirm this hypothesis or find new explanation for the phenomenon of breathing activation. Since the bubble train will evidently increase the flow resistance in the microchannel, theoretical analysis and corresponding design modification should be made in the future to minimize the need for breathing activation in the working µDMFC.

The leakage pressure is measured and summarized in table 2. Since r_{eff} and θ_{eff} are difficult to measure, equation (4) can not be applied directly. The theoretical value is hence calculated from equation (2), using the nominal diameter specified by the manufacturers. Our data shows this estimation of leakage pressure is too conservative for all of the four experiments.

Table 2*. Leakage pressure: calculated and measured value*

	Porous polypropylene			Porous PTFE		
	nominal diameter	calculated value	measured value	nominal diameter	calculated value	measured value
10M Methanol	0.2µm	22psi	> 35psi *	3µm	1.5psi	~5psi
DI water		110psi	> 35psi *		7.4psi	16psi

*membrane breaks at 35 psi

The irregular-hole model (as figure 3 shows) is also confirmed by SEM pictures of the two relevant hydrophobic porous membranes, as shown in figure 8.

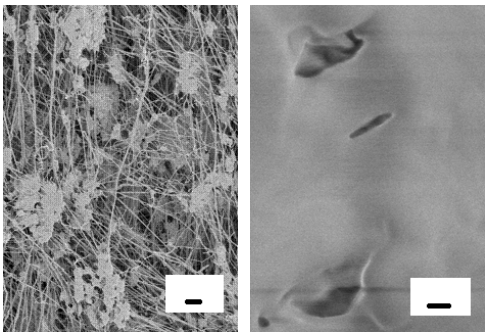

(a) porous polypropylene (b) porous PTFE

Figure 8. *SEM picture of porous membranes' surface*

CONCLUSIONS

Benefited from micron/submicron hydrophobic breathing holes, the membrane breather achieved >35psi leakage prevention pressure for 10M methanol and demonstrated stable breathing function in the microchannel. This paves the way for the distributed breather application in µDMFC's. The well-established membrane industry provided ample resources for the optimization of this breather to ensure its functionality in µDMFCs, as well as other fluidic applications. Further investigation of bubble dynamics, which account for phenomenon like breathing activation, may elucidate the behaviors of microscopic bubbles/droplets inside the breathing holes.

ACKNOWLEDGEMENT

This work has been supported by DARPA Micro Power Generation Program. The authors wish to thank Professors C. Y. Wang, X. Zhang and X. Zhong, as well as T. J. Yen, G. Q. Lu, Y. Lu and H. W. Lu for their discussion and help.

REFERENCES

[1] T. J. Yen, N. Fang, X. Zhang, G. Q. Lu, and C. Y. Wang, "A Micro Methanol Fuel Cell Operating At Near Room Temperature," *Applied Physics Letters*, vol. 83, pp. 4056-8, 2003.

[2] D.-S. Meng, J. Kim, and C.-J. Kim, "A Distributed Gas Breather for the Micro Direct Methanol Fuel Cell," Proc. *IEEE Int. Conf. Micro Electro Mechanical System (MEMS 2003)*, Kyoto, Japan, 2003, pp. 534-7.

[3] M. Chiao, K. B. Lam, and L. Lin, "Micromachined Microbial Fuel Cells," Proc. *IEEE Int. Conf. Micro Electro Mechanical System (MEMS 2003)*, Kyoto, Japan, 2003, pp. 383-6.

[4] Z. Yang, S. Matsumoto, and R. Maeda, "A prototype of ultrasonic micro-degassing device for portable dialysis system," *Sensors and Actuators A*, vol. 95, pp. 274-80, 2002.

[5] K. D. Pickering, L. Y. Hammond, and J. L. Garland, "Immobilized Microbe Microgravity Water processing System (IMMWPS) Flight Experiment," Proc. *Bioastronautics Investigetors' Workshop*, Galveston, Texas, 2001.

[6] A. Guenther, M. Jhunjhunwala, M. A. Schmidt, and K.F.Jensen, "Liquid mixing using inert gas and an integrated gas-liquid separator.," Proc. *7th Int. Conf. Miniaturized Chemical & BioChemical Analysis Systems (µ-TAS)*, Squaw Valley, CA, 2003, pp. 465-8.

[7] J. Kim and C.-J. Kim, "Nanostructured Surfaces for Dramatic Reduction of Flow Resistance in Droplet-based Microfluidics," Proc. *IEEE Int. Conf. Micro Electro Mechanical System (MEMS 2002)*, Las Vegas, 2002, pp. 479-82.

[8] T. Cubaud and C.-M. Ho, "Transport of Bubbles in Square Microchannels," *To Be Published*, 2004.

INTEGRATED MICRO FUEL CELL POWER SUPPLY

André D. Taylor and Levi T. Thompson
University of Michigan
Ann Arbor, Michigan 48109-2136

ABSTRACT

An integrated thin film micro fuel cell power supply design is described in this paper. The device incorporates: 1) a microfabricated micro-fuel cell, 2) integrated heaters and temperature sensors, and 3) a novel electrode design configuration. The architecture of this design allows this device to be completely fabricated using standard micromachining techniques.

INTRODUCTION

Fuel cells are an attractive alternative to batteries for portable electronic devices. Microfabricated micro-fuel cells hold promise for being highly efficient with low cost. Several approaches have been reported for the fabrication of micro-fuel cells [**1-4**] using micromachining techniques. Most of these devices include micromachined fuel cell components combined with conventional macro MEAs (membrane electrode assemblies) [**1-4**]. Previous work has demonstrated the possibility of a completely microfabricated micro-fuel cell [**5**]. The present work combines surface and bulk micromachining technologies to produce thin film micro-fuel cells of various geometries with integrated heaters and temperature sensors. This novel device design demonstrates a truly integrated micro-fuel cell based power supply that is compatible with existing CMOS processes.

FABRICATION OF UM-µPEMFC

A seven mask process for the UM-µPEMFC has been developed. Figures 1a and 1b show the closed and exploded views of the device structure respectively.

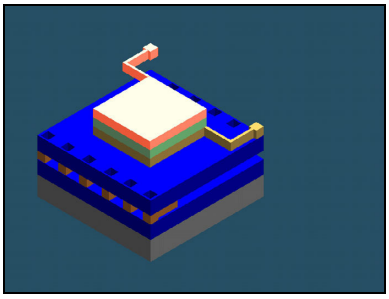

Figure 1a. *Closed view of the UM-µPEMFC.*

Travel support has been generously provided by the Transducers Research Foundation and by DARPA MEMS and DARPA BioFlips programs.

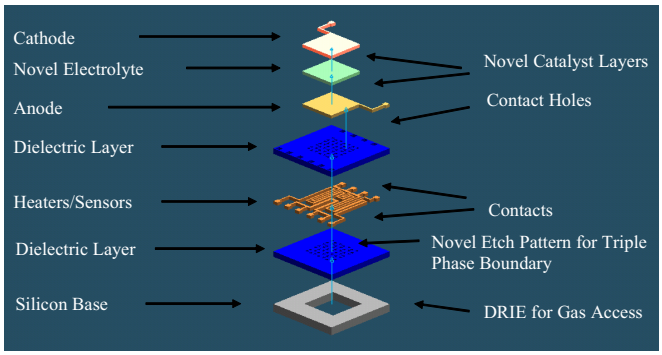

Figure 1b. *Exploded view of the UM-µPEMFC.*

A stress relieved oxide-nitride-oxide (1 µm) dielectric layer was deposited onto a silicon substrate via LPCVD (low pressure chemical vapor deposition). A 6000 Å layer of polysilicon was deposited on top of the oxide and was subsequently doped with phosphorous for a sheet resistance of 18 Ω/□. Using RIE (reactive ion etching), the polysilicon layer was patterned into the heaters and temperature sensors shown in Figure 2.

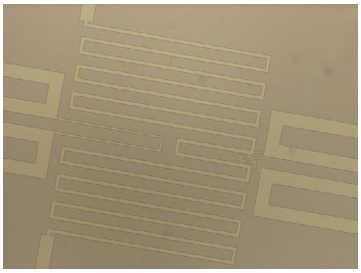

Figure 2. *Heaters and Temperature Sensors of UM-µPEMFC.*

A 0.5 µm protective layer of oxide layer was deposited via LPCVD on top of the heaters and temperature sensors in order to isolate them from the electrodes. The fuel cell (Ti/Pt) anode and catalyst layers were patterned onto the oxide surface using Electron Beam (E-beam) evaporation and metal lift-off techniques. Figure 3 shows the anode on top of the oxide layer above the heaters and temperature sensors. (Further details about the electrode will be illustrated later in the paper.)

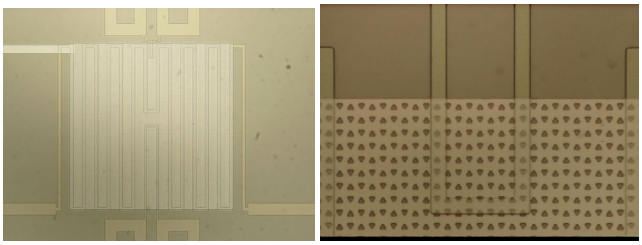

Figure 3. *UM-µPEMFC Anode above Heaters/Sensors.*

The electrode was subsequently patterned with photoresist for an RIE step that takes place in the triangular openings of the electrode down to the silicon substrate. A second RIE processing step

0-9640024-5-0/hh2004/$20©2004TRF
DOI 10.31438/trf.hh2004.40

removed the oxide layer above the heater and temperature sensor contact pads. A thin film of Nafion® solution (5% of a 950 weight equivalent) was spin casted onto the anode at 500 rpm for 45 seconds. The film was then cured in an oven set at 150 C for 45 min. It has previously been shown that Nafion® films cured under these conditions have excellent adhesion and chemical resistance [**6**]. The spin cast speed vs. thickness and stress of the Nafion® thin films are reported for the first time in Figure 4.

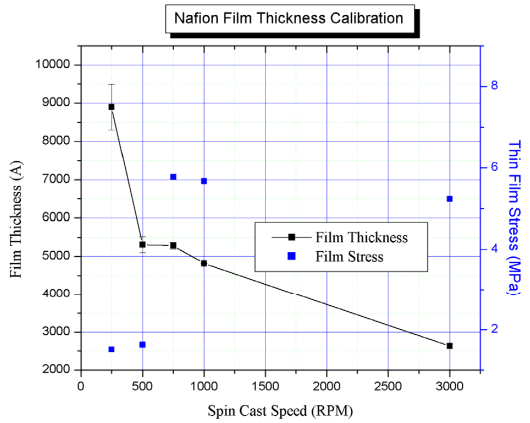

Figure 4. *Nafion® thickness and stress correlation.*

From the Figure 4 one can conclude that the stress contribution from the Nafion® thin film will not be significant (>100 MPa) for the overall thin film structure. The Nafion layer was then patterened with photoresist to open up contacts to the anode, heater, and temperature sensor contact pads. The fuel cell (Pt/Ti) catalyst and cathode layers were deposited and patterned on top of the Nafion® in a manner similar to the anode. The backside of the wafer was patterned with photoresist using backside alignment and the front side was bonded to a carrier wafer. Gas access to the anode was accomplished by using RIE and DRIE (deep reactive ion etching). The oxide/nitride/oxide layer was removed from the backside using RIE in the areas not protected by photoresist. DRIE is then used to selectively etch the silicon substrate down to the oxide dielectric layer. After DRIE the device wafer was separated from the carrier wafer. The integrated micro fuel cell was thus supported by the stress relieved oxide-nitride-oxide dielectric layer.

ELECTRODE DESIGN CONFIGURATION

In an effort to improve the active area of the triple phase boundary region, triangular vias were developed. This should result in improved intrinsic performance relative to designs reported by Morse et al [**5**]. In the Morse design cylindrical vias were used to provide continuous porosity for the anode and cathode shown in Figure 5.

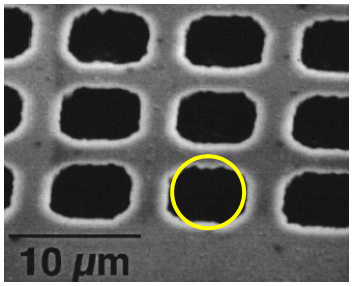

Figure 5. *Morse et al. electrode design [5].*

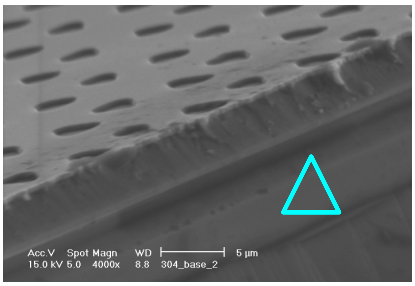

Figure 6. *UM-µPEMFC electrode design..*

By taking the ratio of the electrode opening perimeter to area, the following comparison between the circular and triangular designs can be made (Figure 7).

$$Ratio = \frac{Perimeter}{Area}$$

$$R_C = \frac{2\pi R}{\pi R^2} = \frac{2}{R} \qquad R_T = \frac{4}{R}$$

Figure 7. *Ratio comparison of electrode via openings.*

A direct comparison of the two shapes illustrates that triangular vias have twice the active surface area compared to the circular vias. Another advantage that triangular openings have over circular is with regard to nearest neighbor feature approach. By alternating the positions of the triangles (illustrated in Figure 3), it is possible to pack more via openings on a given electrode size while at the same time maintaining a fixed distance from opening to opening.

HEATER AND TEMPERATURE SENSOR DESIGN

Previous work has demonstrated the performance of micro fuel cells either at room temperature or with the use of an external heating source. Towards the realization of a fully integrated micro fuel cell for portable electronic applications, we integrated these devices with internal heating sources.

The heaters and temperature sensors for the micro fuel cell were tested and calibrated. Figure 8 illustrates the temperature vs. resistance for the polysilicon RTD.

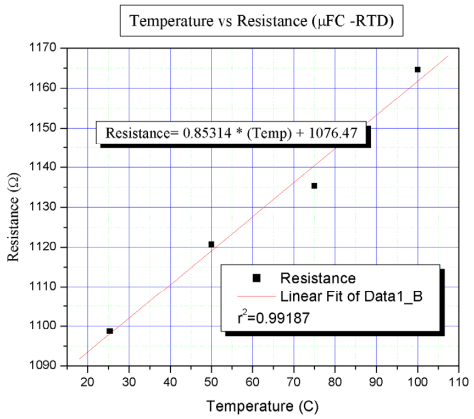

Figure 8. *Polysilicon RTD temperature versus resistance.*

The Polysilicon RTD was calibrated in a thermal chamber that was controlled by a Labview® program written by the author. The parameters were then tabulated into a linear best fit equation which was used to control the power supply to the heaters. It was possible to control the heaters based on the response of the temperature sensor.

RESULTS AND CONCLUSIONS

This paper reports the design and fabrication of an integrated micro fuel cell power supply. A novel electrode design was presented that optimizes several micromachining techniques in order to improve the triple phase boundary region. In addition, the integration of heaters and temperature sensors was introduced as a possible method to improve the fuel cell reaction and hence device performance. Several device geometries have been fabricated using the device architecture described above. These results will be presented in a forthcoming publication. Figure 9 illustrates an integrated micro fuel cell with a dime mounted on a PC board prior to testing.

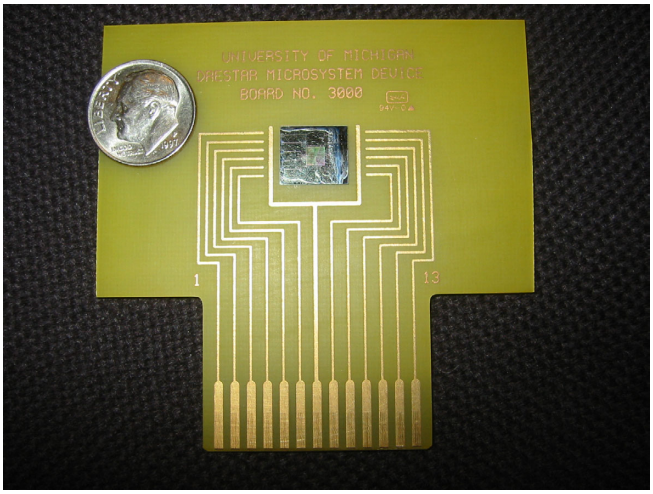

Figure 9. *Integrated UM-μPEMFC on PC board.*

REFERENCES

1. J.P. Meyers and H.L. Maynard, "Design Considerations for Miniaturized PEM Fuel Cells", Journal of Power Sources, 109, (2002), pp. 76-88.

2. S.C. Kelly, G.A. Deluga, and W.H. Smyrl, "Miniature Fuel Cells Fabricated on Silicon Substrates", AIChE Journal, 48, 5, (May 2002), pp. 1071-1082.

3. R. O'Hayre, T. Fabian, S.J. Lee, and F.B. Prinz, "Lateral Ionic Conduction in Planar Array Fuel Cells", Journal of The Electrochemical Society, 150 (4), (2003), pp. A430-A438.

4. G.Q. Lu, C.Y. Wang, T.J. Yen, and X. Zhang, Development and Characterization of a Silicon-Based Micro Direct Methanol Fuel Cell, Electrochim Acta, 49 (5), (FEB 25 2004), pp. 821-828.

5. J.D. Morse, A.F. Jankowski, R.T. Graff, and J.P. Hayes, "Novel Proton Exchange Membrane Thin-Film Fuel Cell for Microscale Energy Conversion", Journal of Vacuum Science, Technology A, 18(4), (Jul/Aug 2000), pp. 2003-2005.

6 B. Ilic, P. Neuzil, G.J. Maclay, E.L. Ginzston, "Batch Fabricated Amperometric Relative Humidity Sensor",, Electrochemical Society Proceedings, 98-14, (1998), pp. 140-147.

PIEZOELECTRIC MICRO POWER GENERATOR FOR ENERGY HARVESTING

R. Sood, Y.B. Jeon, J.-h. Jeong and S.G. Kim
Department of Mechanical Engineering, Massachusetts Institute of Technology
Cambridge, MA 02139

ABSTRACT

A thin film lead zirconate titanate $Pb(Zr,Ti)O_3$ (PZT), power generating device is developed. It is designed to resonate at specific vibrational frequencies from an ambient, vibrational energy source, thereby creating electrical energy via the piezoelectric effect. The energy harvesting device uses the piezoelectric d_{33} mode and is fabricated with three mask steps. Our cantilever device was designed to have a flat structure with a proof mass added to the end. A method for controlling the bowing curvature of the cantilever was applied by modulating the residual stress and elastic properties of the composite beam. The top electrode of Ti and Pt was patterned into an interdigitated shape on top of the sol-gel-spin coated PZT thin film in order to employ the d_{33} mode of the piezoelectric. This d_{33} mode design can generate at least a 20 times higher voltage than that of the d_{31} mode design. The device was mechanically excited by base shaking experiments, which revealed that our device has three resonance modes. The base-shaking experiments at the first resonant frequency (13.9 kHz) demonstrated that the generated charge is proportional to the tip displacement of the cantilever with an approximate linearity coefficient of 4.14 pC/μm. The total system can deliver 1μW of continuous electrical power to a 5.2MΩ resistive load at 2.4V DC. The corresponding energy density is 0.74 mW-h/cm^2, which compares favorably to current chemical batteries (i.e. lithium ion). We expect the optimized design to generate a much higher power level than we have now by targeting and harvesting from lower frequency vibrations.

INTRODUCTION

Energy harvesting from the environment has been actively explored using many methods such as solar power (most familiar ambient energy source), electromagnetic fields (used in RFID tags, inductively powered smart cards, etc.), thermal gradients, fluid flow, energy produced by the human body, and the action of gravitational fields [**1**]. Most of all, mechanical vibration is a potential power source which can be used for conversion to electrical energy through Microelectromechanical systems (MEMS) technology. Piezoelectric materials are perfect candidates for harvesting power from ambient vibration sources because they can efficiently convert mechanical strain to an electrical signal [**2,3**]. Several bulk piezoelectric generators have already been developed using the d_{31} piezoelectric mode [**1,4,5**], but there has been no d_{33} thin-film piezoelectric generators at the scale of MEMS. In this study, we describe a MEMS-based power scavenger employing the piezoelectric thin film with the d_{33} mode, named here as the Piezoelectric Micro Power Generator (PMPG).

DESIGN

The energy conversion from mechanical vibration into electrical power can be formulated as a general model given mathematically by Eq. (1) [**1,6**]:

$$m\ddot{z}_o + (b_e + b_m)\dot{z}_o + kz_o = -m\ddot{z}_i \tag{1}$$

where z_o is the device output (tip) displacement, z_i is the input (base) displacement, m the lumped mass, b_m the mechanical damping coefficient, b_e the electrically induced damping coefficient, and k the stiffness of the MEMS device.

The power converted to the electrical system is given by:

$$P = \frac{1}{2} b_e \dot{z}_o^{\,2} \tag{2}$$

PMPG devices should be designed so that they mechanically resonate at a frequency tuned to the ambient vibration source in order to generate maximum electrical power. The resonance frequency is approximately given as $\omega_n = \sqrt{k/m}$ by its stiffness (k), and mass (m). Thus, the devices could be tuned at different frequencies by varying the beam dimensions and/or mass of the moving parts (i.e. layer thicknesses and the inclusion of a proof mass, if necessary). Eqs. (1) and (2) provide us with the converted power at resonance [**1**]:

$$|P| = \alpha\omega^3 Y^2 = \alpha\frac{A^2}{\omega} \tag{3}$$

where $\alpha = \frac{m\zeta_e}{4\zeta_T^2}$, Y is the displacement magnitude of input vibrations, A is the acceleration magnitude, ζ_e and ζ_T the electrical and total damping ratios.

In order to get as much power as possible, we initially hypothesized that the device needed to be operated at a high frequency and have a high amplitude vibration source. However, it should be noted that the displacement amplitude decreases rapidly as the frequency goes up. We also found that most of the available environmental vibrations were at low frequencies and had high acceleration magnitudes. We will optimize the design in the next generation device fabrication.

A cantilever beam structure was chosen for the geometric design. There are two piezoelectric modes (d_{31} and d_{33}), which are commonly used in piezoelectric devices. Figure 1 is a cross-sectional view of these two device modes. They are distinguished by whether the electric field direction is perpendicular to the input strain direction (d_{31}) or parallel to it (d_{33}). Eqs. (4) and (5) show the relation between stress σ_{xx} (or strain x_3) and electric field E_i (or voltage V_{3i}).

$$x_3 = d_{3i}E_i \tag{4}$$

$$V_{3i} = \sigma_{xx} g_{3i} L_i \tag{5}$$

where x_3 is the strain, V_{3i} the open circuit voltage, d_{3i} (V/m) and g_{3i} (Vm/N) the piezoelectric constants, and L_i is the distance between electrodes which could be either t_{pzt} or L. The d_{3i} coefficient is directly proportional to g_{3i} via the dielectric coefficient (ε_{pzt}) of the piezoelectric.

While the d_{31} type must have separate top and bottom electrodes, the d_{33} type eliminates the need for a bottom electrode by employing an interdigitated (IDT) top electrode. This reduces the number of photo masks needed for a d_{33} piezoelectric device compared with the d_{31} device. In the d_{31} case, L_1 from Eq. (5) is

0-9640024-5-0/hh2004/$20©2004TRF
DOI 10.31438/trf.hh2004.41

Solid-State Sensors, Actuators, and Microsystems Workshop
Hilton Head Island, South Carolina, June 6-10, 2004

limited to the thickness of the PZT layer t_{pzt}, while L_3 can be independently long (~10*t_{pzt}) in the d_{33} case. In addition, since the magnitude of the d_{33} and g_{33} coefficients are 2 to 2.5 times larger than their d_{31} and g_{31} counterparts, the generated, open-circuit voltage of a d_{33} type device will be much larger (20 times or greater) than a d_{31} type transducer of similar beam dimensions. This then enables the activation of the rectifying circuit. In this regard, the d_{33} mode was employed to make our PZT micro cantilever device.

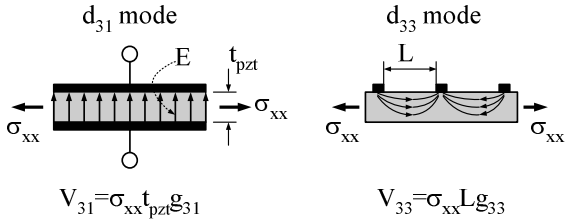

Figure 1. *Two modes of piezoelectric conversion from input mechanical stress.*

FABRICATION

A d_{33} mode, thin film, lead zirconate titanate (also known as PZT) cantilever device was fabricated using three photo masks. Figure 2 shows the device schematic of the d_{33} mode PMPG device. The alternating plus and minus potentials are imposed upon the mini-electrodes when the PZT is poled. The basic design of the multilayer structure consists of five layers as follows: membrane layer (SiO_2 and/or SiN_x) for controlling bow of the cantilever structure, diffusion barrier/buffer layer (ZrO_2) for preventing electrical charge diffusion from the piezoelectric layer, piezoelectric layer (PZT), top IDT electrode (Pt/Ti), and optional proof mass layer (SU-8).

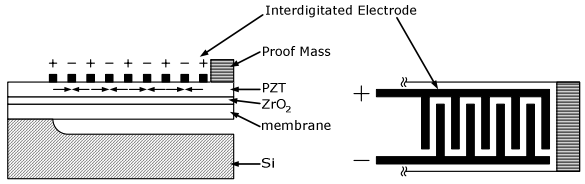

Figure 2. *Schematic of d_{33} mode piezoelectric device.*

First, the membrane layer is deposited on the Si wafer. In order to control the residual stress of the cantilever beams, several different kinds of membrane/buffer layer combinations were deposited such as 0.05μm ZrO_2/0.4μm thermal oxide, 0.05μm ZrO_2/0.4μm PECVD oxide, and 0.05μm ZrO_2/(0.1μm PECVD oxide/0.4μm SiN_x). Each PECVD oxide layer is annealed at 750°C for 30 minutes. The 50 nm thick ZrO_2 layer is deposited via a sol-gel spin-on process, then dried at 350°C for 1 minute, and annealed at 700°C for 15 minutes.

The PZT solution (Mitsubishi Materials Co.) has a composition of Pb/(Zr+Ti) of 118/100 along with a Zr/Ti ratio of 52/48. The solution is spun on the substrate at 500 rpm for 3 seconds and 1500 rpm for 30 seconds. The precursor gel film is pyrolyzed at 350°C for 5 minutes on a hot plate in several repeated cycles to create a PZT layer with 0.48μm thickness. The PZT film is then annealed at 700°C for 15 minutes. The PZT layer and membrane layers are patterned via RIE with BCl_3:Cl_2 (30:10) for 70 min with the first mask. The top IDT electrode is deposited next with 20 nm Ti and 200 nm Pt via e-beam evaporation and patterned using a lift-off procedure with the second mask. The SU-8 is spin-coated on top of the existing layers and patterned with the third mask to create the proof mass. A wet etching process such as KOH etch was initially used to release the cantilever structure, but it showed stiction problems and the KOH was found to attack the PZT layer. We solved this problem by employing an isotropic XeF_2 vapor etching which uses the PZT layer itself as the etch mask. This was possible because XeF_2 has a high etch selectivity between Si and the other layers. An SEM image of the fabricated PMPG device is shown in Figure 3.

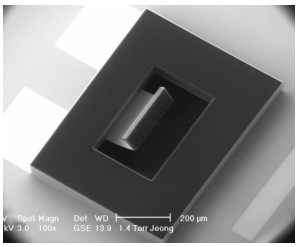

Figure 3. *SEM of the fabricated PMPG device with bond pads.*

The bow of the composite cantilever beam was controlled by changing its bottom layer from thermal SiO_2 to PECVD SiO_2, then to SiN_x. This approach was used for optimizing the residual stress and elastic modulus. On the basis of the data in Table 1, we have calculated the bow curvature as a function of residual stress and elastic modulus and determined that reducing the bow requires two parts: changing the residual stress of the bottom layer from compressive to tensile and increasing its elastic modulus.

Figure 4 shows that our strategy is appropriate. The first device, with thermal SiO_2 of about -300 MPa being the bottom layer, has a severely curled cantilever (Fig. 4(a)). In Fig. 4(b), this bow was greatly diminished by depositing SiO_2 via PECVD, by which the residual stress in the bottom layer is reduced to only tens of MPa. There is a trade off in choosing the elastic modulus. In the smaller elastic modulus regime, it is easier to control the curvature. However, even a small perturbation of the intended stress can result in a very large change of the final curvature. Selecting a large elastic modulus actually gives us more robustness in fabricating the device. For this reason, a SiN_x layer of high elastic modulus (313 GPa) and tensile stress (190 MPa) was selected as the bottom layer. A nearly flat cantilever beam was obtained as can be seen in Fig. 4(c).

Table 1. *Mechanical properties and residual stresses of films deposited for the cantilever structure. PZT number indicates the order in which the PZT film was deposited on top of the ZrO_2 layer. The stress was measured by a curvature method.*

	PZT1**[7]**	PZT 2	PZT3	PZT 4	ZrO_2 **[8]**	SiO_2 **[9]** (thermal)	SiO_2 **[9]** (PECVD)	SiN_x **[10]**
Elastic Modulus [GPa]	63	63	63	63	244	69	69	313
Poisson Ratio	0.30	0.30	0.30	0.30	0.27	0.15	0.15	0.29
Residual Stress [MPa]	630/610	-115/-125	75/65	113/105	400/350	-280/-330	35/-15	210/170

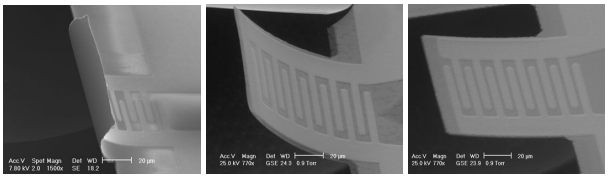

(a) (b) (c)

Figure 4. *SEM images of the stress-controlled cantilevers consisting of (a) PZT/ZrO_2/SiO_2(thermal), (b) PZT/ZrO_2/SiO_2(PECVD) and (c) PZT/ZrO_2/SiO_2(PECVD)/SiN_x.*

CHARACTERIZATION

The PMPG device acts as an AC current generator in parallel with a complex output impedance. While the PMPG is mechanically resonating ($z_o(t)$) at frequency ω_n, the PZT thin film experiences a time-varying change in mechanical stress ($\sigma(t)$), alternating from tensile to compressive. This results in a time-varying generated charge within the PZT layer, which is the source of the AC current. Taking the first time derivative of the charge function Q(t) gives the AC current source $I_P(t)$. A rectifying circuit and electrical storage capacitor are required for rectifying and storing the electrical energy for each device (Fig. 5).

The device chip was packaged on a multiple pinned ceramic package. Each device has two bond pads (Fig. 3), which are connected via wire bonding and soldering to the measurement electronics (charge amplifier) and proto board containing the external rectification circuitry, storage capacitor, and resistive load. The device was heated to 100 °C on a hot plate and poled at 90V DC for 30 minutes. The temperature was then cooled down to room temperature while maintaining the 90 V applied voltage.

The rectification bridge circuit consists of four STMicroelectronics® 1N5711 small signal Schottky diodes and a 10 nF mylar storage capacitor. These diodes were chosen specifically because, compared to most discrete components, they have the smallest forward voltage drop (approximately 0.2V). This allows for the largest possible DC voltage to develop across the capacitance/load. The 10 nF mylar cap was chosen because it has a very low leakage current.

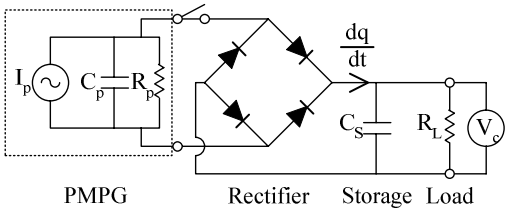

Figure 5. *Equivalent electrical model of the PMPG power system.*

RESULTS AND DISCUSSION

The polarization properties of the PZT thin films were measured using the Radiant Technologies© RT-66A High Voltage Interface with Trek® Model 601C in the form of a P-V hysteresis curve. The spontaneous polarization (P_s), remanent polarization (P_r), coercive field, and dielectric constant are 50 μC/cm^2, 20 μC/cm^2, 38 kV/cm, and 1200ε_0, respectively.

In order to find out the resonance mode and tip displacement, the PMPG device of 170 μm×260 μm was directly excited by a ±3V AC voltage source and swept from 0 to 200 kHz. At the same time, the cantilever tip displacement was measured by a laser vibrometer. Figure 6 reveals three resonant modes: 13.9, 21.9 and 48.5 kHz. The 13.9 kHz mode is the uniform bending mode of concern, and also demonstrates the largest tip displacement amplitude. The 48.5 kHz is also a bending mode, but the beam bends both upward and downward in a snake-like fashion, while the 21.9 kHz mode demonstrates a twisting type motion (torsional mode). Since the 13.9 kHz 1st resonance mode shows the largest amplitude of displacement, we can obtain the highest power output from it.

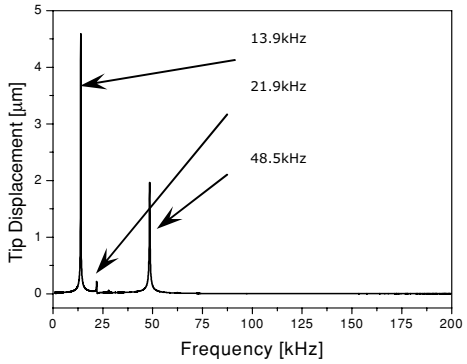

Figure 6. *Cantilever tip displacement vs. AC frequency.*

Having determined the 13.9 kHz 1st mode resonance, a piezoelectric shaker was then used to apply vibration directly to the PMPG at that frequency. The magnitude of the base displacement was varied by changing the shaker drive voltage amplitude. Cantilever tip displacement and the corresponding closed-circuit charge (measured by a closed-circuit charge amplifier) were then measured against the input base displacement (Fig. 7). Here, base displacement is simply the displacement of the silicon substrate to which the micro cantilever is attached. The tip displacement was amplified by approximately 90 times over the base displacement during resonance. On the whole, tip displacement was linear to base displacement except during large base displacements.

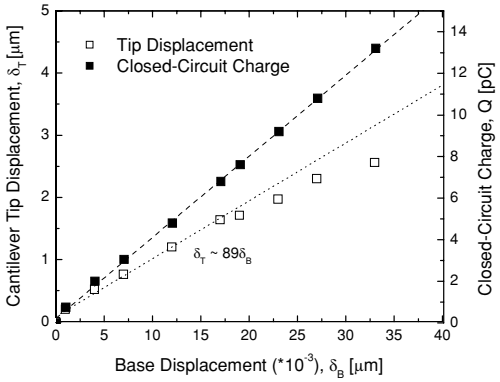

Figure 7. *Cantilever tip displacement and generated closed-circuit charge vs. base displacement.*

The amount of charge developed on the IDT electrode is approximately linear in proportion to tip displacement (In fact, the charge is more linear with the base displacement). This is because the axial stress developed within the PZT layer also increases linearly with tip displacement. A maximum generated charge of 13.2 pC was measured at a maximum tip displacement of 2.56 μm. The charge increases linearly with tip displacement with a linearity coefficient of 4.14 pC/μm.

For the next set of base shaking experiments, the PMPG device was connected to a bridge rectifying circuit with a resistive load across the storage capacitor, as shown in Fig. 5. The load voltage was measured as a function of load resistance with a fixed base displacement magnitude of 14 nm at a shaking frequency of 13.9 kHz. Figure 8 shows the load voltage and power delivered to the load. As expected, the load voltage increases with the increased load, up to 3 V at 10.1 MΩ. However, the power delivered to the load will not increase indefinitely. There is a maximum point, 1.01 μW for the 5.2 MΩ load, after which the electrical power decreases with increased load resistance. A 2.4V DC voltage was achieved at the 1.01 μW power level. Given the device area (including room for on-chip rectification and energy storage circuitry), this translates to an energy density of 0.74 mW-h/cm^2, which compares favorably to current chemical battery solutions (i.e. lithium ion). The storage capacitor charging and discharging times were approximately 0.2 and 0.3 seconds, respectively.

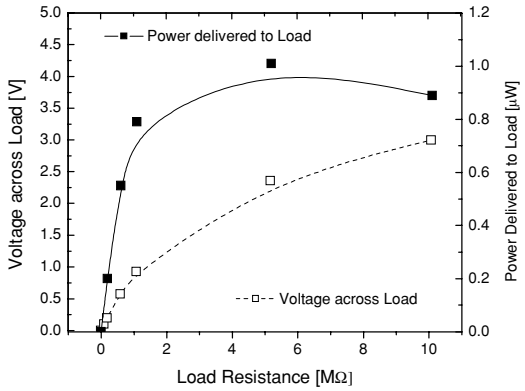

Figure 8. *Load voltage and power delivered to the load vs. load resistance at 13.9 kHz resonance.*

Going back to Eq. (3), the power is inversely proportional to the frequency and proportional to the square of the vibration amplitude. It is known that the amplitude of an ambient vibration source is inversely proportional to the square of its frequency; that is, $Y \sim 1/\omega_n^2$ [**1**]. Considering this property of the vibration source, the power decreases with frequency because the decreasing input base displacement amplitude dominates the increasing frequency contribution. This indicates that, in order to harness the most power from the available energy spectrum, the PMPG should target a lower frequency, perhaps in the few hundreds of Hz. From a conservative viewpoint, the power may not increase exactly linearly with decreasing frequency. Nevertheless, we should be able to achieve at least an order of magnitude more power by tuning the resonance frequency down to several hundred Hz.

However, there is one limitation in scaling down the frequency: The PZT material has a strain limit of approximately 10^{-3} to bear the vibration amplitude. Currently, the tip displacement of the PMPG for the 1.01 μW power generation is approximately 2 μm, roughly corresponding to a PZT strain of below 10^{-4} for the 170 μm long cantilever beam. Consequently, this lower frequency device has more capacity for getting a higher power output, but we have to compromise it within the PZT strain ability.

CONCLUSIONS

A MEMS-based d_{33} mode PMPG device was designed to have a high open-circuit voltage and power output while requiring only three photo masks for fabrication. Adjusting the residual stress and elastic modulus of the bottom membrane layer of the composite beam successfully controlled the bowing and resulted in a flat cantilever composite beam.

The cantilever has three different resonance modes: two bending (13.9 and 48.5 kHz) and one torsional (21.9 kHz). The packaged PMPG device was shaken by a piezoelectric shaker with a base displacement of 14 nm. A maximum DC voltage of 3V was generated across the load (10.1 MΩ), and a continuous electrical power of over 1μW was delivered to the 5.2 MΩ load. The corresponding energy density is 0.74 mW-h/cm^2, which compares favorably to current lithium ion chemical battery solutions. This d_{33} type, thin film, piezoelectric micro cantilever device could be used for various applications such as batteryless and wireless micro sensors and micro power generators. Targeting of the ambient power spectrum at lower frequencies could result in a higher power PMPG device in the future.

REFERENCES

1. S. Roundy, P. K. Wright, and J. Rabaey, "A Study of Low Level Vibrations as a Power Source for Wireless Sensor Nodes", *Computer Communications,* 26**,** 1131 (2003).

2. C. W. Wong, Y. Jeon, G. Barbastathis, and S-G. Kim, "Strain-Tuning of Periodic Optical Devices: Tunable Gratings and Photonic Crystals", *Technical Digest of the 2002 Solid-State Sensor and Actuator Workshop*, Hilton Head Isl., SC, 6/2-6/02, Transducer Research Foundation, Cleveland (2002), pp. 342-345.

3. K. Hwang, M. Koo, and S. Kim, "High-Brightness Projection Display Systems Based on the Thin-Film Actuated Mirror Array (TFAMA)", *Proc. of SPIE, Sep. 20-24*, 3513, *Santa Clara* (1998), pp. 171-180.

4. P. Glynne-Jones, S. P. Beeby and N. M. White, "Towards a Piezoelectric Vibration-Powered Microgenerator", *IEEE Proc.-Sci. Meas. Technol.*, 148, (2001), pp. 69-72.

5. J. Kymissis, C. Kendall, J. Paradiso and N. Gershenfeld, "Parasitic Power Harvesting in Shoes", *Proc. of the Second IEEE International Conference on Wearable Computing (ISWC)*, (1998), pp. 132-39.

6. C. B. Williams and R. B. Yates, "Analysis of a Micro Electric Generator for Microsystems", *Proceedings of the Transducers 95/Eurosensor IX*, (1995), pp 369-372.

7. T. S. Low and W. Guo, "Modeling of a Three-Layer Piezoelectric Bimorph Beam With Hysteresis", *J. MEMS*, 4, 230 (1995).

8. J.F. Lynch, C.G. Ruderer and W.H. Duckworth, "Engineering Properties of Selected Ceramic Materials", *American Ceramic Society*, (1966), Based on report AFML-TR-66-52.

9. M. Fukuhara and A. Sanpei, "Effects on High-Temperature-Elastic properties on α-/β-Quartz Phase Transition of Fused Quartz", *J. Mater. Sci. Lett.*, 18, 751 (1999).

10. S. Sakaguchi, N. Murayama, Y. Kodama, and F. Wakai, "The Poissons Ratio of Engineering Ceramics at Elevated Temperature", *J. Mater. Sci. Lett.*, 10, 282 (1991).

ELECTRONIC COOLING SYSTEMS BASED ON FIXED-VALVE MICROPUMP NETWORKS

Christopher J. Morris, Jone Y. Chung*, Patricia E. Rahm and Fred K. Forster
Department of Mechanical Engineering, University of Washington
Seattle, WA 98195-2600 USA
Dan Faulkner and Reza Shekarriz
MicroEnergy Technologies, Inc.
Vancouver, WA 98660

ABSTRACT

Thermal control of electronics in portable computers and space vehicles where compactness, weight, efficiency, simplicity, reliability and cost are important is an area ideally targeted for MEMS-based approaches. Micropumps based on diaphragm actuation and utilizing fixed-geometry valves may meet all the above criteria when used for fluid transport in closed-loop forced-convection thermal management systems. To investigate this potential application, an integrated cooling module was designed, fabricated and tested. It consisted of a network of four planar micropumps fabricated in plastic and a copper microchannel heat sink. Plastic allowed rapid prototyping and resulted in a multilayer pump network 32x32 by 11 mm thick. Other materials could reduce the total thickness significantly. To our knowledge this work is the first application of a scalable network of micropumps. Thermal power handling of 35 W was possible at a flow rate of 11 ml/min using water as the coolant.

INTRODUCTION

Cooling individual electronic components and systems where mass and reliability are extremely important, such as on micro-satellites is receiving significant attention. In addition, size, efficiency and cost are critical factors in the choice of thermal management method for portable computers. While a number of approaches have been reported, such as thermosyphons [**1**] electroosmotic forced convection [**2**] and spray cooling[**3**], optimization of all characteristics for specific applications is far from complete. In space applications, single-phase cooling may be the proper choice for highest reliability when conductive heat transfer is insufficient. In other applications, two-phase cooling may be the best choice even though pressure and flow instabilities pose problems and driving pressure required increases dramatically with small increases in vapor to liquid mass ratio (quality) [**4**].

In this study we investigated the use of planar membrane micropumps that utilized fixed-geometry valves, which are simple to fabricate and have no moving parts except for the flexure of a piezoelectrically or electrostatically driven membrane [**5**–**7**]. These pumps currently do not produce the high pressure of electroosmotic pumps, but are attractive in many if not all other ways previously mentioned. Presented here are our initial efforts to utilize this approach in the form of a pump network fabricated in plastic. The network was configured in parallel to achieve high flow, but could be configured in series to develop higher pressure necessary for two-phase cooling. We know of no other reports of scalable networks of micropumps.

*Travel support has been generously provided by the Transducers Research Foundation and by the DARPA MEMS and DARPA BioFlips programs.

MICROPUMP-HEAT EXCHANGER MODULE

One overall goal of this project was to develop a compact micropump/heat exchanger unit, the design of which is shown in Fig. 1. The Teflon fluid distribution block and inlet-outlet header were designed to accommodate various 1 cm^2 microchannel arrays. For this initial study v-shaped channels approximately 60 μm wide and 200 μm deep produced with laser micromachining were utilized (Pacific Northwest National Laboratory, Richland, WA). The unit was also designed to accommodate a combination of stacked planar micropumps as shown. For this study a network of four micropumps arranged in parallel was used to attain relatively high flow rate. The piezoelectric drivers were arranged electrically in pairs as shown schematically in Fig. 2. To eliminate the need for a fluid capacitor between the pump network and the fluid load, the individual pumps in each pair operated in phase while each pair operated out of phase from the other.

Reduced-order linear system modeling was used to maximize pump resonance and evaluate numerous design parameters [**8**]. Since the planform dimensions were fixed at 2.5 cm^2, and since the target flow rate was higher than we had attempted with past pump designs, the starting point for the design process was a 20 mm diameter pump chamber diameter. With that dimension fixed, most of the other parameters were determined through the design for resonance described above using properties of acrylic. However, although valve size was determined by this design process, valve shape was not. Figure 3 shows two pump layers, each utilizing different Tesla-type valves designs. The one used in the pump labeled fvp1 has been used in a number of other pump designs, while that used in pump fvp2 was determined from a computational fluid dynamics-based optimization process that substantially improved single-chamber pump performance [**9**].

Machining of all pump features was accomplished with miniature end mills ranging from 125 to 1700 μm in diameter. SurfCAM (CNC Prose) was used to translate CAD drawings into machine code for a mini-milling machine (Model 5410, Sherline Products Inc., Vista, CA), modified for numerical control (999-6100-005, MicroKinetics Corp., Kennesaw, GA). This process allowed rapid prototyping

0-9640024-5-0/hh2004/$20©2004TRF
DOI 10.31438/trf.hh2004.42

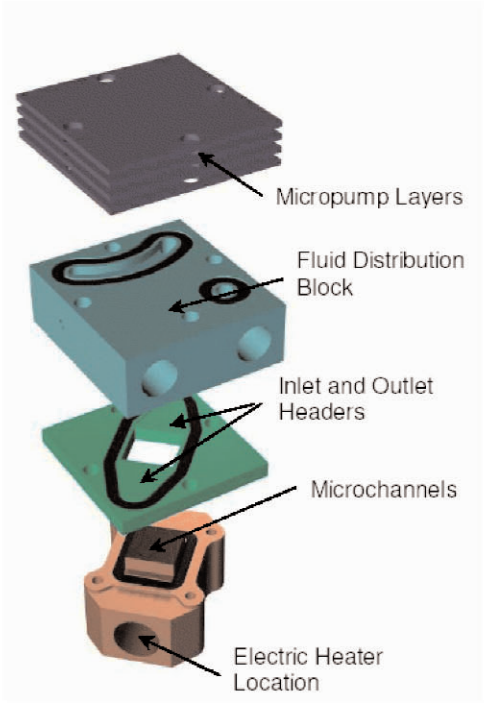

Figure 1. *Schematic of the prototype pump/heat sink assembly. The pump network consisted of a stacked array of micropumps to demonstrate scalability of fluid transport without increase in footprint size.*

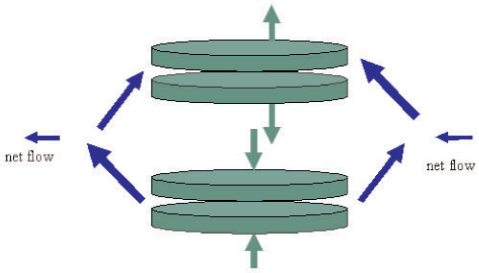

Figure 2. *Schematic of how two pairs of actuators operating out of phase with the elements in each pair operating in phase and deliver steady flow at the network outlet. Two pump chambers are positioned in between each pair of actuators. Arrows are shown for one half of a pump cycle, with relative flow magnitudes into and out of each pump chamber shown.*

compared with silicon-based microfabrication. The process also allowed easy three-dimensional profiling of multiple-depth features, such as the transition between deep valves and shallow chambers as shown in Fig. 4.

Two machined 1.6 mm acrylic layers of the type shown in Figs. 3(a) and (b) were used in each of two pump pairs, separated by a plain 0.5 mm polycarbonate layer. A total of nine layers comprised the pump network, six for the two pairs of pumps. The seventh was a 3.2 mm acrylic spacer be-

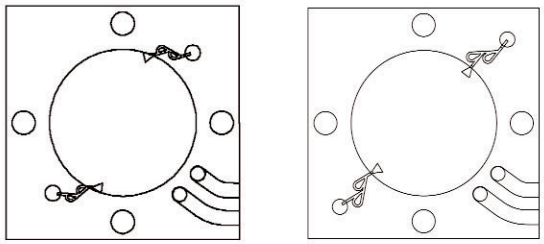

(a) fvp1 (b) fvp2

Figure 3. *Valve-pump chamber layers for micropump network. Shown are 20* mm *diameter pump chambers, two-element valves, each having a transverse dimension of 300* μm*: (a) the Tesla-type A for the pump fvp1 and (b) the Tesla-type G for pump fvp2. Also shown are four through holes for attachment to the heat exchanger and channels at the lower-right corner for routing electrical connections.*

Figure 4. *Valve fabricated in acrylic using micro milling techniques.*

tween pump pairs with a cavity milled on each side to allow for actuator clearance. The eighth and ninth acrylic layers, each 1.6 mm thick, formed a bearing surface for the fluid distribution block and accommodated variable spacing between valve ends (see Figs. 1 and 3). Rapid cure cyanoacrylate (Loctite 420 Superbonder) was used to bond all plastic layers except the acrylic spacer, which was bonded with epoxy. Cyanoacrylate was also used to bond the piezoelectric driver elements to the appropriate acrylic layer. The height of the completed network stack was 11 mm with transverse dimensions of 32 mm.

TEST METHODS

A micropump/heat exchanger module incorporated into a closed-loop test apparatus is shown in Fig. 5. Thermocouples were used to measure inlet and outlet coolant and cooper block temperature. Tubing carried heated coolant from the microchannel heat exchanger to a macroscopic fan-driven heat exchanger in which the fluid temperature re-

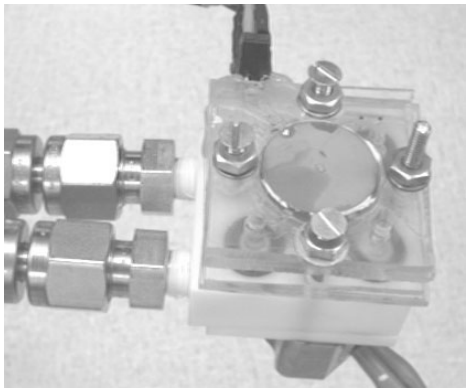

Figure 5. *The pump network/heat exchanger assembly incorporated into the closed-loop test system. Electrical leads to a 400 W, 33Ω cartridge heater can be seen below the assembly.*

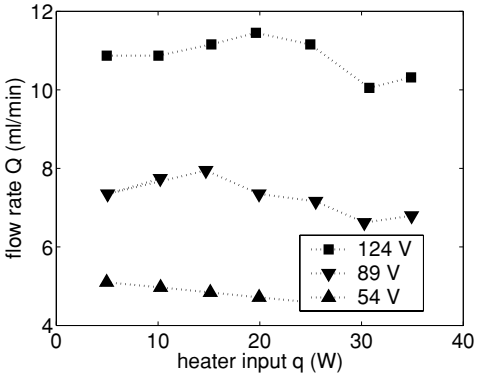

Figure 6. *Flow rate delivered by micropump fvp1 at three different excitation voltage levels versus electrical power to heater. Lines added for clarity.*

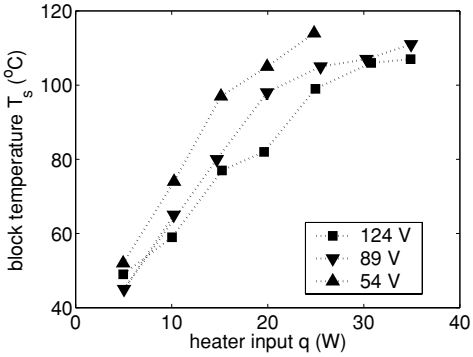

Figure 7. *Heat exchanger temperature versus electrical power to heater for a range of micropump excitation voltages applied to pump fvp1. Lines added for clarity.*

turned to the ambient level. The cooled fluid then passed through a float-in-tube flow meter (Key Instruments, p/n GS60410, Trevose, PA) and finally returned to the micropump, which delivered it back to the microchannel array. Characterization of the test loop was performed with a syringe pump (KD Scientific, model 200, Hollistion, MA). During thermal tests the apparatus was wrapped with insulation (Kaowool S Blanket, Thermal Ceramics, Augusta, Georgia). With insulation in place, external temperatures of the tubing in the region of the coolant thermocouples differed by less than 2 °C from the coolant temperatures. Also, the electrical power delivered averaged 16% higher than the heat gain of the fluid as determined from fluid temperatures. For data taken with a micropump, deionized water was degassed by heating and the piezoelectric actuators were driven with a sinusoidal signal from a signal generator (Model 19, Wavetek, United Kingdom) and amplified (Piezo Linear Amplifier, Piezo Systems Inc., Cambridge, MA). All voltage levels are given as the amplitude of the sinusoidal signal.

RESULTS AND DISCUSSION

Pump fvp1 produced a no-load flow rate of approximately 11 ml/min at 100 V and 330 Hz, which was close to model predictions. The no-load flow rate for pump fvp2 was only 4.1 ml/min at 210 Hz, and it was not tested further. Bonding material may have been deposited in some valves causing the pump network to operate unsymmetrically with a significant reduction in performance. Data were taken for the remaining pump over four days with the system running for up to six hours, which demonstrated that dissolved gas did not pose a problem. Flow rates delivered by pump fvp1 to the microchannel heat exchanger versus heater input are shown in Fig. 6 for various pump excitation voltages. The microchannel heat exchanger temperature T_s versus heater input is shown in Fig. 7 for the corresponding pump excitation levels. The maximum thermal power transferred to the fluid was approximately 35 W at 11 ml/min. Some boiling occurred at all three pump excitation levels for $T_s > 100\,^{\circ}$C. The junction-ambient thermal resistance[1] for the highest micropump excitation level for $T_s < 100\,^{\circ}$C., i.e. $q < 25$ W, was approximately 3 K/W. At 35 W it was approximately 2.3 K/W. The heat transfer coefficient for microchannel array[2] ranged from 400 to 1000 W/m^{2}K over the range of heater input and pump excitation levels considered.

Given the number and size of piezoelectric drivers used in the pump network, an estimate was made of the peak instantaneous power $P_o = \pi f C V_o^2$ based on the capacitance of the drivers. For one 190 μm by 18 mm disk of PZT-5A the capacitance $C = 0.028\,\mu$F, based on a permittivity of $1.5 \times 10^{-2}\,\mu$F/m. For $V_o = 100$ V and $f = 300$ Hz, $P_o = 200$ mW. For four elements, the corresponding instantaneous power was therefore estimated to be 800 mW. Peak power for typical single chamber pumps for which net power has been measured is 5 to 10 times higher than average power[**10**]. Thus, the average power of the pump network described here was estimated at between 80 and 160 mW.

[1] $\Theta_{JA} = (T_s - T_{in})/q$, where T_{in} is the inlet coolant temperature

[2] $h = q/A(T_s - T_{mean})$, where A is the surface area of the heat exchanger, and $T_{mean.}$ is the mean fluid temperature

CONCLUSIONS

We have demonstrated that a fixed-valve diaphragm micropump network used in conjunction with a microchannel array was capable of handling thermal loads of 35 W and 35 W/cm^2. The prototype system, when fabricated in plastic, produced a stacked four-micropump network with a total thickness of 11 mm. With stiffer materials, such as metal for the diaphragm, and better packaging, the overall size could be reduced significantly. Lastly, it was estimated that the net power consumption was less than 200 mW. Thus, on the basis of these results, this approach for cooling appears to be attractive in terms of size, weight, efficiency and simplicity. Further work is needed to investigate these attributes more quantitatively along with evaluations of reliability and cost.

ACKNOWLEDGMENTS

This work was supported in part by a subcontract to the University of Washington from NASA Goddard Space Flight Center contract NASS-03059 to MicroEnergy Technologies Inc. (MET), and by Washington and Technology Center Research Technology Development Agreement WTC FTI 03-10. Support was also provided by a Roy E. and Irene C. Grossmann Memorial Scholarship.

REFERENCES

[1] A. Pal, Y. Joshi, M. H. Beitelmal, C. D. Patel, and T. M. Wenger. Design and performance evaluation of a compact thermosyphon. *IEEE Trans. Comp. Pack. Tech.*, 25(No. 4, December):601–607, 2002.

[2] L. Jiang, J. Mikkelsen, Jae-Koo Koo, D. Huber, S. Yao, L. Zhang, P. Zhou, J. G. Maveety, R. Prasher, J. G. Santiago, T. W. Kenney, and K. E. Goodson. Closed loop electroosmotic microchannel cooling system for VLSI circuits. *IEEE Trans. Comp. Pack. Tech.*, 25(No. 3, September):347–355, 2002.

[3] C. E. Bash, C. D. Patel, and R. K. Sharma. Inkjet assisted spray cooling of electronics. In *International Electronic Packaging Technical Conference and Exhibition*, Maui, July 6–11 2003 (paper IPACK2003-35058).

[4] S. G. Kandlikar. Fundamental issues related to flow boiling in minichannels and microchannels. *Exp. Thermal Fluid Sci.*, 26:389–407, 2002.

[5] F. Forster, R. Bardell, M. Afromowitz, and N. Sharma. Design, fabrication and testing of fixed-valve micropumps. In D. C. Wiggert et al., editors, *Proceedings of the ASME Fluids Engineering Division, ASME International Mechanical Engineering Congress and Exposition (San Francisco)*, volume 234, pages 39–44, New York, November 12-17 1995. ASME.

[6] T. Gerlach and H. Wurmus. Working principle and performance of the dynamic micropump. In *Micro Electro Mechanical Systems, MEMS '95 (Amsterdam)*, pages 221–226, New York, Jan. 29 - Feb. 2 1995. IEEE.

[7] A. Olsson, P. Enoksson, G. Stemme, and E. Stemme. A valve-less planar pump in silicon. In *Transducers '95 (Stockholm)*, volume 2, pages 291–294, New York, June 25–29 1995. IEEE.

[8] C. J. Morris and F. K. Forster. Low-order modeling of resonance for fixed-valve micropumps based on first principles. *J. Microelectromechanical Syst.*, 12(3):325–334, 2003.

[9] A. R. Gamboa, C. J. Morris, and F. K. Forster. Optimized fixed-geometry valves for laminar flow micropumps. In *ASME International Mechanical Engineering Congress and Exposition (IMECE 2003), Fluids Engineering Division*, Washington, D.C., Nov. 15–21 2003 (in press & on CD as paper IMECE2003-55036).

[10] R. Bardell, R. Sharma, F. K. Forster, M. A. Afromowitz, and R. Penney. Designing high-performance micro-pumps based on no-moving-parts valves. In L. Lin, K. E. Goodson, et al., editors, *Micro-Electro-Mechanical Systems (MEMS), ASME International Mechanical Engineering Congress and Exposition (Dallas)*, volume DSC-234/HTD-354, pages 47–53, New York, November 16-21 1997. ASME.

A LOW-POWER, LOW-LEAKAGE, BI-STABLE PLANAR ELECTROLYSIS MICRO GATE VALVE

Jeremy A. Frank and Albert P. Pisano
Berkeley Sensor & Actuator Center, Department of Mechanical Engineering
University of California, Berkeley, California 94720-1774

ABSTRACT

The micro gate valve presented in this paper demonstrates improved sealing over previous planar silicon valves [1]. This is achieved using a wafer-level, five-mask fabrication process that removes the leakage paths above and below the moving gate, a problem that plagued earlier valve versions. Current valve designs exhibit closed fluidic resistances as high as 3.9×10^{15} Ns/m^5 with fluidic-resistance ratios greater than 3,500. This valve uses low-power electrolysis of the working fluid for actuation, making it suitable for portable microfluidic applications where battery energy is limited. These valves require as little as 9 μJ (0.23 μW) to open and 22 μJ (0.6 μW) to close at 5.0 V. No energy is required to maintain the state of the valve. The inert nature of the silicon and Pyrex® fabrication materials also makes this valve suitable for high-temperature and corrosive environments in addition to the biological applications discussed here.

INTRODUCTION

This microvalve is designed for integration into a portable bioassay microfluidic system where all of the energy and working fluid are stored on board the device. Thus, the valves are designed to be both low leak and low power as well as straightforward to fabricate and easy to integrate with other fluidic components to form complete microfluidic bioassay systems.

Portable microfluidic devices have a very limited supply of working fluid and the use of this fluid must be tightly budgeted to increase the life of the system. The microvalves used for these applications must have low leakage rates to increase the precision with which fluid is distributed to other parts of the system. Large leakage rates waste more fluid, decrease system life, and reduce the overall performance of the system as the leakage will induce uncertainty in the position of fluid relative to assay chambers and sensors. This does not mean that a valve must possess an infinite closed fluidic resistance to be functional. While there are applications for very well sealing valves [2], the delivery of both 100 mg/dL and 500 mg/dL concentrations of insulin to an adult could be controlled by a valve with a fluidic-resistance ratio of 3,500.

Additionally, due to the meager amount of energy available from the system battery, the valves are required to have low power consumption. The energy consumption of the valves is designed to make up only a fraction of that deliverable by the system battery, ensuring that the majority of the energy budget can be allocated to sensing and drug/antidote delivery.

Electrolysis actuation is chosen because of the low-power nature of electrolysis. The bi-stable valve would seal equally as well under thermal-bubble or electrostatic actuation because the sealing force is due to the suspension and valve seat geometry and not the specific actuation mechanism. The actual means of actuation would be defined by other system parameters such as power budget and operation speed.

The valve design is also planar, making it easy to integrate with other planar components such as mixers and pumps. Planar systems offer the potential for reduced dead volume within the device, as components can be placed adjacent to one another, obviating any large-volume through-wafer fluidic passages.

Additionally, the inert nature of the materials comprising the valve, Pyrex®, silicon and platinum, suggest that the valve is also suitable for long-term use as well as in high-temperature and corrosive scenarios.

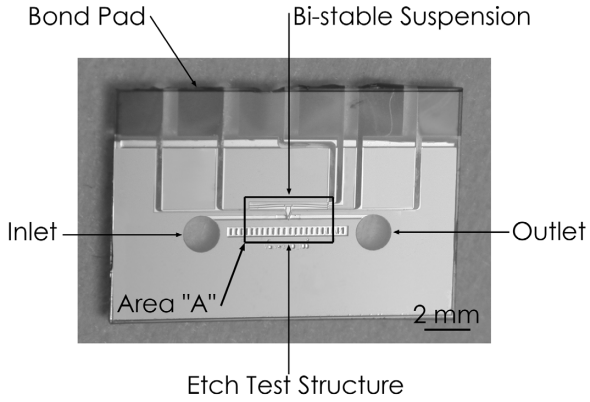

Figure 1. *A photo of the top view of the valve, looking through the Pyrex® cover wafer. Visible are the inlet, outlet, bi-stable suspension, platinum bond pads and a test structure used to monitor lateral silicon etch progression. Area "A" is enlarged in Fig. 2.*

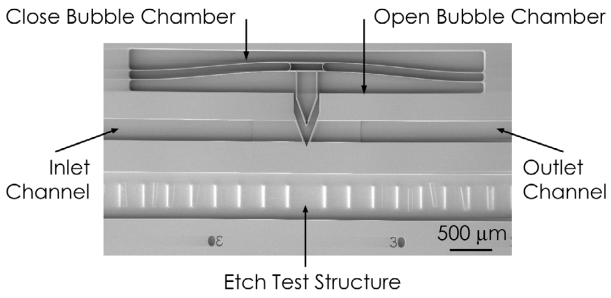

Figure 2. *Area "A" of Fig. 1 shows a close-up picture of the bi-stable suspension for a valve in the open position. Visible are the inlet and outlet channels, close and open bubble chambers and the lateral etch test structure.*

VALVE DESIGN AND FABRICATION

Each valve consists of an inlet, outlet and movable gate etched into the device layer of an SOI wafer, Fig. 1. The fluidic channels etched in the silicon are capped with a patterned Pyrex® wafer that is anodically bonded to the silicon surface. The actuating platinum electrodes are evaporated onto the surface of the Pyrex® and are located above the bubble-actuation chambers. The gate obstructs the fluid flow when the valve is closed and is anchored to the surrounding silicon by a bi-stable suspension. This suspension maintains the state of the valve by holding the gate open or closed, Fig. 2. Thus, no power is required to hold the state of the valve, reducing the overall energy consumption. In addition, the suspension is necessary to prevent loss or misalignment during fabrication. Previous planar valve designs had problems with the loss of free-floating parts during fabrication [3].

0-9640024-5-0/hh2004/$20©2004TRF
DOI 10.31438/trf.hh2004.43

Solid-State Sensors, Actuators, and Microsystems Workshop
Hilton Head Island, South Carolina, June 6-10, 2004

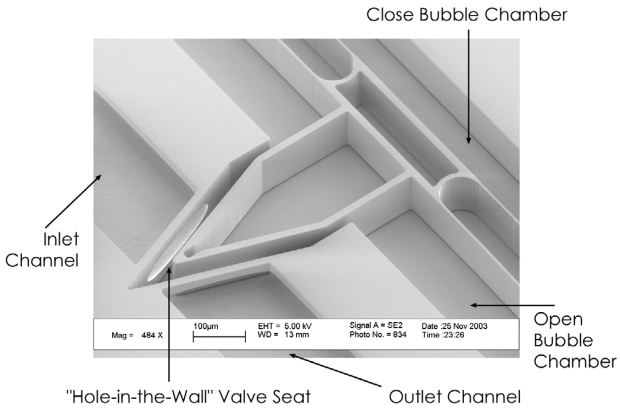

Figure 3. *SEM showing the valve seat. Valve is in the open position. Visible are the inlet and outlet channels, close and open bubble actuation chambers and the valve seat fabricated with the "hole-in-the-wall" process.*

Fluid must flow through a hole etched in the center of the sidewall of a channel, Fig. 3. This hole creates a valve seat that completely encompasses the flow, reducing leakage above and below the gate when the valve is closed. The hole is the key artifact of the fabrication process, Fig. 4, and is responsible for the improved sealing.

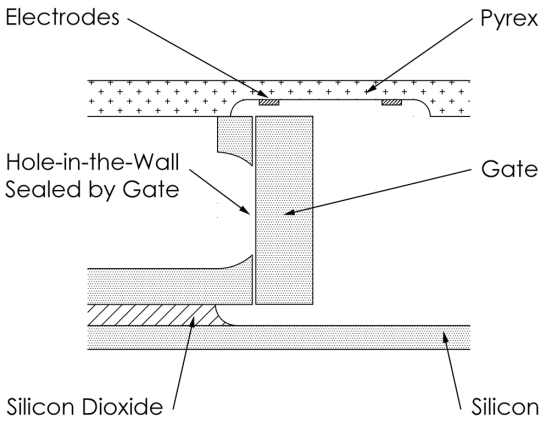

Figure 4. *Cross-sectional view of the valve seat shows how the gate can be brought in contact with the seat, removing the leakage paths above and below the gate.*

The valve is actuated with bubbles of hydrogen and oxygen created by electrolysis of the working fluid, deionized water. Bubbles are grown in the appropriate chamber and apply increasing pressure to the suspension members, eventually flipping the suspension and changing the state of the valve, Figs. 5, 6. The platinum metal used in the electrodes is necessary to catalyze the reaction of the hydrogen and oxygen gas to water, thereby collapsing the bubbles. This helps remove the bubbles from the chamber and allows the valve state to be changed at an increased rate.

The fabrication process is similar to that detailed in [4]. It uses a five-mask, wafer-level process that is typical of the hole-in-the-wall fabrication method. Trenches of two different depths are etched in the device layer of a silicon-on-insulator wafer (100 μm device layer, 4 μm buried oxide). Deep trenches are etched to the buried oxide and serve as the majority of the fluidic pathways. The shallow channels are necessary to fabricate the valve seat.

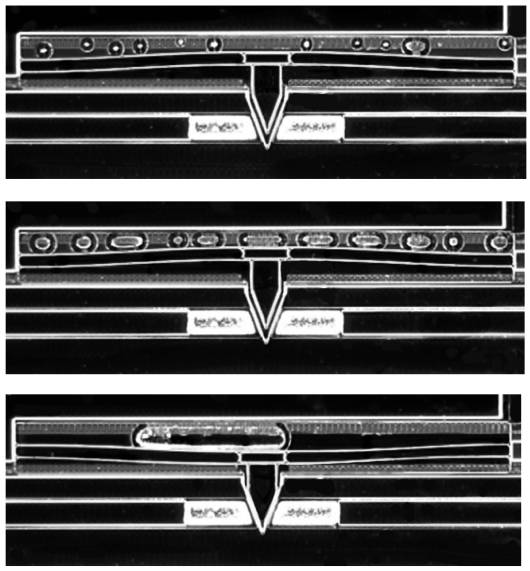

Figure 5. *Sequential photos show the closing process. Bubbles of hydrogen and oxygen grown in the close bubble chamber apply increasing pressure to the bi-stable suspension that flips the gate and closes the valve.*

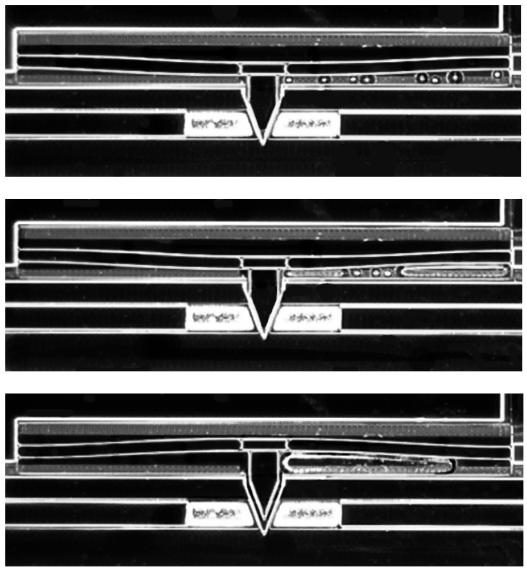

Figure 6. *Sequential photos show the opening process. It was discovered that only one of the two opening bubble chambers was necessary to open the valve. This reduces the energy consumption of the valve.*

All exposed silicon is then passivated in a wet oxidation step that performs two functions: it protects the silicon during the subsequent isotropic etch step and it serves as an oxide polish step that removes the DRIE scallops from the valve seat positioned in the side wall of the channel and improves sealing.

The oxide is removed from the bottom of the shallow channels using a directed plasma etch, exposing the silicon. The buried oxide layer is thick enough to remain following this step.

An isotropic plasma etch of silicon is performed which etches laterally beyond the oxide passivation of the shallow channels, puncturing the thin wall and forming the valve seat, Fig. 7.

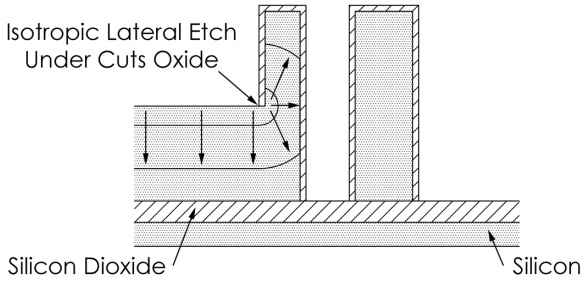

Figure 7. *The isotropic silicon etch progresses laterally under the oxide passivation, puncturing the silicon wall and forming the valve seat.*

The fifth mask is used to define backside through-wafer interconnects that can be omitted if in-plane interconnects are used [5].

The silicon wafer is then subjected to an isotropic HF acid etch to remove all of the passivating oxide to release the moving parts and prepare for the anodic bond.

The capping Pyrex® wafer is patterned with reliefs to ensure that the moving parts of each valve do not become bonded to the Pyrex®. Platinum (titanium adhesion layer) is evaporated onto the Pyrex® and patterned using a lift-off technique.

The Pyrex® wafer is aligned and anodically bonded to the silicon wafer. The wafer stack is then diced following a scheme detailed in [6] that ensures that the microfluidic channels are not contaminated with the cooling water of the dicing saw. Additionally, portions of the silicon can then be broken off to expose the bond pads on the Pyrex® for the open and close electrodes.

The progression of the isotropic lateral etch is of paramount concern during the fabrication as it will define the final geometry of the orifice. This orifice geometry must be tightly controlled if the performance of valves fabricated on different wafers is to be the same. A test structure has been developed that allows for in-situ monitoring of the lateral etch, allowing one-micron resolution of the etch progression, Fig. 8.

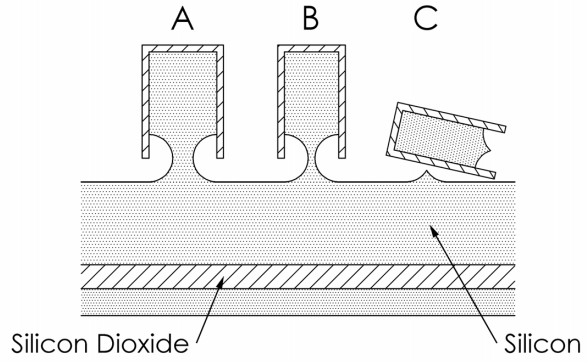

Figure 8. *Mesas A, B, and C are of decreasing thickness. The lateral etch progression is monitored by the fall of the mesas.*

Mesas of differing widths are etched during the shallow-trench etch in the fabrication process. These mesas become undercut during the isotropic silicon etch and topple sequentially, indicating the extent of the lateral etch. Using these test structures, it has been shown that the lateral etch differs only by +/- 1 micron across the wafer which results in a difference in orifice height of +/- 4%. This is important as a basic analysis done in [4] suggests that there is an optimum orifice height that can increase the fluidic-resistance ratio by a factor of 10 or more.

EXPERIMENTAL SETUP

The fluidic resistance of the valves was measured using a syringe pump and a pressure sensor, Fig. 9. The pressure sensor measured the pressure drop across the valve for a range of volumetric flow rates of deionized water set by the syringe pump. This experiment was performed for both the open and closed states of the valve, Figs. 10-12. Additionally, actuation time as a function of energy consumption was investigated, Fig. 13.

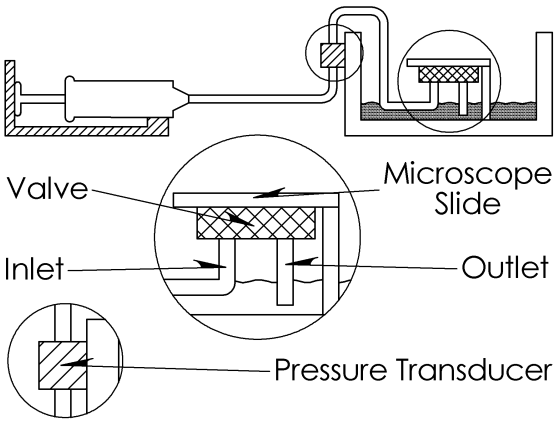

Figure 9. *The valves were tested in an experimental setup like the one shown here. The outlet of the valve was submerged in water to ensure that the outlet pressure was not affected by evaporation or dripping of the exiting fluid.*

RESULTS AND DISCUSSION

The closed and opened fluidic resistance for one of the fabricated valves is presented in Figs. 10 and 11. Data was taken for 12 actuations over a period of 96 hours. The fluidic capacitance of the testing setup greatly increased the time to equilibrium of the pressure drop across the valve for a set flow rate.

The actuation time of the valve was dependent upon the amount of energy used to close the valves. Greater energy was required for faster actuation times as the gas generation rate is proportional to the current flowing between the electrodes. The valves took as little as 22 μJ to close and 9 μJ to open at 5.0V. It was noticed that the actuation of only one open bubble chamber was necessary to open the valve, a discovery that reduced the energy consumption of the valve.

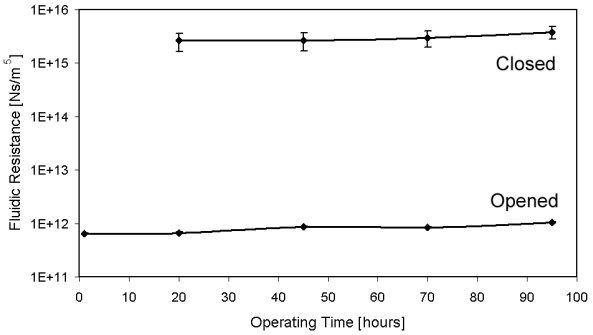

Figure 10. *The fluidic resistance for one valve in both the opened and closed states over time. Data is given for a 95% confidence interval.*

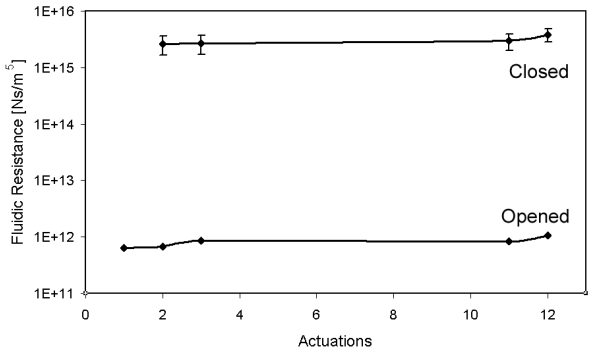

Figure 11. *The fluidic resistance for the same valve as a function of the number of actuations.*

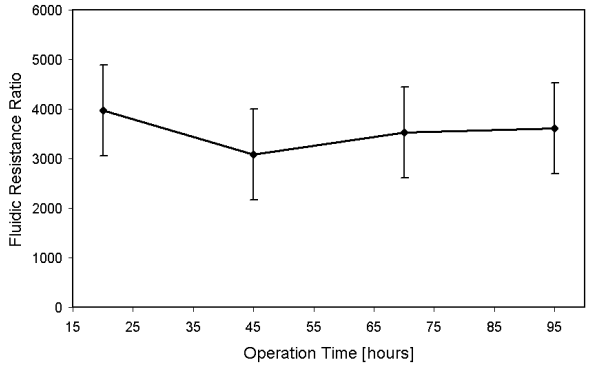

Figure 12. *The fluidic-resistance ratio of the valve remained fairly steady over the duration of the tests. Data is given for a 95% confidence interval.*

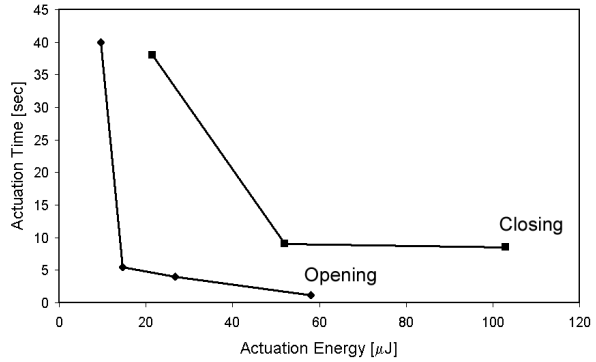

Figure 13. *Actuation energy is inversely proportional to the actuation time. Energy consumption as low as 9 μJ was achieved for an actuation time of 40 seconds (0.23 μW). An actuation time of 1.2 seconds was achieved for an energy consumption of 58 μJ (48 μW).*

The data shows that the fluidic resistance of the valve differs by 25% over the length of the tests. This variation is most likely due to a misalignment between the wedge-shaped gate and the seat. The valve design uses a large safety factor in the bi-stable suspension design to ensure that the valve closes under the pressure available from the electrolysis bubble [7]. This results in long, thin beams (3mm) that are compliant enough to allow for rotation of the gate during actuation. Thus, one side of the gate makes contact with the seat before the other and it is conceivable that the overly weak bi-stable suspension is not sufficiently forceful to guide the gate completely home. This design flaw is easily repairable in future versions of the valve.

CONCLUSION

A planar gate valve fabricated with the hole-in-the-wall process has been shown to have acceptable fluidic resistance and fluidic-resistance ratios for microfluidic applications. The fabrication process is wafer-level and easily allows for the integration of the valve with other planar components. This helps reduce the dead volume of the system, as components can be placed adjacent to one another.

The hole-in-the-wall fabrication process removes the leakage paths above and below the moving gate that plagued earlier planar valve designs, improving performance. The bi-stable suspension reduces the energy consumption of the valve by allowing the valve to only require power to change state. This bi-stable suspension also enables wafer-level fabrication, as the moving parts remain tethered to the substrate during fabrication. Thus, no free-moving parts are lost in the process as in previous planar examples.

Closed fluidic resistances of up to 3.9×10^{15} Ns/m^5 with fluidic-resistance ratios greater than 3,500 have been achieved. Energy and power consumptions were shown to be as low as 9 μJ (0.23 μW) to open and 22 μJ (0.6 μW) to close at 5.0 V. Shorter actuation times of 10 seconds to close can be achieved with an increase in power consumption to 48 μW.

Travel support has been generously provided by the Transducers Research Foundation and by the DARPA MEMS and DARPA BioFlips programs.

REFERENCES

1. A.P. Papavasiliou, A.P. Pisano, and D. Liepmann, "High-Speed and Bi-Stable Electrolysis-Bubble Actuated Gate Valves", *Technical Digest of TRANSDUCERS '01*, Munich, Germany, 6/10-13/01, Transducer Research Foundation, Cleveland (2001), pp. 940-43.

2. J. Xie, X. Yang, X. Wang, and Y.C. Tai, "Surface Micomachined Leakage Proof Parylene Check Valve", *Technical Digest MEMS 2001, 14th IEEE International Conference on Micro Electro Mechanical Systems,* Interlaken, Switzerland, 1/21-25/01, IEEE (2001), pp. 539-42.

3. A.A. Deshmukh, D. Liepmann, and A.P. Pisano, "Characterization of a Micro-Mixing, Pumping and Valving System", *Technical Digest of TRANSDUCERS '01*, Munich, Germany, 6/10-13/01, Transducer Research Foundation, Cleveland (2001), pp. 950-53.

4. J.A. Frank and A.P. Pisano, "Low-Leakage Micro Gate Valves", *Technical Digest of TRANSDUCERS '03*, Boston, MA, 6/8-12/03, Transducer Research Foundation, Cleveland (2003), pp. 143-46.

5. S. Zimmermann, J.A. Frank, D. Liepmann, and A.P. Pisano, "A Planar Micropump Utilizing Thermopneumatic Actuation and In-Plane Flap Valves", *Technical Digest MEMS 2004, 17th IEEE International Conference on Micro Electro Mechanical Systems*, Maastricht, The Netherlands, 01/25-29/04, IEEE (2004), pp. 462-65.

6. S. Zimmermann, D. Fienbork, B. Stoeber, A.W. Flounders, D. Liepmann, "A Microneedle-Based Continous Glucose Monitor: Fabricated on a Wafer-Level Using In-Device Enzyme Immobilization", *Technical Digest of TRANSDUCERS '03*, Boston, MA, 6/8-12/03, Transducer Research Foundation, Cleveland (2003), pp. 99-102.

7. J. Qiu, J.H. Lang, A.H. Slocum, "A Centrally-Clamped Parallel-Beam Bistable MEMS Mechanism", *Technical Digest MEMS 2001, 14th IEEE International Conference on Micro Electro Mechanical Systems,* Interlaken, Switzerland, 1/21-25/01, IEEE (2001), pp. 353-5.

A PIEZOELECTRIC LIQUID-COMPATIBLE MICROVALVE FOR INTERGRATED MICROPROPULSION

Choonsup Lee and Eui-Hyeok (EH) Yang
MEMS Technology Group, NASA Jet Propulsion Laboratory, California Institute of Technology
4800 Oak Grove Dr., Pasadena, CA 91109
Phone: 818-393-7140, Fax: 818-393-6047, E-mail: Choonsup.Lee@jpl.nasa.gov

ABSTRACT

A leak-tight, low-power, liquid-compatible, piezoelectric microvalve has been designed, fabricated, and fully characterized. The measured leak rate of the microvalve for Helium gas is 3 x 10^{-6} scc/sec. The measured forward flow rate using deionized (DI) water is approximately 64 mg/min at 20 psi with the applied voltage of 50V. The resonance frequency of the microvalve is about 11.1 kHz. The measured dynamic power consumption of the microvalve is approximately 60 mW at 50Hz. The measured static power consumption is approximately 2.5 mW at 20V. The microvalve is designed for proportional flow control of liquid propellant for integrated micropropulsion.

INTRODUCTION

Micro/nano spacecraft concepts are of great interest in the aerospace community [1]. Reduction in the mass and size of a space instrument or subsystem results in a nearly exponential savings in launch costs as well as a significant increase in mission duration. In order to enable the construction of such 'microspacecraft', each subsystem will also have to be reduced in size and adapted in function to fit within the spacecraft size and mass envelope, and thereby require extensive miniaturization. Furthermore, thrust levels and impulse bits will have to be reduced in magnitude. The reduction in thrust levels and impulse bits requires fine control of very low propellant flow rates. Microvalves are therefore needed to control such propellant flow.

The authors' group has already demonstrated gas-compatible microvalves for Xenon Electric Propulsion [2]. Recently, JPL has initiated the development of 1-kg-class microspacecraft test-beds, requiring leak-tight, liquid-compatible microvalves, capable of providing precisely controlled, low propellant flow from a liquid propellant tank. Due to the limited resources of propellant and power, such a microvalve must exhibit leak-tight and low power operation (See Table 1). Previously reported liquid-compatible microvalves using electromagnetic and thermal actuators have high power consumption and/or slow actuation [3, 4], both of which are unacceptable for micropropulsion applications. Other liquid-compatible microvalves using either electrostatic or piezoelectric actuators do not meet the demanding requirements of low leak rate or large pressure ranges [5, 6]. Therefore, in this paper, we present the results of development of our leak-tight, low-power, fast-actuation microvalve for proportional flow control of liquid propellant.

Table 1. Microvalve specifications for controlling NASA's 1-kg-class microspacecraft propulsion.

	Generic microvalve requirements
Propellant type	Liquid
Inlet Pressure	~ 50 psi
Leak Rate	< 5 x 10^{-5} scc/sec (helium)
Response Time	< 0.1 msec
Power consumption	< 4 mW

DESIGN OF MICROVALVE

Our microvalve is actuated using a custom-designed piezoelectric stack actuator, which is bonded onto silicon-based components consisting of a valve seat, a lower boss, and an upper boss, as shown in Figure 1. The piezoelectric actuator consists of two active zones surrounding a central inactive zone. Active zones expand vertically as a voltage is applied to the piezoelectric stack. Unlike in our previous microvalve design for high-pressure Xenon Electric Propulsion [2], the microvalve reported in this paper has a silicon membrane called the upper-boss, for isolating the piezoelectric actuator from the liquid propellant. Because the liquid propellant remains inside the silicon chamber, it does not cause electrical shorting within the piezoelectric actuator. The upper boss layer is compression bonded to the lower boss using Au bonding metallization. The bonded boss stack is subsequently bonded to the valve seat. Finally, the custom-designed piezoelectric actuator is epoxy bonded to the top of the upper boss layer.

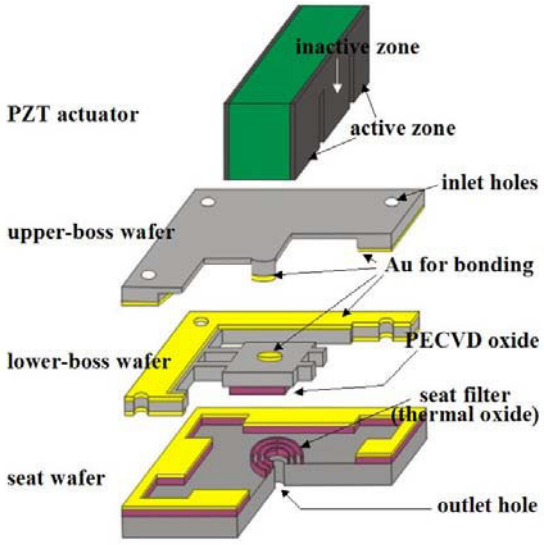

Figure 1. *Structure of the liquid microvalve. All silicon components are metal-to-metal compression bonded and the custom-designed piezoelectric stack is bonded on top of the upper-boss wafer.*

0-9640024-5-0/hh2004/$20©2004TRF
DOI 10.31438/trf.hh2004.44

Solid-State Sensors, Actuators, and Microsystems Workshop
Hilton Head Island, South Carolina, June 6-10, 2004

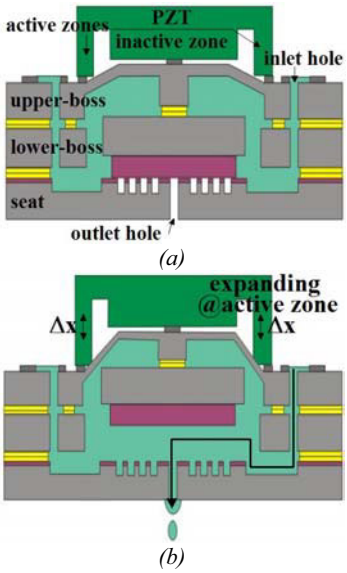

Figure 2. *Operating principle of the microvalve. (a) normally-closed "off" state (b) actuated "on" state:*

Figure 2 shows the microvalve operation principle. The microvalve is the normally closed ("off" state), as shown in Figure 2 (a). The normally closed condition is achieved by applying an initial seating pressure on the valve seat during the bonding of the piezoelectric actuator to the silicon assembly [2]. Application of a voltage to the piezoelectric actuator makes the active zones of the piezoelectric actuator expand vertically, lifting up the lower-boss center plate from the valve seat, as shown in Figure 2(b). This raising action opens up a flow path between the inlet and outlet holes. Proportional flow control of the fluid is achieved by controlling the upward displacement of the piezoelectric actuator by changing the applied voltage.

FABRICATION

The "knife-edge" seat rings are formed on the valve seat by patterning and etching a thermal oxide film using 10:1 Buffered Oxide Etchant (BOE). Subsequently, the wafer is etched using a deep reactive ion etcher (DRIE). Following DRIE, a Cr/Pt/Au film is deposited on the oxide film and patterned using a lift-off process. This metallization is used for the Au-Au compression bonding. Following the metallization step, a central outlet hole is formed using DRIE. On the lower boss plate, a 2-*μm-thick* Plasma Enhanced Chemical Vapor Deposition (PECVD) silicon dioxide is deposited and patterned. As in the previous case a Au-Au compression bonding metallization consisting of Cr/Pt/Au sandwiched layers are formed on both sides of the wafer. A final DRIE process is performed for defining the tether and the center plate. On the upper boss plate, the thin membrane is defined using DRIE, followed by the deposition and patterning of the Cr/Pt/Au bonding layer. Four inlet holes are formed subsequently in each corner of the boss plate using DRIE. Scanning Electron Microscope (SEM) images of the microfabricated silicon components are shown in Figure 3. In Figure 3, the valve seat has an outlet hole, concentric "knife-edge" rings (which also act as a particle filter) and the Au bonding metallization. On the upper boss plate, there are 4 inlet holes, a thin membrane, and the Au bonding metallization. On the lower boss plate, the tether, center plate, inlet holes, and the Au bonding metallization are seen.

Figure 4 shows the fully assembled and packaged microvalve. The inlet gas tube is connected to the inlet hole in the upper boss plate. Also seen are the wires for applying voltage to the piezoelectric actuator and the outlet hole in the seat wafer. The outlet hole diameter is about 200 *μm*.

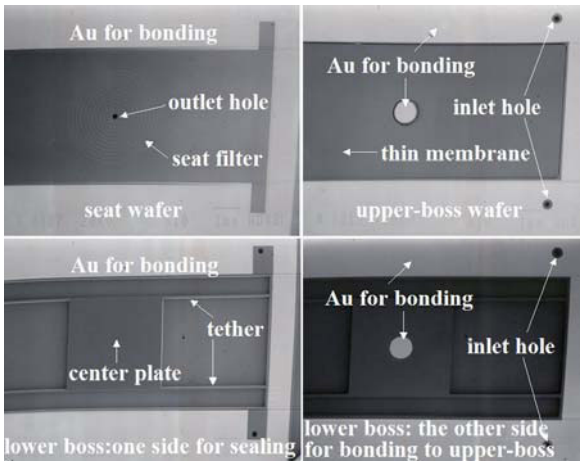

Figure 3. *SEM images of the (a) valve seat, (b) upper boss plate, and (c) valve sealing surface of the lower boss plate and (d) upper boss bonding side of the lower boss plate.*

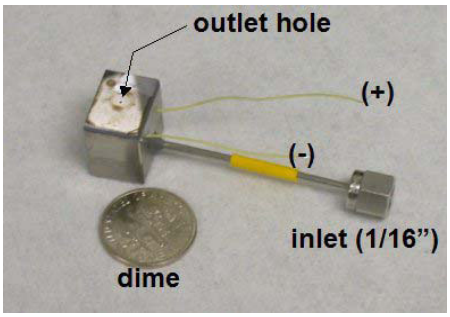

Figure 4. *Fully assembled and packaged microvalve.*

MEASUREMENTS

We measured the stroke of the piezoelectric actuator before and after bonding to silicon components. As shown in Figure 5, there is negligible difference in stroke between the two conditions. This implies that the piezoelectric actuator essentially exerts a very high seating force and can provide robust on-off operation for the microvalve. The blocking force of the stacked multi-layer piezoelectric actuator used in the microvalve is estimated at approximately 1000 N. The measured deflection of the piezoelectric actuator is about 4 *μm* and – 1*μm* respectively at the applied voltages of 50 V and – 10 V.

Leak rate (off state) and flow rate (on state) testing of the packaged microvalves were conducted using both Helium-gas and DI water. The flow test block diagram is shown in Figure 6. Flow rate was measured using an external Mass Flow Meter (MFM) with a measurement resolution of approximately 1.0 x 10^{-2} scc/s.

Helium leak rates were measured using a Helium leak detector. The measured leak rates ranged from 3 x 10^{-6} scc/sec to 4 x 10^{-5} scc/sec at an inlet pressure of 50 psi, as shown in Figure 7. We believe that the low leak rates are attributable to the combination of the smooth hard-seat surfaces (RMS surface roughness is 0.3 nm) and the pre-loaded seating configuration [2].

The measured forward flow rates at various inlet pressures for deionized (DI) water are shown in Figure 8. As the voltage applied to the piezoelectric actuator increases, the vertical deflection increases, increasing the flow of the DI water. The measured flow rate is approximately 60 mg/min at an inlet pressure of 20 psi (for an applied voltage of 40V).

As shown in Figure 9, we measured the DI water flow rate versus the various duty ratios of the pulsed voltage signal for different inlet pressures. The measured dynamic flow rate is 30 mg/min at 90% pulse width for a 15 psi inlet pressure.

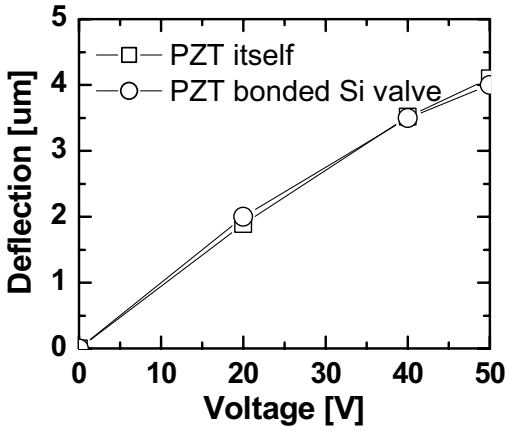

Figure 5. *PZT actuator vertical displacement vs. applied voltage in the unbonded and bonded states.*

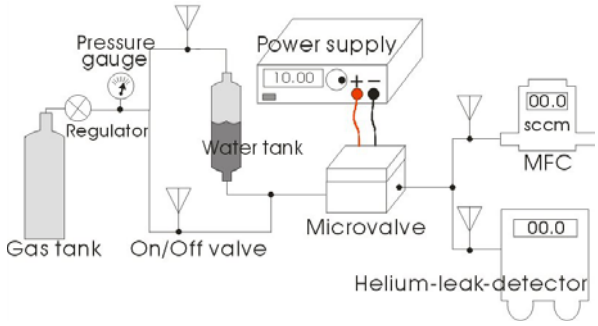

Figure 6. *Schematic diagram showing the microvalve test setup.*

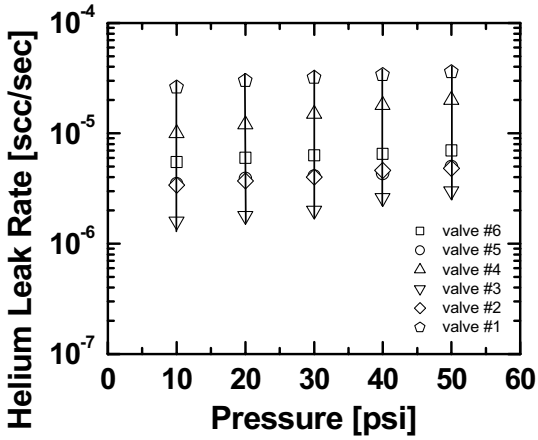

Figure 7. *Measured leak rates for six normally-closed (non-actuated) microvalves.*

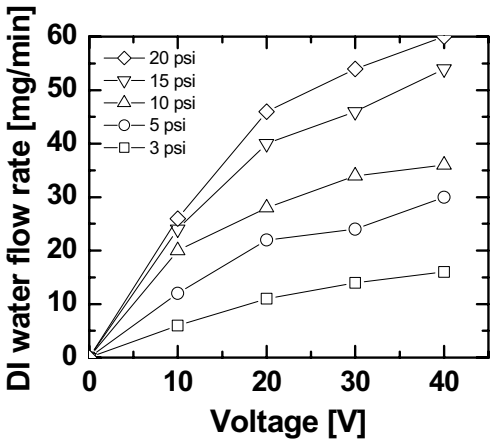

Figure 8. *Measured flow rates for an actuated microvalve at various inlet pressures.*

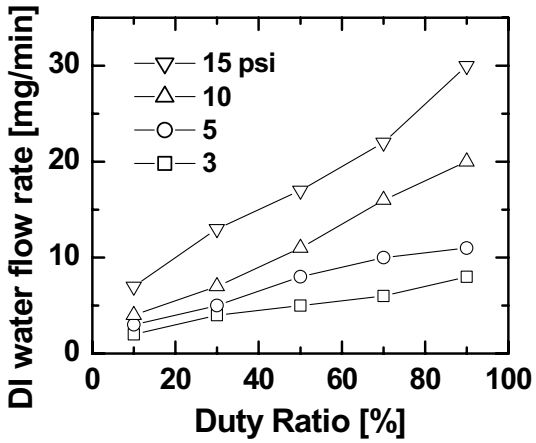

Figure 9. *Measured flow rates for a microvalve actuated with voltage pulses with varying duty ratios for various inlet pressures. (An 18 V square pulse was applied)*

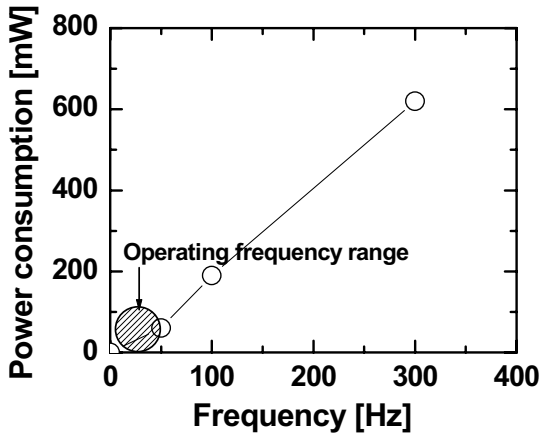

Figure 10. *Power consumption versus operating frequency for a microvalve operated with 10 V_{p-p} sinusoidal signals.*

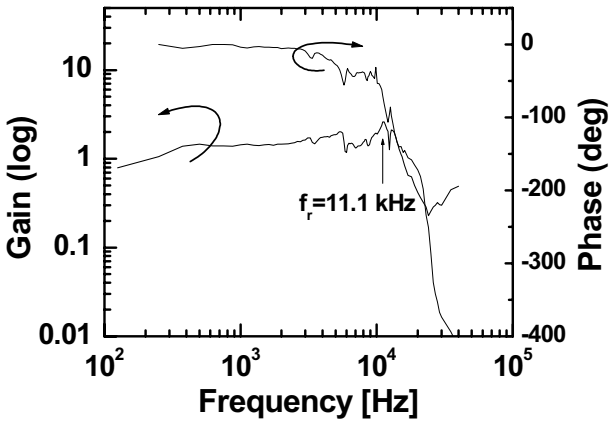

Figure 11. *Measured frequency response of the microvalve. The estimated transient response time is about 30 μs.*

The measured static power consumption is primarily due to the leakage current in the piezoelectric actuator and was measured at 2.5 mW at 20 V. The dynamic power consumption was measured by taking the phase delay into account. Figure 10 shows the dynamic power consumption measurement results. For instance, the dynamic power consumption is about 60 mW for 10 V_{p-p}, 50 Hz actuation. This value is very low compared to the power consumed by either thermally-actuated or magnetically-actuated microvalves. This power consumption is further reduced to a few milli watts when the microvalve is operated in a static proportional flow control mode.

We have also measured the resonance frequency of the piezoelectric actuator bonded to silicon microvalve using a laser doppler vibrometer, as shown in Figure 11. The measured valve is about 11.1 kHz, which shows that the microvalve is capable of fast transient response.

CONCLUSIONS

We have successfully demonstrated piezoelectrically-actuated liquid-compatible silicon microvalves. The measured leak rate of a microvalve using Helium gas is 3 x 10^{-6} scc/sec. The measured static power consumption is approximately 2.5 mW at 20V. The measured dynamic power consumption of the microvalve is approximately 60 mW at 50Hz. The microvalve is capable of proportional flow control of liquid propellant for integrated micropropulsion applications.

ACKNOWLEDGEMENTS

The research described in this paper was performed by the Jet Propulsion Laboratory (JPL), California Institute of Technology under a contract with the National Aeronautics and Space Administration. The authors would like to thank Dr. Thomas George for technical discussions and for reviewing the paper, Mr. Larry Wild for the valve assembly, and Mr. David Bame for the help in the flow test. Travel support has been generously provided by the Transducers Research Foundation and by the DARPA MEMS and DARPA BioFlips programs.

REFERENCES

1. J. Mueller, “A Review and Applicability Assessment of MEMS-Based Microvalve Technologies for Microspacecraft Propulsion”, *Micropropulsion for Small Spacecraft*, Progress in Astronautics and Aeronautics, Vol. 187, edited by Micci, M. and Ketsdever, A., AIAA , Reston, VA, 2000, Chap. 19.

2. E.H. Yang, Choonsup Lee, J. Mueller, "Normally-Closed, Leak-Tight Piezoelectric Microvalve with Ultra-High Pressure Upstream Flow Control for Integrated Micropropulsion," *IEEE MEMS Conference*, Jan. 2003, pp. 80-83.

3. Capanu, M., Boyd, J.G,, and Hesketh, P.J., "Design, Fabrication, and Testing of a Bistable Electromagnetically Actuated Microvalve," *IEEE/ASME Journal of MEMS*, vol. 9, Jun 2000, pp. 181-189.

4. Kawada, H., Yoshida, H., Kamakura, M., Yoshida, K., Saitou, M., Kawahito, K., and Tomonari, S., "Thermally Driven Microactuator Containing Thermal Isolation Structure with Polyimide and It’s applications to Microvalve," *Transducer’03,* 2003, pp. 1935-1938.

5. S. Messner, J. Schaible, J. Vollmer, H. Sandmaier, and R. Zengerle, "Electrostatic Driven 3-Way Silicon Microvalve for Pneumatic Applications," *IEEE MEMS Conference*, Jan. 2003, pp. 88-91.

6. S. Kluge,G. Neumayer, U. Schaber, M. Wackerle, M. Maichl, P. Post, M. Weinmann, and R. Wanner, "Pneumatic Silicon Microvalves with Piezoelectric Actuation," *Transducers’01*, 2002, pp. 924-927.

GEOMETRIC SURFACE MODIFICATION OF NOZZLES FOR COMPLETE TRANSFER OF LIQUID DROPS

Ui-Chong Yi and Chang-Jin "CJ" Kim
Mechanical and Aerospace Engineering Dept., University of California, Los Angeles (UCLA)
Los Angeles, California 90095

ABSTRACT

We report a new and unique way of promoting the complete transfer of discrete liquid drops from a nozzle to printing surfaces when the transfer (i.e., printing) is made by the wettability differences between two surfaces as used in soft printing devices reported previously. Hypothesizing that the complete transfer of droplets can be promoted by reducing the surface energy at the nozzle surface, we propose a new nozzle design with serrated circumference. By geometrically limiting the liquid-solid contact area on the nozzle surface, the effective energy holding droplets back can be reduced. Tests of droplet transfers (~1 μl in volume) from hydrophobic nozzles (~500 μm in diameter) to hydrophilic printing surfaces (e.g., glass surfaces) confirm that the residual droplets can be eliminated and perfect transfer can be accomplished when the nozzles are made serrated.

INTRODUCTION

Printing microscopic liquid droplets onto solid surfaces has become an important scientific/engineering issue in recent years, in demand by such major areas as inkjet printing and DNA/protein microarrays. For microarrays, the amounts of target molecules are determined by the droplet volumes printed on each spot; the variations in the droplet volume would cause an error in the detection of genes or gene expressions. The printing of droplets with consistent volume is an important issue.

Soft printing (i.e., droplet transfer through liquid-solid contact only) has been developed to avoid the tip deformation in pin-based printing and splashing in inkjet-based printing **[1]**. It is worth noting that the concept of soft printing assumes liquid is available as discrete droplets prior to printing by such mechanism as electrowetting on dielectric (EWOD). While consistent volumes of droplets were generated in the printhead, this consistency was found lost after printing, unfortunately, because each printing action leaves a small residual volume behind at the nozzle **[1]**. It is the main goal of this paper to eliminate the residual droplets and restore the volume consistency of the printed droplets.

By promoting complete transfers of discrete drops without residuals on nozzles, different samples can be printed through one nozzle, enabling a flexible and compact system. It also speeds up the printing processes by minimizing the cleaning steps typically employed to avoid cross contamination among printed spots. Further, the concept has possible applications to other areas such as inkjet printings (for elimination of satellite droplets) and DNA solid pin "Replicator" (for reducing the need for cleaning). As droplet-based microfluidics become widely accepted, the complete transfer of liquid droplets will play an important role.

We developed a simple and effective method for the complete transfers of liquid droplets from a printhead to the printing surfaces by micro-engineering the inside circumference of the nozzle (Figure 1) based on the concept of minimizing effective surface energy **[2, 3]**. By generating artificial roughness on hydrophobic surfaces, the effective liquid-solid surface energy can be reduced far beyond the intrinsic material property allowing a dramatic drag reduction (> 95%) for moving droplets inside a channel **[3]**. We apply a similar idea to the transfer of droplets from printheads to print surfaces by soft printing. Soft printing uses hydrophobic printheads and hydrophilic printing surfaces (e.g., glass plate) so that the droplets favor the printing surfaces when they are pulled apart after the soft contact. By reducing the effective energy on the nozzle circumference with serrated structures thus minimizing the pull back of the printhead during soft printing, we promote a complete transfer with no new cost.

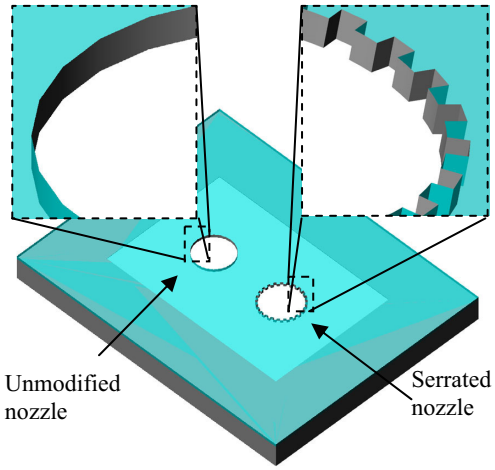

Figure 1. *Unmodified and serrated nozzles*

THEORY

Figure 2 illustrates an analytical model for droplet separation during transfer. The figure only illustrates the printing steps after soft contact between liquid from the nozzle and the top hydrophilic printing surface for simplicity. Chadov *et al.* **[4]** had performed a similar analysis to study

Travel support has been generously provided by the Transducers Research Foundation and by the DARPA BioFlips programs

droplet behaviors during the transfer between two solid surfaces. In the study, he predicted the volume ratio of separated drops based on droplet volumes and surface properties.

Once the contact between the liquid and the plate is made, the hydrophilic top plate moves away from the hydrophobic nozzle, and the droplet necking occurs to preserve the volume of the droplet. Contact angle θ measured from the side surface of the nozzle to the liquid meniscus must be reduced simultaneously as seen in figure 2. As the necking progresses, the air-liquid interfaces at that region finally meet at the center, separating the liquid into two drops at a corresponding separation contact angle θ_{sep}.

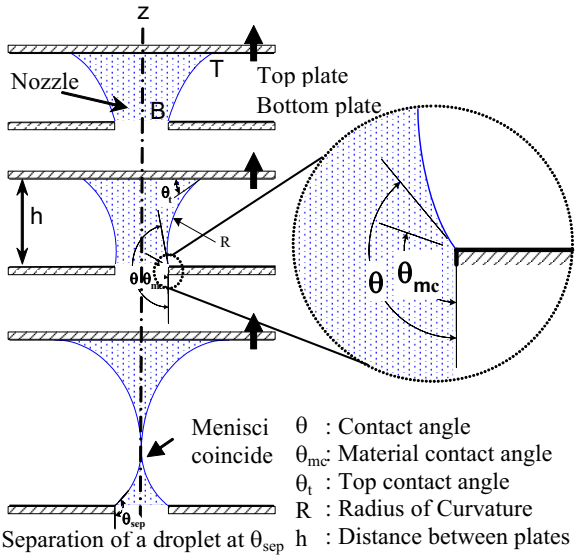

Figure 2. *Analytical model for separation during transfer*

Assuming the droplet shape is approximately formed by the rotation of the circular arc *TB* with radius of curvature *R* around the *z* axis, the separation can be predicted by calculating θ_{sep} for a given drop volume and surface properties of the nozzle and the printing plate as well as dimensions. The calculated separation angles of droplets are plotted against droplet volumes normalized with the nozzle radius in figure 3. For the calculation of separation contact angles, the droplet volume was assumed to be constant, and no effect of contact angle hysteresis was considered.

For a liquid drop to be separated into two smaller drops, contact angle θ must reach the value of the separation contact angle θ_{sep}. However, the contact angle can not be reduced beyond the value of the intrinsic material contact angle θ_{mc} of the nozzle side surface. If θ_{sep} is smaller than the value of θ_{mc} for a given volume of liquid and surfaces, the top plate will continue to pull the liquid without separation until the transfer is complete. By increasing the material contact angle θ_{mc} (i.e., minimizing effective surface energy) through geometrically modifying the surface as shown in figure 1, we propose complete transfers of droplets can be achieved. A droplet on a nozzle (i.e., normalized volume $V^* = 64$) would be separated into two drops with θ_{mc} less than θ_{sep} (= 133°) for the given volume (Figure 3). For example, a 1 µl droplet on a nozzle with 500 µm in diameter would be separated when printed through a regular (i.e., unmodified) nozzle coated with Cytop® (θ_{mc} = 105°). However, if the surface contact angle is increased to over 133°, the drop will be transferred to the top plate without any residual drop on the nozzle side.

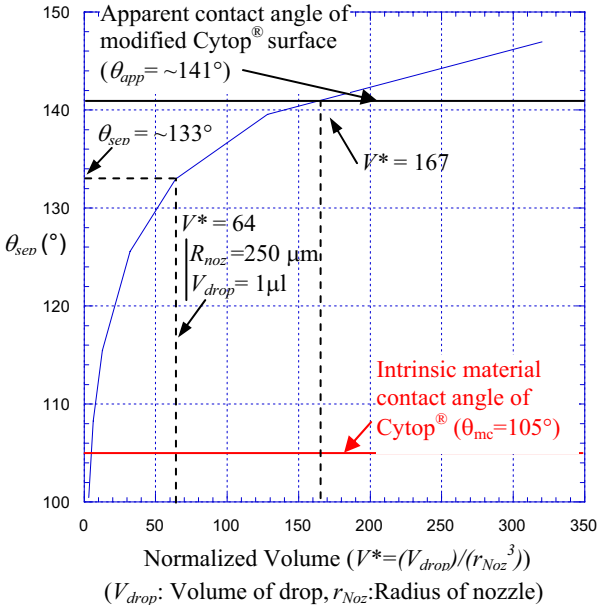

Figure 3. *Angle of separation with contact angle of intrinsic and modified surface of Cytop®*

The apparent contact angle on a roughened surface is expressed by Cassie's equation [5]

$$\cos\theta_{app} = f_1 \cdot \cos\theta_{mc} - f_2 \qquad (1)$$

where $\cos\theta_{app}$ is the apparent contact angle on the modified surface and $\cos\theta_{mc}$ is the intrinsic material contact angle. f_1 and f_2 are the area fractions of liquid-solid and liquid-air contacts. As can be seen from the equation, the reduction in f_1 leads to the increase in the surface contact angle and can be used for promoting complete liquid transfers.

DESIGN AND FABRICATION

The samples are designed (Figure 4) and fabricated through micromachining based on the calculations from the above criteria. Three degrees of nozzle modifications are included with size variations in serrated structures to evaluate the performance. For the variations in structures, the lengths of the liquid-solid contact area (i.e., *f1* in figure 4) are designed to be 2 µm, 5 µm, and 16 µm to test size effect on liquid transfers. Unmodified, 1/4 serrated, 1/2 serrated, and fully serrated nozzles are designed to determine the minimum modification required to promote the complete transfers. In all the designs, the size of the nozzle is set to be 500 µm in diameter and the area reduction of the solid-liquid area is about 70 % compared with the unmodified surface. 70 % reduction in solid-liquid contact

area results in the increase of the contact angle of hydrophobic side surface of the nozzle (i.e., Cytop®-coated surface) to θ_{app} of ~141° from θ_{mc} of ~105° according to equation 1. With the increased θ_{app}, a droplet with $V^* <$ ~167 would completely transfer to the printing surface, according to the criteria. The results of the calculations for the designs are co-plotted in figure 3 with separation contact angles.

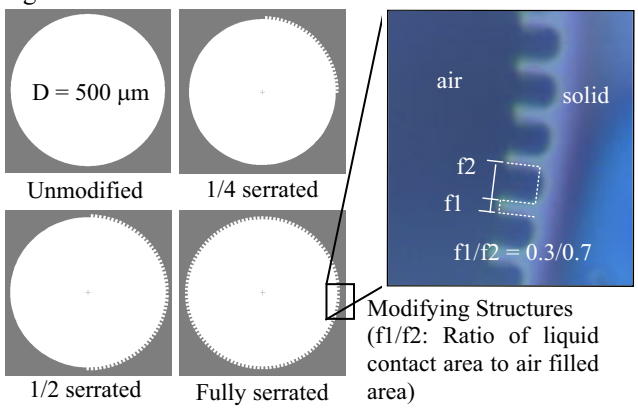

Figure 4. *Four types of nozzles (different degrees of modification around nozzle) and fabricated serrated structures*

Figure 5 illustrates the schematic cross-sectional view of a fabricated testing device, micromachined from a 100 µm-thick silicon wafer. The wafer was deposited with thermal silicon dioxide (SiO_2) and LPCVD silicon nitride (Si_3N_4) layers to be used as protection layers against KOH etching. A 2 µm-thick low stress nitride (LSN) layer was deposited on the top side as a structural top layer. The top and bottom side of the wafer are then etched by RIE to form nozzles. The top side LSN layer was carefully patterned to form nozzles with their corresponding serrated circumferences. The bottom side SiO_2 and Si_3N_4 layers were also patterned to form the LSN membranes later. The patterned wafer went through KOH silicon etching step to form LSN membrane, which works as a structural transparent top layer. The device was then spin coated with ample amounts of Cytop® solution, which was chosen for its better wetting property on nitride surface over Teflon®. A bottom glass plate is also coated with Cytop® to be used as a bottom channel surface.

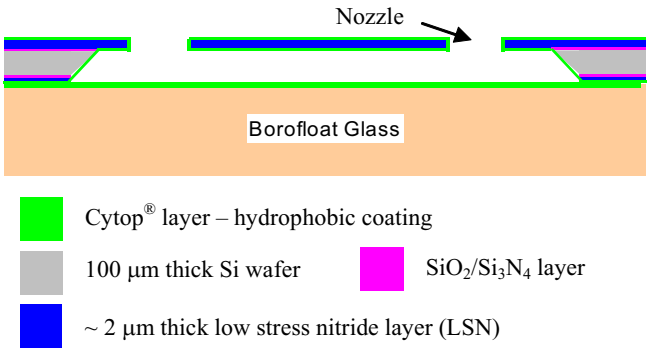

Figure 5. *Cross section view of micromachined printhead test device*

TESTS AND RESULTS

The procedures for testing are illustrated in Figure 6. A small volume (~1 µl) of liquid is pipetted on a Cytop®-coated glass substrate surface, the LSN membrane plate is placed over it and manually pushed down to have the droplet bulge up through the nozzle. The top membrane plate and the bottom substrate plate are then temporarily bonded with 3M® double-stick tapes during the remaining printing test steps. A glass printing plate is then lowered to make the soft contact with the liquid and then moved away, completing one printing cycle. A microscope was used for the visualization and recording of the test from the side.

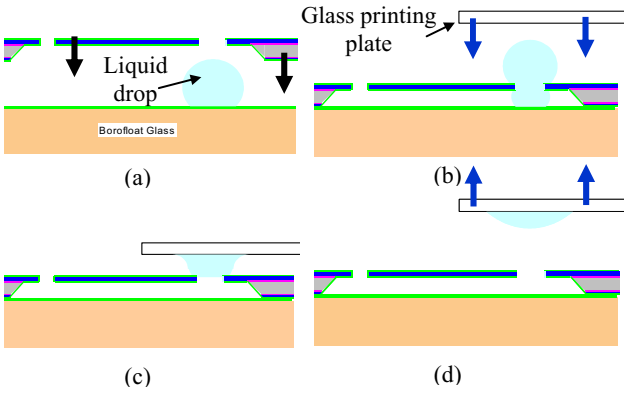

Figure 6. *Printing test. (a) Loading liquid and positioning the membrane plate down (b) Moving a glass plate down (c) Establishing liquid-solid contact (d) Pulling the glass plate away and completing the transfer*

Figure 7 illustrates the result of droplet transfer tests done with water. While the unmodified nozzle leaves residual water behind, all three types of serrated nozzles show complete transfers onto the glass plates. The

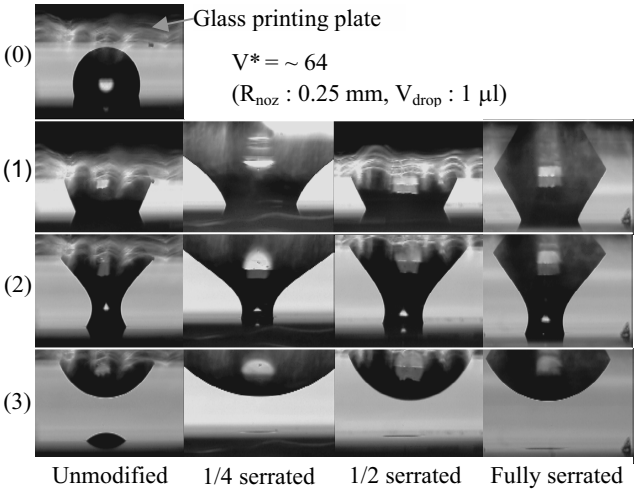

Figure 7. *Water printing tests with 4 different nozzle types (0) before contact (1) after initial contact (2) during top glass plate pulling away (3) after transfer of droplet*

normalized volumes of the droplets were attempted to be at 64 during the tests. The exact detaching moment could not be captured with our current camera (60 frames/sec.). We did not observe any apparent effect of the size variations for the transfers; nozzles with the same design with different dimensions of serrated structures showed the same results. We conclude that the ratio of solid-liquid contact area to liquid-air contact area is the dominant factor.

The nozzles were also tested with a DNA solution (Calf Thymus, 4 μg/ml) successfully (Figure 8). The test results verified that complete transfers are obtained if at least 1/2 of the nozzle circumference is modified, leaving rooms of success for even more challenging solutions with lower intrinsic material contact angles.

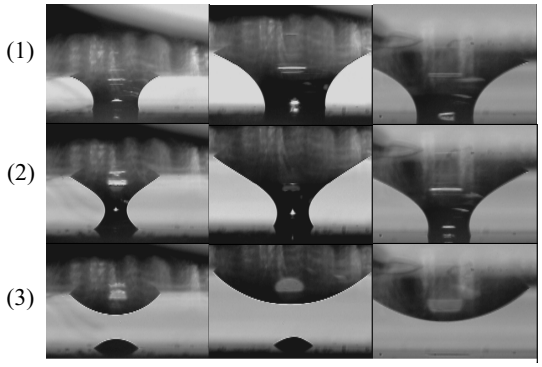

Figure 8. *DNA solution tests with 3 different nozzle types (1) after initial contact (2) during top glass plate pulling away (3) after transfer*

DISCUSSIONS AND FUTURE WORK

We have not performed any measurement or characterization on the sizes of printed spots since the proposed concept utilizes small discrete droplets readily available prior to actual transferring process. The consistency of the printed spots would be achieved if uniformly sized droplets are delivered to the nozzles and whole droplets are printed without residuals. As used in soft printing, EWOD is inherently capable of generating and transporting small and consistent discrete droplets and the proposed concept of serrated nozzles can be easily integrated with little difficulties. The characterization of the printed spots will be pursued in the future once an integrated device is available for testing.

During the transfer tests with diluted DNA solutions, we have observed that a higher degree of modification is needed to achieve the complete transfer compared with DI water. The need for more modification is suspected to be from the differences in solution properties, such as the contact angle. In our previous contact angle measurement of a diluted DNA solution on Cytop® coated surface, a ~ 5 to 10 ° lower contact angle was observed while the contact angle for DI water was ~ 105°. The properties of liquids to be printed are one of the major considerations for determining the design of nozzles and need to be studied further. More tests, including contact angle measurements and transferring tests, with various biological solutions will be performed in the future.

CONCLUSIONS

The concept of the complete transfer of a liquid droplet by modifying printing nozzles has been proposed and demonstrated with micromachined testing devices. The reduction of effective interfacial energy and its effect on promoting total transfers were analytically predicted and modeled as a function of the surface geometry and the contact angle for the design of nozzles. We have successfully verified the concept by demonstrating the total transfers of water and diluted DNA solution droplets onto the glass plates. We expect the technology to be useful for microfluidic printing systems, especially those employing small discrete droplets.

ACKNOWLEDGEMENTS

This work was supported by the National Science Foundation (NSF) “Engineering Microsystems: XYZ on a Chip” (CMS-99-80874) and NASA through the Instritue for Cell Mimetic Space Exploration (CMISE). The author would like to thank Dr. J.-Y. Yoon for the preparation of DNA solutions.

REFERENCES

1. U.-C. Yi and C.-J. Kim, “Soft Printing of Droplets Digitized by Electrowetting”, *Digest of Technical Papers of the Transducers 2003,* Boston, MA, 6/8-6/12, (2003) pp. 1239-1242.

2. D. Oner and T. J. McCarthy, “Ultrahydrophobic Surfaces. Effect of Topography Length Scales on Wettability”, *Langmuir, 16*, pp. 7777-7782 (2000).

3. J. Kim and C.-J Kim, “Nanostructured Surfaces for Dramatic Reduction of Flow Resistance in Droplet-based Microfluidics”, *Proceedings of the IEEE Conference on MEMS,* Las Vegas, NV, 1/20-1/24, (2002), pp. 479-482.

4. A. V. Chadov and E. D. Yakhnin, “Investigation of the Transfer of a Liquid from One Solid Surface to Another. I. slow Transfer, Method of Approximate Calculation”, *Kolloidnyi Zhurnal, 41, 4*, pp. 817-820 (1979).

5. A. W. Adamson, “Physical Chemistry of Surfaces, 5th edition”, John Wilely & Sons, Inc., New York, NY (1990), pp. 387-389.

A FULLY-INTEGRATED MULTI-SITE PRESSURE SENSOR FOR WIRELESS ARTERIAL FLOW CHARACTERIZATION

Andrew DeHennis and Kensall D. Wise
NSF Engineering Research Center for Wireless Integrated MicroSystems
Department of Electrical Engineering and Computer Science
The University of Michigan, Ann Arbor, MI 48109-2122
ph: (734) 615-7020; email: hde@umich.edu

ABSTRACT

This paper presents a fully-integrated battery-free sensing system that uses a two-site wireless pressure measurement for the detection of arterial stenosis. The remotely-powered system uses a backscatter-modulated passive-telemetry interface and transmits sensor as well as reference information to an external system. The monolithic process used to realize the system integrates a 3μm BiCMOS circuit with silicon-on-glass absolute pressure sensors and an on-chip antenna. The wireless sensor interface consumes 340μW and uses capacitance-to-frequency conversion for readout of the vacuum-sealed pressure transducers. The integrated device has a 200μm profile and a volume of 2mm^3. The system can sense a reduction in flow of 13%, which corresponds to a differential pressure of 3mmHg.

INTRODUCTION

Present stroke-prevention procedures utilize carotid artery angioplasty followed by stenting to minimize effects from plaque build-up and increase arterial flow. However, the implantation of stents can sometimes cause restenosis of the artery during the healing process. Currently, the diagnosis of restenosis requires catheterization. To replace this procedure, technology to implement sensors along with the stent itself is currently being pursued [**1**]. Implementing wireless sensors that can be deployed during the stenting procedure would allow transcutaneous querying of the effects of restenosis and potentially the ability to diagnose other concerns in the cardiovascular system. Implementation of this technology requires a batteryless low-profile, transduction system that can be remotely powered to take queried measurements. An illustration of such a system is shown in Figure 1.

Cardiologists primarily rely on the measurement of arterial blood flow when diagnosing patients. Acute measurement of blood flow can be performed through guide-wire tip instrumentation to either directly or indirectly measure the flow across an occlusion. One of the indirect methods of measuring flow is utilizing a multi-site pressure measurement system [**2, 3**]. The complex relationship between pressure and flow is a result of the non-newtonian fluidic properties of blood and the elastic arterial walls. However, models that are not based on finite element modeling of arterial flow still use the Navier-Stokes formulas to build an equivalent circuit model for the relationship. The Navier-Stokes formula defines the differential pressure to distance relationship as

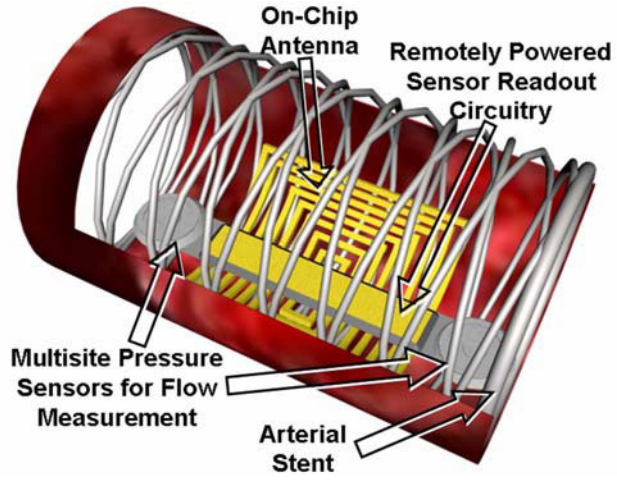

Figure 1. *Illustration of the implantable, wireless system embedded inside an arterial stent.*

$$-\frac{\Delta P}{\Delta x}=\left(\frac{8\eta}{\pi R_i^4}\right)Q+\frac{\rho}{\pi R_i^2}\frac{dQ}{dt} \qquad (1)$$

where Q is the flow rate, η is the viscosity, ρ is the density, and R_i is the lumen radius. The first term defines the situation for constant flow and the second term adds the effects from a time-varying flow rate, which is the case in cardiovascular applications. The implementation of differential pressure measurement in diagnosing the cardiovascular system is shown in Figure 2.

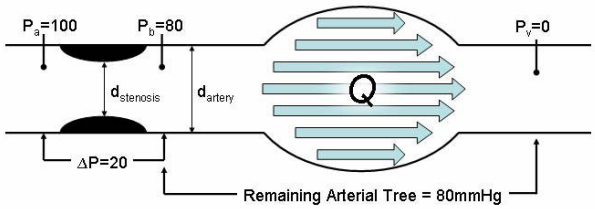

Figure 2. *Illustration of the multisite pressure measurement enabling monitoring for arterial restenosis.*

The narrowing of the artery from the build up of plaque between the two sensing sites causes a reduction of effective lumen radius from $d_{artery}/2$ to $d_{stenosis}/2$. As the narrowing progresses, a differential pressure measurement can be used to diagnose the percent stenosis of the artery defined by the ratio of $d_{stenosis}/d_{artery}$. The differential pressure through the narrowed section can also indirectly measure a reduction in arterial flow.

SYSTEM DESIGN

The system interface is based on backscatter-modulated passive telemetry. This wireless scheme allows an implanted system to function from transcutaneous power delivered by an external system. The coupling of the external and internal antennae provides not only the power transfer but also the ability to sense the load on the wireless subsystem through the carrier waveform. Backscatter modulation is implemented by actively

0-9640024-5-0/hh2004/$20©2004TRF
DOI 10.31438/trf.hh2004.46

loading the secondary system which creates an amplitude modulation (AM) of the carrier signal [**4**]. An overview of the coupled telemetry system is shown in Figure 3. The external system is composed of both a power amplifier, which generates the carrier waveform, and envelope detector, which implements AM

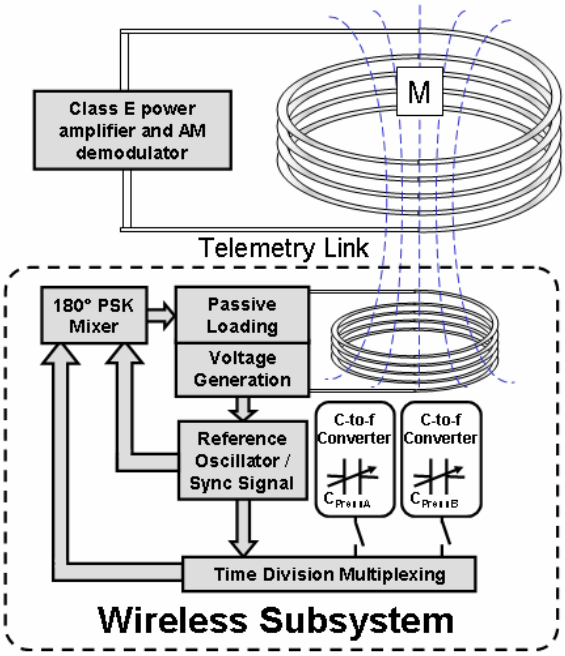

Figure 3. *Schematic of the wireless systems showing the loosely coupled transformer system as well as the block diagram for the wireless subsystem.*

demodulation of the carrier. The external system has been updated from previous systems that have implemented class E power amplifiers and AM envelope detectors that were developed for transcutaneous stimulation and RFID tags [**5, 6**]. The power amplifier operates with a resonant tank at 4MHz with a quality factor of 100, which balances the tradeoffs between power efficiency and signal recovery bandwidth that is inherent in using the same antenna to simultaneously transmit and receive signals. The demodulator has a passband and carrier suppression of 30dB between 1-30kHz and -15dB at 3MHz, respectfully.

The wireless subsystem is composed of three sections: the RF front-end for power recovery and passive loading, the transducers and their interface circuitry, and the sensor and reference multiplexing and mixing. The RF front-end implements a full-bridge, bipolar rectifier along with a shunting transistor for resistive loading of the front-end LC resonant tank that has been previously presented [**7**]. This system, however, integrates the antenna along with the circuitry and uses 0201 surface mount capacitors for the front-end LC tank and power regulator. This implementation minimizes the area needed for active circuitry and minimizes the profile of the system

The capacitive pressure transducers are formed using a bulk-micromachined diaphragm along with the silicon-on-glass dissolved wafer process and are designed for a target pressure range between 700-900mmHg [**8**]. The technique used for vacuum sealing of the absolute transducers implements a silicon-gold eutectic and anodic bonding [**9**]. The Si-Au eutectic enables reflow of a dry etched feedthrough tunnel which is sealed during the anodic bonding process between the Si and glass substrates.

The sensor interface utilizes a capacitive-to-frequency converter implemented using a relaxation oscillator that is based on an oscillator implemented by Song, *et al.* [**10**]. Figure 4 shows the schematic of the relaxation oscillator along with the V_t current source and SR flip-flop digitizer. With the frequency of the oscillator proportional to both the bias current and the sensor capacitance, the current sources can be designed to obtain the desired frequency range for the base capacitance of each sensor.

An on-chip reference oscillator is also implemented using

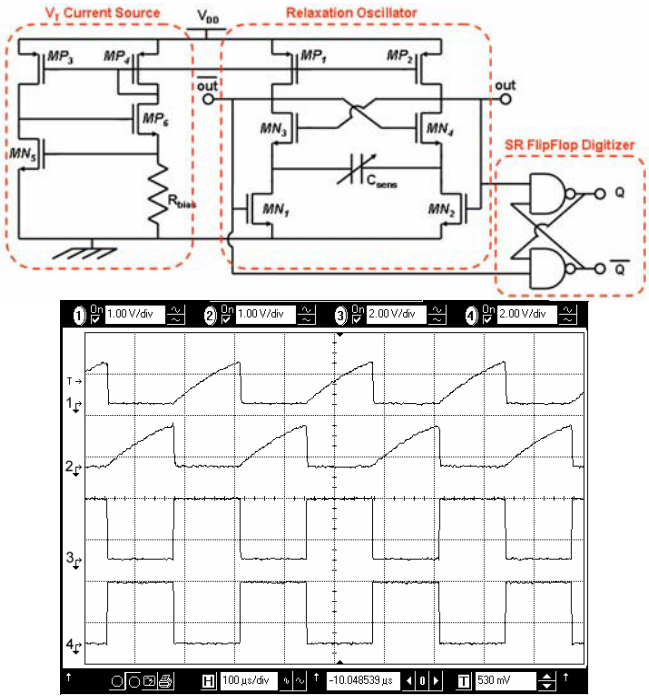

Figure 4. *(upper) Schematic of the capacitance-to-frequency conversion circuitry. (lower) Oscilloscope measurement of the branches of the relaxation oscillator, (traces 1 and 2) and its digitized output (traces 3 and 4).*

the same relaxation oscillator along with integrated poly-to-poly capacitors. This reference oscillator not only provides the ability to query the regulated power of the wireless device, but also the on-chip clock to control the multiplexing between the two transducers. Since backscatter modulation provides only a serial data stream between the two systems, a frequency mixer that combines the frequency content from the two sensors and the reference oscillator has been implemented. Figure 5 shows the block diagram of the mixer that time division multiplexes the two-sensor interface oscillators and mixes in the reference oscillator frequency through phase-shift-keying (PSK) as well as the waveforms measured on the probe station before deposition of the antenna and anodic bonding of the sensors. The PSK modulated signal is then used to load the carrier signal. The amplitude modulation frequency then corresponds directly to the frequency information from the PSK signal, which contains the reference and

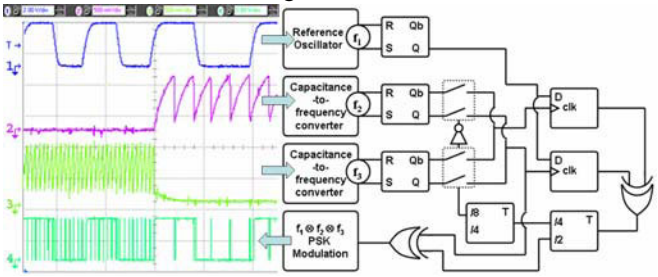

Figure 5. *Schematic of the time-division multiplexed, phase shift keyed (PSK) frequency synthesizer along with oscilloscope waveforms.*

transducer information.

INTEGRATED FABRICATION PROCESS

The fabrication process for this system combines previous work that integrated boron diffused pressure sensors along with a 3µm BiCMOS process [**11**] with the combination anodic-eutectic bonding used to seal the cavity [**9**]. The fabrication steps are implemented in 22 masks with 8 masks for the transducer and 14 for the antenna and circuitry. A final cross section of this process is shown in Figure 6. Photographs of the monolithic device are

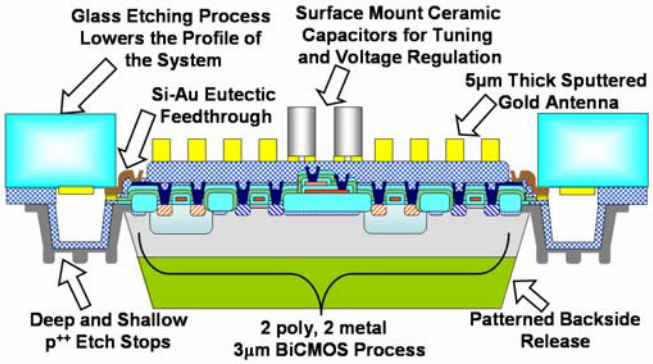

Figure 6. *Cross section of the device showing the integration of the 3µm BiCMOS process with the silicon-on-glass dissolved wafer process and an on-chip antenna.*

shown in Figure 7. The on-chip antenna is realized in a 5µm thick gold layer that overlaps the circuit area and extends to form wings that will wrap around the surface of the artery or stent. Gold was used as the antenna material due to its high level of malleability to enable the curvature of the wings. The sensors are formed using consecutive deep and shallow boron diffusion after the p-well is implanted and the recess areas are etched. The n-epi/p-well CMOS process builds-in isolated, npn-bipolar transistors which are used in the RF front-end of the system. Since bulk silicon is bonded to glass through 3000Å of oxide, the glass is recessed to accommodate the topology from the CMOS and antenna features. After bonding, the backside of the silicon is patterned and etched using a Deep Reactive Ion Etcher (DRIE). This etch thins the antenna wings and sensor areas to approximately 80µm so that the EDP release etch will not reach the circuit area before the sensors are defined and the wings are etched through to their underlying shallow boron diffusion.

After etching and metallization, the 500µm thick glass wafers are pre-diced to a depth of 4mils. Then, following the anodic bonding and DRIE etching of the silicon wafer, the backside of the glass is also diced along the same lines to a depth of 4mils. The two wafer stack is mounted in wax on the silicon side and the backside of the glass wafer is etched in 49% hydrofluoric acid until the backside dice lines meet the front. This process not only thins the glass to approximately 100µm, but also rounds the corners. This process is very sensitive to over etching since the HF will quickly undercut the wax and attack any exposed silicon after the glass punched through between the front side and back side dice lines. A cross-section and SEM shots of the glass thinning process are results are shown in Figure 8. The wafer is then removed from the wax mount and placed in EDP for release of the integrated devices. The only die level assembly needed for the system is the placement of the two surface-mount capacitors for power regulation and resonant tuning of the LC front-end. The devices are then encapsulated in parylene for electrical isolation during testing [**1**].

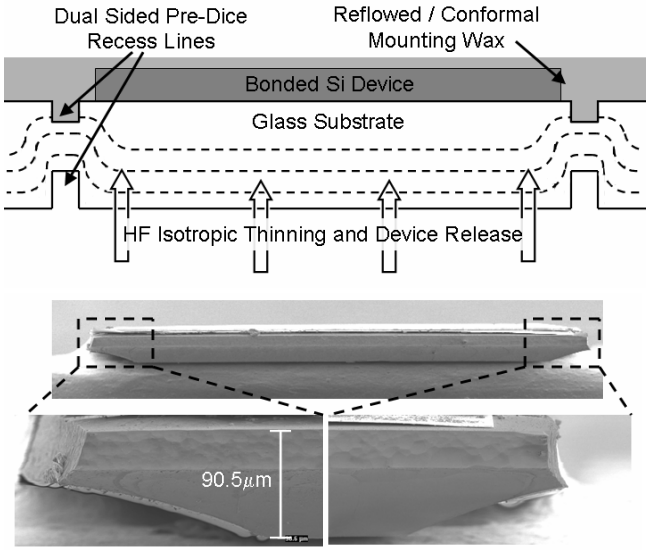

Figure 8. *Cross section (upper) and SEM images (lower) showing the glass thinning process that is used to reduce the vertical footprint of the wireless system.*

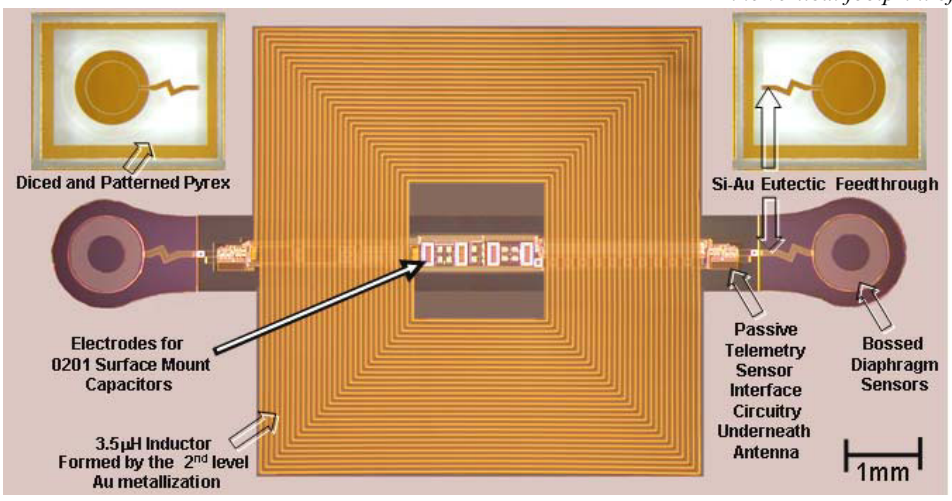

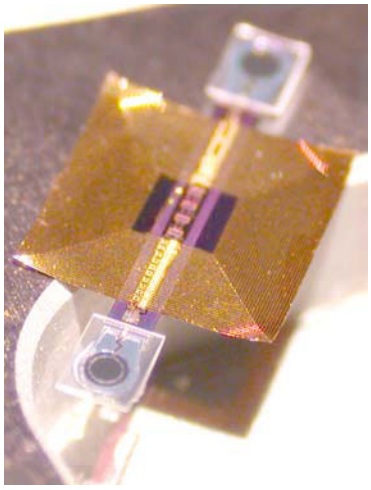

Figure 7. *(left) Die photograph of the device before bonding showing the pressure sensors, interface circuitry, on-chip antenna and corresponding patterned glass electrode used for each capacitive transducer. (right) Photograph of the released, wireless system.*

TEST RESULTS

The passive telemetry interface circuit has a power consumption of 340μW from a 3V supply. The capacitive pressure transducers have a sensitivity of 10fF/mmHg after the parylene deposition and the c-to-f converter shows a response of 750Hz/pF at 10kHz. Since analog frequency transmission is used for wireless readout, the resolution of the system is found through integration of the phase noise spectrum of the oscillator. This analysis finds a resolution of 25Hz at a 100Hz measurement bandwidth, which corresponds to a pressure resolution of 3mmHg.

The test setup used for flow characterization utilized a rigid, 6mm diameter piece of tubing and a voltage controlled gear pump to simulate flow within a stented carotid artery with deionized water. The wireless system is then remotely queried by the external system through the 1mm wall of the tube. Pressure versus flow characterization of the test setup found a transducer sensitivity of 43(ml/min)/mmHg. Due to the large radius, the pressure drop across the 1cm distance between the sensors is below the detection limit when no occlusion is present. The difference between the two sites based on the theory from Eqn (1)

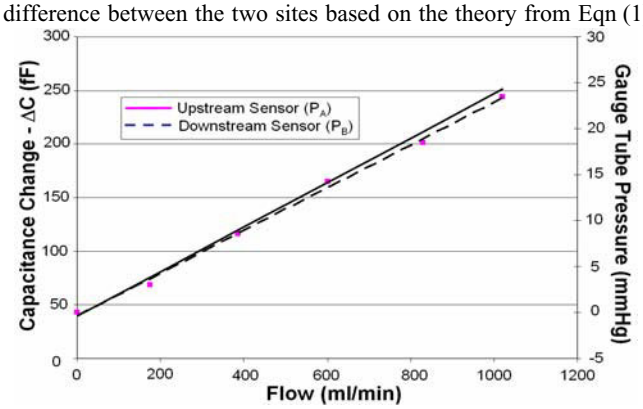

Figure 9. *Pressure versus flow rate characterization of the test setup using the wireless system.*

is a shown in Figure 9 along with the measured flow versus pressure results. In characterizing the system to sense the build up of plaque in an artery, the tube radius between the two sensing sites was reduced to restrict the flow and simulate the effects of arterial restenosis. The differential pressure measurements as the percent occlusion increases are shown in Figure 10 along with the theoretical results predicted from Eqn (1) as well as the corresponding reduction in flow. The measurements show that an occlusion of 60% can be sensed with this system which corresponds to a 13% reduction in arterial flow. This condition is similar to the qualifications for angioplasty intervention, which is

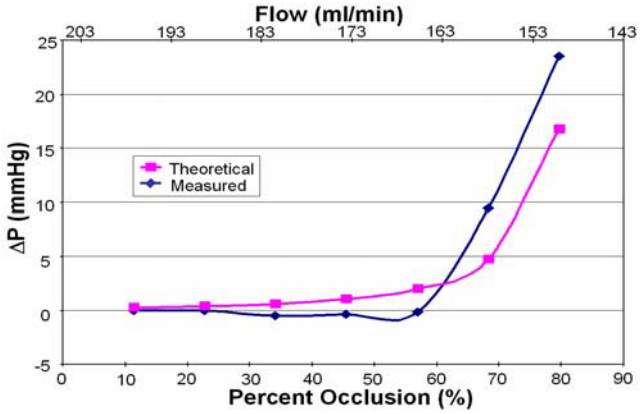

Figure 10. *Pressure versus flow rate characterization of the system as the tube becomes occluded.*

an occlusion of 50% for the carotid artery [**12**].

CONCLUSION

The realization of a wireless arterial flow characterization system has been presented. The system uses two capacitive pressure transducers to monitor for stenosed restriction in arterial flow. The capacitance-to-frequency sensor interface oscillator has a sensitivity of 750Hz/pF and a base oscillation frequency of 10kHz. A digital frequency synthesizer has been developed to provide asynchronous data transmission of the dual site pressure measurements, as well as, the reference signals through a backscattered modulation transmission scheme. The fabricated system has a volume of $2mm^3$ and can detect a 13% reduction in peak arterial flow.

ACKNOWLEDGMENTS

This work is supported by the Engineering Research Centers Program of the National Science Foundation under Award Number EEC-9986866 and by a gift from Ms. Polly Anderson. The authors would like to thank Mayurachat Gulari for assistance in the BiCMOS fabrication process. Travel support has been generously provided by the Transducers Research Foundation and by the DARPA MEMS and DARPA BioFlips programs.

REFERENCES

[1] K. Takahata, et al., "A wireless microsensor for monitoring flow and pressure in a blood vessel utilizing a dual-inductor antenna stent and two pressure sensors," MEMS '04, Maastricht, Netherlands, 2004.

[2] J. Ji, et al., "An ultraminiature CMOS pressure sensor for a multiplexed cardiovascular catheter," IEEE Transactions on Electron Devices, vol. 39, pp. 2260-2267, 1992.

[3] N. H. J. Pijls and B. De Bruyne, Coronary Pressure. Boston: Kluwer Academic Publishers, 1997.

[4] K. Finkenzeller, RFID Handbook. Chichester, England: John Wiley & Sons Ltd., 1999.

[5] T. Akin, "An integrated telemetric multichannel sieve electrode for nerve regeneration applications," in Electrical Engineering and Computer Science. Ann Arbor: University of Michigan, 1994.

[6] "MicroID 13.56MHz RFID System Design Guide," Microchip Technology Inc. 2001.

[7] A. DeHennis and K. D. Wise, "A passive-telemetry-based pressure sensing system," presented at Solid State Sensors and Actuators Workshop, Hilton Head, SC, 2002.

[8] A. V. Chavan and K. D. Wise, "Batch-processed vacuum-sealed capacitive pressure sensors," IEEE Journal of MicroElectroMechanical Systems, pp. 580-588, 2001.

[9] A. DeHennis and K. D. Wise, "An all-capacitive sensing chip for temperature, absolute pressure, and relative humidity," Transducers '03, Boston, MA, 2003.

[10] B. Song, H. Kim, Y. Choi, and W. Kim, "A 50% power reduction scheme for CMOS relaxation oscillator," presented at IEEE Asia-Pacific Conference on ASIC, Seoul, Korea, 1999.

[11] A. V. Chavan and K. D. Wise, "A monolithic fully-integrated vacuum-sealed CMOS pressure sensor," IEEE Transactions on Electron Devices, vol 49, pp. 164 - 169, Jan. 2002

[12] Y.-H. Tsai, et al.,"Angioplasty with stenting in treatment of carotid artery stenosis: report of a 3-year series," Chinese Journal of Radiology, vol. 28, pp. 361-366, 2003.

INTRACELLULAR NEURONAL RECORDING WITH FLEXIBLE MICRO-MACHINED PROBE IMPLANTS

Anupama V. Govindarajan[1], Tai C. Chen[1], Russell C. Wyeth[2], A. O. Dennis Willows[2] and Karl F. Böhringer[1]
[1]Department of Electrical Engineering, [2] Department of Zoology, University of Washington
Seattle Washington 98195

ABSTRACT

We present an implantable sub-micron silicon probe device, with flexible interconnects, that is capable of intracellular neuronal recording. The silicon probe device's ability to penetrate and record from neurons in an isolated brain of the sea slug *Tritonia diomedea* was tested, and we demonstrate that, for the first time, an implantable device can record intracellular action potentials from a single neuron (Pd5 of the *Tritonia* brain). Our group has focused on intracellular neuronal recording with stand-alone silicon needles in the past. In this paper we present the integration of the needle, using standard microfabrication techniques, with a flexible interconnect to an aluminum base pad where electrical connections to the device can be made. Intracellular signals provide detailed information about the functioning of single neurons by directly tracking the transmembrane voltage, as opposed to only recording the field potentials caused by large changes in the transmembrane voltage as is the case in extra-cellular recordings. We have found that the silicon probes (needles) have lower impedances than the Ag/AgCl glass capillary electrodes used conventionally for similar intracellular recording purposes. The success of this prototype is a major step toward self-contained, implantable devices suited for intracellular neuronal recording from freely behaving animals.

INTRODUCTION

MEMS devices are particularly promising as neuronal recording tools due to their small dimensions, compact geometry, and the ease with which multi electrode recording and integration with on-chip electronics can be performed. Recent research has successfully demonstrated electrical microprobes made from silicon that are suitable for neuronal recording [1]. These silicon microprobes with typical cross-sections of tens of micrometers can penetrate living tissue without causing significant trauma [1,2].

Many MEMS devices for extra-cellular neuronal recording have been presented [1-5]. However, to answer many interesting neurobiological questions, intracellular neuronal recordings are needed. Neurons process inputs and produce outputs through modulation of the transmembrane voltage. By directly measuring the DC state of the cell, intracellular recordings can provide detailed information about the functioning of single neurons and their synaptic interactions. In contrast, extracellular recordings, at best give only the timing of action potentials fired by a single neuron – a far more limited view of the neuron's activity.

Standard techniques for intracellular recording consist of glass capillaries and fine conducting wires. Pulled glass capillaries or micropipettes can be transformed into intracellular neuronal probes by filling them with an electrolyte and placing an Ag/AgCl electrode in the electrolyte. The glass walls provide ionic insulation and ensure low leakage current, while the tapered tip produced by pulling the capillary is small enough to penetrate neurons without damaging them. However these micropipettes have overall large dimensions and limited ability to integrate with components such as memory, amplifiers and power sources in a compact manner that will allow measurements from freely behaving animals [6]. Previous MEMS based approaches for intracellular neuronal recording using silicon probes used stand-alone needles, which are not suitable for implantation. [7].

In this paper we outline the significant changes to the process flow described in [6-8] that have enabled the integration of the high aspect ratio, sub-micron silicon probes to a larger silicon base bearing an aluminum pad for electrical connections (Fig. 1). The interconnecting scheme uses two polyimide layers to sandwich a metallic aluminum layer (Pi-Al-Pi interconnect). The metal layer forms the electrical connection between the Al pad on the large silicon base and the silicon needle, while the polyimide layers provide the flexible insulation. This new device was tested on neurons in an isolated brain of the sea slug *Tritonia diomedea*. We have demonstrated that intracellular action potentials from a single neuron (Pd5 of the *Tritonia* brain) can be recorded by the silicon needle device, connected via the Al pad to a conventional neurobiological amplifier. Our success is a major step toward the larger goal of self-contained, implantable devices suited for intracellular neuronal recording from freely behaving animals (Fig. 2).

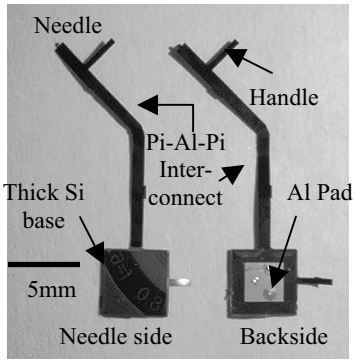

Figure 1. *Completed sub-micron silicon probe devices produced by a combination of micromachining and precision laser cutting.*

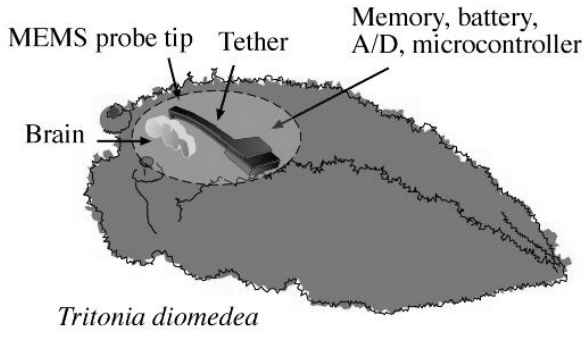

Figure 2. *Schematic of* Tritonia diomedea *with envisioned stand-alone neural recording implant [8]. Animal length is 10cm, neurons can be as large as 400μm. Brain dimensions are several mm. (Integrated electronics not included in current needle design.)*

Travel support has generously been provided by the Transducers Research Foundation and the DARPA MEMS and DARPA BioFlips programs.

FABRICATION

We started with a 400μm thick, 4", <100> DSP boron doped silicon wafer with a resistivity of 0.1-0.6 Ω-cm. First a 1000Å aluminum etch-stop layer was patterned (Fig. 3b). This protects the polyimide interconnect during the needle sharpening in SF_6 plasma. Next the wafer was backside aligned and patterned with photoresist AZP4620 (Clariant), to define the needle, release trench and large silicon base using the standard Bosch process in the Deep-Reactive-Ion-Etching (DRIE) system (Fig. 3c). The needle probes (385μm tall) had protective rings around them to ensure positive profiles while sharpening. Removal of DRIE residue required treatment with CF_4O_2 plasma in addition to EKC 830 resist strip.

The wafer was flipped over and the Pi-Al-Pi interconnect was defined (Fig. 3d-f). The second layer of polyimide was cured at a higher temperature than the first layer. This approach terminates any route for water transmission through the boundary between the base and top polyimide layers [9], ensuring a sound electrical connection between the needle and the Al pad. This curing approach also anneals the Al, ensures better adhesion and a reduced contact resistance.

Before sharpening, the Pi-Al-Pi side was covered with a layer of resist, to prevent the etching of the polyimide in SF_6 plasma from the under side of the wafer, as well as to protect the Al electrical connection layer when the Al etch stop layer is etched away following the sharpening. Needles were simultaneously sharpened (Fig. 3g) by Reactive-Ion-Etching (RIE) using SF_6 plasma. During the sharpening the protective ring is etched away. Fig. 4 shows a sharpened silicon needle with a sub μm tip inset. The silicon at the base of the trench is also etched away during the sharpening, exposing the Al etch stop layer.

At this point the device is attached to the wafer only at the polyimide tabs and in the trench surrounding the thick silicon base. The Al etch stop layer was etched away (Fig. 3h) by carefully immersing the wafer in Al etchant (etch rate~ 3500Å/min at 40^0C) keeping the wafer in vertical position so as to prevent the weight of the etchant from stressing the needle devices. After this the protective backside resist was stripped. The wafer was finally immersed in Isopropyl Alcohol (IPA), which cleaned the wafer before it evaporated leaving a dry surface. At this point we have high aspect ratio, sub micrometer silicon needles connected to a silicon base through a Pi-Al-Pi sandwich. The individual devices are finally released by laser ablation, in which the polyimide tabs that hold the device to the wafer are cut.

RESULTS AND DISCUSSION

The resistance between the silicon probe (needle) and a ground wire, both immersed in sea water, was 1MΩ, on the application of a 100Hz +/–10nA square wave current generated by A-M Systems neuroprobe 1600 amplifier in combination with a stimulator (Medical systems Corp. Model S-90). The resistance of traditional Ag/AgCl glass capillary electrodes is 5-60MΩ. The rough contour of the needle leads to increased surface area for the given needle geometry. This increased surface area might contribute to lowering the impedance of the needle.

We used the sea slug *Tritonia diomedea* as a model system to measure the intracellular action potentials for a variety of reasons, the foremost being that the brain of this animal has been extensively studied and the extremely large neurons in its brain make for very easy conventional recordings. To measure the action potentials, the brain of *Tritonia* was isolated in a dish containing seawater along with a ground wire. Using scissors, a dorsal

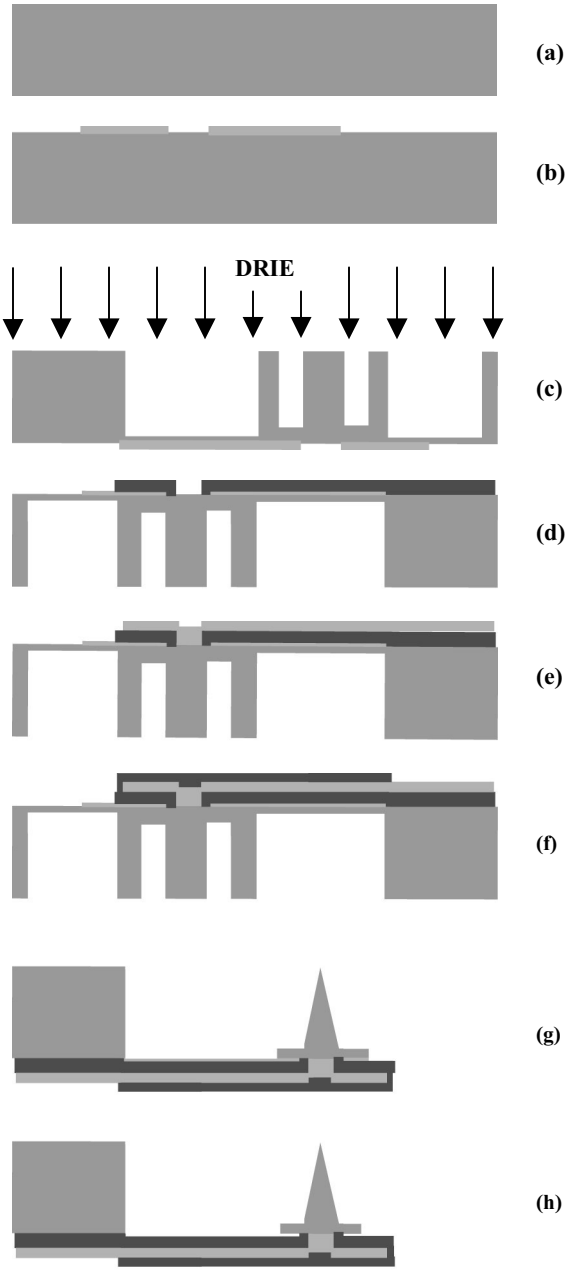

***Figure 3**. Fabrication of the sub-micron silicon probe device; (a) Bare Si wafer, (b) Al etch stop layer patterning on wafer backside, (c) Defining Si probes with DRIE on needle side, (d) Polyimide layer 1 patterning and curing on wafer backside, (e) Al electrical contact layer patterning, (f) Polyimide layer 2 patterning and curing, (g) Needle front side sharpening with RIE, (h) Al etch stop layer etch. Individual devices released by laser cutting.*

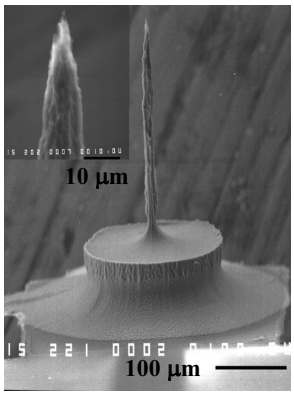

Figure 4. *SEM images of the sub-micron silicon probe with tip inset.*
Needle height is ~ 400µm.
Needle tip diameter is far less than 1µm.

Needle: Magnification 221x, scale bar 100µm.
Tip: Magnification 2000x, scale bar 10 µm.

incision was made overtop of the brain. All nerves emanating from the brain were cut, along with the associated connective tissue, allowing its removal from the body of the animal. The isolated brain was then pinned in a dish, stretched taut and any remaining connective tissue was dissected away. This configuration promotes conventional micropipette penetration of brain neurons, and we reasoned would do the same for silicon needle recording. Figure 5 shows a picture of an isolated *Tritonia* brain.

We measured the voltage between the needle inserted in the Pd5 neuron and the ground wire immersed in the seawater surrounding the isolated brain, using an A-M Systems Neuroprobe 1600 Amplifier. The headstage of the amplifier was connected to the needle probe via the Al pad on the large silicon base. The voltage signal was digitized using a Cambridge Electronic Design Micro1401 MkII with Spike 2 Version 4 software (Fig. 6). As the needle was not insulated, a non-conductive layer of mineral oil was dispensed over the brain to record only from the probe tip because the needle pushed through the oil into the neuron. The oil layer molded to the surface of the brain, creating a high resistance path between the probe tip and the ground wire, reducing the short to the ground enough to allow us to record neuronal signals.

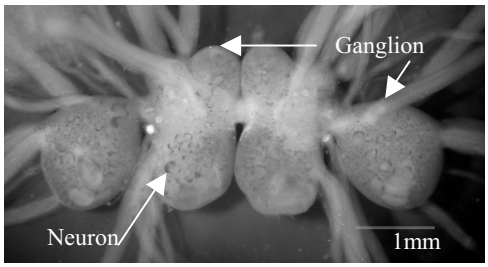

Figure 5. *Isolated brain of* Tritonia diomedea*, showing the ganglia and neurons.*

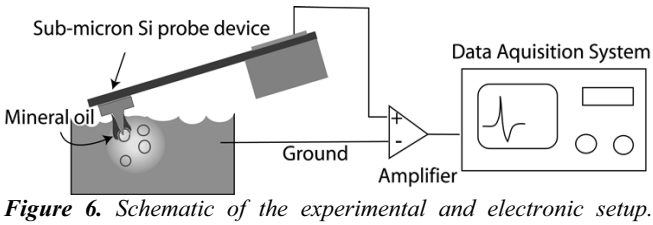

Figure 6. *Schematic of the experimental and electronic setup. (Mineral oil layer is shown only on the neuron of interest for clarity).*

For penetration experiments, the needle tip was manipulated by a tapered glass capillary, which was glued to the back side of the needle base using cyanoacrylate glue (Fig. 7). The non tapered end of the capillary was attached to a micromanipulator. Similarly, the large silicon base of the needle device containing the Al base pad connected to the amplifier headstage was held in another micromanipulator. Both the silicon needle device and the tapered capillary were manipulated into position over a target neuron, before a penetration attempt was made. Fig. 8 shows the needle on top of the Pd5 neuron just before penetration. Penetration comprises slowly advancing the needle along its tip-to-base axis, interspersed with very gentle taps of the manipulator - an identical method to penetration using conventional micropipettes. The flexible interconnect arm allows a range of independent movement of the needle, facilitating final manipulations during penetration. In this fashion we were able to penetrate single neurons and measure intracellular transmembrane potentials with an implantable device.

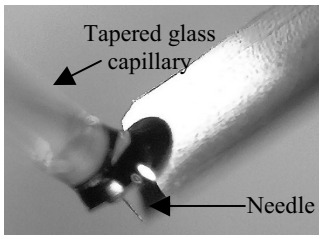

Figure 7. *Preparation for cell penetration. (silicon probe is manipulated by tapered glass capillary attached by veterinary glue).*

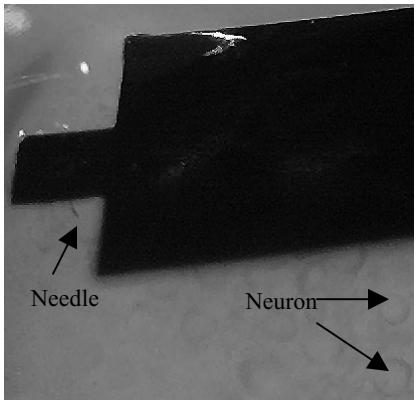

Figure 8. *Implantation of a sub-micron silicon probe into a specific neuron - Pd5 of the brain of* Tritonia diomedea.

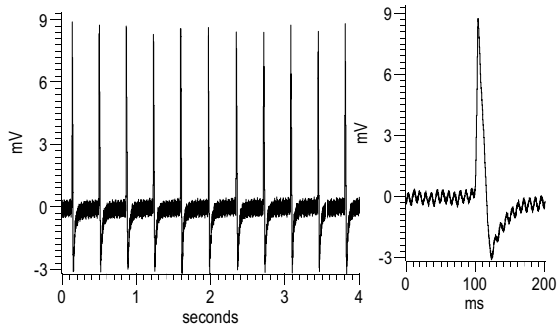

Figure 9. *Intracellular action potentials recorded from Pd5 neuron of the* Tritonia *brain using a sub-micron silicon probe; (a) Train of action potentials, (b) Single action potential with its three phases: a fast initial depolarization, a fast repolarization, followed by a slow hyperpolarization before returning to the baseline.*

Fig. 9 shows the intracellular action potentials recorded from the Pd5 neuron of the *Tritonia* brain with the implantable silicon probe device. The 12mV potentials have the form of attenuated, low frequency filtered action potentials recorded using conventional glass electrodes. In particular, they show all three major phases of an action potential: a fast initial depolarization, a fast repolarization, followed by a slow hyperpolarization before

returning to the baseline. Circumstantial evidence supports the hypothesis that these action potentials are intracellular:
1) The spike shapes look like intracellular, particularly after the hyperpolarization, which is quite distinctive. 2) The spike sizes, though small, are in the intracellular range. Extracellular action potentials would be in the range of μV. Further, the amplitude of the recording did not increase as we advanced the probe, rather the recording started with a discrete change from no activity to full potentials, consistent with sudden intracellular penetration.

FUTURE WORK

It is tempting to speculate that the imperfect insulation provided by the oil allowed some short to the ground, reducing the size of the action potentials. While using glass micropipettes the cell membrane attaches itself to the sides of the glass electrode thus sealing the neuron from the external environment. With this in mind the next step in our process would be needle insulation with SiO_2. The major challenge here is the deposition of SiO_2 on the polyimide as well as the needle.

Implantation of the silicon probe device into the brain of a freely moving organism would require efforts to ensure that the probe does not move relative to the neuron it has penetrated. After penetration the base of the needle needs to be glued to the perineurium – the acellular layer that bounds the brain in sea slugs. This will create a low profile bump on the brain, which we hope will not be susceptible to movement of the brain inside the animal. For this, the needle will have to be manipulated with a detachable device rather than the glued and tapered glass capillary. Changing the geometry of the polyimide arm to a spiral shape will increase the flexibility of the connection between the needle and the large silicon base, so that when they move relative to one another there will be reduced stress on the needle.

We would also like to extend the capability of our device to perform neurostimulation by coating the tip of the needle with metals of high exchange current density [10].

SUMMARY

In conclusion, we have fabricated implantable silicon probe devices with flexible interconnects suitable for intracellular neuronal recording. These probes were implanted into a specific neuron (Pd5) of the *Tritonia* brain and for the first time we have shown that an implantable device can successfully measure intracellular action potentials. The silicon probes have reduced impedances compared to the Ag/AgCl glass capillary electrodes used conventionally for intracellular neuronal recording. These probes can be easily integrated with electronic circuitry to make them self-contained.

ACKNOWLEDGEMENT

The authors would like to thank Dr. Giles Dennler (Linz Institute for Plastic Solar Cells, Johannes Kepler University of Linz, Linz, Austria) for detailed discussions about the behavior of PECVD deposited SiO_2 on Polyimide.

This research was supported by David and Lucile Packard Foundation grant 2000-01763.

REFERENCES

1. L. Lin and A. P. Pisano, “Silicon-Processed Microneedles”, IEEE Journal of Microelectromechanical Systems, vol. 1, no. 1, March 1999.

2. K. Najafi, K. D. Wise and T. Mochizuki, “A High-Yield IC-Compatible Multichannel Recording Array”, IEEE Transactions on Electron Devices, vol.ED-32, (1985), pp.1206-1211.

3. D. J. Anderson, K. Najafi, S. J. Tanghe, D. A. Evans, K. L. Levy, J. F. Hetke, X. Xue, J. J. Zappia, and K. D. Wise, “Batch Fabricated Thin-Film Electrodes for Stimulation of the Central Auditory System”, IEEE Transactions on Biomedical Engineering, vol. 36, (1989), pp. 693-704.

4. G. T. A Kovacs, C. W. Storment, M. Halks-Miller, C. R. Jr. Belczynski, C. C. D. Santina, E. R. Lewis and N. I. Maluf, “Silicon-Substrate Microelectrode Arrays for Parallel Recording of Neural Activity in Peripheral and Cranial Nerves”, IEEE Transactions on Biomedical Engineering, vol. 41, (1994), pp. 567-577.

5. P. K. Campbell, K. E. Jones, R. J. Huber, K. W. Horch and R. A. Normann, “A Silicon Based, Three Dimensional Neural Interface: Manufacturing Processes for an Intracortical Electrode Array”, IEEE Transactions on Biomedical Engineering, vol. 38, (1991), pp. 758-768.

6. Y. Hanein, C. G. J. Schabmueller, G. Holman, P. Luecke, D. D. Denton, K. F. Böhringer, "High-Aspect Ratio Submicrometer Needles for Intracellular Applications", IOP Journal of Micromechanics and Microengineering (JMM) 13(4):S91-S95, July 2003.

7. Y. Hanein, U. Lang, J. Theobald, R. Wyeth, K.F. Böhringer, T. Daniel, D.D. Denton, and A.O.D. Willows, “Intracellular Recording with High Aspect Ratio MEMS Neuronal Probes”, Proceedings of the International Conference on Solid-State Sensors and Actuators (Transducers), (2001), Munich, Germany.

8. G. Holman, Y. Hanein, R. C. Wyeth, A. O. D. Willows, D. D. Denton, K. F. Böhringer, “Silicon Micro-Needles with Flexible Interconnections”, Second International IEEE-EMBS Special Topic Conference on Microtechnologies in Medicine & Biology, pp. 255-260, May 2-4, 2002, Madison, Wisconsin.

9. K. Lee, A. Singh, H. Zhu, G. Coryell, B. Olsen, B. kim, G. Raupp and J. He, “Fabrication of Implantable Polyimide Based Neural Implants with Flexible Regions to Accommodate Micromovement”, Twelfth International Conference on Solid State Sensors, Actuators and Microsystems, vol. 2, June 8-12 2003, Boston, pp. 1221-1224.

10. G. T. A. Kovacs, "Introduction to the Theory, Design and Modeling of Thin-Film Microelectrodes for Neural Interfaces", chapter in, Enabling Technologies for Cultured Neural Networks, D. A. Stenger and T. McKenna, Eds., Academic Press, 1994, pp. 121-166.

11. S. Takeuchi, T. Suzuki, K. Mabuchi and H. Fujita, “3D Flexible Multichannel Probe Array”, IEEE The Sixteenth Annual International Conference on Micro Electro Mechanical Systems, Jan 19-23 2003, Kyoto, Japan, pp. 367-370.

MEASUREMENT OF IN-SITU FLOW VELOCITY USING SINGLE-MOLECULE DETECTION FOR THE APPLICATION OF BIOMOLECULE QUANTIFICATION

Shu-Yi Chao*, Chunyang Zhang and Tza-Huei Wang
Mechanical Engineering Department and Whitaker Biomedical Engineering Institute, Johns Hopkins University
Baltimore, Maryland 21218, USA

ABSTRACT

This paper describes a novel method for measuring flow velocity within a micro capillary using single-molecule detection. A custom confocal fluorescence spectroscopic system is implemented to detect fluorescent bursts of single molecules flowing through a minute laser focal volume. Durations of single-molecule fluorescent bursts, which are found to be strongly related to the molecular transit times through the detection volume, are statistically analyzed to determine the in-situ flow speed. Low concentration (<1 pM) of small fluorophores (< 1 nm) can be used for analysis, rendering it a minimally invasive flow measurement technique. This single-molecule method simultaneously determines both the number of flow-through biomolecules and the associated fluid volume, and therefore can be used for quantitative analysis of biomolecules.

INTRODUCTION

The ability to detect and measure precise quantities of biomolecules, such as DNA and proteins, is of great importance to the fields of genomics, proteomics, and medical diagnostics. Quantifying the transcriptional and translational levels of specific genes and proteins is essential to studies of gene function and disease. To date, a variety of techniques have been developed for quantifying specific mRNA and proteins. Among those, polymerase chain reaction (PCR) based assays provide the most sensitive method for quantitative detection [**1**,**2**]. However, the problems of contamination and variation in the amplification efficiency complicate the application of PCR for precise quantification [**3**]. Recent advances in confocal fluorescence spectroscopy have enabled detection of biomolecules with single-molecule sensitivity [**4-6**]. Single-molecule detection (SMD) provides an opportunity to detect low-abundance of biomolecules without amplification. The concentration of biomolecules (e.g. gene expression level) can be determined according to the number of targets detected, cross-sectional area of the focused laser beam, and the flow speed at the focal region. In practice, however, precise calculation is difficult to achieve because of the uncertainty in measuring flow velocity. The actual velocity of the detected molecules cannot be simply deduced from the volumetric flow rate, since the streamwise velocity varies across the microchannel due to hydrodynamic shear (Figure 1a). This velocity depends on the position of the focused laser beam in the microchannel, which is undefined.

Several methods have been reported for probing flow velocity inside microstructures. For example, micro particle image velocimetry (micro-PIV) [**7**,**8**] was applied to measure the flow profile in a microstructure by first recording positions of many small tracer beads embedded in the fluid and then utilizing a special image cross correlation process to determine the detailed flow velocity field. One deficiency of micro-PIV is its invasiveness for both the flow field and the bioanalytical environment. The beads introduced may alter the flow condition and, more importantly, may interact with the biomolecules, incurring inaccuracy in counting of biomolecules and in measurement of flow speed. Micro flow profiling using fluorescence correlation spectroscopy (FCS) was recently reported [**9**,**10**]. The principle of FCS is based on analysis of fluctuations in the fluorescence signal due to passage of a number of fluorescent molecules through the confocal detection volume. The flow speed at the focal point can be determined by performing autocorrelation analysis of the fluorescent variations associated with the bulk flow. Although less invasive and small fluorophores are used for determining the flow speed, the fluorescence from the imported tracing agents can interfere with the signal from the fluorescently labeled targets, adding difficulty in separating signal from the noises.

In this paper, we developed a flow measurement technique that achieves noninvasiveness by directly using the fluorescent signal from target biomolecules to determine the in-situ flow speed (Figure 1b and 1c). Aside from its application to quantitative detection of biomolecules, this technique can be used for general flow profile measurement with high resolution (< 0.5 µm).

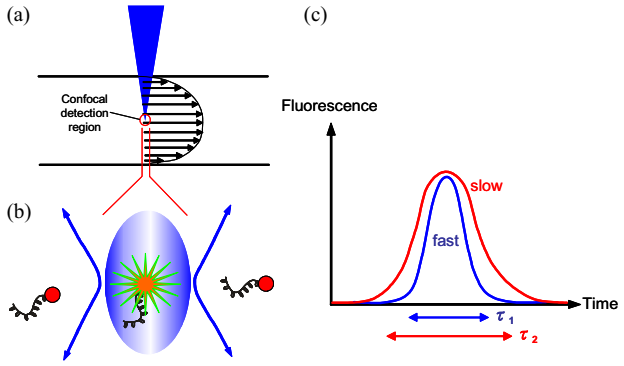

Figure 1. *(a) The molecule/flow velocity within the detection volume is uncertain due to the undefined position of the confocal detection volume and the parabolic velocity profile in the microchannel. (b) A fluorescently labeled biomolecule is excited and emits fluorescence while it passes through the detection volume. (c) Molecular transit time decreases as flow velocity increases.*

SINGLE-MOLECULE DETECTION

We recently achieved single-protein (human I1-2) detection using quantum dots and fluorescent colloidal nanobeads, based on confocal fluorescence spectroscopy [**6**]. Similarly, we accomplished detection of DNA using molecular beacon probes at the single-molecule level (Figure 2a) [**4**,**12**]. Molecular beacons are single-stranded, hairpin-structure oligonucleotide probes that become fluorescent only upon hybridization with their complementary target sequences [**11**]. We used molecular beacons

* Travel support has been generously provided by the Transducers Research Foundation and by the DARPA MEMS and DARPA BioFlips programs.

as homogenous assay (separation-free) probes for detecting specific DNA sequences. Figure 2b and 2c shows a 20-s representative histogram of fluorescent signal of molecular beacons in the absence and presence of complementary targets. The discrete fluorescent bursts (Figure 2c) represent the events of individual fluorescent target-probe hybrids passing through the confocal detection volume. Thus, the number of targets detected can be determined according to the number of fluorescent bursts.

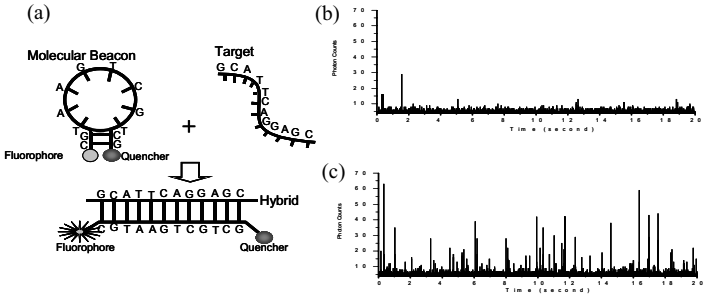

Figure 2. *(a) A molecular beacon probe whose hairpin structure is destroyed when hybridized with a target, restoring fluorescence. (b) A histogram of background fluorescence of molecular beacons in the absence of target DNA. (c) A histogram of single-molecule fluorescent bursts from molecular beacons-target DNA hybrids.*

METHOD AND PRINCIPLES

The technique to measure the flow velocity at the focal point is based on analysis of single-molecule fluorescent histograms detected by the confocal optical apparatus. The duration of a fluorescent burst represents the transit time of a molecule passing through the detection region (Figure 1). The molecular transit time is decided by both the flow velocity at the detection point and Brownian motion of the molecule. When molecules are detected in a fast flow condition, the influence of Brownian motion on the molecular transit time can be neglected. In this regime, one would expect that increase in flow velocity results in decrease in transit time (Figure 1c). The in-situ flow velocity can then be measured through its correlation with the molecular transit times.

To better quantitatively describe this concept, an assumption is first made that the average transit time T_{avg} of a molecule passing through the probe volume is inversely proportional to the flow velocity v as follows:

$$v = \frac{k}{T_{avg}}$$

, where k is a proportionality constant. This assumption is validated through experiments described in the Results and Discussion section.

The constant k is determined via a calibration process, which is performed by first measuring the flow speeds at two positions (position 1 and 2) with a known separation S in the translational direction in between.

$$v_1 = V_0\left[1-\left(\frac{r_1}{R}\right)^2\right] = \frac{k}{T_{avg_1}} \;;\; v_2 = V_0\left[1-\left(\frac{r_1+S}{R}\right)^2\right] = \frac{k}{T_{avg_2}}$$

, where R is the radius of the microcapillary, r_1 is the distance between the center and position 1, and V_0 is the flow velocity at the center and is calculated according to the volumetric flow rate. After the average transit times at position 1 and position 2, T_{avg_1} and T_{avg_2}, are calculated using the measured fluorescent burst data, both of the two unknown variables, r_1 and k, can be determined accordingly.

EXPERIMENTAL SETUP

A schematic diagram of the custom-made single-excitation, single-emission confocal fluorescence spectroscopic system is shown in Figure 3. A 488 nm wavelength light beam from an air-cooled argon laser (Melles Griot) is directed through a dichroic mirror and an oil immersion apochromatic objective (100×, N.A. 1.3, Olympus) to be focused into a microcapillary (250μm in diameter, Polymicro Technologies). A neutral density filter (1.0 o.d.) is used to attenuate the laser power. The higher wavelength emission fluorescence is collected by the same objective and passes through the dichroic mirror (Chroma Technology) which allows light of wavelength greater than 505 nm to pass through. A 50 μm pin hole (Melles Griot) is used to suppress out-of-focus fluorescence and background noise, thus increasing the signal-to-noise ratio. The fluorescence is then filtered by a bandpass filter before detected by a single-photon avalanche photodiode (APD) (EG & G). Samples are injected into the microcapillary through a 1000μL gastight syringe (Scientific Glass Engineering) by a high-precision syringe pump (Harvard Apparatus). A program written in LabView (National Instruments) and a digital counter (National Instruments) are used to perform data acquisition and data analysis. The excitation laser power is kept at 300 μW during the experiments.

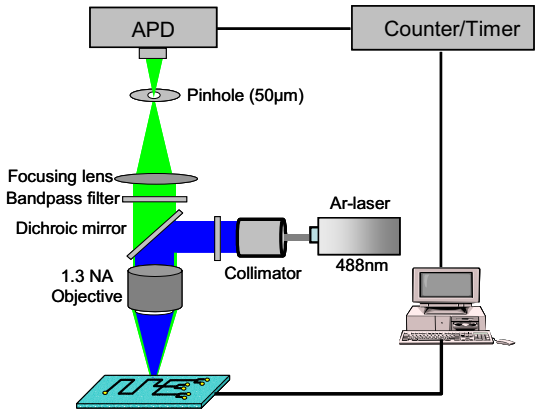

Figure 3. *Schematic diagram of the single-excitation, single-emission confocal fluorescence spectroscopic system.*

SAMPLE PREPARATION

We used pBR322 DNA (New England Biolabs) as target biomolecules to demonstrate the single-molecule detection-based flow measurement. A pBR322 DNA is a commonly used plasmid cloning vector in E. coli. The molecule is a double-stranded circle, 4361 base pairs in length. DNA is labeled with YOYO-1 iodide (Molecular Probes) at a ratio of 1 dye molecule/10 bp to maximize dye-DNA reaction efficiency and to minimize the noise level. YOYO-1 iodide has one carbon atom bridging the aromatic rings of the oxacyanine dye and exhibits absorption /emission maximum of 491/509 nm when bound to double-stranded DNA [**13**]. The resulting solution contained base pairs of DNA at 10^{-8} M along with YOYO-1 at 10^{-9} M and the reaction proceeded for 30 min at room temperature. The solution is further diluted 10 times with deionized water and final concentration of pBR322 DNA is 2.3×10^{-13} M.

RESULTS AND DISCUSSION

Figure 4 shows a 10-s trace (histogram) of fluorescent bursts from pBR322 DNA labeled with YOYO-1 flowing in a micro

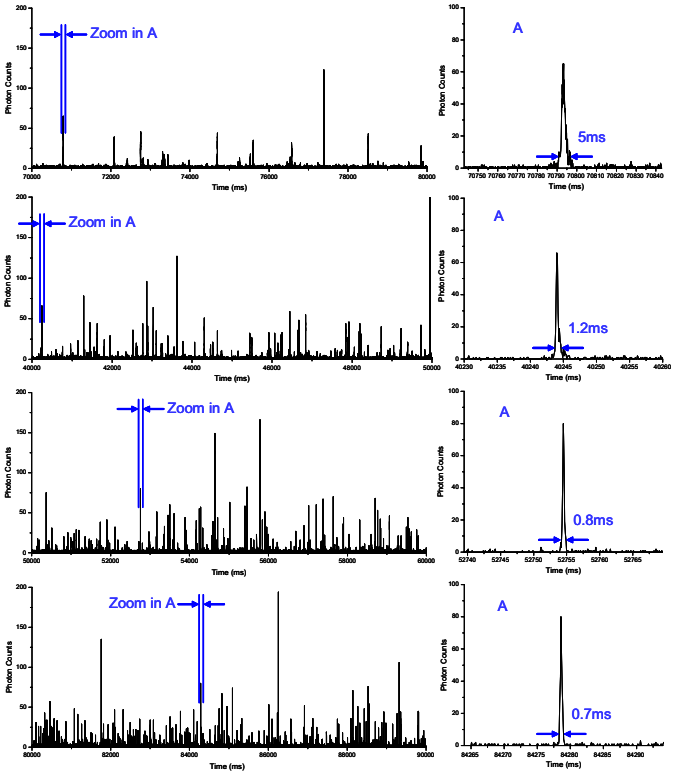

Figure 4. *A 10-s trace of fluoresecent bursts histogram and a representative zoom-in of a single fluorescent burst from pBR322 DNA labeled with YOYO-1 flowing in a microcapillary (250μm in diameter) with different volume flow rate. The corresponding volume flow rate is 1 μL/min, 5 μL/min, 10 μL/min and 15 μL/min from top to bottom. The bin time is 100μs.*

capillary and a representative zoom-in of a single fluorescent burst for different flow conditions. The bin time (signal integration time) is 100μs. Each peak represents a single DNA molecule passing through the probe volume defined by a laser beam with Gaussian intensity profile. The number of fluorescent bursts increases as the flow speed is accelerated, while the duration of a fluorescent burst decreases correspondingly.

The magnitude of a photon burst depends on the fluorescence quantum yield of the fluorescent dye, the trajectories of molecules passing through the probe region and the collection efficiency of the system [**14**].

$$I(t) = Q \int_{-\infty}^{\infty} p(\vec{r}) C(\vec{r},t)\, dV$$

, where Q stands for the combination of fluorescence quantum yield, the excitation cross section of fluorescence molecules, and detection quantum efficiency of detector as well as optical filtering losses in the experimental setup. C is the concentration of fluorescent molecules and p is the combination of the excitation intensity and collection efficiency function which can be approximated by Gaussian distribution:

$$p(\vec{r}) = I_0 e^{-2(x^2+y^2)/w_1^2} e^{-2z^2/w_2^2}$$

, where I_0 is the excitation intensity at the center of the focused laser beam, and w_1 and w_2 are the radius and half height of the probe volume respectively, at which the intensity has dropped by a factor of e^{-2}. The variation of magnitude of single-DNA fluorescence bursts is attributed to the different trajectories of molecules through the non-uniform intensity within the detection volume.

When a fluorescent molecule passes exactly through the center of probe region, a burst with maximal intensity and duration is detected. In contrast, a burst with smaller intensity and duration is measured when a molecule passes through the edge of the detection volume. The probability distribution of duration of a burst is a function of the intensity distribution within the focused laser beam.

To characterize the overall transit time at the focal point, a statistical histogram of burst duration times is plotted for different flow conditions as shown in Figure 5. The background count rate is below 3 photon counts per bin in the current setup. Only bursts with a photon count rate above 8 counts per bin time are considered true events to avoid complications from the background noise. A program written in Matlab is used to determine peak duration time and perform total peak counting. The total analysis time for each measurement is 90s. As shown in Figure 5, the mean of the burst duration distribution decreases as the volume flow rate increases. In addition, the deviation and the width of the right tail in the distributions also decreases with the increase in flow rate, indicating that the influence of Brownian motion on the transit time is less significant in faster flow conditions.

The average duration is used as a characteristic transit time to determine the in-situ flow speed. Figure 6a depicts the average transit time as a function of volumetric flow rate (square). The reciprocal of the average transit time shows a linear relationship with volumetric flow rate (circle) (Figure 6b), showing that flow measurement based on average fluorescent durations is satisfactorily accurate. The plot in Figure 6a can be used as a standard curve to determine the molecule/flow velocity at any detection position inside the micro flow passage. The measured flow velocity starts to deviate from this linear behavior when the flow speed is smaller than 1 mm/s because the Brownian motion effect is becoming more apparent. Therefore, for quantitative detection application, the measurement needs to be carried out in a fast flow condition in order to achieve high accuracy. A good linear relation between the number of molecules detected and

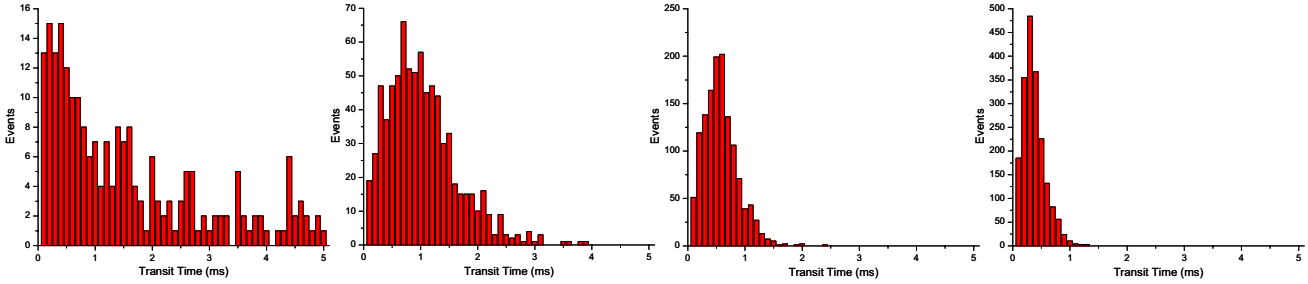

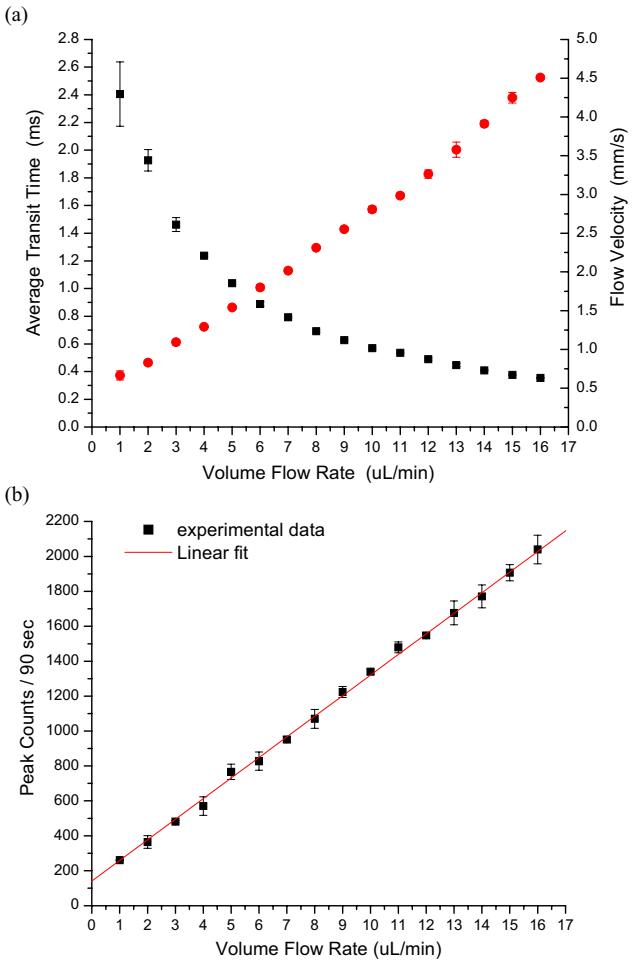

Figure 6. *(a) Average transit time (square) and in-situ flow velocity (circle) as a function of volume flow rate. (b) The number of molecules detected in 90 sec as a function of volume flow rate.*

volume flow rate observed in Figure 6b demonstrates the capacity of high-reliability quantification of biomolecules using single-molecule detection and counting in a micro flow system.

CONCLUSION

Quantification of biomolecules based on single-molecule detection in a micro flow system provides several advantages over conventional methods: extremely high sensitivity and resolution (both at the single-molecule level), requirement of low sample consumption (< 5μL) and rapid analysis (< 2min). The development of in-situ flow velocity measurement enables accurate quantification with high reliability. We have described a generic flow measurement method which can be implemented in a variety of detection assays using different fluorescent tags. In addition, this technique can directly use the fluorescence data from the tags labeled to the molecules, without addition of extra particles to determine the flow velocity, enabling a non-invasive measurement.

ACKNOWLEDGEMENTS

This work is supported by the Whitaker Foundation. The authors thank the Transducers Research Foundation and DARPA MEMS and DARPA BioFlips programs for travel support.

REFERENCES

1. S. A. Bustin, "Absolute Quantification of mRNA Using Real-Time Reverse Transcription Polymerase Chain Reaction Assays", *Journal of Molecular Endocrinology*, 2000, vol 25, pp. 169-193.
2. C. T. Wittwer, M. G. Herrmann, A. A. Moss, R. P. Rasmussen, "Continuous Fluorescence Monitoring of Rapid Cycle DNA Amplification", *Biotechniques*, 1997, vol 22, pp. 130-138.
3. W. W. Wilke, L. D. Sutton, and R. N. Jones, "Automation of Polymerase Chain-Reaction Rests to Achieve Acceptable Contamination Rates", *Clinical Chemistry*, 1995, 41(4), pp. 622-623.
4. T. H. Wang, S. Masset, and C. M. Ho, "A Zepto Mole DNA Microsensor", *Proc. MEMS 2001*, pp. 431-434.
5. T. H. Wang, P. K. Wong, and C. M. Ho, "Electrical Molecular Focusing for Laser Induced Fluorescence Based Single DNA Detection", *Proc. MEMS 2002*, pp. 15-18.
6. H. C. Yeh, E. Simone, C. Zhang, and T. H. Wang, "Single Bio-Molecule Detection with Quantum Dots in a Microchannel", *Proc. MEMS 2004*, pp.371-374.
7. J. G. Santiago, S. T. Wereley, C. D. Meinhart, D. J. Beebe, R. J. Adrain, "A Particle Image Velocimetry System for Microfluidics", *Experiments in Fluids*, 1998, vol 25, pp. 316-319.
8. S. Devasenathipathy, J. G. Santiago, S. T. Wereley, C. D. Meinhart, K. Takehara, "Particle Imaging Techniques for Microfabricated Fluidic Systems", *Experiments in Fluids*, 2003, vol 34, pp. 504-514.
9. M. Gösch, H. Blom, J. Holm, T. Heino, and R. Rigler, "Hydrodynamic Flow Profiling in Microchannel Structures by Single Molecule Fluorescence Correlation Spectroscopy", *Analytical Chemistry*, 2000, vol 72, pp. 3260-3265.
10. B. H. Kunst, A. Schots, and A. J. W. G. Visser, "Detection of Flowing Fluorescent Particles in a Microcapillary Using Fluorescence Correlation Spectroscopy", *Analytical Chemistry*, 2002, vol 74, pp. 5350-5357.
11. S. Tyagi, F. R. Kramer, "Molecular beacons: Probes that fluoresce upon hybridization", *Nature Biotechnology*, 1996, vol 14(3), pp. 303-308.
12. T. H. Wang, Y. F. Chen, S. Masset, C. M. Ho, and Y. C. Tai, "Molecular Beacon Based Micro Biological Detection System", *Proc. of The International Conference on Mathematics and Engineering Techniques in Medicine and Biological Sciences (METMBS'00)*, Las Vegas, NV, U.S.A., 2000, pp. 295-300.
13. R. P. Haugland, "Handbook of Fluorescent Probes and Research Products", *Molecular Probes Inc*.
14. C. Zander, J. Enderlein, R. A. Keller, "Single Molecule Detection in Solution - Methods and Applications", *Wiley-Vch*, 2002.

Integrated Interface Technology for Microfluidic Systems

Ki-Ho Han[1], Rachel D. McConnell[2], Jerome P. Ferrance[2], James P. Landers[2] and A. Bruno Frazier[1]
[1]School of Electrical and Computer Engineering, Georgia Institute of Technology, Atlanta, GA 30032-0250
[2]Department of Chemistry, University of Virginia, Charlottesville, VA 22908

ABSTRACT

This paper introduces a generic packaging approach for microfluidic systems. The 'integrated microfluidic interface' (IMI) provides a simple method for realizing complex arrangements of on-chip to off-chip fluid interconnects, optical windows, and general fluid control components such as pumps / valves into a single package. The fluid interconnects were designed for "one step" fabrication using stereolithography and post assembly of o-rings to ensure a tight seal. The normally open latex microvalves had zero dead volume and were pneumatically actuated by a gauge pressure of ~400kPa. The IMI was demonstrated in a glass-based genetic sample preparation application in which the total analysis system contained microchannels and sub-compartments with different analytical functions. Optical windows in the IMI were utilized for an infrared mediated polymerase chain reaction compartment and for the fluorescence detection in the capillary electrophoresis compartment. The performance of the sample preparation system with the IMI was experimentally characterized, showing that this approach can provide a simple and reliable macro-micro interfacing solution for complex microfluidic systems.

INTRODUCTION

For more than two decades, analytical microfluidic devices [1-3] have been developed for manipulating biological substances. Some of the advantages, when compared to macroscale devices, include smaller size, shorter analysis times, less sample/reagent consumption, and disposability. Many researchers have successfully demonstrated single-functional microfluidic devices [4,5] and transducers [6,7] for fluid manipulation. However, the development of integrated complex microfluidic systems has shown more modest growth, because integration of analytical functions and multiple chips into a total analysis system has technical difficulties such the need for more complex packaging, the possibility of cross biochemical contamination, and the possible need for different substrate materials for the compartment functionalities.

In this work, the IMI fabricated by stereolithography (SLA) is demonstrated to be a flexible method for packaging microfluidic systems with complex arrangements of fluid interconnects and the need for on-chip fluid control. One of the benefits of the IMI is the ability to incorporate microfluidic interconnects, which enables interconnection between chips and interconnections between macroscale and microscale system components. Since the approach results in monolithic fluid interconnects as opposed to the conventional method of post assembling individual connectors, it enables much closer spaced, complex arrangements of fluid interconnects. The IMI can be aligned and bonded to glass, silicon, or plastic microfluidic systems by using common registration techniques such as tooling holes or edge / feature alignment. Furthermore, using o-rings to achieve tight fluid seals avoids the possibility of clogging the fluid microchannels with adhesive when the IMI is bonded to the underlying microfluidic system. In addition, it allows for the integration of other component functionalities such as the incorporation of electrical, mechanical, and optical components into the interface as part of the build process. We demonstrate integration of multiple latex microvalves into the build process for on-chip fluid control. Additionally, we demonstrate optical windows for infrared heating and fluorescence detection.

DESIGN

The miniaturized sample preparation system consists of a cell separation system, cell lysing operation, DNA extraction from the cell lysate, PCR amplification of the DNA, and a DNA separation system, as shown in Fig.1. The cell separation chip contains functionality for introduction of whole blood, purification and separation of red/white blood cells, and cell lysing. The DNA chip contains the functionality for solid phase extraction (SPE), polymerase chain reaction (PCR), and capillary electrophoresis (CE).

First, the cell separation system separates out white blood cells from whole blood. The separated white blood cells are chemically broken down in the cell lysis compartment. In the DNA separation system, the SPE compartment extracts genomic DNA from the white blood cells, and the infrared mediated PCR compartment allows amplification of the target DNA fragments from the extracted DNA. Next, the amplified target DNA fragments are separated using on-chip CE, and subsequently detected with laser-induced florescence.

We have previously shown SPE of DNA from biological samples on independent microdevices [8-10], with a discussion of the technical difficulties associated with integrating these analytical functions with additional functions [10]. These issues include prevention of the solid phase matrix from being established in other regions of the integrated device, contamination of the PCR region with inhibitory reagents used in the SPE process, specifically guanidine and isopropyl alcohol, and prevention of the PCR chamber coating from coating the SPE compartment. Elimination of these problems in simple glass chips without the use of the IMI is not possible.

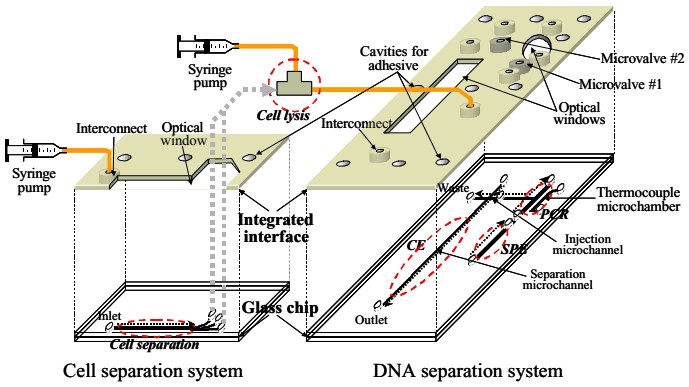

***Figure 1**. Schematic view of the IMI for the miniaturized sample preparation system.*

0-9640024-5-0/hh2004/$20©2004TRF
DOI 10.31438/trf.hh2004.49

Solid-State Sensors, Actuators, and Microsystems Workshop
Hilton Head Island, South Carolina, June 6-10, 2004

Integration of the PCR and the CE compartments has been shown by a number of groups [10-14], but again difficulties remain [10]. Inhibitor effects of CE sieving buffers on the PCR amplification are possible, and the coating used in the PCR chamber can adversely affect the injection process if it gets into the separation domain. Direct sizing of the PCR fragments during the CE separation is also an important issue to ensure correct amplification or to allow multiplex amplification with sizing. This would require addition of internal standards after PCR amplification or co-injection of a DNA marker. One other problem encountered in the integration of PCR with a separation domain was the heat denaturing of the CE sieving matrix during the PCR thermocycling. This led to broad peaks in the subsequent CE separation.

To solve these problems, the IMI for the DNA separation system consists of seven microfluidic interconnects, two microvalves and two optical windows, as shown in Fig.1. The IMI fluid interconnects are designed as a "one step" plug-in interconnect (Fig.2) to facilitate simple connection of capillary tubing. The o-rings are used to avoid clogging of the microchannels by the UV-adhesive during bonding of the glass chip with the IMI and to provide a tight seal between the external capillary tubing and the IMI fluid interconnects. Figure 3 shows the formation of the monolithic microvalve when the IMI is aligned and bonded to the surface of the glass based sample preparation system. As can be seen from the schematic, the microvalve is designed to have zero dead volume.

FABRICATION PROCESS

Stereolithography is a technique where a laser is used to cure a photosensitive polymer structure layer-by-layer. The laser beam diameter of the SLA system (Viper SI2, 3D Systems Corp., USA) is 75 µm ± 15 µm, and the vertical resolution of the platform motion is 25 µm. First, the integrated interface is drawn using 3-D design software (Pro/Engineer®, Parametric Technology Co., USA). The drawing is imported into the SLA system, and then multiple copies of the single drawing are built in an automated fashion with the photosensitive polymer (SL5510™, 3D Systems Corp., USA). Once the part is formed, it is removed from the platform and cleaned to remove the excess uncured photopolymer resin. A five-minute immersion in 100% isopropyl alcohol in an ultrasonic bath is used as the cleaning process, followed by curing using an ultraviolet source.

Figure 4 shows the fabrication process of the sample preparation system with the integrated interface fabricated by SLA. Bottom glass wafers (Borofloat glass of 1.1 mm thick, Howard Glass Co., Worchester, MA) of the cell and DNA separation systems are etched 50 µm and 60 µm in 25% HF solution, respectively. The bottom glass wafers contain microchannels for each of the sample preparation compartments (i.e., cell separation, SPE, PCR, and CE). The cell separation compartment consists of an etched microchannel (3 cm long, 400 µm wide) with an electroplated nickel wire (50 µm high and 100 µm wide) centered in and running the length of the microchannel. The SPE compartment consists of an etched microchannel 2.2 cm long with a width of 400 µm. For the DNA separation system, the top glass wafer, containing only the PCR and thermocouple microchambers, is etched 150 µm deep to allow access for the thermocouple. For proper alignment between the microchannels of the bottom glass and the fluidic ports of the top glass, a drilling guide fabricated by SLA is used, as shown in Fig.4(a). By using glass-to-glass thermal bonding (Fig.4(b)) at 685°C for 3.5 hours, the glass chips of the cell and DNA separation systems are completed.

The IMI is used to realize the microfluidic interconnects, microvalves and optical windows on the glass chip, as shown in Fig.4(c). Nitrile rubber o-rings (Size 001-1/2, McMASTER-CARR, Atlanta, GA) are used for sealing the microfluidic interconnects, and a latex sheet (120 µm thick, McMASTER-CARR, Atlanta, GA) is used for the microvalves. The integrated interface and the glass chip are aligned and clamped in a clamping jig fabricated by SLA, as shown in Fig.4(d). A UV adhesive (Product 1187-M, DYMAX Co., Torrington, CT) is dropped into the openings on the integrated interface, and capillary forces pull the adhesive into the gaps between the integrated interface and the glass chip. The UV adhesive is then cured by placing it under a UV light for 30 minutes, completing the fabrication of the microfluidic device, as shown in Fig.4(e).

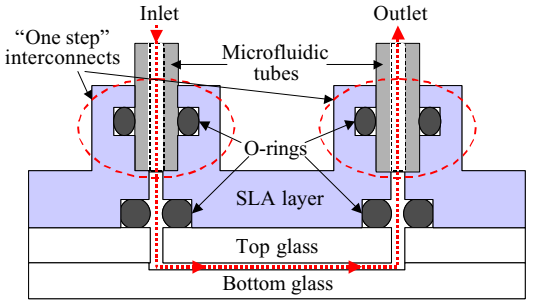

***Figure 2**. Schematic cross-section view of the microfluidic interconnects.*

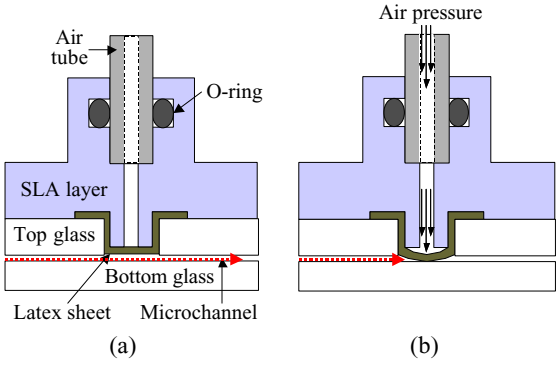

***Figure 3**. Schematic cross-section view of the microvalve: (a) normally open state; (b) pneumatically closed state.*

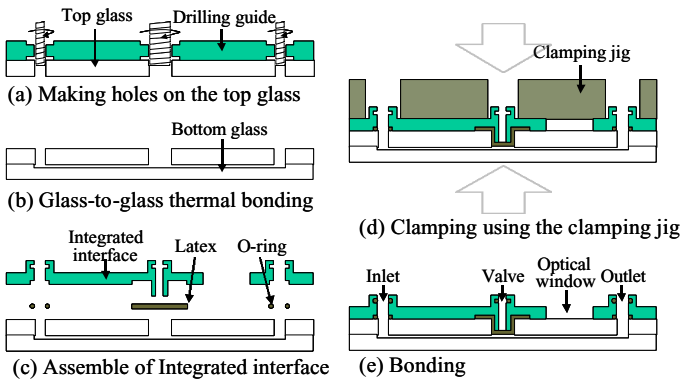

***Figure 4**. Fabrication process.*

RESULTS AND DISCUSSION

Figures 5(a) and (b) show the fabricated cell separation system and DNA separation system with the integrated interfaces. In the cell separation system, the microfluidic interconnect and the optical window are used for readily and effectively introducing the whole blood, and for monitoring the cell separation, respectively. Figure 6 shows that white blood cells are separated from whole blood in microchannel of the cell separation system. In the DNA separation system, microfluidic interconnects are used for introducing the biological/chemical samples into their respective compartments. Microvalve #1 is used to isolate the SPE channel during filling and curing of the sol-gel. Microvalve #2 is used to isolate the CE microchannel while filling the microchannel with polymer, and for preventing the PCR reagent from leaking into the CE compartment during the PCR amplification. Figure 7 shows the maximum fluid pressure before valve leakage for a range of valve pressures from 0 to 400 kPa. Figure 8 shows red dye flowing through each single-function microfluidic compartment in the DNA separation system controlled by the pneumatically actuated microvalves (gauge pressure of ~400 kPa). A DNA extraction profile from the integrated SPE compartment is shown in Fig.9. The optical window for the PCR compartment enables rapid thermocycling between 60 °C and 94 °C using IR-mediated, non-contact heating instrumentation, as shown in Fig.10. These experimental results demonstrate the usefulness of integrated interfaces for complex microfluidic systems.

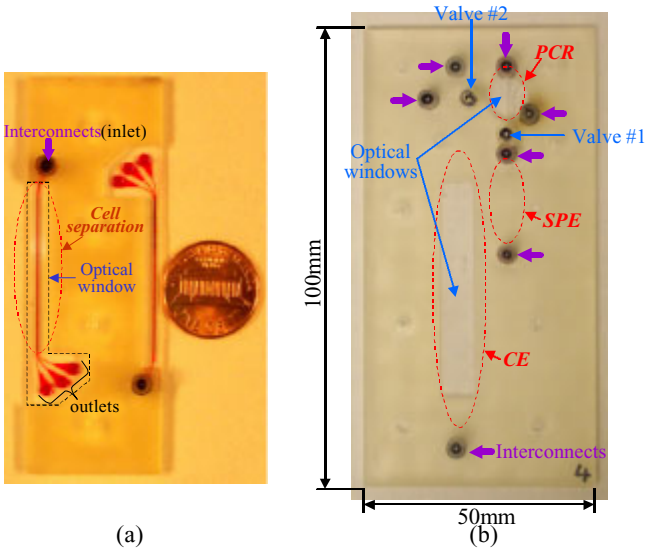

***Figure 5**. Fabricated sample preparation system: (a) cell separation system; (b) DNA separation system.*

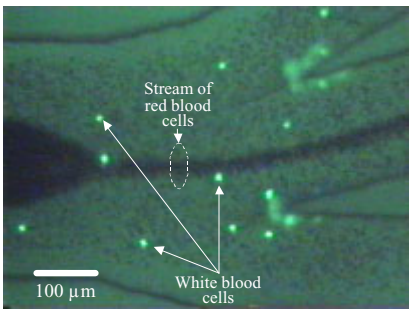

***Figure 6**. Blood cells being separated in the cell separation system.*

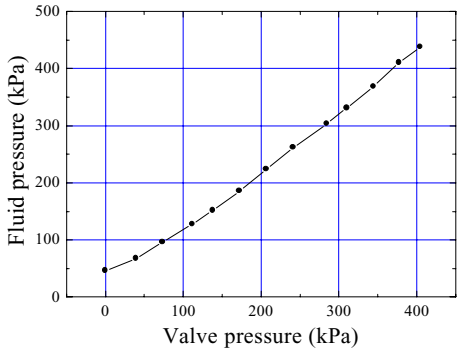

***Figure 7**. Fluid pressure before valve leakage for varying valve pressures.*

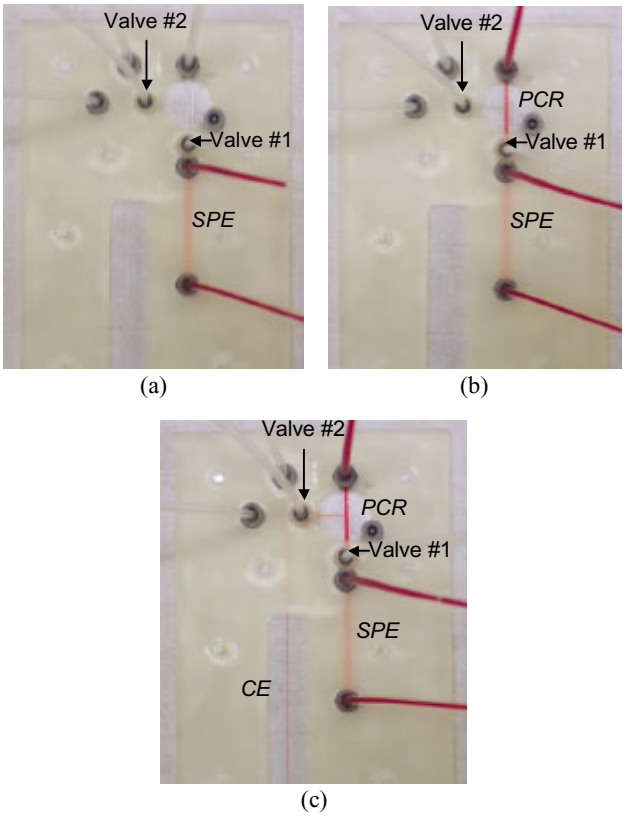

***Figure 8**. Red dye flowing through the microfluidic compartments in the DNA separation system with microvalve #1 and microvalve #2: (a) closed, closed; (b) open, closed; (c) open, open, respectively.*

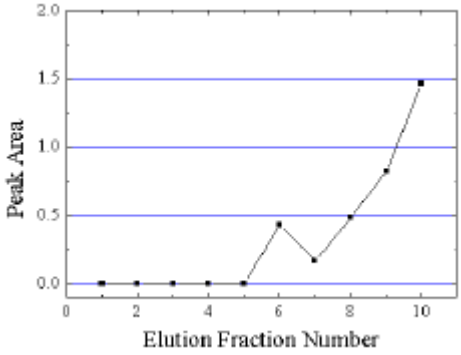

***Figure 9**. Extracted DNA profile from the SPE compartment.*

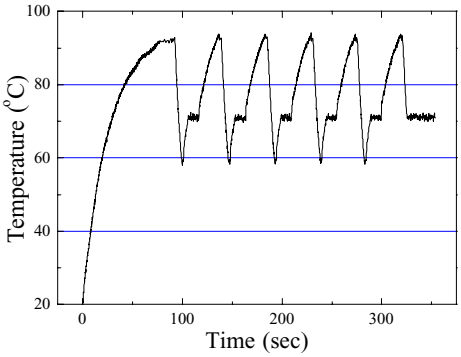

Figure 10. *PCR thermocycling using IR-mediated, non-contact heating.*

CONCLUSION

In this paper, we presented an integrated interface based on stereolithography for a sample preparation system, which consists of a cell separation system and a DNA separation system. The integrated interface contains microfluidic interconnect, microvalve, and optical window components for realizing the integrated sample preparation system.

In the cell separation system, the integrated interface has a "one step" microfluidic interconnect for readily introducing whole blood to the inlet, and one optical window for monitoring the cell separation. In the DNA separation system, the integrated interface consists of seven "one step" microfluidic interconnects, two microvalves for controlling fluids, and two optical windows for optically interfacing with the PCR and CE compartments. The microfluidic interconnects were easy to use and effective for creating fluidic interconnections for each compartment. The microfluidic interconnects were used for curing of the SPE sol-gel, and enabled stopping the flow through the PCR microchamber during DNA amplification. The normally open microvalves, designed to have zero dead volume, were pneumatically actuated by a gauge pressure of ~400 kPa. Microvalve #1 was used to isolate the SPE chamber. Microvalve #2 was used to prevent contamination of the PCR microchamber while filling the CE separation microchannel with polymer, and for preventing the PCR reagent from leaking to the CE compartment during DNA amplification. The optical window over the PCR chamber enabled rapid thermocycling between 60 °C and 94 °C using IR-mediated, non-contact heating instrumentation.

By demonstrating the performance of the single-function compartments of the sample preparation system, this paper has proven that the IMI is a facile and reliable solution for interface technology of complex microfluidic systems.

ACKNOWLEDGEMENTS

This work was supported by the National Institutes of Health (NIH) / National Institute for Environmental Health Sciences (NIEHS) under Grant ES10846. The authors would also like to express thanks for travel support provided by the Transducers Research Foundation and the DARPA MEMS and DARPA BioFlips programs.

REFERENCES

1. S. C. Terry, J. H. Jerman, and J. B. Angell, "A Gas Chromatographic Air Analyzer Fabricated on Silicon Wafer", *IEEE Transactions on Electron Devices, ED-26*, 1880 (1979).
2. O. Bakajin, T. A. J. Duke, J. Tegenfeldt, C.-F. Chou, S. S. Chan, R. H. Austin, and E. C. Cox " Separation of 100-Kilobase DNA Molecules in 10 Seconds", *Analytical Chemistry, 73*, 6053 (2001).
3. Y. Huang, S. Joo, M. Duhon, M. Heller, B. Wallace, and X. Xu, "Dielectrophoretic Cell Separation and Gene Expression Profiling on Microelectronic Chip Arrays", *Analytical Chemistry, 74*, 3362 (2002).
4. A. Y. Fu, C. Spence, A. Scherer, F. H. Arnold, and S. R. Quake, "A Microfabricated Fluorescence-Activated Cell Sorter", *Nature Biotechnology, 17*, 1109 (1999).
5. K. S. Chang, S. Tanaka, C. L. Chang, and M. Esashi, "Combustor-Integrated Micro-fuel Processor with Suspended Membrane Structure", *in Tech. Dig. 12th Int. Conf. Solid-State Sensors and Actuators Workshop (Transducers'03)*, Boston (2003), pp.635-638.
6. W. H. Grover, A. M. Skelley, C. N. Lui, E. T. Lagally, and R. A. Mathies, "Monolithic Membrane Valve and Diaphragm pumps for Practical Large-Scale Integrated into Glass Microfluidic Devices", *Sensors and Actuators B, 89*, 315 (2003).
7. A. Han, O. Wang, M. Graff, S. K. Mohanty, T. L. Edwards, K.-H. Han, and A. B. Frazier, "A Multi-Layer Plastic/Glass Microfluidic Systems Containing Electrical and Mechanical Functionality ", *Lab-on-a-Chip, 3*, 150 (2003).
8. K. A. Wolfe, M. C. Breadmore, J.P. Ferrance, M.E. Power, J.F. Conroy, P.M. Norris, and J.P. Landers, "Toward a Microchip-Based Solid-Phase Extraction method for Isolation of Nucleic Acids", *Electrophoresis, 23*, 727 (1997).
9. M. C. Breadmore, K. A. Wolfe, I. G. Arcibal, W. K. Leung, D. Dickson, B. C. Giordano, M. E. Powers, J. P. Ferrance, S. Feldman, P. M. Norris, and J. P. Landers, "Microchip-Based Purification of DNA from Biological Samples", *Analytical Chemistry, 75*, 1880 (2003).
10. J. P. Ferrance, Q. Wu, B. C. Giordano, C. Hernandez, Y. Kwok, K. Snow, S. Thibodeau, and J. P. Landers, "Developments Toward a Complete Micro-Total Analysis System for Duchenne Muscular Dystrophy Diagnosis", *Analytical Chimica acta, 500*, 233 (2003).
11. E. T. Lagally, P. C. Simpson, and R. A. Mathies, "Monolithic Integrated Microfluidic DNA Amplification and Capillary Electrophoresis Analysis System", *Sensors and Actuators B, 63*, 138 (2000).
12. A. T. Woolley, D. Hadley, P. Landre, A. J. deMello, R. A. Mathies, and M. A. Northrup, "Functional Integration of PCR Amplification and Capillary Electrophoresis in a Microfabricated DNA Analysis Device", *Analytical Chemistry, 68*, 4081 (1996).
13. J. Khandurina, T. E. McKnight, S. C. Jacobson, L. C. Waters, R.S. Foote, and J.M. Ramsey, "Integrated System for Rapid PCR-Based DNA Analysis in Microfluidic Devices", *Analytical Chemistry, 72*, 2995 (2000).
14. E. T. Lagally, I. Medintz, and R. A. Mathies, "Single-Molecule DNA Amplification and Analysis in an Integrated Microfluidic Device", *Analytical Chemistry, 73*, 565 (2001).

ULTRASONIC MICROINJECTION CHARACTERIZED BY INTEGRATED MICRO-OPTICAL FORCE ENCODER

Xiaojing Zhang, Stefan F. Zappe, Calvin F. Quate, Matthew P. Scott* and Olav Solgaard
Edward L. Ginzton Laboratory, Department of Electrical Engineering
*Department of Developmental Biology, and of Genetics, School of Medicine
Stanford University, Stanford, CA 94305

ABSTRACT

The effect of ultrasonic agitation on the required penetration force for microinjection in Drosophila embryos was studied, using an integrated optical MEMS force encoder for in-vivo characterization of the dynamic penetration forces. Two modes of operation were investigated. In the first mode of operation, the injector was brought into contact with the embryo to give a fixed bias offset of the two encoder gratings, and the vibration amplitude of the microinjector was increased till penetration occurred. We observed a linear decrease in the penetration force of 2.5 μN with every 0.1 m/s tip velocity increase. In the second mode of operation, the vibration amplitude was kept constant and the injector was pushed into the embryo until penetration. We measured the injection force over the frequency range of 0~16 kHz with actuation voltage up to 150 volts. The average penetration force was calculated based on injections on multiple embryos for each experimental condition. The achieved minimum peak penetration force was 15.6 μN (~29.7 % of the static penetration force), while the minimum average penetration force was 2.7 μN (5.1 % of the static penetration force).

INTRODUCTION

Minimally invasive microsurgical tools for localized and accurate trans-membrane delivery of genetic material into biological model systems, such as Drosophila, will enable a variety of studies of developmental biology and genetics. Vibration is a well-known method for reducing the cutting force of macroscopic tools. For microsurgical devices, improved efficiency was first observed in dissecting cataractous lenses using piezoelectrically-actuated, centimeter-scale silicon cutters [1]. The cutting force was later characterized using piezoresistors [2].

Recently, we demonstrated a micro-optical, encoder-based force sensor for characterization of the force required for penetration and injection of Drosophila embryos [3]. Minimization of the penetration force is critical to the design of high throughput micro-manipulating instruments [4,5,6] for biology and genetics studies, such as RNAi for gene silencing [7]. In this paper, we report on penetration force minimization through ultrasonically actuation of silicon-nitride microinjectors. Actuated by piezoelectric actuators, the injectors are longitudinally vibrated with tip velocities controllable by actuation frequency and voltage. The forces are measured using MEMS optical-encoder force sensors integrated with the vibrating microinjectors.

THEORY

Ultrasonic microinjection was performed with silicon-nitride probes vibrated by piezoelectric actuators, as shown in Figure 1. The probes have integrated force sensors consisting of two vertically-separated microgratings. With no force applied, the two gratings are perfectly aligned. The upper index grating is connected to the microinjector, and has a resonant frequency of f_0=14 KHz. The static diffraction characteristics of the force encoder under normal plane-wave illumination can be analyzed by Fraunhofer diffraction theory [9].

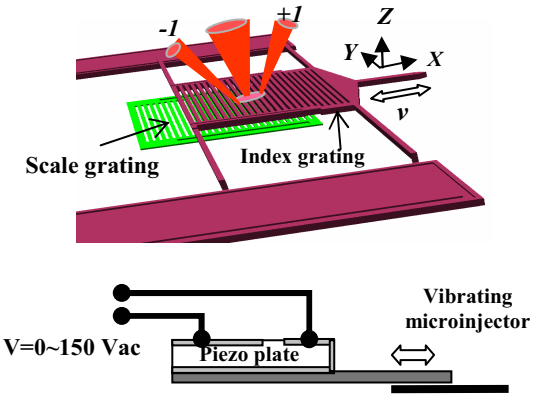

***Figure 1**. Ultrasonic microinjection characterized by integrated optical MEMS force encoder. A piezoelectric stack is bonded onto the backside of the force sensor chip. The probe displacement at maximum actuation voltage of 150 V is 17.4 μm±2.0 μm.*

The first diffraction mode intensity I_1 is a periodic function of injector displacement $d(t)$, as shown by the solid curve in Figure 2. Under ultrasonic actuation, the index grating vibrates along with the microinjector and hence changes its position relative to the fixed scale grating. The force on the injector is determined by the relative displacement $d(t)$ of the two gratings, which is determined by the intensity distribution of the diffraction orders. For the first diffraction mode, we have:

$$I_1[d(t)]=I_0\cdot N^2\cdot\left[\frac{\operatorname{sinc}^2\frac{N\cdot d(t)}{2L}}{\operatorname{sinc}^2\frac{d(t)}{2L}}\right]\cdot\left\{[L-d(t)]\cdot\operatorname{sinc}\frac{[L-d(t)]}{4L}\right\}^2\cdot\sin^2\phi_0\cdot G[d(t)] \quad (1)$$

where I_0 is the illuminating light intensity, N is the number of grating periods under illumination, $\phi_0(x)=(2\pi/\lambda)\cdot(n_1-n_0)\cdot t$ is the phase-delay over the thickness of one grating finger, $2L$ is the period of the grating, $G[d(t)]=\sin^2\{\pi[L+|d(t)-L|]/4L\}$ is phase-modulating term, $d_0(t)$ is the quasi-static relative displacement of the two gratings caused by the linear motion of the microinjector relative to the target, $d_V(t)$ is the sinusoidal displacement of the injector under piezoelectric actuation. The relative displacement can be expressed:

$$d(t)=d_0(t)+d_V(t) \quad (2)$$

Travel support has been generously provided by the Transducers Research Foundation and by the DARPA MEMS and DARPA Bioflips programs

where

$$d_V(t) = A \cdot \sin(\omega_p \cdot t + \varphi_p) = \alpha \cdot V_a \cdot \sin(2\pi \cdot f_P \cdot t + \varphi_P) \qquad (3)$$

and α=0.116μm/V, V_a, f_p are the piezoelectric constant, the actuation voltage, the driving frequency of the piezo-actuator, specifically. The force is related to the displacement through the spring constant, k_x, of the encoder:

$$F = k_x \cdot d(t) \qquad (4)$$

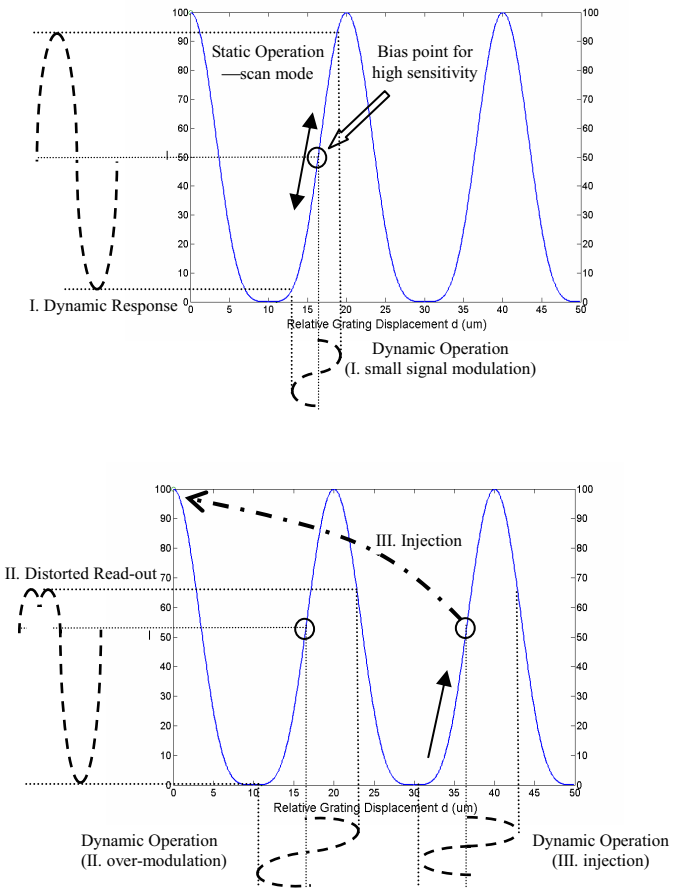

***Figure 2**. The sensor output evolves from a sinusoidal signal at small injector displacement (top), to a distorted output as the tip velocity increases (bottom). After penetration, the encoder bias point recovers to zero and the output signal doubles in frequency.*

The penetration of the embryo membrane can be caused by either linear or vibration motion of the microinjector. We assume the microinjector interacts with the membrane during the full vibration cycles till penetration. In our studies, the linear translation velocity of the microinjector is much smaller than that of the vibration. The average (or peak) penetration force can be derived from the average (or peak) relative displacement of the two gratings. The measured spring constant of encoder k_x is 1.85 N/m.

The dotted lines in Fig. 2 show how the force sensor output evolves from a sinusoidal signal at small injector displacement (case I), to a distorted signal (case II) as the injector vibration amplitude A increases. Penetration, caused by either increased vibration or translation, significantly reduces the force on the injector. Consequently, the average relative grating displacement goes to zero, and the output signal abruptly changes to a periodic signal with doubled frequency (case III).

DESIGN AND FABRICATION

The force encoders were fabricated by LPCVD deposition and patterning of two silicon nitride layers for the dual gratings, separated by low temperature sacrificial oxide, on the silicon substrates. The fabrication process is described in detail in [8].

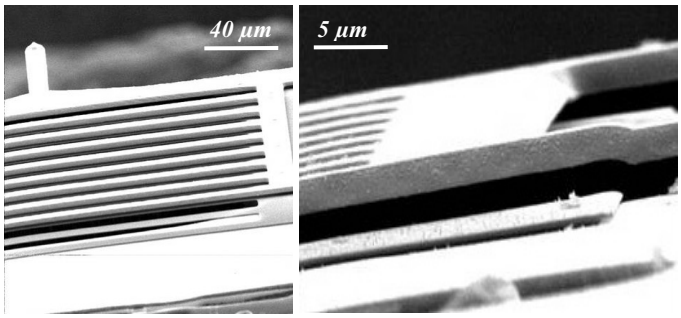

***Figure 3** Scanning electron micrographs show the force probe integrated with the movable index grating (left), and 3 μm uniform vertical gap between the dual gratings (right).*

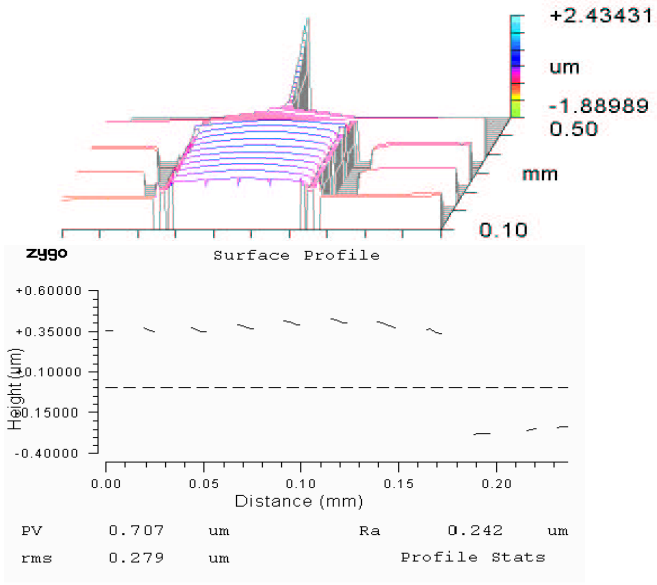

***Figure 4** Movable index grating optical surface profile with roughness 50 nm peak-to-peak and uniformity 1.25% (data acquired using Zygo white-light 3D surface profiler).*

Scanning electron micrographs (SEMs) of the micromachined optical encoder force sensor, with large vertical gaps suitable for ultrasonic actuation, are shown in Fig. 3. The SEMs show the force probe that is integrated with the movable index grating, the index and scale gratings with 20 μm pitch, and a close-view of the 3 μm vertical gap and junction between the gratings and the supporting beams.

The silicon nitride grating layers, deposited under NH_3-rich conditions, have excellent optical surface quality. Figure 4 shows the surface topography characterization results of the encoder gratings using optical phase-shifting interferometry (Zygo white-light 3D surface profiler). The index grating surfaces show less than 50nm root-mean-square roughness. Note that the overhanging probe appears to be bending upwards. This is caused

by the shift of optical reference plane due to the removal of the silicon substrate under the probe.

The sensor chip is completed by bonding a piezoelectric stack, consisting of many piezoelectric ceramic layers that are assembled in series mechanically and in parallel electrically, onto the back side of the chip (Fig. 1). The piezoelectric stack is used to vibrate the microinjector longitudinally in the *X*-direction. The piezo-actuator has a resonance frequency of 69 kHz, and the displacement at the maximum drive voltage of 150 volts is 17.4 µm± 2.0 µm.

EXPERIMENTAL RESULTS AND DISCUSSION

The measurement set-up for ultrasonic microinjection and in-vivo penetration force characterization is shown in Figure 5.

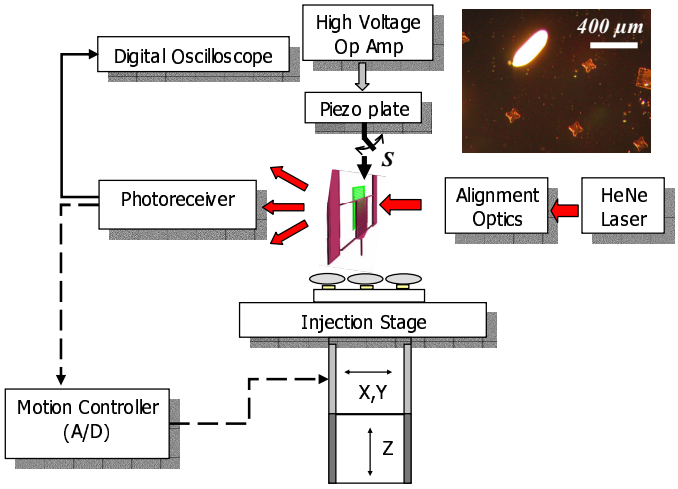

Figure 5. *Experimental set-up for operating optical encoder force sensor on Drosophila embryos positioned on 2-D self-assembly chip(shown in the embedded optical micrograph). The power in the first-order diffracted mode is measured with a photo detector.*

Newly hatched Drosophila embryos [10] were positioned on 2-D micro-fluidic self-assembly chip [6] ready for vertical injection. The encoder was illuminated by a HeNe laser (633nm/4mW) with spot sizes ranging from 60 to 160 µm to achieve tunable sensitivity, and the output intensity signals were detected using a photoreceiver connecting to an oscilloscope. Spatial filtering was preformed to minimize the cross-talk between diffraction orders and therefore optimize the contrast. In earlier static penetration measurements (switch *S* open), we found an average penetration force of 52.5±13.2% µN and an embryo deformation of 58±5.2% µm [3].

During ultrasonic microinjection experiments (*S* closed), the injector is translated towards the target while vibrating. The index-grating vibrates along with the injector and hence changes its position relative to the fix scale grating. The force acting on the injector is determined by the relative displacement of the two gratings, which is determined by the intensity distribution of the first diffraction order under observation.

Two sets of ultrasonic microinjection experiments were performed. First the injector was brought into contact with the embryo to give a fixed bias offset of the two gratings. At each bias point, the actuation voltage, and therefore the injector tip velocity, was increased till penetration (f_p=14 kHz). The critical peak-to-peak actuation voltage V_a for penetration can be used to calculate probe vibration amplitude $d_y = \alpha V_a$ and tip velocity $v_p = 4 \cdot d_y \cdot f_p$.

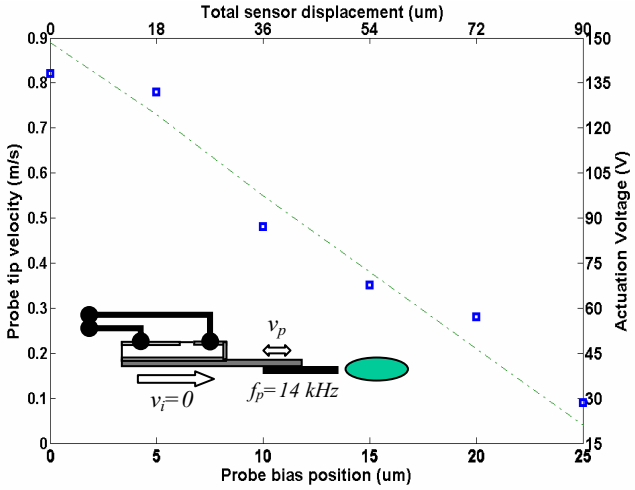

d_0 (µm)	V_a (V)	d_y (µm)	v_p (m/s)	F_p (µN)
0	126	14.64	0.82	27.08
5	120	13.93	0.78	35.02
10	74	8.57	0.48	34.35
15	54	6.25	0.35	39.31
20	43	5.00	0.28	46.25
25	14	1.61	0.09	49.23

Table 1 *Peak penetration force F_p versus bias position d_0, actuation voltage V_a, vibration amplitude d_y and tip velocity v_p.*

Figure 6. *Experimental results for ultrasonic microinjection into Drosophila embryos. The injector was pushed into the embryo till a fixed bias point. For each bias point, the actuation voltage, and therefore the injector tip velocity, was increased (f_p=14 kHz) till penetration occurred. A linear relationship is found between probe tip velocity at penetration and probe bias position, showing the peak penetration force decreasing by ~2.5 µN with every 0.1m/s tip velocity increase.*

As shown in Fig. 6, with zero static force bias, the minimum tip velocity needed for penetration is v_p=0.82 m/s (actuated at f_p=14 kHz and V_a=126 V). This corresponds to a peak penetration force of 27.1 µN, or 48.5% reduction compared to the static penetration without vibration. Table 1 summarizes the calculated tip velocity and the associated peak penetration force at each fixed bias offset of the microinjector. In a series of experiments, we observed a linear decrease in the penetration force of ~2.5 µN with every 0.1m/s tip velocity increase.

In the second set of experiments, the vibration amplitude was kept constant and the injector was pushed into the embryo until penetration. Both peak and average penetration force were measured. Figure 7 shows the measured peak penetration force as a function of actuation voltage and frequency. Each of the 170 points on the surface represents an averaged peak penetration force measured on 3 to 5 embryos. The read-out of the total linear injection-stage displacement upon penetration is scaled with respect to the encoder pitch period to get the linear displacement d_0 between the two gratings, while the amplitude of microinjector vibration can be calculated based on the actuation frequency and voltage. The peak force can then be derived from the total relative displacement of the two gratings.

Both the average and the peak penetration force decreases as the driving frequency and/or actuation voltage increases. At fixed actuation voltage, the penetration force reached a minimum at the encoder resonant frequency of 14 kHz. At the maximum actuation

voltage of 150 V, the minimum tip velocity for penetration was 0.96 m/s. The minimum peak penetration force was 15.6 μN, ~29.7 % of the static penetration force, while the minimum average penetration force was 2.7 μN, ~ 5.1 % of the static penetration force.

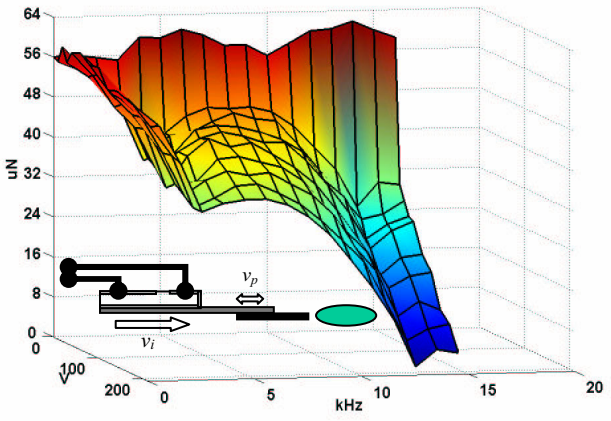

Figure 7. *The peak penetration force was measured over the frequency range f_i=0~16 kHz with the actuation voltage V_j varying from 0 to 150 volts. The average force was calculated based on injections on multiple embryos under each of the 170 experimental conditions (f_i, V_j). The penetration force reached its minimum at the encoder resonant frequency of 14 kHz.*

CONCLUSIONS

Minimally invasive microsurgical tools with integrated sensors are critical for a wide range of studies in biology and medicine, including calibrated trans-membrane delivery of genetic material into biological model systems, such as Drosophila embryos, to enable high throughput screening of gene functions. We demonstrated penetration force minimization through ultrasonically actuation of silicon-nitride microinjectors. The forces are measured using MEMS optical-encoder force sensors integrated with the microinjectors. Significant force reduction through dynamic tip-membrane interaction was achieved. For vibration-only operation, the force is reduced by 4.8% for every 0.1 m/s velocity increase. When the motion of the force probe is a combination of vibration at the encoder resonance and linear translation, the peak force is reduced by 70.3%, while the average force is reduced by 94.9% with respect to the force required for linear translation alone.

ACKNOWLEDGEMENTS

This project was funded by DARPA [Bio:Info:Micro] program (MDA972-00-1-0032). The device fabrication and characterization were performed at the National Nanofabrication Users Network (NNUN) facilities at the Center for Integrated systems and Edward L. Ginzton Lab at Stanford University. The authors wish to thank Matthew Fish for preparing Drosophila embryos for microinjection experiments.

REFERENCES

[1] A. Lal and R.M. White, "Micromachined Silicon Needle for Ultrasonic Surgery", Proc. of *IEEE Ultrason. Sym.*, 1593-95, 1995.

[2] A. Lal, "Silicon-based Ultrasonic Surgical Actuators", *Proc. of the 20th Annual International Conference of the IEEE Engineering in Medicine and Biology Society*, Piscataway, NJ, USA, 2785-90, vol. 6, 1998.

[3] X.J. Zhang, S. Zappe, R.W. Bernstein, O. Sahin, C.-C. Chen, M. Scott and O. Solgaard, "Integrated Optical Diffractive Micrograting-based Injection Force Sensor", *Proc. of the International Conference on Solid State Sensors and Actuators*, p1051-1054, Boston, USA, 2003.

[4] S. Zappe, X.J. Zhang, I.W. Jung, R.W. Bernstein, E. Furlong, M. Fish, M. Scott and O. Solgaard, "Micromachined Hollow Needle With Integrated Pressure Sensor For Precise, Calibrated Injection Into Cells and Embryos", *Proc. of the International Symposium on Miniaturized Chemical and Biochemical Analysis Systems*, vol.2, p682-684, November 3-7, Nara, Japan, 2002.

[5] R.W. Bernstein, X.J. Zhang, S. Zappe, M. Fish, M. Scott and O. Solgaard, "Characterization of Drosophila Embryos Immobilized by Fluidic Microassembly", *Proc. of the International Conference on Solid State Sensors and Actuators*, vol. 2, p987-990, June8-12, Boston, USA, 2003

[6] X.J. Zhang, C.C. Chen, R.W. Bernstein, S. Zappe, M.P. Scott and O. Solgaard, "Micro-optical Detection and Modeling of Microfluidic Self-assembly in Biology", *Journal of Microelectromechanical Systems* (in review).

[7] P.A. Sharp and P.D. Zamore, "RNA Interference", *Science* 287, 2430, 2000

[8] X.J. Zhang, S. Zappe, R.W. Bernstein, O. Sahin, C.-C. Chen, M. Scott and O. Solgaard, "Micromachined Silicon Force Sensor Based on Diffractive Optical Encoders for Characterization of Microinjection", *Sensors and Actuators, Phy. A*, in press, appeared online on January 22, 2004.

[9] J.W. Goodman, *Introduction to Fourier Optics*, 2nd ed., 1996.

[10] Drosophia embryos 50 minutes after hatching are dechlorinated in 60% bleach for 1.5 minutes and then rinsed thoroughly with water (20° C). Properly staged embryos are selected and desiccated for 15 min in a sealed glass jar containing calcium sulfate ($CaSO_4$) desiccant. Finally, embryos are covered in Halocarbon 700 oil (Aqua-Air Industries Inc., Harvey, LA) and ready for microinjection.

RF MEMS SWITCHES WITH METAL ALLOY ELECTRIC CONTACTS

Ronald A. Coutu, Jr.* **and Paul E. Kladitis**
Air Force Institute of Technology, AFIT/ENG, Wright Patterson AFB (WPAFB), OH, 45433

LaVern A. Starman
Air Force Research Laboratory – Sensors Directorate, Hanscom AFB, MA, 01731

Robert L. Crane
Air Force Research Laboratory – Materials and Manufacturing Directorate, WPAFB, OH, 45433

ABSTRACT

This paper is the first to report on the design, fabrication, and testing of radio frequency (RF) microelectromechanical systems (MEMS) contact switches with metal alloy electric contacts. The micro-switches in this study were fabricated with sputtered gold (Au)-platinum (Pt) (Au-(6%)Pt) and gold-palladium (Pd) (Au-(2%)Pd) alloy contact metals. For comparison, micro-switches with sputtered Au electric contacts were also fabricated and tested. The micro-switches with alloy electric contacts exhibited contact resistance (R_c) values between 1-2 Ω and switching lifetimes that were approximately 2-2.7 times greater than micro-switches with sputtered Au electric contacts.

INTRODUCTION

Reliable micro-switches with R_c < 1-2 Ω and capable of switching lifetimes > 10^8 "hot-switched" cycles are needed for future RF applications like space-based and phased array radar. Previous work concentrated on optimizing mechanical designs rather than investigating different electric contact metallurgies [**1**]. Notable exceptions are Majumder, et al.'s and Duffy, et al.'s utilization of "platinum group" and platinum (Pt) contact metals, respectively [**2**, **3**]. These metals were chosen over gold for their increased hardness and improved wear characteristics. In order to achieve acceptable contact resistance values, Majumder, et al.'s switches required multiple (i.e. 4 to 8), parallel contacts and were packaged in a hermetic environment while Duffy, et al.'s switches required high actuation voltages of > ~ 80 *V*. Schimkat studied gold-nickel (Ni) alloy (Au-(5%)Ni) macro-switch contacts in a low-force test configuration but not actual MEMS switches [**4**].

In this study, contact resistance and switching lifetime were investigated using MEMS test structures fabricated with sputtered metal contact materials. The alloys and compositions in this study were chosen to avoid two-phase regions, intermetallic compounds, high actuation voltages, and allow for the testing of un-packaged devices. These considerations help ensure that device fabrication is consistent and repeatable. The contributions of this work include: the design and fabrication of cantilever-style, series switches with sputtered Au and sputtered metal alloy electric contacts, the use of Au-(6%)Pt and Au-(2%)Pd alloys, the fabrication of hemispherical-shaped upper contacts using timed re-flow, and a comparison of measured pull-in voltage, contact resistance, and switch lifetime test results.

DESIGN AND FABRICATION

In metal contact micro-switches, initial switch closure is defined by the pull-in voltage. At pull-in, physical contact between the switch's electric contacts is established with minimal contact force. As the actuation voltage is increased, contact force increases resulting in lowered contact resistance [**5**]. Contact resistance and switch lifetimes were investigated using the cantilever test structures shown in Figures 1 and 2.

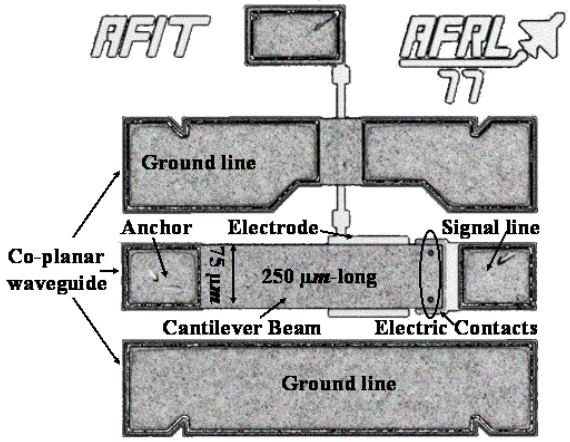

Figure 1. *Captured video image of an electrostatically actuated, cantilever-style, RF MEMS switch (*75 μ*m*-wide by 250 μ*m*-long*). The electric contacts located at the end of the beam and the actuation electrode's center is located 150* μ*m from the anchor.*

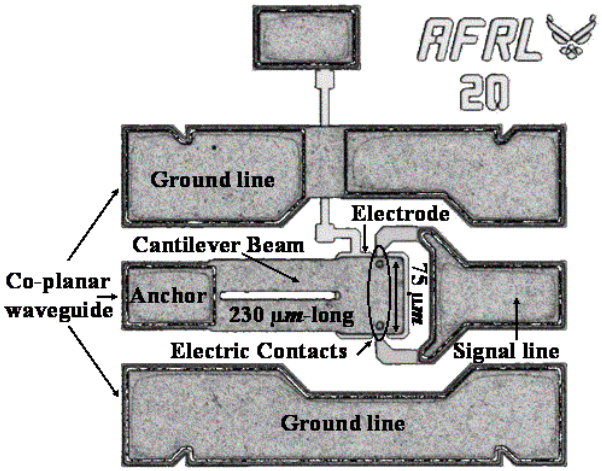

Figure 2. *Captured video image of an electrostatically actuated, cantilever-style, RF MEMS switch (*75 μ*m*-wide by 230 μ*m*-long*). The electric contacts and actuation electrode co-located near the end of the beam.*

* Corresponding Author: R. A. Coutu, Jr., AFIT/ENG, 2950 Hobson Way, WPAFB, OH, 45433
Tel: (937) 255-3636 ext 4595, Fax: (937) 656-4055, Email: ronald.coutu@afit.edu or ronald.coutu@wpafb.af.mil

0-9640024-5-0/hh2004/$20©2004TRF
DOI 10.31438/trf.hh2004.51

The effects of changing actuation voltages and applied contact force locations were investigated in this study. In the device shown in Figure 1 the electric contacts are located at the end of the beam while the center of the actuation electrode is located 150 μ*m* from the beam's anchor. The force placement in this design allows for mechanical cleaning (i.e. wiping) of the switch's electric contacts with each switch actuation. In addition, this design allows for overdriving the beam to collapse. In the Figure 2 device, the electric contacts and actuation electrode are co-located in the vicinity of the electric contacts (i.e. near the beam's end). This allows for the application of higher actuation voltage and consequently higher contact force without increasing the likelihood of collapsing the beam onto the bottom electrode.

The micro-switches in this study were fabricated as part of a co-planar waveguide (CPW) structure on highly resistive sapphire substrates. Three wafers of devices, each with different contact metals (i.e. sputtered Au, Au-(6%)Pt, and Au-(2%)Pd), were individually fabricated using the fabrication process illustrated in Figure 3. Refer to Figure 3 for the following discussion.

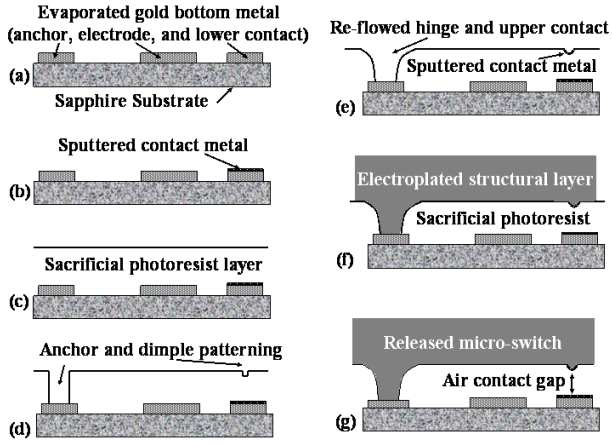

Figure 3. *Illustration of the micro-switch fabrication process.*

The actuation electrode and lower electric contact layers were approximately 3000 Å of evaporated Au patterned using a standard metal lift-off technique **(a)**. A thin (200 Å-thick) chromium (Cr) layer was used under the evaporated Au layer to help the Au remain adhered to the substrate. The lower electric contact metal was sputter deposited (500 Å-thick) and patterned using a metal lift-off technique **(b)**. Due to the conformal nature of sputtered materials, "wings" or raised metal "edges" shown in Figure 4, remain after performing sputtered metal lift-off.

The beam's gap or sacrificial layer was approximately 3 μ*m*-thick and created using MicroChem's polydimethylglutarimide (PMGI) based photoresist **(c)** [**6**]. The switch's hinge geometry was defined in the sacrificial photoresist using standard photolithography techniques while the upper contact geometries were defined by a partial expose and develop of the sacrificial photoresist layer **(d)**. A timed re-flow in an oven with flowing nitrogen was used to reform the dimple into a hemispherical-shaped upper contact bump **(e)**.

The upper contact metals were also sputter deposited (500 Å-thick), and patterned into the switch's dimple area using standard photolithography techniques **(e)**. The excess metal (outside of the dimple area), however, was removed using an etch-back technique, instead of lift-off, to avoid damaging the sacrificial photoresist layer. The upper contact material, located only on the hemispherical-shaped upper contact, is highlighted in Figure 4.

After electroplating the cantilever's gold structural layer (~ 5 μ*m*-thick) **(f)**, the devices were released using a CO_2 critical point dryer and tested to ensure proper operation and performance **(g)**.

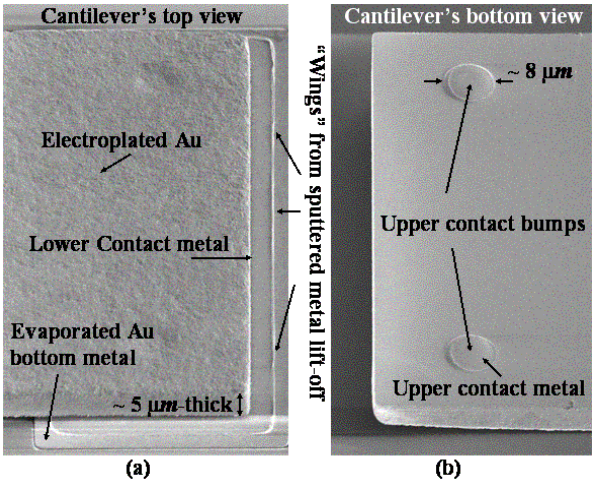

Figure 4. *Scanning electron micrograph (SEM) images of a 75 μm-wide by 250 μm-long beam: (a) top view (b) bottom view.*

Single-phase (i.e both elements have the same crystal structure) Au-(6%)Pt and Au-(2%)Pd metal alloy compositions were chosen as the electric contact materials to avoid two-phase regions (i.e. mixture of two different phases) and intermetallic compounds (i.e. crystal structure that is different from either element). The Au-Pt and Au-Pd phase diagrams for are provided in Figure 5 [**7**].

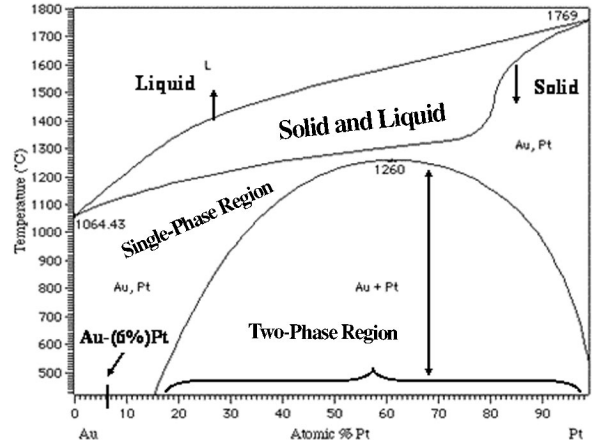

Figure 5*. Equilibrium binary alloy phase diagrams used for selecting single-phase (a) gold-platinum (Au-Pt) and (b) gold-palladium (Au-Pd) alloys.*

The Au-Ni alloy composition that Schimkat studied was a stable, two-phase material. Due to variations in metal alloy deposition processes (i.e. temp, pressure, etc.), however, this precise Au-Ni composition is difficult to reliably duplicate from fabrication run to fabrication run.

EXPERIMENTAL SETUP

A series of 20 micro-switches (10 Figure 1 and 10 Figure 2 designs) were tested on three different wafers (60 switches total) to experimentally characterize pull-in voltage, contact resistance, and switch lifetime. The experimental setup is illustrated in Figure 6.

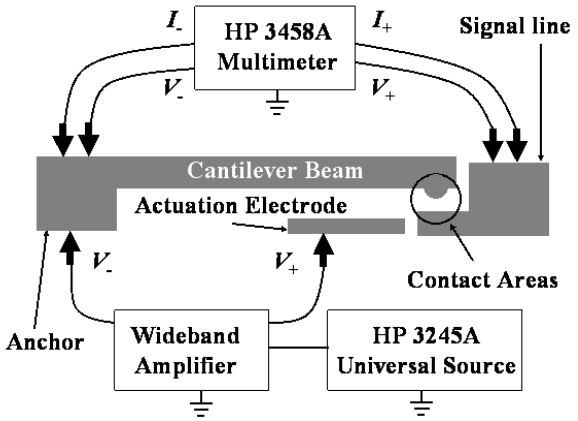

Figure 6. *Schematic illustration of the experimental setup used to measure pull-in voltage, contact resistance, and switch lifetimes. The micro-switch depicted is a Figure 1 style device.*

The micro-switches were tested by wafer probing using an Alessi Rel-4100A microprobe station with standard microprobes. The actuation voltage was applied using an HP 3245A universal source and a Krohn-Hite wideband amplifier. Closed switch resistance was measured using an HP 3458A multimeter in a four-point probe configuration. Contact resistance was found by subtracting the measured beam resistance from the closed switch resistance measurements.

During contact resistance testing, a voltage ranging from 0 to 110 *V* in 0.5 *V* increments was applied between the cantilever beam and the actuation electrode. The micro-switch closes when the actuation voltage exceeds the pull-in voltage (V_{pi}). As the applied voltage is increased, beyond the pull-in voltage, contact force increases and contact resistance decreases. Contact resistance data were collected each time the actuation voltage was incremented.

During lifecycle testing, the micro-switches were actuated with a 50% duty cycle square wave input. The waveform's "on" voltage level was set to V_{pi} plus approximately 1-5 *V* for increased contact force. The input waveform's frequency was set below the beam's resonant frequency. The micro-switches were cycled continuously until they failed open (i.e. infinite resistance) or closed (i.e. stuck down). Contact resistance data were collected every 30 seconds by increasing the input waveform's duty cycle to 90% and lowering its frequency to 1 *Hz* for 2 seconds. The multimeter's open circuit voltage of (~ 8.2 *V*) was present on the electric contacts for all the switching events (i.e. "hot-switching"). The success criteria for this testing was closed switch resistance of less than approximately 3 Ω and infinite open switch resistance.

RESULTS COMPARISON

Contact resistance versus actuation voltage data, for selected micro-switches, are plotted on Figure 7. The Figure 1 style micro-switch, with different contact metals, is compared on Figure 7(a) and the Figure 2 style micro-switch is compared on Figure 7(b).

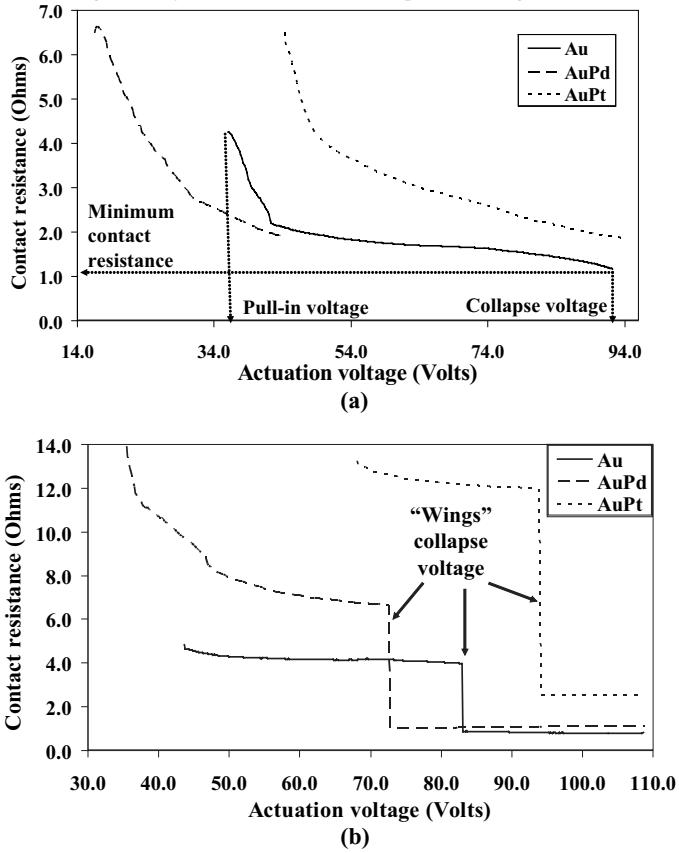

Figure 7. *Contact resistance vs. actuation voltage data plots for selected micro-switches: (a) Figure 1 design (b) Figure 2 design.*

Figure 7(a) (Figure 1 design) shows that pull-in and beam collapse voltages are located at the lower end of the voltage axis (higher contact resistance values) and the higher end of the voltage axis (lower contact resistance values), respectively. Minimum contact resistance is observed immediately prior to reaching the beam collapse voltage. Once the beam collapses onto the actuation electrode, the Figure 1 micro-switch shorts out and is no longer operable. The pull-in voltage, collapse voltage, and minimum contact resistance, for a Figure 1 micro-switch with sputtered Au electric contacts, are highlighted on Figure 7(a).

Figure 7(b) (Figure 2 design) shows pull-in voltages, located at the lower end of the voltage axis, and minimum contact resistance values, located at the higher end of the voltage axis. A sharp decrease in contact resistance, labeled as the *"wings" collapse voltage* on Figure 7(b), is observed. We believe that this anomaly was caused by the Figure 2 micro-switch upper contacts impacting the bottom contact "wings" prior to reaching the planar portion of the bottom contact. Bottom contact "wings" are illustrated on Figure 8(a). This anomaly did not cause the Figure 2 micro-switches to short because the electric contact bumps did not allow the beam to come into contact with the actuation electrode. Figure 1 micro-switches did not exhibit this anomaly because the bottom contacts were larger and the "wings" were ~20 µm away from the upper contact bumps. The larger Figure 1 bottom contacts are illustrated in Figure 8(b).

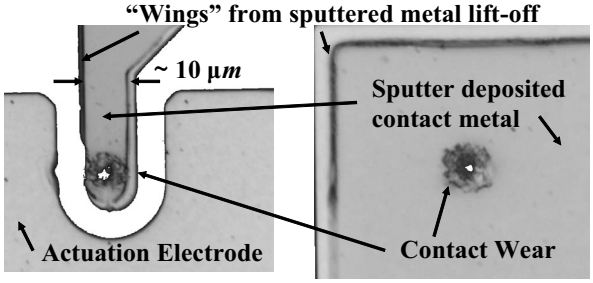

Figure 8. *A captured video image illustrating wear on Au-(6%)Pt lower electric contacts: (a) Figure 2 design and ~ 8.8*10^8 switch cycles (b) Figure 1 design and ~ 2.7*10^8 cycles.*

The pull-in voltages and minimum contact resistance values, depicted on Figure 7, are summarized in Table 1. As expected, the measured contact resistance values for micro-switches with metal alloy electric contacts was higher than for devices with Au electric contacts.

Table 1. *Summary of pull-in voltage (V_{pi}) and minimum contact resistance (R_c) measurements found on Figure 7.*

Contact Metals		V_{pi} (*V*)	Min. R_c (Ω)
Au	(Figure 1 design)	36.2	1.2
Au-(2%)Pd	(Figure 1 design)	16.5*	1.9
Au-(6%)Pt	(Figure 1 design)	44.3	1.9
Au	(Figure 2 design)	43.5 (83.3)**	3.9 (0.9)**
Au-(2%)Pd	(Figure 2 design)	28.7* (75.2)**	6.7 (1.0)**
Au-(6%)Pt	(Figure 2 design)	68.3 (94.1)**	11.7 (2.6)**

* Devices on this wafer exhibited lower pull-in voltage due to a thinner (3.2–4.2 μ*m*) than expected beam thickness.
** "Wings" collapse voltage and corresponding contact resistance.

Contact resistance versus switch cycle data, for selected micro-switches, are plotted on Figure 9.

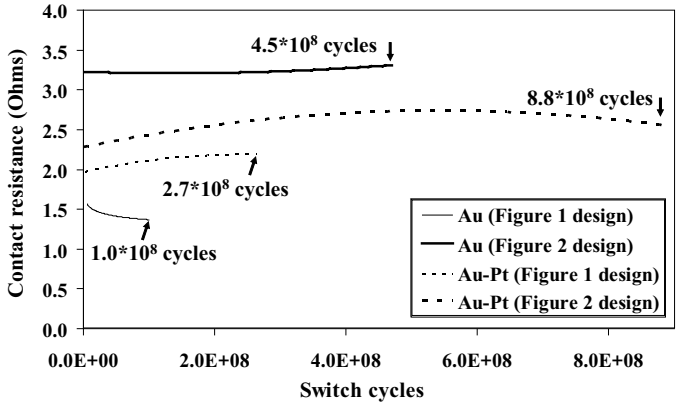

Figure 9. *Contact resistance vs. switch cycles data plots.*

The raw lifecycle data was curve fitted and the resulting trendlines were plotted on Figure 9. Micro-switches fabricated with Au-(2%)Pd electric contacts were not effectively lifecycle tested because all of the devices exhibited lower than usually restoring force due to a thinner than expected (~ 3.2–4.2 μm versus ~ 5 μm) electroplated Au beam thickness. The low restoring force is evidenced by the low measured pull-in voltages, for micro-switches on the Au-(2%)Pd wafer, that are illustrated in Figure 7 and summarized in Table 1.

Generally, micro-switches with Au electric contacts are limited to ~ 10^6 "hot-switched" cycles because evaporated Au (typical micro-switch bottom contact metal) is a soft metal and prone to wear [**2**]. Majumder, et al. reports greater than 10^7 "hot-switched" cycles and ~ 10^{11} "cold-switched" cycles for devices with "platinum group" electric contacts [**2**]. Duffy, et al. does not report lifetime results for their switches with Pt contacts [**3**].

The micro-switches with metal alloy electric contacts, in this study, were "hot-switched" and exhibited approximately 2-2.7 times longer lifetimes than devices with sputtered Au electric contact metals. This was most likely due to the increased material hardness of the sputtered metal alloys. Also, the switches with sputtered Au contacts, in this study, outperformed other micro-switches with evaporated Au contacts [**2**]. Once again, this was most likely due to the increased material hardness of the sputtered Au contact metals. The measured Meyer hardness of evaporated Au, sputtererd Au, and sputtered Au-(6%)Pt thin (500 Å) films were ~ 1 *GPa*, ~ 2 *GPa*, ~ 2.2 *GPa*, respectively.

CONCLUSIONS

The purpose of this work was to show the design, fabrication, and test results for micro-switches with metal alloy electric contacts, optimized for increased wear (> 10^8 "hot-switched" cycles), low contact resistance (1-2 Ω), and actuation voltages less than approximately 65 *V*. Overall, the results in this study show increased micro-switch wear performance at the expense of a small increase in contact resistance.

ACKNOWLEDGEMENTS

This work was sponsored by the Materials and Manufacturing Directorate, Air Force Research Laboratory, USAF, under project order number QGWSML02722002, POC: Dr. Robert L. Crane. The authors would like to acknowledge the Sensors Directorate, Air Force Research Laboratory, in particular, Dr. Rob Reid, Dr. Jack Ebel, Dr. Rick Strawser, Dr. Becky Cortez, and Dr. Kevin Leedy for switch design inputs and helping develop the custom micro-switch fabrication process.

REFERENCES

1. D. Peroulis et al., "Electromechanical Considerations in developing Low-Voltage RF MEMS Switches", *IEEE Trans.ns on Microwave Theory and Techniques*, **51**:1 (2003), pp. 259-270.
2. S. Majumder et al., "MEMS Switches", *IEEE Instrumentation and Measurement Magazine*, Mar 2003, pp. 12-15.
3. S. Duffy et al., "MEMS Microswitches for Reconfigurable Microwave Circuitry", *IEEE Wireless and Components Letters*, **11**:3 (2001), pp. 106-108.
4. J. Schimkat, "Contact measurements providing basic design data for microrelay actuator", *Sensors and Actuators, A*., **73** (1999), pp. 138-143.
5. R. Holm, Electric Contacts: Theory and Applications, (Berlin, Springer, 1967).
6. MicroChem Corp., http://www.microchem.com, 2003.
7. H. Baker, ed., ASM Handbook Volume 3 Alloy Phase Diagrams, (Ohio, ASM International, 1992).

SILICON CARBIDE FOR ENHANCED MEMS RELIABILITY

Di Gao, W. Robert Ashurst, Carlo Carraro,
Berkeley Sensor & Actuator Center, Department of Chemical Engineering, University of California Berkeley, CA 94720

Roger T. Howe
Departments of Electrical Engineering and Computer Sciences and Mechanical Engineering, University of California, Berkeley, CA 94720

Roya Maboudian
Department of Chemical Engineering, University of California, Berkeley, CA 94720

ABSTRACT

The tribological characteristics of SiC films, both as a structural material and as a thin passivating coating, are characterized using micromachined cantilever beam arrays, doubly clamped beams, and sidewall adhesion and friction testers. Our results indicate that using SiC as the substrate or structural layer or thin film coating significantly reduces stiction of free-standing structures to the substrate, and virtually eliminates stiction and wear of sidewall MEMS structures.

INTRODUCTION

A major reliability problem with silicon-based MEMS is unwanted adhesion, friction and wear (collectively called tribology). Adhesion, which is also referred to as "stiction" in MEMS research community, results from the dominance of surface forces, such as capillary, chemical, electrostatic, or van der Waals, over body forces at the micrometer scale. Stiction can be categorized into two classes: release stiction and in-use stiction. Release stiction occurs during the release step of MEMS devices, where the sacrificial material is removed in liquid etchants and the microstructures are subsequently dried. During the drying process, the liquid capillary forces produced at the liquid-vapor interface are sufficient to draw compliant microstructure surfaces into contact and cause stiction. The stiction remains if the restoring force generated by the micromechanical structure is not large enough to overcome the adhesion. Release stiction problems are most commonly solved by designing new processes to dry the MEMS devices without creating the liquid-vapor interface (such as critical point drying technique), and modifying the surface texture to reduce the contact area (such as roughening the surfaces and using dimples) or changing the water meniscus shape (such as self-assembled monolayer coating technique). Although release stiction can be avoided using these techniques, microstructure surfaces may still come into contact and impact or shear against each other when the device is in operation, in storage or improperly handled after the release stage, which may lead to the second class of stiction, in-use stiction. The in-use stiction poses a great threat to MEMS reliability, and in most cases requires surface modification of the structural material to prevent it from occurring.

To date, coating the MEMS devices with either solution-based or vapor-based anti-stiction monolayers appears to be an effective method to overcome the in-use stiction problem. However, some microstructures, such as the hubs on microgears, experience tremendous wear in operation, which is another issue that plagues the MEMS reliability. Although some of the anti-stiction monolayers are shown to significantly reduce the static friction between the sliding surfaces, they are susceptible to large number of wear cycles. Therefore, the integration of hard materials, as either structural or coating layers, into MEMS technology is of great interest to the current research on the wear issue in MEMS. One approach is to find a material that can be processed by microfabrication methodologies, and is able to reduce the in-use stiction and to provide wear resistance simultaneously. SiC is one such promising material. Recent advances in polycrystalline SiC technology for MEMS [**1,2**] enable the use of SiC both as a structural layer and as a thin passivating coating for MEMS devices. In this paper, we report on the tribological characteristics of SiC films for enhanced MEMS reliability. These include the characterization of SiC-to-Si and SiC-to-SiC stiction, as well as the effectiveness of SiC as a wear resistant coating material. In addition, SiC-to-SiC sidewall stiction is examined. Our results indicate that using SiC as the substrate or structural layer or thin film coating significantly reduces stiction of free-standing structures to the substrate, and virtually eliminates stiction and wear of sidewall MEMS structures.

EXPERIMENTAL DETAILS

The SiC films used in our experiment are deposited by a low-pressure chemical vapor deposition (LPCVD) process at 800 °C using a single precursor 1,3-disilabutane (DSB) in a commercial 3-inch horizontally oriented hot-wall tubular reactor (TekVac CVD-300-M). Details of the LPCVD process are described elsewhere [**3**]. When the SiC films are used as substrate or structural materials, hydrogen-diluted ammonia (5% NH_3 in H_2) is introduced to the reactor along with the precursor DSB (with flow rate ratio of 1:5 for diluted NH_3 to DSB) to dope the SiC films. The resistivity of the SiC films is about 45 mΩ·cm in experiments reported here. The SiC films are etched using HBr/Cl_2 transformer coupled plasmas (TCP) in a commercial LAM TCP 9400 etcher [**4**]. The etch process parameters are chosen so that relatively straight SiC sidewalls are obtained.

Cantilever beam arrays (CBA) and doubly clamped beams are employed to characterize the SiC-to-Si and SiC-to-SiC stiction when SiC is used either as the structural or substrate material. Specifically, structures with the following combinations of structural and substrate materials are fabricated and tested: SiC on polycrystalline Si (poly-Si), SiC on SiC, and poly-Si on SiC. As a comparison, stiction of poly-Si structures to poly-Si substrate is also examined. To characterize the stiction of SiC-to-SiC sidewalls, sidewall stiction testing structures are employed. Such a structure consists of a doubly clamped beam and an anchored pad with one side of their sidewalls facing each other. Schematic views of these testing structures are shown in Fig. 1. The fabrication of these structures involves the following steps: (i) deposition of the substrate material (~1 μm thick) on Si wafers, (ii) deposition of sacrificial silicon oxide (~2 μm thick), (iii) deposition of the structural material (~2 μm thick), (iv) patterning the structures using one mask photolithography, and (v) etching of the structural

Travel support has been generously provided by the Transducers Research Foundation and by the DARPA MEMS and DARPA BioFlips programs.

0-9640024-5-0/hh2004/$20©2004TRF
DOI 10.31438/trf.hh2004.52

Solid-State Sensors, Actuators, and Microsystems Workshop
Hilton Head Island, South Carolina, June 6-10, 2004

material. All the test structures are released by time-etching the sacrificial silicon oxide in 49% HF aqueous solution, followed by rinsing with deionized water and isopropanol. They are dried in air of normal laboratory ambient (20 °C and 40% relative humidity) to examine the release stiction. To characterize the in-use stiction, the surfaces to be examined are manually pushed into contact by a tungsten probe while sustaining the contact pressure for several seconds. Some testing parts adhered together due to the release stiction are manually separated using tungsten probes before investigating the in-use stiction. The residual strain information for the structural layer is obtained from the strain gauges fabricated around the stiction testing structures to provide parameters for the calculation of the apparent work of adhesion [**5**].

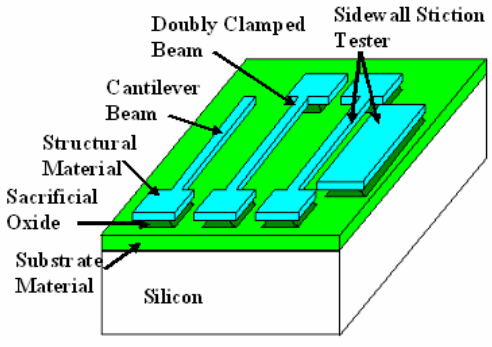

Figure 1. *A schematic view of the testing structures employed to characterize the stiction of the structural material to the substrate (cantilever beam and doubly clamped beam), and the sidewall stiction of the structural material (sidewall stiction tester).*

To evaluate the effectiveness of SiC as a coating material, sidewall friction testers fabricated from poly-Si are coated conformally with a thin SiC coating. The design and the testing scheme of the sidewall friction testers are detailed elsewhere. [**6**]. Briefly, the device consists of a fixed post and a flexible beam. The beam is pulled to contact and rub against the post during the wear test. Before the structures are encapsulated with SiC, poly-Si sidewall friction testers are released and coated with an octadecene-based monolayer to avoid the stiction and to protect the poly-Si surface from being oxidized by air [**7**]. The samples are next transferred into the LPCVD reactor and coated with ~40 nm SiC films. The SiC films are not doped when used as coating materials in these experiments. With these devices, the static friction coefficient of the SiC films is obtained as a function of the wear cycles and compared with that of the native oxide on poly-Si surfaces.

The probing system used for all micromachine actuation is a Lucas-Signatone S-1160 with a Mitutoyo FineScope 60 microscope, equipped with a Sony CCD-IRIS camera. A Nomarski style differential interference contrast prism (manufactured by Olympus) is used with a Mitutoyo M Plan Apo 10× objective on the microscope to measure the detachment length of CBA. The testing structures are also examined by scanning electron microscopy (SEM) afterwards.

RESULTS AND DISCUSSION

CBA with poly-Si beams (0.1 to 1.5 mm long, 10 μm wide, 2 μm thick and 2 μm away from the substrate) are fabricated on both poly-Si and SiC substrates and tested. The in-use stiction results for poly-Si to poly-Si and poly-Si to SiC contacts are listed in Table 1. The apparent work of adhesion is calculated from the detachment length using Eqn. (1) [**8**].

$$\gamma_s = \frac{3Et^3h^2}{8l^4}, \qquad (1)$$

where γ_s is the apparent work of adhesion, E is the Young's modulus of the structural material, h is the thickness of the sacrificial layer, t is the thickness of the beam, and l is the detachment length.

Table 1*. In-use stiction results for contacts of poly-Si to Si and poly-Si to SiC surfaces. The apparent work of adhesion is calculated from the detachment length of cantilever beams.*

Structural Material	Substrate Material	Treatment	Cantilever Beams	
			Detachment Length (μm)	Apparent Work of Adhesion (mJ/m^2)
poly-Si	poly-Si	After release	200	20
poly-Si	SiC	After release	>1500	<0.006
		After exposed to room air for 1 week	>1500	<0.006
		After exposed to room air for 2 weeks	1000	0.034

It is observed that the apparent work of adhesion of newly released poly-Si to SiC contacts is more than 4 orders of magnitude less than that of poly-Si to poly-Si contacts, which makes the detachment length of cantilever beams more than 1.5 mm long. The detachment length only begins to decrease (and hence, the work of adhesion to increase) after the structure is exposed to room air (40% relative humidity) for two weeks. Even then, the replacement of poly-Si with SiC still significantly reduces the stiction of MEMS structures. We expect that under hermetic encapsulation, SiC will retain its extremely low stiction characteristics indefinitely.

The AFM image of the SiC film as a substrate material is shown in Fig. 2. We believe that the relatively rough surface and the film topography with sharp spikes contribute significantly to the reduced in-use stiction.

Due to the relatively high residual strain gradient (8×10^{-5} μm^{-1}) of the SiC films, SiC cantilever beams curve down, making the stiction characterization by CBA impractical. Doubly clamped SiC beams (0.5 to 4 mm long, 10 μm wide, 2 μm thick and 2 μm away from the substrate) are also present on the mask set. All the doubly clamped SiC beams up to 4 mm-long (the longest on the mask set) on both Si and SiC substrates are found to be free-standing after being released and dried in air without employing the critical point drying technique, and remain stiction-free after manually pushing into contact with the substrate (Fig. 3). Since no beam was observed to adhere to the substrate, the detachment length could not be determined. If one assumed it to be equal to the length of the longest beam in the mask set, one would determine an upper bound to the apparent work of adhesion from Eqn. (2) after taking the residual strain ε_R into account [**8**]:

$$\gamma_s = \frac{128Et^3h^2}{5l^4}\left[1+\frac{4l^2}{21t^2}\varepsilon_R+\frac{256}{2205}\left(\frac{h}{t}\right)^2\right]. \qquad (2)$$

Because of the large residual strain of the SiC films (1.14×10^{-3}), the upper bound to the apparent work of adhesion is found to be

~7 mJ/m^2 versus about 20 mJ/m^2 for Si-to-Si contacts. Although the actual apparent work of adhesion for SiC-to-Si and SiC-to-SiC contact is not acquired from this set of experiments, the result is still promising for SiC MEMS devices with clamped-clamped structures, which are very likely free of both release and in-use stiction.

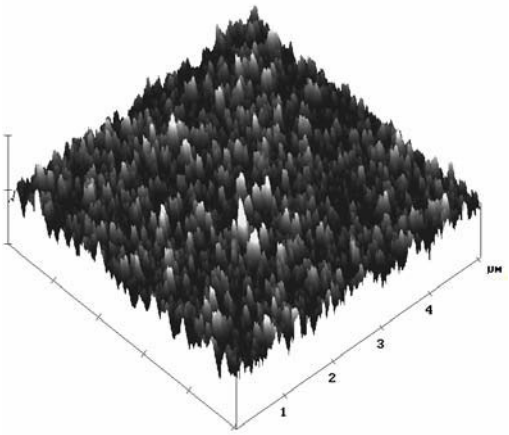

Figure 2. *AFM image of the SiC film as a substrate material. The SiC film is about 1 μm thick, and has a RMS roughness of 12.4 nm. The scan size is 5x5 μm, and vertical scale bar is 100 nm.*

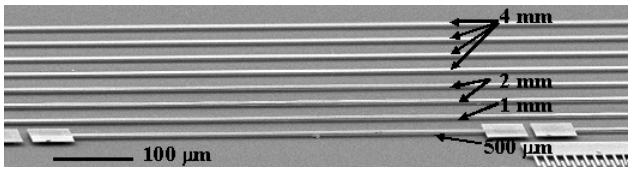

Figure 3. *SiC doubly clamped beams up to 4 mm long on Si substrates. The beams are free-standing after being released and dried in air (without employing the critical point drying technique), and remain stiction-free after manually pushing them into contact with the substrate.*

Figure 4 shows the SiC sidewall stiction testers after they are released and manually actuated. The doubly clamped beams are 0.5 to 4 mm long, 2 μm wide, 2 μm thick and 2 μm away from the fixed sidewall. Similar to the in-plane stiction testing, stiction on the SiC-to-SiC sidewall is not observed either upon release and drying, or upon manual actuation.

Sidewall friction testers (Fig. 5) fabricated from poly-Si are tested with and without SiC coating. The SEM image of a rubbing beam of a SiC-coated side-wall friction tester after 1 million wear cycles is shown in Fig. 6(a). Another rubbing beam without any coating which has failed due to high friction and wear after about 11,000 cycles is shown in Fig. 6(b). By comparing these two images, one can clearly see the wear debris and the worn surface of poly-Si without SiC coating, which are not obviously observed with SiC coating. This observation is consistent with earlier reports of enhanced wear resistance observed by AFM studies on 3C-SiC coated Si (deposited by dual precursor APCVD method) compared to uncoated Si [**9**]. It is postulated that the enhanced wear resistance of the SiC film is due to the higher hardness and fracture toughness of SiC.

Static friction coefficient as a function of rubbing cycle is reported in Fig. 7 and compared to the base line of Si-to-Si contact (i.e., without SiC coating). As is observed, without any coating, the friction coefficient increases as the wear cycles increase and the device fails after 11,000 cycles. But with a thin SiC coating, the device still works after a million rubbing cycles, and the friction coefficient first decreases and then stabilizes as the number of wear cycles increases, indicative of the self-lubricating characteristics of SiC. A similar behavior has been reported previously when SiC-SiC contacts are exposed to oxygen with partial pressures greater than 1 Pa [**10**]. The authors attribute the tribochemically generated lubrication to the sp^2-hybridized carbon. We suggest that a similar phenomenon might be responsible for the observed reduction in the friction coefficient in our experiments.

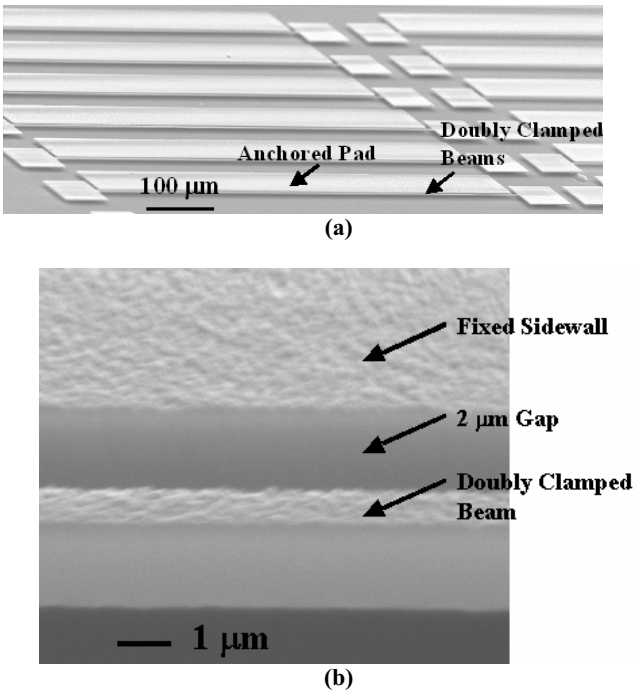

Figure 4. ***(a)*** *The SiC-to-SiC sidewall stiction testers. The SiC doubly clamped beams are 0.5 to 4 mm long, 2 μm thick, and 2 μm wide and separated from the anchored sidewalls by 2 μm. Only the 0.5 mm long testers are shown in this image.* ***(b)*** *A close-up of the sidewalls and gap of the tester in (a). Stiction is never observed either upon release and drying in air, or upon manual actuation of these testers.*

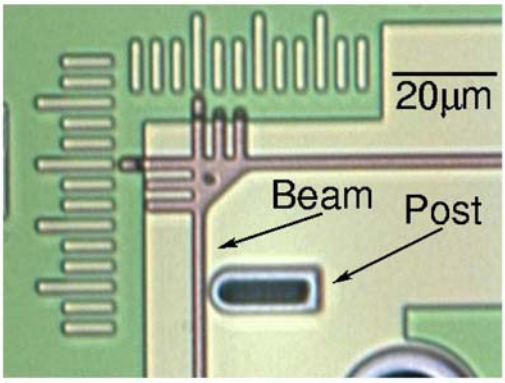

Figure 5. *An optical image of the contacting parts of the sidewall friction tester.*

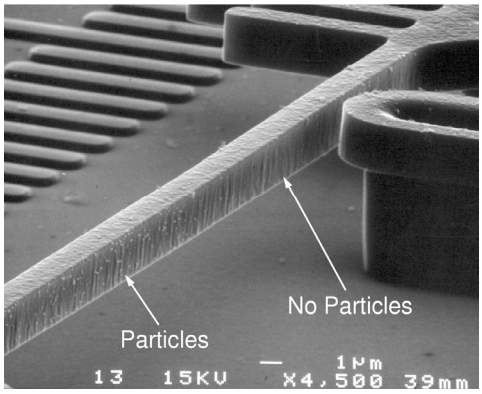

(a)

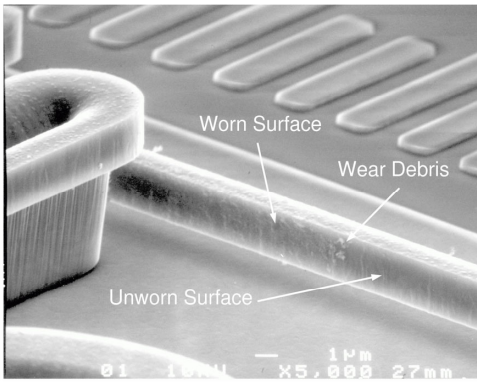

(b)

Figure 6. *(a) SEM image of the rubbing beam of a SiC-coated side-wall friction tester after 1 million wear cycles. Note the absence of wear scarring or debris formation on the beam. (b) SEM of the tester without any coating which has failed due to high friction and wear after about 11,000 cycles. Note the wear debris in this case.*

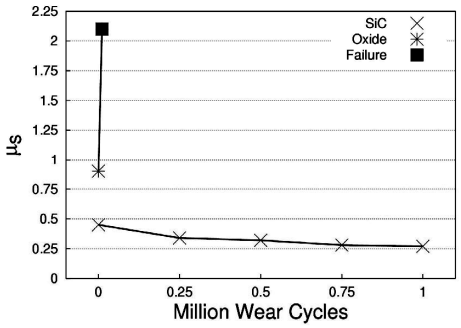

Figure 7. *Wear information for sidewall friction testers with various surface treatments. In the case of oxide samples, the last data point represents failure of the device. The SiC device was not observed to fail by wear.*

CONCLUSIONS

We have investigated the stiction, friction, and wear characteristics of SiC films, when used as structural materials and as thin coatings for MEMS devices. Our results indicate that using SiC as the substrate or structural layer significantly reduces the in-use stiction of MEMS structures, and the application of a thin coating of SiC can dramatically improve the wear resistance of MEMS devices. In addition, self-lubricating phenomenon is observed for SiC-SiC sidewall contacts during wear and friction testing.

ACKNOWLEDGMENT

The authors wish to thank Dr. Muthu Wijesundara for his assistance with the SiC film deposition. The financial support of DARPA MTO NMASP and MPG programs and the Sandia National Laboratories is gratefully acknowledged. One of the authors (D. Gao) acknowledges additional support from the Applied Materials, Inc. in the form of a graduate fellowship.

REFERENCES

1. C. R. Stoldt, C. Carraro, W. R. Ashurst, D. Gao, R. T. Howe and R. Maboudian, "A Low-Temperature CVD Process for Silicon Carbide MEMS," *Sensor Actuat. A*, vol. 97, 410 (2002).

2. D. Gao, M.B.J. Wijesundara, C. Carraro, C. W. Low, R. T. Howe, and R. Maboudian, "High Modulus Polycrystalline 3C-SiC Technology For RF MEMS," in *Proc. Transducers'03*, *The 12th Int. Conf. Solid-State Sensors & Actuators* (2003), pp.1160-1163.

3. M.B.J. Wijesundara, G. Valente, W. R. Ashurst, R. T. Howe, A.P. Pisano, C. Carraro, and R. Maboudian,"Single-source chemical vapor deposition of 3C-SiC films in a LPCVD reactor I. Growth, structure, and chemical characterization," *J. Electrochem. Soc., 151* (3), C210 (2004).

4. D. Gao, R. T. Howe, and R. Maboudian, "High-selectivity Etching of Polycrystalline 3C-SiC Films using HBr-based Transformer Coupled Plasma," *Appl. Phys. Lett*., *82(11)*, 1742 (2003).

5. D. Gao, M.B.J. Wijesundara, R. T. Howe, and R. Maboudian, "Characterization of Residual Strain in SiC Films Deposited using 1,3-Disilabutane for MEMS Applications," *J. Microlithography, Microfabrication, & Microsystems*, 2 (4), 259 (2003).

6. W. R. Ashurst, C. Yau, C. Carraro, R. Maboudian, and M. T. Dugger, "Dichlorodimethylsilane as an anti-stiction monolayer for MEMS: A comparison to the octadecyltrichlosilane self-assembled monolayers," *J. Microelectromech. Syst. 10 (1)*, 41 (2001).

7. W. R. Ashurst, C. Yau, C. Carrao, C. Lee, G. J. Kluth, R. T. Howe, and R. Maboudian, "Alkene based monolayer films as anti-stiction coatings for polysilicon MEMS," *Sensors and Actuators A* 91, 239 (2001).

8. C. H. Mastrangelo, "Adhesion-related failure mechanisms in micromechanical devices," *Tribol. Lett., 3*, 223 (1997).

9. S. Sundararajan, and B. Bhushan, "Micro/nanotribological studies of polysilicon and SiC films for MEMS applications," *Wear, 217*, 251 (1998).

10. J. M. Martin, and T. le Mogne, "Interpretation of friction and wear of ceramics in terms of surface analysis," *Surface and Coatings Technology, 49,* 427, (1991).

EXPERIMENTAL VALIDATION OF MECHANICS-BASED PROCESS MODELS FOR DIRECT WAFER BONDING

Kevin T. Turner and S. Mark Spearing
Massachusetts Institute of Technology
Cambridge, MA 02139

ABSTRACT

Direct wafer bonding, also known as fusion bonding, is a common technique used in the fabrication of microsystems. While the process adds tremendous design flexibility, establishing robust processes has often proved to be a challenge. A mechanics-based model to predict failure in direct wafer bonding processes is reported in this work. An energy-based bonding criterion was implemented in a finite element model to allow the shape and size of the bonded area to be predicted as a function of the wafer geometry, etch patterns, elastic properties, and surface chemistry. The modeling approach has been validated through experiments in which the bonded area was predicted across a series of bonded wafers with specific etch patterns and wafer-scale flatness variations. The modeling approach and experiments reported establish a basis for developing advanced mechanics-based process models for wafer bonding.

INTRODUCTION

Direct wafer bonding is an important technology in the manufacture of microsystems. It significantly increases design flexibility, permits the construction of three-dimensional devices, and allows for the integration of dissimilar materials. Direct bonding is not a new technology, originally developed for the fabrication of silicon-on-insulator substrates, the technology has been widely adopted by researchers developing micro-electromechanical systems. A range of devices have been realized using direct bonding, including pressure sensors [1], accelerometers, and microfluidic systems [2]. While the technology offers significant benefits and has been demonstrated in numerous devices, process failures have increased as the technique has been employed in the fabrication of more complex devices. In particular, the bonding of multiple wafers has presented significant challenges, as high yields are required in each step and the process is fundamentally more difficult because of the thicker and hence stiffer pieces that must be bonded [3]. The process is further complicated by the need to bond wafers with a high fraction of etched area, which reduces the surface energy available to drive the process, or deposited residually stressed films on the surface, which may increase the surface roughness and deform the wafer. These various factors combine to significantly reduce the process window and make process development considerably more difficult.

Challenges such as these have been acknowledged and empirical solutions developed for specific devices [3]. However, solutions such as these are often time consuming, expensive to develop, and do not readily translate to processes for other devices. As such, there is a clear need to have a fundamental understanding of the direct bonding process and how factors such as etch patterns, wafer geometry (thickness, bow, warp, surface waviness), surface energy, and bonding tools effect process yield. A quantitative understanding of such factors would permit models to be developed that would enable intelligent device and process design and allow tolerances to be set such that pre-bond metrology can be employed. The current work reports a numerical model and experiments that demonstrates the effects of wafer geometry and etch patterns may be quantified using a mechanics-based approach.

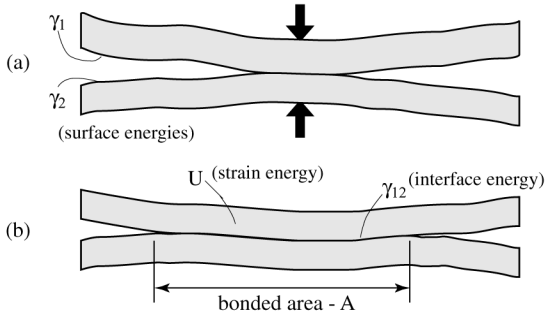

Figure 1. *Schematic of wafer deformation during direct bonding.*

THEORY AND MODELING

The basics of the direct bonding process have been understood for some time [4]. In the process, two flat and smooth wafers are initially contacted at room temperature, bond via the formation of short-range van der Waals and hydrogen bonds, and are then subsequently annealed to strengthen the interface. As it is undesirable to apply pressure during the thermal treatment step, it is critical that the wafer surfaces are held in intimate contact by the room temperature bond. Success in the room temperature bond step is contingent on the fact that the surface forces are sufficient to bring the wafers into contact. Wafers are typically not flat (surface waviness, bow, and warp) and as such they must elastically deform to a common shape (Fig. 1) during the bonding process. This fact was recognized early and researchers developed simple expressions that compare the total strain energy required to form a bond to the surface energy available to do so [4,5]. While these expressions demonstrate the essential scaling of bonding difficulty with the geometry and elastic properties of the wafers, they do not provide a clear route to quantitatively connect these factors to bonding failure. These simple expressions proved sufficient for almost a decade, as the majority of bonding processes being developed typically only required the bonding of two prime grade silicon wafers, a relatively easy task that is typically not limited by flatness variations. As more complicated bonding processes have been attempted though [3], it has become clear that a better understanding of the mechanics of the process is required.

A quantitative modeling framework that allows wafer geometry, etch patterns, and surface energy to be related directly to size of the bonded area was reported by current authors in [6]. This modeling framework is based on energy considerations as well, but rather than simply considering the total strain energy as was done in [4], the strain energy per unit area required to advance the bond front was considered. This approach is essentially the application of fracture mechanics to an adhesion problem and is similar to analyses that have been employed in the assessment of stiction in surface micromachined structures [i.e. 7]. As described in [6], the criterion for bond advance is,

$$\frac{dU}{dA} \le W, \tag{1}$$

Travel support has been generously provided by the Transducers Research Foundation and by the DARPA MEMS and DARPA BioFlips programs.

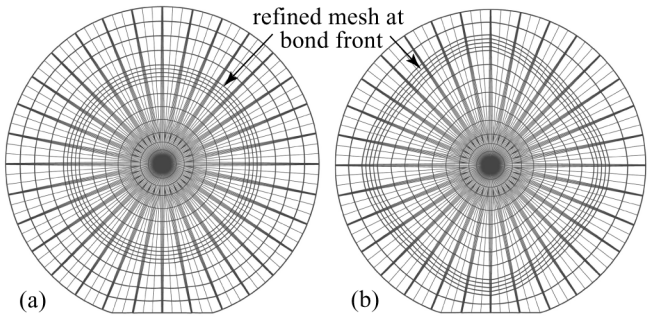

Figure 2. *Top view of finite element mesh before (a) and after (b) iteration to determine the equilibrium bond front position.*

where U is the strain energy, A is the bond area, and W is the work of adhesion ($W=\gamma_1+\gamma_2-\gamma_{12}$). The term dU/dA, the strain energy accumulation rate, is a function of the geometry, elastic properties, and mounting of the wafers and represents the strain energy accumulated in the wafers as the bond advances. In previous work, the case of bonding wafers with axisymmetric curvature (wafer bow) was examined and dU/dA was calculated analytically [6,8]. While that work demonstrated the impact that wafer-scale shape variations, etch patterns, and mounting can have on bonding, only qualitative agreement between the analytical model and experiments was achieved [9].

The primary factor that resulted in the differences between the model and experiments in [9] was that the model was axisymmetric, while the wafers in the experiments were asymmetric. In order to obtain better agreement between the model and experiments and to permit the modeling framework proposed in [6] to be applied to real cases with arbitrary geometries and etch patterns, a finite element implementation of Eq. (1) has been developed and is reported here.

The chief difficulty with predicting bonded areas in wafer pairs with asymmetric shape and etch patterns is that the size and shape of the bond front are not known a priori (in the axisymmetric case, the shape of front is known to be circular). The bond area shape and size is determined by the requirement that equilibrium is satisfied along the entire bond front. This requires that $dU/dA=W$ at all points on the bond front. To implement this criterion for a wafer with an arbitrary shape and etch pattern a three dimensional finite element model that allows for dU/dA to be calculated locally along the bond front and for the equilibrium bond shape and size to be determined iteratively was developed.

The bonding of wafers with asymmetric shape and an axisymmetric spoke etch pattern (Fig. 5(b)) was considered. A three-dimensional finite element model with the mesh shown in Fig. 2 was constructed. The wafers have a 100 mm diameter, a 32.5 mm long flat along the [110] direction, and the anisotropic elastic properties of silicon. The spoke pattern was defined in the mesh and consisted of a central un-etched area with a 7 mm radius and 32 spokes that narrow in width from approximately 1.37 mm at r=7 mm to 0.41 mm at r=50 mm. The mesh around the bond front was refined. The shape and thickness of the two wafers in the pair were defined from measurements on actual wafers. The model consisted of two elements through the thickness of each wafer and the in-plane distribution shown in Fig. 2. All elements were 20 node solid elements and the mesh density was selected after extensive convergence studies. The mesh was created using a MATLAB script and was solved using the commercial finite element package ABAQUS.

The strain energy accumulation rate, dU/dA, was calculated locally along the bond front by adapting the virtual crack closure technique (VCCT) that is commonly used in fracture mechanics to compute the strain energy release rate [10]. Using the VCCT, dU/dA may be calculated along the bond front from the reaction forces, F, and the gap between the wafer surfaces, δ, at the nodes of the elements immediately behind and ahead of the bond front,

$$\frac{dU}{dA}=\frac{1}{2}\frac{F_i\delta_i}{\Delta A}, \qquad (2)$$

where ΔA is an area that depends on the element size. Equation (2) is the basic formulation, the exact reaction forces and gaps that are included in the calculation depend on the position of the node (mid-side or corner) and the element type. A comprehensive list of VCCT equations for standard elements may be found in [10]. The expressions in [10] for the VCCT have been developed for fracture analyses. The only change that must be made when applying these equations to an adhesion analysis is in the calculation of the gap ahead of the bond front. For fracture problems, $\delta=u_A-u_B$, where u_A and u_B are the nodal displacements of wafer A and B. In adhesion analyses, there is an initial gap between the nodes at the interface, δ_o, that must be accounted for, $\delta=\delta_o+u_A-u_B$. The VCCT was chosen as it allows dU/dA to be calculated locally along a given bond front from a single finite element solution without significant mesh refinement.

The position of the nodes along bond front must be varied in a systematic fashion to determine the equilibrium size and shape. This was accomplished using a quasi-Netwon iteration scheme that was based on work in [11] for predicting crack growth in composites. In this approach, an initial bond shape is assumed, dU/dA is calculated locally along the bond front using the VCCT, and the equilibrium convergence criterion $dU/dA=W$+/-1% is checked. If the front is not in equilibrium, a new bond front position is calculated and dU/dA is evaluated along the new front. This procedure is repeated until convergence is achieved – typically 20-50 iterations are required.

Figures 2, 3, and 4 show an example of this modeling process for a real wafer pair. Figure 2(a) shows the initial mesh with an assumed circular bond front. Figure 3 shows maps of the shapes of the two wafers used in this example. One wafer has a large and nearly axisymmetric curvature due to the presence of a residually stressed film while the other has an asymmetric shape variation that is a result of the wafer manufacturing process. Using the model, the shape of front is iterated from the initial assumed shape, Fig. 2(a), to the equilibrium shape, Fig. 2(b). By running the model multiple times for different work of adhesions, the bonded area may be mapped out as a function of W. Figure 4 shows the predicted positions of the bond front for several different values of work of adhesion for the wafer pair shown in Fig. 3.

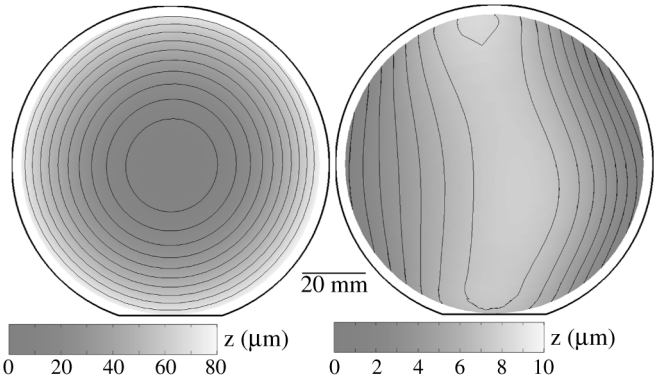

Figure 3. *An example shape measurements of two 100 mm silicon wafers. The 'shape' is defined as the distance between (out-of-plane) the wafer and a reference plane.*

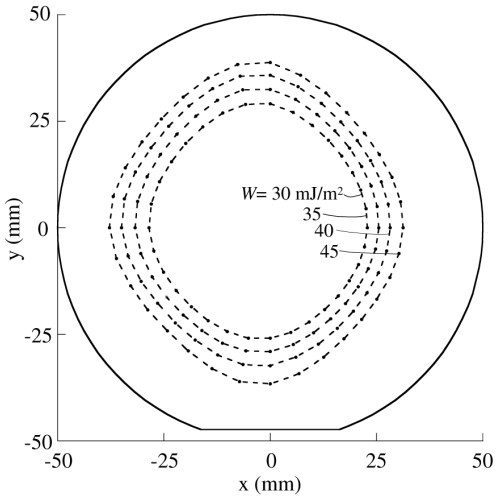

Figure 4. *Predicted bond fronts for the wafer pair shown in Fig. 3 for work of adhesion values from 30-45 mJ/m^2.*

EXPERIMENTAL DETAILS

Experiments were conducted in which two 525 μm thick, 100 mm, (100) silicon wafers were bonded. The basic experimental configuration, which consisted of one nominally flat wafer with a shallow etch pattern bonded to a wafer with a tensile stressed silicon nitride film on the back surface, is shown in Fig. 5(a). The thickness of the nitride film was varied to obtain different levels of wafer shape. The pattern shown in Fig. 5(b) was etched 2-3 μm deep into one wafer in the pair using deep reactive ion etching. The wafers were cleaned immediately prior to bonding using a standard RCA clean to yield a hydrophilic surface.

The wafers were bonded at room temperature by supporting the wafers at the center and initiating contact with a small pressure. The resulting bond was imaged using a standard IR transmission inspection system [2]. The geometry of each wafer was measured on a commercially available capacitance gage (ADE 9900, ADE Corp., Westwood, MA) that provided maps of the thickness and shape (i.e. Fig. 3) that could be imported directly into the numerical model described. A total of five pairs with a range of different bows (minimum bow ~30 μm, maximum bow ~80 μm) were bonded.

RESULTS AND DISCUSSION

There are two comparisons that may be done to assess the accuracy of the bonding criterion proposed in [6] and the numerical model described in this work: 1) comparison of the predicted shape of the bonded areas to those observed experimentally, and 2) comparison of the work of adhesion values across the different pairs. Since the pairs have different geometries, but similar surface conditions, the extracted work of adhesion values will only be constant among the tests if the model properly accounts for the geometry of the pairs. It is important to note though that since only wafer scale geometry effects are being measured and accounted for in this work, the work of adhesion value that is being calculated is a function of the surface chemistry as well as smaller scale flatness variations such as roughness and waviness. To ensure that roughness and waviness were consistent across the wafers in the experiments, all wafers were taken from the same manufacturing lot and the roughness (AFM) and waviness (optical profilometry) were measured on several wafers at several locations to ensure consistency.

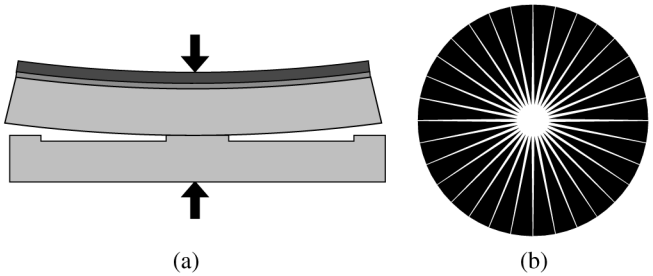

Figure 5. *Bonding configuration (a) and etch pattern (b) used.*

Of the five pairs that were bonded in this work, one bonded completely and the four others bonded over a portion of the wafer. IR images of the four pairs that bonded partially and bond fronts predicted using the model for each pair are shown in Fig. 6. For each wafer pair, the shapes of the individual wafers were imported into the model and bond fronts were mapped out for a range of work of adhesion values (similar to Fig. 4). The work of adhesion value for each pair was determined by selecting the prediction that matched the experimentally observed front the best. In all of the images in Fig. 6, the prediction with the smaller size corresponds

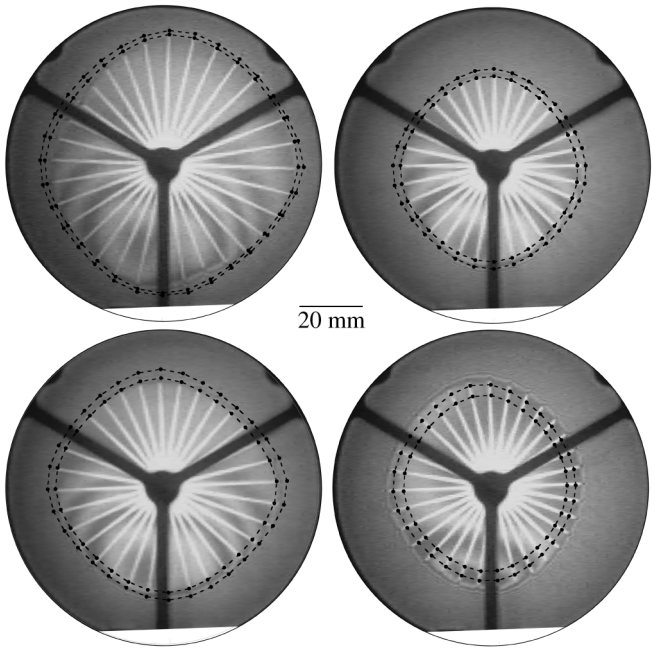

Figure 6. *IR transmission images of four bonded wafer pairs and model predictions of the bond front (dashed lines). In all images the predictions correspond to W=35 mJ/m^2 and W= 40 mJ/m^2.*

to a work of adhesion of 35 mJ/m^2 and the larger to 40 mJ/m^2. The work of adhesion values determined from the size of the bonded area and the wafer geometry for each pair using the numerical model reported here and the axisymmetric analytical model reported in [6] are shown in Fig. 7. The large error bars in the axisymmetric calculations are a result of asymmetries in the wafer and bond shape that make defining a single value for the bond front radius and wafer curvature impossible. For the analytical case, the markers in the plot correspond to *W* if the average values of curvature and bond front position are used in the calculation while the error bars represent the calculated *W* when the minimum and maximum values of bond radius and curvature are used.

The results in Fig. 6 show that there is good agreement between the shape of the bond front predicted by the model and that observed in experiments. This suggests that the numerical model can accurately account for the effects of wafer shape and etch patterns in bonding. The consistency of the work of adhesion

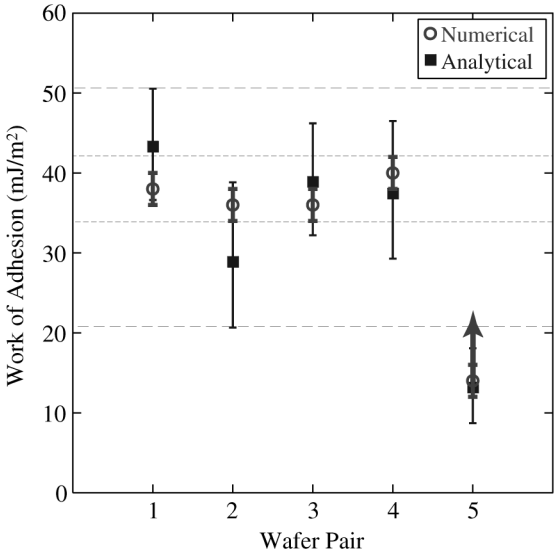

Figure 7. *Summary of the work of adhesion values obtained across 5 wafer pairs using the analytical and numerical model.*

values predicted across the pairs using the numerical model, as seen in Fig. 6 and 7, further validates the modeling approach and demonstrates that the bonding criterion proposed in [6] is effective in accounting for the effects of wafer geometry and etch patterns in direct wafer bonding. Pair 5 in Fig. 7, is the pair that bonded completely and as such there is no bond front that can be measured to allow for the work of adhesion to be calculated. However, a lower bound on the work of adhesion for that pair may be determined by calculating the work of adhesion required for the bond front to advance to the wafer edge, this is the value plotted in Fig. 7 for pair 5.

The work of adhesion values calculated from these pairs are reasonable for hydrophilic bonding. The work of adhesion, as used in this context, is a lumped parameter that includes the effects of surface chemistry (types and density of bonds on the surface) and small-scale flatness variations such as roughness. In the experiments performed, the position of the bond front (and hence the work of adhesion) was observed to be a function of time and would grow several millimeters if the pair was left for several hours. To mitigate the effect of time in the experiments all images were taken 10 min after bonding, the point at which the bond front was observed to not grow a noticeable amount over a 5 minute period. Presumably, the rate at which the bond front grows is associated with the dynamics of bond formation on the surface. To fully understand the nature of the work of adhesion, further studies are clearly required. However, for the purposes of the experiments here, where the primary interest is in the mechanics of the process, comparing work of adhesion values from multiple pairs at a specific time is a good approach.

CONCLUSIONS

In this work, a numerical model to predict failure in direct wafer bonding processes has been reported. The model incorporates a bonding criterion based on the strain energy accumulated in the wafers during bonding and allows the effect of wafer geometry, etch patterns, elastic properties, and work of adhesion to be accounted for. The model was validated through comparison to experiments, from which it was shown that the size and shape of the bond front is accurately predicted using the model. The experiments described verify the general bonding criterion proposed in [6] and the numerical modeling approach described here.

The results of this work demonstrate that failure in direct wafer bonding processes can be quantified and modeled. The bonding criterion and modeling approach that have been experimentally validated in this work provide a basis for the development of advanced process models that are essential for realizing robust wafer bonding processes.

ACKNOWLEDGEMENTS

All microfabrication and experiments were performed at the MIT Microsystems Technology Laboratory (MTL). The assistance of the ADE Corporation (P. Hester) in obtaining wafer shape measurements is greatly appreciated. This work was supported by the Cambridge MIT Institute (CMI-059/P-IR(FT) MEMS).

REFERENCES

1. K. Petersen, P. Barth, J. Poydock, J. Brown, J. Mallon, and J. Bryzek, "Silicon Fusion Bonding for Pressure Sensors," *Technical Digest of the 1998 Solid-State Sensor and Actuator Workshop*, Hilton Head Isl., SC, 6/6-9/88, IEEE, New York, NY (1988), pp. 144-7.

2. M.A. Schmidt, "Wafer-to-Wafer Bonding for Microstructure Formation," *Proc. IEEE*, 86, 1575-85 (1998).

3. N. Miki, X. Zhang, R. Khanna, A.A. Ayon, D. Ward, and S.M. Spearing, "A Study of Multi-Stack Silicon-Direct Wafer Bonding for MEMS Manufacturing," *Technical Digest MEMS 2002*, Las Vegas, NV, 1/20-24/02, IEEE, Piscataway, NJ (2002), pp. 407-10.

4. Q.Y. Tong and U. Goesele, "Semiconductor wafer bonding: recent developments," *Mater. Chem. Phys.*, 37, 101-27 (1994).

5. A. Ploessl and G. Kraeuter, "Wafer direct bonding: tailoring adhesion between brittle materials," *Mat. Sci. Eng.*, R25, 1-88 (1999).

6. K.T. Turner and S.M. Spearing, "Modeling of Direct Wafer Bonding: Effect of Wafer Bow and Etch Patterns," *J. Appl. Phys.*, 92, 7658-66 (2002).

7. M.P. de Boer and T.A. Michalske, "Accurate Method for Determining Adhesion of Cantilever Beams," *J. Appl. Phys.*, 86, 817-27 (1999).

8. K.T. Turner and S.M. Spearing, "Mechanics of Wafer Bonding: Effect of Clamping," *J. Appl. Phys.*, 95, 349-55 (2003).

9. K.T. Turner and S.M. Spearing, "Role of Wafer Bow and Etch Patterns in Direct Bonding," *Proceedings of the 7th International Symposium on Semiconductor Wafer Bonding" Science, Technology, and Applications*, Paris, France, 4/27-5/2/03, Electrochemical Society, Pennington, NJ (2003), pp. 166-74.

10. R. Krueger, "The Virtual Crack Closure Technique: History, Approach, and Applications," *ICASE Report*, NASA/CR-2002-211628, 1-59 (2002).

11. D. Hitchings, P. Robinson, and F. Javidrad, "A Finite Element Model for Delamination Propagation in Composites," *Comput. Struct.*, 60, 1093-1104 (1996).

A SACRIFICIAL-POLYMER-BASED TRENCH REFILL PROCESS FOR POST-DRIE SURFACE MICROMACHINING

Christophe G. Courcimault* and Mark G. Allen
School of Electrical and Computer Engineering, Georgia Institute of Technology,
Atlanta, GA 30332-0269

Joseph P. Jayachandran, Paul A. Kohl, and Sue Ann Bidstrup-Allen
School of Chemical Engineering, Georgia Institute of Technology,
Atlanta, GA 30332-0269

ABSTRACT

We present a trench refill process allowing post-DRIE surface micromachining by formation of planar silicon dioxide membranes encapsulating etched silicon cavities. This process can be used to fabricate diverse structures such as enclosed silicon channels, structures fabricated on top of movable DRIE-etched silicon devices, or could even be considered as the first step toward a low-temperature hermetic encapsulation process. Unlike traditional solvent-based sacrificial dissolution processes, the technology is based on the use of heat-degradable polymers as sacrificial materials. Two polymers were studied: a developmental poly(cyclohexene carbonate) and a commercially-available polypropylene carbonate. Formation of air-filled cavities many microns in depth planarized by encapsulating silicon dioxide layers with nonplanarities less than 150 nm have been realized. The planarization quality as well as the post-processing capabilities have been demonstrated by surface microfabrication of a nickel-electroplated microactuator, exhibiting feature sizes as small as 1 um, over a silicon resonator structure defined by a set of multimicron-deep DRIE silicon trenches.

INTRODUCTION

Many microsystems benefit from a combination of attributes from both bulk and surface micromachining. For example, consider the case where a surface micromachined device is to be fabricated on top of a bulk-etched silicon structure. In most cases, when bulk-micromachining is needed to accomplish device fabrication, the deep etching step is performed at the end of the process [**1**]. The resulting non-planar topography of the substrate surface makes it difficult to consider further surface-micromachining, especially if the surface micromachined structures have exceedingly fine features. Several processes have been introduced in order to address this problem, including LPCVD silicon dioxide deposition, LPCVD polysilicon deposition, and thermal oxide growth, combined with various etch-back methods [**2,3,4**]. The trench-refill process presented here is CMOS compatible and not restricted to very narrow DRIE trenches. The technology is based on the processing of a low-temperature degradable polymer as a sacrificial material. The sacrificial polymer is used here as the refilling material that will transform the trench into a gas-filled (or vacuum-filled) cavity capped with SiO_2 after decomposition. The "gas-refilled" trench can then be subjected to a wide range of post-processing, ranging from construction of surface micromachined structures to full encapsulation.

HEAT-DEGRADABLE SACRIFICIAL POLYMERS

Sacrificial layers are key elements in the fabrication of microsystems, as they allow freeing moving structures or define gaps and cavities. Silicon dioxide has been extensively used as a sacrificial material since its deposition and growth are well understood, and its etching can be very selective to silicon. Metals, such as copper, titanium or chromium are also easily accessible and selectively removable. In some cases, because of the large volumes of sacrificial materials required, metals, oxides or nitrides are not appropriate candidate materials; instead, dissolvable polymers such as photoresists are commonly used. However, the development of a suitable fabrication sequence based on these materials can be quite challenging. Polymer layers may reflow, crack, or shrink under post-processing conditions such as temperature changes or stress introduced by overcoating materials. Even if this issue can be resolved, long dissolution times in solvents are typically required to remove substantial volumes of polymer; and polymeric residues (e.g., for encapsulation applications) can remain a significant problem.

The process presented in this paper focuses on the use of heat-degradable polymers as sacrificial layers for MEMS applications. Such materials typically decompose into volatiles when heated to appropriate temperatures. Several candidate materials have recently emerged which combine microfabrication processability with thermal decomposition properties. The use of heat-degradable functionalized polynorbornenes and polycarbonates has been introduced for the fabrication of air-gaps [**5,6**], with the application of production of low-dielectric-constant materials for high frequency chip interconnection, a key point highlighted by the National Technology Roadmap for Semiconductors [**7**]. When heated to temperatures varying between 250˚C to 400˚C, these materials decompose into volatile compounds. The decomposition reaction of suitable polycarbonates as well as the fabrication of air gaps is described in detail by Jayachandran et al. [**8**]. The typical fabrication process involving these materials mimics that of a photoresist-based sacrificial polymer process. The polymer is spin-cast onto a substrate from solution, soft-baked to remove excess solvent, and then photo-defined or dry-etched to form regions of sacrificial polymer. Various over-coating materials, such as low temperature PECVD silicon dioxide, polyimides, or epoxies, are then deposited or cast onto the sacrificial polymer. An interesting characteristic of these overcoats is that they have been demonstrated to be permeable to the decomposition products of the polymer. Therefore, upon heating, the polymer decomposes and the products diffuse through the overcoat, forming encapsulated channels. These channels can be used as low-dielectric-constant supports for high frequency interconnects or for microfluidic applications.

*Travel support has been generously provided by the Transducers Research Foundation and by the DARPA MEMS and DARPA BioFlips programs.

0-9640024-5-0/hh2004/$20©2004TRF
DOI 10.31438/trf.hh2004.54

In this work, two polycarbonate materials were studied for more advanced MEMS applications. The two materials chosen were poly(cyclohexene carbonate), referred to as PCC; and polypropylene carbonate, referred to as PPC. The latter polymer is commercially available from Promerus, Inc. under the name of Unity 2203P. The chemical structures of the two polymers are shown in Figure 1.

Although planarization results will be shown for both polymers, the fabrication sequence will be described for PCC since the processing of the two polymers is substantially similar. The application of interest is a trench-refill process allowing surface-micromachining after a DRIE step, with the ultimate goal of fabricating multilevel stacked resonators. The fabrication sequence presented in Figure 2 shows how the PCC is temporarily used as a refill material prior to being decomposed through a porous PECVD silicon dioxide layer, which has been deposited on top of it. This decomposition process leaves behind an "empty" trench which is capped by the planarized silicon dioxide layer. Since the inorganic capping layer is not susceptible to solvent-induced wrinkling or cracking, thick sacrificial layers without the usual polymer drawbacks are enabled.

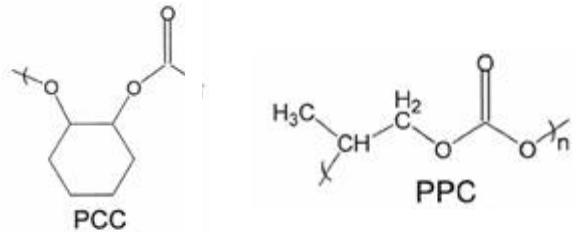

Figure 1. *Chemical structures of poly(cyclohexene carbonate), left, and polypropylene carbonate, right.*

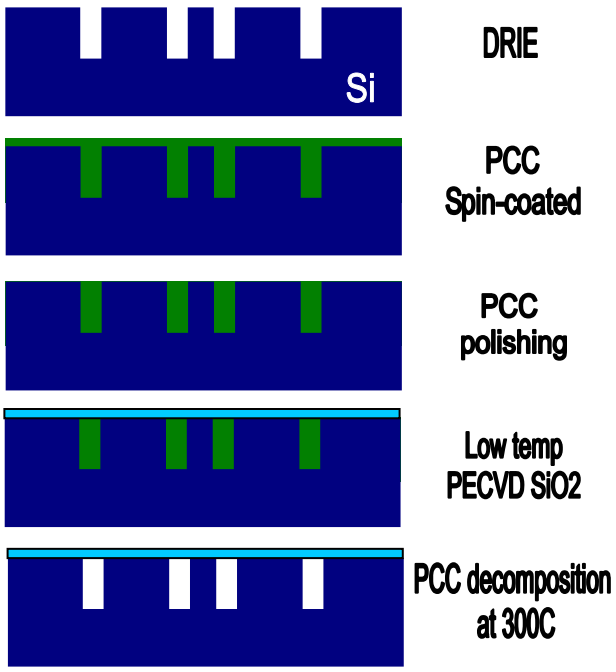

Figure 2*. Fabrication Sequence.*

The details of the process are given below. Trenches 15 µm deep and up to 5 µm wide are etched into a silicon wafer using an ICP etch. The sacrificial polymer is then spin-coated on the surface and soft-baked. Due to the excellent planarization properties of the PCC, the material flows into the etched trenches as well as coats the surface of the wafer. The excess polymer in the fields is removed by gentle polishing, leaving the polymer present only in the trenches. A 1.7 µm thick layer of porous silicon dioxide is deposited at low temperature (100˚C) using PECVD. The sacrificial polymer is decomposed and vaporized through the porous SiO_2. The PCC is decomposed in a nitrogen-purged tube furnace using the following heating steps: the temperature is ramped from room temperature to 150˚C at 3˚C /min, 150˚C to 300˚C at 1˚C/min and held at 300˚C for 3 hours. At this stage of the process, the trenches are free of polymer, and the wafer surface is flat. The silicon dioxide layer can be optionally densified, and the substrate can now be subjected to various micromachining processes such as high temperature steps, photolithography, wet and dry etchings, or material depositions. It should be noted that all of the steps up to this point are low-temperature and CMOS-compatible.

PLANARIZATION RESULTS

The planarization of the substrate surface and the range of post-processing available for surface-micromachining will determine the viability of the trench-refill process. Unlike previous polymer approaches, the process presented here possesses the desirable feature that the trenches are refilled with air. As long as the SiO_2 membrane is not removed, a wide variety of post-processing options are available. Figure 3a) shows a cross-sectional scanning electron micrograph of a trench refilled by PCC, polished, and coated with low temperature PECVD oxide. As shown in Figure 3b), the surface of the substrate after oxide deposition but before PCC removal analyzed using a Tencor Alpha-Step surface profilometer presents a nonplanarity of only 115 nm over the 3 µm width of the 15 µm deep trench. Depending on the measurement sample, both depressions as well as peaks were observed; but in all cases the magnitude of the nonplanarities was less than 300 nm. The PCC was then thermally decomposed. A cross-sectional view of the trench after decomposition of the PCC through the porous SiO_2 is shown in Figure 4a). The trench is free of polymer and residue and the SiO_2 membrane has neither visibly sagged nor broken. Furthermore, the profilometer trace shown in Figure 4b) confirms that the SiO_2 membrane is not affected by the decomposition step and reaffirms the quality of the surface planarization. Again, depending on the measurement sample, both depressions as well as peaks were observed, but in all cases the magnitude of the nonplanarities was less than 300 nm. In this particular case, the surface of the substrate exhibits a 120 nm depression. A similar planarization trace for PPC is shown in Figure 5. Here, after decomposition, an additional post-processing metal layer of Ti/Cu/Ti, with the Cu layer 4 µm in thickness, has been deposited, illustrating the robustness of the capping SiO_2 layer. The planarization of the resultant surface exhibits a 300 nm nonplanarity over the width of the trench.

POST-PROCESSING DEMONSTRATION

In order to demonstrate the capabilities of post-DRIE surface-micromachining using this approach, a nickel electroplated microactuator is fabricated on top of the "air-refilled" cavities. The fabrication sequence is presented in Figure 6. The SiO_2 layer, used for encapsulation of the silicon cavities, also acts as a sacrificial layer for the microactuator. A seed layer (Ti: 15nm / Cu:100 nm / Ti:15 nm) is then deposited on top of the oxide and a 10 micron thick Shipley

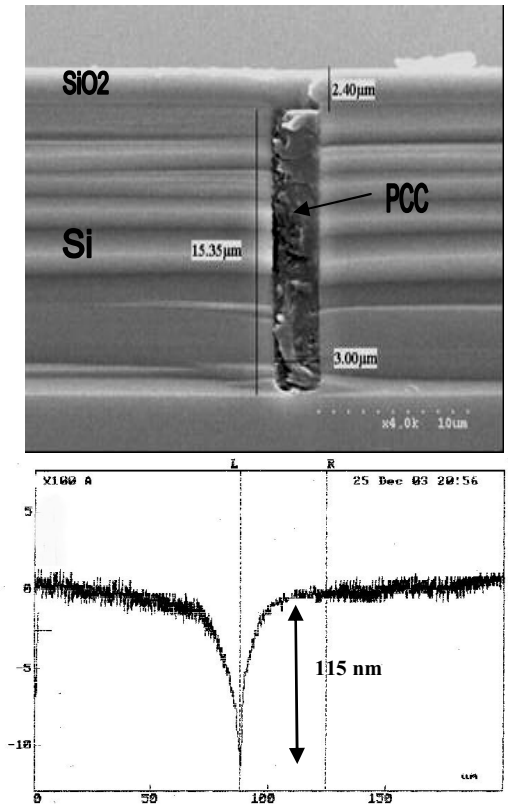

Figure 3. *a) SEM or the trench after PCC refill, polishing and low-temperature SiO_2 deposition. b) Profile of the substrate surface.*

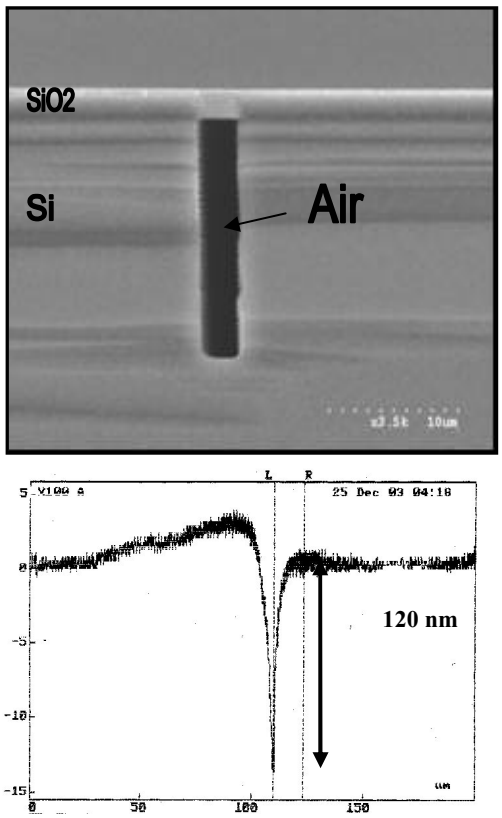

Figure 4. *a) SEM of the trench, after PCC decomposition. b) Profile of the substrate surface above "empty" trench.*

photoresist (SPR220-7) is spun, soft-baked, exposed, post-baked and developed to define an electroplating mold. Using a sulfamate nickel bath, a nine micron thick nickel layer is electroplated. After removal of the mold, the silicon dioxide layer is time-etched using a buffered oxide etch solution (6:1) to release the microactuator and re-open the silicon trenches.

The microactuator is electrostatically actuated by means of a set of comb-drive electrodes. Figure 7 shows an SEM of the interdigitated fingers. Due to the excellent substrate planarization, high resolution photolithography can be performed, allowing fine feature definition. Note the gap between fingers is in the order of 1.1 microns, over a thickness of nine microns (aspect-ratio: 1:8). Figure 8a shows an overall view of the device, and Figure 8b displays the microactuator shuttle free-standing above an empty and clear trench. The microactuator has also been electrically tested. In this device, the 1.7 micron thick silicon dioxide layer serves two purposes: first, for encapsulating the trenches during the microactuator fabrication; and second, to provide electrical insulation of the actuator electrodes. The microactuator exhibits lateral displacement between the interdigitated finger gap. The full range of displacement, 1.1 micron, is obtained under the application of 30 V DC voltage. The insulating properties of the porous, low temperature PECVD oxide have also been examined. Pad-to-pad bias voltages of up to 100 V have been applied to the device without breaking down the 1.7 micron layer of SiO_2. this demonstration device verifies the suitability of the trench-refill process for subsequent surface micromachining.

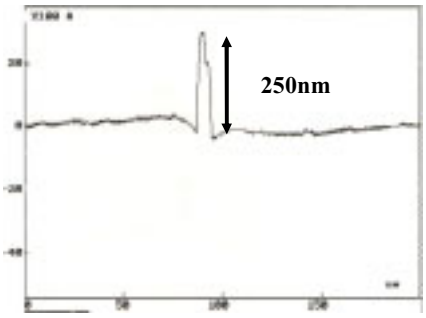

Figure 5.*. Profile of the substrate surface above "empty" trench after PPC decomposition and deposition of a 4 micron Ti/Cu/Ti layer.*

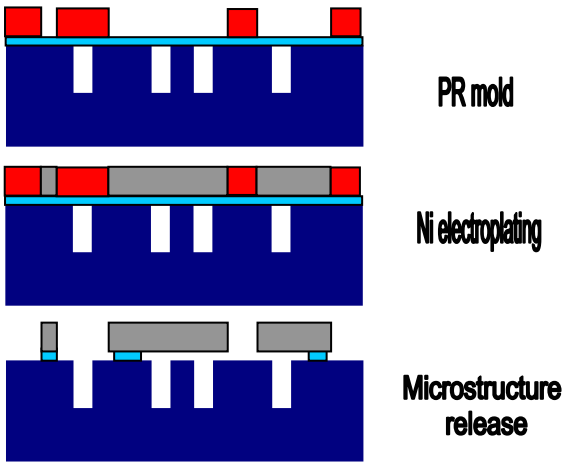

Figure 6. *Fabrication sequence of the electroplated actuator above the DRIE trenches.*

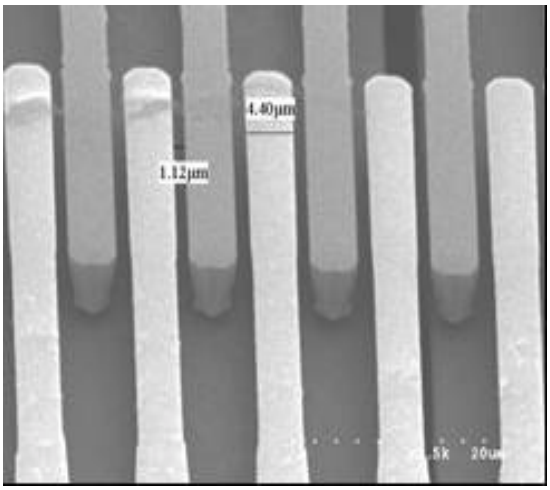

Figure 7. *Electroplated nickel though photoresist mold. The fingers are 4.4 um wide, 9 um thick, and spaced by a 1.1 um gap (A.R= 1:8).*

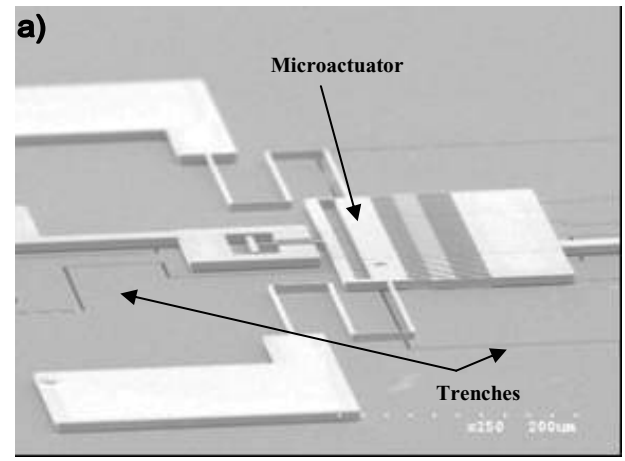

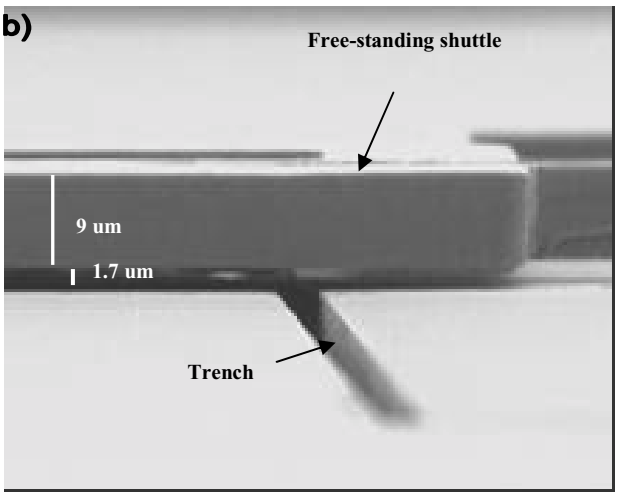

Figure 8 *a) Overall view of the microactuator fabricated over the trenches. b) Released microactuator shuttle standing on top of a trench.*

CONCLUSIONS

The formation of air cavities from DRIE silicon trenches encapsulated by PECVD silicon dioxide after thermal decomposition of various polycarbonates was demonstrated as a suitable method for post-DRIE surface micromachining. The process is CMOS-compatible due to the low temperature heat degradable polycarbonate, is applicable to wider trenches than previously-reported refill processes, and does not affect the size of the trenches. Excellent planarization of the process was observed, allowing the fabrication of micron-scale features directly on top of the sealed trenches. Although the application presented here was for post-DRIE surface micromachining, further applications such as large surface planarization, silicon buried air channels and vacuum encapsulation of microsystems are enabled by this process.

ACKNOWLEDGMENTS

This work was supported in part by the U.S. Defense Advanced Research Projects Agency under the NMASP Program. Microfabrication was carried out in the Georgia Tech Microelectronics Research Center with the assistance of the staff.

REFERENCES

1. T. Muller et al., ”An industrial CMOS process family adapted for the fabrication of smart silicon sensors”, *Sensors and Actuators* 84 (2000), pp. 126-133

2. C. Zhang, K. Najafi, “Fabrication of thick silicon dioxide layers using DRIE, oxidation and trench refill”, *Micro Electro Mechanical Systems, 2002. The Fifteenth IEEE International Conference on*, 20-24 Jan. 2002, pp 160 -163.

3. K. Shenai., “A novel planarization technique using polysilicon refill, polysilicon oxidation and oxide etchback” *IEEE transactions on electron devices*, vol.40, no.2, February 1993, pp 459-463.

4. F. Ayazi, K. Najafi, “High aspect-ratio combined poly and single-crystal silicon (HARPSS) MEMS technology”, *Journal of Microelectromechanical Systems*, vol. 9 , Sept. 2000 pp 288-294.

5. Paul A. Kohl, et al., “Air-gaps for electrical interconnections”, *Electrochemical and Solid-State Letters*, 1 (1) 49-51 (1998).

6. Hollie A. Reed, et al., “Fabrication of microchannels using polycarbonates as sacrificial materials” , *J. Micromech. and Microeng.*, 11 (2001) 733-737.

7. *The National Technology Roadmap for Semiconductors,* Semiconductor Industry Association, San Jose, CA, 1997.

8. J. Jayachandran, et al., “Air-channel fabrication for microelectromechanical systems via sacrificial photosensitive polycarbonates”, *Journal of Microelectromechanical Systems*, vol. 12, no. 2, April 2003, pp 147-159.

TOWARDS INTEGRATED MICRO-MACHINED SILICON-BASED NANOPORES FOR CHARACTERIZATION OF DNA

Hung Chang[1], Farhad Kosari[4], George Andreadakis[4], George Vasmatzis[4], Ed Basgall[5], Alexander H. King[2], and Rashid Bashir[1,3] (bashir@ecn.purdue.edu)
[1]School of Electrical and Computer Engineering, [2]School of Materials Engineering,
[3]Department of Biomedical Engineering, Purdue University, West Lafayette, IN 47907-1285.
[4]Mayo Clinic, Rochester, MN 55905. [5]Penn State University, University Park, PA 16802.

ABSTRACT

The direct characterization, detection, and identification of single nucleic acid molecules can revolutionize genomics, expression analysis, and many areas of biological sciences. A nanopore fabricated using micro and nano-fabrication technique is a viable sensor for such single molecule studies. Here we report the fabrication and processes characterization of silicon-based nanopores using e-beam lithography and TEM-based processing. We performed investigations on the fabrication process in depth. Experiments of metal deposition on the nanopore were also performed to observe the interactions between the metal and the surface oxide.

INTRODUCTION

The concept of characterizing biological single molecules such as nucleic acids with a single pore has been investigated in the recent years. The idea is essentially a coulter-counter based approach, in which the electric detection is achieved by fluctuations of the ionic current in the system when the interested species passes through the single pore. Chang et al. [1] fabricated a silicon-based micro-pore and performed characterization of bacteria as they moved through the pore under an electric field. In his work, ionic currents dropped when the bacteria were passing through the micropore and the current recovered to the original level when the bacteria passed through the micropore. Characteristics of the bacteria could be extracted from the time-sampled current plots. To apply this idea to DNA and related nucleic acids, a pore with 2-4 nm in diameter has to be realized. Kasianowicz et al. [2] pioneered the use of a single 2 nm diameter α-hemolysin channel for the electrical detection of a single DNA molecule, as the molecule traversed the channel. Meller et al. [3] later applied the same channel to discriminate between purines and pyramidines. The channel used in the above works was protein-based. A silicon-based nanopore has also subsequently been reported [4, 5]. In Li's work [4], a feedback controlled ion milling process was used to sculpt a nanopore. A 60 nm hole shrank into a 1.8 nm nanopore after being focused by an ion beam. The same group also performed DNA trans-location measurements through the nanopore [6]. Translocation times and folding of double-stranded DNA with different lengths were thus obtained. Storm et al. recently reported the fabricated of a nanopore with e-beam lithography and TEM techniques. Their method realized an in-situ observation of pore size, and the size could precisely be controlled at the nanometer level. Our fabrication process, though developed independently, is similar to [4]. In this paper, we present further details and characterization of the fabrication process for the nanopore. We also investigated placing thin metal films around the pore and explored the shrinkage of the pore with metal layers around them. The eventual goal of those preliminary works is to fabricate robust nanopores for the characterization of nucleic acid molecules within integrated biochips.

Travel support has been generously provided by the Transducers Research Foundation and by the DARPA MEMS and DARPA BioFlips programs.

NANOPORE FABRICATION

The simplified cross sections of the process flow are illustrated in Fig. 1. The nanopore fabrication commenced with double polished SOI wafers. The buried oxide and SOI layers were 400 nm and 190 nm thick, respectively. A 100 nm thermal oxide was grown on the SOI wafer. An LPCVD nitride layer was deposited and etch windows (~670 μm by 670 μm area) were formed on the backside. The nitride and oxide was etched and the handle layer of the wafer was etched from the back side in TMAH at 90C. The handle silicon layer was etched through, and the etch process stopped on the buried oxide to form a diaphragm of around 80 μm by 80 μm area. The nitride was stripped off in boiling phosphoric acid at 180C, and electron beam lithography was performed on the front to define 100 nm by 100 nm openings on the diaphragm. Next, a short TMAH etch at 60C was performed to etch the SOI, in an inverted pyramid shape, down to the buried oxide. When the buried oxide was removed, a pore of less than 100 nm diameter was formed. Thermal oxide was then grown to shrink the pore to less than 50 nm. Finally, the pore was examined and processed in a transmission electron micrograph and shrank to the desired nanometer dimension utilizing the in-situ observation.

RESULTS AND DISCUSSION

The metamorphosis of the pore by TEM is a complicated process. Not only shrinkage but also expansion of the pore occurred in the experiments.

0-9640024-5-0/hh2004/$20©2004TRF
DOI 10.31438/trf.hh2004.55

Fig. 2 shows TEM images of pore shrinking in the TEM. A 91 nm by 94 nm pore (before the final oxidation) was used to form a 75 nm by 78 nm pore after 100 nm thermal oxide was grown on the pore (Note: TEM pictures are shown when pore was 51 nm by 54 nm). Subsequent observation in the TEM resulted in shrinking of the pore, as shown in Figure 2. The average shrinkage rate of one of the pore was 0.57 nm/min, as shown in Fig. 3.

The pore shown in Fig. 4 was 168 nm by 172 nm after a 90 nm thermal oxide was grown on the pore. The pore expanded to 206 nm and 208 nm within 58 min. Occurrences of shrinkage or expanding depend on the initial pore size and the thickness of the oxide grown on the pore. The critical radius of the pore was suggested in [5] and [7] as: $r_c = d/2$, where r_c is the critical radius, d is the oxide thickness. The pore shrinks if the radius is smaller than d/2; it expands, if radius is greater than d/2. When being examined under high electron energy, the oxide covering the pore flows to reduce the surface energy. A void region, the pore, has lower surface energy when the radius of the pore is below the critical value. In the opposite case, the void region has a higher surface energy; the pore expands. Table 1 shows radii, oxide thicknesses and shrinkage/expanding of some of our pores. The table shows that indeed the pores shrink or expand depending on the ratio of the pore radius to the oxide thickness, and validates the proposed model i.e. $r/d>0.5$ results in expanding the pore and $r/d<0.5$ results in shrinking the pore.

The shrinkage rate varied over time and especially as a function of starting size. The pore seemed to shrink faster at the beginning, and the initial shrinkage rates were between 0.6 to 2.6 nm/min. The rates were also observed to be related to the oxide thickness; the pore with a thicker oxide had a higher initial shrinkage rate. The shrinkage rate reduced down to 0.3 nm/min in all cases, when the pore radius went below 10 nm. Table 2 shows the initial shrinkage rates and the oxide thicknesses of some pores. Figure 3 shows the change shrinking rate vs. time for two pore diameters. The average shrinkage rates are the slopes of the fitted curves, and it is obvious that pores with different oxide thicknesses have different shrinkage rates.

It was also found that non-circular pores could be rounded by the TEM processing. Fig. 5 shows TEM images of an oval pore turning into a rounded one. Fig. 6 shows the plot of the dimensions of the pore (the long and the short axes of the oval pore) vs. time. The shrinkage rates of the long and the short axes were obviously different. The short axis didn't change much for sometime while when the long axis was shrinking. Once the axes became the same size (a circle), then the newly formed circular pore continues to shrink further. This interesting fact is also related to a surface energy of the pore. According to the observation described in the last paragraph, the pore initially shrank faster and shrinkage slowed down after a while. This phenomenon gives a hint that a larger vacant space (as long as below the critical radius) has a larger surface energy comparing to a smaller one. Therefore, the long axis has a higher shrinkage rate than the short one in an oval pore. It can be postulated that the surface energy of the pore due to the long axis is locally higher than that due to the short one, and hence the oxide along the long axis flows faster.

Preliminary experiments involving deposition of a thin metal layer on the pore was also performed before the shrinkage step in TEM. The electron beam was then focused on the pore covered with both the surface oxide and the thin metal layer. This experiment was to investigate if a thin metal layer moves under e-beam irradiation, along with the pores. Two sets of chips were prepared, one with 10 nm Ti only, and one with 10 nm Ti and 5 nm gold film. Fig. 7 shows the case with the 10 nm Ti film. In this case, the metal seems to move along with the pore as it shrinks, since the metal edge cannot be clearly discerned. Fig. 8 shows pore with the 10 nm Ti and the 5 nm gold. In this case, the film does not seem to move along with the pore as the metal edge can be clearly seen away from the pore itself. More experiments need to be performed and this information can be very useful when designing the placement of metal electrodes at the nanopore for tunnel electrodes to laterally measure the passage of DNA through the pore.

CONCLUSION

We have fabricated nanopores in silicon-based membranes using micro and nano-fabricated processes along with Transmission Electron Microscope (TEM)-induced pore size reduction. The process is shown to produce nano-pores, even when starting with non-circular openings. Thin metal films could also be placed on the pore and were found to shrink and move along with the oxide for some films. The measurement of DNA translocation through these nanopores is in progress.

ACKNOWLEDGMENTS

The authors would like to acknowledge the support of NIH NIBIB (R21 RR15118-01) and NASA Institute of Nanoelectronics and Computing at Purdue (Award no. NCC 2-1363) for funding the work, and the Birck Nanotechnology Center for fabrication facilities at Purdue University.

REFERENCES

1. H. Chang, A. Ikram, T. Geng, F. Kosari, G. Vasmatzis, A. Bhunia, and R. Bashir, "Electrical characterization of microorganisms using microfabricated devices", *Journal of Vacuum Society and Technology B, 20*, 2058 (2002).

2. John. J. Kasianowicz, Eric Brandin, Daniel Branton and David W. Deamer, "Characterization of individual polynucleotide molecules using a membrane channel", *Proc. Natl. Acad. Sci., 93*, 13770 (1996).

3. Amit Meller and Daniel Branton, "Single molecule measurements of DNA transport through a nanopore", *Electrophoresis, 23*, 2583 (2002).

4. Jiali Li, Derek Stein, Ciaran McMullan, Daniel Branton, Michael J. Aziz and Jene A. Golovchenko, "Ion-beam sculpting at nanometer length scales" *Nature, 412*, 166 (2001).

5. A. J. Storm, J.H. Chen, X.S. Ling, H.W. Zanderbergen and C. Dekker, "Fabrication of solid-state nanopores with single-nanometre precision", *Nature Materials, 2,* 537 (2003).

6. Jiali Li, Marc Gershow, Derek Stein, Eric Brandin and Jene A. Golovchenko, "DNA molecules and configurations in a solidstate nanopore microscope" *Nature Materials, 2*, 611 (2003).

7. M. Lanxner, C. L. Bauer and R. Scholtz, "Evolution of hole size and shape in {100},{110} and {111} monocrystalline thin film of gold", *Thin Solid Film, 150*, 323 (1987).

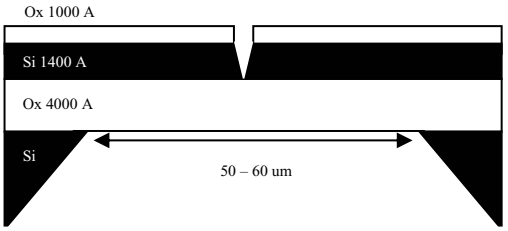

(a) After TMAH etch on both sides.

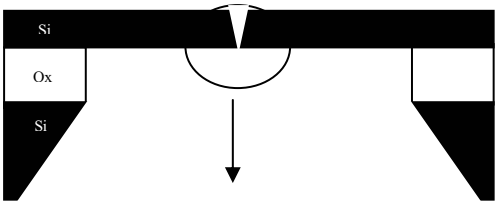

(b) A pore was opened after buried oxide layer was removed.

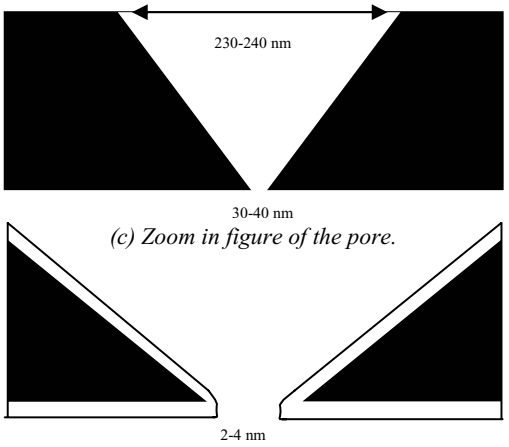

(c) Zoom in figure of the pore.

(d) Grow thermal oxide and shrink the pore by TEM.

Figure 1. *The simplified cross sections of the process flow.*

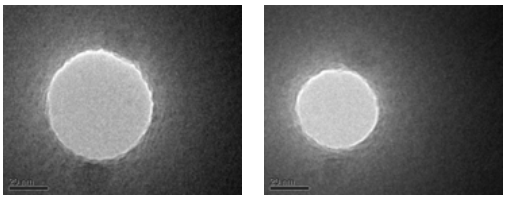

(a) 51 nm x 53nm pore after the last thermal oxidation

(b) 38 nm x 40 nm 20 mins in TEM

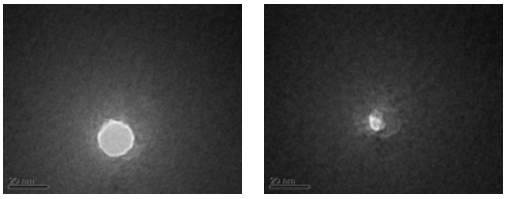

(c) 17 nm x 17 nm 45 mins in TEM

(d) 4.2 nm x 4.6 nm 83 mins in TEM

Figure 2 (a-d). *Shrinking of the nano-pore to the desired size using TEM. Fabrication was in situ observed and pore size could be accurately controlled at nanometer level. All images are in 1,000,000 X.*

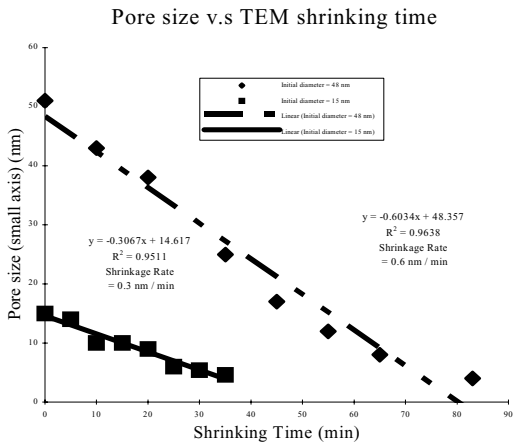

Figure 3. *Slopes in the plot are the shrinkage rates. Different initial pore size had different shrinkage rates.*

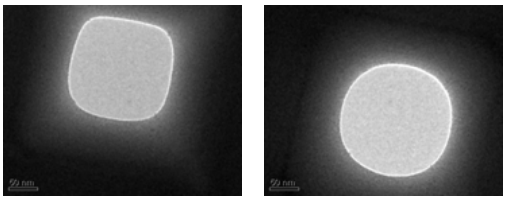

(a) 168nm x 172 nm Pore after the last Thermal oxidation

(b) 187 nm x 189 nm after 20 mins in TEM

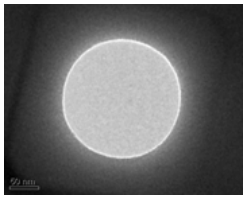

(c) 200 nm x 201 nm 45 mins in TEM

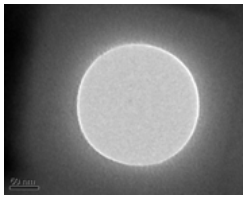

(d) 206 nm x 208 nm 58 mins in TEM

Figure 4 (a-d). *Pore with larger initial size (just prior in TEM) expanded, not shrank. All images are in 300,000 X.*

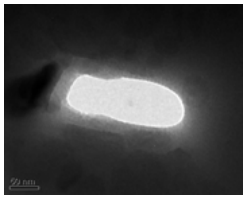

(a) 69 nm x 198 nm Initial pore

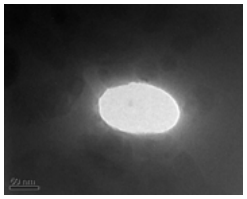

(b) 80 nm x 156 nm 90 mins

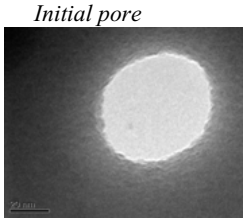

(c) 48 nm x 57 nm 250 mins

(d) 3.3 nm x 3.5 nm 334 mins

Figure 5. *Oval pore turned round by TEM. The first two images are in 300,000 X, and the last two images are in 1,000,000 X.*

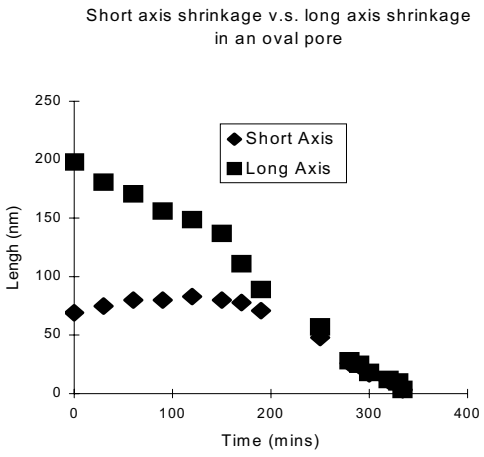

Figure 6. *Long and short axes had different shrinkage rates. Diamond marks are the trends of the short axis and square ones are for the long axis.*

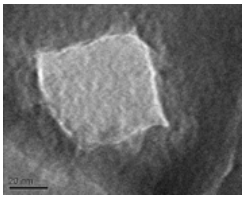

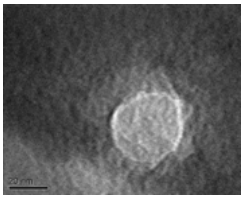

Figure 7. *Nanopore with 10 nm Ti deposition. (a) Initial image of the pore. (b) Pore with 10 nm Ti after 30 mins TEM observation.*

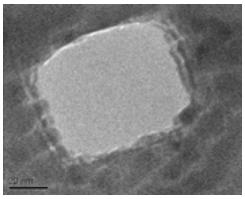

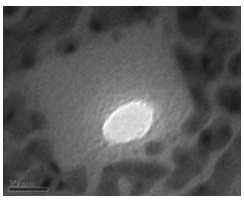

Figure 8. *Nanopore with 10 nm Ti and 5 nm gold deposition. (a) Initial image of the pore. (b) Pore shrank after 30 mins.*

Pore Name Exp./Shr.	Average radius of the pore r (nm)	Grown oxide thickness d (nm)	The ratio of r/d
103003_4 Shrunk	9	79	0.11
102503_4 Shrunk	38	100	0.38
110603_2 Shrunk	51.5	130	0.40
091603_6m Expanded	82	90	0.91
082703_5m Expanded	138	120	1.15
091603_7m Expanded	110	54	2.04

Table 1. *Radii, oxide thicknesses and shrinkage/expanding of some of our pores. For ratio of r/d>0.5, the pores generally expanded and for ratio r/d<0.5, the pores generally shrank.*

Pore Name	Grown oxide thickness d (nm)	Initial pore radius r (nm)	Initial shrinkage rate (nm/min)
103003_4	79	9	0.6
102503_4	100	38	1.6
110603_2	130	51.5	2.6

Table 2. *The last grown oxide, initial pore radius and the initial shrinkage rates of some pores.*

SELF-ASSEMBLY OF MICRO PUMPS WITH HIGH UNIFORMITY IN PERFORMANCE

Jiandong Fang, Kerwin Wang, Karl F. Böhringer
Department of Electrical Engineering
University of Washington
Seattle, WA 98195-2500

ABSTRACT

In this paper we report a novel capillary-force-driven self-assembly technique which proceeds in an air environment. We demonstrate this technique for the self-assembly of piezoelectric driving elements (PZT) for diffuser valve micropumps: with the agitation of an orbital shaker, square PZT actuators self-align and mount to the hydrophilic trench binding sites with electric connections by heat curable lubricant oil and conductive physical contact between the PZT actuators and the substrate. 28 pumps are fabricated on a 4-inch bonded pyrex/silicon substrate. The resonance frequencies of all the pumps show high performance uniformity: the average is 80.1 kHz and standard deviation is 2.0 kHz. This technique provides fast, parallel and well-controlled bonding of bulk PZTs for micro pumps with yield ratio up to 100%.

INTRODUCTION

Assembly of microdevices is a key aspect for the development of multi-component integrated micro systems, and capillary-force-driven self-assembly is a prime candidate for the method-of-choice in many situations [1-2]. Previously we reported self-assembly of micro parts in an aqueous environment [3], which limits the application range as follows: 1) parts are soaked in water for a long time, 2) bonding adhesive's volume can not be easily controlled, 3) part tilting is difficult to avoid [4], 4) bonding to hydrophobic binding sites is not strong, 5) electroplating is needed to establish electrical contact. To overcome these disadvantages, this paper reports a novel capillary-force-driven self-assembly technique which proceeds in an air environment. Here we demonstrate this technique for the self-assembly of piezoelectric driving elements for fixed-valve micropumps [5]. The pump consists of a shallow chamber with thin membrane actuated by a PZT actuator, two check valves controlling the flow direction and two channels connecting the check valves to the inlet and outlet holes, respectively. This type of micropump is a good candidate for further miniaturization using self-assembly given the current trend toward control and transport of liquids from microliters to nanoliters [6].

To achieve good performance in piezo driven pumps, the bonding of PZT should have the following properties: 1) adequate stiffness for the pump membrane to bend up and down as the PZT actuator expands and contracts; 2) accurate alignment of the PZT on the pump membrane; 3) controllable bonding thickness without tilt; 4) electrical connections. Usually, highly viscous electrically conductive silver epoxy is used to glue the PZT manually onto these pumps, which is a serial process without good control of process parameters: epoxy thickness can not be controlled easily, epoxy is not uniformly distributed underneath PZT, and alignment errors are difficult to avoid. Using this self-assembly technique, the PZT can be bonded on the pump membrane in a well-controlled parallel process with strong adhesion.

FABRICATION

Micro pumps are fabricated on a 4" single side polished silicon wafer using two DRIE (System 100 with ICP 380, Oxford Instruments Plasma Technology Ltd, UK) processes and one anodic bonding (Fig. 1). We choose diffuser valves for the micro pumps because they are well understood and reliable [7-9]. AZ4620 (Clariant Inc.) is patterned by photolithography to be the DRIE mask with the following steps: 1) singe the wafer on a 110 °C hotplate for one minute; 2) spincoat primer P20 and AZ4620 at the speed of 2200 RPM for 30 sec in sequence; 3) prebake wafer on a 110 °C hotplate for 3 minutes; 4) expose with 4" IR contact aligner (AB-M, Inc, USA) UV light for 30 sec; 5) develop in solution AZ400K / DI water = 1/4 for 2 minutes; 6) postbake on a 110 °C hotplate for 10 minutes. 1st DRIE is for pump chamber (5mm in diameter, 25 μm deep), and 2nd DRIE is for diffuser valves and channels (275 μm deep), Fig. 2 shows the depth uniformity of DRIEs. The shallow and large etched chamber makes the 2nd photolithography of AZ4620 for the channels and valves DRIE feasible, because conformal coating of photoresist on the surface with trenches is difficult. A laser cutter (Model 4410, ESI, USA) is used to drill the inlet and outlet holes. Then a 500 micron-thick 7740 pyrex wafer (Plan Optik, Germany) is anodically bonded to the etched silicon wafer on a 550 °C hotplate at the voltage of 1200 volts. In order to get thin pump chamber membranes, HF (49%wt) is used to etch the bonded pyrex wafer down to 230 microns in thickness at the rate of 6.75 μm/min. To prepare for the self-assembly of PZT, a layer of Cr/Au (50/1000 Å) is deposited by thermal evaporation and patterned by Cr/Au etching to form the 3mm square binding sites with photoresist AZ1512 as the mask, then AZ1512 is stripped by acetone, finally the exposed pyrex inside the binding sites is etched by HF (49%wt) to 24 μm in depth with the patterned gold as the etching mask. During the above two HF etches, a piece of blue tape is attached to the backside of the pump substrate in order to keep the pump channels and chamber clean from the HF solution.

PZT SELF-ASSEMBLY

PZT parts are fabricated from a 2.85" square PZT sheet (PSI-5H4E, Piezo Systems, Cambridge, MA) with the following steps: 1) AZ1512 is spin coated on the PZT sheet and patterned with the mask protecting the 3mm square bonding areas from UV exposure, after developing only the bonding areas are coated with AZ1512; 2) Cr/Au (50/1000 Å) is deposited on both sides of the PZT sheet by two thermal evaporations; 3) the PZT sheet is rinsed in acetone so that AZ1512 and the gold on AZ1512 is removed, the nickel bonding areas are exposed (Fig. 3a); 4) the PZT sheet is diced into 4mm square parts; 5) the diced parts are cleaned with acetone, IPA and DI water in sequence inside a sonicator. Finally the cleaned parts are collected to a piece of filter paper and dried by baking on a 100°C hotplate for 5 minutes.

Travel support has been generously provided by the Transducers Research Foundation and by the DARPA MEMS and DARPA BioFlips programs.

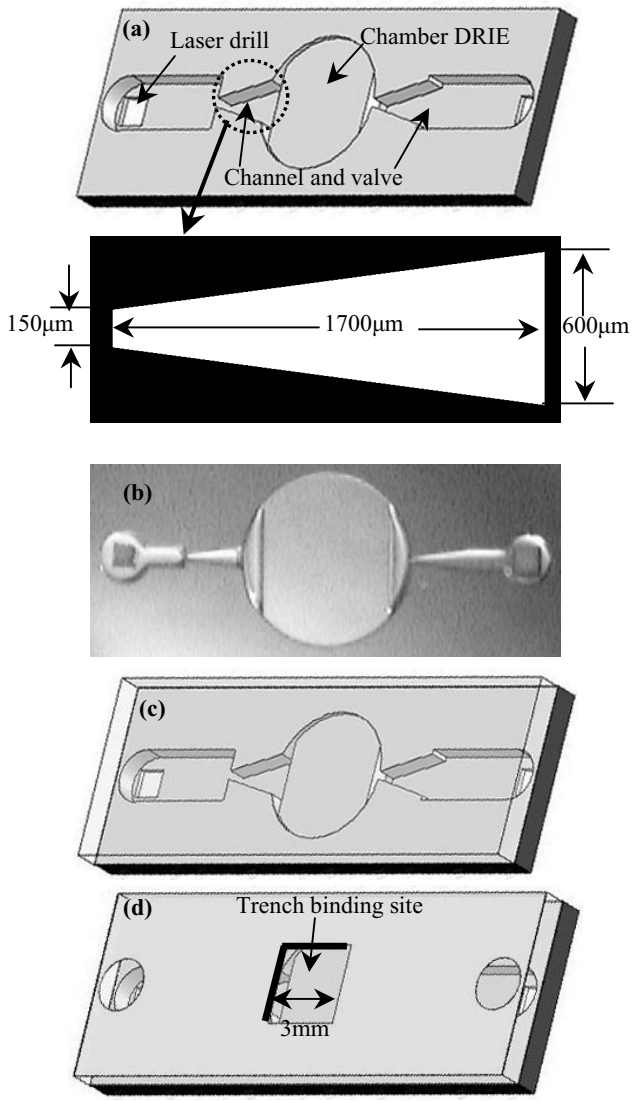

Fig.1. *Pump fabrication processes (schematic diagrams not to scale).* ***(a)*** *pump structure after 2 DRIEs and laser drilling;* ***(b)*** *microscope image of the pump structure;* ***(c)*** *anodic boding of pyrex 7740 wafer to the substrate;* ***(d)*** *Cr/Au patterned on the pyrex for the trenched PZT binding sites (two 1mm diameter holes on gold are used for alignment of pump with testing stage holes, see Fig. 8).*

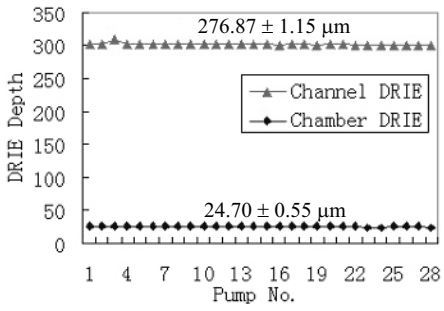

Fig.2. *Depth uniformity of two DRIEs: 28 pumps on a single wafer are numbered from top to bottom and from left to right (see Fig. 6).*

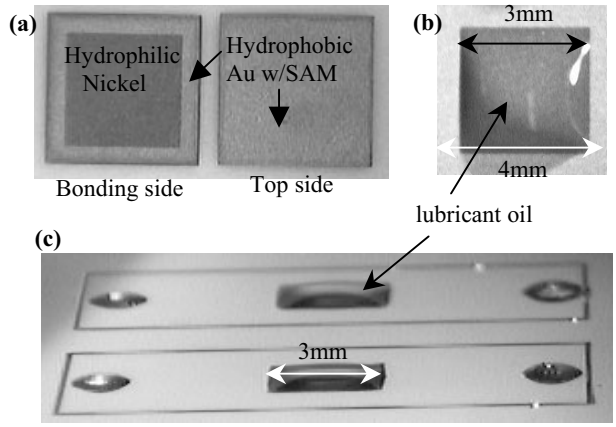

Fig.3. *Pump substrate and square PZT part in an air environment.* ***(a)*** *two sides of PZT part;* ***(b)*** *lubricant oil covers only hydrophilic nickel surface of PZT part bonding side;* ***(c)*** *lubricant oil covers only the hydrophilic trench binding sites.*

To prepare for self-assembly, the pump substrate and PZT parts are soaked in alkanethiol solution (48μl 1-dodecanethiol diluted in 100 ml ethanol) for selective adsorption of self-assembled-monolayer (SAM). The gold area on the substrate and parts become hydrophobic after adsorbing SAM from alkanethiol solution by chemical bonding, while the pyrex area on the substrate and nickel area on the PZT parts remain hydrophilic without SAM adsorption after an ethanol rinse.

This self-assembly technique exploits the surface tension force to self-align the PZT parts to the defined 3mm×3mm×24μm hydrophilic trench binding sites (Fig. 1d). In an air environment heat curable lubricant oil (acrylate-based adhesive) [2] only wets the hydrophilic areas such as the trench binding sites and nickel area on the PZT parts (Fig. 3) and is repelled by hydrophobic SAM coated gold area. Dry PZT parts are introduced manually onto the lubricant oil droplets on the binding sites with the nickel area facing down. The global minimum of the total surface energy can be achieved when the part is aligned with the binding site on the substrate. If the part is not well aligned, the capillary force of the lubricant oil will cause aligning the part with the binding site to minimize the total surface energy. Because the part is larger than the binding site, the part tends to stay in tilt and touches the substrate by its corner or edge, which prevents the capillary force from aligning the part to the binding site. An orbital shaker (Model 51300-00, Cole-Parmer Instrument Company) is used to provide a centrifugal force to the parts, which is uniform everywhere on the shaker stage. The centrifugal force drags and balances the parts on the lubricant oil droplets without touching the substrate so that the parts can self-align with the binding sites by the capillary force to the global minimum surface energy state (Fig. 4).

Finally a 4" pyrex wafer is used to squeeze out the excessive lubricant underneath aligned PZT parts (the top side of the PZT is a hydrophobic SAM coated gold surface, which can prevent the squeezed lubricant from climbing along the hydrophilic sidewalls of the PZT to the top side, otherwise, the lubricant could bond the pressing pyrex wafer with the PZT top side), and electrical connections between the PZTs with surface roughness of about 1μm and the substrate are established (Fig. 5). The lubricant oil is polymerized on an 85 °C hotplate for about half an hour. The top electrode of the PZT is connected by wire bonding (Fig. 5c).

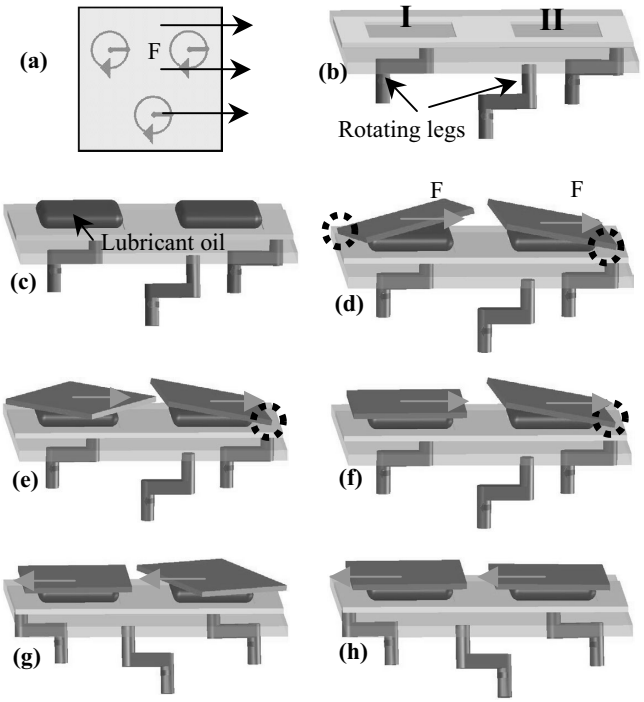

Fig.4. *Schematic diagrams for the mechanism of orbital shaker assisted self-alignment.* ***(a)*** *top view of orbital shaker at the phase when the centrifugal force is in the direction to the right;* ***(b)*** *a substrate with two hydrophilic binding sites is attached to the orbital shaker platform;* ***(c)*** *lubricant oil covers only hydrophilic binding sites;* ***(d)*** *two PZT parts are attracted to lubricant oil droplets and stay in a tilt state (one corner is touching the substrate);* ***(e)*** *centrifugal force to the right drags and balances part I on the lubricant oil droplet;* ***(f)*** *part I self-aligns with the binding site;* ***(g)*** *the centrifugal force to the left makes part II flat;* ***(h)*** *part II self-aligns with the binding site.*

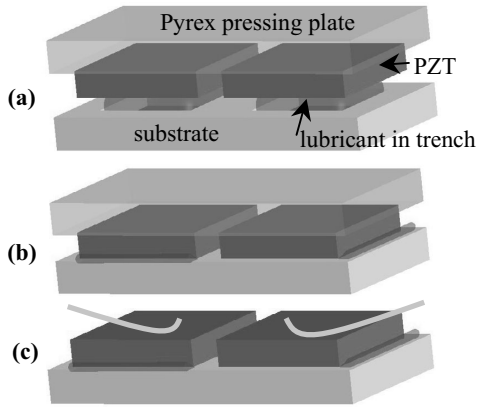

Fig.5. *A 500 micron thick pyrex wafer is used to squeeze out excessive lubricant.* ***(a)*** *pyrex wafer is applied on the substrate in parallel;* ***(b)*** *lubricant is squeezed out and PZTs touch the substrate;* ***(c)*** *wires bonded to the PZT top surface for testing use.*

PUMPING TEST

To demonstrate the performance uniformity of all the 28 pumps on a single wafer (Fig. 6), a laser vibrometer is used to obtain the resonance frequency without any fluid load (Fig. 7). Pump # 9 is chosen for an ethanol pumping test on the reusable testing stage (Fig. 8). During the pumping test, the inlet and outlet Teflon tubes (both tubes are about 15 cm long) are mounted to a level workstation surface, and the time is measured for the water column head to move through a selected region (1cm long) in the outlet tube. Because the tube fluidic resistance increases with the length of the tube [10], the water column head speed will drop as it moves towards the end of the outlet tube if the driving signal on the PZT does not change. To keep consistency between different frequencies, the water column head is reset to the same initial position before applying a new driving frequency. The result shows the first resonance frequency is about 7.1 kHz, and pumping rate at this resonance frequency is about 0.386 μl/sec when the applied voltage is 90 volts (p-p) (Fig. 9).

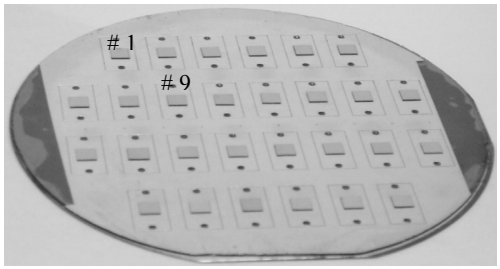

Fig.6. *28 PZTs assembled on pump chamber membranes on a 4-inch wafer by orbital shaker assisted self-assembly method. Yield ratio is 100%.*

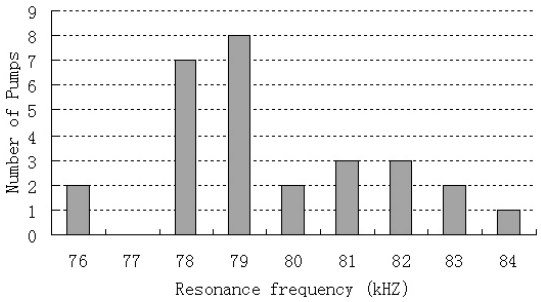

Fig.7. *Distribution of resonance frequency of 28 pumps on a single wafer. The average is 80.1 kHz, and standard deviation is 2.0 kHz. Here the pump wafer is not bonded to the testing stage.*

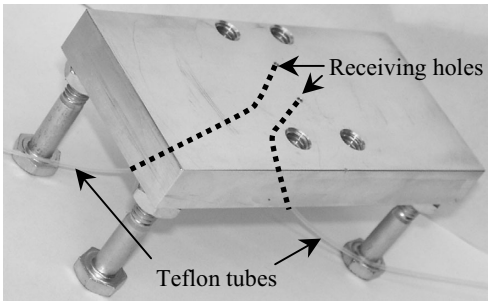

Fig.8. *A reusable pump testing stage. Pump wafer was bonded to the stage using silicone rubber, which provides strong bonding and can be de-bonded without any residue by applying an appropriate shear force on the wafer.*

ADHESION TEST

A de-bonding test was performed to compare the adhesion strength of the bonding between in-air assembly method and in-water assembly method. To measure the de-bonding force, a digital

scale is used (Fig. 10): the bonded stack is held vertically with the PZT resting on a pushing tip that is attached to the digital scale. Then the digital scale reading is zeroed out, and a force is applied to the top of the stack until the PZT is de-bonded or damaged. The final scale reading (in kilograms) multiplied by g = 9.81 N/kg is the de-bonding force. The result shows that bonding to a hydrophilic site without SAM in air is much stronger than bonding

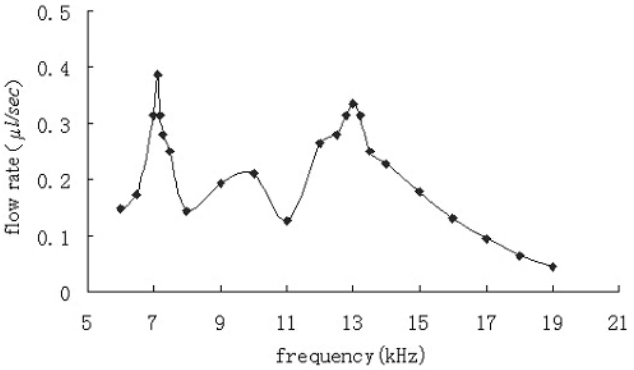

Fig.9. *Flow rate vs. frequency of pumping ethanol. The base resonance frequency is about 7.1 kHz. Here pump is bonded to the testing stage.*

to a hydrophobic site with SAM in water: the maximum shear stresses for in-air and in-water self assembled PZTs are greater than 2.22×10^6 Pa (PZT edge damaged by pushing tip at this stress) and 8.89×10^5 Pa, respectively.

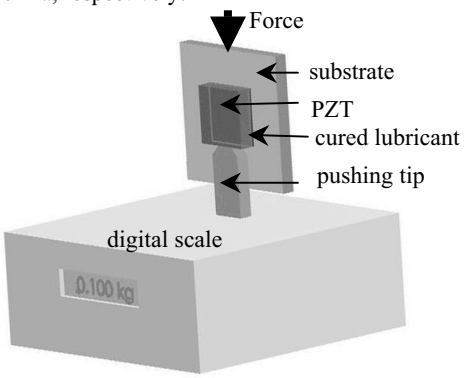

Fig.10. *Bonding strength test: 1) 3mm square PZT bonded by in-water assembly can be de-bonded by the shear force of about 8 Newtons and the de-bonding is at the interface between lubricant and substrate, which means the SAM on the binding site weakens the bonding; 2) the pump PZT bonded by in-air assembly still stays bonded at the force of 20 Newtons, when the PZT edge is damaged by the pushing tip.*

CONCLUSIONS

An orbital shaker assisted self-assembly technique in air is used to construct fixed valve micro pumps, and all the pumps work with high uniformity. This technique demonstrates many benefits of this method: precise placement, tilt free, strong bonding, well-defined bonding layer thickness by HF etching, and contact electrical connections by pressing. With batch process capabilities, this self-assembly technique supports the construction of more versatile and miniaturized micro systems.

ACKNOWLEDGEMENTS

This work is supported by NIH Center of Excellence in Genomic Science and Technology grant 1-P50-HG002360-01. The authors would like to thank Fred Forster and Yael Hanein for inspiring discussions, Brian Williams and Chris Morris for helping with the pump design and pumping test, Tai-Chang Chen for helping with laser cutting, and group members for helpful discussions.

REFERENCES

[1] J. Lienemann, A. Greiner, J. G. Korvink, X. Xiong, Y. Hanein, K. F. Böhringer, "Modelling, Simulation and Experimentation of a Promising New Packaging Technology - Parallel Fluidic Self-Assembly of Micro Devices." *Sensors Update* 13(1):3-43, December 2003.

[2] U. Srinivasan, M. H. Helmbrecht, C. Rembe, R. S. Muller, R. T. Howe, "Fluidic Self-Assembly of Micromirrors onto Microactuators Using Capillary Forces," *Journal on Selected Topics in Quantum Electronics,* 8(1), pp. 4-11, 2002.

[3] X. Xiong, Y. Hanein, J. Fang, Y. Wang, W. Wang, D. T. Schwartz, K. F. Böhringer, "Controlled Multi-Batch Self-Assembly of Micro Devices." *IEEE Journal of Microelectromechanical Systems* 12(2), pp.117-127, 2003.

[4] K. L. Scott, R. T. Howe, C. J. Radke, "Model for Micropart Planarization in Capillary-based Microassembly," *Transducers 2003*, pp.1319-1322.

[5] F. K. Forster, R. L. Bardell, M. A. Afromowitz, N. R. Sharma, A. Blanchard, *Proceedings of the ASME Fluids Engineering Division, ASME International Mechanical Engineering Congress and Exposition* (San Francisco), vol. 234 , pp. 39–44. 1995.

[6] B. E. Williams and F. K. Forster. "Micropump design of optimum pressure/flow characteristics". Micro-Electro-Mechanical Systems (MEMS), vol. MEMS-3 *ASME International Mechanical Engineering Congress and Exposition* (New York), 2001.

[7] K. Yang, I. Chen, B. Shew, C. Wang, "Investigation of the flow characteristics within a micronozzle / diffuser". Journal of Micromechanics and Microengineering, Vol.14, pp.26-31, 2004.

[8] A. Olsson, G. Stemme, E. Stemme, "A numerical design study of the valveless diffuser pump using a lumpedmass model", *J. Micromech. Microeng*. 9, 34-44, 1999.

[9] M. Heschel, M. Muellenborn, S. Bouwstra, "Fabrication and characterization of truly 3-D diffuser/nozzle microstructures in silicon", *IEEE J. Microelectromech. Systems*, Vol. 6, No. 1, 41-47, March 1997.

[10] C. J. Morris, F. K. Forster, "Low-order modeling of resonance for fixed-valve micropumps based on first principles", *IEEE Journal of Microelectromechanical Systems* 12(3), pp.325-334, 2003.

CMOS/BICMOS SELF-ASSEMBLING AND ELECTROTHERMAL MICROACTUATORS FOR TUNABLE CAPACITORS, GAP-CLOSING STRUCTURES AND LATCH MECHANISMS

Altug Oz* and Gary K. Fedder*†
*Department of Electrical and Computer Engineering and †The Robotics Institute
Carnegie Mellon University, Pittsburgh, PA 15213, USA

ABSTRACT

CMOS/BiCMOS MEMS micromovers that use the principles of self-assembly and electrothermal actuation have been designed, fabricated and tested. These micromovers exhibit lateral micro-positioning of up to 25 µm. Three main applications are demonstrated: tunable capacitors, gap-closing structures and latch mechanisms. A 2.17 to 1 capacitor tuning range was measured from 400 fF to 866 fF within a 5 V control voltage. Mechanical latch structures that operate by sequencing micromovers enable zero-power stand-by operation of the capacitors. Micromovers are also used to form 300 nm gaps, which are integrated into a microresonator design. Finite-element simulation of displacements of the lateral self-assembly and actuation match measured results to within 20%.

INTRODUCTION

There is an increasing interest for technologies to integrate MEMS actuators on CMOS or BiCMOS chips. The actuators should have small footprints and CMOS compatible control voltages (<5V). Electrothermal actuators can provide smaller footprints and smaller control voltages compared to the electrostatic actuators. They also provide large force and large displacements. However, thermal actuators consume more power than electrostatic actuators. Generally thermal actuators are also slower than the electrostatic actuators. Usually thermal time constants are longer than the electrical and mechanical time constants. To alleviate these two problems, the thermal mass of the actuators should be designed as small as possible.

Our prior electrothermal micromover design in a 20 µm by 200 µm area demonstrated 3.5 µm deflection with 18 mW heater power [1]. Lateral bending moments in the actuator are achieved by offsetting the metal layers embedded within the CMOS-MEMS beams. Larger displacement is desirable for many applications, but without increasing actuator footprint and power. Different techniques have been used to get larger displacements in compact areas. One of the techniques is to use both electrothermal and electrostatic actuation at the same time. One actuator design in a 0.03 mm^2 area produced 30 µm lateral deflection with 40 mW power [2]. Another design with the same technique was demonstrated for a RF MEMS switch [3]. A power of 400 mW was consumed during switching, but the 10 V electrostatic latch mechanism operated with close to zero continuous power. Another technique used current passed through V-shaped bent-beams anchored at two ends to cause a thermal expansion at the center of the actuator [4]. To increase the displacements, rotary actuators and inchworm designs were demonstrated by using multiple bent-beam actuators orthogonally [5]. For rotary actuator designs, the displacement was increased from 3 µm to 33µm, but power is increased from 40 mW to 375 mW.

Travel support has been generously provided by the Transducers Research Foundation and by the DARPA MEMS and DARPA BioFlips programs.

LATERAL MICROMOVERS

CMOS-MEMS micromovers exploit lateral stress gradients by embedding metal layers that are offset from the centerline of the beam [1]. The folded-flexure microactuator in Fig.1 illustrates the change in metal offset along the length of the actuator beams. Built-in differences in residual stress in the aluminum and silicon dioxide layers create a gradient driving self-assembly upon micro-structural release. The released beam bends into an S-shape resembling the static mode-shape of a guided-end beam. Electrothermal actuation generates a stress gradient from the different temperature coefficients of expansion of the offset materials and, in most CMOS technologies, acts to retract the beam back to its layout position when heated. The length, width and metal offset of the actuator beams are the primary design parameters that determine displacement characteristics.

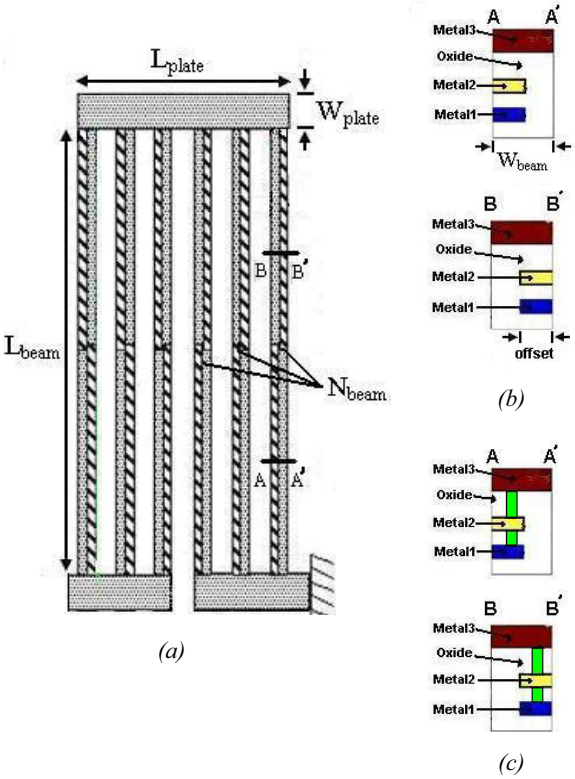

Figure 1. *(a) Layout and design parameters for a folded-flexure micromover, (b) Cross section of the micromover beams at two positions, showing the embedded metal offset, (c) Cross section of the micromover beams with vias between metal layers.*

Displacement magnitudes of the lateral self-assembly and actuation are verified quantitatively by finite element analysis (FEA), using Coventorware [6]. For FEA, a simulation

temperature, T_{set}, is calculated to model the lateral actuation magnitude upon release of the actuator.

$$T_{set} = -T_0 + T_{sim} + T_d \quad (1)$$

where, T_{sim}, is the simulator initial temperature, which is 273 K, and T_d is the ambient temperature. T_o denotes the characteristic temperature, defined as the temperature at which a beam with embedded offset metal layers exhibits zero deflection relative to layout. To perform a simulation in Coventorware, the characteristic temperature for that type of actuator must be known. This information can be measured from lateral curl of a simple beam test structure, by determining the temperature at which the structure is completely straight. An SEM of a test cantilever structure at room temperature is shown in Fig.2(a). The verniers at the tip of the beam aid in measuring lateral displacement.

Micromovers were designed in the Jazz Semiconductor 4-metal 0.35 µm BiCMOS process by using the lower three metal layers. All of the test micromovers have a symmetric dual folded flexure design. An example simulation of displacement is shown in Fig.2(b) for device #1A, which has its design parameters given in Table 1. The characteristic temperature of 367 K used in the simulation was measured from a test beam with the same design parameters. The simulated self-assembly lateral displacement is 12.4 µm. The thermal coefficient of expansion (TCE) values, that are used in the simulations are 28.3 µ/K for metal layers and 0.4 µ/K for oxide layers.

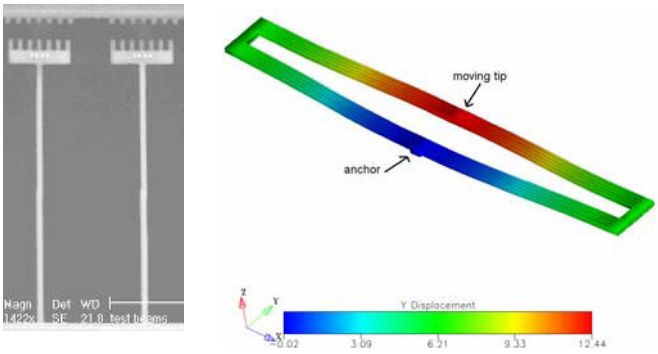

(a) *(b)*

Figure 2. *(a) Scanning electron micrograph (SEM) of test cantilever structures at room temperature, (b) Simulated self-assembly lateral displacement of device #1A.*

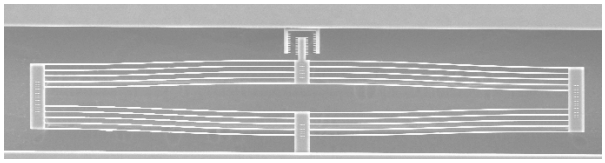

Figure 3. *SEM of a fabricated micromover in the Jazz process.*

Device #	L_{beam}	W_{beam1}	offset	L_{plate}	W_{plate}	N_{beam}	Via Between Metal layers
1A	200 µm	1.2 µm	0.6 µm	40 µm	10 µm	5	No
8A	200 µm	1.5 µm	0.9 µm	40 µm	10 µm	5	No
6B	200 µm	1.5 µm	0.9 µm	40 µm	10 µm	5	Yes
4B	100 µm	1.5 µm	0.9 µm	40 µm	10 µm	5	No

Table 1. *Design parameters for four dual folded-flexure micromover designs.*

Device #	Lateral self-assembly		Lateral electrothermal actuation		
	Measured displ.	Simulated displ.	T of the actuator	Measured displ.	Simulated displ.
1A	10.5 µm	12.4 µm	325 K	5.5 µm	4.3 µm
			350 K	10.5 µm	8.33 µm
			375 K	16 µm	12.27 µm
			400 K	21 µm	16.43 µm
			425 K	25.5 µm	20.46 µm
			450 K	---	24.48 µm
8A	1.8 µm	2.0 µm	325 K	4 µm	2.9 µm
			350 K	7.5 µm	5.5 µm
			375 K	10.5 µm	8.1 µm
			400 K	13 µm	10.5 µm
			425 K	15.5 µm	12 µm
			450 K	---	15.4 µm
6B	11 µm	12.8 µm			
4B	0.3 µm	0.4 µm			

Table 2. *Simulated and measured lateral displacement from self-assembly and electrothermal actuation.*

An SEM of the fabricated device #1A is shown in Fig.3. Measured and simulated displacement magnitudes of the lateral self-assembly and electrothermal actuation for different micromover test structures are given in Table-2. The temperatures in Table-2 are set with external heat sources and thermal sensing equipment for monitoring the temperature. Measured and simulated results match within 20%.

Some new techniques are used to improve the maximum displacement from the same actuator area. One technique is using vias between metal layers, as shown in Fig.1(c), to increase the lateral motion at the tip of the actuator. Device #6B has same design parameters as device #8A with the addition of the vias between metal layers. Device #6B has 6.1 times larger lateral displacement compared to device #8A for self-assembly.

Mechanical frequency response due to electrothermal actuation was measuried optically using a MIT microvision system [7]. Measurement results are shown in Fig.4 for a micromover in the Jazz process with the design parameters: L_{beam}= 168 µm, W_{beam1}= 1.5 µm, W_{beam2}= 0.9µm, L_{plate}= 43 µm, W_{plate} = 12 µm, and N_{beam}= 5. The 3dB bandwidth is 178 Hz. The measured mechanical resonant frequency (f_{res}) in Fig.4 is 26.3 kHz. Thermal bandwidth of the actuator is smaller than the mechanical bandwidth, so the system is dominated by the first-order thermal

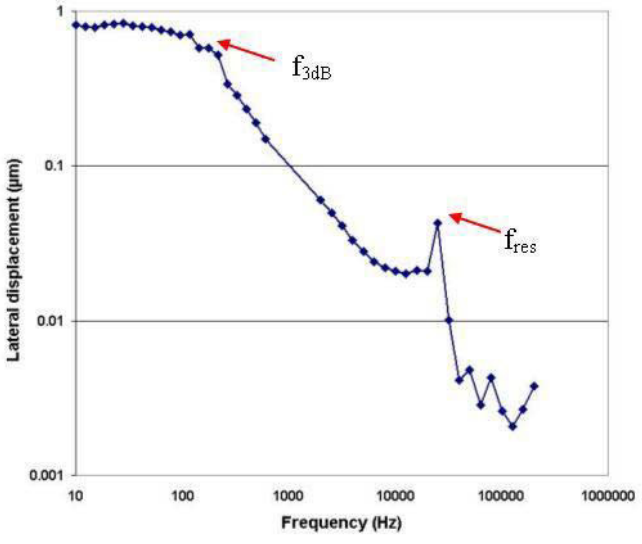

Figure 4. *Mechanical frequency response of a dual folded-flexure micromover during electrothermal actuation.*

response at frequencies below the mechanical resonance. The calculated 3dB bandwidth value from an equivalent first-order thermal model is 127Hz. The estimated thermal conductance and capacitance in the model are 5.832×10^{-5} W/K and 6.51×10^{-8} J/K, respectively.

LATERAL LATCH MECHANISM

Electrothermal actuators consume far more power in continuous operation compared to electrostatic actuators. It is advantageous to latch the micromovers into desired positions to eliminate continuous power supply. One basic latch mechanism is a "peg" in a slot, shown in Fig.5. The two micromovers start at zero power with the peg and one of the slots in an engaged position. This engaged position is formed through self-assembly of the micromovers. In the first actuation step, the latch micromover is actuated, pulling the slot away from the peg. After this, the device micromover is actuated to a new position corresponding to a different second slot. In the second step, heating power to the latch micromover is turned off and the peg becomes engaged with the second slot. In the third step, heating power to the device micromover is turned off, and the slot and peg contact each other keeping the device in its new position.

LATCHED TUNABLE CAPACITOR

Several tunable RF capacitors with a latching mechanism were fabricated in the Jazz process. A representative comb-finger capacitor design is shown in Fig.6. The latching function demonstrated upon release is shown in Fig.7(a) and corresponds to C_{MIN} = 280 fF. The second intended C_{MAX} latch state was not functional because the comb fingers could not engage. The alternate second latched position is shown in Fig.7(b) and corresponds to C_{MAX} = 380 fF, when the comb truss beams contact mechanically.

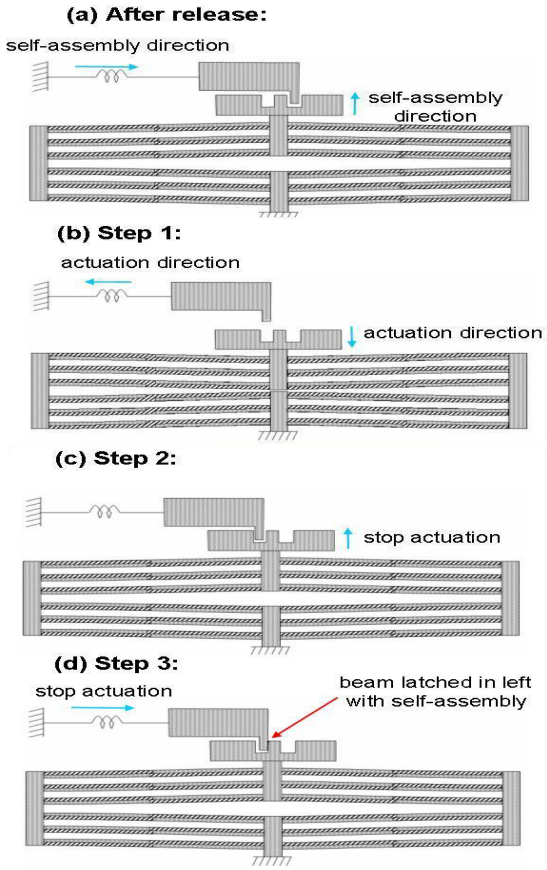

Figure 5. *Sequential steps for lateral latch mechanism.*

The measured tuning range of 36% is believed to be limited by a thin layer of sidewall polymer that acts as a dielectric spacer. This polymer is deposited during the CMOS-MEMS dielectric etch.. The comb engagement problem was due to bloat of the metal-4 layer, from which the mask defining the finger sidewalls was formed, and exacerbated by further comb finger widening from polymer deposited on the sidewalls.

Alternate capacitor designs were made with long interdigitated beams operating in a parallel-plate mode. This design has a measured minimum capacitance of 400 fF when the beams are centered with maximum gap and a maximum capacitance of 866 fF when the beams are actuated and touching, similar to the latch state in Fig.7(b) (but without the comb fingers). These limiting capacitance values, corresponding to a 2.17:1 tuning range, are about twice as large as the previous generation design [1]. The simulated values of C_{MIN} = 310 fF and C_{MAX} = 800 fF match with the measured values within 25%. The latch mechanism also functions for this design.

These sidewall parallel-plate capacitors are used in a voltage controlled oscillator (VCO) that provides 700 MHz frequency tuning range around a 2.45 GHz center frequency [8]. Similar capacitors are used in a RF filter to provide 490 MHz frequency tuning range around 2.1 GHz center frequency [8]. This capacitor design also enabled a low-power VCO design, by having a high quality factor over 30 for 1.5 GHz to 2.5 GHz [9].

GAP CLOSING STRUCTURE

Another application of the micromovers is in assembling nanometer-scale sidewall gaps for large capacitance and large

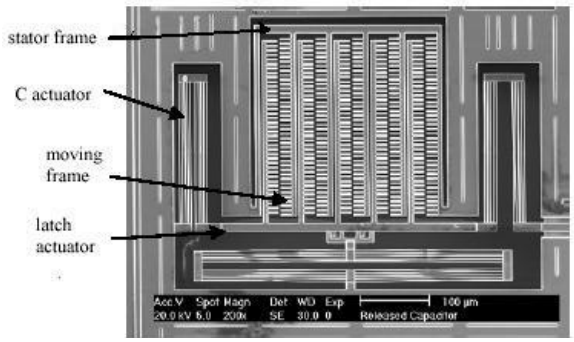

Figure 6. *An unengaged comb-finger tunable capacitor.*

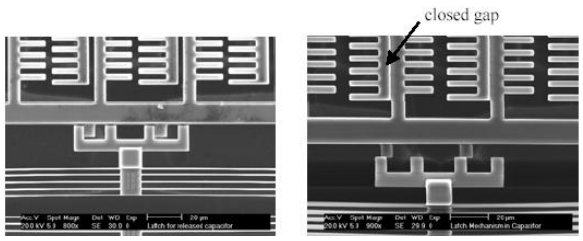

(a) *(b)*

Figure 7. *Capacitor latching. (a) A disengaged comb finger latch state, (b) A different latch state, where the comb truss beams contact mechanically.*

electrostatic force per area. Desirable gap sizes range from about 50 to 500 nm. Such small gaps are particularly useful for improving the gain of high-frequency microresonators. Conventional optical lithography and etching limits gap width in the CMOS microstructures to around 0.5 µm. Smaller gaps have been made in other micromachining processes, for example by forming a thin sacrificial oxide layer between silicon or polysilicon electrodes. In our assembly approach, the gap as drawn in layout is much larger than the final dimension, as depicted in Fig.8. One electrode of the gap is a resonator, exemplified by the fixed-fixed beam in Fig.8. A micromover shifts the other electrode in the direction to narrow the gap. A self-assembly micromover is ideal for this application, requiring zero power. A rigid limit stop sets the desired final gap value. Since the limit stop edge and the beam edge face the same direction, any global manufacturing variation in the sidewall etch will not affect the gap dimension. Theoretically, the gap can be set to an arbitrarily small value, however the practical minimum gap will be determined by the surface roughness of the sidewalls.

The gap closing mechanism is fabricated in the Jazz process for a cantilever resonator application. The gap closing result is given in Fig.9. The initial gap between the resonator and the micromover electrode was 1.1 µm, while the gap between the micromover and the limit stop was 0.8 µm. A 0.3 µm nanometer-scale gap was achieved after the release etch. For reference, the width of the beams on the resonator are 1.4 µm.

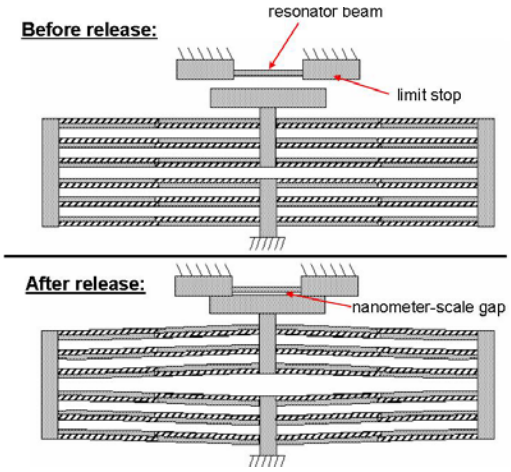

Figure 8. *Gap closing mechanism by using micromover self-assembly.*

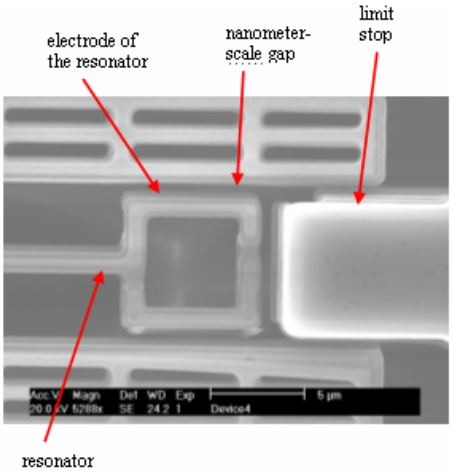

Figure 9. *SEM of a nanometer scale gap-closing mechanism.*

CONCLUSIONS

Maximum displacements of 10.5 µm for self-assembly and 25.5 µm for actuation enable applications where relatively large stroke in a compact footprint are needed. The micromovers are capable of sufficient motion to engage relatively long comb fingers. A 8:1 C_{MAX}:C_{MIN} tuning ratio is expected by compensating the metal-4 bloat in future layout. Design optimization may increase the tuning ratio further. The reasonable match between measured and simulated micromover displacement values verifies that the simulations are adequate for predictive design, but that second-order model refinement remains to be done. Zero-power standby capacitor tuning was demonstrated using the latch mechanism. Future work will investigate refinement of actuated latch mechanisms and quantify the improvement in resonator performance by using gap-closing mechanisms.

ACKNOWLEDGEMENT

This work was funded by the MARCO/DARPA Center for Circuits, Systems, and Software (C2S2).

REFERENCES

1. A. Oz, G. K. Fedder, "RF CMOS-MEMS capacitor having large tuning range," in *Proc. 2003 IEEE Int. Conference on Solid-State Sensors and Actuators (Transducers' 03),* Boston, MA, June 2003, Page(s): 851-854.

2. X.-Q. Sun, X. Gu, and W. N. Carr, "Lateral in-plane displacement microactuators with combined thermal and electrostatic drive," in *Proc. Solid-State Sensor and Actuator Workshop*, Hilton Head, SC, June 1996, pp. 152–155.

3. Ph. Robert, D. Saias, C. Billard, S. Boret, N. Sillon, C. Maeder-Pachurka, P. L. Charvet, G. Bouche, P. Ancey, P. Berruyer, "Integrated rf- mems switch based on a combination of thermal and electrostatic actuation," in *2003 IEEE Int. Conference on Solid-State Sensors and Actuators (Transducers' 03)*, Boston, MA, June 2003. Page(s): 1714-1717.

4. L. Que, J.-S. Park, and Y. B. Gianchandani, "Bent-beam electrothermal actuators -I: single beam and cascaded devices," in *J. MEMS*, vol. 10, pp. 247–254, June 2001.

5. J.-S. Park, L. L. Chu, A. D. Oliver, and Y. B. Gianchandani, "Bent-beam electrothermal actuators—Part II: Linear and rotary microengines," in *J. MEMS*, vol. 10, pp. 255–262, June 2001.

6. Coventor web page, http://www.coventor.com.

7. D. Freeman, A. Aranyosi, M. Gordon, S. Hong, "Multi-dimensional Motion Analysis of MEMS Using Computer Microvision", *Solid State Sensor & Actuators Workshop*, Hilton Head Is., SC, 1998, p. 150-155.

8. D. Ramachandran, A. Oz, V. K. Saraf, G. K. Fedder, T. Mukherjee, "MEMS-enabled reconfigurable VCO and filter", *2004 IEEE MTT-S Int. RFIC Symposium Dig.,* June 2004.

9. V. K. Saraf , D. Ramachandran, A. Oz, G. K. Fedder, T. Mukherjee, "Low-Power LC-VCO using integrated MEMS passives", *2004 IEEE MTT-S Int. RFIC Symposium.Dig.,* June 2004.

DYNAMIC ARRAY MANIPULATION OF MICROSCOPIC PARTICLES VIA OPTOELECTRONIC TWEEZERS

Aaron T. Ohta, Pei-Yu Chiou, and Ming C. Wu
Department of Electrical Engineering, UCLA
Los Angeles, CA 90095-1594

ABSTRACT

We report on the first dynamic array manipulation of microparticles using optoelectronic tweezers. Polystyrene particles with 20 and 45-μm diameters are individually trapped by light patterns generated by a digital light projector with digital micromirror device (DMD). Self-organization and individual addressing of the particles are demonstrated. Movement of 45-μm polystyrene particle is measured to be 35μm/sec (a force of 15 pN).

INTRODUCTION

Cellular-scale manipulation is an important tool in biological research. Technologies that have demonstrated the capability for such microscopic manipulation include optical tweezers and dielectrophoresis [1, 2]. While optical tweezers affords very fine control of microparticles, it suffers from high optical power requirements. Dielectrophoresis has been demonstrated to trap particles as small as 14 nm [3]. However, dielectrophoresis requires a static pattern of electrodes, and is not easily reconfigurable.

We have demonstrated another method of manipulating micrometer-scale objects: optically-induced dielectrophoresis, or optoelectronic tweezers [4]. Using a laser to induce dielectrophoretic forces, we have demonstrated controlled movement of 25-μm latex particles, and *E. coli* bacteria [4, 5]. This technique allows the use of very low optical power levels, enabling us to perform particle manipulation with an incoherent light source [6]. The use of a spatial light modulator in our optical system also allows us to dynamically reconfigure particle traps, providing us with increased versatility in particle manipulation over conventional dielectrophoresis. In this paper, for the first time, we present dynamic *array manipulation* of microparticles using optoelectronic tweezers. We demonstrate the self-organization of particles into an array, and the formation of single-particle arrays, with the capability to individually address each particle.

THEORY

Dielectrophoresis (DEP) refers to the forces induced upon a particle in the presence of a non-uniform electric field, which are typically generated by a variety of electrode configurations. A particle within an electric field forms an induced dipole, which will experience a force due to the field gradient [2].

The direction of the induced dielectrophoretic force is dependent upon the frequency of the electric field and the permittivity and conductivity of the particle and the surrounding medium. Positive DEP results in particle attraction to electric field maxima. In contrast, negative DEP causes particles to be repelled from field maxima. Applying an ac electric field thus allows the tuning of the type of DEP force induced on a particle, as well as negating any electrophoretic effects, or particle movement due to its surface charge.

Our optoelectronic tweezers (OET) device enables optically-induced dielectrophoresis. Unlike conventional DEP, no electrode pattern is required to introduce non-uniformities into an applied electric field; instead, a photoconductive layer is used to form virtual electrodes. Focusing incident light onto the photoconductor greatly increases its conductivity as compared to the dark areas, effectively creating an electrode in the illuminated area, analogous to the patterned electrodes in conventional DEP. In addition, the virtual electrodes used by OET are movable and reconfigurable, unlike the static electrodes of conventional DEP.

To illustrate, a repulsive OET trap is shown in Fig. 1(a). This single-particle rectangular trap has inner dimensions of 70 μm by 50 μm. A sphere with a diameter of 45 μm is surrounded by light "walls" 25 μm in width. The corresponding cross-sectional distribution of the square of the electric field shows that width of the trap as experienced by the particle is approximately 50 μm, as DEP force depends on the gradient of this distribution (Fig. 1(b)). If negative DEP forces are induced by the trap pattern, all particles outside the trap area will be repelled by the electric field maxima forming the trap perimeter. Any particle within the enclosed trap area will feel similar repulsive forces, but these forces balance, trapping the particle. Once a particle is contained within the rectangular pattern, the trap can be moved, transporting the particle to a desired location. Furthermore, multiple traps can be used as building blocks to form arrays of trapped particles. Such arrays can be arbitrarily arranged, and dynamically reconfigured.

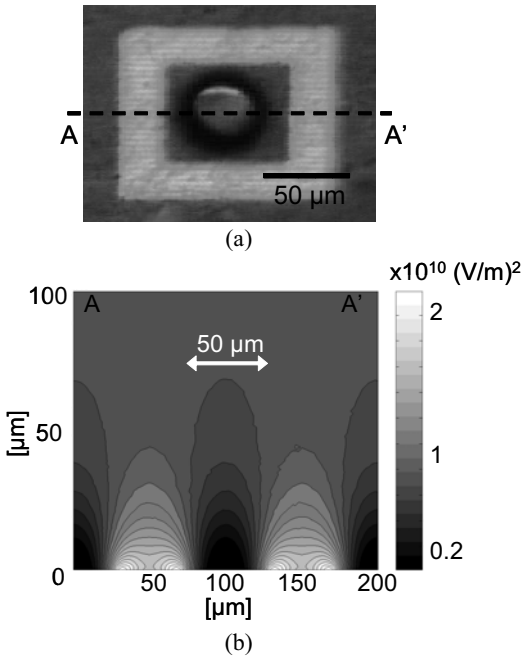

Figure 1. *(a) A single particle OET trap. A 45 μm polystyrene sphere is contained by optically-induced negative DEP.*
(b) Distribution of the square of the electric field for the single particle trap in (a) along the cross-section A-A'. DEP force is proportional to the gradient of this distribution.

0-9640024-5-0/hh2004/$20©2004TRF
DOI 10.31438/trf.hh2004.58

The optical power required to induce DEP forces in OET is much lower than that of optical tweezers, as the light energy does not directly trap the particles. Early experiments using OET showed movement of 25 μm particles at 4.5 μm/sec with an optical power of 1 μW, corresponding to an incident power density of 440 mW/cm^2 [4]. In comparison, a 1 μm diameter optical tweezers trap, at a minimum trapping power of 1 mW, has an optical power density of 32 kW/cm^2.

The low optical power requirements of OET offer many advantages in the system design. Inexpensive incoherent light sources can be employed instead of lasers to provide the illumination necessary for OET [6]. In addition, we can produce light patterns by imaging rather than scanning techniques. Furthermore, with no need to focus all optical energy, we can use a simple spatial light modulator to pattern images, rather than the holographic techniques employed by optical tweezers arrays [7]. In our experiments, we used the digital micromirror device (DMD) [8] in a light projector to image the virtual electrodes.

The optoelectronic tweezers device is formed by evaporating a 10-nm-thick aluminum film onto a glass substrate for electrical contact. A 1-μm-thick undoped amorphous silicon (a-Si) photoconductive layer is then deposited by plasma-enhanced chemical vapor deposition. To protect the photoconductive film, a 20-nm-thick silicon nitride layer is deposited over the a-Si. The liquid buffer layer containing the particles of interest is sandwiched between this photoconductive device and indium-tin-oxide (ITO) glass (Fig. 2). An applied ac bias across the ITO and a-Si produces the electric field.

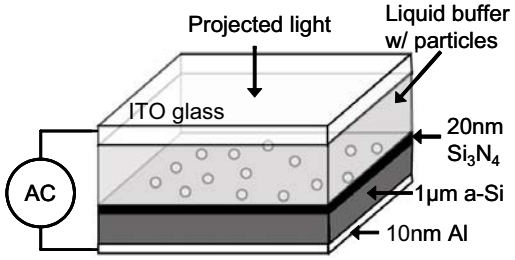

Figure 2. *Optoelectronic tweezers device. The liquid buffer containing the particles of interest is contained between the upper ITO glass layer and the lower photoconductive layer. To separate the top and bottom layers, 100-μm thick spacers are used (not shown).*

Amorphous silicon has a dark conductivity of 0.01 μS/m to 1 μS/m. Thus, in the dark, the a-Si has a much lower conductivity than the liquid buffer (which has a conductivity of 10 mS/m), causing the majority of the voltage to drop across the silicon layer. Incident light focused onto the photoconductive layer, greatly increasing its conductivity, results in a non-uniform electric field surrounding the illuminated area, as most of the voltage now drops across the liquid buffer layer. In this manner, the light incident on the OET device can pattern virtual electrodes.

EXPERIMENTAL SETUP

A DMD-based projector (InFocus LP335) is used to display images drawn on a PC, via Microsoft PowerPoint software. The projector provides both the optical source (a 120W, 1000-ANSI lumen high-pressure mercury lamp) and the DMD-to-PC interface. The output of the projector is collected, collimated, and directed into an Olympus MSPlan10 10X objective lens (NA = 0.30), projecting an image onto the OET device. The power at the projector output was measured to be approximately 600 mW. Approximately 7% of this power is collected by the objective lens and focused onto the OET device. Therefore, the power of the light incident on the OET is 42 mW, corresponding to an intensity of 12 W/cm^2.

The buffer solution consists of deionized water and KCL salt, mixed to obtain a conductivity of 10 mS/m. Polystyrene microspheres (45 and 20 μm, from Polysciences, Inc.) are mixed into the buffer solution, and sandwiched into the OET device. Observation of the particles under test is done via a Nikon TE2000U inverted microscope. A CCD camera attached to the observation port of the microscope recorded images and video of our experiments. A schematic of the optical setup is shown in Fig. 3. To produce the electric field necessary for DEP, an ac voltage of 10Vpp at 100 kHz (Agilent 33120A) was applied across the top ITO surface and the bottom photoconductive surface of the OET device.

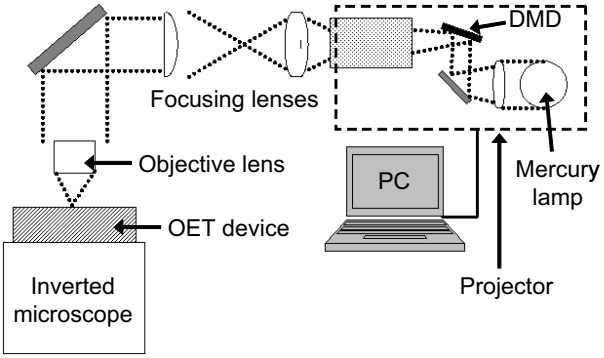

Figure 3. *Experimental setup. The image from an InFocus LP335 DMD-based projector is focused into a 10x objective lens, and projected down onto the OET device. Particle movement is observed via the Nikon TE2000U inverted microscope.*

EXPERIMENTAL RESULTS

We have demonstrated the self-organization of randomly distributed 45-μm polystyrene spheres into an array (Fig. 4). A simple grid pattern consisting of orthogonal horizontal and vertical lines, drawn in PowerPoint, is then projected onto the OET device. The pattern activates the optically-induced DEP, repelling particles from the illuminated areas due to negative DEP forces. This mechanism causes the self-organization of the particles once the grid pattern is illuminated; the particles are pushed into the non-illuminated cells. After a settling period, the particles are trapped within the of an array cells.

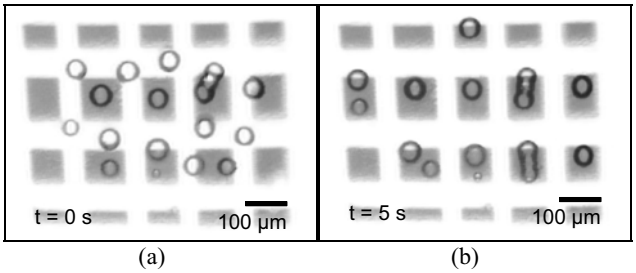

Figure 4. *Self-organization of 45-μm polystyrene spheres into an array configuration. After the initial grid illumination (a), the randomly arranged particles move towards the dark areas via negative DEP. After five seconds, all particles are contained within the array cells (b).*

Due to a large trap relative to the particle size, the initial self-organization may result in more than one particle per array cell (Fig. 4(b)). In this array, the largest cells are 80 µm by 100 µm. It may be possible to form self-organizing arrays with a single particle per array cell by optimizing the dimensions of a single array cell trap, such that only one particle may fit into the trap's potential well at any time.

In addition, we found that certain particles within the self-organized array are able to escape when the array is moved around the image plane. This phenomenon occurs for the array cells that contain multiple particles. This occurrence, along with subsequent manipulation of the self-organized array in Fig. 4(b), allowed us to obtain an array with a single particle per cell (Fig. 5a). We were able to move the resulting array of single particles around the image plane at approximately 25 µm/sec.

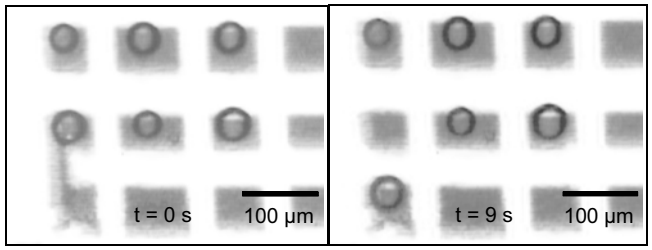

Figure 5. *Single-particle manipulation within the array. A particle in the lower-left side of the array is made to change its array by combining cells (a), the re-splitting the cell, moving the particle to the adjacent array position (b).*

Particles can be moved individually between adjacent cells, as illustrated in Fig. 5. The adjacent cells are merged by first removing the dividing wall, and then re-separating the cells. All movement of the trap walls are controlled in real time by the operator. To improve on the speed of this technique, a moving light wall can be used to facilitate the transportation of the particle between cells. This enables a single particle to be transferred to any cell of the array, using repeated transfers between adjacent cells.

Since the patterns for manipulating the particles in the array are created dynamically by optical illumination, a wide variety of operations can be performed by simple software programming. For example, to flush the particles in a single row of the array, we remove the dividing walls of that row and use a moving wall to sweep out the particles (Fig. 6).

In addition to self-organizing behavior, arrays can be formed from multiple single-particle traps. Each randomly positioned particle is first contained within a square trap. This is performed by drawing a rectangle around each particle in PowerPoint. The multiple traps can then be positioned to form an array of individually addressable cells. Using this technique, we are able to form a 4x5 array of single particle traps (Fig. 7). Though the operation was performed manually, it can potentially be automated by combining OET with a vision system. Biological applications of such an array include studies on single-cell behavior and interaction.

Since each cell of the array is an independent single particle trap, the array has the capability of being dynamically rearranged. To illustrate, an array consisting of 45 µm and 20 µm polystyrene spheres are reorganized under operator control (Fig. 8). This demonstrates the addressability of each particle trap, as well as the dynamic nature of the OET patterns.

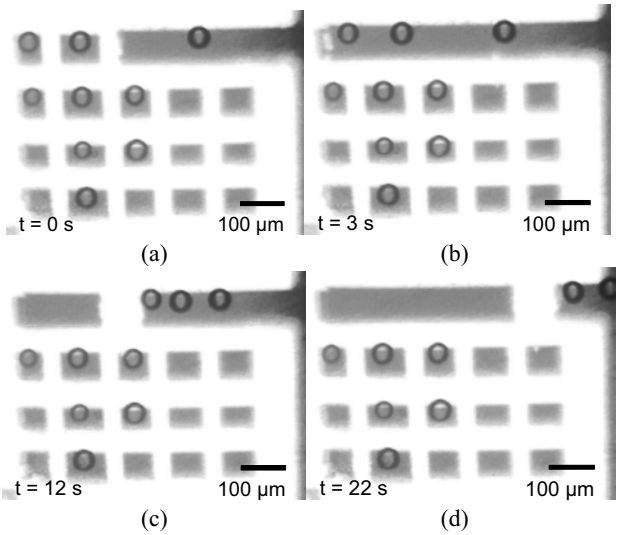

Figure 6. *Flushing an array row (to remove undesired particles from the array). First, the walls of the cells in the row to be flushed are removed (top row in (a)). The particles are no longer bounded in the lateral direction (b). An operator-controlled light bar is then used to push the particles out of the array (c, d).*

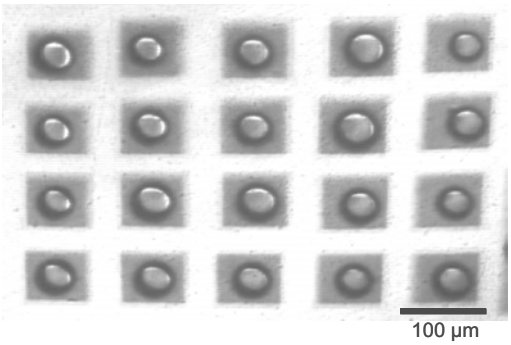

Figure 7. *An array of single particles, formed from multiple single particle square traps. Each particle is individually addressable. The time required to form this array of 20 particles was 3 minutes.*

DISCUSSION

Movement of a single 45-µm sphere due to negative DEP has a maximum velocity of approximately 35 µm/sec. This corresponds to an estimated force of 15 pN, based upon Stoke's Law. The maximum velocity of a 20-particle array is limited to approximately 25 µm/sec. Thus, the minimum holding force of each individual array cell is 10 pN. This force is less than that experienced by a single 45 µm particle, probably due to slight non-uniformities in image sharpness over the entire array area. The more defocused areas will have less of an electric field gradient, and a correspondingly lower DEP force. Thus, this 10 pN force reflects the minimum trapping force of all of the array cells.

The forces attained in these experiments, using an optical power density of 12 W/cm^2, are in rough agreement with our earlier results using a 632-nm laser light source [4]. Our earlier data suggests that the optical power density necessary to achieve a force of 15 pN is 6.6 W/cm^2. The difference between this predicted power density requirement and our experimental findings can be attributed to losses through the additional optics needed for our current experiment.

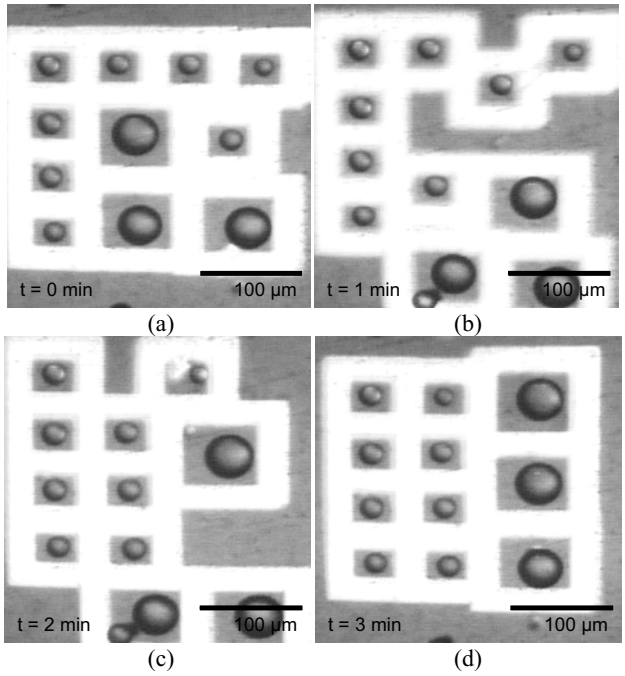

Figure 8. *Dynamic rearrangement of an array containing both 45 µm and 20 µm particles. An array is rearranged by moving individual cells into a desired configuration. Total rearrangement time is 3 minutes.*

Our results compare favorably to other microparticle manipulation techniques. Conventional dielectrophoresis uses static electrode patterns, and is thus not reconfigurable. In addition, our device is less expensive to produce, as no photolithographic steps are needed. Addressable DEP arrays have also been demonstrated using CMOS technology [9], but these devices are expensive to produce, and the minimum electrode size is limited by the required CMOS circuits (20 µm in [9]). Both conventional DEP and optical tweezers are capable of manipulating particles a few nanometers in diameter. The minimum size of the virtual electrode in OET is limited by the 115-nm ambipolar diffusion length of the a-Si [10].

The OET can operate over a large area (~ 1 x 1 mm^2), which is much greater than the 20 x 20 μm^2 for optical tweezers [7]. Though holographic tweezers can generate multiple traps, direct imaging using a DMD is more versatile. It can generate any arbitrary pattern with high contrast ratio. No computation is required to generate the desired pattern. Furthermore, OET can induce repulsive forces on transparent dielectric particles such as biological cells, and form cell cages, which is not possible with optical tweezers. On the other hand, optical tweezers traps are three-dimensional, whereas our trap patterns are limited to two dimensions. We are also must be more selective in our choice of buffer solutions, as the conductivity of the solution plays a crucial role in the DEP phenomenon.

CONCLUSIONS

We have demonstrated the self-organizing of 45-um polystyrene particles into an array, and the creation of an array from multiple single particle traps utilizing optoelectronics tweezers. Single particle movement within the array has been demonstrated, showing the ability to address individual array cells. Movement of single 45 µm polystyrene spheres was measured to be 35 µm/sec (a force of 15 pN). Movement of a 20-particle array was performed at 25 µm/sec (a force of 10 pN). Such particle manipulation techniques have many applications to experiments with biological cells and microparticles.

ACKNOWLEDGEMENTS

This project is supported by the Center for Cell Mimetic Space Exploration (CMISE), a NASA University Research, Engineering, and Technology Institute (URETI). Travel support has been generously provided by the Transducers Research Foundation and by the DARPA MEMS and BioFlips programs.

REFERENCES

[1] A. Ashkin, J. M. Dziedzic, J. E. Bjorkholm, and S. Chu, "Observation of a single-beam gradient force optical trap for dielectric particles," *Optics Letters*, 11(5), pp. 288-290, 1986.

[2] H. A. Pohl, *Dielectrophoresis*. Cambridge: Cambridge University Press, 1978.

[3] T. Muller, A. Gerardino, T. Schnelle, S. G. Shirley, F. Bordoni, G. Degasperis, R. Leoni, and G. Fuhr, "Trapping of micrometer and sub-micrometer particles by high-frequency electric fields and hydrodynamic forces," *J. Physics D – Applied Physics*, 29(2), pp. 340-349, 1996.

[4] P. Y. Chiou, Z. Chang, Zehao, and M. C. Wu, "A Novel Optoelectronic Tweezer Using Light Induced Dielectrophoresis," *Proc. IEEE/LEOS International Conf. Optical MEMS*, pp. 8-9, 2003.

[5] P. Y. Chiou, W. Wong, J. C. Liao, and M. C. Wu, "Cell Addressing and Trapping Using Novel Optoelectronic Tweezers," *Proc. IEEE MEMS*, pp. 21-24, 2004.

[6] A. T. Ohta, P. Y. Chiou, and M. C. Wu, "Dynamic DMD-Driven Optoelectronics Tweezers for Microscopic Particle Manipulation," to be published in the *Proc. Conference on Lasers and Electro Optics (CLEO)* 2004.

[7] D. G. Grier, "A revolution in optical manipulation," *Nature*, vol. 424, pp. 810-816, 2003.

[8] L. J. Hornbeck, "Deformable-Mirror Spatial Light Modulators," *Spatial Light Modulators and Applications III, SPIE Critical Reviews*, vol. 1150, pp. 86-102, 1989.

[9] N. Manaresi, A. Romani, G. Medoro, L. Altomare, A. Leonardi, M. Tartagni, R. Guerrieri, "A CMOS Chip for Individual Cell Manipulation and Detection," *Proceedings of IEEE International Solid-State Circuits Conference 2003*, vol. 1, pp. 192-487, 2003.

[10] R. Schwarz, F. Wang, M. Reissner. "Fermi-level dependence of the ambipolar diffusion length in amorphous silicon thin film transistors," *Applied Physics Letters*, vol. 63, p.1083, 1993.

LOW-COST ELECTROPLATED VERTICAL COMB-DRIVE

Zhihong Li and Norman Tien
Berkeley Sensor and Actuator Center, Department of Electrical and Computer Engineering
University of California, Davis, CA 95616

ABSTRACT

A low-cost, vertical comb-drive actuator has been developed employing a thick photoresist and electroplating process. The thickness of the metallic structures can be varied from a few microns to tens of microns. Utilizing this technique scanning mirrors with a reflecting area of 500μm×500μm and scanning angle up to ±10 optical degrees at resonant mode have been designed, fabricated and tested.

INTRODUCTION

Vertical comb-drive actuators (VCA's) have received significant research attention as they can directly provide torque and large out-of-plane motion, which is very important for optical applications such as scanning mirrors for raster scanning displays and optical communications [1-5]. VCA's have also been reported to realize other devices such as tunable capacitors with a high tuning ratio [6].

Previously reported methods of fabricating VCA's utilized DRIE, backside through-wafer etching, wafer bonding or double-sided alignment on expensive SOI wafers [1-5]. Such processes would result in high fabrication costs for products containing VCA's. In this work, we utilize the process of electroplating with a photoresist mold to fabricate VCA's, which is very inexpensive and can be applied to any substrate [7, 8]. Only two masks, neither requiring critical alignment, are employed. In addition, the thickness of the structures, as well as the overlap between upper comb fingers and lower comb fingers, can easily be varied from a few microns to tens of microns by using different photoresists and process parameters. If SU-8, an ultra-thick and high aspect ratio photoresist [9, 10], is employed, structures may be realized with thickness greater than 100μm. The metallic structures are advantageous for RF applications due to the low resistivity.

DEVICE DESIGN

Fig.1 (a) and Fig.1 (b) show micrographs of torsional scanning mirrors with different configurations (called Type A and Type B herein), which were designed and fabricated to validate the technique discussed. The reflecting area of the mirrors was 500μm×500μm and the length of comb fingers was 100μm or 200μm. The designed width and spacing of comb fingers were (5μm, 5μm), (4μm, 6μm) or (6μm, 6μm) to find an optimized design. In the Type A mirror, the width and length of the torsional beams were 4μm and 100μm respectively, while they were 5μm and 300μm in the Type B mirror.

Fig.2 shows a 3-dimesional schematic drawing of the scanning Type A mirror, in which the substrate is recessed by KOH etching to increase the maximum achievable tilt angle and to decrease the damping coefficient due to the squeezing film effect. Under electrostatic actuation, the torque, T, resulting from the change of capacitance is derived from [4, 5]

$$T = \frac{\partial C}{\partial \theta}\frac{V^2}{2} \tag{1}$$

where V is the applied voltage, C is the capacitance between fixed comb fingers and moving comb fingers, and θ is the angular displacement. Ignoring the fringing filed, the capacitance, C, is a function of θ [4]:

$$C = 2\frac{N\varepsilon_0 A(\theta)}{g} \tag{2}$$

where N is the number of pairs of the comb fingers, ε_o is the permittivity of free space, $A(\theta)$ is the overlap area as a function of θ, and g is the spacing between comb fingers. Under DC actuation, θ reaches the maximum value at maximum capacitance, i.e., the maximum overlap area, $A(\theta)$. The tilt angle under AC actuation can be much larger than DC actuation if the mechanical quality factor (Q) is high enough, because the comb fingers could go beyond the balanced position due to overshooting. The maximum tilt angle is dependent on the geometry of the device, the quality factor, and the waveform of the AC actuations. This will not be discussed in detail in this paper.

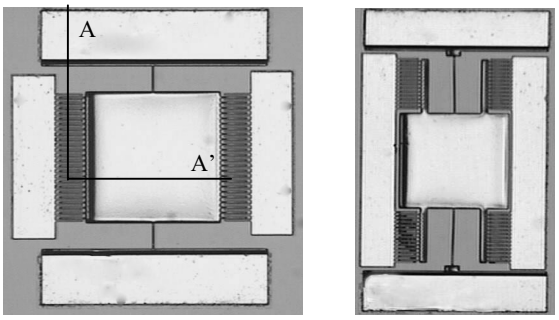

(a) Type A (b) Type B

Figure 1. *Micrographs of the fabricated mirrors with different layouts.*

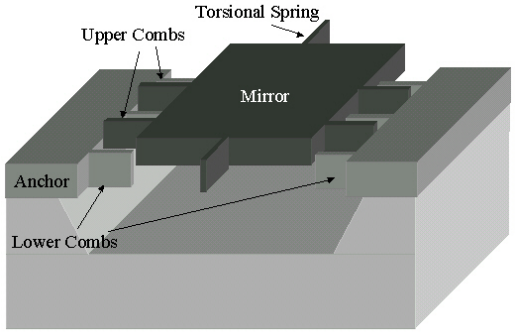

Figure 2. *3-dimensional schematic drawing of the scanning mirror.*

0-9640024-5-0/hh2004/$20©2004TRF
DOI 10.31438/trf.hh2004.59

PROCESS

A typical process flow along cross section A-A' (indicate cross section line) in Fig.1 (a) is shown in Fig.3. In the process, a PECVD oxide layer was employed as a plating-block mask for the lower comb fingers and anchors, and a Cu layer served as both a sacrificial and lifting layer for the mirrors and upper comb fingers. Therefore, self-aligned asymmetric upper comb fingers and lower comb fingers were achieved with a single step Ni plating. (a) A layer of Ni/Cr (1000Å/100Å) was evaporated as a seed layer on a 4' silicon wafer with 1.1µm thermal oxide. (b) A 0.3 µm PECVD oxide was deposited and patterned by RIE to form a plating-block for the lower comb fingers and anchors. (c) 20µm of AZ4620 photoresist was spun (double coating) and patterned with a Karl Suss MA4 contact aligner to form an electroplating mold. The designed width and spacing of comb fingers was 5µm, and the aspect ratio was 4:1. (d) An 8µm Cu layer was electroplated onto the mirror and upper comb fingers, while the anchors and lower comb fingers were not plated because they were covered with the PECVD oxide layer. (e) A 9µm Ni layer was electroplated on both the Cu layer and the Ni seed layer after a BOE strip of the oxide. Therefore, the thickness of both upper and lower comb fingers was 9µm with a 1µm overlap. The Ni was plated in *Technics Nickel S* sulfamate solution (Technics Inc.) at 40°C under pulsed direct current with a current density of 60mA/cm^2, a frequency of 1kHz and a duty cycle of 50%. A 15mL/Ga stress reducer/brightener was added to the solution to reduce the residual stress and to increase surface reflectivity. (f) The Cu layer was etched in $C_2H_4O_2$:H_2O_2:H_2O (1:1:20) solution to release the structures. (g) After the seed layer was removed, thermal oxide was etched in BHF to expose the area to be recessed. (h) The silicon substrate was etched by 22.5 *wt.%* KOH at 70°C to create a 15µm recess.

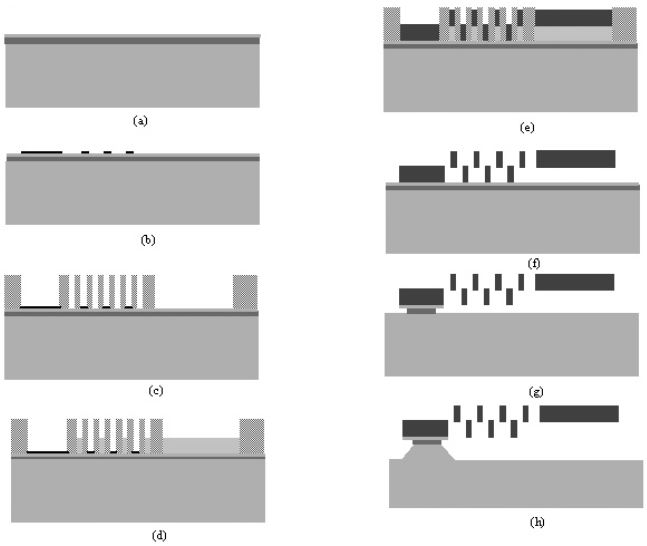

Figure 3. *A typical process flow to fabricate mirrors with electroplated vertical comb drive actuators.*

RESULTS

Fig.4 (a) and Fig.4 (b) show asymmetric comb fingers with different magnifications, where the length of comb fingers was 100µm, while the designed width and spacing were 4µm and 6µm, respectively. No significant buckling resulting from a residue stress gradient was observed on either the mirror or the comb fingers because of the thick structure and utilization of nickel sulfamate solution. However, some long beams (300µm) in the Type B mirror bent laterally with up to 5µm of deformation. The deformation was not observed before KOH etching. Therefore, the deformation was most likely caused by the air bubbles during KOH etching. This will be further investigated in the future. The results showed that the mirror with the designed geometry of 4µm comb finger width and 6µm comb finger spacing had higher yield and performance than one with 5µm comb finger width and 5µm spacing. In fact, the measured width of the comb fingers was about 5µm for the designed 4µm comb due to the lithography process. The mirror with the designed 6µm comb finger width and 6µm spacing had a bit higher yield than the same device with 4µm comb finger width and 6µm spacing, but the driving voltage was higher. The lower beams were about half micron narrower than the upper ones because of the profile of the photoresist mold. Before electroplating, the wafer was cut into pieces containing 4-6 dice. The deviation of thickness of photoresist mold was within 10%.

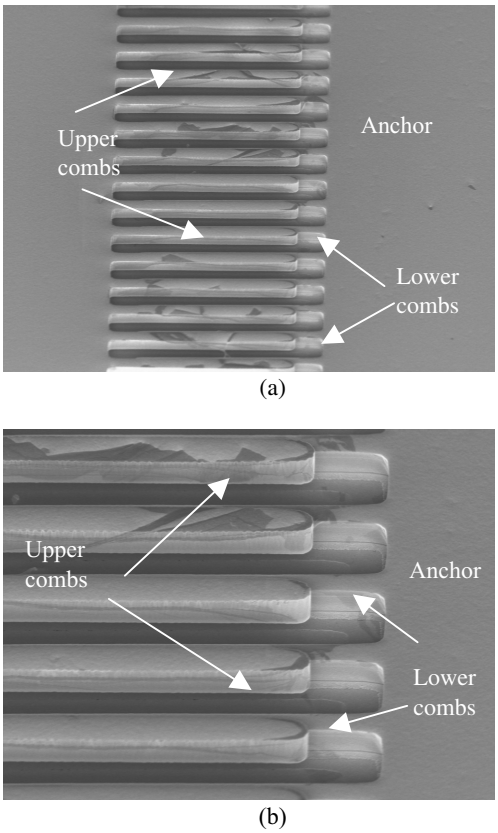

Figure 4. *SEM micrographs of asymmetric comb fingers with different magnifications. The length of comb fingers was 100µm, while the designed width and spacing were 4µm and 6µm, respectively.*

The mirrors were designed to operate at resonance, but they could also operate by being driven statically. The tilt angles under DC and AC actuation and frequency response were measured. In all of our measurements, the voltage was applied to a single side of the comb drives.

Fig.5 shows the peak-to-peak tilt angle as a function of an applied square wave voltage with a 50% duty cycle at the resonant frequency. The maximum tilt angle was ±9.8 optical degrees at about 3.8kHz and 78V for the Type B mirror with 100μm-long comb fingers. The Type A mirror with 100μm-long and 5μm-wide comb fingers had the maximum tilt angle of ±5 optical degree at about 4.6kHz and 65V. The mirror with 200-μm-long comb fingers had lower driving voltage, but the maximum tilt angle was much smaller.

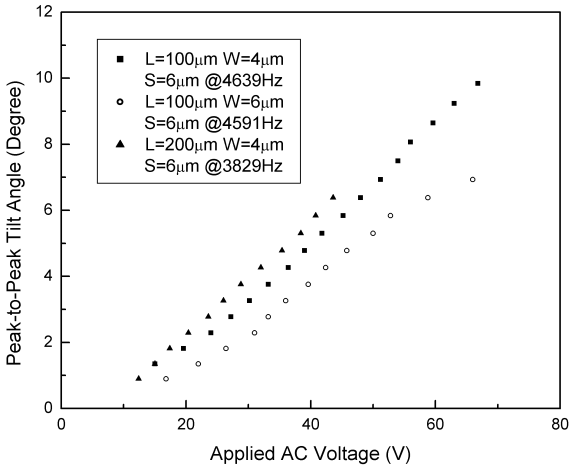

(a)

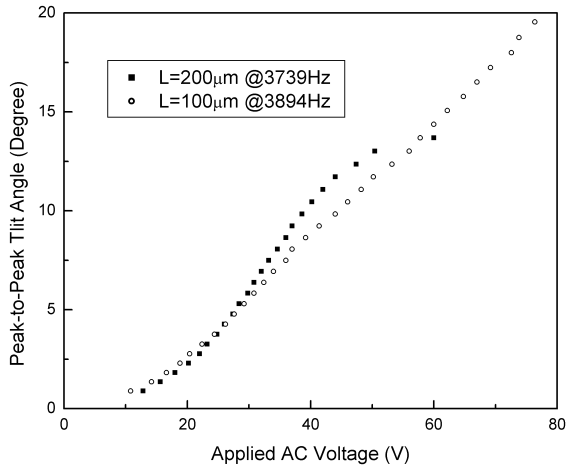

(b)

Figure 5*. The peak-to-peak tilt angles as a function of the applied pulsed DC voltage at 50% duty cycle at the resonant frequency for (a) the Type A mirror and (b) the Type B mirror, where L, W and S are the designed length, width and spacing of the comb fingers. In the Type B mirror, the width and spacing of comb fingers are 4μm and 6μm.*

Fig.6 presents the frequency response of the mirrors. The resonant frequency of the Type A mirrors with the designed comb finger length of 100μm was about 4.6kHz, with no significant difference for different comb widths, while the frequency of the mirrors with designed comb finger length of 200μm was about 3.8kHz. The resonant frequencies of the Type B mirrors with comb finger length of 100μm and 200μm were 3.7kHz and 3.9kHz, respectively.

Fig.7 shows the DC voltage dependence of tilt angles. The Type A mirror with the designed comb finger length of 100μm, width of 4μm and spacing of 6μm reached the maximum tilt angle of 2.8 optical degree at 141V, after which the mirror was balanced. The angle coincided with the calculated value of 2.7 optical degrees, at the maximum capacitance position. The Type B mirror with 200μm-long comb fingers and 100μm-long comb fingers reached the maximum tilt angle of 2.5 optical degrees at 130V, and 2.4 optical degrees at 200V, respectively. The values were smaller than the calculated angle of 3.7 optical degrees. The reason was that the displacements other than rotation (normal translation or lateral translation) occurred when a DC voltage was applied to a single side of the comb fingers, because the design of torsional beams was not optimized.

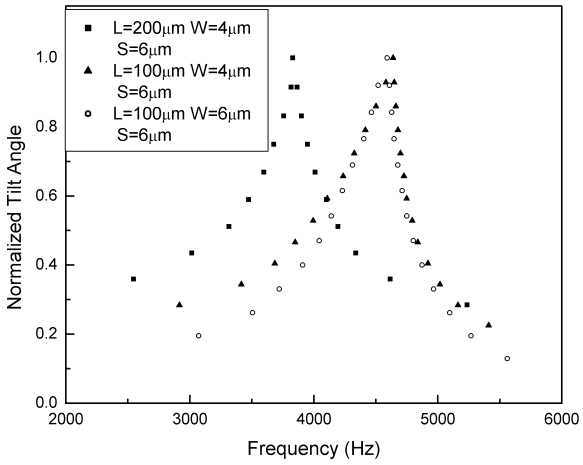

(a)

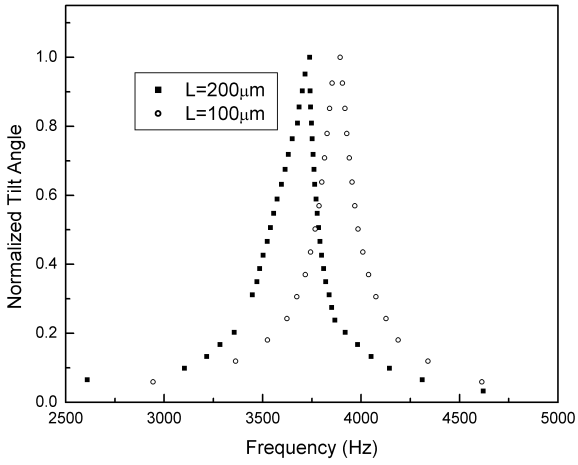

(b)

Figure 6*. The frequency response for (a) the Type A mirror and (b) the Type B mirror. The tilt angle is normalized by the maximum tilt angle for each device.*

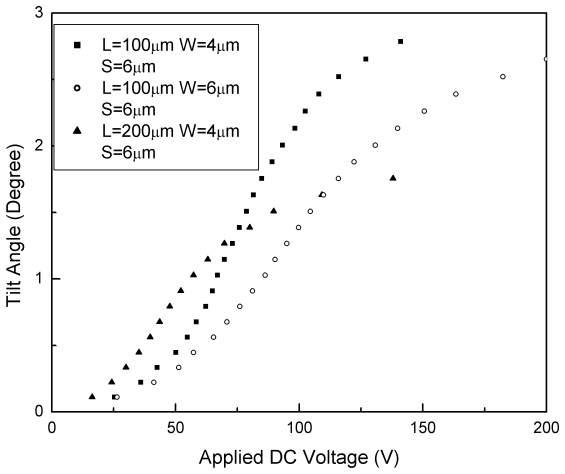

(a)

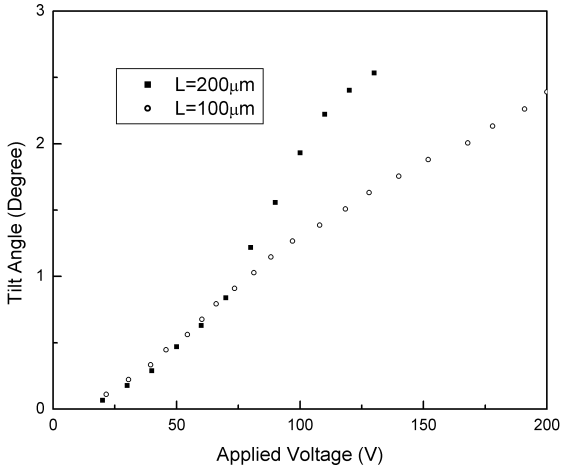

(b)

Figure 7*. The DC voltage dependence of tilt angles for (a) the Type A mirror and (b) the Type B mirror*

CONCLUSIONS

Utilizing a thick photoresist and electroplating process, a low-cost, vertical comb-drive actuator has been developed. In the process, a buried PECVD oxide mask and a Cu layer as a sacrificial and lifting layer allows Ni vertical asymmetric comb drives to be fabricated with self-alignment. Using this technique, two types of scanning mirrors with a reflecting area of 500μm×500μm have been designed, fabricated, and tested. The maximum tilt angle was ±9.8 optical degrees at about 3.8kHz and 78V for the Type B mirror with 100μm-long comb fingers, while the Type A mirror with the designed comb length of 100μm, width of 4μm and spacing of 6μm reached the maximum tilt angle of 2.8 optical degree at 141V DC voltage.

The evaluation of additional design parameters such as surface roughness, curvature, and reflectivity, and the application of the vertical comb-drive for tunable capacitors are in progress.

AKNOWLEDGEMENT

The authors would like to thank Dr. Daniel T. McCormick for his help in measurement and Mr. Qingquan Liu for Ni plating process.

REFERENCES

1. Y. Mizuno, O. Tsuboi, N. Kouma, H. Soneda, H. Okuda, Y. Nakamura, S. Ueda, I. Sawaki, and F. Yamagishi, "A 2-Axis Comb-Driven Micromirror Array for 3D MEMS Switches", *Conference Digest of 2002 IEEE/LEOS International Conference on Optical MEMS, 8/20-23/02,* Lugano, Switzerland (2002), pp. 17-18
2. V. Milanovic, S. Kwon, and L. P. Lee, " Monolithic Vertical Combdrive Actuators for Adaptive Optics", *Conference Digest of 2002 IEEE/LEOS International Conference on Optical MEMS,* 8/20-23/02, Lugano, Switzerland (2002), pp. 57-58
3. D. Hah, S. Huang, H. Nguyen, H. Chang, J. –C. Tsai, M. C. Wu, " Low Voltage MEMS Analog Micromirror Arrays with Hidden Vertical Comb-Drive Actuators", *Technical Digest of the 1994 Solid-State Sensor and Actuator Workshop*, Hilton Head Isl., SC, 6/13-16/94, Transducer Research Foundation, Cleveland (1994), pp. 11-14
4. D. McCormick, Ph. D. Dissertation, Cornell University, 2003
5. J. A. Yeh, H. Jiang, and N. C. Tien, "Integrated Polysilicon and DRIE Bulk Silicon Micromachining for an Electrostatic Torsional Actuator", *Journal of Microelectromechanical Systems, 8,* 4(1999), pp.456-465
6. H. Nguyen, D. Hah, P. R. Patterson, W. Piywattanametha, M. C. Wu, " A Novel MEMS Tunable Capacitor Based on Angular Vertical Comb Drive Actuators", *Technical Digest of the 1994 Solid-State Sensor and Actuator Workshop*, Hilton Head Isl., SC, 6/13-16/94, Transducer Research Foundation, Cleveland (1994), pp. 277-279
7. X. Li, S. Kiyawat, and C.-J. Kim, "High-Aspect-Ratio Electroplated Structures with 2μm Beamwidth, *Proc. MEMS (MEMS-Vol. 1), ASME Int. Mechanical Engineering Congress and Exposition, Nashville, TN,* (1999), pp. 25-30.
8. J. Quemper, S. Nicolas, J. P. Grandchamp, A. Bosseboeuf, T. Bourouina, and E. Dufour-Gergam, "Permalloy Electroplating through Photoresist Molds", *Sensors and Actuators,* 74 (1999), pp. 1-4
9. H. Lorenz, M. Despont, N. Fahrni, N. Labianca, P. Renaud and V. Vettiger, "SU-8: a Low-cost Negative Resist for MEMS", *J. Micromech. Microeng*, 7(1997), pp. 121-124
10. E. H. Conradie and D. F. Moore, "SU-8 Thick Photoresist Processinf as a Functional Material for MEMS Applications", *J. Micromech. Microeng*, 12(2002), pp. 368-374

BULK MICROMACHINED TITANIUM MICROMIRROR DEVICE WITH SLOPING ELECTRODE GEOMETRY

Masa P. Rao[1], Marco. F. Aimi[2], and Noel C. MacDonald[1, 2]
[1]Mechanical & Environmental Engineering Department, University of California, Santa Barbara (UCSB), Santa Barbara, CA 93106
[2]Materials Department, University of California, Santa Barbara (UCSB), Santa Barbara, CA 93106

ABSTRACT

This paper reports the fabrication of a bulk micromachined hybrid torsional micromirror device composed of titanium mirror structures bonded to an underlying silicon sloping electrode structure. The fabrication of the device is enabled by two recent innovations: 1) the Metal Anisotropic Reactive Ion etching with Oxidation (MARIO) Process [**1**], which provides, for the first time, high aspect ratio micromachining capability in bulk titanium; and 2) the High Aspect Ratio Laminated Metal Micromachining (HARLMM) Process, which allows for creation of complex, multilayer titanium devices and heterointegration of these devices with dissimilar material substrates. This work represents the first demonstration of the MARIO and HARLMM Processes in a device application. Details on the fabrication of the device are presented illustrating the simplifications made possible by these two processes and additional simplifications made possible by the single-mask process used to create the sloping electrode structure.

INTRODUCTION

The advent of high aspect ratio bulk micromachining has provided the opportunity for extension of microfabrication capability into the third dimension well beyond that possible using surface micromachining. This has enabled the development large, rigid, highly planar MicroElectroMechanical Systems (MEMS) with highly predictable and reproducible mechanical response. However, material selection in high aspect ratio micromachining has been limited almost exclusively to single crystal silicon, due primarily to the predominance of Deep Reactive Ion Etching (DRIE) Processes, such as the Bosch Process.

While silicon has proven to be an excellent micromechanical material for many applications, no one material can satisfy the requirements of all applications. Consequently, there exists a need for microfabrication techniques that provide greater materials selection capability for high aspect ratio micromechanical applications. The development of the MARIO Process addresses this need by enabling the fabrication of high aspect ratio structures in titanium.

Titanium has a number of properties that make it an attractive alternative to silicon, one of which is its high fracture toughness, which has implications for enhanced durability, shock resistance, flaw tolerance, and notch insensitivity. Interest in these attributes, as well as many others, has motivated efforts to develop process technology that enables implementation of titanium on the micro-scale. Methods such as surface micromachining [**2**] and bulk micromachining via wet/electrochemical etching [**3,4**] have been reported, but each suffers from aspect ratio restrictions that limit design flexibility and functionality. The MARIO Process, in contrast, has no such limitation. It allows definition of arbitrarily complex structures with micron-scale features and tall vertical sidewalls in bulk titanium substrates.

The utilization of titanium also provides added benefit with regards to process simplification and design complexity through the HARLMM Process. The high fracture toughness of titanium allows foils as thin as 10 μm to be handled and processed without the need for fixation to temporary carriers. This enables the fabrication of complex structures with significant cross-sectional variation though-the-thickness by sequential bonding of thin foils. The HARLMM Process also enables heterogeneous integration of high aspect ratio, multi-level, titanium-based MEMS with dissimilar material substrates, therefore providing considerable flexibility with respect to device design, fabrication, and functionality. Similar operations in silicon are possible, but generally require the use of temporary fixation to prevent damage to the delicate thin silicon layers or donation of thin device layers from Silicon on Insulator (SOI) wafers. These methods can add significant cost and impose undesirable constraints on the device design, fabrication, and packaging.

In this paper, the MARIO and HARLMM Processes are used to fabricate a hybrid micromirror device composed of titanium mirrors that are heterogeneously integrated with underlying fixed silicon sloping electrode structures. The sloping electrode structure is utilized to reduce the drive voltage and is created using a simple single-mask process based on the exploitation of Reactive Ion Etching (RIE)-lag.

THEORY

Recent work has shown that utilization of non-parallel plate electrode geometries, such as terraced [**5**] or sloping electrodes [**6,7**], offers the potential for reduced drive voltage relative to comparable parallel plate designs without compromising angular displacement or switching speed. Figure 1 shows a schematic of a particular sloping electrode geometry in which the inside edge of the sloping electrode is not aligned along the centerline defined by the mirror's axis of rotation (i.e. $x = 0$), but is instead spaced a finite distance, x_0, away.

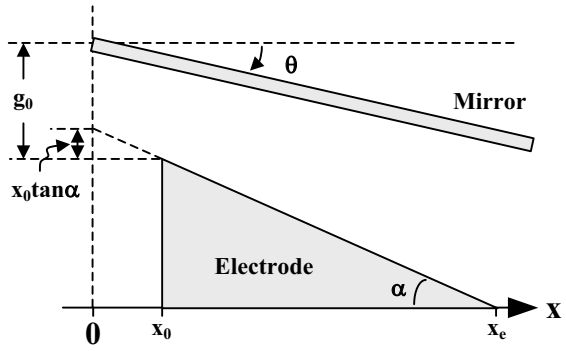

***Figure 1. Sloping electrode schematic**. Note: only half of the electrode geometry is shown, plane designated by x=0 is the symmetry plane.*

The electrostatic torque for this electrode geometry can be expressed as

0-9640024-5-0/hh2004/$20©2004TRF
DOI 10.31438/trf.hh2004.60

$$T_E = \int_0^{x_e} xF_E(\theta, x)dx - \int_0^{x_0} xF_E(\theta, x)dx \qquad (1)$$

where x is the moment arm, F_E is the electrostatic attraction force per unit length, and θ is the mirror tilt angle. The first term is the torque applied by a sloping electrode that begins at the centerline and extends out to length x_e, and the second term subtracts the torque produced by the missing inner portion of the electrode that extends from $x = 0$ to $x = x_0$. The electrostatic force, F_E, can be approximated by

$$F_E = \frac{\varepsilon_0 w V^2}{2g(\theta, x)^2} \qquad (2)$$

where ε_0 is the dielectric constant, w the width of the mirror, V the applied voltage, and g the effective gap between the mirror and sloping electrode. The effective gap varies as a function of the mirror tilt, position along the x-axis, and the electrode slope, and can be defined as

$$g = g_0 - x_0 \tan\alpha + x\tan(\alpha - \theta) \qquad (3)$$

where g_0 is the initial gap distance between the highest point on the electrode and the mirror in its rest state (i.e. $\theta = 0$), and α is the slope angle of the electrode. It should be noted that the above expression does not take into account any vertical 'piston-like' displacement of the mirror. In the current device, such displacement is considered to be negligible due to the resistance to out-of-plane bending afforded by the high aspect ratio torsion springs ($a/b \geq 10$). It should also be noted that the above analysis does not account for any fringing field effects.

Figure 2 shows a plot of the torque curves produced by evaluation of Eqs. 1-3 for both sloping and parallel plate electrode geometries compared to the restoring torque produced by the torsional springs. The torque enhancement provided by the sloping electrode geometry is clearly evident. For the given case, pull-in voltage is reduced from 147.2 V for the parallel plate electrode to 57.2 V for the sloping electrode, representing a 61% reduction in drive voltage.

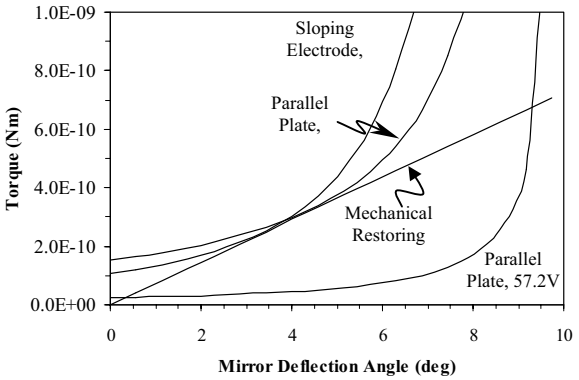

Figure 2. Plot of electrostatic attraction torques for sloping and parallel plate electrodes at varying voltages vs. mechanical restoring torque. *Device dimensions used for the calculation were: 100x100x10μm mirror;1x10x60μm springs; x_0 = 5μm; x_e = 49.24μm; α = 10°; and g_0 = 0.88μm.*

EXPERIMENTAL DETAILS

As illustrated in the previous section, the sloping electrode geometry holds promise for significant reduction of drive voltage. Fabrication of structures with such surface gradient topography is by no means simple, however. Methods reported in the literature for fabrication of sloping electrode micromirror devices [**5-7**] rely on rather complex fabrication routes that could conceivably have detrimental implications on performance, cost, manufacturability, and/or reliability. In this section we present a fabrication method that is far simpler to implement.

The micromirror device is composed of two discrete die, the Electrode Die and the Mirror Die, that are fabricated separately then bonded together in the final step using gold thermocompression bonding. Both die are fabricated via simple, single-mask bulk micromachining processes.

The Electrode Die is fabricated in single crystal silicon substrates using a single-mask, DRIE-based process flow that relies on the phenomena of RIE-lag to simultaneously define all structures on the die. The process begins with lithographic patterning of the silicon wafer in which all components of the Electrode Die are defined, including: sloping electrodes; interconnect lines; remote bondpads; bonding frames that set the mirror/electrode gap height; and grounded landing pads that prevent the mirror from physically contacting the drive electrodes during snap down. Figure 3 shows a portion of the mask pattern used to fabricate the Electrode Die.

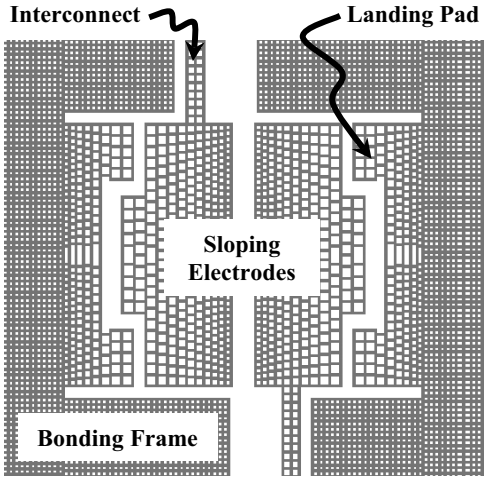

Figure 3. Portion of the Electrode Die mask pattern.

After lithographic patterning the wafer is etched using DRIE, the photoresist mask is stripped, and the wafer is thermally oxidized. The oxidation time is determined by the time needed to oxidize through all thin-walled structures above the etched floors. The oxidized structures are then removed via wet etching in hydrofluoric acid, thus yielding a surface whose topography is defined by the previous DRIE etch depth variation.

Once the HF etch has been performed, all structures on the Electrode Die have been physically defined, however, these structures are not yet electrically active nor isolated from one another. Electrical isolation is achieved by thermally oxidizing the wafer, which isolates the surfaces of the raised structures from the underlying silicon substrate. Electrically active surfaces and connections are then created by blanket gold metallization using e-beam evaporation. The complete process flow for the Electrode Die is summarized in Figure 4.

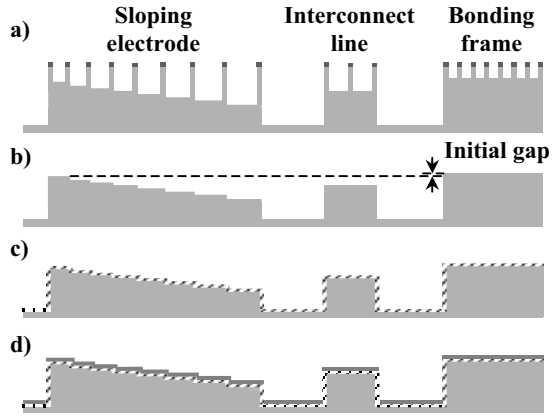

Figure 4. Electrode Die process flow. *a) lithographic patterning on single crystal silicon followed by DRIE; b) thermal oxidation followed by HF-based wet etching; c) thermal oxidation; and d) blanket gold metallization.*

The Mirror Die is fabricated in free-standing 10 μm thick bulk titanium foil which has been chemical mechanical polished (CMP) to facilitate lithographic patterning. A titania etch mask is deposited using reactive sputtering and is patterned using a CHF_3-based dry etch. The foil substrate is then deep etched using the MARIO Process, which is a cyclic etch/passivation dry etch recipe consisting of a chlorine-based etch step and a passivating oxidation step. Further details regarding the MARIO Process can be found in reference 1. Etching is carried out until the pattern is completely etched through the foil, resulting in a die with free-standing mirrors supported by high aspect ratio springs. The die is then coated with gold on the backside using e-beam evaporation and finally bonded to the Electrode Die using gold thermocompression at 350 ºC and ~7 MPa applied pressure.

RESULTS & DISCUSSION

Figure 5 shows the completed Electrode Die prior to bonding of the Mirror Die. As can be seen, fabrication of complex, 3-dimensional structures with multiple levels and sloping surfaces is achieved with a single lithographic masking step. Modulation of the etch via dimensions in the mask pattern causes variation in etch depths across the pattern due to transport limitations imposed by the narrow via dimensions. This etch depth variation is then translated into surface height variation by removal of the thin-walled structures above the etched floors using thermal oxidation and HF-based wet etching.

Utilization of thermal oxidation and wet etching allows for incorporation of both thick- and thin-section structures in the same mask pattern, e.g. the large electrodes and thin interconnect lines of the current device. This provides greater design flexibility relative to other lag-based methods that rely on isotropic etching to remove the structures above the etched floors [**8,9**]. Fabrication of complex structures such as the Electrode Die would not be possible with these methods due to the aggressive undercutting that occurs as a result of isotropic etching.

The use of narrow etch vias for the definition of the device structures causes the etch rate to lag well behind that of the surrounding open areas, therefore defining raised structures with tall vertical sidewalls that stand at varying heights above the substrate floor. Once these structures have been oxidized (Fig. 4c), the vertical sidewalls enable electrical isolation of the upper surfaces of the structures from one another and the surrounding substrate floor due to the poor step coverage of the e-beam metallization (Fig. 4d). Deposition does not occur on surfaces that are parallel to the deposition direction, i.e. the vertical sidewalls, thus electrical isolation is achieved by virtue of the topography of the surface. This therefore enables the definition of all electrically active surfaces without the need for additional patterning steps.

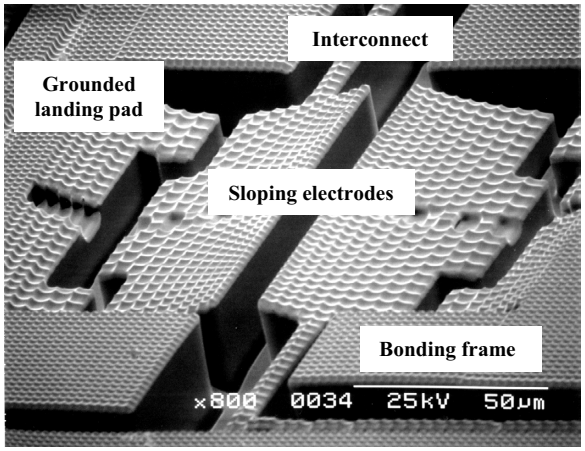

Figure 5. Scanning electron micrograph of the completed Electrode Die prior to bonding of the Mirror Die. *The bright regions are gold, while darker regions are thermal oxide. Metallization does not occur on the vertical sidewalls of the structures due to the poor step coverage of the e-beam deposition technique.*

The completed micromirror device with the titanium Mirror Die bonded to the silicon Electrode Die is shown in Figure 6. Alignment accuracy is good and the bonded foil shows no apparent signs of deformation, damage, or delamination, therefore indicating that neither bonding pressure nor thermal mismatch-induced residual stresses are a detriment to the current device.

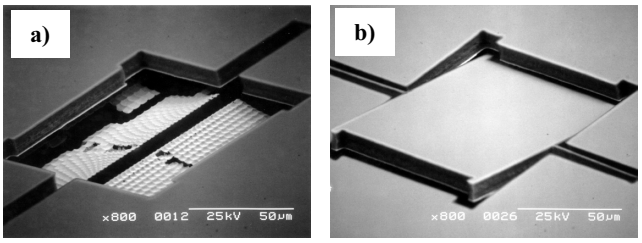

Figure 6. Scanning electron micrographs of the completed hybrid titanium/silicon micromirror device. *a) mirror removed to show underlying sloping electrodes with one of the grounded landing pad visible at upper left; b) tilted mirror showing landing tips at corners. The tilted mirror in (b) resulted from stiction after multiple snap down cycles.*

Quantitative characterization of the mirror surface quality was carried out using white light optical profilometry. As can be seen in Figure 7, planarity of the mirror surface is rather poor. The average surface roughness of the mirror surface is 95 nm and the maximum peak-to-valley height differential is 216 nm. The large surface height variation across the mirror prevented accurate measurement of the mirror curvature. Further optimization of the CMP process is currently underway to reduce the roughness.

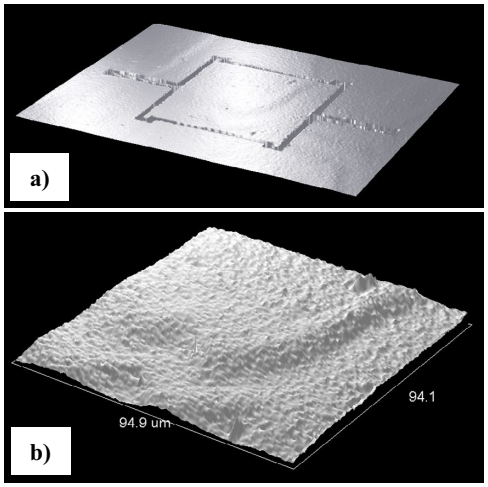

Figure 7. Optical profilometry images of the mirror device. *a) image of a single mirror and it's surroundings; and b) close up of the mirror surface itself.*

Preliminary dynamic testing of the mirrors shows that intermittent stiction occurs during operation in the digital snap-down mode. This stiction occurs despite the attempt to minimize contact area through the use of narrow landing tips on the mirror, and prevent charging or current-induced welding through the use of complimentary grounded landing pads on the Electrode Die. Stiction in this case most likely results from the presence of gold on both contacting surfaces, therefore it is anticipated that the problem could be remedied to a large extent by removal the gold from the backside of the mirror. However, incorporation of additional strategies, such as application of adhesion-inhibiting surface coatings and novel biasing schemes may be needed as well to ensure complete elimination of stiction.

Operation of the device in the analog scanning mode shows more promising results. Dynamic testing using Laser Doppler Vibrometry, as seen in Figure 8, indicates that pneumatic-damping enables reduction of settling times to well under 1 ms, without resorting to the use of drive signal shaping. These times compare rather favorably to the 1-3 ms settling times often quoted for other large micromirror devices.

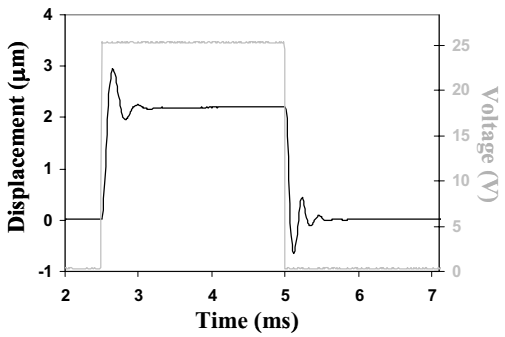

Figure 8. Dynamic response of the mirror device driven in air at 200Hz with a 25V square wave signal. *Resonant frequency is ~4.2 kHz and settling times are well under 1 ms.*

CONCLUSIONS

The simplicity of the process presented here lies in direct contrast to other methods proposed for the fabrication of sloping electrode-based micromirror devices which require: a) the use of costly SOI wafers to provide the thin silicon layer needed for the mirror and springs [**5**]; b) careful optimization of multiple electrodeposition and planarization steps to develop the desired sloping electrode geometry and flat, low roughness mirrors [**6**]; or c) thorough optimization of solder pad geometry and location to ensure accurate and consistent reflow-based self-assembly [**7**]. Utilization of the MARIO, HARLMM, and RIE-lag processes circumvents these issues, providing a potentially simple and robust method for fabrication of high performance micromirror devices.

ACKNOWLEDGMENTS

The authors would like to thank. G. D. Cole, M. Napoli, and the Materials Technology Office at the Defense Advanced Research Projects Agency.

REFERENCES

1. M. F. Aimi, M. P. Rao, N. C. MacDonald, A. S. Zuruzi, and D. P. Bothman, "High-Aspect-Ratio Bulk Micromachining of Titanium," *Nature Materials, 3,* 103 (2004).

2. C. O'Mahony, M. Hill, P. J. Hughes, and W. A. Lane, "Titanium as a Micromechanical Material," *J. Micromech. Microeng., 12,* 438 (2002).

3. T. N. Pornsin-sirirak, Y. C. Tai, H. Nassef, and C. M. Ho, "Titanium-alloy MEMS Wing Technology for a Micro Aerial Vehicle Application," *Sens. Actuators A Phys., 89,* 95 (2001).

4. P. –F. Chauvy, C. Madore, and D. Landolt, "Electrochemical Micromachining of Titanium Through a Patterned Oxide Film," *Electrochem. Solid St., 2,* 123 (1999).

5. R. Sawada, J. Yamaguchi, E. Higurashi, A. Shimizu, T. Yamamoto, N. Takeuchi, and Y. Uenishi, "Single Si Crystal 1024ch MEMS Mirror Based on Terraced Electrode and a High-Aspect Ratio Torsion Spring for 3-D Cross-Connect Switch," *2002 IEEE/LEOS International Conference on Optical MEMS: Optical MEMS 2002*, Lugano, Switzerland, 8/20-23/02, IEEE Laser and Electro-Optics Society, Piscataway, NJ (2002), pp. 11-12.

6. K. Reimer, R. Engelke, M. Witt, and B. Wagner, "16k Infrared Micromirror Arrays with Large Beam Deflection and Tenth Millimeter Pixel Size," *Proceedings of the SPIE Conference on Miniaturized Systems with Micro-Optics and MEMS,* Vol. 3878, Santa Clara, CA, 9/20-22/99, The International Society of Optical Engineering, Bellingham, WA (1999), pp. 272-90.

7. B. McCarthy, V. Bright, and J. Neff, "A Multi-Component Solder Self-Assembled Micromirror," *Sens. Actuators A Phys., 103*, 187 (2003).

8. T. Bourouina, T. Masuzawa, and H. Fujita, "MEMSNAS: Microloading Effect for Micromachining 3D Structures with Nearly Arbitrary Shapes: Application to Micro-optics on Silicon," *2001 IEEE/LEOS International Conference on Optical MEMS: Optical MEMS 2001*, Okinawa, Japan, 9/25-28/01, IEEE Laser and Electro-Optics Society, Piscataway, NJ (2001), pp. 81-82.

9. T. –K. A. Chou and K. Najafi, "Fabrication of Out-of-Plane Curved Surfaces in Si by Utilizing RIE-Lag," *15th IEEE International Conference on Micro Electro Mechanical Systems MEMS 2002,* Las Vegas, NV*,* 1/20-24/02, IEEE, Piscataway, NJ (2002), pp. 145-148.

ELECTROTHERMAL SCS MICROMIRROR WITH LARGE-VERTICAL-DISPLACEMENT ACTUATION

Ankur Jain, Hongwei Qu, and Shane Todd
Department of Electrical & Computer Engineering
University of Florida, Gainesville, FL 32611-6200

Gary K. Fedder
Department of Electrical & Computer Engineering
Carnegie Mellon University, Pittsburgh, PA 15213

Huikai Xie
Department of Electrical & Computer Engineering
University of Florida, Gainesville, FL 32611-6200

ABSTRACT

This paper reports a novel large-vertical-displacement (LVD) microactuator that can generate large piston motion at low driving voltage. A LVD micromirror device has been fabricated by using a unique DRIE CMOS-MEMS process that can simultaneously provide thin-film and single-crystal silicon microstructures. With only a 0.7 mm by 0.32 mm sized device, the LVD micromirror demonstrated a vertical displacement of 0.2 mm at an actuation voltage of 6 V d.c. This device can also perform bidirectional rotational scanning through the use of two bimorph actuators. The micromirror can rotate ± 20°, and has negligible initial tilt angle and high scanning speeds (~2 kHz).

INTRODUCTION

Fast-scanning mirrors with piston-motion are required by applications for wave-front shaping in adaptive optics [**1**], biomedical imaging, interferometry systems [**2**], laser beam scanning, and by spatial light modulators [**3**]. Other applications that require large vertical displacements include scanning tunneling microscopes, tunable lenses for confocal microscopy [**4**], microvalves, actuators on magnetic recording heads, and precision micropositioning systems.

Numerous piston-motion actuation designs have been reported in literature. Vertical displacements of 7.5 μm [**5**] and even as high as 50 μm [**4**] have been achieved through the use of electrostatic vertical comb drives. Deformable mirrors with electromagnetic and electrostatic actuations for use in adaptive optics demonstrated vertical displacements of 20 μm [**6**] and 6 μm [**1**], respectively. Other vertical actuation mechanisms include a piezoelectric cantilever with displacements up to 25 μm [**7**], and an electrothermally-actuated trampoline-type micromirror with a maximum displacement of 2 μm [**8**]. Most of these actuators can only generate up to a few tens of microns of vertical displacement.

This paper presents a novel large-vertical-displacement (LVD) micromirror design that can perform optical scans, as well as large piston motion at low driving voltages. Out-of-plane displacement of the micromirror is provided by a pair of electrothermal actuators. It is well known that there is large *z*-displacement at the tip of a long rotational beam. The innovation of this LVD device is converting the large tip displacement into a pure *z*-axis displacement of a flat micromirror. The LVD microactuator design can potentially achieve maximum vertical displacements of a few millimeters with millimeter-sized devices.

In this paper, the LVD concept, device design and fabrication process will be described first. Then the experimental results, including frequency response, piston-motion and bi-directional scanning, are reported.

LVD MICROMIRROR DESIGN

In prior work, we demonstrated single-crystal silicon (SCS) based 1-D and 2-D scanning micromirrors with large rotation angle for transverse scanning in optical coherence tomographic (OCT) imaging [**9,10**], but the unidirectional operation, non-stationary center of rotation, and large initial tilt angle of those micromirrors complicated the device packaging and optical design. The LVD micromirror consists of two complementary electrothermal actuators in a folded structure which allows the mirror plate to remain parallel to the substrate surface, while still taking advantage of the large stroke lengths provided by the actuators.

The schematic drawing of the LVD micromirror is illustrated in Fig. 1(a). The mirror plate is attached to a rigid silicon frame by a set of aluminum/silicon-dioxide bimorph beams. A polysilicon resistor is embedded within the silicon dioxide layer to form the heater for the thermal bimorph actuator. As this set of beams directly actuates the mirror, it is referred to as the *mirror actuator*. The movable frame is connected to the silicon substrate by another set of identical bimorph beams. This second set of beams actuates the frame, and is referred to as the *frame actuator*. After the mirror is released during fabrication, the beams curl up due to the tensile stress in the upper aluminum layer and compressive residual stress in the bottom silicon dioxide layer, as illustrated in Figs. 1(b) and 2. The rigidity of the frame and the flatness of the

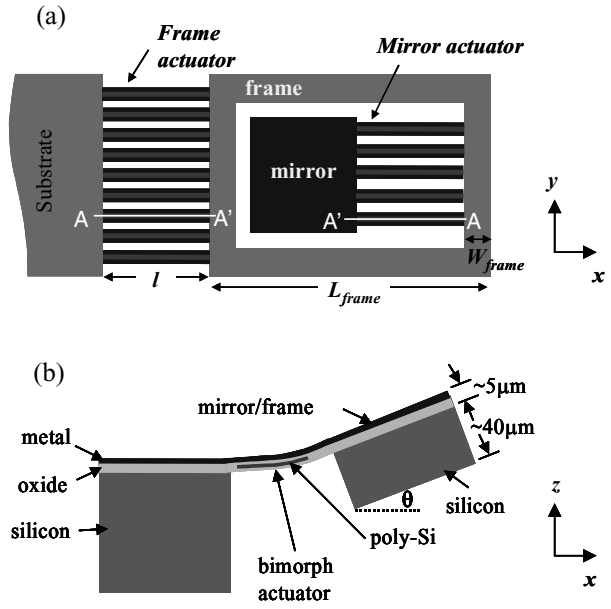

Figure 1.*Design schematic of the LVD micromirror. (a) Top-view; (b) crossectional view of A-A'.*

Travel support has been generously provided by the Transducers Research Foundation and by the DARPA MEMS and DARPA BioFlips programs.

0-9640024-5-0/hh2004/$20©2004TRF
DOI 10.31438/trf.hh2004.61

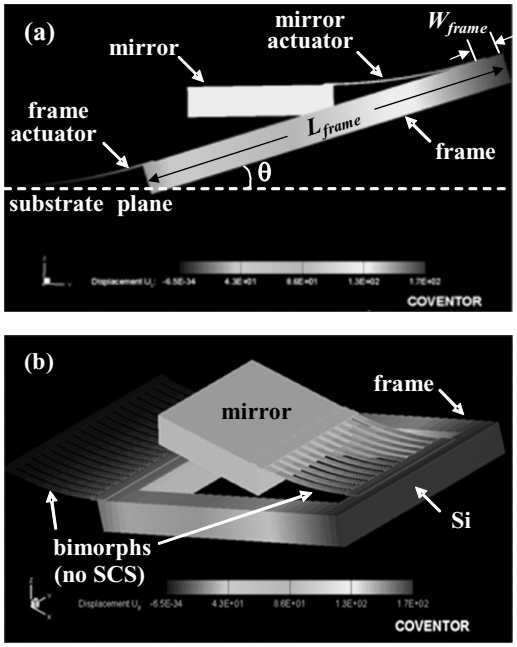

Figure 2. *(a) Side-view; and (b) 3D model of the LVD micromirror illustrating the initial curling of the bimorph actuators. The mirror surface is parallel to the substrate plane, i.e., no initial tilt, as the curling of the two bimorph actuators compensate each other. The mirror plate is located 0.13mm above the substrate plane.*

mirror are guaranteed by the thick SCS layer underneath the frame and mirror. In contrast, the bimorph actuators do not have the SCS layer and thus are thin and compliant in the *z*-direction. The mirror surface is coated with aluminum for high reflectivity. The fabrication details are given in the next section.

FEM thermomechanical simulation was conducted using Coventorware [**11**]. The simulation result is shown in Fig. 2, where the curling of the two sets of bimorph beams compensate each other resulting in a zero initial tilt. The initial elevation of the mirror plate above the chip plane, Z_{mirror}, due to the curling of the thermal actuators can be calculated from:

$$Z_{mirror} = (L_{frame} - W_{frame}) \sin\theta$$

where L_{frame} *and* W_{frame} are the length and beam-width of the frame, respectively. θ, the initial tilt angle of the frame, can be computed from $\theta = l / \rho$; where l and ρ are the length and radius-of-curvature of the thermal actuator, respectively. For a frame with L_{frame} = 0.5 mm, W_{frame} = 40 μm, and θ = 17°, the initial rest position of the mirror Z_{mirror} is 0.135 mm. The simulation results in Fig. 2 show that the mirror plate is located 0.132 mm above and parallel to the substrate plane. There is no substrate underneath the mirror plate. Thus, the mirror plate can move down below the chip plane. From experiment, it was found that the maximum displacement below the chip plane is roughly equal to Z_{mirror}, thereby resulting in a maximum *z*-displacement, $Z_{max} = 2Z_{mirror}$ = 0.27 mm. Much larger vertical displacements can be achieved by simply increasing the frame and/or the actuator lengths.

The mirror and frame actuators rotate the mirror in opposite angular directions. There exist two basic modes of operation: (1) Bi-directional scanning by alternatively applying voltage to the mirror and frame actuators, and (2) Large piston motion by simultaneously applying voltage to both actuators. Equal angular rotation by the two actuators will result in pure vertical

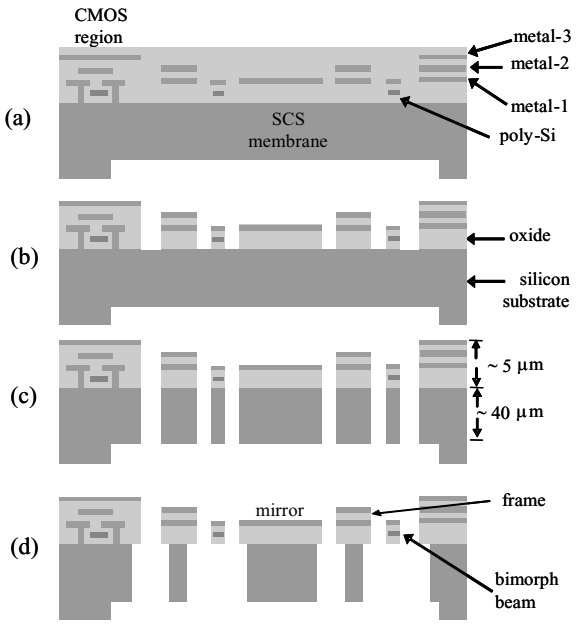

Figure 3. *DRIE CMOS-MEMS process flow: (a) backside Si etch; (b) oxide etch; (c) Deep Si etch; and (d) Si undercut.*

displacement of the mirror. Large *z*-axis displacement is achieved via the angular amplification due to the long arm length of the frame.

DEVICE FABRICATION

The micromirror is fabricated using deep-reactive-ion-etch (DRIE) CMOS-MEMS processing [**12**]. The process flow, outlined in Fig. 3, uses only four dry etch steps and can produce mixed thin-film and bulk-Si microstructures. The process starts with a backside deep anisotropic silicon etch to form a thick SCS membrane (~40 μm). This SCS membrane is required to keep the mirror flat. The second step is a frontside anisotropic oxide etch that uses the CMOS interconnect metal (i.e., Al) as an etching mask. Next, a deep silicon trench etch is done to release the microstructure. The last step is an isotropic silicon etch, performed to undercut the silicon to form bimorph thin-film beams which are approximately 2 μm thick. These thin-film beams provide *z*-axis compliance for out-of-plane actuation, and form bimorph actuators with an embedded polysilicon heater. There are no substrate or other microstructures directly above or below the mirror microstructure, so large actuation range is allowed. This process is mask-less, uses only dry etch steps, and is completely compatible with foundry CMOS processes.

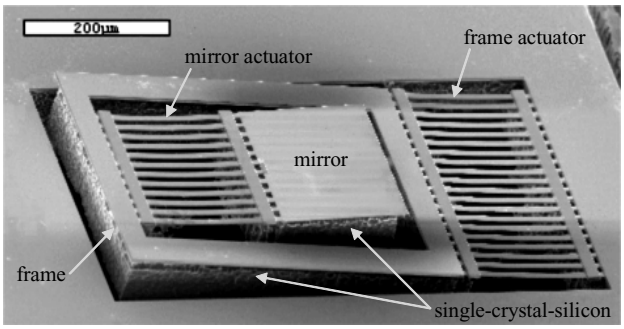

Figure 4. *SEM of a fabricated LVD micromirror device.*

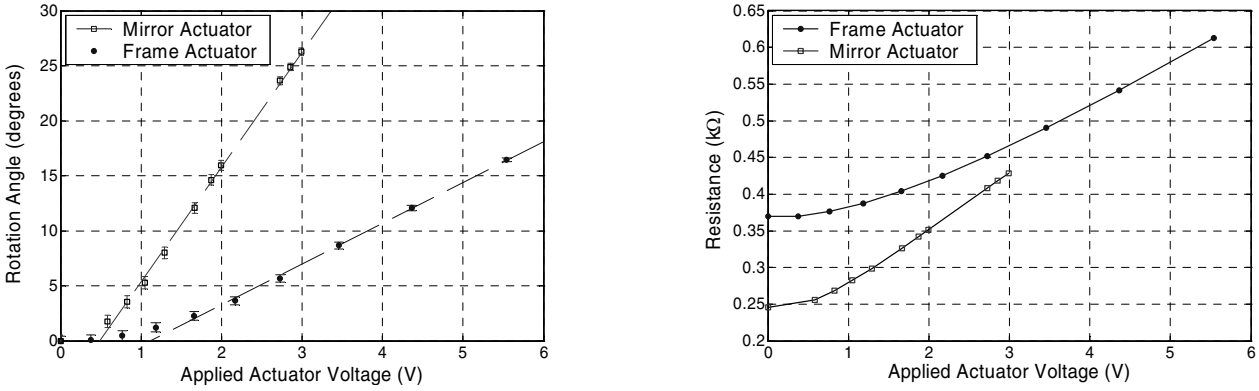

Figure 5. *Device characterization. (a) Plot of the rotation angle, and (b) plot of the polysilicon heater resistance versus applied voltage for the two actuators.*

A fabricated 0.7 mm by 0.32 mm LVD micromirror device is shown in Fig. 4. The initial tilt angle of the frame with respect to the substrate surface is typically 13°. This tilt angle is dependent on the over-etch of the top aluminum layer of the bimorph beams. The heating element in the 10-μm wide bimorph beams is a set of 200 μm long, 7 μm wide, polysilicon strips oriented along the beams. The gaps (9 μm) between the beams are used to undercut the underneath silicon to form the thin-film bimorph beams (Fig. 3(d)). The frame actuator and mirror actuator are constituted of 20 and 12 bimorph beams, respectively. The measured open circuit polysilicon resistances of the mirror and frame actuators are 240 Ω and 365 Ω, respectively. The peak-to-valley surface deformations are within 40 nm over the 190 μm mirror plate. This small mirror size is just used to demonstrate the concept. Since the mirror plate is supported by bulk silicon, much larger mirrors can be made.

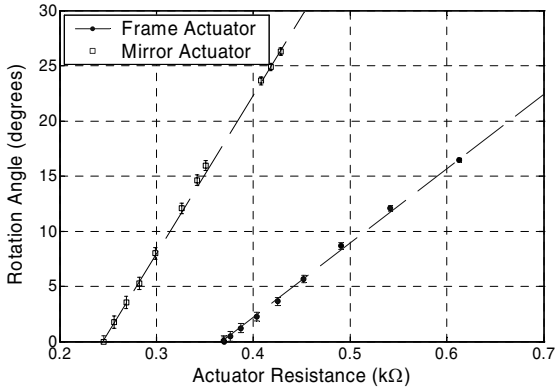

Figure 6. *Plot of the linear correlation between rotation angle and the polysilicon resistance for the two actuators.*

EXPERIMENTAL RESULTS

An experimental setup with a laser beam incident on the mirror and a d.c. voltage applied to the two actuators was used to measure the static deflection angles. The mechanical scan angle of the mirror was obtained by measuring the scan distance of this reflected laser beam on a screen. Fig. 5(a) shows the linear responses between the measured angles of rotation and the actuation voltages for the mirror and frame actuators, respectively. The mirror has a maximum rotation of 26.5° when 3 V d.c. is applied to the mirror actuator. Both the mirror and the frame rotate when a voltage is applied only to the frame actuator. A maximum deflection of -16.5° is observed when 5.5 V d.c. is applied to the frame actuator. The same actuation voltage causes a larger rotation angle by the mirror actuator than the frame actuator due to the polysilicon resistance difference between the two actuators, and also because the mechanical structure of the frame provides additional thermal isolation to the mirror actuator. The polysilicon resistance of the bimorph actuators change with applied voltage, and is plotted in Fig. 5(b). There is a large increase in the polysilicon resistance because the heating effect of the actuation current causes a temperature change, which in turn induces stress change in the bimorph beams. As evident from Fig. 6, there exists a linear correlation between the rotation angle and the polysilicon resistance for each of the two actuators. The resulting error (< 2% of full-scale value) in fitting the actuator rotation and resistance data to a linear plot is within the rotation-angle measurement experimental-error. This linear relationship allows for independent control of rotation angle of each actuator by monitoring its polysilicon heater resistance. Thermal coupling between the two actuators can be accounted for by monitoring their individual polysilicon heater resistances.

Vertical piston motion of the mirror can be achieved by equal but opposite angular rotations of the two actuators. By using the rotation-angle versus actuation-voltage data, a mirror-actuator drive-voltage versus frame-actuator drive-voltage plot for same angular rotation values is obtained. The slope of this experimentally determined plot, shown in Fig. 7(a), provides the driving voltage ratio for the two actuators that would maintain no tilting of the mirror plate. A voltage divider was used to drive the two actuators with a voltage ratio of 3:7 (determined from plot). A maximum vertical displacement of 200 μm was obtained. The vertical displacement of the mirror as a function of the drive voltage is shown in Fig. 7(b). By using a linearly-fitted voltage ratio, some tilting of the mirror plate (less than 1°) was observed.

The frequency response of the LVD micromirror was measured using a Polytec OFV-511 laser Doppler vibrometer, as shown in Fig. 8. Resonant peaks were observed at 1.18 kHz and 2.62 kHz. These results are a close match to the modes observed at 1.14 kHz and 2.76 kHz from the modal analysis simulations using Coventorware.

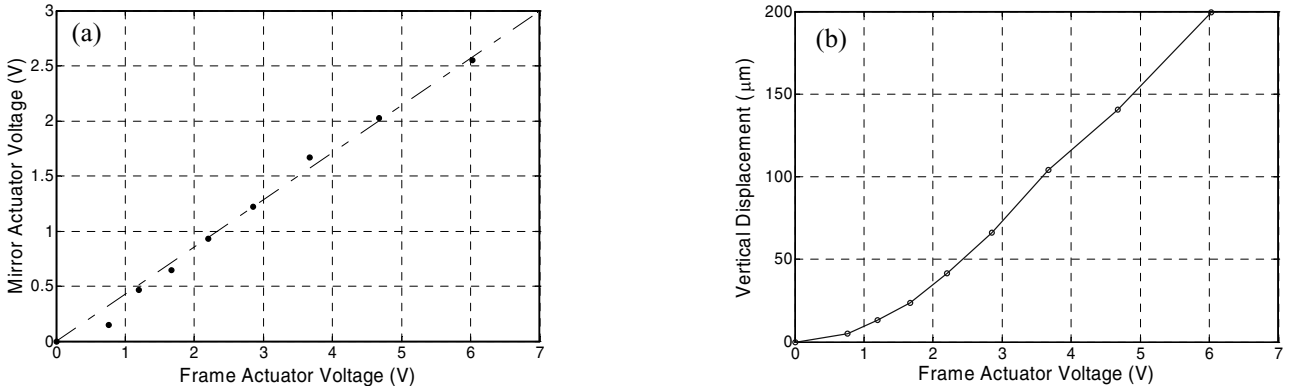

Figure 7. *(a)Plot of mirror actuator voltage versus corresponding frame actuator voltage that is required to maintain zero angular tilt of the mirror. (b) Vertical displacement of the mirror as a function of frame actuator voltage. The voltage applied to the mirror actuator is 43% of the frame actuator voltage, which is provided by a voltage divider. With this voltage ratio the maximum tilt of the mirror in the entire 200 μm travel range is less than 1°.*

CONCLUSIONS

A micromirror with a novel large-vertical-displacement electrothermal-actuation mechanism was successfully demonstrated. 200 μm vertical displacement has been achieved with a microdevice of only 0.7 mm by 0.32 mm. Much larger vertical displacement can be achieved by simply increasing the length of the frame and/or the initial tilt angle of the frame. The fabrication process is simple and compatible with CMOS processes; therefore control circuits can be integrated with the mirror on the same chip. This device is capable of large piston motion, and can also operate as a bidirectional scanner with high scanning speed. The large actuation range and fast scanning speeds make this device very suitable for use in interferometry, laser beam steering, biomedical imaging, and phase modulation applications. Based on this LVD microactuator concept, various devices such as tunable microlenses for use in confocal microscopy can also be developed.

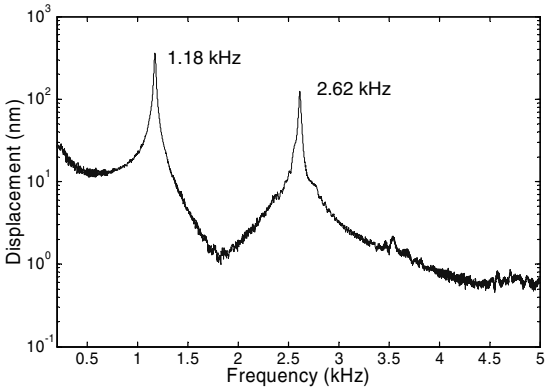

Figure 8. *Frequency response of the LVD micromirror device. The actuation signal was a 1 V sine wave.*

REFERENCES

1. M. A. Helmbrecht, U. Srinivasan, C. Rembe, R. T. Howe, and R. S. Muller, "Micromirrors for Adaptive-Optics Arrays," *Technical Digest of the 11th Intl. Conf. on Solid State Sensors and Actuators (Transducers '01)*, Munich, Germany, June 10-14, 2001.

2. A. P. Lee, C. F. McConaghy, G. Sommargren, P. Krulevitch, and E. W. Campbell, "Vertical-Actuated Electrostatic Comb Drive with In Situ Capacitive Position Correction for Application in Phase Shifting Diffraction Interferometry", *J. of Microelectromechanical Systems, 12,* 960-971 (2003)

3. S. –W. Chung, and Y. –K. Kim, "Design and fabrication of 10 x 10 micro-spatial light modulator array for phase and amplitude modulation," *Sensors and Actuators, 78*, 63-70 (1999).

4. S. Kwon, V. Milanovic, and L. P. Lee, "Vertical Microlens Scanner for 3D Imaging", *Technical Digest of the 2002 Solid-State Sensor and Actuator Workshop*, Hilton Head Isl., SC, June 2002, pp. 227-230.

5. D. Lee, U. Krishnamoorthy, K. Yu, and O. Solgaard, "High-Resolution, High-Speed Microscanner in Single-Crystalline Silicon Actuated by Self-Aligned Dual-Mode Vertical Electrostatic Combdrive with Capability for Phased Array Operation", *Technical Digest of the 12th International Conference on Solid State Sensors, Actuators and Microsystems (Transducers '03)*, Boston, MA, June 8-12, 2003, pp. 576-579.

6. O. Cugat, P. Mounaix, S. Basrour, C. Divoux, and G. Reyne, "Deformable magnetic mirror for adaptive optics: first results," *IEEE 13th Annual Intl. Conf. on MEMS*, Miyazaki, Japan, Jan 2000, pp. 485-490.

7. D. E. Glumac, and W. P. Robbins, "A planar unimorph-based actuator with large vertical displacement capability. I. Experiment," *IEEE Transactions on Ultrasonics, Ferroelectrics and Frequency Control, 45*, 1145-1150 (1998).

8. A. Tuantranont, L. –A. Liew, V. M. Bright, W. Zhang, and Y. C. Lee, "Phase-only micromirror array fabricated by standard CMOS process," *Sensors and Actuators A, 89*, 124-134 (2001).

9. H. Xie, A. Jain, T. Xie, Y. Pan, and G.K. Fedder, "A Single-Crystal Silicon-Based Micromirror with Large Scanning Angle for Biomedical Applications," *CLEO Technical Digest*, Baltimore, MD (2003).

10. A. Jain, T. Xie, Y. Pan, G. K. Fedder, and H. Xie, "A Two-Axis SCS Electrothermal Micromirror for Biomedical Imaging," *2003 IEEE/LEOS International Conference on Optical MEMS*, Waikoloa, HI, Aug 2003, pp. 14-15.

11. CoventorWare 2003 Reference Manual, Coventor, Inc., Cary, NC.

12. H. Xie, L. Erdmann, X. Zhu, K. Gabriel, and G.K. Fedder, "Post-CMOS processing for high-aspect-ratio integrated silicon microstructures," *J. of Microelectromechanical Systems, 11*, 93-101 (2002).

TIP-TILT-PISTON ACTUATORS FOR HIGH FILL-FACTOR MICROMIRROR ARRAYS

Veljko Milanović, Gabriel A. Matus, Daniel T. McCormick

Adriatic Research Institute
828 San Pablo Ave., Suite 115E, Berkeley, CA 94706
veljko@adriaticresearch.org

ABSTRACT

Tip-tilt-piston actuators for optical phased arrays with large deflection angle, large piston range, and fast update rates are demonstrated. The devices include bonded low-inertia micromirrors on top of actuators aimed to achieve >96% fill-factor arrays. The gimbal-less design methodology enables scaling devices down to a few 100 μm to allow future implementation of large arrays with <100 μsec update. Several different design architectures have been successfully fabricated and tested as individual devices, and as a 2x2 element array. Devices with square layouts are demonstrated with 800 μm down to 400 μm on a side. In each case the devices consist of 4 vertical combdrive rotators connected by 2 degree-of-freedom (DoF) linkages to a central stage. Each actuator can rotate bi-directionally to raise or lower its linkage, giving the stage the required 3 DoF. The stage is used as a platform for bonding of a thin, low-inertia mirror plate which then completely covers the actuator. A representative high field-factor actuator of 500 μm x 500 μm dimensions achieves optical deflection angles beyond -20° to 20° for both axes and greater than -12 μm to 12 μm pistoning, at <80V actuation. In comparison, a larger low field-factor device with a 600 µm diameter integrated micromirror is also demonstrated which utilizes 3 bi-directional actuators radially offset by 120° to achieve tip-tilt-piston actuation with -10° to 10° deflection in all axes and -30 µm to 30 µm pistoning.

I. INTRODUCTION

A. Background

Various optical applications require large adaptive apertures with rapid reconfiguration rates. Even in the case of simple beam steering, increasing the mirror size results in significantly increased response times due to increased inertia. Therefore, it is desirable to replace large mirrors with phased arrays of smaller micromirrors. This offers several advantages such as significantly higher steering speeds and remarkably improved optical and mechanical properties. Past efforts have emphasized the need for such arrays ([1],[2]) but have not achieved all three degrees of freedom (3-DoF, tip-tilt-piston,) nor sufficiently high speeds of operation. Namely, if such 3-DoF device-phased arrays were available, it would enable more sophisticated optical beam shaping, multiple-beam steering, and a variety of general adaptive optics application.

In Figure 1a, four tip-tilt-piston actuators are arranged in a 2x2 array with minimal spacing between the actuators to achieve high fill-factor of the reflecting surfaces in Figure 1b. Each actuator in Figure 1a is rectangularly arranged with 400 µm on each side, and its central stage can be actuated to tip-tilt-piston, as will be discussed in more detail in Sec. II. After transfer and bonding of separately fabricated single-crystal silicon mirrors (Figure 1b,) the devices can be used independently, as four scanners, or together, as one larger (800 x 800 µm) aperture, etc. The elements in Figure 1b are not functional as it is impossible to reach the actuating electrodes beneath the micromirrors, but were used for bonding demonstration purposes. In the future, larger arrays with perhaps 1000s of elements could therefore have remarkable impact in numerous photonics applications.

B. Two-axis scanners and the gimbal-less approach

Recently, we have developed independently and linearly controllable vertical comb drives using only a single SOI device

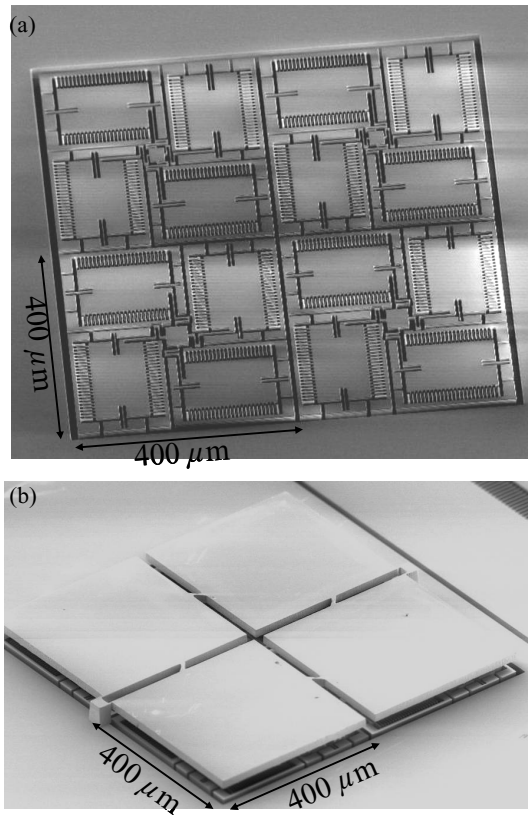

Figure 1. SEM micrographs of a fabricated 2x2 element array of high aspect-ratio tip-tilt-piston actuators: (a) actuators as fabricated in the SOI device layer and before micromirror bonding, and (b) after bonding of a 2x2 array of low-inertia micromirrors, still tethered together for simultaneous transfer and alignment.

layer, thereby realizing monolithic structures with isolated actuators [3]. These devices are fabricated in the Multilevel-beam SOI-MEMS process [4]. Our goal was primarily to expand their use to two-axis micromirror scanning applications, while maintaining the high-speed operation possible in the one-axis devices and minimizing cross-coupling between axis. An additional goal has been to achieve devices with tip-tilt-piston capability, i.e. 3 DoF actuation, for phased array applications. Such applications have an additional requirement that the devices should easily scale down to small dimensions.

The most common method of implementing two-axis (two degrees of freedom, 2DoF) rotation has been through the use of a gimbaled structure [5],[6],[7], although packaging-based methods with one-axis scanners are utilized as well. However, to implement 2DoF gimbaled micromirror without cross-talk between driving voltages, electrical isolation of the mechanical coupling linkages is required. Backfilling of isolation trenches by an additional deposition layer followed by a chemical mechanical polishing (CMP) step has been used to achieve the electrically isolated mechanical coupling [7],[8]. The additional deposition and CMP steps significantly increase both the complexity and cost of the fabrication process. Typically, gimbaled designs result in non-symmetric and relatively slower achievable response frequencies

0-9640024-5-0/hh2004/$20©2004TRF
DOI 10.31438/trf.hh2004.62

Solid-State Sensors, Actuators, and Microsystems Workshop
Hilton Head Island, South Carolina, June 6-10, 2004

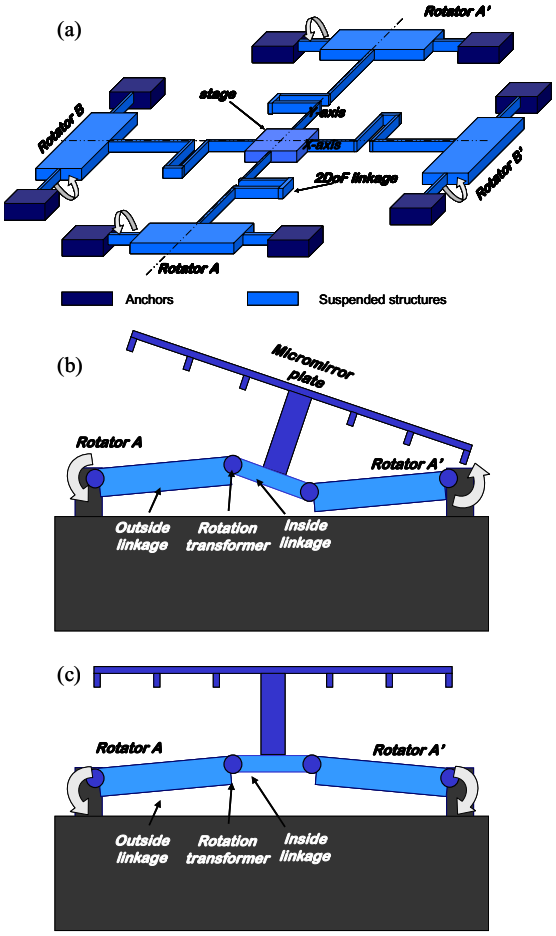

Figure 2. Gimbal-less tip-tilt-piston scanner's operation: (a) 4 bi-directional rotators, here shown just as torsion beams working in pairs to provide each of two axes of rotation. (b) cross-section A-A' example of x-axis actuation, actuator A and A' both turn in the same direction, giving micromirror rotation with a virtual axis at center. (c) cross-section A-A' in an example where both actuators A and A' lift the central stage in common-mode, achieving pistoning.

between the two axes due to the gimbal's slower outer axis. Our approach for high-speed two-axis scanning in [9] was based on pre-engaged vertical combdrives in SOI and gimbal-less design.

In that methodology, we utilize the previously demonstrated one-axis vertical combdrive-based rotation actuators [3], which are discussed in more detail below. These rotators are then combined utilizing mechanical linkages that allow 2DoF of rotation for a central micromirror in differential operation (Figure 2b,) and pistoning in common-mode operation (Figure 2c.)

II. Background and Device Principles

A. One-axis rotators

The basic building block for our two-axis and tip-tilt-piston scanners is a one-axis rotator. Due to the capabilities of the Multilevel-beam SOI-MEMS process [4] to provide isolated combdrives with different actuation force directions, a designer can choose optimized combdrives in a given application. The four types of actuators we most commonly use are shown in the micrographs of three fabricated devices in Figure 3. Figure 4 depicts their cross-sections.

1) The first type of actuator in Figure 4(i) utilizes Down combs and Up combs on opposing sides of the axis of rotation to achieve uni-directional pure rotation. During counter-clockwise rotation, overlap area increases on both sides, increasing capacitance. As

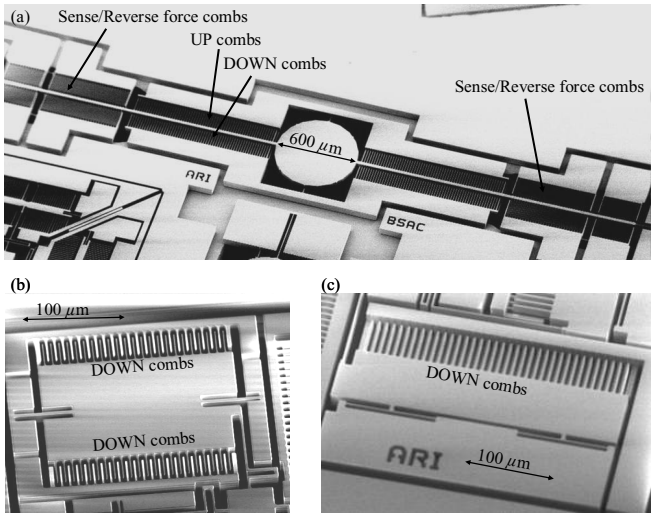

Figure 3. Uni- and Bi-directional one-axis rotators which are the main building blocks of two-axis scanners and tip-tilt-piston actuators: (a) one-axis pure-rotation with integrated and isolated sense capacitance/reverse force actuation fingers, (b) bi-directional DOWN rotation actuator, and (c) uni-directional DOWN actuator.

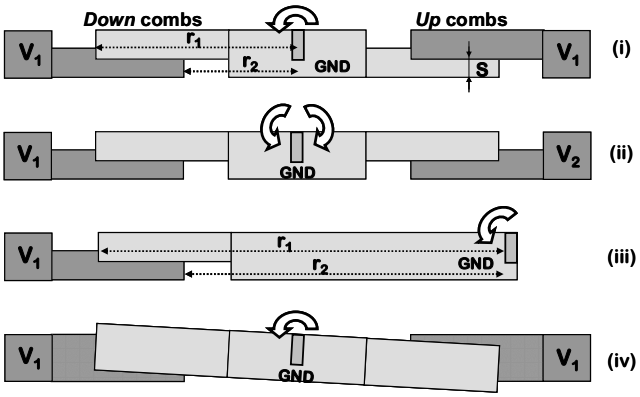

Figure 4. Schematic cross-sections of SOI device layer arranged to achieve 4 distinct modes of operation, such as bi-directional rotation and pistoning.

discussed in [9], it is difficult to represent the desired quantity $dA/d\theta$ in closed-form. However it can be estimated to within ~5% by a simple and useful expression:

$$dA/d\theta \approx 0.5 \cdot \left(r_1^2 - r_2^2\right), \tag{1}$$

where r_1 is the distance of the rotor finger tip from the rotation axis, and r_2 is the distance of the stator finger tip from the rotation axis (Figure 4(i)). Because the fingers are initially pre-engaged such that linear operation from onset can be assumed, we can make a further approximation, neglecting fringing field effects:

$$\frac{dC}{d\theta} \approx 2\frac{\varepsilon_0}{g} \cdot \frac{dA}{d\theta} \approx \frac{\varepsilon_0}{g}\left(r_1^2 - r_2^2\right), \tag{2}$$

where ε_0 is air permittivity and g is the gap distance between combfingers. The factor 2 in (2) comes from the fact that a combfinger has two sides which contribute to the capacitance.

We then plug (2) into the well-known electrostatic torque equation,

$$\tau = N\frac{1}{2} \cdot \frac{dC}{d\theta} \cdot V^2 \approx \frac{N \cdot \varepsilon_0}{2g}\left(r_1^2 - r_2^2\right) \cdot V^2, \tag{3}$$

accounting for N combfingers in an actuator. Rotation eventually causes the fingertips to disengage. As the combfinger tips pass

through, the rate $dA/d\theta$ is no longer constant and drive no longer follows the voltage squared law. Combdrive stroke and combfinger length are the main parameters that determine this disengagement angle. The simplest approximation for the maximum angle is thus simply $\theta_{max\_lin} \approx tan^{-1}(S/r_1)$ (Figure 4 (i)). The drive will continue to rotate past θ_{max_lin}, but the rate $dA/d\theta$ decreases and eventually changes sign, i.e. the area begins to decrease and the vertical comb drive loses drive ability. Therefore, the approximations in (1)-(3) are only valid in the range $0° < \theta < \theta_{max\_lin}$.

2) The type of actuator in Figure 4(ii) utilizes Down combs on both sides, resulting in bi-directional rotation when one side is activated at a time, though with some unwanted lateral and vertical motion. With both sides activated, it gives pistoning Down motion. The same approximations from the case 1) above apply, except that only one half of the total number of combfingers actuate in either direction.

3) The third type of actuator in Figure 4(iii) utilizes only Down combs to provide uni-directional rotation. The trade off is that, given the same space considerations as in (ii) and (i), the torque arm can be twice as long giving four times the torque.

4) The fourth type of actuator in Figure 4(iv) utilizes full thickness, High beams for combfingers which are perfectly overlapping at $\theta=0$. However, as θ increases beyond zero to either direction, applying voltage to this actuator gives reverse-force, i.e. force to return to $\theta=0$. The 2nd purpose for such combdrives is to utilize them as isolated sets of capacitance sense fingers, as in the device of Figure 3a. In that case, during the device operation, monitoring the capacitance on those combdrives provides position feedback for closed-loop feedback control which is described in [14].

Equations governing these types of combfingers follow from above, approximating the area change and therefore torque as:

$$\tau \approx -\frac{N \cdot \varepsilon_0}{2g} \cdot \left(r_1^2 - r_2^2\right) \cdot V^2. \qquad \theta \neq 0 \tag{4}$$

When used in capacitive sensing circuits such as [14], reference capacitors are fabricated on chip utilizing the same layout in order to insure matched capacitances.

B. Two-axis scanners with integrated micrormirrors

As mentioned above in Sec. I*B*, to achieve the goal of fast two-axis scanning, we combine multiple one-axis actuators positioned orthogonally, and utilize mechanical linkages to allow two-axes of rotation for a central micromirror, as first demonstrated in [9]. Two one-axis rotators are utilized for each axis of the overall two-axis scanner. For the *x*-axis, actuators A and A' are utilized, and for the *y*-axis, actuators B and B'. The actuators are attached to the mirror through a set of beams and a mechanical rotation transformer. The problem of combining one-axis actuators discussed above in Sec. II*A*, and allowing their operation to be mostly unaltered by the other axis' operation, is addressed as follows. Each linkage that connects an actuator to the central micromirror is actually designed to be a two degree of freedom (2 DoF) mechanical component which allows rotation via transformers, and allows de-coupling from the orthogonal axis via torsional compliance.

An important design feature is that the position of the mechanical rotation transformer in Figure 2b governs the mechanical rotation gain *G* between the micromirror's and actuator's rotation. Namely, since the actuator rotates about its axis, and the micromirror stage rotates about a virtual stationary axis (due to opposing actuations on either side in Figure 2b,) the angles relate as $\theta_{mirror} / \theta_{act} = G = d_2/d_1$. In that, d_2 is the length of the inside linkage from the transformer to the mirrors center, and d_1 is the length of the outside linkage from the actuator's axis to the

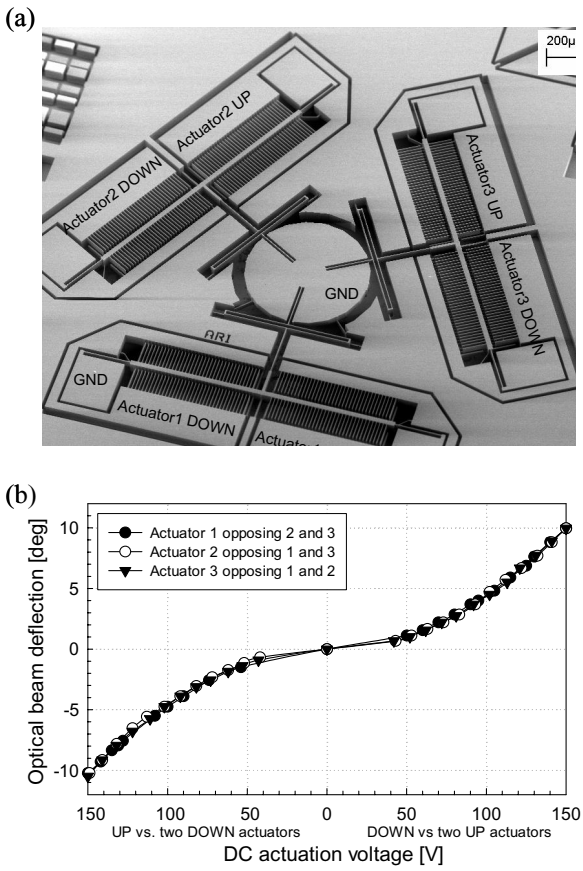

Figure 5. Large tip-tilt-piston "Triangle" device with integrated 600 µm diameter micromirror demonstrating the use of 3 bi-directional rotators arranged around the central stage for tip-tilt-piston operation (b) optical beam deflection measurement in 3 axes, with actuators working in differential modes (2 opposing 1) and (c) pistoning characterization with all actuators working in common mode (all three Up or all three Down).

transformer. This feature is very beneficial due to the following: the maximum angle of each rotator is given by combdrive dimensions as discussed in Sec. II*A* above, while the micromirror angle can be arbitrarily increased by using $G>1$. Moreover, proper design use of mechanical gain can significantly increase overall device speed as $G^{-1/2}$, because it allows increased finger length and torque while achieving same desired large angles of micromirror rotation.

By utilizing these principles and increasing the length of each rotator to obtain large torques and better stability, most recent devices with integrated 600 µm diameter micromirrors achieve >20° optical deflection while maintaining lowest resonances > 4.4 kHz.

C. Implications to Tip-Tilt-Piston array elements

In order to achieve the goal of large optical phased arrays with high fill factor (e.g. >96%,) and tip-tilt-piston actuation of each element, several significant issues have to be addressed and improved on the previous monolithic two-axis scanner work:

1) The actuators must be completely covered beneath the micromirror's reflecting plate for high fill-factor, therefore additional fabrication/packaging solutions are required. Some examples of previous work are given in [1],[5],[10]-[12]. We currently address this issue by separately fabricating low-inertia silicon micromirrors and transferring/bonding them into place on top of the provided actuators stages. This is described in Sec. III*C*.

2) The actuators must be designed in a way to provide independently controllable pistoning in addition to tip-tilt actuation,

for phase correction. As shown in Figure 2, this can be achieved if all rotators are bi-directional. In their common mode operation, pure pistoning is achieved, while in differential mode operation, tip- or tilt- rotation. We have demonstrated this concept in a large device with three bi-directional actuators arranged at 120 degree positions relative to each other (Figure 5a.) Measurements for the device are given in Figure 5b and Figure 5b. It was tested for three different axes. Namely, the device shown has 3 bi-directional actuators, such that any of the actuators can either actuate the linkages Up or Down, depending on which electrode is activated. For example, for testing of the actuator 1 axis in the positive angle direction, we actuate the actuator 1 Down while actuating actuators 2 and 3 Up. The actual axis of that rotation is parallel to actuator 1 shuttle, through the micromirrors center. The opposite arrangement results in a negative angle deflection. Analogous configurations were employed for each of the remaining axis. In the common-mode arrangement full-stroke pistoning actuation was measured from -30 μm to 30 μm.

3) The actuators must be reduced in size significantly to fit beneath a mirror with an edge dimension of less than 600 μm, while maintaining large torque and therefore high speed operation.

4) In an array of such elements, routing of signals to each element must be provided.

In the present work, we address issues 1) thru 3), demonstrate proposed actuator designs, and discuss results. The routing and packaging solutions for 4) are planned as future work.

III. DEVICE FABRICATION

A. Summary of Multilevel beam SOI-MEMS process layers

All of the actuators in this paper were fabricated using the multilevel beam SOI-MEMS process, described in detail in [4], which will be only briefly summarized here, as it applies to the array-element actuators.

The process requires three photolithography masks and three DRIE etches in order to achieve the desired 3-level beams as shown in Figure 6. In the process aimed at larger devices (e.g. Figures. 5 and 6) with significant vertical displacement during actuation, back-side etching is also required to provide large cavities for such movement. Those therefore require a total of four masks. For small array elements, that do not include a large integrated micromirror, back-side etching can be eliminated since there is no requirement for providing space for large vertical displacements and rotations. Therefore, as shown in Figure 6, three masks are used to DRIE etch into the device layer of an SOI wafer and achieve isolated sets of vertical combdrives with *UP* or *DOWN* actuation.

The first layer of photolithography is applied to the device wafer's backside prior to SOI wafer formation, which allows for the mask *Backup* to be etched into that wafer before SOI bonding. After the SOI bonding, grinding and polishing, the remaining two masks are applied on the front of the device layer and aligned to the pre-etched *Backup* mask in the SOI wafer. Two timed DRIE etches on the front side of the wafer complete the shaping of the device layer, resulting in four types of beams, *High*, *Upper*, *Lower* and *Middle*. *Upper* and *Lower* are approximately three fifths of the device layer thickness with an overlap of approximately one fifth, while *High* beams are of full device layer thickness. The resulting structures are high aspect ratio, fully monolithic single crystal silicon structures.

B. Design and fabrication of low-inertia micromirrors

Low inertia micromirrors are fabricated in a separate SOI wafer employing a 3-level selective DRIE process (Figure 8). The mirrors are realized from monolithic single crystal silicon and consist of a full-height pedestal, thinned mirror plate, and mid level trusses. The pedestal provides a bonding surface for attachment to

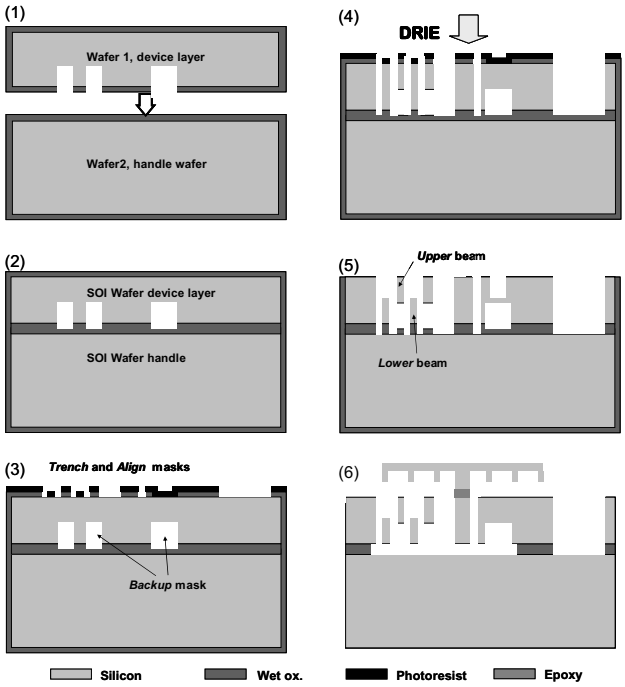

Figure 6. Schematic of the process steps to fabricate the high fill-factor devices with bonded mirrors in this work.

the designed receiving platform on the actuators; it also serves as a stand-off, providing separation between the mirror and actuator to allow sufficient rotation. Thinning of the mirror plate results in a significant reduction of the device's moment-of-inertia. Minimizing the inertia and mass of the structure allows higher resonant frequencies to be achieved without reducing the compliance of the actuation structure's suspension. The fabrication process also incorporates truss structures in order to provide a stiffening backbone for the thin mirror. Analytical and finite element models (FEM) of the device are employed to optimize the design of the mirror and truss structures in order to minimize the inertia as well as dynamic deformation of the mirror plate. Furthermore, FEM is utilized to avoid undesirable, excitable modes. The trusses are also designed to allow the thin mirror plates to be metalized with approximately 100 nm of aluminum with minimal warping and static deformation.

The fabrication of the low inertia micromirrors is initiated by growing a thick oxide layer (~2μm) on an SOI wafer with a device layer thickness equal to the desired thickness of the pedestal plus the mirror plate. The oxide layer is then patterned with three consecutive lithography steps and RIE oxide etches (Figure 8a). These etches define a multi-tiered oxide hard-mask for the subsequent DRIE silicon etches. During the first DRIE step only the silicon that will be etched down to the buried oxide layer is exposed; the depth of this trench etch is greater than the desired thickness of the mirror plate. A blanket RIE oxide etch then completely removes the thinnest oxide hard-mask, while thinning the remaining oxide masks. The second DRIE determines the thickness of the trusses by recessing the mirror plate to the desired depth. A second oxide etch removes the truss hard-mask. The final DRIE step lowers the parimeter trench, truss beams and mirror plate simultaneously; after the buried oxide layer is reached at the bottom of the outer trench the etch is terminated when the desired mirror thickness is achieved (Figure 8b). Finally the mirrors are released in concentrated hydro-fluoric acid (HF) (Figure 8c).

In the present work the thickness of the pedestal is 50μm, the trusses are 15μm and the mirror thicknesses is 2μm. SEMs of example fabricated mirror structures are presented in Figure 9.

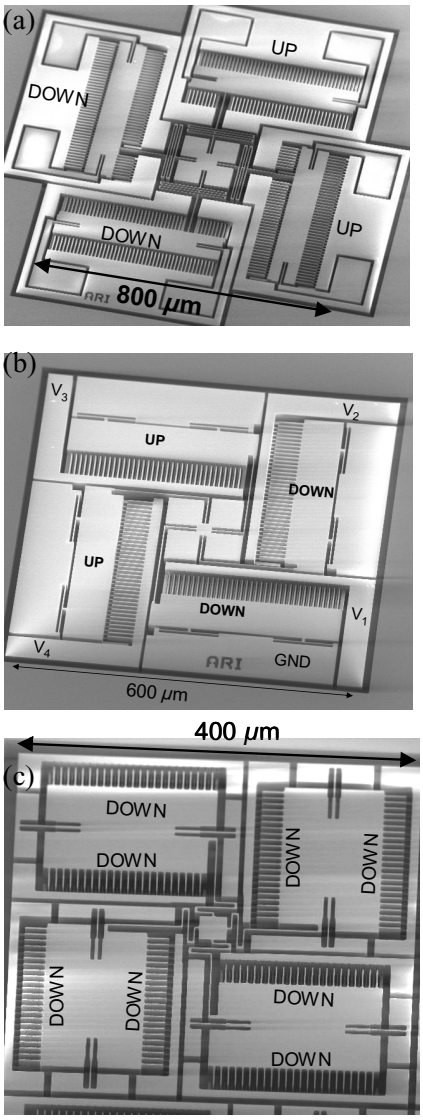

Figure 7. a) 0.8 mm x 0.8 mm (HFF800) device with large pads for prototype testing, four one-directional rotators are arranged around a central stage. (b) 0.6 mm x 0.6 mm (HFF600) device with different (L-shaped) type of 2DoF linkages between one-sided rotators and the central pedestal, and (c) a 0.4 mm x 0.4 mm device (HFF400) showing four bi-directional rotators around the central pedestal. HFF500 devices (0.5 mm x 0.5 mm) were also fabricated as a scaled version of the HFF400 devices, with same layout.

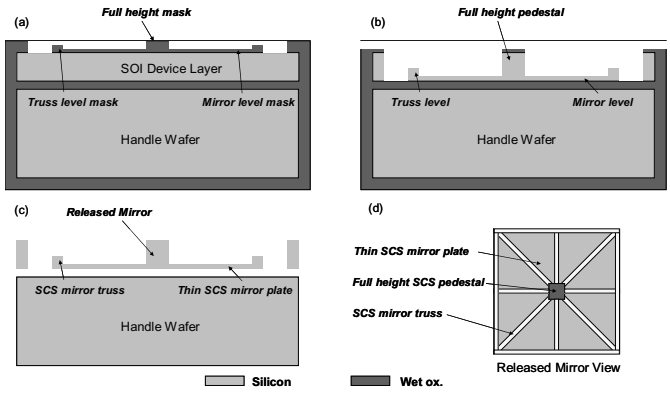

Figure 8. Schematic fabrication process steps for the three-level low-inertia micromirrors in a separate SOI wafer.

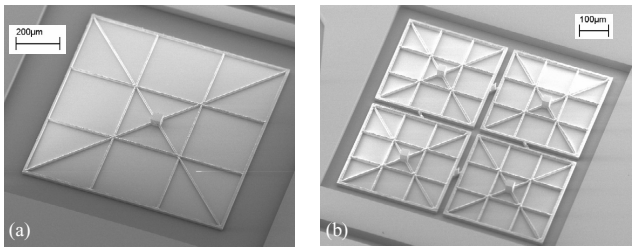

Figure 9. Fabricated low-inertial mirrors before release from the SOI wafer. Three thicknesses are visible, the thin mirror plate, thicker trusses for robust and flat support and the tall pedestal.

C. Transfer and bonding of low-inertia micromirrors onto actuators

The low inertia micromirrors must be attached to the actuators, which are realized on a separate wafer. Transfer and bonding of individual thinned micromirrors onto the actuators was achieved using custom fabricated "capillary pickup fingers," [13] which hold the micromirror from the top, flat side. In this work a small quantity of optical epoxy is applied to the actuator's pedestal platform using a micromanipulator and a simple tungsten probe tip. The mirror is held by the capillary pickup fingers, on a separate micromanipulator. Following optical alignment of the mirror and actuator while viewing on the microscope, contact is made between the pedestal and platform. The surface forces tend to bring the pedestal into perfectly flat alignment with the stage as soon as contact is made, and the capillary pickup fingers then release the mirror. Finally the epoxy is exposed to ultra-violet light followed by a curing step in a 125°C oven.

Batch bonding and alignment of multiple mirrors for large-scale, high fill-factor arrays is an on-going effort, with the 2x2 array in Fig. 1c demonstrated to date.

IV. CHARACTERIZATION AND CONCLUSIONS

A variety of designs of high fill-factor (HFF) actuators have been designed and fabricated, as shown in Figure 7, in all cases utilizing 4 one-directional actuators arranged around the central mirror. Several devices of each kind were tested. By electrically activating the proper pair of electrodes, different actuation modes have been independently demonstrated. By observing the deflection of a laser beam against a metric wall, we measured the rotations of both the micromirror as well as the actuators which reflect a small portion of the beam (the laser beam covers the entire device.) In that way we are able to verify the overall performance as well as the mechanical gain between the center stage and actuator rotation. For pistoning mode characterization we utilized a Laser Doppler Velocimeter.

Large numbers of devices have been successfully tested as fabricated on a probe station, with a summary of the results is given in Table 1. The smallest device (400 μm on a side) measured >20° of optical deflection in both axes and >64 kHz and >30 kHz resonant frequency in rotation and pistoning, respectively, prior to mirror bonding. A representative high field-factor actuator of 500 μm x 500 μm dimensions (HFF500) achieves optical deflection angles beyond -20° to 20° for both axes and greater than -12 μm to 12 μm pistoning, at <80V actuation, as summarized in Figure 10.

It is also important to note, as shown in Figure 11 for a 500 μm actuator and an 800 μm actuator, that for devices with bonded micromirrors the quality factor (Q) (which is extracted from the measured step response) decreases significantly. The Q of the 800 μm device is reduced from ~50 to 2.50 with a bonded micromirror, and for a 500 μm device the final Q was 1.46. This reduction in Q is the result of increased damping due to the effects of surrounding air, and is highly desirable for faster settling time operation. A settling time of ~ 2 ms in open loop actuation was extracted from the plots.

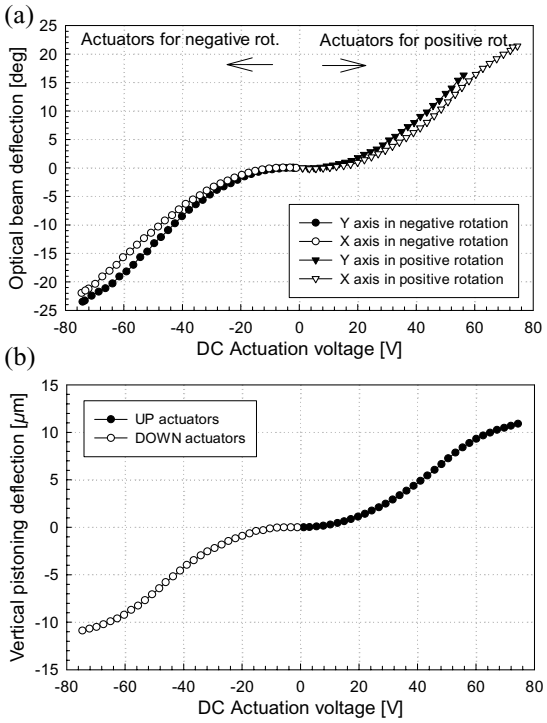

Figure 10. Measured HFF500 actuator in (a) bi-directional rotation for both axes, and (c) bi-directional pistoning actuation..

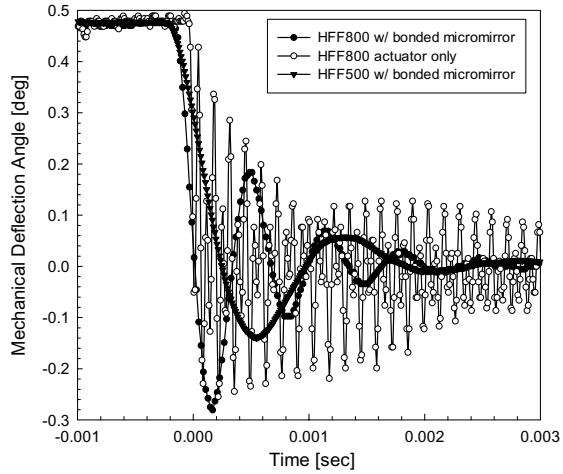

Figure 11. Measured comparison of an HFF800 device step response before and after mirror bonding, showing an approximate 10x reduction in resonant frequency of the ringing, and similarly a very significant decrease of the quality factor from ~ 50 to 2.5 due to the effects of the air surrounding the micromirror. Superimposed is the step response for the HFF500 device with the bonded micromirror with Q of 1.46.

The present methodology is very promising for high speed and large static deflection 2D scanning applications as well as high fill factor arrays of small mirrors with tip-tilt piston capability for each individual element. It enables the designer to significantly optimize independent components and achieve desired overall performance. The actuators and mechanical linkages allow static two-axis rotation of for micromirrors without need for gimbals, or other specialized isolation methodology. The design presented

	X-axis scan optical °	Y-axis scan optical °	Res. freq no mirror [Hz]	Res. freq W/ mirror [Hz]
Triangle	-10 to 10	-10 to 10	n/a	4096
HFF800	0 to 12.5	0 to 14.5	22727	1977
HFF600	0 to 16	0 to 16.1	13157	4000*
HFF500	-22 to 22	-23 to 16	11378	697.9
HFF400	-12.5 to 14	-15 to 6	64900	15500*
				*predicted results

Table 1. Table of measured characteristics of 5 types of devices, Triangle from Figure 5 with integrated mirror, and 4 high fill-factor actuators for mirror bonding. HFF600 and HFF400 have not been characterized with bonded mirrors to date.

utilizes a combination of actuators for making micromirrors capable of two-axis scanning as well as pistoning. Symmetry of the design allows both axes to have similar angular rotation and speed, which is highly desirable for applications such as vector or non-raster scanning. Smooth actuation of the device from onset greatly simplifies implementation of control systems.

V. Acknowledgements

The authors would like to thank M. Cohn, R. Roehnelt, and K. Castelino for many useful discussions on the actuator design and micromirror bonding and transfer, as well as C. Keller for many useful discussions and assistance with micromirror transfer.

VI. References

[1] J.-C. Tsai, *et al*, "Analog Micromirror Arrays with Orthogonal Scanning Directions for Wavelength Selective 1xN2 Switches," *Transducers '03*, pp. 1776-1779, Jun. 2003.

[2] Krishnamoorthy, U., *et al,* "Dual-Mode micromirrors for Optical Phased Array Applications", *Transducers'01,* Munich, Germany, June 2001.Germany, Jun. 2001.

[3] V. Milanović, S. Kwon, L. P. Lee, "Monolithic Vertical Combdrive Actuators for Adaptive Optics," *IEEE/LEOS Int. Conference on Optical MEMS*, Switzerland, Aug. 2002.

[4] V. Milanović, "Multilevel-Beam SOI-MEMS Fabrication and Applications," *J. of MEMS,* vol. 13, no. 1, pp. 19-30, Feb. 2004.

[5] P. R. Patterson, *et al*, "A MEMS 2-D Scanner with Bonded Single-Crystalline Honeycomb Micromirror," *Late news, Proc. Solid-State Sensor and Actuator Workshop*, Hilton Head, South Carolina, pp. 17-18, Jun. 2000.

[6] S. Kwon, V. Milanović, L. P. Lee, "A High Aspect Ratio 2D Gimbaled Microscanner with Large Static Rotation," *IEEE/LEOS Int. Conf. on Optical MEMS'02*, Switzerland, Aug. 2002.

[7] H. Schenk, *et al*, "Large Deflection Micromechanical Scanning Mirrors for Linear Scans and Pattern Generation," *IEEE J. of Selected Topics in Quantum Electronics*, vol. 6, no. 5, Sep./Oct. 2000.

[8] T. Brosnihan, et al, "Embedded Interconnect and Electrical Isolation for High-Aspect-Ratio, SOI Inertial Instruments," *1997 Int. Conf. on Solid-State Sensors and Actuators*, Chicago, June 16-19, 1997.

[9] V. Milanović, et al, "Monolithic High Aspect Ratio Two-axis Optical Scanner in SOI," Int. Conf. on Microelectromechanical Systems, MEMS2003, Kyoto, Japan, pp. 255-258, Jan. 2003.

[10] F. Niklaus, S. Haasl and G. Stemme, "Arrays of monocrystalline silicon micromirrors fabricated using CMOS compatible transfer bonding," J. of MEMS , v 12, n 4, Aug. 2003, p 465-469.

[11] U. Srinivasan, et al, "Fluidic self-assembly of micromirrors onto microactuators using capillary forces," IEEE J. of Spec. Topics in Quantum Electronics, vol. 8 (1), pp. 4-11, Jan. 2002.

[12] C. Rembe, *et al*, "Stroboscopic interferometer with variable magnification to measure dynamics in an adaptive-optics micromirror,"
2000 IEEE/LEOS Int. Conf. on Optical MEMS, 21-24 Aug. 2000

[13] http://www.memspi.com

[14] B. Cagdaser, et al, "Capacitive Sense Feedback Control for MEMS Laser Beam Steering Mirrors," *Proc. Solid-State Sensor and Actuator Workshop*, Hilton Head, South Carolina, Jun. 2004.

OPTICAL AND MECHANICAL CHARACTERIZATION OF AN EVANESCENT COUPLER OPTICAL SWITCH

Marcel W. Pruessner[1,2], Kuldeep Amarnath[2], Madhumita Datta[1,2], Daniel P. Kelly[1,2], S. Kanakaraju[3], Ping-Tong Ho[2], and Reza Ghodssi[1,2]

[1]MEMS Sensors and Actuators Laboratory (MSAL) and Institute for Systems Research (ISR),
[2]Department of Electrical and Computer Engineering, University of Maryland, College Park, Maryland 20742
[3]Laboratory for Physical Sciences (LPS), College Park, Maryland 20740

ABSTRACT

An InP-based optical switch with evanescent coupling mechanism is presented. Switching is achieved by electrostatic actuation of two parallel waveguides. Actuation at 5.4 V has been achieved with coupling efficiency of 60 % resulting in 2.2 dB loss. The device exhibits 47 dB channel isolation in the off state and is compact with an active area of 500 μm x 5 μm.

INTRODUCTION

Indium phosphide (InP) is attractive for optical communications due to its direct bandgap and suitability as a substrate material for active optical devices operating at the 1550 nm wavelength. To date, InP-based MEMS efforts have mainly concentrated on tunable filters [**1**], likely due to the small displacements required for these types of devices. However, we previously demonstrated that InP is suitable for MEMS devices with several micron displacement range [**2**]. We also previously characterized suspended InP-based waveguides for use in optical MEMS [**3**] and now present an optical waveguide MEMS switch.

Contrary to free-space switches, which typically use relatively large mirrors, we are developing a moving waveguide switch. Compared to previously developed MEMS serially-coupled waveguide switches [**4, 5**], our evanescent parallel-coupled switch is smaller and potentially enables variable power coupling so that it can also function as a variable power splitter/attenuator. Passive evanescent couplers are commonly used as optical power splitters. Active couplers have used thermal heating to perform optical switching by varying the refractive index, *n*, between two *fixed* parallel waveguides [**6**]. However, these devices typically draw significant current. Other approaches have utilized expensive electro-optic materials [**7**] to vary *n* and achieve switching.

Our device uses electrostatic actuation to vary the spacing between two *movable* suspended waveguides, resulting in low-power and relatively high-speed operation (compared to thermal couplers [**6**]). We chose InP due to its potential for optical gain at 1550 nm. However, for passive operation our device is not limited to expensive semiconductors [**7**] and can be fabricated in relatively inexpensive materials – i.e. polymer waveguides on silicon actuators – without significant design changes.

THEORY

The MEMS coupler consists of two movable parallel waveguides that are electrostatically actuated until pull-in so as to vary the spacing between them (Figure 1). Optical switching then occurs by evanescent coupling and mode-interference. If two single-mode waveguides are brought close together, then the compound waveguide structure can support two modes: even and odd [**8**]. These modes travel at different velocities (propagation constants, β) along the length *z* of the waveguide. The optical power measured at the output will be the contribution of both even and odd modes, resulting in a constantly varying exchange of power between BAR and CROSS waveguides throughout the interaction length (Eq. 1). The coupling coefficient, κ, depends exponentially on the waveguide gap (Eq. 2), as well as on the waveguide geometry, refractive index and optical polarization.

$$P_{BAR} = P_{IN}\cos^2(\kappa \cdot z) \quad \text{and} \quad P_{CROSS} = P_{IN}\sin^2(\kappa \cdot z) \tag{1}$$

$$\kappa \propto \exp(-gap) \tag{2}$$

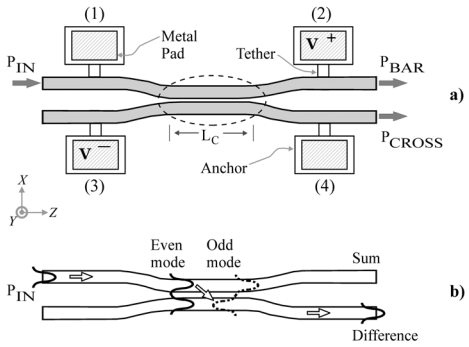

Figure 1. *a) Top view schematic of coupler, b) evanescent coupling via mode interference. The 2 μm wide waveguides are normally straight with 1 μm gap before actuation.*

FABRICATION

Processing of our device (Figure 2) is similar to that in Refs. [**2, 3**]. We patterned 7000 Å SiO_2 using positive resist, projection lithography, and reactive ion etching (RIE). The top 5 μm (4 μm waveguide layers and part of the $In_{0.53}Ga_{0.47}As$ sacrificial layer) were etched by methane-hydrogen RIE, resulting in vertical sidewall profiles (88 degrees) and less than 50 nm roughness. After removal of the SiO_2 mask, Ni-Ge-Au-Ni-Au ohmic contacts were deposited and patterned by lift-off followed by a 40 second rapid thermal anneal at 400 °C. We cleaved the devices and etched the InGaAs layer in $HF:H_2O_2:H_2O$ (1:1:8) with complete selectivity over InP followed by supercritical CO_2 drying. A complete switch is shown in Figure 3.

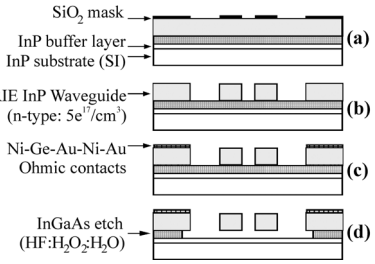

Figure 2. *Process flow of the InP coupler optical switch.*

Travel support has been generously provided by the Transducers Research Foundation and by the DARPA MEMS and DARPA BioFlips programs.

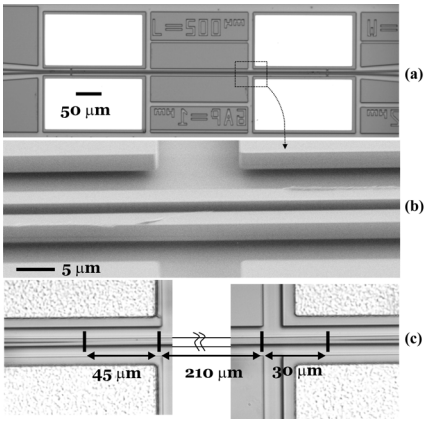

Figure 3. *a) Fabricated coupler, b) close up of n-type suspended waveguides, c) measured coupling length: $L_{PULL\text{-}IN}$ = 285 μm.*

EXPERIMENTAL DETAILS

Initial testing of the device was performed with S-polarized light (electric-field perpendicular to wafer plane) at 1550 nm wavelength. The experimental setup consisted of a tunable laser, a polarization control unit and input/output lensed fibers controlled by piezoelectric XYZ-stage. A probe station and function generator were used to actuate the device. Electrical actuation signals and optical output power were fed to an oscilloscope. We measured the BAR and CROSS outputs separately.

Prior to actuation, we measured less than 0.6 nW of optical power in the CROSS waveguide for 30 μW power in the BAR waveguide resulting in a channel isolation of 47 dB (in the 'off' state). Next, a 5.4 Vp-p, 10 Hz square wave with DC offset was used to modulate the waveguide gap and achieve pull-in during the optical measurements. The results in Figure 4 show 60 % coupling of power from the BAR to the CROSS waveguide during pull-in (relative to P_{BAR} in the uncoupled state), resulting in 2.2 dB coupling loss. The uncoupled BAR power at pull-in is 10 %.

Figure 5 shows the switching speed of the device in response to a 10 Hz square wave actuation pulse. The rise- and falltime is 1 ms. However, there is a 400 μs delay in the risetime. This delay is due to the exponential dependence of evanescent coupling on the waveguide separation (Eq. 2): the 400 μs delay is the time required for the beams to come into close proximity in order for coupling to occur. The beams separate immediately after removal of the actuation voltage so that the falltime does not exhibit this delay in the response. It turns out that the switching speed is dominated by *thermal* actuation, as discussed below.

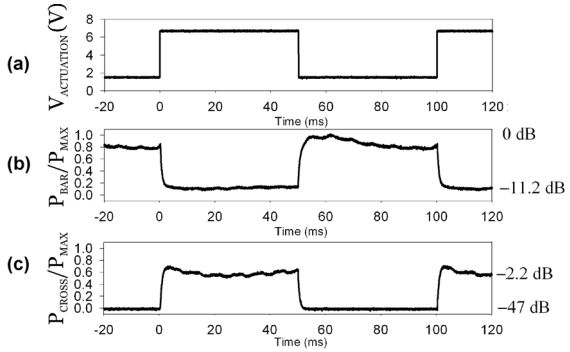

Figure 4. *a) Actuation signal, b) normalized BAR, and c) normalized CROSS signals, where P_{MAX}=maximum BAR power (S-polarization: electric field E=E_Y, λ=1550 nm wavelength).*

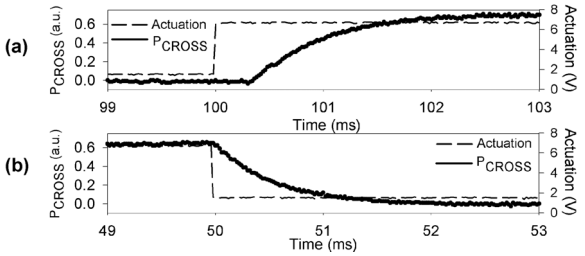

Figure 5. *Measured a) risetime and b) falltime. The speed is t_{SWITCH} < 1.4 ms (S-polarization: E=E_Y, λ=1550 nm).*

THERMAL ISSUES

The 1.4 ms total switching time (Figure 5) is slow compared to typical electrostatic pull-in actuators: the reason is that the tested device was actually *thermally* actuated. Figure 2a shows a 0.45 μm thick InP buffer layer grown on top of a semi-insulating (SI) InP substrate. The buffer layer is typically grown before any additional epilayers in order to obtain uniform surface conditions for crystal growth. Undoped InP *as grown* by MBE is n-type conducting with n~10^{16}/cm^3. This results in significant substrate leakage currents. In Figure 1a a voltage is applied between terminals 2 and 3 to actuate the device. The measured resistance between terminals 1 and 3 was $R_{13} = R_{LEAKAGE} \cong 300\ \Omega$, and the waveguide resistance (i.e. terminals 1 and 2) was around 5 kΩ (measured on separate samples without the InP buffer layer, but with similar waveguides and doping). Therefore, terminals 1 and 3 are at similar potential and significant current flows through the waveguide resulting in a combination of electrostatic and thermal actuation. Measurements have shown that 2.5 mW of thermal power are dissipated in the waveguides during actuation at 5.4 V.

Simple calculations shed some insight on the electro-thermal behavior of our device. The induced (thermal) strain required to actuate the waveguides is [**2**]:

$$\varepsilon_{THERMAL} = -\left[\frac{\pi^2}{4}\left(\frac{dx}{L}\right)^2 + \frac{\pi^2}{3}\left(\frac{w}{L}\right)^2 + \varepsilon_O\right], \qquad (3)$$

where dx = 0.5 μm is the actuation distance of each waveguide during switching, L = 500 μm is the waveguide length, and w = 2 μm is the waveguide width. The first term represents the induced axial strain, the second is the *Euler* buckling strain, and ε_o is the intrinsic tensile strain of the waveguides. Assuming ε_o = 0.04 % (the designed intrinsic tensile strain), the necessary thermal strain is $\varepsilon_{THERMAL}$ = −0.0455 %. The coefficient of thermal expansion is $\alpha = 4.56\times10^{-6}$/K [**9**], which implies a temperature increase of $\Delta T = \varepsilon_{THERMAL}/\alpha$ = 100 K in order to thermally actuate the switch. Based on our calculations and the measured switching speed and heat dissipation, we conclude that *thermal* heating is the dominant actuation mechanism, not *pull-in*.

The thermal effects on the characteristics of our device are discussed below. Future devices will use epiwafers without an InP buffer layer and with pn-junctions between waveguide and sacrificial layers to avoid substrate leakage currents.

OPTICAL CHARACTERIZATION

After the initial experiments, we repeated our measurements with P-polarized light (E-field parallel to wafer plane), again at 1550 nm wavelength. In these experiments we obtain 10 % coupling, significantly less than for S-polarization (Figure 6).

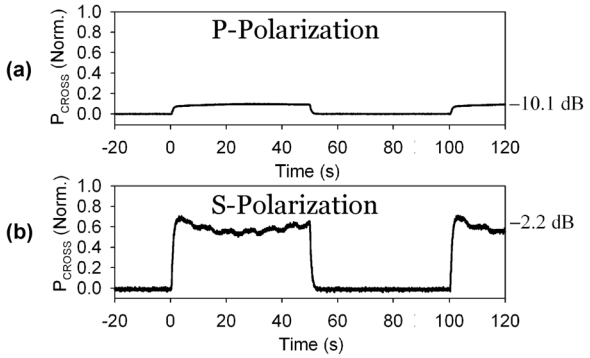

Figure 6. *Experimentally measured coupling efficiency to CROSS waveguide: a) P-polarization: 10%, and b) S-polarization: 60%.*

For our optical analysis we approximate the coupling length (L_C in Figure 1) as the pull-in length, which equals 285 μm (Figure 3c). If we know the coupling coefficient κ, then we can obtain the coupled power (P_{CROSS}) using Eq. 1. We can obtain the coupling coefficient κ by simulation. While it is difficult to precisely know the waveguide gap during actuation, we assume the switching gap to be greater than twice our maximum sidewall roughness (> 2 × 50 nm = 100 nm). This gives us an estimate and starting point for the gap in our simulations.

Polarization-dependent coupling was analyzed by simulating [**10**] the effective refractive index ($n_{effective}$) for even and odd modes for both S- and P-polarizations for various gaps (Figure 7). From $n_{effective}$ we calculate the coupling coefficient [**8**]:

$$\kappa = (\beta_{even}-\beta_{odd})/2 = (n_{even}-n_{odd})k_o/2, \quad (4)$$

where $k_o=2\pi/\lambda_o$ and λ_o=1550 nm. After simulations for various gaps, we find that a 120 nm separation between the waveguides at pull-in gives us the best agreement between simulation and experiment (Table 1). Using a 120 nm gap and a coupling length of L=285 μm (as measured in Figure 3c) we expect 54.7 % and 1.07 % coupling for the S- and P-polarizations, respectively (Figure 8), similar to the 60 % obtained experimentally for S-polarization, but significantly smaller than our measured 10 % for P-polarization (Figure 6).

A possible source of discrepancy between our measurements and simulation is that the exact waveguide gap at pull-in is not known. Also, our waveguides are not strictly single-mode. The 2 μm × 2 μm waveguide core cross-section (Figure 7) was chosen for mechanical robustness. Subsequent simulations have shown that the core cross-section should be less than 0.7 μm × 0.7 μm for single-mode behavior. This explains the larger than expected measured coupled power for P-polarization due to higher order mode coupling.

Another concern is that thermal actuation of our waveguides will cause a shift in the refractive index. The temperature dependence of the refractive index for InP is $dn/dT = 1.9\times10^{-4}$/K at 1550 nm wavelength [**9**], resulting in an increase of 1.9 % in the refractive index during thermal actuation (assuming ΔT = 100 K). Repeating our simulations [**10**] for a 2 % increase in the refractive index, we obtain P_{CROSS} = 49.0 % for S-polarized light and P_{CROSS} = 0.86 % for P-polarized light, similar to the results in Table 1. We conclude that the thermally-induced increase in the refractive index of our waveguides does not significantly change our coupling analysis.

While our analysis assumes single-mode waveguides (the waveguides support more than one mode), the general agreement between measured and simulated coupling efficiency for different polarization is insightful for future device design and suggests that our device behavior is dominated by the fundamental mode. Future devices, however, should utilize single-mode waveguides to ensure fundamental mode-coupling.

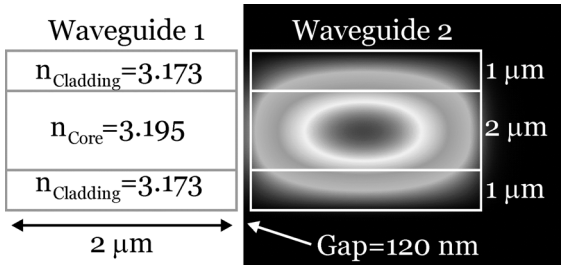

Figure 7. *Half-structure cross-section simulation (right) of the optical mode in the coupler from which $n_{effective}$ is obtained [**10**].*

Gap=120 nm	P-Polarization	S-Polarization
$n_{effective}$ (even)	3.163234	3.166794
$n_{effective}$ (odd)	3.163054	3.165353
κ (μm^{-1})	3.648300×10^{-4}	2.920668×10^{-3}
$P_{CROSS,\ L=285\ \mu m}$ (%)	54.7	1.07

Table 1. *Simulated Coupling for S- and P-Polarizations.*

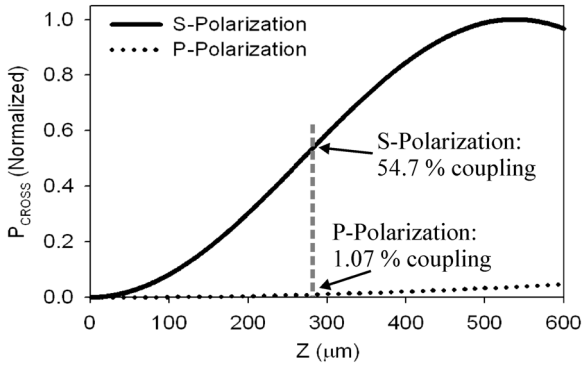

Figure 8. *Predicted coupling for S- and P-polarizations vs. coupling length, neglecting losses. For 285 μm coupling length (dashed vertical line), P-polarization yields 1.07 % and S-polarization gives 54.7 % coupling.*

MECHANICAL CHARACTERIZATION

The complete coupler switch does not simply consist of the device shown in Figures 1 and 3. Rather, it has sets of optical inputs and outputs connected to the coupled-region via S-curved waveguides (Figure 9). These S-curved waveguides are suspended in air by 1.5 μm wide, 5 μm long tethers using the same 'suspended waveguide' technology presented in [**3**]. The effects of tether compliance were studied by experiment and simulation.

We gauged tether compliance by measuring the displacement of the S-curve region during actuation of the two waveguides in the coupled region (Figure 9). An ideal tether would be completely rigid and would result in zero movement of the S-curve. Measurements were performed using an optical profilometer [**11**] while actuating the coupled waveguides. We measured 700 nm total S-curve displacement for $V_{ACTUATION}$ = 5 Vp-p at 800 Hz (Figure 10). Note that this did not result in pull-in of the coupled-waveguide region.

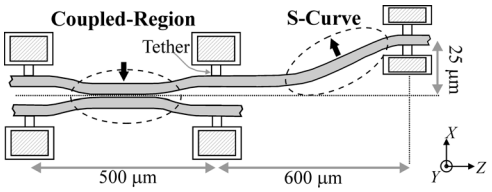

Figure 9. *Actuation of the coupled region causes oscillation of the S-curve due to compliance and the pivot action of the tether.*

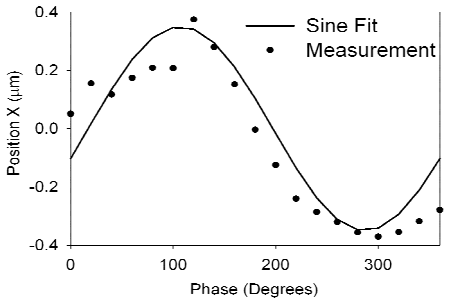

Figure 10. *Measured x-direction displacement of the S-curve (due to thermal effects) in response to a sine wave actuation signal (5 Vp-p, 800 Hz). Electrostatic actuation should limit this effect.*

Static load ANSYS simulations showed that while we expect only small tether movement (< 3 nm) during actuation, the tethers also rotate slightly, resulting in significant displacement (~150 nm) of our S-curves. However, this is still much less than the 700 nm S-curve displacement measured experimentally. The additional movement of the S-curve is the result of thermal expansion of the coupled waveguides during actuation.

Future devices will rely on electrostatic rather than thermal actuation by preventing substrate leakage currents. Based on ANSYS simulations, this should prevent any significant movement of the S-curve waveguides and will result in more efficient actuation in terms of both power consumption and switching speed. Initial pull-in actuation of devices fabricated on new epiwafers (without InP buffer layer and including pn-junctions between waveguide and sacrificial layers) result in switching times as low as 30 µs based on electrical measurements and pull-in voltages as low as 3.7 V. This performance is comparable to that of serially-coupled MEMS waveguide switches [**4, 5**], but with much smaller device area. The substrate leakage is negligible with measured R_{13} and R_{24} (Figure 1) in the tens of MΩ range. This reduces the power consumption to the µW-range, significantly smaller than for thermal couplers [**6**]. A concern with pull-in actuators, however, is that they are prone to stiction, posing a significant concern that needs to be addressed [**12**].

CONCLUSIONS

We have presented an InP-based optical MEMS switch with evanescent coupling mechanism in which we control the spacing between two semiconductor waveguides by application of a voltage. The device is compact, low voltage, relatively low loss and enables dense integration on a chip. We believe it can find applications in photonic circuits and devices, including tunable filters [**13**]. Other applications include optical network restoration in which switching speeds of 1 ms are more than adequate.

Although designed for electrostatic pull-in actuation, the current device exhibits thermal actuation due to substrate leakage currents. Future devices will be based on electrostatic pull-in, resulting in more efficient switches with lower power consumption and expected switching speeds in the sub-100 µs range. While the present waveguides are multi-mode, the demonstrated device can be scaled down in dimensions (i.e. reducing the waveguide cross-section) to obtain single-mode waveguides without significant change in the design. We expect that reducing the device size will further decrease the switching time. Stiction and reliability is a concern, however. Future devices could utilize actuators that do not exhibit pull-in, thereby increasing the device reliability. In this manner, variable coupling can also be achieved so that the device acts as a switch and as a variable power splitter or attenuator.

ACKNOWLEDGMENTS

The authors especially thank Mr. L. C. Calhoun for assistance with the MBE wafer growth, and Mr. L. C. Olver and the Laboratory for Physical Sciences (LPS) staff for access to the cleanroom facilities. This work is supported by a National Science Foundation (NSF) CAREER award (R. Ghodssi) and by the LPS.

REFERENCES

1. S. Irmer, J. Daleiden, V. Rangelov, C. Prott, F. Römer, M. Strassner, A. Tarraf, and H. Hillmer, "Ultralow Biased Widely Continuously Tunable Fabry–Pérot Filter," *IEEE Phot. Tech. Lett. 15* (3) 434-436 (2003).

2. M. W. Pruessner, T. T. King, D. P. Kelly, L. C. Calhoun, and R. Ghodssi, "Mechanical property measurement of InP for optical communications," *Sens. Actuators A*, *105* (2), 190-200, (2003).

3. D. Kelly, M. W. Pruessner, K. Amarnath, M. Datta, S. Kanakaraju, L. C. Calhoun, and R. Ghodssi, "Monolithic Suspended Optical Waveguides for InP MEMS," *IEEE Phot. Tech. Lett.*, in press, May 2004.

4. E. Ollier, "Optical MEMS devices based on moving waveguides," *IEEE J. Sel. Top. Quan. Elec.*, *8*, 155-162, (2002).

5. T. Bakke, C. P. Tigges, J. J. Lean, C. T. Sullivan, and O. B. Spahn, "Planar microoptomechanical waveguide switches," *IEEE J. Sel. Top. In Quan. Elec.*, *8* (1), 64-72 (2002).

6. Q. Lai, W. Hunziker, and H. Melchior, "Low-Power Compact 2×2 Thermooptic Silica-on-Silicon Waveguide Switch with Fast Response," *IEEE Phot. Tech. Lett.*, *10* (5), 681-683 (1998).

7. V. R. Chinni, T. C. Huang, P. K. A. Wai, C. R. Menyuk, and G. J. Simonis "Performance of Field-Induced Coupler Switches," *IEEE J. Quant. Elec., 31* (11), pp. 2068-2074 (1995).

8. Katsunari Okamoto, "Fundamentals of Optical Waveguides," Academic Press: San Diego (2000).

9. E. Gini and H. Melchior, "Thermal Dependence of the Refractive Index of InP Measured with Integrated Optical Demultiplexer," *J. Appl. Phys., 79* (8), pp. 4335-4337 (1996).

10. Apollo Photonics, OWMS 1.21: Optical Waveguide Mode Solver, Waterloo, Canada.

11. Model: Wyko NT1100 with dynamic MEMS (DMEMS) option, available from Veeco Instruments, Woodbury, New York.

12. H. Lim, C. Carraro, R. Maboudian, M. W. Pruessner, and R. Ghodssi, "Chemical and Thermal Stability of Alkanethiol and Sulfur Passivated InP(100)," *Langmuir*, *20*, pp. 743-747, 2004.

13. M.-C. M. Lee and M. C. Wu, "A MEMS actuated tunable microdisk resonator," *Proc. 2003 IEEE/LEOS Conf. on Optical MEMS*, Hawaii, (2003), pp. 28-29.

Poly-Wire-Coupled Single Crystal Silicon HARPSS Micromechanical Filters Using Oxide Islands

Reza Abdolvand, Gavin K. Ho, and Farrokh Ayazi
School of Electrical and Computer Engineering, Georgia Institute of Technology
Atlanta, GA 30332-0250

ABSTRACT

This paper reports on the implementation of single crystal silicon micromechanical filters coupled through a thin polysilicon wire using a SOI-based HARPSS process. The formation of suspended thin poly wires, which provide weak mechanical coupling between high quality factor thick microresonators, are enabled by the use of thick sacrificial oxide islands created between adjacent single crystal silicon resonators. The oxide islands are also used beneath the input and output pads of the filters to reduce the parasitic capacitances to substrate. Mechanical coupling of microresonators using thin-film wires provides superior design flexibility since the material and thickness of the coupling element can be chosen independent of those of the resonators. Measurement results obtained from 800kHz two-pole HARPSS micromechanical filters with thin poly wire are presented.

INTRODUCTION

Previously reported micromechanical filters have shown high selectivity, narrow bandwidth, and low insertion loss in the range of low to high frequency **[1-3]**. The bandwidth of these filters is primarily determined by the stiffness ratio of the coupling element to resonator **[4]**. To date, a few implementations of mechanically-coupled resonator filters have been reported using polysilicon surface micromachining technology, in which the vibrating resonator and the coupling element thickness is limited by the deposition thickness of the thin film polysilicon (typically a few microns).

The mixed-mode HARPSS fabrication technology has the ability to create sub-100nm vertical capacitive gaps along tens of microns thick high-Q single crystal silicon (SCS) resonators **[5,6]**. This in turn provides stronger capacitive transduction and lower motional resistance. Electrically-coupled micromechanical filters have been demonstrated using HARPSS resonators **[7,8]**; however, mechanical coupling of laterally-vibrating SCS HARPSS resonator was not demonstrated in the past. Figure 1 illustrates two ways of coupling SCS resonators through axially loaded coupler beams. In Fig. 1a, the coupler has the same thickness as the resonator structures, while in Fig. 1b the coupler is a thin wire such as a surface-deposited beam. One of the main challenges in implementing narrow bandwidth filters is providing a small coupling strength between constituent resonators. Thick coupling elements have large spring constants and consequently wider filter bandwidth. Reducing the width of the coupling element to decrease the stiffness is limited by lithography and long compliant couplers may cause excessive mass loading. Thin coupling wires present a viable solution to narrow bandwidth filtering, if they can be easily fabricated. Both the axial and flexural stiffness of a beam are directly proportional to its thickness (*i.e.* height), which can be greatly reduced in a thin-film deposition process. Therefore, compliant thin-film wires have great potential for resonator coupling in narrow bandwidth filters and is the main focus of this work (Fig. 1b).

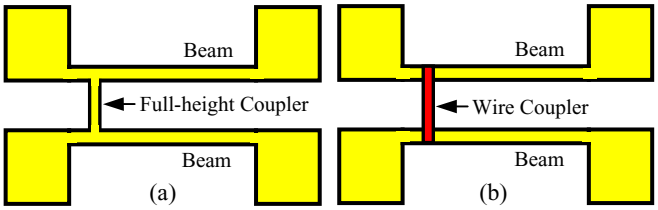

Figure 1. *Coupling of two HARPSS beam resonators via a) full-height silicon beam; and b) surface-deposited beam (e.g. poly wire)*

The resonance frequencies and mode shapes for the flexural modes of a beam resonator are:

$$f_n = \frac{\beta_n^2 w}{4\sqrt{3}\pi}\sqrt{\frac{E}{\rho}} \tag{1}$$

$$\phi_n(x) = C_n[\sinh\beta_n x - \sin\beta_n x + \alpha_n(\cosh\beta_n x - \cos\beta_n x)] \tag{2}$$

where w is the width of the beam, E is the Young's modulus, ρ is the density, and $\beta_n L$ = 4.7300, 7.8532, 10.995 for the first three modes **[9]**. Modeling the beam resonator as a single degree of freedom system for the fundamental flexural mode, $\omega_o = 2\pi f_o = \sqrt{k_{eff}/m_{eff}}$ where the effective mass m_{eff} and effective stiffness k_{eff} are evaluated at a particular point of interest. For a 1D homogeneous continuous system, these parameters are:

$$m_{eff} = \frac{KE_{tot}}{\left(\frac{1}{2}\right)\dot{\phi}_c^2} = \rho w h \frac{\int_L \phi^2(x)dx}{\phi_c^2}, \quad k_{eff} = \omega_o^2 m_{eff} \tag{4),(5}$$

where ϕ_c and $\dot{\phi}_c$ are the modal displacement and velocity at $x=x_c$. In a lumped model of a two-pole mechanically-coupled bandpass filter with a coupling stiffness k_c (Fig. 2), the frequency separation between the resonances is approximated by:

$$\Delta f = f_2 - f_1 \approx f_1 \frac{k_c}{k_{eff}} \tag{3}$$

A large k_{eff} can be obtained via low-velocity coupling **[2]**, where the modal displacement ϕ_c is small. It is therefore advantageous to place coupling element closer to the resonator clamped boundary.

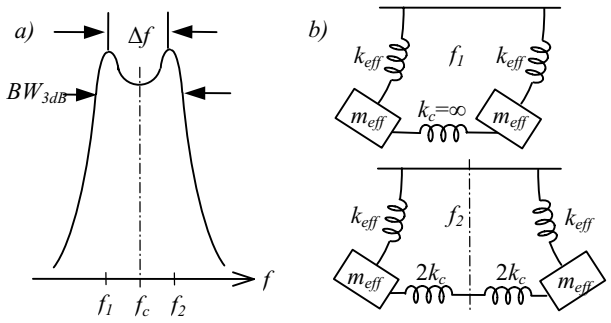

Figure 2. *a) Frequency response of a two-pole filter, b) vibration modes of a discrete 2DOF mechanical system.*

Travel support has been generously provided by the Transducers Research Foundation and by the DARPA MEMS and DARPA BioFlips programs.

FABRICATION PROCESS

In this work, the SOI-based HARPSS process is augmented with thick silicon dioxide islands to enable formation of suspended thin poly wires. Placement of such thick oxide islands beneath the input and output wire-bonding pads has the added benefit of substantially reducing the parasitic capacitances to the substrate.

The process begins on an SOI wafer with a 5-50µm thick device layer. The first step involves etching narrow trenches for isolation and oxide island formation. Numerous 1.5µm wide trenches are etched on a 1.5µm pitch into the SOI device layer (Fig. 3a), followed by subsequent thermal oxidation of the wafer to consume the remaining silicon and create the thick silicon dioxide islands. To ensure formation of voidless oxide islands, a 0.5µm LPCVD oxide layer is then deposited, followed by plasma etch back of the oxide on the surface (Fig. 3b).

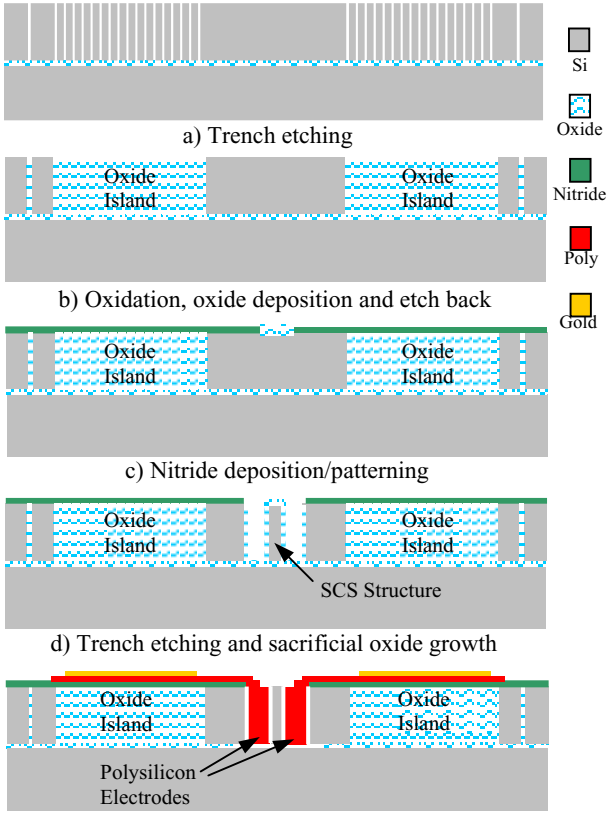

Figure 3. *Fabrication process flow of the SOI-based HARPSS process with thick oxide islands.*

To protect the solid oxide islands from the final HF release of the device, a 0.4µm LPCVD nitride layer is deposited and patterned to cover the oxide (Fig. 3c). After this, 5µm wide trenches are etched into the silicon device layer and subsequently filled with thin layers of oxide and polysilicon. The thickness of the thin sacrificial oxide defines the capacitive transduction gaps (Fig. 3d). The polysilicon layer is patterned on the surface to form the poly pads and coupling wires. In the next step, a thin layer of gold is deposited on top of polysilicon pads through a lift-off process. The last lithography step is performed to etch polysilicon inside the trenches and define electrodes. Finally, the device is released in HF:H_2O (1:1) solution (Fig. 3e). Figure 4 shows a cross section of a smooth polysilicon bonding pad with a solid oxide island underneath implemented on a 15µm thick SOI substrate.

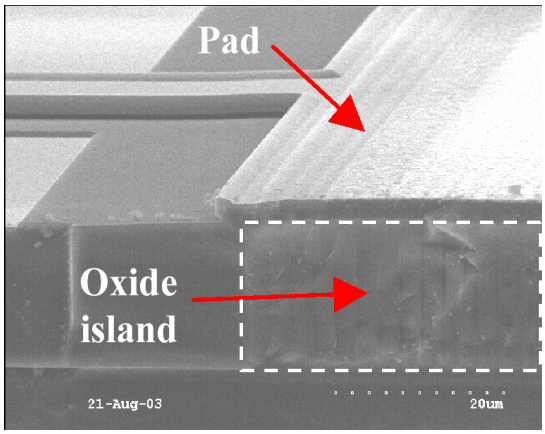

Figure 4. *Cross-section of a bonding pad and the solid oxide island created in the 15µm thick silicon device layer of an SOI wafer.*

Suspended Poly Wire

A polysilicon coupling wire can be incorporated into this modified version of the HARPSS process without any additional processing steps. The oxide islands, used for reduction of the pad capacitance, are also created between adjacent resonators for this purpose (Fig. 5a). In a second poly deposition and patterning step, a poly wire is patterned on the oxide island, which connects the neighboring resonators at the top surface (Fig. 5b). Since these oxide islands are not protected with nitride, they are etched in the final HF release step, and a suspended coupling wire is created (Fig. 5c).

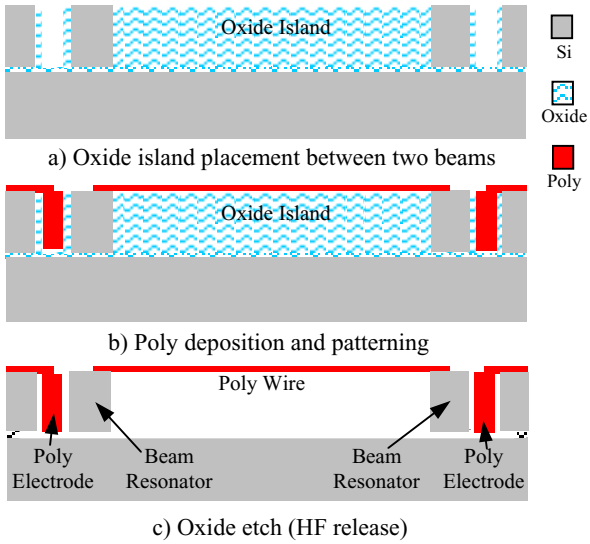

Figure 5. *Fabrication process for formation of the poly wire*

In this process, polysilicon was used for the coupling wire to minimize the number of mask layers. However, any other process compatible material (*e.g.* HF resistant metals) can be used to make the wire. Figure 6 shows an SEM of an electromechanical HARPSS filter consisting of two 300µm(*l*)×9µm(*w*)×15µm(*h*) single crystal silicon clamped-clamped beams coupled with a suspended poly wire centered at 10µm from the clamped boundary. Figure 7 is the close up of the poly wire and 15µm thick SCS

beams. Figure 8 is the SEM of a HARPSS filter with similar SCS beams coupled with a full-height SCS beam.

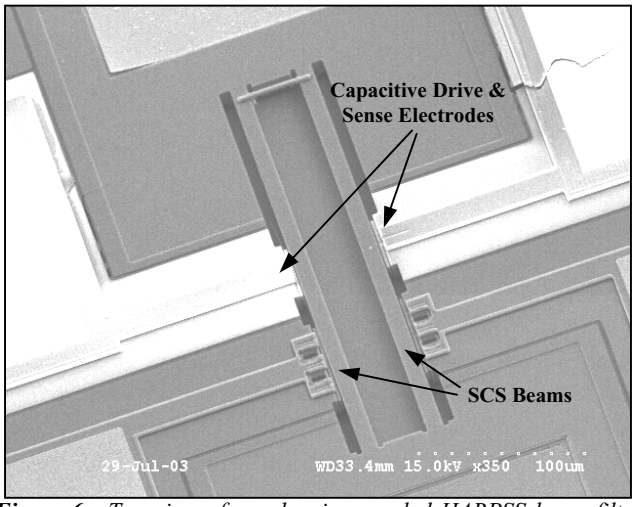

Figure 6. *Top view of a poly-wire-coupled HARPSS beam filter consisting of two 300µm×9µm×15µm beams. The poly-wire is centered at 10µm from the beam resonator support.*

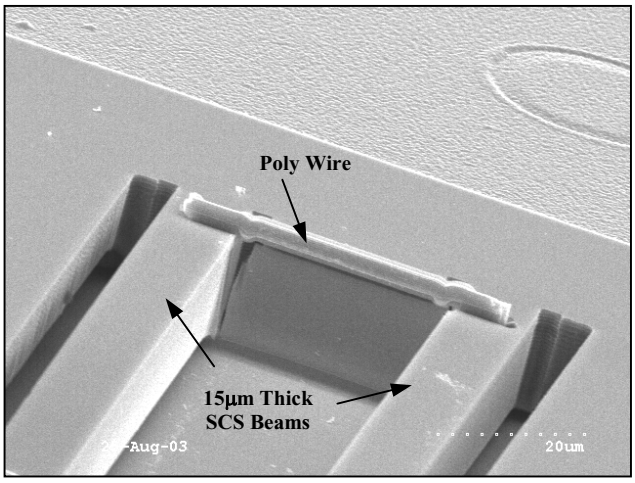

Figure 7. *Close up view of the poly wire of Fig. 6.*

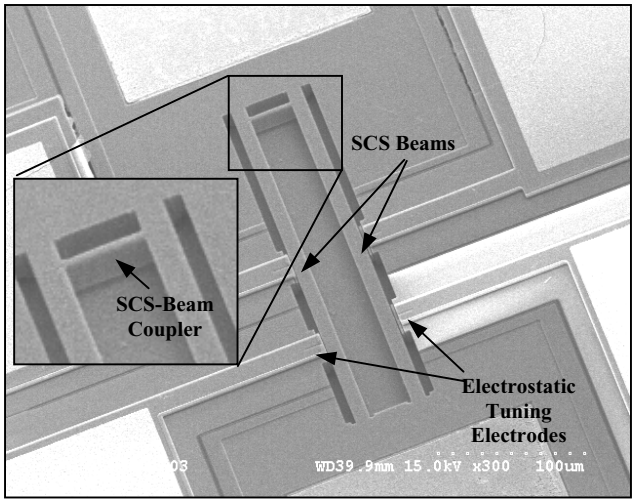

Figure 8. *SEM picture of a fabricated HARPSS beam filter with a full-height SCS beam coupler*

EXPERIMENTAL RESULTS & ANALYSIS

The specifications of the devices in Figs. 6 and 8 are listed in Table 1. Their frequency responses were measured under vacuum and are shown in Figs. 9a and 9b respectively. The frequency separation between two resonance peaks in the poly-wire-coupled device (12kHz) is 3 times lower than that of the SCS-beam-coupled device (35kHz). Since the dimensions of the constituent resonators and the coupling locations are the same in both devices, the implementation with the poly-wire coupling element is clearly advantageous for reducing the frequency separation. The measured Q for each individual peak in Fig. 9 is 7300.

Table 1. *Poly-wire-coupled and full-height SCS-beam-coupled device dimensions*

Parameter	Poly-Wire	SCS-Beam
Resonator $l \times w \times h$ [µm]	300×9×15	300×9×15
Coupler Material	Polysilicon	SCS
Coupler Modulus	150 GPa	168 GPa
Coupler $l \times w \times h$ [µm]	30×2×3	30×2×15
Coupling Dist. from Beam End	10µm	10µm

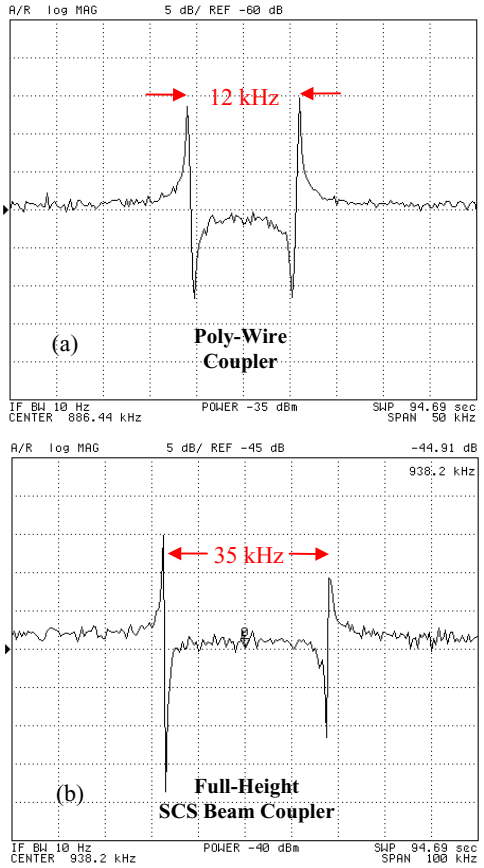

Figure 9. *Frequency response plots measured for a) the poly-wire-coupled device of Fig. 6, and b) the SCS-beam-coupled device of Fig. 8.*

For the device dimensions in Table 1, the effective mass m_{eff} at the coupling location for both devices were found to be 1800 times the resonator mass using Equation 4. Noting that m_{eff} is much larger than the mass of the coupling element m_c, mass loading is negligible. In the out-of-phase mode, the coupling beam is axially

loaded, so the stiffness and effective mass of the coupling element are

$$k_c = \frac{E_c wh}{L} \quad \text{and} \quad m_{c,eff} = \frac{m_c}{8}. \qquad (6),(7)$$

The coupling strength k_c is proportional to the height of the coupling beam and the advantage of using thin poly-wires for coupling is evident. Substituting Equation 6 with specifications in Table 1 into Equation 3, the calculated Δf are 3.4kHz and 28kHz for the poly-wire- and SCS-beam-coupled devices respectively. The analytical results are consistently smaller than experimental data, indicating that through-support coupling **[3]** which was not included in this model provides additional coupling in this topology.

To obtain a filter response from the poly-wire-coupled device, the motional resistance was reduced by applying polarization voltages of 65V, and external termination resistances were placed at both the input and output. Figure 10 is the filter response obtained with resistive termination.

The electrostatic tuning electrodes on each beam (Fig. 8) offer a tuning mechanism to alter the resonator frequency and compensate for the fabrication non-idealities. The minimum coupling-limited frequency separation occurs when the two resonators are matched **[1]**. The variation in the frequency separation of the poly-wire coupled filter is shown in Fig. 11.

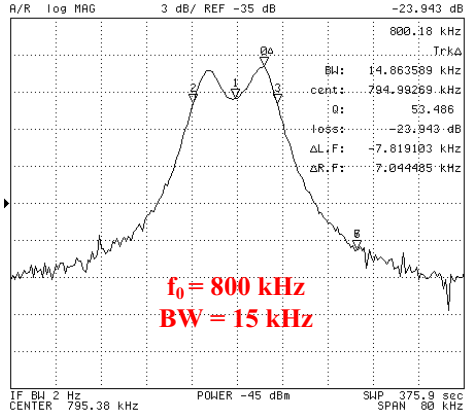

Figure 10. *Filter characteristic from an array of two 300μm×10μm×15μm poly-wire-coupled beams.*

CONCLUSIONS

The structural coupling of adjacent laterally-excited micromechanical resonators using a coupling element of a different material to enable narrow bandwidth filters was demonstrated. Thick oxide islands incorporated into a new HARPSS process enabled fabrication of a thin suspended polysilicon wire with a good structural bond to the single crystal silicon resonators. This wire-fabrication technology is applicable for coupling other resonator geometries and has potential for minimally-invasive resonator anchoring schemes.

ACKNOWLEDGMENTS

The authors wish to thank Siavash Pourkamali and the cleanroom staff of the Georgia Tech Microelectronics Research Center for their assistance. This work was funded under the DARPA NMASP program.

REFERENCES

1. K. Wang and C. T.-C. Nguyen, "High-order medium frequency micromechanical electronic filters", *IEEE Jnl. of Microelectro-mechanical Systems (JMEMS),* V8, N4, (1999), pp. 534-557.
2. K. Wang, F. D. Bannon III, J. R. Clark, and C. T.-C. Nguyen, "Q-Enhancement of Microelectromechanical Filters Via Low-Velocity Spring Coupling," *Proc. of 1997 IEEE Ultrasonics Symp*, (1997), pp. 323-327.
3. G. K. Ho, R. Abdolvand, and F. Ayazi, "Through-Support-Coupled Micromechanical Filter Array," *Proc. IEEE MEMS'04 Conf.*, Maastricht, The Netherlands (2004), pp. 769-772.
4. R. A. Johnson, *Mechanical Filters in Electronics*, 1983.
5. S. Pourkamali, A. Hashimura, R. Abdolvand, G. Ho, A. Erbil, and F. Ayazi, "High-Q Single Crystal Silicon HARPSS Capacitive Beam Resonators with Sub-micron Transduction Gaps," *IEEE Journal of Microelectromechanical Systems*, Vol. 12, No. 4, August 2003, pp. 487-496.
6. S. Pourkamali and F. Ayazi, "SOI-Based HF and VHF Single-Crystal Silicon Resonators with Sub-100 Nanometer Vertical Capacitive Gaps," *Tech. Digest 12th Int'l Conf. on Solid State Sensors, Actuators and Microsystems (Transducers'03)*, Boston MA (2003), pp. 837-840.
7. S. Pourkamali, R. Abdolvand, and F. Ayazi, "A 600kHz Electrically Coupled MEMS Bandpass Filter," *Proc. IEEE Int'l MEMS Conf.* (MEMS'03), Kyoto, Japan (2003), pp. 702-705.
8. S. Pourkamali, R. Abdolvand, G. K. Ho, and F. Ayazi, "Electrostatically Coupled Micromechanical Beam Filters", *Proc. of IEEE MEMS'04 Conf.*, The Netherlands (2004), pp. 584-587.
9. S. S. Rao, *Mechanical Vibrations*, 3E, 1995, Addison Wesley, Reading MA, pp. 526-527.

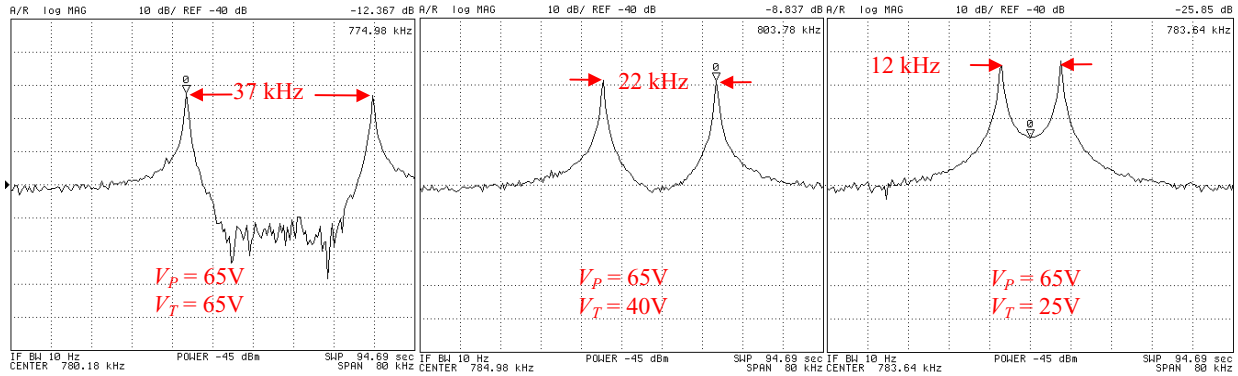

Figure 11. *Electrostatic tuning for frequency matching to produce a coupling-limited filter bandwidth (V_T is applied to one tuning electrode with the remaining tuning electrode grounded). A polarization voltage V_P of 65V was applied to the body of the resonators.*

EFFECTS OF BORON CONCENTRATION ON $Si_{1-x}Ge_x$ PROPERTIES FOR INTEGRATED MEMS TECHNOLOGY

Marie-Ange N. Eyoum[1,a], Yu R. Su[2], Brian L. Bircumshaw[2], Dimitry Kouzminov[3], Hideki Takeuchi[1], Roger T. Howe[1,2], and Tsu-Jae King[1]

[1]Department of Electrical Engineering and Computer Sciences, [2]Berkeley Sensor & Actuator Center, University of California, Berkeley, CA 94720 USA

[3]Materials Analytical Services, Sunnyvale, CA 94085 USA

[a]Tel: 1-510-643-2558 FAX: 1-510-642-2739 e-mail: meyoum@eecs.berkeley.edu

ABSTRACT

The effects of boron (B) concentration on the chemical, electrical, and mechanical properties of p+ polycrystalline germanium (poly-Ge) and p+ polycrystalline silicon-germanium (poly-$Si_{1-x}Ge_x$) films are reported. Experimental results show that heavy B doping is beneficial for increasing the deposition and etch rates, as well as for reducing the surface roughness of p+ poly-Ge sacrificial films. However, structural poly-$Si_{1-x}Ge_x$ films become more compressive, and show a slight increase in strain gradient, with increasing B content. Analytical models fit to the experimental data for conductivity, residual stress, and strain gradient have been generated as a guide for co-optimization of B and Ge content.

INTRODUCTION

Polycrystalline silicon-germanium (poly-$Si_{1-x}Ge_x$) is an attractive material for post-CMOS integration of MEMS with electronics because it can be used to form high-quality structural films with a thermal process budget that is compatible with standard electronics [1-2]. Germanium (Ge) is an attractive sacrificial material because it can be deposited rapidly at low temperatures (< 350°C) and readily etched selectively to metals, Si, SiO_2, Si_3N_4, and $Si_{1-x}Ge_x$ ($x < 0.7$) in a heated peroxide (H_2O_2) solution [3]. *In-situ* p-type doping is preferred because it provides enhanced deposition rate and lower resistivity [1]. Previous studies of structural poly-$Si_{1-x}Ge_x$ layers focused on very heavily boron doped films (B concentration exceeding 10^{20} cm^{-3}) for minimum electrical resistivity (<1 mΩ·cm) and maximum deposition rate. Recently, however, heavy boron doping was reported to enhance the etch rate of p+ $Si_{1-x}Ge_x$ ($x > 0.7$) in H_2O_2, which compromises the etch selectivity between the p+ Ge sacrificial material and the $Si_{1-x}Ge_x$ structural layer(s) during the long etch needed to release the MEMS structures [4].

The effects of boron concentration on the properties of poly-Ge films and poly-$Si_{1-x}Ge_x$ films are presented in this paper, which aims to highlight the tradeoffs for process optimization. The B-doping dependence of Ge deposition rate, etch rate, and surface roughness is first discussed. Experimental data are then reported for p+ $Si_{1-x}Ge_x$ ($x < 0.7$) films, to show the effects of boron content on residual stress and strain gradient. It should be noted that all of the films studied in this work are suited for post-CMOS processing, since they are deposited at a temperature less than or equal to 425°C with no post-deposition annealing treatment.

EXPERIMENTAL DETAILS

P-type Ge films were deposited at 350°C and 300mT onto oxidized Si wafers, with a very thin (<10nm thick) amorphous-Si seed layer, in a conventional low-pressure chemical-vapor deposition (LPCVD) system using GeH_4 (170 sccm) as the Ge precursor gas, and B_2H_6 as the dopant gas. The B_2H_6 is diluted (to 10%) in H_2 and is introduced from the back of the furnace through an injector in order to minimize gas depletion effects, while the GeH_4 is simply introduced through a ring at the front of the tube. Because of this arrangement, the B concentration and Ge content are dependent on wafer position inside the tube (**Fig. 1**). The B concentration in each of the deposited films was determined by Secondary Ion Mass Spectrometer (SIMS) analysis. The sheet resistance of the films was measured at several points on each wafer using a four-point probe instrument; average values are reported herein. The Ge films were patterned into test structures using conventional optical lithography and reactive ion etching (RIE) using Cl_2/HBr chemistries. The film thickness was then determined from step-height measurements using a Dektak surface profilometer. The Ge etch rate in a 90°C H_2O_2 solution was then characterized by monitoring the step height in-between etch treatments, for films of various Ge contents.

P-type poly-$Si_{1-x}Ge_x$ films were deposited at 425°C and 400mT in the same LPCVD system, onto oxidized Si wafers (p-type, 1 ohm/square) coated with ~2.2μm of undoped low temperature oxide (LTO). SiH_4 was used as the precursor Si gas (**Fig. 1**). The B concentration and Ge content in the deposited films were determined by SIMS analysis (2.5% accuracy), and varied from $1\times10^{19}cm^{-3}$ to $5\times10^{21}cm^{-3}$ and 61% to 67%, respectively. In order to determine thin film stress, wafer curvature measurements were made using a Tencor FLX-2320 instrument before and after $Si_{1-x}Ge_x$ deposition (with the backside $Si_{1-x}Ge_x$ film removed). The films were patterned into cantilever-beam test structures (**Fig. 2**) and then released using a timed etch in 49% concentrated HF. Then, a Veeco Instruments WYKO interferometer was used to measure the tip deflection of 100μm- and 50μm-long beams to determine the strain gradient.

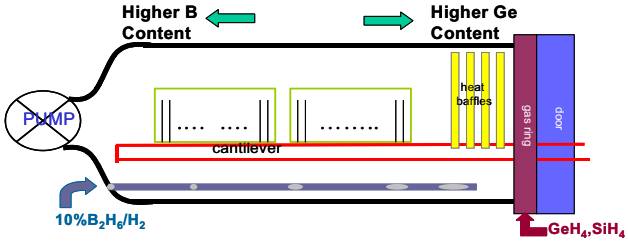

Figure 1: *Schematic Diagram of LPCVD furnace that was used to deposit p+ sacrificial Ge and p+ structural $Si_{1-x}Ge_x$ films.*

0-9640024-5-0/hh2004/$20©2004TRF
DOI 10.31438/trf.hh2004.65

Solid-State Sensors, Actuators, and Microsystems Workshop
Hilton Head Island, South Carolina, June 6-10, 2004

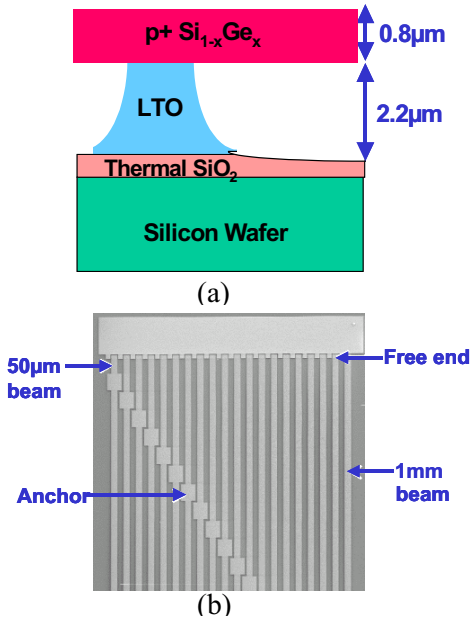

Figure 2: *(a) Schematic cross-section and (b) SEM micrograph of cantilever beams that were used to determine the strain gradient of the structural p+ poly-Si_xGe_{1-x} films.*

RESULTS AND DISCUSSION

A. Effect of Boron Doping on Sacrificial Ge Properties

Ideally, a sacrificial material is deposited at a high rate with minimal surface roughness, and is rapidly and controllably etched selectively to the structural material. Thus, we investigated the deposition rate, etch rate (in a 30% H_2O_2 solution maintained at 90°C), and surface roughness of p+ Ge films as a function of B concentration ([B]). **Fig. 3** shows that the deposition rate increases with [B], and saturates above ~1.8×10^{21} cm^{-3} at a deposition rate of ~160Å/min. The etch rate also increases with [B]. As expected, the resistivity drops with increasing [B] (**Fig. 4**). However, it shows an abrupt increase at ~2×10^{21} cm^{-3} since that deposition condition leads to an amorphous film. Because of the enhancement in deposition rate that accompanies an increase in [B], the atoms adsorbed on the wafer surface have less time to migrate to the lowest energy crystal sites before the next atoms arrive. Thus, as [B] increases, the degree of disorder in the film increases (average grain size decreases – see **Fig. 6**), until ultimately the film is deposited in amorphous form at very high levels of [B].

Atomic force microscopy (AFM) measurements indicate that the more heavily boron doped Ge films are smoother (**Fig. 5**), which is consistent with their higher deposition rate (resulting in smaller average grain size – see **Fig. 6**). Clearly, high [B] is desirable for increasing process throughput, etch selectivity, and film smoothness for sacrificial Ge films. It is important to note that, although the deposition rate can be substantially increased by increasing the deposition temperature, the film roughness also increases. Thus, it is preferable to keep the p+ Ge deposition temperature below 400°C.

B. Effect of Boron Doping on Structural $Si_{1-x}Ge_x$ Properties

The etch rate of p+ poly-$Si_{1-x}Ge_x$ films in a 30% H_2O_2 solution maintained at 90°C was measured and found to be relatively low (25A/min) and independent of B concentration, for

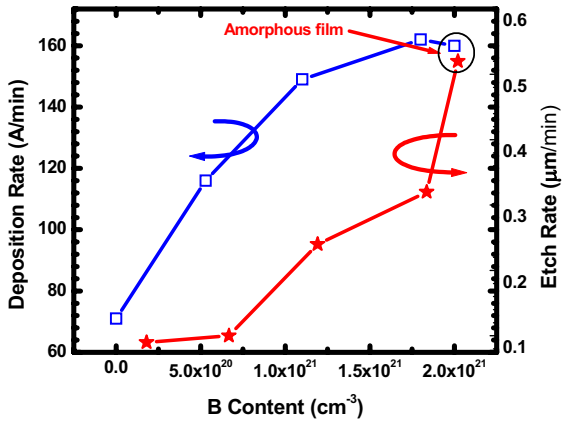

Figure 3: *Deposition and etch rates of Ge sacrificial layer as a function of B content. The p+Ge films were deposited at T=350°C, P=300mtorr, GeH_4=170sscm. B_2H_6/H_2 flow rate was varied from 0sscm to 60sscm.*

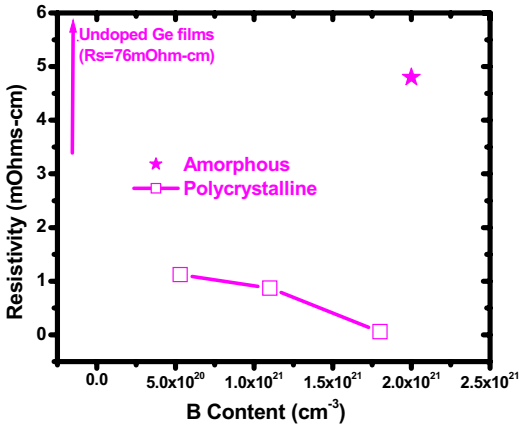

Figure 4: *Resistivity of p+ Ge sacrificial layer as a function of B content. The p+Ge films were deposited at T=350°C, P=300mtorr, GeH_4=170sscm. B_2H_6/H_2 flow rate was varied from 0sscm to 60sscm.*

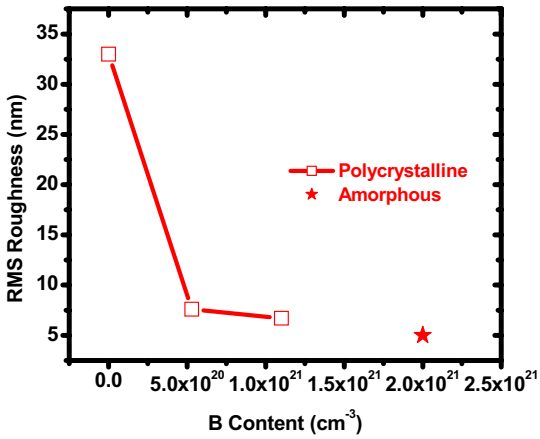

Figure 5: *Surface roughness of Ge sacrificial layer as a function of B content. The p+Ge films were deposited at T=350°C, P=300mtorr, GeH_4=170sscm. B_2H_6/H_2 flow rate was varied from 0sscm to 60sscm.*

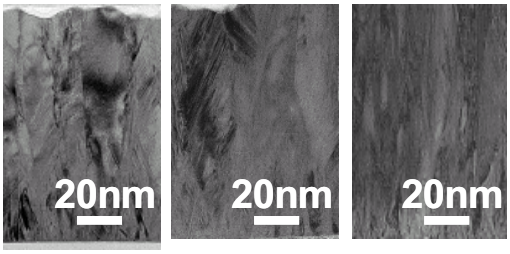

(a) (b) (c)

Figure 6: *X-TEM of p+ Ge films reported in Fig(s).3, 4 and 5. (a)[B]=5.3×10^{20}cm^{-3} (b)[B]=1.1×10^{21}cm^{-3} and (c)[B]=1.8×10^{21}cm^{-3}. Average grain size becomes smaller as B content increases because of the higher deposition rate of heavily doped p+Ge. films.*

films with Ge content below 65%. Thus, good etch selectivity between sacrificial p+ Ge and structural $Si_{1-x}Ge_x$ can be achieved so long as x does not exceed 0.65. The conductivity of poly-$Si_{1-x}Ge_x$ films as a function of B concentration is plotted in **Fig. 7**, and is seen to improve with increasing [Ge] as well as increasing [B]. This is likely due to improved dopant activation and hole mobility with increasing Ge content [5], due to increased grain size [6].

Using a regression analysis methodology that accounts for all the measured data, the best-fitting surface plots for conductivity, residual stress, and strain gradient as a function of B concentration and Ge content were generated (**Fig. 7** and **Fig. 8**). The fitting confidence is 99.5% for conductivity, 89% for residual stress, and 81% for strain gradient. The average residual stress decreases (*i.e.* the film becomes less compressive) with increasing [Ge], but increases for very high [B] (**Fig. 8a**). The strain gradient decreases with increasing [Ge] and decreasing [B] (**Fig. 8b**). Thus, optimization of the boron concentration involves a trade-off between electrical properties (conductivity) and mechanical properties (stress and strain gradient). Electrical and mechanical properties each improve with increasing Ge content. Thus, the Ge content should be maximized at ~65%, so that good etch selectivity of Ge in heated H_2O_2 solution is maintained.

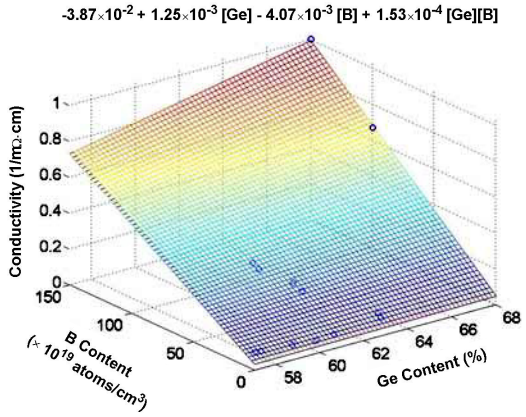

Figure 7: *p+ poly-$Si_{1-x}Ge_x$ conductivity as a function of Ge and B content. The p+$Si_{1-x}Ge_x$ films were deposited at T=425℃, P=400mtorr. SiH_4, GeH_4 and B_2H_6 flow rates were varied. In the modeling equation of conductivity (1/mΩ-cm), [Ge] is in % of Ge content and [B] is in atoms/cm^{-3}/10^{19}.*

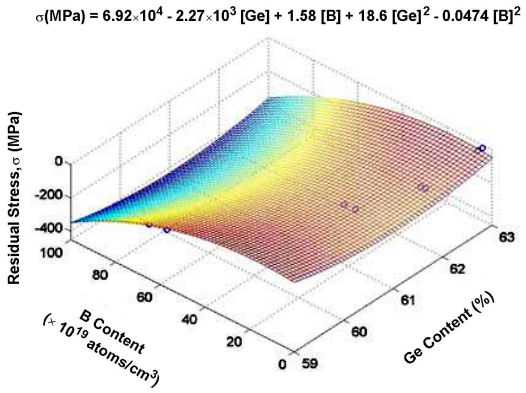

(a)

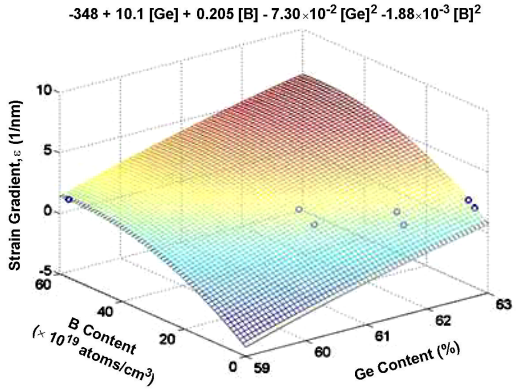

(b)

Figure 8: *p+ poly-$Si_{1-x}Ge_x$ (a) residual stress (b) strain gradient as a function of Ge and B content. The p+ $Si_{1-x}Ge_x$ films were deposited at T=425℃, P=400mtorr. SiH_4, GeH_4 and B_2H_6 flow rates were varied. In the modeling equations of residual stress (MPa) and strain gradient (nm^{-1}), [Ge] is in % of Ge content and [B] is in atoms/cm^{-3}/10^{19}.*

For [B]=2.5×10^{20}cm^{-3}, the strain gradient is 1.3×10^{-3} μm^{-1}, which corresponds to a vertical deflection of 1.7 μm at the tip of a 100 μm-long, 0.8 μm-thick cantilever beam. Although this is too high for inertial MEMS device applications (*e.g.* accelerometers and gyroscopes), it may be acceptable for nanoscale MEMS devices such as RF filters. Approaches to reducing the strain gradient include the use of a bi-layer [7] and the use of pulsed excimer-laser annealing (ELA) [8]. Based on the best-fit analytical models, the optimal B concentration for a low resistivity poly-$Si_{0.42}Ge_{0.58}$ film is ~5.1×10^{20}cm^{-3} to achieve minimal residual stress (~0.0012 MPa) and strain gradient (~3.75×10^{-3} μm^{-1}). However, it is important to note this optimal point is an approximation since the models are based on relatively few data points.

Hall measurements were performed to compare the dopant activation level in two p+ $Si_{0.37}Ge_{0.63}$ films: Sample A (with [B] ≅ 4.5×10^{19} cm^{-3}, σ = -22 MPa) and Sample B (with [B] ≅ 9.7×10^{20} cm^{-3}, σ = -79 MPa). The results are summarized in **Table I**, and they indicate that all of the B is activated in Sample A, whereas this is not the case for Sample B. Therefore, the fact that the p+ $Si_{1-x}Ge_x$ structural films become more compressive at very high B concentrations is likely due to segregation/clustering of boron atoms.

***Table I**: Hall Effect Measurement Results for p+ $Si_{0.37}Ge_{0.63}$. Sample A (σ = -22 MPa), Sample B (σ = -79 MPa)*

	Sample A	Sample B
Boron Concentration	4.5×10^{19} cm^{-3}	9.7×10^{20} cm^{-3}
Carrier Concentration	4.5×10^{19} cm^{-3}	5.1×10^{20} cm^{-3}

Due to the large strain gradient which causes the released structures to bend up (out of plane), it was not possible to operate the fabricated comb-drive test structures in order to obtain measurements of the mechanical quality factor (Q) for this study. Q values of ~20,000 at 19 kHz resonant frequency have previously been reported for very heavily doped (~[B] > 6×10^{20} cm^{-3}) poly-$Si_{0.38}Ge_{0.62}$ films [9]. The Q was found to increase with post-deposition annealing (RTA) temperature**.** To investigate possible causes for this change, we annealed similarly doped poly-$Si_{0.38}Ge_{0.62}$ films for 1 minute in N_2 at various temperatures (450°C to 600°C) and then performed Hall measurements as well as X-ray diffraction (XRD) analyses. The Hall measurement results did not indicate a significant increase in dopant activation with annealing, which would suggest that excess (non-ionized) B atoms remain. The XRD analysis results show that the as-deposited film has weak (111) texture, which changes to a strong (110) texture after a rapid thermal annealing treatment. The diffraction peaks for the annealed films were significantly larger and narrower, indicating a larger average grain size, as well. Thus, it seems that the improvement in Q with annealing is attributable to improved microstructure, rather than a reduction in segregated B atoms.

C. Ge and B Quantification by SIMS

Since SIMS was used in this work to quantify the concentrations of B and Ge atoms in the $Si_{1-x}Ge_x$ films, it is appropriate to highlight here some of the limitations of this characterization technique. SIMS is based on the linear relation between the concentration of the element of interest and its secondary ion yield in a given matrix. It was shown that correctly chosen analytical conditions and quantification techniques allowed SIMS analysis to generate highly accurate and precise data for B implants into $Si_{1-x}Ge_x$ structures for bipolar applications [10]. SiGe bipolar structures are typically characterized by relatively small contents of Ge, up to 10-15 atomic percent. On the other hand, CVD layers for MEMS applications require very high Ge contents, typically 60-70%. The ability to perform highly accurate quantification of doping elements in high Ge content $Si_{1-x}Ge_x$ films is a major challenge for SIMS. In the current study, quantification of Si and Ge was done with a $Si_{0.4}Ge_{0.6}$ epitaxially grown standard and the so-called "missing Si" approach. SIMS measurements were performed on Cameca 4FE7 secondary ion mass-spectrometer, with 4 keV Cs+ primary ion beam and negative detection mode ($28Si^-$, $70Ge^-$, $11B28Si^-$, $11B70Ge^-$). The measurement uncertainty achieved in the current study was 2.5% atomic concentration and was assessed by performing SIMS measurements on identical samples.

CONCLUSION

In-situ B doping is beneficial for improving the deposition and etch rate, as well as the surface smoothness, of LPCVD p+ Ge sacrificial films. Heavy B doping does not increase the etch rate of poly-$Si_{1-x}Ge_x$ structural films in heated H_2O_2 solution, as long as the Ge content is below 65%, so that high etch selectivity can be maintained for a Ge sacrificial material. Increasing the B concentration is beneficial for decreasing electrical resistivity, but results in more compressive stress at very high concentrations, as well as slightly higher strain gradient.

ACKNOWLEDGEMENTS

The authors would like to thank Sunil Bhave for designing the mask used to fabricate the mechanical test structures for this study, Carrie W. Low for providing Figure 1 as well as useful discussion on SIMS analysis, finally the DARPA BioFlips Program and the Transducer Research Foundation for the Student Travel Award Fund. Funding for this project is through the DARPA NMASP program, Dr. D. J. Radack, Program Manager.

REFERENCES

1. A. E. Franke, Y. Jiao, M. T. Wu, T.-J. King, R. T. Howe, "Post CMOS modular Integration of poly SiGe microstructures using Poly-Ge sacrificial layers," *Technical Digest of the 2000 Solid State Sensor and Actuator Workshop*, pp. 18-21 (2000).
2. C. Rusu, S. Sedky, B. Parmentier, A. Verbist, O. Richard, A. Witvrouw, F. Larmer, S. Kronmuller, V. Leca, and B. Otter, "New low-stress PECVD poly-SiGe layers for MEMS," *Journal of Microelectromechanical Systems*, **12**, 6 (2003).
3. B. Li, B. Xiong, L. Jiang, Y. Zohar, M. Wong, "Germanium as a versatile material for low-temperature micromachining," *Journal of Microelectromechanical Systems*, **8**, 4 (1999).
4. B. L. Bircumshaw , M. L. Wasilik, E. B. Kim, Y. R. Su, H. Takeuchi, C.W. Low, C. Liu, A. P. Pisano, T.-J. King, R. T. Howe, "Hydrogen peroxide etching and stability of P-type poly-SiGe films," *Proceedings of the 17th International Conference on Micro-electromechanical Systems,* pp. 514-520 (2004).
5. T.-J. King, J. P. McVittie, K. C. Saraswat, J. R. Pfiester, "Electrical properties of heavily doped polycrystalline silicon-germanium films," *IEEE Transactions on Electron Devices* **41**, 228 (1994).
6. T.-J. King and K. C. Saraswat, "Deposition and properties of low-pressure chemical-vapor deposited polycrystalline silicon-germanium films," *Journal of the Electrochemical Society* **141,** 2235 (1994).
7. B. C.-Y. Lin, T.-J. King, R. T. Howe, "Optimization of poly-SiGe deposition processes for modular MEMS integration," *Proceedings of the MRS 2003 Fall Meeting, Symposium A: Micro- and Nanosystems* (Boston, MA), (2003).
8. S. Sedky, R. T. Howe, T.-J. King, **"**Pulsed laser annealing, a low thermal budget technique for eliminating stress gradient in poly-SiGe MEMS structures," to appear in *Journal of Microelectromechanical Systems* (2004).
9. S. A. Bhave, B. Bircumshaw, W. Z. Low, Y.-S. Kim, A. P. Pisano, T.-J. King, R. T. Howe, "Poly-SiGe: A high-Q structural material for integrated RF MEMS," *Technical Digest of the 2002 Solid-State Sensor and Actuator Workshop,* pp. 34-37 (2002).
10. D. Kouzminov and J. Hunter, "Characterization of SiGe-based HBT structures by SIMS," *14th Annual Conference on SIMS*, Phoenix, AZ (2001).

A High-Q Widely-Tunable Gigahertz Electromagnetic Cavity Resonator

SM Hou[1], JH Lang[1], AH Slocum[2], AC Weber[2], JH White[2]
EECS[1] & ME[2] Departments, MIT, Cambridge, MA, 02139, USA

Abstract

This paper describes the design, fabrication and testing of a quasistatic electromagnetic cavity resonator fabricated using KOH etching, shallow RIE, metalization and wafer bonding. The resonator is distinguished by its simultaneous high Q near 200, and wide high-frequency tuning range, 2.5 GHz to 4.0 GHz for the experimental resonator presented here. When combined with an integrated actuator, it should be suitable for use in electronically-tunable RF band-pass filters and oscillators. The experimental resonator, however, is tuned with an external piezoelectric actuator for simplicity.

1. Introduction

RF systems such as cell phones and local wireless communication networks often need high-frequency widely-tunable high-Q band-pass filters for channel selection filters and local oscillators. This paper describes the design, fabrication and testing of a quasistatic electromagnetic cavity resonator designed for such applications. It is fabricated using standard MEMS technologies, and is distinguished by its simultaneous high Q near 200 or higher, and its wide high-frequency tuning range, 2.5 GHz to 4.0 GHz for the experimental resonator presented here. While the experimental resonator is tuned with an external piezoelectric actuator, it could be tuned with integrated internal actuation.

Figure 1 shows a cross section of the resonator. It consists of a square central capacitor surrounded by a square toroidal inductor etched jointly as a single cavity into a bonded pair of silicon wafers. The cavity is lined with gold to enable high-Q operation. Both electric and magnetic coupling to the resonator are possible. The figure shows magnetic coupling using a wire loop inserted through the wall of the cavity. Alternatively, electric coupling could be made through direct connections to the capacitor electrodes. Because the cavity is smaller than an electromagnetic wavelength, it is quasistatic with identifiable capacitor and inductor regions. This simplifies tuning, which is performed by compressing the cavity to close the capacitor gap.

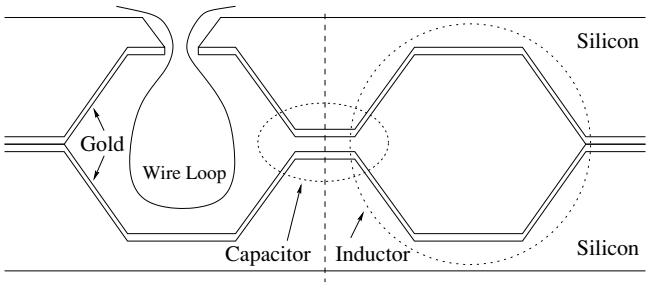

Figure 1: cross section view of a cavity resonator with magnetic coupling.

Travel support has been generously provided by the Transducers Research Foundation, and by the DARPA MEMS and DARPA BioFlips programs.

Alternative technologies provide wide tuning or high Q, but not both. For example, crystal resonators exhibit exceptionally high Q, but they are generally not tunable. Mechanical MEMS resonators can also exhibit very high Q, but they are not widely tunable, and do not generally operate in the gigahertz range [1,2,3,4,5]. Finally, resonators that employ tunable MEMS capacitors can be widely tunable [6], but the associated inductor, often formed through surface micromachining or with a bonding wire, is usually so lossy that a high-Q resonator can not be obtained [7,8,9]. In contrast, the cavity inductor shown in Figure 1 exhibits a higher Q.

2. Fabrication

Figure 2 shows the resonator fabrication process flow. A silicon wafer is first masked using silicon-nitride (Si_3N_4), and then etched using potassium-hydroxide (KOH) to form the inductor cavity (Figure 2A). Corner compensation [10] is used to preserve the shape of an interior square island that will support the capacitor electrode. A single-sided etch is used to form a half cavity, while a double-sided etch is used to form an additional slit through which a magnetic coupling loop may be inserted. Next, reactive-ion etching is used to remove the Si_3N_4 mask over the capacitor island, and additional KOH etching is used to open the capacitor gap (Figure 2B). The KOH etch is timed to produce a 20-μm gap, and is performed on only one of the two wafers in Figure 1. The remaining Si_3N_4 mask is then removed using hot phosphoric acid, and the wafer receives approximately 2 μm of sputtered gold. This gold thickness is slightly more than the 1.8-μm skin depth of gold at 2 GHz. Finally, the wafer is diced, and gold-gold thermocompression bonding of two die is used to form a closed cavity resonator (Figure 2C). Figure 3 shows a photograph of one half-cavity die before bonding; the die does not contain slits for the magnetic coupling loop.

KOH etching is important to cavity fabrication because it results in very smooth and open side walls, and open cavity corners. It is otherwise not possible to coat the cavity with a continuous low-resistivity film of gold. In contrast, deep-reactive-ion etching of silicon, and hydrofluoric-acid etching of glass, were not successful. The resulting cavity side walls were to steep and rough, and the resulting cavity corners were too sharp, to permit good metalization.

3. Modeling & Design

At 3 GHz, the wavelength of light is 10 cm. Since a 3-GHz resonator of the type shown in Figure 1 is much smaller than 10 cm, it is a quasistatic device [11]. Therefore, it has identifiable capacitive regions in which electric-field energy storage dominates, and inductive regions in which magnetic-field energy storage dominates. This argument holds for higher frequency resonators too because size will scale down as frequency scales up. In the resonator shown in Figure 1, the

0-9640024-5-0/hh2004/$20©2004TRF
DOI 10.31438/trf.hh2004.66

Solid-State Sensors, Actuators, and Microsystems Workshop
Hilton Head Island, South Carolina, June 6-10, 2004

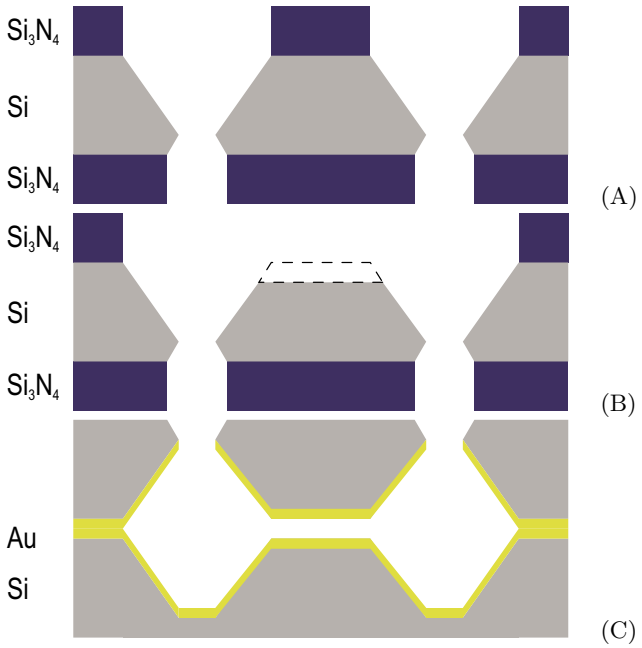

Figure 2: cavity resonator fabrication process flow.

Figure 3: photograph of one half-cavity die.

central region functions as a parallel-plate capacitor while the surrounding toroidal cavity functions as a single-turn inductor. Together, the central capacitor and the toroidal inductor form a parallel resonant tank.

As fabricated in Figures 2 and 3, the capacitor has nearly square electrodes. Denote their side length by X, and the distance across their gap by G. Then, the capacitance of the tank, $C_{\rm T}$, is approximated by

$$C_{\rm T} \approx \frac{\epsilon_\circ X^2}{G} \tag{1}$$

where $\epsilon_\circ$ is the free-space permittivity. Fringing is ignored in (1) since $X \gg G$.

Also as fabricated in Figures 2 and 3, the inductor has a square outer perimeter. Denote its outer side length by W and the depth of its cavity by D. In this case, the mean path length of the solenoidal magnetic field through the toroid is approximately $(4X + \pi(W - X)/2)$, and the cross sectional area through which the magnetic field passes is approximately $D(W - X + D\cot(54.7^\circ))/2$. The inductance of the tank, $L_{\rm T}$, is thus approximately

$$L_{\rm T} \approx \frac{\mu_\circ D(W - X + D\cot(54.7^\circ))}{8X + \pi(W - X)} \tag{2}$$

where $\mu_\circ$ is the free-space permeability. Better approximations for $L_{\rm T}$ can be obtained from [12].

Since $D \ll (W - X)$ for the resonators considered here, the series resistance of the inductor is dominated by the resistance of the metal covering the floor and ceiling of the inductor cavity. In this case, the path length of the solenoidal current around the inductor toroid is approximately (X-W), and the mean cross sectional area through which the current passes is approximately $\delta(X + W)/2$. The series resistance of the tank inductor, $R_{\rm LT}$, is thus approximately

$$R_{\rm LT} \approx \frac{W - X}{2\sigma\delta(W + X)} \tag{3}$$

where σ is the metal conductivity, and δ is the smaller of the metal thickness and its skin depth. Note that when δ is a skin depth, then $R_{\rm LT}$ is a function of frequency. Again, better approximations for $R_{\rm LT}$ can be obtained from [12].

To approximate the series resistance of the tank capacitor, model the capacitor electrodes as disks of radius R and thickness δ. Further, assume that the electrodes are uniformly charged, which is the case for a high-Q capacitor. In this case, the radial current density J in the electrode at the radius r from the center is $ri/2\pi\delta R^2$, where i is the total current leaving the capacitor. By integrating the power dissipation density J^2/σ over the volume of both capacitor electrodes, and equating the result to $R_{\rm CT}i^2$, the series resistance of the tank capacitor, $R_{\rm CT}$, is approximated by

$$R_{\rm CT} \approx \frac{1}{4\pi\sigma\delta} \quad . \tag{4}$$

Note that when δ is a skin depth, then $R_{\rm CT}$ is also a function of frequency. Once again, better approximations for $R_{\rm CT}$ can be obtained from [12].

By combining (1) and (2), the resonant frequency of the tank, $\omega_{\rm T}$, is determined according to

$$\omega_{\rm T} = \frac{1}{\sqrt{L_{\rm T}C_{\rm T}}} \approx \sqrt{\frac{G(8X + \pi(W - X))}{\epsilon_\circ\mu_\circ DX^2(W - X + D\cot(54.7^\circ))}} \quad , \tag{5}$$

which is tuned by compressing the resonator to decrease G. Using (1) through (5) the quality factors of the capacitor, $Q_{\rm CT}$, the inductor, $Q_{\rm LT}$, and the tank, $Q_{\rm T}$, are determined from

$$Q_{\rm LT} = \frac{\omega_{\rm T}L_{\rm T}}{R_{\rm LT}} \quad \& \quad Q_{\rm CT} = \frac{1}{\omega_{\rm T}R_{\rm CT}C_{\rm T}} \tag{6}$$

$$Q_{\rm T}^{-1} = Q_{\rm CT}^{-1} + Q_{\rm LT}^{-1} \quad . \tag{7}$$

For the experimental resonator described below, $W = 18$ mm, $X = 4$ mm, $D = 1$ mm, and $G = 23.2$ μm, as fabricated for an uncompressed resonator. From (1), (2) and (5) it is therefore expected that $C_{\rm T} = 6.11$ pF, $L_{\rm T} = 243$ pH, and $\omega_{\rm T}/2\pi = 4.13$ GHz. At this frequency, the skin depth of gold is $\delta = 1.22$ μm. From (3), (4), (6) and (7) it is therefore expected that $R_{\rm LT} = 6.35$ mΩ, $R_{\rm CT} = 1.59$ mΩ, $Q_{\rm CT} = 3970$, $Q_{\rm LT} = 920$, and $Q_{\rm T} = 795$. In general, the inductor is always more lossy than the capacitor.

The wire loop and toroidal inductor form a transformer, and so the magnetically-coupled resonator is modeled as shown in Figure 4. There, α is the ratio of the loop cross sectional area to the inductor cross sectional area, $L_{\mathrm{L1}} + L_{\mathrm{L2}}$ is the leakage inductance of the loop, C_{P} models the distributed parasitic capacitance of the loop, and R_{P} models eddy currents induced by the loop in the inductor walls. From terminal impedance measurements alone, it is not possible to uniquely determine α, L_{T}, C_{T}, L_{P2}, and $R_{\mathrm{T}} \equiv R_{\mathrm{LT}} + R_{\mathrm{CT}}$. Therefore, C_{T} will be taken to be 6.11 pF, as given by (1) for the as-fabricated dimensions.

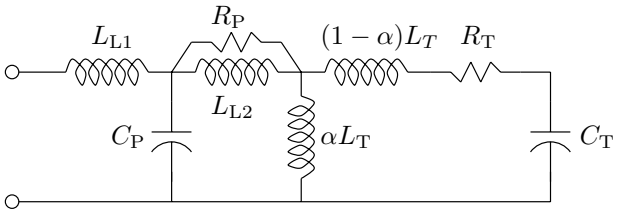

Figure 4: electrical model of the experimental resonator.

4. Experimental Results

Resonator impedance is measured as a function of frequency with an Agilent PNA/E8362B network analyzer as shown in Figure 5. The resonator is mounted on a block, and a manipulator inserts the magnetic-coupling wire loop into the cavity as in Figure 1. The wire loop is kept away from the cavity walls to minimize the induction of parasitic eddy currents and losses in the walls. The wire loop connects to the analyzer through an SMA connector. Finally, impedance is measured as a calibrated piezoelectric actuator pushes on the resonator through a hole in the block to compress the cavity, thereby closing the capacitor gap and tuning the resonator.

Figures 6 and 7 show two impedance measurements, one with no cavity compression and one with a 13.9-μm compression of the capacitor gap. The figures show the tunable resonance of the tank, which shifts from 3.97 GHz to 2.54 GHz, as well as other dynamics caused by the wire loop. From the measured impedance of the uncompressed resonator, and the assumption that $C_{\mathrm{T}} = 6.11$ pF, the model parameters in Figure 4 are determined to be $L_{\mathrm{T}} = 266$ pH, $\alpha = 0.431$, $L_{\mathrm{L1}} = 769$ pH, $L_{\mathrm{L2}} = 6.82$ nH, $C_{\mathrm{P}} = 747$ fF, $R_{\mathrm{T}} = 22.4$ mΩ and $R_{\mathrm{P}} = 11$ kΩ. These parameters are very close to those predicted in Section 3. Further, the match between the modeled and measured impedance is extremely good up to and beyond 5 GHz, with less than a 1% error in magnitude and phase. Thus, the modeled and measured impedance would be indistinguishable in Figures 6 and 7, hence the modeled impedance is omitted. At frequencies above 6 GHz, the modeled and measured impedance diverges, most likely due to distributed wire loop dynamics that is not captured by the lumped-parameter model of Figure 4. Note that to compute the modeled resistances, the frequency-dependent skin depth of gold was used in (3) and (4).

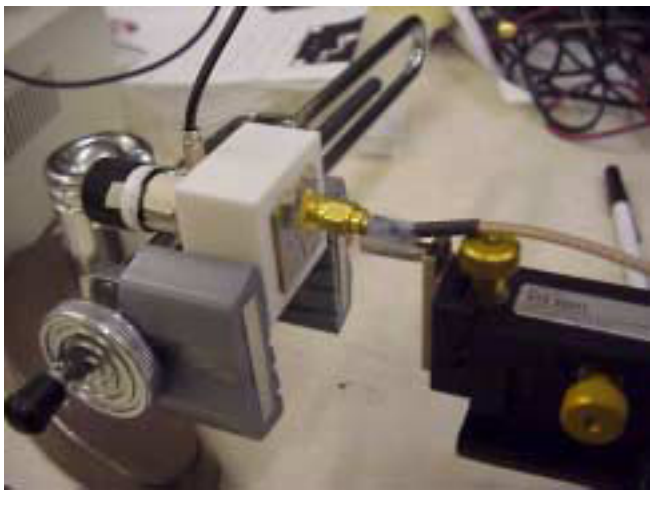

Figure 5: experiment to measure resonator impedance.

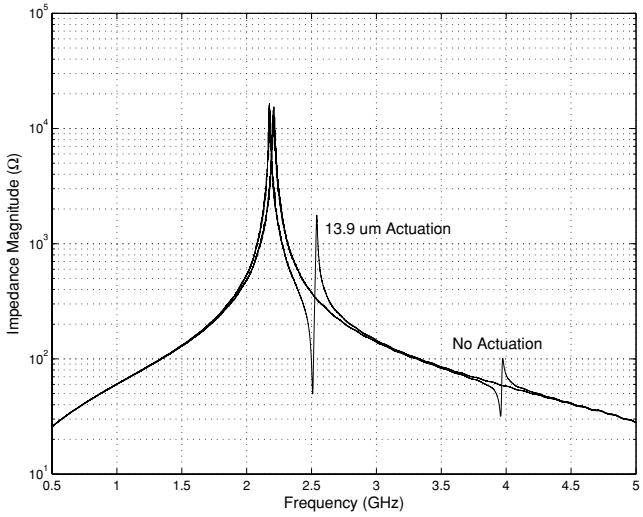

Figure 6: resonator impedance magnitude as a function of frequency for 0-μm and 13.9-μm capacitor gap compression.

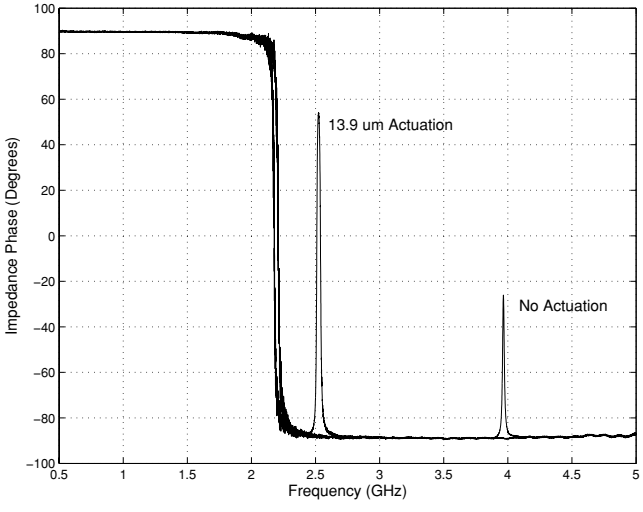

Figure 7: resonator impedance phase as a function of frequency for 0-μm and 13.9-μm capacitor gap compression.

With a capacitor gap compression of 13.9 μm, (1) predicts a tuned C_{T} of 15.2 pF. With only this change to its parameters, the model of Figure 4 predicts the tuned impedance shown in Figure 6 with the same level of accuracy as it does the untuned impedance. Similar tests were repeated for all capacitor gap compressions from 1 μm to 13 μm in 1 μm steps with identical results. Thus, it can be concluded that the resonator behaves as predicted in Section 3.

Figure 8 shows the measured tank resonant frequencies that result from each 1-μm step in capacitor gap compression, together with a theoretical prediction based upon (1), (5) and the fitted value of L_{T}, 266 pH. The good match under-scores the validity of the analysis of Section 3. Figure 9 shows the corresponding measured Q of the resonator, and the estimated Q of the tank alone based on (7) and the fitted parameters of the model in Figure 4. Note that the Q of the tank is generally higher than that of the complete resonator owing to the losses induced by the wire loop. It is not, however, as high as predicted in Section 3 and Figure 4.

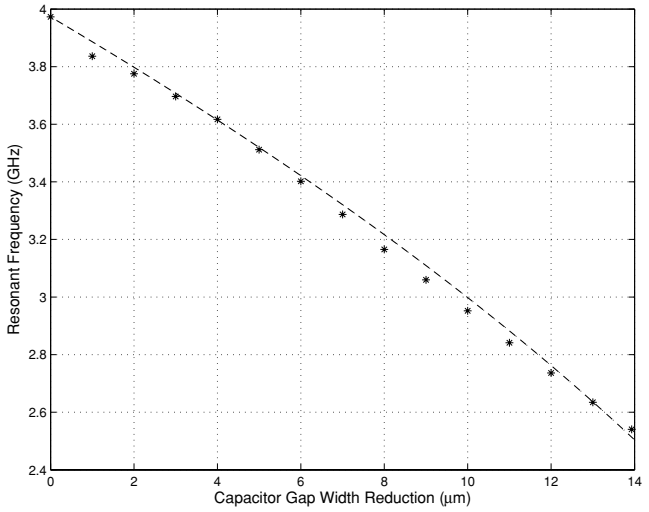

Figure 8: measured ($*$) and predicted ($-$) tank resonant frequency ω_{T} as a function of the decrease in capacitor gap.

5. Conclusions

The primary conclusion of this paper is that a cavity resonator can exhibit both high-Q, approaching 300, and a wide high-frequency tuning range. Further, it can be relatively simple to fabricate. In order to become acceptable to most applications, however, two modifications to the resonator as presented here must be made. First, direct electrical coupling to the capacitor should replace the magnetic coupling through a wire loop. The leakage inductance, and parasitic capacitance and resistance, of the wire loop appear to be generally too high. Second, the cavity structure must be made less rigid than that shown in Figures 1 and 3 so as to permit tuning with lesser mechanical effort.

Acknowledgments

The work reported here was supported by a grant from the MIT Deshpande Center. The authors also wish to thank the staff of the MIT Microsystems Technology Laboratories for their help with resonator fabrication, Christine Tsau of MIT for her help with gold-gold bonding, and David Wentzloff of MIT for his help in conducting the impedance measurements.

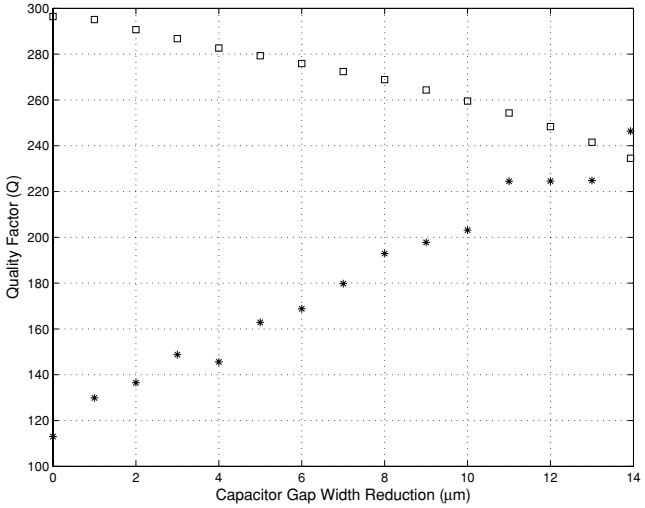

Figure 9: measured resonator ($*$) and estimated tank ($\square$) quality factors at the resonance of ω_{T} as functions of the decrease in capacitor gap.

References

[1] Lin et al, "Microelectromechanical filters for signal processing", *JMEMS*, *7*, #3, 286–294, September 1998.

[2] Wang et al, "High-order medium frequency micromechanical electronic filters", *JMEMS*, *8*, #4, 534–557, December 1999.

[3] Wang et al, "VHF free-free beam high-Q micromechanical resonators", *JMEMS*, *9*, #3, 347–360, September 2000.

[4] Piazza et al, "Voltage tunable piezoelectrically-transduced single-crystal silicon resonators on SOI substrate", *MEMS 03*, 149–152, January 2003.

[5] Wang et al, "Self aligned 1.14 GHz vibrating radial mode disk resonators", *Transducers 03*, 947-950, June 2003.

[6] Borwick et al, "A high Q, large tuning range, tunable capacitor for RF applications", *MEMS 02*, 669–672, January 2002.

[7] Dahlmann et al, "High Q achieved in microwave inductors fabricated by parallel self-assembly", *Transducers 01*, 3C2.02, June 2001.

[8] Grenier et al, "Integrated RF MEMS for single chip radio", *Transducers 01*, 4C1.01, June 2001.

[9] Yoon et al, "3D lithography and metal surface micromachining for RF and microwave MEMS", *MEMS 02*, 673–676, January 2002.

[10] Long et al, "Design of compensation structures for anisotropic etching", *International Conference on Modeling and Simulation of Microsystems*, 124–127, San Juan, PR, 1999.

[11] Haus and Melcher, *Electromagnetic Fields and Energy*, Prentice Hall, 1989.

[12] Hammond, *Energy Methods in Electromagnetism*, Oxford University Press, 1981.

FABRICATION AND MEASUREMENT OF AN IC-COMPATIBLE GHZ-RANGE PIEZOELECTRIC LONGITUDINAL BAR RESONATOR

D. J. D. Carter, J. Kang, D. White, and A. E. Duwel
The Charles Stark Draper Laboratory
Cambridge, MA 02139

ABSTRACT

We report on the fabrication and measurement of a piezoelectrically-actuated, longitudinal-mode acoustic MEMS resonator designed to operate in air with high Q and low impedance in the ~50 MHz – 2 GHz frequency range. Since the longitudinal-mode frequency is set lithographically by the lateral bar dimensions, a wide range of resonator frequencies can be created on a single chip. Device processing is IC compatible, offering the potential for integration in transceiver applications.

This first set of fabricated devices had resonator lengths ranging from 3 to 30 microns, corresponding to frequencies from 100 MHz to 1.3 GHz, on a single wafer. We discuss the fabrication process for these aluminum nitride (AlN) devices and present measurements on resonators with frequencies ranging from ~100-700 MHz.

INTRODUCTION

Radio-frequency transceivers used today rely on off-chip components for highly frequency selective resonant elements. The ability to integrate extremely small, high quality factor (Q) resonators will significantly impact size and performance in existing transceivers [**1**]. In addition, new system architectures will take advantage of ultra-dense arrays of resonators to make chip-scale filter banks and frequency synthesizers, enabling a new generation of small, universal transceivers.

Towards these goals, relevant performance metrics of the resonators include small size, high Q, frequency scalability over 0.3-3 GHz, RF integrated circuit process compatibility, RF impedance compatibility, linearity, and power handling. On all fronts, the thin-film resonator (TFR) technology, which uses piezoelectric actuation, is particularly advanced. Resonators at 0.8-3 GHz with Q's ranging from 450-2000 and impedance levels in the range of 50 Ohms are reported [**2,3,4**]. Quartz resonators have been demonstrated with Q's above 13,000 at 590 MHz [**5**]. Several capacitively actuated resonator designs that are easily scalable have also demonstrated impressive Q's. In [**6**], a disk-mode resonator at 1.14 GHz produced Q=1500 in air. Capacitively actuated designs are challenged however by high impedance levels (in the range of 10kΩ) and process compatibility.

The Draper piezoelectric longitudinal bar (L-Bar) resonator design strategically addresses key requirements for RF applications. In the following sections, we review the resonator design and several of its merits. The fabrication process is next described in detail. Finally, we present results from initial device measurements.

RESONATOR DESIGN

The L-Bar resonator physically resembles a suspended capacitor. Figure 1 shows a solid model of the center bar suspended above a silicon substrate via tethers. The bar is metalized on top and bottom. These electrodes apply a field through the thickness of the AlN. At most frequencies, the device response is that of a capacitor. At the mechanical resonance, however, the electrical impedance drops by orders of magnitude, depending on the device Q.

The choice of a piezoelectrically actuated, in-plane longitudinal mode MEMS device is unique and the design addresses important application metrics. The frequencies of in-plane longitudinal modes are lithographically scalable over ~50 MHz – 2 GHz, allowing arrays on a single chip. These modes are also robust to package (thermal) stress. The piezoelectric actuation allows for impedance matching. The suspended bar structure and materials choices enable extremely high Q designs. In addition, the use of aluminum nitride (AlN) as a structural and transduction material has multiple advantages. AlN can be deposited at temperatures well below 400°C for process compatibility, it has a low dielectric loss tangent, the dielectric breakdown is ~ 10^6 V/cm (allowing for high power handling), and the response is extremely linear. Finally, the electrode geometry enables a self-aligned, manufacturable process and minimizes spurious modes so that additional mode selection filters are not necessary.

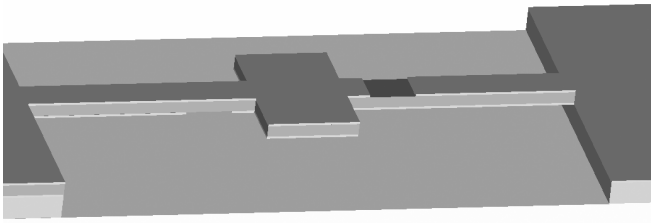

Figure 1. *Schematic of the L-bar device. The suspended resonator is made of piezoelectric aluminum nitride sandwiched between metal layers. The resonant structure is suspended over a gap by tethers. Nominal dimensions for an 800MHz resonator are 5 um long x 3 um wide with a 1.5 um wide tether.*

PROCESS OVERVIEW

Figure 2 shows an overview of the process flow for the resonator. The starting point is the following materials stack on a silicon wafer: a release layer (0.5 – 1 μm thick) of thermally-grown SiO_2, a thin (~200 Å), "seed" layer of AlN, 1500Å of Mo, and 5000Å of polycrystalline, c-axis-oriented, piezoelectric AlN. Approximately 2000Å of Ni is then patterned by evaporation and liftoff.

The patterned nickel serves as an etch mask for wet etching of AlN, which serves as an etch mask for RIE of the Mo bottom metal and a further wet etch of the seed AlN. At this point the mechanical form of the resonator, support tethers, and probe pads has been defined into the stack. Figure 3 shows a scanning-electron micrograph of an etched stack test structure.

0-9640024-5-0/hh2004/$20©2004TRF
DOI 10.31438/trf.hh2004.67

Solid-State Sensors, Actuators, and Microsystems Workshop
Hilton Head Island, South Carolina, June 6-10, 2004

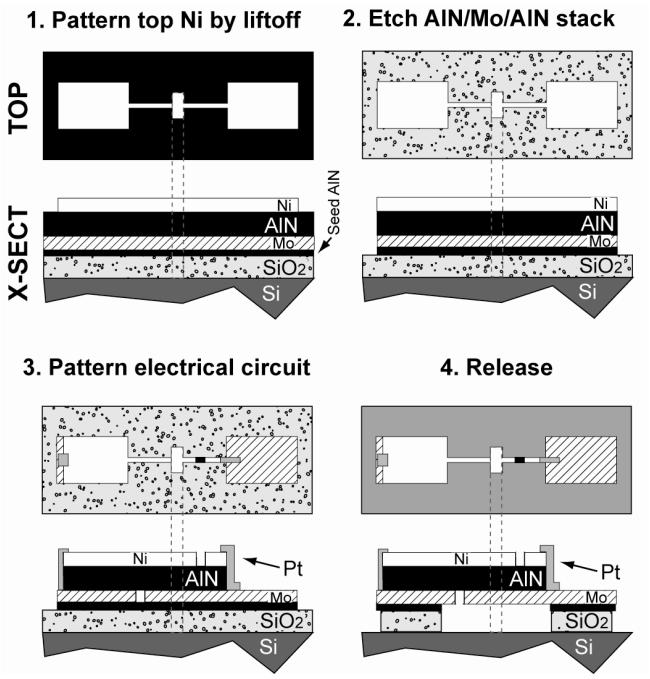

Figure 2. *Schematic of L-bar process flow. Mechanical form of resonator, including critical alignments, is defined in first mask level. Each layer in the device film stack serves as a self-aligned etch mask for subsequent layers. Several etch steps pattern the electrical circuit. The release etch is self aligned.*

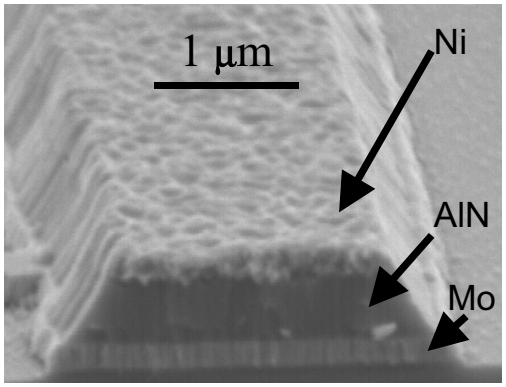

Figure 3. *Scanning-electron micrograph of etched stack structure. Nickel, patterned by liftoff, serves as an etch mask for the underlying AlN, which is wet etched in AZ400k photoresist developer. The Ni and AlN serve as etch masks for RIE of the molybdenum bottom metal in CF4 plasma.*

The next sequence of steps forms the proper electrical circuit. To minimize parasitic capacitances (*i.e.* top/bottom metal overlap other than on the resonator), breaks are etched into the tether Mo and Ni on opposite sides of the resonator. Then the Ni and AlN are removed by wet etching on the probe pad opposite the bottom metal break to allow electrical access to the Mo for testing. To complete the electrical circuit, isolated top and bottom metal islands on the tethers are shorted to appropriate pads by liftoff of a platinum "patch."

The device is released by etching the underlying SiO_2 in BHF. Figure 4 shows scanning-electron micrographs of two released resonator devices.

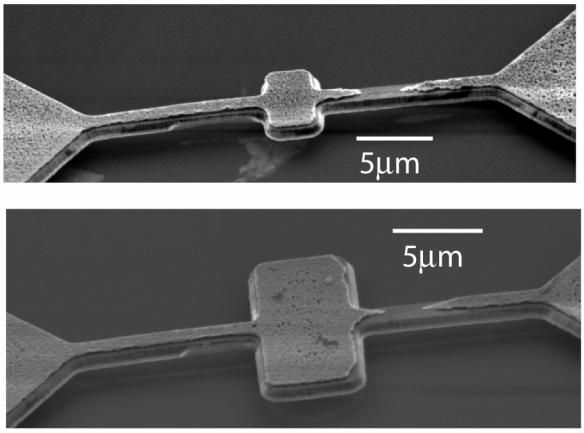

Figure 4. *Scanning-electron micrographs of released resonator structures. TOP: 5 μm long x 3 μm wide resonator. BOTTOM: 10 μm long x 6 μm wide resonator.* ***Tethers are approximately 1 μm wide for both devices.***

FABRICATION DETAILS

CRITICAL ALIGNMENTS: The small device size requires precise alignments in the structure. For example, the resonator should be centered on the tethers to minimize sensing of non-longitudinal modes, and the resonator and tethers should be centered on the support structure to allow minimization of acoustic wave propagation into the supports through tether-length "tuning." This process incorporates all of these alignments into the first mask level, which patterns the nickel. Since the nickel serves as an etch mask for the entire stack, the device definition is self-aligned. Additionally, the patterned device structure serves as a self-aligned etch mask for its own release.

MATERIAL/PROCESS CHOICES: Tradeoffs among device electrical characteristics, IC-compatible processing, and piezoelectric film growth requirements dictated materials selection.

Our AlN films were deposited by a commercial vendor [**7**]. Their best-quality process, which typically yielded an x-ray rocking curve FWHM of ~1.5 degrees, dictated the bottom of the piezoelectric stack (seed AlN/Mo/AlN). Nickel was chosen as the top metal for its suitability as an etch mask for both wet etching and Cl-based dry etching [**8**] of AlN, as well as for a ratio of density to electrical conductivity comparable to that of molybdenum.

The choice of molybdenum, aluminum nitride, and nickel required a unique set of selective etch chemistries, shown in Table 1.

rate/ notes	**20:1:1 DI:HF:H_2O_2**	**AZ400k developer**	**CF_4/O_2 RIE [9]**	**XeF_2**	**BHF**
Ni	~1000Å/min	x	x	x	x
AlN	x	self-limiting (see text)	x	x	x
Mo	x	x	anisotropic ~133Å/min	isotropic, undercut	x
SiO_2	not exposed	x	not exposed	x	re-lease

Table1. *Etch chemistries used to fabricate resonator.*

The Mo/AlN stack is deposited by sputtering/reactive sputtering at 400°C or below. No high-temperature steps are used in the subsequent processing of the device, making this process IC-compatible.

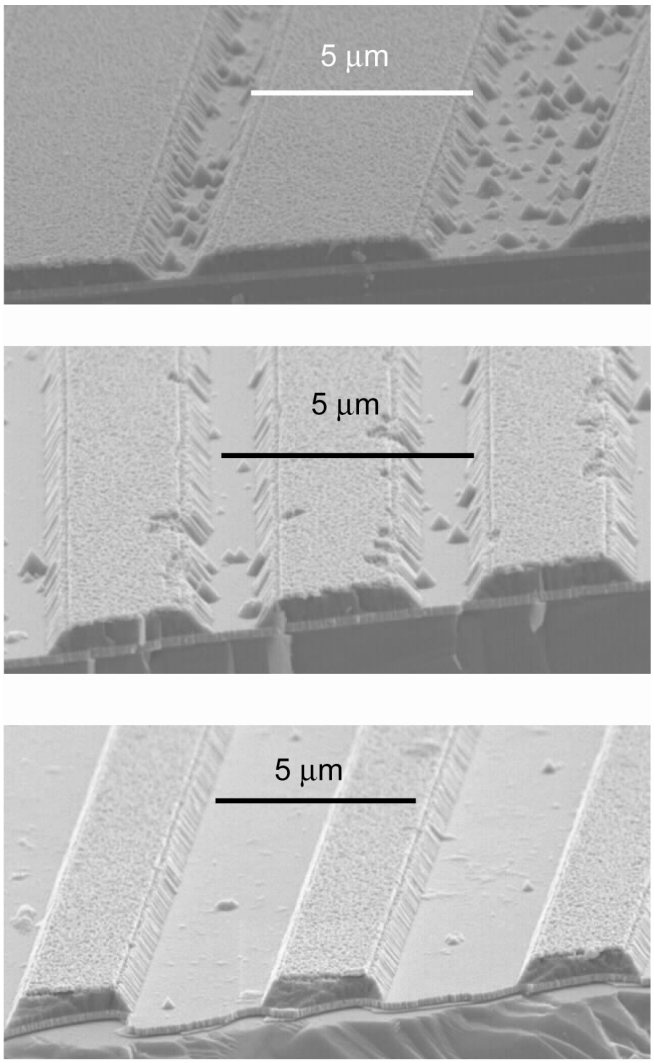

Figure 5. *Scanning-electron micrograph of progress of AlN wet etch in AZ400k photoresist developer. The top Ni etch mask protects the underlying AlN film, which is on a Mo bottom layer. The surface of the exposed AlN quickly roughens into conical-shaped structures that slowly etch to the underlying Mo. TOP: 1:30 etch. MIDDLE: 2:30 etch. BOTTOM: 10:00 etch. The AlN etch is self-limited at the sidewall angle shown (~50x overetching showed no change in the structure).*

WET ETCHING OF AlN: For our AlN films, wet etching in AZ400k photoresist developer was self-limiting at a fixed sidewall angle of approximately 55°. Figure 5 shows scanning-electron micrographs of a time sequence of the AlN etch. In unprotected regions, the etch produces conical structures. As the etch progresses, these cones shrink in size, eventually disappearing. Note that in the protected areas the film is dense, *i.e.* no etchant infiltrates from the sides.

The self-limiting nature of this etch is quite high; ~50x overetching showed no change in the structure. Previous literature on etching of AlN in AZ400k does not mention film roughening, conical structures, or self-limited etching [**10, 11**]. This effect is beneficial to our process, but not well understood at this time.

UNDERCUT ETCHING OF Mo: Minimizing stray capacitance required a break to be patterned in the top and bottom tether metal. For the top metal, this was a rather straightforward wet etch with a photoresist mask, but for the Mo bottom metal, an undercut etch was required.

To execute this etch, a resist window was opened in the area around the bottom metal break, and a XeF_2 etch [**12, 13**] was used to etch the Mo. XeF_2 gave high selectivity to all other materials in the structure, and was a highly isotropic etch.

DEVICE MEASUREMENTS

Resonator testing was conducted at the wafer level, in air, at room temperature, using GGB Industries probe tips on a Cascade Microtech probe station and an Agilent 8753 Network Analyzer. The device is wired in a series configuration for two-port measurements.

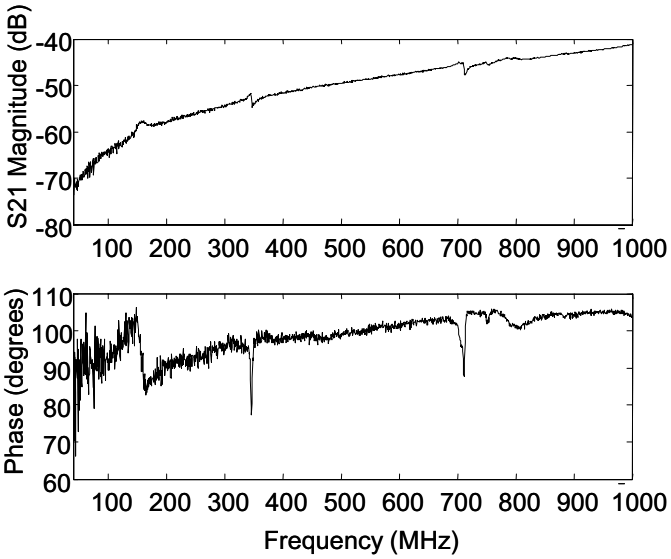

Figure 6. *S21 measurement of a 10-μm x 5-μm L-bar resonator. Two longitudinal-mode resonances are evident, corresponding to the length and width modes of the device.*

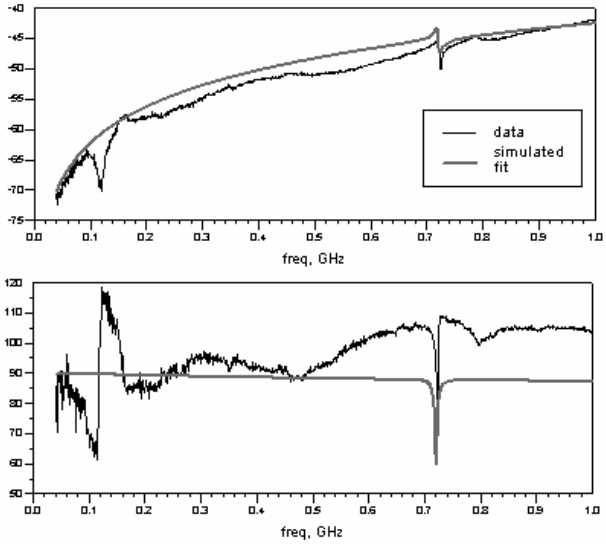

Figure 7. *S21 data from a different 10-μm x 5-μm device, along with fit to a BVD model. This model gives a Q of 125. Q values as high as 550 at 700 MHz have been measured on these devices.*

Figure 6 shows an S21 measurement of a 10 µm long x 5 µm wide resonator over a wide frequency sweep. Two longitudinal-mode resonances are evident, corresponding to the length and width modes, at approximately 350 and 700 MHz, respectively. The spurious feature at 120 MHz, which is currently not well understood, is present in all devices as well as non-resonant calibration structures.

Figure 7 shows a fit to a 5 µm width mode from a different resonator. The fit uses a Butterworth van Dyke (BVD) model [**14**] for the mechanical resonance. Parasitics were modeled as port capacitance and resistance. The BVD circuit parameters were R= 35 kΩ, L= 1 mH, C=0.047 fF, and Co=2.7 fF. This corresponds to a Q of 135. Q values as high as 550 at 700 MHz have been measured on fabricated devices.

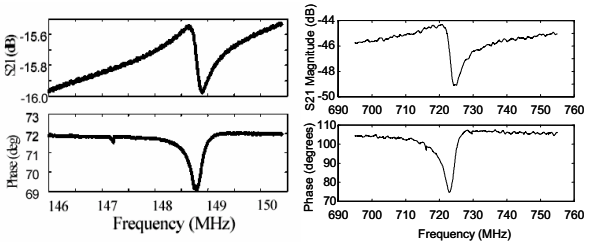

Figure 8. *Closeups of S21 data from two other devices. LEFT: 25 µm length mode. RIGHT: 5 µm width mode.*

Figure 8 shows detailed S21 data of resonances from two other devices. Figure 9 shows a plot of frequency vs. inverse length. The slope of 3.7 GHz–µm is consistent with calculations based on the AlN and metal layer mechanical properties for a simple longitudinal mode.

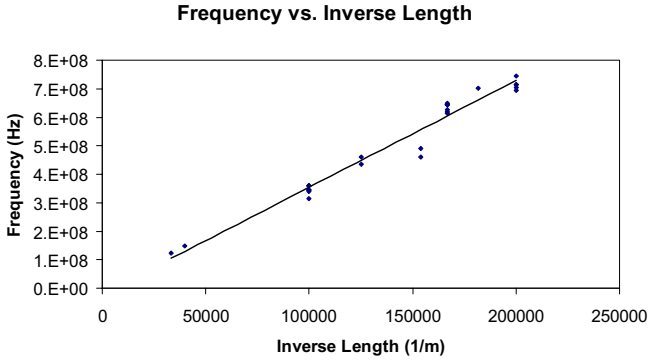

Figure 9. *Frequency vs. inverse length for a number of resonators.*

CONCLUSIONS

A new RF MEMS resonator has been designed, fabricated, and measured. The design addresses key performance parameters including quality factor, frequency scalability, mode isolation, and impedance matching. The design allows for a self-aligned fabrication process enabling high dimensional precision even as feature sizes are pushed to sub-micron ranges. A unique undercut etch is used to isolate the electrical leads and form the basic overlap capacitor structure. Initial measurements verify that well-isolated longitudinal modes are excited in the devices. Although measured quality factor and electrical admittance are much lower than theoretical limits predict, ongoing work will address electrical parasitics and process improvements. These first experimental results verify that the RF resonator design is widely scalable in frequency, confirm that the modes are well-isolated, and demonstrate an IC-compatible fabrication process.

ACKNOWLEDGEMENTS

The authors would like to thank the many Draper Laboratory staff and technicians who contributed to this work, particularly Connie Cardoso, Mert Prince, and Mark April for their work in the fabrication of the devices, Mark Mescher and Mathew Varghese for helpful discussions about many aspects of the work, and Jim Sitomer for program management support. This material is based upon work supported by the U.S. Army Aviation and Missile Command under Contract No. DAAH01-01-C-R204. Any opinions, findings and conclusions or recommendations expressed in this material are those of the authors and do not necessarily reflect the views of the Charles Stark Draper Laboratory, Inc.

REFERENCES

1. C.T.-C. Nguyen, "Micromechanical components for miniaturized low-power communications," *Proceedings*, 1999 IEEE MTT-S International Microwave Symposium RF MEMS Workshop, Anaheim, CA, June 18, 1999, pp. 48-77.

2. K.M. Lakin, "Thin Film Resonators and Filters," 1999 IEEE International Ultrasonics Symposium, Paper M-1, October 17-21, 1999.

3. M. Hara, J. Kuypers, T. Abe, M. Esashi, "MEMS Based Thin Film 2 GHz Resonator for CMOS Integration," IEEE MTT-S Digest, p. 1797, 2003.

4. R. Ruby, P. Bradley, Y. Oshmyansky, A. Chien, "Thin Film Bulk Wave Acoustic Resonators (FBAR) for Wireless Applications," IEEE Ultrasonics Symposium, p. 813, 2003.

5. D. T. Chang, *et al.*, "A New MEMS-based Quartz Resonator Technology," Hilton Head 2004.

6. J. Wang, Z. Ren, C.T.-C. Ngyuen, "Self-aligned 1.14-GHz vibrating radial-mode disk resonators," 12th International Conference on Solid State Sensors, Actuators and Microsystems, Boston, June 8-12 2003.

7. Advanced Modular Sputtering (AMS), Goleta, CA, www.amsincorp.com.

8. A. N. Cleland, M. Pophristic, and I. Ferguson, "Single-crystal aluminum nitride nanomechanical resonators," *Appl. Phys. Lett. 79(13)*, 2070 (2001).

9. Yue Kuo and J. R. Crowe, "Slope control of molybdenum lines etched with reactive ion etching," *J. Vac. Sci. Technol. A 8(3)*, 1529 (1990).

10. J. R. Mileham *et al.*, "Wet chemical etching of AlN," *Appl. Phys. Lett. 67(8)*, 1119 (1995).

11. . J. R. Mileham *et al.*, "Patterning of AlN, InN, and GaN in KOH-based solutions," *J. Vac. Sci. Technol. A 14(3)*, 836 (1996).

12. Xactix,, Inc., Pittsburgh, PA, www.xactix.com.

13. Patrick B. Chu *et al.*, "Controlled Pulse-Etching with Xenon Difluoride," *Digest of Technical Papers, Volume 1, 1997 International Conference on Solid-State Sensors and Actuators (Transducers 97)*, Chicago, IL, pp. 665-668 (1997).

14. Lakin, K. M., "Modeling of thin film resonators and filters," *IEEE MTT-S International Microwave Symposium Digest*, Albuquerque, NM, pp. 149-152, June 1992.

FABRICATION OF A HIGH SPEED MICROSCALE TURBOCHARGER

Hanqing Li, Nicholas Savoulides, Linhvu Ho, Stuart A. Jacobson, Ravi Khanna, Chiang-Juay Teo, Li Wang, Dennis Ward, Alan H. Epstein, and Martin A. Schmidt
Massachusetts Institute of Technology
Cambridge, MA 02139

ABSTRACT

Microscale turbocharger devices have been fabricated and tested. The device, formed by fusion bonding six silicon wafers, consists of a free rotor (with a compressor and turbine) contained within a static structure. A pressure differential across the turbine generates a torque that spins the rotor, producing flow and pressure rise through the compressor. This paper addresses fabrication issues critical to high speed operation of this device, such as journal bearing profile control, nozzle and thrust bearing process control and integration, rotor integration, and rotor imbalance, providing the first discussion of fabrication innovations developed specifically for the turbocharger. Preliminary test results are also included.

INTRODUCTION

A turbocharger has been fabricated as part of a program to build a microfabricated gas turbine generator (GTG) [1,2]. As the GTG is a highly complex system, its development has included several intermediate devices of increasing complexity. The turbocharger is far along the path to the GTG, lacking only the electric generator and having its turbine and compressor flow paths independent (Figure 1). The fabrication processes for the turbocharger are directly applicable to the GTG. As such, the turbocharger is a test vehicle for developing fabrication processes and turbomachinery/bearing technology.

Unlike previous devices in this program that had either a compressor or a turbine, the turbocharger rotor is formed from two aligned wafers, one containing a compressor and one containing a turbine. The turbocharger rotor diameter (8.2 mm) is twice that of previous devices. The increased mass of the rotor and its two wafer design place stringent requirements on the fabrication process. These requirements can be separated into two groups. The first results from tight specifications of the critical components that control the rotor performance, such as journal bearings, thrust bearings, and nozzles. The second results from factors that affect the imbalance of the rotor when spinning, such as mask misalignments and wafer bonding misalignment (in plane), and blade DRIE etch non-uniformity (out of plane).

TURBOCHARGER STRUCTURE

The micro turbocharger is a six layer fusion-bonded MEMS device as schematically shown in Figure 1. The rotor is composed of a compressor in layer 3 (L3) bonded to a smaller diameter turbine in layer 4 (L4). The rotor is radially supported by a gas journal bearing located in the gap between the outer edge of the compressor and the stator ((6) in Figure 1). In some device builds, a second journal bearing is included in the gap between the outer edge of the turbine and the stator ((7) in Figure 1). The turbocharger is referred to as a dual bearing device when the turbine gap is 15 μm, small enough to act as a journal bearing, and as a single bearing device when the turbine gap is much wider, 50 μm in the current design. The journal bearings are supplied with gas from a plenum (8) located in L4, on the backside of the compressor. A thrust bearing gap (6) is etched into L5 to provide vertical clearance that during operation is maintained by gas flow through nozzles (2) in both L2 and L5. The thrust bearing nozzles are supplied from plena (5) located in L2 and L5. Compressor blades (3) and turbine blades (4) are etched partly into L3 and L4 respectively. A SEM picture of a sectioned turbocharger is shown in Figure 2.

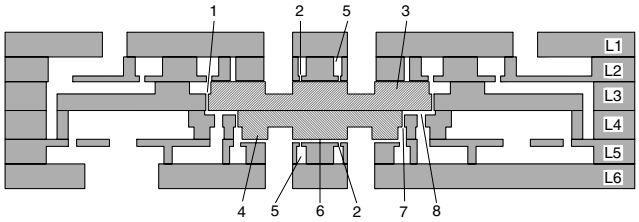

***Figure 1**. Cross-section of the turbocharger. The hatched structure is the rotor, free to spin within the device. Other critical components include: (1) compressor journal bearing, (2) thrust bearing nozzles, (3) compressor blades, (4) turbine blades, (5) thrust bearing supply plena, (6) thrust bearing gap etch, (7) turbine journal bearing, and (8) journal bearing supply plenum.*

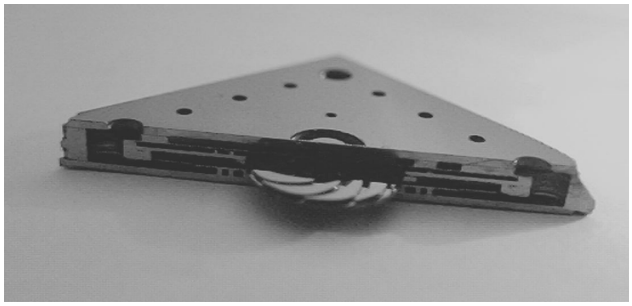

***Figure 2.** SEM picture of a sectioned turbocharger with rotor reinserted (taken from [2]). The device is formed by fusion bonding six silicon wafers. Die dimensions are 23 mm x 23 mm x 2.9 mm. Compressor diameter = 8.2 mm. Turbine diameter = 6.0 mm.*

JOURNAL BEARING PROFILE CONTROL

The journal bearing is a narrow, deep and straight donut shape trench etched by DRIE into L3, and also into L4 in the dual bearing design, as seen in Figure 1. The design specifications are 16 +/- 0.75 μm in width and 330 μm in depth for the L3 compressor journal bearing, and 15 +/- 0.75 μm in width and 330 μm in depth for the L4 turbine journal bearing. These tight specifications make the journal bearing profile control a challenge.

One major difficulty we encountered in developing the journal bearing etch process was profile repeatability. Although in-spec journal bearing profiles could be obtained with our baseline DRIE (deep reactive ion etch) recipes [3,4], defects such as blowup tops (large initial openings that quickly taper down), steps, spikes, bellies, positive taper and negative taper appeared from time to time. We found that these defects were related to

0-9640024-5-0/hh2004/$20©2004TRF
DOI 10.31438/trf.hh2004.68

both DRIE conditions and inconsistency in masking material profiles.

The masking materials used in our device are a thick photo resist AZ9260 layer on top of a thermally grown silicon oxide film. The oxide film is included to protect the bonding surfaces of the wafers. Since it typically takes more than 4 hours to etch the narrow and deep journal bearings, two layers of the photo resist, totaling about 22 μm, are coated on the wafers. The journal bearing etch pattern is transferred to the photoresist by an integral exposure of 5 x 15 seconds, development in AZ440 for 2 – 3 minutes, and post bake at 95°C for 30 minutes. The photoresist pattern is then transferred into the underlying oxide film with a BOE (buffered oxide etch) etch. The photo resist pattern edges have 40 to 60 degree slopes that depend mainly on the baking conditions. The oxide, though only 0.5 to 2 μm thick, typically has a slope of 45 degrees or less. The etch rate of the photoresist is in the range of 2 - 3 μm/hour and the etch rate of the oxide is about 1 μm/hour. Figure 3 shows the resist etch rate dependence on DRIE chamber pressure. The etch rate decreases significantly with increasing SF6 pressure. The inset is a SEM picture of the resist and oxide profile.

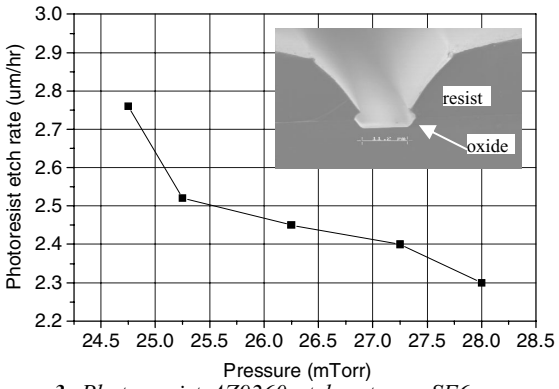

Figure 3. *Photo resist AZ9260 etch rate vs. SF6 pressure. The inset is a SEM picture of the resist/oxide bi-layer profile after BOE etch of oxide. The resist slope is the result of baking before BOE. The opening is about 9 um wide at the bottom of oxide.*

Due to the long etch time required to achieve a depth of greater than 300 μm in the silicon, the photoresist and oxide etch rates are large enough to result in significant mask material removal during the silicon etch. Thus the mask profiles determine the evolution of the journal bearing profiles. As the resist and oxide patterns recede from their original positions during DRIE, the opening of the journal bearing becomes larger. At the same time, with increasing depth, the amount of etching species needed to remove Si at the bottom and on the side of a straight journal bearing trench increases. If the masking materials recede faster than the speed at which the etching species can remove Si to make the journal bearing straight, a blow up or steps would appear in the journal bearing profile, as often seen in samples with shallow resist slopes. The SEM pictures in Figure 4 show the time dependence of the profiles of journal bearings patterned from the same mask (8 μm width) and DRIE recipe. The oxide is 1 μm thick and the resist is about 22 μm thick for all these samples. After 1 hour and 2 hours the journal bearings remain straight. This is probably because of the low aspect ratio of the trench and the slower mask recession rate that is now still mainly determined by the BOE etched oxide slope. After 3 hours, however, a step of about 1-2 μm appears indicating a sudden change in the mask recession rate when the 1 μm thick and roughly 45 degree slope in oxide is completely etched away and resist starts dominating the mask recession rate. As the etch continues, the step moves further down as shown by the arrows.

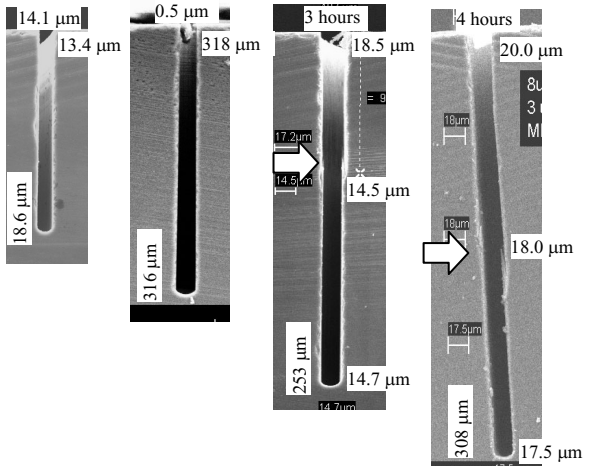

Figure 4. *Journal bearing profile evolution with DRIE time taken from 4 samples prepared with same recipes. The photo mask width was 8 μm. The resist and oxide are 22 μm and 1 μm thick respectively. Steps shown by the arrows start to show after 3 hours and moved downward. The apparent tilt of the rightmost picture is just an artifact from the SEM.*

With the same DRIE recipe and resist process, increasing the oxide thickness delays the appearance of steps or sudden width change in the journal bearing because the recession rate of the oxide is slower than that of the resist due to the slower etch rate of oxide (assuming similar slope), as seen in Figure 5. All three samples were prepared the same way except for their oxide thickness, 0.5 μm, 1.0 μm and 2.0 μm from left to right. The DRIE etch was done for 4 hours. The step in the 0.5 μm oxide sample is lower than in the 1.0 μm oxide sample, and a straight journal bearing with no step is obtained in the 2.0 μm oxide sample.

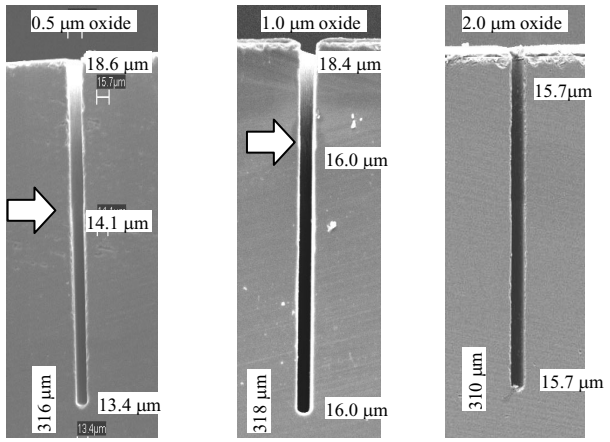

Figure 5. *Influence of oxide thickness on journal bearings in 3 samples with different oxide thickness. Steps labeled by the arrows were visible in the 0.5 μm sample, moved up in the 1.0 μm sample and disappeared in the 2.0 μm sample. Journal bearing depth is labeled on the left and width on the right of the trenches*

Obviously increasing the resist slope angle can reduce its recession rate and therefore prevent the steps, but steeper slopes, if more than 45 degrees, could cause ion deflection onto the side walls of the journal bearing, eroding the passivation film thereon

and forming bellies. Therefore to form narrow and straight journal bearings it is necessary to use a thick layer of oxide, 2 μm or more, that gives a larger window in photoresist profile control, though with a cost of increased complexity in the BOE step.

However, a thick layer of oxide not only makes the photolithography and BOE etch hard to control, but also causes wafer bow. To avoid wafer bow, we use a LOCOS (local oxidation of silicon) oxide pattern for the journal bearing in our device. As an example, Figure 6 shows the layer 4 journal bearing process flow. Nitride film is deposited and patterned in step 3, as the LOCOS oxidation barrier. A thick thermal oxide film is grown locally in the pattern defined by the nitride pattern in step 5, followed by BOE and DRIE of the journal bearing in steps 6 and 7, respectively. To protect the journal bearing from the subsequent blade etch (not shown) on the opposite side of the wafer, a thin layer of thermal oxide is grown in the trench, as seen in step 9. Another feature of this layer is a 30 μm recess (the journal bearing supply plenum, (8) in Figure 1) that joins the journal bearing on one side. To form this recess without damaging the journal bearing profile, we use a nested mask that is patterned in step 2 and protected by nitride in step 9, and isotropically etch away a small Si ring adjacent to the journal bearing in step 11, which is now under the protection of oxide. The oxide in the journal bearing trench is now thicker than the oxide on the surface, so the surface can be stripped of oxide by a timed BOE (or HF) etch for bonding and there is still a protective layer of oxide inside the journal bearing, as seen in step 12.

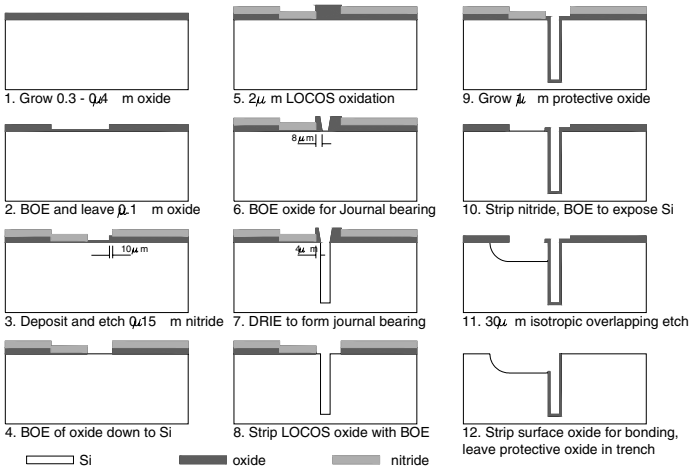

Figure 6. *Journal bearing process flow of turbine layer (L4). The journal bearing was etched using LOCOS oxide (steps 5-7) formed by a nitride barrier (step 3) and protected by oxidation (steps 8 and 9). A 30 μm deep trench joined one side of the journal bearing by isotropic etch (step 11) through a nested mask. The photoresist is not drawn for clarity.*

Careful control of the profiles of the photoresist and the oxide resulted in a significant improvement in the journal bearing process repeatability. For example, a wafer yield of over 80% can now be achieved for specifications of 15 - 16 +/- 0.75μm width and 330 +/- 5 μm depth. Our ongoing journal bearing process development effort includes fine tuning of the DRIE recipes for various specifications and side wall roughness improvement for better performance of the device.

THRUST BEARING AND NOZZLES

A total thrust bearing gap (see Figure 1) of 5.5 μm is etched into L5, and the rotor shifts axially downward by half this gap during centered operation, once it is freed. Each thrust bearing is supplied with pressurized air through 20 nozzle holes that are 100 μm deep and 10 μm in diameter, etched in L2 and L5. The process flow requires that these nozzles breakthrough into a 350 μm deep plenum that has already been etched into the back of the wafers. Proper performance of the thrust bearings requires precise control of the nozzle dimensions and good uniformity between the nozzles. The nozzles have a mean diameter tolerance of +/- 1 μm and mean length tolerance of +/- 10 μm, with allowable standard deviation between the nozzles about a factor of 5 less than the tolerances. Thus careful control of the photo process, BOE etch, and DRIE are necessary, as well as close inspections of both the nozzles and plena. For example, if nozzle patterning is done after the plenum DRIE, the protection of the bonding surface on the plenum side (usually protected with a layer of photoresist) is difficult to control because the baking before the nozzle BOE tends to make the protective resist flow away from the deep trench edges, exposing oxide there to BOE. When oxide undercut occurs, the Si bonding surface the oxide is supposed to protect is roughened by BOE, resulting in a degradation of the wafer bonding strength. One possible solution we are exploring is to use DRIE to etch through both the oxide and Si on the nozzle side. The solution we are currently using successfully is to do the photolithography and BOE steps for the nozzles and plena at the same time.

ALIGNMENTS AND ASSEMBLY

As seen in Figure 1, the rotor of the turbocharger is a two layer structure, with compressor blades on top of L3 and turbine blades on the bottom of L4. L3 and L4 are bonded together before the blades on either side are etched, but after the journal bearings are etched. This bonding must be done with very small misalignment to minimize the rotor imbalance. Because the journal bearing trenches form sealed cavities when the two wafers are in contact, L3/L4 bonding is usually done in "fusion bonding" mode, in which the two wafers are separated by metal flags during alignment, clamped, pumped to about 10^{-3} torr, and pressed at room temperature in vacuum after the flags are pulled out. Due to post alignment clamping and flag motion, the fusion bonding mode usually has less alignment accuracy than the "silicon direct bonding (SDB)" mode, in which the wafers are put in contact in air right after alignment. The disadvantage of SDB mode is that any sealed cavity has trapped air in it that has the potential to cause plastic deformation of the Si wafer if annealed at high enough temperature.

To achieve better alignment in the rotor, we bonded L3 and L4 using the SDB mode of the bonder. The annealing was done at 600ºC rather than the usual 1050ºC to avoid plastic deformation. This is feasible because the subsequent blade etch opens the sealed journal bearing cavity and a high temperature annealing is done later for the final assembly. L3/L4 bonding misalignment of less than 2 μm is regularly obtained with this process, with no bonding quality degradation observed from infrared images.

The misalignment between patterns, front to front or front to back, also contributes to rotor imbalance. Using a contact aligner, we can achieve mask misalignments of about 2 μm or better. Further improvement should be possible with the use of a stepper and precise measurement of front to back misalignment.

BLADE HEIGHT UNIFORMITY

Another major source of rotor imbalance is DRIE etch non-uniformity of blades in L3 and L4. With the rotor diameter set at 8.2 mm and journal bearing depth set at 330 μm, blade depth

variation has to be smaller than 3 μm to meet the design imbalance specification. This limits blade heights to less than 250 μm due to machine tolerance. The wafers are rotated multiple times during DRIE of blades to control depth uniformity. Figures 7a and 7b show blade etch variation around the circumference of a compressor and SEM picture of the compressor blades. With careful process control, experimental measurements show that a typical rotor has its center of mass offset from its geometric center by 3-5 μm.

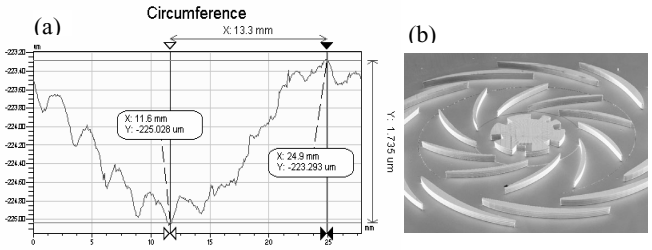

Figure 7. *(a) Blade etch variation on the circumference of a compressor. The maximum peak-to-valley difference is 1.7 μm. (b) SEM picture of compressor blades of a single bearing device.*

ROTOR RELEASING

Two ways for freeing the rotors were investigated. The first was to retain the rotor by bonding the center of the compressor top to oxide bonding pads in L2 before the L4 blade etch, and releasing the rotor with HF after dicing. This approach subjects the bonded wafers of L1 to L4 to several wet process steps and makes the wafer cleaning and bonding afterward very difficult. The current approach is to free the rotors from the L3/L4 stack, set them aside, finish all the layers, and drop the rotors back in during the final assembly. The free rotor method significantly simplifies the fabrication process. Although the free rotor approach eliminates the ability to perform fixed rotor flow tests, it opens the possibility for external characterization and dynamic balancing of the rotors prior to final assembly.

TESTING

During operation, turbine supply pressure is increased, and bearing pressures are adjusted to ensure rotordynamic stability. A high bandwidth fiber optic displacement sensor is used to measure rotor speed. Figure 8 shows measurements of the pressure ratio and mass flow rate obtained across the compressor for two runs of the same single bearing device. The compressor exhaust is throttled back to atmospheric pressure using an external valve. The throttle was set to a slightly different value for each of these runs. The compressor achieved a pressure ratio of 1.2 (17% of design pressure rise) with a flow rate of 0.14 g/s at 480,000 rpm (40% of design speed). The measured pressure ratio is consistent with model expectations. The rotor destructively crashed at 460,000 rpm. The test data indicates that the crash resulted from the failure of the thrust bearings to provide sufficient angular stiffness to contain tilting torques applied to the rotor from asymmetries in the design. Further refinements to the fabrication process will be necessary to achieve design speed operation.

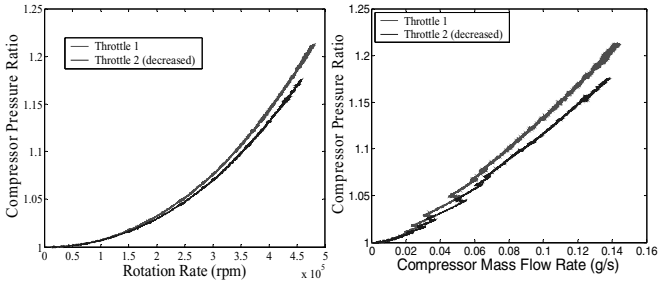

Figure 8. *Test results for two different compressor throttle settings, showing significant pressure rise and flow rate through the compressor. The sharp flow rate changes occur when the journal bearing pressure is adjusted, which acts as a throttle on the compressor. Uncertainties: pressure ratio +/- 0.04, flow rate +/- 0.004 g/s.*

CONCLUSIONS

This paper discussed key fabrication issues related to the high speed operation of a microscale turbocharger. Proper control of the masking material profile was found to be critical for meeting the journal bearing dimensional specifications with high yield. Blade height uniformity of less than 2 μm in the 8.2 mm rotors was achieved. The thrust bearing nozzle etch process was improved. A new free rotor method was developed to simplify the etching and assembly process. These process improvements resulted in a turbocharger device that achieved a speed of 480,000 rpm. Future work will focus on further improving rotor balance and process repeatability.

ACKNOWLEDGEMENTS

The authors would like to thank the staff of the MIT Microsystems Technology Laboratories for their help in fabrication. This work was supported by the Army Research Laboratory (DAAD19-01-2-0010) under the Collaborative Technology Alliance in Power & Energy program, managed by Mr. John Hopkins (ARL) and Dr. Mukund Acharya (Honeywell), and by the Army Research Office (DAAG55-98-1-0292) managed by Dr. Tom Doligalski.

REFERENCES

1. Epstein, A.H., Senturia, S.D. et al., "Power MEMS and Microengines," Transducers '97, The 9th International Conference on Solid-State Sensors and Actuators, Chicago, IL, June 1997.
2. Epstein, A.H., "Millimeter-Scale, MEMS Gas Turbine Engines," Paper GT-2003-38866, Proceedings of ASME Turbo Expo 2003, Atlanta, GA, June 2003.
3. Fréchette, L. G, Jacobson, S. A., Breuer, K. S., Ehrich, F. F., Ghodssi, R., Khanna, R., Wong, C.W., Zhang, X., Schmidt, M. A., and Epstein, A.H., "Demonstration of a Microfabricated High-Speed Turbine Supported on Gas Bearings," Hilton Head Solid-State Sensor & Actuator Workshop, Hilton Head Island, SC, June 4-9, 2000, pp. 43-47.
4. Liu, L.X., Teo, C.J., Epstein, A.H., and Spakovszky, Z.S., "Hydrostatic Gas Journal Bearings for Micro-Turbomachinery," Paper DETC2003/VIB-48467, Proceedings of DETC'03, Chicago, IL, September 2-6, 2003.

A TRANSISTORLESS MICROMECHANICAL HIGH VOLTAGE GENERATOR USING A DC-POWERED SELF-OSCILLATING RELAY

Kabir Udeshi[1] and Yogesh B. Gianchandani
Engineering Research Center on Wireless Integrated Microsystems
University of Michigan, Ann Arbor, USA

ABSTRACT

This paper describes a DC powered high voltage generator that neither uses transistors nor requires a clock signal for its operation. The system, that operates on the principle of an induction coil voltage converter, is assembled using a self-oscillating mechanical relay and a wire wound inductance. Two versions of this high voltage generator have been implemented. The first version, assembled to have a footprint of less than 4 mm x 4 mm, uses an inductor and generates peak voltages > 200 V from a 4 V DC supply. An alternate version uses a transformer that provides electrical isolation and has been used to generate peak voltages > 500 V with a peak voltage gain > 300. The self oscillating relay is fabricated using low temperature UV-LIGA process, that can be appended to a CMOS process. Experimental results used to characterize system performance show that the self oscillating relay consumes not more than 15 % of input power. Circuit simulations closely track observed experimental trends.

I. INTRODUCTION

A large number of micromachined devices ranging from electrostatic actuators [1], to microfluidic electrokinetic pumps [2], to microplasmas [3], all need high voltages for their operation. This requirement for high voltages is what prevents the use of these devices in integrated microsytems and portable devices as they can only be powered by a single low-voltage DC supply. The need for high voltage generators extends to automotive transducers and a variety of portable electronic devices that use LCD display technology. In order to meet this demand, schemes have been proposed to integrate an additional miniaturized high voltage power source [4, 5]. These however occupy large footprints and entail the additional overhead of power management and distribution. The preferred solution is to step up voltage from the low voltage DC power source such as a battery. A typical implementation of such a high voltage generator utilizes an inductor in conjunction with a switch that periodically breaks the current through the inductor. The miniaturization and integration of this high voltage generator has been limited by the need for an efficient inductive element as well as a high power, high voltage switch.

Traditionally microelectronic transistors have been used as switches for high voltage generators. However, in standard CMOS technology transistors are severely limited by their dielectric and junction breakdown voltages, making them unsuitable for any application that demands even moderately high voltage or power levels [6]. The use of hybrid high voltage CMOS technology results in increased costs, and yet can handle only voltages up to about 80 V. In addition to the voltage limitation, transistors need electrical control signals that determine their switching characteristics. These control signals are generally obtained from an oscillator. The inductive element may be microfabricated, but typically results in modest inductance values [7]. An alternative approach is to integrate wire wound inductors using microassembly techniques [8].

This paper reports a high voltage generator that eliminates the need for a transistor. It operates using a fully mechanical self-oscillating relay and an assembled wire wound inductive element, without the need for any electronic circuitry. The system operates from a single DC power source. The first section describes the operation of the high voltage generator that has been implemented in two configurations. The next section reports experimental results that show a microsystem generating peak voltages in excess of 200 V. Then experimental results are compared to with circuit simulations and further conclusions drawn.

I. SYSTEM OPERATION

The high voltage generator works on the principle of an induction coil voltage converter [9]. One version of the microsystem, Version I, is similar to a boost converter [10] (Fig. 1). The current through an inductor is cut periodically by the action of a switch. In the portion of the operating cycle that the switch is closed, the input current, *Iin*, is on, and energy is stored in the inductor. Once the current is turned off by the switch, the stored magnetic energy is converted into electric potential, which results in the generation of a high output voltage spike, *Vout*, across the load impedance, *Zload*. The cycling of the switch between its open and closed positions results in these high voltage spikes being generated at regular intervals. The pulsed

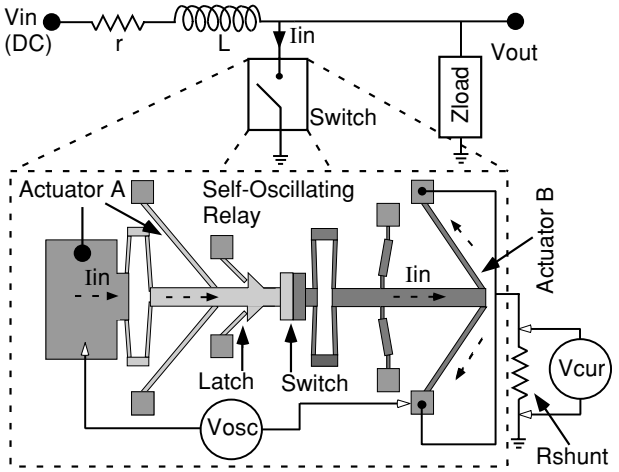

Fig. 1: Circuit diagram of Version I of the high voltage generator with a schematic of the self-oscillating relay. Rshunt=1Ω.

[1] Address: 1301 Beal Ave., Ann Arbor, MI 48109-2122, USA; E-mail: kudeshi@umich.edu

0-9640024-5-0/hh2004/$20©2004TRF
DOI 10.31438/trf.hh2004.69

Solid-State Sensors, Actuators, and Microsystems Workshop
Hilton Head Island, South Carolina, June 6-10, 2004

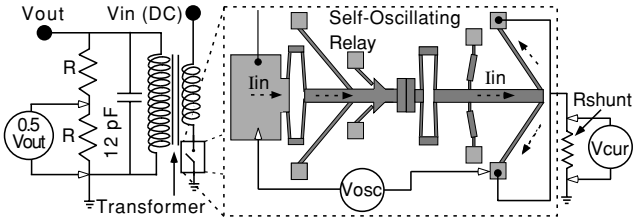

Fig. 2: Version II: High voltages have been generated using transformers that provide electrical isolation.

output could directly power a variety of devices or be converted to a high voltage DC. The periodic switching in the circuit is achieved by using a self oscillating relay [11]. The relay, operated by an electrothermal actuator, is connected directly in the current path of the circuit, and requires no additional electrical connections.

An alternative implementation, Version II, uses a miniature transformer in a manner similar to a flyback converter [12] (Fig. 2). The use of a transformer instead of an inductive coil provides electrical isolation as well allows for the capability to generate higher output voltages by choosing a suitable turns-ratio.

I. CIRCUIT ANALYSIS

Both versions of the high voltage generator may be analyzed using the circuit in Fig. 1 consisting of a DC voltage source, *Vin*, parasitic resistance of the coil winding, *r*, an inductor, *L*, a switch, and the load impedance, *Zload*. The circuit has two phases of operation. In the first phase, the switch is closed and the current through the circuit ramps up resulting in energy being stored in the inductor. The differential equation that describes the change in current, *Iin*, with time, *t*, during this phase of operation and its solution is given by [9]:

$$r\,Iin + L\frac{dIin}{dt} = Vin \quad ; \quad Iin = \frac{Vin}{r}\left(1 - e^{\frac{-rt}{L}}\right) \qquad (1)$$

The equation is derived under the assumption that when the switch is closed, no current flows through *Zload*, which is much larger than the parasitic resistance of the closed switch.

The circuit goes into its second phase of operation at the instant the switch starts opening. As the current falls to zero, the e.m.f. of the coil adds itself to that of the source leading to a high voltage across the output load. Since there are numerous physical phenomena occurring at this moment, including potential arcing across the switch, it is not easily described by a closed form expression. However, the output voltage generated, *Vout*, is known to be a function of the rate of change of current, *Iout*, that flows through the load during this phase of operation [9].

Version II of the high voltage generator may be

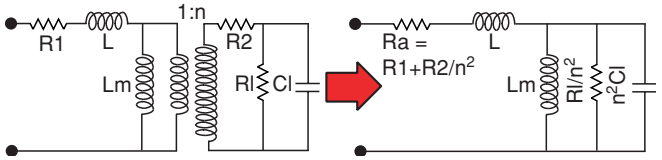

Fig. 3: The model of a transformer can be converted to an equivalent circuit with an inductor.

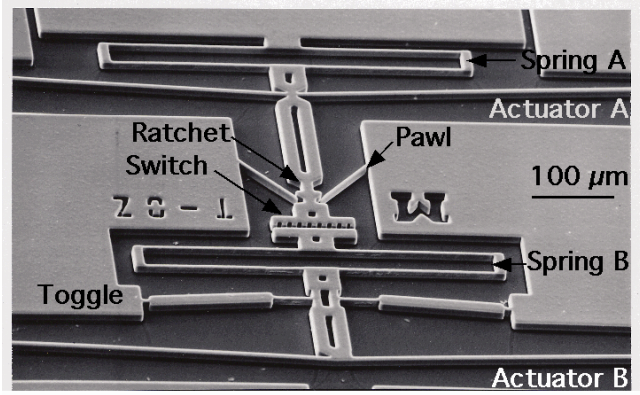

Fig. 4: SEM image of fabricated self-oscillating relay.

analyzed in a similar manner by converting the model of a transformer into an equivalent circuit containing inductors. Figure 3 shows the model of a transformer where *R1*, *R2* represent the primary and secondary coil resistances respectively, *L* the leakage inductance, *Lm* the magnetization inductance, *n* the turns ratio and *Rl* and *Cl* represent the load resistance and capacitance, respectively [13]. *Lm* corresponds to the inductance that produces magnetic flux in the transformer. The equivalent circuit eliminates the transformer and scales the load connected to the secondary circuit by a factor determined by the turns ratio. This circuit can be simulated using SPICE. The parameter that needs to be set is the rate of change of output current, which can be derived from experimental data.

I. FABRICATION & ASSEMBLY

The self-oscillating switch was fabricated using a single mask UV-LIGA process using SU-8 resist [14]. Thirty micron thick structures were fabricated from electroplated copper with a minimum feature size of 3 μm. A SEM of the oscillator is shown in Fig. 4. The low temperature process used to fabricate the switch allows it to be appended to a CMOS process.

The coil was wound using a coil winder on a cylindrical steel core, and assembled onto a PCB along with the die of the oscillator. The microsystem shown in Fig. 5 has a footprint of 4 mm x 4 mm. The dimensions of the inductor may be significantly reduced by the use of toroidal, nickel-iron cores.

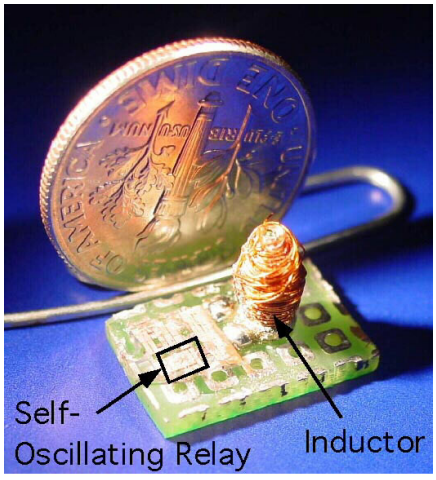

Fig. 5: A photograph of Version I of the high voltage generator made by assembling the self-oscillating relay with a wire wound inductor

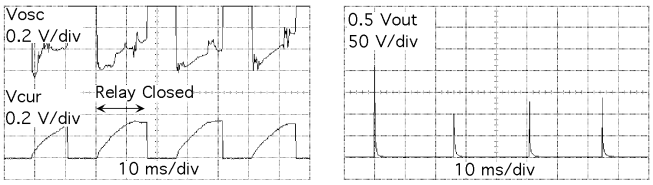

Fig. 6: Output waveforms as obtained on an oscilloscope for Version II of the high voltage generator.

I. MEASUREMENT RESULTS

The system was tested and characterized for a variety of input parameters and operating conditions. The experimental characteristics were compared with circuit simulations to explain trends observed.

To verify the operation of the high voltage generator, the nodal voltages and circuit current were dynamically recorded using the setup of Fig 2. When the switch (Fig. 2) is closed, the current flowing through the primary of the transformer, *Vcur*, ramps up (Fig. 6), and the voltage across the relay, *Vosc*, is at a small value corresponding to the small resistive voltage drop across a closed switch. Opening of the switch causes *Vosc* to rise to the supply voltage and the current to drop rapidly leading to the generation of a high voltage, *Vout*, across the load. Variations in the magnitude of peak *Vout* could be due to digital sampling carried out by the oscilloscope. The high voltage spikes do not temporally coincide with the location of the falling current because separate oscilloscopes were used to capture these waveforms using independent trigger signals. The observed waveforms verify the operation of the high voltage generator as described by the theory of an induction coil voltage converter.

In Version I, the self-oscillating relay has been integrated with a hand wound 450 μH inductance, as shown in Fig. 5, and has been used to generate voltages up to 208 V from a 3.8 V DC supply while driving a 1 MΩ, 12 pF load. The peak output voltage (Fig. 7) increases with input power (a), while the peak voltage gain remains constant at about 50 (b). In power calculations, it is assumed that while the switch is closed, no current flows through the output load. This assumption is valid as the resistance of the relay in the closed state (≈15 Ω) is negligible compared to that of the output load (which is in the KΩ to MΩ range). Thus, Vosc x Iin gives the input power consumption by the relay, while Vin x Iin gives the total input power. The fraction of input power consumed by the self-oscillating relay is 5-14 % (Fig. 7c). Since up to 95 % of the input power is delivered to the inductor at high output voltage levels, optimized circuit parameters can result in acceptable energy efficiency.

Simulated values of peak output voltage obtained, track experimental results (Fig 7a). In order to simulate circuit performance, an input parameter required is the rate of change of current. The self-oscillating relay was modeled as a linear resistor whose resistance changes from 0 Ω to 100 MΩ as the switch opens. The time rate of change of this resistance is used to determine the rate of change of current. A resistance change time of 450 μs allows simulated results to track those obtained experimentally.

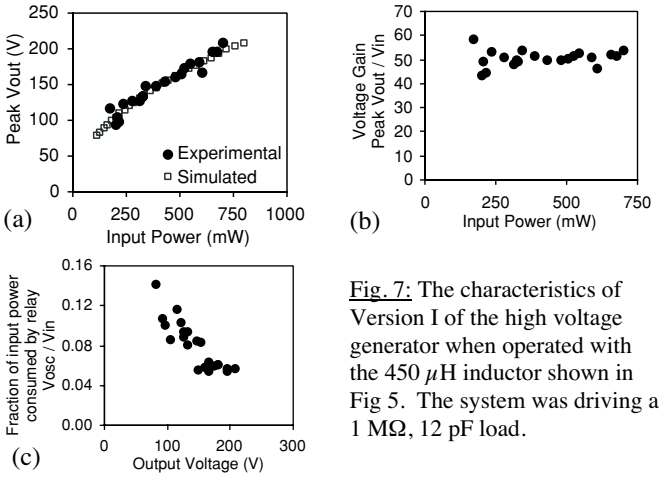

Fig. 7: The characteristics of Version I of the high voltage generator when operated with the 450 μH inductor shown in Fig 5. The system was driving a 1 MΩ, 12 pF load.

Version II of the high voltage generator uses a transformer and provides electrical isolation between the input and output as shown in Fig. 2. A study of the operating characteristics under different resistive loading conditions was carried out, using a transformer with a magnetization inductance of 3.5 μH and 12 pF capacitive load in parallel with the resistive load (Fig. 8). The peak output voltage (a) and voltage gain (b) decrease with smaller load resistance values due to higher current flow rates. The higher currents also cause an increase in the input power consumed by the microsystem (c). The low fraction of input power consumption by the relay (<15 %) indicates that even though driven by an electrothermal actuator, it is energy efficient (d).

In order to simulate the circuit performance, the parameters *Lm*, *L*, *n*, *R1* and *R2* of a physical transformer need to measured. The coil resistances *R1* and *R2* can be measured using an ohmmeter. The other parameters are calculated using [15]:

$$Lm = M^2 / L_2o \quad ; \quad L = L_1o - M^2 / L_2o$$
$$n = L_2o / M \quad ; \quad M = \sqrt{L_1o(L_2o - L_1s)} \qquad (2)$$

where, *L*, is the measured inductance, with the first subscript indicating the side of the transformer; 1 indicates the primary and 2 the secondary. The second subscript indicates the condition of the adjacent winding while

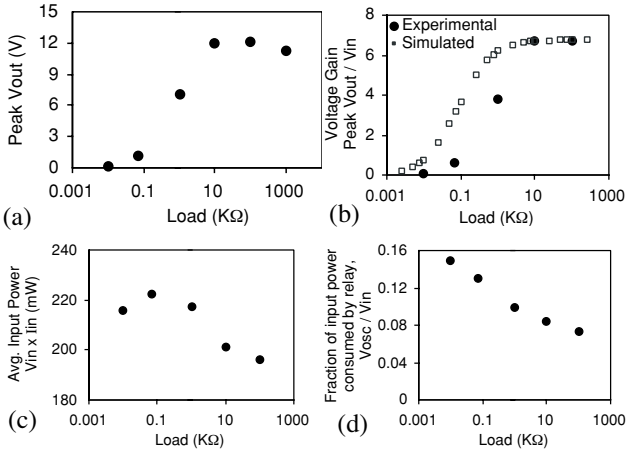

Fig. 8: Version II tests: A study of the operating characteristics under different resistive loading conditions.

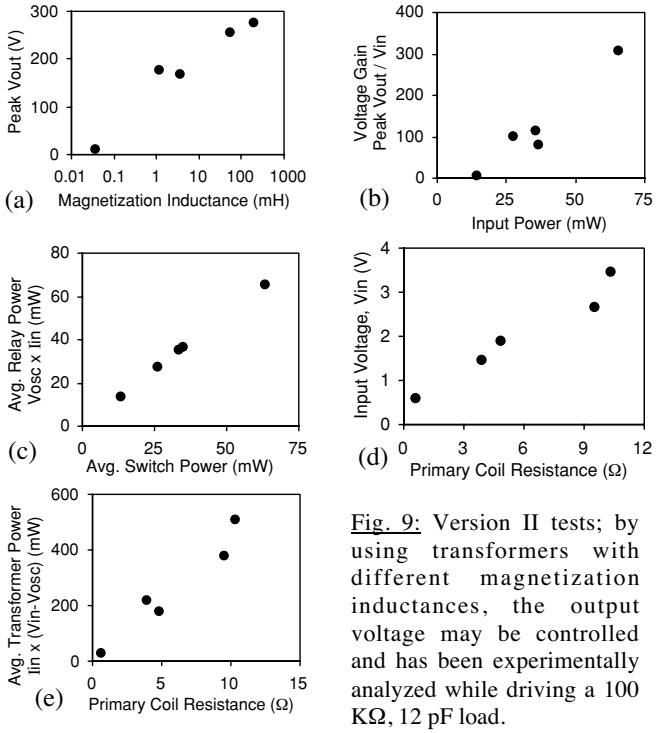

Fig. 9: Version II tests; by using transformers with different magnetization inductances, the output voltage may be controlled and has been experimentally analyzed while driving a 100 KΩ, 12 pF load.

carrying out the inductance measurement; whether open, *o*, or shorted, *s*.

The measured transformer characteristics were used to simulate the performance of the circuit and are compared with experimentally obtained values of peak output voltage in Fig. 8(b). The S-shaped curve can be explained by observing the nature of the load. At small values of load resistance, most of the output current flows through the resistor. However at high values of resistive load, the charging current of the capacitor becomes dominant. Since a fixed capacitance was used while carrying out the experiments, the peak voltage gain saturates at large resistive loads.

Output voltages generated by the system may be changed by varying the magnetization inductance, *Lm*, of a transformer (Fig 9). The output voltage (a) and voltage gain (b) increase with higher values of inductance due to greater energy storage capacity. The input voltage of the system (d), as well as transformer power consumption (e) depends significantly on coil resistance, which may be greatly reduced by the use of superior winding coil material. Power consumption of the oscillating relay is found to depend mainly on the power drop across the contact resistance of the relay switch (c).

II. CONCLUSIONS

The high voltage generator reported in this paper can generate high voltage spikes from a DC source without the use of transistors. Version I of this system uses an inductor and has been assembled along with a self oscillating relay to have a footprint of less than 4 mm x 4 mm and can generate voltages in excess of 200 V from a 4 V DC supply. Version II uses a transformer that provides electrical isolation and allows greater control over the output voltage through the turns ratio. The system performance has been characterized under various power levels, loads and inductance values. The self-oscillating relay consumes less than 15 % of the input power indicating that the system has a high energy efficiency. Results of circuit simulations, with a single fitting parameter, closely track experimental results, indicating that the system operates as predicted by theory. A reliable and optimized design of the high voltage generator reported can power high voltage sensors and allow complete integrated microsystems to operate using a single a low voltage DC power source.

ACKNOWLEDGEMENTS

This work was supported primarily by the Engineering Research Centers Program of the National Science Foundation under Award Number EEC-9986866. The facilities used for this research include the Solid-State Electronics Laboratory (SSEL) at the University of Michigan. Travel support has been generously provided by the Transducers Research Foundation and by the DARPA MEMS and DARPA BioFlips programs

REFERENCES

[1] W. Tang, T. Nguyen, M. Judy, R. Howe, "Electrostatic Comb-Drive of Lateral Polysilicon Resonators," *Sensors and Actuators A (Physical)*, v A21, n 1-3, Feb. 1990, p 328-31

[2] S. Zeng, H. Chen, J. Mikkelsen, J. Santiago, "Fabrication and characterization of electrokinetic micro pumps," *Thermo-mechanical Phenomena in Electronic Systems*, v 2, 2000, p 31-36

[3] C. Wilson, Y. Gianchandani, "Spectral Detection of Metal Contaminants in Water using an On-Chip Microglow Discharge," *IEEE Trans. Electron Devices*, v 49, n 12, Dec. 2002, p 2317-22

[4] J. Lee, Z. Chen, M. Allen, A. Rohatgi, R. Arya, "A miniaturized high-voltage solar cell array as an electrostatic MEMS power supply," *J. MEMS*, v 4, Sept. 1995, p102-108

[5] J. Bates, G. Gruzalski, C. Luck, "Rechargeable solid state lithium microbatteries," *IEEE MEMS, 1993*, p 82-86

[6] H. Jiang, W. Carr, "On-chip integration of high-voltage generator circuits for an electrostatic micromotor," *Intl Conf. on Solid-State Sensors and Actuators*, v 1, 1995, p 150-53

[7] C. Ahn, M. Allen, "A comparison of two micromachined inductors (bar and meander-type) for fully integrated boost DC/DC power converters," *IEEE Transactions on Power Electronics*, v 11, n 2 , March 1996, p 239-45

[8] G. Skidmore, M. Ellis, A. Geisberger, K. Tsui, K. Tuck, R. Saini, T. Udeshi, M. Nolan, R. Stallcup, J. Von Ehr II, "Assembly Technology Across Multiple Length Scales From the Micro- Scale to the Nano-Scale," *IEEE MEMS, 2004*, p 588-92

[9] H. Armagnat, *The theory, design and construction of induction coils*, New York, McGraw publishing company, 1908

[10] R.Jaeger, *Microelectronic Circuit Design*, McGraw-Hill, 1997

[11] K. Udeshi, Y. Gianchandani, "A DC-Powered, Tunable, Fully Mechanical Oscillator Using In-plane Electrothermal Actuation," *IEEE MEMS, 2004*, p 502-06

[12] N. Mohan, T. Undeland, W. Robbins, *Power electronics: converters, applications, and design*, New York, John Wiley & Sons, Inc., 1995

[13] W. Flanagan, *Handbook of transformer design and applications*, McGraw-Hill, Inc., 1993

[14] H. Lorents, M. Despont, N. Fahrni, N. LaBianaca, P. Renaud, P. Vettiger, "SU-8: a low-cost negative resist for MEMS," *J. Micromech. Microeng* , v 7, n 3, 1997, p 121-24

[15] J. Stewart, A. Boyd, *Theory and design of capacitor-storage ignition systems*, Technical Report, Univeristy of Michigan, Ann Arbor, 1956

PALLADIUM-NANOSTRUCTURES ON PLATINUM-BLACK CATALYSTS INTEGRATED INTO A MICROFABRICATED SI-BASED MICROFUEL CELL

R. S. Jayashree, J. Spendelow, E. R. Choban, and P. J. A. Kenis
Department of Chemical and Biomolecular Engineering
University of Illinois
Urbana, IL 61801

J. Yeom, and M. A. Shannon*
Department of Mechanical and Industrial Engineering
University of Illinois
Urbana, IL 61801

ABSTRACT

In this work, we investigate the effect of the structure and composition of the catalyst on the electro-oxidation of formic acid, first in an electrochemical cell and then in a microfabricated silicon-based membrane electrode assembly (silicon-MEA). The silicon-MEAs consist of two grids that serve as the catalyst support and current collector, and they guide the flow of fuel/oxidant to the anode/cathode and carbon dioxide away from the anode. Different dendritic Pt-black catalyst support structures were fabricated by varying electrodeposition conditions. Bimetallic Pt/Pd catalyst tailored to formic acid-DI water fuel mixtures were obtained by spontaneous deposition on high surface area Pt structures. These Pt/Pd catalyst structures increase the activity towards electro oxidation of formic acid by up to an order of magnitude over long times. In addition, the initial silicon-MEAs with Pt/Pd catalyst grids exhibit doubled power density in fuel cell testing.

INTRODUCTION

Research and commercialization of Proton Exchange Membrane Fuel Cells (PEMFC) are gaining momentum as a "clean" energy source. While hydrogen and methanol are typically used as the fuels, recently formic acid has been shown to be a promising alternative for powering MEMS devices at ambient temperatures [**1**]. Compared to hydrogen it is easier to store, and formic acid has faster kinetics and exhibits less tendency for crossover across the proton exchange membrane than methanol [**1**]. Microfuel cells for use in portable applications in particular benefit from formic acid, since the fast kinetics of dissociating H^+ ions at room temperature eliminates the necessity to introduce additional heating elements, which reduce the overall performance of the fuel cell system. Kelley *et al.* have reported a miniaturized fuel cell with performance comparable to large-scale fuel cells [**2**]. Recently, we have been successful in miniaturizing silicon MEAs using MEMS type microfabrication techniques [**3**]. This method facilitates the integration of key components of MEAs including microchannels, current collector, and catalyst on a single chip. In comparison to traditional MEAs in which the catalyst is painted as a layer onto the Nafion membrane, the silicon grids with Pt-catalyst structures presented here offer the advantages of: (1) rapid diffusion/transport of fuel towards the catalyst structures; (2) easy removal of CO_2 from the catalyst/fuel interface to the outside world; and (3) low-resistant contact between the catalyst structures and the Nafion membrane.

In the work presented here, we describe the deposition of high surface area Pt/Pd catalyst structures with dendritic morphologies on silicon-grid MEAs. Electrochemical studies have recently shown that Pt/Pd bimetallic catalysts obtained by spontaneously Pd on Pt nanosphere particle catalysts perform well in the electro-oxidation of formic acid, yielding significantly higher currents at a given potential [**4**]. Unfortunately, nanoparticle Pt/Pd catalysts are usually contained in a Nafion®-based ink that is painted onto the Nafion PEM, which is not compatible with MEMS fabrication techniques for the MEA. Therefore, we have developed a spontaneous deposition method to deposit Pd onto high surface area electrodeposited Pt catalyst structures that is compatible with our silicon-based MEAs to improve the performance of the formic acid fuel cells.

EXPERIMENTAL DETAILS

1. Microfabrication of silicon MEAs

Silicon-based membrane electrode assemblies (MEAs) were prepared using various microfabrication processes. Briefly, a double- sided <100> oriented polished wafer was covered on the front side with a 1000 Å Au layer and patterned into a circular mesh with 100 µm square holes by photolithography followed by liftoff. Next, the front/back side was covered with a polyimide layer that was further patterned using photolithography, followed by deep reactive ion etching to yield the silicon-based grid with 100 µm square holes. After catalyst deposition (see section 2) two of these grids, which serve both as the current collector and catalyst support, are bonded to a Nafion membrane to yield a silicon-based MEA shown in Figure 1. A detailed description on the fabrication of the silicon-MEA can be found elsewhere [**3,5**].

2. Synthesis of catalyst structures

2.1 Preparation of Pt catalyst structures

High surface area Pt-black was deposited onto the Au-covered silicon grids by electrodeposition using a plating bath made with 120 ml of water, 5g of chloroplatinic acid (H_2PtCl_6.

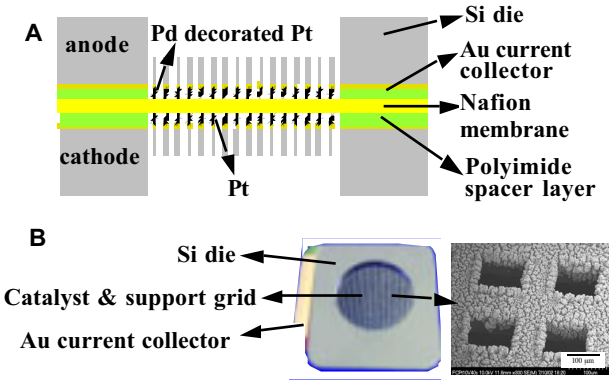

***Figure 1**. (A) Schematic diagram of silicon-based MEA. (B) Photograph of Membrane Electrode Assembly (MEA) prepared by silicon MEMS fabrication processes, with a mesh of 50 µm thick and 150 µm width, and 100 µm square holes to facilitate gas diffusion to the electrode.*

Travel support has been generously provided by the Transducers Research Foundation and by the DARPA MEMS and DARPA BioFlips.

$6H_2O$), and 30 g of lead acetate ($Pb(C_2H_3O_2)_2$) [**6**]. Figure 2 shows two SEM micrographs of the dendritic structures that can be electroplated with this bath. In the present study, we investigate the effect of structure on the catalytic activity of the Pt during formic acid electro-oxidation.

We varied the morphology of the catalyst electrode structures using the following deposition conditions.

1. Flat, shiny Pt deposited by e-beam evaporation.
2. Pt-black electrodeposited at constant voltages of 2, 5 and 10 V using Pt foil as the counter electrode.
3. Pt-black electrodeposited at a constant current of 250 mA.

2.2 Spontaneous deposition of Pd onto Pt catalyst structures

The rate of electro-oxidation of formic acid typically increases on bimetallic Pt/Pd catalysts up to an optimum coverage of dispersed Pd before decreasing with further increase in Pd coverage [**4**]. Therefore, we deposited Pd islands on the Pt catalyst structures by spontaneous deposition using the process that was reported to maximize the electro-oxidation rate [4]. The electrodes with Pt catalyst structures were first cleaned electrochemically in 0.1 M H_2SO_4 by cycling between 0 and 1.5 V vs. RHE. Then the electrodes were placed in a 5 mM palladium nitrate + 0.1 M H_2SO_4 solution for 5 min, followed by thorough rinsing with Milli-Q water. These electrodes were electrochemically annealed by cycling five times between 0 and 0.95 V in 0.1 M H_2SO_4. This spontaneous deposition procedure was repeated five times to yield Pd decorated Pt catalyst structures on the silicon grids. Note, however, that the resulting structures are of Pd on a various dendritic Pt structures, which for cases (2) and (3) described above are different from the structures previously reported in reference [4]. The inset of Fig. 2 shows a cartoon of one Pt dendrite decorated with Pd adatom islands.

3. Electrochemical Characterization

3.1 Cyclic Voltammetry (CV)

All silicon grids with catalyst structures were cleaned in a 0.1 M H_2SO_4 solution by cycling from 0.0 to 1.5 V vs. RHE at a scan rate of 500 mV/s. Next, cyclic voltammograms of these electrochemically cleaned silicon grids with catalyst structures were recorded in a 0.1 M H_2SO_4 solution in the presence of 0.1 M formic acid between 0.05 and 1.25 V vs. RHE at a scan rate of 50 mV/s.

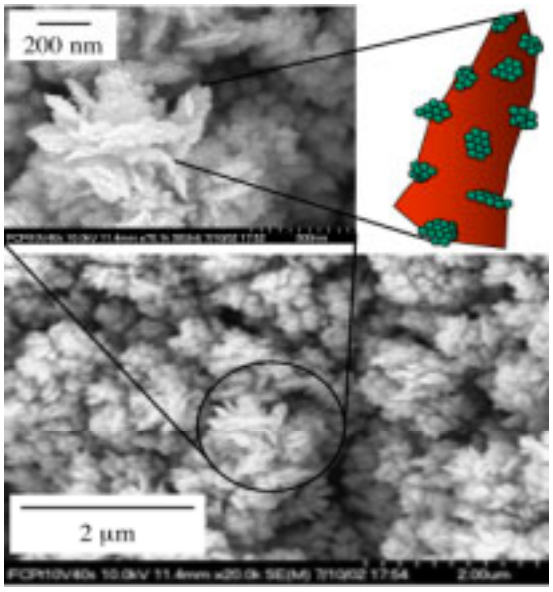

Figure 2. *SEM micrographs of dendritic catalyst structures, with cartoon of a decorated Pt dendrite.*

3.2 Chronoamperometry (CA)

The voltage potential is varied in steps between 0.95 V and 0.01 V to the silicon grids with Pt structures for 1 s and repeated 4 times to ensure complete removal of surface-bound CO. After the cleaning steps the silicon-based electrodes were held at 0.2 V and 0.3 V vs. RHE for 600 s and the current was recorded as a function of time.

3.3 Fuel Cell Test Apparatus

Figure 3 shows a diagram of the test fixture for the silicon-based MEA. The silicon-based MEA is clamped between two PTFE casings, which contain electrical contacts as well as fluidic inlets and outlets. 10 M formic acid was fed into the anode chamber at a flow rate of 1 ml/min and oxygen gas was fed into the cathode chamber at 10 sccm. I-V curves were obtained by applying different potentials to the cell and recording the current at these different potentials. The obtained current values were normalized to the geometric surface area (0.44 cm^2) of the silicon-based MEA.

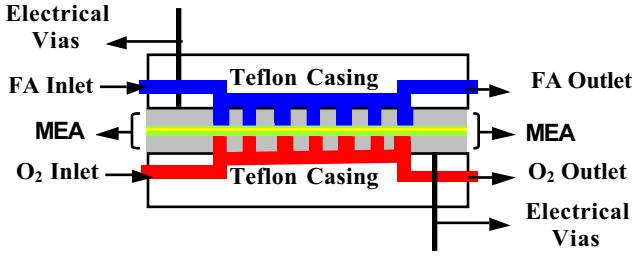

Figure 3. *Schematic of silicon-MEA test fixture (FA: Formic Acid).*

RESULTS AND DISCUSSION

In the present study, we performed an initial investigation of the effect of structure on the catalytic activity of the Pt/Pd during formic acid oxidation. The structure affects both the total surface area and the average size and density of the dendrites that grow out from the bush-like configuration shown in Fig. 2. Figure 4 shows SEM micrographs of the different Pt catalyst structures. Deposition of Pt via evaporation resulted in a uniform covering of the microfabricated grids (Fig. 4A). Figures 4B-D shows the dendritic-morphology of Pt catalyst structures grown at different constant potentials. At, lower potentials (2V, Fig. 4B) lower surface coverage and a non-uniform deposition of Pt is observed, which can be explained by Ostwald ripening of the electroplated structure. This mechanism proposes that the growth of larger crystals occurs at the expense of smaller ones [**7**]. Deposition at higher potentials (5V, Fig. 4C, and 10V, Fig. 4D) results in a higher surface coverage of uniformly distributed dendritic structures. Figure 4E shows Pt-black catalysts structures deposited at constant current conditions. These different Pt black catalysts structures shown in Figs. 4A-E will exhibit different performance when integrated in a silicon-MEA, due to differences in surface area as well as differences in the nature of the contact between these dendritic structures and the Nafion membrane. Catalyst structures that are uniform in height are expected to lead to better contact.

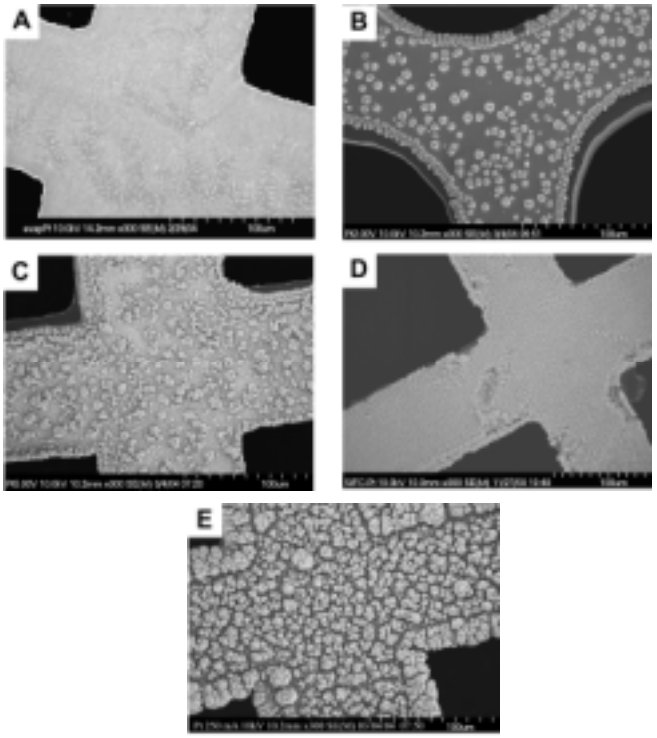

Figure 4*. SEM micrographs of Pt catalysts on Au surface are shown here. A corresponds to evaporated Pt, B, C and D correspond to Pt structures electrodeposited at a constant voltage of 2, 5 and 10 V respectively, and E represents the morphology of Pt structure electrodeposited at a constant current of 250 mA.*

1. Electrochemical Characterization

1.1 Cyclic Voltammetry (CV)

The cyclic voltammogram (CV) of silicon grids with Pt catalyst structure (Figure 4D) is shown in Figure 5a. The CV data shows two peaks at 0.65 V (all potentials vs. RHE) and 1 V during the scan, and one peak at 0.9 V on the reverse sweep. Lu *et al.* suggest that the first anodic peak corresponds to formic acid oxidation to CO_2 on Pt surface sites uncovered by CO, while the second peak corresponds to the oxidation of CO on Pt sites and increased formic acid oxidation resulting from the release of CO from the Pt surfaces [**4**]. The peak appearing at 0.9 V during the cathodic sweep can again be attributed to the oxidation of formic acid to CO_2, which extends to 0.3 V. Figure 5b shows the cyclic voltammogram of silicon grids with Pd-modified Pt catalyst. The peaks on the positive-going sweep appear at 0.45 V and 0.8 V, while on the negative-going sweep a peak appears at 0.75 V. These results indicate that the Pt electrodes decorated with Pd have a higher intrinsic activity for formic acid oxidation than pure Pt electrodes. This increase in activity for transient formic acid oxidation is carried over into an increased activity for steady-state formic acid oxidation, as reflected in the chronoamperometry results (see below).

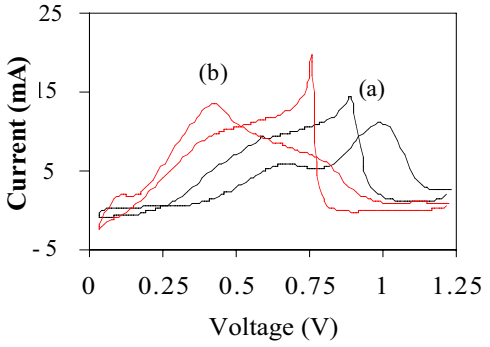

Figure 5. *Cyclic Voltammograms of silicon based Pt-black electrodes in 0.1 M Formic Acid + 0.1 H_2SO_4 (a) without and (b) with Pd-atoms.*

1.2 Chronoamperometry (CA)

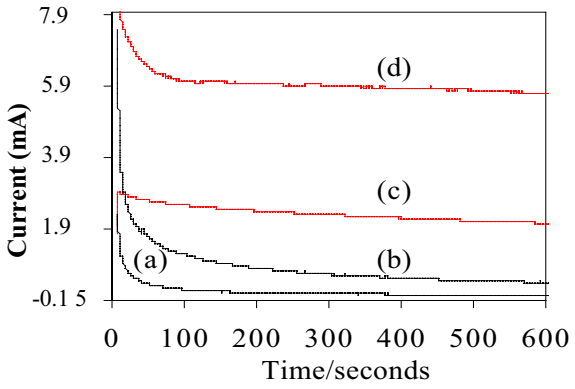

Figure 6. *Chronoamperometric data of Pt-black electrodes with and without Pd in an aqueous solution of 0.1 M formic acid + 0.1 M H_2SO_4. The lines (a,b) and (c,d) correspond to electrodes without and with Pd ad-atoms, respectively. Profiles (a) and (c) are measured at 0.2 V vs. RHE, while (b) and (d) are obtained at 0.3 V vs. RHE.*

Figure 6(a-d) show the chronoamperometric plots corresponding to formic acid oxidation on Pt electrodes with and without Pd. At a given potential, the steady-state currents from the Pd/Pt bimetallic catalysts structures are significantly higher in comparison to plain Pt electrodes, reflecting an increased intrinsic activity for formic acid oxidation on Pd islands, as well as a decreased susceptibility to CO poisoning. Indeed, FTIR experiments on Pt(111) modified by Pd show no CO formation on Pd islands during formic acid oxidation [**8**]. However, Pd islands are not necessarily immune to poisoning during formic acid oxidation. Several reports have demonstrated deactivation of Pt/Pd electrocatalysts during formic acid oxidation, an effect that has been attributed to the presence of interfacial CO_2 [**4,9**], adsorbed formic acid, formate, or other reaction intermediates [**4**] or adsorbed OH and anions [**8**]. Nevertheless, the improved steady-state activity of Pd-modifed Pt, as demonstrated in the chronoamperometry results, clearly demonstrates that Pd-modified Pt catalyst structures can serve as better catalysts for formic acid oxidation.

1.3 Fuel Cell Testing

Figure 7 shows the I-V curves and performance for silicon based fuel cells with and without Pd. The current densities and the power densities are significantly higher (~2 times) for the silicon-MEA tested that has Pt/Pd bimetallic catalysts structures, as opposed to Pt only catalyst structures. These electrochemical studies clearly indicate that the Pt/Pd bimetallic catalyst structures enhance formic acid electro-oxidation, allowing formic acid oxidation to occur at a lower anode overpotential, and thus increasing the cell potential at a given current density (Figure 7), similar to fuel cells developed with nafion ink catalysts [1]. The spontaneously deposited Pd structures on the electroplated Pt-black, therefore, gains the advantages of the Pt/Pd bimetallic catalyst, without the issue of requiring ink in the fabrication.

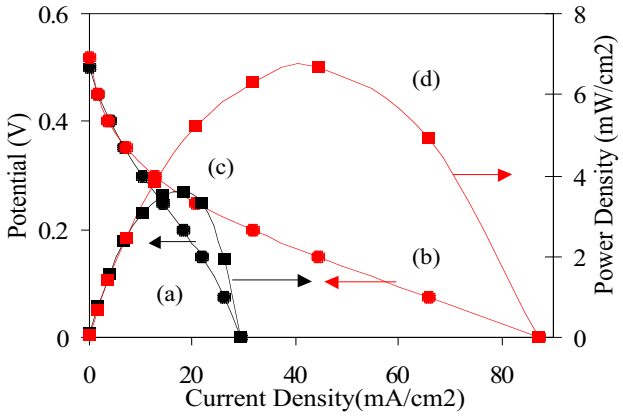

***Figure** 7. The I-V curves for silicon based fuel cells (a) without Pd and (b) with Pd are shown. Power density curves (c) without Pd, and (d) with Pd.*

CONCLUSIONS

Silicon based MEAs comprised of microfabricated grids with Pt or Pt/Pd catalysts structures show promise for application in microfuel cells. Unlike in traditional polymer electrolyte membrane fuel cells in which the catalyst is deposited as an ink, the morphology of the catalyst structures studied here can be precisely controlled by varying electrodeposition conditions. Electrochemical analysis shows that silicon-grid with Pt/Pd bimetallic catalyst structures increases the activity towards electro oxidation of formic acid by up to an order of magnitude over long times. In addition, the initial silicon-MEAs with Pt/Pd catalyst grids exhibit doubled power density in fuel cell testing. In sum, these silicon-MEAs show promise towards integrated, all-silicon microfuel cells.

ACKNOWLEDGEMENTS

The authors thank DARPA for financial support under U. S. Air Force Grant F33615-01-C-2172.

REFERENCES

1. C. Rice, S. Ha, R. I. Masel, P. Waszczuk, A. Wieckowski, and T. Barnard, "Direct formic acid fuel cells", *J. Power Sources, 111,* 83 (2002).
2. S. C. Kelley, G. A. Deluga, and W. H. Smyrl, "Miniature methanol/air polymer electrolyte fuel cell", *Electrochem. Solid-State Lett. , 3,* 407 (2000).
3. G. Z. Mozsgai, J. Yeom, A. Asthana, B. R. Flachsbart, P. Waszczuk, E. R. Choban, P. J. A. Kenis, and M. A. Shannon, "A Silicon Microfabricated Direct Formic Acid Fuel Cell", *First International Conference on Fuel Cell Science Engineering and Technology,* ASME, 4/21-23(2003), Rochester, (2003), 267.
4. G. Q. Lu, A. Crown, and A. Wieckowski, "Formic acid decomposition on polycrystalline platinum and palladized platinum electrodes", *J. Phys. Chem.,* 103, 9700 (1999).
5. J. Yeom, G. Z. Mozsgai, B. R. Flachsbart, A. Asthana, E. R. Choban, P. J. A. Kenis, and M. A. Shannon, "Fabrication and characterization of a silicon-based millimeter scale, microfabricated PEM fuel cell operating with gaseous hydrogen, methanol, or formic acid as fuels", *Manuscript in preparation.*
6. A. C. Hill, R. E. Patterson, J. P. Sefton, and M. R. Columbia, "Effect of Pb(II) on the morphology of platinum electrodeposited on highly oriented pyrolytic graphite", *Langmuir,* 15, 4005 (1999).
7. R. Boistelle, and J. P. Astier, *J. Cryst. Growth,* 90, 14 (1988).
8. M. Arenz, V. Stamenkovic, T. J. Schmidt, K. Wandelt, P. N. Ross, and N. M. Markovic, "The electro-oxidation of formic acid on Pt–Pd single crystal bimetallic surfaces", *Phys. Chem. Chem. Phys.* 5, 4242 (2003).
9. M. J. Llorca, J. M. Feliu, A. Aldaz, and J. Clavilier, "Formic acid oxidation on Pd_{ad} + Pt(100) and Pd_{ad} + Pt(111) electrodes", *J. Electroanal. Chem.,* 376, 151 (1994).

A ROBUST LOW-COST PDMS PERISTALTIC MICROPUMP WITH MAGNETIC DRIVE

Eleanor Kai[1], Tingrui Pan[1,2] and Babak Ziaie[1,2]
[1]Department of Electrical and Computer Engineering
[2]Department of Biomedical Engineering, University of Minnesota
Minneapolis, MN 55414

ABSTRACT

In this paper, we present a low-cost PDMS peristaltic micropump with magnetic drive. The fabrication process is based on soft molding and bonding of three PDMS layers. A base layer incorporates the microchannels while a middle actuating layer houses three miniature permanent magnets covered by a top flat layer. A small DC motor (6mm in diameter and 15mm in length) with three permanent magnets (NdFeB) stagger-mounted on its shaft is used to pull down and actuate the membrane-mounted magnets. A maximum flow rate of about 24μL/min at the speed of 4000rpm with power consumption of 14mW was demonstrated.

Keywords: Magnetic Drive, Microfluidics, Micropump, Peristaltic Pump, PDMS, Soft Lithography

INTRODUCTION

Micropumps play an important role in a wide variety of chemical and biological microsystems, such as drug delivery and microfluidic devices. Over the past decade, several different micropump designs have been developed. These include electroosmotic, nozzle-diffuser, positive displacement, and peristaltic [1-8]. Depending on the pumping liquid and required pumping rate and back pressure, various actuation mechanisms and fabrication techniques can be used. Elecroosmotic pumps have the advantage of high backpressures and simple designs, but require very high voltages and a charged liquid. The nozzle-diffuser pump design is likewise simple and easy to fabricate. Positive displacements pumps require a complex fabrication method for creating two check-valves and an actuating chamber. Several peristaltic pumps have also been demonstrated using various fabrication and actuation techniques such as thermopneumatic, piezoelectric, electrostatic, and magnetic. Piezoelectric drives require high voltages, whereas, for electrostatic actuation one needs to create small gaps complicating the fabrication process. Magnetic drives can provide large forces over extended displacements. However, one frequently needs to integrate microcoils and ferromagnetic materials.

In this paper, we report on the design, fabrication, and test of a simple low-cost PDMS peristaltic micropump with magnetic actuation. Figure 1 shows a perspective view of the PDMS micropump. It consists of three PDMS layers; the bottom one incorporates the microchannel while the middle layer houses three small permanent magnets loaded in small reservoirs separated from the microchannels by a thin PDMS layer (membrane). Finally, a top flat sheet covers the magnets and seals the middle layer. Positioning another set of three magnets at different phase angles on the rotor of a small DC motor creates the serial membrane actuation needed for a peristaltic pump. The polarity of adjacent magnets in the reservoir is reversed in order to prevent simultaneous actuation of two neighboring magnets. By varying the rotation speed the flow rate can be easily adjusted. The micropump has a small power consumption (<20 mW), mainly determined by the power requirements of the small DC motor.

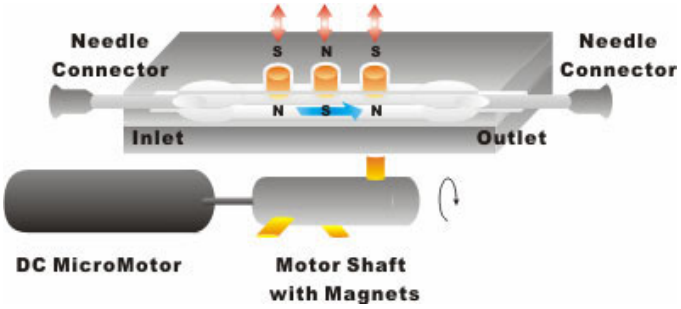

Figure 1. A perspective view of the PDMS micropump.

DESIGN AND FABRICATION

Figure 2 shows the expanded diagram of the micropump. Silicone elastomer (Ellsworth Adhesive, WI) is the only structure material used for the body of the pump. The first fabrication step is creating two separate molds, one for the microfluidic channel and one for the actuation membranes (middle layer). The top layer is a simple sheet and does not require any mold.

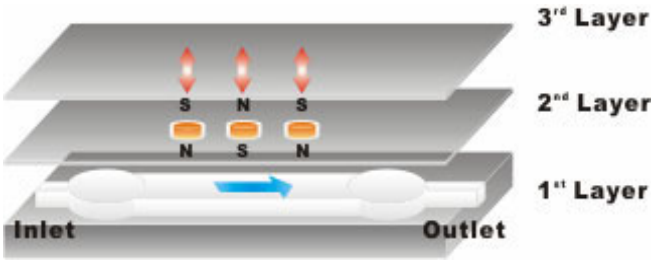

Figure 2. Expanded diagram of the micropump.

The design used in this paper, which is for 2mm square magnets, incorporates a 13mm x 3mm channel with 300µm x 8.5mm needle insertion points at both ends. The middle layer includes 300µm x 3mm x 6mm membranes on which three small magnets are attached. The membranes are spaces 1mm apart. Alignment marks were also added to assist in bonding the bottom and middle layers.

The mold for casting the PDMS was fabricated using SU-8 (2100, MicroChem Corp., MA). SU-8 was processed according to the recommended directions, but particular care was taken to keep its thickness as uniform as possible. Bubbles were found to form in the photoresist during spinning, but if these were punctured, the photoresist healed after sitting for 10 minutes. Due to the long required bake time, the wafers were rotated every 5 minutes. As an additional measure, the wafers were overexposed by 80mJ/cm^2 on top of the 550mJ/cm^2 recommended for the desired thickness (250µm) to prevent structures detaching from the wafer during development. The final molds were found to have a height variation of 200µm to 385µm across the wafers.

PDMS (Silgard 184, 10:1 ratio) was subsequently mixed and cast over the SU-8 mold. For the fluidic channel PDMS layer, 800µm spacers were used whereas for the actuation PDMS layer 650µm spacers were employed to ensure a membrane thickness of at least 250µm (thinner membranes were hard to release from the mold without tearing). Next a transparency was slowly placed on the uncured PDMS, taking care to not introduce bubbles into the film and a 2lb weight was placed on top of the mold and spacer to achieve the desired PDMS layer thickness [9]. This set up was heated to 100°C in an oven for 15 minutes to speed up the curing process. To prevent the SU-8 molds from cracking and buckling during this step, the oven had to be ramped up slowly from 55°C to 100°C before curing for 15 minutes and then ramped back down to 55°C. Immediately after curing, the two PDMS surfaces were exposed to the oxygen plasma (100W, 100mTorr for 30sec) and bonded by applying a pressure of 0.1MPa [9]. After bonding, the PDMS was heated to 200°C for 5 minutes to drive out moisture and strengthen the bond.

Magnets were marked (to indicate poles) and loaded into the membrane chambers. By varying the magnet polarity in adjunct chambers, the interference of magnet-actuated membrane motion is minimized. Finally, the magnets are encapsulated in the chambers by a top PDMS layer and 27 gauge needles are used to create the interface via the needle insertion points provided in the pump's design. Figure 3 shows a photograph of the peristaltic micropump loaded with magnets.

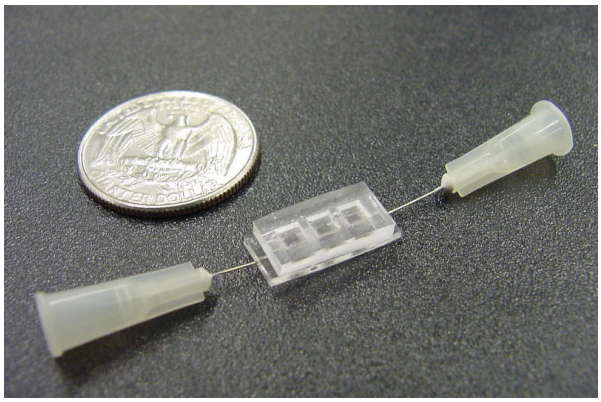

Figure 3. A photograph of the peristaltic micropump loaded with magnets.

EXPERIMENTAL SETUP AND RESULTS

Figure 4 shows the test and measurement setup. Three external NdFeB magnets stagger positioned (120^o separation) around the shaft of a 0615N4.5S DC coreless micromotor (MicroMo Electronics Inc., FL, 6mm diameter and 15mm length) are used to actuate the internal magnets (Flexible Sheet, ceramic ferrite magnetic powder with flexible thermoplastic binder, Dexter Magnetics). The separation between the external and internal magnets is 1mm. The external magnets are mounted on the shaft of the DC motor using Polyvinylsiloxane (Coltène Whaledent, OH) molded into a cylinder. The pump was placed on the surface of a plastic box that houses the micromotor. This provides an easy way to place the pump over the rotating magnets while protecting the micromotor from any accidental water damage. The pump was primed by water before performing the measurements.

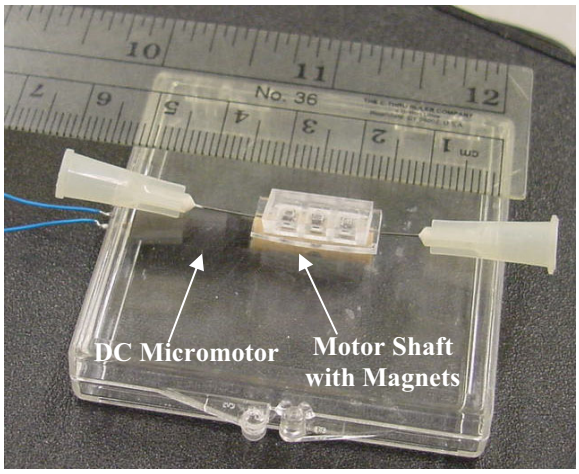

Figure 4. Test and measurement setup. The external magnets are positioned at different phase angles to generate a waveform channel membrane movement.

Pumping rate measurements were made at pump level by measuring the amount of water that entered the pump over a 15 minute time period using a 1mL syringe. Voltage and current measurements were also taken during this 15 minute time period. Motor speed can be roughly estimated using the speed constant given by the manufacturer (4727rpm/V). Figure 5 shows the pumping rate vs. the speed of the micromotor. As expected, at lower frequencies the flow rate follows an approximately linear relation to the rotation speed. However, at higher frequencies this relationship caps and eventually drops. This happens when the driving frequency approaches and exceeds the mechanical oscillation frequency of the structure (i.e., membrane) itself. Power consumption versus rotation speed was calculated from the current and voltage measurements, Figure 6. For this particular pump, a maximum flow rate of about 24μL/min at the speed 4000rpm with a power consumption of 14mW was obtained. The micropump power consumption is rather low compared to other reported pumps most having power consumptions of > 100mW. An additional advantage of our pump is its low operating voltage (< 1V) making it suitable for portable battery powered applications.

We also conducted several tests to measure the pumping backpressure. For these measurements, the inlet needle was connected to a reservoir of water via a primed tube while the outlet needle was connected to a tube raised to various heights. A graph of pumping backpressure versus rotation speed is shown in Figure 7. As can be seen, the backpressure is rather low. This is due to the back flow associated with the incomplete closure of the microchannel by the actuating membrane. This can be remedied by a modified design using a stronger magnet and a better alignment. As mentioned previously, although the external magnets were NdFeB, the internal ones were of lower strength magnetic flexible sheets. This was chosen to simplify the loading process. Using SmCo or NdFeB internal magnets will increase the flow rate and backpressure. This, however, has to be done by changing the design to allow for tighter holding chambers in order to restraint the strong attraction of the internal magnets during the loading process. Figure 8 shows an improved design allowing the usage of stronger internal magnets. As can be seen, four layers are used in this design with the bottom layer again serving as the microfluidic channel. A flat PDMS sheet will serve as the membrane whereas another layer with cylindrical holes will be used to hold and restrain the magnets. A top layer will be used to seal the device as was in the case for the described micropump.

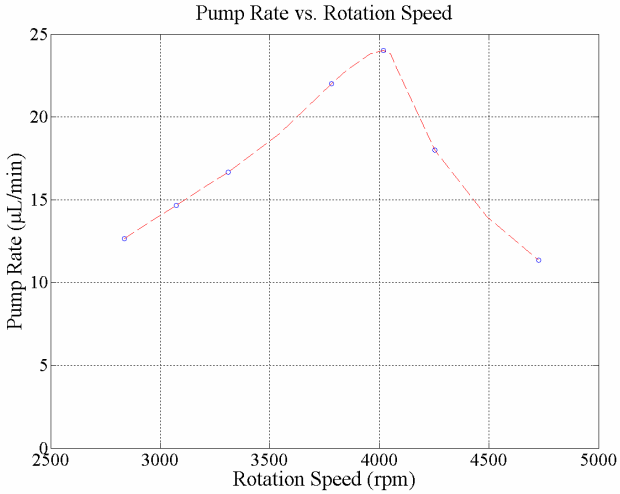

Figure 5. Pumping rate vs. motor rotation speed.

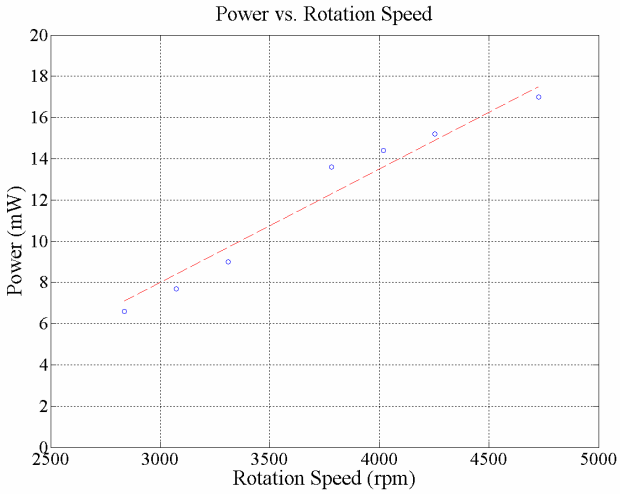

Figure 6. Power consumption vs. motor rotation speed.

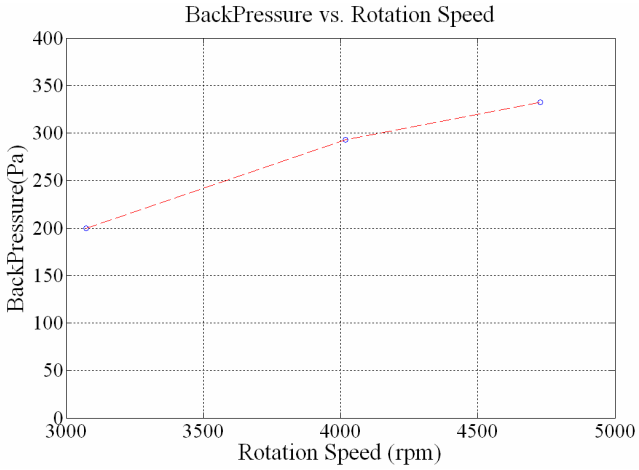

Figure 7. Pumping backpressure vs. motor rotation speed.

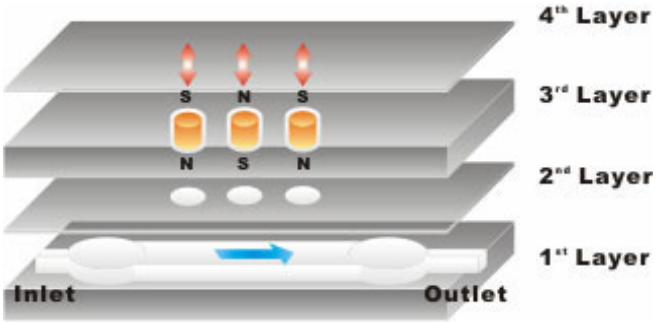

Figure 8. Improved design for higher backpressures and pumping rates.

CONCLUSIONS AND FUTURE WORK

In this paper, we reported a low-cost peristaltic PDMS micropump with a magnetic drive. The pump is fabricated using three PDMS layers. Actuation is achieved using three external magnets attached to a micromotor pulling down three internal magnets loaded in small reservoirs and separted from the microchannel by a thin membrane. The maximum pump rate was found to be 24μL/min with a maximum backpressure of 300Pa. The power consumption at this pumping rate is 14mW which is one of the lowest reported in the literature. Future work includes design improvements and optimizations to achieve higher backpressures and flow rates.

ACKNOWLEDGEMENT

The authors would like to thank Mr. Scott McDonald and Mr. Woohyek Choi for their help with fabricating the device. We also would like to thank Mr. Kevin Roberts for helping to dice the magnets.

REFERENCES

[1] D. J. Laser, A. M. Myers, S. Yao, K. F. Bell, K. E. Goodson, J. G. Santiago, T. W. Kenny, "Silicon Electroosmotic Micropumps for Integrated Circuit Thermal Management", *IEEE Transducers Conference 2003*, Boston, MA, pp. 151-154, 2003.

[2] A. Olsson, P. Enoksson, G. Stemme, E. Stemme, "Micromachined Flat-Walled Valveless Diffuser Pumps", *Journal of Microelectromech. Systems*, vol. 6 (2), pp. 161-166, 1997.

[3] J.-H. Tsai and L. Lin, "A Thermal-Bubble-Actuated Micronozzle-Diffuser Pump", *Journal of Microelectromech. Systems*, vol. 11 (6), pp. 665-671, 2002.

[4] M. Khoo and C. Liu, "A Novel Micromachined Magnetic Membrane Microfluid Pump", *IEEE EMBS International Conference 2000*, Chicago, IL, pp. 2394-2397, 2000.

[5] F. C. M. van de Pol, H. T. G. van Lintel, M. Elvenspoek, and J. H. J. Fluitman, "A Thermopneumatic Micropump Based on Microengineering Techniques, " Sensors and Actuators A, Vol. 21-23, pp. 198-202, 1990.

[6] C. Grosjean and Y.-C. Tai, "A Thermopneumatic Peristaltic Micropump", *IEEE Transducers Conference 1999*, Sentai, Korea, pp. 1776-1779, 1999.

[7] L. Cao, S. Mantell, D. Polla, "Implantable Medical Drug Delivery Systems using Microelectromechanical Systems Technology", *Conf. on Microtech. in Medicine and Biology, 2000*, Lyon, France, pp. 487-490, 2000.

[8] S. Na, S. Ridgeway, and L. Cao, "Theoretical and Experimental Study of Fluid Behavior of a Peristaltic Micropump", *IEEE Microelectronics Symposium, 2003,* Boise, ID, pp. 312-316, 2003.

[9] B. H. Jo, L. M. Van Lerberghe, K. M. Motsegood, D. J. Beebe, "Three-Dimensional Micro-Channel Fabrication in Polydimethylsiloxane (PDMS) Elastomer", *Journal of Microelectromech. Systems*, vol. 9 (1), pp. 76-81, 2000.

Controlled Vesicle Self-Assembly in Continuous Two Phase Flow Microfluidic Channels

Andreas Jahn, Wyatt N. Vreeland, Laurie E. Locascio, Michael Gaitan
Semiconductor Electronics Division and Analytical Chemistry Division
National Institute of Standards and Technology
Gaithersburg, MD 20899

ABSTRACT

This paper describes a method to form monodisperse populations of liposomes in a continuous 2-phase flow microfluidic network with precision control of their size from 100 nm to 300 nm by manipulation of the fluid flow rates. We demonstrate that water-soluble reagents can be encapsulated in the liposomes enabling formulations for therapeutic or drug delivery applications. We conclude that by creating a solvent-aqueous interfacial region in a microfluidic format that is homogenous and controllable on the length scale of a nanoparticle self-assembly process, we can facilitate the fine control of its size and polydispersity.

INTRODUCTION

Liposomes [**1**] are one example of nanoparticles that have been used for a wide variety of medical applications including targeted drug delivery and DNA transfection [**2,3**]. Liposomes are cellular mimetics composed of a lipid bilayer membrane that encapsulates and sequesters species inside from species residing outside the membrane. Traditional liposome preparation methods [**4,5,6,7,8,9,10,11,12,13**] are all conducted through mixing of bulk phases, leading to inhomogeneous chemical and/or mechanical conditions during liposome formation; hence liposomes are often polydisperse in size and lamellarity. Liposome size and size distribution are important for *in vivo* applications where size ultimately determines drug dosage. The traditional methods to formulate liposomes require additional steps such as membrane extrusion or sonication in order to yield the desired homogeneous liposome populations. Methods that can control liposome size during formation without the need for additional steps would be of great benefit. Here we report on a method that shows promise towards this goal.

METHOD

In our approach to liposome formation, we employ the laminar characteristics of fluidic flow in a micrometer-scale channel to precisely control the distribution of chemical conditions and mechanical forces so that they are constant on a length scale equivalent to that of the liposome. We find that forming liposomes in a micrometer-scale flow field results in more homogenous conditions during liposome self-assembly and the resultant liposome populations are more uniform in size, and hence of low polydispersity. A schematic diagram of the microfluidic device is shown in Figure 1. We hydrodynamically focus [**14**] an isopropyl alcohol solution containing dissolved phospholipids [**15**] (center inlet channel) at a microchannel cross-junction between two aqueous buffer streams (side inlet channels).

When the lipid solution comes into contact with the aqueous solution, the isopropyl alcohol rapidly diffuses into the aqueous phase and *vice versa*. Diffusive mixing typically requires a

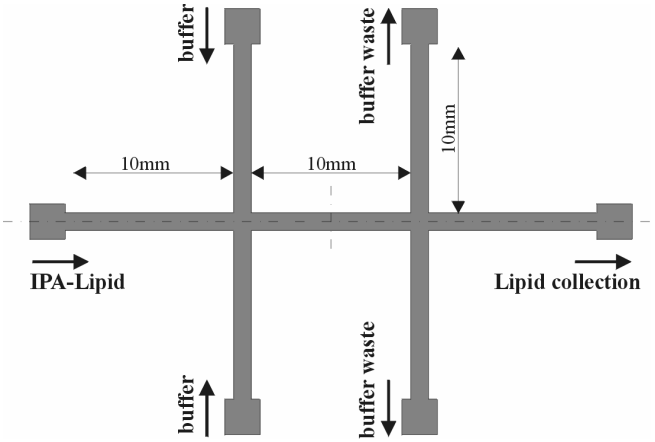

Figure 1. *Schematic microchannel design with corresponding fluid flows; microchannels have trapezoidal cross-section; maximum width is 200 μm, minimum width is 146 μm and depth is 40 μm.*

substantial amount of time and space to complete. However, fast mixing can be obtained by reducing the length scale over which the fluid must diffusively mix by hydrodynamically focusing the injection stream. The flow rates of the isopropyl alcohol and buffer channels are adjusted to control the degree of hydrodynamic focusing, which affects the chemical and mechanical conditions at the lipid-buffer interface and ultimately the liposome size. The lipids assemble into liposomes when the alcohol is diluted to a concentration where lipids are no longer soluble. The focusing stream width can be controlled by varying the flow ratios between the sample and buffer, as can be seen in Figure 2.

Immediately downstream of the first cross intersection, the fluorescent intensity of the center stream containing phospholipids increases sharply indicating the formation of the lipids into liposomes. This effect is due to an increased quantum efficiency of the fluorescent dye used in this experiment ($DiIC_{18}$) upon incorporation into a lipid membrane. This effect is most dramatically illustrated in Figure 3.

After the formation process is completed at the fist cross intersection, the liposomes continue to flow along the stream to the second cross intersection in a tightly focused stream, owing to the low Reynold's number laminar flow typical of microfluidics and their comparatively low diffusion coefficient. At this second cross intersection, excess buffer is removed via the two side outlet channels and the liposome suspension is collected via the center outlet channel. The liposomes form (as demonstrated by increased fluorescence of the $DiIC_{18}$) along the boundary between the isopropyl alcohol and water. At all flow rates tested, a ridge of increased fluorescence is clearly visible as the aqueous streams focus the isopropyl alcohol solution. Fluorescence intensity increases to its maximum value immediately downstream of the minimum width of the isopropyl alcohol stream indicating the highest concentration of liposomes.

0-9640024-5-0/hh2004/$20©2004TRF
DOI 10.31438/trf.hh2004.72

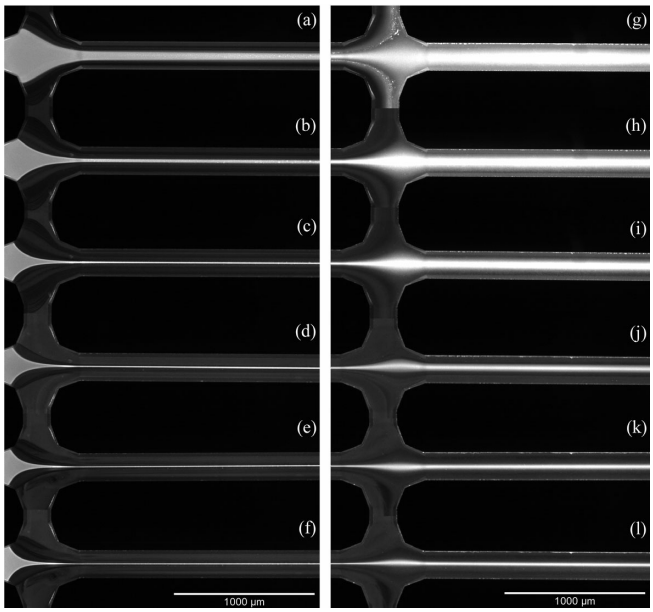

Figure 2. *Fluorescent images of $DiIC_{18}$ in IPA-lipid mixture at different flow ratios; (a)-(f) shows the focusing of IPA at the first intersection at different volumetric flow rates. IPA-lipid mixture fed in from the left into the middle channel at constant volumetric flow rate of 0.7 µl min^{-1}; PBS is fed in from the side inlets at volumetric flow rates of (a) 1, (b) 5, (c) 10, (d) 15, (e) 20 and (f) 25 µl min^{-1}, respectively; images (g)-(l) show the variation of the IPA-lipid stream at the second intersection at the flow rates according to (a)-(f). The silicon/glass microchannels have trapezoidal cross sections with the following dimensions: depth = 40 µm, maximum width = 200 µm, minimum width = 146 µm.*

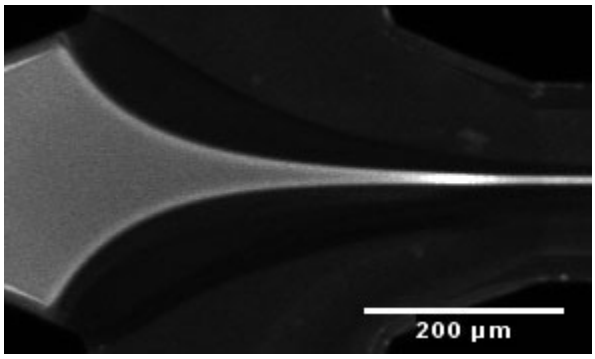

Figure 3. *Magnified view of the injection stream of Figure 2d showing increased fluorescence of the $DiIC_{18}$ due to its increased quantum efficiency upon incorporation into a lipid membrane.*

DEVICE FABRICATION

The device consists of a silicon wafer containing the microfluidic structures, a borofloat glass wafer (BSG) to seal the microchannels and fluidic connectors to inject fluid through

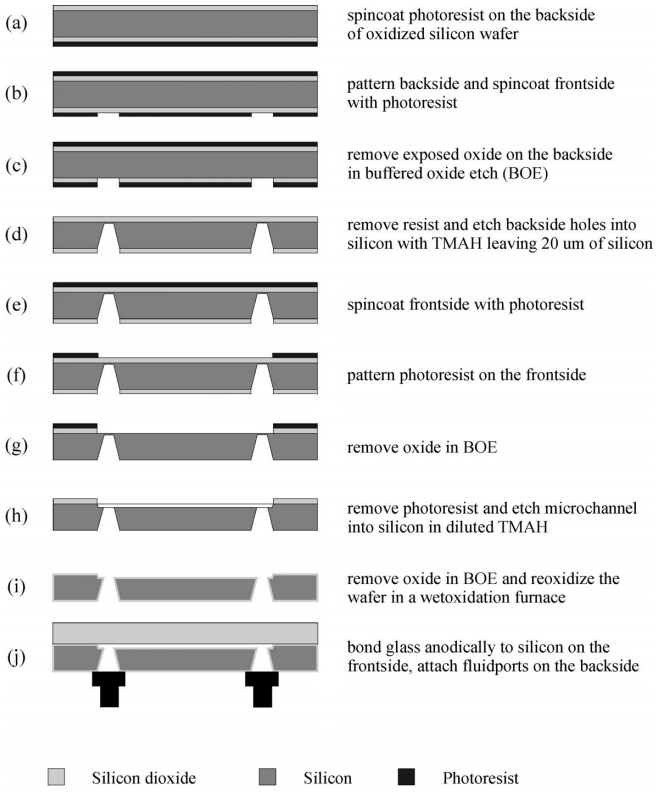

Figure 4. *Fabrication process flow; drawing not to scale.*

syringes via PEEK capillary tubing. Figure 4 shows the details of the fabrication process flow.

A layer of 1.3 µm thick positive resist (MicroChem S1813) is spin-coated and patterned on the back side of an oxidized silicon wafer followed by an HF dip to pattern the exposed oxide. Fluidic through-holes are then partially etched anisotropically through the back side using 2:1 mixture of H_2O and 25% tetramethylammoniumhydroxide (TMAH) heated to 80 ºC leaving a thin silicon membrane of approximately 20 µm thickness. Afterwards, the oxide on the front side of the silicon wafer is patterned with a microfluidic network of 200 µm wide and 40 µm deep microchannels that are anisotropically etched using the same TMAH process. The oxide is removed completely and the wafer reoxidized to form a homogenous surface for the following anodic bonding process.

Prior to bonding, the glass wafer (75 mm diameter, 0.1 mm thick, Corning Pyrex 7740) and the silicon wafer are thoroughly cleaned and dehydrated to ensure intimate contact between the wafers. The wafers are then anodically bonded at 400 ºC for 60 min with a ramp rate of 25 ºC min^{-1} and a bonding voltage of 800 V. The thermal expansion coefficient (TEC) of borofloat glass (BSG) is well matched to that of silicon below 400 ºC which greatly reduces the stress of the microchannel network device.

We use fluidic nanoports (F-124S, Upchurch Scientific, USA) for our fluidic connections between capillary tubing and the microchannel network in order to minimize volume to the fluid path. The nanoports are bonded to the backside of the silicon wafer using adhesive rings that are provided with the nanoports by clamping them to the wafer between two metal plates and curing them in a convection oven at 121 ºC for 90 min. PEEK™ capillary tubes deliver the fluid from glass syringes to the microchannel network.

EXPERIMENTAL DETAILS

Reagent transfers were obtained using gastight syringes interfaced to the microchannel network through capillary tubing (PEEK Tubing, Upchurch Scientific) and capillary connectors (Nanoports, Upchurch Scientific) that were bonded to the fluid through-holes etched in the silicon wafer. Two programmable high accuracy syringe pumps PHD 2000 from Harvard Apparatus were used to inject sample and buffer solution into the microchannel. A Labview software interface ensured the precise control of the sample and buffer flowrates. Sample consumption of the lipid solution was on the order of 5-15 nl s^{-1} and experiments were performed with as little sample as 100 µl.

Dimyristoylphosphatidylcholine (DMPC) and cholesterol in a molar ratio of 1:1 were diluted in chloroform (all from Aldrich) with 1 wt% of 1,1'-dioctadecyl-3,3,3',3'-tetramethilindocarbocyanine perchlorate ($DiIC_{18}$) added for fluorescent imaging. The chloroform solvent was evaporated under a stream of nitrogen at room temperature to form a lipid film on the bottom of a test tube. The test tube was then placed in a vacuum desiccator for at least 24 h to ensure dryness. The dried lipid mixture was resolubilized with 500 µl dry isopropyl alcohol yielding a 10 mM concentration of lipid solution. Phosphate buffered saline solution (10 mM phosphate, 27 mM potassium chloride, 137 mM sodium chloride, pH = 7.4) was used as a hydration buffer. To demonstrate the encapsulation process, a fluorescent dye, carboxyfluorescein (CF), was incorporated into the buffer stream at a concentration of 1 mM. Upon formation of the liposomes at the interface between isopropyl alcohol and buffer solution, the liposomes encapsulated a discrete volume of buffer, and with that entrapped dissolved CF. The liposome formulations were collected at each flow condition in polycarbonate cuvets. After collection, phosphate buffered saline solution (10 mM) was added to each formulation and sealed for further characterization.

The flow profile in the microchannel were imaged with a fluorescence microscope (Axioplan 2, Carl Zeiss, Thornwood, NY, USA) using a halogen lamp as an excitation source with appropriate filters for excitation and detection of $DiIC_{18}$ (excitation 540 nm ± 12.5 nm; beam splitter 565 nm; emission 605 ± 27.5 nm) and carboxyfluorescein (excitation 470 nm ± 20 nm; beam splitter 510 nm; emission 515 nm) and digitalized using a high sensitivity Hamamatsu Photonics Orca-ER CCD camera.

The size of the liposomes were determined at 21 ºC by quasi elastic light scattering (QELS) with a Nanosizer (Coulter® N4MD, Coulter Electronics, USA). Samples containing 100-200 µl of liposome solutions were collected in polycarbonate cuvets at the lipid collection port of the microchannel and diluted with 1 mL of 10 mM buffered saline solution. The cuvets were then placed into the sample compartment of the light scattering device. Five measurements were taken and averaged for each sample (Figure 5).

Cryo transmission electron microscopy (Cryo-TEM) involves the examination of a vitrified hydrated sample directly on a cryo stage in the TEM. Five microliter drops of liposome suspensions were placed on 1000-mesh copper EM grid. Specimens were frozen by clamping each grid into spring-loaded forceps of a Leica KF80 freezing machine. The grid was blotted with filter paper to leave a thin film of liposome suspension just prior to plunging the grid into liquid ethane cooled to -180 ºC by liquid nitrogen. The frozen grid was then loaded under liquid nitrogen into a Gatan model 626 specimen holder and cryotransferred into an FEI CM120 transmission electron microscope (Philips) equipped with Gatan anticontaminator blades. Suitably thin specimen regions were imaged at a beam voltage of 120 kV and at an electron dose of less than 1000 electrons per square nanometer using a Gatan GIF100 post-column imaging filter equipped with a 1024x1024 pixel cooled CCD camera. Contrast was enhanced by energy-filtering the transmitted electrons and by underfocusing the objective lens to about 500 nm.

The main advantage here is that no other preparation is necessary, and the presence of unwanted ice crystals is easily detected. The liposome diameter of approximately 100 nm observed with the cryo-TEM (Figure 6) was in agreement with that determined by quasi-elastic light scattering (95 nm ± 30 nm).

flow ratio /1/	mean diameter /nm/	1σ /nm/
2	233	68
10	207	46
20	150	40
30	106	28
40	100	20

Figure 5. *Liposome size and standard deviation (σ) vs. different flow ratios. IPA-Lipid mixture is injected at a constant volumetric flowrate of 1.0 µl* min^{-1}*. Flow ratio is defined as the center flowrate to the total aqueous flowrate from the two side channels.*

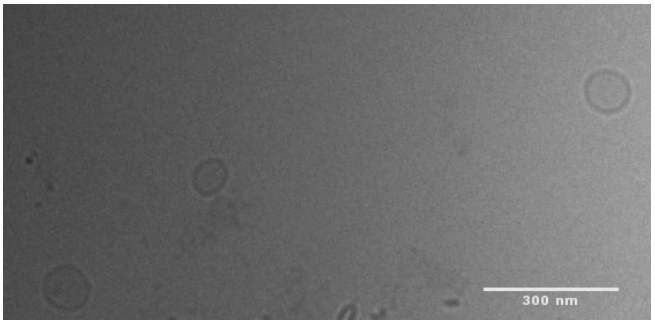

Figure 6. *Cryo-TEM of unilamellar liposomes at 120 kV beam voltage and less than 1000 electrons per square nanometer electron dose. The image shows unilamellar liposomes produced by this method.*

CONCLUSION

By changing the length scale of the fluidics in which lipids self-assemble into liposomes and simultaneously manipulating both the length scale and the shear forces applied to the vesicles upon formation, we have achieved fine control of liposome size and homogeneity. Microfluidics allows us to adjust the flow fields precisely using the simple principle of hydrodynamic focusing. We anticipate that this method could be used to manufacture liposome formulations on demand and thus avoid issues of poor shelf life that have been problematic with other processes.

ACKNOWLEDGEMENTS

We gratefully acknowledge Dr. M. Richter of the Fraunhofer Institute IZM for supporting the guest researcher opportunity for A.J. at NIST. We also acknowledge the NIST/NRC Postdoctoral

Associate Program for support of W.N.V. and funding from the NIST Director's Single Molecule Manipulation and Measurement Program. We also acknowledge Dr. Richard Leapman at NIH for his support with the cryo transmission electron microscopy imaging.

REFERENCES

1. A. D. Bangham, M. M. Standish, J. C. Watkins, "Diffusion of Univalent Ions Across the Lamellae of Swollen Phospholipids", *J. Mol. Biol.* **13**, 238-253 (1965).
2. G. Gregoriadis, "Liposome Technology Volume 3; Targeted Drug Delivery and Biological Interactions", (CRC Press, Boca Raton, 1983).
3. D. D. Lasic, D. Papahadjopoulos, "Liposomes Revisited", *Science* **267**, 1275-1276 (1995).
4. G. Gregoriadis, H. da Silva, A. T. Florence, "A Procedure for the Efficient Entrapment of Drugs in Dehydrationrehydration Liposomes (DRVs)", *Int. J. Pharm.* **65**, 235-242 (1990).
5. F. C. Szoka, D. Papahadjopoulos, "Procedure for Preparation of Liposomes with Large Internal Aqueous Space and High Capture by Reverse Phase Evaporation", *Proc. Natl. Acad. Sci. U.S.A.* **75**, 4194-4198 (1978).
6. C. Pidgeon, S. McNeely, T. Schmidt, "Multilayered Vesicles Prepared by Reverse Phase Evaporation: Liposome Structure and Optimum Solute Entrapment", *Biochemistry* **26**, 17-29 (1987).
7. H. Hauser, "The Effect of Ultrasonic Irradiation on the Chemical Structure of Egg Lecithin", *Biochim. Biophys. Res. Commun*. **45**, 1049-1055 (1971).
8. S. Batzri, E. D. Korn, "Single Bilayer Liposomes Prepared without Sonication", *Biochem. Biophys. Acta.* **298**, 1015-1019 (1973).
9. T. H. Fischer, D. D. Lasic, " A Detergent Depletion Technique for the Preparation of Small Vesicles", *Mol. Cryst. Liq. Cryst. Lett.* **102**, 141-145 (1984).
10. H. Kikuchi, H. Yamauchi, S. Hirota, "A Spray-Drying Method for Mass-Production of Liposomes", *Chem. Pharm. Bull*. **39**, 1522-1527(1991).
11. A. Wagner, K. Uhl-Vorauer, G. Kreismayer, "The Crossflow Injection Technique - an Improvement of the Ethanol Injection Method", *J. Lip. Res*. **12**, 259-270 (2002).
12. T. S. Aurora, W. Li, H. Z. Cummins, "Preparation and Characterization of Monodisperse Unilamellar Phospholipid Vesicles with Selected Diameters from 300 to 600 nm", *Biochimica et Biophysica Acta* **820**, 250-258 (1985).
13. P. L. Luisi, P. Walde, "Giant Vesicles", (John Wiley & Sons, Chichester, 2000).
14. J. B. Knight, A. Vishwanath, J. P. Brody, J. P., R. H. Austin, "Hydrodynamic Focusing on a Silicon Chip: Mixing Nanoliters in Microseconds", *Phys. Rev. Lett.* **80** (17), 3863-3866 (1998).
15. L. Locascio-Brown, A. L. Plant, V. Horvath, "Liposome Flow Injection Immunoassay: Implications for Sensitivity, Dynamic Range, and Antibody Regeneration", *Anal. Chem*. **62**, 2587-2593 (1990).

A REMOTELY ADJUSTABLE MICROMACHINED CHECK-VALVE WITH A VARIABLE LENGTH CANTILEVER-BEAM STRUCTURE FOR IMPLANTABLE BIOMEDICAL MICROSYSTEMS

Tingrui Pan and Babak Ziaie
Department of Electrical and Computer Engineering
Department of Biomedical Engineering, University of Minnesota
Minneapolis, MN 55455

ABSTRACT

In this paper, we present a remotely adjustable micromachined check-valve with a variable length cantilever-beam structure for implantable biomedical microsystems. The adjustable cantilever-beam structure is fabricated by gold thermo-compression bond of a thin silicon wafer over a glass substrate. The evaporated gold forms anchors on the silicon and strips on the glass substrate. Electrochemical dissolution of gold anchors and strips by a constant DC current (obtained via a telemetry link) is used to adjust the microfluidic characteristics of the valve (opening pressure and flow rate). The anchor pads are 10x10μm^2 in size with 10μm separation while strips are 50μm wide and 1.5mm long. A current density of 35mA/cm^2 resulted in the release of gold anchors in 2 minutes with gold strips completely removed in 10 minutes.

Keywords: Electrochemical Release, Implantable Biomedical Microsystem, Microfluidics, Microvalve, Thermo-Compression Bonding

INTRODUCTION

Micromachined passive check-valves play an important role in a wide variety of implantable biomedical microsystems (e.g., drug delivery and therapeutic pressure relief devices) [1, 2]. In many applications, it is highly desirable to be able to remotely vary the opening pressure set-point over a period of time. For example, glaucoma drainage devices incorporate a passive check valve to reduce the intraocular pressure (IOP) [3]. The ability to remotely change the set-point after surgery provides surgeons more flexibility in regulating the IOP [2, 3]. We previously reported an adjustable SU-8 micromachined check-valve array based on electrochemical dissolution of gold membrane [2]. In this paper, we report on an alternative approach using a variable length cantilever-beam structure. Figure 1 shows a perspective view of the microvalve along with its fluidic schematic. It consists of a silicon cantilever beam bonded to a glass bottom plate containing an ultrasonically drilled inlet hole. The bonding is done using gold thermo-compression technique over selected areas defined by an array of gold anchor pads on the silicon substrate and thin gold strips on the glass substrate. The gold anchors and strips define various lengths and hence opening pressures for the valve. The strips can be electrochemically removed in sequence, lowering the opening pressure accordingly.

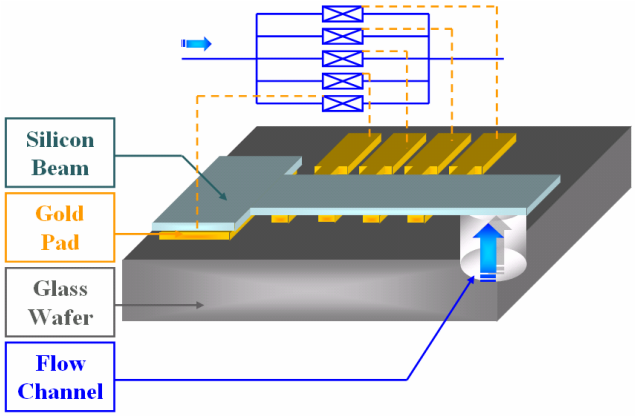

Figure 1. A perspective view of the microvalve along with its fluidic schematic.

DESIGN AND FABRICATION

Figure 2 shows the fabrication sequence. The silicon substrate fabrication process starts with a thermal oxidation step of a thin silicon substrate (200μm thick). A 0.5μm silicon dioxide is grown to prevent silicon diffusion during thermo-compression bond [4]; this also serves as an isolation layer during the electrochemical dissolution. The backside oxide layer is patterned for the final etching step. A Ti/Au (10nm/1.0μm) bonding layer is then deposited by electron beam evaporation and patterned on the silicon wafer by lift-off process to create an array of gold bonding pads. The glass fabrication process starts with the deposition and patterning of the Ti/Au (10nm/1.0μm) bonding strips on a Pyrex 7740 glass substrate. A flow channel of 600μm in diameter is then ultrasonically drilled on the glass substrate. The bonding surfaces of the two substrates are exposed to oxygen plasma for 5 minutes to completely remove organic remains before wafer alignment. During the alignment process of two substrates, three spacers and three clamps on a bonder fixture are loaded consequentially to separate the wafers and hold them in position. The gold-to-gold thermo-compression is carried out in Karl Suss SB6 VAC bonder (Suss MicroTec, Germany) under atmospheric pressure. Following the withdrawal of the clamps, the temperature is ramped up and stabilized at 350°C for 30 minutes, 0.01MPa pressure was applied over the wafer and then spacers are withdrawn.

Travel support has been generously provided by the Transducers Research Foundation and by the DARPA MEMS and DARPA BioFlips programs.

Then a bonding pressure of 0.1MPa is applied across the two substrates for 15 minutes (corresponding to 5MPa of pressure on the gold anchor pads). Afterwards, the temperature is ramped down slowly [4]. To machine the silicon substrate into a cantilever shape, we use deep reactive ion etch (DRIE) from the backside of the silicon wafer. Finally, the devices are diced and separated into individual 8x8mm^2 chips. The overall size is compatible with the currently implanted glaucoma drainage devices, *e.g.*, Ahmed glaucoma valve (which is the most widely used implantable devices) is 13mm wide, 16mm long, and 2mm thick.

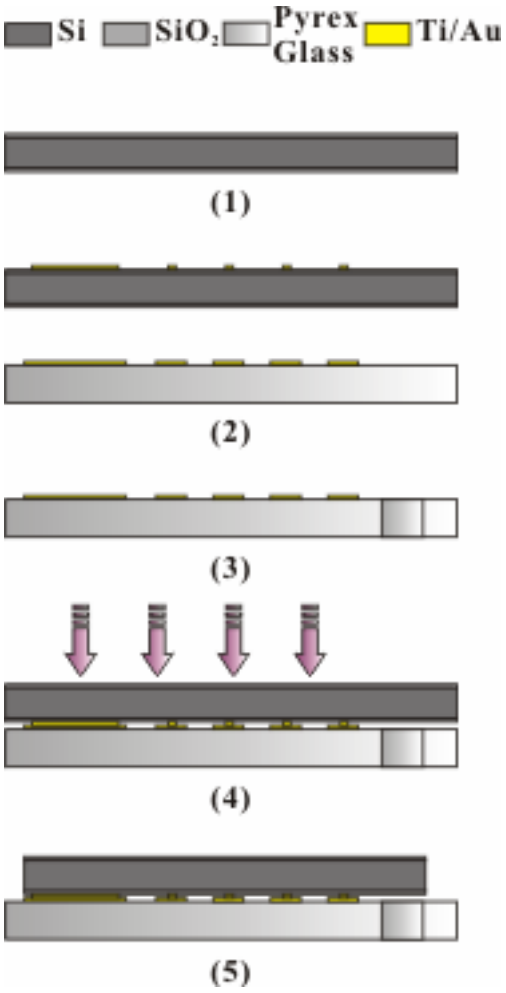

Figure 2. Fabrication process includes: (1) thermal oxidation of silicon wafer; (2) e-beam evaporation and patterning of Ti/Au; (3) ultrasonic drilling of the flow channel; (4) thermo-compression bonding of Si-Glass; (5) DRIE Si from the backside followed by wafer dicing.

The release and activation mechanism is based on the electrochemical etching of gold anchors. Gold is a biocompatible metal and its ionic compounds have many medical applications (e.g., Au^{I} salts used for treatment of rheumatoid arthritis). It has also been shown that one can dissolve gold in a saline solution by applying + (0.8~1.2) volts (with respect to a saturated calomel reference electrode). Gold dissolution occurs through the formation of water-soluble chloro-gold III complexes (Au^{III}) [5, 6]. An array of 10x10µm^2 gold anchor pads with 10µm separation is used in our design. On the glass substrate, the gold pattern is a continuous narrow strip of 50µm wide connected to the outside pads. Figure 3 shows photographs of the front and the backside of the adjustable micromachined check-valve.

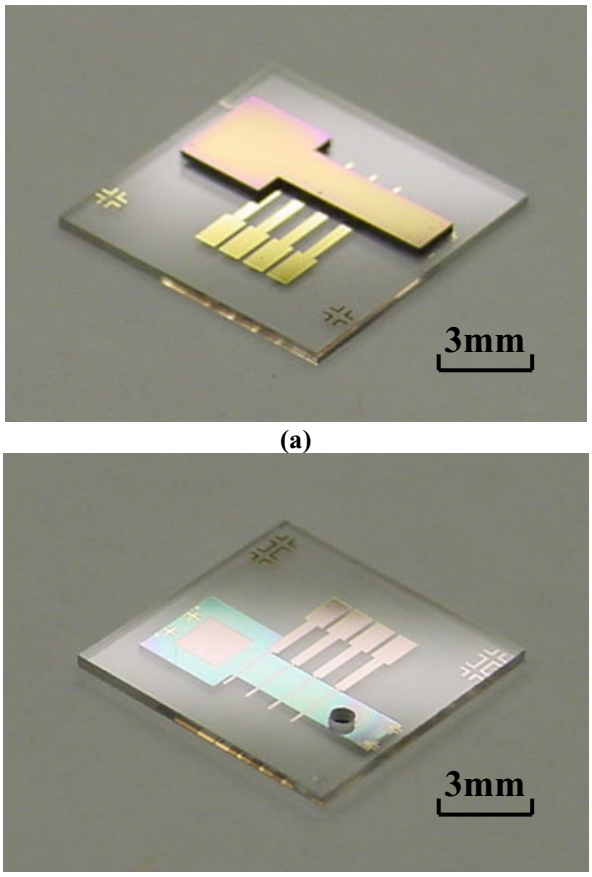

Figure 3. Photographs of (a) the front view and (b) the backside view of the adjustable micromachined check-valve.

EXPERIMENTAL SETUP AND RESULTS

As was mentioned previously, in our design, electrochemical dissolution of gold anchors is used to adjust the length of the cantilever beam, and therefore change the fluidic characterization of the microvalve. This is accomplished by a constant DC current obtained via a telemetry link. Figure 4 shows the test and measurement setup. For present experiments, we are using surface mount devices (SMD) to implement the receiver circuitry with a CMOS integrated version currently under design and fabrication. An AC source (4MHz, 20V_{p-p}) is used to inductively power a receiver. The received voltage is used to generate a constant current for the electrochemical dissolution. The receiver circuitry consists of a LC tank, a full wave rectifier (RH02 DICT-ND, Diodes Inc.) followed

by a capacitive filter and an adjustable current source (LM334M-ND, National Semiconductor). A current density of 35mA/cm^2 resulted in a release of gold anchors in 2 minutes and gold strips are completely removed in 10 minutes. Figure 5 shows microscopic photographs of the valve gold strips before and after complete release.

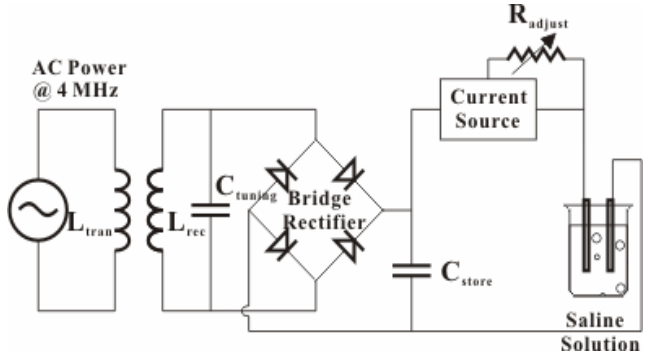

Figure 4. Schematic of the telemetry experimental setup and receiver circuitry.

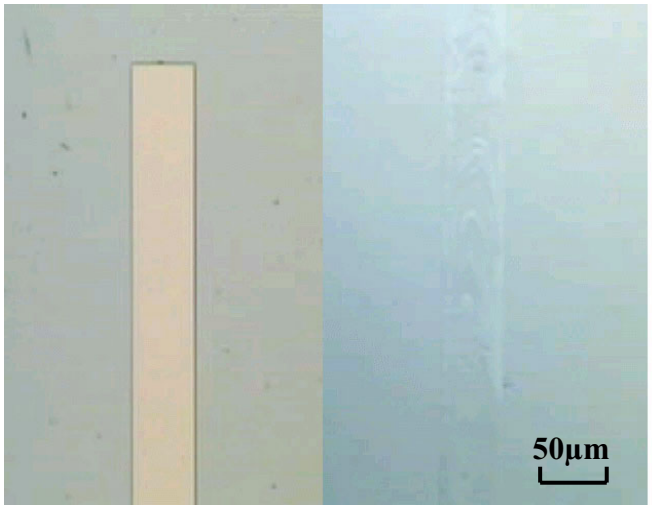

(a) **(b)**

Figure 5. Microscopic photographs of a gold strip on the valve (a) before and (b) after release.

Both gravity and syringe-pump driven flow were used to characterize the valve performance [7]. These can be easily achieved by using the following setup shown in Figure 6. The setup consists of a syringe pump (KDS Inc.) connected to a glass standpipe (1.1 mm ID) or a pressure sensor via a 3-way stopcock. The third outlet is connected to the valve through a silastic tubing. All tests are carried out at the atmosphric pressure and room temperature.

In the gravity-driven flow tests, the branch connected to the syringe pump is closed and the valve is subjected to the gravitational force of the fluid head, which forces the valve open and drains the fluid out until the gravitational head is reduced to the level at which the valve is closed. The flow rate through the device can be calculated as

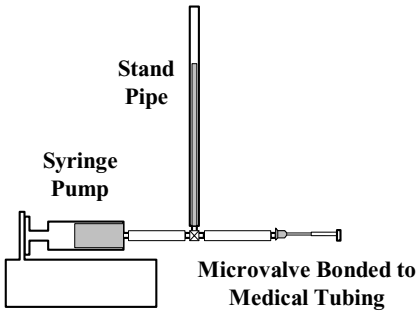

Figure 6. Schematic of *in vitro* microfluidic test setup.

$$Q = A\,dh/dt \qquad (1)$$

where A is the cross-section area of the standpipe and h is the height of the fluid in it. The flow resistance, defined by the pressure drop P over the flow rate Q, can be obtained from

$$R = \frac{P}{Q} = \frac{P}{A\,dh/dt} \qquad (2)$$

This configuration allows the flow resistance to be measured over a wide range of flow rates. Figure 7 shows the measurement results of the pressure head (left) and flow resistance (right) vs. flow rate of a microvalve with the cantilever flap having a width of 1.5mm and a length of 4mm. As expected, the valve exhibits nonlinear fluidic behavior due to the pressure response of the cantilever beam structure, *i.e.*, the higher the pressure, the larger the displacement of valve flap, and therefore the much larger the flow rate and smaller the flow resistance. Figure 7 also indicates a closing pressure of 7mmHg.

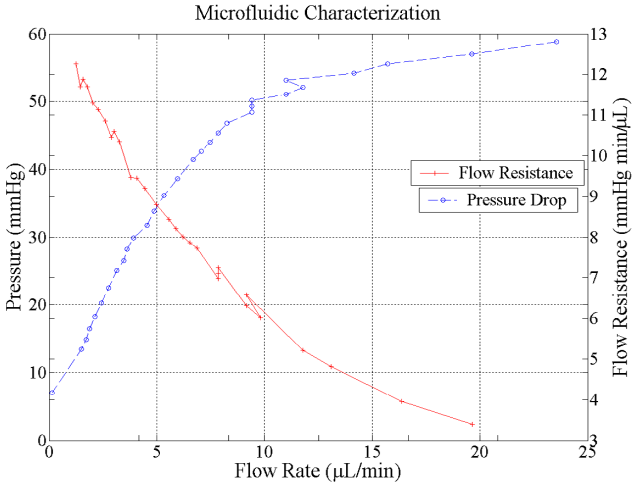

Figure 7. The measurement results of the pressure head (left) and flow resistance (right) vs. flow rate of a microvalve with the cantilever flap having a width of 1.5mm and a length of 4mm.

In the syringe-pump driven tests, the syringe pump provides a constant flow rate and pressure variation across the valve is monitored using the standpipe or a pressure sensor. This configuration also simulates the operation of pressure activated passive check valves encountered in actual physiological settings (*e.g.*, constant aqueous humor inflow in the eye) [8]. Following the dissolution of each anchor, deionized (DI) water at 10μL/min flow rate is injected into the microvalve. Figure 8 shows the pressure measurement results for the check-valve illustrating the basic forward operation of the device. Opening pressures of 178, 78, 26, 12mmHg and stablized pressure of 145, 72, 22, 7mmHg show four-stage performance by releasing the gold strips sequentially.

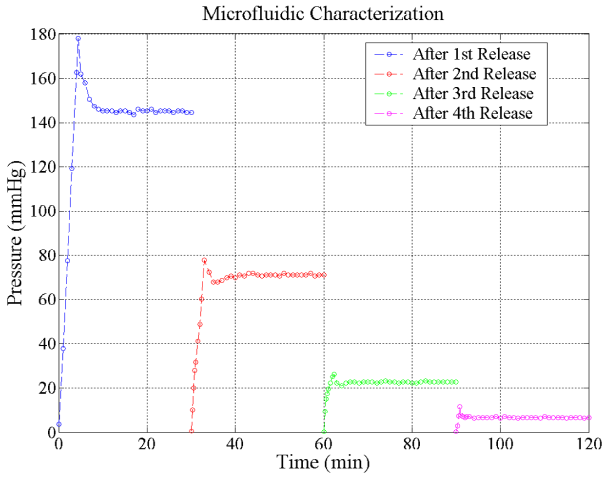

Figure 8. The pressure measurement results for the check-valve characteristic tests illustrating the basic forward operation of the device.

CONCLUSIONS AND FUTURE WORK

In this paper, we report on a remotely adjustable micromachined check-valve with a variable length cantilever-beam structure for implantable biomedical microsystems. The adjustable cantilever-beam structure is fabricated by gold thermo-compression bond of a thin silicon wafer over a glass substrate. A current density of 35mA/cm^2 resulted in a release of gold anchors in 2 minutes and gold strips are completely removed in 10 minutes. Both gravity and syringe-pump driven flow were used to characterize the valve performance. Nonlinear valve behavior and four-stage valve behavior have been clearly demonstrated. A CMOS integrated version of the receiver circuitry is currently under design and fabrication.

ACKNOWLEDGEMENTS

The authors would like to express our gratitude to Dr. David Brown of the Ophthalmology Department of University of Minnesota and Drs. Jay McLaren and Douglas Johnson of the Mayo Clinic and Foundation for valuable discussions. We also would like to Mr. Kevin Roberts in the fabrication of the device. This work was supported by the NSF CAREER award (BES-00936029) to Dr. Babak Ziaie.

REFERENCES

[1] L. Low, S. Seetharaman, K. He, and M. J. Madou, "Microactuators toward Microvalves for Responsive Controlled Drug Delivery," *Sensors and Actuators B*, vol. 67, pp. 149-160, 2000.

[2] T. Pan, W. Zheng, M. Lei, B. Cavanagh, and B. Ziaie, "A Remotely Adjustable Check-Valve Array with an Electrochemical Release Mechanism for Implantable Biomedical Microsystems," *IEEE Transducers Conference*, 2003, Boston, MA, pp.115-118, 2003.

[3] T. Pan, Z. Li, J. D. Brown, and B. Ziaie, "Microfluidic Characterization of a Valved Glaucoma Drainage Device with Implication for Enhanced Therapeutic Efficacy," *IEEE EMBS 2003*, Cancun, MX, 2003.

[4] C. H. Tsau, S. M. Spearing, and M. A. Schmidt, "Fabrication of Wafer-Level Thermocompression Bonds," *Journal of Microelectromechanical Systems*, vol. 11, pp. 641-647, 2002.

[5] J. Santini, A. Richards, R. Scheidt, M. Cima, and R. Langer, "Microchips as Controlled Drug-Delivery Devices," *Angewandte Chemie*, vol. 39, pp. 2396-2407, 2000.

[6] J. Santini, M. Cima, and R. Langer, "A Controlled-Released Microchip," *Nature*, vol. 397, pp. 335-338, 1999.

[7] J. M. Porter, C. H. Krawczyk, and R. F. Carey, "In vitro Flow Testing of Glaucoma Drainage Devices," *Ophthalmology*, vol. 104, pp. 1701-1707, 1997.

[8] J. D. Brown and R. F. Brubaker, "A Study of the Relation between Intraocular Pressure and Aqueous Humor Flow in the Pigment Dispersion Syndrome," *Ophthalmology*, vol. 96, pp. 1468-1470, 1989.

AN ELECTROSTATICALLY ACTUATED LOW-LEAKAGE SILICON MICROVALVE

Joachim Sihler[1], Alexander H. Slocum[1], Jeffrey H. Lang[2]
ME[1] & EECS[2] Departments, Massachusetts Institute of Technology
Cambridge, MA 02139, USA

ABSTRACT

The microvalve reported here is developed for sample preparation and injection in a miniature gas chromatograph; hence, leakage rate is of particular importance to prevent cross contamination within the system. Fabricated and tested prototypes exhibit leakage rates of $5.8 \cdot 10^{-6}$ atm-cc/sec and are made only of silicon and silicon dioxide. The prototype valves are capable of switching pressures of 8 psi with open flow rates of 8.4 sccm of N_2. Operation voltages are less than 35 V.

INTRODUCTION

Recent advances in microsystem design and microfluidics include the development of Micro Total Analysis Systems (uTAS), where chemical or physical processes or analyses are carried out on a very small scale, essentially on the surface of a microchip. One branch of these types of systems is miniature gas chromatographs. In gas chromatography systems, a small amount of sample gas is first trapped and isolated from the main stream and then a carrier gas is used to push the sample gas through a long capillary, called the separation column. In the separation column, the components of the gas are separated due to their unique travel times. For sample preparation and injection, microvalves are needed to handle the sample and carrier gases.

Many different microvalves have been introduced over the years for a variety of purposes and with a large range of actuator principles. For application in gas chromatography systems, the leakage rate is of particular importance in order to prevent cross contamination of sample and carrier gases within the system. From this point of view, there are only a few microvalves where leakage tests have been performed and relatively low leakage rates have been observed. Unfortunately, different research groups use different units for pressure, flow rate, leakage rate etc. Additionally, the specific conditions (i.e. temperature and pressure) at which gas flow rate values are given are not always explicitly and consistently reported, which makes a detailed comparison difficult. However, an attempt is made here to convert all data into common units. Furthermore, leakage rates in the literature have been measured under substantially different valve inlet pressures. To account for this, we have divided the leakage rate values by the inlet pressure at which the leakage rate was measured, which yields a value that may be interpreted as a "leakage conductance". This value represents the leakage rate in $Pa \cdot m^3/s$ per Pa of inlet pressure. The requirements given for our gas chromatography valve is a leakage rate on the order of 10^{-8} atm-cc/sec near 1 atm of pressure drop, which corresponds to 10^{-14} $Pa \cdot m^3/s/Pa$. Table 1 shows a comparison of the relevant references where, after conversion to common units, leakage conductance values on the order of 10^{-12} $Pa \cdot m^3/s/Pa$ or less have been found. To our knowledge, the lowest leakage rates for silicon microvalves were reported by Hirano [2] and Yang [4]. Both valves achieved acceptable leakage rates, but both need an externally attached actuator. The lowest leakage rates for microvalves with integrated micro actuation were reported by Goll [1] and Carlen [3]. However, their valves use materials that are not appropriate for gas chromatography applications due to their insufficient thermal, chemical, and/or physical performance. The microvalve reported here exhibits a leakage rate comparable to those with integrated microactuators in Table 1. Further, it is made of only silicon and silicon dioxide, and is therefore compatible with, and suitable for, most gas chromatography systems.

Ref.	Pressure	Open Flow Rate (gas)	Leakage con-ductance	Type of actuator	Voltage	Power
units	**[MPa]**	**[Pa·m³/s]**	**[Pa·m³/s/Pa]**	**[--]**	**[V]**	**[mW]**
[1]	0.04	$3.3 \cdot 10^{-5}$ (N_2)	$3.33 \cdot 10^{-12}$	TH	)*	)*
[2]	0.1)**	$3.2 \cdot 10^{-4}$ (He)	$5.8 \cdot 10^{-15}$	EM/EXT	30	)*
[3]	0.107	$1.67 \cdot 10^{-4}$ (N_2)	$7.83 \cdot 10^{-12}$	TH	)*	100
[4]	2.07	0.0868 (He)	$1.21 \cdot 10^{-14}$	PZ/EXT	30	3
Our) [1]	**0.069**	**0.014 (N_2)**	**$5.8 \cdot 10^{-12}$**	**ES**	**17**	**0.001**
Our) [2]	**5.0**	**0.1 (N_2)**	**N/A**		**34**	

NOTE: most values obtained after unit conversion
)* = not reported;)** = concluded from paper, not explicitly given
) [1] = actual prototype fabricated and data obtained from measurements;) [2] = predicted data, this prototype is not fabricated yet
ES = electrostatic, EM = electromagnetic, TH = thermal, PZ = piezo, EXT = external actuator

Table 1: Comparison of references

VALVE DESIGN

Figure 1 and Figure 2 show schematic views of the microvalve design and the fluid flow through it. The microvalve consists of a silicon substrate made from an SOI wafer. The device layer of this SOI wafer is etched to form the circular valve cavity, and the buried oxide layer is patterned to form the valve seat, valve plate

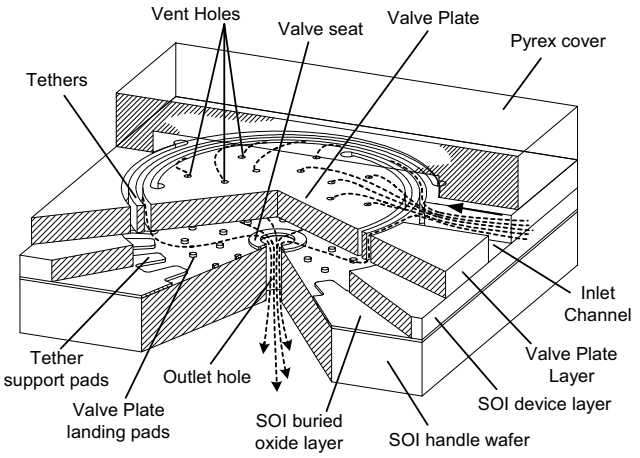

Figure 1: Microvalve structure

0-9640024-5-0/hh2004/$20©2004TRF
DOI 10.31438/trf.hh2004.74

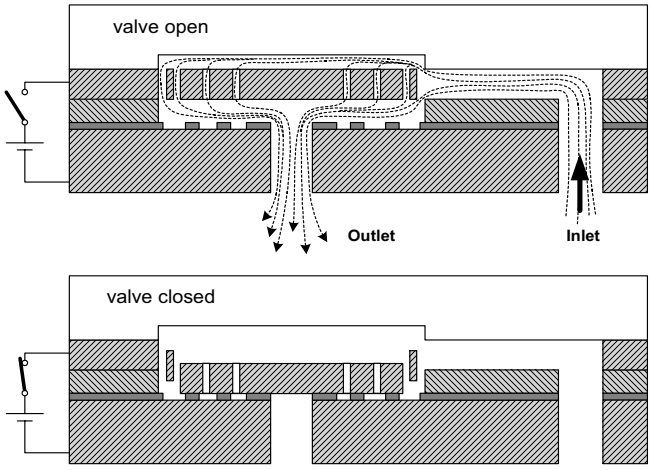

Figure 2: Microvalve operation

landing pads, and tether support pads. A through-hole etched in the SOI handle wafer forms the valve outlet. The valve plate layer is bonded on top of the SOI wafer and it is etched to create the inlet channel and the circular valve plate with the suspending tethers. A Pyrex wafer with a relief recess is bonded on top of the structure to form a cover. To give an impression of the size, the valve plate has a diameter of approximately 2.5mm. If a pressure is applied, the gas enters the valve cavity through the inlet channel on the right hand side and flows around the tethers and through the vent holes towards the central outlet. The valve is normally open. If it is to be closed, an electric potential can be applied between the SOI handle wafer and the valve plate layer, which causes the valve plate to pull in onto the valve seat, blocking the fluid flow. If the voltage supply is disconnected, the elastic spring force of the tethers pulls the valve plate off of the valve seat to open the valve.

MATHEMATICAL MODELING

We have developed a mathematical model to capture the behavior of the valve, i.e. the flow rate of the valve as a function of pressure drop when the valve is not actuated, and the flow rate for a given pressure drop as a function of the applied actuation voltage.

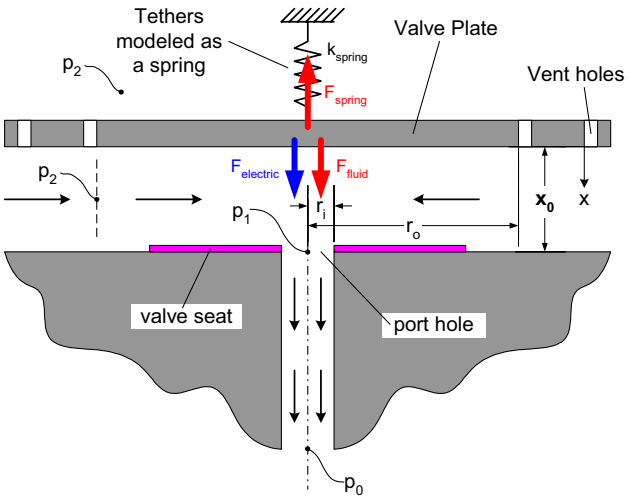

Figure 3: Lumped parameter model of the valve

Figure 3 shows the lumped parameter model for the force balance on the valve plate. When the gas flows past the valve plate into the outlet, the pressure drops first across the valve plate from p_2 to p_1 at the entrance to the port hole, and then finally from p_1 to atmospheric p_0 across the port hole. The pressure on both sides of the valve plate is equalized for the most part due to the vent holes, but there is a section in the center near the valve seat where there are not any vent holes and a pressure drop occurs. This section is within the radius r_o. This is also the area of the valve plate that contributes to the fluid force term. The Navier-Stokes Equation was used to obtain an expression for the fluid force as well as the flow rate.

The force balance on the valve plate can be written as

$$F_{fluid} + F_{electric} = F_{spring} \ .$$

The spring force is a linear function in x, and the electrostatic force can be obtained from the parallel capacitor equation. These terms are

$$F_{fluid} = \frac{\pi \cdot (r_o^2 - r_i^2)}{2 \cdot \ln(\frac{r_o}{r_i})} \cdot (p_2 - p_1) = A \cdot (p_2 - p_1)$$

$$F_{electric} = \frac{\varepsilon \cdot \pi \cdot d_{electrode}^2}{8} \cdot \frac{V^2}{(x_0 - x)^2} = C \cdot \frac{V^2}{(x_0 - x)^2}$$

$$F_{spring} = k_{spring} \cdot x \, ,$$

where A and C summarize the constant terms. The flow rate of the radial flow and the flow rate through the port hole can both be obtained from the Navier-Stokes Equation. For the radial flow, these are

$$Q = \frac{\pi}{6 \cdot \mu \cdot \ln\left(\frac{r_o}{r_i}\right)} \cdot (x_0 - x)^3 \cdot (p_2 - p_1)$$

$$= B \cdot (x_0 - x)^3 \cdot (p_2 - p_1)$$

For the flow through the outlet hole

$$Q = \frac{\pi \cdot r_i^4}{8 \cdot \mu \cdot L} \cdot p_1 = \frac{1}{R_h} \cdot p_1 \, ,$$

where B and R_h again summarize the constant terms.

For the case of no actuation ($F_{electric} = 0$), the combination of the above equations will yield the following relationship between the inlet pressure p_2 and the flow rate Q through the valve

$$Q = B \cdot \left(x_0 - \frac{A}{k_{spring}} \cdot (p_2 - R_h \cdot Q) \right)^3 \cdot (p_2 - R_h \cdot Q) \, ,$$

and for the case of a non-zero actuation voltage ($F_{electric} \neq 0$) this equation will be

$$Q = A \cdot (p_2 - R_h \cdot Q) + C \cdot V^2 \cdot \left(\frac{Q}{B \cdot (p_2 - R_h \cdot Q)} \right)^{-\frac{2}{3}}$$

$$- k_{spring} \cdot \left(x - \left(\frac{Q}{B \cdot (p_2 - R_h \cdot Q)} \right)^{\frac{1}{3}} \right)$$

These equations are solved numerically using Matlab®. The results and their comparison with data obtained experimentally are presented later in this paper.

DEVICE FABRICATION

The fabrication sequence of the valve is shown in Figure 4. An SOI wafer with a 525 micron thick handle wafer, a 0.5 micron thick buried oxide layer, and a 10 micron thick device layer is used (1). First, a circular valve cavity is etched into the device layer by DRIE etching (2). Then, the buried oxide layer is etched by wet BOE to form the valve seat as well as the landing pads (3). The

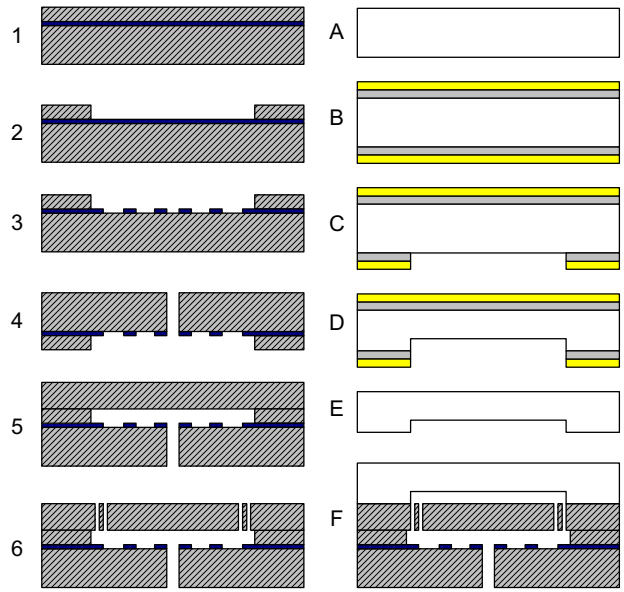

Figure 4: Fabrication process

wafer is flipped over and the backside outlet port hole is etched into the handle wafer by DRIE etching (4). After an RCA clean, a thinned 110 micron thick wafer, called the valve plate layer, is fusion bonded on top of the SOI wafer (5). The valve plate layer wafer is then etched by DRIE to form the valve plate and the suspending spring tethers. (6).

The second part of the process is to fabricate the Pyrex wafer that forms a lid to enclose the valve. On a plain Pyrex wafer (A), a layer of titanium (200A) and a layer of gold (1000A) is deposited by e-beam evaporation (B). These layers are deposited on both sides and serve as the wet etch mask. One side of the wafer is

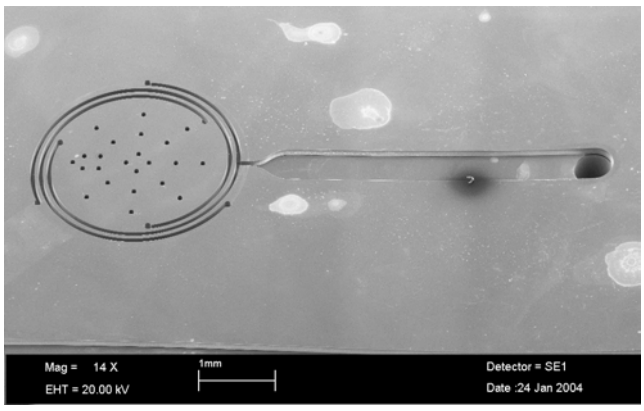

Figure 5: SEM image of a valve prototype

patterned and etched first with Aqua Regia to remove the Au, then with CR-7 to remove the Cr layer to expose the Pyrex (C). The Pyrex is then etched in diluted HF to create a slight recess (D) to prevent the valve plate from bending to the glass later in the process. The Au and the Cr mask layers are the conveniently stripped in the same Aqua Regia and CR-7 beakers (E). In a final fabrication step, the glass wafer is anodically bonded to the valve wafer (F). A dicing operation separates the wafer into individual valves.

Figure 5 shows an SEM image of a fabricated valve. Since Pyrex glass is not transparent to e-beam imaging, the Pyrex glass cover was etched off by using 49% HF prior to microscopy.

EXPERIMENTAL RESULTS

Three different performance parameters of the valve are measured. These are the Nitrogen flow rate as a function of inlet pressure without actuation voltage, the Nitrogen flow rate as a function of actuation voltage for different inlet pressures, and the

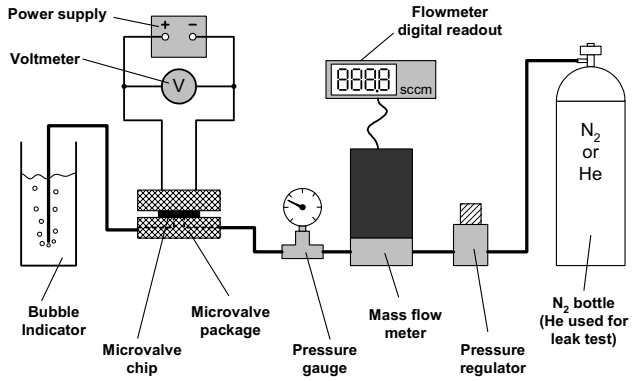

Figure 6: Test setup

Helium leakage rate. Figure 6 shows the test setup. For these tests, the valve is packaged into a two part polycarbonate housing where the fluidic connections are made by using Buna-N rubber O-rings. The electrical contacts are established with needle probes inserted through properly placed holes in the package. The Nitrogen is supplied by a pressure bottle and it flows through a pressure regulator, a mass flow meter, and a pressure gauge into the valve inlet. A voltage supply is used to provide the electrical actuation. A bubble indicator is connected to the outlet of the valve to easily

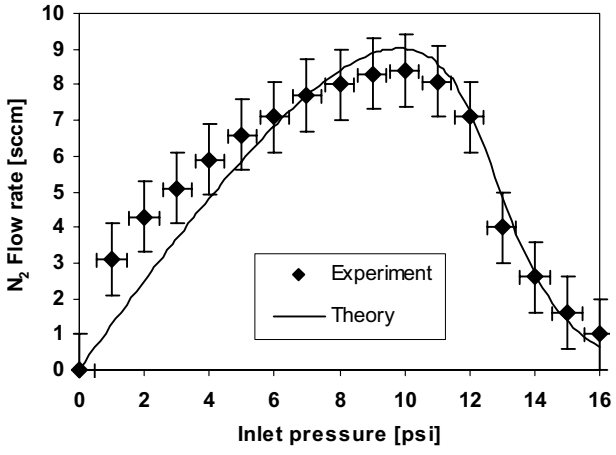

Figure 7: Flow rate as a function of inlet pressure

visualize whether the valve is open or closed. It consists of a jar of water with the end of the tubing submerged under the water line. If the valve is open, bubbles will rise from the end of the pipe.

Figure 7 shows the experimental and theoretical flow rate of Nitrogen as a function of the inlet pressure when there is no actuation voltage supplied. Initially, the flow rate increases with pressure, but then the fluidic force on the valve plate increases and the valve closes slowly thereby reducing the flow rate. The theory curve was obtained from the above equations, and the geometric variables contained in the constants A, B, C, and R_h introduced earlier were adjusted within dimensional measurements taken from the as fabricated devices to best fit the curve of Figure 7. The theoretical curves of Figures 8 and 9 were then obtained using these adjustments.

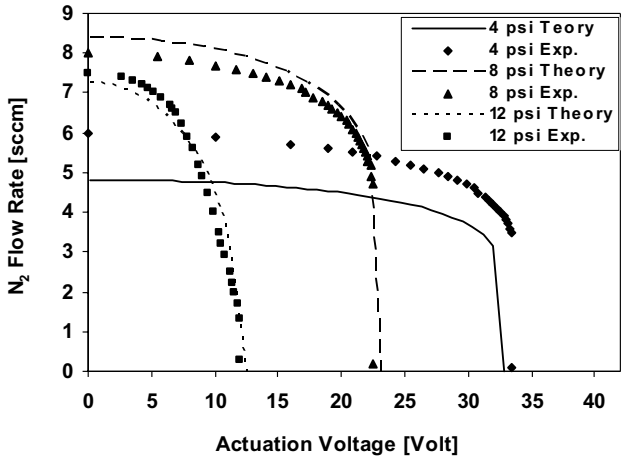

Figure 8:Flow rate as a function of actuation voltage for different inlet pressures

Figure 8 shows theory and experiment of the flow rate as a function of the actuation voltage supplied to the valve for different inlet pressures. The voltage required to close the valve, i.e. the pull-in voltage, decreases as the inlet pressure increases. The reason for this is that the inlet pressure actually "helps" the

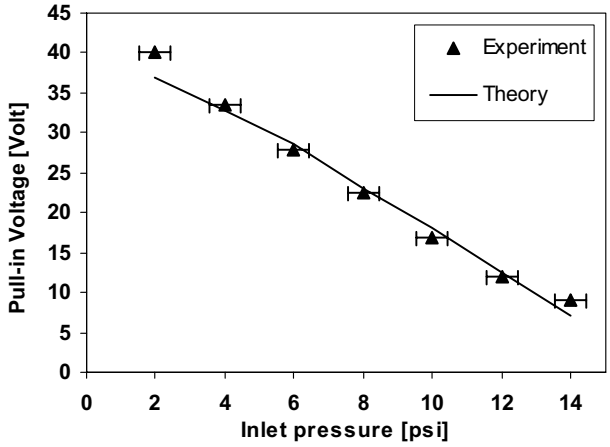

Figure 9: Pull-in voltage as a function of inlet pressure

electrostatic actuator to close the valve. We call this phenomenon the *pressure assisted pull-in effect*. Figure 9 shows this phenomenon more explicitly. By exploiting this effect it is conceivable to design microvalves capable of switching much greater inlet pressures while keeping the electrostatic actuation voltage within reasonable limits, i.e. within the limits of electrical breakdown. A predicted set of data is shown in Table 1.

The leakage rate is measured by attaching a Varian 979 He-leakage tester to the outlet of the valve package. The Nitrogen bottle is replaced by a Helium bottle and the system is flushed to guarantee that there is enough Helium present to flow through the potential leak. For a pressure drop across the closed valve of approximately 1 atm, a leakage rate of $5.8 \cdot 10^{-6}$ atm-cc/sec is measured. This value is converted to a "leakage conductance", and is added to Table 1 for comparison.

The leakage rate was also measured using a valve wafer from an earlier build. This wafer was neither capped nor diced into individual valves. Direct optical access to the valve plate was needed for measuring the displacement due to the electrostatic force by means of an optical profilometer. After the electric tests, the He-leakage tester was connected to the backside port holes by using PEEK tubing and two-part epoxy. The leakage rates measured here were as low as $1.8 \cdot 10^{-9}$ atm-cc/sec. This wafer did not have the vent holes in the valve plate, and therefore, we suspect that the DRIE process caused less roughening of the underside of the valve plate since ion back-bounce through the vent holes could not occur. This is consistent with our analysis that the leakage rate is very sensitive to the surface roughness.

CONCLUSIONS AND FUTURE WORK

We have demonstrated a gas-chromatography-compatible microvalve that can achieve a leakage rate comparable to other valves that incorporate integrated microactuators, but use incompatible materials. Microvalves that report lower leakage rates require a separate external actuator. We also have experimental evidence that the valve concept presented here can achieve significantly lower leakage rates. Finally, we have identified a pressure assisted pull-in effect associated with the specific geometry of our valve which can be used to design microvalves that handle much higher inlet pressures. In the future, we plan to fabricate double-sided microvalves with an upper SOI layer identical to the lower half. Such valves will be able to switch a flow of gas from an inlet port to either of two outlet ports.

ACKNOWLEDGEMENTS

This work was supported by research grants from ABB Corporate Research Ltd. and Ford Motor Corporation.

REFERENCES

1. C. Goll, W. Bacher, B. Bustgens, D. Maas, W. Menz, W.K. Schomburg, "Microvalves with bistable buckled polymer diaphragms", *Journal of Micromechanics and Microengineering*, Vol. 6, No 1, pp. 77-79, March 1996

2. M. Hirano, K. Yanagisawa, H. Kuwano, S. Nakano, "Microvalve with ultra-low leakage", *10th IEEE Annual Workshop on Micro Electro Mechanical Systems, MEMS '97*, Page(s): 323 - 326. 26-30 Jan. 1997.

3. E.T. Carlen, C.H. Mastrangelo, "Surface micromachined Paraffin-Actuated Microvalve", *Journal of Microelectro-mechanical Systems*, Vol. 11, No. 5, October 2002.

4. E.H. Yang, C. Lee, J. Mueller, "Normally-closed, leak-tight piezoelectric microvalve under ultra-high upstream pressure for integrated micropropulsion" *16th IEEE Conference of Micro Electro Mechanical Systems*, Kyoto, Jan. 19-23, 2003, Page(s): 80 -831.

THREE-DIMENSIONAL TOWER STRUCTURES WITH INTEGRATED CROSS-CONNECTS FOR 3-D CULTURING OF NEURONS

Yoonsu Choi*, Seungkeun Choi, Richard Powers, and Mark G. Allen
School of Electrical and Computer Engineering, Georgia Institute of Technology
Atlanta, GA 30332-0250

Yoonkey Nam and Bruce C. Wheeler
Department of Electrical and Computer Engineering
Univ. of Illinois at Urbana-Champaign
Urbana, IL 61801

Ashley Marr and Gregory J. Brewer
Department of Medical Microbiology and Immunology
Southern Illinois Univ. Sch. of Med.
Springfield, IL 62794-9626

ABSTRACT

As the complexity of bioengineered systems continues to increase, there is a need for the creation of geometrically-controlled three-dimensional scaffolds for cellular growth and culturing. Since the size scale of micromachined structures meshes well with that of cells, MEMS technology can be utilized for this application. In this work, three-dimensional (3-D) scaffolds have been generated for 3-D cell culturing. The scaffolds consist of high-aspect-ratio SU-8 towers (for high surface area) and towers with three-dimensional cross connect 'bridges', extending from tower to tower, which form highly complex structures for scaffolds. Towers and cross-connects of several dimensions have been tested to find optimal structures of scaffolds for cell culturing. Typical sizes for towers range from 500~700 µm in height and 50~250 µm in diameter. To further promote 3-D culturing, 20~100 µm width cross-connects, bridging from tower to tower, were fabricated. A micro-assembly technique was developed to create a highly complex set of scaffolds from a single tower and cross-connect array. Hippocampal neurons of rat embryos have been cultured on the various developed structures and 3-D interconnection between neurons was successfully observed.

INTRODUCTION

The *in vitro* culturing of living cells is a valuable technique for examining the properties and functionality of different cell types without the limitations of, or reliance on, a living host organism. In addition to the study of cells and cellular networks, cell cultures are an important intermediate step towards the engineering of living tissues, e.g., for prosthetics or other applications. As an example, consider the culturing of neural cells. Two-dimensional neuronal culturing has become routine for basic science studies ranging from toxicity to cell attachment and growth [1][2]. However, it is critical to develop cellular systems for *in vitro* measurement that mimic the 3-D *in vivo* environment as closely as possible, for enhanced cellular survival as well as functionality in networks more representative of tissue-engineered structures and systems [3][4].

As a simple example of a scaffold for growth of 3-D cellular networks, consider an array of high aspect ratio polymeric towers extending normally from an integral polymeric substrate. This configuration facilitates neuronal cell growth on and between the towers in addition to enabling future perfusion, stimulation and monitoring capabilities via pores and electrodes. 3-D cultures may be expected to be more active in modeling the brain because of greater opportunities for connections in the additional dimension.

Photodefinable epoxies such as SU-8 have been demonstrated to be biocompatible under appropriate conditions [5] and are used commercially in two-dimensional microelectrode arrays for neuronal culturing [6]. Recently, there have been large advances in the fabrication of three-dimensional structures based on photosensitive epoxies [7]. The purpose of this work is to investigate whether such 3-D structures would be suitable for neuronal culturing, and to initiate geometric optimization as a first step toward fully exploiting these 3-D structures.

DESIGN AND FABRICATION

Two types of structures considered as scaffolds for growth of 3-D cellular networks are shown in Figure 1. The first is a relatively simple 'tower' structure, and is composed of high-aspect-ratio SU-8 pillars extending from either glass or silicon substrates. The second is similar, with the exception that multiple-level 'bridges' or cross-connects are suspended from tower to tower to provide additional horizontal surfaces for cells to adhere.

The fabrication sequence for the simple 'tower' structure is straightforward and is shown in Figure 2. To promote adhesion,

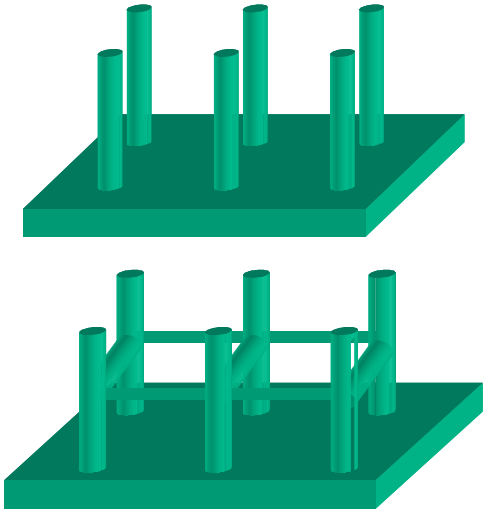

Figure 1. *Three-dimensional scaffolds developed in this work. Top: tower structures; bottom: tower structures with hotizontal cross-connects. For clarity, only one horizontal level of cross-connects is shown.*

*Travel support has been generously provided by the Transducers Research Foundation and by the DARPA MEMS and DARPA BioFlips programs.

RIE treatment is used to roughen the substrate surface. This treatment is followed by the deposition of a titanium adhesion layer. A 700 µm thick layer of SU-8 is then applied and patterned to make the tower structures. The tower diameters and spacing ranged from 50µm to 250µm. Structural tower arrays of 8x8 and 16x16 towers were fabricated and tested as a foundation for cellular culturing of neurons. Figure 3 shows the completed tower structures

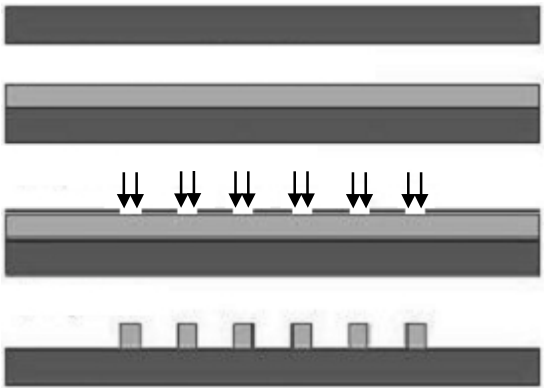

d) Development and Oxygen plasma treatment

Figure 2. *Fabrication sequence for tower arrays*

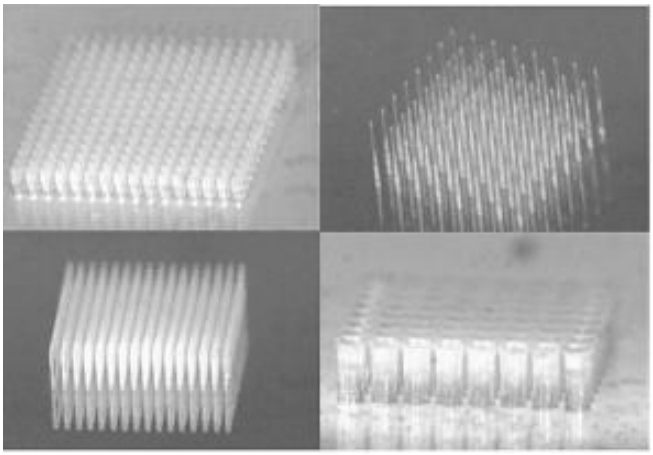

Figure 3. *16x16 and 8x8 arrays of SU-8 Towers*

The fabrication sequence for the cross-connect scaffolds cosists of two parts: generating individual arrays of structures, and assembling them into a complex 3-D structure. Figure 4 shows the fabrication sequence of the individual structures. A 20 µm thick layer of SU-8 is spun on a glass substrate and the tower and associated SU-8 substrate support patterns are subsequently exposed. After post-baking to cross-link the exposed area, an additional 300µm thick SU-8 layer is added without developing the first layer. This additional layer serves as a basis for the cross-connect pattern and extends the substrate. The cross-connect and extended substrate patterns are exposed and post-baked to cross-link the patterns. Finally, all layers of the sample are developed simultaneously.

The individual arrays are then assembled into micromachined molds to form the final scaffold structures as discussed below. Individual structures with cross-connects are separated from the substrates as shown in Figure 5. Note that each structure consists

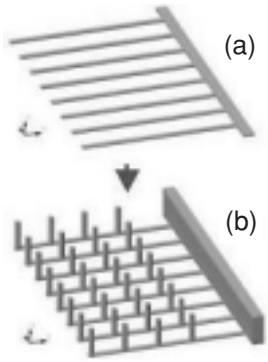

Figure 4. *Fabrication scheme of cross-connects*

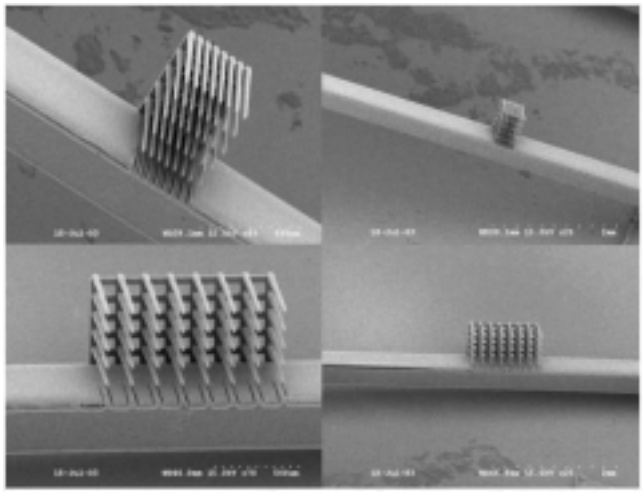

Figure 5. *Individual structures with cross-connects*

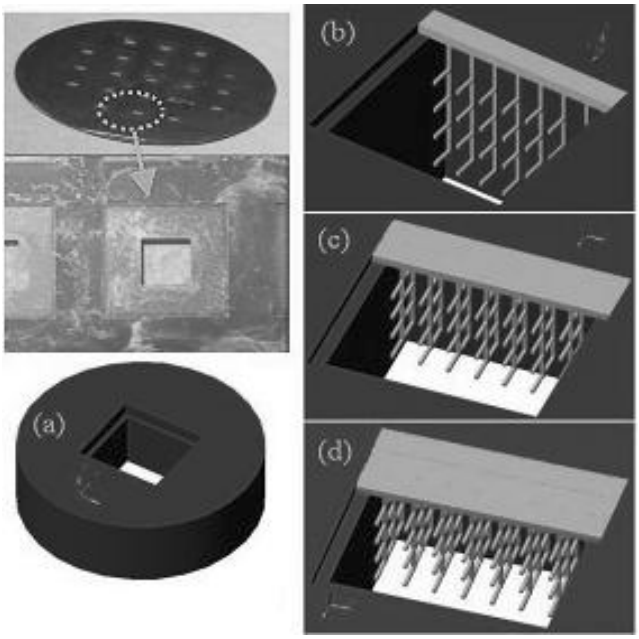

Figure 6. *Assembly scheme*

of the scaffold structure as well as a substrate 'bar' of material that can be used for handling and assembly. These individual structures are then consecutively placed in an ICP-etched silicon mold as seen in Figure 6. The silicon mold is created by 300 µm deep ICP etching followed by IR-laser cutting to make the square through holes. The 300 µm depth recess is used as a guide to efficiently place the individual arrays. After filling the mold with individual structures, a thin bonding layer of SU-8 is spun on and patterned in squares to adhere the assembled structure and complete the device. To augment biocompatibility, a thin layer of parylene is then coated over the entire surface. Figure 7 shows the completed tower structures with associated cross-connects.

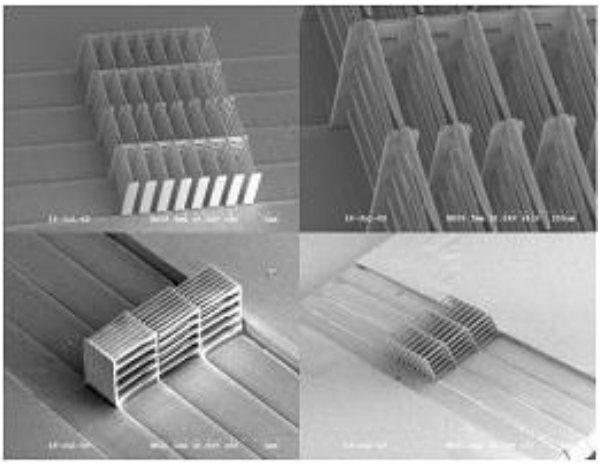

Figure 7. *Completed tower and cross-connect* structures

CELL CULTURE

Prior to application of cells onto the tower structures, a sequence of sterilization steps is required to ensure the viability of the neural culture. First, substrates are soaked in ethanol overnight to leach out any potential organic contaminants that can be toxic to cell growth. After soaking, the samples were dried under vacuum at 90°C for at least 2 hr to remove any solvents that might remain from the soaking process. The samples are then soaked in a solution of PDL (poly-D-lysine, 0.1 mg/mL in deionized water, Sigma) for 1 – 2 hours. PDL is a common protein that promotes cell adhesion. After PDL adsorption, samples are rinsed thoroughly in deionized water to remove any unbound PDL and gently dried with nitrogen gas. Extra care was taken during the blow-dry process so as not to damage the three-dimensional structures. As a final step, the samples were soaked briefly (20 s) in 70 % ethanol to prevent microbial contamination and after blow-drying the sample, it was quickly transferred to a sterile Petri-dish.

Hippocampal neurons are taken from embryonic day 18 rats, mechanically dissociated and delivered in Hibernate E from BrainBits^{TM} (Brainbits, Springfield, IL). Hippocampus tissues were triturated and plated at a density of 200 cells/mm^2 under serum-free and glia-free conditions [6]. The cell plating medium was Neurobasal/B27 (Invitrogen, Carlsbad, CA) containing 25 M glutamate and 0.5 mM glutamine. Plated cells were incubated at 37 C in 9% O_2 5% CO_2 through the culture. After 4 days, one-half of the medium was changed with Neurobasal/B27 medium containing 0.5 mM glutamine.

RESULTS AND DISCUSSION

Some preparation steps were required to take pictures of cultured neurons using the scanning electron microscope (SEM). First, half of the media was removed and the culture was rinsed in 1x PBS (phosphate buffer solution, pH 7.4) twice very gently. Fixative, 4% paraformaldeyde in PBS, was added at room temperature for 20 min. After the primary fixation, the culture was rinsed in a buffer (1xPBS) and dehydrated through a series of ethanol solutions in ascending percentages (25 %, 50 %, 75 %, 100 %). After ethanol dehydration, the culture was dried by soaking in hexamethyldisilazane (HMDS) for 3 min twice and put in a dessicator under house vacuum for at least 1 hr. Finally, it was mounted on an SEM stub with carbon stub adhesive and sputter-coated with gold/palladium for 60 sec. After conductive coating, silver paint was utilized to form a ground connection with the conductive coating.

Figure 8 shows SEM pictures of 3-D neuronal cell cultures on SU-8 towers without cross-connects. Cell bridging and web-like connections of 3-D neuronal networks show the possibility of 3-D cell culturing with these scaffolds.

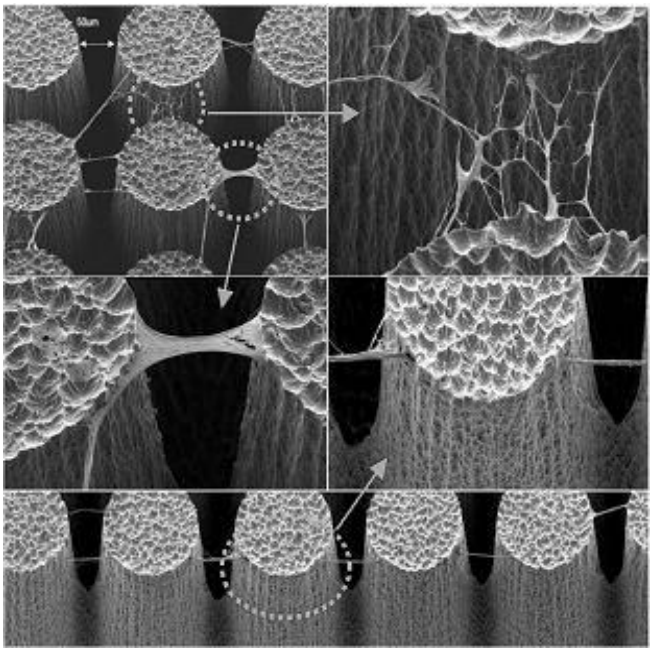

Figure 8. *Cell bridging in 3-D networks of cultured cells*

Figure 9(a) shows a perspective view of 3-D structures with neurons growing on cross-connects. Two neurons which are well spread and attached to the round-shaped surface can be seen in the inset. The outgrowth of neurites are very healthy and presumably making connections between each other. Due to the low plating density, there are a few cells available for each bars. Some cells are bridging the edge and make web-like connections as shown in Figure 9(b). At the left top corner, there is a healthy neuron attached to the vertical wall. One can see growth cones in this cell. Figure 9(c) shows a healthy neuron growth on the flat SU-8 surface beside the 3D structure. The status of the culture was judged by observing the cell growth in this region. Figure 9(a) and 9(b) were taken by SEM while Figure 9(c), 9(d), and 9(e) were made by transmitted light microscopy (phase contrast).

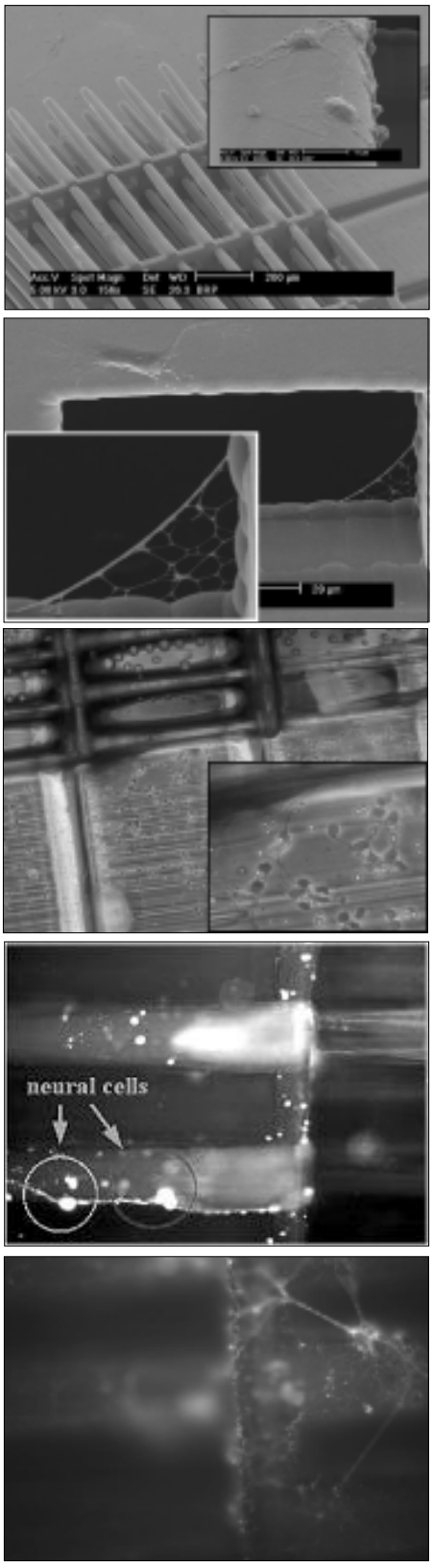

Figure 9. *Cell culture on cross-connect*

CONCLUSIONS

This work has demonstrated that cell culturing on complex 3-D MEMS structures, including bridging, is feasible, and opens the possibility of cell growth on highly functionalized scaffolds for tissue culturing and engineering applications. The cross-connect configuration facilitates neuronal cell growth on and between the towers in addition to enabling future perfusion, stimulation and monitoring capabilities via pores and electrodes.

ACKNOWLEDGEMENT

This work was supported in part by the National Institutes of Health [NIH-BRP (EB00786-01)]. SU-8 epoxy material donation by Microchem, Inc., is gratefully acknowledged.

REFERENCES

1. Q. He, E. Meng, Y. Tai, C.M. Ruthergleri, J. Erickson, and J. Pine, "Parylene neuro-cages for live neural networks study", *TRANSDUCERS 2003*, Boston, MA (2003) pp. 995-998.

2. W.L.C. Rutten, and J. van Pelt, " Activity patterns of cultured neural networks on micro electrode arrays", *Proceedings of the 23rd Annual International Conference of the IEEE Engineering in Medicine and Biology Society,* (2001) pp. 737 – 740.

3. C.S. Chen, " Microengineered systems to directly manipulate and probe living cells", *Micro Total Analysis System 2003,* Squaw Valley, CA, (2003) pp. 433 – 436.

4. M. Li, J.D. Glawe, H. Green, D.K. Mills, M.J. McShane, B.K. Gale, "Effect of high aspect ratio microstructrues on cell growth and attachment", *1st Annual International IEEE-EMBS Special Topic Conference on Microtechnologies in Medicine & Biology*, Lyon, France (2000).

5. J. Ross, G. Prado, Y. Choi, M. Allen, M. LaPlaca, and S. DeWeerth, "A novel system for measurement of electrophysiological signals associated with traumatic neuronal injury", *Micro Total Analysis System 2003,* Squaw Valley, CA, (2003) pp. 1061 – 1063.

6. See, e.g., Ayanda Biosystems, http://www.ayanda-biosys.com/

7. Y. Yoon, R. Powers, Y. Choi, C. Courcimault, and M.G. Allen, "Micromachined Polymeric Microvasculatures: A Three-Dimensional Microfluidic System Using Inclined SU-8 Structures and Laser Machining", *226th American Chemical Society National Meeting,* (2003).

8. G. J. Brewer, J. R. Torricelli, E. K. Evege, and P. J. Price, "Optimized survival of hippocampal neurons in B27-supplemented Neurobasal, a new serum-free medium combination", *Journal of Neuroscience Research*, (1993) vol. 35, pp. 567-576.

A MICROMACHINED STAINLESS STEEL CUFF FOR ELECTROMAGNETIC MEASUREMENT OF FLOW IN BLOOD VESSELS

Kenichi Takahata* and Yogesh B. Gianchandani
Department of Electrical Engineering and Computer Science, University of Michigan, Ann Arbor

ABSTRACT

This paper reports a micromachined cuff that senses blood flow velocity inside a blood vessel. Utilizing two electrically isolated electrodes in the cuff, the sensor produces a voltage proportional to the flow rate in the presence of a magnetic flux, which is to be externally read out by an implanted circuit chip. The cuff structure is fabricated from planar stainless steel foil using batch-compatible micro-electro-discharge machining and subsequently plastically reshaped into a ring by inflating a cylindrical balloon inside a blood vessel. The cuff has a pair of electrodes which are separated from each other by insulating links. A dielectric layer coats all surfaces except the electrodes. Devices deployed inside 3-mm i.d. silicone tubes demonstrate linear and symmetric responses of 3.1-4.3 V per cm/sec over 180 cm/sec with fields of about 0.25 T created by a local permanent magnet of 25x25x9 mm^3. Output dependences on the orientation of electrodes, magnetic field, and degree of stenosis (blockage inside a blood vessel) are also theoretically evaluated.

I. INTRODUCTION

Chronic measurement of blood flow is important for long-term monitoring of vascular diseases, including coronary artery disease, which is commonly treated by a medical procedure called balloon angioplasty with stent implantation. However, re-closures often occur due to recoil of the blood vessels or further plaque deposition. Wireless monitoring of blood flow can provide advance notice of such failures. Detection mechanisms proposed in the past for implantable sensors include thermal resistor [1], blood conductivity [1] and differential pressure measurement using capacitive diaphragms [2]. Electromagnetic detection [3] is another promising candidate since it has several potential advantages over each of these options, which include linear relationship between the output and flow, less output dependence on cross-sectional flow profile, and elimination of the sensing diaphragms, which can potentially improve reliability and lifetime. Electromagnetic flow sensors typically have two electrodes located on inner walls of the fluid channel. In the presence of a magnetic field, a voltage proportional to the flow velocity is developed between electrodes. The principle has been demonstrated in micro domain as well [4]. Two of the possible configurations for micromachined blood flow sensors are illustrated in Fig. 1: (A) a C-shaped cuff with penetrating electrodes is wrapped around and a blood vessel, and (B) a circular cuff is located inside a blood vessel. In this effort, the latter approach is explored. The voltage is intended to be read out and transmitted by a separate device.

II. DESIGN & FABRICATION

When all three orientations of blood flow, magnetic field, and electrical sense axis are perpendicular each other, the induced voltage E is maximized and given by:

$$E_{\max} \quad D \cdot B \cdot v \qquad (1)$$

where D is the diameter of the flow channel, B is the magnetic flux density and v is the cross-sectional average velocity of the flow. This linear equation assumes that (a) the magnetic field is spatially uniform, (b) the flow velocity profile is axially symmetric, and (c) the fluid is electrically conductive. The condition (b) is valid in typical arterial vessels and also downstream of a narrowed site if the location is reasonably away from the blockage. It is worth noting that despite the condition (c), the output voltage is independent of conductivity over a wide range [5].

The cuff presents challenges in both form and material. In the recent past, we have reported a fabrication technique for cardiac stents that are machined from planar steel foil by batch-compatible micro-electro-discharge machining (EDM) [6] and plastically reshaped into a tubular shape by a standard balloon angioplasty procedure [7]. The completed structure did not use any bonded or hinged joints, and demonstrated excellent mechanical strength. The balloon expansion technique is suitable for tailoring the final diameter of the cuff to actual inner diameter of an artery at the location of the implant. The fabrication process of the stent is also useful for the cuff because it provides a planar approach to the micromachining of stainless steel, which is a suitable structural material. However, it does not accommodate insulating segments that will permit electrical isolation of different parts of the structure which is essential for the cuff sensor, and must be modified to meet the needs of the cuff.

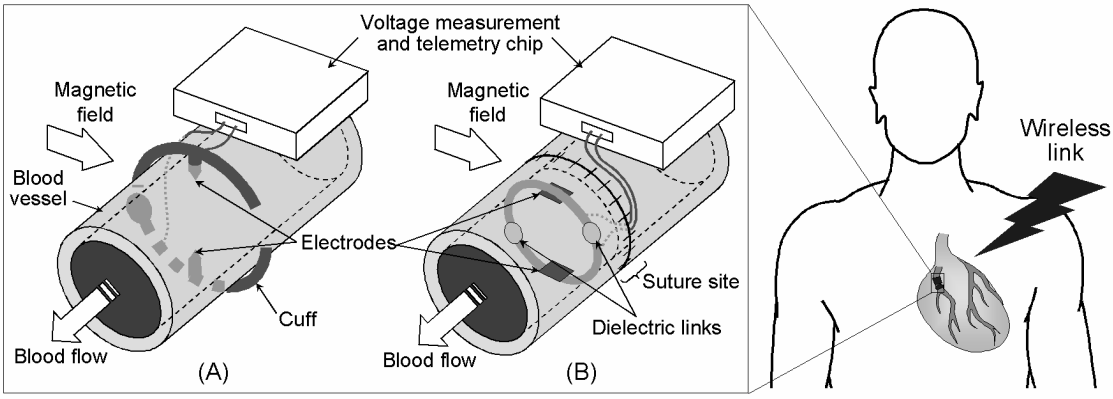

Fig. 1: Conceptual diagram of the device implementation options: (A) A C-shape cuff with penetrating electrodes wrapped around a blood vessel; (B) a ring cuff implanted inside a blood vessel upon vascular surgery. Lead transfer is located at suture sites.

*Corresponding author: 1301 Beal Avenue, Ann Arbor, MI 48109-2122, USA; Tel: +1-734-647-1782; Fax: 763-9324; Email: ktakahat@eecs.umich.edu

0-9640024-5-0/hh2004/$20©2004TRF
DOI 10.31438/trf.hh2004.76

The planar design of the ring cuff has a pair of meander bands comprised of 50 µm-wide beams, electrode plates, and two dielectric links which mechanically tie the bands but electrically insulate them each other (Fig. 2). This pattern is EDMed in 50 µm-thick #304 stainless steel foil so that two bands are connected to the original foil, maintaining 100- m gaps at the links. Insulating cement is used to bridge the gaps, and then the device is released from the foil (Fig. 3). This is similar to the process flow for a Kelvin probe described in [8]. Lead wires are bonded to the electrodes with conductive adhesive. All surfaces of the device except front-side planes of the electrodes are coated with an insulating layer. (Without this, spatial averaging will reduce the voltage.) The electrode may optionally be coated with an anti-fouling layer. This feasibility experiment used two-part epoxy and enamel for the cement and the insulation layer respectively.

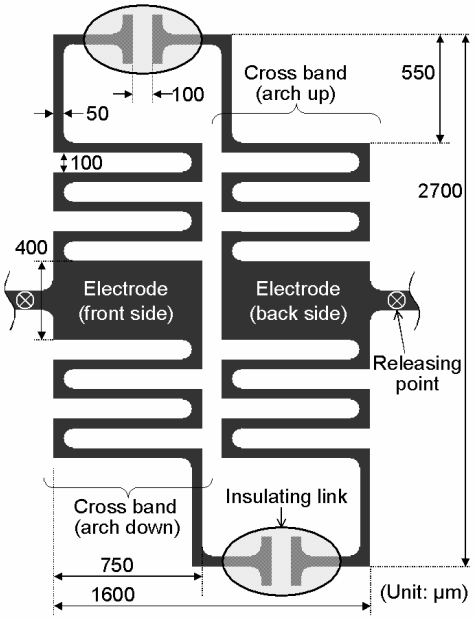

Fig. 2: A layout of the planar cuff structure.

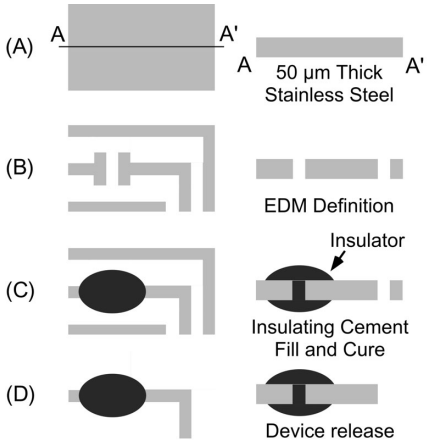

Fig. 3: Fabrication process flow [8].

The planar structure (Fig. 4) is mounted on a deflated balloon, which was a standard angioplasty catheter in this case (Fig. 5), so that one of the bands is located above the balloon whereas the other band is below it (Fig. 6). The device is then deployed near a chronically or potentially diseased location in a blood vessel. Although this device is deployed by an angioplasty balloon, its deployment requires access to both inside and outside of the blood vessel. Thus, it is most appropriate for use during a bypass procedure in which the blood vessels are severed. The lead transfer through the walls of the vessel, as noted previously, can be located at the suture sites. The cuff is expanded by the balloon before the vessel is sutured. Figure 7 shows a device that is expanded inside a silicone tube with 3-mm i.d.. The balloon is inflated up to 7 atm. causing the lumen to expand to 3.5 mm in diameter. When the balloon is deflated and removed the expanded cuff remains within the tube (Fig. 8). Tests with flow velocities up to 2 m/s show that both the structure and its placement are robust and immovable. (Maximum arterial flow is typically ≈1.6 m/s.)

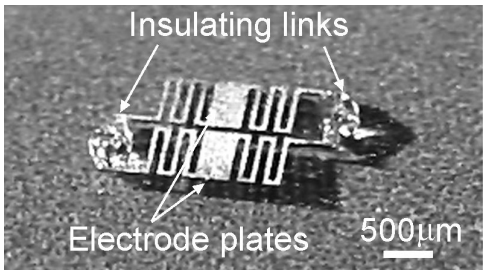

Fig. 4: A stainless steel cuff in the planar form.

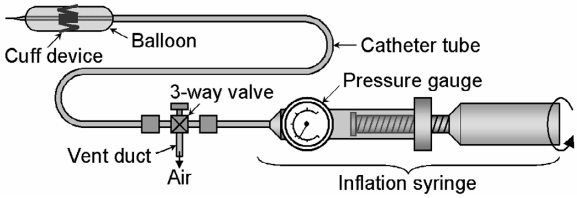

Fig. 5: A set-up for deployment of a cuff device.

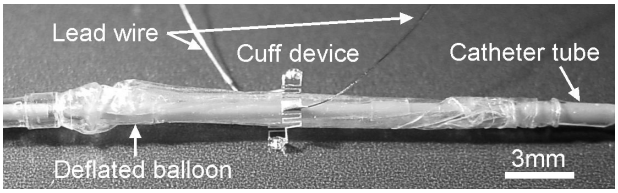

Fig. 6: A planar cuff structure mounted on a standard catheter balloon in the deflated state.

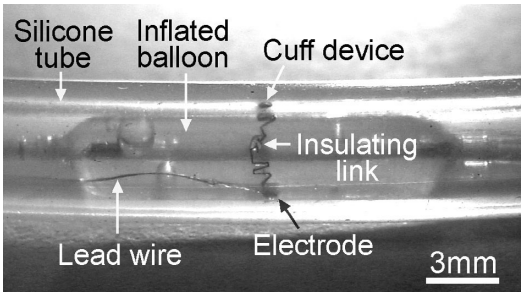

Fig. 7: The stainless steel cuff plastically expanded to a ring shape inside a silicone tube/mock artery by inflation of the balloon.

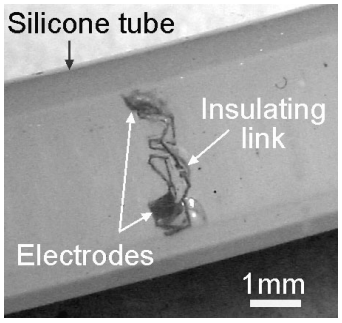

Fig. 8: The cuff remains attached to the on inner walls of the tube by pressure after the balloon is deflated and removed. (The lead wires have been removed.)

III. EXPERIMENTAL RESULTS

Figure 9 shows the measurement set-up: a pump/flow-controller regulates the flow of 2 % wt. saline and a voltmeter measures voltage between the electrode leads. A permanent magnet with dimensions of 25x25x9 mm^3 was used to provide magnetic field in this setup. The field orientation was perpendicular to both flow direction and the voltage sense axis defined by the locations of the two electrodes. The magnetic field was characterized by an InAs Hall sensor (F. W. Bell, FL, model BH-205) and measured to be ≈0.25 T at the location of the cuff. The presence of the cuff had no detectable impact on the externally measured magnetic field. To determine the electromagnetic effect, voltage change due to varying flow rate was measured with opposing orientations of the magnetic field as shown in Fig. 10. The voltage change relative to a baseline value, which is associated with polarization and electrochemical effects, is plotted in Fig. 11. The voltage linearly and symmetrically increases or decreases depending on the orientation. The voltage response and sensitivity in this test were 3.1-4.3 V per cm/sec and 50-70 ppm per cm/sec, respectively.

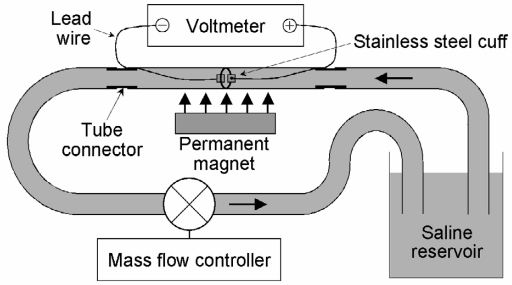

Fig. 9: A set-up for flow measure-ment.

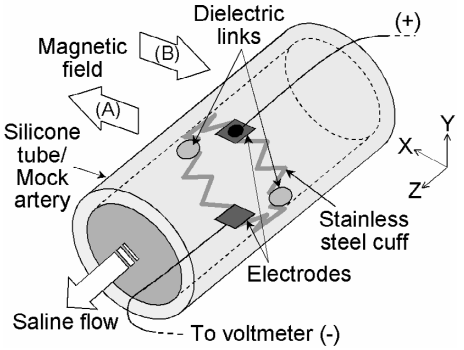

Fig. 10: A close-up of the device in the set-up with different orientations of magnetic field.

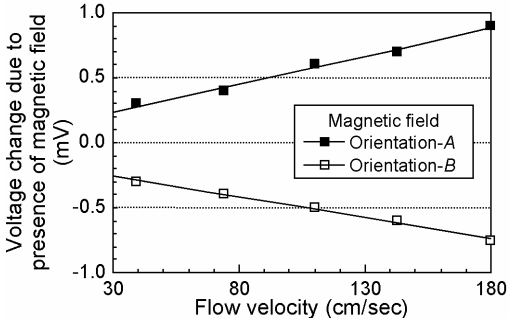

Fig. 11: Measurement result showing linear dependence on flow velocity and symmetric responses with opposing magnetic fields.

IV. ANALYSIS AND DISCUSSION

Since the output signal may depend on orientation of the magnetic field, it is important to evaluate the extent of this. Figure 12a illustrates magnetic fields misaligned by θ in the *X-Z* plane and φ in the misaligned plane perpendicular to the *X-Z* plane. The cuff is parallel to the *X-Y* plane which is perpendicular to a flow direction. The electrodes are located at $\varphi = 90^{o}$ as seen in Fig. 12a. The induced potential at φ on the circular perimeter in the *X-Y* plane is $(E_{max}/2)\cdot\sin\varphi$ [5]. When the electrodes are located on walls of the flow channel, the modified output voltage that incorporates these angular errors can be expressed as:

$$E \quad E_{\max}\cdot\cos\varphi\cdot\cos\theta \qquad (2)$$

Figure 12b shows a contour map of voltage normalized by the maximum value i.e. E_{max} ($\theta=\varphi=0$) as a function of θ and φ up to 90 , where *E* becomes zero. For example, when the magnetic field is tilted by 15 for both θ and φ, the signal loss is estimated to be 6.7%. As seen in eqn. (2) or the map impact of the angular error is less for smaller angles. This deviation can be minimized by having an external magnet with a proper harness that fits to the geometry of skin surfaces.

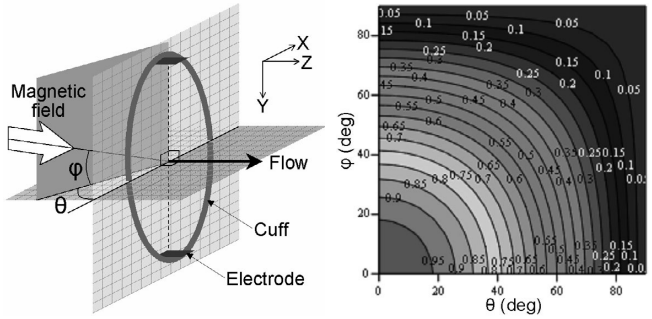

Fig. 12: (a-left) Definition of misaligned angles of magnetic field; and (b-right) a normalized voltage (E/E_{max}) map on θ-φ axes.

Using eqn. (1) with *D*=3 mm and *B*=0.25 T, the calculated output voltages are plotted with a dotted line (Cal-1) in Fig. 13b. Although at lower flow velocity the prediction matches well with the experimental result (also plotted in Fig. 13b with square dots), it deviates as the flow velocity is increased. Figure 13a shows actual electrode positions observed in the expanded cuff, where they are not actually on a diametrical line but are shifted by approximately 50 in total during the balloon expansion. This non-uniform expansion can lower the output voltage. Two hypothetical cases are evaluated and plotted in Fig. 13b: each of electrodes is equally offset by 25 as shown in Fig. 13a (Cal-2), and one of electrodes is offset by the whole 50 (Cal-3). The plots indicate that the latter case shows closer match to the measurement, although the deviation from the measured values is still not negligible. A potential cause for this mismatch is a loss associated with non-ideal profile of flow velocity. The presence of electric leads which are connected to the electrodes and/or the cuff itself can disturb the flow. The sensitivity to local flow velocity varies across the channel and rapidly increases close to the electrodes [9]. Thus, the disturbance near an electrode due to the boundary irregularities can potentially require a correction factor to be introduced into the theoretical estimate, which is otherwise idealized. Lead wires that were attached directly to the electrodes

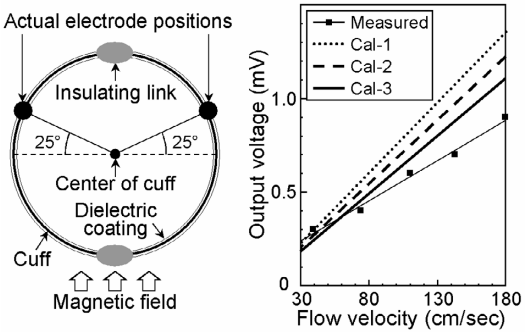

Fig. 13: (a-left) Electrode positions in the cuff structure; (b-right) measured and projected voltages as a function of flow velocity.

and the use of relatively large electrodes (400x750 m^2) in the set-up may have also contributed to the reduced response. However, the latter tends to reduce the sensitivity to the electrode position error because of the averaging effect. These issues open an avenue for design optimization of the cuff in the future.

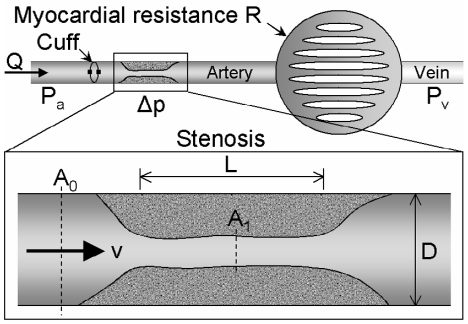

Fig. 14: Simplified model of the vascular system with a stenosis.

The impact of a blockage in a blood vessel (stenosis) on the sensing signal was evaluated using a simplified coronary circulation model with a narrowed artery, as shown in Fig. 14. This model assumes oscillating laminar flow in a rigid-wall vessel and blood as a Newtonian fluid, which is reasonable assumption for arteries with >ϕ1mm [10]. The pressure and flow rate used in this analysis were time-averaged values for one cardiac cycle. The blood flow rate in a normal artery is given by [10]:

$$Q \quad \frac{P_a \quad P_v \quad \Delta p}{R_p} \tag{3}$$

where Q is voluminal flow rate, P_a and P_v are arterial (upstream of the stenosis) and venous pressures respectively, R is myocardial resistance, and Δp is the pressure drop across the stenosis. This analysis uses P_a=100 mmHg, P_v=0 mmHg, and R≈0.4 mmHg/(ml/min) [11]. The pressure drop can be expressed as [12]:

$$\Delta p \quad K_v \frac{4 \ Q}{\pi D^3} \quad K_t \ \alpha \quad 1^{\ 2} \frac{8\beta\rho Q^2}{\pi^2 D^4} \tag{4}$$

where α is the ratio of average area of unobstructed artery to minimum cross-sectional area of stenosis i.e. A_0/A_1 in Fig. 14, β is a function of flow waveform whose average value is about 2.5 [12], ρ is density of blood, and is viscosity of blood. K_v and K_t are coefficients that depend on stenosis shape and entrance/exit geometrical characteristics, respectively. This analysis assumes a stenosis with circular cross section and constant channel diameter across its length L, where the coefficients can be approximated to be K_v≈32(L/D)α^2 and K_t≈1.5 for blunt ends, which includes both entrance and exit effects [13]. Using eqns. (3) and (4), the dependence of flow rate Q on the stenosis ratio α can be obtained. Assuming conditions for eqn. (1) and that the cuff is located upstream of the stenosis as shown in Fig. 14, the output voltage can be calculated with the flow rate, or velocity. Figure 15 plots the result as a function of percent stenosis, which means percent reduction of channel area, i.e., (1-1/α)100, with different diameters of the artery. The plot shows that the growth of the stenosis can be detected earlier for a narrower blood vessel. The analysis indicates that, for example, when D=2 mm, 10% change in the output voltage is induced by 39% stenosis. (Left main coronary artery disease is defined as >50% narrowing.)

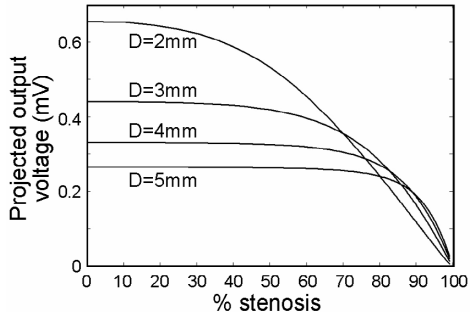

Fig. 15: Projected output voltages vs. percent stenosis with different blood vessel diameters.

V. CONCLUSION

A micromachined stainless steel cuff for electromagnetic flow sensing in a blood vessel has been investigated. A 50- m thick planar microstructure with overall dimensions of 2.7x1.6 mm^2 was designed and fabricated to have a pair of electrodes that were mechanically coupled but electrically isolated by dielectric links. The planar structure was then assembled on a deflated angioplasty balloon, and plastically expanded to ring shape by inflation of the balloon inside a silicone tube. The expanded cuff was lodged on inner walls of the tube by its own pressure and remained immovable in at least 2-m/s flow. Fluidic tests that used saline and DC magnetic field of 0.25 T demonstrated linear response of electromagnetically induced voltage to varied flow speed. The measurement result exhibited reasonable match to theoretical analysis. To circumvent polarization sensitivity and allow amplification of the output signal, the future use of AC magnetic field instead of the DC operation will be continued.

ACKNOWLEDGEMENT

This research was supported in part by a grant from the National Science Foundation. Travel support has been generously provided by the Transducers Research Foundation and by the DARPA MEMS and DARPA BioFlips programs.

REFERENCES

[1] A. Bolz, V. Lang, B. Merkely, M. Schaldach, "First Results of an Implantable Sensor for Blood Flow Measurement," *IEEE Conf. EMBS*, pp. 2341-3, 1997

[2] A. DeHennis, K.D. Wise, "A Fully-Integrated Multi-Site Pressure Sensor for Wireless Arterial Flow Characterization," *Solid-State Sensor and Actuator Workshop (Hilton Head)*, 2004

[3] B.H Brown, R.H. Smallwood, D.C. Barber, P.V. Lawford, D.R. Hose, "Medical Physics and Biomedical Engineering," *Institute of Physics Publishing, Bristol and Philadelphia*, pp. 608-11, 1999

[4] H.J. Yoon, S.Y. Kim, S.W. Lee, S.S. Yang, "Fabrication of a Micro Electromagnetic Flow Sensor for Micro Flow Rate Measurement," *SPIE Symp. Smart Struc. Mat.*, pp. 264-71, 2000

[5] A. Kolin, "An Alternating Field Induction Flow Meter of High Sensitivity," *Rev. Sci. Instrum.*, 16(5), pp.109-16, 1945

[6] K. Takahata, Y.B. Gianchandani, "Batch Mode Micro-Electro-Discharge Machining," *IEEE J. MEMS*, 11(2), pp.102-10, 2002

[7] K. Takahata, Y.B. Gianchandani, "Coronary Artery Stents Microfabricated from Planar Metal Foil: Design, Fabrication, and Mechanical Testing," *IEEE Conf. MEMS*, pp. 462-5, 2003

[8] L.L. Chu, K. Takahata, P. Selvaganapathy, J.L. Shohet, Y.B. Gianchandani, "A Micromachined Kelvin Probe for Surface Potential Measurements in Microfluidic Channels and Solid-State Applications," *IEEE Conf. Solid-State Sensor, Actuators, and Microsystems (Transducers)*, pp. 384-7, 2003

[9] J.A. Shercliff, "The Theory of Electromagnetic Flow-Measurement," *Cambridge University Press*, 1962

[10] D.F. Young, "Fluid Mechanics of Arterial Stenosis," *J. Biomech. Eng.*, 101, pp. 157-75, 1979

[11] P. Segers, G. Fostier, J. Neckebroeck, P. Verdonck, "Assesing Coronary Artery Stenosis Severity: In Vitro Validation of the Concept of Fractional Flow Reserve," *Catheter. Cardiovasc. Interv.*, 46, pp. 375-9, 1999

[12] A.C. Roth, D.F. Young, N.R. Cholvin, "Effect of Collateral and Peripheral Resistance on Blood Flow through Arterial Stenosis," *J. Biomech.*, 9, pp. 367-75, 1976

[13] D.F. Young, "Some Factors Affecting Pressure-Flow Relationships for Arterial Stenosis," *ASME Conf. Appl. Mech. Bioeng. Flu. Eng.*, pp. 87-90, 1983

MEMS CALORIMETER FOR REAL-TIME BIOCHEMICAL TESTING AND FLUID CHARACTERIZATION

Yuyan Zhang and Srinivas Tadigadapa
Department of Electrical Engineering, Pennsylvania State University
University Park, PA -16802

ABSTRACT

This paper presents a calorimetric microfluidic sensor which can be used to measure the molar enthalpy change of enzymatic reactions and to characterize the thermal properties of fluids at low sample volumes. The device consists of a microthermopile with the hot junctions located on a 2μm thick, freestanding silicon nitride-silicon dioxide-silicon nitride membrane and the cold junctions on bulk silicon substrate and integrated with glass microfluidic channels. The p^+-polysilicon/gold microthermopiles fabricated on the thermally isolated membrane showed a sensitivity of 0.94V/W and a time constant of less than 100ms. Enzymatic catalysis of glucose, hydrogen peroxide and urea, were performed using glucose oxidase/catalase mixture, catalase, and urease respectively in the integrated microfluidic device. A sensitivity of 53.5μV/M for glucose, 26.5μV/M for hydrogen peroxide and 17μV/M for urea was obtained. Based on the measurements a rather low detection limit for glucose of ~ 2 mM (30 pmole) was obtained. The primary reason for this result is the low volume of analytes sampled. The device has also been used for the measurement of the thermal conductivity and thermal diffusivity of fluids. This was achieved by introducing a periodic heat signal through the analyte and detecting the frequency dependent thermal signal response in the presence of various fluids. In this mode, the sensor design is configured to allow for the heat to primarily travel through the fluid and this coupled with the integrated temperature sensor makes a promising tool for the thermal characterization of small quantities of fluids.

INTRODUCTION

Microcalorimetry is a critical technique for the measurement of enzyme function, cell metabolism, the identification of drug effects on specific cell types, and the study of protein folding, structural transitions and other biological phenomena [1-5]. Thermopile based microcalorimeters can be configured as highly selective biochemical sensors that operate by detecting the heat of reaction to measure the concentrations of substances in gases and liquids, or the change of thermal properties such as thermal conductivity and thermal diffusivity to monitor the reaction process[2]. The device presented in this paper consists of a freestanding microthermopile integrated with glass microfluidic channels. [Figure 1] The proposed device measures the heat of reactions thermoelectrically by measuring the temperature difference created between the junctions on a freestanding membrane (hot junctions) and the junctions on the silicon substrate (cold junctions) [6]. By introducing a periodically varying heat signal in to the fluid sample using the integrated polysilicon heater, and measuring the amplitude and the phase of the heat wave traveling though the fluid due to conduction using the integrated thermopile, the thermal conductivity and the thermal diffusivity of the fluid can be accurately detected [7]. The important criteria for obtaining high resolution here is to be able to confine the largest amount of heat flow through the test fluid. Accomplishment of this goal can be used to characterize the evolution, development, and detection of various biochemical reactions and reactants with very high sensitivity.

The thermopile is located on top of a freestanding membrane, which is fabricated from 2 μm thick stress compensated dielectric layers of silicon nitride-Silicon dioxide-Silicon nitride. The thermopile itself is made from 10^{19} cm^{-3} p-doped polysilicon/Gold and consists of 16 thermocouples connected in series. The thermopile hot junctions are located on the freestanding membrane whereas the cold junctions of the thermopile are located on the rim of the silicon chip. The large thermal mass and good thermal conductivity of the rim keeps the cold junctions at room temperature whereas the thermally unconstrained membrane, where the reaction occurs, rises in temperature due to the heat of reaction. In addition a polysilicon heater was integrated onto the membrane. The polysilicon heater provides a technique for the calibration of the thermopile and for the measurement of the thermal properties of the fluid assays. A Pyrex 7740 glass substrate in which the 30μm deep microfluidic channels were etched was then aligned and anodically bonded onto the thermopile structure. Inlet and outlet fluidic ports were drilled in the glass substrate using a diamond drill prior to bonding. The integration of glass microfluidic channels and reaction chamber on top of the freestanding membrane allows for the introduction of controlled quantities of the analyte and enzyme, which are

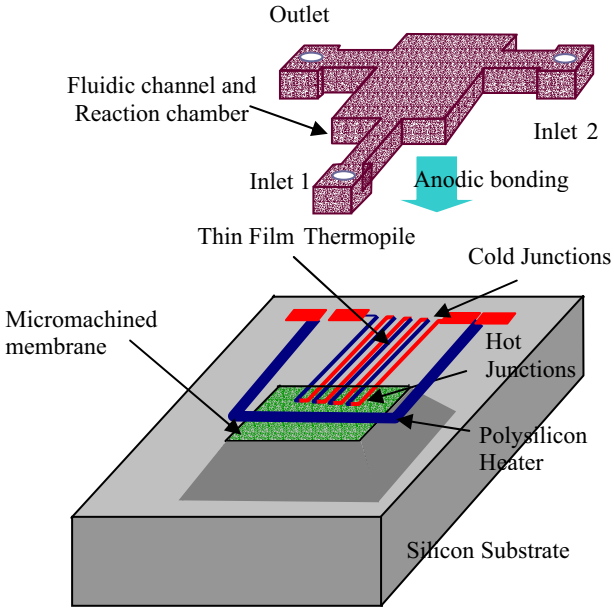

Figure 1. *A three-dimensional schematic of the proposed microcalorimeter with integrated microfluidic channels.*

* *Travel support has been generously provided by the Transducers Research Foundation and by the DARPA MEMS and DARPA BioFlips programs*

0-9640024-5-0/hh2004/$20©2004TRF
DOI 10.31438/trf.hh2004.77

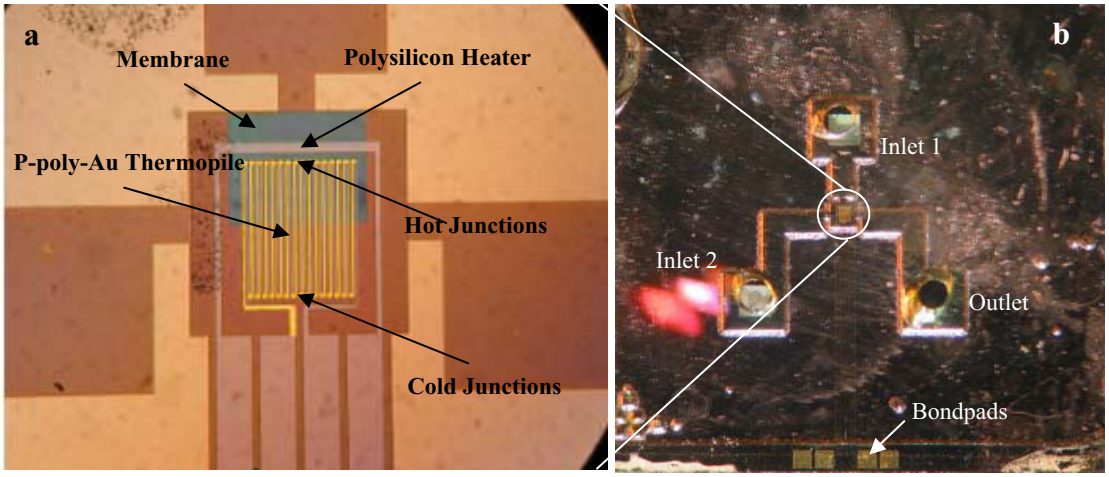

Figure 2. *Optical photographs of the fabricated device. (a) Shows a close-up view of the microthermopile consisting of 16 Au-p^{+}polysilicon thermocouples connected in series and the heater structure on the membrane. (b) Shows the complete microcalorimeter with the bonded glass chip and the bonding pads.*

made to mix on the hot junctions by virtue of the design of the reaction chamber design. Figure 2 shows the top-vew optical pictures of the fabricated microthermopiles. A poly(dimethylsiloxane) PDMS layer is then attached on to the glass substrate that allows for easy fluidic connection to the inlet and outlet ports on the chip for testing. Using the integrated heater on the membrane, the sensitivity of the microthermopiles was measured to be 0.94V/W while the time constant was better than 100ms [8].

ENZYMATIC REACTION

Enzymatic catalysis of glucose, hydrogen peroxide and urea, were performed using glucose oxidase-catalase, catalase, and urease respectively in continuous flow configuration using the integrated microfluidic channel. Both the substrates and enzymes were pumped into channel at a fixed rate of 0.5ml/hr, which gave out the highest output voltage for same substrate and enzyme concentration. The enthalpy changes for these three reactions are 180kJ/mol, 100kJ/mol and 61kJ/mol. Since the reaction of 1 mole of glucose to gluconic acid using glucose oxidase requires a mole of oxygen which could not be delivered in the closed glass reaction chamber, this reaction produced no output. This problem was circumvented by mixing 1moles of hydrogen peroxide with glucose solution and 800U of catalase enzyme with 240U of glucose oxidase. This resulted in the production of A sensitivity of 53.5µV/M for glucose, 26.5µV/M for hydrogen peroxide and 17µV/M for urea was obtained. [Figure 3] Detection limit for glucose in the continuous flow mode is ~ 2 mM (30 pmole). This moderate sensitivity is due to the small volume of the analyte used and relatively poor mixing region in the reaction chamber, which depends on the diffusion coefficient and time. The real mixing region is two orders less than the chamber dimension.

THERMAL PROPERTIES OF FLUIDS

In addition to the direct measurement of heat of reactions, the fabricated calorimeter can also be used for the investigation of the thermal properties of the analytes. In order to accomplish this, an integrated heater is used to introduce a controlled amount of heat which travels through the freestanding membrane and the fluid on the membrane to the thermopile sensor hot junctions. The magnitude of the signal and the phase difference for periodically varying heat input can be used to determine the thermal conductivity and the thermal diffusivity of the fluid under investigation respectively.

For a system in thermal equilibrium, the temperature difference between two locations can be calculated as

$$T(x_1) - T(x_2) = Q * R_{therm} \qquad (1)$$

where Q is thermal flow and R_{therm} is thermal resistance, which equals:

$$R_{therm} = \frac{L}{KA} \qquad (2)$$

L, A, K are the length, cross-sectional area and thermal conductivity of the thermal conductor respectively. A

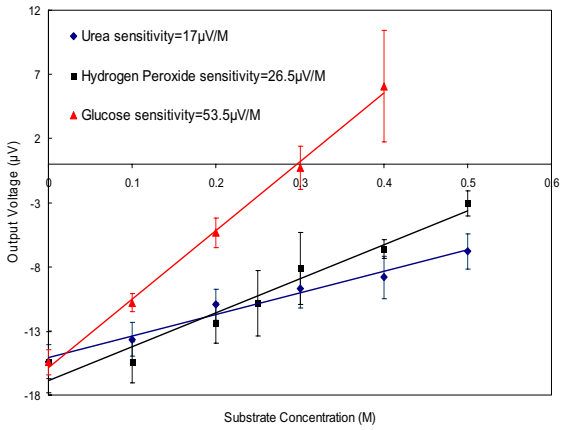

Figure 3. *Output of the microthermopile as a function of urea, hydrogen peroxide, and glucose concentration catalyzed by Urease, Catalase, and Glucose Oxidase/Catalase mixture.*

simplified lumped-element model of the sensor is shown in Figure 4. Accounting for all the possible paths for heat transfer, several idealized direct thermal resistances need to be considered such as the resistance due to: (i) the air under the membrane (R_A), (ii) the membrane (R_M), (iii) the fluid (R_L) from heater to thermopile. Heat also travels indirectly through fluid (R_{LV}) to the glass channel (R_C) and then back to fluid (R_{LV}). Of all these four paths, the thermal resistances of fluid and membrane are the dominating ones. For the fabricated device, the membrane has an effective thermal resistance of 0.081K/W. For the investigated fluids, the thermal resistance varied from 0.056K/W (DI-water) to 1.28K/W (air). The resolution of this technique depends upon the thermal influence the fluid has in relation to the structures constituting the sensor such as the membrane, the glass channel etc. For an accurate thermal characterization of the fluid, a significant amount of heat must flow through the fluid. The design and materials of the sensor must be chosen to maximize this possibility.

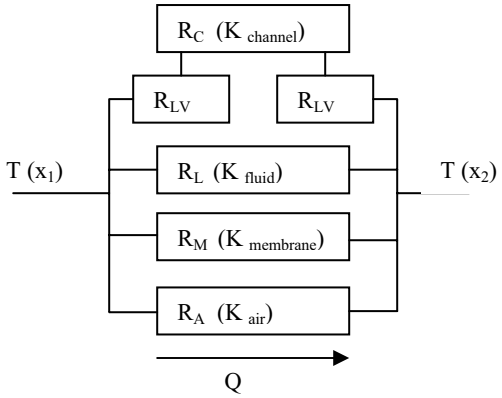

Figure 4. *Lumped-element model consisting thermal resistance of channel, fluid, membrane and air.*

As shown in Fig. 1 & 2, the microthermopile structure on the membrane was integrated with a polysilicon heater. By adding a periodic voltage on the heater, a heat wave is generated on the membrane. The thermal signal detected by thermopiles is a function of the thermal properties of the liquid in the chamber. A fluid volume of around 15nl defined by the channel geometry was brought into contact with one side of the membrane. The measurements were carried out in quasi-stationary fluids, i.e., at a flow rate of 20µl/hr. This low flow rate allows for the validity of the steady state conditions and at the same time removes the influence of thermal properties change of the fluids due to the temperature increase. The heater signal voltage used was a sinusoidal function without offset. Since both the positive and the negative part of the sine wave result in heating of the polysilicon heater, the temperature function detected by the thermopile exhibits an output signal at double the input voltage frequency. An SRS830 lock-in amplifier has been used to measure the output voltage amplitude of the thermopile. The input voltage signal to the polysilicon heater of frequency f was used as the reference signal and the $2f$ signal from the microthermopile was detected. This method naturally rejects any noise at frequency f by electrical coupling. Figure 5 shows the output voltage amplitude of the

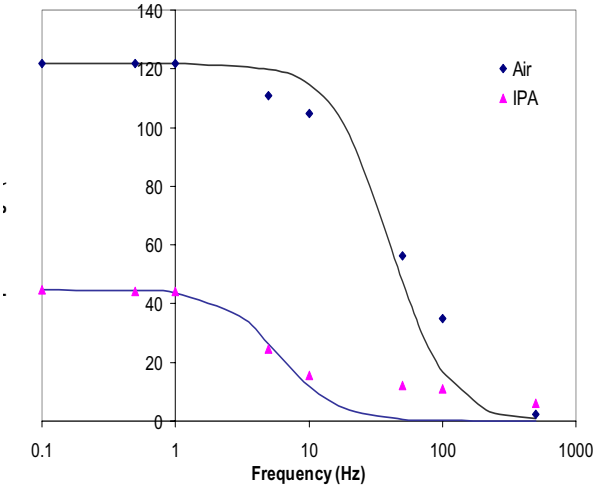

Figure 5. *Thermopile output amplitude versus sinusoidal signal frequency as measured in air.*

thermopile as function of the applied signal frequency in air and IPA. The dots in the figure are the measurement results and the lines represent the behavior of a first order low-pass filter. The low pass filter has a cutoff frequency of 40Hz for air and 6Hz in the presence of IPA. At low frequency (< 1Hz) the output signal does not change with frequency. Thus a time constant of 25ms in air and 167ms in IPA can be inferred from this measurement. As expected, the higher heat capacity of IPA results in a larger time constant.

For a fixed amplitude of the heating signal in the polysilicon heater, the output voltage of the microthermopile was measured in the presence of fluids and fluid mixtures of different thermal properties in the integrated microfluidic channel. The *rms* amplitude of the output signal corresponding to the effective thermal conductivity K of the fluid in the microfluidic channel is shown in Figure 6. The experiments were performed at 0.1Hz and 0.5Hz separately with air, acetone, IPA, ethanol, water and IPA/water mixture. The two sets of results are nearly identical, which confirms

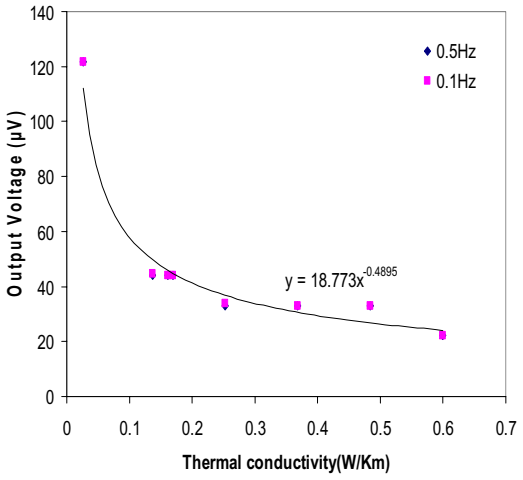

Figure 6. *RMS output of the microthermopile as a function of effective thermal conductivity for air, IPA, acetone, ethanol, IPA/water, and water.*

the result from Fig, 5 for frequencies within the plateau region at low frequencies.

For a mixed fluid, the effective thermal conductivity can be calculated as [9]:

$$K = v_{water}K_{water} + v_{IPA}K_{IPA} \qquad (3)$$

v is the volume fraction of the two components of the mixture. All the tested fluids, and their thermal conductivities obtained from literature are shown in Table 1. The thermal conductivity and thermal response has nonlinear relationship due to the isocaloric signal approach.

Fluid	K($WK^{-1}m^{-1}$)
Air	0.026
IPA	0.137
Acetone	0.161
Ethanol	0.169
75%IPA+25%water	0.253
50%IPA+50%water	0.369
25%IPA+75%water	0.484
DI water	0.6

Table 1. *Investigated fluid and the effective thermal conductivity of the fluids and fluid mixtures investigated.*

For the present design, the polysilicon heater surrounded the thermopile and thus the heat was generated all around the thermopile. Thus the generated thermal waves reaching the thermopile hot junctions are expected to have different phases. Since thermopile output signal was the average of all these heat waves, information about fluids thermal diffusivity could not be easily extracted. One of the methods of increasing the heat generated by the segment of polysilicon heater adjacent to the thermopile hot junctions is to decrease the width of this section relative to the rest of the heater structure. By this arrangement a much better phase correlation between the input and output signals was seen in a preliminary experiment. Five degrees of phase change was observed when the fluid in the microfluidic channel was changed from air to DI-water. More accurate measurements of the phase shift required for determination of the thermal diffusivity of fluids requires modifications to the design of the heater and will be reported in future studies.

CONCLUSIONS

A microthermopile calorimeter with integrated microfluidic channel has been presented, which can be used to monitor enzymatic reactions. Because of the extremely small chamber volume, the device is capable of detecting glucose solutions up to 2 mM (30 pmole) catalyzed by glucose oxidase enzyme. The device also showed the capability of characterizing thermal properties of different fluids. In relation to other work done so far, this paper represents the smallest volumes of fluids sampled for heat of reaction and thermal property measurements. Since the total heat produced in any biochemical reaction is proportional to the volume of the reacting fluid, the sensitivity of the device is relatively low. Even using immobilized enzymes confined to the hot junction area as opposed to continuous flow configuration are not expected to improve the sensitivity of the device due to the reduced volume of the reactants. For example for a volume of 10μl and an immobilized enzyme area of $1mm^2$, Herwaaden et al [6] report a sensitivity of 450 μV/M as opposed to the a sensitivity of 56 μV/M in our work using a volume of 10nl. Thus unless a temperature sensing technique capable of resolving temperatures in the sub-mK range is developed, the ultimate resolution of the thermal sensor reported here cannot exceed a μM for glucose sensing [8]. Future work for the sensor will involve improvements of the design of the sensor for more accurate measurements of the thermal diffusivity and thermal conductivity of biochemical fluids and a way to characterize biochemical reactions by real-time monitoring of the change in the thermal properties of reacting fluids.

ACKNOWLEDGEMENTS

This work is supported by a grant from the National Science Foundation, ECS-0097468.

REFERENCE

[1] Introduction to Cellular Metabolism www.mc.maricopa.edu/~tdclark/Chapter6.pdf

[2] I. Wadso, “Isothermal Microcalorimetry for the characterization of interactions between drugs and biological materials”, Thermochimica Acta 267 (1995) 45-59

[3] K. Welfe, R. Misselwitz, R. Sabat, H.D. Volk, J. Schneider-Mergener, U. Reineke, and H. Welfle, “Interaction of a designed interleukin-10 epitope mimic with a antibody studied by isothermal titration microcalorimetry”, J Mol Recognit 14-2(2001) 89-98

[4] B. W. Sigurskjold, “Exact analysis of competition ligand binding by displacement isothermal titration calorimetry”, Anal. Biochem. 277 (2000), 260-266.

[5] P.E. Morin and E. Freire, “Direct calorimetric analysis of the enzymatic activity of yeast cytochrome c oxidase”, Biochemistry 30 (1991), 8494-8500.

[6] A.W van Herwaarden, P.M. Sarro, J.W. Gardner and .Bataillard, “Liquid and Gas Micro-calorimeters for (Bio)chemical Measurements”, Sensors and Actuators A, 43(1994) 24-30

[7] H. Ernst, A. Jachimowicz and G. Urban, “Dynamic Thermal Sensor-Principles in MEMS for Fluid Characterization”, IEEE Sensors Journal, 1-4(2001), 361-367

[8] Y. Zhang and S. Tadigadapa, “Calorimetric Biosensors with Integrated Microfluidic Channels”, Biosensors and Bioelectronics, Accepted for Publication, (2004).

[9] A. Salazar, “On thermal diffusivity”, Eur. J. Phys. 24 (2003), 351-358.

Integrated Silica-Bead Separation Column for On-Chip LC-ESI

Qing He, Jun Xie, and Yu-Chong Tai
Electrical Engineering Department, California Institute of Technology,
Pasadena, CA 91125
Yunan Miao and Terry D. Lee
Division of Immunology, Beckman Research Institute of the City-of-Hope
Duarte, CA, 91010

ABSTRACT

This paper presents the first direct delivery of silica beads into separation columns using bead/photoresist mixture for on-chip Liquid Chromatography (LC) – Electrospray Ionization (ESI) applications. Instead of packing beads into an existing column from off-chip, this new method uses photoresist mixed with surface-functionalized LC silica beads for a modified photolithography (including spin-coat, exposure and development) and parylene-channel process, followed by sacrificial photoresist removal (by acetone) to release the silica beads inside the LC column. The substantiation and validation of this new technique is demonstrated on an LC-ESI chip integrated with particle filters, silica-bead LC column, and electrospray nozzle, which has been tested both physically and chemically.

INTRODUCTION

High Performance Liquid Chromatography (HPLC) is one of the most powerful, versatile, and widely-used separation techniques. It allows separation, identification, purification, and quantification of the chemical compounds in complex mixtures. HPLC separation column is usually packed with micron-sized particles with a diameter from 1 to 10 μm. The particles are coated with surface-functional groups (stationary phase) to interact with the sample and eluent (mobile phase). When the injected sample plug is carried through the column by the liquid eluent, different sample components interact with the stationary phase differently, thus partition their time in stationary and mobile phase variously, and therefore migrate through the column at different speeds, and exit the column at different time.

Normally, LC columns are made by externally packing beads into a capillary tube. Although highly desirable, on-chip LC (unlike electrophoresis) is rarely published [**1-7**] partly because the integration of LC columns without external packing remains a difficult challenge. To make columns, packing with on-chip frit [**1**] [**2**] and packing without frit [**3**] have been demonstrated. Alternative methods have also been proposed to avoid packing, such as open-tubular [**4**], coating nanoparticles on channel surface [**5**], coating micromachined posts arrays [**6**], and monolith [**7**]. We have previously demonstrated the on-chip separation and detection of seven-anion mixture with externally packed Ion Liquid Chromatography microchip with integrated frits/filters, injector, conductivity detector, and column externally-packed with ion-exchange LC beads [**1**]. Unfortunately, although it may seem to be straightforward to pack a fabricated channel, the packing process is laborious, time-consuming and one column at a time. Therefore, we propose a new in-process bead-delivering technique to make integrated LC columns. This method is batch manufacturable, can be easily integrated with other devices, and does not depend on bead types.

The combination of liquid chromatography and Mass Spectrometry (LC-MS) is a very powerful merger for separation and detection, where ESI is usually used for coupling. Microchips with LC-ESI capabilities are highly desirable. We have successfully made parylene freestanding ESI nozzles before [**8-9**]. This work for the first time integrates the LC beads column with ESI nozzle, using the above-mentioned beads integration technology.

DESIGN AND FABRICATION

The major steps for integrating beads into a micromachined LC column are shown in Figure 1. First the beads are mixed with photoresist. The mixture is spin-coated and photo-patterned together. Parylene is used to form channels and filters, where filters are channels with height smaller than the bead diameter. After photoresist removal by Acetone, the beads are free to move in the channel but trapped by filters at ends of the channel. Figure 1(d) illustrates a densely packed column with 5μm-diameter LC silica beads with C18 coatings.

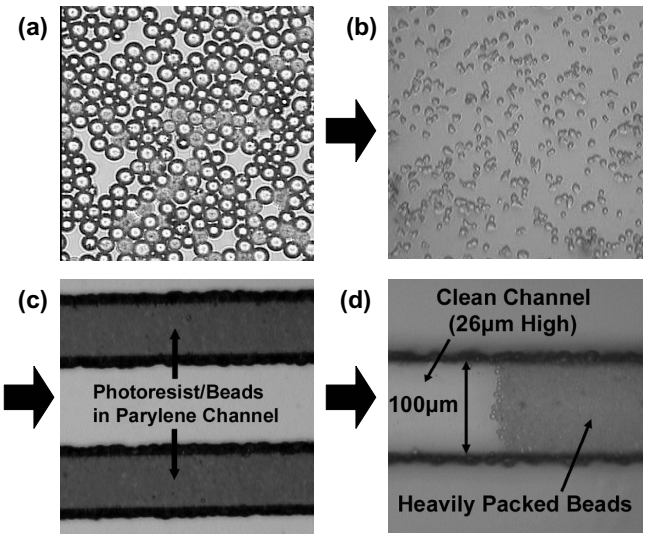

Figure 1. *Pictures illustrating the major steps for integrating beads into parylene channel.*

The photo-patterning process can leave a bumpy surface after developing. This is due to beads either exposed on or removed from the top surface during developing. Therefore, the photo-patterned structure surface roughness is about ± bead diameter. Those beads that are exposed after photo-patterning tend to stick to subsequently deposited parylene and do not release from parylene

Travel support has been generously provided by the Transducers Research Foundation and by the DARPA MEMS and DARPA BioFlips programs.

0-9640024-5-0/hh2004/$20©2004TRF
DOI 10.31438/trf.hh2004.78

even after photoresist removal (Fig. 2 (a)). To prevent beads sticking to channel-top parylene, a buffer photoresist layer can be spin-coated on top of the mixture film and patterned together with the mixture. The result can be seen in Figure 1 (d) and 5 (d) where essentially no bead stuck to top parylene. Furthermore, beads/photoresist scums also like to stick to bottom substrate after developing, which is very hard to remove even with ultrasonic agitation (Fig. 2 (b)). The solution is a bottom buffer photoresist layer spun before the mixture film, which prevents direct beads-to-substrate contact. In summary the bottom buffer photoresist, the beads/photoresist mixture, and the top buffer photoresist are spin-coated in sequence and patterned all-together.

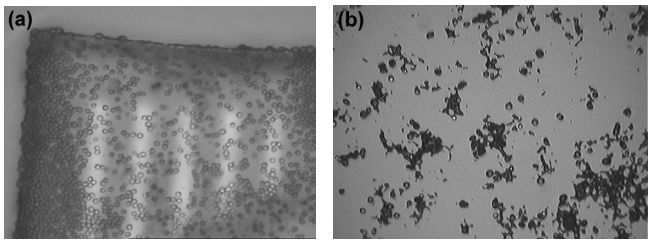

Figure 2. *Processing challenges. (a) Beads stick to top parylene if no top buffer photoresist is applied; (b) Beads/photoresist scums stick to substrate if no bottom buffer photoresist is used.*

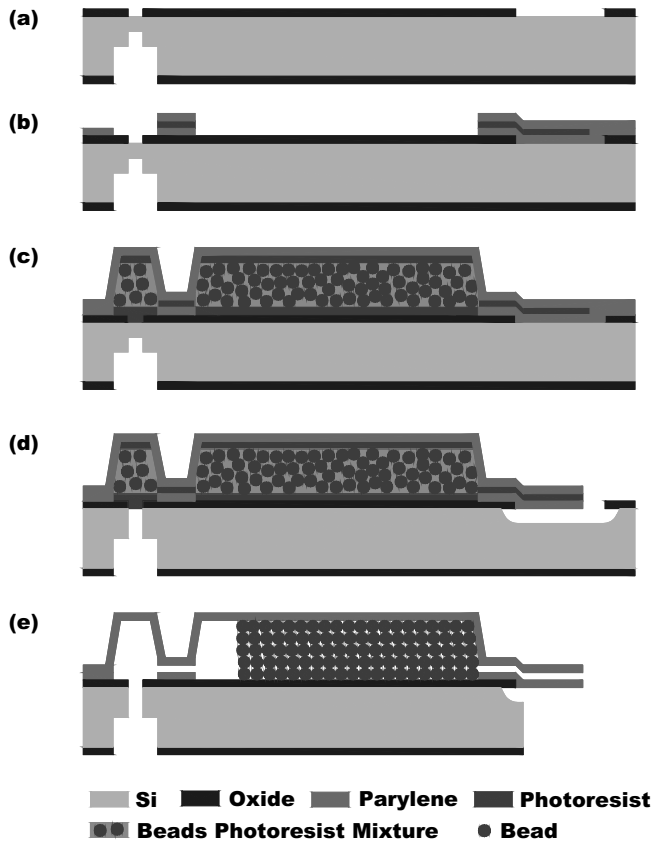

Figure 3. *Simplified process flow. (a) Pattern backside oxide and DRIE two-step backside holes; Pattern frontside oxide; (b) Deposit 1st parylene layer, pattern photoresist; Deposit 2nd parylene layer; Pattern the three layers; (c) Spin bottom buffer photoresist layer; Spin beads and photoresist mixture; Spin top buffer photoresist layer; Pattern the multiple photoresist layers; Deposit 3rd parylene layer. (d) Pattern parylene layers to open nozzle; DRIE opens backside holes; BrF_3 releases nozzle and makes trench (not shown). (e) Acetone dissolves photoresist; Break chip along trench to free nozzle; Pack the released beads into a column with pressurized flow.*

The thickness of the spin-coated mixture film depends on the spin rate, type of bead and photoresist used, and mixing ratio. The higher the beads content in the mixture, the thicker the resulting film, due to increase in the effective viscosity of the mixture. In order to successfully pattern the beads-embedded thick photoresist, multiple exposure-developing cycles may be needed. It is different from simply increasing exposure and developing time, in which only the mixture top part gets overexposed, since the beads may block the bottom parts from exposure. By developing away the exposed top part before the next exposure, the bottom parts of the photoresist can be fully exposed.

Despite the a few novel aspects detailed above, this process is still mainly a photolithography process, which allows its easy integration with other processes and/or devices. An integrated LC column –Electrospray Ionization (ESI) nozzle chip is fabricated by incorporating the above with a parylene ESI nozzle process similar to the one used in [**8**]. A simplified process flow is shown in Figure 3. The beads used are 5µm-diameter C18 porous silica beads, which is the most popular type for reverse-phase LC column. Photoresist AZ4620 was used to mix with beads at 1:10 (beads: photoresist) volume ratio. The mixture is spin-coated at 2.5krmp after a 2.5µm-thick bottom buffer photoresist coating and before a 5µm-thick top buffer photoresist coating. The total thickness of all photoresist layers is about 27µm. The filters height is 3µm. The fabricated column cross-section is 100µm wide by 26µm high, which shares the same cross-sectional area as a 58µm ID capillary. ESI nozzle freestanding overhang is 600µm in length. The nozzle opening is 3µm high by 15µm wide. The thicknesses of the parylene layers are 3µm (bottom), 3µm (middle), and 5µm (top). Figure 4 shows various parts of a fabricated LC-ESI chip, both before and after photoresist removal.

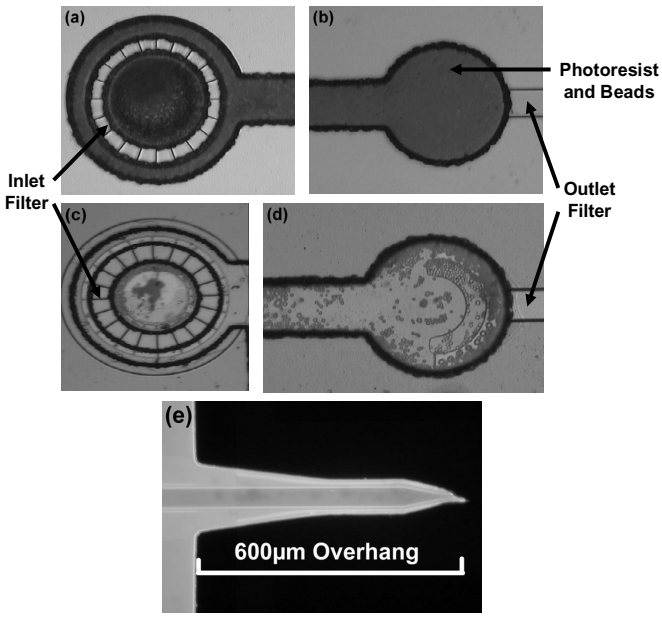

Figure 4. *Fabricated device pictures. (a) Column inlet and inlet filter before removing photoresist; (b) Column outlet to nozzle and outlet filter before release; (c) (d) After release, it can be seen that the beads are loosely released inside the channel; (e) Fluorescent picture of the freestanding parylene ESI nozzle. The nozzle opening*

is 3μm high by 15μm wide. The freestanding overhang part is 600μm long.

RESULTS AND DISCUSSION

While the beads are embedded in photoresist during processing, they are loosely released inside the column after photoresist removal. The beads can be easily packed into a dense column with a pressure flow (e.g. 15psi water flow). Figure 5 shows series of photomicrograph of released beads moving in a channel.

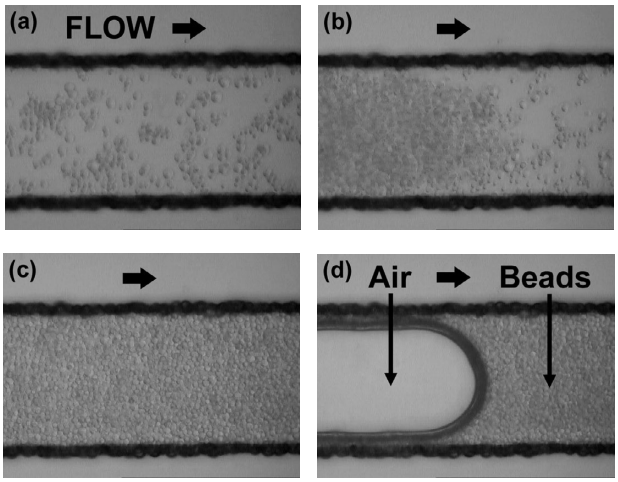

Figure 5. *Series snapshots of released beads moving with liquid from left to right in a microchannel. The channel is 100μm wide and 26μm high. Beads diameter is 5μm; (a), (b), (c) Beads move with liquid; (d) Air pushes liquid and beads.*

Figure 6 shows the column packing process and electrospray to a Mass Spectrometer. The full channel length (L_f) is 6800μm (Fig. 6 (a)). Since the nozzle end is a much smaller opening than the column inlet end, the beads pack to some degree at the nozzle end automatically during drying of the column, as shown in Figure 6 (b). After packing (Fig. 6 (c)), the LC column length (L_c) is 2700μm, which corresponds to 40% packing ratio (L_c/L_f). This ratio means 1cm-long channel with beads loosely released inside will turn into 4mm-long column heavily packed with beads. The ratio is dependent on original beads/photoresist mixing ratio. The higher the beads content in the mixture, the higher the packing ratio. The current 40% packing ratio is for original 1:10 beads-to-photoresist volume mixing ratio. To have long packed columns, large reservoirs instead of long serpentine channels can be used. The packing is done at 15psi with water. The flow rate during packing is on average 17nL/sec. After packing, the flow rate drops to 3nL/sec because of the increased flow resistance. The breakthrough time for an unretained sample to travel through this column and nozzle is 2.3sec. And because of integration, the post column volume is only 0.05nl including outlet filter and nozzle. Using the original mixing ratio and column packing ratio, the porosity of the bead column is estimated to be 0.75, which is consistent with externally-packed capillary columns (Fig. 8 (a)). The testing results of the column physical properties are summarized in Table 1.

The electrospray test is performed at 15psi with 98:2 Acetonitrile/water and 0.1% formic acid. The electrospray voltage of 1.2kV is applied off-chip at the upstream using the method described in [**9**]. When the voltage is off, the liquids coming out the nozzle form a droplet (Fig. 6(d)). When the ESI voltage is on, the sample liquid electro-sprays into the Mass Spectrometer. A typical electrospray figure obtained is shown in Figure 7. An eight-hour continuous spray testing is done without failure of the nozzle or observable nozzle performance degradation.

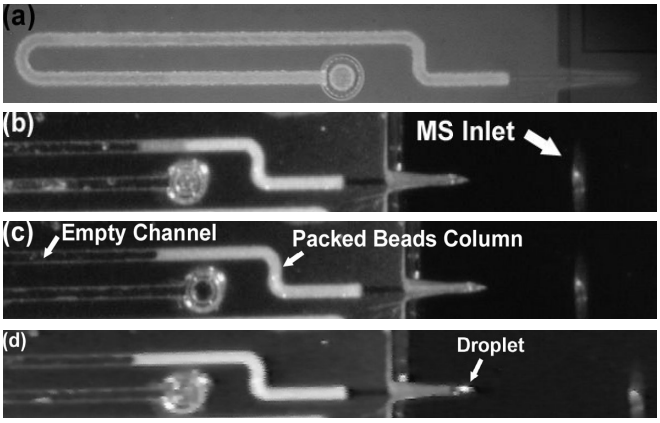

Figure 6. *Snapshots of packing a column and electrospray to a Mass Spectrometer (MS). (a) Fluorescent picture of the device used; (b) Before packing; (c) After packing; (d) Droplet forms at nozzle tip when electrospray voltage is off.*

	Column Properties
Beads Type	Porous Silica 5μm Diameter C18, pore size 100Å
Cross Section Dimension	100μm wide by 26μm high
Equivalent Column ID	58 μm
Full Channel Length (L_f)	6800 μm
Packed Column Length (L_c)	2700 μm
Packing Ratio (L_c/L_f)	40%
Flow Rate during Packing	17 nl/sec
Flow Rate after Packing	3 nl/sec
Breakthrough Time	2.3 sec
Post Column Volume	0.05 nl
Column Porosity	0.75

Table 1. *Summary of an on-chip column properties.*

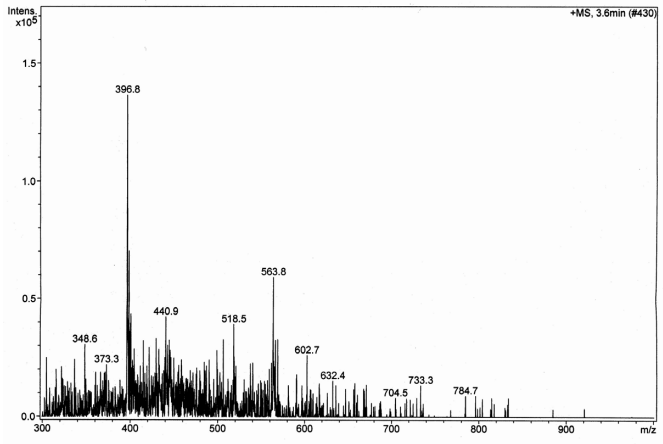

Figure 7. *A typical electrospray spectrum from the on-chip LC column and ESI nozzle.*

It is important to validate that the C18 silica beads function as normal after photoresist contamination and acetone cleaning. To do so, a capillary column-nozzle (Fig. 8(a)) packed with photoresist-

contaminated-then-acetone-cleaned C18 beads is used to separate Cytochrome C tryptic digest standard, using reverse-phase LC with gradient elution. The sample concentration is 0.1μM. Injection volume is 1μL. The MS data (Fig. 8 (b)) shows the column still achieves separation with performance comparable to similar capillary columns packed with fresh C18 beads. However, it is also found that the background noise level does depend on the cleanness of the column, as the background drops with more flushing cleaning of the beads column.

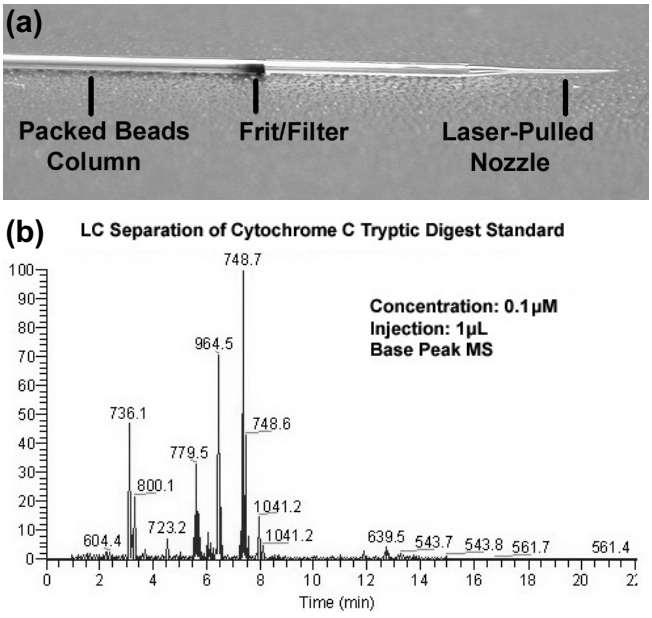

Figure 8. *(a) Picture of externally-packed capillary LC column and ESI nozzle; (b) MS data for LC separation of digested Cytochrome C using the capillary column packed with photoresist-contaminated-then-cleaned C18 beads.*

Future work includes performing on-chip LC separation and ESI to MS for detection, and comparing the separation capability of on-chip columns to conventional capillary columns.

CONCLUSIONS

In summary, a novel method to integrate beads into micromachined devices has been developed, which is wafer-scale batch processing, can be easily incorporated into other processes, and does not depend on bead types. This process is used to make an LC column – ESI nozzle on-a-chip. The column physical properties have been characterized. The ESI nozzle functions without problem in eight-hour continuous spray. Although the integrated beads have been contaminated with photoresist during device fabrication, their separation performance is not found to be affected, using a capillary column packed with contaminated-then-cleaned LC beads.

ACKNOWLEDGEMENTS

This work is supported by NIH (R01 RR06217) and NSF ERC Center at Caltech (EEC-9402726).

REFERENCES

1. Q. He, C. L. Pang, Y.-C. Tai, and T. D. Lee, "Ion Liquid Chromatography On-a-Chip with Beads-Packed Parylene Column", *Proceedings of the 17th IEEE International Conference on MicroElectroMechanical Systems (MEMS 2004)*, Maastricht, The Netherlands, January, 2004, pp. 212-215.

2. G. Ocvirk, E. Verpoorte, A. Manz, M. Grasserbauer, and H.M. Widmer, "High performance liquid chromatography partially integrated onto a Silicon chip", *Analytical Methods and Instrumentation*, Vol. 2 No. 2, 74-82 (1995).

3. L. Ceriotti, N.F. Rooij, and E. Verpoorte, "An integrated fritless column for on-chip capillary electrochromatography with conventional stationary phases", *Analytical Chemistry*, 2002, 74, 639-647.

4. A. Manz, Y. Miyahara, J. Miura, Y. Watanabe, H. Miyagi, and K. Sato, "Design of an open-tubular column liquid chromatography using silicon chip technology", *Sensors and Actuators B1*, (1990) 249-255

5. J.P. Murrihy, M.C. Breadmore, A. Tan, et al., "Ion chromatography on-chip", *Journal of Chromatography A*, 924 (2001), 233-238.

6. B. He, N. Tait, and F. Regnier, "Fabrication of nanocolumns for liquid chromatography", *Analytical Chemistry*, 1998, 70, 3790-3797.

7. A.K. Singh, D.J. Throckmorton, J.S. Brennan, and T.J. Shepodd, "Gradient-elution reversed-phase electrochromatography in microchips", *Proceedings of μTAS 2003*, pp. 1163-1166.

8. J. Xie, J. Shih, Q. He, C. L. Pang, Y.-C. Tai, Y. N. Miao, and T. D. Lee, "An Integrated LC-ESI Chip With Electrochemical-Based Gradient Generation", *Proceedings of the 17th IEEE International Conference on MicroElectroMechanical Systems (MEMS 2004)*, Maastricht, The Netherlands, January, 2004 , pp. 334-337.

9. L. Licklider, X. Q. Wang, A. Desai, Y.-C. Tai, and T. D. Lee, "A Micromachined Chip-Based Electrospray Source for Mass Spectrometry", *Analytical Chemistry*, 2000, 72, 367-375

A HIGH-PERFORMANCE TEMPERATURE-PROGRAMMED GAS CHROMATOGRAPHY COLUMN

Masoud Agah, Joseph A. Potkay, Andrea L. Elstro, Glambert R. Lambertus, Richard D. Sacks, and Kensall D. Wise

Engineering Research Center for Wireless Integrated MicroSystems
University of Michigan, Ann Arbor, MI 48109-2101

ABSTRACT

This paper reports the design and fabrication of high-performance Si-glass μGC separation columns having integrated heaters and temperature sensors for temperature programming and integrated pressure sensors for flow control. These 3m-long 150μm-wide 250μm-deep columns, integrated on a 3.33cm square die, were fabricated using a silicon-on-glass dissolved-wafer process. The 2000ppm/°C TCR of the temperature sensors and the 52fF/kPa sensitivity of the pressure sensors satisfy the requirements needed to achieve reproducible separations in a μGC system. Using these columns, highly-resolved twenty-component separations were obtained with analysis times a factor of two faster than the isothermal responses.

INTRODUCTION

Gas chromatography (GC) systems are instruments that separate the different components of a gaseous mixture in space and time [**1, 2**]. In a GC system, a gas sample is vaporized and injected into a separation column that has been coated with a stationary phase. Different gaseous molecules spend different amounts of time in the stationary phase coating while traversing the column so that they emerge from it separated in time. The gases then pass over a detector, generating an electrical output signal proportional to the concentration of the compound. The delay through the column identifies the species present [**1-3**].

Conventional GCs tend to be large, fragile, and relatively expensive table-top instruments with high power consumption, but they are known to deliver accurate and selective analysis. Microsystems based on chromatography are a promising approach to gas analysis and are rapidly moving toward small portable microinstruments. Such systems will make gas chromatography a pervasive method of gas analysis, with applications in homeland security, monitoring food freshness, industrial process control, and improving environment quality [**2**]. They promise to actually increase performance while drastically decreasing size and cost.

The basic – and heart – of a μGC system is its separation column. There have been many efforts to miniaturize such columns (along with the rest of the instrument) [**1-6**]; however, column development faces difficult challenges in minimizing power and in implementing the complex temperature and pressure control needed to enhance performance. Temperature programming can be used to separate samples over a broad boiling range and reduces the analysis time [**2, 7**]. Pressure control is also required to achieve reproducible separations since variations in the flow rate affect the retention times [**8**].

This paper reports the first high-performance μGC separation columns having integrated heaters and temperature sensors for temperature programming as well as integrated pressure sensors for flow control. These columns are part of a μGC intended for an environmental monitoring system currently under development as part of the National Science Foundation Engineering Center for Wireless Integrated Microsystems. The following sections describe the theory, fabrication, and experimental results for these microfabricated columns.

THEORETICAL DISCUSSION

A common way to express the performance of GC columns is to determine the number of theoretical plates (N) as well as the height-equivalent-to-a-theoretical-plate (*HETP*). A theoretical plate is a discrete section in which a solute molecule equilibrates between the stationary and mobile phases. For square channels, *HETP* is given by [**1**]:

$$HETP = 2\frac{D_g}{u} + \frac{1+9k+\frac{51}{2}k^2}{105(1+k)^2}\frac{uw^2}{D_g} + \frac{8h^2ku}{3D_l(1+k)^2} \tag{1}$$

where D_g and D_l are the diffusion coefficients in the gas and liquid phases, respectively, k is the retention factor, h is the thickness of the liquid phase, and w is the channel width. To determine the total resolving power of a column, the total number of plates, N, is calculated as:

$$N = \frac{L}{HETP} \tag{2}$$

where L is the column length.

Analysis time is also a key factor in determining the quality of chemical analyzers, especially when it comes to near real-time applications. In a GC system, a gas mixture is separated as its components distribute between mobile and stationary phases over time. All components spend the same time in the mobile phase, equal to the unretained peak time, given by:

$$t_m = \frac{L}{\overline{u}} \tag{3}$$

where $\overline{u}$ is the average carrier gas velocity. Retention time (t_r) is the time spent by a compound in both phases. The adjusted retention time considers only the time spent in the stationary phase:

$$t_r' = t_r - t_m \tag{4}$$

and finally, the retention factor or capacity factor of a solute is defined as:

$$k = t_r' \big/ t_m \tag{5}$$

The capacity factor is specific for a given compound and is constant under constant conditions [**9**].

Column temperature has a significant influence on component retention and separation. At a given temperature, the elution order of compounds will not depend on other GC conditions. However, in a temperature programming scenario,

0-9640024-5-0/hh2004/$20©2004TRF
DOI 10.31438/trf.hh2004.79

Solid-State Sensors, Actuators, and Microsystems Workshop
Hilton Head Island, South Carolina, June 6-10, 2004

analytes may change their relative positions as the temperature changes while they pass through the column [**9**]. Temperature programming will cause a continuous, monotonic change in the retention factor for each analyte [**9-11**]:

$$\ln k = A + \frac{B}{T} \tag{6}$$

where A and B are empirical constants and T is the temperature. Increasing the temperature reduces the retention factor and hence decreases the analysis time.

It is shown explicitly in [**11**] that an isothermal GC in comparison to a temperature-programmed GC provides the highest separation capacity but at the expense of noticeably longer analysis time. Using longer columns in a temperature-programmed GC compensates for its disadvantage in separation capacity while still retaining considerably shorter analysis time. It is important to note that raising the column temperature reduces the carrier gas viscosity and hence for a constant inlet pressure, the flow rate decreases. Therefore, flow control is required to maintain a constant flow rate during analysis in order to prevent variations of retention times and degradation of the separation efficiency [**8**].

For the columns utilized in the WIMS ERC µGC, 30-110°C and 40°C/min are selected as the targets for the column temperature range and temperature programming rate, respectively, so as to separate 30 volatile organic compounds in less than 10min. Also, the depth, width and length of the Si-glass columns are 250µm, 150µm, and 3m, respectively, representing a trade-off among the analysis time, *HETP,* and volumetric flow rate. Moreover, air — instead of hydrogen and helium — is used as the carrier gas to eliminate the need for gas storage and to allow further miniaturization [**1**].

FABRICATION

The fabrication is based on a silicon-on-glass dissolved-wafer process. First, recessed areas are created in the silicon to form the cavities and flow tunnel for the pressure sensors and the lead tunnel for the glass electrodes. Then, a 1.2µm-thick thermal oxide is grown to protect the cavities during a deep boron diffusion (Fig. 1a). Using patterned PR9260 as a mask, DRIE is used to etch the silicon to form rectangular microchannels in a 3.33cm square area and reduce the thermal mass of the silicon rim. After stripping the resist, highly boron-doped etch-stops are diffused into the channel area (Fig. 1b), followed by a 4µm-shallow boron diffusion to form the sensor membranes. Then, a 2000Å oxide is grown on the back as an electrical isolation layer and subsequently 250/500Å of Ti/Pt is evaporated and patterned using lift-off to form the heaters and temperature sensors. A 3000Å-thick LTO deposition on both sides of the wafer is used to stress-compensate the tensile p++ diaphragm [**12**] and anneal the temperature sensors. The LTO thickness on the front should not exceed the aforementioned value, otherwise it will degrade the anodic bonding performance [**13**]. A 1µm-thick LTO layer is deposited on the back side to serve as a mask in EDP (Fig. 1c). Bottom electrodes and metal interconnects for the pressure sensors are patterned onto the glass wafer with an evaporated Ti/Pt/Au stack. Then, the wafers are anodically bonded to seal the channel at 400°C, 1000V, and 200N of pressure. Next, the back oxide is patterned to open EDP etch windows and contact areas for the heaters, temperature sensors, and the bulk. Cr/Au is then sputtered and patterned on the back of the silicon substrate to form metal interconnects and cover the silicon rim for heat distribution (Fig. 1d). After that, the glass wafer is thinned in HF for 45min to reduce the thermal mass. It should be noted that a support wafer is

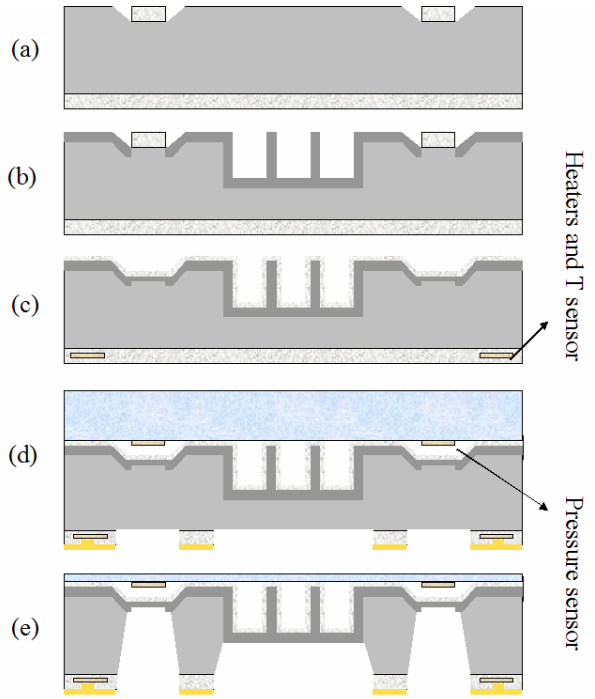

Figure 1. *Silicon-on-glass dissolved wafer process flow.*

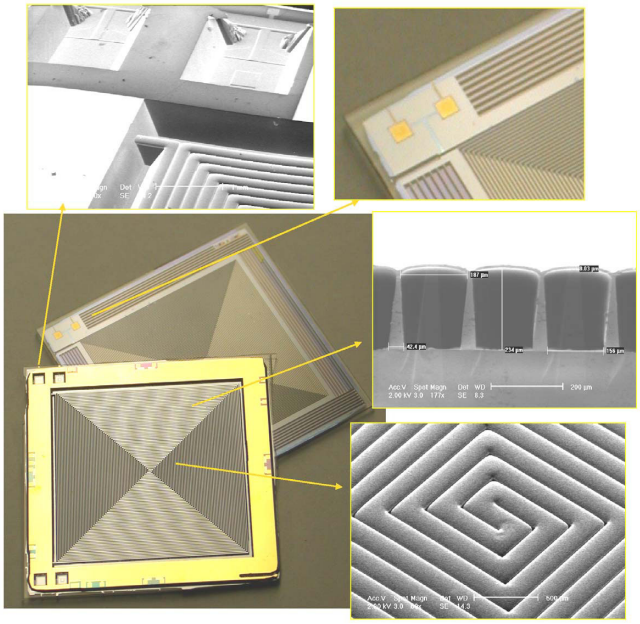

Figure 2. *Center left: Top and bottom views of the fabricated separation column. Clockwise from top left: (1) SEM image of the column entry and the pressure sensors, (2) the pressure sensor electrodes, the column entry and the silicon rim that is etched to reduce the thermal mass, (3) cross-sectional view of a non-thinned etched-back column, and (4) SEM image of the column back.*

temporarily attached to the back side to protect it during this long etch. In addition, the solution is stirred to obtain a smooth surface. This step thins the glass to less than 80µm. Following glass thinning, EDP is employed to etch back the column and release the pressure sensors (Fig. 9e). With the columns fabricated, fused silica capillaries are attached to the side ports for fluidic

interconnects, and the columns are coated with polydimethylsiloxane, a non-polar stationary phase.

Fig. 2 shows the fabricated etched-back column. Each column port has its own pressure sensor; consequently, measurements of pressure differences are independent of ambient fluctuations and the column temperature. The SEM photo of the pressure sensors displays a device without the gold ring, causing significant undercut. As seen in Fig. 2, the silicon rim has been selectively etched to reduce the thermal mass. Different temperature sensors were also defined on the die to explore the thermal behavior of the column at various points. Moreover, one heater was integrated on each side of the die to suppress temperature gradients around the heaters and reduce temperature non-uniformity of the column during transients [**2**].

THERMAL BEHAVIOR

Details of the steady-state power requirements of the Si-glass simple columns are discussed in [**2**]. The thermal behavior of the etched-back columns is similar to those of simple columns listed in Table 1 except for their transient response. Analogous to its electrical counterpart, the thermal time constant can be estimated as:

$$t_{th} = R_{th} \times C_{th} \tag{7}$$

where R_{th} and C_{th} are the effective thermal resistance and capacitance of the system. Thermal resistance and power consumption (P_{ss}) are related as:

$$P_{ss} = \frac{\Delta T}{R_{th}} \tag{8}$$

where ΔT denotes the temperature rise of the column. To lower the power consumption, the thermal resistance should be increased by isolating the column from its surrounding environment, using standoffs and vacuum packaging to reduce both convective and conductive losses and covering the column surface with a low emissivity material such as gold to shrink radiative losses [**2**].

The thermal capacitance is given by:

$$C_{th} = \sum C_{th,i} = \sum_i m_i \widetilde{C}_i \tag{9}$$

where m and $\widetilde{C}$ are the mass and the specific heat of each component of the column, respectively. For the same input power, the etched-back columns show a similar steady-state temperature but a much higher heating rate due to their lower thermal mass. To obtain a temperature ramp of 40°C/min with a final temperature of 100°C under the vacuum conditions listed in Table 1, the power source should deliver 1.2W and 600mW for a simple and etched-back columns, respectively, during transients. Although the cool-down of the etched-back columns is also faster due to the lower mass, for the 3m-long silicon-glass columns, this thermal time constant is still very significant. For columns having a thermal capacitance of 0.7J/°C, the thermal time constant in vacuum at 100mW of steady-state power consumption is still about 9min.

Table 1. *Required sustained power for T_{column}=100°C [2].*

Directly on PCB @ atmospheric pressure	Free space	4.4W
	7.5mm-high package	3.4W
Standoffs, gold protection, and metal package	Atmospheric pressure	650mW
	Vacuum	100mW

SERPARATION PERFORMANCE

The temperature sensors integrated with these columns have TCRs of 2000ppm/°C, sufficient to allow column temperature to be controlled to <0.5°C. The pressure sensors should be operated in the vicinity of the flow rate where the *HETP* is minimized. It has been found experimentally that the maximum separation efficiency is obtained with a flow velocity of ~10cm/s, corresponding to a pressure drop of 5-10kPa across the 3m column. Around this point, the pressure sensors have a sensitivity of 52fF/kPa, allowing adequate flow control to ensure reproducible separations. The burst pressure of the columns is above 50psi.

With the sensors calibrated, different experiments were conducted to explore the separation capabilities of the columns. The chromatograms used air as the carrier gas and a commercial flame-ionization detector. Experimentally, the number of plates can be calculated as [**1**]:

$$N = 5.545\left(\frac{t_R}{w_{1/2}}\right)^2 \tag{10}$$

where $w_{1/2}$ is the width of the peak at half height. The numbers of plates were calculated using an isothermal separation and were found to be approximately 8000. This is significantly higher than the previously reported value of 4900 [**1**] due to improvements in the coating techniques for the μGC columns.

Fig. 3a displays the separation of 20 compounds obtained at room temperature. While the first five compounds are separated in about one minute, it takes about 10min for chlorobenzene – which has a high boiling point (132°C) – to elute from the column. Fig. 3b shows a separation of the same mixture with the column run at 30°C for 1min followed by a temperature ramp of 5°C/min for 5min. Although less effective for low boiling compounds, this temperature program has reduced the analysis time for chlorobenzene by a factor of two. Using higher programming rates decreases the retention time more effectively but at the cost of resolution.

CONCLUSION

This paper has reported silicon-glass μGC columns having integrated heaters and temperature sensors for temperature programming as well as pressure sensors for flow control. Twenty compounds are separated in less than 6min. The 2000ppm/°C TCR of the temperature sensors and the 52fF/kPa sensitivity of the pressure sensors are sufficient to achieve reproducible separations in a μGC system. The thermal time constant and transient power requirements of these columns are half of those of their predecessors [**2**].

ACKNOWLEDGMENTS

This work was supported primarily by the Engineering Research Centers Program of the National Science Foundation under Award Number EEC-9986866. Travel support has been generously provided by the Transducers Research Foundation and by the DARPA MEMS and DARPA BioFlips programs.

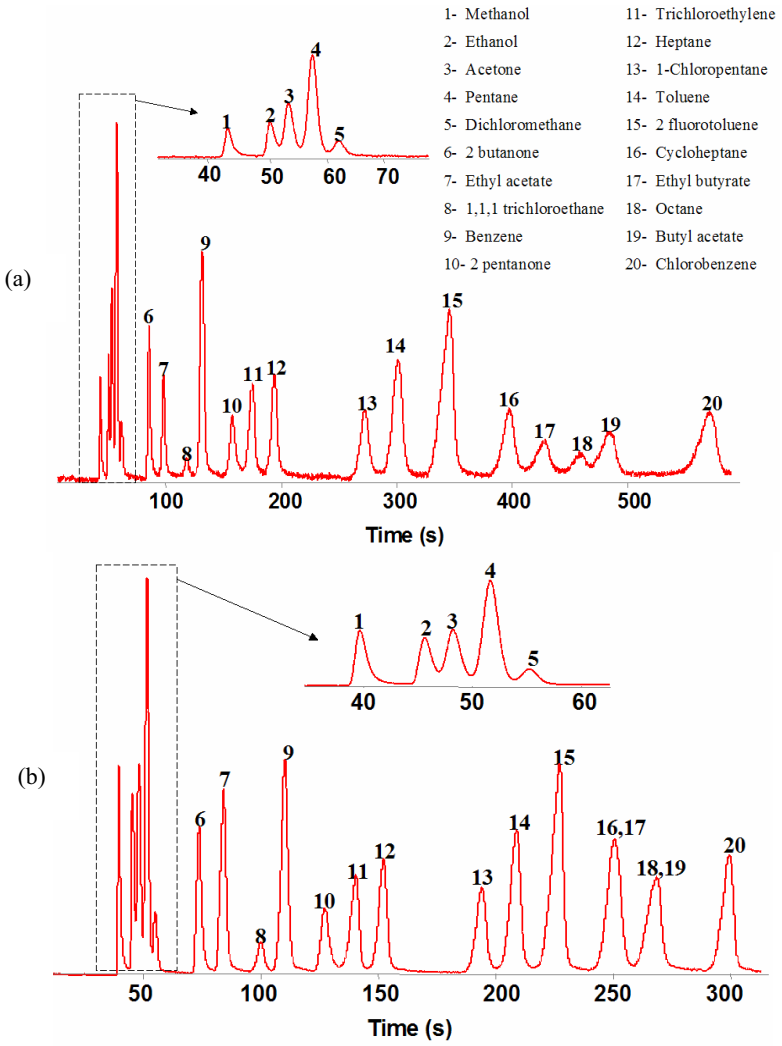

Figure 3. *Chromatograms achieved using the 3m column. Air is used as the carrier gas: (a) isothermal run at room temperature, (b) isothermal run at 30℃ for 1min followed by temperature programming for 5min with a rate of 5℃/min.*

REFERENCES

1. J. A. Potkay, J. A. Driscoll, M. Agah, R. D. Sacks, and K. D. Wise, "A High-Performance Microfabricated Gas Chromatography Column," *IEEE MEMS Conf.*, pp. 395-398, 2003.
2. M. Agah, J. A. Potkay, J. A. Driscoll, R. D. Sacks, M. Kaviany, and K. D. Wise, "Thermal Behavior of High-Performance Temperature-Programmed Microfabricated Gas Chromatography Columns," *IEEE Int. Conf. on Solid-State Sensors, Actuators and Microsystems*, Boston, pp. 1339-1342, June 2003.
3. E. S. Kolsear and R. R. Reston, "Review and Summary of a Silicon Micromachined Gas Chromatography System," *IEEE Trans. Components, Packaging, and Manufacturing Technology*, 66, pp. 481-486, 1998.
4. H. Noh, P. J. Hesketh, and G. D. Frye-Mason, "Parylene Gas Chromatographic Column for Rapid Thermal Cycling," *IEEE J. of Micoelectromech. Syst.*, 11, pp. 718-725, 2002.
5. R. W. Tjerkstra, M. de Boer, E. Berenschot, J. G. E. Gardeniers, A. van den Berg, and M. C. Elwenspoek, "Etching Technology for Chromatography Microchannels," *Electrochimica Acta*, 42, pp. 3399-3406, 1997.
6. E. B. Overton, H. P. Dharmasena, U. Ehrmann, and K. R. Carney, "Trends and Advances in Portable Analytical Instrumentation," *Field Analytical Chemistry and Technology*, 1, pp. 87-92, 1996.
7. H. M. McNair and G. L. Reed, "Fast Gas Chromatography: The Effect of Fast Temperature Programming," *J. of Microcolumn Separation*, 12, pp. 351-355, 2000.
8. F. R. Gonzalez and A. M. Nardillo, "Theoretical and Practical Aspects of Flow Control in Programmed-Temperature Gas Chromatography," *J. of Chromatography A*, 757, pp. 97-107, 1997.
9. R. Ong, P. Marriott, P. Morrison, and P. Haglund, "Influence of Chromatographic Conditions on Separation in Comprehensive Gas Chromatography," *J. of Chromatography A*, 962, pp. 135-152, 2002.
10. L. M. Blumberg and M. S. Klee, "Elution Parameters in Constant-Pressure, Single-Ramp Temperature-Programmed Gas Chromatography," *J. of Chromatography A*, 918, pp. 113-120, 2001.
11. L. M. Blumberg and M. S. Klee, "Quantitative Comparison of Performance of Isothermal and Temperature-Programmed Gas Chromatography," *J. of Chromatography A*, 933, pp. 13-26, 2001.
12. A. DeHennis and K. D. Wise, "A Double-Sided Single-Chip Wireless Pressure Sensor," *IEEE MEMS Conf.*, pp. 252-255, 2002.
13. J. A. Plaza, J. Esteve, and E. Lora-Tamayo, "Effect of Silicon Oxide, Silicon Nitride and Polysilicon Layers on the Electrostatic Pressure during Anodic Bonding," *Sensors and Actuators A*, 67, pp. 181-184, 1998.

High Performance MEMS Sensor for Low Dew Point Humidity Detection

Anis Zribi[1], **Aaron Knobloch**[1], **Wei-Cheng Tian**[1], **Gerald Schultz**[2]

[1]Micro and Nano Structures Technologies
General Electric Global Research Center,
Niskayuna, NY 12309

[2]General Eastern Instruments
Wilmington, MA 01887

ABSTRACT

A highly sensitive micro-machined humidity-sensor using novel detection techniques have demonstrated the ability to measure humidity within the range of 6 ppmw (0.04% RH, -60°C DP) to 11 pptw (60.7% RH, 15°C DP) at ambient with a resolution of approximately 2 ppm, a sensitivity of 69.6 Hz/°C DP, a non linearity of 0.14% and a low hyteresis of approximately 0.07%. This sensor operates in two distinct schemes where the measurand is either the heat or mass exchange associated with the adsorption/desorption of water vapor onto a hygroscopic polystyrene sulfonic acid thin film. While operation in both modes has been demonstrated, this paper will focus on the resonant sensor concept and performance. The sensor consists of two dual freestanding rectangular silicon nitride membranes with a Pt/Ti current carrying conductor, stretched on top of a silicon frame. Only one of the two membranes is loaded with the sensing film. The second membrane is designed for use as a reference cell to compensate for noise parameter effects (e.g. pressure, temperature…etc). The membrane is driven into resonance using out-of-plane Lorentz forces, which are generated due to interaction of an external magnetic field with the AC powered conductor. Because of its low power consumption (less than 140 μW) and its high performance over a broad range of humidity, the sensor appears to be suitable for many applications ranging from industrial gas monitoring to medical diagnosis where there is a growing need for miniaturized gas and vapor sensors with lower detection limits while maintaining short response times and high chemical stability.

INTRODUCTION

The increasing need and the more stringent requirements for humidity sensors in applications such as process control, appliances, microelectronics, semiconductor, medical applications, and automotive have been continuously driving research and development of novel and high performance devices and sensor materials [**1**]. The areas of improvement for humidity sensors typically include sensor material stability, fouling, hysteresis, response speed, humidity range, operating environment, power consumption, size, and cost. Traditionally, these performance issues have been addressed by a wealth of sensing materials and transducers designed for specific applications with various properties. Accordingly, even the best of these sensors suffer from limitations regarding the sensitivity ranges, chemical stability, response speed, size, or simplicity.

A recent review by Rittersma [**2**] discussed the five main transduction techniques of state-of-the-art humidity sensors: capacitive, resistive, hygrometric, gravimetric, and optical. Among these transduction mechanisms, capacitive, gravimetric, and optical methods appear to be the best suited for low dew point humidity sensing considering their high sensitivity, low response times, low power consumption, and miniaturizability. Other sensing methods have shown promise in detection of humidity at low dew points [**3**]. MEMS-based batch fabrication techniques can significantly reduce sensor cost and allow for integrated electronics.

The majority of commonly used transducers for humidity sensing are based on capacitive concepts. These approaches are based on the measurement of the change in dielectric properties and/or dimensions of hygroscopic thin films upon absorption of moisture. Both resonant [**4**] and non-resonant [**5**] sensors have been built using this concept. However, regardless of the resonant nature of these sensors, their performance is primarily determined by the material properties and the electrode geometry.

Porous ceramics [**6**], high-humidity-uptake dielectric polymers and polymer composites [**7**] are the most frequent sensor materials used in capacitive humidity sensors. More recently, porous silicon [**2**] has been introduced for specific applications. While porous ceramics and silicon appear very attractive because of their large surface area, long-term structural stability, and their batch manufacturability, they suffer serious limitations in comparison to polymers in terms of response linearity, drift due to chemisorption of hydroxyl groups, and susceptibility to contaminants such as smoke.

Although capacitive transducers, in general, have demonstrated fast responses and high sensitivities on the order of a few hundred percent as published in the literature [**1**], the response time and signal to noise ratios of capacitive humidity sensors are still the main areas where improvements are required. According to Nitta and Cunningham [**6, 8**], the response time of capacitive sensors is dictated by the kinetics of water absorption, which is a diffusion-limited mechanism initiated by capillary condensation. The indication is that minimizing the response time of a sensor requires optimization of the material and transducer response simultaneously.

Numerous gravimetric humidity sensors are described in the literature with various operation mechanisms and performances [**2, 9**]. These devices measure the effect of a combination of sensor material, mass change and/or mechanical properties variation, induced by humidity uptake. The change in the sensor material properties produces a change in the resonance frequency of the sensor, which is the direct output of the sensor. Quartz Crystal Microbalances (QCMs), capacitive and piezoelectric Flexural Wave Plates (FPWs), capacitive nano/micro cantilevers and magnetoelastic films and ribbons are the most widely known transducers used in gravimetric humidity sensors. QCMs and capacitive plates/cantilevers are excited and driven into resonance by electrical energy whereas magnetoelastic sensors take magnetic energy as an input. Because of well-understood [**2, 10**] technical considerations, the bandwidth of these sensors is fairly narrow. QCMs, for example, operate at MHz frequencies with a total resonance peak shift for the entire RH range on the order of a kHz or less. As a result, these devices rely on complex and specific electronics to achieve high sensitivities and high signal to noise ratios. In contrast, the device presented in this paper is a gravimetric sensor designed to achieve high bandwidth, high sensitivity at a low cost.

0-9640024-5-0/hh2004/$20©2004TRF
DOI 10.31438/trf.hh2004.80

THEORY

The performance of resonant, gravimetric humidity sensors depends equally on the performance of the resonant and the chemical transducers. In an effort to develop a complete transfer function relating the performance of our sensor to all important variables (i.e. geometry, materials properties…etc), we created an analytical and a numerical model of the membrane and current carrying conductor system shown in Figure 1. The membrane is a low stress silicon nitride membrane, which is uniformly stretched by a tension T (force per unit length) from all four sides. The tension T is the result of the residual stress σ built into the membrane during processing as described in the experimental section. The membrane has a mass m, a density ρ, an elastic modulus E, a Poisson ratio ν and it has the dimensions a, b, and h as displayed in Figure 1. The boundary of the membrane, where the silicon frame is attached to the nitride, is treated as a Dirichlet boundary with zero displacement along the edges.

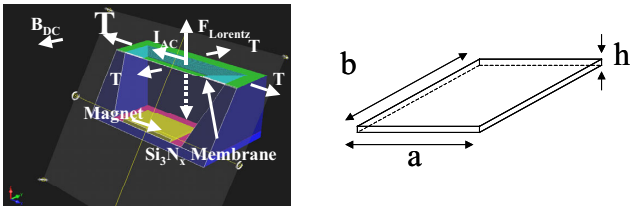

Figure 1. *Operating principles of the sensor and its geometry.*

In the absence of external forces, the wave equation describing the motion of the membrane is

$$\mu \frac{\partial^2 \delta}{\partial t^2} = -D\nabla^4 \delta + T\nabla^2 \delta, \quad \delta = \delta(x, y, t) \qquad \text{(Eq.1)}$$

where δ is the out of plane displacement of point M on the membrane identified by it coordinates x and y in the selected cartesian reference. The mass per unit area, μ, of the membrane is defined as

$$\mu = \frac{m}{ab} = \rho h \qquad \text{(Eq.2)}$$

and D describes the flexural rigidity of the membrane as defined by

$$D = \frac{Eh^3}{12(1-\nu^2)}. \qquad \text{(Eq.3)}$$

The boundary conditions of the membrane are zero displacement Dirichlet conditions and are expressed by the following

$$\begin{aligned} &\delta(0, y, t) = 0, \ y \le b \\ &\delta(a, y, t) = 0, \ y \le b \\ &\delta(x, 0, t) = 0, \ x \le a \\ &\delta(x, b, t) = 0, \ x \le a \end{aligned}, \qquad \text{(Eq.4)}$$

and the initial condition is a uniformly distributed mechanical perturbation

$$\delta(x, y, 0) = \delta_0, \ 0 \le y \le b \ and \ 0 \le x \le a. \qquad \text{(Eq.5)}$$

Using the method of separation of variables, we can express δ by

$$\delta(x,y,t)=f(X)g(Y)\tau(t), \qquad \text{(Eq.6)}$$

where f, g, and τ are sinusoidal functions. By plugging this expression back into equations 1, 4, and 5, we can solve for the resonance frequency of the first fundamental mode of the membrane:

$$f_r = \sqrt{\frac{\pi^2 Eh^2}{48\rho(1-\nu^2)}\left(\frac{1}{a^2}+\frac{1}{b^2}\right)^2 + \frac{T}{4\rho h}\left(\frac{1}{a^2}+\frac{1}{b^2}\right)}. \qquad \text{(Eq.7)}$$

According to (Eq.7), the resonance frequency of the membrane is a function of the residual stress in the membrane as well as the mass of the membrane. The cumulative effect of mass and stress change of the membrane is the basis of our sensing scheme. In fact, the polystyrene sulfonate (H^+ state), a hygroscopic film, is a polyelectrolyte that swells considerably upon uptake of moisture in addition to a mass increase on order of 20 % wt at equilibrium. The swelling mechanism and the high humidity uptake of the sensor film have been discussed extensively in the literature [**11**].

The sensitivity of the transducer to mass (S_m) and stress change (S_{st}) can be derived from (Eq.7). The differential of the resonance frequency with respect to mass and tension is related to these sensitivities by

$$\begin{aligned} df_r &= \left(\frac{1}{2m}\right)\left(-f_r dm + \frac{ab}{4}\left(\frac{1}{a^2}+\frac{1}{b^2}\right)\frac{1}{f_r}dT\right) \\ &= S_m dm + S_T dT \end{aligned}. \qquad \text{(Eq.8)}$$

The cross sensitivity of this transducer to mass and stress variations is then expressed by

$$\begin{aligned} S_{transducer} &= \left| \ S_m * S_T \ \right| \\ &= \frac{1}{16\rho^2_{Si_3N_x}}\frac{1}{abh^2}\left[\frac{1}{a^2}+\frac{1}{b^2}\right]. \end{aligned} \qquad \text{(Eq.9)}$$

The indication of this simple model is that thinner membranes and smaller membranes have a higher sensitivity than larger and thicker diaphragms.

DEVICE DESIGN & FABRICATION

The micromachined humidity sensor consists of two parts: silicon micromachined resonant membrane and the sensing material. The platform contains dual rectangular silicon nitride membranes with the metal conductor on top of it. The sensing material is applied to the backside of the membrane in the sensing cell but no sensing film is required for the reference cell. The reference cell is designed to compensate for the cross-sentivity to noise parameters (e.g. pressure, temperature, etc). Different sensing materials, such as polystyrene sulfonic acid (PSSA) or a

Table 1. *Design of experiment examining the role of device geometry.*

Design	Metal width (μm)	Metal length (μm)	Final Membrane Size (μm)	Chip Size (μm)
1/2 X Straight	150	2005	1500x1800	6650x6650
1/2 X Serpentine	50/50	21505	1500x1800	6650x6650
1/3 X Straight	100	2003	1000x1300	6650x6650
1/3 X Serpentine	35/35	15653	1000x1300	6650x6650

functionalized self-assembled monolayer, have been used to maximize the device sensitivity.

This study examines the effects of the membrane dimension on sensor performance. The geometrical design of experiment has been performed to optimize the performance of the micromachined humidity sensors, as shown in Table 1. The straight or serpentine microresistor design can be used for either resonance frequency shift or differential scanning nanocalorimetry measurement. For the resonance frequency shift experiment, the straight-line design is preferred because it can generate a larger Lorentz force and stable vibration modes. The metal dimension determines the electrical current passing through the conductor and thus, modulates the Lorentz force at a given magnetic flux. The dimensions of the membrane control the coverage area for the sensing material. The two contact pads are used to flow current through the conductor.

A relatively simple and robust process has been developed based on bulk micromachining. A layer of low stress silicon nitride (~200 MPa) with a thickness of 0.5 or 1 μm is deposited on the surface of the 300 μm thick (100) n-type silicon substrate. The current carrying conductor and contact pad consist of 5/40 nm thick Ti/Pt, which are patterned via a metallization and lift-off process. Finally, the etch windows are opened at the backside of the wafer using Reactive Ion Etching of silicon nitride and a 30% Potassium Hydroxide (KOH) etch with a rate of 1.1 μm/min at 80°C, to release the silicon nitride membranes. During the KOH etching, the front side of the wafers is protected by a special wafer holder so the KOH will not attack the metal conductor. This process has a yield of approximately 100%. The inset of Figure 2 shows a final packaged humidity sensor.

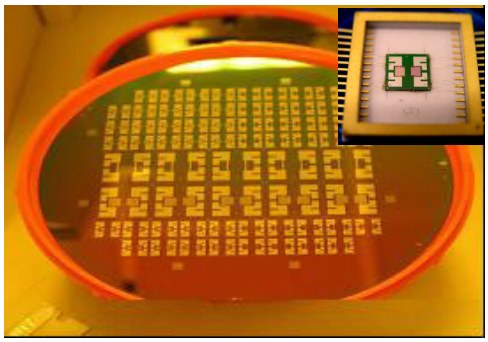

Figure 2. *Picture of a completely processed wafer of humidity sensors. The inset photo shows a packaged die for humidity sensor testing.*

EXPERIMENTAL RESULTS

Dies were coated individually with 2 μL of 0.01 M Poly Styrene Sulfonic Acid (PSSA) co-polymer. Table 2 shows the water absorption capability of four different formulations of PSSA. Thermal Gravametric Analysis (TGA) was used to determine the weight change of different four different formulations of PSSA. Graphs of the water absorption behavior showed that the H+ co-polymer had a stable water uptake with temperature in comparison with some of the more highly absorptive formulations. One risk of using a highly adsorptive polymer is the generation of high stresses on the membrane structure causing device failure. The PSSA was applied to the backside the membrane with a small syringe and allowed to dry for 5-10 minutes.

Table 2. *Weight change due to water absorption for various co-polymer PSSA formulations.*

	Percent Weight Change
Li^+	26.9%
Cs^+	10.5%
Mg^{2+}	30.6%
H^+	18.0%

Figure 3 shows a schematic of the test setup used to examine the resonant response of the humidity sensor. The individual dies were placed in a Teflon™ jig that included a small permanent magnet located underneath the chip, spring-loaded probes, and an interrogation hole for the laser vibrometer. The permanent magnet is approximately 12 mm^3 and generates a weak magnetic field of approximately 3 T. This jig was fixed to a port of a stainless steel pressure vessel. The fixture also included a hole which allowed the atmosphere of the chamber to interact with the polymer on the backside of the membrane. The atmosphere of the chamber was controlled through the use of a Dew Point Generation (DPG) system and a chilled mirror humidity sensor. Dry Nitrogen gas was used as the carrier gas for the humidity. A network analyzer in conjunction with a laser vibrometer was used to drive the membrane into resonance and measure the resonant frequency.

Each test consists of two phases: desorption and adsorption. First, a DC power supply was used to desorb the absorbed water in the PSSA using a power of approximately 40 mW. Simultaneously, the Dew Point Generator set to the desired setpoint and its output is checked with the chilled mirror. The chamber humidity is allowed to stabilize during the desorbtion of water from the polymer. Once the sensor has fully desorbed water from the polymer material, the DC power supply is terminated. The polymer is allowed to adsorb humidity from the humidity

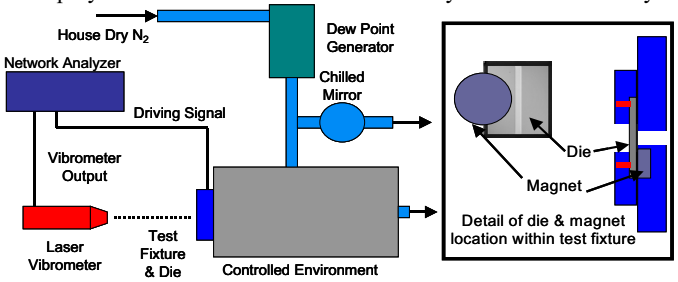

Figure 3. *Experimental setup for resonant frequency measurements at specified humidity.*

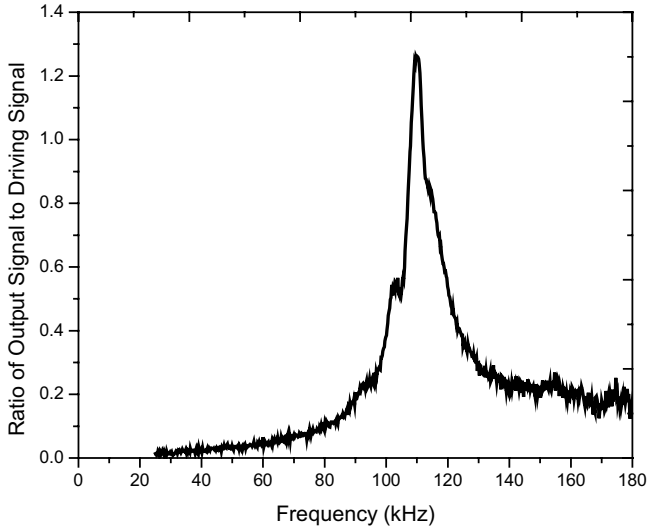

Figure 4. *Resonant frequency response for a 1 by 1.3 mm, 0.5 μm thick membrane at 217 ppm water.*

Table 3. *Humidity Sensor performance with respect to geometry.*

Membrane Area (mm^2)	Membrane Thickness (μm)	Sensitivity (Hz/°C DP)	Max Non-linearity	Max Hysteresis	Resolution (°C DP)
2.7	1.0	20.58	0.14%	0.07%	4.37
2.7	0.5	69.28	0.40%	0.40%	1.30
1.3	1.0	39.85	0.37%	0.39%	2.26
1.3	0.5	69.64	0.44%	0.66%	1.29

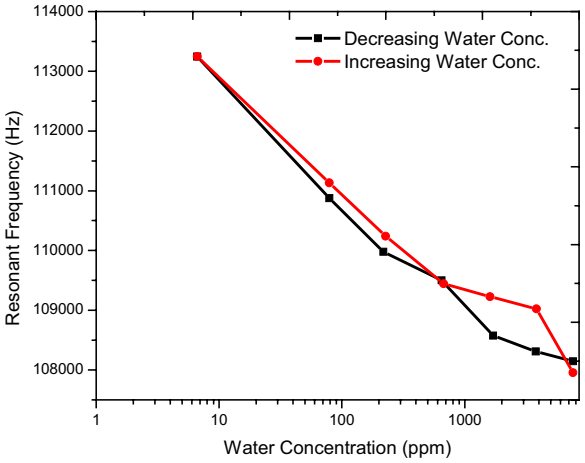

Figure 5. *Hysteresis over a 7500 ppm range of a 1 by 1.3 mm, 0.5 μm thick membrane structure.*

controlled environment for approximately 5 minutes. This time is required to ensure a homogenous environment with our high volume chamber. The network analyzer then drives the membrane into resonance by scanning a range of frequencies between 0-200 kHz at an output power of 15 dbs @ 1.26 Volts. A measurement is made of the ratio of the output of the vibrometer divided by driving signal generated by the network analyzer.

Figure 4 shows a typical resonant peak for a 1.0 by 1.3 mm 0.5 μm thick membrane. Tests for each design were performed at dew points ranging from -60°C up to 10°C at intervals of 10°C which corresponds to a range of water concentrations of 7 to 7600 ppm. Table 3 summarizes the response for each of the designs in terms of the sensitivity, non-linearity, and hysteresis. Figure 5 summarizes the resonant testing results examining the effect of the membrane geometry on sensitivity. Hysteresis measurements were performed by cycling the humidity from -60°C up to 10°C to determine if the membrane or polymer has any memory of its previous state.

Drift of the sensor was tested over a time span of 1 hour and examined the accuracy of the measurements. Measurements were taken at three different humidity levels (-60°C, -30°C, 10°C) to determine if there were any differences in drift at different humidities. Sensor drift was limited to 100 Hz that did not vary with humidity. This corresponds to a maximum resolution of the 1.0 by 1.3 mm, 0.5 μm thick membrane of 2.5°C dew point.

An analysis of the data suggests that increased sensitivity can be achieved by optimizing the membrane geometry. Reducing the thickness of the membrane improves the sensitivity of the sensor, which is consistent with the conclusions provided by Eq.9. Smaller geometry membranes also improve the sensitivity of the device although this effect becomes minimal at very thin geometries where the effect of thickness is more considerable.

CONCLUSIONS

Humidity sensors based on resonant frequency shift due to a mass change of polystyrene sulfonic acid were fabricated and tested. Small membrane structures with very thin membranes showed a very linear response over a wide bandwidth and at low dew points. Sensitivities, hysteresis, and resolution of this resonant-based sensor compare very favorably to polyimide sensors based on resonant structures [**4**] or capacitive schemes [**12**]. Further testing is necessary determine if sensitivity improvements can be obtained with PSSA formulations that exhibit better water adsorbtive properties such as Mg^{2+} or Li^{+}. Materials such as self-assembled monolayers or zeolites could also show improved sensitivity and resolution due to their higher surface area and nanomorphology. In order to mass produce humidity sensors based on polyelectrolytes, low cost coating techniques are being developed.

ACKNOWLEDGMENTS

The authors would like to thank the support and hard work of Joe Krisciunas, Stacey Goodwin, Laura Meyer, Glenn Claydon, and Dennis Cusano.

REFERENCES

1. T. Hayes and R. Bayrer, “Chemical Sensors: Liquid, Gas, and Biosensors”, The Freedonia Group, Inc., April 2002.
2. R. E. Cavicchi, et. al., “Microdifferential Scanning Calorimeter for Combustible Gas Sensing”, *Sensors and Actuators B* 97 (2004) pp. 22-30.
3. Z. M. Rittersma, “Recent achievements in miniaturized humidity sensors-a review of transduction techniques”, *Sensors and Actuators* A 96 (2002) pp. 196-210.
4. T. Harpster, B. Stark, and K. Najafi, “A passive wireless integrated humidity sensor”, *Proceedings of the 14th IEEE International Conference on MEMS*, Interlaken, Sweden, January 21-25 2001, pp. 553-557.
5. A. Foucaran, et. al., “Porous Silicon Layer Coupled with a Thermoelectric Cooler: A Humidity Sensor”, *Sensors and Actuators A*, 79, (200), pp. 189-193.
6. T. Nitta and S. Hayakawa, “Ceramic Humidity Sensors”, *IEEE transactions on components, hybrids, and manufacturing technology*, Vol. CHMT3, No.2 June 1980.
7. W. H. Tao, et. al., “The humidity sensing properties of Organic Inorganic (AMPS/SiO_2) hybrid materials”, *Proceedings of IEEE Sensors*, Taipei, Taiwan, June 12-14 2002, Vol. 1, pp. 641-646.
8. R. Cunningham and R. Williams, *Diffusion in Gases and Porous Media*, Plenum Press, New York, 1980.
9. A. Schroth, et. al., “A resonant Polyimide-based humidity sensor”, *The 8th international conference on solid state sensors and actuators, and Eurosensors IX*, Stockholm, Sweden, June 25-29 1995, Vol. 2, pp. 740-742.
10. C. Grimes, D. Kouzoudis, E. Dickey, D. Qian, M. Anderson, R. Shahidain, M. Lindsey, and L. Green, “Magnetoelastic Sensors in Combination with Nanometer-scale Honeycombed Thin Film Ceramic TiO2 for Remote Query Measurement of Humidity”, *Journal of Applied Physics*, 87, 9 (2000).
11. M. Rubinstein, R. H. Colby, A. V. Dobrynin, J.-F. Joanny, “Elastic modulus and equilibrium swelling of Polyelectrolyte Gels”, *Macromolecules*, 29, 398-406, (1996).
12. C. Laville and C. Pellet, “Interdigitated Humidity Sensors for a Portable Clinical Microsystem”, *IEEE Transactions on Biomedical Engineering*, 49, 10, 1162-1167, (2002).

IN SITU MONITORING OF NATIVE OXIDE FILM BEHAVIOR AT MEMS CONTACT INTERFACES THROUGH BASIC ELECTRICAL MEASUREMENTS

L. Kogut, A. Lumbantobing, and K. Komvopoulos
Department of Mechanical Engineering, University of California, Berkeley, CA 94720

ABSTRACT

Special surface micromachines were used to study the behavior of polysilicon/native oxide/polysilicon contact interfaces. Contact voltage measurements obtained during monotonic and cyclic contact loading were analyzed in the context of an electrical contact resistance theory in order to elucidate the contact behavior of the native oxide film. The results indicate that the oxide film remains nearly intact under monotonic contact loading, while it ruptures under cyclic contact loading, resulting in the formation of polysilicon/polysilicon asperity contacts, which decreases significantly the contact voltage for constant current across the interface. The erratic behavior of the contact voltage during cyclic contact loading is attributed to the pronounced effects of the insulating oxide film and fine oxide debris trapped at the contact interface. A reliable method to remove the native oxide film from the asperity contacts is presented, and its efficacy to change the contact interface behavior from nonohmic to ohmic is demonstrated by current versus contact voltage measurements. A good agreement was found between experimental and theoretical results for the current-contact voltage response. This study shows that the native oxide film can be removed from the contact interfaces of micromachines by electromechanical means without inducing surface damage.

INTRODUCTION

In view of the increasing number of microelectromechanical systems (MEMS) involving surface contact, understanding of the behavior of MEMS contact interfaces is imperative. Touch-mode MEMS devices are advantageous in many applications, such as electrostatic actuators [**1**], microswitches [**2**], and microrelays [**3**]. The performance and lifetime of such microdevices depend on the behavior of their contact interfaces. However, basic knowledge of MEMS contact interfaces is sparse due to limitations of conventional microscopy techniques to access hindered contact interfaces [**4**].

Polysilicon oxidizes readily upon exposure to air. When two polysilicon surfaces are brought into contact (Fig. 1) and electric current is passed through their contact interface, the flow of electrons is impeded by the constriction resistance (R_{ci}) of the asperity contacts [**5**] and the tunnel resistance (R_{ti}) of the thin insulating native oxide film separating the two surfaces [**6**]. Thus, the contact voltage measured across the interface can be used to characterize the contact behavior [**5**,**6**]. Ohmic contacts are desirable in a variety of applications, such as microrelays [**7**]. However, the potential barrier due to the presence of an insulating film dominates the charge transport, resulting in nonohmic behavior at the contact interface.

The main objective of this study was to explore the feasibility of current and contact voltage measurements as a nondestructive *in situ* means of monitoring the behavior of MEMS contact interfaces To accomplish this objective, a special microdevice was designed and fabricated using surface micromachining with poly-silicon as the structural material. A simple and reliable procedure was developed to remove the native oxide film from asperity contacts and, hence, change the contact resistance behavior from nonohmic to ohmic. The efficiency of this technique was demonstrated by current versus contact voltage measurements. The MEMS devices were tested under a variety of operating conditions and the results were interpreted in the context of an electrical contact resistance (ECR) theory [**6**], thus providing new insight into the characteristics of MEMS contact interfaces.

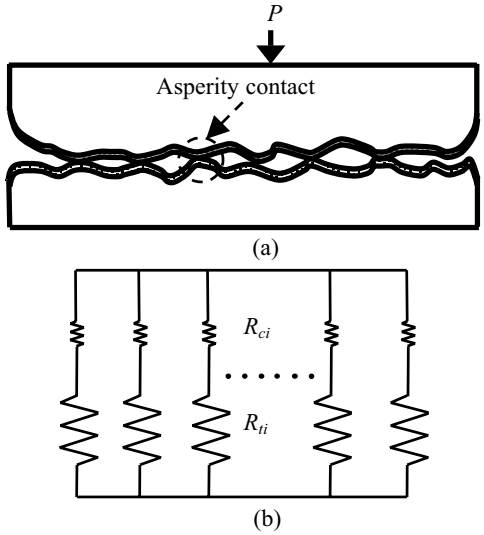

Figure 1. *(a) Polysilicon surfaces in normal contact separated by an insulating native oxide film, and (b) electrical analog of the contact interface consisting of constriction resistance R_{ci} and tunnel resistance R_{ti} at each asperity contact.*

EXPERIMENTAL PROCEDURES

Figure 2 shows a scanning electron microscope (SEM) micrograph of the MEMS device used in the present experiments. The main part of the microdevice is a microstructure (shuttle) connected to pad A. The shuttle is suspended above the substrate by a folded-flexure suspension. Four 10 μm × 10 μm dimples at the corners of the bottom surface of the shuttle are used to control the contact area. Three electrodes below the shuttle – the center electrode (connected to pad B) and two electrically connected side electrodes (connected to pad C) that are isolated from the center electrode – are used to actuate the shuttle in the normal direction and to obtain electrical measurements. The shuttle and center electrode and the shuttle and side electrodes form an electrostatic closing gap actuator, which is used to pull the shuttle into contact with the side electrodes at the dimples. It is reasonable to postulate that the dimples share equally the contact load, and that the contact interface behavior of the four dimples and the two side electrodes is analogous to that of four identical resistors in parallel.

The test microdevice was fabricated by surface micro-

Travel support has been generously provided by the Transducers Research Foundation and by the DARPA MEMS and DARPA BioFlips programs.

0-9640024-5-0/hh2004/$20©2004TRF
DOI 10.31438/trf.hh2004.81

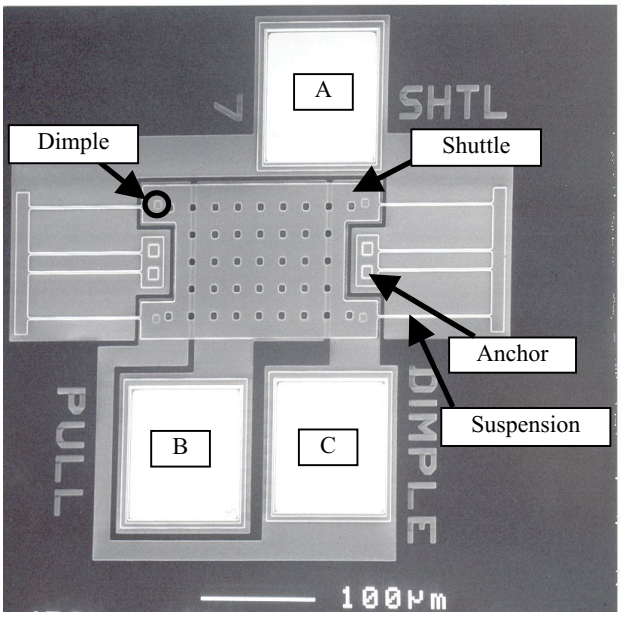

Figure 2. *Scanning electron micrograph of the microdevice.*

machining using multi-user MEMS processes (MUMPs). The three electrodes consist of a 0.5 μm thick polysilicon layer (poly 0) and are isolated from the n-type Si(100) substrate by a 0.6 μm thick SiN layer. The suspension system consists of a 2 μm thick polysilicon layer (poly 1). The fabrication of the shuttle was completed by stacking the poly 1 and poly 2 layers (total thickness equal to 3.5 μm) in order to increase the rigidity of the shuttle. The 0.75 μm in height dimples at the bottom surface of the shuttle were fabricated from poly 1. A 0.5 μm thick Au layer was evaporated on the pads in order to minimize the ECR at the microprobe/pad contact interfaces. The actual dimensions of the microdevice were measured before testing to insure accurate modeling. The post-fabrication lateral dimensions and film thickness of the microdevice were measured with a SEM and an optical interferometric profiler, respectively. Relatively small discrepancies (less than 10%) were observed between actual and design dimensions. The surface topographies of the side electrodes were examined with an atomic force microscope (AFM) using a silicon tip of nominal radius of curvature equal to 10 nm. Three 1 μm × 1 μm AFM images with a lateral resolution of 2.5 nm, obtained at various locations on the electrode surfaces, were used to examine the homogeneity of the surface topography.

The experiments were performed in a high-vacuum multi-probe station (MMR Technologies, Inc., California) mounted on a vibration isolation table. A mechanical roughing pump and a turbo pump were used to evacuate the chamber to pressures as low as 10^{-6} Torr. The chamber, connected to a source of dry nitrogen (99.998% purity) via a dehumidifying filter, was first pumped down to 10^{-6} Torr and then refilled with dry nitrogen. Unless otherwise stated, the experiments were carried out in dry nitrogen, room temperature, and atmospheric pressure.

RESULTS AND DISCUSSION

Monotonic contact loading

Measurements of contact voltage versus monotonically increasing contact pressure were obtained under constant current in order to determine the thickness of the native oxide film and to analyze its response to mechanical stresses. The shuttle was first pulled down by slowly increasing the DC bias voltage applied to the center electrode V_P (Fig. 3). When the bias voltage reached a critical value [**8**], instability occurred and the shuttle snapped into contact with the substrate, forming four contact interfaces between the dimples and the side electrodes across which the contact voltage was to be measured. At that instant, the gap between the shuttle and the center electrode was equal to the height of the dimples (0.75 μm). Subsequently, V_P was increased gradually to produce a monotonically increasing contact load. At each load level, the contact voltage across the interface of the four dimples and two side electrodes was measured via a voltmeter by applying a constant current of 10 μA across the interface.

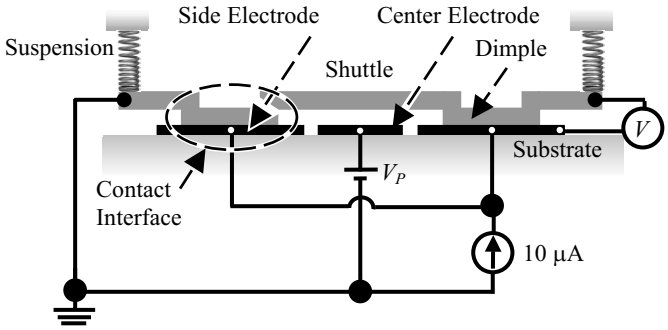

Figure 3. *Schematic cross-sectional view of the microdevice showing the circuit used for contact voltage measurement in the monotonic and cyclic contact loading experiments.*

Figure 4 shows the contact voltage versus apparent contact pressure p_a, defined as the ratio of the contact load to the apparent contact area. Each data point and error bar represents the average contact voltage and standard deviation, respectively, obtained from 36 microdevices selected from three different dies and tested at a given apparent contact pressure. The measured contact voltages correspond to ECR values of the order of 100 kΩ, i.e., about five orders of magnitude higher than those obtained with MEMS devices possessing gold (ohmic) contacts (~1 Ω) [**9**]. Since the microdevices consist of heavily doped polysilicon with specific resistivity only three orders of magnitude higher than that of gold [**9**], the five orders of magnitude higher ECR values shown in Fig. 4 indicate the presence of an insulating (oxide) thin film at the contact interface (nonohmic contact). The moderate decrease of the contact voltage with the increase of the apparent contact pressure is indicative of a nonohmic contact behavior. This is a characteristic of the tunnel resistance of a thin insulating film. The tunnel resistance increases with the decrease of the voltage drop across each asperity contact due to the increase of the effective barrier height [**10**]. The increase in the apparent contact pressure produces a larger contact area and, hence, lower ECR, which, for fixed current flow (10 μA), yields a smaller voltage drop across the interface. This increases the asperity contact tunnel resistances, thereby compensating the decrease of the contact voltage [**6**].

Polysilicon surfaces are known to readily oxidize upon exposure to room air. On average, a microdevice was exposed to the atmosphere for about 2 h prior to testing in dry nitrogen. Based on experimental results [**11**], it was predicted that a 6.5 Å thick native oxide film formed on the polysilicon surfaces during the exposure to the ambient conditions. Since the thickness of the oxide film is significantly less than the measured rms surface roughness (137 Å), it may be postulated that the oxide film did not possess a uniform thickness. Therefore, the 6.5 Å value was treated as the rms value of the oxide film thickness, implying that an oxide film of effective thickness equal to 9.2 Å existed at the dimple/electrode contact interfaces.

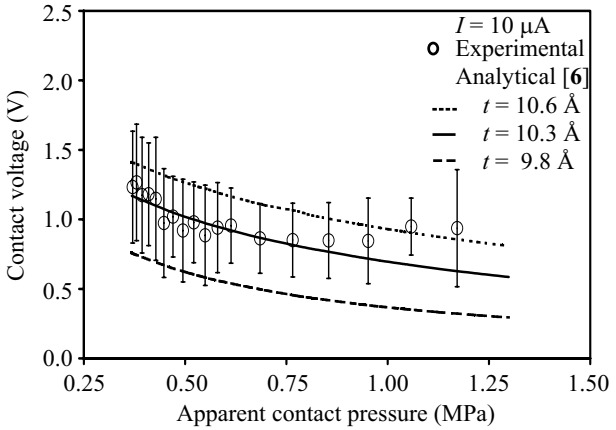

Figure 4. *Contact voltage versus apparent contact pressure for monotonic contact loading.*

The ECR theory reported in Ref. [**6**] for conductive rough (fractal) surfaces separated by a thin insulating film was used to analyze the experimental results shown in Fig. 4. In the low-pressure regime (p_a < 0.75 MPa), the experimental data show a 25% decrease in average contact voltage with the increase of the apparent contact pressure. This behavior agrees well with the analytical solution obtained for insulating film thickness t = 10.3 Å. The error bars in the experimental data are bounded by solutions corresponding to t = 9.8 and 10.6 Å. The 10.3 Å film thickness is close to the predicted effective thickness of the native oxide film (9.2 Å). The fairly accurate theoretical predictions of the contact voltage in the low-pressure regime suggest that contact voltage measurements together with appropriate theoretical treatment can be used to determine *in situ* the thickness of the native oxide film at MEMS contact interfaces.

The agreement between experimental and analytical results decreases in the high-pressure regime (p_a > 0.75 MPa). The measured contact voltage reaches a plateau and then increases slightly with the increase of the apparent contact pressure, contrary to the trend predicted by the analytical solutions. This is a result of the significant bending of the shuttle due to the high electrostatic force, resulting in partial surface separation of the dimples from the side electrodes. As a consequence, the contact area decreased and, in turn, the contact voltage increased (for constant current) [**6**]. This effect compensated the decrease of the contact voltage due to the increase of the apparent contact pressure, producing a contact voltage plateau.

Cyclic contact loading

The response of the oxide film to cyclic contact loading was examined by applying and removing a bias voltage V_P to the center electrode (Fig. 3) in order to simulate the loading and unloading stages of a contact loading cycle. A bias voltage (maintained constant throughout a single test) was applied for 1 s during each loading stage. The cycle frequency was set at 0.5 Hz, and contact voltage measurements were acquired during both loading and unloading for a constant current of 10 μA applied across the contact interfaces (Fig. 3). In these tests, the electrostatic force during contact was varied between 0 and 24 μN (low-load range) and 0 and 95 μN (high-load range), sufficiently high to initiate contact without causing excessive bending of the shuttle, for a minimum of 10^5 contact loading cycles using 10 and 8 microdevices, respectively. However, despite the removal of the electrostatic force, the shuttle was permanently adhered to the side electrodes, as indicated by the finite contact voltage measured during unloading. Stiction of the shuttle to the substrate occurred due to the relatively smaller restoring force than the adhesion force generated at the contact interface. Regardless of this limitation, valuable insight into the contact behavior was obtained from the cyclic contact loading experiments.

Figure 5 shows characteristic examples of contact voltage responses obtained during the loading stage of the cyclic contact loading experiments for electrostatic force in the high-load range. A significantly erratic behavior of the contact voltage occurred during testing. Similar results were observed for electrostatic force in the low-load range. The analytical results shown in Fig. 4 reveal that the decrease in the contact voltage can only be attributed to thinning of the insulating oxide film at asperity contacts, leading to the formation of third-body oxide debris. Using the ECR theory presented in Refs. [**5**] and [**6**], it was predicted that rupturing of the oxide film from all the asperity contacts or only from the smallest asperity contact should yield contact voltages of the order of 10^{-3} and 10^{-2} V, respectively. Therefore, the contact voltage fluctuations may be attributed to redistribution of fine oxide debris produced from rupturing of the oxide film at several asperity contacts. Because only normal contact occurred, oxide debris remained within the vicinities of asperity contacts. Despite the fact that the dimples and side electrodes remained attached throughout testing, separation of several asperity contacts occurred during unloading, providing a means for oxide debris to redistribute at the contact interface and, thus, cause fluctuations in the contact voltage response.

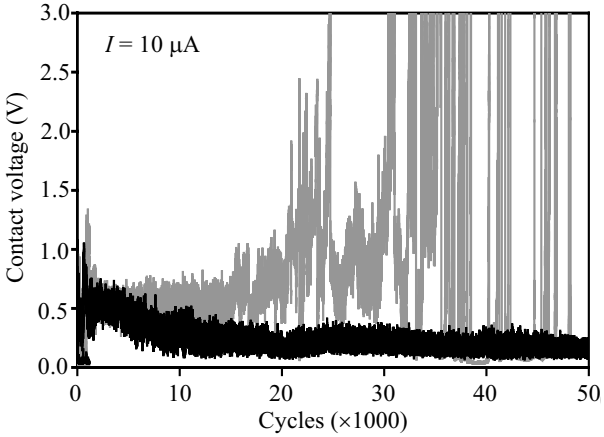

Figure 5. *Examples of contact voltage responses obtained during the loading stage of cyclic contact loading experiments performed under electrostatic force varied between 0 and 95 μN.*

Transition from nonohmic to ohmic behavior

Since cyclic contact loading did not produce a stable ohmic response, additional experiments were performed in order to develop a reliable procedure for altering the contact behavior from nonohmic to ohmic. Figure 6 shows a schematic of the microdevice and the electrical connections used to obtain current versus contact voltage measurements. By applying a potential V_D to the side electrodes and grounding the shuttle and the center electrodes (V_P = 0), electrostatic force was generated between the side electrodes and the free-standing shuttle. To establish contact between the shuttle and the substrate, V_D was gradually increased until the shuttle snapped into contact with the underlying side electrodes. Once contact was established, current flow commenced between the side electrodes and the shuttle, resulting in zero electrostatic force. However, the shuttle remained stuck to the electrode surfaces, as mentioned earlier. This enabled the

measurement of the current in terms of the contact voltage (by varying V_D), thereby allowing characterization of the contact interface without changing the contact load. All the results presented below were obtained from experiments conducted under working pressure of 10^{-6} Torr.

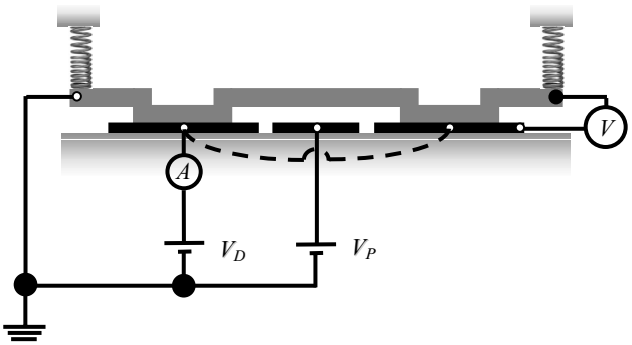

Figure 6. *Schematic cross-sectional view of the microdevice showing the circuit used in the current versus contact voltage characterization.*

Figure 7 shows a comparison between experimental and analytical results [**6**] of the current as a function of contact voltage. The experimental results were obtained from 11 microdevices selected from two different dies. For each microdevice, the current was measured for different contact voltages, while ramping V_D up and down in the range of 0–5 V. Solutions for the current versus contact voltage (not shown here for brevity) were obtained for different contact loads using the theory presented in Ref. [**6**]. A good agreement was found between experimental and theoretical results for a contact load (including adhesion) equal to 36 μN. Since the restoring force generated by the suspension was equal to 14 μN, the adhesion force [**12**] was estimated to be equal to 50 μN. This high adhesion force resulted in permanent adhesion (stiction) of the shuttle to the side electrodes. As shown in Fig. 7, the contact interface exhibited a nonohmic behavior that is attributed to the nonohmic tunnel resistance.

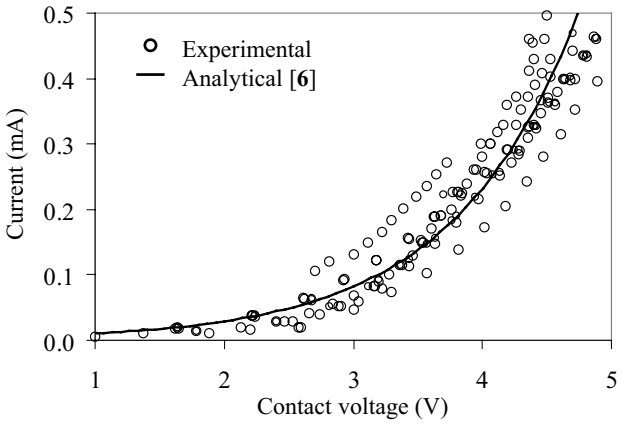

Figure 7. *Current versus contact voltage after pulling the shuttle into contact showing nonohmic behavior.*

Figure 8 shows that the corresponding power dissipation, obtained by multiplying the current by the contact voltage (Fig. 7), increases with the contact voltage. Since thermal softening of gold contacts occurred for similar values of power dissipation [**9**], it was necessary to examine whether the contact interface was altered during the measurements. Hence, instead of using the same microdevice (Fig. 4), contact voltage measurements for a given apparent contact pressure were obtained with a new microdevice. In these experiments, electrical energy about two orders of magnitude less than that in the monotonic contact loading experiments (Fig. 4) was supplied to the contact interfaces, which reduced the possibility of thermal softening. A total of 12 microdevices were used to measure the contact voltage for 12 different values of apparent contact pressure covering the entire apparent contact pressure range shown in Fig. 4. The results obtained from these experiments were found to be in good agreement with those obtained using the original testing procedure. Therefore, it is concluded that thermal softening did not occur during testing and that the variation of the contact voltage in Fig. 4 is solely due to the effect of the contact load on the real contact area.

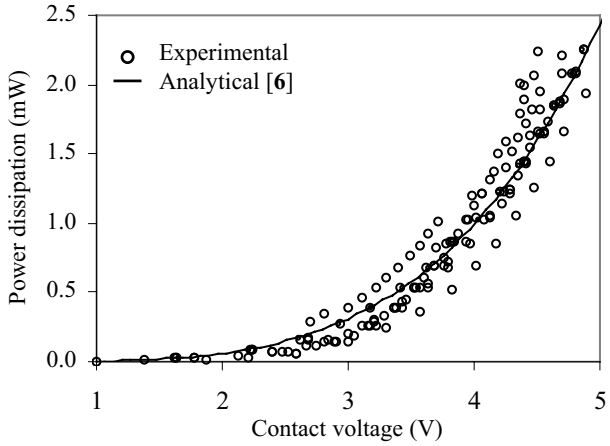

Figure 8. *Power dissipation versus contact voltage response corresponding to the results shown in Fig. 7.*

Figure 9 shows representative results for the current versus contact voltage behavior of a stuck microdevice (curve denoted original). The common method for releasing adhered microdevices by a mechanical microprobe was employed in these experiments. The released microdevice was pulled again into contact by increasing gradually the voltage V_D, following the procedure described earlier. The variation of the current with contact voltage (1^{st} release) shows again nonohmic behavior, suggesting that the native oxide film was not ruptured during mechanical probing. The behavior obtained after repeating this process (2^{nd} release) reveals a similar trend. Thus, the microdevice continued to exhibit nonohmic contact behavior even after it was released based on this technique. For constant contact voltage, the current decreased after each release process, presumably due to surface roughening caused by the abruptness of the probing process.

As mentioned in the previous section, applying a high electrostatic force to the shuttle by biasing the center electrode caused downward bending of the shuttle. This bending of the shuttle was examined as a means of releasing the stuck shuttle and also altering the current-contact voltage response. In these experiments, the shuttle was first pulled into contact by using the aforementioned approach based on the gradual increase of V_D. Then, the voltage V_P applied to the center electrode (Fig. 6) was increased slowly, while the current flow corresponding to a constant voltage V_D was monitored continuously. Only a moderate increase in the current (compared to the values obtained upon initial contact) occurred up to $V_P = 90$ V, as discussed previously.

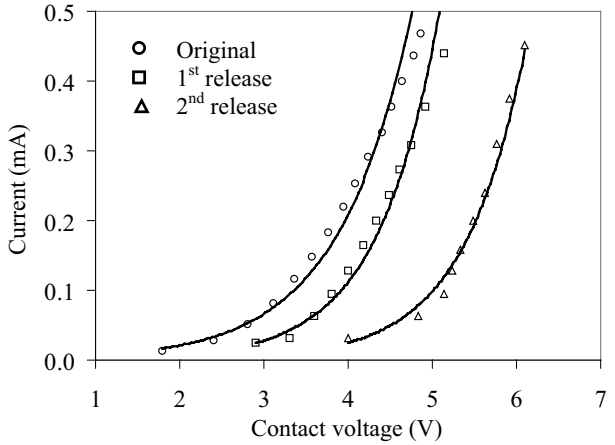

Figure 9. *Current versus contact voltage for a microdevice released with a mechanical microprobe.*

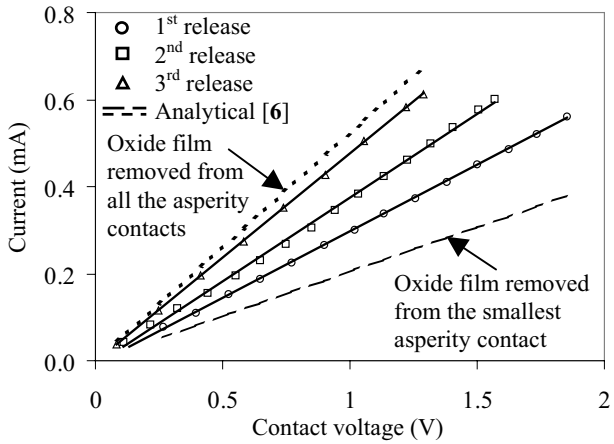

Figure 10. *Current versus contact voltage for a microdevice released by applying and removing a relatively high electrostatic force to cause bending and snapping back of the shuttle. The analytical results were obtained from the theory presented in Ref. [6] assuming that the native oxide film was removed from the smallest asperity contact and all the asperity contacts.*

However, the abrupt decrease in the current observed when $V_P >$ 90 V suggested that excessive bending of the shuttle occurred, causing rocking of the dimples. As a consequence, the real contact area between the dimples and the side electrodes decreased, thus reducing the magnitude of the adhesion force at the contact interfaces. Consequently, upon the removal of the voltage V_P, the shuttle snapped back to its original free-standing position, as indicated by the current measurements (open contact).

After the first successful release using the previous method, the shuttle was pulled again into contact with the substrate by applying a voltage V_D to the side electrodes. Figure 10 shows a linear current versus contact voltage response (1st release) that reveals an ohmic behavior, indicating the removal of the oxide film from the asperity contacts. ECR simulations based on the theory presented in Ref. [**6**] confirmed the ohmic behavior and yielded a current-contact voltage response similar to that shown in Fig. 10 for the extreme cases where the oxide film was either absent from all the asperity contacts or only from the smallest one. The aforementioned process was repeated (e.g., 2nd and 3rd release in Fig. 10) resulting in a progressive increase of the current (for constant contact voltage) towards values predicted for conductive rough surfaces (ohmic contacts) [**5**]. The contact interface always exhibited an ohmic behavior after each release process, contrary to the erratic behavior obtained by cyclic contact loading, suggesting the permanent removal of the oxide debris from the asperity contacts comprising the real contact area. This is probably due to the bending of the shuttle that caused relative slip between the dimples and the side electrodes. Such microscopic interfacial slip resulted in the permanent removal of the oxide debris from the asperity contacts, producing a stable ohmic behavior characterized by a linear current versus contact voltage response.

Figure 11 shows the power dissipation versus contact voltage corresponding to the results shown in Fig. 10. For constant contact voltage, the power dissipation increases with the number of release cycles due to the increase of the current flow. However, for a given contact voltage, the power dissipation of microdevices with ohmic contacts assumes higher values than those with nonohmic contacts (Figs. 11 and 8, respectively) due to the higher current intensities produced (Figs. 10 and 7, respectively). The higher power dissipation may result in thermal damage of a MEMS device operating under a high contact voltage. While for ohmic contacts the power dissipation versus contact voltage is parabolic (power dissipation is proportional to the contact voltage squared and inversely proportional to the contact resistance, Fig. 11), for

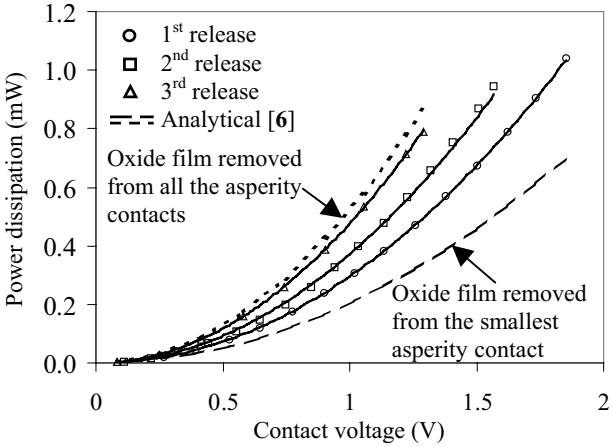

Figure 11. *Power dissipation versus contact voltage responses corresponding to the results shown in Fig. 10.*

nonohmic contacts, the contact resistance depends on the contact voltage and, therefore, the relationship of the power dissipation and the contact voltage is not parabolic (Fig. 8).

Figure 12 shows the variation of the current with time when the stage temperature was increased from 35 °C to 155 °C in four steps of 2 min each. In the first minute of each cycle, the stage temperature increased linearly at a rate of 30 °C/min. The temperature was maintained constant during the second minute of each step. As shown in Fig. 12, the current response lagged the temperature change by a few seconds (typically 5 to 8 seconds) and the current decreased with the increase of the stage temperature. The time lag is probably a result of the thermal resistance of the microdevice-stage interface and the contact interfaces between the polysilicon surfaces. The change in the current is relatively small (less than 10% of the original value for a temperature change of 120 °C). However, the current variation of ~1 mA can easily be resolved with a standard ampermeter of resolution equal to 1 μA, corresponding to a temperature resolution of 0.12 °C for a dynamic range of 120 °C. This demonstrates the possibility of using current measurements in MEMS devices possessing contact interfaces as a means of *in situ*

surface temperature sensing. The small temperature effect on the current is attributed to the fact that the tunnel resistance is practically independent of temperature [**13**], and the constriction resistance, which increases with the increase of the temperature, is much smaller than the tunnel resistance [**6**]. Therefore, for increased sensitivity, devices with ohmic contacts are more advantageous.

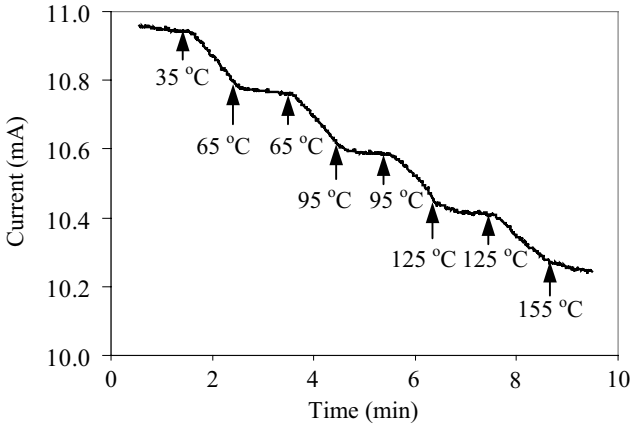

Figure 12. *Current versus time showing the thermal response at the contact interface. The temperatures shown are stage temperatures, and the heating rate was equal to 30 °C/min.*

The present work can be extended to analyze *in situ* the deformation behavior of an insulating film at contacts of microswitches and microrelays. The approach derived in this study for removing the native oxide film, which is responsible for the nonohmic behavior of MEMS contact interfaces, is straightforward and can easily be adopted in various microdevices to improve the reliability and operation performance.

CONCLUSIONS

The design of a polysilicon microdevice fabricated by surface micromachining, suitable for characterizing the native oxide film at MEMS contact interfaces through basic electrical measurements, was demonstrated in this study. The electrical response of the contact interface was interpreted in terms of an earlier ECR theory to provide insight into the behavior of the oxide film under various contact loadings. Based on the presented results and discussion the following main conclusions can be drawn from this investigation.

(1) Under monotonic contact loading, the voltage decreases with the increase of the apparent contact pressure due to the increase of the real contact area. The measured voltage is less sensitive to changes in the contact pressure than ohmic contacts due to the intrinsic behavior of nonohmic contacts.

(2) The thickness of the oxide film extracted from voltage versus contact pressure measurements and an earlier ECR theory was found to be equal to ~10 Å. The fact that the oxide thickness was not affected by contact loading is indicative of the durability of the oxide film under monotonically increasing contact loads.

(3) Cyclic contact loading promoted rupturing of the oxide film, resulting in polysilicon/polysilicon asperity contacts that reduced the contact voltage significantly. However, redistribution of oxide debris at asperity contacts produced erratic contact voltage response.

(4) The removal of the oxide film from asperity contacts through the application of electrostatic forces resulted in the release of the initially adhered microdevice and the transition from nonohmic to ohmic contact behavior.

(5) The current decreased with the increase of the temperature at the contact interface in a characteristic manner, illustrating the potential for *in situ* measurement of temperature changes at MEMS contact interfaces.

ACKNOWLEDGEMENTS

This research was supported by the National Institute of Standards and Technology under Grant No. 60NANB1D0078. The authors are grateful to S. J. Timpe for assistance in redesigning the MEMS devices.

REFERENCES

1. C. Cabus, E. I. Cabuz, T. R. Ohnstein, and R. Maboudian, "Factors Enhancing the Reliability of Touch-Mode Electrostatic Actuators," *Sens. Actuators A, 79,* 245 (2000).

2. S. Majumder, N. E. McGruer, G. G. Adams, P. M. Zavracky, R. H., Morrison, and J. Krim, "Study of Contacts in an Electrostatically Actuated Microswitch," *Sens. Actuators A, 93,* 19 (2001).

3. H.-S. Lee, C. H. Leung, J. Shi, S.-C. Chang, S. Lorincz, and I. Nedelescu, "Integrated Microrelays: Concept and Initial Results", *J. Microelectromech. Syst., 11,* 147 (2002).

4. I. De Wolf and W. M. van Spengen, "Techniques to Study the Reliability of Metal RF MEMS Capacitive Switches," *Microelectron. Reliab., 42,* 1789 (2002).

5. L. Kogut and K. Komvopoulos, "Electrical Contact Resistance Theory for Conductive Rough Surfaces," *J. Appl. Phys., 94,* 3153 (2003).

6. L. Kogut and K. Komvopoulos, "Electrical Contact Resistance Theory for Conductive Rough Surfaces Separated by a Thin Insulating Film," *J. Appl. Phys., 95,* 576 (2004).

7. I. Schiele and B. Hillerich, "Comparison of Lateral and Vertical Switches for Application as Microrelays," *J. Micromech. Microeng., 9,* 146 (1999).

8. M.-H. Bao, *Handbook of Sensors and Actuators, vol. 8: Micro Mechanical Transducers, Pressure Sensors, Accelerometers, and Gyroscopes*, S. Middelhoek, Ed., New York: Elsevier, 2000, pp. 140-142 and 144-150.

9. E. J. J. Kruglick and K. S. J. Pister, "Lateral MEMS Micro-contact Considerations," *J. Microelectromech. Syst., 8,* 264 (1999).

10. J. G. Simmons, "Generalized Formula for the Electric Tunnel Effect Between Similar Electrodes Separated by a Thin Insulating Film," *J. Appl. Phys., 34,* 1793 (1963).

11. W. B. Ying, Y. Mizokawa, Y. Kamiura, K. Kawamoto, and W. Y. Yang, "The Chemical Composition Changes of Silicon and Phosphorous in the Process of Native Oxide Formation of Heavily Phosphorous Doped Silicon," *Appl. Surf. Sci., 181,* 1 (2001).

12. L. Kogut and K. Komvopoulos, "Analysis of Interfacial Adhesion Based on Electrical Contact Resistance Measurements," *J. Appl. Phys., 94,* 6386 (2003).

13. J. G. Simmons, "Electric-Tunnel Effect and its Use in Determining Properties of Surface Oxides," *Trans. Metall. Soc. AIME., 233,* 485 (1965).

STICTION IN MICROFLUIDIC ENVIRONMENTS

Elizabeth E. Parker[a,b], W. Robert Ashurst[b], Carlo Carraro[b], Roya Maboudian[b]
[a]Honeywell Federal Manufacturing & Technologies, LLC*, Kansas City, MO 64141
[b]Department of Chemical Engineering, University of California, Berkeley, CA 94720

ABSTRACT

Although much insight has been gained into the problem of stiction for MEMS operating in air, no systematic investigation of the phenomenon in microfluidic environments has been performed. With the increased interest in BioMEMS and microfluidic applications, the characterization of microstructure adhesion in fluids becomes important. The adhesion characteristics of oxide-terminated and SAM-coated polycrystalline Si (polysilicon) cantilever beams in various solvents are investigated. It is found that surfaces behave quite differently in microfluidic environments, when compared to their behavior in air. Oxide-terminated surfaces are found to exhibit much reduced adhesion in water, in comparison to air. In contrast, hydrophobic SAM-coated surfaces experience strong adhesion in water, a behavior opposite to what is observed in air. It is also observed that oxide-terminated surfaces exhibit greater adhesion in hydrocarbons, compared to SAM-coated surfaces, while surfaces show no adhesion in isopropyl alcohol regardless of surface termination.

INTRODUCTION

One of the biggest problems that plagues MEMS is the occurrence of stiction [1], the adhesion that takes place when surfaces of MEMS come into contact. One method that has been suggested to reduce adhesion consists of coating the microstructure surfaces with self-assembled monolayer (SAM) films [2-4]. These monolayer coatings help overcome adhesion by making the microstructure surfaces hydrophobic. This hydrophobicity prevents suspended surfaces from being attracted to each other or to the substrate due to surface tension forces when they are brought out of the liquid phase associated with the release step. It also reduces adhesion during device operation.

Although the performance of oxidized and SAM-coated microstructures operating in air has been the subject of much analysis, little has been done to systematically study what occurs when these films are subjected to fluidic environments. This may be crucial to the BioMEMS and microfluidic technologies, which involve valves, pumps, and diverse fluidic environments such as blood samples. In these instances, SAM coatings have been investigated as a means to control the movement of liquids in microfluidic devices [5, 6]. By rendering capillaries in microfluidic devices hydrophobic or hydrophilic, the flow of liquid can be manipulated. It is in regards to these applications that adhesion in microfluidic environments has been investigated in this paper.

EXPERIMENTAL DETAILS

Release and Coating Procedures:

The structures that were investigated in this paper consisted of arrays of polysilicon cantilever beams, so-called cantilever beam arrays (CBA), ranging in length from 150 to 1700 μm in 50 μm increments. All beams were 18 μm wide, with a thickness of 2.5 μm and suspended approximately 2 μm from the substrate surface (Fig. 1). These structures were fabricated using the Sandia SUMMiT IV™ process. Four surface treatments and four solvents were used in this study. The surface treatments were chemically grown silicon oxide, and three organic monolayer coatings derived from the following precursors: dichlorodimethylsilane, $(CH_3)_2SiCl_2$ (DDMS) (Alfa Aesar, 99+%), octadecyltrichlorosilane, $C_{18}H_{37}SiCl_3$ (OTS) (Aldrich Chemical Co, 90+%), and 1H, 1H, 2H, 2H-perfluorodecyltrichorosilane, $CF_3(CF_2)_7(CH_2)_2SiCl_3$ (FDTS) (Lancaster Synthesis Inc, 96%). The precursor OTS was deposited through liquid means, while DDMS and FDTS were deposited from both liquid and vapor phases. Coatings were deposited using both methods in order to determine if deposition method affected adhesion behavior. The solvents were DI H_2O (18 Ω-cm), isopropyl alcohol (IPA), anhydrous iso-octane, and hexadecane (HD) (Aldrich Chemical Co.). These solvents were chosen because of the similarities to fluids that may be used in micro-fluidic applications and also to explore the effect of polar versus nonpolar solvents, and short-chained versus long-chained hydrocarbons.

Each release/coating cycle consisted of two dies containing cantilever beam array (CBA) structures and a Si(100) piece. The processing began by releasing the structures in a 1:1 (v/v) HF (49 wt%)/HCl (36 wt%) solution and oxidizing the surface in a piranha solution (2:1 (v/v) sulfuric acid/hydrogen peroxide (30 wt%)). After oxidation, the chips were placed in a series of DI H_2O rinses until the pH remained neutral in the last DI H_2O rinse.

For chips undergoing the oxide surface treatment only, one die and the Si(100) piece were pulled directly from the water rinse, and left to dry through evaporation. These samples were used as control samples to ensure process robustness. The other chip was removed from the water rinse and placed in a vial of the desired solvent through a series of intermediate rinse steps.

For chips undergoing liquid monolayer coatings, bulk water was removed through a series of solvent rinses before they were placed in the coating solution with the appropriate precursor. The intermediate rinses consisted of methanol, followed by IPA, and iso-octane. Iso-octane was used as the solvent for the SAMs solution, with precursor concentrations of 1 mM for DDMS, 0.5 mM for OTS, and 1 mM for FDTS in a pre-conditioned (with the particular precursor) glass container. The chips were left in the covered container until the contact angle measured on the Si(100) piece was within the expected range for the particular precursor used in the coating [7, 8]. Once the expected contact angles were reached, the chips were stepped back through the iso-octane rinses. The series of rinses used for each environment can be seen in Table 1. The other chip and the Si(100) piece followed the standard coating process by continuing through the IPA rinses, the methanol rinse, and by finishing in a DI H_2O rinse. Once pulled from the water rinse, these chips were dry.

For chips undergoing DDMS and FDTS monolayer coatings deposited in the vapor phase (V-DDMS and V-FDTS), the chips were placed in a methanol rinse after the DI water rinses, and were then placed in vials of methanol. The chips were kept in methanol for at least 24 hours and then dried using a Tousimis model 815 "Autosamdri" supercritical carbon dioxide dryer. The samples were then plasma-cleaned and coated with either DDMS or FDTS in the vapor phase as described elsewhere [8]. Once coated, the chips were placed in IPA to wet the surfaces, transferred to a rinse of the desired solvent, and then placed in a vial of the solvent until tested.

*Operated by the United States Department of Energy under Contract No. DE-ACO4-01AL66850.

0-9640024-5-0/hh2004/$20©2004TRF
DOI 10.31438/trf.hh2004.82

Table 1: The series of rinses used for bringing SAM-coated dies into a given environment.

Desired Environment	Rinse 1	Rinse 2	Rinse 3	Rinse 4	Final Step
Air	Iso-octane	IPA	Methanol	Water	Air
Water	Iso-octane	IPA	Water	--	Water Vial
IPA	Iso-octane	IPA	--	--	IPA vial
Iso-octane	Iso-octane	--	--	--	Iso-octane vial
Hexadecane	Iso-octane	Hexadecane	--	--	Hexadecane vial

Probing Techniques in Solution

Chips were kept in vials of solvent for at least 24 hours before testing. This was to ensure that the sample surface had come to equilibrium with the fluid. A 4.25" diameter glass dish with an approximate 9/16" sidewall was used to hold the chips during testing. The dish was placed in a UVO cleaner to remove any undesirable contaminants from the surface. The dish was then placed under a Mitutoyo Finescope 60 microscope with a Nomarski style differential interference contrast (DIC) prism, and viewed with a Mitutoyo M Plan Apo 10x objective. The dish was filled with the desired solvent, and the chip was placed in the dish while maintaining the liquid meniscus. Before any testing, all beams were insured to be free from the surface. Signatone SE-SMS probe tips were used to probe the beams. A color change determined which beams were adhered to the surface, as seen in Fig. 1(a). To insure that the coatings were not altered by storage in the various fluids, the testing was performed within 5 days of film formation.

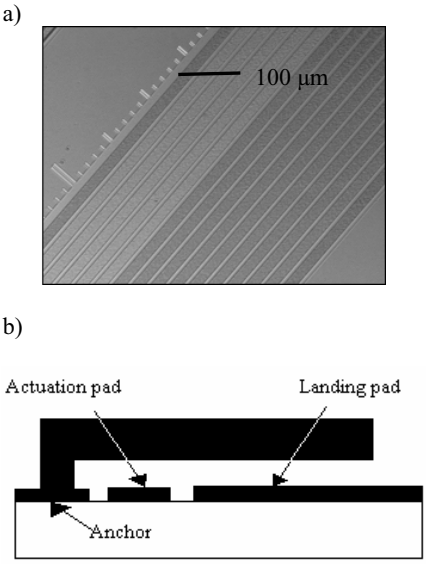

Figure 1. *(a) Differential Interference Contrast (DIC) image of DDMS-coated beams in iso-octane after probing manually. Light beams are adhered to the substrate. The beam at the far right is 950 μm, while that at the far left measures 1700 μm. (b) Side view schematic of a cantilever beam.*

Manual Actuation and Analysis

Beams were probed systematically at the very tip of the beam. Any beams that remained adhered after immediate probing were recorded. A second pass was then performed on all beams that remained free-standing. These beams were brought into contact with the substrate and held there for thirty seconds. Adhered beams were recorded. Finally, the procedure was repeated a third time, but for a probing time of one minute on any remaining free-standing beams. In this last cycle, rarely were additional beams adhered. Once testing was complete, the chip was returned to its vial and the dish was rinsed.

Using the adhered beam data from the cantilever beam probing, the average detachment length, l_d, was calculated based on the probability that a beam of length, l, was adhered to the substrate [9]. From this, the apparent work of adhesion was then obtained [7].

AC Electrostatic Actuation

Similar to the method described under the manual probing, an electrostatic method was employed to test cantilever beams in various environments. This electrostatic probing method was modified from a version used by Sounart and Michalske [10]. Two Signatone SE-10T probe tips were used to actuate the cantilever beam array by applying an AC square wave signal between the actuation pad and the ground plane, see Fig. 1(b) [11]. Voltages and frequencies were varied to avoid electrolysis. Adhered beams were recorded after an immediate voltage was applied and released, after 30 seconds of sustained applied AC voltage, after 1 minute of sustained applied AC voltage, and finally after 5 minutes of sustained applied AC voltage. The adhered beam data were then used to determine the work of adhesion, as done for manual actuation.

RESULTS

Results of Manual Probing

The work of adhesion data for actuation in air and water can be seen in Table 2. When water was used as the fluidic environment, cantilever beams displayed behavior opposite of that observed in air. While in air, beams with only an oxide treatment adhered to the substrate for beams less than 250 μm, corresponding to values for the work of adhesion of 1020 $\mu J/m^2$, oxide beams showed no tendency to adhere in water. In fact, the longest beams (1700 μm) were routinely free-standing in water even when held in contact with the substrate for a prolonged period, which yielded values for the apparent work of adhesion of $<0.5\ \mu J/m^2$. However, SAM-coated beams adhered strongly to the substrate in water, while displaying much longer detached beams in air.

Independent of surface treatment, beams remained free in IPA despite contact with the substrate for a prolonged period, corresponding to values for the work of adhesion of $<0.5\ \mu J/m^2$.

For actuation in iso-octane and hexadecane, although SAM-coated beams would stick to the substrate, there was not a strong attraction to the surface. In some cases, beams could be probed with a probe tip to the free position after being adhered to the substrate. However, in the case of oxide-terminated beams, they were strongly adhered to the substrate. These beams were more difficult to probe to a free position than beams with SAM coatings. Values for the work of adhesion for the various surface treatments in iso-octane and hexadecane can be seen in Tables 3 and 4.

Table 2: Detachment lengths and work of adhesion data for various surface treatments in air, water, and IPA, using manual actuation. Water and hexadecane contact angles are also listed. The relative humidity of the ambient environment was 50 ± 10%.

Surface Treatment	Contact Angle in Water	Contact Angle in Hexadecane	Detachment length, l_d (μm)			Work of Adhesion (μJ/m^2)		
			Air	Water	IPA	Air	Water	IPA
Oxide	<30º	<20º	250	1700	1700	1020	<0.5	<0.5
DDMS	103º	38º	516	150	1700	56	>7870	<0.5
V-DDMS	103º	38º	531	150	1700	50	>7870	<0.5
OTS	110º	38º	680	150	1700	19	>7870	<0.5
FDTS	115º	68º	667	150	1700	20	>7870	<0.5
V-FDTS	115º	68º	1000	150	1700	4	>7870	<0.5

Results of AC Electrostatic Actuation

Electrostatic actuation was not performed on beams in water since they were either completely free, as in the case of oxide-terminated beams, or all strongly adhered, as in the case of SAM-coated beams (Table 2). Because all beams despite surface treatment were free-standing in IPA, beams were not electrostatically actuated in this environment either.

As mentioned in the experimental section, estimates of the voltages and frequencies were obtained for the actuation in iso-octane and hexadecane. In this paper, we present results using 94 V actuation voltage and frequencies above 10 Hz. It was found that 94 V was enough to insure good contact between the beams and the substrate, and beams actuated at voltages greater than 94 V became electrostatically shorted to the actuation pad under them. Frequencies lower than 10 Hz caused electrolysis in the fluid. Results of the electrostatic actuation in iso-octane can be found in Table 3, along with the results from manual probing as a comparison. Although prolonged actuations of 1 and 5 minutes were performed, the results did not differ from those found at 0.5 minutes. Therefore, one value is reported for each combination of voltage and frequency.

The results for actuation in hexadecane of the monolayer-coated beams can be seen in Table 4. It can be observed that the values of the work of adhesion of the SAM-coated beams are at least one order of magnitude less than the values for oxide-terminated beams. Results for prolonged probings of 1 minute and 5 minutes did not differ from the results for 0.5 minutes. Therefore, one value is displayed for these coatings in hexadecane.

DISCUSSION

The oxide-terminated beams are found free-standing in water, for any beam length. Because oxide-terminated beams are hydrophilic, the surfaces can more effectively form hydrogen bonds with the surrounding water than with each other. As a result, these surfaces interact weakly with each other in favor of forming the hydrogen bonds with the surrounding water [12].

In contrast, SAM-coated beams are found to strongly adhere to the substrate in water. This behavior can be attributed to hydrophobic interaction [12]. Because of this interaction, when the hydrophobic surfaces of the SAM-coated beams and the substrate come together, they squeeze out water molecules between the surfaces in favor of forming vapor cavities. This lowers the free energy of the system since the ejected water molecules are able to form hydrogen bonds in the bulk, resulting in adhered surfaces.

Independent of surface treatment, none of the beams are adhered to the substrate in IPA. It is observed that the contact angle of isopropyl alcohol measures less than 20˚ for all the surface treatments. Because IPA completely wets all of the surfaces, it is not energetically favorable for vapor to condense at contact sites as expected in the case for SAM-coated surfaces in water. Results are consistent with this argument.

For oxide-terminated beams in both iso-octane and hexadecane, it can be observed that the standard deviation is quite large compared to the values of the work of adhesion. During actuation, the detachment lengths never varied more than 150 μm per array of beams. However, since the detachment lengths were rather small in these fluids, ranging between 200 and 400 μm, Δl_d of 50 μm has a significant impact on the standard deviation of the work of adhesion due to $\Delta l_d / l_d^5$ scaling. For large detachment lengths as seen with the SAM-coated beams in these fluids, l_d^{-5} causes the standard deviation of the work of adhesion to become small, compared to that of the oxide-terminated beams.

With the highest values for contact angles in both water and hexadecane, it would be expected that beams coated with FDTS would be adhere at shortest beam lengths in iso-octane and hexadecane, and would therefore have the greatest values for the apparent work of adhesion. Although this is observed for vapor FDTS-coated samples, it is not observed for liquid-deposited FDTS samples. Differences between the vapor-deposited and liquid-deposited FDTS coating quality may arise from the particle generation inherent in the liquid deposition method (vapor-deposited coatings usually exhibit less particles). A rougher surface due to more particles may actually decrease the work of adhesion since less surface area will be contacting when compared to a smooth surface. As a result, one might expect lower values for the work of adhesion for liquid-deposited FDTS-coated beams, than those with vapor-deposited FDTS. This is consistent with the experimental observation.

It would also be expected that beams coated with DDMS and OTS would have comparable values for the detachment lengths and apparent work of adhesion since both precursors yield films with similar contact angle values (and both have lower contact angles than FDTS). This is consistent with results, with both liquid- and vapor-deposited DDMS samples. Although deposition method makes a difference in the values of work of adhesion for FDTS-coated samples, no such difference is observed for the two methods of deposition for DDMS. This can be attributed to the fact that the liquid method of DDMS deposition yields few particles for this precursor [4].

Although it was observed that some of the detachment lengths from manual actuation after electrostatic actuation were lower than the lengths found before actuation, corresponding to higher works of adhesion for the manual actuation, these differences were small and may be due to slight rearrangement of the coating molecules on the surfaces due to electrostatics. After electrostatic actuation, the ground pad and actuation pad were visibly changed where the probe tips touched the pad. It

Table 3: Work of adhesion of various surface treatments in iso-octane after manual and electrostatic actuation. A "V" stands for vapor-deposited coating, while those coatings without a "V" imply deposition in the liquid phase.

Testing Conditions	Work of adhesion in iso-octane ($\mu J/m^2$)					
	Oxide	DDMS	V-DDMS	OTS	FDTS	V-FDTS
manual (original)	492 ± 331	7 ± 1	2± 0.7	5 ± 1	9 ± 3	397 ± 146
94v, 10Hz	185 ± 147	6 ± 1	1 ± 0.5	4 ± 1	5 ± 1	44 ± 79
94v, 100Hz	790 ± 688	5 ± 1	1 ± 0.4	5 ± 1	8 ± 2	44 ± 79
94v, 1kHz	185 ± 147	4 ± 1	1 ± 0.4	5 ± 1	5 ± 1	44 ± 79
manual (repeat)	395 ± 144	7 ± 1	2± 0.9	5 ± 1	13 ± 0	322 ± 112

Table 4: Work of adhesion of various surface treatments in hexadecane after manual and electrostatic actuation. A "V" stands for vapor-deposited coating, while those coatings without a "V" imply deposition in the liquid phase.

Testing Conditions	Work of adhesion in hexadecane ($\mu J/m^2$)					
	Oxide	DDMS	V-DDMS	OTS	FDTS	V-FDTS
manual (original)	2490 ± 0	4 ± 0	2 ± 0.6	2 ± 0.4	4 ± 0.4	221 ± 70
94v, 10Hz	2490 ± 0	3 ± 1	2 ± 0.5	1 ± 0.1	1 ± 0.4	184 ± 56
94v, 100Hz	2490 ± 0	3 ± 1	2 ± 0.3	1 ± 0.1	1 ± 0.4	184 ± 56
94v, 1kHz	2490 ± 0	3 ± 1	2 ± 0.3	1 ± 0.2	1 ± 0.3	184 ± 56
manual (repeat)	2490 ± 0	10 ± 2	2 ± 0.4	3 ± 1	4 ± 0.4	266 ± 152

appeared that particles were accumulated where the probe tip has been. In manual actuation, no visible damage was seen at the end of the beams where the probe tip was placed.

CONCLUSIONS

It has been shown that the behavior of modified surfaces in microfluidic environments differs greatly than that observed in air for the same treatments. For oxide-terminated surfaces, the apparent work of adhesion is <0.5 $\mu J/m^2$ in water, but as much as 1020 $\mu J/m^2$ in air. For SAM-coated surfaces, the apparent work of adhesion is smallest in air, ranging from 19-56 $\mu J/m^2$, depending on the precursor, while it is the greatest in water, >7870 $\mu J/m^2$. In IPA, beams undergoing any of the surface treatments are free-standing. In iso-octane and hexadecane, oxide-terminated beams yield the largest values for work of adhesion when compared to any of the SAM-coated beams. DDMS- and OTS-coated beams yield similar works of adhesion in both of these environments while vapor-deposited FDTS-coated beams yield higher works of adhesion, compared to DDMS and OTS, but lower works of adhesion when compared to oxide-terminated beams. Liquid-deposited FDTS-coated beams yield values for the work of adhesion comparable to DDMS- and OTS-coated beams, and lower than vapor-deposited FDTS-coated beams in these fluidic environments. This is attributed to the presence of particles on liquid-deposited FDTS films. Finally, two methods of actuation for the cantilever beams are demonstrated for determining detachment lengths, and therefore the apparent work of adhesion in fluid, with similar results for both methods.

ACKNOWLEDGEMENTS

The authors wish to gratefully acknowledge the financial support of Honeywell FM&T through the Technical Fellowship program, NSF (grant #0099765), and Sandia National Labs.

REFERENCES

1. R. Maboudian and R.T. Howe, ″Critical review: Adhesion in Surface Micromechanical Structures," *Journal of Vacuum Science and Technology B*, *15* (1997).
2. R. Maboudian, ″Surface Processes in MEMS Technology," *Surface Science Reports, 30* (1998).
3. R. Maboudian, W.R. Ashurst, and C. Carraro, ″Self-Assembled Monolayers as Anti-Stiction Coating for MEMS: Characteristics and Recent Progress," *Sensors and Actuators A, 82* (2000).
4. R. Maboudian, W.R. Ashurst, and C. Carraro, ″Tribological Challenges in Micromechanical Systems," *Tribology Letters, 12*, 2 (2002).
5. Hobbs, E.D. and A.P. Pisano, "Micro Capillary-Force Driven Fluidic Accumulator/Pressure Source," *Proceedings of the 12th International Conference on Solid-State Sensors, Actuators, and Microsystems, Transducers '03*, Boston, MA (2003), pp.155-158.
6. N. Roxhed, "Designing Passive Microfluidic Control Components, in Signals, Sensors and Systems," Master Thesis, Royal Institute of Technology, Stockholm (2003).
7. U. Srinivasan, et al., ″Self-assembled Fluorocarbon Films for Enhanced Stiction Reduction," *Proceedings of the 9th International Conference on Solid-State Sensors and Actuators, Transducers '97*, (1997), pp. 210-213.
8. W. R. Ashurst, et al., ″Wafer Level Anti-stiction Coatings for MEMS," *Sensors and Actuators A*, *104*, 3 (2003).
9. W. R. Ashurst, "Surface Engineering for MEMS Reliability, in Chemical Engineering," PhD thesis, University of California, Berkeley (2003).
10. Sounart, T.L. and T.A. Michalske, "Electrostatic Actuation Without Electrolysis in Microfluidic MEMS," *Proceedings of the 12th International Conference on Solid-State Sensors, Actuators, and Microsystems, Transducers '03*, (2003), Boston, MA pp. 615-618.
11. M. R. Houston, R.T. Howe, and R. Maboudian, ″Self-Assembled Monolayer Films as Durable Anti-Stiction Coatings for Polysilicon Microstructures," *Technical Digest, Proceedings of the 1996 Solid-State Sensor and Actuator Workshop*, Hilton Head Isl., SC, Transducer Research Foundation, Cleveland (1996), pp. 42-47.
12. J. N. Israelachvili, *Intermolecular and Surface Forces*. 2 ed., London: Academic Press (1992).

PATTERN DENSITY BASED PREDICTION FOR DEEP REACTIVE ION ETCH (DRIE)

Tyrone F. Hill , Hongwei Sun, *Hayden K. Taylor, Martin A. Schmidt, and Duane S. Boning

Microsystems Technology Laboratories
Massachusetts Institute of Technology
Cambridge, MA 02139, USA

*Cambridge University
Engineering Department
Cambridge CB2 1PZ, UK

ABSTRACT

A quantitative model capturing Deep Reactive Ion Etch (DRIE) pattern density effects is presented. Our previous work has explored the causes of wafer-level variation and demonstrated die-level interactions resulting from pattern density and reactant species consumption [1]. Several reports have focused on experimental evidence and modeling of feature-level (aspect ratio) dependencies [2]. In contrast, in this work we contribute a computationally efficient and effective modeling approach that focuses on layout pattern density-induced nonuniformity in DRIE. This is a key component in an integrated model combining wafer-, die-, and feature-level DRIE dependencies to predict etch depth for an input layout and a characterized etch tool and process. A micro-scale engine turbopump layout is used to demonstrate the model, which was calibrated to fit across-die variation within 1% and intra-die variation to within 0.1% (normalized RMS error).

INTRODUCTION

Deep Reactive Ion Etch (DRIE) is a key technology for realizing the high aspect-ratio structures that are so prevalent in MEMS. The Bosch etch method used here consists of time-multiplexed cycles of polymer deposition (C_4F_8 feed gas) and chemical etching of silicon (SF_6 feed gas). Recent work on DRIE has included optimizing process parameters [3], exploring aspect ratio dependencies [2], and identifying die-to-die effects (Sun et al.) [1]. Our work seeks to develop a model to capture and predict pattern or layout dependent effects in DRIE, as summarized in Fig. 1.

In this paper, we focus on the center component in Fig. 1, where we contribute a pattern density based model. By pattern density, we mean the area fraction of exposed surface on the wafer (that portion not blocked by an etch mask), and thus we are concerned with design or layout-specific variation in etch depth or rate due to pattern density variations across the chip and wafer. Our pattern density model convolves an etch "impulse response" with a local pattern density map for any given device layout, in order to predict die-level etch perturbations for that design. The layout for the full wafer (typically with multiple die) is analyzed, so that pattern-density based interactions between die are captured, as well as within-die pattern density perturbations. In addition, wafer level nonuniformities based on an empirically derived model are applied, resulting in predicted etch maps for each die across the wafer.

In the following, we first present the pattern density model. This is followed by discussion of feature-level effects, and a brief summary of the previously developed wafer-level variation model used in the framework of Fig. 1. Application of the model to a microscale turbopump is then presented. Finally, limitations in the current model and directions for future work are summarized.

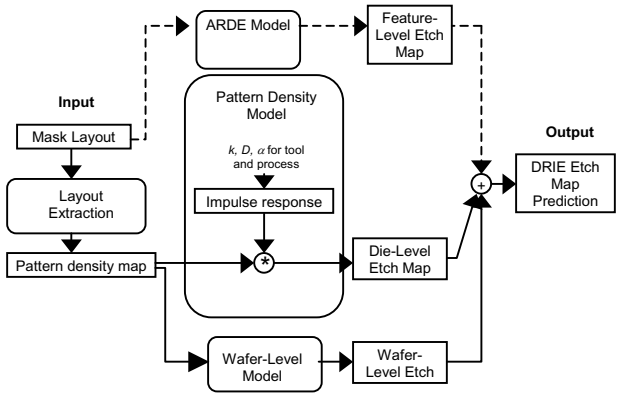

Figure 1. *Framework for pattern dependent modeling in DRIE. The solid lines show components included in the present work.*

DIE-LEVEL MODEL

The physical rationale behind the pattern density model is next described, followed by model derivation and implementation.

Physical Motivation for Pattern Density Effects

The Bosch process involves two major mechanisms: ion-assisted dry chemical etching, and the deposition of a polymer inhibiting layer. During the etch cycle, we assume that the ion-assisted etch rate will be affected by the concentration of the reactant species. That is to say, we assume key reactions are:

$$SF_6 + e^- \longrightarrow S_x F_y + S_x F_y^{\bullet} + F^{\bullet} + e^- \quad (1)$$

$$Si + nF^{\bullet} \longrightarrow SiF_n \quad (2)$$

Eq. 1 represents the dissociation of SF_6 into neutral fluorine radicals and ions. The fluorine radicals reach the wafer by diffusion, and are responsible for removing silicon. We assume that localized concentration gradients of fluorine radicals create spatial variations in etch rate. Pattern density dependencies thus result from the localized consumption of reactants on different regions of the wafer. We find that these depressions in concentration can occur on relatively long length scales, i.e., across several millimeters, and thus result in interaction between multiple die on a wafer. Qualitatively, die that are surrounded by highly loaded areas will etch more slowly, since they encounter more competition for reactants.

Pattern Density Model Development

Die-level interactions are empirically modeled through the use of an "etch impulse response." This idea is analogous to a filter-based inter-layer dielectric (ILD) thickness prediction scheme for CMP proposed by Ouma et al. [4]. If *f(x,y)* represents the spatial response to an impulse of pattern density, and *d(x,y)* is a function

Travel support has been generously provided by the Transducers Research Foundation and by the DARPA MEMS and DARPA BioFlips programs.

describing the local spatial pattern density of a layout, then the die-level variation *z(x,y)* is given by a convolution operation:

$$z(x,y) = f(x,y) \otimes d(x,y) \tag{6}$$

In our current model, the impulse response is based on the diffusion equation solution for a spherical coordinate system with an inverse distance (1/*r*) dependence. An expression for the filter function is obtained for the reduction *C* of reactant concentration at a radius *r* from an arbitrary point on the wafer surface. Eq. 7 represents diffusion of the species *C*, with surface area limited to a half sphere. By rearranging terms and integrating we can obtain an expression for the concentration (Eq. 8). In this equation, there are two important parameters: the reaction rate *k* and the diffusion coefficient *D*, which represent the consumption rate of silicon and transport rate of etchant to the wafer surface.

$$2\pi r^2 D \frac{\partial C}{\partial r} = k \tag{7}$$

$$C = -\frac{k}{D}\frac{1}{2\pi r} \tag{8}$$

Based on Eq. 8, we have the (negative) impact on background reactant concentration as a function of distance away from each area of exposed silicon. This impulse response thus forms a filter, as given by Eq. 9 below and illustrated in Fig. 2, that we can convolve with a representation of the open area (local pattern density) across the wafer. We allow for an empirical constant α in order to scale the filter with respect to wafer-level effects.

$$f = -\alpha\left(\frac{k}{D}\right)\frac{1}{2\pi r} \tag{9}$$

While Eq. 9 gives a 1/*r* spatial dependence and a magnitude scaling parameter (the aggregate of *k*, *D*, α, and constants), other spatial forms may also be appropriate. For example, solution of the diffusion equation in cylindrical coordinates gives rise to a ln(*r*) dependence. An alternative approach is to empirically fit the spatial dependence, e.g., to $a/(c+r)^b$, allowing constants *a*, *b*, and *c* to be determined empirically.

Pattern Density Model Implementation

In our implementation of the etch variation model (as summarized in Fig. 1), the pattern density model consists of the information related to the filter function. Specifically, the pattern density model consists of the filter function structure (1/*r* in this case), and an aggregate scaling parameter which is fit using characterization data for a fixed etch recipe. An AutoCAD layout for the design of interest is processed through a layout density extraction tool (provided courtesy of Praesagus, Inc.). The local layout pattern density map is convolved with the filter function to produce the pattern density perturbation to the etch rate or depth. Increased computational efficiency may be achieved by using an FFT approach rather than direct convolution. We assume that wafer-, die, and feature-level etch perturbations are additive: pattern density based variation is added to a wafer-level uniformity prediction to produce an etch variation map for the entire wafer

A set of test masks was designed to fit the pattern density model for a specific recipe. The masks have a small region (or a pair of regions) on the wafer consisting of concentric circles with pattern densities varying from 10 to 90%. Etch experiments are performed and etch depths measured at a variety of distances from the patterned regions. These give the spatial extent and magnitude of pattern density-induced etch perturbation to fit the model. The filter parameters were extracted on a 1mm x 1mm size grid; additional amplitude scaling of the filter may be necessary when applied to a layout having a smaller discretization.

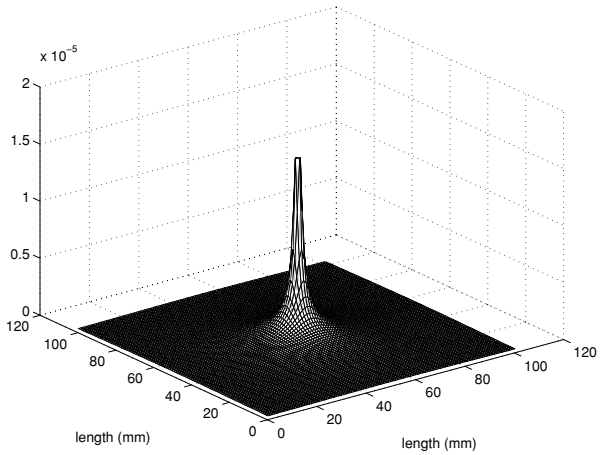

***Figure 2**. 3-d image of filter impulse response f(x,y)*

For the experiments shown here, the recipe had a pressure trip of 94.0 mT (meaning that the upper pressure limit for the chamber is 94mT) and an automated pressure control value (APC) setting of 75°. The etch cycle used a 105 sccm flow rate (SF_6), 100W of platen power, and 750W coil power. The passivation cycle had a 40 sccm flow rate (C_4F_8), 60W of platen power, and 600W of coil power. The experiments were carried out in an Inductively Coupled Plasma (ICP) etcher manufactured by Surface Technology Systems of Newport, UK.

FEATURE-LEVEL MODEL

Feature-level effects include variations due to differing aspect ratios (depth to width) in individual etch features. It is thought that these variations are related to the probability of reactant transmission to the bottom of the feature, as described by Coburn and Winters [5]. Recent efforts by Yeom et al. to separate effects suggest a connection between pattern density and feature level uniformity [2]. Our work does not presently include feature-level effects; addition of an existing or new feature-scale model must be done with care to be consistent with the pattern density model.

WAFER-LEVEL MODEL

Wafer-level variation spans the entire wafer, and is related to ion and neutral transport in the plasma, as well as asymmetries in the geometry of the chamber [1]. For low loading densities ion transport is believed to be the dominant factor in determining uniformity. As a result, layouts with low loading (<10%) generally exhibit a “hot spot” with a higher than average etch rate. As the etch rate increases, the behavior is governed by neutral transport, resulting in a “cold spot.”

For the etch variation model in this work, we use an empirical characterization of the wafer-level variation for a given recipe. A separate set of test masks with uniformly spaced measurement locations is used. Each mask has a different uniform pattern density, and thus the wafer-level uniformity map corresponding to different global loadings can be empirically captured.

Fig. 3 shows a normalized (to highest etch rate location) wafer-level spatial etch map corresponding to 4.4% global loading. In some etch applications (including the turbopump example shown later), the wafer is rotated multiple times during the total etch. The wafer level model thus averages the spatial uniformity map through equivalent rotations.

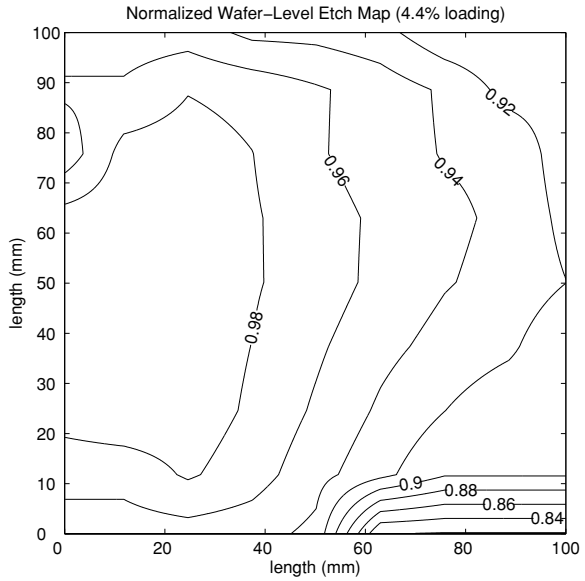

***Figure 3**. Normalized wafer-level etch map for 4.4% loading.*

MODEL APPLICATION

While DRIE has been successful in a research environment, issues with uniformity remain a challenge for use in high volume MEMS manufacturing. An example of such a barrier can be found in the fabrication of microscale rotating power devices in silicon. These devices consist of bulk-micromachined layers bonded together, and rely heavily on DRIE. Etch nonuniformity can create variation in feature height, which may lead to imbalance in rotation and device failure [6]. The etch depth variation possible in a single device, based on WYKO measurement, is shown in Fig. 4. The individual turbopump is replicated multiple times on the wafer, resulting in a local density map as shown in Fig. 5.

The extraction shown in Fig. 5 is performed on a 100 μm by 100 μm grid. The white areas represent an open etch area, while the black areas represent a masked area. The local density map is convolved with the impulse response to obtain the percentage variation due to pattern density. The result is added to the normalized global etch map corresponding to the layout (4.4% loading in the case), with rotation.

The etch variation map was compared to a wafer etched for 90 minutes with a layout based on the extraction given in Fig. 4. The chamber parameters are identical to those used to obtain the filter coefficients. The wafer was rotated 90° four times to control the effects of wafer-level variation. Fig. 4 is an experimentally obtained spatial etch map for the upper left die in the layout. The etch depths range from 250 μm to 268 μm, resulting in 6.7% across die variation. Fig. 6 shows a close-up of the same die based on pattern density model predictions, which predicts an across die variation of 7%. Predictions for the turbopump mask, based on filter coefficients tuned using the characterization mask, are within 1% root-mean-square (RMS) error.

As a further test, etch rate variations are also considered on a scale internal to a single die. In order to measure intra-die variation, depth measurements were taken at a 2.2 mm radius from the center of each die. Taking measurements at a constant radius minimizes feature-level effects, since the feature opening will be similar along the circumference. The numbering scheme for these positions is shown in Fig. 7.

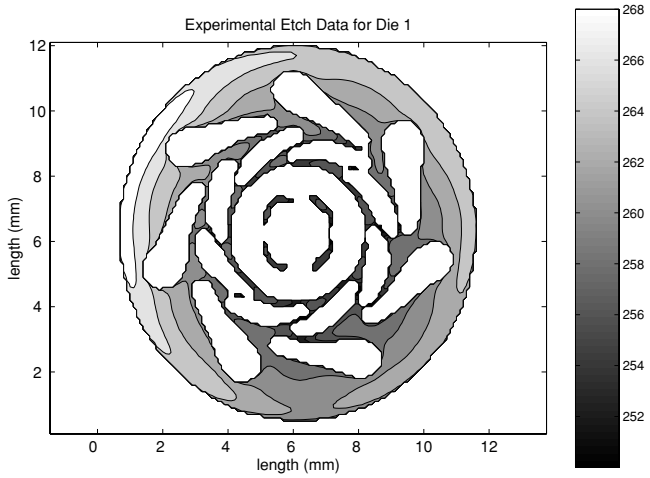

***Figure 4**. Measured etch depths (in μm) for a turbopump pattern. A 6.7% across-die variation is observed.*

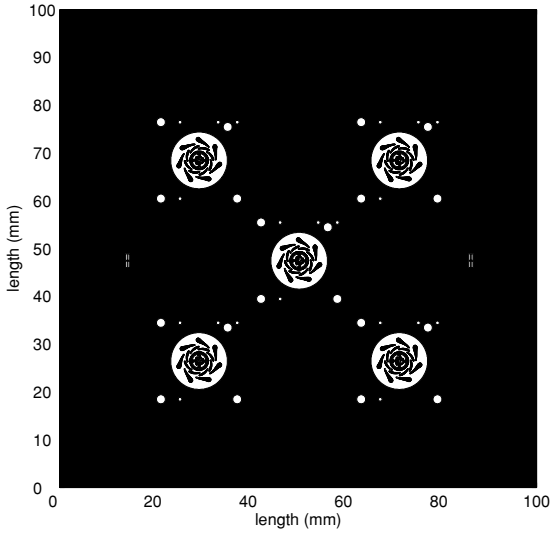

***Figure 5**. Image of pattern density extraction resulting from AutoCAD layout of turbopump.*

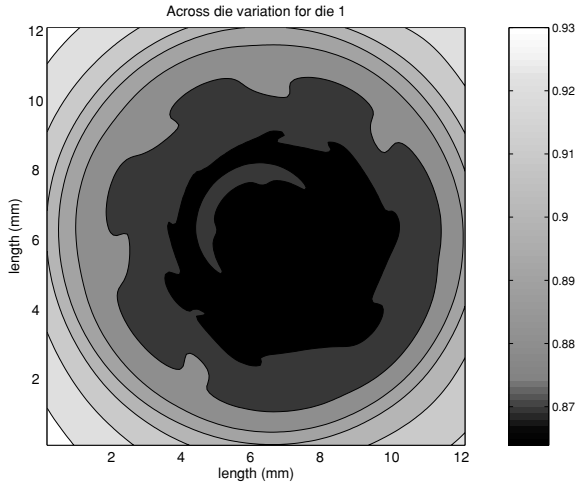

***Figure 6**. Spatial map of etch variation predicted by the pattern density model. The scale represents normalized etch rate. The model predicts across die variation of 7%.*

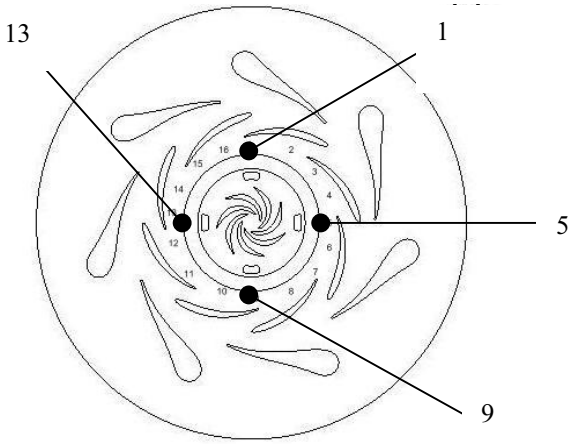

***Figure 7**. Experimental measurement positions for Fig. 8. The measurements were taken at a 2.2 mm radius from the die center, with a phase difference of π/8 radians between them.*

The pattern density model is able to capture the subtle spatial pattern of etch nonuniformity within this ring, as seen in Fig. 8 which shows predictions and experimental measurements for the upper left die. The trends in the figure can be understood qualitatively: positions nearest to the center of the layout have a higher pattern density, and experience a slower etch rate. The empirical scaling coefficient α is tuned to the turbopump data; without tuning, the correct spatial trends are captured but our 1% error results in offsets in the trends of Fig. 8. The filter magnitude tuning appears necessary to overcome model limitations. An α value of 2.34 was found to fit the data, with a normalized root-mean-square (RMS) error of 0.087% for the die.

LIMITATIONS AND FUTURE WORK

A pattern density based model has been presented for spatial mapping of layout dependent effects in DRIE. The model is able to capture the large across-die variations (6-7%) existing in DRIE applications, such as the turbopump. The model can also capture subtle within-die effects, with additional tuning to achieve 0.1% accuracy. The pattern density model can serve as the basis for layout optimization (e.g. dummy fill generation [7]) to improve DRIE uniformity.

Several limitations and possibilities for future improvements can be noted. First, alternative functional forms for the pattern density filter function (e.g. $1/r^b$) may be considered, or may apply in different etch circumstances. Second, feature-level or aspect-ratio dependent effects have not been included. Work is needed to understand how pattern density effects evolve over time as feature aspect ratios change. Third, the wafer-level model can be improved to predict wafer uniformity across varying global etch loadings by way of an improved physical model. Finally, alternative ways of combining these three components (e.g. in a multiplicative rather than additive manner) can be considered to account for wafer-, die-, and feature-level interactions.

ACKNOWLEDGEMENTS

This work was supported in part by the Cambridge-MIT Institute. The turbopump layout is courtesy of the MIT Microengine Project. We also thank Praesagus, Inc. for assistance with layout file extractions.

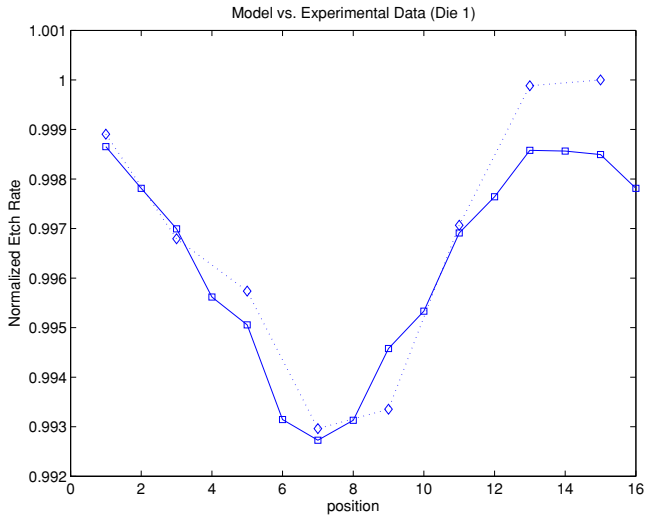

***Figure 8**. Comparison between model (squares) and experimental data (diamonds) for the upper left die, normalized to the fastest etching location in the die.*

REFERENCES

1. H. Sun, T. Hill, M. A. Schmidt, and D. Boning, "Characterization and Modeling of Wafer and Die Level Uniformity in Deep Reactive Ion Etching (DRIE)," *2003 MRS Fall Meeting*, Boston, MA, *In press*, Dec. 2003.
2. J. Yeom, Y. Wu, M. A. Shannon, "Critical Aspect Ratio Dependence in Deep Reactive Ion Etching of Silicon," *12th Int. Conf. on Solid State Sensors, Actuators, and Microsystems*, Boston, MA, June 2003.
3. A. Ayon, R. Bayt, C.C. Lin, R.A. Braff, H. Sawin, and M. A. Schmidt, "Characterization of a Time Multiplexed Inductively Coupled Plasma Etcher," *J. Electrochem. Soc.*, vol. 146, no. 1, pp. 339-349, 1999.
4. D. O. Ouma, D. S. Boning, J. E. Chung, W. G. Easter, V. Saxena, S. Misra, and A. Crevasse, "Characterization and Modeling of Oxide Chemical Mechanical Polishing Using Planarization Length and Pattern Density Concepts," *IEEE Trans. on Semicond. Manuf.*, vol. 15, no. 2, pp. 232-244, May 2002.
5. J. W. Coburn and H. F. Winters, "Conductance considerations in the reactive ion etching of high aspect ratio features," *Appl. Phys. Lett.,* vol. 55, no. 26, pp. 2730-2732, Dec. 1989.
6. N. Miki, C. J. Teo, L. Ho, and X. Zhang, "Precision Fabrication of High-Speed Micro-Rotors using Deep Reactive Ion Etching (DRIE)," *Tech. Digest of 2002 Hilton Head Solid-State Sensors and Actuators Workshop,* Hilton Head Island, SC, pp. 265-268, June 2002.
7. Y. Chen, A. Kahng, G. Robins, and A. Zelikovsky, "Area Fill Synthesis for Uniform Layout Density," *IEEE Trans. on CAD*, vol. 21, no. 10, pp. 1132-1147, Oct. 2002.
8. C. Gormley, K. Yallup, W. Nevin, J. Bhardwaj, H. Ashraf, P. Hugget, and S. Blackstone, "State of the Art Deep Silicon Anisotropic Etching on SOI Bonded Substrates for Dielectric Isolation and MEMS Applications," *Fall Meeting of the Electrochem. Society,* Hawaii, USA, pp. 350-661, Oct. 1999.
9. R. A. Gottscho and C. W. Jurgensen, "Microscopic Uniformity in Plasma Etching," *J. Vac. Sci. Technology B,* vol. 10, no. 5, Sept./Oct. 1992.

LEEDUS: A MICROMACHINING PROCESS FOR DIE-SCALE PATTERN TRANSFER IN CERAMICS WITH HIGH RESOLUTION AND THROUGHPUT

Tao Li[1] and Yogesh B. Gianchandani
Engineering Research Center for Wireless Integrated Microsystems
University of Michigan, Ann Arbor, Michigan

ABSTRACT

While ceramics are important materials for electronic and microsystem packaging, they are difficult to pattern lithographically. LEEDUS, a fabrication process combining lithography, electroplating, batch mode micro electro-discharge machining (μEDM) and batch mode micro ultrasonic machining (μUSM), is presented in this paper. This technology provides die-scale pattern transfer capability from lithographic masks onto ceramics, glass or other brittle materials. This is done by using the photomask to create an electroplating mold, then using the electroplated pattern as an electrode to μEDM a hard metal tool, which is finally used in the μUSM of the ceramic substrate. A minimum feature size of 25μm has been demonstrated on the glass-mica (Macor™) ceramic plate with a 4.5mm×4.5mm die size and 34μm cutting depth using a stainless steel microtool. The machining rate in the demonstration was about 18μm/min, and the tool wear ratio for the microtool was 6%. The average surface roughness was Ra 0.55μm. Other process characteristics are also discussed.

I. INTRODUCTION

Ceramics play an increasingly important role in electronic and MEMS packaging areas because of their unique electrical, chemical, mechanical, and physical properties. Typically, they are hard, electrically and thermally insulating with high melting temperatures and high chemical stability. However, they are also brittle, with low toughness and ductility. In addition to conventional semiconductor devices and IC high-performance packaging, ceramics also find attractive applications for microsystem packaging such as hermetic packages made entirely of ceramic or combination of ceramic and metals, in which cases, holes, grooves or complex patterns are often required on the ceramic substrates.

Although superb for packaging applications, the properties of ceramics also make them difficult to process lithographically. Consequently, in conventional IC packaging industry ceramics are often processed by dry pressing or tape casting from a powder form [1]. These additive processes usually face the problems of volume shrinkage, high temperature steps, and varying material properties. Serial subtractive processes like laser drilling or diamond grinding, which are most commonly used for conventional precision machining of ceramics, are less attractive for complex patterns which can be best made when structures are defined by a mask. Reactive ion etching (RIE) is limited by a slow etch rate and varying gas requirements for different ceramics [2]. Powder blasting provides good machining rates, but is limited by V-shaped sidewalls and blast lag [3] [4]. Phosphoric acid or other wet chemical etchings for ceramics suffer from quite limited etching rate and achievable minimum feature size due to lateral undercutting [5]. Thus, a bulk process with pattern-transfer capability is greatly desired.

This paper presents LEEDUS, a fabrication process which utilizes micro ultrasonic machining (μUSM) in batch mode to transfer a mask-defined die-scale pattern from a micro electro-discharge machined (μEDM'ed) microtool into a ceramic plate with high resolution and throughput.

Conventional ultrasonic machining (USM) has been widely accepted as an effective machining process for hard and brittle materials like ceramics, glass and silicon. Since these materials are brittle, it is easier to fracture them than to plastically deform them, and USM produces little or no damage or high-stress deformation at or below the surface. Moreover, it causes no thermal or chemical alterations in the sub-surface characteristics of the machined material, and can achieve precision surface finish of Ra 0.4~0.76μm [6]. However, at the micro level, USM has been used only as a serial process with a rotating cutting tool, thereby limiting both throughput and structural shapes [7] [8]. The batch mode μUSM approach presented in this paper facilitates die-scale transfer of complex lithographic patterns and provides relatively high resolution - the best reported in the past is about 25 μm - as well as high throughput, while retaining the favored characteristics of conventional USM.

II. PROCESS DESCRIPTION

The LEEDUS process flow is illustrated in Figure 1. A copper structure is electroplated into an SU-8 mold on a silicon substrate with lithography-defined negative pattern. Then the silicon die is used as an electrode to batch μEDM a stainless steel or WC/Co microtool, transferring the corresponding positive die-

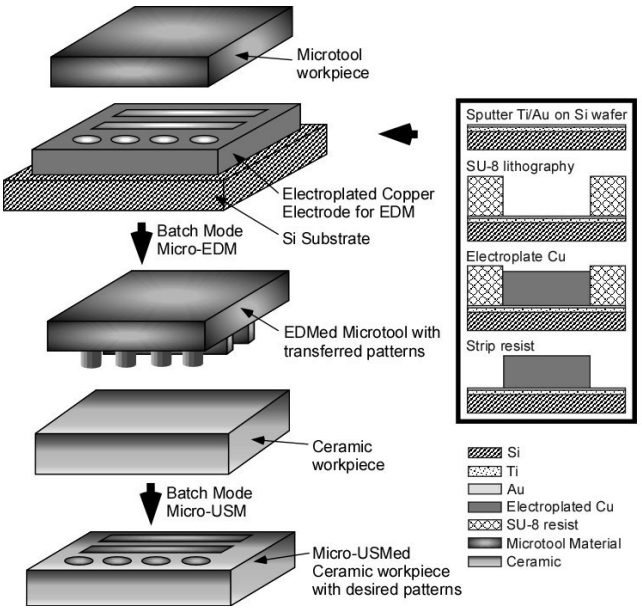

Fig. 1: Concept of LEEDUS: combining Lithography, Electroplating, batch mode micro Electro-Discharge machining, and batch mode UltraSonic machining.

[1] *Corresponding author:* 1301 Beal Ave., Ann Arbor, MI, 48109, USA; Tel: (734) 647-2040, Fax: (734) 763-9324.

0-9640024-5-0/hh2004/$20©2004TRF
DOI 10.31438/trf.hh2004.84

Solid-State Sensors, Actuators, and Microsystems Workshop
Hilton Head Island, South Carolina, June 6-10, 2004

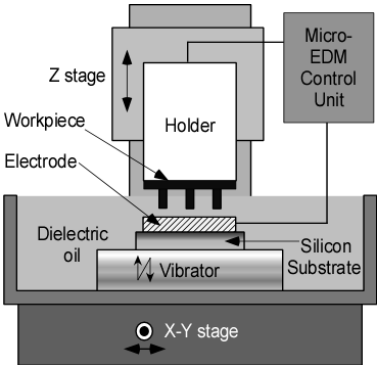

Fig. 2: µEDM setup used for batch mode microtool fabrication.

scale pattern onto the microtool [9] [10]. The microtool is then mounted on an ultrasonic machining setup for batch mode µUSM of a ceramic workpiece, thus having the desired negative pattern transferred onto the ceramic workpiece.

Figure 2 shows a schematic diagram of the setup for µEDM based on the Panasonic µEDM machine MG-ED72W. This setup has X-Y-Z stages with 0.1µm-precision relative positioning of the microtool workpiece and copper electrode. The copper electrode is fixed on a vibrator which can vibrate in the feeding (Z) direction of the microtool workpiece with a frequency of 100Hz and adjustable amplitude. This vibration is necessary to avoid welding when a short circuit occurs between the electrode and the workpiece, as well as to facilitate removal of machining debris.

The schematic diagram for the batch mode µUSM setup is shown in Figure 3. The µEDM'ed microtool is firmly and carefully mounted by epoxy at the tip of the horn where the vibration energy generated by the ultrasonic transducer is maximized. An appropriate abrasive slurry which consists of water and fine abrasive powders is supplied between the tip of the microtool and a ceramic workpiece. The vibrating tip of the microtool is fed into the ceramic workpiece. The ultrasonic motion of the microtool imparts velocity to the abrasive particles on its downward stroke. These particles, in turn, are responsible for the erosion of the workpiece, thus creating the desired cavities in the shape of the microtool.

III. EXPERIMENTAL DETAILS

A 4.5mm×4.5mm silicon die with 50µm high electroplated copper structures was used as the electrode for batch mode µEDM with discharge voltage of 80V and discharge control capacitance of 100pF. Figure 4 shows SEM images of two of the demonstrative copper patterns, both of which have features with lateral

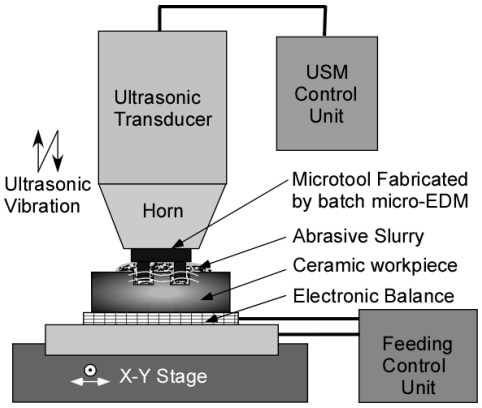

Fig. 3: µUSM setup used for batch mode pattern transfer to ceramic workpiece.

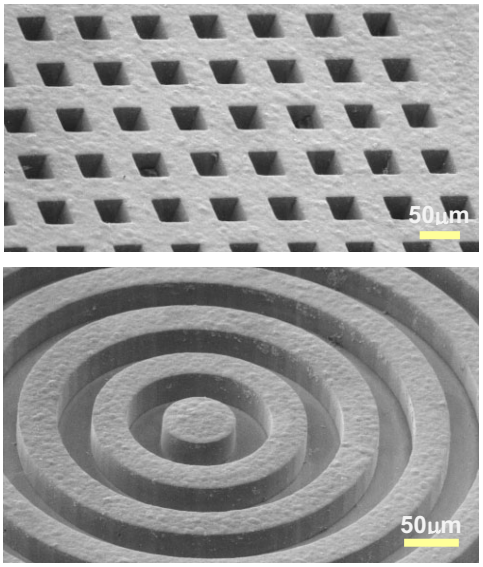

Fig. 4: SEM images of two of the patterns on the electroplated copper electrode die (both have 40µm feature size).

dimension of 40µm. Figure 5 shows µEDM'ed microtools made with stainless steel and WC/Co. The grainy nature of WC/Co leads to a rougher finish. The 40µm features in the copper pattern are reduced to 24µm on the microtool due to the µEDM discharge gap which was measured as about 8µm. This gap is generally determined by the discharge energy and is stable under fixed discharge conditions. The dimension of the electrode patterns should be designed while keeping this gap in mind.

These microtools were then used for batch mode µUSM on a

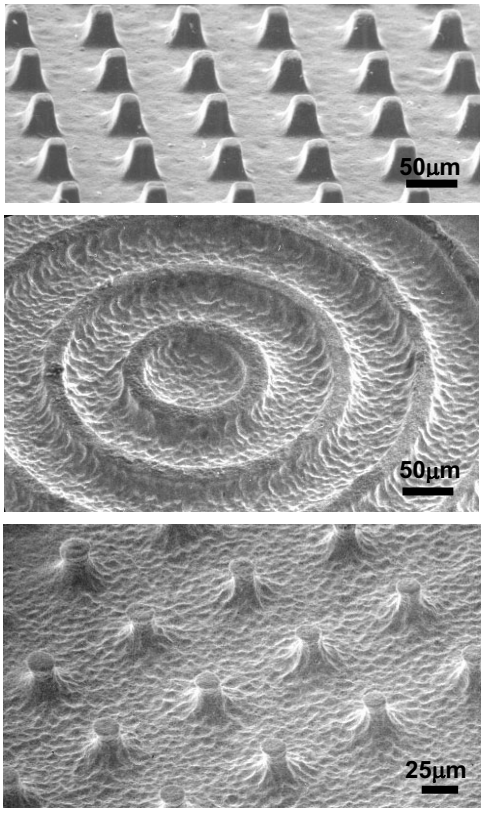

Fig. 5: SEM images of batch mode µEDM'ed microtools: (a) stainless steel microtool pattern of 35µm height; (b) and (c) WC/Co microtool pattern with poles array of 32µm height.

Table I: Properties of the ultra-high temperature glass-mica (Macor™) ceramic plate used in the demonstration (McMaster Carr 8489K231).

Temperature Range	-185˚C ~ 800˚C
Flexural Strength	94 MPa
Compressive Strength	345 MPa
Dielectric Strength	3.94×10^7 volt/m
Thermal Conductivity	1.46 W/m·K
Density	2.5×10^3 Kg/m^3
Others	Nonporous, opaque white

glass-mica (Macor™) ceramic plate whose properties are shown in Table I. The ultrasonic vibration utilized for the demonstration had a frequency of 20 KHz and amplitude of 15µm. The abrasive was WC powder with particle size of 0.5~1µm. Results are shown in Figures 6 and 7. A minimum feature size of 25µm on the ceramic plate was achieved with a machining depth of 34µm. The overall process performance achieved at this time is summarized in Table II.

The average machining rate observed in this demonstration was about 18µm/min, with ~5 mm^2 cutting surface area and ~0.5N machining load. For USM, the machining rate usually increases with any of the following: the brittle fracture hardness of the workpiece material, mean radius of abrasive grains, working load applied in the cutting zone, amplitude of vibration, and frequency of oscillation [11]. Figure 8 shows the change of machining rate with increasing amplitude of ultrasonic vibration. A linear relationship was assumed for the dashed trend line. Although larger amplitude results in faster machining speed, the surface finish becomes rougher and chips can occur.

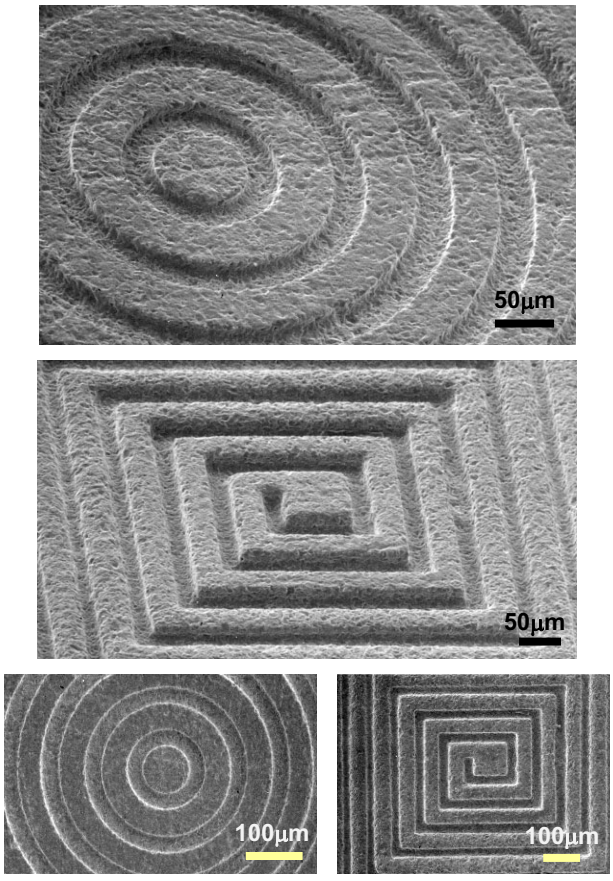

Fig. 6: SEM images of two of the patterns transferred onto ceramic surface in perspective view showing depth, and corresponding top-down view showing fidelity of the features.

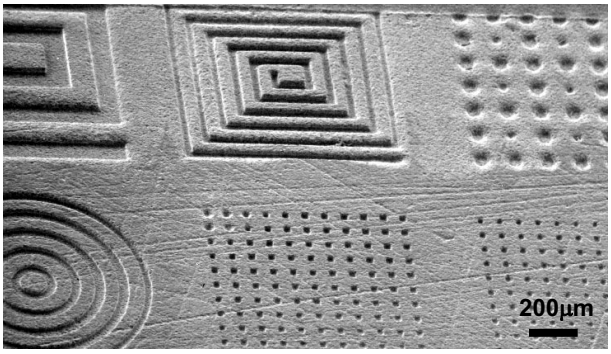

Fig. 7: SEM image of patterns on the ceramic surface transferred from the die-scale microtool.

Table II: Machining parameters for the batch mode µUSM of the Macor ceramic plate.

Transducer frequency	20KHz
Vibration amplitude	15µm
Abrasive powders	WC (0.5~1µm)
Batch machining die area	4.5mm×4.5mm
Avg. machining rate	18µm/min
Machining load	~0.5N
Minimum feature size	25µm
Cutting depth	34µm
Surface roughness (Ra)	~0.55µm (0.4µm for the raw material)
Tool wear ratio(height)	<6% (Stainless steel)

Figure 9 (a) shows the copper electrode after µEDM of the stainless steel microtool. A tool wear ratio of ~29% was measured, which corresponds to ~10µm loss of copper tool height for making a 35µm high microtool. This tool wear can be simply compensated by increasing the SU-8 mold height to get a higher copper electrode, or can be reduced using parallel discharge mode µEDM with partitioned die area as described in [10].

The wear ratio of µUSM microtools usually varies with different tool materials, or changes with machining parameters such as machining load, abrasive powder size, etc. In order to compare microtool materials, the WC/Co microtool was also tested for µUSM under the same machining parameters. Figure 9 (b) and (c) show post-use stainless steel and WC/Co microtools respectively. The stainless steel microtool wore less than 2µm for the 34µm cutting depth, giving a wear ratio of <6%, while the WC/Co microtool showed a tool wear ratio of more than 25%. This suggests stainless steel should be a better choice for this

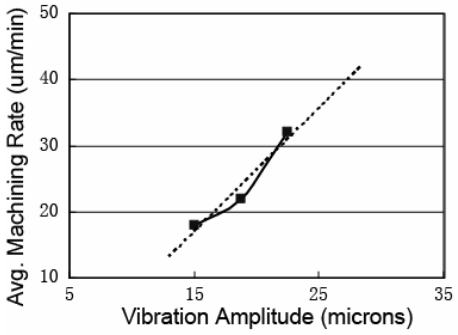

Fig. 8: Variation of machining rate as the amplitude of ultrasonic vibration is increased (Other machining parameters remain the same as in the demonstration).

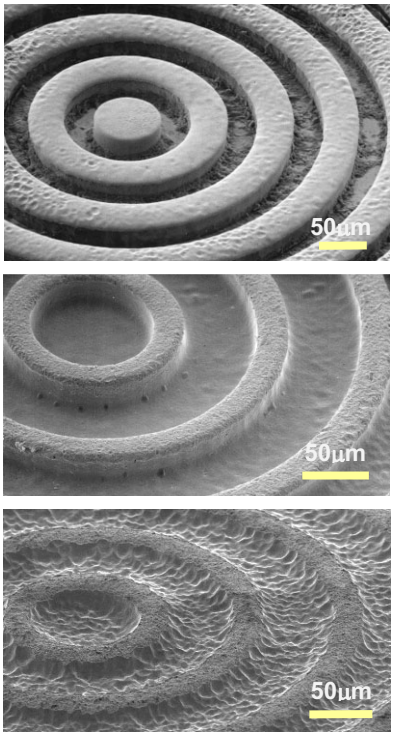

Fig. 9: Post-use SEM images of a: (a) copper electrode used after µEDM of the steel microtool, tool wear ratio ~29%; (b) stainless steel microtool, after µUSM of the ceramic part, tool wear ratio <6%; (c) WC/Co microtool, after µUSM of the ceramic part, tool wear ratio >25%.

application, opposing the usual preference for WC/Co. The reason for this divergence is still under investigation.

Figure 11 shows the hole sizes distribution for the 11×11 array of 30µm features in Figure 10. Average hole width is 29.4µm. The standard deviation of hole sizes is less than 2µm, providing acceptable size uniformity for many applications.

IV. CONCLUSIONS

A new fabrication process which combines lithography, electroplating, batch mode µEDM and batch mode µUSM has been developed to provide die-scale pattern transfer capability from lithographic mask onto ceramics, glass or other brittle materials with high throughput and resolution. A demonstrative die-scale pattern with 25µm minimum feature sizes and spacing was defined with a mask and transferred onto the workpiece by stainless steel and WC/Co microtools with a machining speed of about 18µm/min. The experimental results are very promising for further improvements and will be pursued in future efforts.

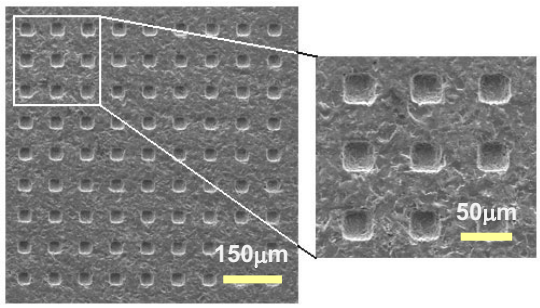

Fig. 10: SEM images of an array of 30µm-width holes fabricated on the ceramic plate.

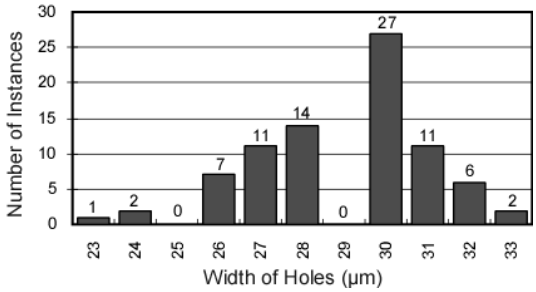

Fig. 11: Variation of features size in the array of Fig.10 - Gaussian distribution of hole widths around the mean value. Mean hole width: 29.4µm. Standard deviation: 1.9µm.

ACKNOWLEDGEMENT

The authors are grateful to the Solid-State Electronics Laboratory (SSEL) colleagues at the University of Michigan, esp. Mr. K. Takahata, Mr. K. Udeshi and Dr. S. McNamara for their help with equipment. The authors also appreciate Prof. K. Najafi and Mr. J. Giachino at UM WIMS ERC for valuable discussions. This work was supported primarily by the Engineering Research Centers Program of the National Science Foundation under Award Number EEC-9986866. Travel support has been generously provided by the Transducers Research Foundation and by the DARPA MEMS and DARPA BioFlips programs.

REFERENCES

1. W. D. Brown, *Advanced Electronic Packaging: with emphasis on multichip modules,* IEEE Press, New York (1999).
2. S. Wang, X. Li, K. Wakabayashi, and M. Esashi, "Deep Reactive Ion Etching of Lead Zirconate Titanate Using Sulfur Hexafluoride Gas," *Journal of the American Ceramic Society,* v 82, n 5, pp. 1339-41 (May 1999).
3. H. Wensink, J. W. Berenschot, H. V. Jansen, and M. C. Elwenspoek, "High resolution powder blast micromachining," *Proc. of the IEEE Micro Electro Mechanical Systems (MEMS),* pp. 769-774 (2000).
4. M. Wakuda, Y. Yamauchi, and S. Kanzaki, "Material response to particle impact during abrasive jet machining of alumina ceramics," *Journal of Materials Processing Technology,* v 132, n 1-3, pp. 177-183 (Jan 10, 2003).
5. E. Makino, T. Shibata, and Y. Yamada, "Micromachining of fine ceramics by photolithography," *Sensors and Actuators A (Physical),* v 75, n 3, pp. 278-288 (Jun. 1999).
6. T. B. Thoe, D. K. Aspinwall, and M. L. H. Wise, "Review on ultrasonic machining," *International Journal of Machine Tools & Manufacture,* v 38, n 4, pp. 239-255 (Apr. 1998).
7. X. Sun, T. Masuzawa, and M. Fujino, "Micro ultrasonic machining and its applications in MEMS," *Sensors and Actuators A (Physical),* v A57, n 2, pp. 159-64 (Nov. 1996).
8. H. Choi, S. Lee, and B. Lee, "Micro-hole machining using ultrasonic vibration," *Key Engineering Materials,* v 238-239, pp. 29-34 (2003)
9. K. Takahata, N. Shibaike, H. Guckel, "High-aspect-ratio WC-Co microstructure produced by the combination of LIGA and micro-EDM," *Microsystem Technologies,* v6, n5, pp.175-8 (2000).
10. K. Takahata, and Y. B. Gianchandani, "Batch Mode Micro-Electro-Discharge Machining," *IEEE/ASME J. Micromechanical Systems,* 11(2), pp. 102-110 (Apr. 2002).
11. M. Komaraiah, and P. N. Reddy, "A study on the influence of workpiece properties in ultrasonic machining," *International Journal of Machine Tools & Manufacture,* v33, n3, pp. 495-505 (1993).

SURFACE MICROMACHINED ELECTROMAGNETICALLY RADIATING RF MEMS

Yong-Kyu Yoon, Bo Pan, Peter Kirby, John Papapolymerou, Manos Tentzeris, and Mark G. Allen
School of Electrical and Computer Engineering
Georgia Institute of Technology, Atlanta, GA 30332

ABSTRACT

Increases in operational frequencies have reduced required RF radiator sizes, while simultaneously advances in 3-D fabrication technology have increased achievable thicknesses, such that **surface micromachined radiators in the 30-300 GHz range (millimeter wave range) are feasible in not only the horizontal dimension but also the vertical dimension**. Much of the new fabrication technology enabling three-dimensional surface micromachining is based on photostructurable epoxies. Since at GHz frequencies, currents are confined to the outermost portions of conductors, small (micron-scale) thicknesses of metals deposited on three-dimensional epoxy scaffolds suffice to create RF subcomponents, the operation of which are indistinguishable from their solid metal counterparts. This concept has been demonstrated previously for simple passive elements such as inductors. In this work, the concept is extended to radiating structures. This approach offers the potential to create surface micromachined vertical radiating structures with higher potential performance than other MEMS-compatible solutions, e.g., conventional printed-circuit patch antennas. To illustrate this approach, a W-band (75GHz~110GHz), coplanar-waveguide (CPW)-fed, quarter-wavelength monopole antenna is designed, fabricated, and characterized. A monopole antenna with a height of 800 μm is shown to radiate at 85 GHz with 16 dB return loss (due to the radiation), which shows good agreement with simulation results.

INTRODUCTION

Millimeter-wave (MMW) devices are highly valued for their ability to provide very-broad-bandwidth wireless communication in both space and terrestrial applications. Examples include satellite, radar, mobile collision detection, imaging, and indoor local communications [**1**, **2**]. One of the key components for a wireless millimeter wave system is its radiating structure, i.e., its antenna. Currently, planar MMW antennas such as microstrip antennas or printed-circuit patch antennas are widely used due to their ease of manufacture, low cost, simple fabrication, and relative ease of integration with monolithic systems. However, patch antennas can suffer from relatively narrow bandwidth, substrate dielectric loss, mutual coupling with their substrate, and surface wave perturbation issues [**3**]. Although wire antennas (e.g., dipole or monopole antennas) or cavity antennas can be considered as alternatives to printed-circuit patch antennas because of their broad bandwidth, low loss, and reduced dependence on substrate, fabrication difficulty has prevented them from being efficiently implemented in a cost effective, integrated fashion.

Now we are at a unique intersection point in time in which increases in operation frequencies of RF systems have pushed characteristic sizes of RF subelements small enough, and advances in fabrication technologies have pushed achievable thicknesses of surface micromachined components large enough, that an intersection has been achieved. Surface micromachined radiators in the 30-300 GHz range (millimeter wave range) are now feasible not only in the horizontal dimension but also in the vertical dimension, offering the potential to create radiating structures with better performance than, e.g., conventional printed-circuit patch antennas. Surface micromachining of these devices also offers the advantages of substrate independence as well as ease of integration with chips or substrates. The purpose of this work is to illustrate the capability of surface micromachining to create radiating structures for MMW applications.

An electromagnetic wave propagating through a good conductor attenuates very quickly in the depth direction of the conductor; the resultant electric current flows through the outermost portion of the conductor. Therefore, thin (micron-scale) metal layers deposited on three-dimensional (3-D) epoxy backbones should be sufficient to create RF components whose electrical characteristics are equivalent to those of their solid metal counterparts. This concept has been demonstrated previously for non-radiating passive elements: RF MEMS based on epoxy-core conductors [**4**], in which fabrication of a high-aspect-ratio RF inductor with height on the order of 1 mm has been successfully demonstrated. The three-dimensionally (3-D) complex structures achievable using mm-thickness, photostructurable resists [**5**-**8**] can now also create attractive geometries for high frequency radiators.

In this work, to illustrate this approach, a W-band (75 GHz ~ 110 GHz), coplanar-waveguide (CPW)-fed, quarter-wavelength monopole antenna is designed, fabricated, and characterized. This antenna has several unique properties. First, it is fed using a coplanar waveguide, which provides easy connectivity to other components and ease of fabrication compared to a via-through-substrate approach. Second, the epoxy core technique is used to provide a simple and efficient methodology for the transition from 2-D CPW structure to 3-D monopole. Third, since the fabricated monopole antenna is achieved by a low-temperature, foundry-compatible process, fully-integrated millimeter wave systems are feasible.

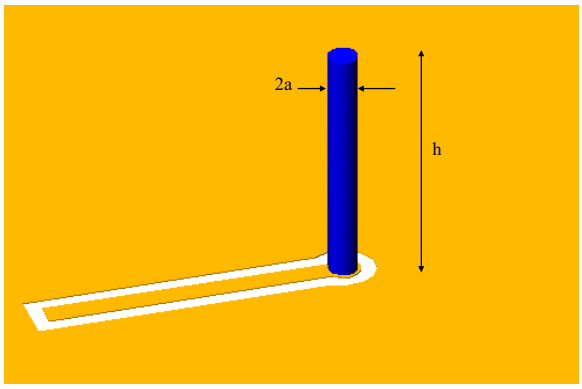

Figure 1. *Schematic of a coplanar-waveguide fed quarter-wavelength monopole antenna.*

Travel support has been generously provided by the Transducers Research Foundation and by the DARPA MEMS and DARPA BioFlips programs.

DESIGN AND SIMULATION

To design an integrated type monopole antenna, fabrication limitations and their associated effect on antenna frequency must be taken into account. Limitations exist for both achievable aspect ratio (height to diameter ratio, *h/2a* in Figure 1) as well as achievable absolute monopole height corresponding to the frequency range of interest.

The height of a quarter wave monopole in W-band (75 GHz ~ 110 GHz) is in the range of 1 mm to 680 µm. The feasibility of tall RF conductor fabrication (up to 1mm) with aspect ratios of 10 to 15 was demonstrated in a previous work [**4**]. In practice, the monopole is cylindrical with a diameter of *2a* rather than an ideal wire with zero thickness. The nonideal cylindrical monopole therefore has an inductive reactance term attributable to the nonzero width of the conductor when it is driven at the radiating resonance frequency of an ideal monopole of the same height. This reactance term results in the nonideal monopole having its actual resonance at a slightly lower frequency than that of an ideal monopole. Alternatively, if a particular resonant frequency is desired, the monopole length can be reduced to achieve the ideal monopole resonant frequency. The magnitude of this height correction depends on the aspect ratio of the cylinder [**9**]; for example, in the case of a typical fabrication-limited aspect ratio of 10, the height *h* of the 'quarter-wave' monopole is given to be *0.228 λ*. The height of the quarter-wavelength monopole required for radiation resonance in W-band is plotted in Figure 2, where the dotted line and the solid line represent an uncompensated ideal monopole and a compensated practical monopole with an aspect ratio of 10, respectively. In addition to the height corrections discussed above, it should be noted that the thicker the cylindrical monopole (i.e., the lower the aspect ratio), the wider its bandwidth becomes, and the less sharp its band-selectivity becomes.

Although the actual radiation resistance should be calculated using methods that take into account parasitics, driving elements, and imperfect ground planes, it is instructive to consider some simplified design equations for the micromachined monopole. For a quarter-wavelength monopole antenna of aspect ratio less than infinity over an ideal ground plane, the empirical radiation resistance R_A is given by Equation 1 [**10**]:

$$R_A = 12.35\,(2\pi h/\lambda)^{2.4} \qquad (1)$$

Using a fabrication-limited aspect ratio of 10, and a resultant height *h* of *0.228 λ*, the predicted radiation resistance is 29.3 Ω. The ohmic resistance R_{ohmic} of the antenna conductor can be calculated using Equation 2:

$$R_{ohmic}[\Omega] = R_s \frac{h}{2\pi a} \quad , \qquad (2)$$

where R_s is the surface resistance or sheet resistance defined as:

$$R_s = \sqrt{\frac{\omega\mu}{2\sigma}} \quad , \qquad (3)$$

and ω, μ, and σ are the radian frequency, permeability of the conductor, and conductivity of the conductor, respectively.

If the wire is made of gold ($\sigma = 4.1 \times 10^7$ S/m), the surface resistance R_s at 85 GHz is calculated to be 0.092 Ω/sq. With *h* of 800 µm and *a* of 40 µm, R_{ohmic} is 0.29 Ω. The ohmic resistance of the wire is less than 1% of the radiation resistance. Therefore, the

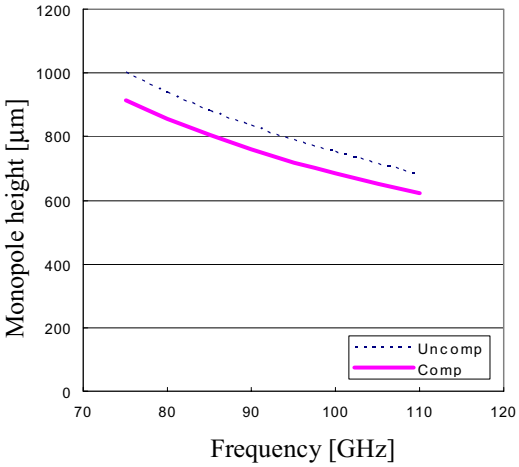

Figure 2. *Height of a monopole required resonance radiating at W-band: Uncomp and Comp represent the height of the ideal monopole and that of a cylindrical monopole, respectively, where the aspect ratio of height to diameter is 10.*

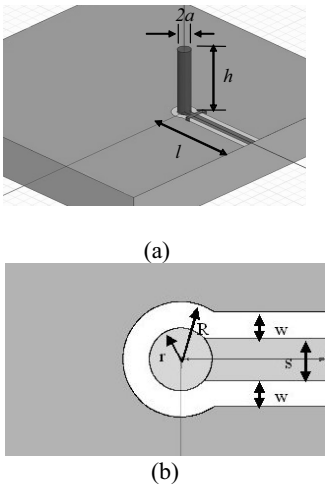

Figure 3. *Monopole antenna fed through coplanar waveguide(CPW): (a) overall view; (b) top view showing geometrical parameters.*

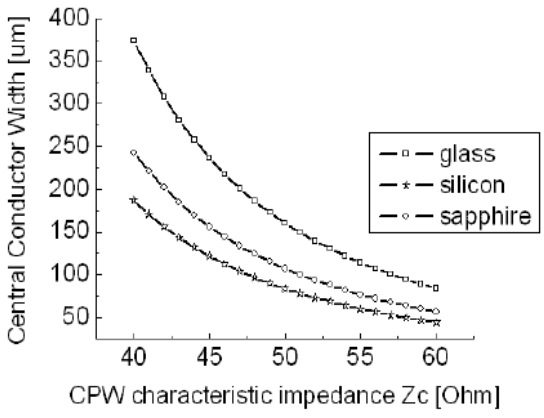

Figure 4. *Central conductor width of CPW according to characteristic impedance Zc on different substrates (gap width is fixed to 50µm).*

antenna input resistance can be approximated by the antenna radiation resistance in resonance mode.

Another consideration of the monopole design is the scheme required to feed it. A monopole is usually fed against a large solid ground plane, which requires via fabrication through the substrate. Instead, here a coplanar-waveguide (CPW) feeding scheme is used as shown in Figure 3, resulting in a via-free and a low-cost solution for an integrated RF transceiver system. The characteristic impedance of CPW lines on silicon (ε_r=11.7), sapphire (ε_r=10), and glass (ε_r=7.8) has been calculated as a function of the normalized center conductor width, using the LineCal functionality of the Agilent advanced design system (ADS) and is shown in Figure 4. The gap width w is fixed to 50 µm and the ground is assumed to be infinite. The calculated characteristic impedance on these substrates is between 50 Ω and 60 Ω with a central conductor width s of 80 µm, which is appropriate for the impedance matching to the system (its characteristic impedance is usually 50 Ω) but may not be good for antenna input impedance matching, which could be solved by CPW geometry optimization.

For a more synthetic analysis, the monopole antenna and the feeding CPW line can be analyzed as a whole using numerical software. Input return loss and radiation pattern have been simulated using the Ansoft high frequency system simulator (HFSS) 9.0 with the parameters listed below on various substrates.

The radius of ground aperture R: 110 µm
The radius of bottom pad of monopole r: 60 µm
Gap between the signal and the ground lines w: 50 µm
Central conductor line width s: 80 µm
Monopole width $2a$: 80 µm
Monopole height h: 800 µm
CPW line length l: 1 mm

The simulation results for a glass substrate are plotted in Figure 5. The monopole shows resonance at a frequency of 85GHz, and the far-field radiation pattern shows an omnidirectional and quite symmetric pattern, as expected.

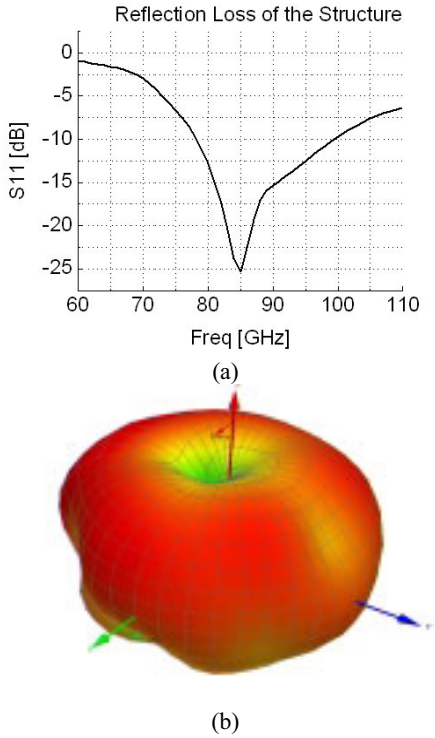

Figure 5. *Simulated (a) input return loss and (b) radiation pattern for the monopole on soda lime glass using Ansoft HFSS.*

FABRICATION AND MEASUREMENT

A polymer core conductor fabrication technique [**4**] has been adopted for the high-aspect-ratio monopole structure. A photodefinable epoxy, SU-8 (Microchem, Inc.), which is favorable for high-aspect-ratio micro patterning [**11**], is used for the monopole backbone, and electroplated gold is used for the electrical conductive path. The skin depth of gold in the W-band (75 GHz ~ 110 GHz) is in the range of 0.30 µm to 0.24 µm. In general, 5 times the skin depth is considered to be sufficient to minimize the RF conductor loss and thereby not degrade the electrical performance. In this case a gold layer of approximately 1.5 µm was used.

Figure 6 details the fabrication process. A chromium coated soda-lime glass (Telic Co.) is used as a substrate. Chromium is patterned for the monopole column definition using standard photolithography *(a)*. SU-8 epoxy (800 µm thick) is coated on the substrate to a thickness that will ultimately define the monopole height. The SU-8 is exposed to a UV source from the substrate side to obtain a uniform column latent pattern. Alternatively, a front side exposure can be used if the substrate is opaque (Si, GaAs, etc.) *(b)*. The latent pattern is developed. Metal deposition of titanium and copper using a DC sputterer is carried out to form a conformal seed layer. Thin SU-8 (5 µm) is spin-coated and patterned for the definition of the signal path as well as ground pads using proximity photolithography due to the uneven surface topography *(c)*. Gold of 2 µm thickness is uniformly electrodeposited through the bottom mold as well as over the column surface. The thin SU-8, the seed layer, and the bottom chromium layer are removed sequentially to complete the process *(d)*. For fabrication simplicity, a two-mask process has been described above. In order to obtain more accurate bottom electrode

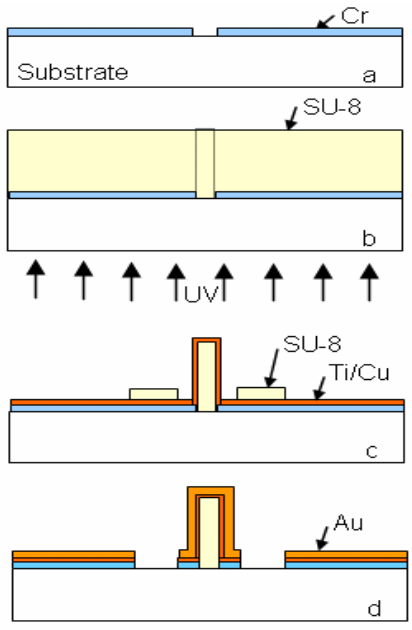

Figure 6. *Fabrication process for a monopole antenna using epoxy core conductor scheme.*

dimensions for the signal and the ground lines, bottom line metallization can be performed separately from the monopole metallization with an additional mask step. Since the maximum temperature of any fabrication step is below 100 °C, the process is CMOS compatible and easily integrable with a variety of substrates. Figure 7a and 7b show a photomicrograph of a fabricated CPW-fed monopole antenna array (3×3) and an SEM image of a single monopole antenna, respectively. The fabricated structure is measured to be approximately 800 μm tall.

An Agilent 8510C vector network analyzer connected to a Cascade GSG 150 probe station has been used for s-parameter measurement after a standard SOLT calibration between 50 GHz and 110 GHz. Figure 8 shows measured and simulated return loss of a single monopole antenna from 50 GHz to 110 GHz. The measurements have been performed with a monopole with a height of 800 μm. A return loss of 16 dB was measured for the monopole resonating at 85 GHz. Good agreement between simulation and measurement is observed for the 800 μm tall sample. Radiation pattern measurements are currently underway.

CONCLUSIONS

A previously-developed epoxy core conductor fabrication concept is extended to millimeter wave applications with radiating structures. To demonstrate the process feasibility, a W-band micromachined monopole, which is vertically mounted on a glass substrate, is reported. A 2-D to 3-D feeding scheme is also proposed and optimized by simulation using a high frequency system simulator. Both the simulation and measurement results agree well. A return loss of 16 dB has been measured for a monopole of 800 μm thick, resonating at 85 GHz. This micromachined monopole, as well as more complex geometries based on this fabrication technology, may have application in low-cost broadband compact millimeter wave communication systems.

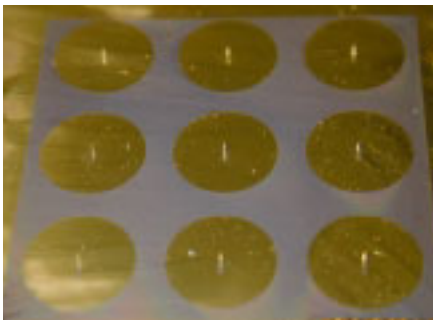

(a)

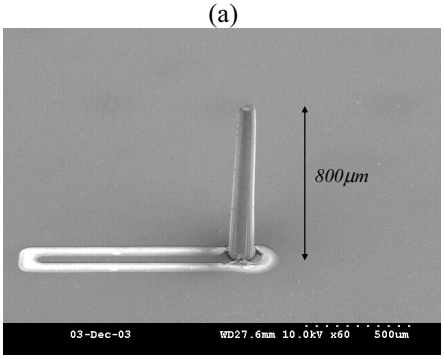

(b)

Figure 7. *Fabricated CPW-fed monopole antenna: (a) photomicrograph of 3X3 monopole array; (b) SEM image of 800μm tall monopole.*

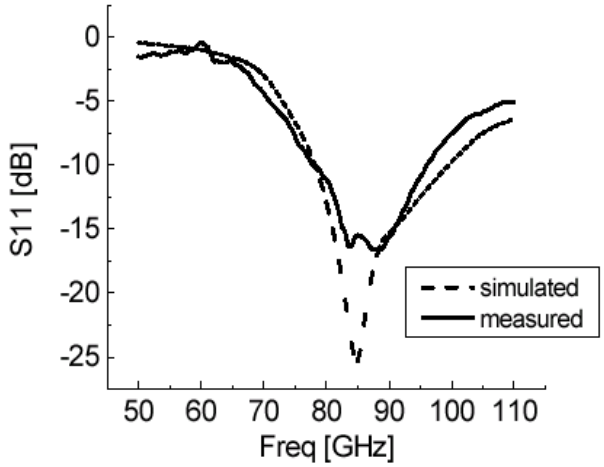

Figure 8. *Measured and simulated reflection power (S11) for a monopole with a pole height of 800 μm.*

REFERENCES

1. F.K. Schwering, "Millimeter Wave Antennss," *Proceedings of the IEEE,* Vol. 80, No. 1, pp. 92-102, January, 1992.

2. G.M. Rebeiz, "Millimeter-Wave and Terahertz Integrated Circuit Antennas," *Proceedings of the IEEE,* Vol. 80, No. 11, pp. 1748-1770, November, 1992.

3. D.M. Pozar, "Considerations for Millimeter Wave Printed Antennas," *IEEE Trans. Antennas and Propagation*, Vol. AP-31, No. 5, pp. 740-747, September, 1983.

4. Y.-K. Yoon, J.-W. Park, and M.G. Allen, "RF MEMS Based on Epoxy-Core Conductors," *Digest of the 2002 Solid-State Sensor, Actuator, and Microsystems Workshop*, Hilton Head Island, South Carolina, pp. 374-375, 2002

5. M. Han, W. Lee, S.-K. Lee, S.S. Lee, "Fabrication of 3D Microstructures with Inclined/Rotated UV Lithography," *Proceedings of the IEEE Microelectromechanical Systems Conference (MEMS)*, Kyoto, Japan, pp. 554-557, 2003.

6. H. Sato, T. Kakinuma, J.S. Go, and S. Shoji, "A Novel Fabrication of In-channel 3-D Micromesh Structure Using Maskless Multi-Angle Exposure and Its Microfilter Application," *Proceedings of the IEEE Microelectromechanical Systems Conference (MEMS)*, Kyoto, Japan, pp.223-226, 2003.

7. Yong-Kyu Yoon, Jung-Hwan Park, Florent Cros, and Mark G. Allen, "Integrated Vertical Screen Microfilter System Using Inclined SU-8 Structures," *Proceedings of the IEEE Microelectromechanical Systems Conference (MEMS)*, Kyoto, Japan, pp.227-230, 2003.

8. Yoonsu Choi, R. Powers, Y.-K Yoon, M.G. Allen, "A Three-Dimensional Microfluidic Network for Cellular Perfusion," *The 7th International Conference on Miniaturized Chemical and BioChemical Analysis Systems (MicroTAS2003),* pp. 1001-1004, Oct. 2003.

9. W.L. Stutzman and G.A. Thiele, Antenna Theory and Design, Chapters 2 and 5, John Wiley & Sons, Inc., New York, 1998.

10. R.F. Schwartz, "Input Impedance of a Dipole or Monopole," *Microwave Journal*, vol. 15, p.22, Dec. 1972.

11. H. Lorenz, M. Despont, N. Fahrni, J. Brugger, P. Vettiger, P. Renaud, "High aspect ratio, ultrathick, negative-tone near-UV photoresist and its applications for MEMS," *Sensors and Actuators*, *Part A, vol. 64*, pp-33-39, 1998.

POROUS POLYSILICON SHELL FORMED BY ELECTROCHEMICAL ETCHING FOR ON-CHIP VACUUM ENCAPSULATION

Rihui He[1], Li Fan[2], Ming C. Wu[2], and Chang-Jin "CJ" Kim[1]
[1]Mecahnical and Aerospace Engineering Department,
[2]Electrical Engineering Department, University of California, Los Angeles (UCLA)
Los Angeles, CA 90095

ABSTRACT

We have developed a novel on-chip vacuum encapsulation technique, which turns a thick polysilicon layer porous "after deposition" so that the process is fully compatible with typical polysilicon surface micromachining. Once the polysilicon shell layer is deposited over the top sacrificial SiO_2 layer and turned porous, the thick porous layer allows for fast removal of sacrificial material underneath, but not the penetration of sealing materials during subsequent vacuum sealing. The sacrificial etching through a thick porous shell is confirmed visually, and the idea of sealing is proved with a dual cavity structure. To showcase the applicability, the proposed process is further demonstrated through the common MUMPs process.

INTRODUCTION

The on-chip packaging approach has long been recognized as a technology to simplify the subsequent packaging and thus reduce the cost of final MEMS product. This technology is especially beneficial to many resonating devices, which frequently require vacuum encapsulation. Despite the anticipated advantages over the usual post-process packaging methods that involve bonding, the monolithic on-chip encapsulation methods have some drawbacks and so far not proven practical.

In the early on-chip encapsulation techniques, the sacrificial layer was removed by allowing the etchant (e.g. HF) to enter the microshell through the lithographically-made etch holes on the shell [1, 2]. In addition to the long etching time and the resulting extended exposure to the etchant, which raises the concern for material degradation [3], the deposition of sealing material on the surface of the encapsulated devices is not negligible, affecting the device characteristics. The problem would be more serious for the recent devices with nanogap [4]. To overcome these drawbacks, thin (below 100 nm), permeable polysilicon, deposited by LPCVD in a certain process condition, was proposed as the shell material [5-7]. However, the permeability was in large part due to the thinness, requiring a separate thick shell layer and using the thin permeable polysilicon only at the etching holes on the shell. Further, a small amount (80Å) of sealing material still penetrated through the thin permeable layer during sealing.

The concept of the new on-chip encapsulation approach is shown in Fig. 1. What is desired is a thick but permeable shell layer, so that it can be a structural material by itself and also block the sealing material from passing through the pores during the vacuum sealing process. Among various porous materials, porous polysilicon is chosen because it can be turned porous by electrochemical etching "after" it is deposited, which makes the process compatible with typical polysilicon surface micromachining processes. If the thick polysilicon is made porous, with vertically-oriented nanopores preferentially, it satisfies most of the desired characteristics: structural layer by itself, resistant but permeable to HF, and effective sealing. The resulting on-chip encapsulation technology is expected to provide a low-cost, high performance packaging solution for a wide variety of polysilicon surface-micromachined devices, especially micro- and nano-resonators.

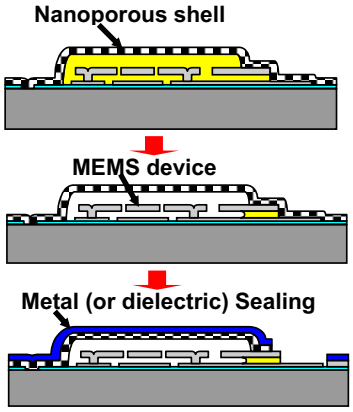

Figure 1. *On-chip encapsulation by thick porous shell*

FORMATION OF POROUS POLYSILICON SHELL

In the traditional electrochemical etching, porous polysilicon is directly formed on top of conductive material [8]. To be used for encapsulation in surface micromachining, the porous polysilicon needs to be formed on top of sacrificial layer, which is usually insulating oxide. Anderson *et al.* [9] has reported lateral porous etching of polysilicon formed between two nitride layers. However, the porous polysilicon layer was sacrificed to make nitride channel, rather than being released as freestanding structure. Since the voltage was applied between the channel ends, it is suspected that the pores are formed laterally and not suitable for our goal of passing the etchant through the thickness.

The process flow to test fabrication of freestanding porous polysilicon shell is outlined in Fig. 2. The 1.5 μm polysilicon shell was fabricated by typical polysilicon surface micromachining steps (Fig.2 (a)). The polysilicon was symmetrically doped from PSG layers on both sides by annealing at 1000 ºC in N_2. The polysilicon thus obtained a resistivity of 0.02 $\Omega \cdot cm$. In order to create an electrical

Travel support has been generously provided by the Transducers Research Foundation and by the DARPA MEMS and DARPA BioFlips programs.

contact between polysilicon and silicon substrate for electrochemical etching, openings were made through nitride layer to the silicon substrate.

After the top PSG layer was stripped off, the wafer was diced, and each die was mounted in the electrochemical etching set-up (Fig. 3). Photoresist was used as a simple mask to define electrochemical etching area. A photoresist with high resistance to electrochemical etching solution, NR 9-8000 negative photoresist, is used. Liquid In-Ga was painted on the backside of the sample to provide good electrical contact between the sample and the copper jig. The polysilicon was electrochemically etched in 49% HF:ethanol = 1:1 solution at 4 mA/cm^2 for 250 sec in room light and temperature. Then, the underlying PSG sacrificial layer was removed by HF, which diffuses through the pores of porous polysilicon. The HF release time was less than 2 minutes regardless of the size of the cavity. The sample was thoroughly rinsed in DI water and methanol. Final drying step used supercritical CO_2 drying to alleviate stiction problem (Fig. 2 (c)). Finally PECVD low stress nitride deposition was performed for vacuum sealing experiment (Fig. 2 (d)).

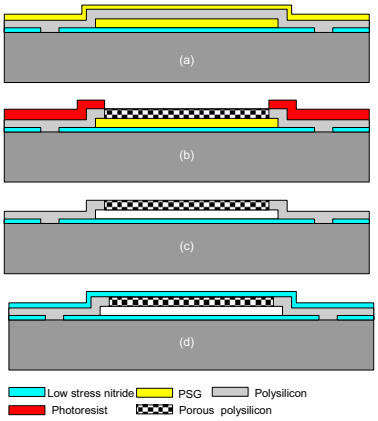

Figure 2. *Process flow of porous polysilicon shell formation, sacrificial etching, releasing, and sealing.*

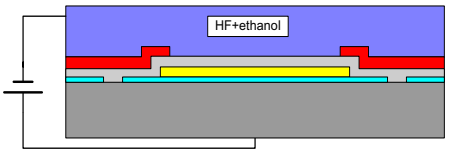

Figure 3. *Schematic view of the electrochemical etching set up. The backside is protected by a copper jig. Pt is used as the counter electrode in HF-ethanol solution.*

The electrochemical etching current has to be carefully chosen. In the electrochemical etching, pore growth rate increases with the current density [10]. In order to prevent photoresist from peeling off in the HF-ethanol electrochemical etching solution and to minimize etching undercut, high current density is preferred. However, high current density etching would create a problem of its own. Fig. 4(a) shows, after 140 sec electrochemical etching at 10 mA/cm^2, a crack is observed in the polysilicon under the edge of the photoresist mask. This is because after polysilicon in the unmasked area is turned porous, this small cross section area is exposed to etching solution and high current density leads to electropolishing of polysilicon. Fig. 4(b) shows the successful result of electrochemical etching when the current is lowered to 4 mA/cm^2. After 255 sec of etching, no electropolishing is observed in the polysilicon area protected by photoresist while the polysilicon in the unmasked area is already porous (indicated by the partial etching of PSG).

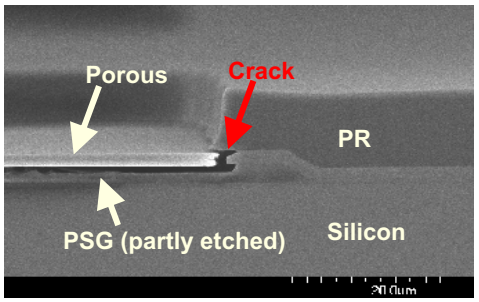

(a)

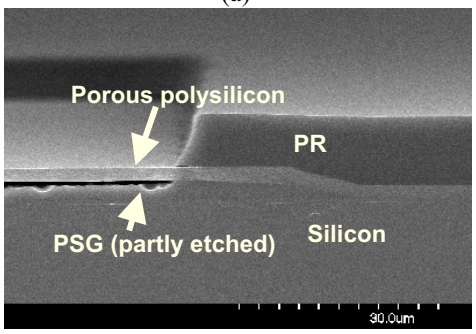

(b)

Figure 4. *SEM cross section images of the polysilicon shell after electrochemical etching at different current density. (a) 140 sec at 10 mA/cm^2, (b) 255 sec at 4 mA/cm^2.*

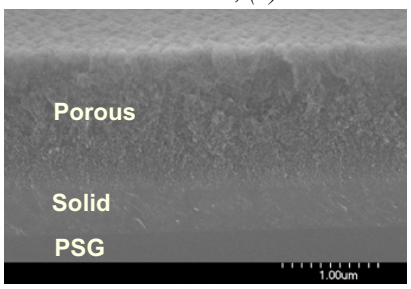

Figure 5. *SEM cross section of polysilicon shell after 200 sec electrochemical etching at 4 mA/cm^2 constant current*

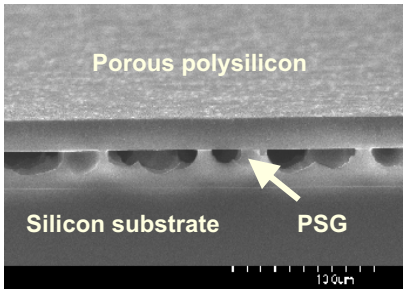

Figure 6. *SEM cross section of polysilicon shell after 250 sec electrochemical etching at 4 mA/cm^2 constant current.*

The process of pore growth during the electrochemical etching can be observed by SEM. Fig. 5 is a cross section of a sample after 200 sec of electrochemical etching. The polysilicon is turned porous in the top region, and the porous area is visually distinguishable from the solid area below. Fig. 6 is the SEM pictures of the cross section after 250 sec of electrochemical etching. There are many trenches observed at the top of PSG sacrificial layer, which indicates that the polysilicon shell has been completely turned porous and HF in the electrochemical solution has diffused through the porous polysilicon shell to attack PSG. The irregular etching pattern in PSG shows the pore growth across the shell area is not uniform. It is suggested that the electrochemical etching current flows mainly along the polysilicon grain boundaries, which leads to a higher pore growth rate and preferential etching of the grain boundaries [8].

Fig. 7 shows the interface of the porous and solid area near the edge of the porous polysilicon cavity. The left side of the shell is porous, while the right side is solid, which was protected by photoresist during the electrochemical etching.

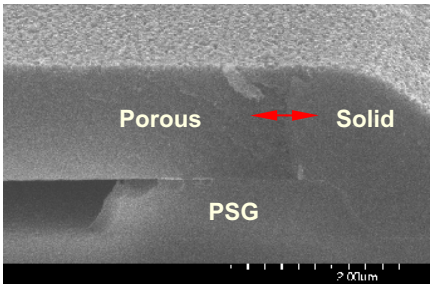

Figure 7. *SEM cross section of polysilicon shell. The interface of porous and solid area is visible. Photoresist, which protected the solid region during the porous etching, has been removed.*

VACUUM SEALING

We used a simple dual cavity design [5] to prove vacuum sealing on porous polysilicon shell. A 150 μm dual cavity with porous polysilicon shell was sealed by 1 μm PECVD low stress nitride deposition (Fig. 8). The deposition pressure was 900 mTorr. To ensure the air in the cavity is fully evacuated, the sample was pumped down in vacuum for more than 2 hours before the nitride sealing.

After the nitride deposition, the profile of one of the cavity was first measured by a Dektak profilometer. Then, the other cavity was broken intentionally by a probe tip before obtaining the profile of the first cavity again. The 1.63 μm height difference indicated the cavities had been sealed in low pressure during the PECVD nitride deposition.

The deflection of the cavity after vacuum sealing is calculated by the model in [11, 12]. The pressure load deflection relationship is given as:

$$p = \frac{C_1 \sigma t h}{a^2} + \frac{C_2 E t h^3}{a^4}, \quad Et = E_1 t_1 + E_2 t_2$$

The Young's modulus of porous polysilicon E_1 is roughly measured to be 30 GPa by load deflection experiment on a porous polysilicon membrane. The Young's Modulus of silicon nitride film E_2 is assumed to be 190 GPa from literature. Residual stress σ is deducted from the shell deflection when the pressure applied is 0. The calculated deflection h from this model is 1.68 μm, which is in good agreement with the measured deflection 1.75 μm.

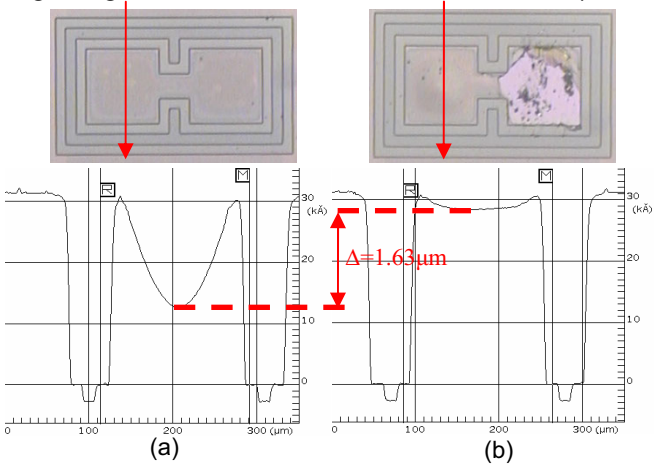

Figure 8. *A 150 μm dual cavity is used to prove sealing effect. Both of the scanning data are from the left cavity, indicated with the arrows. The scan data (a) was obtained before breaking the right cavity and the scan data (b) was obtained after the breakage.*

INTEGRATION WITH MUMPS PROCESS

To demonstrate the general application of this technique, Poly2 layer in MUMPs process has been chosen to form porous polysilicon shell. MUMPs service is widely used for polysilicon surface micromachining.

Fig. 9 is the schematic view of the process. A bridge resonator structure has been designed inside the shell to demonstrate on-chip encapsulation of microdevices. Poly2 layer on top will be partly turned porous by electrochemical etching. Supporting posts are designed to reinforce the polysilicon shell of the large size. The sacrificial oxide is used to isolate the polysilicon shell from the electrical feedthrough by time control of the release in HF.

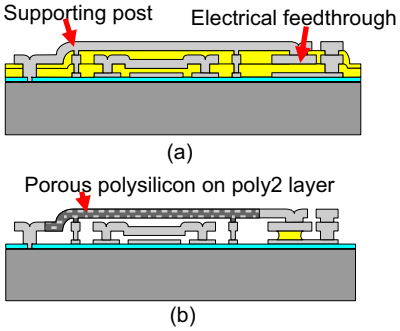

Figure 9. *Schematic view of a MUMPs device. (a) as received. (b) after post process to release bridge structures.*

The post process on the MUMPs chip starts with the removal of all the layers on the backside by RIE. This is necessary to open the electrical contact to the Poly2 layer through the substrate. Using photoresist as a mask, part of

the Poly2 shell is turned porous by electrochemical etching. The structure is then released in less than 4 minutes in 49% concentrated HF.

Fig. 10 is a microscopic top view of the device after release, which shows the color difference between the porous area and non-porous area on the polysilicon shell. Many black dots are observed on the porous polysilicon shell surface. Those black dots are identified as the area with higher porosity from the SEM observation.

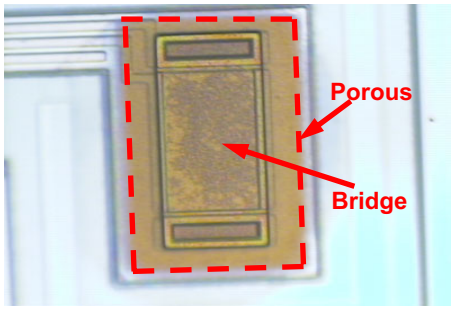

Figure 10. *Optical picture of a released bridge. The area inside the dashed line is the porous area on the Poly2 shell.*

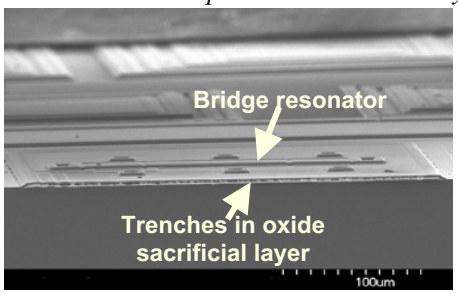

Figure 11. *SEM cross section of porous polysilicon shell on a MUMPs chip.*

Shown in Fig. 11 is the cross section of a device after electrochemical etching. The trenches in oxide indicate HF in the electrochemical etching solution has started to etch sacrificial oxide layer through the pores. The SEM picture in Fig.12 shows the bridge has been successfully released without any stiction.

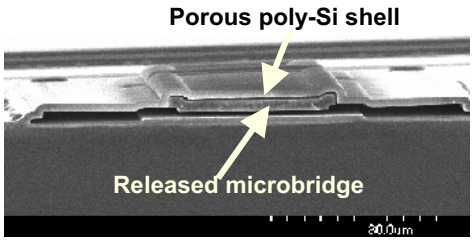

Figure 12. *A released microbridge on MUMPs chip.*

CONCLUSION

We have successfully demonstrated the first on-chip encapsulation using a porous polysilicon shell. The 1.5 μm polysilicon shell is completely turned porous in 255 sec by electrochemical etching. Porous area on the polysilicon shell can be simply defined by photoresist masking. The sacrificial layer under the porous polysilicon shell is cleared in 2 minutes (without device inside) or 4 minutes (with device inside) in 49% concentrated HF regardless of the shell area size. PECVD low stress nitride deposition has successfully sealed the cavity with porous polysilicon shell in vacuum. The process is fully compatible with typical surface micromachining process. Integrating with the common MUMPs process, a bridge structure is successfully encapsulated by this technique.

ACKNOWLEDGEMENT

This work was funded by DARPA MEMS Program. Discussion with Prof. B. Dunn is highly appreciated.

REFERENCES

[1] H. Guckel, D. W. Burns, C. R. Rutigliano, D. K. Showers, and J. Uglow, "Fine grained polysilicon and its application to planar pressure sensor," *Proceedings of the 4th International Conference on Solid-State Sensors and Actuators (Transducer '87)*, 1987, pp. 277-82.

[2] L. Lin, K. M. McNair, R. T. Howe, and A. P. Pisano, "Vacuum-encapsulated lateral microresonators," *Proceedings of the 7th International Conference on Solid-State Sensors and Actuators (Transducers'93)*, Yokohama, Japan, 1993, pp. 270-3.

[3] J. A. Walker, K. J. Gabriel, and M. Mehregany, "Mechanical integrity of polysilicon films exposed to hydrofluoric acid solutions," *Proceedings of the IEEE Micro Electro Mechanical Systems*, Napa Valley, California, USA, 1990, pp. 56-60.

[4] J. R. Clark, W.-T. Hsu, and C. T.-C. Nguyen, "High-Q VHF micromechanical contour-mode disk resonators," *Technical Digest of IEEE Int. Electron Devices Meeting*, San Francisco, California, 2000, pp. 399-402.

[5] K. S. Lebouitz, R. T. Howe, and A. P. Pisano, "Permeable polysilicon etch access windows for microshell fabrication," *Proceedings of the 8th International Conference on Solid-State Sensors and Actuator*, Stockholm, Sweden, 1995, pp. 224-227.

[6] K. S. Lebouitz, A. Mazaheri, R. T. Howe, and A. P. Pisano, "Vacuum encapsulation of resonant devices using permeable polysilicon," *IEEE MEMS Conference*, Orlando, FL, 1999, pp. 470-475.

[7] G. M. Dougherty, T. D. Sands, and A. P. Pisano, "Microfabrication using one-step LPCVD porous polysilicon films," *Journal of Microelectromechanical Systems*, vol. 12, 2003, pp. 418-24.

[8] P. G. Han, M. C. Poon, P. K. Ko, J. K. O. Sin, and H. Wong, "Study of luminescent porous polycrystalline silicon thin films," *J. Vac. Sci. Technol. B*, vol. 14, pp. 824-6, 1996.

[9] R. C. Anderson, R. S. Muller, and C. W. Tobias, "Porous polycrystalline silicon: a new material for MEMS," *Journal of Microelectromechanical Systems*, vol. 3, pp. 10-18, 1994.

[10] V. Lehmann, "The physics of macroporous silicon formation," *Thin Solid Films*, vol. 255, 1995, pp. 1-4.

[11] O. Tabata, K. Kawhata, S. Sugiyama, and I. Igarashi, "Mechanical Property Measurements of Thin Films Using Load-Deflection of Composite Rectangular Membranes," *Sensors and Actuators*, vol. 20, 1989, pp. 135-141.

[12] D. Maier-Schneider, J. Maibach, and E. Obermeier, "A new analytical solution for the load-deflection of square membranes," *Journal of Microelectromechanical Systems*, vol. 4, 1995, pp. 238-241.

MICROBOLOMETERS WITH ADAPTIVE DETECTIVITY USING ELECTROSTATIC ACTUATION*

Woo-Bin Song and Joseph J. Talghader
Department of Electrical and Computer Engineering, University of Minnesota
Minneapolis, MN 55455

ABSTRACT

The first microbolometers with electronically controlled detectivities are reported. Such devices are needed to thermally image scenes containing both very high and low temperatures. In the high detectivity state, the microbolometers are operated similar to standard commercial devices [**1**]. In the low detectivity state, portions of the support beams are brought in contact with the substrate to reduce the sensitivity of the devices. This can be done on a pixel-by-pixel basis. In low voltage testing, the maximum actuation voltage is set to 17V, and the detectivities of a typical device can be switched more than an order of magnitude between $1.8x10^6$ $cmHz^{1/2}/W$ and $1.5x10^5$ $cmHz^{1/2}/W$. The device pixel size is 100μm by 100μm and is designed for an array fill factor of 91%.

INTRODUCTION

Thermal detectors based on small bandgap materials such as $Hg_{0.8}Cd_{0.2}Te$ (MCT), InSb, and others have been studied and commercialized primarily for military and space science applications [**2**]. These photon detectors have very high performance but require cryogenic cooling systems to reduce parasitic dark currents.

With the advent of micromachining technology, it was realized that sufficiently high performance could be achieved with uncooled detectors that operated based on the heating of a small mass. Several classes of devices for reading the rise in temperature were developed. First and most prominent of these was the bolometer[**3,6**], but also developed were pyroelectric detectors [**4**], thermoelectric detectors [**5**], and others. The cost and weight of these devices is dramatically reduced compared to infrared photon detectors because cooling is no longer needed and because the materials involved are much easier to work with. For example, Wood, et. al. [**6**] reported high-quality infrared imaging in an infrared focal plane array using a monolithic silicon-based process. Recent studies have attempted to improve the performance of the basic microbolometer by developing high temperature-coefficient-of-resistance (TCR) materials such as semiconducting YBaCuO (which is well-known for its superconducting superconducting state in other technologies) [**7**], vanadium oxide [**8**], and so on. Also new device structures have been proposed to enhance sensitivity and thermal isolation [**9**].

Typical thermal detectors are designed for high thermal isolation, and this makes them extremely receptive to small differences in background temperature. However, high sensitivity potentially has drawbacks when a scene contains very bright areas that may results from fires, explosions, or engine operation. For example, the most common material used as the TCR layer in microbolometers, vanadium oxide, is thermochromic, meaning that its absorption and resistance properties change if the microbolometer is heated excessively. Also, the electronics used to amplify the signals at the edges of the array would be unable to handle the full dynamic range needed to image the smallest and brightest signals. Intensity-dependent noise and device damage are other possible issues. In this paper, an adaptive microbolometer is shown that is able to handle both high and low intensity signals. It does not require major changes to standard commercial architectures but rather uses an already-existing electrostatic actuator between the ground electrode and detector plate to bring a small area of the supports into contact with the substrate, thereby increasing device thermal conductance. To characterize this adaptive microbolometer, measurements of thermal conductance, responsivity, and detectivity have been made with and without electrostatic actuation.

BACKGROUND

Since the responsivity of a thermal detector is inversely proportional to its thermal conductance, the detectors must be thermally isolated from their surroundings. As implied in the previous section, a good thermal isolation can be achieved by having an air gap between the sensing element and the substrate with only thin support beams connecting them. To insure that the thermal conductance is determined by the support design, detector arrays are packaged under low vacuum conditions in hermetically sealed packages.

Previous research in our group has shown that the thermal conductance [**10,11**] and thermal responsivity [**11**] of micromachined beams and plates can be tuned both continuously and discretely. Continuous tuning of the responsivity was demonstrated over a factor of three and discrete tuning over almost two orders of magnitude. It was shown that the fundamental limit of thermal conductance tuning was about 4 orders of magnitude limited by the thermal contact conductance on the high end and radiation heat transfer on the low end.

While these initial studies were suggestive, the devices used in the demonstration were not designed for high fill factor or high thermal isolation. In addition, it is ultimately the detectivity of a detector that determines performance. The detectivity can be calculated from the expression,

$$D^* = \frac{(A)^{1/2}(\Delta f_{bandwidth})^{1/2}\Re_V}{\sqrt{\overline{V_{noise}}^2}} \qquad (1),$$

where R_V is the responsivity, A is the area of a pixel plate, $\Delta f_{bandwidth}$ is the bandwidth of measurement, and $\overline{V_{noise}^2}$ is the mean square value of the fluctuating noise voltage.

* Travel support has been generously provided by the Transducers Research Foundation and by the DARPA MEMS and DARPA BioFlips programs.

EXPERIMENT AND DISCUSSION

The devices constructed for this study were microbolometers that used an inherent electrostatic actuator to bring its support beams into partial contact with the substrate as shown in Fig. 1. This induced a large change in the thermal conductance of the devices which directly led to similar changes in responsivity and detectivity. The thermal contact conductances of the materials interfaces used in micromachining are high enough [**12**] so that touching a small portion is sufficient to can cause dramatic changes in detectivity. While total thermal contact could change the potential dynamic range by four orders of magnitude [**13**], most imaging requires only a fraction of this range. Partial contact also helps to eliminate stiction during operation. Relatively low actuation voltages can be used due to the low rigidity of the supports.

The adaptive microbolometers are composed of two layers of silicon nitride structural material separated from the substrate and each other by polyimide sacrificial layers. First a 500nm silicon nitride layer is deposited on top of a highly doped silicon wafer for electrical insulation followed by 1500nm of spin-coated polyimide, which is patterned and etched with an O_2 plasma to form anchor points for the 500nm thick PECVD nitride support beams. The support beams are coated with Ti/Au to insure a low resistance for read-out. Then, a second polyimide layer is spin-coated, patterned, and etched with an O_2 plasma to make vias from the Ti/Au to the TCR material (Ti) of the microbolometer plate, which is deposited later. The pixel plate is composed of a 100nm Ti layer, which is the TCR material, sandwiched between two 200nm PECVD nitride layers. Between depositions, vias are opened from the Ti to the Ti/Au of the supports. In the final step, the double polyimide layers are isotropically etched in an O_2 plasma to release the pixel plate and its support beams from the substrate. The designed pixel is 100μm by 100μm and has an array fill factor of 91%. Images of completed devices and a small test array are shown in Fig. 2. Typical device characteristics are given in Table I.

(a)

(b)

Figure 1. *Conceptual diagram of a tunable detectivity microbolometer. In diagram (a), the device stands in a state of low thermal conductance and high detectivity. In diagram (b), the device supports have been actuated into contact with the substrate, creating a high thermal conductivity and low detectivity state. In practice only the edge farthest from the ground support contacts the substrate to prevent stiction.*

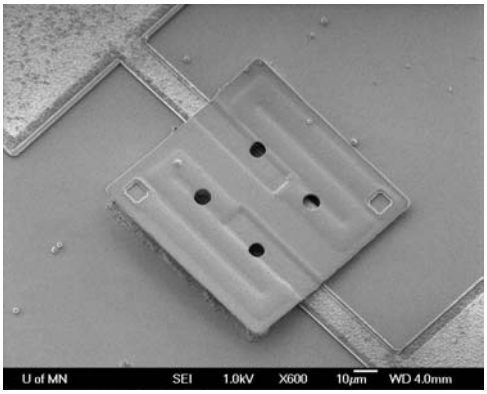

(a)

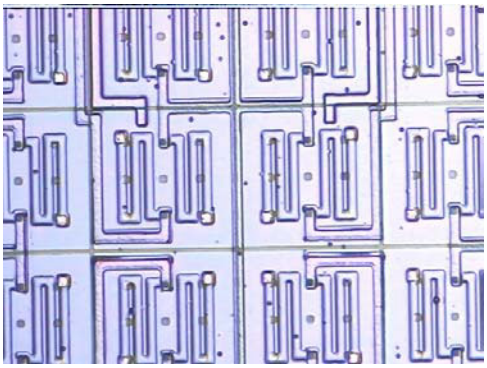

(b)

Figure 2. *(a) SEM image of an individual microbolometer device. The microbolometer pixel dimensions are designed to be compatible with high fill-factor arrays and shown in part (b), an optical image of a portion of a 4 x 4 high fill factor array.*

Parameter	Value
Size of Pixel plate	100 μm x 100 μm
Thickness of Pixel plate	Top plate (PECVD Nitride): 0.2 μm
	TCR layer (Titanium): 0.1 μm
	Bottom plate (PECVD Nitride): 0.2 μm
Length of Support beam	277 μm
Width of Support beam	6 μm
Thickness of Support beam	0.5 μm
Air Gap Spacing	Plate to support beam: 1.5 μm
	Support beam to plate: 1.5 μm
Thermal Coefficient of Resistance	0.2 $\%K^{-1}$ (Titanium)

Thermal Conductivity of PECVD Nitride	0.038 ~ 0.051 W/cm-K
Density of PECVD Nitride	2.22 g/cm^3
Specific Heat of PECVD Nitride	1.31 ~ 1.73 J/g-K
Heat Capacity of Device	2.55 x 10^{-8} J/K
Thermal Time Constant	1.5 msec

Table I. *Measured and calculated parameters for the microbolometer whose data is shown in Figs. 3, 4, and 5.*

The thermal conductances of the devices were measured under vacuum (< 10 mTorr) using a standard electrical method described in [**14**]. In this technique, a current is run through the detector plate which heats the device and changes the device resistance. The amount of heating caused by a given current depends on the thermal conductance of the device, which is extracted from a plot of 1/R vs. I^2, as shown in Fig. 3. A typical device gives a thermal conductance, G = 1.68 x 10^{-5} W/K when unactuated, and G = 2.99 x 10^{-4} W/K using an actuation voltage of 17V.

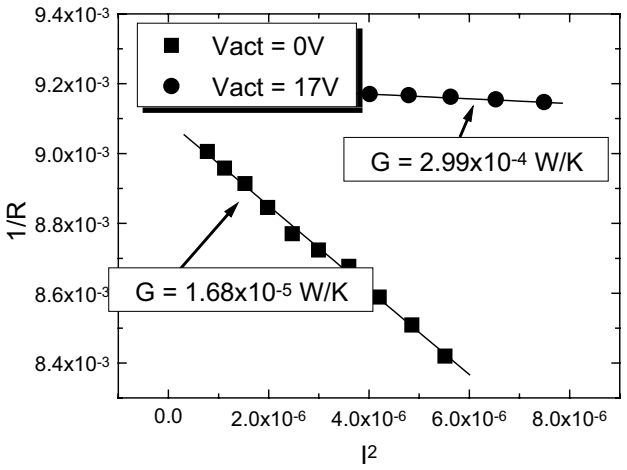

Figure 3. *A plot of the inverse resistance versus current squared for a microbolometer in its unactuated (Vact = 0V) and soft actuation (Vact=17V) states. This type of plot is commonly used for microbolometers because the slope is inversely proportional to the thermal conductance. The plot shows that the thermal conductance of a device is changed by more than an order of magnitude even in a soft actuation state.*

Responsivity and detectivity measurements were also made. The devices were optically heated by a semiconductor laser of λ = 658nm. The frequency of the signal was scanned by directly modulating the laser. The incident intensity was correlated with a detector and to the area of a pinhole aperture that was near to the size of the device under test. The microbolometer output voltage was amplified using a PARC113 preamplifier and examined with an HP35660A dynamic signal analyzer.

The responsivity of the same device from Fig. 3 is shown in Fig. 4. The responsivity varies by over an order of magnitude when the support beam of the device snaps down at a voltage of 17 V. The reponsivities of the device taken at frequencies below 10Hz show substantial scatter because of 1/f noise in our experimental set-up and are therefore not plotted.

Once the responsivity had been measured, the noise spectrum of the devices was obtained directly from the signal analyzer and used to extract the detectivity as described in Eq. 1. Fig. 5 shows the detectivity vs. frequency of the same device as in Figs. 3 and 4. The detectivity varies more than an order of magnitude between 1.8x10^6 cmHz$^{1/2}$/W and 1.5x10^5 cmHz$^{1/2}$/W, in 0 V actuation and 17 V actuation, respectively. As mentioned above, the detectivities below 10Hz were not plotted because of difficulties in measuring 1/f noise at extremely low sampling rates, which made the uncertainty in the detectivity values very large. This problem might be solved by replacing the Ti TCR material with VO_X, because VO_X gives a relatively low 1/f noise characteristic at low frequency range as well as a high TCR of –2.0%/K [**6**]. In this measurement, Johnson noise was around 120 nV/Hz$^{1/2}$, which is somewhat higher than in typical microbolometers. This noise will be reduced in the future with a low-noise resistor for electrical read-out and a high TCR element.

The devices described are the first microbolometers made with a fully adaptable detectivity, but they have a relatively low performance relative to commercial devices. In particular, the device was designed to have a much lower thermal conductance of 7 x 10^{-7} W/K than measured in its unactuated state. This would directly translate to another 1.5 orders of magnitude improvement in responsivity and detectivity. It is suspected that the top layer of polyimide between the plate and the support beam was not fully removed during etch-release. This will be corrected in future processing. In addition, the performance could be further improved by using vanadium oxide instead of titanium as the TCR layer. Commerical VOx has a TCR that is approximately -2%/K compared to a TCR for Ti of approximately 0.2%/K as shown in Fig. 6. It additionally has a very low 1/f noise, indicating further improvement. With these changes the architecture presented here could provide commercial thermal imaging performance with full intensity adaptivity, extending the dynamic range of present-day microbolometers by multiple orders of magnitude.

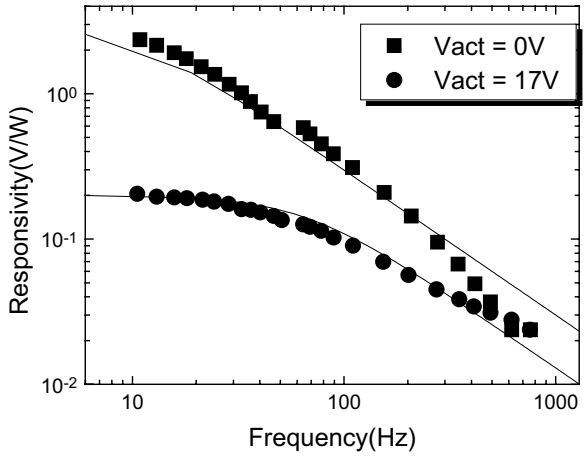

Figure 4. *Responsivity vs. frequency for an adaptive detectivity microbolometer. The response varies by over an order of magnitude when the lowest device support is snapped down at 17V. Note that frequencies below 10Hz were not plotted for consistency with Fig. 5 (see explanation there). The responsivity is artificially low because of the support beam widths and metal thicknesses used in the microbolometer are higher than would be used in a production environment. This represents limitations of*

our available fabrication processes rather than the architecture itself.

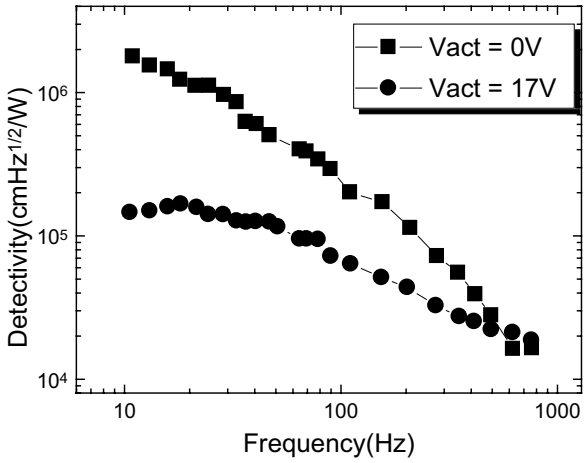

Figure 5. *Detectivity vs. frequency for a typical device. The detectivity is in a high state at 0V actuation and a low state at 17V actuation. Frequencies below 10Hz were not plotted because of the difficulties in measuring 1/f noise at extremely low sampling rates, which made the uncertainty in the detectivity values large at very low frequencies.*

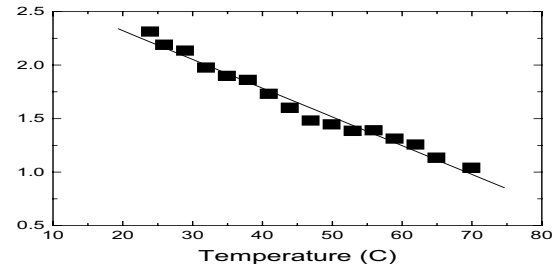

(a) VO_x,unit of Resistance in x-axis: Mohm

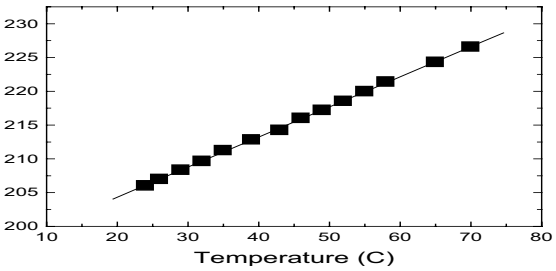

(b) Ti, unit of Resistance in x-axis: ohm

Figure 6. *Resistance vs. temperature measured by point-probe for VOx (a) and Titanium (b). Measured TCR of VO_X and Ti is –1.16%/K and 0.21%/K, respectively. Any potential contribution of the contact points has not been isolated from the material TCR and therefore this graph is the sum of both.*

CONCLUSIONS

The detectivities of adaptive microbolometers have been measured vs. frequency in high and low sensitivity states. These bolometers have been designed to have extended dynamic range to handle both very hot and cool areas within the same image. The high sensitivity state corresponded to normal microbolometer operation. In the low sensitivity state, a portion of the support beam was actuated to be partially in contact with the substrate and thereby increased the thermal conductivity and reduced the detectivity. We reported that the thermal conductance of a typical device could be changed by 1.25 orders of magnitude, the responsivity by one order of magnitude, and the detectivity by 1.2 orders of magnitude.

ACKNOWLEDGEMENT

This work was supported by Defense Advanced Research Project Agency under Grant No. F33615-00-1-1625. The authors would like to thank the staffs at Nanofabrication center at the University of Minnesota.

REFERENCES

1. R. A. Wood, “Monolithic silicon microbolometer arrays”, Ch. 3 in *Uncooled Infrared Imaging Systems and Arrays,* Ed. P. W. Kruse, and D. D. Skatrud, *Semiconductors and Semimetals*, vol. 47, Academic Press, New York, 1997, pp. 43-121.

2. J. A. Cutts and R. W. Capps, “Space science applications of infrared detector technology: a review”, *Proceedings of 4th International Conference of Advanced Infrared Detectors and Systems,* 6/5-7/90, (1990), pp. 125-131.

3. P. W. Kruse, L. D. McGlauchlin, and R. B. McQuistan, “Elements of Infrared Technology”, Ch. 9, Wiley, New York, 1962.

4. D. E. Burgess, P. A. Manning, and R. Watton, “The theoretical and experimental performance of a pyroelectric array imager”, *Proceedings of SPIE, 572,* 2 (1985).

5. I. H. Choi and K. D. Wise, “A silicon-thermopile-based infrared sensing array for use in automated manufacturing”, *IEEE Transanction Electron Devices, ED-33,* 72 (1986)

6. R. A. Wood, C. J. Han, and P. W. Kruse, “Integrated uncooled infrared detector imaging array”, *Technical Digest of the 1992 Solid-State Sensor and Actuator Workshop,* Hilton Head Isl., SC, 6/2-6/92, Transducer Research Foundation, Cleveland (1992), pp. 132-135.

7. P. C. Shan, Z. Celik-Butler, D. P. Butler, and A. Jahanzeb, “Semiconduting YBaCuO thin films for uncooled infrared bolometers”, *Journal of Applied Physics, 78,* 7334 (1995).

8. M. Almasri, D. P. Butler, and Z. Celik-Butler, “Self-supporting uncooled infrared microbolometers with low-thermal mass”, *Journal of Microelectromechanical systems, 10,* 469 (2001).

10. R. N. Supino and J. J. Talghader, “Electrostatic control of microstructure thermal conductivity”, *Applied Physics Letters*, *78,* 1778 (2001).

11. W.-B. Song and J. J. Talghader, “Adjustable responsivity for thermal infrared detectors”, *Applied Physics Letters*, *81*, 550 (2002).

12. W.-B. Song and J. J. Talghader, “Interface thermal conductance for microactuated devices”, *Technical Digest of the 2002 Solid-State Sensor and Actuator Workshop,* Hilton Head Isl., SC, 6/2-6/02, Transducer Research Foundation, Cleveland (2002), pp. 329-332.

13. W.-B. Song and J. J. Talghader, “Thermal contact conductance of actuated interfaces”, *Applied Physics Letters*, *81*, 1216 (2002).

14. P. Erickson, J. Y. Andersson, and G. Stemme, “Thermal characterization of surface-micromachined silicon nitride membranes for thermal infrared detectors”, *Journal of Microelectromechanical systems, 6,* 55 (1997).

LARGE-DEFLECTION STACKED MULTI-ELECTRODE ELECTROSTATIC ACTUATOR

Hanseup S. Kim, Asli B. Ucok, and Khalil Najafi

Center for Wireless Integrated MicroSystems (WIMS ERC)
University of Michigan, Ann Arbor, Michigan 48109-2122

ABSTRACT

This paper presents a large-deflection electrostatic actuator that is comprised of multiple stacked flexible electrodes. This actuator can provide: 1) a large deflection at low voltages due to a small gap between electrodes; and 2) a modal operation of a single electrostatic device with 'n'-different center deflections in an 'n'-layered electrostatic device. The actuator obtains the full deflection by allowing the top flexible electrode to bend consecutively to the next electrodes until reaching the bottom. The top electrode can also be forced to stop at different deflection heights by proper application of voltages selectively to the first few electrodes.

The resultant micro-fabricated actuator achieved a large out-of-plane deflection ($6.09\mu m$) of a top Parylene layer at a low voltage (less than $50V$), which is a considerable reduction, more than 30%, compared to a conventional single electrode actuator. Using three flexible Parylene electrodes, the fabricated actuator showed three different modes of deflections: $1.00\mu m$, $2.66\mu m$, and $6.09\mu m$. The fabricated actuator operated for more than 1,000,000 cycles continuously in a 'touch' mode, where each electrode physically bent and contacted the next electrodes. Although the actuator successfully operated such a long period, it showed signs of stress relaxation and fatigue of polymer electrodes. In atmosphere, the actuator response time is $<91ms$, which was the minimum detectable limit of the equipment.

Key Words: Large Deflection, Stacked Multi-layer actuator, Electrostatic actuator

INTRODUCTION

Diaphragms play a major role in MEMS actuators because they are efficient in volume displacement, offer large area bending, and are easy to fabricate using lithography techniques. Diaphragm based actuators are used to generate fluid flows through micro channels [1] and applied in micro-mirrors for optical applications. [2, 3]. They can be deflected in a controlled manner using various transduction techniques, such as electrostatic [4, 5], electromagnetic [6], piezoelectric [7-9], and thermo-pneumatic [10] actuation.

Electrostatic actuation has many advantages over others in deflecting a diaphragm. It generally uses low power due to its capacitive operation. Even in micro domain, it can generate a large amount of force. Moreover, it is more compatible with CMOS-based processes than electromagnetic and piezoelectric actuation due to its simple structure and its generous material selectivity. In addition, it responds faster than thermo-pneumatic actuation, and is more immune to temperature change than piezoelectric actuation. Therefore, various applications, such as micro pumps and micro mirrors, have adopted electrostatic actuation for their membrane deflection.

Conventional varying-gap electrostatic actuators have a fairly small maximum out-of-plane (vertical) deflection limited by the gap spacing between the two electrodes. The gap cannot be easily increased since it significantly increases the operating voltage. Thus, obtaining a large maximum deflection without increasing the required voltage is a challenge in electrostatic actuators.

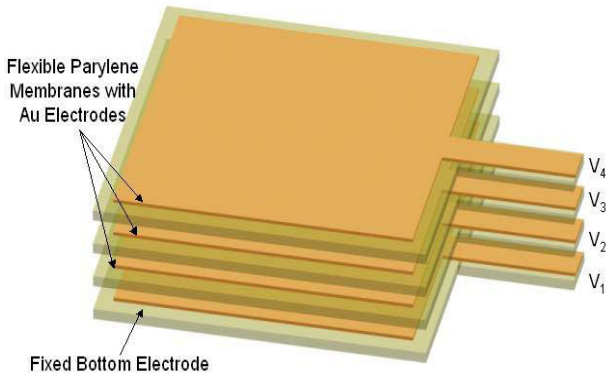

Figure 1. *3D-illustration of stacked multi-layer electrostatic actuator: The bottom electrode is fixed to the substrate while remaining electrodes are on flexible Parylene membranes. Modal deflection depends on both the number of flexible membranes used and the voltages applied to the corresponding electrodes.*

To overcome this challenge, curved electrodes can be used [11] to reduce the effective distance between the two capacitive electrodes around the perimeter of the actuator. However, this requires a more complicated fabrication process. The stacked multi-electrode actuator structure reported in this paper reduces the operating voltage and increases the total deflection by stacking up multiple, free-standing, flexible polymer membrane electrodes on top of each other with small air gaps in between, as illustrated in Figure 1. The small gaps between membrane/electrode pairs enable the top membrane to deflect down to the next layer at a low voltage, and then this pair is pulled down to the layer below. This process repeats to the following layers underneath in a similar way. Thus, the stacked multiple electrode actuators achieve a large deflection of the top membrane with a relatively lower voltage than conventional electrostatic actuators. In addition, the multiple electrode actuators can have a modal operation of multiple deflections by selectively bending the top membrane to certain layers only.

STACKED MULTI-ELECTRODE ACTUATOR

Large deflection at a low voltage

The operation of the multi-electrode electrostatic actuator is similar to a conventional capacitive type electrostatic actuator in that alternative signals are applied to adjacent layers to create attractive forces between them. This force will pull the layers towards each other. In conventional devices one of the two electrodes is fixed. In the stacked actuator all electrodes move towards each other except for the bottom electrode that is fixed.

0-9640024-5-0/hh2004/$20©2004TRF
DOI 10.31438/trf.hh2004.88

To find the pull-in voltage (the voltage at which a diaphragm collapses) of the multi-electrode actuator, we start from the mechanical restoring force and the electrical force equations:

$$F_{Electrical} = \frac{\varepsilon_o}{2} \cdot Area \cdot \frac{V^2}{(d-w)^2} \quad (1)$$

$$F_{Restoring} = k \cdot w \quad (2)$$

where ε_o is the dielectric constant for air, V is an applied electrical voltage, d is an initial distance between two parallel plates, w is a deflection distance, and k is a spring constant.

In the multi-electrode actuator, since both electrodes move equally instead of only one, w is replaced by $2w$ in equation 1, and k is replaced by $2k$ in equation 2. This results in a pull-in voltage value that remains the same as an actuator with a fixed electrode, as shown in equation 3:

$$V = \sqrt{\frac{8 \cdot k \cdot d^3}{27 \cdot \varepsilon_o \cdot Area}} \quad (3)$$

Therefore, the multi-electrode actuator will have the same pull-in voltage between any electrodes including the fixed bottom electrode. A multi-electrode actuator can obviously have a smaller pull-in voltage by reducing the gap distance, d.

Modal operation

To obtain different deflection distances of the top membrane for multi-deflection modes from a single device, signals can be applied to some of layers selectively, as illustrated in Figure 2. Generally, when 'n' layers are used, 'n' different deflections are achievable in a modal operation of the multi-electrode actuator.

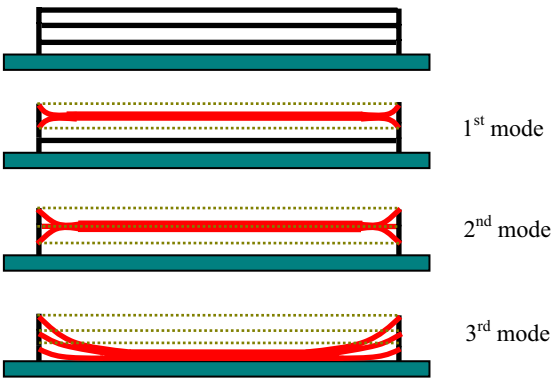

Figure 2. *Illustration of three modal deflections from a three-layered electrostatic actuator*

FABRICATION

A stacked multi-electrode actuator has been designed and fabricated. The actuator has three freestanding flexible Parylene membranes, each coated with thin metal films. Each actuator is a 100μm x 100μm square, with a total height of ~15.7μm, and an average gap of ~2.2μm between individual electrodes. A total of three suspended membranes are used, with the bottom electrode being fixed and on the substrate.

At the beginning, an array of different sizes of single-electrode actuators is formed in order to identify their structural strength to generate a multi-electrode actuator structure, as shown in Figure 3.

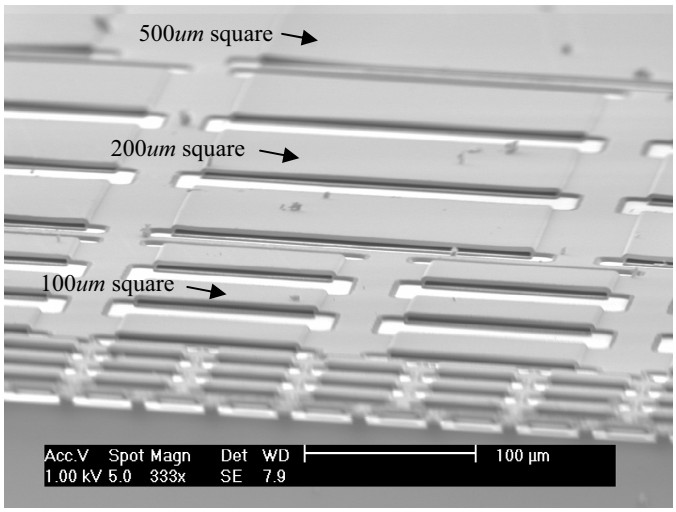

Figure 3. *Microfabricated array of single electrode electrostatic actuator: up to a 200µm square size, single freestanding Parylene membranes were successfully formed.*

Then, the multi-electrode structure is formed by stacking up multiple sets of sacrificial photoresist of AZ1827 (2.7μm), thin Parylene layer (2μm), and conductive thin gold layer (0.3μm), as shown in Figure 4. After patterning of each sacrificial layer photoresist, it is hard baked at 110°C for 30 minutes to create a sloped profile around the edges of the photoresist and provide good step coverage for subsequent metal layers. The hard baked photoresist layers are removed in acetone leaving air-gaps between layers after two sides of Parylene sidewalls have been dry-etched by oxygen flow. The completed actuator is naturally dried to form a stacked multi-electrode electrostatic actuator without stiction, as shown in Figure 5.

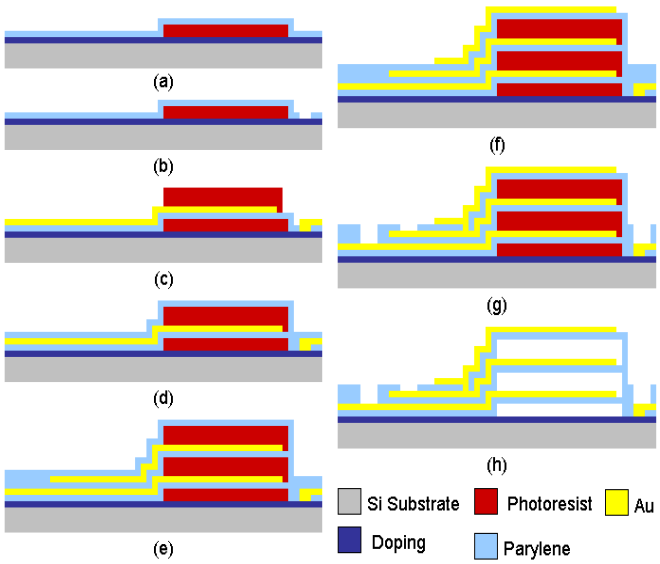

Figure 4. *The process flow for the fabrication of large deflection stacked multi-layer electrostatic actuator utilizing simple photoresist sacrificial layer and acetone dissolution.*

The completed devices are mounted and interconnected to electronic packages. Originally each device is wire-bonded through each device pad that is located on each layer of multiple Parylene stacks. However, each Parylene layer provides too soft surface for a wire-bonding of the electrical pads. Thus, at the electrical pads, a

conductive epoxy, P10, is added to complete the connectivity of wire-bonding from the actuators to outside packages, as shown in Figure 6.

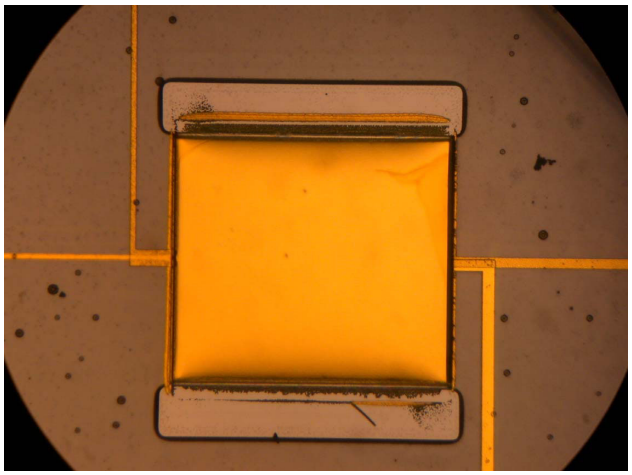

(a)

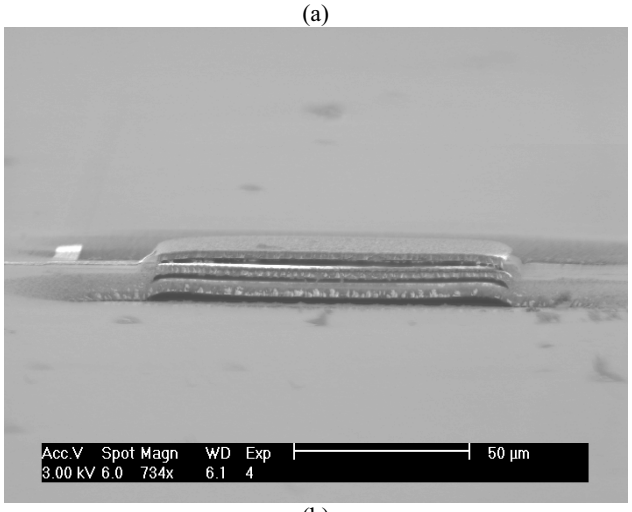

(b)

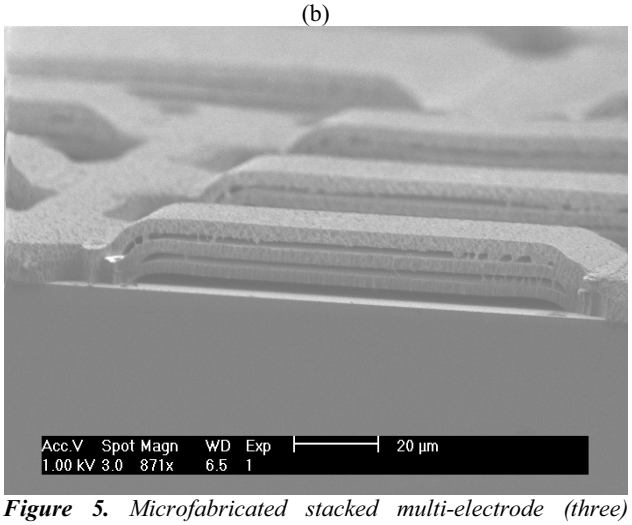

Figure 5. *Microfabricated stacked multi-electrode (three) electrostatic actuator: a) Top view of the completed actuator, b)Side View (SEM), and c) Side view (SEM) of an array of multi-electrode actuator.*

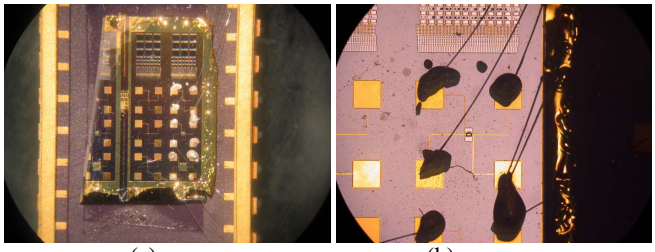

(a) (b)

Figure 6. *Wire-connected multi-electrode electrostatic actuators: a) a piece of actuator die on electronic package wire-bonded, and b) a close-up view of a multi-electrode actuator and interconnections. Conductive epoxy is additionally used for complete interconnection to outside package.*

TEST RESULTS

The fabricated actuators were packaged and then tested using both AC and DC drive signals, as discussed below. First, a full DC deflection was observed through Zygo interferometer by looking at the fringe changes on the actuator surface. Then, the deflection was measured by observing the capacitance change using a HP4284A LCR meter. The maximum deflection happened at DC $13V$ in the beginning stage, however, it was observed that this pull-in voltage drifted up to more than $130V$ as DC signal is continually applied. The maximum deflection caused a $10.776pF$ capacitance change in total. This high capacitance change was due to 1) the fact that the bottom electrode was directly connected the silicon wafer itself, which caused a great deal of parasitic values; and 2) the fact that the metal residue outside membrane areas hanged out and touched membranes' metal layers.

Second, the response time of the actuator was measured by applying 0 volts to 30 volts through the LabView 7.0 software. Here, the 30 volts was applied to make sure the diaphragm fully collapsed in a specific case. The response time was ~$91ms$, as shown in Figure 6. The response time was symmetric for both membrane collapse and release. The response time was measured in atmosphere where air was squeezed out from the space between electrodes through ~$2.2\mu m$ gaps. Faster operation is possible in a vacuum for use in reflective optical display applications.

Third, a lifetime reliability test of the actuator was performed. The actuator was tested by supplying DC signal between 0 volts and 30 volts at $10Hz$. The test was performed more than 24 hours, and resulted in a significant decrease of capacitance change per cycle over time, as shown in Figure 7. The overall decrease of capacitance change was more than 50% after one million cycles. This decrease is possibly due to 1) the stretching of a visco-elastic polymer material, Parylene; 2) the stress charge (stress relaxation) of the Parylene membrane due to heats generated by repeated motions; or 3) the charging effect on the Parylene membrane caused by continual DC voltages. Over time, the polymer membrane stretches and provides a smaller restoring force resulting in smaller moving distance and, thus, smaller capacitance change over time.

Finally, the modal operation was tested by applying voltages selectively to some layers. The modal operation was successfully measured through a Zygo interferometer, as seen in Figure 8. The modal operation resulted in distinctive deflection differences: 1st mode of $1.00\mu m$, 2nd mode of $2.66\mu m$, and 3rd mode (full collapse) of $6.09\mu m$.

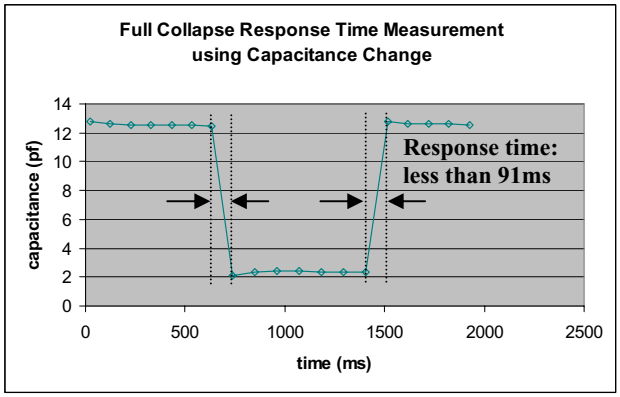

Figure 6. *Response time measurements of a multi-electrode electrostatic actuator*

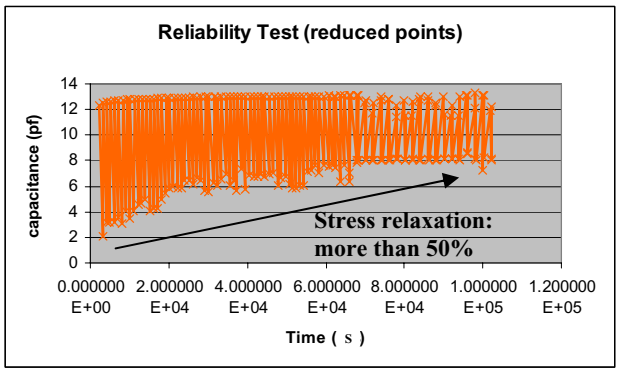

Figure 7. *Capacitance change measurement for a reliability test of a multi-electrode electrostatic actuator*

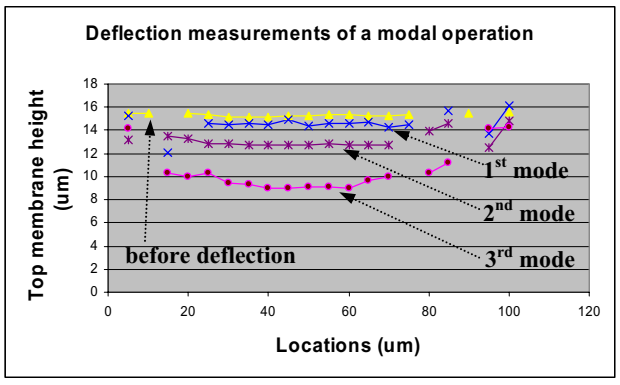

Figure 8. *Modal deflection measurement of a multi-electrode electrostatic actuator*

DISCUSSIONS AND CONCLUSIONS

The stacked multi-electrode electrostatic actuator has demonstrated that it can achieve a large out-of-plane deflection at a low voltage and can be operated in several different deflection modes. The actuator can be used in a variety of applications, including optical devices. For this purpose, the Parylene multi-electrode actuator has shown great potential. First, Parylene can be conformally deposited with precise thickness. Moreover, this flexible Parylene film is used in a simple surface micro-machining fabrication process with a good yield. Second, the actuator can have very high fill factor in an array form when used as a display pixel. This is more feasible especially because the actuator's membrane has an intrinsic tensile stress. Third, the actuator is fabricated under 110°*C*. Thus, the actuator can be added on top of CMOS circuitry through a post-CMOS process.

Several observations and issues were also made during testing. First, frequent failures were observed during multi-layer full collapsing. The failure happened when some of the multi-electrodes did stick together without collapsing to the next layers further. In this case, the failure resulted in much higher operating voltages to move those membranes into the fully-collapsed positions. This implies that further design improvements like corrugation may be needed to facilitate collapse regardless of membrane position. Second, Parylene showed signs of fatigue and stress relaxation over time, and this led to a drift of the pull-in voltage and deflection distance as well as response time. Third, the surface roughness of Parylene membrane was measured by a surface profiler, Datek, showing up to 3000*Å* of roughness. This is higher than expected and needs to be improved. Fourth, DC charging was observed. Combined with Parylene membrane's stress relaxation, the charging effect caused the pull-in voltage to increase to a very high value (more than 150*V*). An attempt to eliminate the charging effect in an 80°*C* oven failed because it caused membranes to touch and stick together due to tiny gaps between. Further work is necessary in this area.

ACKNOWLEDGEMENT

The authors thank Joseph Potkay for valuable help on measurements. This project is funded by the Engineering Research Centers Program of the National Science Foundation under Award Number EEC-9986866. Travel support has been generously provided by the Transducers Research Foundation and by the DARPA MEMS and DARPA BioFlips programs.

REFERENCES

[1] R. Zengerle, S. Kluge, M. Richter, and A. Richter, "A bidirectional silicon micropump," MEMS '95, Netherlands, pp. 19-24, 1995.

[2] D. M. Bloom, "Grating light valves for high resolution displays," Electron Devices Meeting, Technical Digest., International, pp. 343, 1994.

[3] L. J. Hornbeck, "Current status of the digital micromirror device (DMD) for projection television applications," Electron Devices Meeting. Technical Digest., International, pp. 381-384, 1993.

[4] Cabuz-C, Herb-WR, Cabuz-EI, and Son-Thai-Lu, "The dual diaphragm pump," MEMS 2001., Interlaken, Switzerland, pp. 519-22, 2001.

[5] R. J. Linderman, O. Nilsen, and V. M. Bright, "The resonant micro fan gas pump for active breathing microchannels," pp. 1923-1926, 2003.

[6] C. H. Ahn and M. G. Allen, "Fluid Micropumps Based on rotary magnetic actuators," MEMS '95, pp. 408-412, 1995.

[7] T. Gerlach, "Pumping gases by a silicon micro pump with dynamic passive valves," 1997 International Conference on Solid-State Sensors and Actuators, Chicago, pp. 357-360, 1997.

[8] K.-P. Kamper, J. Dopper, W. Ehrfeld, and S. oberbeck, "A self-filling low-cost membrane micropump," MEMS '98, pp. 432-437, 1998.

[9] A. Olsson, G. Stemme, and E. Stemme, "The first valve-less diffuser gas pump," MEMS '97, Nagoya, Japan, pp. 108-113, 1997.

[10] C. Grosjean and Y.-C. Tai, "A thermopneumatic peristaltic micropump," The 10th International Conference on Solid State Sensors, Actuators, and Microsystems, Sendai, Japan, pp. 1999.

[11] H. S. Kim, K. Najafi, P. D. Washabaugh, and L. P. Bernal, "Large-deflection out-of-plane electrostatic buckled-electrode actuator," Transducers '03, Boston, pp. 794-797, 2003.

BUCKLED BEAM LINEAR OUTPUT CAPACITIVE STRAIN SENSOR

J. Guo, H. Kuo, D. J. Young, W. H. Ko
EECS Department, Case Western Reserve University
Cleveland, OH, 44106

ABSTRACT

A capacitive strain sensor employing a mechanical amplification scheme has been designed, analyzed, fabricated, and tested. The mechanical amplifier based on the bending of a buckled beam provides an increased device sensitivity, thus attractive on reducing the sensitivity requirement and power dissipation in the interface circuits. An analytical model was developed to predict the mechanical gain of the structure, which was confirmed by Finite-Element-Analysis (FEA), with an error of less than 1.5% of the measurement results. The fabricated device achieved a sensitivity of 282 atto-farads/microstrain (aF/με). The mechanical thermal noise analysis shows that a sensitivity of 0.1 microstrains (με) with a dynamic range of 10,000 (80dB) over 10 kHz bandwidth can be achieved combining this design with a matching interface circuit.

INTRODUCTION

High-performance strain sensors having large dynamic range and bandwidth are highly desirable in applications such as aerospace, biomedical and power industries. Traditional metal foil strain sensors dominate current market because of their low cost and easiness to handle. However, foil strain sensors suffer from low sensitivity with gauge factors typically around 2 and high power consumption [1]. Silicon piezoresistive strain sensors employing the piezoresistivity effect, which is a phenomenon that a material changes its resistance with stress, can achieve gauge factors typically from 30 to 120. However, the piezoresistive strain sensors suffer from high temperature instability, initial drift, and large resistive thermal noise and power dissipation. Capacitive strain sensors can overcome the above drawbacks and achieve a large dynamic range and bandwidth with a reduced power consumption. This is particularly attractive in biomedical applications where low-power consumption devices are critical. However, the minimum detectable capacitance change of most MEMS capacitive devices is typically on the order of tens of atto-farads (aF); hence, high-sensitivity integrated or nearby interface circuits, and sophisticated packaging schemes are required to maintain an overall system performance, which typically results in high power consumption and cost. Therefore, a capacitive strain sensor with a mechanical amplification is highly attractive as it improves the sensor sensitivity, thus reducing the noise requirement and power dissipation for interface circuits.

Researches were reported on measuring residual stresses utilizing an mechanical amplification scheme achieving a strain resolution of 10 microstrain [2,3]. This paper presents an innovative capacitive strain sensor structure that combines the mechanical amplification of a buckled beam and the comb structure to achieve a high sensitivity below 0.1 microstrain (με) and large linear dynamic range up to 80 db. An analytical model has been developed to predict the mechanical gain of the structure, which has been verified by ANSYS FEA.

DESIGN CONCEPTS

The schematic diagram of the buckled beam mechanical amplification scheme is shown in Figure 1. The structure consists of two buckled beams with a small buckling angle, α, and one sensing beam at center. When a strain, ε, is applied, it causes a lateral displacement, $\Delta x = L_g \varepsilon$. For a small buckling angle, the center deflection of the sensing beam, Δw, is larger than Δx, thus resulting in a mechanical amplification gain, A_{mech}. A linear differential capacitive output can be obtained by designing comb drive fingers at the center sensing beam, as shown in Figure 2. For a compressive strain, the top and bottom beams will move up and the center beam will move down, thus resulting in a differential capacitance change.

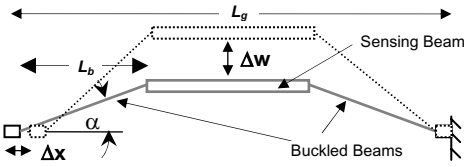

Figure 1. *Principle of the buckled beam amplification scheme.*

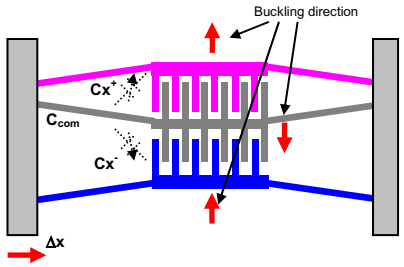

Figure 2. *A buckled beam strain sensor with differential output.*

MODELING

A. Beam modeling

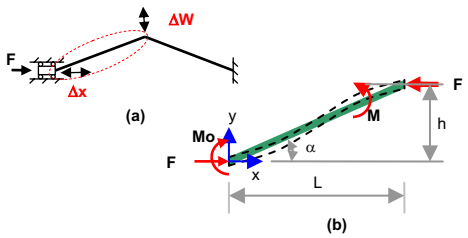

Figure 3. *(a) The simplified structure. (b) Forces acting on the beam.*

0-9640024-5-0/hh2004/$20©2004TRF
DOI 10.31438/trf.hh2004.89

Solid-State Sensors, Actuators, and Microsystems Workshop
Hilton Head Island, South Carolina, June 6-10, 2004

An analytical analysis based on the simple beam theory was developed to predict the mechanical gain of the buckled beam. The sensor structure can be simplified as a simple beam structure constrained as shown in Figure 3.a with one end fixed and the other end guided along the x-axis. The forces acting on the bent beam are shown in Figure 3.b, where F is the equivalent force applied by the external strain, Mo is moment from the guild end, M is the moment in the beam at an arbitrary location (x,y), and the governing equation is given by [5],

$$EI\frac{d^2y}{dx^2} = M_o = M - Fy, \tag{1}$$

where E and I are the Young's modulus and moment of inertia of the beam, respectively.

The boundary conditions are given by,

$$y\big|_{x=0} = 0\ ,\ \frac{dy}{dx}\big|_{x=0} = \tan\alpha\ ,\text{ and }\ \frac{dy}{dx}\big|_{x=L} = \tan\alpha\ . \tag{2}$$

By solving the above equations, and assuming that the changes of angle, α, can be neglected, the center deflection, Δw, can be expressed by [3],

$$\Delta w = 2\frac{\tan\alpha}{k}\tan\left(kL/2\right) - h\ , \quad \text{(for compression)} \tag{3a}$$

$$\Delta w = 2\frac{\tan\alpha}{k}\tanh\left(kL/2\right) - h\ , \quad \text{(for tension)} \tag{3b}$$

where $k = \sqrt{F/EI}$.

The end displacement of the buckled beam can be calculated by,

$$\Delta x = \int_0^L \frac{1}{2}\left(\frac{dy}{dx}\right)^2 dx - L\frac{1}{2}\tan^2\alpha\ , \quad \text{(for compression)} \tag{4a}$$

$$\Delta x = \int_0^L \frac{1}{2}\left(\frac{dy}{dx}\right)^2 dx - L\frac{1}{2}\tanh^2\alpha\ , \quad \text{(for tension)} \tag{4b}$$

Therefore, for a small buckling angle and small lateral displacement, the mechanical gain of the buckled beam can be solved as,

$$A_{mech} = \frac{\Delta w}{\Delta x} \cong \frac{1}{\tan\alpha}\ . \tag{5}$$

An FEA analysis using ANSYS has been performed to confirm the above analytical results. Table 1 shows the comparison between the results obtained analytically using Equation (5) and by FEA by apply a small strain such as 100 με. An error less than 1% was observed, indicating a high accuracy of the modeling.

Table 1. *Comparison of the mechanical gain obtained analytically and by FEA for a buckled bema with length of 300 μm and width of 3 μm.*

Beam height, h (um)	30	40	50	60	70
tan(α)	0.100	0.133	0.167	0.200	0.233
Calculated Gain	10.000	7.500	6.000	5.000	4.286
ANSYS result	9.900	7.450	5.970	4.980	4.270
Error (%)	1.000	0.667	0.500	0.400	0.367

B. Sensor modeling

Based on the results of the beam modeling, the sensor sensitivity, which is defined as the capacitance change per unit applied strain, can be expressed as,

$$S \equiv \frac{\Delta C}{\Delta Strain} = \frac{4NA_{mech}t\varepsilon_e}{g}\ , \tag{6}$$

where N is the number of fingers on each sensing beam, A_{mech} is the mechanical gain, t is the thickness of the beam, ε_e is the dielectric permittivity, and g is the gap between fingers.

An FEA analysis of a full device structure employing a coupled-field analysis method has been performed to verify the above analytical results. Figure 4 shows the capacitance change characteristics obtained by using Equation (6) and FEA. A maximum 11% error for compressive strain and a 5% error for tensile strain at range of 1000 με are observed. These errors are introduced by the change of the beam buckling angle, α, as the applied strain increases and can be improved by optimizing the structure parameters. A nonlinearity analysis of the FEA curve shows a nonlinearity of 1.49%FS for the range of 0 to 1000 με tensile strain, which agrees with measurement results.

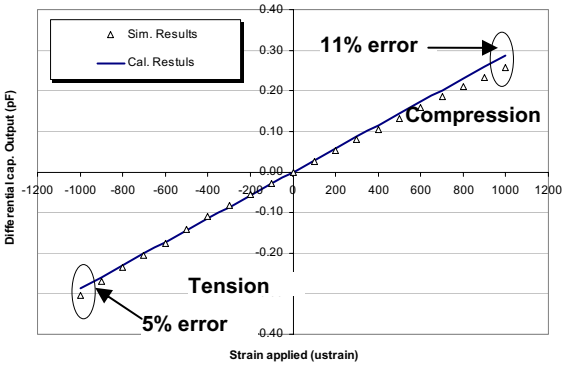

Figure 4. *Simulation results about capacitance change as a function of load strain.*

C. Device resolution analysis

The fundamental sensing resolution is determined by the device noise such as the resistive thermal noise introduced by the device series resistances and the mechanical thermal noise of the structure (Brownian motion) [4]. The mechanical thermal noise is the dominate part as the series resistance is typically on the order of 100 ohms or less. The mechanical thermal noise is introduced by the air damping of a structure and for a second-order mechanical damping system such as the designed strain sensor, the noise is basically determined by the structure mechanical parameters such as resonant frequency (ω_o), damping factor (or quality factor Q) and mass (m). The input strain referred equivalent thermal noise is given by,

$$\varepsilon_n = K_n\sqrt{\frac{4K_BT}{\omega_o{}^3 mQ}}\cdot\sqrt{BW}\ . \tag{7}$$

where ε_n is input strain referred mechanical thermal noise; K_B is the Boltzman constant; T is the absolute temperature with unit of Kelvin; ω_o is the structure resonant frequency; m is the mass; Q is the quality factor; BW is the required signal bandwidth; K_n is the conversion factor between the noise displacement and the input-referred strain, which is a function of mechanical gain and gauge length, and equals to 200 according to the sensor dimensions given in Table 2.

Table 3 lists the mechanical parameters of a designed device; the calculated input strain referred mechanical thermal noise is less than 0.003 με for a bandwidth of 10 kHz. A low noise charge amplifier has been designed to interface with the sensor to achieve a sensitivity of 0.1 με with a dynamic range of 80 dB over a 10 KHz bandwidth.

Table 2 *Design values of the buckled beam strain sensor*

L_g	Gauge Length	1000 um
L_b	Buckled Beam Length	300 um
α	Buckling angle	5.7º
N	Number of Fingers on each sensing beam	37
g	Gap between fingers	3.6 um
A_{mech}	Mechanical amplification gain	10

Table 3. *Device mechanical parameters*

ω_o	Resonant frequency (simulated)	8.8×10^5 rad/s
m	Mass	0.55 µg
Q	Quality factor	~1
BW	Bandwidth	10 kHz

FABRICATION

A single mask fabrication process, as shown in Figure 5, was designed to fabricate the device. The process started with a SOI wafer with device/oxide layer of 20 µm/2 µm and device layer resistivity of 0.5-10 ohm-cm. The wafer was first patterned and etched using a DRIE process. Then the wafer was diced, cleaned, and followed by a timed HF release process. Finally, a 200Å aluminum layer was sputtered on the device to reduce the thermal noise contributed by the device series resistance.

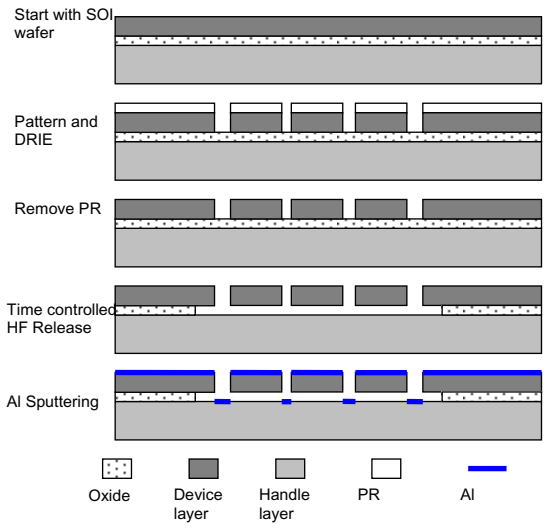

Figure 5*. Major fabrication steps.*

The SEM picture in Figure 6 shows a fabricated strain sensor with four sets of individual sensors. The size of the sensor (not including the anchors or bonding pads) is around 1000 µm by 700 µm with dimensions listed in Table 2. The selection of buckling angle, α, is a trade-off between sensitivity and linearity. The first generation devices were designed for concept verification purpose and the devices were anchored on a silicon substrate and then tested by a three point bending fixture, as will be illustrated in the following section.

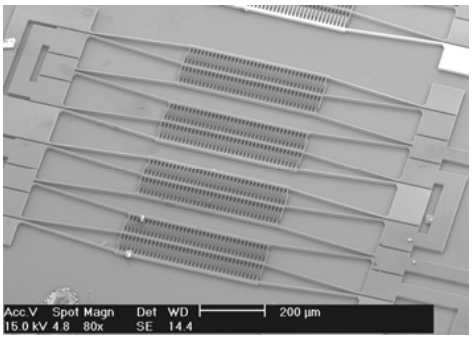

Figure 6. *An SEM picture of a buckled beam capacitive strain sensor.*

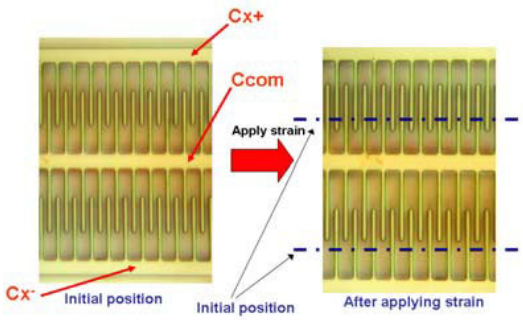

Figure 7. *Microphotograph of fingers under deflection*

Figure 7 demonstrates an example of the differential capacitance change when a strain is applied. The left figure in Figure 7 shows the initial finger positions when no strain is applied. The initial finger overlapping length for Cx^+ and Cx^- are the same. The right figure shows the finger position changes when a strain is applied, Cx^+ increase as Cx^- decreases, indicating a differential capacitive output.

EXPERIMENTAL RESULTS

The strain sensor was tested by bending its substrate on a three-point bending test fixture, as shown in Figure 8. The test strip is 30 mm long with one end clamped and the other end bent by a micrometer. The strain introduced by bending can is calculated by,

$$\varepsilon_{3-pt} = \frac{3t(L - x_{sensor})}{2L^3}\Delta Z \,, \qquad (8)$$

where $\varepsilon_{3\text{-}pt}$ is the strain introduced by bending; t is the sensor substrate thickness; L is the length of the substrate; x_{sensor} is the distance from sensor center to the clamped edge; ΔZ is the displacement applied . By manipulating the micrometer, a strain can be applied on the sensor and the capacitance change can be read out by a commercial available C-V converter chip. Limited by the micrometer, the test setup can achieve a resolution around 1.5 µε.

Figure 9 shows a typical measured sensor capacitance change characteristics as a function of the applied strain. The measured sensitivity of the sensor is 282 aF/µε, which closely matches the hand calculation result (289 aF/µε) and FEA result (284 aF/µε), indicating an agreement between modeling and measurement.

The measured non-linearity of the sensor is around 1.5%FS for tensile strain, which agrees with the simulation results

(1.49%FS) given in Section **MODELING B. Sensor Modeling**. This non-linearity is introduced by the fact that the mechanical gain changes with the applied strain as the buckling angle changes. It can be improved by optimizing the structural parameters such as buckling angle, shape of the buckling beam, etc.

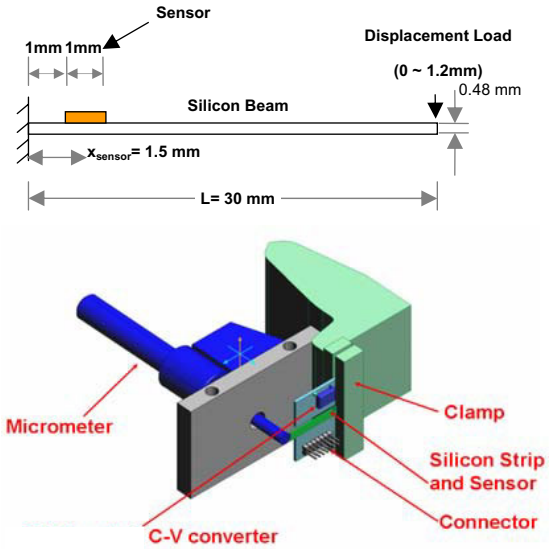

Figure 8. *Three point test fixture*

The test results also show that the maximum hysteresis is less than 1.5 με. Since the resolution of the testing setup is also around 1.5 με, indicating an improved test fixture is needed to obtain an accurate sensor hysteresis characteristic.

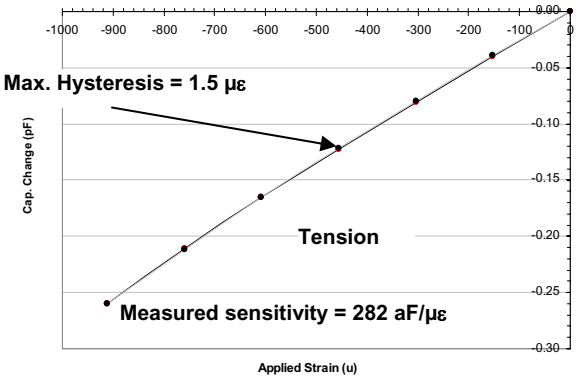

Figure 9. *Capacitance change as a function of applied tensile strain.*

CONCLUSIONS AND FUTURE WORK

An innovative capacitive strain sensor employing a mechanical amplification scheme based on the bending of a buckled beam has been presented. The fabricated prototype device achieved a sensitivity of 282 aF/με, which matches the results obtained analytically and by FEA. The fundamental resolution limit has been studied based on the analysis of the mechanical thermal noise, indicating a sensitivity of 0.1 με with a dynamic range of 80 dB over a 10 KHz bandwidth can be expected with a matching interface circuit.

The future work includes the optimization of the structure to achieve an improved sensitivity, linearity, and the device testing fixture, as well as the development of a packaging scheme which integrates the sensor, read out IC and wire connection.

ACKNOWLEDGMENT

This work was funded by U.S. Army Research Office (ARO) contract # DAAD 19-02-1-0198. Travel support has been generously provided by the Transducers Research Foundation and by the DARPA MEMS and DARPA BioFlips programs.

REFERENCES

[1] M. Nagy, C. Apanius, and J. W. Siekkinen, H. V. Estrada, "A user-friendly, high-sensitivity strain gauge", *Sensors*, June 2001.

[2] Yogesh B. Gianchandani and Khalil Najafi, "Bent-beam strain sensors", *JMEMS*, VOL. 5, No. 1, p52-58, March 1996

[3] Liwei Lin, Albert P. Pisano and Roger T. Howe, "A micro strain gauge with mechanical amplifier", *JMEMS*, Vol. 6, No.4, p313-321, December 1997

[4] Thomas B. Gabrielson, "Mechanical-thermal noise in micromechanical acoustic and vibration sensors", *IEEE Transaction,* ED Vo1. 40, No. 5, 1993

[5] S. P. Timoshenko and S. woiniwsky-Krieger, "Theory of Plates and shells", 2nd edition, McGraw-Hill, 1970

CAPACITIVE SENSE FEEDBACK CONTROL FOR MEMS BEAM STEERING MIRRORS

Baris Cagdaser, Anand Jog, Matt Last, Brian S. Leibowitz, Lixia Zhou,
Eric Shelton, Kristofer S.J. Pister, and Bernhard E. Boser
Berkeley Sensor & Actuator Center
497 Cory Hall, University of California at Berkeley, CA 94720

ABSTRACT

This paper describes a feedback control system for a MEMS dual-axis scanner, which consists of two single-axis torsional mirrors. The mirror position is measured electronically with the sense capacitors and the EAM technique. The feedback system provides electronic damping and improves the dynamic performance of the high Q (~50) mirrors. Closed-loop controlled device achieves 400 s settling time. Due to the feed-through, drive signal mixes with the sense and limits the control bandwidth. Band-pass filtering and pseudo-differential sense attenuates the feed-through in the sense circuit.

INTRODUCTION

MEMS mirrors find their main application in the field of optical communication. In communication systems, MEMS mirrors serve as the beam steering device in a free space laser link **[1,2]** or in an optical cross-connect **[3,4]**. In general, accuracy, speed, and large optical range are the main requirements for a mirror to be used in a communication system. Dielectric charging, poor mirror dynamics, or electrostatic pull-in are some of the reasons why MEMS mirrors fail to meet these requirements in open-loop electrostatic actuation. Closed-loop control can improve the limitations associated with the open-loop actuation. Previous closed-loop controlled mirrors have used the feedback for extending the drive range **[2,3,4]**. All of these devices employ the same dual-axis gimbaled structure, which uses parallel plate actuators for driving the mirror. Nonlinearities of the parallel plate actuation cause natural frequency down-tuning and pull-in resulting in limited angular range. Closed-loop control via feedback linearization **[2,3]** or sliding mode control **[4]** provides stable operation beyond the instability point.

Implementation of the feedback control requires position sense. Capacitive sense is the most commonly used method for position sensing in MEMS devices. In optical beam steering MEMS mirrors, position can also be measured by tracking the beam position by an external optical setup (usually a position sensing diode- PSD). Previous designs for optical cross-connects **[3,4]** use optical measurements to implement the position sense. Capacitive sense has been implemented for only one design with a bigger mirror size **[2]**: 23mm diameter compared to 900 m **[3]**, and 400 m **[4]**. The larger mirror diameter provides more room for the sense capacitor and improves the sensitivity.

Closed-loop control also improves the dynamic performance of a MEMS device. In this design, mirrors have vertical comb drive actuators **[5]**. Unlike parallel plate actuators, vertical comb drive is stable even at high drive voltages (>100V, >20 degrees optical) beyond which side instability ensues. This mirror design, however, has a high Q value (~50 in air) resulting in substantially underdamped step response. Feedback control is used for providing electronic damping. Position sensing is achieved by capacitive sense. Linear control techniques are enough to control the system over a 15 degrees optical steering range with the desired dynamic performance. The sense, drive, and the controller are all implemented using off-the-shelf components.

DESIGN SUMMARY

The MEMS scanner presented here is used as the beam steering device in a free-space optical communication system **[1]**. The acquisition, pointing, and beam stabilization requirements set the mirror specifications. Some key specifications are as follows:

20 degrees optical range for both axes
< 0.014 degrees resolution (1/4 of the laser beam)
< 1ms settling time

Mirrors are fabricated in a multilevel beam SOI process **[5]**. A reflector deposited on the glass package lid optically couples the two single-axis mirrors. Figure 1 shows the scanner and a conceptual sketch of the laser path. As the first mirror (Y-axis scanner) rotates, the laser beam moves along the second mirror (X-axis scanner). In order to meet the steering range requirement, X-axis scanner is designed to be longer than the Y-axis one. The Y-mirror has a round reflector with 600 m diameter. The mirrors are 2nd order systems with resonant frequencies of 1.7kHz (Y-mirror) and 700Hz (X-mirror).

In contrast to previous designs **[2,3,4]**, this mirror lacks squeeze film damping resulting in high Q values even for operation in air. This high Q value results in substantial ringing and extremely long settling times. The damping ratio for an open loop driven mirror is ~0.01, which causes 100% overshoot and ~600msec settling time (within 2%) for the 700Hz X-mirror. As mentioned earlier, feedback control provides the necessary damping for the system, and meets the goal of <1ms settling time. The feedback loop consists of 1) high voltage drive circuit with sufficiently large bandwidth (0-100V, 100kHz); 2) sense circuit using the electromechanical amplitude modulation (EAM) technique; 3) a phase lead controller for phase compensation.

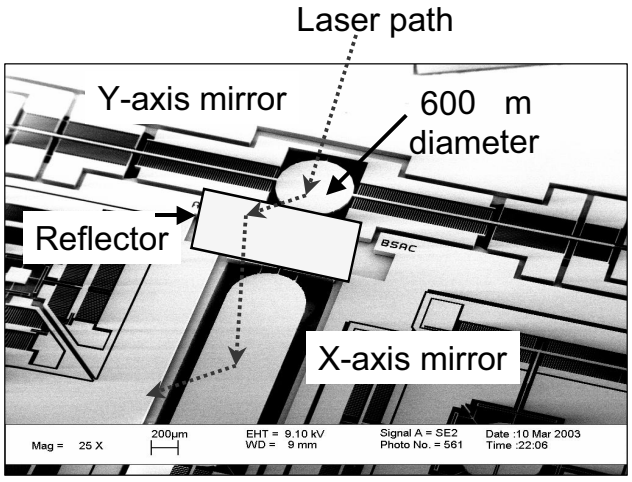

Figure 1. *MEMS scanner with the sketch of optical coupling.*

Travel support has been generously provided by the Transducers Reasearch Foundation and by the DARPA MEMS and DARPA BioFlips programs.

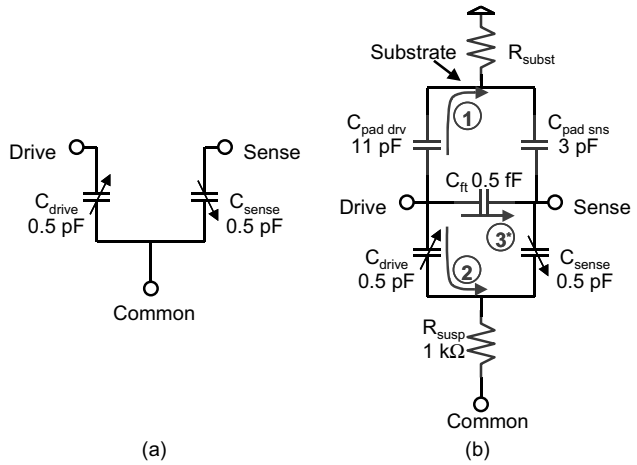

Figure 2. *MEMS mirror electrical model a) ideal; b) actual with parasitics.*

SENSE CIRCUIT

In closed-loop operation, the high voltage drive and the sense operate simultaneously. The sense circuit measures the mirror position while the drive is applying high voltage signals across the drive capacitor. Since drive and sense circuitry are connected to the same electrical network (MEMS), it is important to prevent drive and sense signal interference. This is achieved with the help of separate sense and drive capacitors. Since each capacitor has one plate connected to the MEMS, drive and sense capacitors share a common terminal, Figure 2. In an ideal case, the common terminal is connected to a voltage supply that avoids interference between the drive and sense. In reality, however, there are parasitic effects that create feed-through paths for the drive signal. The three main parasitic effects are 1) finite conductivity of MEMS device layer; 2) parasitic pad capacitors; 3) package parasitics.

MEMS conductivity creates a problem because the common terminal of the sense and drive capacitor is attached to the MEMS. The only physical connection from MEMS to the bonding pads is through the torsion beam. Since torsion beams are long and thin structures, the electrical conductivity of the MEMS strongly determines the value of the parasitic resistor (R_{susp}). In this device, the high conductivity device layer (1mΩ.cm) and a final metal deposition on the die minimize such effects. The 200-300A Al thin-film deposition also enhances the mirror optical reflectance.

Pads on the sides of the mirror suspend the stator fingers of the drive and sense capacitors. In the SOI process, the pads are separated from the substrate by a 2 m oxide layer. The process determines the minimum pad-substrate overlap. After minimizing the pad size, parasitic drive and sense capacitor values are 11pF (C_{pad_drv}) and 3pF (C_{pad_sns}), Figure 2b. Since the connection to the substrate is nonideal (R_{subst}), parasitic pad capacitors also create a feed-through path from the drive terminal to the sense.

The third type of feed-through is due to parasitics created during the packaging step. Closely spaced bond wires and package pins create feed-through paths between each other. In this case, the package parasitics between drive and sense (C_{ft}, 0.5pF) dominates the other two feed-through mechanisms.

As explained above, the physical separation of sense and drive helps to attenuate the feed-through problem but is not a complete solution. In order to further decrease the interference we also separate the two signals in the frequency domain. In the electromechanical amplitude modulation (EAM) technique, a high frequency carrier (V_{mod}, 3Mhz) modulates the common node of the drive and sense capacitors. As the sense capacitor varies with mirror rotation, the amplitude of the resulting sense current also changes. In other words, position change modulates the amplitude of the sense current (I_{sns}), Figure 3. Due to this amplitude modulation, the sense signal (V_{sns}) consists of a carrier and sense sidebands, Figure 4. In addition to these components, the low frequency drive signal (V_{drv}) also couples into the sense through three main parasitic paths discussed earlier.

In the EAM technique, demodulation is used to bring the sense signal down to the baseband. Ideally, this demodulation step modulates drive feed-through to the carrier frequency and brings the sense signal down to the base-band without mixing the two. Demodulator offset (V_{offset}), however, causes feed-through to leak into the base-band where it mixes with the sense signal, Figure 4.

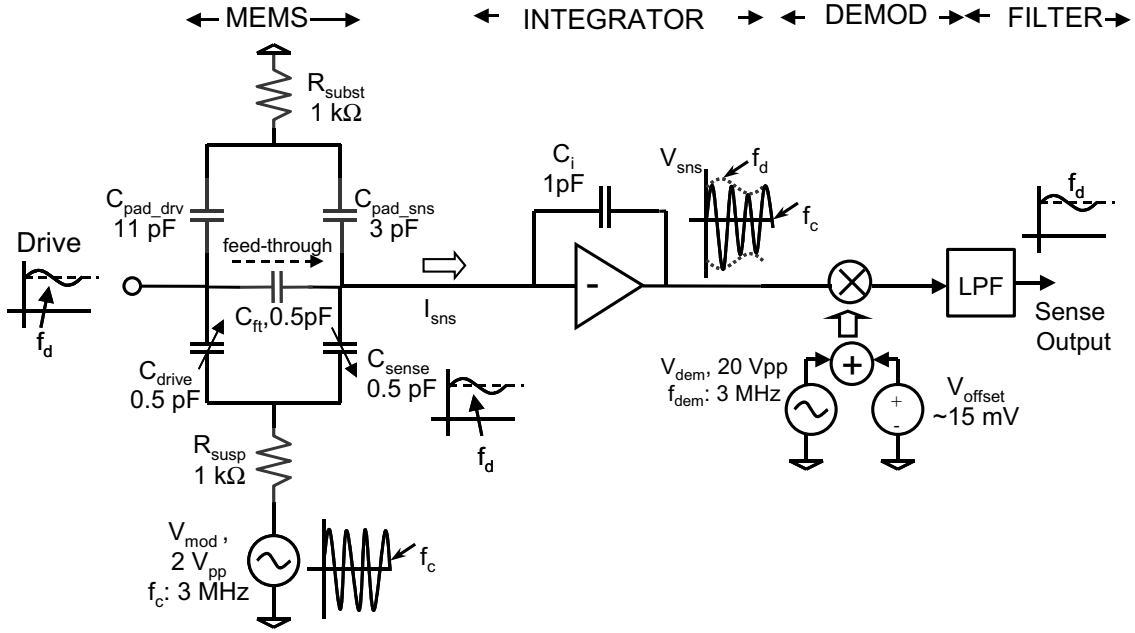

Figure 3. *Capacitive sense with the EAM technique.*

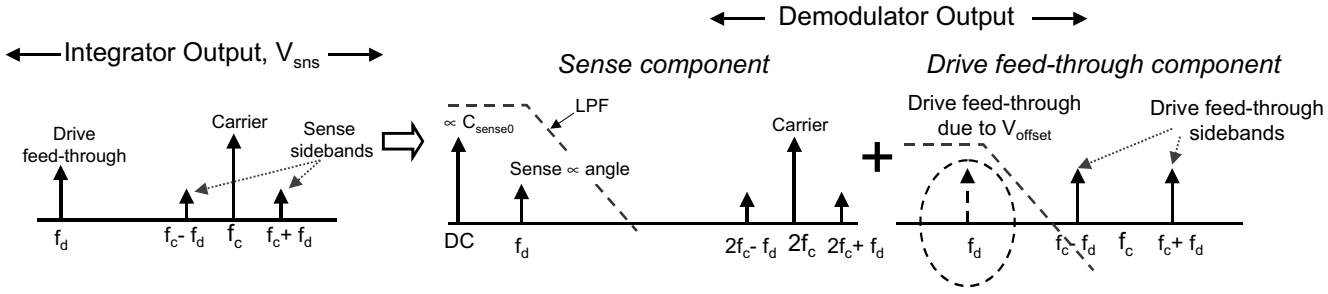

Figure 4. *Modulation, demodulation, and the feed-through.*

Demodulation is an analog multiplication step that multiplies the input signal by the demodulation signal. Consequently, multiplication by the offset is a direct path for the drive feed-through to leak into the baseband and mix with the sense signal.

In order to reduce the feed-through, we use pseudo-differential sense and band-pass filtering, Figure 5. Band-pass filtering eliminates the low frequency drive signal before it leaks into the demodulator. Pseudo-differential sense helps the problem by increasing the sense signal strength. Sense signal is proportional to the modulation signal (V_{mod}) amplitude. Increasing the amplitude of the modulation signal eventually saturates the integrator circuit. In pseudo-differential sense, an external capacitor is connected to the input node of the integrator circuit. The external cancellation capacitor is driven by an out of phase version of the modulation signal resulting in the cancellation of the carrier that has no position information. The carrier amplitude is also much bigger than the sense sidebands. Using the pseudo-differential sense we can increase the modulation amplitude without saturating the integrator. As the sense signal becomes stronger, feed-through effects diminish. Using these circuit techniques, the sense bandwidth has improved by 10x, Figure 6.

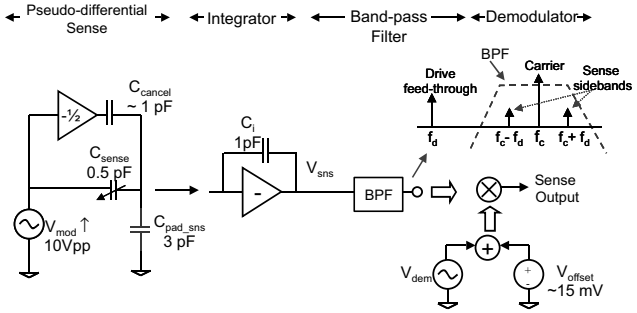

Figure 5. *Bandpass filtering and pseudo-differential sense.*

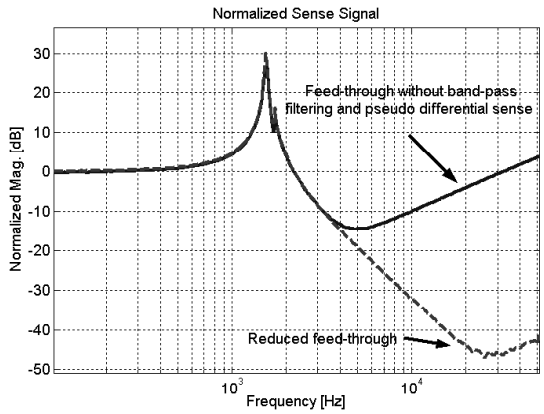

Figure 6. *Feed-through before and after the circuit modifications.*

CONTROLLER DESIGN

Phase compensation and the loop gain are the two main parameters in control loop design. Figure 7 shows the block diagram of the control system. The high voltage drive amplifier is in the gain stage. An analog phase lead filter implements the phase compensator. The main goal of the compensator is to provide enough phase margin for the stability of the feedback loop.

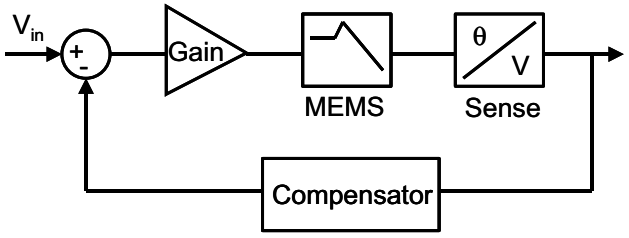

Figure 7. *Closed-loop system block diagram.*

Figure 8 shows the measured overall open-loop transfer function (OLTF) and the compensator. Increasing the loop gain improves the rejection of the disturbances. Higher loop gain also increases the unity gain crossover frequency (ω_u) resulting in a need for phase compensation at higher frequencies. As long as we can provide enough phase, the closed-loop bandwidth also increases with the ω_u. In the control loop, the 2nd order characteristics of the mirror causes a major 180 phase shift at the resonant frequency of the device. Considering that the other components in the loop also contribute to the phase delay, there is a practical limit for the maximum attainable closed-loop bandwidth.

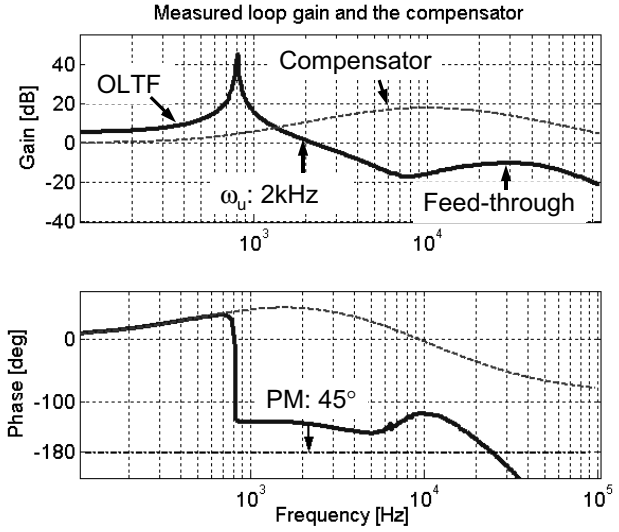

Figure 8. *OLTF and the compensator.*

Ideally, the high voltage drive amplifiers are the slowest components in the loop (100kHz bandwidth) and limit the practical control bandwidth to 10-20kHz. In practice, because the feed-through effects begin to dominate at ~20kHz, we limit the loop gain by a low-pass filter at that frequency. After the filtering is applied the maximum closed-loop bandwidth of the system becomes 2-3kHz with a loop gain of ~10 dB at DC.

EXPERIMENTAL RESULTS

The closed-loop system has been implemented on a PCB with off-the-shelf components. Dimensions of the two channel sense, controller, and drive board are 6cm x 12cm x 4cm. It weights 0.25 lb, and the total power consumption is 5W, Figure 9. The measurements shown here were done with the 700Hz X-mirror. The controller has a zero at 580 Hz, and two poles at 6.4kHz and 16kHz. The second pole of the controller limits the compensator bandwidth in order to suppress the feed-through signal. The feedback system has a 2kHz bandwidth, Figure 10.

The electrostatic drive has nonlinearities primarily due to 1) torque (force) is proportional to the square of the drive voltage; 2) MEMS capacitors vary nonlinearly with the mirror position. The latter one also affects the sense. Consequently, mirror dynamics depend on the mirror position. The linear controller used in the system, however, is able to meet the settling time requirement (< 1ms) for the range of 5 degrees to 20 degrees optical rotation. The best response is achieved at 50V actuation (8 degrees) with 400 s settling time, Figure 11. The dynamic error for the settling time is the quarter beamwidth - 0.014 degree (0.25mrad).

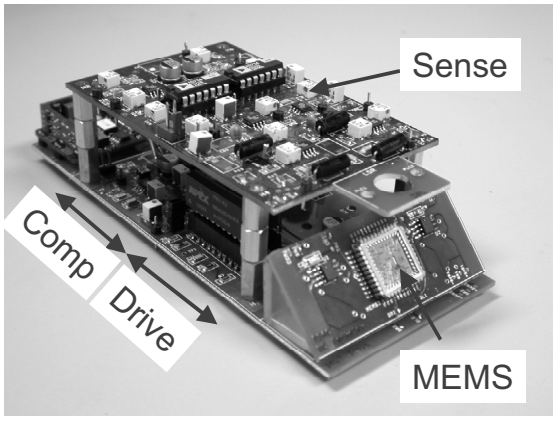

Figure 9. MEMS scanner and the control system.

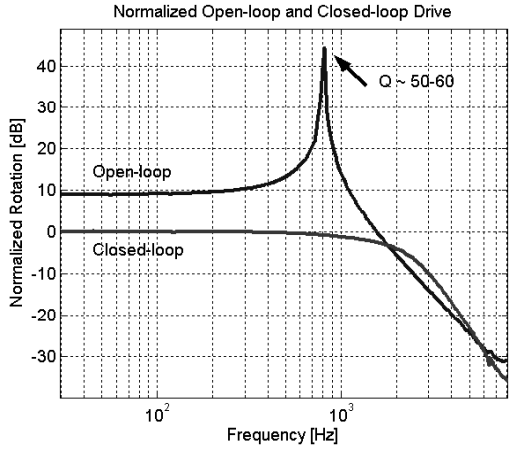

Figure 10. *Measured closed-loop vs. open-loop actuation.*

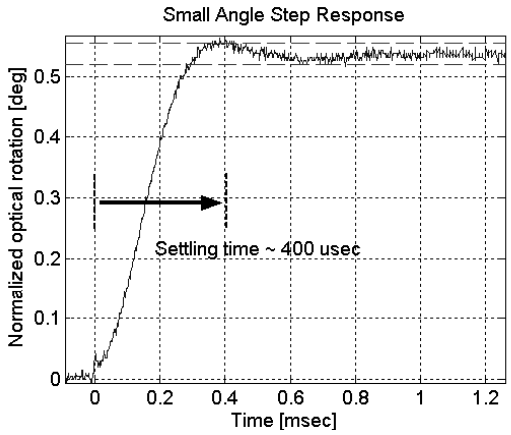

Figure 11. *0.5 degree step response.*

The resolution of the closed-loop controlled single mirror is approximately 0.004 degree-rms (70 rad-rms). The dominant noise source is the demodulator in the sense circuit. The noise contribution of the rest of the system is less than half of the demodulator circuit.

CONCLUSIONS

Feedback control effectively improves the dynamic performance of MEMS mirrors. Minimizing parasitics and using the EAM technique attenuate the feed-through effects. Additional filtering introduced in the loop due to the feed-through limits the control bandwidth.

ACKNOWLEDGEMENTS

This research is funded by DARPA under the agreement DAAH01-00-C-0099.

REFERENCES

1. M. Last, B.S. Leibowitz, B. Cagdaser, A. Jog, L. Zhou, B. Boser, K.S.J. Pister, "Toward a wireless optical communication link between two small unmanned aerial vehicles," *IEEE International Symposium on Circuits and Systems*, vol.3, (2003), pp.930-933.

2. M. Suhonen *et al*, "Scanning micromechanical mirror for fine-pointing units of intersatellite optical links," *Smart Materials & Structures*, vol.10, no.6, December (2001), pp.1204-1210.

3. N. Yazdi *et al*, "Robust sliding-mode control of electrostatic torsional micromirrors beyond the pull-in limit," *Tranducers '03*, Boston USA, vol. 2, June (2003), pp. 1450-1453.

4. T. Juneau *et al*, "Dual-axis mirror positioning using a nonlinear closed-loop controller," *Tranducers '03*, Boston USA, vol. 1, June (2003), pp. 560-563.

5. V. Milanović *et al*, "Monolithic High Aspect Ratio Two-axis Optical Scanner in SOI," *Int. Conf. on Microelectromechanical Systems*, MEMS2003, Kyoto Japan, January (2003), pp. 255-258.

6. V. Milanović, "Multilevel beam SOI-MEMS fabrication and applications," *ICECS 2002 9th IEEE International Conference on Electronics, Circuits and Systems*, vol.1, (2002), pp.281-5.

7. C. Nguyen, "Micromechanical signal processors," Ph.D. Dissertation, Dept. of EECS, University of California, Berkeley, (1994).

TWO-AXIS GIMBALED MICROSCANNER IN DOUBLE SOI LAYERS ACTUATED BY SELF-ALIGNED VERTICAL ELECTROSTATIC COMBDRIVE

Daesung Lee and Olav Solgaard
Edward L. Ginzton Laboratory, Department of Electrical Engineering
Stanford University, Stanford, CA 94305

ABSTRACT

We present a two-axis, bi-directional gimbaled microscanner in double SOI layers actuated by self-aligned, vertical, electrostatic combdrive actuators. The fabrication process is an extension of our previously developed process for fabrication of single-axis scanners in single-SOI material by adding a non-critical backside etch step. Double-stacked SOI layers are used to provide both electrical isolation and mechanical connections. We demonstrate micromirrors with ± 7.5°, ± 7.8° of static optical deflection on the inner and outer axis, respectively. Resonant frequencies are 3.5 kHz with ± 8.8° optical deflection on the inner axis and 980 Hz with ± 10.5° optical deflection on the outer axis.

INTRODUCTION

Micromirrors that measure hundreds of micron on a side and provide separately-controllable tilt on two orthogonal axes are required for high-resolution optical MEMS applications like displays, fiber switches [**1**], and scanning-confocal microscopes [**2**]. Gimbals actuated by vertical combdrives provide an effective way of implementing decoupled two-axis rotation, and such structures have been demonstrated in polysilicon as well as Silicon-on-Insulator (SOI) with one or two layers of device silicon [**3-5**]. Designs based on SOI material with two device layers simplify electrical isolation, enabling more complex electrode structures that provide bi-directional operation of both frames. Compared to polysilicon scanners, SOI-based designs also simplify fabrication of mirrors with high optical quality. Gimbal-less scanners using mechanical rotation transformers have been reported, and have been shown to provide similar scanning speed on both axes [**6**], which is difficult to achieve with gimbals.

We have recently demonstrated a single-axis micromirror capable of bi-directional rotation and piston motions actuated by self-aligned, vertical, electrostatic combdrives in double-stacked SOI layers [**7,8**]. The fabrication process, which requires only front-side processing, offers three structural layers that consist of upper, lower, and double-stacked layers. Two oxide layers under the device layers provide electrode isolation and etch stops for thickness control. Self-alignment of combs in the two device layers is accomplished by creating masking features in the upper layer and transferring them into the lower layer. These process features can be extended to fabricate two-axis, bi-directional gimbaled microscanners by adding a non-critical backside etch step.

In this paper, we present the design, fabrication process, and experimental results of two-axis, bi-directional gimbaled microscanners in double SOI layers actuated by self-aligned, vertical, electrostatic combdrive actuators.

DESIGN AND FABRICATION

Figure 1 shows a schematic of the completed two-axis gimbaled microscanner. The mirror, movable combteeth, and inner torsional springs are fabricated in the upper silicon layer. The outer torsional springs are fabricated in double-stacked SOI, while the fixed combteeth are fabricated either in double-stacked SOI as shown in Fig. 1a, or in the lower silicon layer only. A backside etch window is located beneath the gimbaled structure. Four electrodes in the lower layer allow bi-directional rotation of the inner and outer frames. Typically, all parts of the upper layer are grounded, but in some cases two electrodes in the upper layer for the outer frame are connected to two additional actuation voltages. A dual configuration of the mirror can be implemented by changing the role of the upper and lower silicon layer.

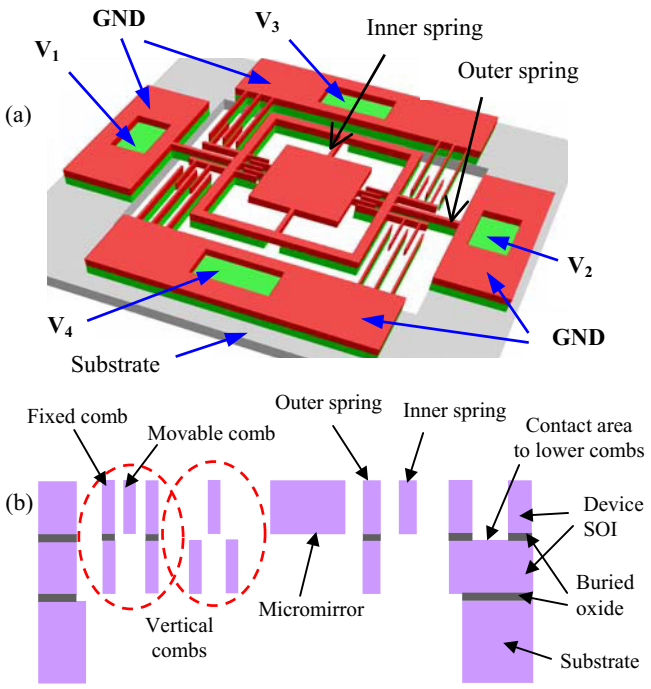

Figure 1. (a) 3D schematic of a two-axis gimbaled micromirror, (b) Cross sectional view of a two-axis gimbaled micromirror

The process starts with DRIE of the device layer (Mask 1) in regular SOI wafers (Fig. 2a). The mask patterns coarse structures encompassing the final dimension of the completed device in the lower device layer with micron scale misalignment margin. The second device layer is created by oxidation, fusion bonding, grinding, and polishing (2b). The two structural layers are both 21 μm thick and the intermittent oxide layer is 0.45 μm thick. A single LTO layer (1.1 μm) is deposited and patterned by two masks, creating two thickness of LTO; 1.1, 0.4 μm. The first of the two masks (Mask 2) is the self-alignment mask and patterned into the full thickness of LTO (2c). Then the partial etch of LTO leaving 0.4 μm is done with Mask 3, which covers the regions for partial etching with micron scale misalignment margin (2d). The

Travel support has been generously provided by the Transducers Research Foundation and by the DARPA MEMS and DARPA BioFlips programs.

process uses two self-alignment steps; Mask 1 to Mask 2, and Mask 2 to Mask 3. The alignment accuracy needed in each step is *g/2* where *g* is the comb gap. At the completion of the process, these three masks make structures in upper, lower, and double-stacked layers.

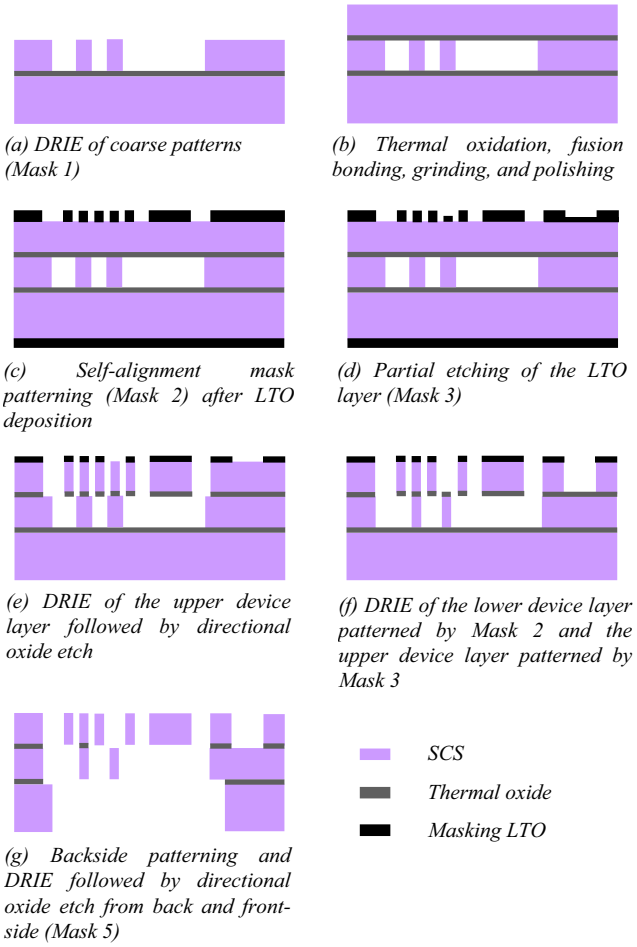

(a) DRIE of coarse patterns (Mask 1)

(b) Thermal oxidation, fusion bonding, grinding, and polishing

(c) Self-alignment mask patterning (Mask 2) after LTO deposition

(d) Partial etching of the LTO layer (Mask 3)

(e) DRIE of the upper device layer followed by directional oxide etch

(f) DRIE of the lower device layer patterned by Mask 2 and the upper device layer patterned by Mask 3

(g) Backside patterning and DRIE followed by directional oxide etch from back and front-side (Mask 5)

Figure 2. Process flow of two-axis gimbaled micromirrors (not to scale)

With the front-side masking with three masks completed, the LTO layer on the backside of the wafer is stripped and alignment marks (Mask 4) are written on the backside of the wafer by etching 0.5 μm of silicon. Next, the upper silicon layer is etched and the exposed parts of the oxide layer and remaining thin LTO (initial thickness: 0.4 μm) are directionally etched (2e). Then the lower and upper silicon layers are etched at the same step with silicon and LTO masks patterned by Mask 2 and 3, respectively (2f). Now the front-side etching is completed and the wafer is bonded to an oxidized handle wafer with 1.6 μm of photoresist for substrate etching. The backside-etch patterns (Mask 5) are prepared with thick photoresist on the backside of the wafer. Here the previously etched patterns in silicon (Mask 4) are used for alignment.

The silicon substrate (500 μm) is then etched by DRIE and the process wafer is separated from the handle wafer by soaking in acetone for 5-7 hours. After being cleaned in Piranha, exposed parts of the oxide layers are directionally etched from the backside. Finally the remaining masking LTO, as well as the exposed intermittent oxide layers are directionally etched from the front-side (2g). Figure 3 and 4 show SEM pictures of a finished device with the mirror fabricated in the upper, and lower silicon layer, respectively. In these SEM pictures, fixed combs consist of double-stacked layers. Devices with fixed combs in one layer were successfully fabricated as well. Here small amount of undercut of device layers at the interface of intermittent oxide layers is observed because over etching of silicon is required due to non-uniformity of the etching rate. Large oxide membranes formed under mirrors after the substrate etching, especially when the mirror is fabricated in the upper silicon layer, were observed to crack during the process. However, the structural layers were not affected, and the directional oxide etch from the backside was sufficient to completely remove exposed parts of the oxide layers.

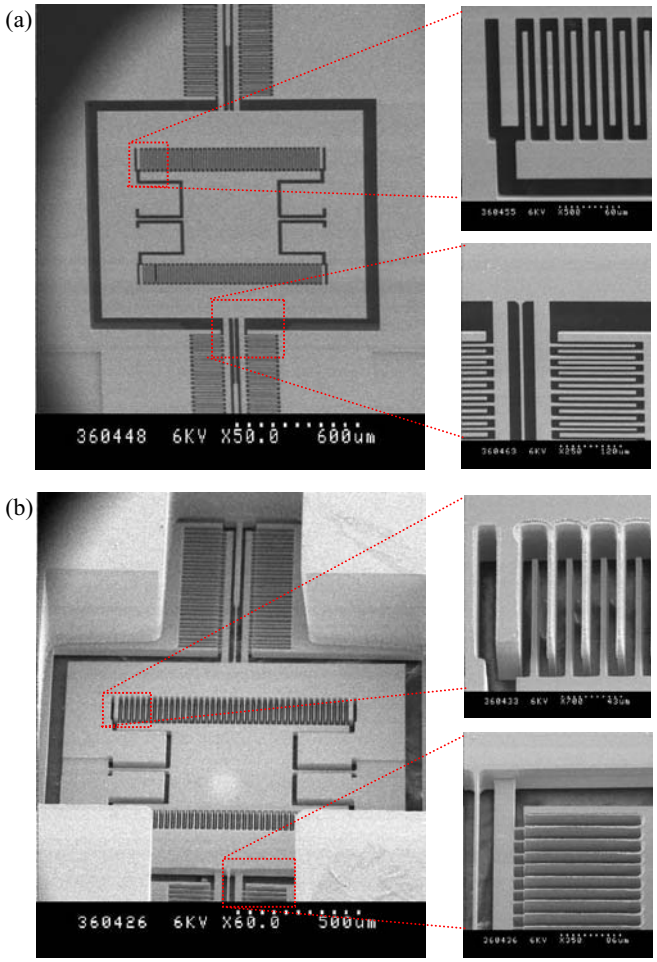

Figure 3. SEM pictures of a two-axis gimbaled micromirror where the mirror is fabricated in the upper silicon layer: (a) Top view, (b) Bottom view

One of the advantages of this process is that isotropic oxide etch is not necessary because directional oxide etch is available both from the front and backside of the wafer. We also observed increased bonding yield by using vacuum bonding to create the second device layer in this process. The sequence of the etch steps is critical. Variations of the process, by switching the order of front and backside etching, have been shown to cause pop-up of mirrors with weak inner torsional springs during the etch of the lower device layer. Double SOI structures after substrate etching were observed to bend, which caused some lateral etching enough to break weak inner torsional springs. This implies that a backside etch window cannot be replaced with a trench fabricated at the

beginning of the process to provide only front-side processing in double SOI layers.

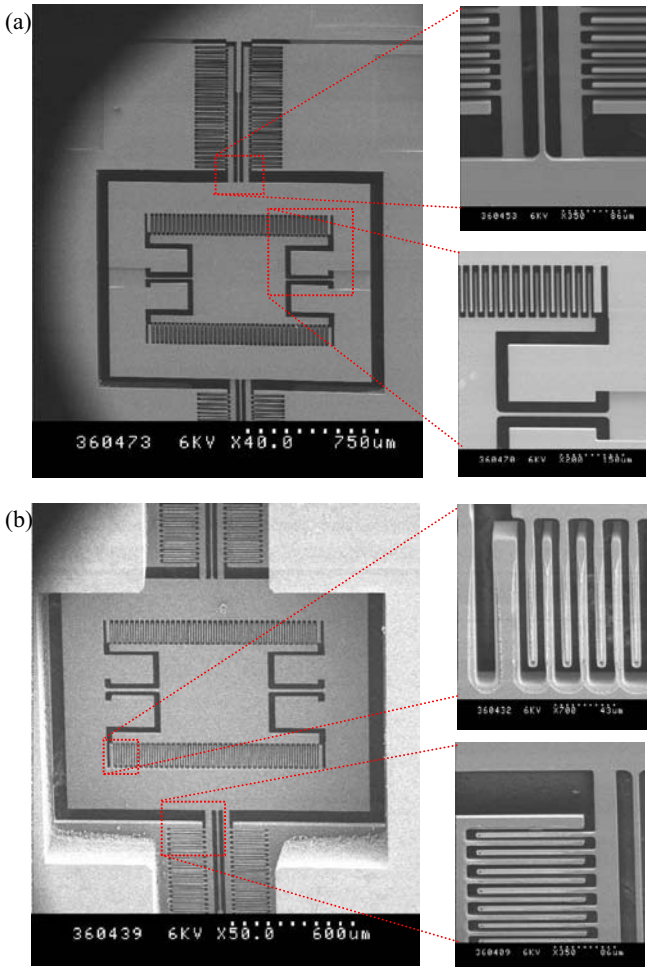

Figure 4. SEM pictures of a two-axis gimbaled micromirror where the mirror is fabricated in the lower silicon layer: (a) Top view, (b) Bottom view

DEVICE CHARACTERIZATION

Single-crystal-silicon (SCS) mirrors have merits of flat and smooth optical surfaces. In most cases, they are made of a single SOI layer. In our process, the frame and outer torsional springs are made of two SOI layers with an oxide layer in between although mirrors are fabricated in a single SOI layer. The following surface profile measurement and device characterization show that the performance of our devices are close to those of devices made in a single SOI layer.

Figure 5 shows the interferometric image of the frame of a finished device measured by WYKO. The dimension of the frame and micromirror is 1580×1160 μm, 500×500 μm, respectively. The peak-to-valley surface deformation of the frame is 0.78 μm for the horizontal direction and 0.94 μm for the vertical direction. The peak-to-valley surface deformation of the micromirror is less than 0.08 μm. The effect of the stress in the structural layers is mainly the elevation of fixed combs in the inner gimbal, causing the degradation in the performance of vertical combdrives. In our case, the elevation and height variation of fixed combs is less than 0.3 μm. The elevation of the movable combs in the outer gimbal is less than 0.2 μm. This shape of surface profile is observed universally across the devices with different spring designs and fabricated from other wafers. The upper and lower silicon layers are 21±1.5 μm thick for all the wafers. The variation of surface deformation of the frame is less than 50 percent.

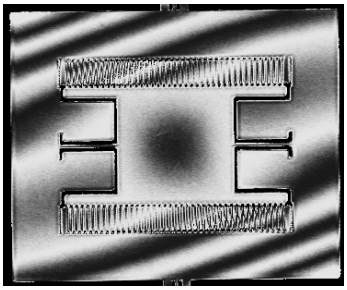

Figure 5. Interferometric surface profile of the frame of the mirror measured by WYKO

The static and dynamic shown in Fig. 6 and 7 are all obtained for mirrors that have torsional springs that measure 250×6×21 μm and 400×6×42.5 μm for the inner and outer frame, respectively. There are 40 combteeth each measuring 115×6×21 μm on the inner frame, and 60 combteeth each measuring 165×6×21 μm on the outer frame. The gaps between combteeth are 6 μm for both axes. The dimension of the frame is the same as that of the micromirror used for surface profile measurements.

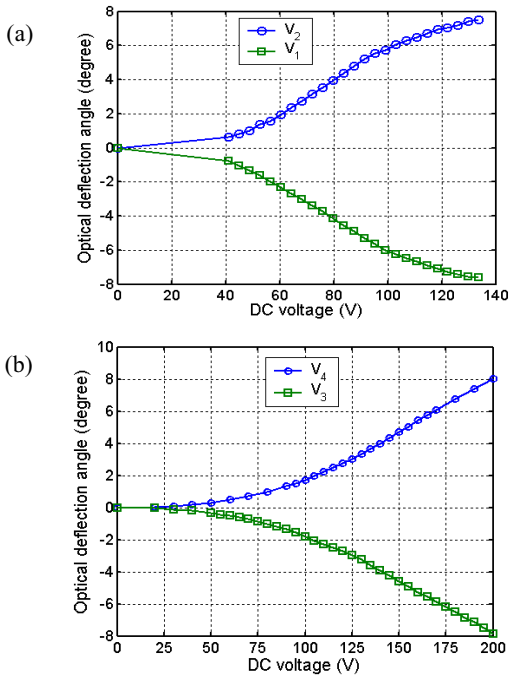

Figure 6. Static optical deflection curves: (a) Inner axis, (b) Outer axis

The measured static optical deflection for a 500×500×21 μm microscanner ranged from −7.6° at V_1=133V to 7.5° at V_2=133V on the inner axis (Fig. 6a) and from −7.8° at V_3=200V to 8.0° at V_4=200V on the outer axis (Fig. 6b). The deflection on the inner axis is close to the calculated maximum of ± 7.8° for static operation, while the maximum of ± 13° deflection on the outer axis could not be achieved with practical voltages.

The observed deflection curves are not quadratic in the voltage because the derivative of the capacitance between combs in the vertical combdrives as a function of rotation is not constant. As the deflection increases the moving combteeth rotate through the full depth of the stationary combteeth, limiting further capacitance increases.

The frequency response was obtained with a driving voltage of (42+10sinωt)V on V_2 for the inner axis (Fig. 7a), and on V_4 for the outer axis (Fig. 7b). The resonant frequency was 3.5 kHz with ± 8.8° optical deflection on the inner axis and 980 Hz with ± 10.5° optical deflection on the outer axis.

The data was collected by measuring the output waveform of a PSD (position sensitive detector) whose input is the reflected beam from the mirror surface. On both axes, three major peaks were observed. The driving frequencies at these peaks are measured to be $\omega_0/2$, ω_0, and $2\omega_0$ where ω_0 is the resonant frequency of the rotational mode. At each of these peaks, the mirror was observed to rotate at the resonant frequency. In addition to the major peaks, we also observed minor peaks at 1/3, 1/4, and 1/5 of the resonant frequency. At these peaks, the rotation was a combination rotation at the driving and resonant frequencies. The peaks below the fundamental resonance are due to the non-linear relationship between voltage and electrostatic force.

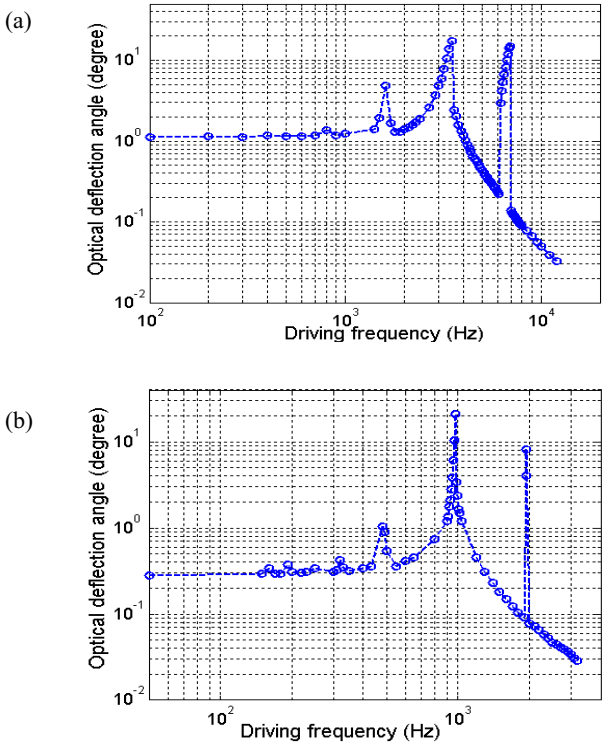

Figure 7. Frequency response: (a) Inner axis, (b) Outer axis

At the peak at $2\omega_0$, the mirror rotates at the resonant frequency, i.e. half the driving frequency. The likely cause is that large parts of the moving combs protrude on the opposite side of the stationary combs when the moving comb rotates through large angles. Under such large angular deflection, the electrostatic force is therefore directed oppositely to its direction under small rotation. The effect of this "backward" electrostatic force is that a drive signal at twice the resonant frequency can give rise to motion at the resonance as observed.

CONCLUSIONS

We have demonstrated two-axis, bi-directional gimbaled microscanners fabricated in SOI material with two devices layers. The fabrication process requires 5 lithography steps, and includes self-alignment and etch stops of all critical etch steps. The two isolated devices layers enable bi-directional operation on both axes while maintaining good surface profiles. We demonstrated static optical rotation of more than ± 7.5° on the inner axis and ± 7.8° on the outer axis of gimbaled scanning mirrors measuring 500×500×21 μm. On resonance, the achieved scan angles are ± 8.8° and ± 10.5° on the inner and outer axis, respectively.

We expect that this type of gimbaled microscanners as well as this process technology will find a variety of applications including displays, scanning-confocal microscopes, wave-front correctors, and optical fiber switches.

ACKNOWLEDGEMENT

The authors gratefully acknowledge support from the Defense Advanced Research Projects Agency under contract (DAAH01-00-C-0089).

REFERENCES

1. R. Ryf, et al, "1296-port MEMS Transparent Optical Crossconnect with 2.07 Petabit/s Switch Capacity", *Technical Digest of Optical Fiber Communication Conference 2001*, Anaheim, CA, USA, Mar. 2001, Post deadline paper PD-28.

2. D.L. Dickensheets, G.S. Kino, "Silicon-Micromachined Scanning Confocal Optical Microscope", *Journal of Microelectromechanical Systems*, vol. 7, no. 1, Mar. 1998.

3. S. Kwon, V. Milanovic, L. P. Lee, "A High Aspect Ratio 2D Gimbaled Microscanner with Large Static Rotation", *2002 IEEE/LEOS Int. Conf. on Optical MEMS,* Lugano, Switzerland, Aug. 2002.

4. N. Kouma, O. Tsuboi, Y. Mizuno, H. Okuda, X. Mi, M. Iwaki, H. Soneda, S. Ueda, I. Sawaki, "A Multi-Step DRIE Process for A 128 x 128 Micromirror Array", *2003 IEEE/LEOS Int. Conf. on Optical MEMS,* Hawaii, USA, Aug. 2003.

5. D. Han, C.-A. Choi, C.-H. Jun, Y. T. Kim, "A Self-Aligned Vertical Comb-Drive Actuator Using Surface Micromachining for Scanning Micromirrors", *2003 IEEE/LEOS Int. Conf. on Optical MEMS,* Hawaii, USA, Aug. 2003.

6. V. Milanovic, G. Matus, T. Cheng, B. Cagdaser, "Monolithic High Aspect Ratio Two-axis Optical Scanners in SOI", *Int. Conf. on Microelectromechanical Systems, MEMS2003,* Kyoto, Japan, Jan. 2003.

7. D. Lee, U. Krishnamoorthy, K. Yu, O. Solgaard, "High-Resolution, High-Speed Microscanner in Single-Crystalline Silicon Actuated by Self-Aligned Dual-Mode Vertical Electrostatic Combdrive with Capability for Phased Array Operation", *Transducers'03,* Boston, USA, Jun. 2003.

8. D. Lee, U. Krishnamoorthy, K. Yu, O. Solgaard, "Single-Crystalline Silicon Micromirrors Actuated by Self-Aligned Vertical Electrostatic Combdrives with Piston-motion and Rotation Capability", submitted to *Sensors and Actuators: A (Physical)*, Jul. 2003 (accepted for publication)

SILICON-ON-INSULATOR-BASED OPTICAL ADD-DROP MULTIPLEXERS

Peter Gulvin, Joel Kubby, Jingkuang Chen, James Diehl, Kathleen Feinberg, Kristine German, Lawrence Herko, Nancy Jia, Pinyen Lin, Xueyuan Liu, Jun Ma, John Meyers, Peter Nystrom, and Yao Rong Wang
Xerox Wilson Center for Research and Technology
Webster, New York 14580

ABSTRACT

Optical Add-Drop Multiplexers (OADMs) are used for independently addressing the various wavelengths in wavelength division multiplexing (WDM) systems. Applications such as network restoration/reconfiguration, time-dependent bandwidth, and fiber to the home all require OADMs with good optical performance, small size, low cost, millisecond-range switching times, low power requirements, and good reliability over a variety of operating conditions.

Xerox has developed a single-chip integrated OADM built on a Silicon-On-Insulator (SOI) wafer that meets these requirements. The optical loss through a switch is less than 2 dB. The entire system from fiber to fiber has 19 dB loss, an extinction ratio of over 40 dB, and an adjacent crosstalk value of more than 30 dB. Smoothing the waveguide sidewalls and decreasing input, output, and gap loss with anti-reflection (AR) coatings should decrease the loss to 12 dB. The high optical index contrast between silicon and air allows for much tighter bending radii of the ridge waveguides than in similar silica-based approaches, reducing the chip size to only 1.5 x 2 cm and decreasing the cost per device. The thermal driving and latching actuators switch within 12 ms, using only 0.8 W of power, for a total of less than 10 mJ per change of state, with no power required to maintain the state. An unpackaged device ran for 17 million switch cycles without failure, and a hermetically-sealed device is expected to have even better reliability. Variable optical attenuators (VOAs) can be integrated with the devices for gain equalization without making any changes in the fabrication.

The devices can be fabricated using a manufacturing process developed through a National Institute of Standards (NIST) and Technology Advanced Technology Program (ATP) grant [**1**]. This process consists of a surface micromachining process done on top of an SOI wafer, allowing for guided as well as free-space optics, the integration of flip-chip bonded light sources, and the possibility of including integrated electronics. This broadly enabling process will allow fabrication of other applications in the same run, increasing volumes to be more cost-effective for the foundry customer.

INTRODUCTION

In WDM, multiple channels of information are encoded as different wavelengths. Independently handling these channels requires OADMs, which allow channels to enter or exit a WDM fiber. Currently OADMs cost $1,000 per channel, restricting their use to long-haul communications. Decreasing the price per channel to $100 would open them up to the metropolitan network level and applications such as network restoration and reconfiguration, time-dependent bandwidth, and fiber to the home [**2**].

To enable this 10X cost reduction of an OADM system, the system size was decreased by about 50X, and all the system components were integrated onto one chip [**3**]. To shrink the system, silicon waveguides were used instead of the more common silica waveguides. The higher optical index of silicon over silica leads to a minimum bending radius of 3 mm, much smaller than the 10 mm minimum bending radius for a comparable silica waveguide. This allows the entire system to fit within a few square centimeters, as compared to the silica version that nearly fills a 6" wafer, cutting the cost by 50X.

Figure 1. *OADM chip on a fingertip*

An OADM system requires a demultiplexer to separate the wavelengths, the switches to route the light to and from add/drop channels, and VOAs to level the output power of the channels. Typically each of these components is on a separate chip, and they are pieced together to create an OADM. This adds a great deal of cost and complexity to packaging. If all of these components could be created with the same fabrication process, then they could be integrated on one chip, saving space, cost, and potentially increasing performance by eliminating loss due to coupling between chips. Xerox's fabrication process is capable of producing the tapered input/output couplers for the fibers, the arrayed waveguide gratings (AWGs) used for multiplexing and demultiplexing, the optical switches, and the VOAs. As such, the process could be used for a wide range of optical systems in addition to OADMs, including λ-routers and optical switches. The current prototype OADM includes the fiber couplers, AWGs, and switches, all on a 2 x 1.5 cm chip.

The primary figures of merit for an OADM are optical insertion loss, extinction ratio, adjacent and non-adjacent crosstalk, power consumption, and reliability. While the current insertion loss of 19 dB is still too high, process development and anti-reflection coatings are expected to lower the loss to 12 dB, which is competitive even when compared to much larger systems. The extinction and crosstalk values of 40 and 30 dB are already competitive, and should only improve as the fabrication process is optimized. The power consumption is 0.8 W during a change of state, and the 12 ms duration of a state change means that it consumes less than 10 mJ. No power is necessary to maintain the state, giving the additional benefit that the switches maintain their state during a power outage. Also, the small size of the system greatly reduces the energy required to maintain its temperature. The unpackaged switches have been run for more than 17 million cycles without failure, and hermetically-sealed packaged die should have increased lifetime.

0-9640024-5-0/hh2004/$20©2004TRF
DOI 10.31438/trf.hh2004.92

THEORY

Ridge Waveguides:

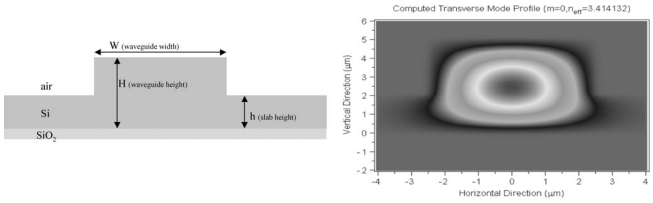

Figure 2. *Ridge waveguide and its transverse mode profile [2]*

An optical fiber guides light by confining it to a high index region (core) surrounded by a lower index material (cladding). A ridge waveguide is similar, except the index differentiation is achieved by changing the material's thickness, as shown in Fig. 2.

To fully understand a ridge waveguide one would have to solve Maxwell's equations for the different thickness regions and match the solutions at the boundaries to determine the allowable eigenmodes. However, one can use the effective index method to determine the effective index of the ridge (larger thickness) region and the slab (smaller thickness) region. In the ridge region the light is mostly confined to the silicon, and thus the index is that of the silicon (n = 3.5). In the slab region a larger percentage of the light is in the air, and the resulting effective index is a weighted average between that of the silicon (n = 3.5) and that of the air (n = 1). To find the actual value modeling software is used to analyze the mode shape and determine the effective index. The example in figure 3 uses BeamPROP[1] optical modeling software to analyze a 5-micron thick, 5-micron wide ridge region and 2-micron thick, infinitely wide slab region. The result is shown as $n_{eff} = 3.414$.

Arrayed Waveguide Gratings:

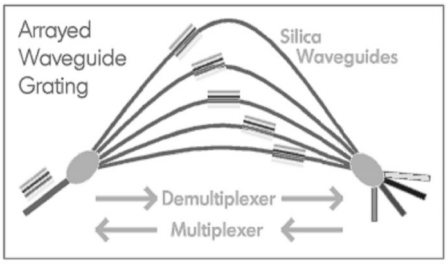

Figure 3. *Conceptual drawing of AWG (www.lightreading.com)*

An arrayed waveguide grating (AWG) uses interference between a large array of waveguides to direct different wavelengths of light to different output channels. When an AWG is acting as a demultiplexer, light enters from a single waveguide and fans out in a region called the "star coupler". The light then enters an array of intermediate waveguides, each of a slightly different length and each carrying part of all the wavelength channels. As a particular wavelength exits the intermediate waveguides, it interferes with the same wavelength exiting the other intermediate waveguides, and is sent through the exit star coupler toward the output waveguides. The output waveguide for a particular wavelength channel is placed at the point where that wavelength has its maximum constructive interference. Thus each wavelength channel is aimed at the proper output waveguide. Increasing the number of intermediate waveguides will strengthen the interference, leading to a more well-aimed, well-defined spot, but at the cost of a larger AWG.

The same process can be turned around, sending light in what were previously output channels, combining them, and then sending them multiplexed together in one waveguide.

Thermal Actuators:

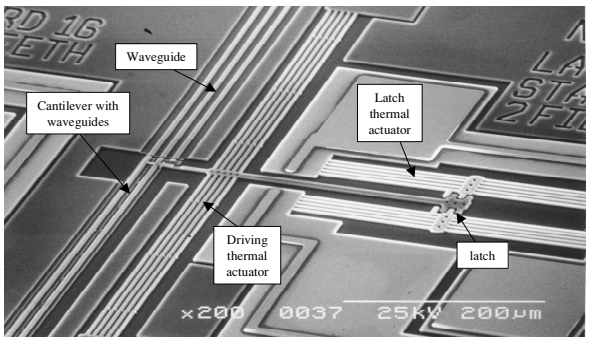

Figure 4. *OADM system [2]*

Thermal actuators in general use electric current to cause Joule heating, and the resulting thermal expansion causes motion. A straight beam between two anchors would buckle unpredictably when heated, so typically the center of the beam is offset slightly to one side to assure motion in that direction. This is known as a "V-beam" actuator.

When a v-beam actuator is subjected to film stress (e.g.: doped silicon or polysilicon), it will either bend more or straighten, depending on whether the stress is compressive or tensile respectively. In an optical switch where one of the states is the as-fabricated position, the displacement that results from stress is highly undesirable.

To eliminate this effect, methods besides an offset must be used to break the symmetry and bias the motion of the actuator in the desired direction. One possibility is to vary the spacing of the beams to alter their rates of heating and cooling, and thus their ultimate temperature. Another is to vary the doping levels of the beams to alter the Joule heating [**2**]. In either case beams on one side heat more and at a quicker rate than those on the other, and the actuator moves in the direction of the beam that expands the most or the most quickly.

Another challenge with thermal actuators, particularly with longer, higher displacement actuators, is that the voltage difference between the beams and the floor beneath them can cause the beams to electrostatically pull down and stick to the floor, causing device failure. To minimize this, the voltage applied to the two ends is not single-ended, but rather bipolar. Thus the center of the beams are at zero potential, and the downward force is minimized (other areas along the length still have a downward force). Another way to minimize this effect is to more heavily dope the beams, decreasing the voltage required to achieve the same current. Since a higher doping level leads to higher stress levels, this further increases the need for a design that doesn't displace easily due to stress.

[1] BeamPROP is produced by RSoft Inc, www.rsoftdesign.com/

EXPERIMENTAL DETAILS

Fabrication process:

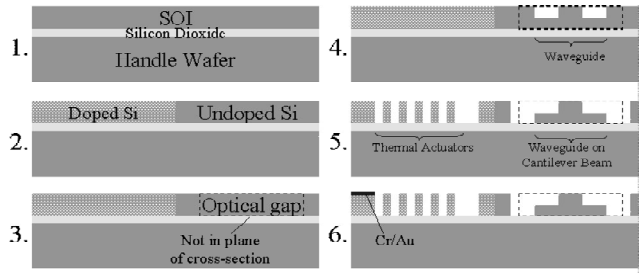

Figure 5. *OADM fabrication process*

1. Starting wafer: The process begins with an SOI wafer with a 5 or 6 micron device layer, and a 1 or 2 micron buried oxide layer.

2. Patterned doping: This provides greater conductivity for the thermal actuators to lower the voltage requirements, while avoiding doping of waveguides to prevent absorption of photons.

3. Critical gap silicon etch: This etch defines the optical gap between the moving and stationary sides of the optical switch, since the resulting Fabry-Perot cavity will have significant loss unless it is tuned to a multiple of half the wavelength or if AR coatings are applied. To get as close as possible to an optimal value the lithography must be very accurate, and the flat silicon at this stage will help.

4. Waveguide etch: This timed partial-depth silicon etch defines the ridge and slab regions of the waveguides.

5. Mechanical silicon etch: This etches all the way through the silicon, stopping on the buried oxide layer. The thermal actuators, cantilever beams, latch beams, traces, and bond pads are defined at this step.

6. Patterned metal: Chrome/Gold is patterned using a lift-off process, coating the bond pads and optionally the traces.

Switch Operation:

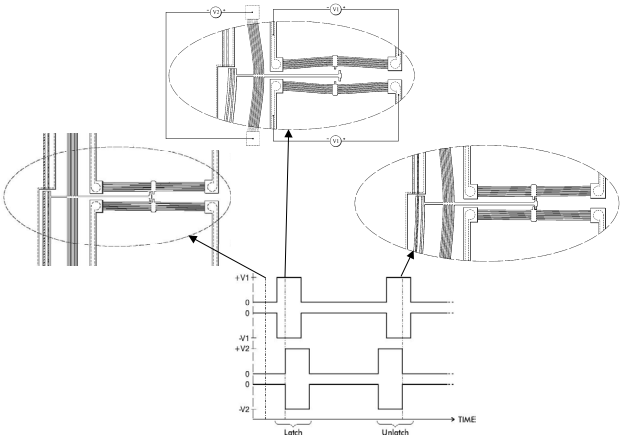

Figure 6. *Diagrams of unlatched, intermediate, and latched states, and a plot of voltage vs. time [**2**]*

Shown above is a diagram of how the devices are latched and unlatched. To latch the device the latch actuators are opened, the drive actuator moves the waveguides so that the latch teeth are beyond where they need to be, the latch actuators close, and the drive actuator relaxes so that the waveguides settle into their latched state. To unlatch the device, the drive actuator is again actuated to separate the latch teeth and prevent friction from causing binding, the latch actuators open, the drive actuator relaxes and moves the waveguides to their original state, and the latch actuator closes. Figure 7 shows what the waveguides look like in their unlatched and latched states.

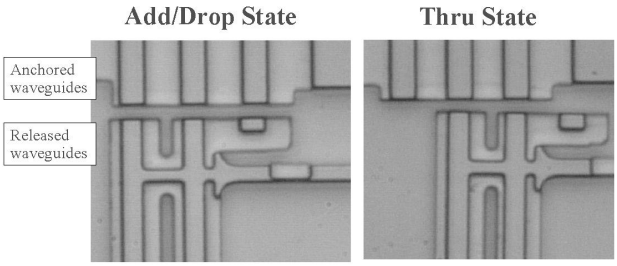

Figure 7. *Close-up view of waveguides in both states[**2**]*

Unpackaged devices have been successfully run for over 17 million latch/unlatch cycles without seeing a failure or any significant drifting in the positions of the states. Some oxidation was evident near the midpoints of the drive actuators, where the maximum temperature is achieved. By hermetically sealing the devices in an inert gas, the oxidation should be eliminated. The devices were left in their latched states for weeks to test whether stiction in the latch teeth might pose a problem, but they started right up without a problem.

Optical Testing:

To test the devices, lensed fibers were used to couple broadband illumination into a waveguide that is tapered in the plane of the chip (no thickness variation). To determine the loss at each wavelength, the spectrum of the input and output light was measured and the difference in power at each wavelength was noted.

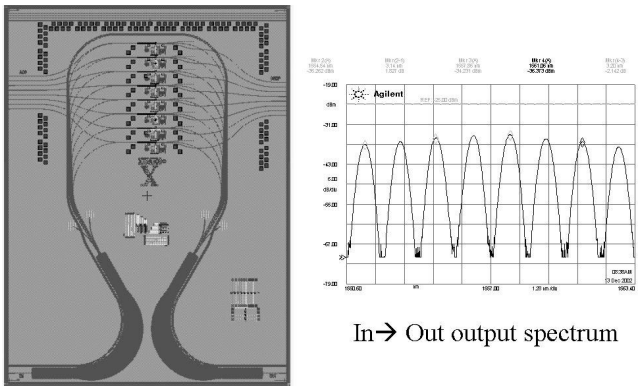

Figure 8. *Example design and the resulting output spectrum*

The insertion loss for an entire system was measured to be 19dB. To determine the loss breakdown by component, a series of test structures were used, such as AWGs by themselves, switches with waveguides, straight waveguides, and curved waveguides. The table below lists the losses that were found, the degree to which the loss can be improved, and the method by which the improvement will occur. The numbers don't add to 19dB since the parts used to measure component losses were not from the exact system that the 19 dB figure came from:

Source of Loss	Current IL	Target IL	Improvement Method
Fiber-WG coupling	4.7dB	<2dB	Add AR coating
Waveguide Loss (5.3cm)	4.3dB	<2.5dB	Sidewall smoothing
2 x AWG	8dB	6dB	Sidewall smoothing/Design Optimization
Waveguide Gap	2dB	1dB	Add AR coating
Crossings, S-bends, etc.	1dB	1dB	None
Total	**20dB**	**<12dB**	

Figure 9. *Table analyzing optical losses*

When an AR coating is added to the waveguide gap, the Fresnel loss in the gap will be eliminated and tight control of the gap width will not be necessary. That will allow the waveguide gap to be etched at the same time as the rest of the mechanical features, saving one mask and a few processing steps and making the process much more manufacturable.

The need for sidewall smoothing is due to vertical striations and other roughness in the reactive ion etching (see figure 10).

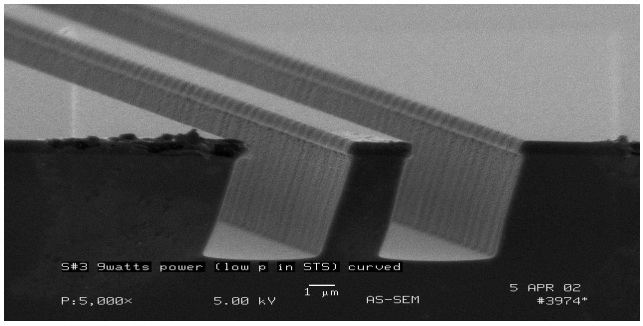

Figure 10. *Etched features showing vertical striations*

Manufacturing Process:

The fabrication process described above is a custom process designed solely to make the OADM. Versions of the device have been made using a manufacturing process developed through an Advanced Technology Program (ATP) grant from the National Institute of Standards and Technology [**1**]. This process consists of a surface micromachining process done atop an SOI wafer, allowing for guided as well as free-space optics, the integration of flip-chip bonded light sources, and the possibility of including integrated electronics. This flexible process will allow fabrication of other applications in the same run, increasing volumes to be more cost-effective for the foundry customer.

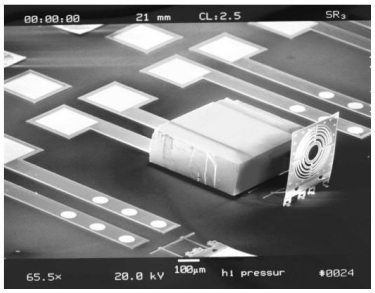

Figure 11. *Flip-chip bonded laser diode and fresnel lens made with ATP process[**4**]*

There are plans to transfer this process developed under an ATP grant to the Infotonics Technology Center in Canandaigua, NY within the year. The Infotonics Center was created with the intent of sharing infrastructure that would be prohibitively expensive and underutilized were one company to purchase it on their own, and the ATP process will be one of the first process qualified in the Center.

CONCLUSIONS

An OADM has been created that performs nearly as well as much larger systems, but with substantial size and cost advantages. With further process development and some work with AR coatings, the OADM should be able to be improved to the point where it is competitive with other OADMs in any cost or size range.

A fabrication process has been created that is capable of making much more than just OADMs. A **λ**-router has also been demonstrated [**2**], and has been shown to function as expected, with extra loss due to the additional pair of AWGs. Other applications such as optical switching may also be possible using the same process.

ACKNOWLEDGEMENTS

Process work performed under Cooperative Agreement #70NANB8H4014, National Institute for Standards and Technology Advanced Technology Program, ATP Project Managers Thomas Lettieri and Carlos Grinspon.

REFERENCES

1. J.A. Kubby on behalf of the MOEMS Manufacturing Consortium, "Combining light with motion: hybrid integration of light emitters and detectors with SOI-based micro-opto-electro-mechanical (MOEMS) systems", *Proceedings of SPIE, 4293,* 32-45 (2001).

2. K. German et al., "Optical MEMS platform for low cost on-chip integration of planar light circuits and optical switching", *Submitted to Proceedings of SPIE, 5357*, 2004

3. J.A. Kubby, "Advances in MEMS integration with planar waveguide devices", *Proceedings of SPIE*, *4654*, 1-12 (2002).

4. P. Gulvin, "Hybrid Silicon-On-Insulator Micromachining Process: 8 Mask Version Design Guide", 2004 www.infotonics.org/Newsroom/documents/scssmmv2.pdf

POLY-SIGE HIGH FREQUENCY RESONATORS BASED ON LITHOGRAPHIC DEFINITION OF NANO-GAP LATERAL TRANSDUCERS

Emmanuel P. Quévy, Sunil A. Bhave, Hideki Takeuchi, Tsu-Jae King, Roger T. Howe
Berkeley Sensor & Actuator Center, Electrical Engineering and Computer Sciences Department,
University of California at Berkeley, Berkeley, California 94720-1774

ABSTRACT

In this paper, we describe a new approach for fabrication of micromechanical resonators for radio-frequency communication applications. The proposed process provides ultra-narrow lateral gaps using lithographically-defined sacrificial Ge blades. By using Germanium as a sacrificial material, we eliminate the need for HF etching to release mechanical structures and thereby simplify the integration of these devices with CMOS electronics. Polycrystalline silicon-germanium (poly-SiGe) is used as the structural material in order to keep the thermal budget low (maximum temperature 425°C), so as to be compatible with CMOS metallization stacks. Resonators with frequencies up to 200MHz and Q ranging from 3,500 to 14,000 are demonstrated.

Index terms – MEMS, resonator, silicon-germanium

INTRODUCTION

Micromachined resonators are promising as on-chip replacements for discrete filters and oscillators which are presently implemented using off-chip quartz and surface-acoustic-wave (SAW) devices in wireless communication systems [1]. The monolithic integration of control, amplification and signal-processing electronics with radio frequency micro-electromechanical devices (RF MEMS) also reduces parasitic capacitances and inductances as well as overall system power consumption. Recent progress toward a low-thermal-budget polycrystalline silicon-germanium (poly-SiGe) MEMS technology promises to make possible the modular cofabrication of high-performance surface-micromachined structures on top of completed CMOS wafers [2]. However, a detailed process integration scheme for poly-SiGe resonator fabrication -- particularly one that provides ultra-narrow lateral gaps between the resonator and drive/sense electrodes -- has yet to be explored.

There are several process requirements for post-CMOS integration of RF resonators. First, the MEMS fabrication thermal process budget must be carefully designed in order to retain the performance and reliability of the CMOS electronics. Interconnect reliability, rather than transistor performance, limits the post-processing temperature, which should not exceed 450°C. High-quality poly-SiGe structural layers with Ge content greater than ~60% can be deposited by conventional low-pressure chemical vapor deposition without exceeding this temperature limit [3]. Second, the metallization stack of the underlying electronics must be protected from chemical attack during the microstructure release etch. The use of Ge rather than SiO_2 as the sacrificial material is advantageous because it can be rapidly etched in a heated H_2O_2 solution which does not attack oxide, metal, poly-Si, or poly-SiGe with a Ge content less than ~70%. Third, extremely small (sub-100 nm) electrode gaps are needed in order to achieve low motional resistances, hence low insertion losses [4]. For the definition of nanoscale lateral gaps, a sidewall sacrificial oxide spacer process has already been developed for poly-Si MEMS technology [4]. In this process, the poly-Si electrode layer (which is deposited after the sacrificial spacers are formed) must be etched with high selectivity to the sacrificial oxide, in order to clear it completely along the sidewalls of the structural poly-Si layer in the areas where the electrode layer must be removed. Because Ge etches more quickly (by a factor of ~3) than poly-SiGe or poly-Si in a standard Cl_2/HBr dry-etch chemistry, the sidewall spacer process cannot be used if Ge is employed as the sacrificial material, however [5]. Therefore, we have developed a simple Damascene process, featuring unconstrained placement of lateral gaps.

DAMASCENE GE-BLADE PROCESS

Figure 1 illustrates the fabrication process; scanning electron microscopy (SEM) pictures at various steps are presented in Figure 2. A Si wafer covered with 1-µm CVD-SiO_2 was used as the starting substrate. For simplicity, a two-mask process was used. First, a 2-µm-thick *in-situ* boron-doped poly-Ge sacrificial film was deposited by LPCVD (350°C, 2hr deposition) and patterned using i-line lithography. The structures include 0.5µm minimum-width lines to define the transducer's lateral gaps (Figure 1.a). Photoresist ashing in O_2 plasma was used to reduce the minimum line width to 50nm (Figure 1.b and Figure 2.a). The photoresist pattern was then transferred to the Ge layer using a HBr/Cl_2 chemistry in a transformer-coupled plasma (TCP) etcher. Figure 2.b shows SEM images of a high-aspect-ratio (10~20) Ge blade. Note that sidewall taper in the etched Ge structures, due mainly to a tapered photoresist profile, must be minimized for peak resonator performance. (Sidewall taper is undesirable for the aforementioned sidewall sacrificial oxide spacer process as well.) To avoid any potential adhesion issue for the narrow Ge-blades on SiO_2, the Ge was not etched all the way down to the underlying SiO_2; rather, a second mask was used to define anchoring contacts to the SiO_2 (Figure 1.c). Next, a 2.2µm-thick *in-situ* boron-doped poly-$Si_{0.35}Ge_{0.65}$ structural layer was deposited by LPCVD (425°C, 400mtorr, $SiH_4/GeH_4/B_2H_6$[10% in H_2] = 100/60/60sccm, 4hr40min. deposition) as shown in Figure 1.d and 2.c. This deposition step accounts for the majority of the total thermal process budget. Figure 2.d shows that the poly-$Si_{0.35}Ge_{0.65}$ is deposited conformally over the Ge blade. After chemical mechanical polishing (CMP) of the poly-$Si_{0.35}Ge_{0.65}$ layer, the sacrificial poly-Ge layer was removed in H_2O_2 at 90°C. Figure 2.e shows an SEM image of a fabricated Double-Ended Tuning Fork (DETF) resonator. Figure 2.f shows a cross-sectional SEM image of the nanoscale gap. Due to high compressive stress and strain gradient in the poly-$Si_{0.35}Ge_{0.65}$ film, the gap is reduced to almost zero and the resonator is vertically displaced from the electrodes by ~100nm, respectively. Optimization of the poly-$Si_{0.35}Ge_{0.65}$ deposition process is underway to minimize these effects.

0-9640024-5-0/hh2004/$20©2004TRF
DOI 10.31438/trf.hh2004.93

Solid-State Sensors, Actuators, and Microsystems Workshop
Hilton Head Island, South Carolina, June 6-10, 2004

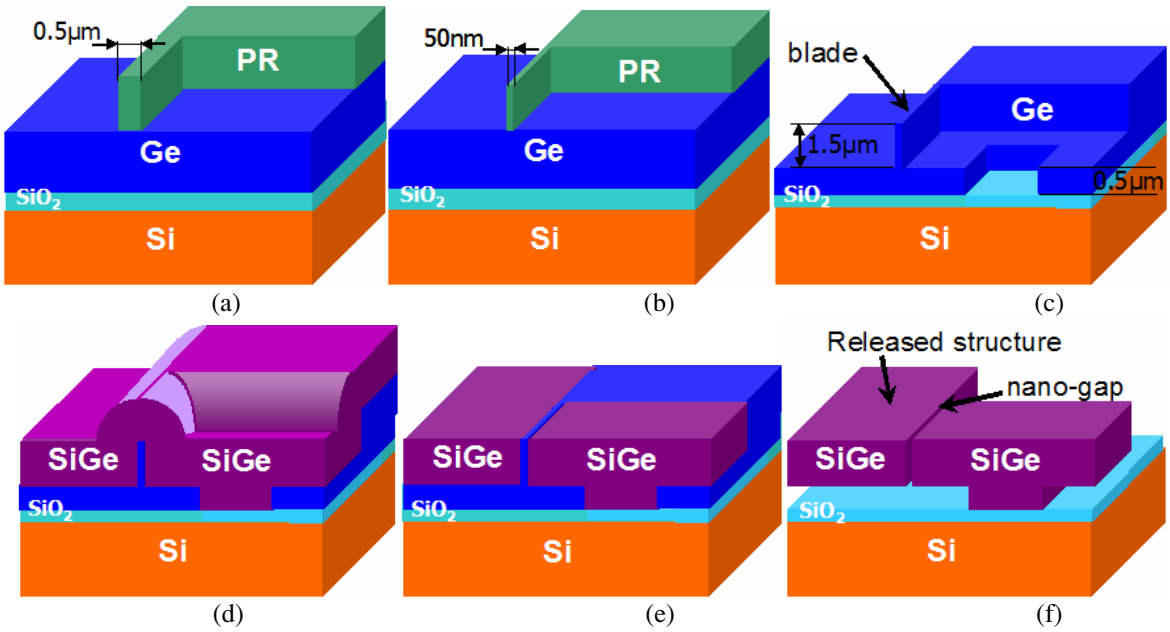

Figure 1: Outline of the 2-mask Germanium Blade Damascene Process which provides ultra-narrow gaps.

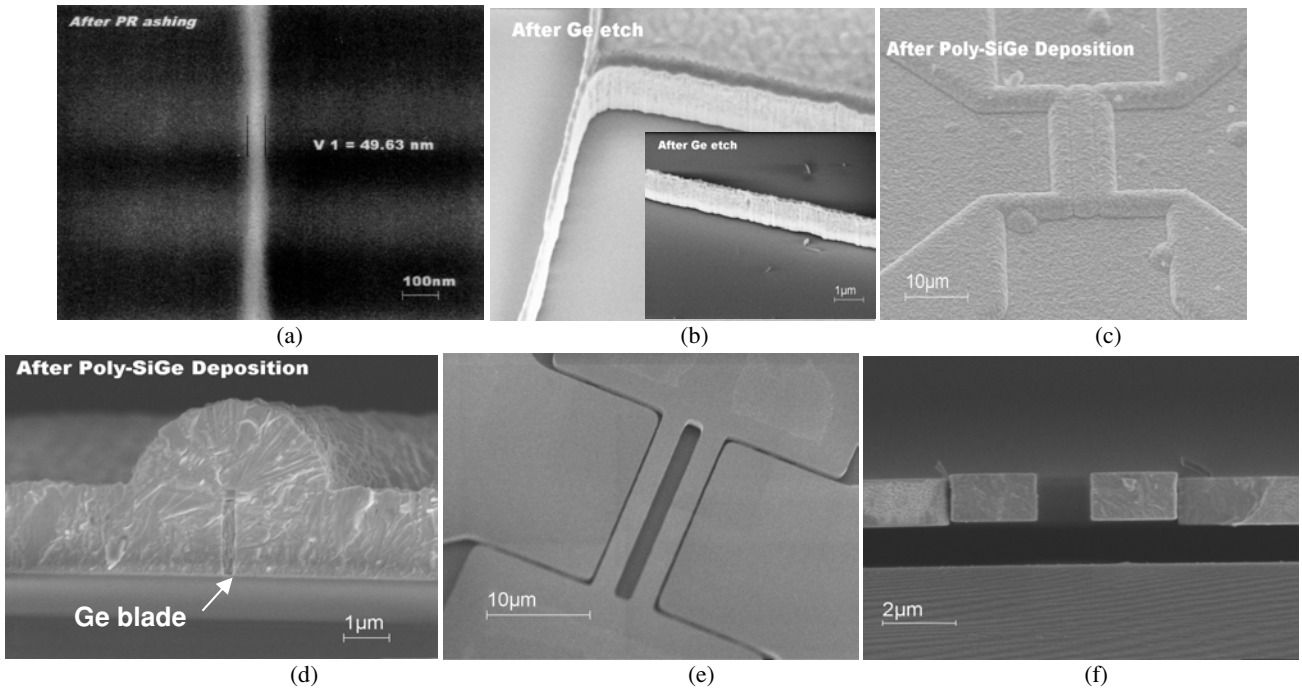

Figure 2: SEM pictures corresponding to various steps depicted in Figure 1 in the case of a double-ended tuning fork (DETF): **(a)** 50nm line definition by lithography and photoresist ashing; **(b)** High-aspect-ratio Ge blade; **(c)** top view and **(d)** cross-section after SiGe structural layer deposition; **(e)** Released DETF top view and **(f)** cross-section

This new process provides significant advantages for manufacturing. First, a single deposited layer is used to form the resonator structure and drive/sense electrodes, so that there is no need for a highly selective etch process in order to avoid the formation of unwanted "stringers" along the resonator sidewalls. Because the number of film deposition steps is reduced, the thermal process budget is substantially reduced. Second, nanoscale lateral gaps are achieved by lithographically patterning ultra-narrow lines rather than spaces. Line patterning technology for ~100nm features is well established, as 50nm physical gate-length transistors are now used in products at the 90nm CMOS technology node. This is because the well-controlled formation of ultra-narrow line widths is feasible using photoresist ashing [6] or hard-mask trimming [7] techniques. Also, because of the unique etching characteristics of Ge, the width of a Ge blade after it is formed by dry etching can be further reduced in a controllable manner, in hot (~90°C) deionized water. Finally, the unconstrained placement of lateral gaps is an additional advantage of this method as compared to the sidewall spacer process.

HIGH-FREQUENCY SIGE DEVICE CHARACTERIZATION

Devices fabricated using the 2-mask damascene Ge-blade process were characterized using various methods:

2-port measurement method:

The main problem encountered in testing of MEMS resonators is the feed-through capacitance. Indeed, using direct 2-port measurement of the 24MHz resonator in Figure 2.e, the peak height achievable was only 0.5dB. To address this problem, we used a differential drive/sense scheme as illustrated in Figure 3. The proof mass is used either as a drive or sense element, allowing better efficiency but higher direct feed-through via capacitive transduction. The use of a power combiner/splitter adds flexibility, allowing actuation of both symmetric/asymmetric modes, and providing feed-through cancellation for the asymmetric differential mode in particular.

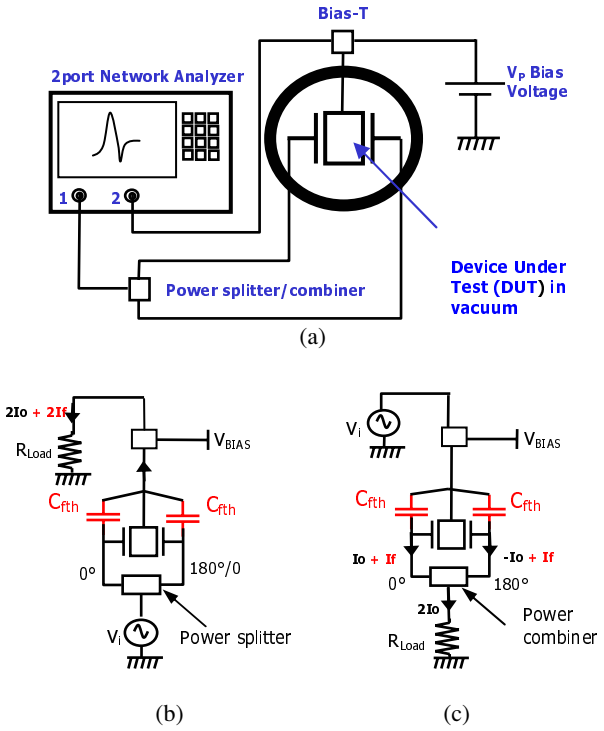

Figure 3: (a) Experimental set-up for Transmission Measurement with Differential Drive Configuration (b) and Differential Sense Configuration (c)

Using the differential drive/sense scheme, the transmission characteristic of the same DETF is shown in Figure 4.a, exhibiting a resonance peak increased to 8dB at 24.05MHz, and a quality factor of 4800. Based on frequency pulling extraction, the effective gap was determined to be 295nm, which accounts for the low transduction efficiency. This gap broadening can be attributed primarily to insufficient etch selectivity (of Ge *vs.* $Si_{0.35}Ge_{0.65}$) during the long release etch in H_2O_2 [5], which can be remedied by using a structural layer with Ge content below 65%. Poor critical-dimension (CD) control on the blade definition mask may also have contributed to the gap broadening.

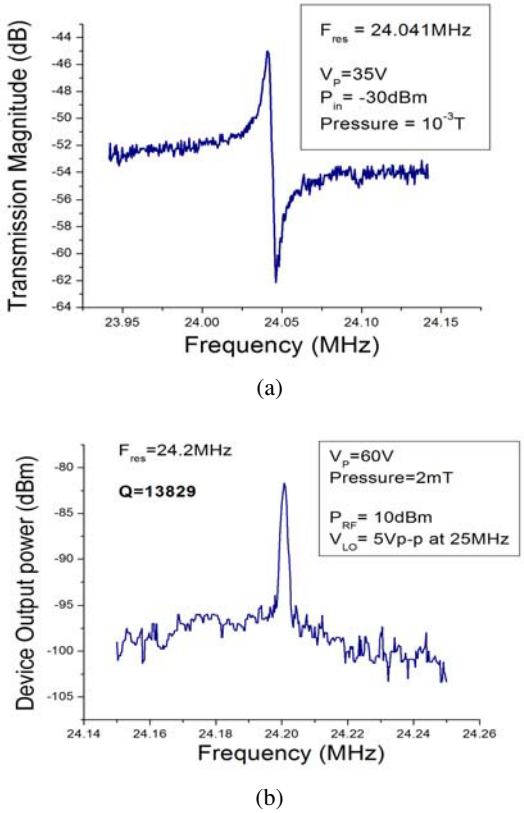

Figure 4: Transmission Magnitude of the Double-Ended Tuning Fork shown in Figure 2.e, in the case of Differential Sense Configuration for the asymmetric mode (a), and RF/LO technique for the symmetric mode (b)

RF/LO technique:

The RF/LO technique [8] was used to perform characterization of fabricated device at higher frequencies. Indeed, this technique takes advantage of the capacitive non-linearity of the transducer to perform mixing and thus further minimize the influence of any parasitic feed-through in the resonance band.

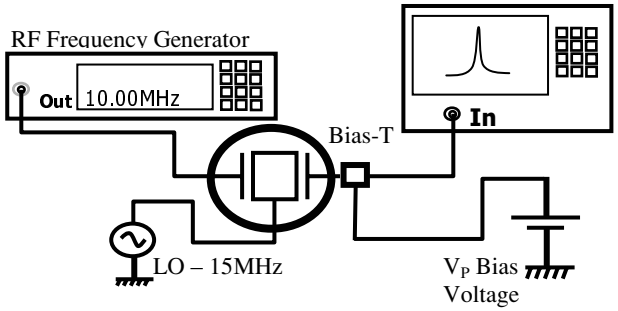

Figure 5: Experimental set-up for RF/LO measurement technique

In the case of the 24MHz tuning fork, this technique was used to characterize the symmetric mode and to extract an expectedly higher Q of 13,800 (Figure 4.b).

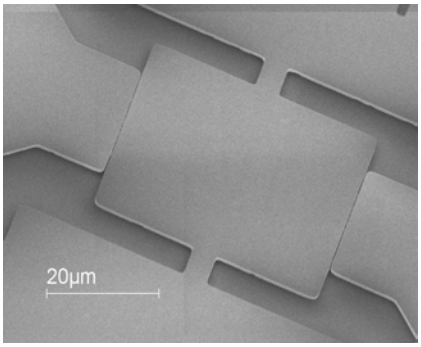

Figure 6: SEM picture of bulk-longitudinal resonator.

A 40µm-long and 32µm-wide bulk-longitudinal resonator (Figure 6) was also characterized using this technique. A 74.4MHz resonance was observed for the fundamental mode, while the third harmonic mode was visible at 205MHz, as shown in Figure 7.a and 7.b. The quality factors were measured to be 2,900 and 3,500 respectively.

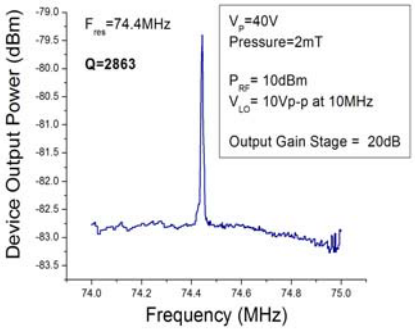

(a)

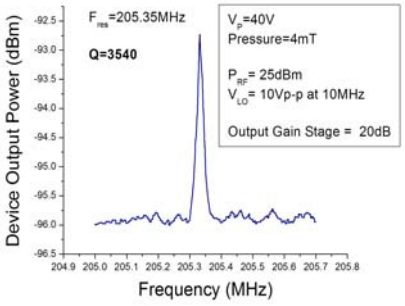

(b)

Figure 7: Device output power of the Bulk Longitudinal Resonator shown in Figure 6 using the RF/LO measurement technique: (a) Fundamental Mode (b) Third Harmonic

Temperature Drift:

Figure 8 presents the temperature dependence of the DETF, which exhibits TC_F = -85ppm/°C, greatly influenced by the compressive stress due to thermal-expansion mismatch between the SiGe structure and Si substrate. Using a simple model, the corresponding TC_F for SiGe was extracted to be -104ppm/°C. On the same plot, a simulated curve shows the benefit of matching the thermal expansion coefficients of the substrate and the structure, resulting in a lower TC_F of -48ppm/°C. Although these values are higher than for poly-Si, it is possible to take advantage of such a mismatch to integrate efficient temperature-sensing structures for compensation purpose.

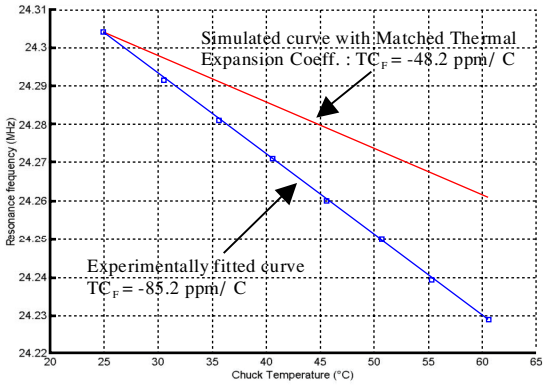

Figure 8: Measured and Simulated Frequency dependence versus Temperature for a DETF

CONCLUSIONS

A new Ge-Blade Damascene Process is proposed and successfully applied to fabricate a high-frequency DETF resonator. Due to its low thermal budget, HF-free release process, and highly-planar surface topography, this new process is promising for post-CMOS integration of nano-mechanical resonators applicable for RF communication systems.

ACKNOWLEDGEMENT

This work was supported by the DARPA NMASP program, with Dr. D. J. Radack, Program Manager. Travel support has been generously provided by the Transducers Research Foundation and by the DARPA MEMS and DARPA BioFlips programs.

REFERENCES

1. C.T.-C. Nguyen, L.P.B. Katehi, G.M. Rebeiz, "Micromachined Devices for Wireless Communications," *Proc. of the IEEE*, Vol. 86 (8), pp. 1756-1768 (1998)
2. A.E. Franke, J.M. Heck, T.-J. King, and R.T. Howe," Polycrystalline Silicon–Germanium Films for Integrated Microsystems," *Journal of Microelectromechanical Systems*, Vol. 12 (2), pp.160-171 (2003)
3. S.A. Bhave, B.L. Bircumshaw, W.Z. Low, Y.-S. Kim, T.-J. King, R.T. Howe and A.P. Pisano, "Poly-SiGe: A high-Q structural material for integrated RF MEMS," *Technical Digest, Solid-State Sensor and Actuator Workshop*, pp. 34-37 (2002)
4. J.R. Clark, W.-T. Hsu, and C.T.-C. Nguyen, "High-Q VHF Micromechanical Contour-Mode Disk Resonators," *Technical Digest, IEEE Int'l Electron Devices Meeting*, San Francisco, CA, pp. 493-496 (2000)
5. B. Bircumshaw, *et al.* "Hydrogen Peroxide Etching and Stability of P-type Poly-SiGe Films," *Technical Digest, IEEE MEMS Conference* (Maastricht, The Netherlands), pp. 514-519 (2004)
6. J. Chung, M. Jeng, J. E. Moon, A. T. Wu, T. Y. Chan, P. K. Ko, and C. Hu, "Deep submicrometer MOS device fabrication using a photoresist ashing technique," *IEEE Electron Device Letters,* Vol. 9, pp. 186–188 (1988)
7. K. Asano, Y.-K. Choi, T.-J. King, and C. Hu, "Patterning Sub-30-nm MOSFET Gate with I-Line Lithography," *IEEE Trans. on Electron Devices*, Vol. 48(5), pp. 1004-1008 (2001)
8. J. Wang, Z. Ren, and C. Nguyen "Self-aligned 1.14GHz vibrating radial-mode disk resonators," *Proceedings of the 12th International Conference on Solid-State Sensors, Actuators, and Microsystems (Transducers'03)*, Boston, MA, pp. 947-950 (2003)

ACTIVE TEMPERATURE COMPENSATION FOR MICROMACHINED RESONATORS

Matthew Hopcroft[1], Renata Melamud[1], Rob N. Candler[1], Woo-Tae Park[1], Bongsang Kim[1], Gary Yama[2], Aaron Partridge[2], Markus Lutz[2], Thomas W. Kenny[1]

[1]Stanford University,
Departments of Mechanical and Electrical Engineering
Stanford, CA 94305

[2]Robert Bosch Corporation,
Research and Technology Center, North America
Palo Alto, CA 94304

ABSTRACT

Encapsulated micromechanical resonators have been fabricated from single crystal silicon and a method for stabilizing their resonant frequency over temperature has been demonstrated. The method uses high-frequency AC signals applied directly to the resonant structure in order to heat it. By adjusting the power of the heating signal, varying amounts of heat could be added to the resonant structure in order to compensate for the effects of changing external temperature and the variation in resonant frequency was reduced significantly. This method requires minimal changes to existing resonator designs and is applicable to any resonator with a current path through its structure. The resonators examined here exhibited temperature coefficients of resonant frequency of over 210 Hz/°C (170 ppm/°C) without temperature compensation. With compensation, the temperature coefficient was reduced to less than 5 Hz/°C (4 ppm/°C).

INTRODUCTION

Micromachined resonators are of interest for applications in on-chip high frequency signal manipulation and integrated circuit timing [1, 2]. Silicon is a preferred material for high-performance micromechanical resonators because of its high mechanical stiffness and IC compatibility; however, it exhibits a temperature coefficient of stiffness as high as 75 ppm/°C, and a significant temperature coefficient of expansion, 2.6 ppm/°C. These effects cause resonators fabricated in silicon to exhibit large variations in resonant frequency over practical operating temperature ranges. Many important applications require a small variation of resonant frequency with temperature (< 1 ppm/°C), so there is interest in novel integrated temperature compensation approaches. This paper describes the first demonstration of resonator temperature compensation based on direct heating of the resonator structure within a wafer-scale encapsulation. This work is a first step towards our goal of a "micro-oven" consisting of a temperature-regulated encapsulation structure, and demonstrates the ability to merge the electrical connections necessary for thermal measurement, heating, and resonator operation with the wafer-scale hermetic encapsulation process previously developed [3, 4].

FABRICATION

The resonator designs chosen for these experiments are doubly-clamped tuning forks [5], shown in Figure 1. Each beam of the tuning fork measures 220μm x 20μm x 8μm, and the device has a resonant frequency and quality factor (Q) of approximately 1.24 MHz and 12,000 respectively at 23°C.

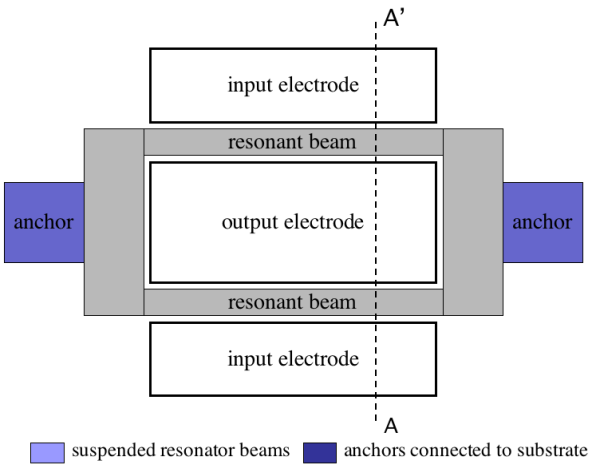

Figure 1 *Schematic plan view of the double-clamped tuning fork resonator design.*

The resonators are fabricated in a silicon-based, IC-compatible, encapsulated process [3, 4], illustrated in Figure 2. Structures are defined in the device layer of an SOI wafer and then encapsulated with a layer of epitaxial silicon. Openings are etched to allow HF vapor release of the resonator, and the final seal is completed with a second epitaxial silicon deposition. A SEM cross-section of a device, taken after the encapsulation has been deposited, is shown in Figure 3.

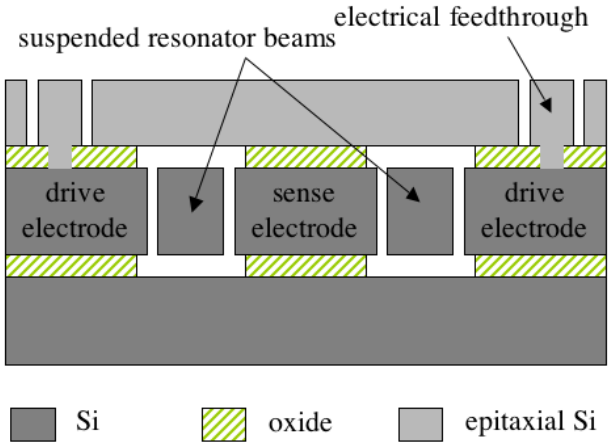

Figure 2 *Schematic cross-section of the encapsulated silicon resonators. The section is from the line A-A' in Figure 1. Electrical feedthroughs permit contact with the encapsulated device. The substrate and device layers are single crystal silicon, and the top encapsulation layer is epitaxial polysilicon.*

Travel support has been generously provided by the Transducers Research Foundation and by the DARPA MEMS and DARPA BioFlips programs.

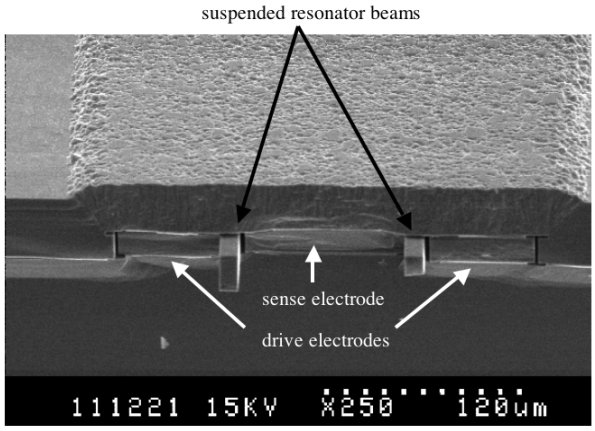

Figure 3 *SEM cross-section of a resonator during fabrication. The section is approximately on the line A-A' in Figure 1, with the resonator beams protruding.*

THEORY

Silicon is an attractive material for microresonator construction because it can be produced with a nearly ideal crystal structure, which should allow for perfectly reproducible. fatigue-free mechanical operation. However, like many semiconductors, silicon exhibits a high material sensitivity to temperature. Values found in literature for temperature coefficient of stiffness are as high as 75 ppm/°C, and a temperature coefficient of expansion of 2.6 ppm/°C. These effects cause the resonant frequency of silicon resonators to exhibit a strong temperature dependence [6]. Figure 4 shows the measured change in resonant frequency of a typical double-clamped tuning fork micromechanical resonator plotted against temperature. The change in resonant frequency with temperature is 214 Hz/°C, or 173 ppm/°C. The relationship is linear in this temperature range. This large temperature coefficient of frequency is attributed to differential thermal expansion between the device layer and the encapsulation layer leading to temperature-induced stress in the resonator.

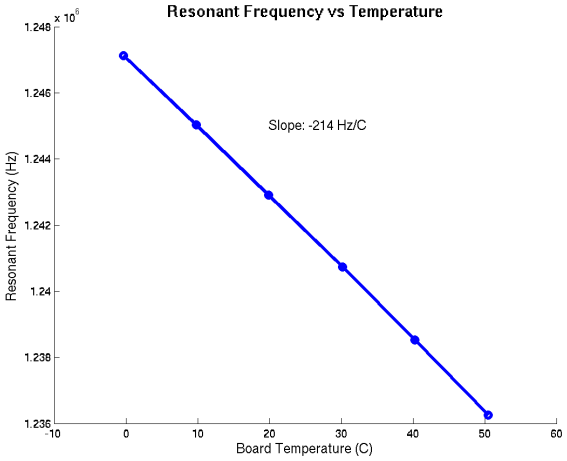

Figure 4 *Plot of resonator resonant frequency vs temperature for a double-clamped tuning fork resonator with a resonant frequency of 1.24 MHz at 25°C. This represents a sensitivity to temperature of 173 ppm/°C.*

Our approach to alleviating this dependence on external temperature is to add heat directly to the resonator beam. For these experiments, a high-frequency AC signal was applied to the beams to raise their temperature by Joule heating. The heating power could then be adjusted as necessary to compensate for the effects of external temperature. A 5 MHz signal frequency was chosen for applying heat power so that the additional voltage on the resonator beams would not interfere with the resonant frequency measurement. Figure 5 shows the relationship between applied heating power and resulting resonant frequency, at various temperatures. The resulting plots are linear, as we expect from the temperature data in Figure 4.

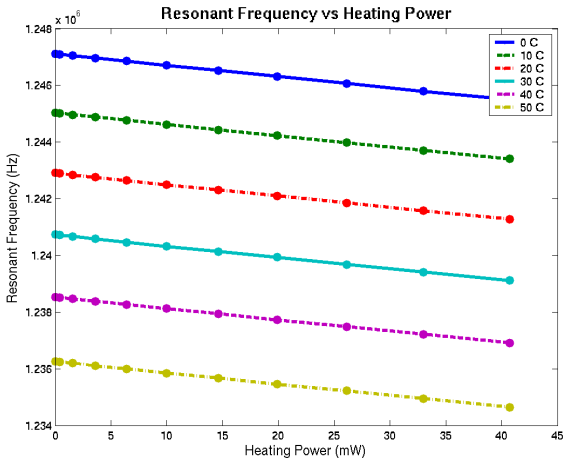

Figure 5 *Plot of resonator resonant frequency vs applied heating power, at various temperatures. The maximum power applied was limited by the capability of the function generator used to generate the heating signal. This corresponds to a maximum frequency change of approximately 1700 ppm.*

There are two ways in which the applied heating power can cause a shift in resonant frequency. First, there is heating of the resonator structure, which causes softening of the bulk modulus of the silicon and compressive stress in the resonator beams due to differential thermal expansion of the beam, the substrate, and the encapsulation layers. There are many unknowns related to heating the resonator structure, including the initial stress in the beam, compressive stress in the beam due to thermal expansion, additional stress induced by the packaging, and the temperature conditions inside the encapsulated cavity. It is clear that the temperature distribution in the resonator due to the applied heating power is not uniform, unlike the temperature distribution due to environmental temperature, and the specific interactions governing the relationship between resonant frequency and temperature are complex.

A finite element model of the microresonator is being developed to study the interactions between external/internal temperature, heater current, and resonant frequency. In this model, we begin by calculating the distribution of the electric current throughout the beam, and then extract the heat deposition as a function of location. A thermal model of the resonator takes the heat input information and computes the temperature distribution within the resonator. This temperature distribution can be used to calculate the local change in bulk modulus as well as thermal expansion effects on the dimensions and effective stiffness of the resonator, and so the resonant frequency can be calculated. Some modeling results for the temperature of the silicon beam are shown in Figure 6. At maximum heating power, the peak temperature of

the beam is expected to be 9-12°C above the ambient, at room temperature (23°C). This correlates with the measured change in resonant frequency, which corresponds to an approximate 10°C change in temperature.

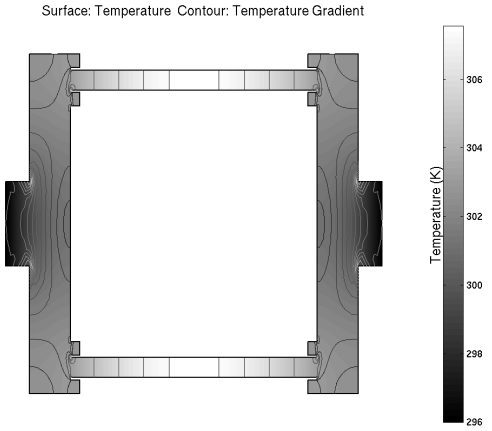

Figure 6 *Plot of calculated temperature distribution due to Joule heating of the resonator beam. Higher temperatures are lighter colors. The temperature gradients are shown by the contour lines.*

The second way in which the applied heating power can cause a shift in the resonant frequency is an electrostatic spring softening effect due to the rectification of the AC heating voltage signal by the quadratic force-voltage relationship in the electrostatic actuator. In our doubly-clamped resonators, differential thermal expansion is dominant. We estimated that the change in resonant frequency due to spring softening was less than 80 ppm, which is the noise due to typical uncontrolled temperature drift. However, the response of the resonator to applied heating is measured, as in Figure 5, and this data is used to calibrate the compensation feedback process, so all of the contributions to resonant frequency change are included in the frequency compensation control.

RESULTS

The resonators were packaged in surface mount IC packages and mounted on printed circuit boards for testing. The temperature of the resonator environment was controlled using a Thermotron S-1.2 temperature chamber, which is capable of maintaining the air temperature in the chamber at +/- 0.1°C. A semiconductor temperature sensor, the LM35 from National Instruments, was used to measure the temperature of the immediate resonator environment with 0.01°C precision.

The resonators are actuated and measured electrostatically, and a DC electrostatic bias is applied to the resonator beams to increase the charge present in the capacitors. As discussed above, a 5 MHz AC signal, generated by a SRS DS345 function generator, was applied to the resonator beams in order to compensate for the effects of external temperature. A circuit, based on the "Bias-T" of Clark, et al [7], was used to apply a DC electrostatic bias to the beam without affecting the DC bias required for the capacitive readout, as shown in Figure 7. The modified bias-T used here is basically high-pass and low-pass filters joined to allow the coupling of the DC bias and the heating signal. A DC blocking capacitor prevents the bias from creating a potential drop across the beam.

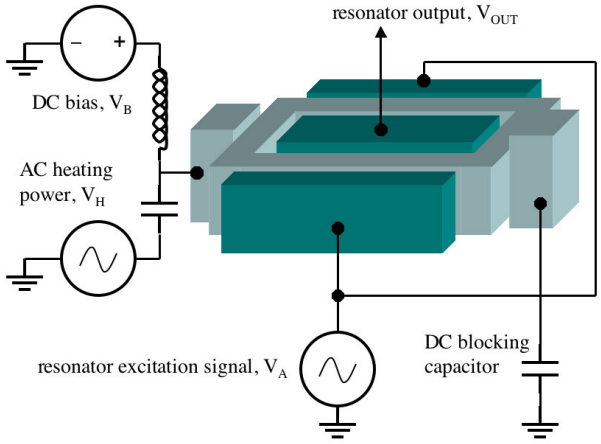

Figure 7 *Electrical connections for measuring the resonator. A "modified Bias-T" circuit allows the AC heating signal to be applied to the resonator beam without allowing the DC bias voltage to create a potential drop across the beam.*

The resonators were measured using a HP4395A network analyzer, which provided a sinusoidal actuation signal to the drive electrodes, and simultaneously measured the response at the sense electrode. The frequency of the actuation signal and input measurement are swept over a frequency range and the amplitude and phase of the response is recorded (divided by the actuation signal to cancel out the effects of any irregularities in the output). A typical resonator measurement is shown in Figure 8. The measurement system was automated so that measurements could be taken over long periods of time. The network analyzer built-in peak detection algorithm was used to determine the frequency at the maximum response, and hence the resonant frequency.

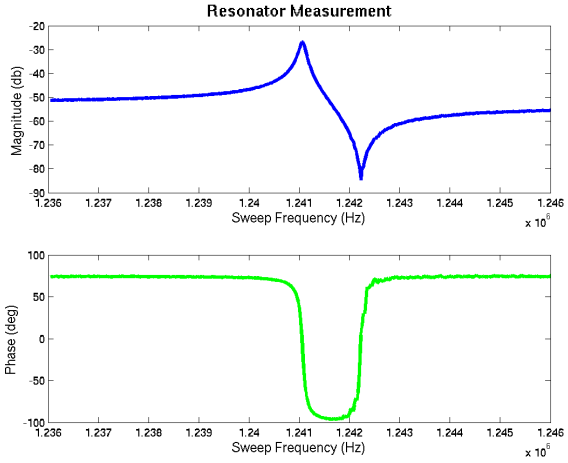

Figure 8 *Bode plot of typical 1.24 MHz resonator response.*

For temperature compensated operation, the temperature inside the chamber was measured. The output power that was required to keep the resonator temperature constant was then computed, based on the results of measurements of the responsiveness of the device to external temperature and to applied heating power (e.g. the data in Figures 4 and 5). This heating power was then applied to the resonator, and measurements were taken. Figure 9 compares the resonant frequency with and without temperature compensation as the ambient temperature is swept over 22 - 15°C. The variation in frequency is reduced over 40x, to

4 ppm/°C, with temperature compensation. The relative temperature range for compensation experiments was limited to slightly less than 10°C, as in Figures 5 and 9, by the amplitude output of the function generator.

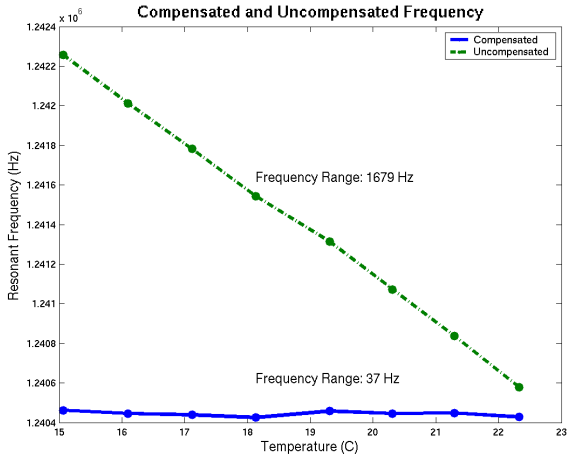

Figure 9 *Plot of resonant frequency vs temperature. Each data point represents an average of 5 measurements, with an average deviation of 2.2 Hz. The change in frequency without compensation is 170 ppm/°C, and with compensation it is 4 ppm/°C.*

Measuring the frequency of the resonator, as described above, required between 60 and 180 seconds to accomplish per measurement, depending on the resolution of the measurement. Temperature fluctuations during that time are the primary source of error in the measurements. These fluctuations were typically less than 0.05°C, which corresponds to approximately 10 Hz (8 ppm) error in each individual measurement of resonant frequency. Averages of multiple measurements were used to reduce the experimental error to less than 5 Hz.

CONCLUSION

A method for directly heating silicon micromechanical resonators in order to achieve resonant frequency stability over temperature has been demonstrated. This approach has the advantage of requiring limited modifications of existing designs, and general applicability to many other designs, and these devices represent an excellent platform for development of compensation approaches that can eventually lead to silicon resonators for high-stability applications. There are some drawbacks in the requirements for external circuitry and the high-frequency signal source; more significantly, because the distribution of heating is uneven, the direct heating approach leads to significant temperature gradients throughout the resonators, and to complex effects on the resonant frequency of the structure. Nonetheless, the results presented here show the feasibility of the direct heating method.

The definitive solution to temperature stability issues is to situate the resonator inside an isothermal chamber with temperature regulation. Our ultimate goal is to produce such a device within a wafer-level encapsulation process. An intermediate step, which has been fabricated but not yet tested, involves localization of the heating at the edges of the resonator, so that the beams are uniformly heated, and more likely to follow a predictable thermal control scheme. Results from these devices are being gathered, and will be presented at the meeting. Future work will be focused on fabrication processes and operational methods for resonators that are encapsulated within truly thermally-regulated enclosures.

ACKNOWLEDGEMENTS

This work was supported by DARPA HERMIT (ONR N66001-03-1-8942), the Robert Bosch Corporation Palo Alto Research and Technology Center, a CIS Seed Grant, The National Nanofabrication Users Network facilities funded by the National Science Foundation under award ECS-9731294, and The National Science Foundation Instrumentation for Materials Research Program (DMR 9504099).

The authors would also like to acknowledge the assistance of Klint A. Rose of Stanford University with some problems in computational methods.

REFERENCES

[1] Nguyen, C.T. *Micromechanical components for miniaturized low-power communications (invited plenary).* in *IEEE MTT-S International Microwave Symposium RF MEMS Workshop on Microelectromechanical Devices for RF Systems: Their Construction, Reliability, and Application.* 1999. Anaheim, California,, pp. 48-77.: IEEE.

[2] Nguyen, C.T. *Transceiver Front-End Architectures Using Vibrating Micromechanical Signal Processors.* in *Topical Meeting on Silicon Monolithic Integrated Circuits in RF Systems.* 2001. Ann Arbor, Michigan, USA: IEEE.

[3] Partridge, A., et al. *New thin film epitaxial polysilicon encapsulation for piezoresistive accelerometers.* in *Micro Electro Mechanical Systems, 2001. The 14th IEEE International Conference on.* 2001.

[4] Park, W.-T., et al. *Wafer Scale Encapsulation of MEMS Devices.* in *InterPack 2003, International Packaging and Technical Conference and Exhibition.* 2003. Maui, Hawaii USA.

[5] Candler, R.N., et al. *Investigation of Energy Loss Mechanisms in Micromechanical Resonators.* in *Transducers '03.* 2003. Boston, MA USA.

[6] Hsu, W.-T. and C.T.-C. Nguyen. *Geometric stress compensation for enhanced thermal stability in micromechanical resonators.* in *Ultrasonics Symposium, 1998. Proceedings., IEEE.* 1998.

[7] Clark, J.R. and C.T.-C. Nguyen. *Measurement techniques for capacitively-transduced VHF-to-UHF micromechanical resonators.* in *Transducers '01 / Eurosensors XV, The 11th International Conference on Solid-State Sensors and Actuators.* 2001. Munich, Germany: Springer.

ENHANCEMENT OF DRIVE-MODE BANDWIDTH IN MEMS VIBRATORY GYROSCOPES UTILIZING MULTIPLE OSCILLATORS

Cenk Acar and Andrei Shkel
Mechanical and Aerospace Engineering Department, University of California Irvine
Irvine, CA, 92697. USA.

ABSTRACT

The limitations of photolithography-based micromachining technologies defines the upper-bound on the performance and robustness of micromachined gyroscopes. Conventional gyroscope designs based on matching the drive and sense modes are extremely sensitive to variations in system parameters. Non-conventional design concepts have been reported that increase bandwidth to improve robustness, but with the expense of response gain reduction. This paper presents a new approach that may yield vibratory MEMS gyroscopes with wider drive-mode bandwidth, without significant sacrifice in response gain. The approach is based on utilizing multiple drive-mode oscillators with incrementally spaced resonant frequencies to achieve wide-bandwidth response in the drive-mode. Enhanced mode-decoupling is also achieved by distributing the linear drive-mode oscillators radially and symmetrically, to form a multi-directional linear drive-mode and a torsional sense-mode; minimizing quadrature error and zero-rate-output. The approach has been implemented on bulk-micromachined prototypes fabricated in a SOI-based process, and experimentally demonstrated.

INTRODUCTION

The tolerancing capabilities of the current photolithography processes and micro-fabrication techniques are inadequate compared to the requirements for production of high-performance inertial sensors. The resulting inherent imperfections in the mechanical structure significantly limit the performance, stability, and robustness of MEMS gyroscopes [1], [2]. Thus, fabrication and commercialization of high-performance and reliable vibratory MEMS gyroscopes have proven to be one of the most challenging tasks in the micro-domain.

The operation principle of the vast majority of existing micromachined vibratory gyroscopes relies on detection of the sinusoidal Coriolis force induced on a vibrating proof-mass. The proof-mass is driven into a constant-amplitude oscillation in the drive direction, generally at resonance. When the gyroscope is subjected to an angular rotation, the sinusoidal Coriolis force is induced in the sense direction. To achieve the maximum possible response gain, the conventional gyroscopes are generally desired to operate at or near the resonance peak of both drive and sense modes. This is typically achieved by designing and electrostatically tuning the drive and sense resonant frequencies to match [3].

The drive and sense mode matching (or near-matching) requirement in vibratory gyroscopes renders the system response very sensitive to variations in system parameters, e.g. due to fabrication imperfections and fluctuations in operating conditions, which shift the drive or sense resonant frequencies [2]. Vacuum packaging of the devices to enhance sensitivity results in extremely narrow response bandwidth, leading to much tighter mode-matching requirements. Extensive research has focused on design of symmetric drive and sense-mode suspensions for mode-matching and minimizing temperature dependence [11]. However, especially for lightly-damped devices, it is recognized by many authors that the mode-matching requirement is well beyond fabrication tolerances; and none of the symmetric designs can provide the required degree of mode-matching without a feedback control [4], [5].

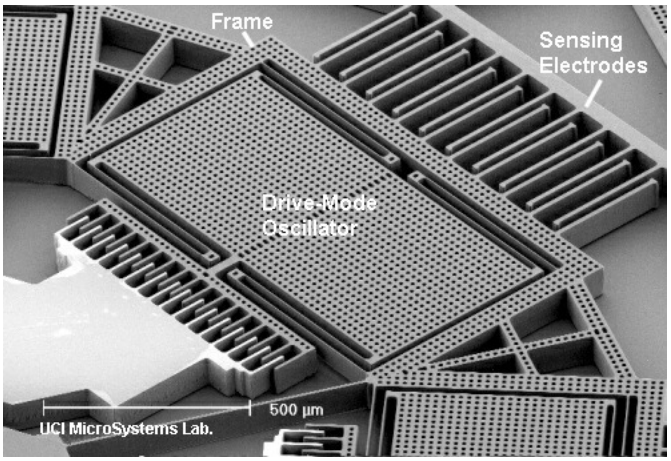

Fig. 1. *SEM micrograph of a distributed-mass micromachined gyroscope prototype, utilizing multiple drive-mode oscillators with incrementally spaced resonance frequencies.*

Furthermore, as the modes are matched closer, the mechanical interference between the modes becomes more significant, resulting in operation instability and drift. In order to suppress coupled oscillation and drift and to minimize the resulting zero-rate drift, various devices have been reported employing decoupled suspension systems for the drive and sense modes [9], [10]. The approach of decoupling drive and sense modes led to the first integrated commercial MEMS gyroscopes produced by Analog Devices.

The mode-matching problem and the quadrature error due to the structural imperfections are the two major challenges in MEMS gyroscope design. We have previously reported gyroscope systems that offer improved robustness by expanding the degree-of-freedom of the dynamical system [6], [7]. Even though increased-DOF gyroscope systems provide significantly increased bandwidth (over 1 kHz), the objective is achieved with the expense of sacrificing the response gain. This paper presents a novel approach that provides wider drive-mode bandwidth in vibratory MEMS gyroscopes with minimal sacrifice in response gain; based on utilizing multiple drive-mode oscillators with incrementally spaced resonance frequencies. The concept was introduced in [8] by these authors, with the preliminary experimental results on the first generation prototypes. In this paper we generalize the approach, theoretically and experimentally explore the involved design trade-offs to achieve a wide drive-mode bandwidth, and present the experimental characterization results that demonstrate the feasibility of the design concept.

THE APPROACH

The proposed approach explores the possibility of increasing the drive-mode response bandwidth of micromachined gyroscopes, without sacrificing gain, by utilizing multiple resonators in the drive-mode. Also, by distributing the drive-mode oscillators symmetrically around the center of a supporting frame, multi-directional linear drive-mode and a single torsional sense-mode are formed (Figure 2),

0-9640024-5-0/hh2004/$20©2004TRF
DOI 10.31438/trf.hh2004.95

Solid-State Sensors, Actuators, and Microsystems Workshop
Hilton Head Island, South Carolina, June 6-10, 2004

effectively decoupling the drive and sense modes. Thus, zero-rate-output and quadrature error due to mechanical mode coupling are suppressed effectively in the presence of structural imperfections. Furthermore, the sensing electrodes attached to the supporting frame do not deflect due to the drive-mode oscillations.

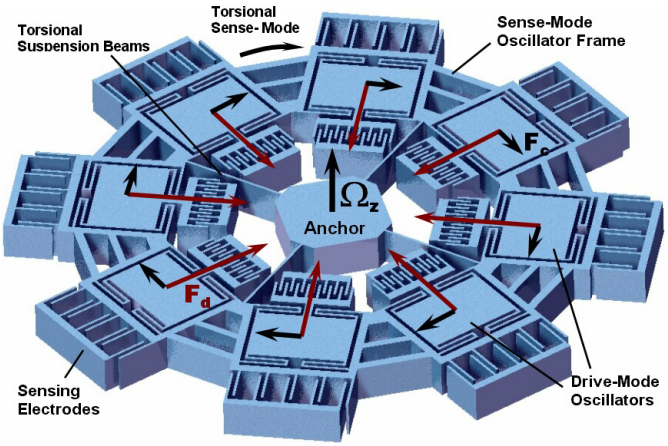

Fig. 2. *Conceptual illustration of the distributed-mass gyroscope with 8 symmetric drive-mode oscillators, where F_d and F_c denote the drive and the Coriolis forces on each mass, respectively.*

The distributed drive-mode oscillators are driven in-phase along the axes normal to the tangents of the supporting frame, and constrained in the tangential direction with respect to the supporting frame. In the presence of an angular rotation rate about the z-axis, the Coriolis force $F_{ci} = 2m_i\Omega_z\dot{x}_i$ is induced on each proof mass orthogonal to each drive-mode oscillation direction (Figure 2). Thus, each of the induced Coriolis force vectors lie in the tangential direction, combining to generate a resultant sinusoidal moment on the supporting frame. The net moment excites the supporting frame into torsional oscillations about the z-axis, which is detected by the sense capacitors, providing measurement of angular rate. Thus, the simplified equation of motion of the supporting frame in the sense-direction becomes

$$I_z\ddot{\phi} + D_z\dot{\phi} + K_z\phi = \sum_{i=1}^{n} \vec{r}_{ci} \times \vec{F}_{ci} = \sum_{i=1}^{n} 2r_c m_i \Omega_z \dot{x}_i \cdot \hat{k}$$

where r_{ci} is magnitude of the position vector $\vec{r}_{ci}$ of the i^{th} oscillator center-of-mass, ϕ is the torsional deflection of the supporting frame, I_z denotes the moment of inertia of the supporting frame combined with the proof masses, D_z is the sense-mode torsional damping ratio, and K_z is the torsional stiffness of the suspension.

Wide-Bandwidth Operation

In the presented design concept, a wide-bandwidth operation region is achieved in the drive-mode frequency response, by designing or actively tuning the resonance frequency of each drive-mode oscillator to be incrementally spaced (Figure 3a). When the tangential Coriolis forces induced on each proof mass are combined, a constant-amplitude sinusoidal Coriolis moment is achieved over a wide frequency range (Figure 3b). The device is nominally operated in the flat region of the Coriolis moment frequency response. Thus, fluctuations in system parameters that shift oscillator resonance frequencies will not result in a significant change in the total Coriolis torque through the operation frequency band. If the sense-mode resonance frequency is designed to be accommodated in the same frequency band (Figure 3b), the requirement on the degree of mode-matching is relaxed, and robustness against structural and thermal parameter fluctuations is achieved.

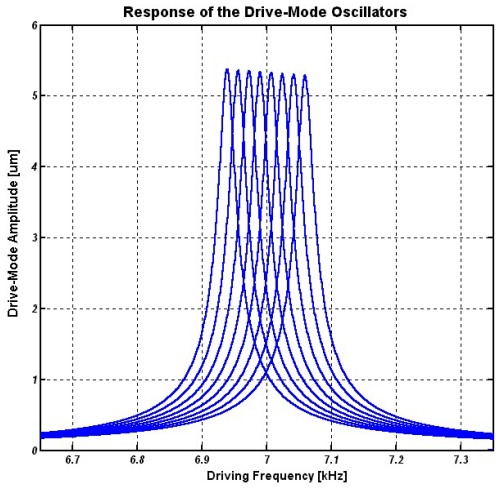

(a)

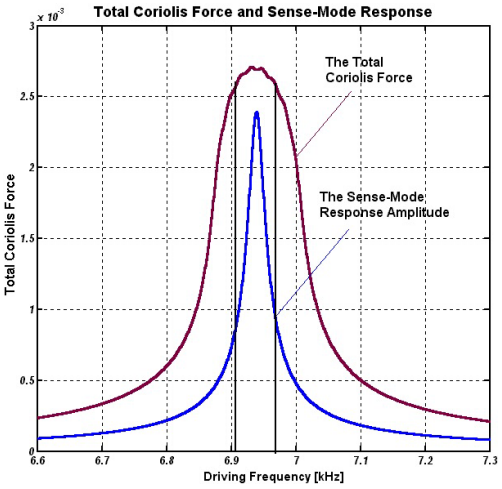

(b)

Fig. 3. *(a) The frequency responses of the distributed drive-mode oscillators; (b) The frequency spectrum of the total Coriolis torque generated by the distributed drive-mode oscillators.*

It should be noticed that the resonance frequency separation of the oscillators are dictated by the bandwidth of the response, which is determined by damping. In order to obtain a flat operation region in the drive-mode, the frequency separation should be less than the bandwidth of a single oscillator. If the separation of frequencies is large for high-Q resonators, the individual resonance peaks become more emphasized in the response (Figure 4), and the flat operation region will not be achieved in the drive-mode response; which is experimentally illustrated in the next section.

EXPERIMENTAL ANALYSIS OF TRADE-OFFS

Fabrication of Prototypes

The wide-bandwidth design concept was analyzed experimentally using bulk-micromachined prototype structures, fabricated in the UCI Integrated Nano-Systems Research Facility (Figure 1). Two different prototype gyroscope structures utilizing the wide-bandwidth design concept were designed: one type of structure employing comb-drive actuation to achieve large drive amplitudes, and another type employing parallel-plate actuation for a wide electrostatic tuning range.

For the fabrication of the prototypes, a one-mask process based on SOI (Silicon-on-Insulator) wafers was developed. The process relies

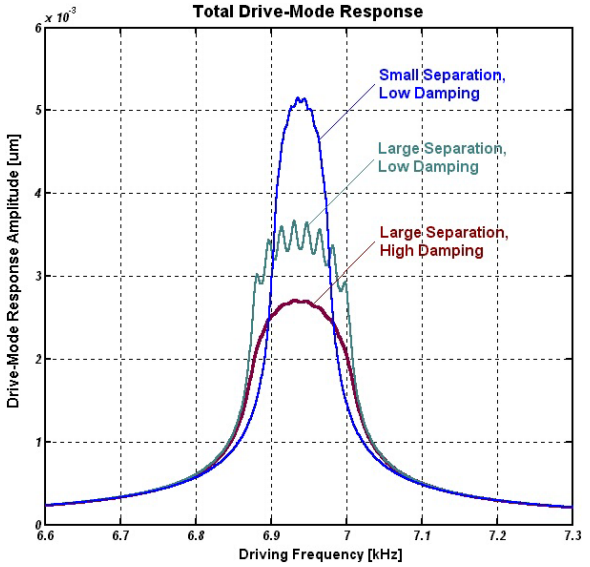

Fig. 4. *The effect of damping and resonance frequency separation on the drive-mode response gain and bandwidth (effecting sensitivity and robustness, respectively).*

on deep-reactive ion etching (DRIE) through the $100\mu m$ device layer of the SOI wafer, and front-side release of the structures by etching the Oxide layer in HF solution. The process and the device design was optimized to minimize notching at the Oxide interface and excessive undercutting. In the device, $15\mu m \times 15\mu m$ holes were used to perforate the suspended structures, and $10\mu m$ gaps were used in the sensing and actuation electrodes. Anchors were designed as unperforated areas larger than $40\mu m \times 40\mu m$.

Through Finite Element Analysis simulations using the package MSC Nastran/Patran, the resonance frequency of the drive-mode oscillators were obtained at 6.98kHz with an elastic modulus of 130GPa for single-crystal Silicon in (100)-direction. The torsional sense mode resonance frequency of the structure about the sense axis was then located at ω_z =6.79kHz with four torsional suspension beams, by iteratively optimizing the beam length.

Experimental Results

The dynamic response of the linear drive-mode oscillators and the torsional sense-mode of the prototype gyroscope were characterized in a cryogenic MMR vacuum probe station. The frequency response of the prototype devices were acquired under varying pressure values and at room temperature, using off-chip sensing electronics. One-port actuation and detection was employed for characterization of the drive-mode oscillators, where a single electrode was used for both driving and sensing at the same time.

The resonance frequencies of the drive-mode resonators were observed to be scattered between 4.546 kHz and 5.355 kHz within a 809Hz frequency band (Figure 5a). The random separation of the identically-designed drive-mode resonance frequencies resulted from the fabrication imperfections. The deviation of approximately 26% from the FEA results were attributed to lateral over-etching during DRIE, the resolution of the mask used in fabrication, and the exposure and development steps of the photolithography process.

Figure 5b presents the experimentally acquired frequency responses of the Port-1 oscillator, from atmospheric pressure to 1 Torr. Least-square curves were fit to each experimental data curve for estimation of the Q factor and the bandwidth, which are summarized in Table 1.

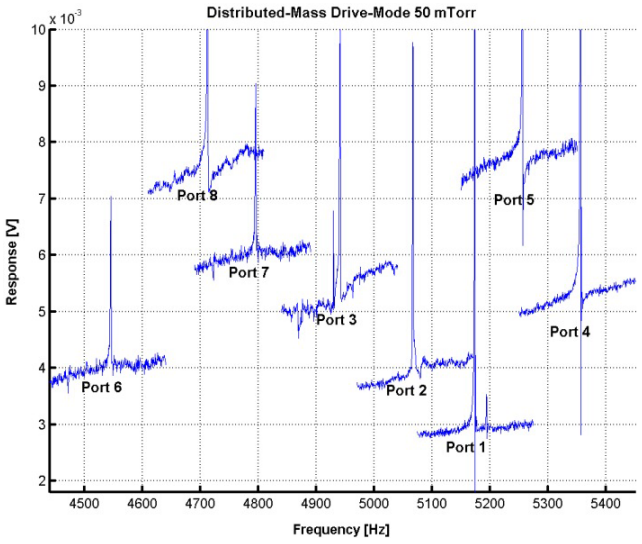

(a)

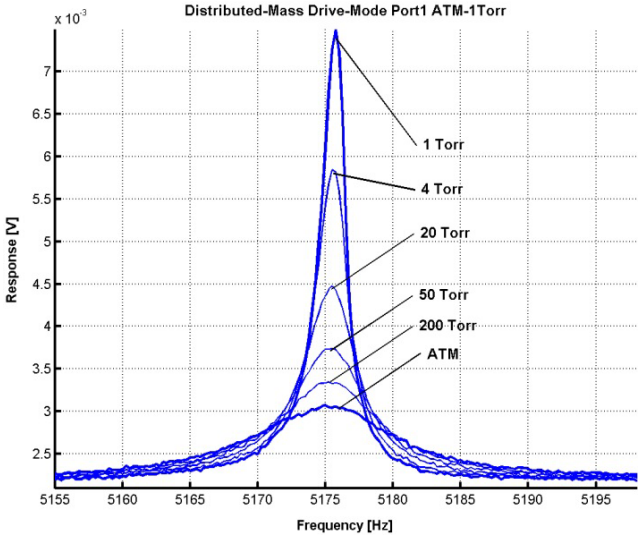

(b)

Fig. 5. *(a) Experimental frequency response measurements of the 8 drive-ports at 50mTorr pressure; (b) Experimental measurements of the drive-mode frequency response of one of the oscillators, at different pressure values.*

Drive-Mode

Pressure	Q Factor	BW
1 Torr	4187	1.24Hz
4 Torr	2912	1.78Hz
20 Torr	1861	2.78Hz
50 Torr	1339	3.87Hz
200 Torr	985	5.25Hz
ATM	598	8.65Hz

Sense-Mode

Pressure	Q Factor
1 Torr	921
10 Torr	430
100 Torr	119
200 Torr	87
ATM	42

Table 1. *The calculated Q factor and the bandwidth values from the least-square curves for each pressure.*

The bandwidth of the drive-mode response even at atmospheric pressure was observed to be too narrow to achieve wide-band operation without electrostatic tuning of the drive-mode frequencies. In order to achieve a wider range of electrostatic tuning, the prototype with the parallel-plate actuated drive-mode oscillators (Figure 1) was tested, and the resonance frequencies of each drive-mode oscillator were electrostatically tuned to achieve uniform and smaller separation of frequencies.

After electrostatic tuning of the parallel-plate oscillators for 10Hz spacing, the close spacing of the drive-mode resonance frequencies allowed all of the resonators to be excited together, to jointly generate a resultant Coriolis moment. The total Coriolis moment, which is obtained by summing the experimentally measured response of the eight drive-ports, was observed to provide a flat range of over 140Hz (Figure 6). When the experiments were repeated at reduced pressures, the resonance peaks in the flat region of the overall response became more emphasized, as was theoretically illustrated in the previous section. Based on the experimental results, it was concluded that 200 to 300 Torr is the optimal pressure for the parallel-plate devices to achieve a flat wide-bandwidth drive-mode response with 10Hz spacing.

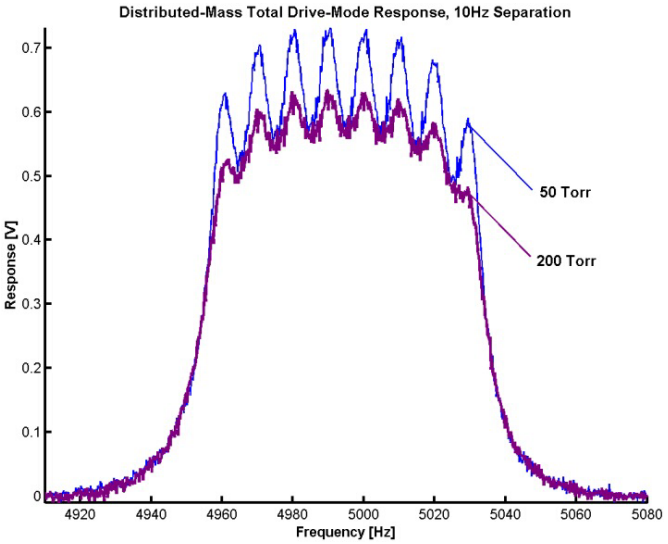

Fig. 6. *Experimental frequency response measurements of the total Coriolis force induced in the sense-mode, obtained by summing the measured drive-mode response of the drive ports.*

The sense-mode resonance frequency of the frame was measured at 3.758kHz with 20V DC bias voltage. Figure 7 presents the experimentally acquired frequency responses of the torsional sense-mode, from atmospheric pressure to 10 Torr. At pressures around 200 Torr, the parallel-plate devices were observed to provide a flat wide-bandwidth drive-mode response with individual tuning for 10Hz spacing, and sufficient off-resonance sense-mode gain.

CONCLUSION

A novel design approach based on utilizing multiple drive-mode oscillators with incrementally spaced resonance frequencies was presented, which provides wider drive-mode bandwidth in vibratory MEMS gyroscopes without significant sacrifice in response gain. The operational principles were theoretically illustrated, and experimentally verified. The linear drive-mode oscillators and the torsional sense-mode of the prototype gyroscope structures were characterized under varying pressure values. The resonance frequencies of the identically-designed drive-mode resonators were observed to be scattered within a 809Hz frequency band, due to the mask resolution and the fabrication imperfections. This phenomenon could be exploited in future designs, to naturally provide the required frequency separation. The bandwidth of the drive-mode response even at atmospheric pressure was observed to be too narrow to achieve wide-band operation without electrostatic tuning of the drive-mode frequencies. After electrostatic tuning of the parallel-plate oscillators for 10Hz spacing, the close spacing of the drive-mode resonance

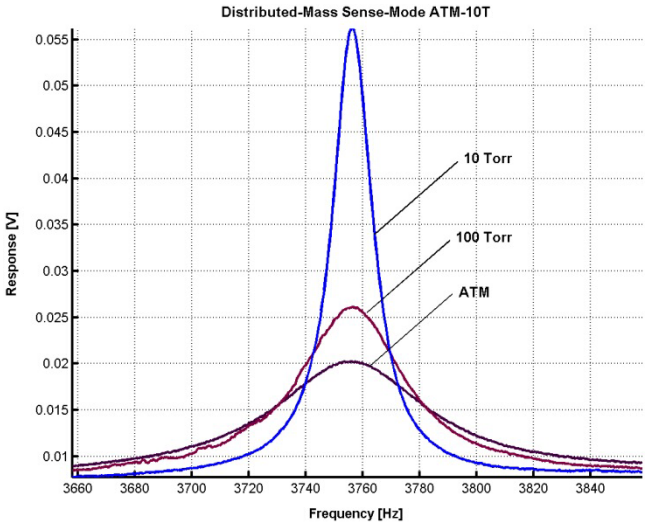

Fig. 7. *Experimental measurements of the torsional sense-mode frequency response, under different pressure conditions.*

frequencies allowed all of the resonators to be excited together, to jointly generate a resultant Coriolis torque. The total Coriolis torque was observed to provide a flat range of over 140Hz. At pressures around 200 Torr, the flat wide-bandwidth drive-mode response was achieved together with sufficient off-resonance sense-mode gain, experimentally demonstrating the feasibility of the wide-bandwidth drive mode principle. The next generation prototypes will be fabricated using higher resolution masks to minimize random scattering of the drive-mode resonance frequencies, thus allowing to use comb-drive oscillators for larger drive-mode amplitudes.

ACKNOWLEDGEMENTS

Travel support has been generously provided by the Transducers Research Foundation and by the DARPA MEMS and DARPA BioFlips programs.

REFERENCES

[1] A. Shkel, R. Horowitz, A. Seshia, S. Park and R.T. Howe. Dynamics and Control of Micromachined Gyroscopes. *American Control Conf., CA*, 1999.

[2] A. Shkel, R.T. Howe, and R. Horowitz. Modeling and Simulation of Micromachined Gyroscopes in the Presence of Imperfections. *Int. Conf. on Modeling and Simulation of Microsystems*, 1999.

[3] W.A. Clark, R.T. Howe, and R. Horowitz. Surface Micromachined Z-Axis Vibratory Rate Gyroscope. *Proc. Solid-State Sensors and Actuators*, Hilton Head, SC, June 1996.

[4] S. Park and R. Horowitz. Adaptive Control for Z-Axis MEMS Gyroscopes. *American Control Conference, Arlington, VA*, June 2001.

[5] R.P. Leland. Adaptive Tuning for Vibrational Gyroscopes. *Proceedings of IEEE Conference on Decision and Control, Orlando, FL*, Dec. 2001.

[6] C. Acar, A. Shkel. Four Degrees-of-Freedom Micromachined Gyroscopes. *Journal of Modeling and Sim. of Microsystems, Vol. 2*, pp. 71-82, 2001.

[7] C. Acar, A. Shkel. Non-Resonant Micromachined Gyroscopes with Structural Mode-Decoupling. *IEEE Sensors Journal, Vol. 3, No. 4, pp. 497-506*, 2003.

[8] C. Acar, A. Shkel. Distributed-Mass Micromachined Gyroscopes for Enhanced Mode-Decoupling. *IEEE Sensors Conference, September 2003, Toronto, Canada*.

[9] J.A. Geen. A Path to Low Cost Gyroscopy. *Solid-State Sensor and Actuator Workshop*, Hilton-Head, SJ, 1998, pp. 51-54.

[10] W. Geiger, et.al. Decoupled Microgyros and the Design Principle DAVED. *IEEE Sensors Journal*, 2001, pp. 170-173.

[11] S.E. Alper, and T. Akin. A Symmetric Surface Micromachined Gyroscope with Decoupled Oscillation Modes. *Sensors and Actuators A*, Vol. 97, 2002, pp. 347-358.

HIGH FREQUENCY MICROMECHANICAL PIEZO ACTUATED DISK RESONATOR

Le Yan[†], Wei Pang*, Jian Wu[§], William C. Tang[‡], and Eun-Sok Kim*

[†]Dept of Mechanical and Aerospace Engineering
[§]Dept. of Electrical Eng. and Computer Science
[‡]Department of Biomedical Engineering
University Of California, Irvine
Irvine, CA, 92697-2715

[*]Dept. of Electrical Engineering
University of Southern California
Los Angeles, CA, 90089-0271

ABSTRACT

This paper presents the design, simulation, fabrication and testing of a piezo transduced high frequency micromechanical resonator. The resonator is designed to operate in the wine-glass mode and the anchors are optimized to both suppress spurious modes and minimize the energy loss into the substrate. The resonator is fabricated with a simple 4-mask low temperature process from SOI wafer. The highest temperature during the process is 250°C, allowing post-COMS integration compatibility. A prototype resonator with measured diameter of 100 μm was tested in air using non-optimized experimental setup, with measured resonant peaks at 44.97 MHz and 138.5 MHz, which match the simulated result from Ansys©. The quality factor of 35 at 138.5 MHz is extracted, and is expected to be substantially higher if measured in vacuum with calibrated RF cables.

INTRODUCTION

Due to their small sizes, on-chip integration potential, and better performance, micromechanical resonators are attractive as replacements for the off-chip filters and oscillators currently used in communication systems. Significant process has been made in the last decade in this technology, with high quality factors (>10,000) in GHz range with impedance matching being the main focuses of current research activities. The state-of-research reported in [**1**] and [**2**] a *Q* factor of 14,600 at frequency of 1.2 GHz. However, the impedance matching between the resonators and signal pickup circuits remained unsolved, and the nanometer-scale capacitive gap required by this approach posed a fabrication challenge. An SOI based high frequency disk resonator was presented in [**3**], in which a Quality factor of 39,300 at 147.8 MHz was reported. This result was superior than its polysilicon counterpart [**4**], but the nano-gap remains inevitable for electrostatic transduction. A piezoelectric thin film micromechanical beam resonator was reported in [**5**], and SOI counterpart of this clamp-clamped beam resonator was demonstrated in [**6**], although the *Q* values were high, the frequencies were in the KHz to low MHz range.

In RF range, piezoelectric transduction may provide significant advantages over capacitive transduction, especially in impedance matching, since the admittance ratio between piezoelectrically transduced clamp-clamp beam resonator and electrostatically transduced plate resonator is proportional to the second-order resonant frequency [**5**]. The current work is motivate by the need to solve the impedance matching problem of capacitively transduced resonator while reaching a frequency and quality factor of the same order. This paper introduces the first wineglass mode disk resonator using piezoelectric transduction to circumvent the nano-gap fabrication requirement and to enable impedance matching. The design, simulation, fabrication and characterization results at the first and second wineglass mode are presented.

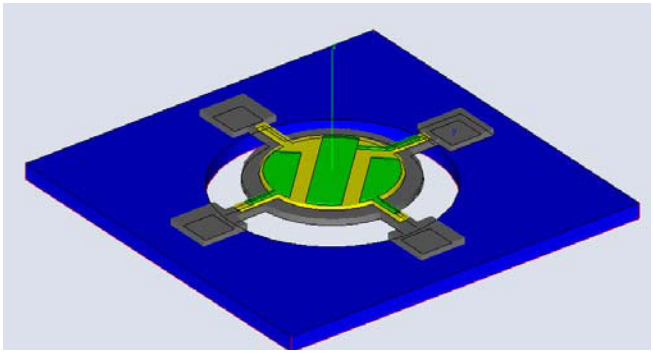

Figure 1. *The perspective view of the wine-glass mode resonator design. The resonator is supported by four anchor beams at its quasi-node positions, and the length of the anchor beams is designed to be quarter acoustic wavelength to minimize energy loss. [8]*

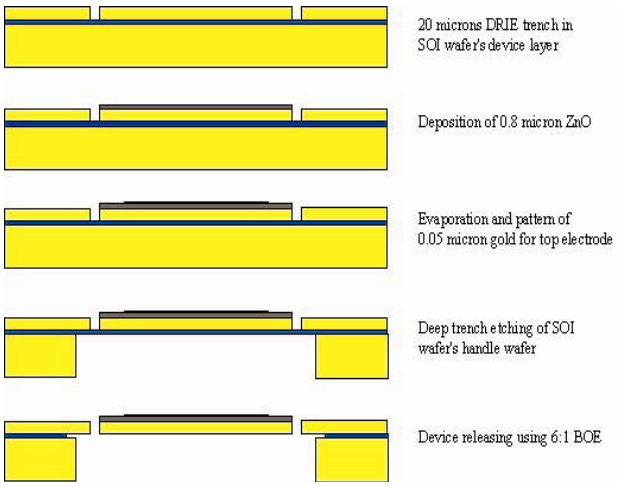

Figure 2.*The detailed process flow for the piezo transduced disk resonator, The highest process temperature is 250°C at the zinc oxide sputtering step.*

RESONATOR FABRICATION

Figure 1 shows the perspective view of the resonator. This resonator is fabricated with a 4-mask process from SOI wafer, eliminated the need for high-temperature deposition of structural and sacrificial thin films.

The highest processing temperature was the ZnO sputtering at 250ºC, which offers the opportunity for post-CMOS integration. Also, the single-crystalline silicon is superior to polysilicon because of its higher material quality factor, lower intrinsic stress,

Travel support has been generously provided by the Transducers Research Foundation and by the DARPA MEMS and DARPA BioFlips programs.

and more predictable mechanical and electrical properties. Thin-film zinc oxide is chosen as the piezoelectric transducer for its high electromechanical coupling coefficient and mature fabrication process [**7**]. A thin layer of gold (500Å) is used for top electrode and the heavily-doped silicon serves as both structure layer and the bottom electrode [**8**], which simplifies the process by eliminate one step of metal evaporation and patterning. Structural layer is designed to be 20 μm thick to suppress the out-of-plain spurious modes. Figure 2 shows the cross-sectional views of the process flow.

The first masking and etching step defined the resonator, in which 10-μm-wide trenches were etched through the thickness of the <100> device layer of the SOI wafer with inductively coupled plasma (ICP) deep reactive ion etching (DRIE), exposing the buried oxide layer. A thin layer of zinc oxide (0.8 μm) was then deposited by RF sputtering with the Sputtersphere822 system in the USC MEMS group. The zinc oxide was then etched using solution of acetic acid, phosphorus acid and DI water with concentration of 1:1:110. This wet etching process produced substantial undercut and was the main cause for yield loss. 500Å of Gold was evaporated and patterned with lift-off to form the top electrode. The bottom side of the SOI wafer was patterned with double-side alignment and etched through with DRIE to the oxide layer. This backside opening was necessary to facilitate removal of the buried oxide layer with 6:1 Buffered Oxide Etchant (BOE), which was substantially faster than etching from the front side. Two prototypes of the resonators are shown in Fig. 3. Figure 4 shows the side wall profile of the DRIE-etched disk. The scalloping surface roughness was typical of an un-optimized DRIE process, and very likely contributed to surface losses.

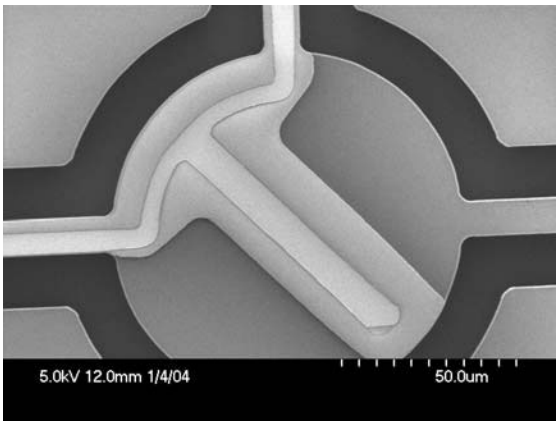

(a)

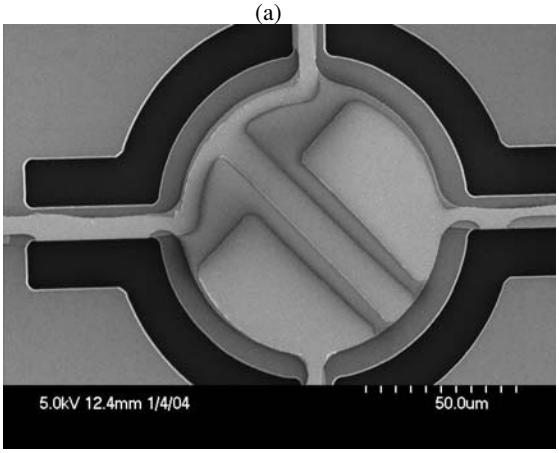

(b)

Figure 3. *The SEM pictures of 100-μm-diameter resonators in (a) one Port and (b) two-port configuration.*

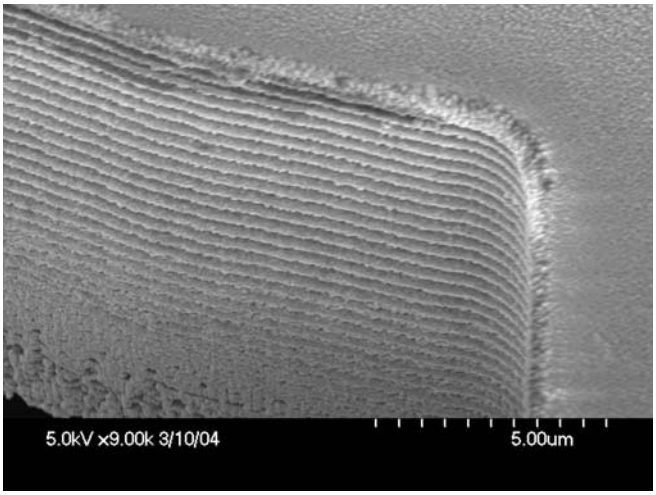

Figure 4. *SEM of the side wall profile of the disk resonator. The scalloping surface is typical of some DRIE process, and may likely contribute to surface energy loss.*

MEASUREMENT AND SIMULATIONS

The one port resonator with diameter of 100 μm and four supporting beams (10 μm wide by 42.6-μm-long) was tested with HP8753D network analyzer under atmospheric pressure. This initial test setup was not optimized. The uncalibrated DC cables and probes induced significant signal loss and partially contributed to the observed low quality factors. Figure 5 shows the measured microwave reflection coefficient S_{11}. The impedance (Z) was evaluated from the measured S_{11} with:

$$S_{11} = (Z - 50)/(Z + 50)$$

The calculated impedance is plot in Fig. 6. The resonant peaks were determined at zero imaginary impedance, and were 44.97 MHz and 138.5 MHz for the first and second modes, respectively. The quality factors were calculated with the following formula [**9**]:

$$Q = \frac{f}{2}\frac{\partial Z_{\text{phase}}}{\partial f}$$

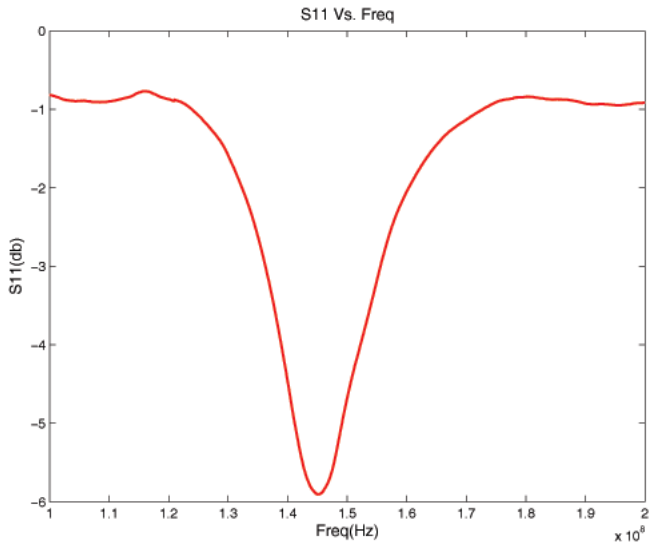

Figure 5*. The measured S_{11} from a one port disk resonator.*

The evaluated Q values were 3 and 30 for the first and second resonances, respectively.

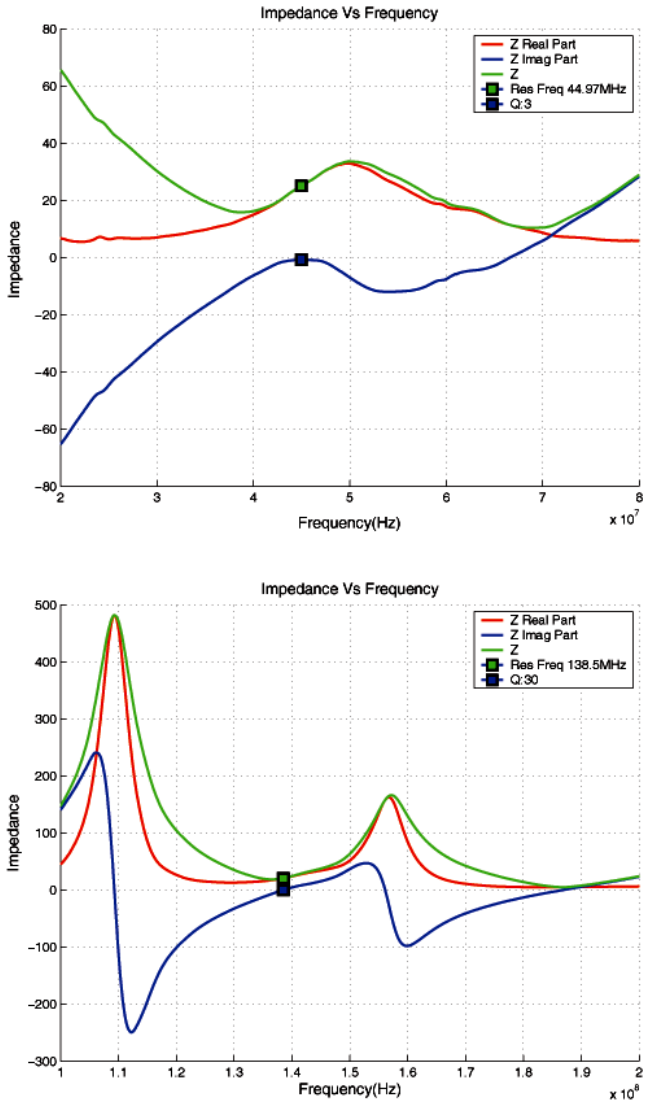

Figure 6. *The calculated impedance of the one port resonator with diameter of 100μm at (top) sweeping frequency from20 MHz to80 MHz and (bottom) sweeping frequency from 10 MHz to 200 MHz.*

The resonator was simulated with Ansys©. The first and second wineglass modes were obtained at 43.5 MHz and 126 MHz, respectively. These simulated results matched the measured resonant peaks well (within 3% and 9%, respectively) and validated the vibration modes. Figure 7 shows the simulation results.

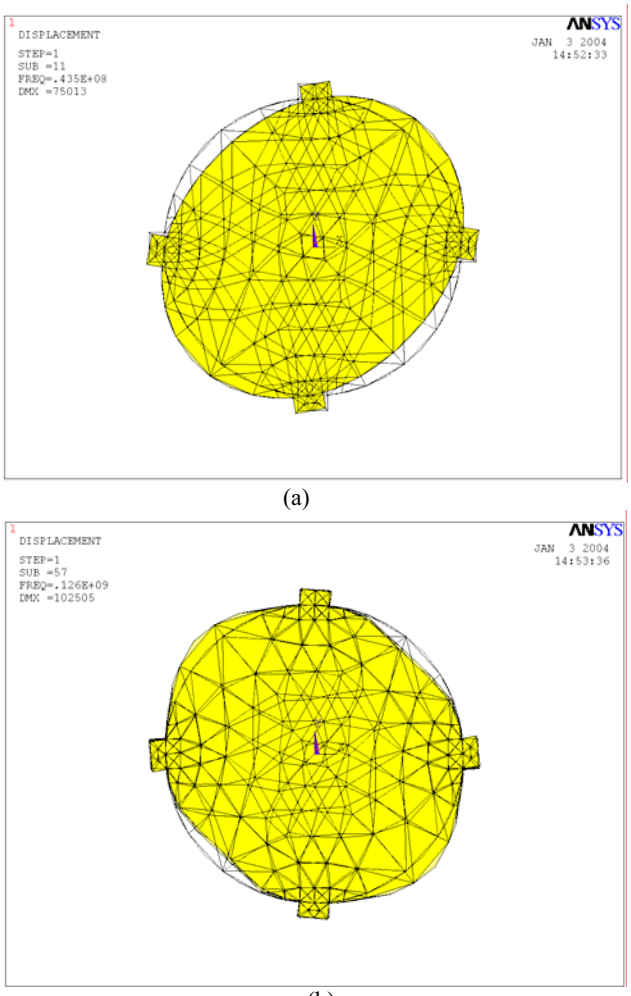

Figure 7. *The simulation result of the 100-μm disk resonator at the first and second wineglass resonant modes, which corresponds to resonant frequencies of 43.5 MHz and 126 MHz, respectively.*

CONCLUSIONS AND FUTURE RESEARCH

By employing piezoelectric transduction, the nano-gap fabrication required for capacitive transduction is eliminated, and, more importantly, the impedance has been demonstrated for the first time, to match the 50 ohm transmission line at 44.97 MHz and 138.5 MHz. The first-generation devices were fabricated, revealing needs for improvements. The test setup will also be optimized to ascertain more accurate Q values. Future efforts will concentrate on raising the resonant frequencies from VHF to UHF by moderately reducing the diameter and improving Q substantially by optimizing the design and fabrication processes. First, the sidewall scalloping roughness can be substantially reduced by carefully tuning the DRIE process. Further smoothness may be achieved with a brief thermal oxidation and oxide removal with 2% HF, as shown in [**10**]. Second, the beam design will be improved to enhance Q factors. The current 10-μm width of the supporting beams is overly conservative and thus contributes to energy loss. It will be reduced to level comparable with [**3**] in future devices. The number of anchor beams should also be reduced, as indicated in [**11**] and [**12**]. Third and finally, excessive ZnO at unnecessary location has been proven to contribute to low quality factors and should be removed. It has been demonstrated in

[**6**] that the quality factor could be improved by a factor of 2 by removing unnecessary ZnO.

REFERENCES

1. J. Wang, J. E. Butler, T. Feygelson and C. T.-C. Nguyen "1.51 GHz Nanocrystalinge Diamond Micromechanical Disk Resonator With Material-Mismatched Isolating Support," *Proceedings of the 17th IEEE International Conference on Micro Electro Mechanical Systems,* Maastricht, The Netherlands, Jan. 25–29, 2004, pp 641–644.

2. S. Li, Y. Lin, Y. Xie, Z. Ren and C. T.-C. Nguyen "Micromechanical 'Hollow-Disk' Ring Resonator," *Proceedings of the 17th IEEE International Conference on Micro Electro Mechanical Systems,* Maastricht, The Netherlands, Jan. 25–29, 2004, pp 821–824.

3. S. Pourkamali and F. Ayazi, "SOI-Based HF and VHF Single-Crystal Silicon Resonators with Sub-100 Nanometer Vertical Capacitive Gaps," *Technical Digest of the 12th International Conference on Solid State Sensors, Actuators and Microsystems*, Boston, June 8–12, 2003, pp 837–840.

4. J. R. Clark, W.-T. Hsu, and C. T.-C. Nguyen, "High-*Q* VHF Micromechanical Contour-Mode Disk Resonators," *Proceedings of the IEEE International Electron Devices Meeting,* San Francisco, CA, Dec. 11–13, 2000, pp 399–402.

5. Don L. DeVoe, "Piezoelectric Thin Film Micromechanical Beam Resonators," *Sensors and Actuators A,* Vol. 88 (2001) pp 263–272.

6. G. Piazza, R. Abdolvand, and F. Ayazi, "Voltage-Tunable Piezoelectrically-Transduced Single-Crystal Silicon Resonators on SOI Substrate," *Proceedings of the 16th IEEE International Conference on Micro Electro Mechanical Systems*, Kyoto, Japan, Jan. 19–23, 2003, pp 149–152.

7. T. Xu, G. Wu, G. Zhang and Y. Hao, "The compatibility of ZnO Piezoelectric Material with Microfabrication Process," *Sensor and Actuator A,* Vol. 104, pp 61–67.

8. Analog Devices product specification 100.126401

9. H. Kim, B. Ju, Y. Lee, S. Lee, J. Lee and S. Kim, "A Novel Suspended Type Thin Film Resonator (SFTR) Using the SOI Technology," *Sensors and Actuators A,* Vol. 89 (2001), pp 255–258.

10. R. E. Mihailovich, and N. C. MacDonald, "Dissipation Measurements of Vacuum-Operated Single-Crystal Silicon Microresonators," *Sensors and Actuators A ,* Vol. 50, 199, (1995)

11. W. Pang, H. Zhang, S. Whangbo and E. S. Kim, "High Q Film Acoustic Wave Resonator from 2.4 Ghz to 5.1GHz," *Proceedings of the 17th IEEE International Conference on Micro Electro Mechanical Systems,* Maastricht, The Netherlands, Jan. 25–29, 2004, pp. 805–808.

12. M. Abdelmoneum, M. Demirci, and C. T.-C. Nguyen, "Stemless Wineglass Mode Disk Micromechanical Resonators," *Proceedings of the 16th IEEE International Conference on Micro Electro Mechanical Systems, Kyoto*, Japan, Jan. 19–23, 2003, pp 698–701.

NANORIBBED TORSIONAL OSCILLATORS OPTIMIZED FOR HIGH-FREQUENCY FORCE SENSING

Benjamin W. Chui, Charles T. Rettner, H. Jonathon Mamin, Raffi Budakian, and Daniel Rugar
IBM Research Division, Almaden Research Center, San Jose, CA 95120
ben.chui@california.com, rugar@almaden.ibm.com

ABSTRACT

In this paper, we focus on ultrasensitive cantilevers for the detection of nuclear magnetic resonance (NMR) at frequencies that coincide with the nuclear spin precession (Larmor) frequency, around 1 MHz. The small size of these cantilevers precludes the usual practice of locating the reflective paddle near the tip, so a torsional configuration has to be used to allow the paddle to be situated at the distal end, providing improved optical access. These torsional oscillators, fabricated in part with electron-beam lithography, have ribs 200 nm wide and 1.5 μm tall attached to arms 200 nm thick and 12 μm long. Fabrication details and characterization results are presented.

INTRODUCTION

Previously, we have reported on mass-loaded cantilevers for magnetic resonance force microscopy (MRFM) **[1]**. These diving-board style cantilevers, which were 90 μm long with a natural frequency around 5 kHz, have been used to detect electron spin resonance with close to single-spin sensitivity. In that experiment, the cantilevers measured the low-frequency modulation of the *longitudinal* component of the electron spin **[2]**. Ultimately, we hope to extend this capability to nuclear-spin detection and explore a new mode of operation where the cantilever oscillates synchronously with the *transverse* component of the spin precession **[3]**. In the case of hydrogen nuclei (i.e., protons) in a 250-Gauss magnetic field, this precession frequency (called the Larmor frequency) is approximately 1 MHz.

In order to operate at megahertz frequencies while maintaining attonewton force sensitivity, the cantilever must be thin (e.g., 300 nm thick) and short (e.g., 20 μm or less) if the standard diving-board configuration is to be used. Sensing cantilever motion with our standard technique of optical interferometry in this case, however, could be challenging. Since the cantilever is positioned very near (and in our case perpendicular to) the sample, the sample can block optical access to the tip where the reflective paddle is located (Fig. 1a). If the paddle is moved further back (away from the tip and towards the base), a mechanical disadvantage would be introduced with respect to tip motion, ultimately reducing optical detection sensitivity. Ideally, one would like to spatially separate the optically sensed region from the probe-tip region *without* introducing a mechanical disadvantage or sacrificing high-frequency operation (Fig. 1b).

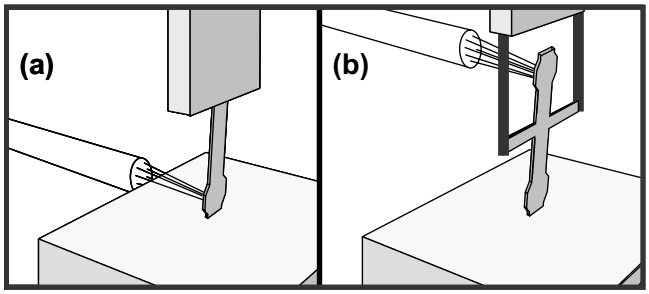

Figure 1: *(a) Conventional and (b) torsional cantilevers used in scanning. In (a), if the cantilever is small and the paddle is located close to the tip, the optical path from the laser interferometer to the paddle can be blocked by the sample. Using a torsional cantilever as shown in (b) can improve optical access.*

DEVICE DESIGN

To meet these challenges, we have designed and fabricated torsional oscillators with the following characteristics:

- Resonance frequency of approximately 1 MHz, with spring constant below 1 N/m (i.e., low-mass, small-size)
- High Q (use single-crystal silicon)
- Adequate frequency separation between the fundamental mode and spurious higher-order modes
- Optical sensing unaffected by sample proximity (i.e., place the reflective paddle on the arm that is *opposite* the tip)

The resulting optimized design is shown in Fig. 2. Note the small size of the device (12 μm-long arms and 2 μm-long hinges, both 120 nm thick) compared to our previous ones **[1, 4]**. To stiffen the unwanted flapping modes without adding excessive mass, a tall but narrow "nanorib" (1.5 μm by 200 nm) is incorporated along the arms perpendicular to the plane of cantilever.

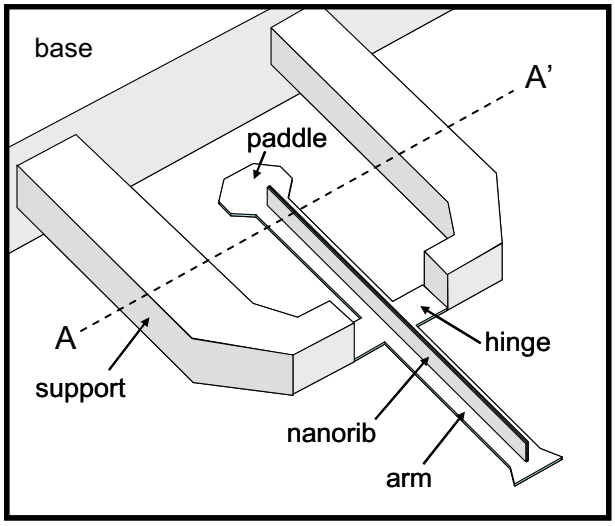

Figure 2: *Nanoribbed torsional cantilever design. The arms and the hinge are all 120 nm thick. Each of the two arms is 12 μm long and 2 μm wide. The hinge on each side of the arm is 2 μm long and 2 μm wide. The nanorib is 200 nm wide and 1.5 μm tall. Note that the supports are thickened for rigidity.*

0-9640024-5-0/hh2004/$20©2004TRF
DOI 10.31438/trf.hh2004.97

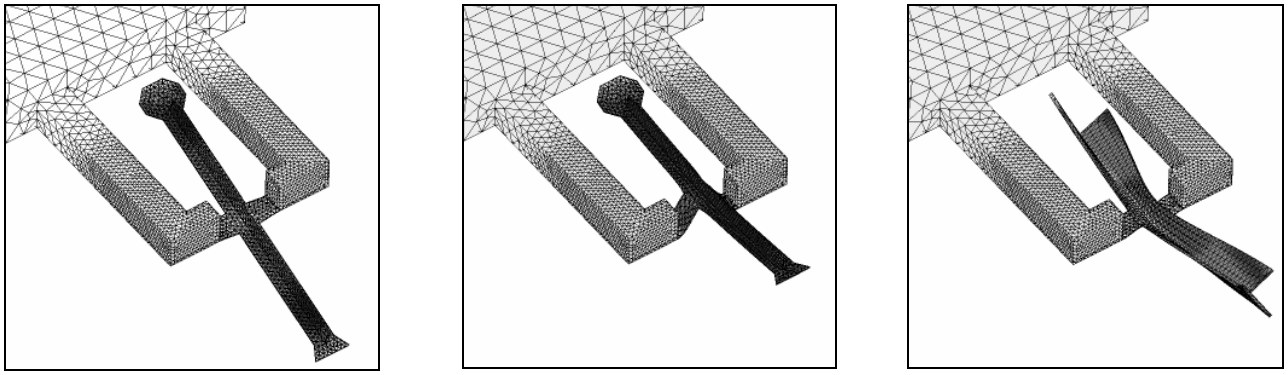

Figure 3: *The fundamental (torsional) mode of the cantilever is at 1.20 MHz according to finite element analysis, while the next two modes are at 6.31 MHz and 10.0 MHz respectively, i.e. at least five times higher than the fundamental.*

The fundamental, torsional mode is designed to be at 1.2 MHz, and the next mode is more than five times higher according to finite element analysis (Fig. 3). The calculated torsional stiffness is 0.6 N/m. As required, the reflector paddle is located at the opposite end to the tip, providing improved optical access.

DEVICE FABRICATION

The fabrication process is shown in Fig. 4. Note that electron-beam lithography is used to pattern the nanoribs. In fact, e-beam lithography is juxtaposed with conventional lithography and multi-step plasma etching to form sub-micron, high-aspect-ratio features coupled to larger, flat structures. Also note that for our application, the cantilever tip must protrude from the edge of the chip in order to access the sample; i.e., a surface-released device **[5]** would not be suitable. We therefore had to adopt a bulk-release approach.

The starting material for our process is a silicon-on-insulator (SOI) wafer with a 1.5-μm top silicon layer (Fig. 4a). A 200-nm thermal oxide layer is grown and patterned (Fig. 4b), and on top of that a second pattern is written with e-beam on 300-nm spin-on-glass (SOG) type resist (Fig. 4c). The oxide mask defines the gross features of the device (the base and support), while the electron-beam mask defines the sub-micron rib. The wafer with the composite oxide-SOG mask is then subject to a timed plasma etch that forms the rib (Fig. 4d). Note that the etch stops just short of the SOI buried oxide. In this case a highly non-isotropic etch is desirable since it creates a uniform cross-section for the thin, narrow rib. Etch-rate uniformity across the wafer is also important, since the amount of top silicon left after the etch determines the final thickness of the arm. The oxide-SOG mask is then removed with HF.

A low-temperature-oxide (LTO) layer is grown and patterned, and is used as a mask for the ensuing selective epitaxy deposition (Fig. 4e). In this step, areas not covered by oxide (i.e., the base and most of the support) will be thickened by the growth of single-crystal silicon epitaxy (Fig. 4f), making them more rigid and less susceptible to unwanted low-frequency modes. An additional lithographic step (not necessarily e-beam) plus one more plasma etch (stopping on the buried oxide) is used to define the arms of the

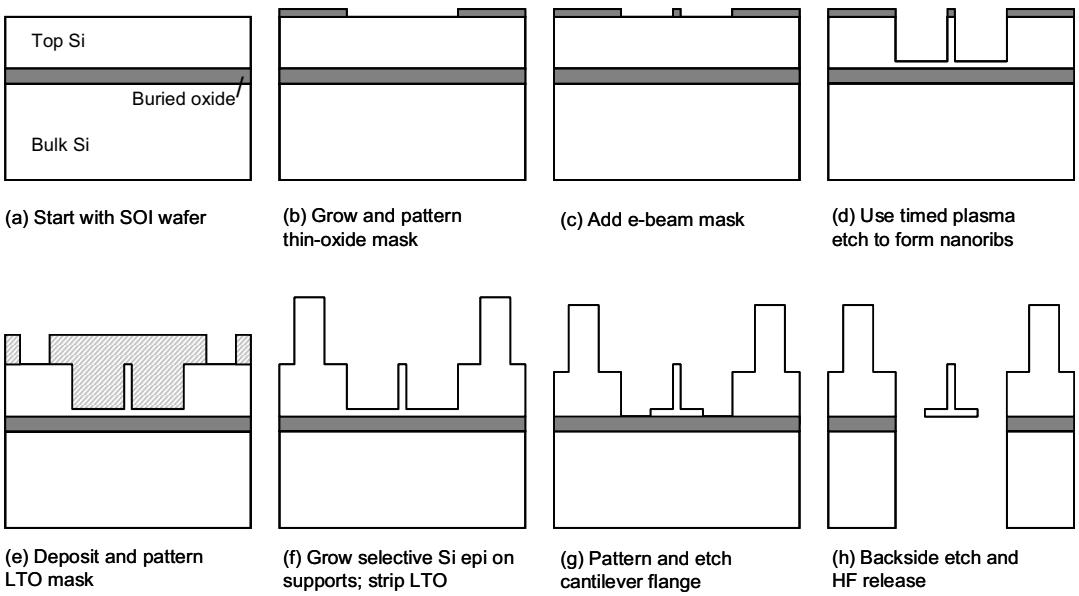

Figure 4: *Fabrication process flow for the nanoribbed torsional cantilever (viewed along section AA' of Figure 2). Note the electron-beam lithography step (c) and the subsequent timed plasma etch (d) used to define the high-aspect-ratio ribs. In spite of the very delicate cantilever structure, a bulk-release approach based on through-wafer backside deep reactive ion etch (DRIE) is used so that the resulting device can protrude from the edge of the chip just like a scanning probe tip.*

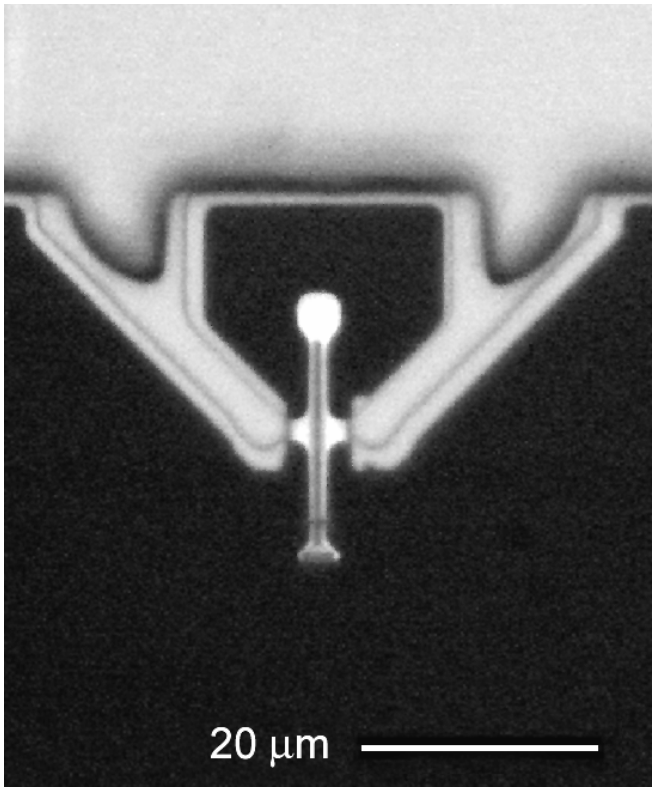

Figure 5: *Optical image (top view) of a fully released torsional cantilever. Note that when used in actual scanning, the tip will be functionalized with an appropriate magnetic particle or coating.*

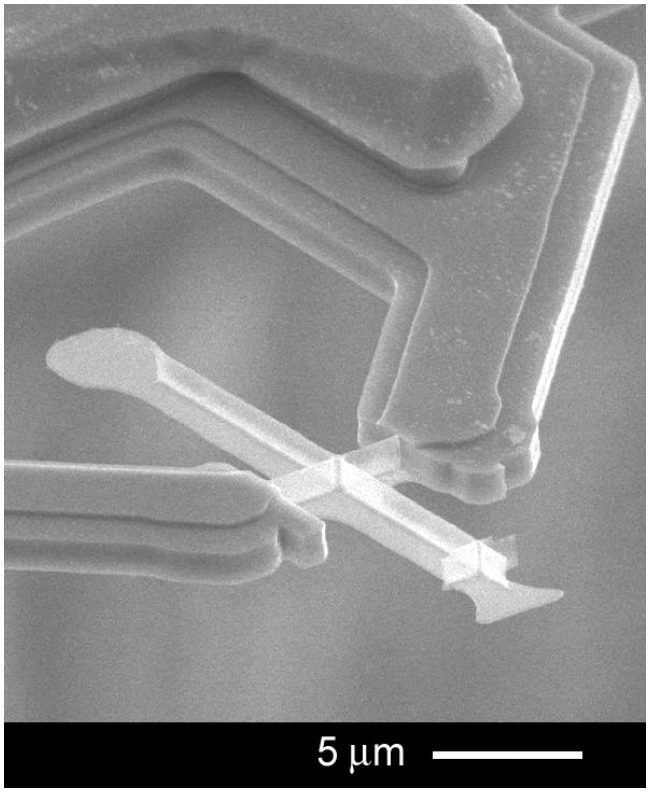

Figure 6: *Scanning electron microscope image of a fully released torsional cantilever. Shown here is an alternate design with a rib on the hinge in addition to the existing one on the arm.*

cantilever (Fig. 4g). Finally, a nitride-LTO bi-layer is grown to protect the top side of the wafer, and a backside DRIE step (with the buried oxide as the etch-stop) is used to create through holes in the wafer. The top-side nitride is then plasma-etched away, and finally an HF vapor etch is used to remove the buried oxide and top-side LTO and release the finished devices (Fig. 4h).

Optical and SEM images of fully released, single-crystal silicon torsional oscillators are shown in Figures 5 and 6. Figure 5 shows a standard cantilever design, while Fig. 6 shows a design variation that has an extra nanorib across the hinge for reinforcement. Both designs exhibit the same basic torsional behavior.

DEVICE CHARACTERIZATION

A standard-design torsional cantilever has been characterized in vacuum at room temperature, indicating that f_0 = 1.42 MHz and Q ~ 6000 (Fig. 7). In comparison, finite element analysis predicts f_0 = 1.20 MHz. Primary sources of discrepancy, we believe, include lithographic alignment error and thick photoresist-related distortion, as well as deviations in cantilever hinge thickness due to etch-rate non-uniformity across the wafer. (The resonant frequency of the cantilever is highly sensitive to hinge thickness.)

Efforts are also being made to study the behavior of f_0 and Q in vacuum at low temperatures (down to liquid N_2 and eventually liquid He temperatures). One practical difficulty we encountered with the optical measurement apparatus is that the small size of the cantilever paddle, which is 4 μm in diameter, requires the optical alignment to be extremely precise and stable at all temperatures; otherwise the laser beam would drift off the paddle causing a loss of optical signal. We have discovered that process of cooling the optical measurement apparatus does introduce a sufficiently large temperature-related mechanical shift that the laser beam becomes misaligned, and as a result we are planning to install an active beam-steering mechanism inside the vacuum chamber to combat this problem.

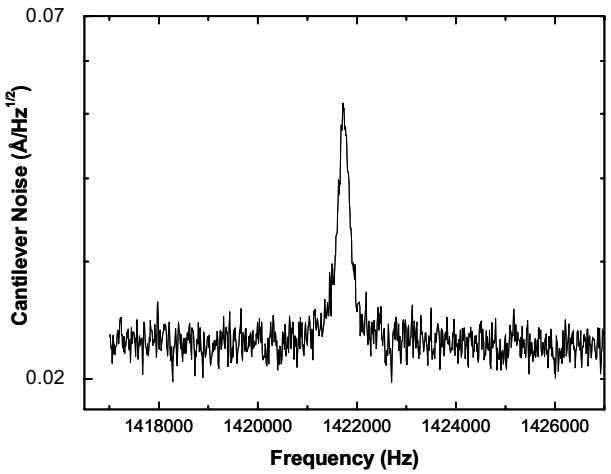

Figure 7*: Frequency-domain plot of thermal noise of torsional cantilever in vacuum at room temperature, showing a fundamental frequency of 1.42 MHz with a Q of approximately 6000.*

FUTURE WORK

While the present nanoribbed cantilever largely satisfies our design and performance requirements, fabrication yields are unacceptably low due to widespread breakage during final release. Upon investigation, we have found that microtrenching tends to occur at the base of the ribs (where they meet the arm) during the rib plasma etch of Fig. 4d. This phenomenon, which is a side-effect of our highly non-isotropic plasma etch recipe, can cause cracks that extend most of the way through the thickness of the arm, eventually causing structural failure.

We have therefore completely re-designed our device to have a truss-like structure composed mostly of vertical elements, minimizing the occurrence of corners between vertical and horizontal surfaces. Prototypes of the new design have been successfully fabricated (Fig. 8). As seen in Fig. 8, the cantilever body is essentially a truss, in this case defined exclusively by electron-beam lithography. (The use of a hollow structure preserves the low-mass and high-frequency characteristics of the oscillator.) Note that the hinge is now vertically oriented as well. While reminiscent of past Hexsil devices **[6]**, the present device is made of a different material (single-crystal silicon), is much smaller in scale and is fabricated using a substantially different process. The fabrication process largely follows that of Fig. 4, except that in step 4(d) the plasma etch now extends all the way down to the buried oxide. The one flat component of the device that remains after the plasma etch—the paddle—corresponds to a pre-fabricated mesa on the substrate. Further evaluation of the new device is in progress.

This work was supported by the DARPA MOSAIC program administered through the Army Research Office. The cantilevers were fabricated at the NSF National Nanofabrication User Network facility at Stanford University. The authors would like to thank T.W. Kenny, Y. Hishinuma, R. Shenoy, G. Yama, A. Partridge, M. Lutz, and J. McVittie for their assistance.

REFERENCES

[1] B.W. Chui, Y. Hishinuma, T.W. Kenny, H.J. Mamin, R. Budakian, D. Rugar, "Mass-loaded cantilevers with suppressed higher-order modes for magnetic resonance force microscopy," *Transducers 2003 Tech. Digest*, Boston, June 2003, pp. 1120-3.
[2] H.J. Mamin, R. Budakian, B.W. Chui, D. Rugar, "Detection and manipulation of statistical polarization in small spin ensembles," *Phys. Rev. Lett.,* Vol. 91, Art. 207604, Nov. 2003.
[3] J.A. Sidles, J.L. Garbini, G.P. Drobny, "The theory of oscillator-coupled magnetic resonance with potential applications to molecular imaging," *Rev. Sci. Instrum.,* Vol. 63, No. 8, pp. 3881-99, Aug. 1992.
[4] T.D. Stowe, K. Yasumura, T. Pfafman, T.W. Kenny, D. Botkin, D. Rugar, "Torsional Force Probes Optimized for Higher Order Mode Suppression," *Transducers 1997 Technical Digest*, Chicago, June 1997, pp. 141-4.
[5] S. Evoy, D.W. Carr, L. Sekaric, A. Olkhovets, J.M. Parpia, H.G. Craighead, "Nanofabrication and electrostatic operation of single-crystal silicon paddle oscillators," *J. Appl. Phys.,* Vol. 86, No. 11, p. 6072-7, Dec. 1999.
[6] C.G. Keller, R.T. Howe, "Hexsil tweezers for teleoperated microassembly," *Proceedings of MEMS 1997*, Nagoya, Japan.

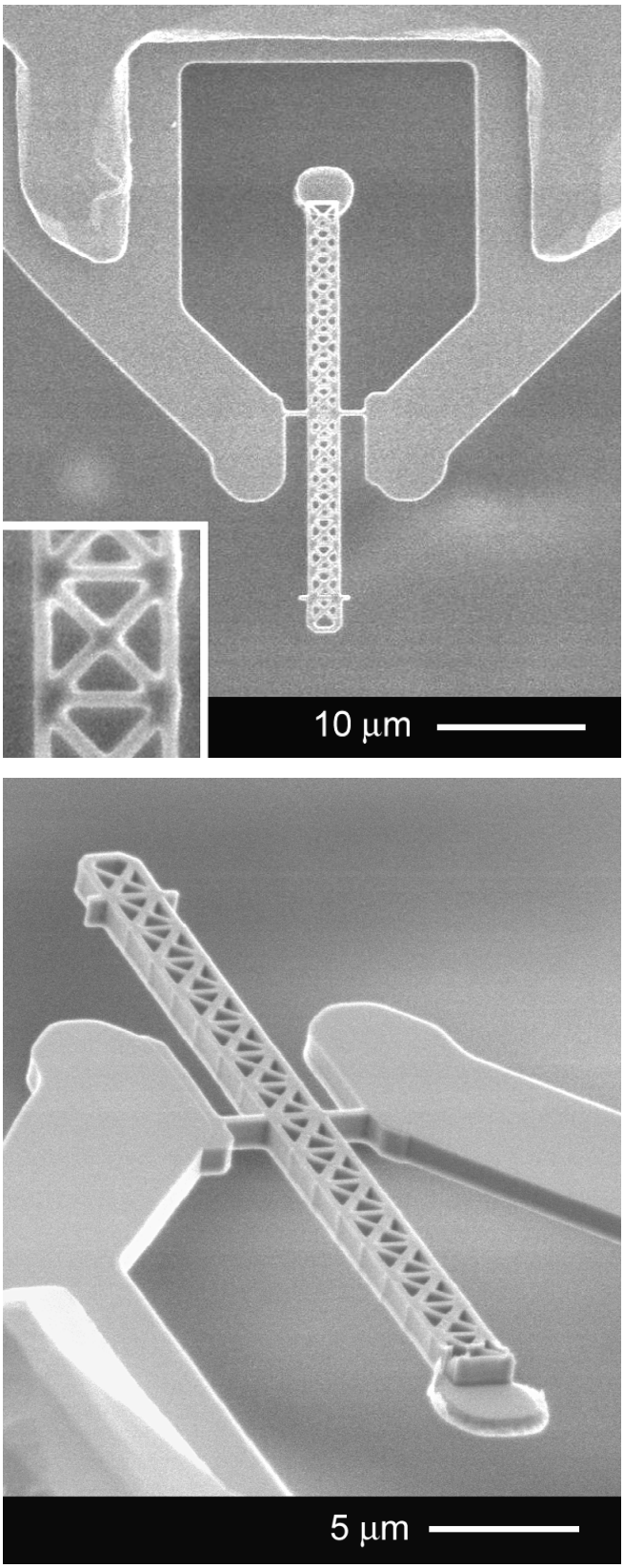

Figure 8: *SEM's of fully released truss-style torsional cantilever, made of single-crystal silicon. The two arms (16×2×1 μm each) are trusses formed by e-beam lithography and plasma etch. Note vertically oriented hinges (2×1×0.25 μm each) and flat paddle. INSET: details of truss segment; the "unit square" is 2×2 μm.*

Compensated Tunable Capacitive Thin Film Hydrogen Sensor

D. J. Kirby, J. J. Zinck, D. T. Chang, F. P. Stratton

HRL Laboratories, LLC, 3011 Malibu Canyon Road, Malibu, CA, 90265-4799, USA

ABSTRACT

We report on the development of a compensated, integrated, differential capacitive hydrogen sensor based on the lattice expansion of $LaNi_{5-x}M_x$ thin films. Fabricated devices demonstrate a stable response to hydrogen as measured over 0.1 to 1 atm. We have measured the intrinsic response time of $LaNi_{4.4}Al_{0.6}$ films as τ =10 s. We have determined a Sieverts type dependence of the $LaNi_{4.4}Al_{0.6}$ film response to hydrogen as a function of partial pressure. Additionally, we have shown the integrated sensor sensitivity to be better than 0.01 atm with the ability to detect hydrogen at pressures > 2 atm.

INTRODUCTION

Recently there has been considerable focus on the emergence of a hydrogen economy, underscoring the need for low-cost wide dynamic range hydrogen sensors. While there are many commercially available sensors that respond in the range suitable for threshold sensors (< 4% hydrogen), many have issues associated with gas specificity and robustness. There are only a few examples of concentration sensors (4-100% hydrogen) [**1**], and similar considerations apply. In this paper we report on a novel hydrogen sensor concept based on the lattice expansion of a metal hydride thin film, which has the potential to meet the demands of a broad range of sensing applications [**2**]. In this paper we will describe the thin film material characterization, and the wafer level fabrication and testing of a compensated thin film $LaNi_{4.4}Al_{0.6}$ capacitive hydrogen sensor.

Alloys of the formula $LaNi_{5-x}M_x$ absorb hydrogen to form metal hydrides reversibly and exhibit a substantial lattice expansion as a consequence of absorption [3]. This physical property of $LaNi_{5-x}M_x$ alloys is used as the basis of a capacitive sensor. This sensor is ideally suited for hydrogen detection because the lattice expansion is specific to hydrogen and the temperature and pressure of hydriding can be tuned by varying the alloy composition. Thus, maximum sensitivity can be adjusted for specific operating conditions rendering a high dynamic range for detection of hydrogen.

THIN FILM RESULTS

We have prepared thin films of $LaNi_{4.4}Al_{0.6}$ on Si (100) substrates by DC magnetron sputtering using elemental targets. We have measured the lattice expansion of these films using a tilted plate capacitance dilatometer [**4**] in a temperature-controlled oven, equipped with N_2 and H_2 gas handling capability. An expansion of the lattice is measured as a change in the capacitance gap of the dilatometer. Figure 1 shows a response time of τ = 10s for a 2 m-thick $LaNi_{4.4}Al_{0.6}$ film on exposure to 0.8 atm of hydrogen, as measured at T= 103°C. The capacitance change of a bare silicon wafer on exposure to 0.8 atm hydrogen is plotted for reference. In this case, hydrogen does not adsorb on silicon or absorb into the silicon lattice, hence no expansion occurs and the measured capacitance change is due to the dielectric constant change of vacuum to hydrogen only.

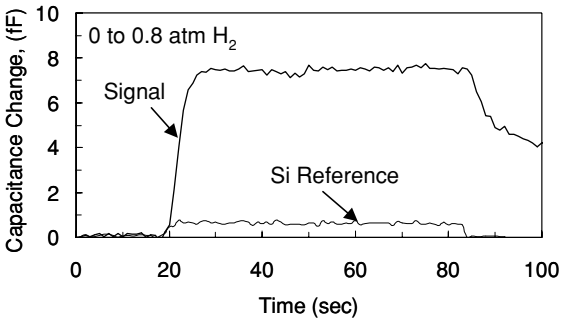

***Figure 1**. Response time of 2 m thick $LaNi_{4.4}Al_{0.6}$ film to 0.8 atm hydrogen showing τ_{90} = 10s at T=103°C. Silicon substrate response is shown for dielectric constant change only. Measurement integration time = 0.03 seconds.*

For sensor calibration, we have also measured the steady state response of films as a function of partial pressure of hydrogen. The thin films exhibit a Sieverts type dependence as shown in Figure 2, ($\Delta C \alpha P^{1/2}$). Therefore the films have a larger fractional response at lower pressures indicating the potential for threshold sensor applications. Films have been tested from 0.1 to 3.0 atm of hydrogen at temperatures of 70 to 120°C.

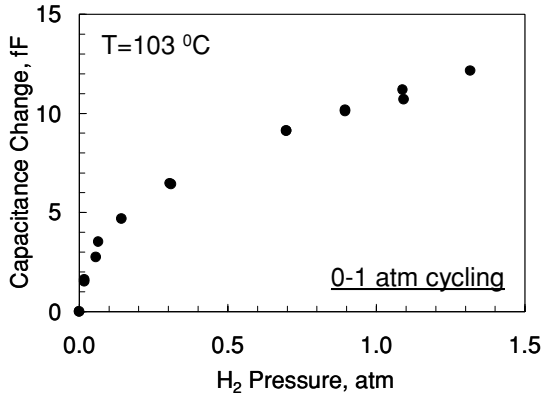

***Figure 2**. Sieverts type dependence of steady state response of 4 m $LaNi_{4.4}Al_{0.6}$ film to hydrogen observed over 0 to > 1 atm.*

0-9640024-5-0/hh2004/$20©2004TRF
DOI 10.31438/trf.hh2004.98

INTEGRATED DEVICE RESULTS

We have successfully implemented these films in a compact differential device, which is designed to compensate for the effect of extraneous gases and thermal effects on the capacitance measurement. Our two-wafer process and the completed device are shown schematically in Figure 3. Two capacitors, signal and reference, are formed in close proximity. Gas delivery channels supply the same gas flow and mixture to both signal and reference capacitors in the sensing region so as to allow compensation for thermal and dielectric effects, other than the response to hydrogen.

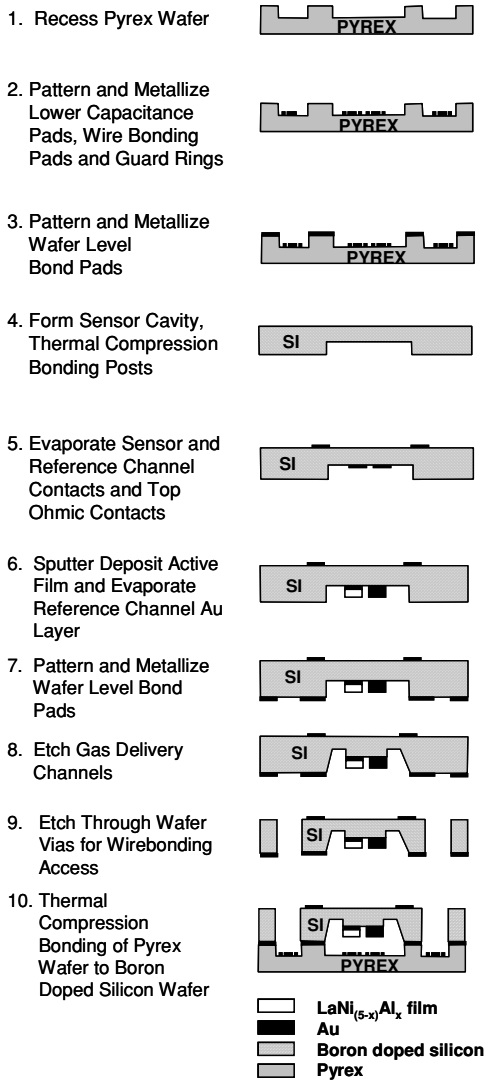

Figure 3. *Hydrogen sensor two-wafer fabrication process. Active film areas are: 200 m^2, 500 m^2 and 1000 m^2.*

Figure 4 shows the differential response of a 500 m^2 integrated device to cycling of hydrogen between vacuum and 1 atm, illustrating a burn in of approximately 12 cycles at T= 72°C. The differential signal is the signal capacitance minus the reference capacitance. The negative abscissa values reflect that the reference capacitance is slightly higher than that of the signal. An initial cycle of N_2 is used as an inert calibration gas to confirm that the lattice expansion occurs in the presence of hydrogen only. Figure 5 demonstrates that sensor sensitivity is better than 0.01 atm hydrogen at T=90 °C, based on the signal to noise of the differential capacitance.

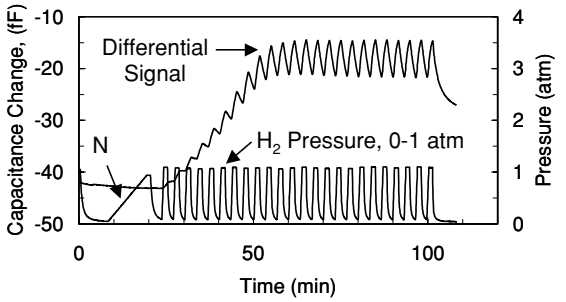

Figure 4. *Response of 500 m^2 integrated sensor to 0-1 atm of hydrogen at T= 72 °C. Burn-in = 12 cycles.*

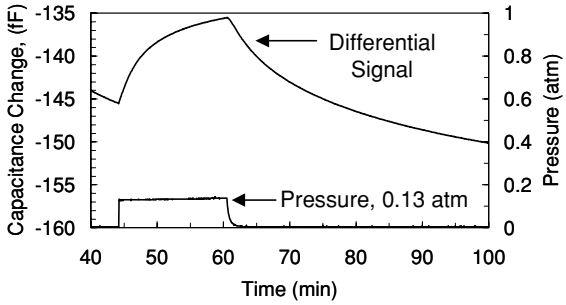

Figure 5. *Differential response of 500 m^2 integrated sensor to 0.13 atm of hydrogen at T= 90 °C.*

SUMMARY

In summary, we have demonstrated the feasibility of integrating a differential capacitive hydrogen sensor based on the lattice expansion of $LaNi_{5-x}M_x$ thin films. The devices demonstrate a stable response to hydrogen as measured over 0.1 to 1 atm. Integrated devices have a burn-in of typically 12 cycles of hydrogen after which the amplitude of the response stabilizes. We have measured the intrinsic response time of $LaNi_{4.4}Al_{0.6}$ films as τ =10 s, and it is expected that the devices will also demonstrate a τ =10 s in the absence of a process contamination. We have determined a Sieverts type dependence of the $LaNi_{4.4}Al_{0.6}$ film response to hydrogen as a function of partial pressure, indicating the potential for threshold sensor applications. We have demonstrated an integrated sensor sensitivity better than 0.01 atm and tested films over 0 - 2 atm of hydrogen partial pressure with stable response.

ACKNOWLEDGMENTS

This work was supported by General Motors - FCA division.

REFERENCES

[1] Baselt D R, el al, 2003, *Sensors and Actuators* B **88** 120; see also www.h2scan.com.

[2] Zinck J J and Kirby D J, 2003, Thin film metal hydride hydrogen sensor, *U. S. Patent* # 6,539,774

[3] Gupta M and Schlapbach L, 1988, *Hydrogen in Intermetallic Compound* I, Topics in Applied Physics, **63** 182 (Springer-Verlag)

[4] Genossar J and Steinitz M, 1990, *Review Sci. Instrum.*, **61** 2469.

DROPLET ARRAYS IN MICROFLUIDIC CHANNELS FOR COMBINATORIAL SCREENING ASSAYS

Wen-Chi Chao[a], John Collins[b], Mark Bachman[a, b], G. P. Li[a, b], and Abraham P. Lee[b,c]

[a]Department of Electrical and Computer Engineering, [b]Department of Biomedical Engineering, and [c]Department of Mechanical & Aerospace Engineering,

University of California at Irvine

A microfluidic droplet array that allows dynamic reconfiguration of droplet volume and concentration is reported. Microfluidic droplet technology [1, 2] shows tremendous promise for high throughput combinatorial screening assays by varying the chemical compositions in successive droplets [3]. However, in order to study long term (hours to days) chemical changes (e.g. protein crystallization, enzymatic reactions) inside droplets, active trapping is necessary for temporal and spatial analysis of each droplet in place. The major challenge is to avoid droplet coalescence that would destroy the encapsulated content. Stabilization methods include polymerization and the addition of surfactants to the droplets, but these may ultimately affect the evaporation rate and the chemical content of the droplet [4]. In addition, the ability to successively vary the sizes of the droplets is critical for nucleation and solubility assays based on the evaporation rate of the droplet [5, 6].

The droplet array microfluidic chip is shown in Fig 1, which utilizes a PDMS channel junction to generate droplet emulsions as described in [1]. For trapping droplets, a

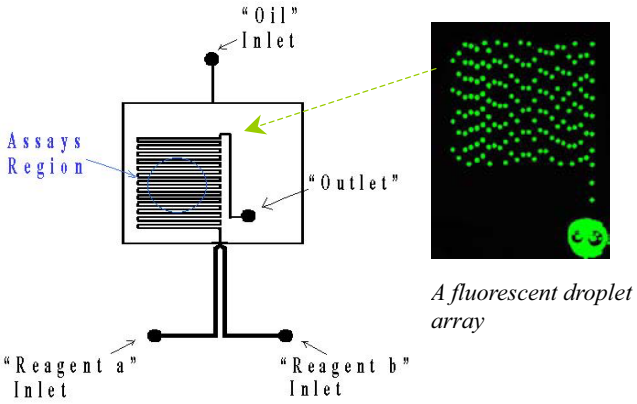

Fig. 1. *Schematics of microfluidic chip.*

zero-dead-volume single-pole double-flow valve from the Lee Company served to divert the flow from the inlets. The control pulses applied to these valves are in phase with each other so that the valves are synchronized. However, many manufacturers claim their microfluidic component to have "zero-dead-volume" when in reality there exits a small dead volume. In addition, even after the flow is switched to a shunt outlet, residual pressure will continue to generate uncontrolled droplets; therefore, trapping droplet arrays in place is challenging. In order to overcome these two problems (dead volume and residual pressure), after the Lee valve diverts the inlet flow to the shunt, the inlet is subsequently exposed to atmospheric pressure in a "timely" manner. The purpose is to control the volume of flow "released" towards the outlet to be balanced by the volume "returned" to the inlet. By doing this process, the droplet arrays are trapped in place to be identified as shown in Fig 2.

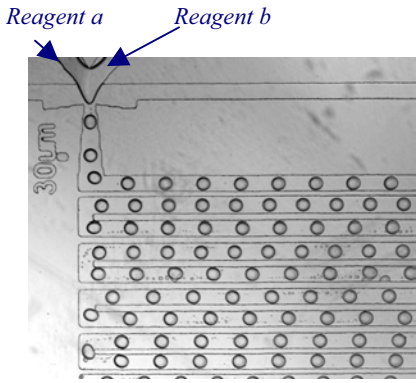

Fig. 2a. *A droplet array carrying two reagents in flow*

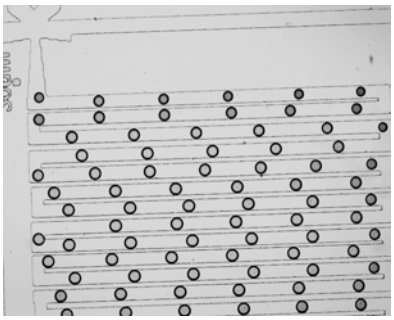

Fig. 2b. *A droplet array trapped in microfluidic channels for screening. After trapping, the droplet is round due to the disappearance of the viscous shearing forces.*

In our experiments, the droplet sizes and chemical concentrations are ramped by programming the flow rates of oil and one of the chemical reagents, respectively, by using Harvard 2000 syringe pumps, controlled by an RS232

Travel support has been generously provided by the Transducers Research Foundation and by the DARPA MEMS and DARPA BioFlips programs.

0-9640024-5-0/hh2004/$20©2004TRF
DOI 10.31438/trf.hh2004.99

interface. Preliminary results are shown in Fig 3 and Fig 4 with droplets having volume gradients and chemical gradients, respectively. As these plots illustrate the sizes of the droplets were more easily controlled (Fig 3) than the concentration (Fig 4). In Fig 3 and Fig 4, Q_a is the flow rate of reagent a; Q_b is the flow rate of reagent b, and Q_o is the flow rate of mineral oil. As seen in Fig. 4, the end pinching effect results in instability of concentration ramping. The images are recorded with a high-speed camera at 500 frames per second.

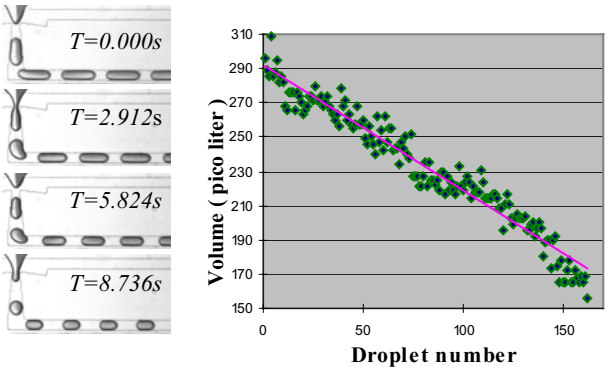

Fig. 3. *Dynamic droplet volume ramped in 8.736s shown in a series of video frames. Q_a =0.7μl/min, Q_b =1.3μl/min, and Q_o =0.4~2.4μl/min*

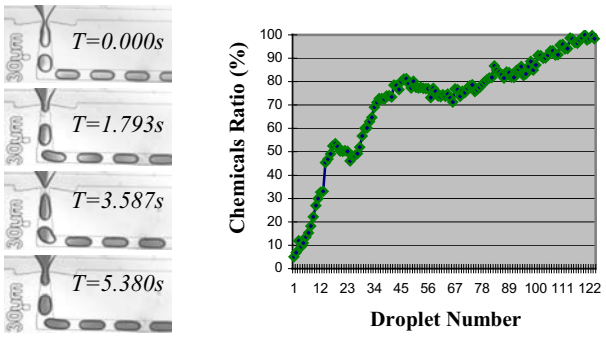

Fig. 4. *Dynamic chemical concentration ramped in 5.380s shown in a series of video frames. Qa =0.7μl/min, Qb =0.6~3.0μl/min, and Qo =1.3μl/min.*

A preliminary experiment of a combinatorial screening assay is demonstrated by observing salt solubility in droplets containing NaCl solution. As shown in Fig 5, crystallization occurred in droplets having higher salt concentration; however, temperature is an important parameter in salt crystallization as shown in Fig 6, as the solubility is higher at higher temperatures. Our droplet device forms a platform to generate multidimensional solubility diagrams for various chemicals.

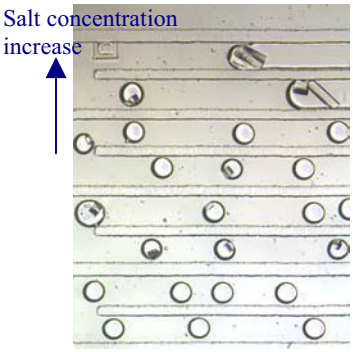

Fig. 5. *Solubility assay based on the salt concentration gradient of microfluidic array. (Scale bar, 100μm)*

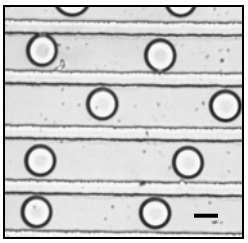

Temp. = 25ºC right after trapping

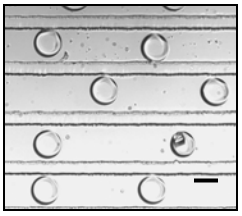

Temp. = 5ºC fort 20 mins

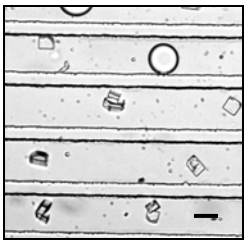

Temp. = -10ºC for 1 hrs

Fig. 6 . Salt c*rystallization observed as the temperature cooled down. (Scale bar, 50μm)*

REFERENCES

[1] Yung-Chieh Tan, John Collins, and Abraham P. Lee, 7th International Conference on Miniaturized Chemical and Biochemical Analysts Systems, October 5-9, 2003

[2] Helen Song, Joshua D. Tice, and Rustem F. Ismagilov, Angew. Chem. Int. Ed. 2003, 42, No.7

[3] Michael Spaid, Andrea Chow, Yevgeny Yurkovetsky, Micro Total Analysis Systems 2003, 445-448, October 2003

[4] T. Thorsen, R.W. Roberts, F.H. Arnold and S.R. Quake, Phys. Rev. Lett. 86: 4163-6 (2001)

[5] P. D. Collingsworth, Terry L. Bray, Gayle K. Christopher, Crystal Growth 219, 283-289 (2000).

[6] Bo Zheng, L. Spencer Roach, and Rustem F. Ismagilov, J. American Chemical Society 2003, 125, 11170-11171

TOWARDS INERTIAL GRADE VIBRATORY MICROGYROS: A HIGH-Q IN-PLANE SILICON-ON-INSULATOR TUNING FORK DEVICE

Mohammad Zaman, Ajit Sharma, Babak Amini, and Farrokh Ayazi
School of Electrical and Computer Engineering, Georgia Institute of Technology
Atlanta, GA 30332-0250

ABSTRACT

This paper reports on the design and implementation of an in-plane solid-mass single-crystal silicon tuning fork gyro that has potential to achieve inertial-grade performance. A novel design is devised to achieve high Q in the drive and sense resonant modes (Q_{drive}=84,000 and Q_{sense}=64,000) with effective decoupling. The gyroscope was fabricated on 40µm SOI using a two-mask process. The drive and sense resonant modes were matched electronically to within 0.07% of each other and the measured rate results show a sensitivity of 1.25mV/º/s in a bandwidth of 12Hz.

MOTIVATION

MEMS vibratory gyros have yet to achieve inertial grade performance, i.e., rate resolution and bias stability better than 0.1º/h. To achieve this, a vibratory gyroscope must attain very high quality factors (>30,000), large sense capacitances (>1pF), large mass (>100µg) and large drive amplitude (>5µm) [**1, 2**]. This calls for innovative designs and radical advances in fabrication technology. In an effort to reach this goal, we have introduced an in-plane, solid-mass silicon tuning fork device that incorporates very high Q, a large mass per unit area, and in-plane operation within a single framework – unlike previously reported tuning fork gyroscopes (TFG) [**3, 4**]. The operating principle is based upon a standard tuning fork's response to rotation. In this design (see Fig.1) the proof-masses are driven to resonance along the x-axis, and the Coriolis acceleration induced by rotation around the z-axis is sensed along the y-axis.

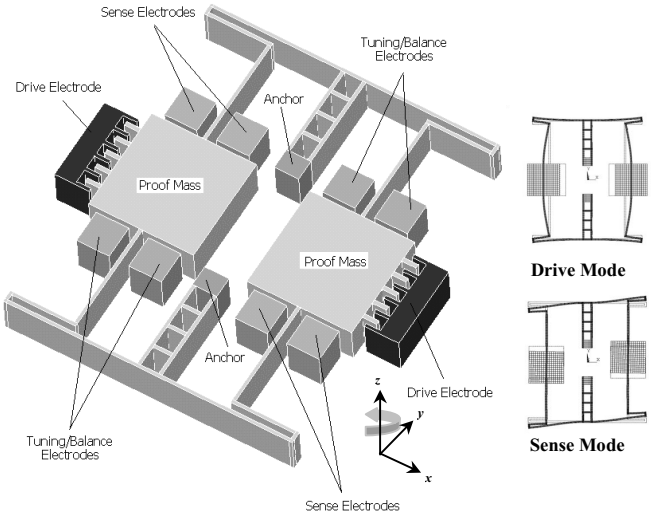

Figure 1. *Schematic diagram of the gyroscope and resonant mode shapes as simulated in ANSYS (exaggerated for clarity).*

A major incentive in utilizing this symmetric tuning fork architecture as opposed to a frame-design or single-mass-design is the differential sensing capability. As a result, linear acceleration/shock signals are rejected as "common mode" without the need for complex electronics. A high Q in the drive mode is necessary to get large drive amplitudes using small drive voltages. A high Q in the sense mode is imperative to substantially increase sensitivity of the device and also lower the Brownian noise floor of the gyroscope. The spring structure design makes it possible to drive the solid proof masses linearly with displacement amplitudes in the range of 4-6µm. The primary energy loss mechanism that leads to Q degradation is support loss [**5**]. The anchor and the flexures were carefully designed to ensure minimal support loss and consequently high Q in the drive and sense modes by torque cancellation/reduction. Detailed ANSYS simulations of the flexures were performed to optimize structural dimensions and to allow the sense mode to occur 50–100Hz higher than the drive mode. Once the device is fabricated, the sense mode is tuned electrostatically using the tuning electrodes to match the drive mode frequency.

FABRICATION

The prototype structures were fabricated on 40µm SOI wafers. SEM pictures of a fabricated device are shown in Figure 2.

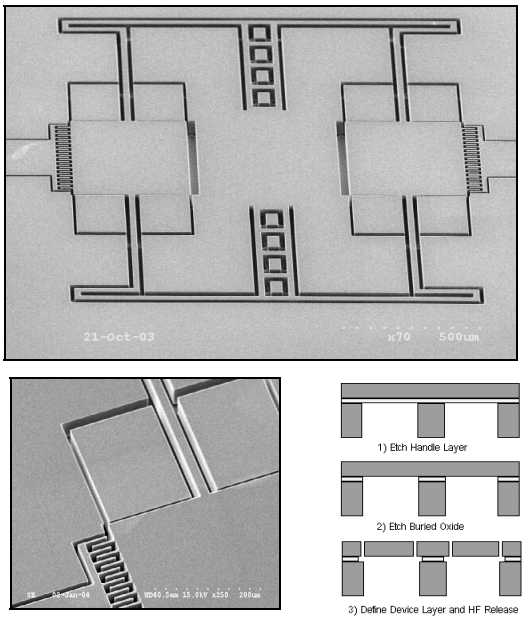

Figure 2. *(Clockwise from top) In-Plane Solid-Mass Silicon TFG, process flow, and close-up of 6µm comb & 2.5µm sense gaps.*

The moving sections of the structure and the areas under the comb drives are first released from the backside of the wafer by etching the handle silicon layer through to the buried oxide layer using the Bosch process. The buried oxide is then removed in a reactive ion etching (RIE) system and finally the top layer is patterned all the way through, leaving behind a suspended structure whose anchors are supported to the handle substrate via several support posts. The final etch step involves a quick HF etch to release areas under these supports. Such a fabrication flow is simple and precludes the requirement of any perforations in the proof mass, resulting in a larger mass per unit area. The simultaneous elimination of the ground plane under the comb drives prevents the excitation of the out of plane modes and detrimental effects of levitation.

0-9640024-5-0/hh2004/$20©2004TRF
DOI 10.31438/trf.hh2004.100

EXPERIMENTATION

A prototype device was tested in vacuum and high Q operation was confirmed. Figure 3 shows the measured drive and sense resonant modes respectively with high Q values (~ 81,000 for drive and ~ 64,000 for sense). As discussed earlier, such high Q's are essential to achieve inertial grade performance in a small bandwidth. Larger bandwidth can be obtained by operating the device in closed loop at the expense of sensitivity.

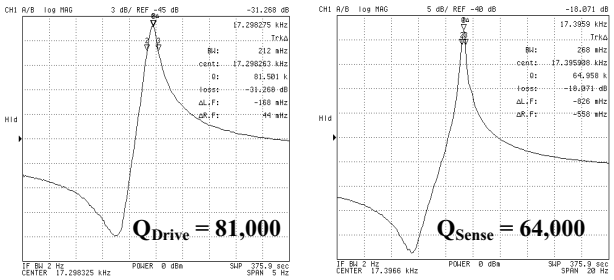

Figure 3. *Measured drive and sense resonant modes.*

The drive and sense frequencies were matched to within 0.07% (12Hz over 17.5kHz) of each other (see Figure 4). Despite a mechanically decoupled design, in practice, fabrication imperfections can lead to non-zero off-diagonal elements in the spring stiffness and damping coefficient matrices [**6**] resulting in significant zero-rate output (ZRO). This quadrature error prevents close matching of the drive and sense resonant modes [**4**]. Inertial grade performance requires that the high Q resonant modes be matched. This lowers the Brownian noise floor by a factor of $\sqrt{Q_{sense}}$ [**1**] and improves stability. The Brownian noise floor is an order of magnitude greater than the electronic noise floor and is therefore the key factor in determining the resolution of the gyroscope. Additionally, any mismatch is undesirable as it reduces the sensitivity and makes it a function of the frequency of input rotation signal.

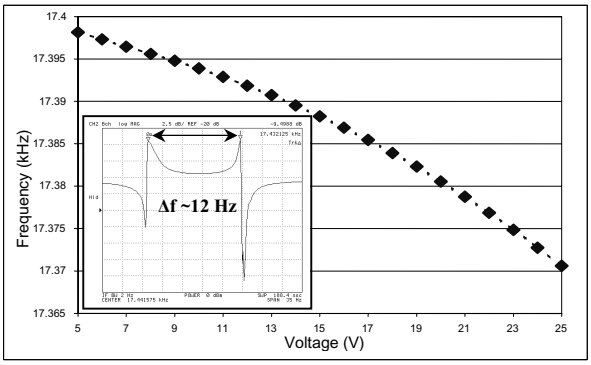

Figure 4. *Tuning characteristics of sense mode frequency. Inset: The resonant modes have been matched to within 12 Hz.*

Measured rate results from the tuning fork gyro with a 12Hz resonant mode mismatch and 1μm drive amplitude yields an open-loop rate sensitivity of 1.25mV/°s, as shown in Figure 5. Table I summarizes the key gyroscope parameters.

CONCLUSIONS AND FUTURE DIRECTIONS

An in-plane, solid-mass silicon tuning fork gyroscope has been designed and implemented on 40μm SOI. This design demonstrates high drive and sense mode quality factors, large drive amplitudes and increased mass – all critical requirements to lower the Brownian noise floor and thereby achieve sub-degree per hour angular rate resolutions.

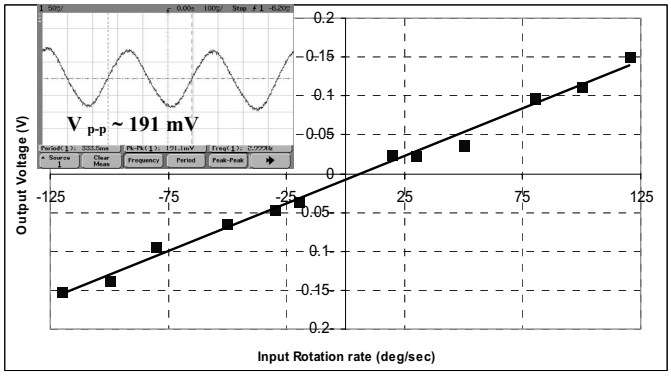

Figure 5. *Output voltage versus input rotation rate. Inset: The response of the sensor to an input of 150 °/s 3Hz signal.*

However, the large capacitance requirements are restricted by the aspect ratio limitations of the current process flow. The HARPSS process [**2**] is being employed to overcome the aspect ratio problem and increase the sense capacitance to >1pF. Finally, strategic electrode placement schemes and electronic feedback control mechanisms are being investigated to achieve complete matching of the high-Q resonant modes and cancel the quadrature error. The high Q operation calls for advancements in vacuum packaging technologies [**7**], which is being pursued as well.

Table I: Summary of the solid-mass Silicon TFG parameters.

Single proof mass dimension (in μm)	400 x 400 x 40
Effective mass	30 μg
Drive mode resonant frequency (in kHz)	ANSYS: 17.413 Measured: 17.298
Sense mode resonant frequency (in kHz)	ANSYS: 17.458 Measured: 17.396
Split of drive and sense resonant frequencies	12 Hz
Rate sensitivity	1.25 mV/°/s
Resolution with 12 Hz freq mismatch	0.01°/s/√Hz
Theoretical Brownian noise floor with matched modes	0.3°/h/√Hz
Electronic noise floor (input ref. noise = 1μV/√Hz)	0.02°/h/√Hz
Measured temp. coefficient of freq. (TCF)	– 59 ppm/°C

ACKNOWLEDGEMENT

This work is supported under the DARPA HERMIT program. The authors wish to thank Dr. Zhili Hao for ANSYS assistance. Travel support has been generously provided by the Transducers Research Foundation and by the DARPA MEMS and BioFlips programs.

REFERENCES

[1] Ayazi, F., "A High Aspect-Ratio High-Performance Polysilicon Vibrating Ring Gyroscope," *Ph.D. Dissertation*, University of Michigan, Ann Arbor (2001).
[2] Ayazi, F. and Najafi, K., "A HARPSS Polysilicon Vibrating Ring Gyroscope" *IEEE/ASME JMEMS*, June 2001, pp. 169-179.
[3] Bernstein, J., et al., "A Micromachined Comb-Drive Tuning Fork rate gyroscope," *Proceedings MEMS 1993*, pp. 143-148.
[4] Schwarzelbach, O., et al., "New Approach for Resonant Frequency Matching of Tuning Fork Gyroscopes by Using a Non-Linear Drive Concept," *Proceedings Transducers 2001*, pp.464-467.
[5] Z. Hao, et al., "An Analytical Model for Support Loss in Micromachined Beam Resonators with In-plane Flexural Vibrations," *Sensors and Actuators A*, Vol. 109, Dec. 2003, pp.156-164.
[6] Clark. W. A., "Micromachined Vibratory Rate Gyroscopes," *Ph.D. Dissertation*, University of California, Berkeley (1997).
[7] Najafi, K., "Micropackaging Technologies for Integrated Microsystems: Applications to MEMS and MOEMS," *Proc. SPIE's Micromachining & Microfabrication Symp. 2003*, pp.1-19.

MEASUREMENT OF TRANSIENT THERMAL RESPONSE OF MICRO-MIRRORS

Craig R. Forest[1]
Mechanical Engineering Department, Massachusetts Institute of Technology
Cambridge, MA 02139

P. Reynolds-Browne,
J. Harris, E. Novak
Veeco Instruments, Inc.
Tucson, AZ 85706-7123

O. Blum-Spahn, C.C. Wong,
S. Mani, F. Peter, D. Adams
Sandia National Laboratories[2]
Albuquerque, NM 87185

ABSTRACT

Metrology of MEMS can provide feedback for modeling of thermal-mechanical behavior and understanding thin film properties. Towards this end, measurements of the transient thermal response of a 500 μm diameter polysilicon mirror were performed, as heated with a 100 μm diameter infrared laser at optical powers up to 600 mW. Stroboscopic interferometry and thermography were utilized to measure mirror surface topography during heating/cooling and correlate the measured deformation with surface temperature. Transient thermal response occured over approximately 2.2 ms, as measured with 0.14 ms temporal resolution. Surface temperatures rose to 179°C with a corresponding surface deformation amplitude of 124 nm near the threshold for plastic deformation. Deformation amplitude and surface temperature were proportional to optical power.

1 INTRODUCTION

Metrology of MEMS is vital to their widespread application in that it provides feedback for design and manufacturing process improvement which leads to predictable, reliable performance. Since MEMS usually contain moving parts, characterization of dynamic behavior is also useful. Metrology at MEMS length and time scales can lead to new understanding of thin film heat transfer properties for better modeling.

1.1 MICRO-SWITCHING SYSTEM

A two-position switch is being developed at Sandia National Laboratories for surety applications [1]. The system features a gear-shaped mirror, a vertical cavity surface emitting laser and a photo-detector. The mirror, shown in Fig. 1, has an off-axis thru-hole; its angular position is controlled by an electrostatic comb drive.

In the design, incident radiation from a laser either passes directly through the off-axis hole and a via in the substrate, or the mirror can be rotated to reflect this radiation. In the latter configuration, radiation incident on the mirror is also partially absorbed, causing localized spot heating. Consequent thermal expansion and deformation create undesirable mechanical and optical performance, such as spurious reflections or binding between the mirror and its hub, which can prevent rotation.

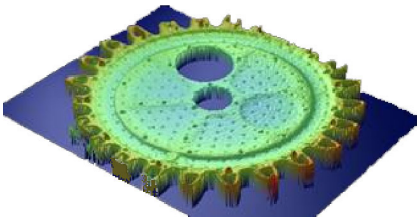

***Figure 1**: Polysilicon micro-mirror, 500 μm diameter.*

Understanding the heat transfer in this system is crucial to mitigating performance concerns. A thermo-mechanical model in which absorbed radiation results in predictable deformation can be used to redesign the switch to prevent binding by minimizing or moving deformation to an area where there is no performance impact [2]. Empirical data is required to generate this model, so we have pursued metrology of the thermally-induced mirror deformation as a function of time, incident optical powers, and surface temperatures.

2 EXPERIMENTAL APPARATUS

To induce thermal deformation, a laser operating at 832 nm was connected to an optical fiber. The 100 μm diameter bare fiber core was then positioned over the micro-mirror at 45° incidence using a translation stage, thereby replicating the configuration for the actual optical switch in which local spot heating occurs.

2.1 DEFORMATION MEASUREMENT

A stroboscopic interferometer (Veeco Instruments, Inc., NT 1100) [3] was modified to capture the mirror thermal deformations as they occurred. A schematic of the experimental setup is shown in Fig. 2 [4]. In the technique, pulse square-wave signals drive the laser, CCD and LED at the same frequency. The phase of the laser heating, ϕ_1, was varied constantly with respect to the phase of the image capture (CCD and LED), ϕ_2. This resulted in a set of data which fully recorded the mirror heating/cooling cycle. Signals at 20 Hz and 50% duty cycle were used. The phase shift, $\Delta\phi = \phi_1 - \phi_2$, was initially zero and was incremented by 1°/cycle.

[1]Travel support has been generously provided by the Transducers Research Foundation and by the DARPA MEMS and DARPA BioFlips programs.

[2]Sandia is a multiprogram laboratory operated by Sandia Corp., a Lockheed Martin Company, for the U.S. Dept. of Energy's Natl. Nuclear Sec. Admin. under Contract DE-AC04-94AL85000.

0-9640024-5-0/hh2004/$20©2004TRF
DOI 10.31438/trf.hh2004.101

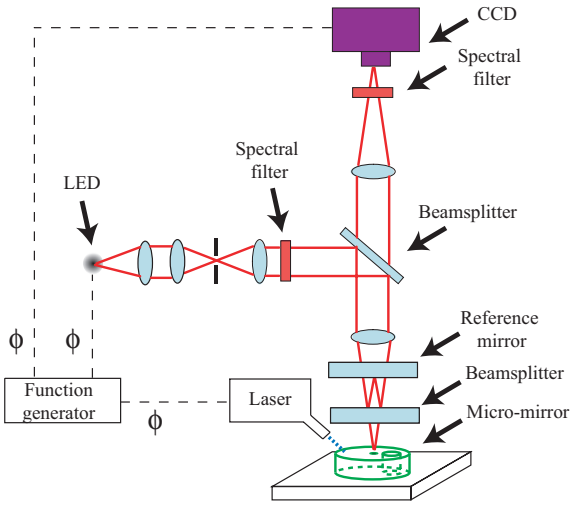

Figure 2. *Stroboscopic interferometry apparatus for transient thermal deformation measurements.*

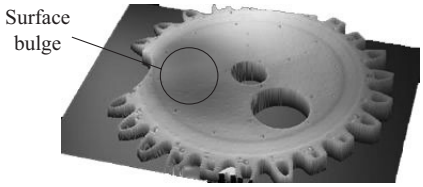

Figure 3. *Deformed mirror–compare with Fig. 1. Data absence at mirror's left edge caused by fiber obstruction.*

For data integrity, the mirror heating/cooling cycle must be repeatable, or purely elastic. To determine the threshold for plastic deformations, mirrors were subjected to constant laser powers up to 600 mW, where local melting was observed. Based on these results, stroboscopic interferometry experiments were performed below the melting threshold, at 150 mW and 300 mW.

2.2 TEMPERATURE MEASUREMENT

Temperatures on the mirror surface were measured with an infrared microscope (EDO Corporation, Infrascope) with 5 μm and 0.1°C spatial and temperature resolutions, respectively. Emissivity was calibrated at 50 and 75°C. Surface temperature measurements were made while the mirror was at steady-state for a range of incident optical powers in the elastic deformation regime.

3 RESULTS AND DISCUSSION

The power threshold for plastic deformation was consistently 400 mW. An interferometric image of a micro-mirror deformed elastically due to local thermal expansion is shown in Fig. 3. By comparing the bulge peak-valley (P-V) vs. optical power and temperature vs. optical power, we computed the linear relationship between bulge P-V and temperature, shown in Fig. 4.

Transient micro-mirror heating/cooling occurs over 2.2 ms, as measured with a 0.14 ms temporal resolution using stroboscopic interferometry. Results are shown in Fig. 5. Without this stroboscopic modification, interferometry can not measure such short-lived deformations.

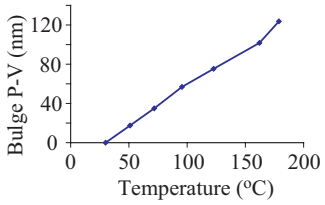

Figure 4. *Bulge P-V vs. surface temperature, revealed by comparing interferometry and thermography results.*

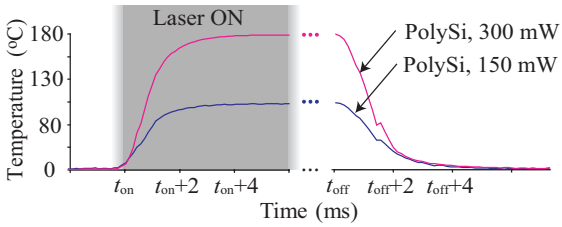

Figure 5*: Interferometric heating/cooling results.*

Incorporation of thermography measurements permits temperature to deformation correlation. Temperatures of the mirror surface ranged up to 179°C at a bulge P-V of 124 nm due to 300 mW of incident radiation. Results indicate that for the <400 mW elastic regime, deformation is proportional to optical power.

4 CONCLUSIONS

The micro-mirror thermal-mechanical behavior has been characterized using a novel application stroboscopic interferometry and infrared thermography. Issues such as how the heat can be better distributed and how deformation can be reduced in critical locations such as the bearing hub can be better understood and solved.

These observations of repeatable, transient MEMS thermal response provide an essential contribution to understanding heat transfer in thin films. The correlation between surface temperature and deformation permits the quantification of radiant and conductive energy rates, which are essential for thermal modeling. Multi-physics analysis software can be validated and improved by comparison with these experimental results. There are numerous other applications in which such dynamic measurement of the transient thermal response of MEMS can be useful, such as bolometers, thermal actuators, and temperature sensitive safety mechanisms.

REFERENCES

1. A.D. Oliver et al., "Microsystems based on surface micromachined mechanisms", *Proceedings of IEEE, Sensors*, 2, pp. 1188-1192 (2002).
2. C.C. Wong and S. Graham, "Investigating the thermal response of a micro-optical shutter", *IEEE Transactions on Components and Packaging Technologies*, 26, 2 (2003).
3. E. Novak et al., "MEMS metrology using a strobed interferometric system", ASPE Winter Topical Mtg. (2003).
4. C.R. Forest et al., "Static and dynamic optical metrology of micro-mirror thermal deformation", NSTI Nanotech Conference (2004).

A CONTINUOUS METHOD FOR MANUFACTURING POLYMER STRINGS AND TUBES

W. Jeong[1], G. Mensing[2], S. Lee[1], D. J. Beebe[2]
[1] Department of Biomedical Engineering, School of Medicine, Dankook University, South Korea
[2] Department of Biomedical Engineering, University of Wisconsin-Madison
Madison, Wisconsin 53706

ABSTRACT

We present a method for the continuous manufacture of micro scale polymer strings and tubes. The method utilizes hydrodynamic focusing and liquid phase photopolymerization. A number of different strings and tubes are demonstrated including the ability to control local properties. Strings and tubes are used in many applications. By including active biomolecules within the micro strings, biosensing strings are demonstrated.

INTRODUCTION

In nature, spiders produce a liquid that solidifies when exposed to air. Here we present an analogous process replacing spontaneous solidification via exposure to air with light initiated solidification. By utilizing 3D multiple stream laminar flow [1] and *in situ* photopolymerization [2], we create a continuous process for the creation of micro scale cylindrical structures.

Strings and tubes are perhaps the most common curved object in both the natural and man-made world enabling a plethora of functions across fields (e.g. medicine, biotechnology). Recent advances in man-made micro scale systems have largely relied on planar two and three dimensional (3D) geometries inherent to integrated circuit derived processes. Recent soft material-based micro systems have provided alternatives in functionality via elastomeric [3] and stimuli responsive materials [2], but their origins are still rooted in pseudo 3D constructs. Extrusion/casting [4], layering [5], or fugitive [6] processes have been used to create small-scale strings and tubes. While these approaches have merit, all have limitations associated with solid-solid and extraction effects for the production of micron-scale tubes or fibers in continuous lengths. The process presented here is conceptually simple using microscale phenomena (e.g. laminar flow, diffusion) and readily scalable to large volume manufacturing. Importantly, the process also allows flexibility in materials choice while providing control over local material properties.

RESULTS AND DISCUSSION

To make micro fibers, the polymerizable sample fluid (4-Hydroxybutyl acrylate (4-HBA)) and non-polymerizable sheath fluid (50 Vol% Polyvinylalcohol (PVA) + 50 Vol% DI water) are combined in stage X of the apparatus illustrated in Fig. 1 to produce a stable sheath flow around a sample stream. Next, the concepts of *in situ* and liquid phase photopolymerization are extended to "on the fly" photopolymerization (i.e. continuous radiation of a moving liquid) to polymerize the sample stream as it flows towards the outlet of the channel. There is no moving solid-solid interface, but rather the moving sample stream is transformed to a solid in a continuous process. By changing the sample and sheath flow rates, the size of the polymerized microstructure can be easily and precisely controlled (Fig 3). By adding a second stage to the apparatus (Fig. 1, left dotted square), micro tubes are fabricated (Fig. 2 bottom; Fig. 5 left). Into stage Y, the core fluid (25 Vol% PVA + 75 Vol% DI water) and sample fluid (4-HBA) are introduced and a core surrounded by sample flow is produced. The core/sample flow then enters stage X where a second sheath fluid (50 Vol% (PVA) + 50 Vol% DI water) is introduced producing a core/sample/sheath flow construct. Upon subsequent and continuous UV exposure, micro tubes are continuously formed.

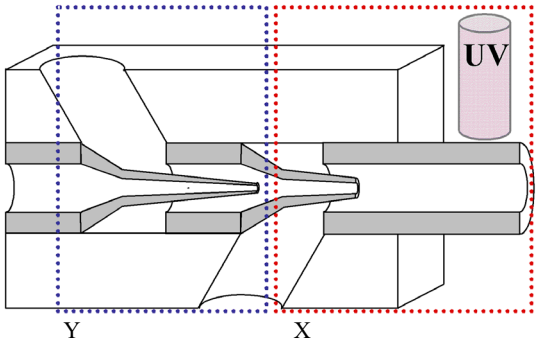

Figure 1. *A schematic diagram of the first (right dotted box) and second stage (left dotted box) channel apparatus. A micropipette puller (P-87, Sutter Instrument Co.) was used to produce the pulled micropipettes with inner diameter of approximately 20 m.*

Examples of the types of strings and tubes produced are shown in Fig 2. Importantly, the use of laminar flow and diffusion enables the local control of the physical and chemical properties of the resultant fibers and tubes. This concept is demonstrated by using two different fluids (one containing a dye and one without the dye) to form the sample stream; the resultant fiber contains a gradient of this dye (Fig. 4). The continuous nature of the process will allow one to scale a simple responsive swatch (Fig. 6) into cloth while simultaneously incorporating local functionality via parametric control combined with upstream microfluidic processing. For example, a "t" channel junction upstream of stage Y enables the creation of local packets within the sample fluid streams providing chemical and physical control of the fibers/tubes along their length while diffusion/gradients allow control along their width. By entrapping enzymes into the sample stream, sensing strings can be mass-produced [7] (Fig. 5 right demonstrates a glucose sensing string).

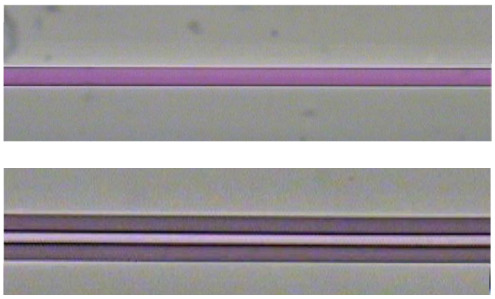

Figure 2. *Top – String output from the first stage (sheath and sample flow). Bottom – Tube output from both stages (sheath, sample and flow flow).*

0-9640024-5-0/hh2004/$20©2004TRF
DOI 10.31438/trf.hh2004.102

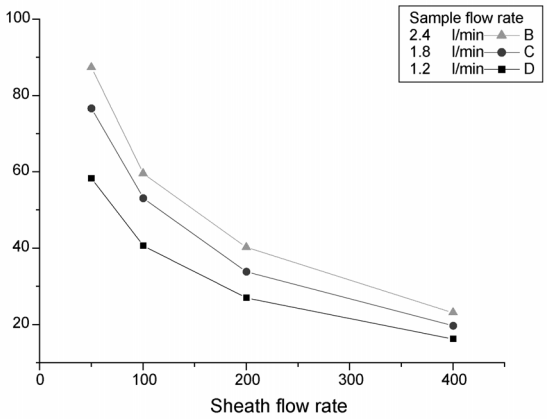

Figure 3. *String diameter (x axis, um) is a function of sample and sheath flow rate. Note strings with outer diameters under 20 microns have been made in our first attempts. Much smaller strings should be possible with optimization of the process.*

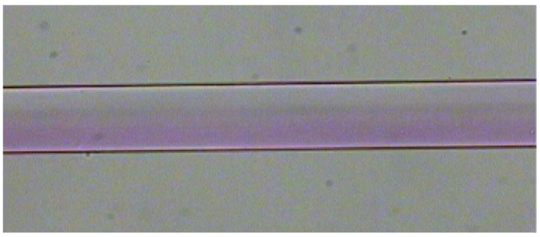

Figure 4. *A gradient is produced from top (low) to bottom (high) across the string.*

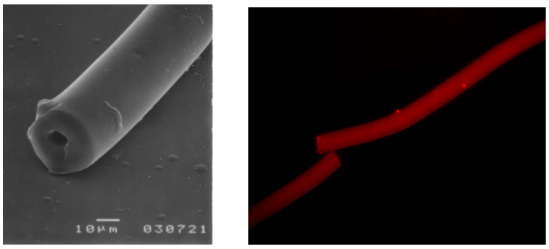

Figure 5*. Left - A scanning electron micrograph of a micro tube. Right –Fluorescent image of a glucose sensing string.*

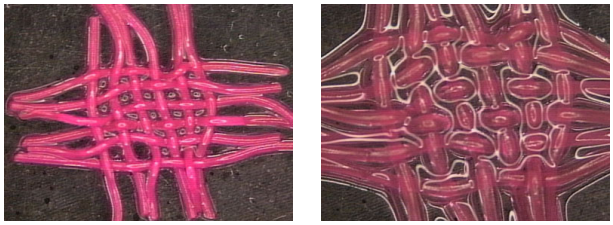

Figure 6*. A patch of woven strings made of pH responsive polymer. Left – unswollen, right – swollen.*

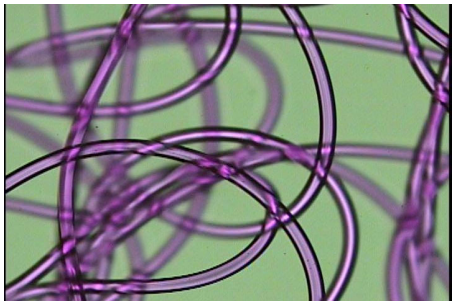

Figure 7*. A jumble of micro polymer string produced using the continuously flowing liquid phase photopolymerization process.*

CONCLUSION

The ability to continuously manufacture micro scale fibers and tubes cost effectively will facilitate their use in many applications. The flexibility of the method across different materials, geometries, and scales is a key advantage over many existing methods that require some form of re-tooling to realize different outcomes. By controlling the flow parameters (steady and time varying hydrodynamic focusing), polymerization parameters (time, distance, intensity), and material parameters (stimuli responsive, viscosity) a wide variety of physical and chemical properties (chemical composition, geometry, scale) can be achieved using a single manufacturing system. Natural shapes can now be readily produced enabling biomimetic designs for medicine (e.g. smart stents, tubular scaffolds) and biotechnology (e.g. embedded functionality, artificial xylem, sensors).

ACKNOWLEDGMENTS

The work was supported under a grant from DARPA-MTO (#F30602-00-1-0570) (Program manager: Dr. Michael Krihak).

REFERENCES

1. Kenis, P.J., Ismagilov, R.F., & Whitesides G.M. Microfabrication inside capillaries using multiphase laminar flow patterning. *Science* **285**, 83-85 (1999).
2. Beebe, D.J. et al. Functional hydrogel structures for autonomous flow control inside microfluidic channels. *Nature* **404**, 588-590 (2000).
3. Unger, M.A., Chou, H., Thorsen, T., Scherer, A., & Quake, S.R. Monolithic microfabricated valves and pumps by multilayer soft lithography. *Science* **288**, 113-116 (2000).
4. Dalton, P. D., Flynn, L., & Shoichet, S. C. Manufacture of poly(2-hydroxyethyl methacrylate-co-methyl methacrylate) hydrogel tubes for use as nerve guidance channels. *Biomaterials* **22**, 3843-3851 (2002).
5. Chou, S.Y., Krauss, P.R., & Renstrom, P.J. Imprint lithography with 25-nanometer resolution. *Science* **272**, 85-87 (1996).
6. Hoffman, W.P., Phan, H.T., & Wapner, P.G. The far-reaching nature of microtube technology. *Mat. Res. Innovat.* **2**, 87-96 (1998).
7. Seong, G.H., Heo, J., & Crooks, R.M., Measurement of enzyme kinetics using a continuous-flow microfluidic system. *Anal. Chem.* **75**, 3161-3167 (2003).

DEVELOPMENT OF A MICROFABRICATED VAPOR PRECONCENTRATOR FOR PORTABLE ION MOBILITY SPECTROSCOPY

Michael Martin, Mark Crain, Kevin Walsh
Department of Electrical and Computer Engineering
University of Louisville
Louisville, Kentucky 40292

R. Andrew McGill, E.J. Houser, D. Mott, Jennifer Stepnowski, Stanley V. Stepnowski, V. Nguyen, Huey-Daw Wu
Naval Research Laboratory
Code 6375, Washington, DC 20375

Stuart Ross
Dstl. Porton Down, Salisbury, UK

David J. Nagel, Ioana Voiculescu
Department of Electrical Engineering
George Washington University, Washington, DC

ABSTRACT

This work is part of the Cascade Avalanche Sorbant Plate ARray (CASPAR) project whose goals are the development of flow through preconcentrators that may be stacked into multiple planes for enhanced performance. These devices act as the front end of a portable Ion Mobility Spectrometer (IMS) for the detection of trace explosive or chemical agent vapors. We report on the design, simulation, fabrication and performance of 7mm x 7mm polyimide preconcentrators. The devices are composed of dual serpentine platinum heaters supported by a 3-6 µm thick layer of polyimide suspended over a silicon frame. Early prototypes have demonstrated an order of magnitude improvement in detection threshold for a single plane when tested with a commercial portable explosive detector.

INTRODUCTION

The chemical preconcentrator described in this paper is a microfabricated hotplate that is coated with a polymer that selectively absorbs the analyte of interest at or near room temperature during the collection phase[1]. In this project the preconcentrator area was maximized to take advantage of the inlet diameter of a commercial hand held IMS explosive detection system[2]. This necessitated designing preconcentrators with active areas of up to 7mm x 7mm which is a significant departure from other approaches[3]. In order to minimize both power consumption and thermal time constant, the heater traces are supported by a thin membrane. Several different approaches to heater support were investigated; a 2 µm thick silicon nitride membrane, a 2 µm thick heavily doped p++ silicon layer, and a 6 um thick polyimide layer. Designs were initially evaluated at the University of Louisville by using the CoventorWare™ Finite Element Analysis (FEA) software package to simulate operational characteristics. Then fabrication approaches were evaluated for the three designs. We report on the polyimide variety in this paper.

DESIGN

A number of design constraints are imposed on the preconcentrator by this application; the foremost being typical considerations for portable sensing. Namely, the component must minimize power consumption, have a small physical footprint and be mechanically robust. The preconcentrator must also have a short thermal time constant (10's-100's ms) while reaching an operating temperature of 100-200 deg C. By minimizing this period, the analyte plug desorbed from the preconcentrator arrives at the detector with increased amplitude, improving the overall signal to noise ratio. The device's efficacy can be maximized by stacking the preconcentrator planes. They are therefore designed with perforations arranged so that a second layer that is rotated by 90° will intercept analyte passing through the holes of previous preconcentrator planes.

Variations on the basic design depicted in Figure 1 were explored. The heater is a platinum dual serpentine either 25 µm or 35 µm wide. It defines an active region that is either 7mm x 7mm or 6mm x 6mm depending on the design variation. It is composed of a sputtered Cr/Pt layer, 0.02µm and 0.16µm thick respectively. The heaters are supported by a 6µm thick layer of polyimide perforated with an array of rectangular openings (375µm x 125µm). The open area fraction within the active region is either ~42% (high perforation density) or ~21% (low perforation density). Relatively large apertures around the outside of the active area serve to isolate it from the cool silicon frame while preventing development of excess pressure drop at flow rates up to 0.5 L/minute.

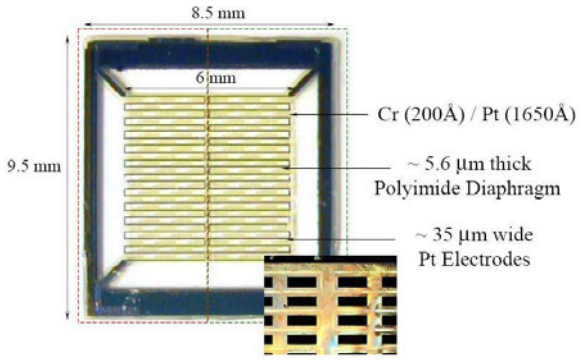

Figure 1 *Micrograph of a 6mm x 6mm prototype CASPAR preconcentrator*

SIMULATION

The finite element analysis (FEA) software, CoventorWare™, was used to model the behavior of the polyimide hotplates. It allows simulation of Joule heating within an electrode and calculation, in three dimensions, of either the transient or steady state thermal distribution. Given that thin film properties vary significantly from their bulk values, the Temperature Coefficient of Resistance (TCR) for the sputtered platinum heater was measured for 22 separate heaters, averaged together and incorporated as a look-up table in the FEA.

A steady state analysis of a single 7 mm x 7mm design variant is presented here. It consists of a 5.6µm thick polyimide layer and

0-9640024-5-0/hh2004/$20©2004TRF
DOI 10.31438/trf.hh2004.103

0.18µm thick platinum traces. The silicon frame and bond pads are not directly incorporated in the model. The geometry has a 35µm wide heater and high perforation density (42% open area). The average preconcentrator operating temperature as a function of voltage was investigated from 5 V to 35 V in 5V increments and compared to experimentally determined values. The data are plotted in Fig. 2. The plot shows reasonable agreement with a significant systematic deviation occurring above 27V (~100°C).

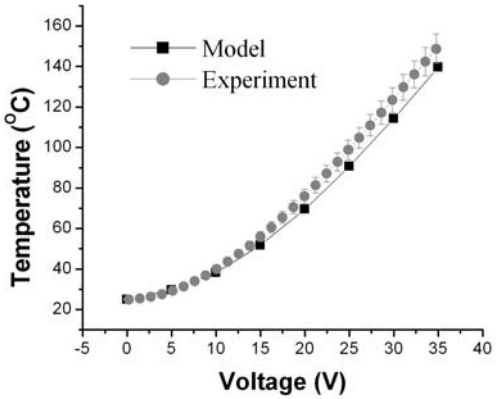

Figure 2 *Comparison of simulated average temperature in the heater to experimental values as a function of voltage.*

At an operating voltage of 30V the corresponding average heater temperature was ~120°C, essentially the target value for the NRL absorbent polymer. The modeled temperature distribution over the hotplate surface at this voltage was investigated as well as the transient thermal response. The simulation data yields a time constant of 41ms while the experimental yields 121ms.

FABRICATION

Devices are fabricated on 525µm thick (100) 4" silicon wafers on which a 0.45µm thick thermal oxide is grown. The oxide acts as both a masking layer on the back of the devices and as a stop layer at the front for Deep Reactive Ion Etching(DRIE). HDMS PI2611 polyimide is spin deposited and cured in a nitrogen atmosphere. The final polyimide thickness is 5.6±0.2 µm. Aluminum is sputtered on the cured polyimide and patterned to act as a masking layer for oxygen plasma etching. The etch step introduces the perforations in the polyimide. After removing the aluminum, a Cr/Pt (0.02±0.03 µm and 0.16±0.03 µm thick, respectively) layer is sputter deposited and patterned using lift-off to produce the heaters. The polished side of the wafer is coated in 7 µm thick positive resist in preparation for back side processing and subsequent dicing. Bulk etch windows for DRIE are opened on the back by spin coating with a 10 µm thick negative resist. The resist is exposed after a back to front alignment to produce 8mm x 8mm openings at the back of each die. The exposed oxide is removed in a buffered oxide etch. Before DRIE, the wafer is diced into individual die. The hotplates are plasma etched in groups of up to 16 in order to minimize etch rate variations caused by the large exposed silicon area on the back. DRIE is performed in a MESC Multiplex from Surface Technology Systems, Plc. for ~4 hours using 3 different platen biases in separate steps. Once the oxide stop layer is exposed the samples are removed from the DRIE and cleaned. Before testing, the sorbent polymer is selectively deposited in the active area using an inkjet printer.

EXPERIMENT

Prototypes were characterized by measuring resistance as a function of temperature in a probe station. The current for the resistance measurement was fixed to 10 µA to avoid heating the hotplate. The chip was mounted on a thermal chuck and the temperature was varied from 25°C to 200°C. During the measurement, nitrogen gas was used to purge the chamber to avoid problems with water condensation.

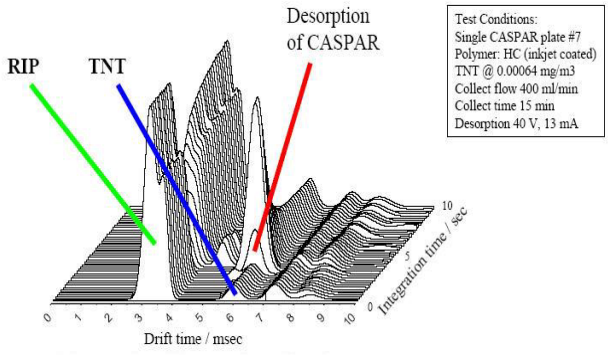

Figure 3 *Initial preconcentrator testing using Vapor Tracer II IMS. The RIP is a Reactive Ion Peak used to transfer charge to the analyte before it is accelerated in the drift tube.*

The temperature versus resistance data were used to determine the temperature coefficient of resistance (TCR). These data were also used as a calibration so that temperature versus power, voltage and time could be found.

The performance of sorbant coated micro-hotplates was qualified by interfacing the device to the front end of an IMS system. 2,4,6-Trinitrotouluene at a concentration just below the inherent detection limit of the IMS was introduced through a thermostatic column for periods ranging from 10 seconds to 30 minutes. Subsequent desorption from a CASPAR prototype produced at least an order of magnitude increase in analyte concentration, see Figure 3.

CONCLUSIONS

A single preconcentrator plane has demonstrated at least an order of magnitude improvement in the detection threshold of a portable IMS explosive detector. The prototype achieved a temperature of 120°C at ~30V in less than 120msec while consuming a total of 175mW in a DC drive mode. Direct measurements of the two dimensional thermal distribution has yet to be performed. However, simulation indicates up to 50°C variation in temperature over the hotplate surface at the operating voltage of 30V and a heater temperature of 120°C. This problem is caused by the relatively low thermal conductivity of the polyimide layer. Future designs will incorporate a metal thermal distribution plate sputtered onto the back of the preconcentrators.

REFERENCES

1. Eric J. Houser, Duane L. Simonson, Jennifer Stepnowski, Stuart K. Ross, Stanley V. Stepnowski III and R. Andrew McGill. "Design of Hydrogen Bond Acidic Polycarbosilanes for Chemical Sensor Applications", ACS Polymer Preprints, 45 (1): March 2004.
2. J.I. Baumbach and G.A. Eiceman,"Ion Mobility Spectrometry: Arriving On Site and Moving Beyond a Low Profile", Applied Spectroscopy, 53, 338A (1999)
3. Manginell, R.P.; Frye-Mason, G.C.; Kottenstette, R.J.; Lewis, P.R.; Channy Wong, C., "Microfabricated planar preconcentrator", Technical Digest. Solid-State Sensor and Actuator Workshop, Hilton Head Isl., SC, Transducer Research Foundation, Cleveland (2000) pgs. 179-182.

18μm THICK HIGH FREQUENCY CAPACITIVE HARPSS RESONATORS WITH REDUCED MOTIONAL RESISTANCE

Siavash Pourkamali and Farrokh Ayazi
School of Electrical and Computer Engineering, Georgia Institute of Technology
Atlanta, GA 30332-0250

ABSTRACT

This paper reports on implementation and high-Q operation of thick bulk mode VHF capacitive disk resonators with reduced motional resistance. Single crystal silicon (SCS) disk resonators as thick as 18μm with capacitive gap size of 160nm (aspect ratio>110) are fabricated on SOI substrates using a three-mask version of the HARPSS on SOI process. The new resonator design with increased number of electrodes as well as larger device thickness results in over 20X lower motional resistance and larger signal to noise ratio comparing to the previously demonstrated thin VHF HARPSS resonators. Quality factor as high as 25,900 is measured for an 18μm thick side-supported disk resonator in air at the frequency of 149.3MHz. The same resonator exhibits a quality factor of 45,700 in vacuum.

INTRODUCTION

A great amount of research is being conducted on silicon based micromechanical resonant devices as viable substitutes for currently off-chip frequency selective components in electronics. Despite recent demonstrations of operating frequencies in the UHF range with high quality factors (>10,000) [1], the major bottleneck for utilization of capacitive resonators as RF components is their extremely high equivalent impedances and low power handling capability. Several techniques have been incorporated in the design of microresonators in order to increase the electrostatic transduction area and reduce the motional resistance of such devices [1,2].

The first VHF SCS capacitive resonator was implemented using a HARPSS-based fabrication process on SOI substrate [3]. Comparing to the surface micromachined polysilicon resonators [1] with thickness limited to 2-3μm, HARPSS SCS resonators can potentially be as thick as a few tens of microns [4] providing much larger transduction area and consequently lower motional resistance and higher power handling. This work is the first demonstration of thick VHF HARPSS resonators using a simple three-mask process. It is shown practically that much lower motional impedances can be obtained from thicker resonators. The measured quality factors for the thick structures are even higher than that of their thin counterparts both in vacuum and air and the resonance frequency is not affected by the resonator thickness.

THREE-MASK HARPSS-ON-SOI PROCESS

A simple three-mask HARPSS on SOI process is developed in this work to fabricate thick SCS resonators with polysilicon sense and drive electrodes. The process flow is shown in Fig. 1. A 1μm thick thermal oxide layer is first grown on the low resistivity SOI substrate. The oxide is patterned and kept only on top of the resonating body of the resonators as well as the polarization voltage wirebonding pads (Fig. 1a) to protect them against the silicon etching plasma. Vertical trenches are then etched using the Bosch process all the way down to the SOI buried oxide to define the shape of the resonators. Therefore the thickness of the resonators is determined by the SOI device layer thickness and can be as large as a few tens of microns. Trench sidewalls are coated with a thin sacrificial LPCVD oxide layer. The thickness of the deposited sacrificial oxide layer determines the capacitive gap size in between the SCS resonators and their polysilicon electrodes and can be reduced to tens of nanometer independently from the lithography limits. Sacrificial oxide is etched back on the surface (Fig. 1b) and trenches are subsequently refilled with p-type doped polysilicon to form the electrodes. The silicon device layer is then patterned to provide electrical isolation between different devices as well as the input, output and body of individual resonators. At the same time the polysilicon inside the trenches is patterned and kept only in the electrode area (Fig. 1c). Structures are finally released and undercut in hydrofluoric acid by removing the sacrificial oxide layer and the underlying buried oxide (Fig. 1d).

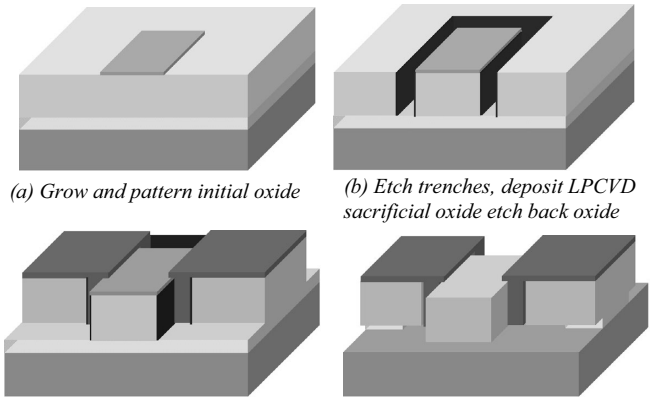

Figure 1. *Fabrication process flow for thick SCS bulk mode resonators on SOI.*

SCS disk resonators designed for operation in their elliptical resonance modes with frequencies in the VHF range were fabricated using the described processing technique. Figure 2 shows the close-up view of a fabricated 18μm thick, 29.2 in diameter side supported disk resonator and its electrodes. To maximize the quality factor, the disk is supported at only one resonance node with a 1.2μm wide, 4.0μm long support beam.

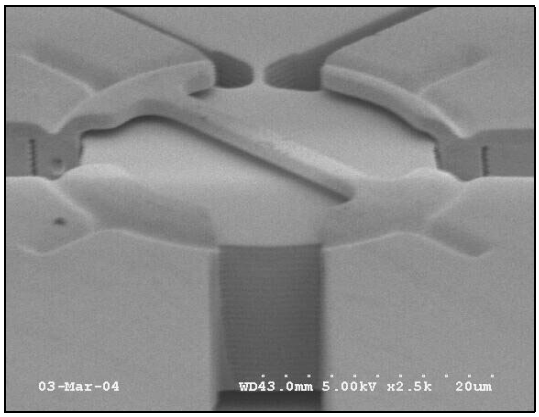

Figure 2. *SEM of a 29.2μm diameter, 18μm thick, SCS disk resonator supported at one resonance node. Gap Size = 160nm.*

0-9640024-5-0/hh2004/$20©2004TRF
DOI 10.31438/trf.hh2004.104

The new design for disk resonators in this work incorporates four electrodes all around the periphery of the disk for maximum signal transduction. Figure 3 is the overall SEM view of the same disk resonator showing all the electrode interconnections. Each pair of confronting electrodes of the resonator is electrically connected. The polysilicon beam bridging over the resonator (Fig. 2) provides electrical connection between two of the electrodes, while the other pair of electrodes are connected by a silicon trace extending around the device (Fig. 3).

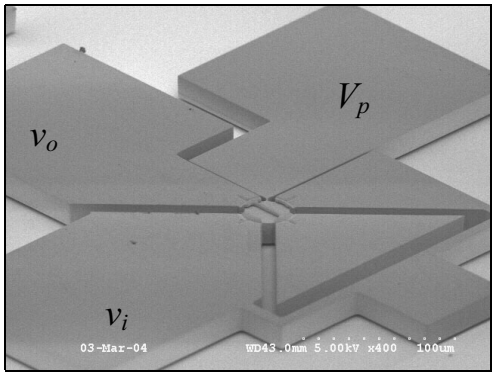

Figure 3. *Overall SEM view of the SCS disk resonator of Fig. 2, showing the electrode interconnections.*

MEASUREMENT AND DISCUSSION

The fabricated resonators were tested in a two-port configuration both in vacuum and atmospheric pressure. Figure 4 shows the frequency response of the 18μm thick disk resonator of Fig. 2, operating in its elliptical bulk mode at 149.3MHz while Fig. 5 is the frequency response of a 3μm thick resonator of the same type. Quality factor of 25,900 was measured for the 18μm thick resonator in air (Fig. 4a), which is over 3X larger than that of the 3μm thick resonator (Fig. 5a) and is the highest reported quality factor in air for VHF capacitive resonators. The measured quality factor for the 18μm thick resonator in vacuum is 45,700 (Fig 4b), slightly larger than that of the 3μm thick resonator (Fig. 5b). Comparing the frequency plots in Figs. 4 and 5, improved signal to noise ratio for the thicker resonator is apparent.

Despite having larger capacitive gap size comparing to the 3μm thick resonators, over 20X lower motional resistances (43.3kΩ in vacuum and 91.2kΩ in air) was measured for the 18μm thick resonator. Lower motional resistance is partly due to increased number of electrodes in the design and partly due to much larger device thickness. Motional resistance of a capacitive elliptical mode disk resonator is given by Eq. 1:

$$R_m = \frac{\sqrt{KM}\,d^4}{Q\varepsilon_0{}^2 L_{eff}{}^2 h^2 V_p{}^2} \propto \frac{d^4}{h.L_{eff}{}^2} \qquad (1)$$

where K and M are the effective stiffness and mass of the resonators, d is the capacitive gap size, ε_0 is the permitivity of the surrounding environment, h is the device thickness, V_p is the applied polarization voltage and L_{eff} is the effective electrode length and is given by Eq. 2:

$$L_{eff} = R.\sin(\theta_e) \qquad (2)$$

where θ_e is the span angle of the electrode and R is the disk radius. Therefore by increasing the number of electrodes from 2 to 4 in the new design, 2X larger effective electrode length and consequently 4X lower motional resistance is obtained. On the other hand 6 times larger device thickness results in an additional 6X lower motional resistance.

Further reduction of the capacitive gap size to 50nm for the same resonator will result in motional resistance values as low as 400Ω that is a reasonable value for RF applications.

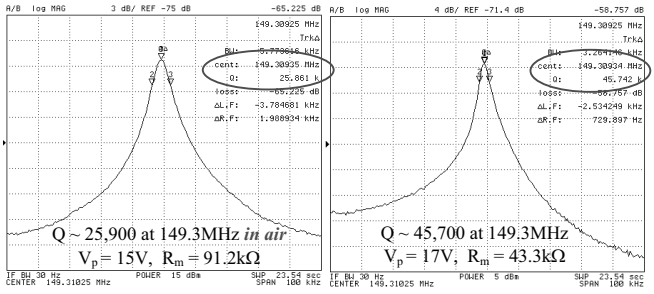

(a) *(b)*

Figure 4. *Frequency response of the 18μm thick, 29.2μm diameter disk resonator: (a) in air, (b) in vacuum.*

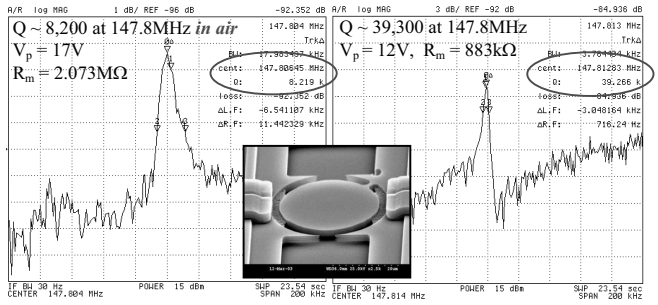

(a) *(b)*

Figure 5. *Frequency response of a 3μm thick, 29.4μm diameter disk resonator with 120nm capacitive gaps:(a) in air,(b)in vacuum.*

CONCLUSION

Thick SCS bulk mode capacitive disk resonators with operating frequencies in the VHF range were fabricated using a three-mask version of the HARPSS on SOI process. The possibility of operation of thick bulk mode resonators without quality factor or resonance frequency degradation was demonstrated for the first time. The fabricated disk resonators exhibited high quality factors of 45,700, and 25,900 in vacuum and atmospheric pressure respectively. Over 20X lower motional resistance and larger signal to noise ratio was obtained for the 18μm thick disk resonators with the new design comparing to the 3μm thick resonator of the same type. Reasonable motional resistances for RF applications can be obtained from the thick resonators by reducing the capacitive size to sub-100nm levels.

ACKNOWLEDGEMENT

This work is supported under the DARPA NMASP program. Travel support has been generously provided by the Transducers Research Foundation and by the DARPA MEMS and DARPA BioFlips programs.

REFERENCES

[1] S. Li, et al, "Micromechanical hollow-disk ring resonators", *MEMS '04*, pp. 821-824.
[2] M. U. Demirci, et al, "Mechanically corner-coupled square microresonator array for reduce motional resistance", *Transducers '03*, pp. 955-958.
[3] S. Pourkamali, and F. Ayazi, "SOI-based HF and VHF single-crystal silicon resonators with sub-100nm nanometer vertical capacitive gaps", *Transducers '03*, pp.837-840.
[4] F. Ayazi and K. Najafi, "High Aspect-Ratio Combined Poly and Single-Crystal Silicon (HARPSS) MEMS Technology", *JMEMS*, Vol. 9, Issue: 3, 288, (2000).

MICRO MOLDED PDMS STRUCTURES FOR CARDIAC MYOCYTE RESTORING FORCE MEASUREMENTS

Yi Zhao, Hui Yu, Biao Li, and Xin Zhang
Department of Manufacturing Engineering and Fraunhofer USA Center for Manufacturing Innovation,
Boston University, Boston, Massachusetts 02215, USA (Tel: 617-358-2702; Email: xinz@bu.edu)

ABSTRACT

This paper presents restoring force measurements of cardiac myocyte using micro molded PDMS structures. Various aspect ratios of the structures were successfully realized by changing pre-curing time for crosslinking. The calcium-activated force was derived from averaged displacement of the micro structures, with nano-newton resolution. This approach has the physiology and pathophysiology potential to be a basis for precise determination of restoring force in cardiovascular study.

INTRODUCTION

Cardiac myocyte, the most heavily worked muscle cell in living body, realizes contractile performance according to ventricular load. The calcium-activated isometric restoring force of cardiac myocyte in response to membrane action potential is critical to maintain heart behavior. Even subtle changes in restoring force can cause serious heart disease, which would not cause any noticeable consequences in other tissues.

To determine the restoring force, Velden et al. attached the isolated cardiac myocyte with silicon glue to a sensitive force transducer and a piezoelectric motor [**1**]. The attachment, however, induces an undesirable external stimulation to the myocyte, and there is an obvious trade-off between transducer sensitivity, which affects noise and drift, and compliance. To minimize the external stimulation to myocyte, Helmes et al. demonstrated an in vitro assay to assess the restoring force by measuring the velocity of recoil in unloaded myocyte after rigor-induced contraction of the force-generated unit (sarcomere) [**2**]. Although the surrogate measurement of restoring force from dynamics sarcomere relengthening was theoretically feasible, a measurement technique is needed for direct force probing. Consequently, investigators have relied on soft materials where the crosslinked chemistry was used to control the mechanical compliance [**3,4**]. Contraction generated deformation was traced by the displacement of beads or microfabricated markers embedded in the substrate, and restoring force can thus be derived. With important advances it made, this approach is, however, limited by the fact that it requires intensive computation of force calibration from continuous substrate deformation.

In this paper, we demonstrate a novel approach for restoring force measurements in isolated myocyte using closely spaced micro molded PDMS structures. This approach fairly isolates force probing from deformation effect of continuous substrate, which allows more accurate probing of restoring forces. With a nano-newton resolution, it has the physiology and pathophysiology potential to be a basis for precise determination of restoring force in cardiovascular study.

FABRICATION

Micro molded PDMS structures were fabricated from silicon molds as illustrated in Figure 1. To make a silicon template containing an array of single spaced holes or walls, silicon wafers coated with photoresist were exposed and developed (Figure 1a), followed by a deep RIE process for high aspect ratio structures (2-5 μm in lateral dimension) (Figure 1b). Prepolymer PDMS (Sylgard 184 with mixing ratio of 10:1) was poured on a glass slide and pre-cured at 65°C (Figure 1c). Then it was put in contact with the silicon template and pumped in vacuum chamber for 5-min degassing. Further curing was subsequently carried out at 65°C for fully crosslinking, making the total curing time up to 1 hour or so. Afterwards, the template was carefully peeled off from PDMS, with the pattern transferred (Figure 1d). It was found that higher aspect ratio associates with smaller pre-curing time and vice versa (Figure 1e), which is believed due to compromise between vacuum intensity and PDMS viscosity. Hence, resulted PDMS structures (Figure 2) are typically shorter in height as compared to their silicon templates. For the mixing ratio used in this work, i.e. 10:1, preferable structures with aspect ratio from 1:3 to 1:4 experience pre-curing time varied from 6 to 9 minutes. As shown in Figure 3, shorter curing causes structures leaning against their neighboring peers (left most); while longer curing compromises with lower force probing sensitivity (two in right most). The elastic modulus of the PDMS structures measured using the Hysitron Triboindenter system yields about 1000 kPa.

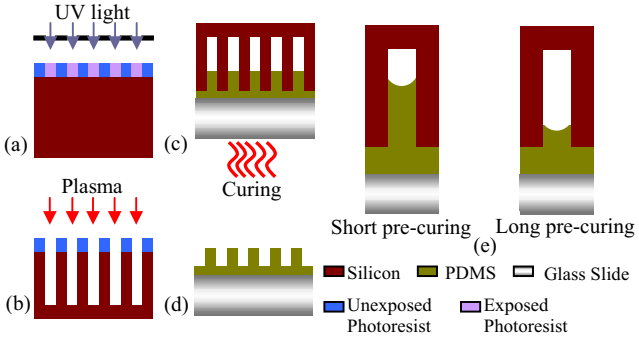

Figure 1. *Micro molding process for PDMS structures.*

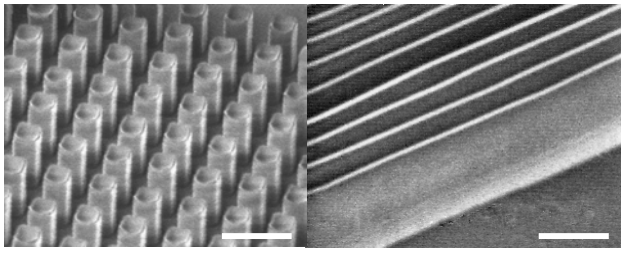

Figure 2. *Micro molded PDMS pillars (a) and walls (b). (Scale bars indicate 10μm).*

EXPERIMENTS AND RESULTS

Fabricated PDMS structure peeled off from glass slide was immerged in medical ethanol for sterilization. Leminin was then coated and kept for 2 hours to enhance adhesion. The heart of Wistar rat was digested with collagenase via langendorf perfusion to obtain isolated, calcium tolerant myocytes. The myocytes were plated on laminin-coated PDMS structure. And the structure with the plated myocytes was put in culture media in a 100 petri dish and stored overnight in a 37°C incubator.

The experimental apparatus used to measure the structure displacement is described as follows. The PDMS substrate with myocytes was placed in a custom-made chamber, which was

Travel support has been generously provided by the Tranducers Research Foundation and by the DARPA MEMS and DARPA BioFlips programs

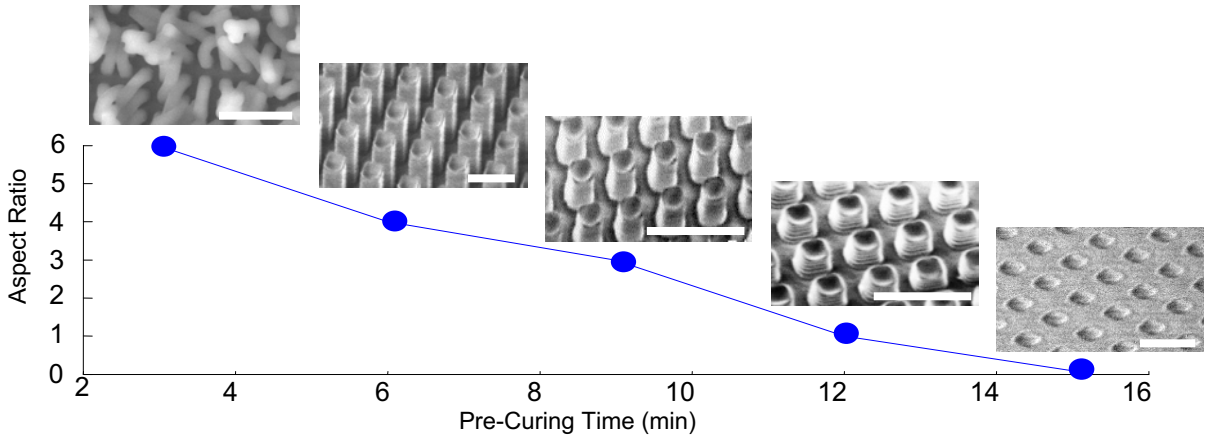

Figure 3. *PDMS structures with various aspect ratios are realized with different pre-curing time. (Space bars indicate 10 μm)*

mounted on an inverted microscope (400×), and stimulated by a digital pacer with periodical voltage pulse. The myocyte contracts in response to the pulse due to the raise of calcium level, followed by a passive relengthening. The process was imaged using a variable frame rate (60-240 Hz) CCD camera, and the images were digitized. The video lines were averaged vertically, and the program performed a Fast-fourier transform (FFT) on the averaged density trace, the peak of the resulting power spectra for various regions in a PDMS structure was thus obtained. The spectra peak represents the structure spacing, which is ultimately converted to the structure displacement. Contraction of the myocyte was traced in the same manner by changing focus to its top surface.

As one of typical results illustrated in Figure 4, the myocyte has an averaged contraction of 8.83 μm (region A) in response to voltage pulse (indicated by black arrows), while the induced displacements of underneath pillars average 0.63 μm (region B). The restoring force can thus be derived, providing Young's modulus and geometry of the pillars. The force probing resolution was calculated as about 2 nN. Furthermore, it was found that the pillars next to the myocyte (region C) do not represent an observable displacement in response to membrane action potential, indicating a fairly good isolation of the restoring force probing from deformation effect of continuous substrate.

Moreover, the non-sliding assumption between myocyte and its underneath PDMS pillars was validated using environmental

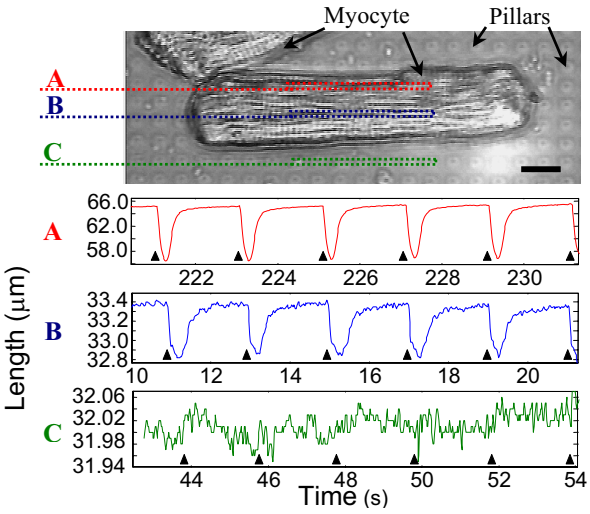

Figure 4. *Tracings were carried out on myocyte surface (region A), pillars underneath the myocyte (region B), and pillars next to the myocyte (region C), respectively. (Scale bar indicates 5 μm)*

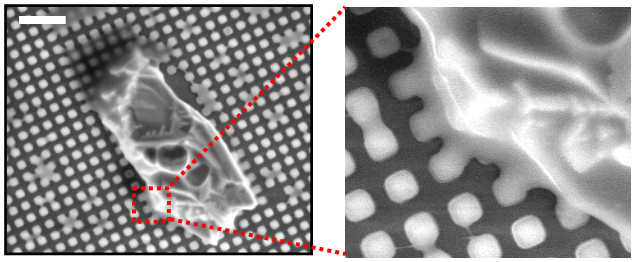

Figure 5. *Environmental SEM observation after force probing indicates good adhesion of myocyte with underneath PDMS pillar arrays. (Scale bar indicates 10 μm)*

SEM after force probing (Figure 5). The good adhesion of the myocyte body with its underneath micro structure ensures the authenticity of the force measurements.

CONCLUSION

In this paper, we have demonstrated a novel approach for myocyte restoring force measurements using closely spaced micro molded PDMS structures. This method not only eliminates direct attachment of myocyte with force transducer, but also isolates force probing from continuous substrate deformation. With nano-newton resolution, it promises the potential with physiology and pathophysiology significance for precise determination of restoring force in cardiovascular study.

ACKNOWLEDGEMENTS

This work is supported by the NSF CAREER Award. The authors would like to thank Dr. Michiel Helmes and his colleagues at Whitaker Cardiovascular Institute, Boston University School of Medicine for their technical advices, and Dr. Richard Schalek at Harvard University Imaging Center for the assistance on environmental SEM observations.

REFERENCES

1. J. Velden, et al., "Force production in mechanically isolated cardiac myocyte from human ventricular muscle tissue", *Cardiovascular Research*, *28*, 414 (1998).
2. M. Helmes, et al., "Time determines the Frank-Starling relation in early diastole", *Journal of General Physiology, 121*, 97 (2003).
3. A. Harris, et al., "Silicone rubber substrata: a new wrinkle in the study of cell locomotion", *Science, 208*, 177 (1980).
4. N. Balaban, et al., "Force and adhesion assembly: a close relationship between studies using elastic micropatterned substrates", *Nature Cell Biology, 3*, 466 (2001).

ISE ARRAYS WITH IMPROVED DYNAMIC RESPONSE AND LIFETIME

Steven M. Martin[1], Jeonghan Ha[2], Jin Wook Kim[2], Timothy D. Strong[1], Geun Sig Cha[2], Richard B. Brown[1]

[1]Dept. of Electrical Eng. and Computer Science, University of Michigan, Ann Arbor, MI USA

[2]Dept. of Chemistry, Kwangwoon University, Nowon-gu, Seoul, South Korea

ABSTRACT

Poly(vinlychloride) (PVC) based ion-selective electrodes (ISEs) exhibit poor substrate adhesion and often fail due electrolytic shunts around the membrane. Silicone rubber (SR) based ISEs have improved surface adhesion, solving the shunt problem, but they have over 15x larger impedances. This increased impedance yields noisy signals and long response times. An ion-selective electrode array with on-chip CMOS buffers was implemented to negate the effects of the silicone rubber membrane's increased impedance. The array was implemented using post-CMOS thin-film fabrication techniques. Theoretical calculations for ISE response time are presented and experimentally verified. Results demonstrated that the dynamic response of on-chip buffered ISEs was 7.5x faster than conventional electrodes, even though they were 225 times smaller. The silicone rubber ISEs demonstrated a 40x increase in lifetime versus PVC membranes, functioning properly for more than 120days.

INTRODUCTION

Poly(vinylchloride) (PVC) is a commonly used membrane in ion-selective electrodes (ISEs) due to its superb electrochemical properties. PVC, however, has poor mechanical adhesion to the silicon substrates often used in micropotentiometric sensors [1]. Poor adhesion is the leading cause of failure in solid-state potentiometric sensors [2]. Membrane matrices having better mechanical properties have been previously investigated. Of these, silicone rubber (SR) has shown exceptional adhesive strength to silicon nitride substrates [3-5].

Compared to PVC, silicone rubber membranes have larger source impedances. Conventional ion-selective electrodes can utilize silicone rubber membranes because the ISEs have large surface areas, and impedance is inversely proportional to area [6]. Solid-state ISE arrays, however, use small geometries which results in ISEs having large impedances, slow responses, and poor detection limits [5]. Membrane impedance may be reduced by engineering the membrane composition. Adding lipophilic salts and various plasticizers can reduce impedance, but they also reduce adhesion [4-5].

In this work, the impedance, response, and lifetime of several silicone rubber membranes were investigated. A solid-state ISE array with on-chip CMOS buffers was developed to enable the use of silicone rubber micropotentiometric sensors. The array was fabricated using a commercial CMOS process and the electrodes and membranes were post-processed on top of the electronics. The membranes were characterized on three electrodes including: conventional liquid junction, passive solid-state, and the CMOS-integrated solid-state electrodes. A model of the ISE response was developed and experimentally verified. Lifetime of the various devices was also examined.

Travel support has been generously provided by the Transducers Research Foundation and by the DARPA MEMS and DARPA BioFlips programs.

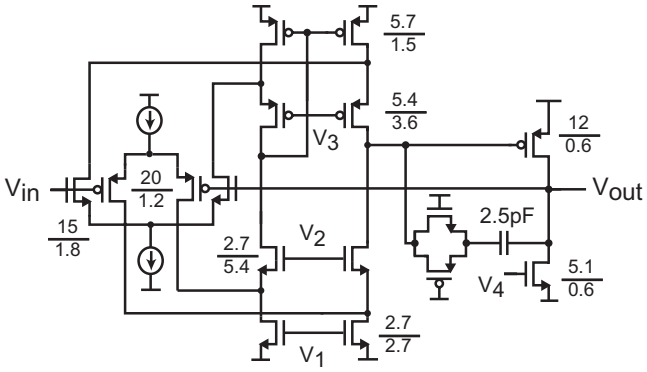

Figure 1. *Unity-gain buffer.*

Table I. *Measured unity-gain buffer characteristics.*

Specification	Conditions	Value
Supply		+/- 1.5 V
Power	R_{load} = 1MΩ	0.9 mW
Open-loop gain	Simulated	100 dB
Closed-loop gain	R_{load} = 1MΩ	-0.98 V/V
3dB Bandwidth	C_{load} = 13 pF	2.1 MHz
Input Impedance	Freq = 0 Hz	> 20 GΩ
Output Impedance		< 100 Ω
Input Common Mode Range		2.6 V
Output Swing	R_{load} = 1MΩ	2.6 V
Slew Rate	C_{load} = 13 pF	20 mV/μs
Settle Time (1 V step)	C_{load} = 13 pF	3.5 μs
Area		0.023 mm^2

EXPERIMENT

Arrays of CMOS op-amps, configured as unity-gain buffers, were fabricated in an AMI Semiconductor (*Pocatello, ID*) 0.5μm, 3V, CMOS process. The folded-cascode op-amps incorporated rail-to-rail input and output stages. Figure 1 shows the schematic of the buffers. Table I lists the measured performance of the unity-gain buffer.

Each die was designed to have six ion-selective electrodes with a 400μm diameter membrane and a 200μm diameter Ag/AgCl electrode. The electrode arrays were fabricated on top of the active die using CMOS-compatible, thin-film processing techniques. Fig-

0-9640024-5-0/hh2004/$20©2004TRF
DOI 10.31438/trf.hh2004.106

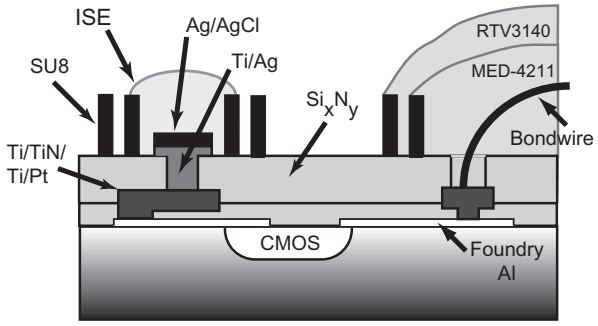

Figure 2. *Cross-section of an active ISE.*

ure 2 shows a cross-section of the completed devices. After delivery from the foundry, the CMOS devices were patterned for interconnect deposition and subjected to a short reactive-ion etch (RIE) to improve step coverage and patterning. A layer of Ti/TiN (40/80nm) was sputter-deposited to prevent interdiffusion between the aluminum and platinum layers. A layer of Ti/Pt (10/1000nm) was then evaporated onto the die and patterned using liftoff. A passivation layer of 400°C PECVD silicon nitride (800nm) was then deposited. Contact openings through the nitride were etched using RIE. Ti/Ag (20/650nm) was then sputter deposited and patterned using liftoff. Thin wells (12µm high) were patterned in SU-8. The SU-8 was cured at 150°C and became a permanent feature on the die. Next, the arrays were diced and bonded. The wirebonds were covered with a two step polymer coating of a silicone elastomer (MED-4211, *NuSil Silicon Technology, Santa Barbara, CA*) and silicone rubber (RTV3140, *Dow Chemical, Midland, MI*). Finally, the Ag electrodes were chloridized by submersion in 1M $FeCl_3$. Passive electrode arrays of identical size were similarly fabricated.

Three different silicon rubber (RTV3140) potassium-selective membranes (labeled K1-K3), and a PVC potassium-selective membrane (K4) were made according to Table II. The common additive potassium tetrakis[3,5-bis(p-chlorophenyl)borate (KTpClPB) and plasticizer dioctylsebacate (DOS) were incorporated into the membranes to study their effects on altering the membrane impedance and performance. The membranes were dissolved in tetrahydrofuran (THF) and dispensed into the SU-8 rings. The rings ensure a repeatable membrane thickness (≈12µm thick). The solvent was allowed to evaporate over several days, leaving behind the selective polymer membrane. Microphotographs of completed devices are shown in Figure 3.

RESULTS AND DISCUSSION

The impedance of the membranes on the different electrode types was recorded using electron impedance spectroscopy (EIS) in a solution of 50mM Tris-H_2SO_4, pH 7.4 plus 0.1M KCl. The results of the EIS experiments were averaged over four different devices

.

Table II. *Membrane compositions.*

Components	K1	K2	K3	K4
Matrix	RTV3140 198 mg	RTV3140 198 mg	RTV3140 198 mg	PVC 66 mg
Additive: KTpClPB	0.6 mg			
Plasticizer: DOS		13.3 mg		133 mg
Ionophore: valinomycin	2.0 mg	2.0 mg	2.0 mg	2.0 mg

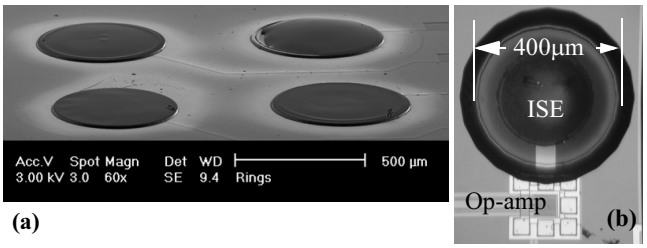

Figure 3. *(a) Scanning electron micrograph of four ISEs cast into the SU-8 containment rings. (b) Microphotograph of an active ISE showing the buffer op-amp and selective membrane.*

Table III. *Measured membrane impedances in MΩ*

Electrode Type	Area (mm^2)	K1	K2	K3	K4
Conventional	28.3	555	127	601	
Solid-State (passive)	0.13	8766	4600	7967	307

and are shown in Table III. The impedance of the active devices could not be measured because of the on-chip buffer, but their impedance should match that of the passive devices. The passive electrodes had impedances well into the gigaohm range even with the various additives. Comparatively, the average impedance of the PVC-based membrane was 307MΩ. These results demonstrate that the silicone rubber membranes were nearly 15x higher resistance.

The selectivity of the membranes was characterized using the matched potential method [7], and the results are shown in Table IV. The selectivity coefficient is a measure of the ratio of primary to interfering ion activity that results in an identical potential change of the sensor. The results indicate that the potassium-selective silicone rubber membranes are over four orders of magnitude more selective towards potassium than the most of other ions examined. The selectivity of the membranes is affected by the addition of the lipophilic salt. The results show that the selectivity is compromised the most in the lowest impedance silicone rubber membrane, K2.

The dynamic response of an ISE can be simulated using a two-time-constant model. The solution/membrane system has an intrinsic time constant, τ_1 [8]. The corresponding dynamic potential change of the membrane is given by

$$\Delta V_{mem}(t) = \frac{RT}{zF}\ln\left(\frac{a_f}{a_i}\right)\left[1 - \exp\left(-\frac{t}{\tau_1}\right)\right] \quad (1)$$

where t is time, R is the gas constant, T is temperature, z is the charge number of the ion, F is Faraday's constant, a_f is the final activity of the ion, and a_i is the initial activity of the ion. A second time-constant, τ_2, is formed by the membrane impedance in series with the input capacitance of the measuring circuit, C_{load}, as shown in Figure 4. Assuming an instantaneous change in activity, the change in output voltage can be derived from Figure 4 such that

$$\Delta V_{out}(t) = \frac{RT}{zF}\ln\left(\frac{a_f}{a_i}\right)\left[1 + \frac{\tau_2\exp\left(-\frac{t}{\tau_2}\right)}{\tau_1 - \tau_2} - \frac{\tau_1\exp\left(-\frac{t}{\tau_1}\right)}{\tau_1 - \tau_2}\right]. \quad (2)$$

Note that the effective impedance of the reference electrode is negligible compared to the resistance of the membrane. A commercial

Table IV. *Measured selectivity coefficients.*

Selectivity log ($K_{k,j}$)	Na^+	Ca^{2+}	Mg^{2+}	NH_4^+
K1 Membrane	< -5.0	< -5.0	-4.2	-2.0
K2 Membrane	-4.8	-4.6	-3.9	-1.9
K3 Membrane	< -5.0	< -5.0	-4.1	-2.0

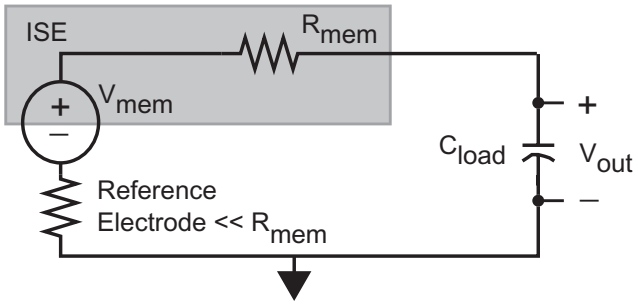

Figure 4. *Simple model for ISE dynamic response.*

15-channel pH meter (*Kosentech, South Korea*), with a measured input capacitance of 1nF, was used for recording. The active devices' input capacitance was approximately 100fF. Table V lists the corresponding time constants. Since the active devices minimize τ_2, τ_1 was empirically fit using the active devices' response. Figure 5 shows both the theoretical and experimentally measured dynamic responses to a decade change in concentration of K^+. The experiments were conducted in a solution of 50mM Tris-H_2SO_4, pH 7.4. Voltage offsets of the responses were eliminated mathematically before plotting. The figure clearly demonstrates the response time dependence on the membrane impedance and load capacitance. The active ISEs responded, on average, nearly 200x faster than passive ion-selective electrodes. The CMOS-buffered ISEs, which are 225x smaller than the conventional electrodes, were 7.5x faster than the conventional electrodes.

Figure 6 shows the measured calibration curves for the potassium-selective electrodes in a solution of 50mM Tris-H_2SO_4, pH 7.4. At room temperature, the theoretically calculated slope for potassium-selective electrodes is 59mV/dec. The percent error of the measured slope versus this ideal slope was 5% and 19% for the active and passive devices, respectively. The standard deviation of the slope was 0.7mV/dec for the active ISEs while the standard deviation of the slope was 3.0mV/dec for the passive sensors.

Figure 7 plots the slope of the calibration curve versus soaking time. The PVC membrane failed after 3days in 50mM Tris-H_2SO_4, pH 7.4, while the passive silicone rubber membrane survived nearly 50days before unexpectedly failing. All six of the passive ISEs failed on the same day indicating some catastrophic failure on the die. This failure is most likely unrelated to failures in

Table V. *Measured time constants in ms.*

Electrode Type	K1		K2		K3	
	τ_1	τ_2	τ_1	τ_2	τ_1	τ_2
Conventional	0.9	560	0.5	130	0.8	600
Solid-State (passive)	0.9	8800	0.5	4600	0.8	8000
Solid-State (active)	0.9	0.9	0.5	0.5	0.8	0.8

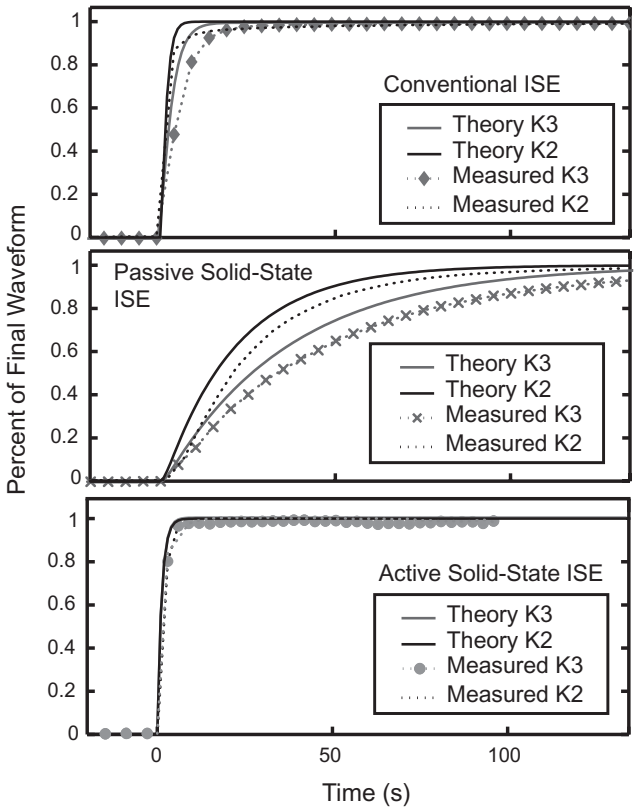

Figure 5. *Theoretical and measured dynamic response for the K2 and K3 membranes on the three electrode types.*

the ion-selective electrodes themselves. The active ISEs with silicone rubber membranes functioned properly for more than 120days.

CONCLUSION

The measured characteristics of the ion-selective electrodes are summarized in Table VI. The impedance of the silicone rubber membranes was shown to be 15x more resistive than PVC membranes. Incorporation of additives such as lipophilic salts into the membrane were unsuccessful at lowering the impedance below 1GΩ. CMOS-integrated ISE arrays were fabricated using thin-film post-processing techniques to enable the use of the high-resistance

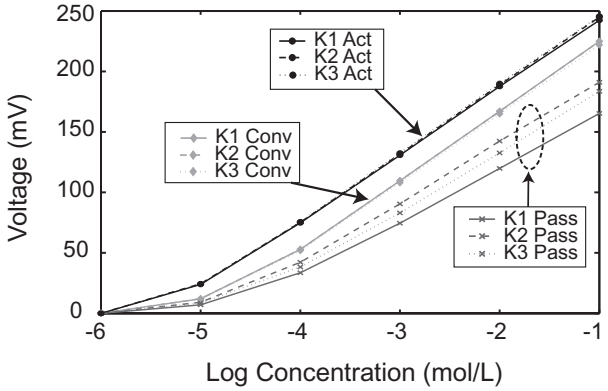

Figure 6. *Measure calibration curves for the ISEs.*

Table VI. *Summary of measured ISE characteristics.*

Membrane	Electrode Type	Impedance (MΩ)	Slope (mV/dec)	Response Time 95% (s)	Detection Limit (μM)	Lifetime (days)
	conventional	555	56.0	5	14	>120
K1	passive	8766	44.1	234	17	46
	active		56.5	1	9.4	>120
	conventional	127	56.0	12	17	>120
K2	passive	4600	49.8	130	12	46
	active		55.9	1	10	>120
	conventional	601	56.5	22	15	>120
K3	passive	7967	48.6	250	15	46
	active		55.0	3	9.9	>120

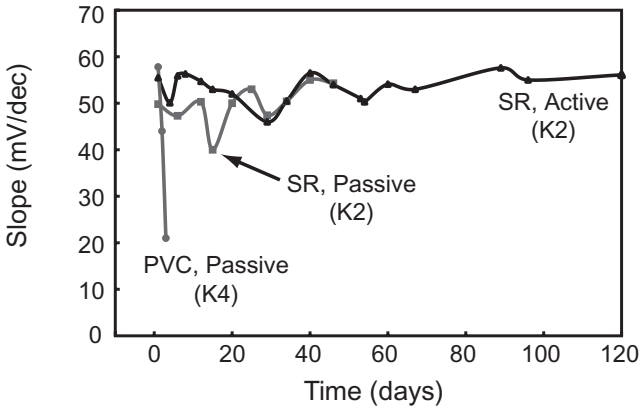

Figure 7. *Measured lifetime of SR and PVC membranes.*

silicone rubber membranes in micropotentiometric sensors. Results indicated that the buffered ISEs had a 200x faster response than passive potentiometric sensors. The active devices were even faster than conventional electrodes while occupying 225x smaller area. The active ISEs improved the slope and linearity of the response versus the passive sensors. The active, SR-based ISEs survived for more than 120days with a response within 5% of ideal and a detection limit of 10μM. Response times, detection limits, and lifetimes for the economically fabricated active sensors were far superior to those of conventional and passive microelectrodes.

ACKNOWLEDGEMENTS

This work was supported in part by the Engineering Research Centers Program of the US National Science Foundation under Award Number EEC-9986866 and under a National Science Foundation Graduate Research Fellowship. The authors would like to thank the MOSIS MEP research support program for fabrication of the CMOS electronics.

REFERENCES

[1] H. Nam, G.S. Cha, T.D. Strong, J. Ha, J.H. Sim, R.W. Hower, S.M. Martin, and R.B. Brown, "Micropotentiometric Sensors," *Proceedings of the IEEE*, vol. 91, pp. 870-880, June 2003.

[2] R.B. Brown, "An Integrated Multiple-Sensor Chemical Transducer," *Ph.D. Dissertation*, University of Utah, 1985.

[3] G.S. Cha, D. Liu, M.E. Meyerhoff, H. C. Cantor, A.R. Midgley, H.D. Goldberg, and R.B. Brown, "Electrochemical Performance, Biocompatibility, and Adhesion of New Polymer Matrices for Solid-State Ion Sensors," *Analytical Chemistry*, vol. 63, pp.1666-1670, 1991.

[4] I.J. Yoon, D.K. Lee, H. Nam, G.S. Cha, T.D. Strong, and R.B. Brown, "Ion sensors using one-component room temperature vulcanized silicone rubber matrices," *Journal of Electroanalytical Chemistry*, vol. 464, pp. 135-142, 1999.

[5] E. Malinowska, V. Oklejas, R.W. Hower, R.B. Brown, and M.E. Meyerhoff, "Enhanced electrochemical performance of solid-state ion sensors based on silicone rubber membranes," *Sensors and Actuators B*, vol. 33, pp. 161-167, 1996.

[6] A. Bard, and L. Faulkner, *Electrochemical Methods: Fundamentals and Applications*, John Wiley & Sons, New York, NY, 1980.

[7] E. Baker, E. Pretsch, and P. Buhlmann, "Selectivity of Potentiometric Ion Sensors," *Analytical Chemistry*, vol. 72, pp. 1127-1133, 2000.

[8] W.E. Morf, E. Lindner, and W. Simon, "Theoretical Treatment of the Dynamic Response of Ion-Selective Membrane Electrodes," *Analytical Chemistry*, vol. 47, pp. 1596-1601, 1975.

FABRICATION AND CHARACTERIZATION OF PHOTOPATTERNED POLYMER MEMBRANES FOR PROTEIN CONCENTRATION AND DIALYSIS IN MICROCHIPS

Simon Song, Anup K. Singh, Timothy J. Shepodd, and Brian J. Kirby
Sandia National Laboratories, PO BOX 969, MS 9951, Livermore, CA 94551

ABSTRACT

Unique capability for processing protein samples in microchips is demonstrated via fabrication of photopatterned nanoporous polymer membranes with engineered pore size. Proteins are electrophoresed into membranes and concentrated by over two orders of magnitude before being injected for analysis. Specific analytes can be extracted from complex samples by flowing sample past a long dialysis membranes and perfusing in counterflow. Protein processing performance is used to characterize membrane porosity and specific diffusivities.

INTRODUCTION

Real-world biological samples require extensive pretreatment before they can be analyzed in a miniaturized device. These pretreatment steps may include preconcentration or desalting of protein solutions before analysis.

Sample preconcentration enables identification and quantification of trace analytes. Previous work with electrophoretic concentration at a barrier[1] has been used to concentrate DNA; however, the nonlinear concentration results in previous work are indicative of dielectric breakdown, leading to perturbative effects on downstream analysis and poor concentration reproducibility.

Desalting and other size-specific extraction techniques are often necessary because small ions reduce the sensitivity and stability of protein analytical tools. Previous work has separated analytes via diffusivity variations [2]; this technique is effective only for simple systems with large diffusivity variations and cannot be used in the more efficient counterflow configuration. Dialysis using sandwiched commercial membranes[3,4], dialysis tubes[5], or dialysis probes[6] does not allow the flexibility or ease of integration required to process subnanoliter volumes of nascent analytes on-chip.

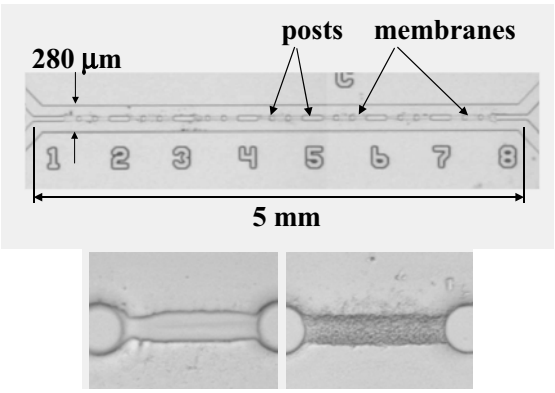

Figure 1. *Top: a counterflow microdialysis channel fabricated in-situ with membranes interspersed between silica support posts. Sample is injected at upper right and exits at upper left; perfusion liquid is injected at lower left and exits at lower right. Bottom: blowup of 35 μm thick 2 kD MWCO (left) and 100 kD MWCO membranes*

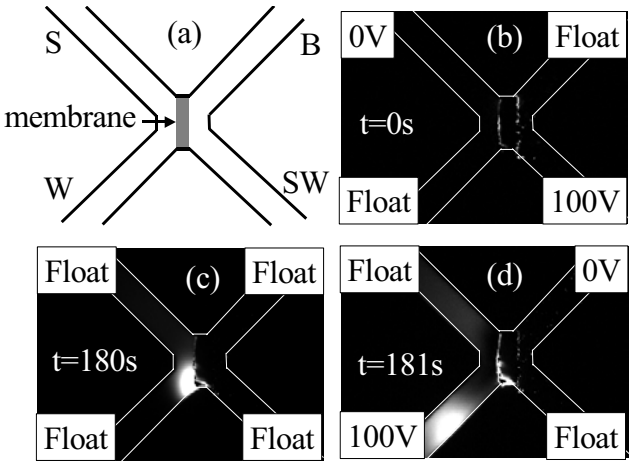

Figure 2. *(a) Capillary electrophoresis cross channel with membrane at the junction. The channel width is 80 μm. (b) the beginning of sample concentration. (c) the end of concentration. Negatively-charged Alexa-Fluor 488-labeled BSA stacks at the membrane. (d) Concentrated BSA is injected into the channel.*

We present a novel method to overcome these limitations and integrate protein concentration and dialysis on microchips by laser-patterning polymer membranes within silica microchannels.

FABRICATION

Thin (5–50μm) nanoporous polymer membranes are fabricated within glass microchannels by using projection optics to define a thin 355 nm laser sheet that photoinitiates polymerization and phase-separation in a thin region within channels previously filled with a monomer/solvent/ photoinitiator solution. The nanoporous membrane remains after unreacted monomer is flushed away. The monomer is 2-(*N*-3-sulfopropyl-*N*,*N*-dimethyl-ammonium) ethyl methacrylate crosslinked with methylene bisacrylamide and the resulting polymer is covalently attached to the glass surface through organosilane surface acrylate functionalization. Membrane shapes and sizes are controlled by shaping the laser sheet, while pore size and molecular weight cutoff are controlled by manipulating the polymer solubility and phase-separation process through changes in the solvent.

For sample preconcentration, 50 μm thick membranes were cast at the junction of a capillary electrophoresis cross microchannel that was pretreated with organosilane-linked linear polyacrylamide to suppress electroosmotic flow. For microdialysis, sets of 35 μm thick membranes were fabricated inside 5 mm long fused silica microchannels (Fig 1). Water:2-methoxyethanol solutions were used as the solvent and different ratios of these two

0-9640024-5-0/hh2004/$20©2004TRF
DOI 10.31438/trf.hh2004.107

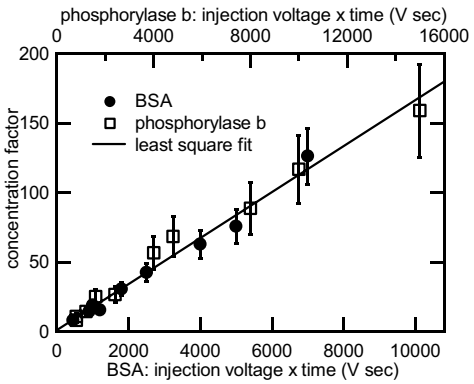

Figure 3. *Linear concentration of two proteins by electrophoresis into a nanoporous membrane. Proteins may be concentrated by over two orders of magnitude; linear response facilitates metered concentration and evinces effecient small-ion transport.*

components were used to generate membranes with different pore sizes.

RESULTS AND CHARACTERIZATION

Protein concentration. Semipermeable membranes patterned at the junction of an electrophoresis cross chip (Fig 2a) enable linear, metered concentration of proteins before injection. The membranes allow the small charge-carrying salt and buffer ions to pass through (membrane electrical resistance is immeasurably small) but prevent passage of proteins above the MWCO. Upon application of voltage, electrophoresis drives proteins toward the membrane where they concentrate (Figs 2b,c). Voltage switching injects the concentrated sample for downstream analysis (Fig 2d). Here the membrane obviates complicated buffer systems required for other concentration techniques (e.g., isotachophoresis, isoelectric focusing). Protein concentrations in injected samples increase linearly (r^2=0.92) with voltage and time over two orders of magnitude (Fig 3) and the extent of concentration is limited only by protein precipitation. The low electrical resistance of the membrane and the linear concentration both result from efficient small ion transport and support the assertion that the concentration process does not affect the buffer electrolyte distribution. This performance is a significant improvement over other electrophoretic concentration techniques [1], which show strongly nonlinear response indicative of dielectric breakdown rather than size-selective membrane transport.

Counterflow mass exchange. Long, 150:1 aspect-ratio membranes (Fig 1) enable counterflow microdialysis, an efficient means for size-selective extraction of analytes from a complex sample. Spatial variation of FITC-labeled analytes (as measured by fluorescence microscopy) during counterflow microdialysis was used to quantify the molecular weight cutoff (MWCO) and analyte-dependent specific diffusivity of the membranes. Samples were injected with pressure at upper right at 10 nl/min and perfused with pressure from lower left with water at 35 nl/min. Concentration profiles observed for two different membranes with several analytes (Fig 4a,b) were combined with a 2D control volume analysis to infer molecular-weight-dependent specific membrane diffusivities (diffusivity in the membrane normalized by that in solution; Fig 4c). Defining the MWCO as the geometrically-interpolated MW at which the specific diffusivity drops to 50% of the value for Rhodamine 560, the two membranes show MWCOs of 2 kD and 100 kD with uncertainties defined by the interpolation. The specific diffusivities of Rhodamine in the 2 kD- and 100 kD-cutoff membranes are 0.3 and 0.6, respectively,

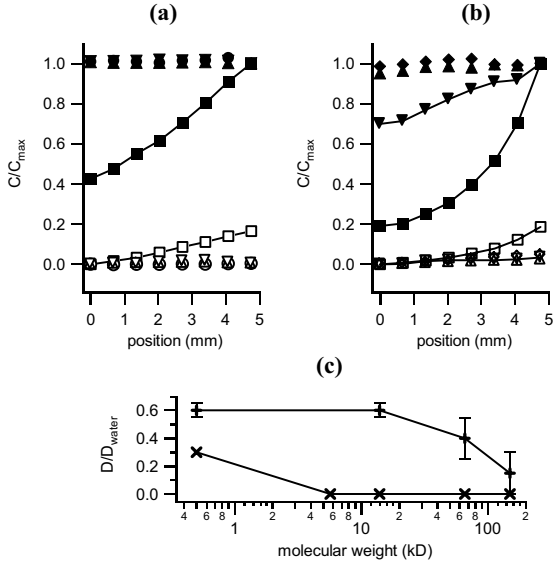

Figure 4. *Counterflow mass transport. Top: concentration profiles with membranes precipitated from (a) 3.7:1 water:2-methoxyethanol and (b) 0.3:1 water:2-methoxyethanol. Closed symbols: sample channel, flow enters at L=5mm and exits at L=0mm. Open symbols: perfusion channel, flow enters at L=0mm and exits at L=5mm.* ■ *Rhodamine 560 (0.5 kD);* ● *monomeric insulin (5.7 kD);* ▼ *lacalbumin (14 kD);* ♦ *BSA (66 kD);* ▲ *anti-biotin (150 kD). Some lines omitted for clarity. Bottom: (c) specific diffusivity through membrane as a function of analyte molecular weight.* × *2 kD membrane.* + *100 kD membrane.*

which are on the same order as specific diffusivities of dyes in agar and polyacrylamide gels.

CONCLUSIONS

The successful fabrication of thin semipermeable membranes patterned within silica microchannels allows for rapid protein sample processing steps, including concentration and dialysis. This architecture allows concentration using the same voltage injection scheme typically used on capillary electrophoresis microchips, and improves on other concentration work by generating linear concentration without perturbing the buffer electrolyte. This architecture shows dialysis performance comparable to commercial membranes and the ability to photopattern allows increased design flexibility, as multiple membranes with varying properties can be constructed in close proximity in a single microanalytical device for processing of nascent analytes.

REFERENCES

1. Khandurina, J.; Jacobson, S.C.; Waters, L.C.; Foote, R.S.; Ramsey, J.M. *Anal. Chem.* **1999**, *71*, 1815-1819.
2. Munson M.S.; Cabrera C.R.; Yager P. *Electrophoresis* **2003**, *23*, 2642-2652
3. Jiang, Y.; Wang, P.-C.; Locascio, L.E.; Lee, C.S. *Anal. Chem.* **2001**, *73*, 2048-2053.
4. Lamoree, M.H.; Van Der Hoeven, R.A.M.; Tjaden, U.R.; Van Der Greef, J. *Mass Spectrom.* **1998**, *33*, 453-460.
5. Canarelli, S.; Fisch, I.; Freitag, R. *J. Chromatogr. A.* **2002**, *948*, 139-149.
6. Lin, S.; Slopis, J.M.; Butler, I.J.; Caprioli, R.M. *J. Neurosci. Methods* **1995**, *62*, 199-205.

ELECTROWETTING-ON-DIELECTRIC FOR ANALYSIS OF PEPTIDES AND PROTEINS BY MATRIX ASSISTED LASER DESORPTION/IONIZATION MASS SPECTROMETRY

Aaron R. Wheeler and Robin L. Garrell
Department of Chemistry and Biochemistry, University of California,
Los Angeles, CA 90095-1569

Hyejin Moon and Chang-Jin "CJ" Kim
Department of Mechanical and Aerospace Engineering, University of California,
Los Angeles, CA 90095-1597

Joseph A. Loo
Department of Biological Chemistry, University of California,
Los Angeles, CA 90095-1597

ABSTRACT

A new technique for preparing samples for matrix assisted laser desorption/ionization mass spectrometry (MALDI-MS) is reported. The technique relies on electrowetting-on-dielectric (EWOD) to move droplets containing proteins or peptides and matrix to specific locations on an array of electrodes for analysis. Standard MALDI-MS reagents, analytes, and concentrations are demonstrated to be compatible with the technique. The results suggest that EWOD may be a useful tool for automating sample preparation for high-throughput proteomics and other applications of MALDI-MS.

INTRODUCTION

The field of proteomics is important as a basic science and for clinical applications ranging from drug discovery to assays for gene expression [1]. Standard methods for proteomics rely on mass spectrometry (MS) coupled with matrix assisted laser desorption/ionization (MALDI). Progress in proteomics would be accelerated by the availability of high-throughput analysis techniques.

Typical proteomics analyses with MALDI-MS require many steps, as depicted in Figure 1. A critical step is the mixing of sample and matrix (Figure 1d); this step is time-consuming and can lead to sample loss, dilution, and contamination. High-end commercial instruments accomplish this step with robotically controlled deposition of reagents. This technology has recently been combined with microfabricated picoliter droplet delivery devices, which enables deposition of arrays of thousands of spots for analysis [**2, 3**].

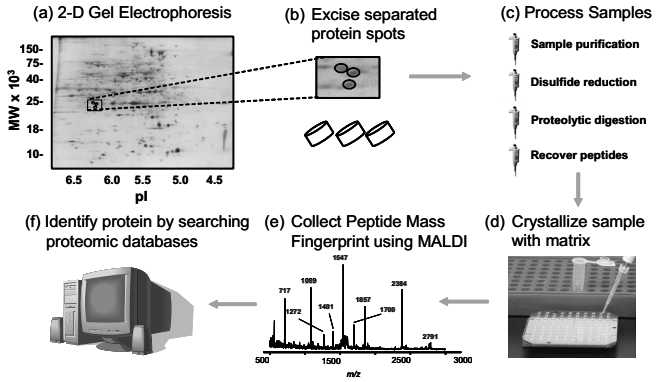

Figure 1. *Schematic depicting the steps required for proteomics analysis with MALDI-MS. The current work focuses on step (d).*

We present a novel method for MALDI sample preparation relying on electrowetting-on-dielectric (EWOD) [**4-7**]. In EWOD, a sequence of potentials is applied to adjacent electrodes buried beneath hydrophobic, dielectric layers. This causes changes in local wettability, which enables transport of aqueous droplets across a surface. EWOD devices are formed in an array geometry, which makes it an attractive technology for use with MALDI-MS.

Unlike droplet dispensing systems [**2, 3**], EWOD-based devices are reconfigurable, require low power, and require no moving parts. We recently presented the design parameters for EWOD devices to dispense, merge, mix, and cut droplets suspended in air [**6**]. This is of critical importance, as MALDI signals are severely degraded by the presence of non-volatile liquids. Thus, other array-based droplet manipulation techniques that rely on silicone or hydrocarbon oils as a suspension medium [**7, 8**] would probably not be suitable for MALDI-MS.

We describe here the fabrication and use of EWOD devices for MALDI-MS analysis of peptides and proteins. This is the first report of using droplet-based microfluidics for proteomics or mass spectrometry applications.

EXPERIMENTAL

EWOD devices were fabricated using procedures similar to those developed previously [**4-6**]. The devices consisted of a top and bottom plate as shown in Figure 2. Electrodes on the bottom plate were formed from doped polysilicon and were buried under thermally grown oxide (1500 Å) and Teflon-AF (7500 Å). The electrodes were 1 mm^2 with a 4 μm gap between each electrode. A single electrode on the top plate was formed from indium-tin-oxide (ITO) buried under a thin layer of Teflon-AF (150 Å). The two plates were joined by three layers of double-sided tape (300 μm).

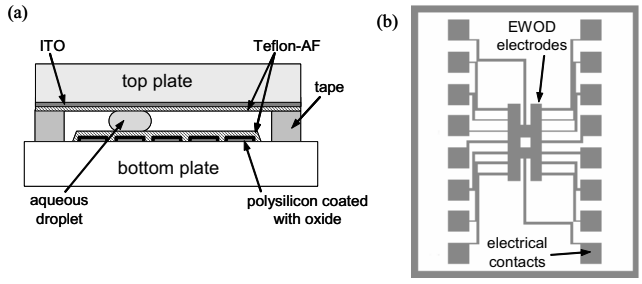

Figure 2. *Side view (a) and top view (b) schematics of EWOD device (not to scale).*

EWOD devices were used to move droplets of sample and matrix, as shown in Figure 3. Typically, droplets were moved several mm in a few seconds, and then dried under vacuum for ~1-2 min. Droplets were routinely driven on and between each line

0-9640024-5-0/hh2004/$20©2004TRF
DOI 10.31438/trf.hh2004.108

Solid-State Sensors, Actuators, and Microsystems Workshop
Hilton Head Island, South Carolina, June 6-10, 2004

of electrodes on each device. Matrix and sample droplets were either moved and dried separately, or two droplets were merged on a device and then dried. Typically, several spots were deposited onto the bottom plate of a device, which was then affixed with double-sided tape to a customized MALDI sample target.

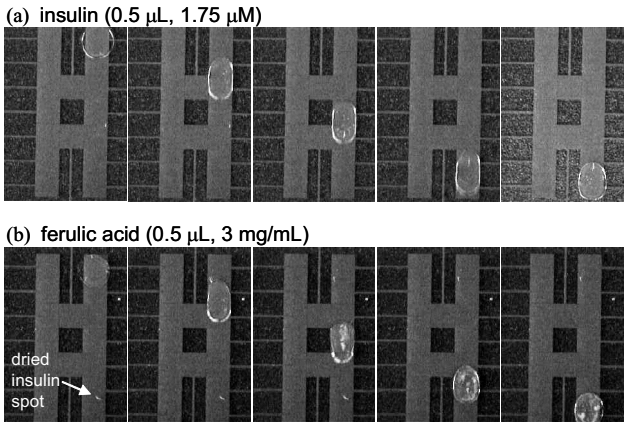

Figure 3. *Video sequence (left-to-right) of EWOD-driven movement of 0.5 μL droplets of insulin and ferulic acid (FA) down the right side of the electrode pattern. In (a), an insulin droplet was moved and dried. In (b), a droplet of FA was driven onto the dried insulin spot.*

A Voyager DE-STR spectrometer (Applied Biosystems) was used to collect MALDI mass spectra from deposited spots of sample and matrix. 500 shots were collected per spectrum, with the laser power adjusted for different matrices. Images and mass spectra of insulin co-crystallized with the common matrices 2,5-dihydroxybenzoic acid (DHB, 10 mg/mL, 0.05% TFA, with 5% acetonitrile), ferulic acid (3 mg/mL, 0.0375% TFA, with 15% acetonitrile), or sinapinic acid (SA, 10 mg/mL, 0.1% TFA, with 50% acetonitrile) are shown in Figure 4.

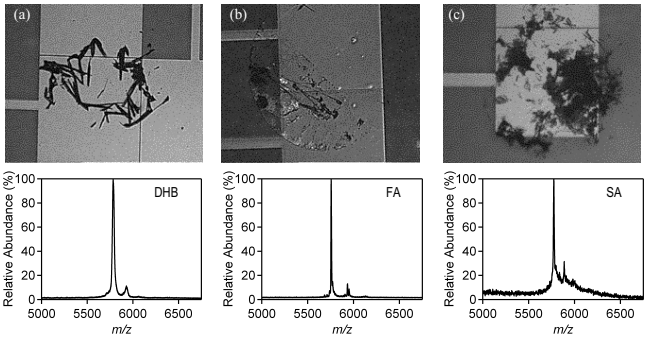

Figure 4. *Images and MALDI mass spectra of insulin (5733 Da) co-crystallized with various MALDI matrices. For each trial, a 0.5 μL droplet of insulin (1.75 μM, 0.025% TFA) was moved by EWOD to a designated electrode and dried. In (a) and (b), insulin deposition was followed by EWOD-driven deposition and drying of a 0.5 μL droplet of matrix. In (c), insulin deposition was preceded by manual deposition and drying of a 0.5 μL droplet of matrix.*

In addition to insulin, several other peptides and proteins were analyzed, including insulin chain B (Fig. 5a), cytochrome c (Fig. 5b), and myoglobin (Fig. 5c). The measured molecular weights for cytochrome c and myoglobin were higher than the expected values, which is believed to be caused by the use of a custom sample target that changes the ion flight path length. In future experiments, EWOD-MALDI mass spectra will be calibrated with known standards. These data demonstrate that EWOD-MALDI can be used to prepare samples with a variety of standard MALDI matrices, and to analyze proteins and peptides having a wide range of molecular weights.

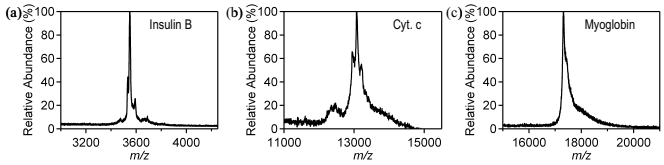

Figure 5. *MALDI mass spectra of (a) insulin chain B (3495 Da, 2 μM, 0.025% TFA), (b) cytochrome c (12.8 kDa 1.85 μM, 0.025% TFA), and (c) myoglobin (16.9 kDa, 1.45 μM, 0.0125% TFA). For each spectrum, a 0.5 μL droplet of peptide or protein was moved by EWOD and dried. The process was then repeated with DHB (10 mg/mL, 0.05% TFA, with 5% acetonitrile).*

CONCLUSIONS

This work represents a potentially important breakthrough for proteomics. Future work will concentrate on extending EWOD-MALDI to devices with dense arrays of electrodes for high-throughput analysis, and on integrating additional sample processing steps, such as sample purification, disulfide reduction, and proteolytic digestion (Fig. 1c).

REFERENCES

1. D. Figeys, "Proteomics in 2002: A year of technical development and wide-ranging applications", *Anal. Chem.*, *75*, 2891-2905 (2003).

2. D. P. Little, T. J. Cornish, M. J. O'Donnell, A. Braun, R. J. Cotter, and H. Koster, "MALDI on a Chip: Analysis of Arrays of Low-Femtomole to Subfemtomole Quantities of Synthetic Oligonucleotides and DNA Diagnostic Products Dispensed by a Piezoelectric Pipette", *Anal. Chem.*, *69*, 4540-4546 (1997).

3. P. Onnerfjord, J. Nilsson, L. Wallman, T. Laurell, and G. Marko-Varga, "Picoliter Sample Preparation in MALDI-TOF MS Using a Micromachined Silicon Flow-Through Dispenser", *Anal. Chem.*, *70*, 4755-4760 (1998).

4. J. Lee, H. Moon, J. Fowler, T. Schoellhammer, and C.-J. Kim, "Electrowetting and electrowetting-on-dielectric for microscale liquid handling", *Sens. Actuators, B*, *95*, 259-268 (2002).

5. H. Moon, S. K. Cho, R. L. Garrell, and C.-J. Kim, "Low voltage electrowetting-on-dielectric", *J. Appl. Phys.*, *92*, 4080-4087 (2002).

6. S. K. Cho, H. Moon, and C.-J. Kim, "Creating, Transporting, Cutting, and Merging Liquid Droplets by Electrowetting-Based Actuation for Digital Microfluidic Circuits", *J. Microelectromech. Sys.*, *12*, 70-80 (2003).

7. M. G. Pollack, R. B. Fair, and A. D. Shenderov, "Electrowetting-based actuation of liquid droplets for microfluidic applications", *Appl. Phys. Lett.*, *77*, 1725-1726 (2000).

8. J. A. Schwartz, J. V. Vykoukal, and P. R. C. Gascoyne, "Droplet-based chemistry on a programmable micro-chip", *Lab Chip*, *4*, 11-17 (2004).

Authors

H

J

K

L

Keywords